



Isolation and Characterization of Cholest-5-en-3-ol Compound from the Ethyl Acetate Extract of Stem Bark Ulin Plant (*Eusideroxylon zwageri* Teijm & Binn)

Heni Yulianti¹ , Adlis Santoni^{1,*} , Mai Efdi¹ 

¹Andalas University, Department of Chemistry, Faculty of Mathematics and Natural Sciences, Padang, Indonesia.

Abstract: Cholest-5-en-3-ol is an organic compound that belongs to the category of steroidal secondary metabolites. The compound has a double bond and a hydroxyl group and is commonly found in plants that contain oils such as coconut, nuts, and others. So far, there have been no reports of isolating the compound cholest-5-en-3-ol from the extract of the stem bark of the ulin plant. This compound has been found in very small amounts. A maceration method was used to obtain the extract. The isolation method used for the isolation of the compound was chromatography, while for the elucidation of the structure of the compound, UV-Vis spectrophotometry, Fourier transform infrared spectroscopy (FTIR), and nuclear magnetic resonance spectroscopy (NMR) were used. The ethyl acetate extract is the most abundant with 85.5 g. The isolation results were obtained as a white needle-like solid. Based on the spectra of UV-Vis spectrophotometry, FTIR spectra, and chemical shifts of NMR, the elucidated compound is the cholest-5-en-3-ol.

Keywords: Isolation, Characterization, Ulin, Cholest-5-en-3-ol.

Submitted: December 12, 2023. **Accepted:** March 20, 2024.

Cite this: Yulianti H, Santoni A, Efdi M. Isolation and Characterization of Cholest-5-en-3-ol compound from the Ethyl Acetate Extract of Stem Bark Ulin Plant (*Eusideroxylon zwageri* Teijm & Binn). JOTCSA. 2024;11(3):919-24.

DOI: <https://doi.org/10.18596/jotcsa.1379263>

***Corresponding author's E-mail:** adlissantoni@sci.unand.ac.id

1. INTRODUCTION

Ulin is one of the indigenous plants of Borneo Island used by the Uud Danum Dayak people living around the Ambalau River. The Uud Danum Dayak tribe often uses ulin leaves to treat fevers, tonics, stomach aches, allergies, and postnatal care (1). Ulin is a plant that is widely used in traditional medicine. A decoction of the bark is used by the people of Kutai and surrounding areas to treat diabetes, toothache, stomach ache, fever, and gynecological problems. In addition to using the ulin plant for furniture, the people of Jambi traditionally use ironwood as a skin medicine (2,3). The bark leaves, and seeds of the ulin plant can be used to treat a variety of ailments. The bark is commonly used for toothache, jaundice, herbal postpartum treatment, and black hair treatment. The leaves and roots can be used for postnatal care, and the seeds can be used for treating black hair (4).

Previously, the presence of secondary metabolites in ulin plants has been reported by LC-MS and GC-

MS analysis, including N-cis-feruloyl tyramine, 3'-O-methylviolanonone, 6-hydroxy-2-[2-(4'-methoxyphenyl)ethyl] chromone, B-asarone, and eusiderin A (4,5). The isolation of compounds from the methanolic extract of the stem bark has been reported previously. As for the five isolated compounds contained in the bark of ulin plant, namely two neolignan-derived compounds of benzodioxane type, one bicyclo (3,2,1) octanoid neolignan compound, one aporphine alkaloid-derived compound, and one phenanthrene alkaloid-derived compound isolated from the methanol extract (6). The stem bark of the ulin plant was extracted using hexane and methanol, but no steroid compounds were successfully isolated. Therefore, an attempt was made to isolate steroid compounds from the ethyl acetate extract of the ulin plant stem bark.

Steroidal compounds have not been previously reported in ulin plants. Some steroid compounds have potential health benefits, such as preventing cancer (anti-carcinogenic), acting as antioxidants, and treating conditions such as hypoglycemia, allergies,

asthma, rheumatism, and inflammation. Therefore, the isolation of steroid compounds is carried out, especially the cholest-5-en-3-ol compound.

Hexane, ethyl acetate, methanol, acetone, dichloromethane, hydrochloric acid, chloroform, distilled water, Liebermann-Burchard reagent, silica gel, and a sample of the stem bark of the ulin plant collected in the village of Selat, Jambi Province, Indonesia, and identified in the Herbarium of Andalas University (ANDA, Number 311/K-ID/ANDA/ IX/2020).

2. EXPERIMENTAL

2.1. Material

Table 1: Characteristics of ulin plant.

Characteristics	Name
Kingdom	Plantae
Divisi	Spermatophyta
Sub Divisi	Angiospermae
Kelas	Dicotiledoneae
Ordo	Lurales
Family	Lauraceae
Genus	Eusideroxylon
Species	<i>Eusideroxylon zwageri</i> Teijsm. & Binn

2.2. Apparatus

Glassware, separating funnel, dark-colored bottles, aluminum foil, analytical balance (KERNABJ220-4NM), test tube rack, dropping pipette, micro pipette, white Whatman filter paper, grinder, water bath, centrifuge, rotary evaporator (Heidolph Laborota 4000), TLC plate, chromatographic column, UV-Vis Spectrophotometer (Thermo Scientific, Genesys 20), FTIR (UATR FTIR PerkinElmer Frontier C90704 Spectrum IR Version 10.6.1), NMR (Bruker-Avance Neo 500 MHz).

2.3. Extraction

A dried sample of up to 5 kg was taken from Selat village, Bulian Regency, Jambi Province. It was macerated in stages with various solvents, starting with n-hexane, ethyl acetate, and methanol.

2.4. Identification of Steroids in Ethyl Acetate Extract

The ethyl acetate extract is dissolved in a mixture of chloroform and water (1:1 v/v) until a layer is formed. The bottom layer was dripped onto the drip plate, and Liebermann-Burchard reagent was added.

2.5. Isolation of Steroidal Compounds

Isolation begins with thin-layer chromatography (TLC), which is an initial screening to determine the type of eluent to be used for isolation by column chromatography. A small amount of ulin extract is dissolved in the solvent used, then the sample is spotted onto the TLC plate and placed in a vessel saturated with the eluent. The TLC plate is left in the vessel until the eluent reaches a predetermined limit mark. The TLC plate is then removed from the vessel, air dried, and then irradiated under an ultraviolet lamp at a wavelength of 254 nm and 365 nm to make the spots on the TLC plate more visible.

A sample of 60 g was isolated by column chromatography using the SGP system. The eluate collected in a vial (10 mL) was examined for the color pattern on TLC. The same color pattern was combined to obtain several fractions. The fraction with a simple color pattern was tested for purity and melting point using a melting point apparatus.

2.6. Characterization of Steroidal Compounds

The compounds obtained were analyzed with UV-Vis, FTIR, ¹HNMR, ¹³CNMR, HMQC, HMBC, and DEPT.

3. RESULTS AND DISCUSSION

3.1. Extraction

The yield of n-hexane extract was 60 g (1.2% yield), 85.5 g of ethyl acetate extract (1.7% yield), and 121.4 g of methanolic extract (3.2% yield).

3.2. Identification of Steroids in Ethyl Acetate Extract

Identification results using the Liebermann-Burchard reagent produced a green color on the drop plate, indicating the presence of steroidal compounds in the ethyl acetate extract.

3.3. Isolation of Steroidal Compound

The isolation procedure is shown in Figure 1. Separation of 60 g of ethyl acetate extract of ulin stem bark using gravity column chromatography with a silica gel stationary phase with a solvent gradient polarity (SGP) eluent system. The falling eluate was collected in 100 mL vials. The eluates were analyzed by TLC at 5 intervals, and those with the same color pattern were combined. After combining, four fractions (A-D fraction) were obtained.

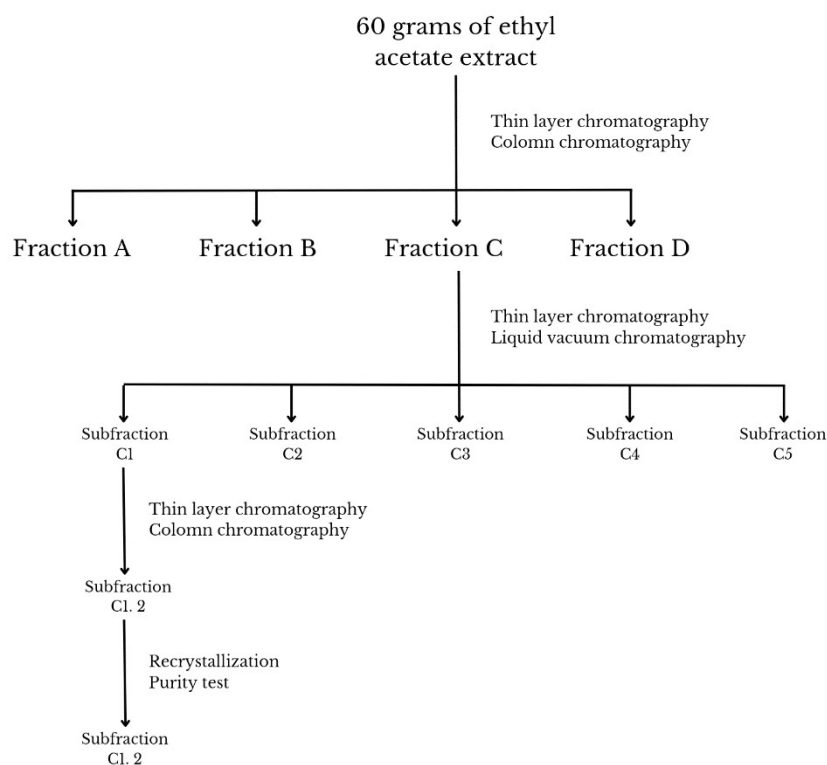


Figure 1: Schematic of the isolation of steroidal compound.

Fraction C was purified using liquid vacuum chromatography with a maximum of 10 grams due to its simpler stain pattern compared to the other fractions. The eluate was collected in a 100 mL vial and separated into 5 subfractions (subfractions C1-

C5) using a TLC plate with the same stain pattern. Additionally, the C1 subfraction of 0.787 grams was subjected to column chromatography for further purification.



Figure 2: Needle-like solid obtained.

Subfraction C1 was selected due to its simple stain pattern compared to other subfractions, and the fact that the eluate was collected in a 10 mL vial. The same eluate was combined into sub-subfractions (C1.1-C1.9). In sub-subfraction C1.2, a white needle-like solid was observed (Figure 2), which led to further purification of the C1.2 sub-fraction through recrystallization.

The solids tested using TLC with an eluent of hexane and ethyl acetate in a ratio of 8.5:1.5 showed a stain pattern that appeared as a single bluish-green color after being sprayed with Liebermann-Burchard reagent and heated (refer to Figure 3) (7). The compound obtained was tested for its melting point, which was found to be 148-150 °C. Therefore, it can be concluded that the compounds isolated are a group of steroid secondary metabolites (8,9).

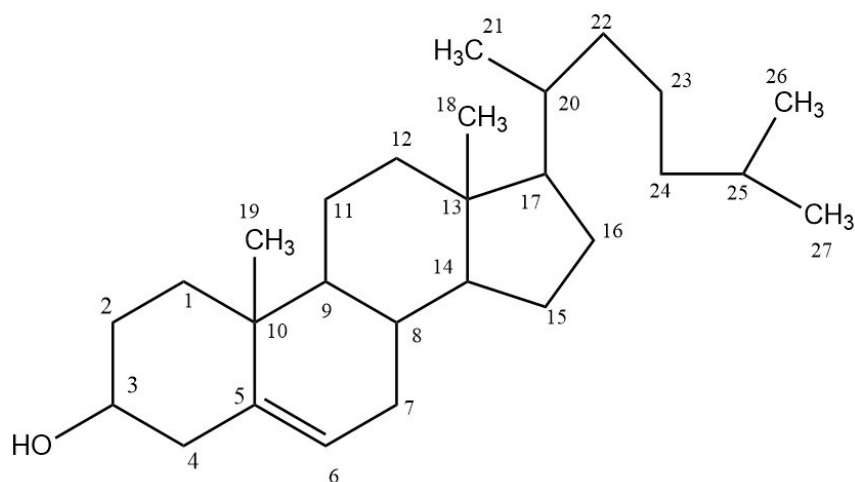


Figure 3: The structure of the cholest-5-en-3-ol.

3.4. Compound Characterization

White powder, UV-Vis λ 207 nm. IR (KBr) ν max 3361.20, 2932.94, 2862.79, 1669.38, 1455.35, 1042.05 cm^{-1} ; $^1\text{H-NMR}$ (d_6 , 500 MHz, δ , ppm) δ_{H} 1.828 (H-1, d, $J=1.48$, 2H), 1.750 (H-2, t, $J=2.15$, 2H), 3.364 (H-3, d, $J=0.88$), 2.181 (H-4, t, $J=2.41$ and 1.48, not observed), 5.282 (H-6, d, $J=1.00$), 1.918 (H-7, dd, $J=1.48$ and dd, $J=1.40$, not observed), 1.953 (H-8, q, $J=1.37$), 0.927 (H-9, d, $J=0.61$), 1.534 (H-11, s, $J=1.38$, 2H), 1.196 (H-12, t, $J=2.46$ and 1.62, not observed), 1.114 (H-14, s, $J=1.62$), 1.559 (H-15, t, $J=1.62$ and 0.61, not observed), 1.848 (H-16, t, $J=2.15$, 2H), 1.236 (H-17, s, $J=1.62$), 0.693 (H-18, s, $J=2.64$), 0.939 (H-19, d, $J=3.50$), 1.171 (H-20, dd, $J=1.37$), 0.840 (H-21, dd, $J=3.69$), 2.292 (H-22, s, $J=2.41$, 2H), 1.274 (H-23, t, $J=2.46$ and 1.38, not observed), 1.188 (H-24, dd, $J=2.57$, 2H) 1.953 (H-25, dd, $J=1.48$), 0.810 (H-26, dd, $J=3.38$), 0.694 (H-27, s, $J=2.64$); $^{13}\text{C-NMR}$ (d_6 , 500 MHz) δ_{C} 37.407 (C-1) 31.667 (C-2) 70.878 (C-3) 42.504 (C-4) 141.524 (C-5) 120.743 (C-6) 31.801 (C-7) 31.945 (C-8) 50.375 (C-9) 36.485 (C-10) 20.964 (C-11) 39.835 (C-12) 42.254 (C-13) 56.825 (C-14) 24.122 (C-15) 28.144 (C-16) 55.980 (C-17) 11.452 (C-18) 19.275 (C-19) 36.111 (C-20) 18.977 (C-21) 33.855 (C-22) 22.909 (C-23) 39.720 (C-24) 31.878 (C-25) 20.628 (C-26) 20.859 (C-27).

3.5. UV-Vis

UV-Vis spectrophotometry was performed in the range of 190 – 500 nm. The measurements revealed a strong absorption peak at a wavelength of 207 nm, indicating the presence of a non-conjugated double bond (C=C) due to the $\pi \rightarrow \pi^*$ electronic transition. This was further confirmed by a thin layer chromatography test, where the eluted TLC plate did not show any fluorescent stains upon irradiation with a UV356 nm lamp (10,11).

3.6. FTIR

The FTIR spectrum of the isolated compound displays absorption at the wavenumber 3361.20 cm^{-1} , indicating the presence of hydroxyl groups (-

OH). Technical abbreviations have been explained upon first use. This is confirmed by the absorption wave number of 1042.05 cm^{-1} , which indicates the presence of the C-O group. The strain between oxygen and hydrogen is also evident. In the absorption spectrum, wave numbers 2932.94 cm^{-1} and 2862.79 cm^{-1} indicate the presence of primary and secondary aliphatic C-H groups, as evidenced by the symmetric stretching. The bending at wave number 1455.35 cm^{-1} is the area for C-H alkane groups. The absorption at wave number 1669.38 cm^{-1} indicates the presence of an unconjugated C=C double bond, while there is no absorption at a wavelength of 1500 cm^{-1} . Based on the spectrum results, it was concluded that the isolated compounds are steroid secondary metabolites. This is supported by the presence of hydroxy groups (-OH) and unconjugated double bonds (10,12).

3.7. NMR

The Nuclear Magnetic Resonance (NMR) used in analyzing the structure of the isolated results, namely $^{13}\text{C-NMR}$, aims to determine the number of carbon atoms and their types in compounds isolated from $^1\text{H-NMR}$, which aims to determine the number of protons or hydrogen atoms and the type of chemical environment.

The compound was analyzed using $^{13}\text{C-NMR}$ (100 MHz) and DEPT 135, revealing the presence of 27 carbon atoms. A carbon signal was observed at 70.878 ppm (C3) in the $^{13}\text{C-NMR}$ spectrum, which is suspected to be bonded to a hydroxyl group (-OH). This was supported by FTIR spectral data, which showed an absorption wave number of 3361.20 cm^{-1} , indicating the presence of a hydroxyl functional group (-OH). The IR spectrum shows an absorption wavenumber of 1669.38 cm^{-1} , indicating the presence of a double bond. This is supported by the carbon signals at chemical shifts of 120.743 ppm (C-6) and 141.524 ppm (C-5). The chemical shifts at $^{13}\text{C-NMR}$ and $^1\text{H-NMR}$ can be compared with those found in the literature (Table 2) (10,13).

Table 2: ¹H-NMR (500 MHz, d₆) and ¹³C-NMR (500 MHz, d₆) isolated compounds and cholest-5-en-3-ol comparatory literature data.

Number of Carbon	DEPT 135	¹³ C-NMR isolated compounds (ppm)	¹ H-NMR isolated compounds (ppm)	¹³ C-NMR Literature (ppm)	¹ H-NMR Literature (ppm)
C1	CH ₂	37.407	1.828 (2H)	37.2	
C2	CH ₂	31.667	1.750 (2H)	31.6	
C3	CH	70.878	3.364	71.8	3.524
C4	CH ₂	42.504	2.181 (not observed)	42.3	2,280
C5	C	141.524	-	140.6	
C6	CH	120.743	5.282	121.4	5.349
C7	CH ₂	31.801	1.918 (not observed)	31.9	
C8	CH	31.878	1.953	31.9	
C9	CH	50.375	0.927	50.2	
C10	C	36.485	-	36.5	
C11	CH ₂	20.964	1.534 (2H)	21.1	
C12	CH ₂	39.835	1.196 (not observed)	39.8	
C13	C	42.254	-	42.3	
C14	CH	56.825	1.114	56.8	
C15	CH ₂	24.122	1.559 (not observed)	24.3	
C16	CH ₂	28.144	1.848 (2H)	28.3	
C17	CH	55.980	1.236	56.1	
C18	CH ₃	11.404	0.693	11.9	0.677
C19	CH ₃	19.275	0.939	19.4	1.006
C20	CH	36.111	1.171	35.8	
C21	CH ₃	18.977	0.840	18.7	0.915
C22	CH ₂	33.855	2.292 (2H)	36.2	
C23	CH ₂	22.903	1.274 (not observed)	23.8	
C24	CH ₂	39.720	1.188 (2H)	39.5	
C25	CH	31.878	1.953	28.0	
C26	CH ₃	20.628	0.810	22.6	0.867
C27	CH ₃	20.859	0.694	22.8	0.862

Based on Table 1, the isolated compound is cholest-5-en-3-ol, as evidenced by the chemical shifts of ¹³C-NMR and ¹H-NMR, which are similar to the shifts of ¹³C-NMR and ¹H-NMR of the compound in the literature.

4. CONCLUSION

The compound cholest-5-en-3-ol was isolated from ulin plants using maceration and chromatography methods. The ulin plant stem bark was the initial source of this compound. After maceration, three extracts were obtained: methanol, ethyl acetate, and methanol. Ethyl acetate extracts were chosen for further isolation as they had not been previously isolated. The isolation product was a white needle-like solid. The compounds were characterized using UV-Vis, FTIR, ¹H-NMR, ¹³C-NMR, and DEPT to determine the number and type of protons and carbons and the position of the compound structure.

5. CONFLICT OF INTEREST

The authors declare no conflict of interest.

6. ACKNOWLEDGMENTS

The authors are grateful to department of Chemistry, Andalas University, Padang, West Sumatera, Indonesia.

7. REFERENCES

- Mariani Y, Yusro F, Konishi Y, Taguchi T, Tominaga A. Regulatory effects of five medicinal plants used by dayak uud danum in west kalimantan Indonesia on the delayed-type hypersensitivity and the inflammation of human colon epithelial cells. *Kuroshio Sci.* 2016;10(1):59–71.
- Irawan B. Soil Properties and the abundance of ironwood (*Eusideroxylon zwageri* Teijsm. & Binn.) Varieties in Jambi, Indonesia | *Jurnal Manajemen Hutan Tropika*. *J Manaj Hutan Trop* [Internet]. 2015;21(3):155–61. Available from: [<URL>](#).
- Kusuma IW, Rahmini, Ramadhan R, Rahmawati N, Suwasono RA, Sari N. Phytochemicals and antidiabetic activity of *Eusideroxylon zwageri* stem bark collected from East Kalimantan, Indonesia. *IOP Conf Ser Earth Environ Sci* [Internet]. 2018 Apr 1;144(1):012030. Available from: [<URL>](#).
- Kristen U, Wacana K, Timotius KH, Rahayu I. Ethnopharmacological relevance of *Eusideroxylon Zwageri* Teijsm. et Binnend: A review. *Syst Rev Pharm* [Internet]. 2021;12(1):1619–23. Available from: [<URL>](#).
- Yoosu S, Namseok C, Minoru T. Two new isomeric lignans from *Eusideroxylon zwageri*. *Chem Nat Compd* [Internet]. 2009 May 14;45(3):356–9. Available from: [<URL>](#).

6. Syamsurizal, Afrida. Synthesis and structure activity relationships of eusiderin a derivatives as antifeedant. *Chem Mater Res* [Internet]. 2012;2(7):2225–0956. Available from: [<URL>](#).
7. Stochmal A, Oleszek W, Kapusta I. TLC of Triterpenes (Including Saponins). In 2008. Available from: [<URL>](#).
8. Nofita SD, Ngibad K, Rodli AF. Determination of percentage yield and total phenolic content of ethanol extract from purple passion (*Passiflora edulis f. edulis Sims*) fruit peel. *J Pijar Mipa* [Internet]. 2022 May 24;17(3):309–13. Available from: [<URL>](#).
9. Dewi BAD, Wardani TS, Nurhayati N. *Fitokimia*. Yogyakarta: Pustaka Baru Press; 2022.
10. Gupta U, Singh V, Kumar V, Khajuria Y. Spectroscopic Studies of Cholesterol: Fourier Transform Infra-Red and Vibrational Frequency Analysis. *Mater Focus* [Internet]. 2014 Jun 1;3(3):211–7. Available from: [<URL>](#).
11. Nguyen H. *UV-Vis Spectroscopy Chapter 6*.
12. Permatasari DAI, Wardani TS. *Elusidasi Struktur*. Yogyakarta: Pustaka Baru Press; 2021.
13. Smith WB. Carbon-13 NMR Spectroscopy of Steroids. In: *Annual Reports on NMR Spectroscopy* [Internet]. Academic Press; 1978. p. 199–226. Available from: [<URL>](#).



Preparation and Physicochemical Characterization of Bioplastics from Vegetable Waste/Poly (Vinyl Alcohol) and Coating with Poly Eugenol

Erwin Abdul Rahim^{1*} , Muhammad Ilham Latif Al Bafadhal¹, Wan Azizah¹, Reza Aulia Putri Prastyo¹, Ni Ketut Sumarni¹, Bambang Sardi¹

¹Tadulako University, Department of Chemistry, Palu, Indonesia.

Abstract: Plastic waste is increasingly piling up because it is not easily destroyed by rain, sunlight, or microbes that live in the soil, thereby it increases environmental damage such as soil pollution. One of the solutions to overcome the problem of using plastic is bioplastic technology. In this study, we aimed to prepare and characterize the physicochemical of bioplastics from different vegetable waste such as green spinach (GS), water spinach (WS), and moringa (M). The preparation of bioplastics was carried out with two variants: the vegetable waste as the base material/PVA and coating with polyeugenol (PEU). Physicochemical analysis of bioplastics includes surface observation by scanning electron microscopic (SEM); crystallinity by X-Ray diffraction (XRD); identification of functional groups by Fourier transform infra-red (FTIR); thermal characteristics analysis by thermogravimetric analysis (TGA), differential thermal analysis (DTA), and differential scanning calorimetric (DSC); and analysis of mineral composition by atomic absorption spectroscopy (AAS) techniques. Analysis by SEM showed that the smoothest surface was WS/PVA coating with polyeugenol (PEU) compared with other vegetable waste. The characterization results showed that the obtained bioplastic had good heat resistance up to 200 °C. XRD analysis showed that vegetable waste/PVA coated with PEU increases the crystallinity and the highest crystallinity value was M/PVA coated with PEU. The FTIR results showed the presence of C-H alkanes, C=O carboxylic acids, OH alcohols, and C-H alkenes and the spectra are similar between GS, WS, and M. Analysis by AAS showed that the bioplastic produced contained some micro and macronutrients including Ca, Cu, Fe, K, Mg, Mn, Na, and Ni and only the mineral Cu was not found in M. Thus, bioplastic from vegetable waste/PVA and coating with PEU were potentially used as mulch and packaging material.

Keywords: Bioplastic, Vegetable waste, Polyvinyl alcohol, Poly Eugenol, Characterization.

Submitted: September 26, 2023. **Accepted:** March 28, 2024.

Cite this: Abdul Rahim, E, Al Bafadhal MIL, Azizah W, Prastyo RAP, Sumarni NK, Sardi B. Preparation and Physicochemical Characterization of Bioplastics from Vegetable Waste/Poly (Vinyl Alcohol) and Coating with Poly Eugenol. JOTCSA. 2024;11(3): 925-32.

DOI: <https://doi.org/10.18596/jotcsa.136723>

***Corresponding author's E-mail:** erwin_abdulrahim@yahoo.com

1. INTRODUCTION

Polymers are a class of chemicals that are widely used in everyday life and industry. Polymers that are widely used are plastic, rubber, fibre, and nylon (1). The use of plastic has expanded and touched almost all areas of life. Various products and equipment are made from this material because it is considered more economical, not easily broken, flexible, and lightweight. One example of a product made from plastic that is most often used by the public is plastic bags and equipment (2). Plastics have become an important necessity and their usage continues to increase. But despite these benefits, plastic is a problem for the environment.

The use of plastic as a packaging material and other equipment has caused environmental problems. Plastic waste is increasingly piling up because it is not easily destroyed by rain, sunlight, or microbes that live in the soil, thereby it can increase environmental damage such as soil pollution. One of the solutions to overcome the problem of using plastic is bioplastic technology. Bioplastics are plastics that are used like conventional plastics but are easily degraded naturally by microorganisms (3). Bioplastics can be developed by utilizing natural resources. The materials used in the manufacture of bioplastics are polymer compounds found in plants such as starch, cellulose, and lignin (4).

The utilization of food waste as a source of bioplastic feedstock is a highly sought-after result, (5) as it can significantly improve the sustainability of our economy following one of the circular economic paradigms: the substitution of plastics resulting from non-renewable sources with biodegradable bioplastics and/or derived from renewable sources (6). An example of conversion of biomass and food waste into modern biodegradable plastics are starch-based plastics, biopolymers and immerge such as polylactic acid, or materials synthesized from biomass such as PHA (7). Proteins have also recently been proposed as structural and functional biopolymers, taking advantage of their biocompatibility and various fabrication strategies (8).

Several researchers have studied the preparation and characteristics of bioplastics, including research on bioplastics from carrot, parsley, turnip, and cauliflower vegetable waste whose characteristics showed mechanical properties similar to polypropylene (PP) and starch-based bioplastics (9), mainly preparation and characterization bioplastic from starch. Among various synthetic polymers, polyvinyl alcohol (PVA) is one of the best choices because of its water solubility and biodegradability (10). On the other hand, eugenol is the main component of clove leaf oil which is mainly produced in Indonesia and polyeugenol (PEU) can be synthesised quickly, and easily, and has strong antibacterial and antioxidant activity (11).

This study aims to prepare and characterize the physicochemical properties of bioplastics derived from various vegetable wastes, including green spinach (GS), water spinach (WS), and moringa (M) added with PVA and polyeugenol (PEU). To the best of our knowledge, there have not been any reports on the preparation and characterization of physicochemical of GS, WS, and M vegetable waste added with PVA and PEU using SEM, FTIR, XRD, TGA, DSC, DTG, and AAS. This research database can be useful for designing and manufacturing bioplastic materials.

2. EXPERIMENTAL SECTION

2.1. Material and Methods

Eugenol (99.99% purity; obtained from Happy Green Co.), vegetable waste from GS, WS, M (Obtained from local market in Palu, Central Sulawesi), distilled water (Obtained from Organic Laboratory, Palu, Central Sulawesi), concentrated sulfuric acid, glacial acetic acid, methanol (p.a), ethyl acetate, n-hexane, anhydrous sodium sulfate, and PVA (all were obtained from Sigma-Aldrich).

2.2. Preparation of Bioplastic

2.2.1. Samples

One kilogram of WS waste is used as one of the samples. The samples were then properly cleaned, chopped into little pieces, and dried for two to three days. Then, using an 80-mesh screen, mix the leftover vegetable waste until it is smooth. The useful vegetable waste powder is available.

2.2.2. Synthesis of Bioplastic Films from Vegetable Waste

The glacial CH_3COOH was diluted to prepare a 1M CH_3COOH solution in water. Water vegetable powder was dissolved in a CH_3COOH solution at a concentration of 1 g of powder, and then it was vigorously stirred to hydrolyze in 20 mL of 1 M CH_3COOH solution. The vegetable dispersion was swirled on a hot-plate at 70 °C for 6 hours to prevent temperature changes, then printed and allowed to cure for around 48 hours at room temperature on a Petri plate. 0.5 g of dry sample was mixed with 0.5 g of PVA in 20 mL of distilled water then stirred at 80 °C for 2 hours then cast in a petri dish, and then the solvent was evaporated at room temperature until it was dry.

2.2.3. PEU Synthesis

10 g of eugenol was weighed in a 250 mL beaker. Then 2.5 mL of $\text{H}_2\text{SO}_4\text{-CH}_3\text{COOH}$ as a catalyst in a ratio of 4:1 (monomer: catalyst) was added gradually into the beaker while continuously stirring (room temperature, \pm 5 minutes) using a magnetic stirrer. Polymer formation was indicated by the release of thick white smoke and the presence of polymer formed on the walls of the beaker. To quench polymerization, 4 drops of methanol was added onto the polymeric crude. Then the crude was left for 24 hours at room temperature until the polymer solidified and dried. Then 40 mL of ethyl acetate and 40 mL of n-hexane were added to from PEU. The mixture was then shaken until the PEU was completely dissolved. Afterwards, it was put into a 250 mL separatory funnel, then 100 mL distilled water, was then shaken and stored for 24 hours until two layers were formed. The bottom and top layers were separated and the top layer was washed for 3 times using distilled water. The top layer which is insoluble in water, PEU was dried over 1 g anhydrous Na_2SO_4 and filtered using a glass funnel. Then the filtrate was placed in a Petri dish and stored at room temperature for 48 hours.

2.2.4. Preparation of Vegetable Waste/PVA/PEU Bioplastics

Mix bioplastic with PVA in a ratio of 50%:50%, where PVA samples were weighed at 0.5 grams, and bioplastic was weighed at 0.5 grams and the mixture was redissolved in 20 mL of distilled water and stirred for 1 hour at 75 °C. Then, the mixture was poured onto a petri dish and let it sit for 24 hours at room temperature. Afterwards, polyeugenol was dissolved in 10 mL of ethyl acetate and sprayed onto the mixture with the best results from the previous treatment.

2.3. Characterization

2.3.1. Surface morphology analysis using SEM

Using a scanning electron microscope (JSM-6510LA), the bioplastics' microstructural examination was completed. After being submerged in liquid nitrogen, two distinct samples, each measuring 0.5 cm², of each bioplastic were randomly fractured to examine the surface of the samples. Double-sided adhesive tape was used to secure the cryo-fractured samples to the support after they had been mounted on aluminium stubs. Lastly, samples were coated with

gold palladium and monitored at a working distance of 10 mm and an accelerating voltage of 10 kV.

2.3.2. Functional group analysis using FTIR

A Thermo Scientific Nicolet iS10 was used to do the FTIR measurements. One light microscope with an auto image connection and one spectrometer. The samples of bioplastics were used for these studies.

2.3.3. X-Ray Diffraction (XRD) Analysis

The bioplastic samples were observed with Rigaku-Nex QC X-ray diffractometer (XRD) at a static position using a Cu $K\alpha$ radiation source ($\lambda=1.5418$ Ao) with operating conditions at 40 kV, 30 mA, angle $2\theta = 10 - 60$ and scan speed $2\theta/\text{min}$.

2.3.4. Micro and Macro Mineral Analysis with AAS

The atomic absorption spectroscopy (AAS) Shimadzu was used to do mineral analysis. The samples of bioplastics were used for these studies and the mineral analysis is Ca, Cu, Fe, K, Mg, Mn, Na and Ni.

2.3.5. Thermal analysis with TGA, DTA and DSC

The thermal characteristics of TGA, DTA and DSC analyses were carried out in the Shimadzu

instrument. The specimen weighed between 10 and 25 milligrams, and its temperature rose by 5 degrees Celsius every minute from 30 to 550 degrees Celsius.

3. RESULTS AND DISCUSSION

3.1. Preparation of Bioplastics from Vegetable Waste

Bioplastics were made using an environmentally friendly water-based method using 0.1M CH_3COOH and blending with PVA using water solvent. The coating with PEU is carried out using the spray method. From vegetable waste which is useless and pollutes the environment, it was made into bioplastic which is useful and environmentally friendly because it can significantly increase the sustainability of our economy following one of the circular economy paradigms: the substitution of plastic produced from non-renewable sources with bioplastic which can decompose and/or come from renewable sources. All 6 samples were made consisting of 3 samples in the form of samples with PVA added and 3 samples coated with PEU. The scheme for making bioplastic can be seen in Figure 1.

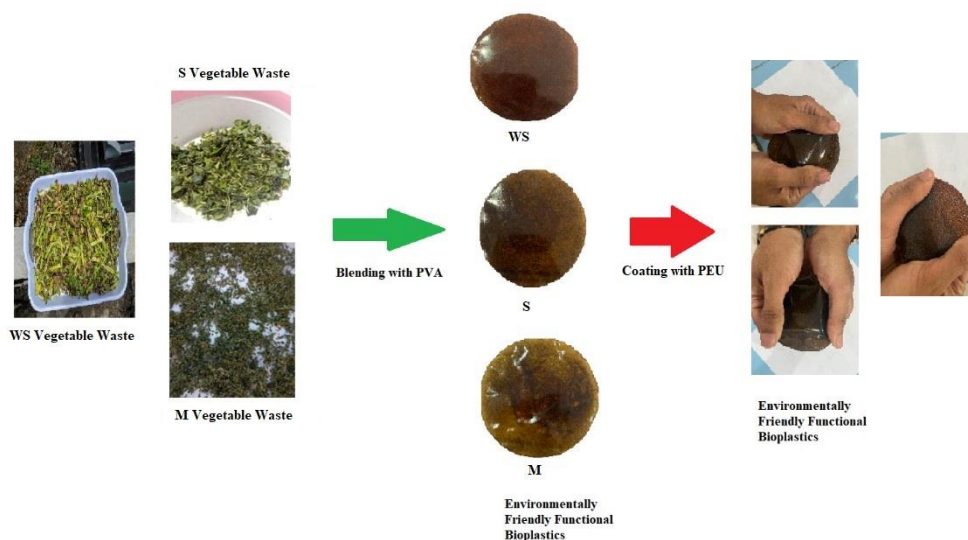


Figure 1: Preparation scheme of bioplastic from vegetable waste.

3.2. Characterization

3.2.1. Surface Morphology

To determine the surface morphology of the resulting bioplastics, analyses were carried out using SEM technique. The results of the analyses can be described as follows:

The surface morphology images of the bioplastic samples were recorded with an SEM instrument with a magnification of 3000 times as shown in Figure 2. All samples showed a smooth surface, no pores, and

some small parts that were less smooth. Adding PVA as a plasticizer improves compatibility, good dispersion, and a homogeneous mixture (12). Coating with PEU makes the resulting bioplastic surface smoother and more homogeneous. The less refined bioplastic part of vegetable waste is caused by an imperfect agglomeration process this can be seen from all the samples in the picture above, except for the bioplastic sample from WS waste /PVA/PEU whose surface structure is very smooth.

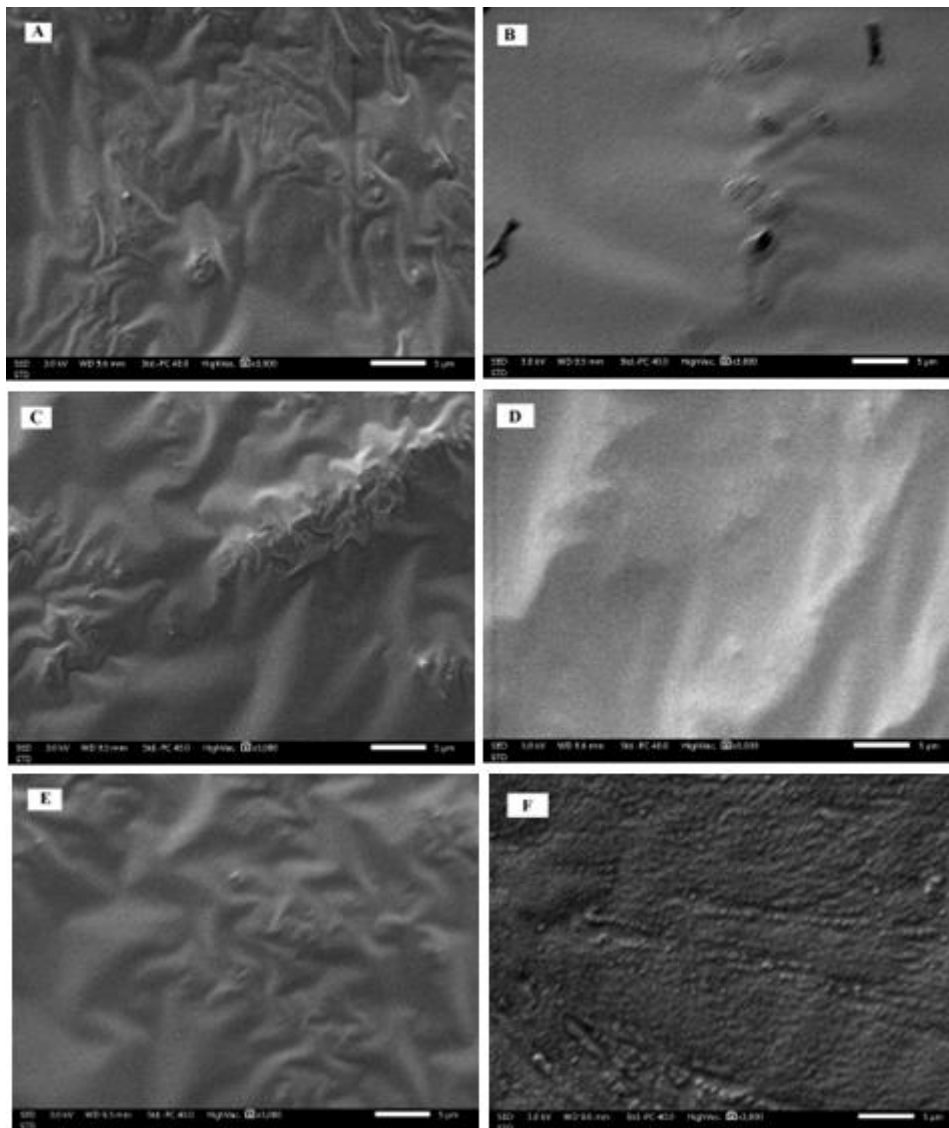


Figure 2: The SEM analyses of: A. GS/PVA, B. GS/PVA/PEU, C.WS/PVA, D.WS/PVA/PEU, E. M/PVA, F.M/PVA/PEU.

3.2.2. Bioplastic Function Group Analysis

To find out the functional groups contained in bioplastics, analysis was done using FTIR and the results of the analysis can be seen in Figure 3. The FTIR spectra analysis shows that there is a similarity between the bioplastic spectra of GS waste, WS waste, and M waste likewise with the addition of vegetable waste with PEU. The results of the FTIR analyses showed that there is absorption at 2966.52 cm^{-1} so the band that appears in the range of $2850\text{--}2970\text{ cm}^{-1}$ is the C-H Alkane group (13). The C-C, C-O, and COOH (carboxylic acid) bonds can be identified by the appearance of an energy band between 800 and 1300 cm^{-1} (14,15). In the results

obtained, the visible group is at $1050\text{--}1300\text{ cm}^{-1}$. An absorption of $1000\text{--}1300\text{ cm}^{-1}$ shows a typical area of the C-O ether group. The presence of the C-O ether group indicates the ability to decompose (16-18). Absorption in the 3500 cm^{-1} region indicates the presence of OH groups. The OH group is hydrophilic because water molecules can cause microorganisms in the environment to enter the bioplastic matrix thereby it damages the bioplastic (19,20). The band that appears in the range of $675\text{--}995\text{ cm}^{-1}$ indicates the presence of the C alkene group. Wiercigroch et al. (2017) (20) also found that the energy band at 926 cm^{-1} is a glycosidic bond in carbohydrates.

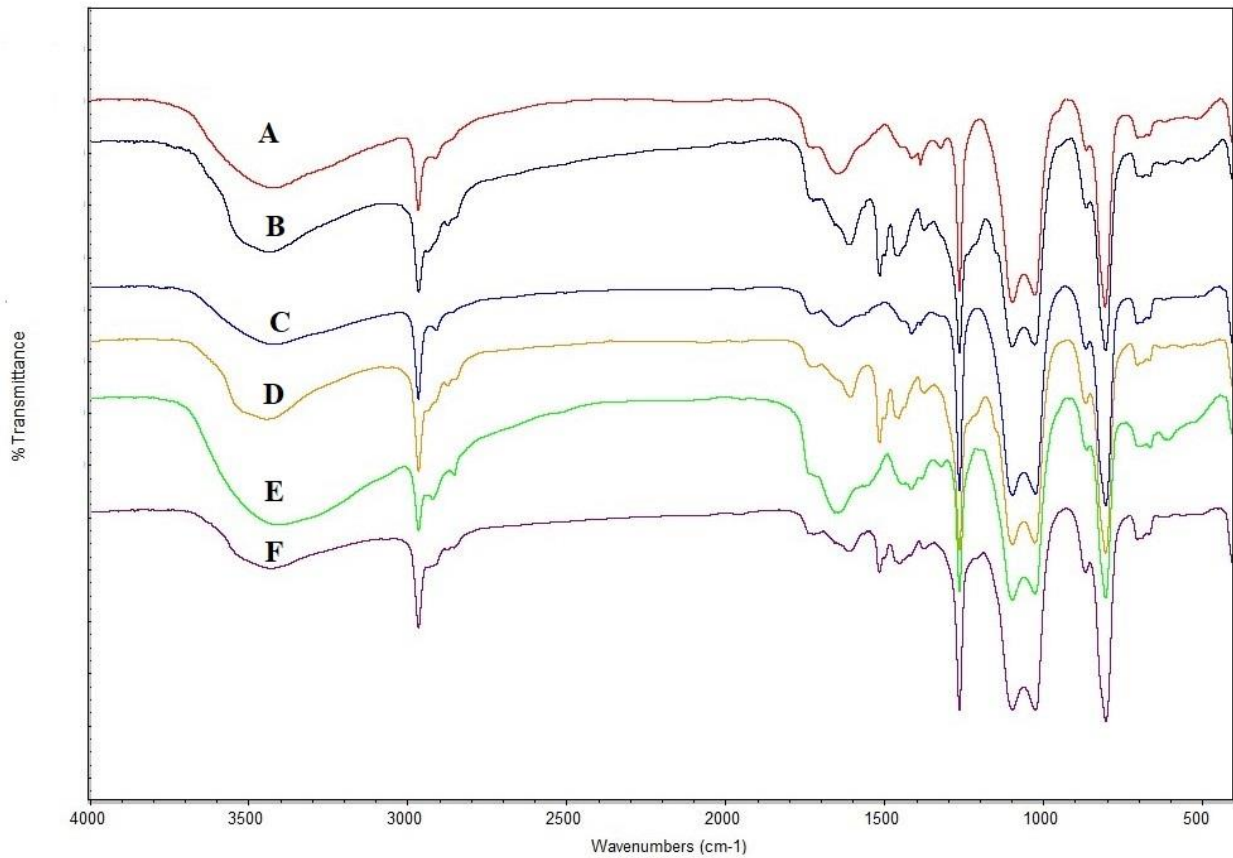


Figure 3: The FTIR spectra bioplastics sample: A. GS/PVA, B. GS/PVA/PEU, C. WS/PVA, D. WS/PVA/PEU, E. M/PVA, F.M/PVA/PEU.

3.2.3. X-Ray Diffraction (XRD) Data Analysis

The XRD spectra showed two combinations of bioplastics (vegetable waste/PVA) and (vegetable waste/PVA/PEU) (Figure 4). The diffractogram pattern of each sample has different intensities at each angle and has peaks marked by sharp curves. These peaks are known as crystal regions (21). From the diffractogram image, it can be shown that bioplastic from vegetable waste/PVA and the addition

of PEU is a material that is amorphous and crystalline. The crystallinity value of bioplastics from vegetable waste/PVA increased with the addition of PEU (Table 1). Based on the results of previous research (22) using XRD, PEU shows peaks which are crystalline areas, so it is concluded that PEU has a crystalline form so that the addition of PEU increases the crystallinity of the bioplastic samples.

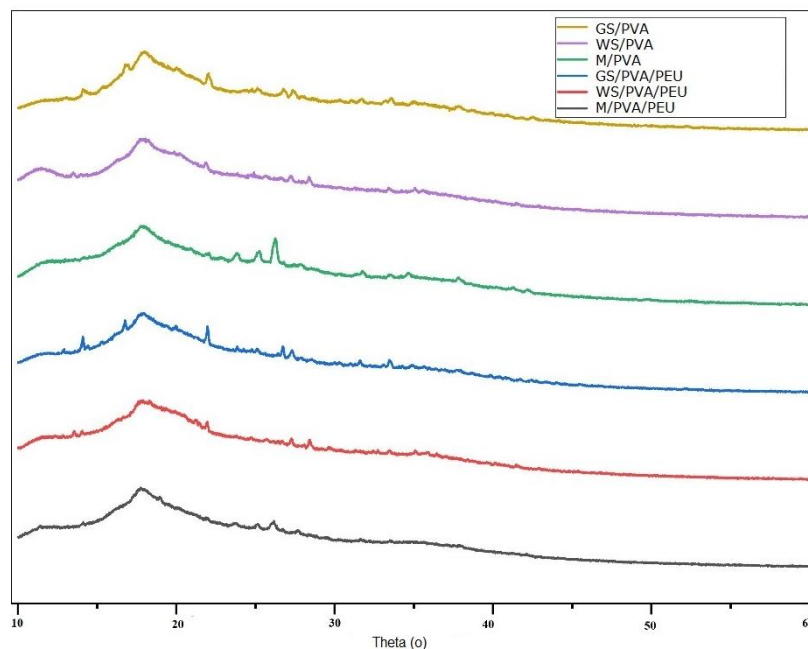


Figure 4: The XRD spectra of GS, WS and M vegetable waste/PVA and coating with PEU.

Table 1: The crystallinity of bioplastic from vegetable waste/PVA and coating with PEU.

Bioplastics	Crystallinity (%)
GS/PVA	36.2
GS/PVA/PEU	42.7
WS/PVA	39.0
WS/PVA/PEU	41.7
M/PVA	40.8
M/PVA/PEU	42.9

3.2.4. Micro and Macro Mineral Analysis with AAS

Furthermore, an analysis of the mineral composition of the selected materials was carried out using AAS to see the bioplastic potential of vegetable waste for application in fertilization. Table 2 shows that the bioplastic material developed from vegetable waste/PVA has the amount of micro and macronutrients needed for plant growth which can be

used as a natural fertilizer. In this way, bioplastic can be used as film mulch which will reduce the use of inorganic fertilizers which are associated with environmental pollution and provide opportunities for the development of more sustainable agricultural systems. Vegetable waste is naturally rich in organic and mineral materials so the application of bioplastic from GS, WS, and M vegetable waste as mulch is very promising.

Table 2: The mineral compositions (mg per kg).

Bioplastics	Mineral Amount (mg per kg)							
	Ca	Cu	Fe	K	Mg	Mn	Na	Ni
GS/PVA	10600.00	5.81	202.17	2.71	4442.53	23.64	4093.69	324.62
WS/PVA	7095.36	0.09	105.33	1.51	1975.06	65.67	6933.99	50.07
M/PVA	12000.00	0	76.40	4478.64	2392.23	33.82	4879.16	118.33

3.2.5. Analysis of Bioplastics with TGA, DTA and DSC

Thermal analysis includes calorimetric differential thermal analysis (TG/DTA). TGA analysis was aimed at analyzing the loss of mass and weight due to thermal degradation. At the same time, DTA analysis aims to analyze the melting point of polymers or materials involved in endothermic exothermic processes (23). The temperature is adjustable from 31.22 to 552.35 °C. The heat of decomposition is shown in Figure 5. The results show that thermal decomposition occurs at temperatures below 155.46 °C due to the loss of light substances such as water. GS/PVA/PEU samples reduced weight by 84.68% at 552.26 °C. A 50% weight loss occurs at the temperature of 359.97 °C. The WS/PVA/PEU sample lost 92.60% at 548.97 °C and 50% weight loss at 325.79 °C. In addition, the M/PVA/PEU sample had a change of 86.20% at the temperature of 552.13 °C. GS/PVA/PEU samples were more heat stable than WS/PVA/PEU samples and M/PVA/PEU samples were more heat stable than WS/PVA/PEU samples. The breakdown of polysaccharides and the evaporation of light compounds and water occurs at this stage. Thermal properties were also analyzed by DTA (24). The results for all samples are shown in Figure 5. At this point, all samples behave on most of the same curves, with four peaks for the exothermic signal. The first endothermic peak refers to the glass transition temperature (T_g). The second endothermic peak also refers to the melting point (T_m). Samples of GS/PVA/PEU T_g 129.83 °C. The GS/PVA/PEU sample had the highest glass transition temperature

of 129.83 °C. All samples had T_g between 125.73 °C and 129.83 °C. The highest T_m was obtained at 196.64 °C for the M/PVA/PEU sample. These results were comparable to those that were obtained from XRD in which the GS/PVA/PEU samples had more crystallinity than WS/PVA/PEU samples and M/PVA/PEU samples had more crystallinity than WS/PVA/PEU samples.

4. CONCLUSION

Biopolymers from vegetable waste/PVA were successfully prepared by casting from a solution and coating with PEU using the spray method. Characterization using SEM shows that the resulting bioplastic has a smooth surface and no pores. The results of FTIR analysis show the presence of C-H Alkane groups, C-C, C-O, and C-O-H bonds (carboxylic acids) and OH. Samples analyzed by XRD showed that the bioplastic produced was semicrystalline. Contains macro and micro minerals and has good heat stability. Based on the characterization results, this bioplastic has the potential to be applied as mulch and food packaging.

5. ACKNOWLEDGMENTS

The authors would like to express their thanks to the DRTPM-Directorate General of Indonesian Higher Education who has funded this research with contract number 063/E5/PG.0200.PL/2023.

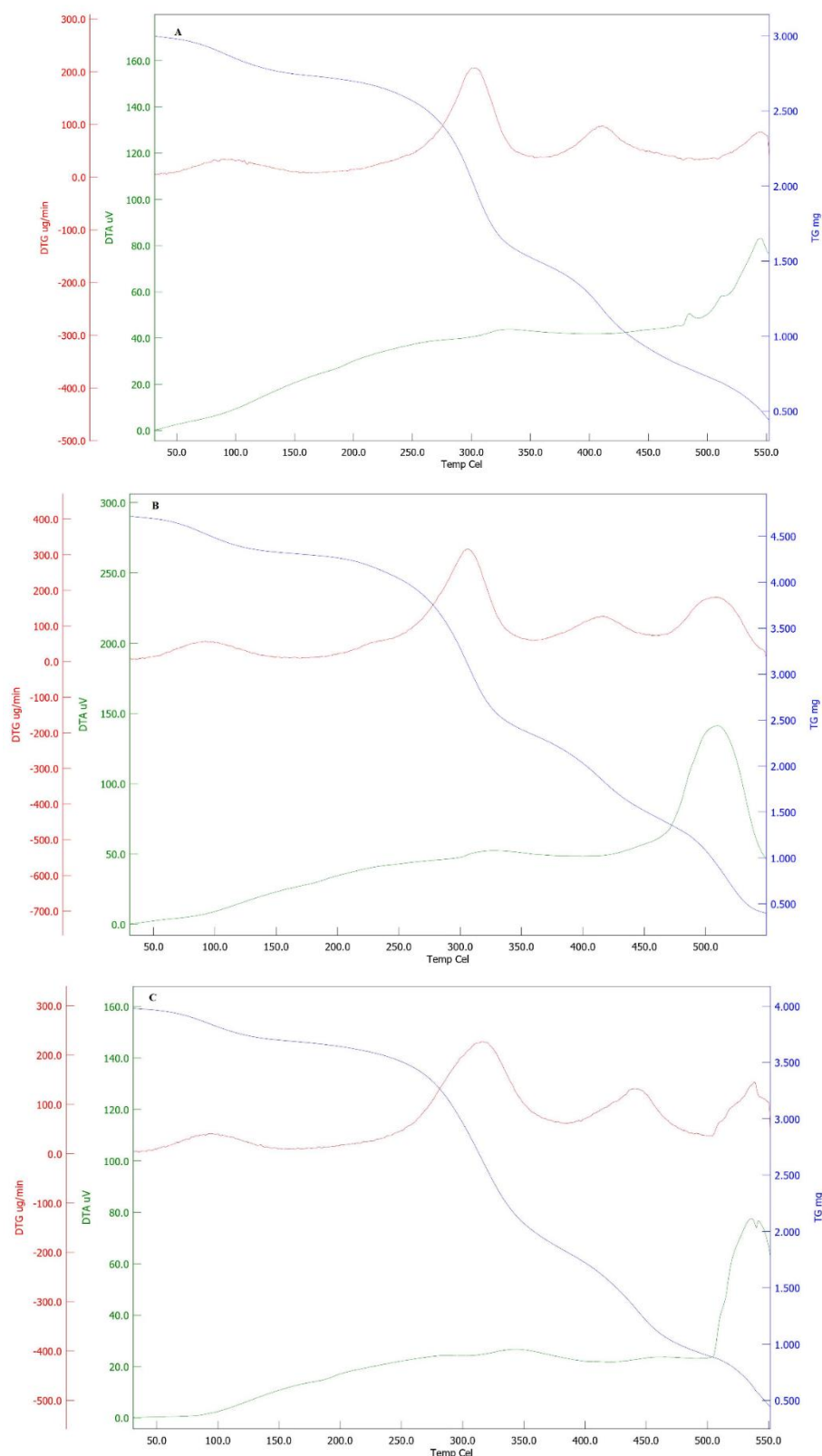


Figure 5: TGA, DTA and DSC analysis result curves for bioplastic samples from vegetable waste: A. GS (top), B. WS (middle), C. M (bottom) added with PVA and PEU.

6. REFERENCES

1. Singh MK, Tewari R, Zafar S, Rangappa SM, Siengchin S. A comprehensive review of various factors for application feasibility of natural fiber-reinforced polymer composites. *Results Mater* [Internet]. 2023 Mar 1;17:100355. Available from: [<URL>](#).
2. Moghaddam Fard P, Alkhansari MG. Innovative fire and water insulation foam using recycled plastic bags and expanded polystyrene (EPS). *Constr Build Mater* [Internet]. 2021 Oct 25;305:124785. Available from: [<URL>](#).
3. Idris SN, Amelia TSM, Bhubalan K, Lazim AMM, Zakwan NAMA, Jamaluddin MI, et al. The degradation

- of single-use plastics and commercially viable bioplastics in the environment: A review. *Environ Res* [Internet]. 2023 Aug 15;231:115988. Available from: [<URL>](#).
4. Rahardiyani D, Moko EM, Tan JS, Lee CK. Thermoplastic starch (TPS) bioplastic, the green solution for single-use petroleum plastic food packaging – A review. *Enzyme Microb Technol* [Internet]. 2023 Aug 1;168:110260. Available from: [<URL>](#).
5. Shen L, Worrell E, Patel M. Present and future development in plastics from biomass. *Biofuels, Bioprod Biorefining* [Internet]. 2010 Jan 7;4(1):25–40. Available from: [<URL>](#).
6. Kiser B. Circular economy: Getting the circulation going. *Nature* [Internet]. 2016 Mar 24;531(7595):443–6. Available from: [<URL>](#).
7. Snell KD, Peoples OP. PHA bioplastic: A value-added coproduct for biomass biorefineries. *Biofuels, Bioprod Biorefining* [Internet]. 2009 Jul 7;3(4):456–67. Available from: [<URL>](#).
8. Vepari C, Kaplan DL. Silk as a biomaterial. *Prog Polym Sci* [Internet]. 2007 Aug 1;32(8–9):991–1007. Available from: [<URL>](#).
9. Perotto G, Ceseracciu L, Simonutti R, Paul UC, Guzman-Puyol S, Tran TN, et al. Bioplastics from vegetable waste via an eco-friendly water-based process. *Green Chem* [Internet]. 2018 Feb 19;20(4):894–902. Available from: [<URL>](#).
10. Phattarateera S, Xin L, Amphong C, Limsamran V, Threepopnatkul P. Comparative studies of starch blends on the properties of PVA films. *Carbohydr Polym Technol Appl* [Internet]. 2023 Dec 1;6:100340. Available from: [<URL>](#).
11. Rahim EA, Istiqomah N, Almilda G, Ridhay A, Sumarni NK, Indriani I. Antibacterial and Antioxidant Activities of Poly Eugenol with High Molecular Weight. *Indones J Chem* [Internet]. 2020 May 9;20(3):722–8. Available from: [<URL>](#).
12. Haghghi H, Gullo M, La China S, Pfeifer F, Siesler HW, Licciardello F, et al. Characterization of bio-nanocomposite films based on gelatin/polyvinyl alcohol blend reinforced with bacterial cellulose nanowhiskers for food packaging applications. *Food Hydrocoll* [Internet]. 2021 Apr 1;113:106454. Available from: [<URL>](#).
13. Ferreira-Villadiego J, García-Echeverri J, Vidal M V, Pasqualino J, Meza-Castellar P, Lambis-Miranda HA. Chemical Modification and Characterization of Starch Derived from Plantain (*Musa paradisiaca*) Peel Waste, as a Source of Biodegradable Material. *Chem Eng Trans* [Internet]. 2018;65:763–8. Available from: [<URL>](#).
14. Sardi B, Altway A, Mahfud M. Bio-oil production from low-rank coal via novel catalytic microwave pyrolysis using activated carbon + $\text{Fe}_2(\text{SO}_4)_3$ and HZSM-5 + $\text{Fe}_2(\text{SO}_4)_3$. *Fuel* [Internet]. 2022 Sep 15;324:124509. Available from: [<URL>](#).
15. Sardi B, Ningrum RF, Ardianyah VA, Qadariyah L, Mahfud M. Production of Liquid Biofuels from Microalgae *Chlorella* sp. via Catalytic Slow Pyrolysis. *Int J Technol* [Internet]. 2022 Jan 20;13(1):147–56. Available from: [<URL>](#).
16. Liu J, Yu H, Wang L, Vatsadze SZ, Chen D, Wu X, et al. One-step synthesis of ferrocenyl glycidyl ethers as combustion catalysts for the thermal decomposition of ammonium perchlorate. *Powder Technol* [Internet]. 2023 Oct 1;428:118772. Available from: [<URL>](#).
17. Sardi B, Rachmawati H, Maulana TF, Setiawati E, Indrawan N, Mahfud M. Advanced bio-oil production from a mixture of microalgae and low rank coal using microwave assisted pyrolysis. *Bioresour Technol Reports* [Internet]. 2023 Feb 1;21:101367. Available from: [<URL>](#).
18. Sardi B, Uno I, Marhum FA, Akbar AA, Arief T, Arif M, et al. Role of novel additives (reservoir rock and activated carbon) in bio-oil synthesis from LRC microwave pyrolysis. *Int J Hydrogen Energy* [Internet]. 2024 Jan 2;49:203–16. Available from: [<URL>](#).
19. Okeke ES, Olagbaju OA, Okoye CO, Addey CI, Chukwudozie KI, Okoro JO, et al. Microplastic burden in Africa: A review of occurrence, impacts, and sustainability potential of bioplastics. *Chem Eng J Adv* [Internet]. 2022 Nov 15;12:100402. Available from: [<URL>](#).
20. Wiercigroch E, Szafraniec E, Czamara K, Pacia MZ, Majzner K, Kochan K, et al. Raman and infrared spectroscopy of carbohydrates: A review. *Spectrochim Acta Part A Mol Biomol Spectrosc* [Internet]. 2017 Oct 5;185:317–35. Available from: [<URL>](#).
21. Heredia-Guerrero JA, Benítez JJ, Porrás-Vázquez JM, Tedeschi G, Morales Y, Fernández-Ortuño D, et al. Plasticized, greaseproof chitin bioplastics with high transparency and biodegradability. *Food Hydrocoll* [Internet]. 2023 Dec 1;145:109072. Available from: [<URL>](#).
22. Djunaidi MC, Astuti Y. Synthesis, characterization and selectivity of molecularly imprinted polymer (MIP) glucose using polyeugenol as a functional polymer. *Rasayan J Chem* [Internet]. 2019;12(02):809–21. Available from: [<URL>](#).
23. Mas I, Hortelano C, Ruiz-Bermejo M, de la Fuente JL. Highly efficient melt polymerization of diaminomaleonitrile. *Eur Polym J* [Internet]. 2021 Jan 15;143:110185. Available from: [<URL>](#).
24. Abdul Rahim E, Sanda F, Masuda T. Synthesis and Properties of Novel Eugenol-Based Polymers. *Polym Bull* [Internet]. 2004 Aug;52(2):93–100. Available from: [<URL>](#).



Mini-Review on Coumarins: Sources, Biosynthesis, Bioactivity, Extraction and Toxicology

Fatima Elmusa^{1*} , Muna Elmusa² 

¹Eskisehir Technical University, Department of Biology, Eskisehir, Turkey.

²Elfurat Engineering Research and Development Limited Company, Ankara, Turkey.

Abstract: Coumarins are a class of naturally occurring compounds found in various plants, fungi, and microorganisms, each with a unique chemical profile. These compounds exhibit a broad range of bioactivities, including antithrombotic, anti-inflammatory, antioxidant, antimicrobial, antiviral, anticancer, and neuroprotective properties. The effective extraction of coumarins, facilitated by methods such as maceration and microwave-assisted extraction, is integral to unlocking their potential across various applications. Nevertheless, safety and toxicology considerations assume paramount importance, particularly in pharmaceuticals, cosmetics, and food additives. While moderate dietary consumption of coumarin-rich foods is generally safe, excessive intake, whether through foods or supplements, raises concerns linked to hepatotoxicity and photosensitivity. Notably, specific coumarin derivatives, including the widely used anticoagulant warfarin, necessitate precise dosing and vigilant monitoring to mitigate the risk of bleeding complications. In conclusion, the versatile biological activities of coumarins underscore their significance; yet, their safety and toxicity profiles are contingent on multiple factors, encompassing compound type, dosage, and individual susceptibility. This review provides a holistic understanding of coumarins, encompassing their natural origins, biosynthesis, bioactivity spectrum, extraction techniques, and insights into safety, and toxicology.

Keywords: Coumarins, Natural Sources, Biosynthetic Pathway, Extraction, Toxicology.

Submitted: January 13, 2024. **Accepted:** April 22, 2024.

Cite this: Elmusa F, Elmusa M. Mini-Review on Coumarins: Sources, Biosynthesis, Bioactivity, Extraction and Toxicology. JOTCSA. 2024;11(3):933-44.

DOI: <https://doi.org/10.18596/jotcsa.1419322>

***Corresponding author's E-mail:** fatima.almousa1998@gmail.com

1. INTRODUCTION

Coumarins, a class of natural compounds characterized by their benzopyrone structure, have been the subject of significant scientific interest and research due to their widespread occurrence in nature and diverse biological activities (1). These compounds, originally identified in tonka beans (*Dipteryx odorata*) and later found in various plants, fungi, and microorganisms, have demonstrated a wide range of pharmacological properties, making them intriguing candidates for applications in pharmaceuticals, food additives, cosmetics, and beyond (2).

The intriguing chemical structure of coumarins consists of a benzene ring fused to an α -pyrone (benzopyrone) ring, creating a scaffold with distinct electronic and steric properties. This structural

arrangement confers upon coumarins a remarkable ability to interact with a myriad of biological targets, resulting in their diverse bioactivity spectrum (3). The presence of coumarins in edible plants and their established usage in traditional medicine practices have long hinted at their potential health benefits (4).

Natural sources of coumarins are abundant and encompass a wide array of botanical species. Plants such as cinnamon, sweet woodruff, and sweet clover are renowned for their coumarin content. Coumarins are distributed across various plant parts, including flowers, seeds, and leaves, with distinct classes such as pyranocoumarins and furanocoumarins contributing to their molecular diversity (5). Fruit and flowers often exhibit higher coumarin concentrations compared to other plant parts, rendering them noteworthy sources for isolation and analysis (6).

Beyond plants, coumarins have also been identified in microorganisms, further expanding their biogeographical distribution. Fungi, in particular, have yielded coumarin derivatives from species isolated in diverse ecological niches (7). These coumarins, typically encountered as secondary metabolites in plants and microorganisms, serve essential functions in protecting against various environmental threats, including herbivores and pathogens (8).

The pharmacological importance of coumarins is undeniable. These compounds have demonstrated a myriad of bioactivities, including antithrombotic, anti-inflammatory, antioxidant, antimicrobial, antiviral, anticancer, and neuroprotective effects (1). Such a versatile pharmacological profile has spurred extensive research into their potential therapeutic applications. Coumarins have found utility in the treatment of various medical conditions, with some derivatives serving as anticoagulants to prevent blood clot formation (9). Additionally, their antioxidant properties make them attractive candidates for the development of novel therapies aimed at mitigating oxidative stress-related diseases (10).

In the context of food and cosmetics, coumarins have been explored as natural additives and functional ingredients. Their fragrance and flavor-enhancing properties have led to their incorporation into perfumes, and food products (11). Furthermore, coumarins have shown potential in the cosmetic industry due to their skin-lightening and antioxidant effects (12).

While coumarins offer remarkable promise, they are not without their challenges and risks. Excessive consumption of coumarin-rich foods or dietary supplements has raised concerns regarding potential adverse effects, including hepatotoxicity and photosensitivity (13). The delicate balance between their beneficial bioactivities and potential health risks underscores the need for a comprehensive understanding of coumarins' safety and toxicology profiles.

This mini-review endeavors to provide an overview of coumarins, encompassing their natural sources, biosynthesis, bioactivities, extraction methods, and safety considerations. We aim to shed light on the multifaceted world of coumarins, offering insights into their potential applications, while emphasizing the importance of responsible use and vigilant monitoring to harness their benefits effectively.

2. NATURAL SOURCES OF COUMARINS

Coumarin is present in numerous vegetables, fruits, spices, and herbs, as illustrated in Figure 1. Within plants, coumarins are distributed across various plant parts, including flowers, seeds, and leaves (5). They exhibit varying concentrations and molecular diversities, with distinct classes such as pyranocoumarins (linear and angular) and

furanocoumarins (linear and angular) (5). Generally, fruit and flowers contain higher coumarin concentrations compared to roots, stem bark, leaves, and seeds (6). Table 1 offers an overview of coumarin and its derivative classes, their isolation from various plant sources, as well as pertinent details such as the source parts and isolation methods, along with the number and types of coumarins identified.

In addition to plants, coumarin and its derivatives have been discovered in microorganisms. In a 2015 study, J. Wang et al. reported the isolation of a novel coumarin derivative from two fungal species found along the shores of the South China Sea, which they subsequently co-fermented (14). Similarly, Uma-shankar et al. published a study in the same year where they extracted three coumarin compounds from *Alternaria* mushrooms isolated from the leaves of *Crotalaria pallida* (15). In a 2020 investigation, a new coumarin derivative was identified, along with pyron-derived compounds, in the *Aspergillus versicolor* fungal strain isolated from *Coridius chinensis* (16). These coumarins, typically encountered as secondary metabolites in plants and microorganisms, serve a critical function in defending against various threats (6).

3. BIOSYNTHESIS OF COUMARINS

Plants synthesize many phenolic compounds (37). These synthesized compounds are classified into four distinct groups according to their carbon scaffolds: 1) phenolic acids (C6-C1), 2) hydroxycinnamic acids (HCs, C6-C3), 3) stilbenes (C6-C2-C6), and 4) flavonoids (C6-C3-C6). The hydroxycinnamic acids class includes p-coumaric acid, caffeic acid, and ferulic acid (38). Phenolic compounds, including p-coumaric acid, caffeic acid, and ferulic acid, are synthesized in plants from phenylalanine or tyrosine through the activity of phenylalanine ammonia lyase (PAL) or tyrosine ammonia lyase (TAL) enzymes. The biosynthesis of coumarins, as depicted in Figure 2, involves the conversion of phenylalanine and tyrosine using PAL or TAL, followed by enzymatic reactions catalysed by 4-cinnamic acid: coenzyme A ligase (4CL) and feruloyl CoA 6'-hydroxylase (F6'H) (also known as 2-oxoglutarate-dependent dioxygenase, 2OGD, or p-coumaroyl CoA 2'-hydroxylase, C2'H) enzymes (37,38). Following deamination by PAL, the initial enzyme in the phenylpropanoid pathway, cinnamic acid is produced and subsequently hydroxylated by cinnamate 4-hydroxylase (C4H) to yield p-coumaric (4-coumaric) acid (39,40). p-Coumaric acid serves as a precursor for coumarin derivatives, including umbelliferone, catalysed by 4CL and F6'H enzymes, and esculetin, which is produced with the participation of coumarate-3-hydroxylase (C3H), 4CL, and F6'H enzymes (38,39). p-Coumaroyl-CoA can be converted to esculetin through a series of enzymatic reactions, starting with hydroxycinnamoyl transferase (HCT) and followed by C3H and HCT enzymes, respectively (41-44). Caffeic acid, derived from the hydroxylation of p-coumaric acid by the C3H enzyme (45), can further undergo

O-methylation via caffeic acid O-methyl transferase (COMT) to produce ferulic acid (38). Ferulic acid is subsequently transformed into scopoletin, one of the coumarin derivatives, through the actions of 4CL and F6'H enzymes (46). The formation of feruloyl-CoA,

an intermediate in the conversion of ferulic acid to scopoletin, can also occur from caffeoyl-CoA via caffeoyl-CoA O-methyltransferase (CCoAOMT) (47).

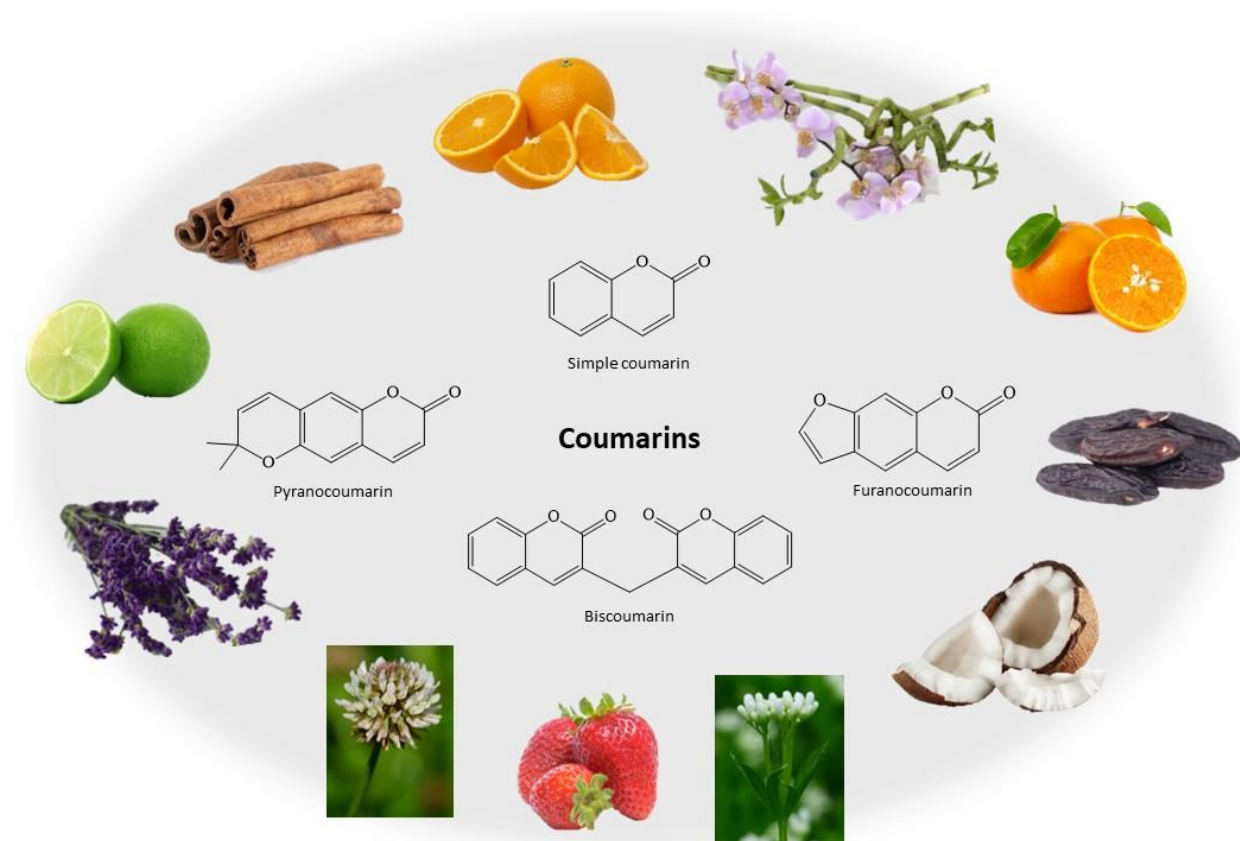


Figure 1: The structure and natural sources of various coumarin classes.

While the conversion of phenylalanine-derived coumaric acid to coumarin has been reported to occur through a single-step ortho-hydroxylation process, except for the para-hydroxylation, this biosynthetic step remains relatively underexplored (48). An alternative pathway for coumarin biosynthesis begins with the conversion of phenylalanine-derived coumaric acid into trans-2-cinnamate by the enzyme cinnamate 2-hydroxylase (C2H) and proceeds through subsequent transformations catalyzed by 2-coumarate O- β -glucosyltransferase (2GT) and β -glucosidase (GBA) (49).

Despite plants' capacity to synthesize various flavonoid compounds, including coumarins, their natural extraction is often insufficient for applications such as drug development. Traditional tissue culture

and chemical synthesis methods prove impractical for large-scale coumarin production (37). Consequently, researchers have turned to microorganisms as an alternative for biosynthesizing phenolic compounds, including coumarins (40,50). These studies involve the transfer of structural genes isolated from plants, fungi, and bacteria into microorganisms like *Escherichia coli* and *Saccharomyces cerevisiae*, resulting in recombinant microbial strains capable of producing phenolic compounds (37). In 2015, Yang et al. achieved the synthesis of coumarin derivatives using *E. coli*. They cloned and transferred Os4CL and IbF6'H2 genes from *Oryza sativa* and *Ipomoea batatas* into *E. coli*. This genetic modification enabled the *E. coli* to produce three coumarin derivatives—umbelliferone, esculetin, and scopoletin—when cultured in media supplemented with hydroxycinnamic acids such as p-coumaric acid, caffeic acid, and ferulic acid (38).

Table 1: Classes and Isolation of Plant-Derived Coumarins.

Sources	Part Of Source	Isolation Method	Solvent	Temperature	Time	Coumarins Number and Type	Ref.
<i>Ailanthus altissima</i> (Mill.) Swingle	Air-dried root barks	-	70% EtOH-H ₂ O	70 °C	3 h	14 compounds (Simple coumarins)	(17)
<i>Angelica dahurica</i>	Air-dried roots	Reflux	95% EtOH-H ₂ O	-	3 h	23 compounds (10 furanocoumarins + 3 furanocoumarin dimers)	(18)
11 species of Bamboo	Leaves	Ultrasound-Assisted Extraction + Centrifugation	70% EtOH-H ₂ O and MeOH	RT and 4°C	30 min	12 compounds (8 simple coumarins + 4 furanocoumarins)	(19)
<i>Bombax ceiba</i>	Dried flowers	-	MeOH and 70% MeOH	55 °C and RT (20 °C)	5 + 20 h	24 compounds (4 simple coumarins + 13 flavones + 3 glycosides + 4 phenolic acids)	(20)
<i>Calophyllum brasiliense</i>	Air-dried leaves	-	Hexane	RT	-	3 compounds (Simple coumarins)	(21)
<i>Calophyllum inophyllum</i>	Air-dried leaves	-	95% EtOH-H ₂ O	-	-	6 compounds (Pyranocoumarins)	(22)
5 species of Citrus	Peels	Percolation	MeOH	RT	5 days	6 compounds (2 simple coumarins + 4 furanocoumarins)	(23)
6 species of Citrus	Dried peels	Centrifugation	80% MeOH-H ₂ O	RT	~1.5 h	27 compounds (6 simple coumarins + 21 furanocoumarins)	(24)
<i>Citrus grandis</i> (L.)	Dried fruits	Reflux	70% EtOH-H ₂ O	-	1.5 h	17 compounds (10 simple coumarins + 7 furanocoumarins)	(25)
<i>Clausena excavate</i>	Air-dried roots	Reflux	95% EtOH-H ₂ O	-	-	9 compounds (pyranocoumarins)	(26)
<i>Cuphea ignea</i> (Lythraceae)	Fresh whole plant	Reflux	Hot EtOH/H ₂ O (3:1)	-	8 h	1 compound (Simple coumarins)	(27)
<i>Ferula sinkiangensis</i>	Seeds	Reflux	95% EtOH-H ₂ O	-	2 h	11 compounds (Simple coumarins)	(28)
<i>Ferulago subvelutina</i>	Milled roots	Percolation	Ethyl acetate	RT	48 h	6 compounds (2 simple coumarins + 4 furanocoumarins)	(29)

<i>Matricaria chamomilla</i> (L.)	Leaves	-	EtOH	-	-	7 compounds (5 simple coumarin + 2 cinnamic acid derivatives)	(30)
<i>Melilotus officinalis</i> (L.)	Air-dried flowering tops	Soxhlet, Ultrasound-Assisted Extraction, Microwave-Assisted Extraction	95% and 50% EtOH-H ₂ O	-	8 h	3 compounds (1 Simple coumarin + 2 phenolic acid)	(31)
<i>Melittis melisophyllum</i> L.	Air-dried and fresh leaves	-	80% MeOH	RT	30 min	1 compound (o-coumaric acid glucoside)	(32)
<i>Murraya paniculate</i> (L.) Jack	Air-dried leaves and stems	-	95% and 50% EtOH-H ₂ O	-	-	19 compounds (Simple coumarins)	(33)
<i>Paxillus involutus</i>	Dried fruiting bodies	-	Ethyl acetate	4°C	~ 4 days	4 compounds (1 furanocoumarins)	(34)
<i>Trifolium repens</i>	Flowers	Soxhlet	Petrol and CHCl ₃ + MeOH and 70% MeOH	RT	8 + 8 h	5 compounds (2 simple coumarins + 3 biscoumarins)	(35)
<i>Zanthoxylum schinifolium</i>	Freeze dried leaves	-	80% MeOH	-	-	9 compounds (Simple coumarins)	(36)

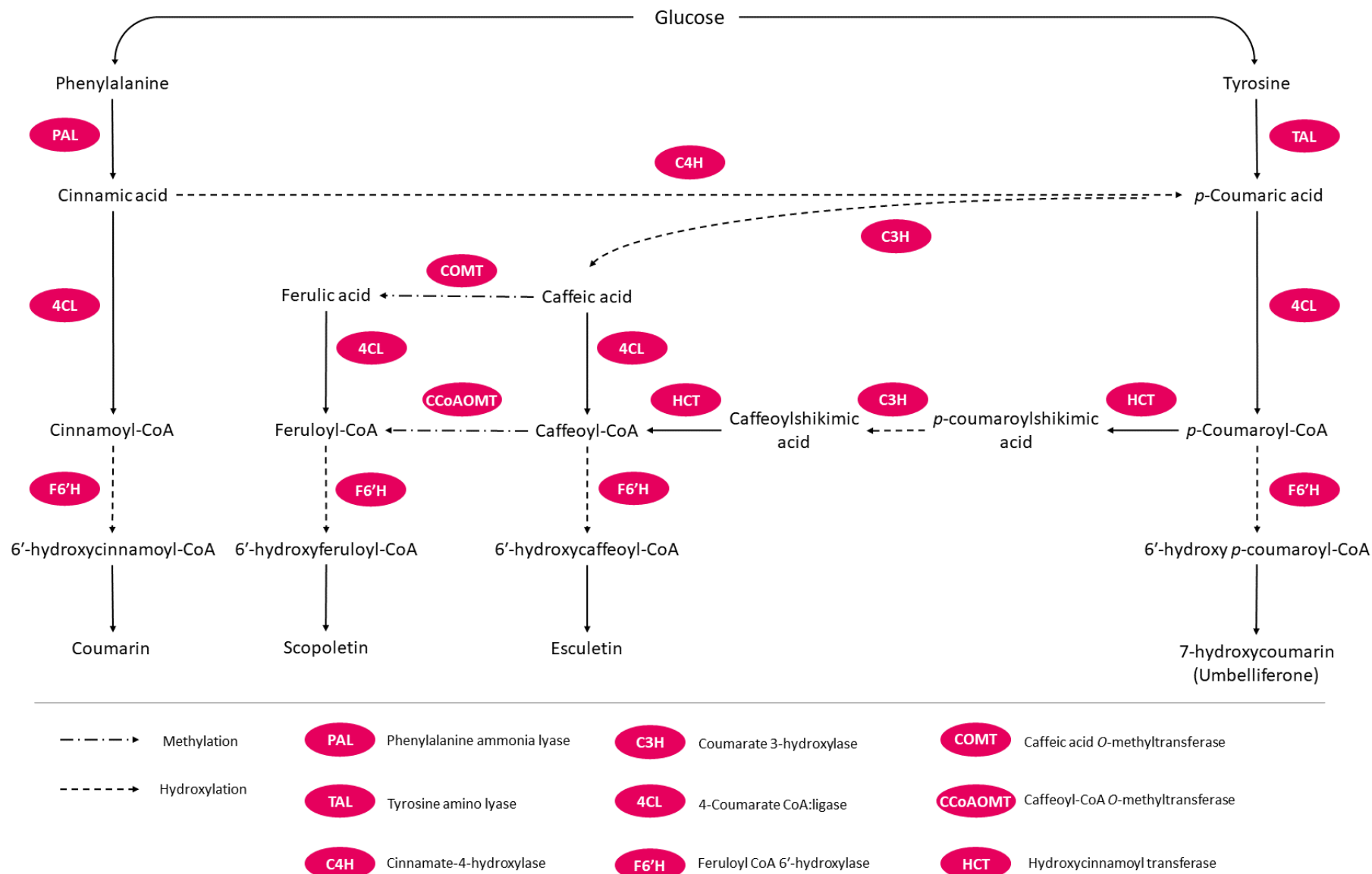


Figure 2: Biosynthesis Pathway of Coumarins.

4. BIOACTIVITY OF COUMARINS

Coumarins, a class of naturally occurring compounds found in various plants, fungi, and microorganisms, have garnered significant attention due to their diverse and promising biological activities (51). These compounds exhibit a wide range of pharmacological properties, making them subjects of extensive research for potential therapeutic applications (2). Below, we delve into some of the notable bioactivities associated with coumarins:

Antithrombotic Activity: One of the well-documented bioactivities of coumarins is their antithrombotic (anticoagulant and antiplatelet) activity (52). The prototypical coumarin derivative, warfarin, has long been used as an oral anticoagulant to prevent blood clot formation. It functions by inhibiting vitamin K epoxide reductase, a key enzyme in the coagulation cascade (53). This property has led to the development of various coumarin-based anticoagulant drugs.

Anti-Inflammatory Properties: Several coumarin compounds have demonstrated anti-inflammatory activity, which can be attributed to their ability to inhibit pro-inflammatory enzymes and cytokines (54). Coumarin derivatives, such as scopoletin and herniarin, have shown potential in attenuating inflammatory responses, making them of interest in conditions characterized by excessive inflammation (10,55).

Antioxidant Effects: Many coumarins exhibit potent antioxidant properties, which can help protect cells and tissues from oxidative damage caused by reactive oxygen species (ROS) (56). These antioxidants scavenge free radicals and reduce oxidative stress, potentially contributing to the prevention of various chronic diseases (57).

Antimicrobial Activity: Coumarins have displayed antimicrobial activity against a wide range of microorganisms, including bacteria (58), fungi (59), and parasites (60). Some coumarin derivatives have been investigated for their antibacterial and antifungal properties, suggesting their potential as natural antimicrobial agents.

Antiviral Activity: Several studies have investigated the effects of coumarin derivatives on various viruses, highlighting their promising role in combating viral infections. Some coumarin derivatives have exhibited the ability to inhibit the replication of certain viruses. This inhibition can occur through different mechanisms, including interference with viral RNA or DNA synthesis, disruption of viral protein function, or inhibition of viral entry into host cells. Coumarins have shown efficacy against a range of viruses, including but not limited to hepatitis virus, Influenza Virus, and HIV (61).

Anticancer Potential: Emerging research has highlighted the anticancer potential of certain

coumarins. These compounds have shown cytotoxic effects on cancer cells and may inhibit tumor growth by various mechanisms, including apoptosis induction and cell cycle arrest (62).

Neuroprotective Effects: Coumarins, such as esculetin and osthole, have exhibited neuroprotective properties by modulating neuroinflammatory responses and protecting neurons from oxidative stress (63). These findings raise the possibility of coumarin-based treatments for neurodegenerative disorders (64).

In addition to the mentioned bioactivities, coumarins have also been investigated for their potential in managing various conditions such as diabetes and cardiovascular diseases (65,66). Their versatile pharmacological profile continues to drive research into their therapeutic applications (2). It is important to note that the bioactivity of coumarins can vary widely depending on their chemical structure, concentration, and the biological context. Further research is necessary to elucidate the specific mechanisms of action and clinical potential of different coumarin derivatives.

5. EXTRACTION METHODS

The efficient extraction of coumarins from natural sources is a critical step in harnessing their potential for various applications, including pharmaceuticals, food additives, and cosmetics (5). The choice of extraction method plays a pivotal role in determining the yield and purity of the extracted coumarins. Below, we explore several extraction techniques commonly employed to isolate coumarins from their natural matrices:

Reflux Method: The reflux method involves heating a mixture of the coumarin-rich source material and solvent in a round-bottomed flask fitted with a condenser. The solvent vaporizes and condenses, creating a continuous cycle. This refluxing process facilitates the extraction of coumarins as the solvent repeatedly comes into contact with the source material. After refluxing for a specified time, the extract is collected (67).

Soxhlet Extraction: Soxhlet extraction is a continuous extraction technique that involves solvent reflux. The raw material is placed in a porous thimble, which is inserted into a Soxhlet extractor. Solvent is continuously boiled, evaporating and condensing in a reflux system. The condensed solvent drips back onto the material, ensuring prolonged contact and efficient extraction. Soxhlet extraction is suitable for coumarins in samples with relatively low coumarin content (68).

Hydrodistillation Method: Hydrodistillation is a method used primarily for extracting essential oils, including those containing coumarins. In this method, steam is passed through the source material, vaporizing compounds. The steam and extracted compounds are condensed and collected

separately, with the essential oil enriched in coumarins obtained as the distillate (69).

Maceration: Maceration is a simple and widely used extraction technique, particularly suitable for extracting coumarins from dried plant material. In this method, the coumarin-rich source is soaked or immersed in a solvent at room temperature for an extended period (at least 3 days). During maceration, the solvent gradually absorbs the coumarins from the plant material. The resulting extract is then filtered to remove solid particles, and the solvent is evaporated to obtain the coumarin-rich extract. Maceration is a relatively gentle method and is especially useful for heat-sensitive compounds (68).

Infusion Method: The infusion method involves soaking the coumarin-rich source material in a suitable solvent, typically at room temperature or slightly elevated temperatures. The solvent gradually absorbs the coumarins over time. After the desired extraction period, the mixture is filtered, and the solvent is evaporated to obtain the coumarin-rich infusion (68). This method is similar to the maceration method but differs in the duration and temperature of the solvent.

Percolation Method: Percolation represents a continuous extraction technique that involves the passage of a solvent through a densely packed bed of coumarin-rich material. This method employs specialized equipment known as a percolator, typically a narrow, cone-shaped glass vessel open at both ends. To initiate the process, finely powdered plant material is moistened with the chosen extraction solvent. Subsequently, an additional quantity of solvent is introduced, and the mixture is allowed to rest. Following this, the content is transferred into the percolator and allowed to stand for 24 hours. This process results in the gradual dissolution of coumarins. Finally, the outlet of the percolator is opened, and the liquid contained therein is allowed to drip slowly. The resulting extract is then separated through filtration (68,70). This method is often used for both small and large-scale extraction processes and allows for precise control of solvent flow rates and extraction times (71).

Supercritical Fluid Extraction (SFE): Supercritical fluid extraction is an advanced method that uses supercritical fluids, such as carbon dioxide (CO₂), to extract coumarins. Under specific temperature and pressure conditions, CO₂ becomes a supercritical fluid with unique solvation properties (72). It can selectively dissolve coumarins from the raw material, and upon depressurization, the coumarins precipitate, leaving behind a concentrated extract. SFE is considered environmentally friendly and offers precise control over extraction parameters (73).

Microwave-Assisted Extraction (MAE): Microwave-assisted extraction is a rapid and efficient method for coumarin extraction. In MAE, the sample is exposed to microwave radiation in the presence of

a suitable solvent. The microwave energy accelerates the extraction process by promoting the release of coumarins from the plant matrix. This method is known for its shorter extraction times and improved efficiency (68).

Ultrasonic-Assisted Extraction (UAE): Ultrasonic-assisted extraction employs high-frequency ultrasound waves to enhance the extraction process. The cavitation generated by ultrasound disrupts cell walls and facilitates the release of coumarins into the solvent (70). UAE is known for its shorter extraction times, reduced solvent consumption, and improved extraction efficiency (74).

In a comparative study conducted by Molnar et al., it was found that the maceration method was at least five times more efficient than the Soxhlet, hydrodistillation, and supercritical CO₂ extraction methods and provided the highest umbelliferone and herniarin extraction (75). In a study by Chanfrau et al., reflux and Ultrasonic-Assisted Extraction methods were compared. As a result of the study, it was found that reflux provides a higher coumarin yield, and the use of low-frequency ultrasound in the extraction method provides a higher coumarin yield than high-frequency ultrasound (74).

As a result, the choice of extraction method should consider factors such as the nature of the source material, the desired coumarin compounds, and the specific requirements for purity and yield. Researchers often optimize extraction conditions, including solvent type, temperature, and extraction time, to maximize the recovery of coumarins while minimizing undesirable co-extracts. Ultimately, the selected method should align with the intended application of the extracted coumarins.

6. SAFETY AND TOXICOLOGY

The safety profile of coumarins has garnered significant interest, given their widespread presence in nature and their versatile applications in pharmaceuticals, food additives, and cosmetics (2). While coumarins offer diverse bioactivities, their consumption and exposure demand careful consideration to mitigate potential health risks.

Coumarins are naturally occurring compounds found in various edible plants like cinnamon, tonka beans, and certain fruits. In these natural forms, coumarins are generally deemed safe when consumed in typical dietary quantities (76). However, excessive consumption of coumarin-rich foods or dietary supplements can raise concerns regarding cumulative exposure (5). While natural coumarins may offer potential health benefits, excessive intake can lead to adverse effects:

Hepatotoxicity: Some coumarins, including coumarin itself, have been linked to hepatotoxicity (liver toxicity) when consumed in excessive amounts. Regulatory authorities in some countries

have established tolerable daily intake (TDI) levels for coumarin, prompting efforts to limit its presence in certain foods (77).

Photosensitivity: Specific coumarins, such as bergapten found in certain citrus fruits, can induce photosensitivity when applied topically or ingested in large quantities. This can result in skin reactions upon exposure to sunlight, including sunburn and blistering (78). Similarly, psoralen can trigger photosensitization reactions when the skin encounters ultraviolet (UV) light, leading to skin irritation, rashes, and an elevated risk of sunburn (79).

Anticoagulant Risk: Certain coumarin derivatives, like warfarin, serve as anticoagulant medications to prevent blood clotting. While effective for their intended purposes, these medications require vigilant monitoring and precise dosing due to their narrow therapeutic window. Overdosing can result in bleeding complications, underscoring the importance of medical supervision (80).

In conclusion, coumarins encompass a wide range of biological activities, but their safety and toxicity profile hinge on various factors, including the specific coumarin compound, dosage, and individual susceptibility. While natural dietary intake is generally safe, vigilance is essential when dealing with coumarin derivatives used in pharmaceuticals and high-concentration cosmetic products. Regulatory guidelines and risk management strategies are vital to ensure the safe utilization of coumarins across various applications.

7. CONCLUSION

Coumarins, with their intriguing benzopyrone structure, have long captivated the attention of researchers and enthusiasts alike due to their widespread presence in nature and versatile pharmacological properties. The plethora of biological activities exhibited by coumarins, including antithrombotic, anti-inflammatory, antioxidant, antimicrobial, antiviral, anticancer, and neuroprotective effects, highlights their vast potential in both pharmaceutical and nutraceutical applications. Moreover, the employment of efficient extraction methods, such as maceration, microwave-assisted extraction, and supercritical fluid extraction, enables the retrieval of these compounds for further investigation and industrial exploitation. However, it is crucial to acknowledge the potential health risks associated with excessive consumption of coumarin-rich substances, including hepatotoxicity, photosensitivity, and anticoagulant effects. Therefore, careful consideration must be given to the safe usage of coumarins, involving thorough risk assessments, stringent quality control measures, and adherence to established regulations. Despite these caveats, the study of coumarins continues to captivate scientists, offering a wealth of opportunities for groundbreaking discoveries and innovations in medicine, food science, and related

disciplines. By responsibly harnessing the power of coumarins, we may unlock novel therapeutic pathways and create new possibilities for improving human health and well-being.

8. CONFLICT OF INTEREST

The authors have no conflicts of interest to declare.

9. REFERENCES

- Sharifi-Rad J, Cruz-Martins N, López-Jornet P, Lopez EPF, Harun N, Yeskaliyeva B, et al. Natural Coumarins: Exploring the Pharmacological Complexity and Underlying Molecular Mechanisms. Gil G, editor. Oxid Med Cell Longev [Internet]. 2021 Aug 23;2021:6492346. Available from: [<URL>](#).
- Annunziata F, Pinna C, Dallavalle S, Tamborini L, Pinto A. An Overview of Coumarin as a Versatile and Readily Accessible Scaffold with Broad-Ranging Biological Activities. Int J Mol Sci [Internet]. 2020 Jun 29;21(13):4618. Available from: [<URL>](#).
- Sharma M, Vyas VK, Bhatt S, Ghate MD. Therapeutic potential of 4-substituted coumarins: A conspectus. Eur J Med Chem Reports [Internet]. 2022 Dec 1;6:100086. Available from: [<URL>](#).
- Hussain MI, Syed QA, Khattak MNK, Hafez B, Reigosa MJ, El-Keblawy A. Natural product coumarins: biological and pharmacological perspectives. Biologia (Bratisl) [Internet]. 2019 Jul 15;74(7):863–88. Available from: [<URL>](#).
- Lončar M, Jakovljević M, Šubarić D, Pavlić M, Buzjak Služek V, Cindrić I, et al. Coumarins in Food and Methods of Their Determination. Foods [Internet]. 2020 May 18;9(5):645. Available from: [<URL>](#).
- Matos MJ, Santana L, Uriarte E, Abreu OA, Molina E, Yordi EG. Coumarins – An Important Class of Phytochemicals. In: Phytochemicals - Isolation, Characterisation and Role in Human Health [Internet]. InTech; 2015. Available from: [<URL>](#).
- Tsvileva OM, Koftin O V., Evseeva N V. Coumarins as Fungal Metabolites with Potential Medicinal Properties. Antibiotics [Internet]. 2022 Aug 26;11(9):1156. Available from: [<URL>](#).
- Xia T, Liu Y, Lu Z, Yu H. Natural Coumarin Shows Toxicity to *Spodoptera litura* by Inhibiting Detoxification Enzymes and Glycometabolism. Int J Mol Sci [Internet]. 2023 Aug 24;24(17):13177. Available from: [<URL>](#).
- Lu PH, Liao TH, Chen YH, Hsu YL, Kuo CY, Chan CC, et al. Coumarin Derivatives Inhibit ADP-Induced Platelet Activation and Aggregation. Molecules [Internet]. 2022 Jun 23;27(13):4054. Available from: [<URL>](#).
- Ghosh R, Singha PS, Das LK, Ghosh D, Firdaus SB. Anti-inflammatory activity of natural coumarin compounds from plants of the Indo-Gangetic plain. AIMS Mol Sci [Internet]. 2023;10(2):79–98. Available from: [<URL>](#).
- Coumarin. IARC monographs on the evaluation of carcinogenic risks to humans. 2000;77:193–225. Available from: [<URL>](#).
- Boo YC. p-Coumaric Acid as An Active Ingredient in Cosmetics: A Review Focusing on its Antimelanogenic Effects. Antioxidants [Internet]. 2019 Aug 4;8(8):275. Available from: [<URL>](#).

13. Eggleston W. Coumarins. In: Encyclopedia of Toxicology [Internet]. Elsevier; 2024 [cited 2024 May 6]. p. 293–7. Available from: [<URL>](#).
14. Wang J, Huang S, Li C, Ding W, She Z, Li C. A New Coumarin Produced by Mixed Fermentation of Two Marine Fungi. Chem Nat Compd [Internet]. 2015 Mar 27;51(2):239–41. Available from: [<URL>](#).
15. Umashankar T, Govindappa M, Ramachandra YL, Chandrappa CP, Padmalatha RS, Channabasava R. Isolation, purification and in vitro cytotoxic activities of coumarin isolated from endophytic fungi, *Alternaria* species of *Crotalaria pallida*. Indo Am J Pharm Res [Internet]. 2015;5(2):926–36. Available from: [<URL>](#).
16. Li TX, Meng DD, Wang Y, An JL, Bai JF, Jia XW, et al. Antioxidant coumarin and pyrone derivatives from the insect-associated fungus *Aspergillus Versicolor*. Nat Prod Res [Internet]. 2020 May 18;34(10):1360–5. Available from: [<URL>](#).
17. Yan ZY, Lv TM, Wang YX, Shi SC, Chen JJ, Bin-Lin, et al. Terpenylated coumarins from the root bark of *Ailanthus altissima* (Mill.) Swingle. Phytochemistry [Internet]. 2020 Jul 1;175:112361. Available from: [<URL>](#).
18. Bai Y, Li D, Zhou T, Qin N, Li Z, Yu Z, et al. Coumarins from the roots of *Angelica dahurica* with antioxidant and antiproliferative activities. J Funct Foods [Internet]. 2016 Jan 1;20:453–62. Available from: [<URL>](#).
19. Wang S, Tang F, Yue Y, Yao X, Wei Q, Yu J. Simultaneous Determination of 12 Coumarins in Bamboo Leaves by HPLC. J AOAC Int [Internet]. 2013 Sep 1;96(5):942–6. Available from: [<URL>](#).
20. Joshi KR, Devkota HP, Yahara S. Chemical Analysis of Flowers of *Bombax ceiba* from Nepal. Nat Prod Commun [Internet]. 2013 May 1;8(5):583–4. Available from: [<URL>](#).
21. Rodríguez-Hernández KD, Martínez I, Agredano-Moreno LT, Jiménez-García LF, Reyes-Chilpa R, Espinoza B. Coumarins isolated from *Calophyllum brasiliense* produce ultrastructural alterations and affect in vitro infectivity of *Trypanosoma cruzi*. Phytomedicine [Internet]. 2019 Aug 1;61:152827. Available from: [<URL>](#).
22. Li Z lin, Li Y, Qin N bo, Li D hong, Liu Z guo, Liu Q, et al. Four new coumarins from the leaves of *Calophyllum inophyllum*. Phytochem Lett [Internet]. 2016 Jun 1;16:203–6. Available from: [<URL>](#).
23. Ramírez-Pelayo C, Martínez-Quiñones J, Gil J, Durango D. Coumarins from the peel of citrus grown in Colombia: composition, elicitation and antifungal activity. Heliyon [Internet]. 2019 Jun 1;5(6):e01937. Available from: [<URL>](#).
24. Dugrand A, Olry A, Duval T, Hehn A, Froelicher Y, Bourgaud F. Coumarin and Furanocoumarin Quantitation in Citrus Peel via Ultrapformance Liquid Chromatography Coupled with Mass Spectrometry (UPLC-MS). J Agric Food Chem [Internet]. 2013 Nov 13;61(45):10677–84. Available from: [<URL>](#).
25. Tian D, Wang F, Duan M, Cao L, Zhang Y, Yao X, et al. Coumarin Analogues from the *Citrus grandis* (L.) Osbeck and Their Hepatoprotective Activity. J Agric Food Chem [Internet]. 2019 Feb 20;67(7):1937–47. Available from: [<URL>](#).
26. Peng WW, Zheng YQ, Chen YS, Zhao SM, Ji CJ, Tan NH. Coumarins from roots of *Clausena excavata*. J Asian Nat Prod Res [Internet]. 2013 Mar 1;15(3):215–20. Available from: [<URL>](#).
27. Moustafa ES, Swilam NF, Ghanem OB, Hashim AN, Nawwar MA, Lindequist U, et al. A coumarin with an unusual structure from *Cuphea ignea*, its cytotoxicity and antioxidant activities. Pharmazie [Internet]. 2018;73(4):241–3. Available from: [<URL>](#).
28. Li G, Li X, Cao L, Zhang L, Shen L, Zhu J, et al. Sesquiterpene coumarins from seeds of *Ferula sinkiangensis*. Fitoterapia [Internet]. 2015 Jun 1;103:222–6. Available from: [<URL>](#).
29. Naseri M, Monsef-Esfehani HR, Saeidnia S, Dastan D, Gohari AR. Antioxidative Coumarins from the Roots of *Ferulago subvelutina*. Asian J Chem [Internet]. 2013;25(4):1875–8. Available from: [<URL>](#).
30. Petruřová-Poracká V, Repčák M, Vilková M, Imrich J. Coumarins of *Matricaria chamomilla* L.: Aglycones and glycosides. Food Chem [Internet]. 2013 Nov 1;141(1):54–9. Available from: [<URL>](#).
31. Martino E, Ramaiola I, Urbano M, Bracco F, Collina S. Microwave-assisted extraction of coumarin and related compounds from *Melilotus officinalis* (L.) Pallas as an alternative to Soxhlet and ultrasound-assisted extraction. J Chromatogr A [Internet]. 2006 Sep 1;1125(2):147–51. Available from: [<URL>](#).
32. Maggi F, Barboni L, Caprioli G, Papa F, Ricciutelli M, Sagratini G, et al. HPLC quantification of coumarin in bastard balm (*Melittis melissophyllum* L., Lamiaceae). Fitoterapia [Internet]. 2011 Dec 1;82(8):1215–21. Available from: [<URL>](#).
33. Liang H, Cao N, Zeng K, Zhao M, Tu P, Jiang Y. Coumarin and spirocyclopentenone derivatives from the leaves and stems of *Murraya paniculata* (L.) Jack. Phytochemistry [Internet]. 2020 Apr 1;172:112258. Available from: [<URL>](#).
34. Zhang JX, Lv JH, Zhao LQ, Shui XX, Zhang J, Wang LA. Coumarin-pi, a new antioxidant coumarin derivative from *Paxillus involutus*. Nat Prod Res [Internet]. 2020 May 2;34(9):1246–9. Available from: [<URL>](#).
35. Kicel A, Wolbis M. Coumarins from the flowers of *Trifolium repens*. Chem Nat Compd [Internet]. 2012 Mar 22;48(1):130–2. Available from: [<URL>](#).
36. Nguyen PH, Zhao BT, Kim O, Lee JH, Choi JS, Min BS, et al. Anti-inflammatory terpenylated coumarins from the leaves of *Zanthoxylum schinifolium* with α -glucosidase inhibitory activity. J Nat Med [Internet]. 2016 Apr 11;70(2):276–81. Available from: [<URL>](#).
37. Malla S, Koffas MAG, Kazlauskas RJ, Kim BG. Production of 7- O -Methyl Aromadendrin, a Medicinally Valuable Flavonoid, in *Escherichia coli*. Appl Environ Microbiol [Internet]. 2012 Feb;78(3):684–94. Available from: [<URL>](#).
38. Yang SM, Shim GY, Kim BG, Ahn JH. Biological synthesis of coumarins in *Escherichia coli*. Microb Cell Fact [Internet]. 2015 Dec 1;14(1):65. Available from: [<URL>](#).
39. Watts KT, Lee PC, Schmidt-Dannert C. Biosynthesis of plant-specific stilbene polyketides in metabolically engineered *Escherichia coli*. BMC Biotechnol [Internet]. 2006 Dec 21;6(1):22. Available from: [<URL>](#).
40. Miyahisa I, Funa N, Ohnishi Y, Martens S, Moriguchi T, Horinouchi S. Combinatorial biosynthesis of flavones and

- flavonols in *Escherichia coli*. *Appl Microbiol Biotechnol* [Internet]. 2006 Jun 1;71(1):53–8. Available from: [<URL>](#).
41. Comino C, Hehn A, Moglia A, Menin B, Bourgaud F, Lanteri S, et al. The isolation and mapping of a novel hydroxycinnamoyltransferase in the globe artichoke chlorogenic acid pathway. *BMC Plant Biol* [Internet]. 2009 Dec 18 [cited 2024 May 6];9(1):30. Available from: [<URL>](#).
42. Jiang NH, Zhang GH, Zhang JJ, Shu LP, Zhang W, Long GQ, et al. Analysis of the Transcriptome of *Erigeron breviscapus* Uncovers Putative Scutellarin and Chlorogenic Acids Biosynthetic Genes and Genetic Markers. Chen S, editor. *PLoS One* [Internet]. 2014 Jun 23;9(6):e100357. Available from: [<URL>](#).
43. Cheeverunnapakul K, Khaksar G, Panpetch P, Boonjing P, Sirikantaramas S. Identification and Functional Characterization of Genes Involved in the Biosynthesis of Caffeoylquinic Acids in Sunflower (*Helianthus annuus* L.). *Front Plant Sci* [Internet]. 2019 Jul 31;10:457795. Available from: [<URL>](#).
44. Mahesh V, Million-Rousseau R, Ullmann P, Chabrilange N, Bustamante J, Mondlot L, et al. Functional characterization of two p-coumaroyl ester 3'-hydroxylase genes from coffee tree: evidence of a candidate for chlorogenic acid biosynthesis. *Plant Mol Biol* [Internet]. 2007 May 27;64(1–2):145–59. Available from: [<URL>](#).
45. Riedelsheimer C, Lisek J, Czedik-Eysenberg A, Sulpice R, Flis A, Grieder C, et al. Genome-wide association mapping of leaf metabolic profiles for dissecting complex traits in maize. *Proc Natl Acad Sci* [Internet]. 2012 Jun 5;109(23):8872–7. Available from: [<URL>](#).
46. Shimizu BI. 2-Oxoglutarate-dependent dioxygenases in the biosynthesis of simple coumarins. *Front Plant Sci* [Internet]. 2014 Nov 3;5:549. Available from: [<URL>](#).
47. Wagner A, Tobimatsu Y, Phillips L, Flint H, Torr K, Donaldson L, et al. CCoAOMT suppression modifies lignin composition in *Pinus radiata*. *Plant J* [Internet]. 2011 Jul 26;67(1):119–29. Available from: [<URL>](#).
48. Bourgaud F, Hehn A, Larbat R, Doerper S, Gontier E, Kellner S, et al. Biosynthesis of coumarins in plants: a major pathway still to be unravelled for cytochrome P450 enzymes. *Phytochem Rev* [Internet]. 2006 Nov 29;5(2–3):293–308. Available from: [<URL>](#).
49. Zou Y, Teng Y, Li J, Yan Y. Recent advances in the biosynthesis of coumarin and its derivatives. *Green Chem Eng* [Internet]. 2024 Jun 1;5(2):150–4. Available from: [<URL>](#).
50. Leonard E, Lim KH, Saw PN, Koffas MAG. Engineering Central Metabolic Pathways for High-Level Flavonoid Production in *Escherichia coli*. *Appl Environ Microbiol* [Internet]. 2007 Jun 15;73(12):3877–86. Available from: [<URL>](#).
51. Tsivileva OM, Koftin O V. Fungal coumarins: biotechnological and pharmaceutical aspects. In: *Studies in Natural Products Chemistry* [Internet]. Elsevier; 2023. p. 441–79. Available from: [<URL>](#).
52. Gao L, Wang F, Chen Y, Li F, Han B, Liu D. The antithrombotic activity of natural and synthetic coumarins. *Fitoterapia* [Internet]. 2021 Oct 1;154:104947. Available from: [<URL>](#).
53. Mur J, McCartney DL, Chasman DI, Visscher PM, Muniz-Terrera G, Cox SR, et al. Variation in VKORC1 Is Associated with Vascular Dementia. Ikram MA, editor. *J Alzheimer's Dis* [Internet]. 2021 Apr 6;80(3):1329–37. Available from: [<URL>](#).
54. Khan S, Shehzad O, Cheng MS, Li RJ, Kim YS. Pharmacological mechanism underlying anti-inflammatory properties of two structurally divergent coumarins through the inhibition of pro-inflammatory enzymes and cytokines. *J Inflamm* [Internet]. 2015 Dec 29;12(1):47. Available from: [<URL>](#).
55. Santibáñez A, Herrera-Ruiz M, González-Cortazar M, Nicasio-Torres P, Sharma A, Jiménez-Ferrer E. Dose-Effect Determination of a Neuroprotector Fraction Standardized in Coumarins of *Tagetes lucida* and Bioavailability. *Pharmaceutics* [Internet]. 2023 Mar 17;15(3):967. Available from: [<URL>](#).
56. Todorov L, Saso L, Kostova I. Antioxidant Activity of Coumarins and Their Metal Complexes. *Pharmaceutics* [Internet]. 2023 Apr 26;16(5):651. Available from: [<URL>](#).
57. Kadhum AAH, Al-Amiery AA, Musa AY, Mohamad AB. The Antioxidant Activity of New Coumarin Derivatives. *Int J Mol Sci* [Internet]. 2011 Sep 7;12(9):5747–61. Available from: [<URL>](#).
58. Basile A, Sorbo S, Spadaro V, Bruno M, Maggio A, Faraone N, et al. Antimicrobial and Antioxidant Activities of Coumarins from the Roots of *Ferulago campestris* (Apiaceae). *Molecules* [Internet]. 2009 Feb 27;14(3):939–52. Available from: [<URL>](#).
59. Lemos ASO, Florêncio JR, Pinto NCC, Campos LM, Silva TP, Grazul RM, et al. Antifungal Activity of the Natural Coumarin Scopoletin Against Planktonic Cells and Biofilms From a Multidrug-Resistant *Candida tropicalis* Strain. *Front Microbiol* [Internet]. 2020 Jul 7;11:1525. Available from: [<URL>](#).
60. Liu GL, Liu L, Hu Y, Wang GX. Evaluation of the antiparasitic activity of coumarin derivatives against *Dactylogyrus intermedius* in goldfish (*Carassius auratus*). *Aquaculture* [Internet]. 2021 Feb 25;533:736069. Available from: [<URL>](#).
61. Mishra S, Pandey A, Manvati S. Coumarin: An emerging antiviral agent. *Heliyon* [Internet]. 2020 Jan 1;6(1):e03217. Available from: [<URL>](#).
62. Wu Y, Xu J, Liu Y, Zeng Y, Wu G. A Review on Anti-Tumor Mechanisms of Coumarins. *Front Oncol* [Internet]. 2020 Dec 4;10:592853. Available from: [<URL>](#).
63. Hassanein EHM, Sayed AM, Hussein OE, Mahmoud AM. Coumarins as Modulators of the Keap1/Nrf2/ARE Signaling Pathway. *Oxid Med Cell Longev* [Internet]. 2020 Apr 25;2020:1675957. Available from: [<URL>](#).
64. Jameel E, Umar T, Kumar J, Hoda N. Coumarin: A Privileged Scaffold for the Design and Development of Antineurodegenerative Agents. *Chem Biol Drug Des* [Internet]. 2016 Jan 16;87(1):21–38. Available from: [<URL>](#).
65. Li H, Yao Y, Li L. Coumarins as potential antidiabetic agents. *J Pharm Pharmacol* [Internet]. 2017 Sep 5;69(10):1253–64. Available from: [<URL>](#).
66. Najmanova I, Dosedel M, Hrdina R, Anzenbacher P, Filipovsky T, Riha M, et al. Cardiovascular Effects of Coumarins Besides their Antioxidant Activity. *Curr Top Med Chem* [Internet]. 2015;15(9):830–49. Available from: [<URL>](#).

67. Chua LS, Latiff NA, Mohamad M. Reflux extraction and cleanup process by column chromatography for high yield of andrographolide enriched extract. *J Appl Res Med Aromat Plants* [Internet]. 2016 May 1;3(2):64–70. Available from: [<URL>](#).
68. Abubakar A, Haque M. Preparation of medicinal plants: Basic extraction and fractionation procedures for experimental purposes. *J Pharm Bioallied Sci* [Internet]. 2020 Jan 1;12(1):1–10. Available from: [<URL>](#).
69. Fotsing Yannick Stéphane F, Kezetas Jean Jules B, El-Saber Batiha G, Ali I, Ndjakou Bruno L. Extraction of Bioactive Compounds from Medicinal Plants and Herbs. In: El-Shemy HA, editor. *Natural Medicinal Plants* [Internet]. IntechOpen; 2022. Available from: [<URL>](#).
70. Pandey A, Tripathi S. Concept of standardization, extraction and pre phytochemical screening strategies for herbal drug. *J Pharmacogn Phytochem* [Internet]. 2014;2(5):115–9. Available from: [<URL>](#).
71. Mukherjee PK. Extraction and Other Downstream Procedures for Evaluation of Herbal Drugs. In: *Quality Control and Evaluation of Herbal Drugs* [Internet]. Elsevier; 2019. p. 195–236. Available from: [<URL>](#).
72. Altemimi A, Lakhssassi N, Baharlouei A, Watson D, Lightfoot D. Phytochemicals: Extraction, Isolation, and Identification of Bioactive Compounds from Plant Extracts. *Plants* [Internet]. 2017 Sep 22;6(4):42. Available from: [<URL>](#).
73. Manjare SD, Dhingra K. Supercritical fluids in separation and purification: A review. *Mater Sci Energy Technol* [Internet]. 2019 Dec 1;2(3):463–84. Available from: [<URL>](#).
74. Rodríguez-Chanfrau JE, Robaina-Mesa M, Rodríguez-Riera Z, Jauregui-Haza U. Ultrasound-assisted extraction of coumarin from *Justicia pectoralis* Jacq. *Rev Mex Ciencias Farm* [Internet]. 2016;47(1):97–104. Available from: [<URL>](#).
75. Molnar M, Mendešević N, Šubarić D, Banjari I, Jokić S. Comparison of various techniques for the extraction of umbelliferone and herniarin in *Matricaria chamomilla* processing fractions. *Chem Cent J* [Internet]. 2017 Dec 5;11(1):78. Available from: [<URL>](#).
76. Yamada T, Katsutani N, Maruyama T, Kawamura T, Yamazaki H, Murayama N, et al. Combined Risk Assessment of Food-derived Coumarin with in Silico Approaches. *Food Saf* [Internet]. 2022;10(3):73–82. Available from: [<URL>](#).
77. Pitaro M, Croce N, Gallo V, Arienzo A, Salvatore G, Antonini G. Coumarin-Induced Hepatotoxicity: A Narrative Review. *Molecules* [Internet]. 2022 Dec 19;27(24):9063. Available from: [<URL>](#).
78. Bruni R, Barreca D, Protti M, Brighenti V, Righetti L, Anceschi L, et al. Botanical Sources, Chemistry, Analysis, and Biological Activity of Furanocoumarins of Pharmaceutical Interest. *Molecules* [Internet]. 2019 Jun 8;24(11):2163. Available from: [<URL>](#).
79. Ellis CR, Elston DM. Psoralen-Induced Phytophotodermatitis. *Dermatitis* [Internet]. 2021 May 1;32(3):140–3. Available from: [<URL>](#).
80. Verhoef TI, Redekop WK, Daly AK, van Schie RMF, de Boer A, Maitland-van der Zee A. Pharmacogenetic-guided dosing of coumarin anticoagulants: algorithms for warfarin, acenocoumarol and phenprocoumon. *Br J Clin Pharmacol* [Internet]. 2014 Apr 20;77(4):626–41. Available from: [<URL>](#).



Investigation of the Effects of Alcohol and Anti-Icing Additives on the Properties of Jet Fuel

Fevzi Yaşar^{1*}

¹Vocational School of Technical Sciences, Department of Chemistry and Chemical Process Technology
Batman University, 72100 Batman, Turkey.

Abstract: In this study, the effects of methanol, ethanol, isopropanol, and Diethylene glycol monomethyl ether (di-EGME) added to jet fuel in certain proportions on the properties of jet fuel such as density, viscosity, freezing point, and ignition point was examined. By adding 2%, 5%, 7%, and 10% of each additive to JP-8 fuel, the required mixture was obtained and tested in the relevant devices. As a result of the experiments, it was determined that the density value of JP-8 fuel was 797 kg/m³ and this value did not vary greatly in the mixed ethanol, ethanol, and isopropanol, but with the addition of di-EGME, it increased significantly and reached 814.5 kg/m³. It was observed that the viscosity value did not vary greatly with the addition of methanol and ethanol but increased to 1.298 mm/s² with the addition of 10% isopropanol and to 1.98 mm/s² with the addition of di-EGM. The ignition point value of JP-8 fuel, which is 46 °C, was measured to be 40 °C with the addition of 10% methanol, 43.4 °C with the addition of 10% ethanol, 42.9 °C with the addition of 10% isopropanol, and 55.4 °C with the addition of di-EGM. The freezing point value of JP-8 fuel, which is -56.7 °C, was measured as -61.7 °C with the addition of 10% methanol, -62.1 °C with the addition of 10% of ethanol, -57.6 °C with the addition of 10% isopropanol and -54.6 °C with the addition of di-EGM.

Keywords: Ethanol, isopropanol, jet fuel, methanol, viscosity, density.

Submitted: September 22, 2023. **Accepted:** February 26, 2024.

Cite this: Yaşar F. Investigation of the Effects of Alcohol and Anti-Icing Additives on the Properties of Jet Fuel. JOTCSA. 2024;11(3):945-58.

DOI: <https://doi.org/10.18596/jotcsa.1364666>

***Corresponding author's E-mail:** fevzi.yasar@batman.edu.tr

1. INTRODUCTION

Energy, which is at the center of sustainable development, is used to transform economies and societies, encourage industrialization, and raise living standards, as well as to meet basic human needs such as nutrition, heating, cooling, and lighting. Energy access can be defined as access to clean and modern energy at reliable and affordable costs. Accessible and clean energy, which is a part of sustainable development, is very important for people's livelihoods and the economic growth of countries, but it is a goal that is not easy to reach. Access to energy directly affects people, cities, and countries on issues such as economic growth, food production, health, clean water, security, education, and employment (1). Today, countries struggle with seemingly contradictory agendas such as the security of energy supply, economic access to energy, and decarbonization of the energy sector. In energy policies, where energy supply security and price stability are at the forefront, decarbonization,

and sustainability criteria have come to the fore in recent years due to the climate crisis, whose negative effects are being felt more and more. On the other hand, energy transformation, the main elements of which are renewable energy, energy efficiency, and the electrification of energy-intensive end-user sectors, has started to play a critical role in energy supply security and economic access to energy, as well as providing decarbonization with the opportunities offered by technological developments and digitalization (2).

As the world economy grows, the desire for fast delivery of products for the trading countries has made it important to use the existing energy resources effectively and then obtain cheap and clean energy resources. One of the most important factors determining the transportation cost in the aviation sector, where the majority of cargo transfers are made, especially passenger transportation by air, is the fuel used in these vehicles. Today, aircraft, using petroleum-derived fuels, harm the increase in

pollutant emissions in the atmosphere. To eliminate these negativities in high-way vehicles, studies have been carried out for the use of alternative fuels for many years; therefore, the countries encourage the use of biofuels to protect the environment and reduce their dependence on oil. Similarly, determining this potential in the aviation industry and examining the usability of alternative fuels have led to this need. In studies conducted for this purpose, the necessity of using biofuels in the aviation industry and the characteristics of alternative fuel types that can be used were examined. As a result, it has been evaluated that alternative fuels that can be used in internal combustion engines and gas turbines may have similar properties, thanks to the fuel systems and original designs of the aircraft to be produced in the future, and this will contribute to economic development and environmental protection by creating a fuel union in high-way and air transport (3). In aviation, some planes can fly on biofuel, which is an alternative to fossil fuels, but these planes are experimental planes that seat only 2 people and do not serve commercial purposes. Fuels developed for commercial aircraft cannot be used alone. These fuels can be used by mixing them with jet fuels at a rate of 5-20%, but the production of biofuels is expensive compared to jet fuels because biofuel production technologies have not been developed enough for this job (4). Soon, we may see commercial aircraft flying in the skies on 100% biofuel. As part of global efforts to avoid the worst effects of climate change, the aviation industry needs to make massive reductions in carbon emissions by 2050. Although the industry will need to pursue multiple strategies, large-scale production and use of biomass-derived aviation fuels (known as bio-jet fuels) will play a critical role in decarbonizing the industry (5).

According to The New York Times issue of July 29, 2015, UPS has agreed to purchase 46 million gallons (about 174 million liters) of biodiesel for ground vehicles over the next three years. This corresponds to 12% of the petroleum-based fuel that the vehicles in the fleet consumed by 2017. It is not new for companies whose fuel costs take an important place in their expenses to try alternative fuels to reduce this, create an alternative to the endless petroleum-based fuels, and minimize the damage they cause to the environment. They have used alternatives such as natural gas, electricity, and biofuels before, and they are still using them in increasing amounts (6).

Yamık et al. (2013) (7) investigated the effects of JP-8 aviation fuel and diesel blends on exhaust emissions in a single-cylinder diesel engine. In the study, it was stated that towards the end of the 1980s, NATO countries determined JP-8 fuel as a common military fuel, thus ensuring standardization in the fuel used; It was emphasized that 99.8% of JP-8 fuel consists of kerosene so that the freezing point is below -40 °C. In the study; JP-8 was mixed at 5%, 10%, 25%, and 50% and experiments were conducted. As a result, it was observed that engine torque decreased, specific fuel consumption increased (may be due to low density and low cetane

number), NO_x value decreased and CO value increased as JP-8 addition to diesel fuel increased (8).

In their study on the use of alternative fuels in aviation, Yılmaz and Atmanlı (2016) (7) stated that biofuels have the greatest potential as an alternative to aviation fuels. They stated that biofuels mean less environmental pollution and economic gain compared to fossil-based fuels. In the study, which draws attention to the fact that the International Airline Transport Association (IATA) and the International Civil Aviation Organization (ICAO) support the use of alternative fuels in aviation, they mentioned the necessity of determining important properties such as flash point, octane number and freezing point of the fuel to be used in commercial flights for flight safety. They also emphasized that the alternative fuel to be produced should provide positive results in terms of the raw material from which it will be obtained, the production process, the storage of the fuel, the compliance of its properties with standards, and its transportation. They stated that the biggest obstacle to the use of alcohol as an alternative fuel is the low calorific value and rapid evaporation feature, but in light of technological developments, the chemical properties of alcohols can be changed in the desired direction. As a result, they pointed out that the establishment of new industries for the production of alternative fuels is costly and laborious due to the aviation sector, but they stated that the alternative fuels obtained in the current way can be developed and made compatible with the aviation sector (7).

In an experimental study of the effects of JP-8 Aviation Fuel, Sunflower Oil Methyl Ester, and Diesel Fuel Blends On Combustion and Engine Performance, experimentally investigated the effects of JP-8, sunflower oil methyl ester, and diesel fuel blends (B25, B50, B75, B100, J100, Diesel) on combustion and engine performance. However, cylinder pressure close to diesel was obtained with B100 and J100 fuels. It was observed that as the biodiesel ratio increased, the KA10 value increased and the combustion time decreased. The maximum combustion time was determined as 99 and 97.92 °KA with diesel and J100 fuels, respectively. The maximum pressure increase rate was determined as 6.13 bar/°KA with J100 fuel. Compared to the other test fuels, it was observed that the values of indicated average effective pressure and in-cylinder temperature decreased with diesel. As a result, they stated that JP-8 and biodiesel fuel blends can be used in diesel engines without any modification (9).

1.1. Advantages of Biofuel

- It reduces dependence on petroleum products by creating an alternative to these products.
- It reduces the import expenses of oil-deprived countries and makes a positive contribution to their foreign trade balance.
- It significantly reduces greenhouse gas emissions, carbon monoxide, and particulates.
- Additionally, biofuel significantly increases vehicle performance.

- The lubricating effect of biodiesel extends the life of the vehicle engine.
- Raw material producers, from which biodiesel is produced, have a positive impact on the development of rural areas.
- It increases the income of the local people by opening new job areas.
- The development of the biofuel sector will increase economic development by creating new sub-sectors.
- Biofuel is a renewable energy, so biodiesel and ethanol do not leave any harmful waste to the environment after burning.
- It is easier to store biofuel than other alternative fuels because the existing infrastructure is suitable for it.
- Biofuel will also play a positive role in climate change policies. This is especially important for developing countries (10-16).

1.2. Use of Biofuel in Aviation

The greenhouse gas (GHG) emissions from aviation have been growing steadily in recent decades and this trend is set to continue (17). This is primarily due to the rise in international tourism, where air travel represents the mainstay of tourist demand for transportation between the source and host regions (18). Being the major driver of air travel, tourism makes a substantial economic contribution to the global and national economies. Geographically, 'traditional' or 'established' destinations in Western Europe and North America are forecast to retain their strategic importance in terms of tourist demand. Concurrently, the rapid acceleration of tourist flows is envisaged in so-called 'emerging' destinations, such as those in East-Central Europe and Asia. Given that tourism growth correlates with air travel, these 'new' tourist markets are likely to contribute significantly to the continued rise of GHG emissions due to aviation (19). Aviation biofuel is technically viable and nearing the commercial stage. In the last ten years, biofuels have moved from relative obscurity to a point where certain types of fuel have become fully certified for commercial use in up to 50% blends with standard jet fuel and commercial partnerships between airlines and biofuel producers are being established. The need to develop commercially viable alternatives to traditional fossil-based liquid fuels for commercial aircraft is intensifying. The rising price of crude oil, potential new carbon emissions legislation, the negative environmental externality effects resulting from fossil-fuel consumption (including, but not limited to, atmospheric pollution and anthropogenic climate change), and growing global demand for air travel have collectively motivated research into sustainable fuel alternatives (20). Aviation is the transport type that is showing significant, steady, and quite rapid growth in the EU. The international aviation segment accounts for 12.8% of the energy consumed, whereas domestic aviation uses only 1.54% of the energy (21). Air transport is the most growing transportation sector, and it is expected to increase steadily by the year 2030. International Air Transport Association approximates that the industry will have grown by over 5% annually by the year 2030. It is also estimated that the demand for aviation fuels is to grow at 2 to 3% every year. Various studies have

proved that the aviation fuel used in the past has several negative effects on the environment and with the increasing usage, the situation is said to be affected the most, which has led to various research to establish other sources of energy that will have little effect on the environment. Researchers have settled on biofuels since they contain more energy, are cheaper, leave a less negative impact on the environment, and have less damage on the engine (22). Combustion of fossil fuels and human activities disturb the environment by the emission of greenhouse gases like nitrous oxide, carbon dioxide, methane, etc. The requirement of oils for transport is growing day by day and it is expected to increase by 1.3% per year up to 2030 (2). There is no unique solution available for these complications so alternative ways such as modification in vehicle designs, development in public transport, and replacement of conventional fuels with alternative advanced fuels and fuel technologies are to be found. It is expected that by 2030, the carbon emission from the transport sector and the energy requirement will have increased up to 80%. Air transport has played a significant role in the everyday life of the modern world. The influence of air travel increased worldwide social contact, especially in improving business and marketing (23).

With the use of biofuel in the aviation industry, an alternative to petroleum-based fuels will be created. The 2% contribution of the airline transportation sector to global carbon dioxide emissions will be reduced to lower levels. In addition, its use and dissemination will be faster and easier than in other transportation sectors (3). The aviation industry continues its efforts to produce the most high-performance fuel at the lowest cost and with the lowest environmental impact (24). Food and water, which are the sources of human life, cannot be used for aviation biofuel. Features required for the raw material required to produce aviation biofuel are as follows: It should grow quickly, should not use the areas used for food production, should not be used as food, should not require large amounts of pesticides, fertilizers, or irrigation, should provide a socioeconomic contribution to the people of the region where it is grown, and lastly, should provide the same or more energy than petroleum-derived fuels, while providing less or even zero carbon footprints (25). Biofuel testing is a must to determine whether that biofuel is suitable for use in aviation. As in every part of the aviation industry, there are very strict standards and safety rules when it comes to biofuel testing. This means that before the use of biofuels, dozens of research and tests were carried out both on the ground and in the air. As a result of these long and tiring studies and tests, it is put into use if the suitability of that biofuel is assured. Safety is the most fundamental criterion in aviation. In an environment, where even conventional petroleum-based fuels are put to the test, the testing criteria for biofuels are even more stringent. After the tests in the laboratory environment, the performance of the aircraft from its movement on the ground to its take-off speed is tested in ground tests. In the meantime, the time between the fuel being taken into the engine and its combustion is measured, and the combustion

performance inside the engine, and its reactions to acceleration and deceleration are also measured. After the laboratory and ground tests are completed, the flight performance of the fuel is tested. Many airlines dedicate their planes to testing. Thus, they can provide information on fuel quality, ensure that it is certified for use in the aviation industry, demonstrate that biofuel is safe to use in real flight, and encourage biofuel research and development. During flight, the pilot tests fuel performance both in normal operation and in extreme conditions. After completing the flight checks, the next stage is the certification stage. Certification of the fuel for commercial use is the responsibility of the authorized approval bodies of the relevant countries. The aviation industry works in cooperation with authorized test and approval organizations (26). As the production technology and thus production of sustainable biofuel increases, it will be economically viable and will reach a level that can cope with petroleum-based fuels. Production of biofuel raw materials, especially in developing countries, will contribute to the economic development of both the region and the country (27). Due to the zero carbon emission of biofuel, governments' tax reductions and incentives will increase its production and use. In many countries, research is focused on many different sources (bacteria and solid waste materials) for cheaper and improved biofuels. However, some infrastructure investments are needed to develop and expand the use of biofuel. Such as sufficient raw material production and the need for a refinery to convert this raw material stock into biofuel (28). The aviation industry around the world consumes 1.5-1.7 billion barrels of conventional Jet A1 fuel. Analysts state that it would be possible to say that biofuel production would be economically meaningful if even 1% of this amount was switched to biofuel (15).

2. MATERIALS AND METHOD

2.1. Fuel and Additives Used

The JP-8 fuel we used in the study was obtained from Petrol Ofisi company by obtaining the necessary permissions. The additives used in the study were purchased from various commercial companies. Before the experimental studies, fuel and additive mixtures were prepared and made ready to be used in the test equipment. All of the test studies were carried out in Batman University Technical Sciences Vocational School, Department of Chemistry and Chemical Processing Technologies Fuel Analysis Laboratories.

2.1.1. Jet fuel

JP-8, widely used in the aviation industry and known as jet fuel, was accepted as military fuel by NATO countries in the 1980s. When its chemical structure is examined, this fuel, which consists of 99.8% kerosene, is a fuel obtained by distilling petroleum between 150-270 °C, which is frequently used in industry (29). One of the most important features of this fuel is that its freezing point is below -40 °C. Today, the most commonly used aviation fuels are JET A1, JP-8, JP-4. While others are mostly used in

civil aviation, JP-8 is used in military aviation because it provides the standard and prevents high expenditures (30). Kerosene, which constitutes a large portion of 99.8% of JP-8 fuel, generally contains the following hydrocarbons in its structure, with some differences depending on the production process: Aromatics (20%), kinds of paraffin and iso-paraffins (60%), cyclo-paraffins (20%).

Kerosene is a colorless, oily, rapidly flammable, and pungent liquid produced by distilling petroleum (10-25% of the total volume). It is a mixture of 10 different types of simple hydrocarbons obtained from different sources. The carbon chain mixture obtained as a result of fractional distillation generally contains between 6 and 16 carbon atoms per molecule. It is less volatile than gasoline and boils at temperatures between 150 and 275 °C. It is generally burned in lamps, heaters, and stoves, and is also used as fuel or as a fuel component in diesel and tractor engines. It is also used as a solvent in jet engines, rockets, and greases or as an herbicide (insecticide). Kerosene is sometimes used as an additive in diesel fuels to prevent gelation and waxing that may occur in low-temperature operations. Paraffin in the structure of gasoline, diesel, and kerosene obtained from petroleum cannot be used in aircraft because it reduces fluidity at low temperatures. In addition to its high flammability, kerosene is widely used as fuel in jet engines because it maintains its fluidity at low temperatures (31). Kerosene is released by the fine distillation of petroleum between 150-270 °C. The freezing point of kerosene, which has a flash point of 40 °C, is between -47 °C and -49 °C. The most commonly used fuel types containing kerosene in jet fuels are; JET-A, JET-A1, JET-B, JP-4, JP-5, and JP-8 (28) According to an oil report by EMRA, 4.786 million tons of jet fuel was produced in Turkey in 2018. The most commonly used fuel types containing kerosene in jet fuels are JET-A, JET-A1, JET-B, JP-4, JP-5, and JP-8 (32).

JP-8 is a kerosene-based jet fuel developed by the United States in 1990. This fuel replaced JP-4 fuel by the US Air Force in the fall of 1996, as it is a lower flammable, less harmful fuel, safer, and has better combat survivability. The US Navy also uses JP-5 fuel of a similar formulation. This fuel was first used in NATO bases in 1978. Its NATO code is F-34. The flash point of JP-8 is 38 °C, which is higher and safer than the -18 °C flash point of JP-4. JP-5 has an even higher flash point (>60 °C) but is also costly. In addition to fueling aircraft, JP-8 (or JP-5) is used as a fuel for heaters, furnaces, and gas tanks, as a substitute for diesel gasoline in the engines of almost all tactical ground vehicles by the US military forces, and as a coolant in electric generators and in some aircraft components. The use of a single type of fuel greatly simplifies logistics (8). Figure 1 was also developed by ALS for the quantitative analysis of non-volatile hydrocarbons in the C10-C40 range after non-polar solvent (hexane) extraction. The extract is analyzed by a gas chromatograph (GC) with a flame ionization detector (FID).

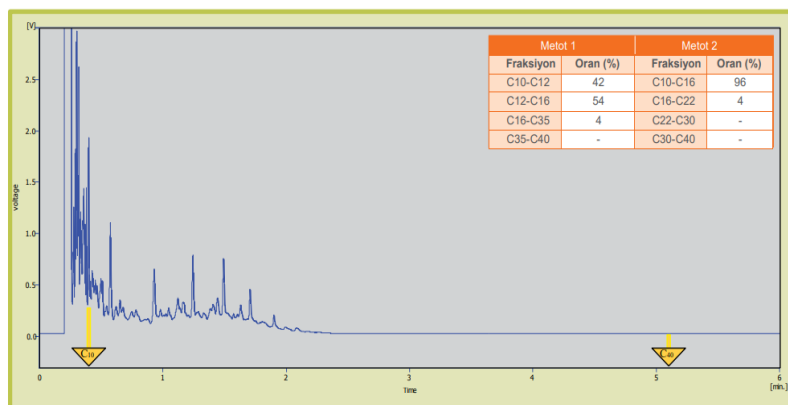


Figure 1¹: JP-8 Gasoline carbon range analysis by Chromatographic Method GC/FID (33).

Table 1 shows the chemical and physical properties and test methods of JP-8. In addition to this information, we examined the basic chemical and physical properties of JP-8 fuel in the laboratory environment before using it in experiments. JP-8 is a kerosene-type aviation fuel containing a military fuel additive package: Static Dissipative Additive (SDA), Lubricity Improver Additive (LIA) (formerly referred to as anti-corrosion/lubricity enhancer additive), and

Fuel System Anti-Icing (FSII-3) and Antioxidant (AO) and Metal Deactivator Additive (MDA). F-34 is used by land-based military gas turbine-powered ground vehicles and equipment in all NATO countries. It is also known as F-34, JP-8, or AVTUR/FSII (32). Table 1. and Table 2. "References and technical approval processes of fuels defined according to ASTM" and "Compositional Data for JP-8" are given respectively.

Table 1: Chemical and Physical properties and test methods of JP-8 (34).

Specifications	Unit	Min	Max	ASTM or IP Test Method
Color				D156 or D6045
Total number of acids aromatics	(mg KOH/g)		0.015	D3242
Sulfur	v/v		25.0	D1319
Sulfur, mercaptan	w/w%		0.30	D129, D1266, D2622, D3120
Flash point	w/w%		0.002	D3227
Density (at 15 °C)	°C	38		D56, D93 , D3828
API (at 60 °F)	kg/L	0.775	0.840	D1298, D4052
Freezing point		37.0	51.0	D1298, D4052
Viscosity (at -20 °C)	°C		-47	D2386 , D5972, D7153
Net heat of combustion	mm ² /s		8.0	D445 or D7042
Hydrogen content	MJ/kg	42.8		D3338, D4529
Smoke point	w/w%	13.4		D3343, D3701, D5291
	mm	25.0		D1322
Corrosion				
Copper strip corrosion, 2 hours at 100 °C (212 °F)			No. 1	D130
THERMAL STABILITY				
Thermal stability (2.5 hours at 260 °C) 10				D3241
Change in pressure drop, mm Hg			25	
Tube rating: One of the following requirements must be met: (1) Annex A1 VTR or (2) Annex A3 ETR or Annex A2 ITR, mean deposit thickness, nm, over 2.5 mm ² area			<3	
ADDITIVES				
Fuel system anti-icing, volume percentage		0.07	0.10	D5006
Fuel electrical conductivity, pS/m 12				D2624

¹ Note: Metot is Method, Fraksiyon is Fraction, Oran is Ratio in the figure.

CONTAMINANTS		
Current gum, mg/100 mL	13	7
Water reaction interface degree		1b
Microseparometer Degree	14	D381 or IP 540 D1094 D3948 or D7224

Table 2: Compositional Data for JP-8 (35).

Compound	Weight (%)
Alkenes	
Tridecene	0.73
Alkyl aromatic	
m-Xylene	0.060
o-Xylene	0.060
1,2,3-Trimethylbenzene	0.27
1,2,3,4-Tetramethylbenzene	1.1
1,3-Dimethyl-5-ethylbenzene	0.62
1-Methyl-2-isopropylbenzene	0.56
1,2,4-Triethylbenzene	0.99
1,3,5-Triethylbenzene	0.60
n-Heptylbenzene	0.25
n-Octylbenzene	0.61
1-Ethylpropylbenzene	0.99
Branched paraffin	
3-Methyloctane	0.040
2,4,6-Trimethylheptane	0.070
2-Methyldecane	0.41
2,6-Dimethyldecane	0.66
2-Methylundecane	1.2
2,6-Dimethylundecane	2.1
Naphthenes	
1,1,3-Trimethylcyclohexane	0.060
1,3,5-Trimethylcyclohexane	0.060
1-Methyl-4-ethylcyclohexane	0.10
Propylcyclohexane	0.14
n-Butylcyclohexane	0.74
Hexylcyclohexane	0.93
Phenylcyclohexane	0.87
heptylcyclohexane	1.0
Diaromatics <i>excluding</i>	
naphthalenes	
Biphenyl	0.63
n-Paraffins	
n-Heptane	0.030
n-Octane	0.090
n-Nonane	0.31
n-Decane	1.3
n-Undecane	4.1
n-Dodecane	4.7
n-Tridecane	4.4
n-Tetradecane	3.0
n-Pentadecane	1.6
n-Hexadecane	0.45
n-Heptadecane	0.080
n-Octadecane	0.020
Naphthalenes	
Napthalene	1.1
1-Methylnapthalene	1.8
2-Methylnapthalene	1.5
1-Ethylapthalene	0.33
2,3-Dimethylnapthalene	0.36
2,6-Dimethylnapthalene	1.3

2.1.2. Methanol

The use of alcohol as an alternative to fuel has a long history. However, the cost of production processes has hindered their widespread adoption. Increasing oil prices have allowed alcohol to become widespread in recent years. Methyl alcohol was used as an active ingredient in this research due to its potential to be used in many fuel studies and to ensure its continuity in our country (36). Technical properties of methanol are given in Table 3.

Table 3: Technical Properties of Methanol.

Specifications	Explanations
Chemical Name	Methanol
Chemical Formula	CH ₃ OH
Appearance	Clear Liquid
Molar Mass	32.04 g/mol
Melting point	-97.6 °C
Cas Number	67-56-1
Density	792 kg/m ³

2.1.3. Ethanol

Thanks to the high octane number of alcohols, allows them to be used even at high compression ratios (37). Ethyl alcohol, due to its structure, has the feature of increasing engine performance while reducing emissions when used as fuel. In this study, we wanted to see what effect ethyl alcohol could have on jet fuel. Technical properties of ethanol are given in Table 4.

Table 4: Technical Properties of Ethanol.

Specifications	Explanations
Chemical Name	Ethanol
Chemical Formula	C ₂ H ₅ OH
Appearance	Colorless Liquid
Molar Mass	46.07 g/mol
Melting Point	-114.1 °C
Cas Number	64-17-1
Density	789 kg/m ³

2.1.4. Isopropanol

This type of alcohol, known by names such as isopropyl alcohol, and IPA, is similar to ethyl alcohol in terms of its structure and is used more as a solvent in industry. We used this type of alcohol as an additive substance in our study because it can be dissolved well with fuels in any ratio and has a strong oxidizing effect. The technical characteristics of isopropanol are given in Table 5.

Table 5: Isopropanol Technical Characteristics.

Specifications	Explanations
Chemical Name	<i>Isopropanol</i>
Chemical Formula	C ₃ H ₈ O
Appearance	Colorless Liquid
Molar Mass	60.1 g/mol
Boiling Point	82.5 °C
Cas Number	67-63-0
Density	786 kg/m ³

2.1.5. Anti-Icing (diethylene glycol monomethyl ether (di-EGME))

In the chemical and dyeing industries, nitrocellulose is used as a solvent for resins and solvents. Purified di-EGME (>99%) is also used as a solvent in cosmetic and dermatological preparations. Di-EGME increases percutaneous absorption through the skin in some pharmaceutical products and it is used in pharmaceutical products in Turkey. Di-EGME is used in shampoos (rinse) at a concentration of up to 5% and conditioners (leave-in) at a concentration of up to 2%, in toiletries, skincare, hair care, or sun care products. It should not be used in products for oral hygiene.

Being a colorless liquid, its use as a solvent for dyes, nitrocellulose, decoctions, and resins stands out among the applications of di-EGME. It is a component of twisting, and conditioning yarns and wood dyes in textile printing products, textile soaps, lacquers, penetration enhancers in cosmetics, drying lacquers, enamels, and brake fluids. Mineral oil soap is used as a neutral solvent in mineral oil-sulfated oil mixtures (by giving fine dispersions in water) and for determining the saponification values of oils. Di-EGME is a very polar, slow-evaporating, water-miscible, odorless solvent. It is an active solvent for cellulose acetate, nitrocellulose, epoxy resins, and many other coating materials. Although diethylene glycol methanomethyl ether is a flammable liquid, it is stable under the recommended conditions. Storage containers made of carbon steel, stainless steel, or phenolic-lined steel are recommended for storage

and preservation. It should also be avoided from contact with strong acids, strong bases, and strong oxidizers. Diethylene glycol monomethyl ether should not be distilled until it is completely dry because it can form unstable peroxides. Diethylene glycol monomethyl ether can be oxidized at high temperatures. Thermal decomposition products may include, yet are not limited to: aldehydes, ketones, and organic acids. The pouring of glycol ethers, including di-EGME, on hot fibrous insulation can lead to a decrease in self-ignition temperatures and possibly spontaneous combustion since it is a flammable liquid and stable under the recommended conditions. The technical characteristics of dietary glycol monomethyl ether are given in Table 6.

Table 6: Technical Characteristics of Diethylene Glycol Monomethyl Ether.

Specifications	Explanations
Chemical Name	Diethylene Glycol Monomethyl Ether
Chemical Formula	C ₅ H ₁₂ O ₃
Appearance	Colorless Liquid
Molar Mass	120.148 g/mol
Boiling Point	194 °C
Cas Number	111-77-3
Density	1020 kg/m ³
Freezing Point	-69 °C

2.2. The Effects of Additives Used in the Study on Fuel Properties

In this study, additives such as methanol, ethanol, isopropanol, and anti-icing were added to jet fuel (JP-8) in the proportions of 2%, 5%, 7%, and 10% and the fuel properties such as density, viscosity, flash point and freezing point of the obtained mixtures were examined. In Table 7, the cumulative results of all experiments with additives added to JP-8 fuel are given. In addition to the results of the pure states of the fuel and additives, the results of the effects of each of the additives added to the jet fuel in the specified proportions on the fuel properties are also seen in the table.

Table 7: Fuel properties of JP-8 and additives used in the study.

(%)	Fuels / Properties	Density 15 °C (kg/m ³)	Kinematic Viscosity 40 °C (mm ² /s)	Flash Point (°C)	Freezing Point (°C)
	Jet fuel (JP-8)	797.0	1.198	46.0	-56.7
Pure	Methanol	793.0	0.597	12.0	-97.8
	Ethanol	795.0	1.102	13.0	-114.1
	isopropanol	789.0	1.768	11.7	-89.0
	Anti-Icing	1020	3.680	96.0	-69.0
	2%	Methanol	796.8	1.156	45.3
Ethanol		796.9	1.160	45.5	-58.6
isopropanol		796.1	1.201	45.0	-56.2
Anti-Icing		799.8	1.410	47.4	-56.3
5%	Methanol	796.5	1.144	43.9	-57.9
	Ethanol	796.7	1.140	44.6	-59.2
	isopropanol	795.6	1.255	44.4	-56.8

	Anti-Icing	803.4	1.530	50.1	-55.8
7%	Methanol	796.1	1.126	42.0	-59.8
	Ethanol	796.5	1.138	44.0	-60.8
	isopropanol	795.0	1.270	43.7	-57.0
	Anti-Icing	808.6	1.750	53.3	-55.1
10%	Methanol	795.5	1.109	40.0	-61.7
	Ethanol	796.2	1.130	43.4	-62.1
	isopropanol	794.4	1.298	42.9	-57.6
	Anti-Icing	814.5	1.980	55.4	-54.6

2.2.1. Density Change

Density is an important quality parameter for gasoline, diesel jet fuel, and all other fuels. It is used to define the product and determine other characteristics. A high density also means that for international product trade, it means the transport of more energy in a low volume. Density (also known as specific gravity) is an indicator of the amount of weight that falls per unit volume of fuel. Density is a basic parameter for all fuels. As the density increases, the amount of energy per unit volume also increases. Since the energy contained by each hydrocarbon in the fuel is different, the types and quantities of components in the jet fuel mixture are very important. Since the density of a fuel is a manifestation of the chemical structure of its composition, it also has the property of being an indicator of its energy value. In general, when looking at fuels with a low density, it is seen that their gravimetric energy content is high, and those with a high density have an excess of volumetric energy

content. Fuels with high volumetric energy, that is, excess density, are preferred in aircraft. Because the volumetric energy per unit volume is greater, the aircraft can travel longer distances with a tank of fuel. As shown in Figure 6, the density of pure JP-8 is higher than pure methanol, ethanol, and isopropanol; and since the mentioned alcohols are added to JP-8 in the specified proportions, it appears that there is a partial, if not a lot, decrease in the density of the resulting fuel mixture. However, since the density of the anti-icing additive used in the study is much higher than JP-8, it has been found that there is a relative increase in the density of the fuel mixtures obtained when JP-8 is added in the specified proportions. This means that if the fuel is injected into the engine at a constant rate, the energy supplied to the engine increases with intensity and thus the engine performance will increase. On the other hand, it can be said that as the density decreases, volumetric fuel consumption will increase due to the above-mentioned reasons.

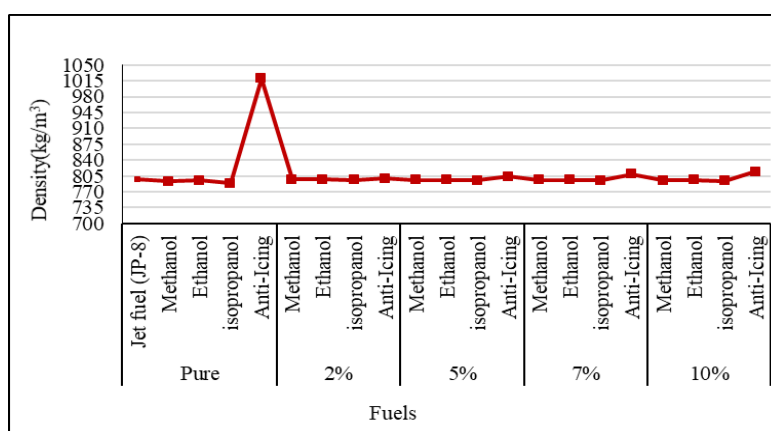


Figure 6: Changes in the density of additives used in pure form and the specified proportions.

2.2.1. Viscosity Change

Viscosity is the resistance of a liquid or gaseous fluid to flow. In other words, it is called the resistance that a liquid or gaseous fluid exhibits to the displacement of a part relative to a part next to it. Viscosity, translated into our language as fluidity, can also be considered as the deceleration force between molecules since the part forced into motion for a fluid will also drag its adjacent parts with it. Such a force prevents the formation of velocity differences in the fluid. For fluids to be transmitted from one place to another by pipelines or to be used as a lubricating material, viscosity is one of the most important factors in determining the forces that resist the flow. In addition, viscosity is used in the regulation of liquid flow in processes such as " spray casting,

spraying, and surface coating". As a result of increasing temperature, the viscosity of liquids decreases, while the viscosity of gases increases rapidly. Therefore, when liquids are heated, liquids flow more easily, but gases are more difficult. Along with this, as the fuel viscosity decreases, it will cause a significant power loss, as there will not be enough fuel supply in the engine as a result of leaks. The high viscosity of the fuel may cause the injection pump not to provide enough fuel to fill the fuel chamber. Failure to provide enough fuel will again cause a loss of power in the engine. Jet fuel should be able to flow easily from the fuel tank located on the wings of the aircraft to the engines through the aircraft fuel system. As the temperature drops as the altitude increases, the fuel in the aircraft's tanks cools down,

in the same way that the fuel in the tanks on the ground faces the risk of freezing during the winter seasons. Under all conditions, jet fuel should maintain its fluidity, it must not freeze, that is, not become viscous. Because the viscosity and freezing points of kerosene-type jet fuels are higher than those of wide-cut jet fuels, they are less suitable for cold climatic conditions. One of the physical properties of jet fuel is the freezing point and viscosity, which are important criteria for its fluidity. Jet fuel is injected into the combustion section of the turbine engine through nozzles. The system sprays the fuel droplets into a fine spray, allowing them to mix with air, while also triggering their immediate evaporation. The size and shape of the droplets in question are related to the viscosity of the fuel. If the viscosity of the fuel is higher than the required value, the engine is forced while taking off. This causes the pressure to drop in the fuel system lines and the fuel pump to operate with excess power to maintain a constant fuel flow rate. For these reasons, the viscosity is limited to the maximum values in the specifications (38). Too high viscosity prevents the jet fuel from being atomized sufficiently. Aircraft engine fuel systems, fuel lines, valves, and pumps are of minimum size and weight and are designed to operate with liquid fuels within a specific viscosity range. Since the viscosity of jet fuels depends largely on temperature, the viscosity of the fuel at the minimum operating temperature should be known. In addition, the effect of viscosity on fuel atomization is important. The performance of pressurized sprayers and air-assisted sprayers largely depends on the fuel viscosity. The subsequent evaporation of the fuel and mixing of the fuel with air to form a flammable mixture depends greatly on the

performance of the fuel nozzle. Engine manufacturers specify a maximum fuel viscosity of 12 centistokes for reliable engine start-up performance, which will limit engine start-up to temperatures of -20 to -30 °C when using JP-5, JP-8, Jet A, or Jet A-1 kerosene fuels. Kinematic viscosity is determined by measuring the time it takes for a fixed volume of fuel to flow through a calibrated capillary tube at a predetermined temperature. The viscosity is calculated from the flow time and the capillary tube diameter and length. In the 1940s and 1950s, the standard viscosity test temperature was -40 °C, but in recent years, international standardization agencies have decided on a -4 °C test temperature. The standard viscosity test method is ASTM D 445, Transparent and Opaque Kinematic Viscosity (39). Figure 7 shows the kinematic viscosity (1.198 mm²/s) of JP-8 used in the study is higher compared to methanol and ethanol used as additives (0.597 and 1.102 mm²/s, respectively). Therefore, it has been observed that when these alcohols are added to JP-8 in the specified proportions, the viscosities of the fuel mixtures obtained also decrease relatively. This is a fact that fuel can easily flow into the engine due to the low viscosity of the fuel as the aircraft rises higher. The viscosities of the isopropanol and anti-icing additives we used in the study (1,768 and 3,680 mm²/h, respectively) are higher than JP-8, and it is observed that the values of the mixtures obtained as a result of measurements partially increase when they are added to the fuel at the rates indicated in our experimental studies. It is expected that this situation can be tolerated and that the addition of these additives to the fuel at the specified rates will not create a problem on flights.

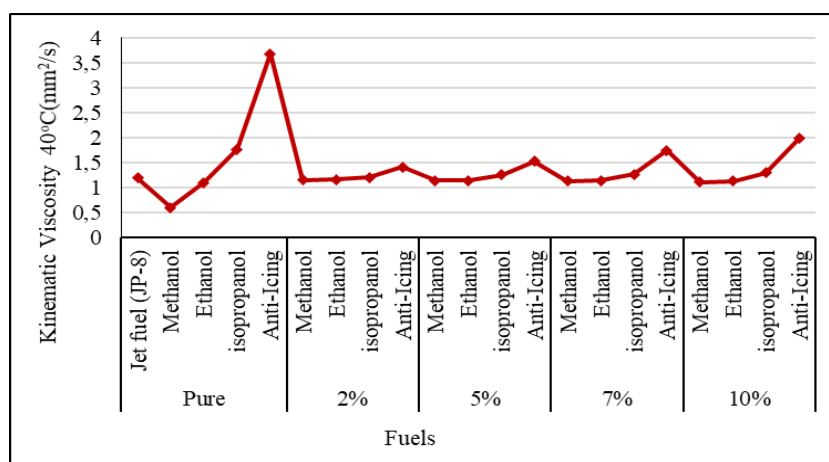


Figure 7: Changes in the kinematic viscosity of additives used in the pure state and the specified proportions.

2.2.1. Flashpoint Exchange

A flash point is the lowest temperature at which a sample of a flammable substance causes its vapor to ignite under certain conditions, according to ASTM. The flash point is one of the most important criteria for determining the hazard of flammable liquids. It can also be called the lowest temperature value that a flammable liquid can produce enough vapor to create a one-second flame. The flash point is often confused with the spontaneous ignition temperature.

The flash point is the lowest temperature at which the fuel vapor will continue to burn even after the ignition source has been removed from the environment. The flame point is higher than the flash point, because at the flash point, steam may not be released quickly enough to keep the combustion going. The flash point is not directly related to the ignition source temperature; however, the ignition source temperature is higher than the flash point. Among the flammable fuels, the flash point is a

distinctive feature. The flash point is also an important parameter for defining the fire hazards of fuels. Fuels with a flash point of less than 37.8 °C are defined as flammable, while fuels with a flash point above this temperature are also called flammable fuels. In gas turbines and jet engines, fuels with a higher flash point and at low cost are preferred. It is safer to transport and process such fuels. The flash point of a liquid is defined as the lowest temperature at which it produces enough vapor to create a "vapor/air" mixture that can ignite (pilot ignition). The vapor pressure of the liquid at this temperature ensures a vapor concentration equal to the lower flammability limit. If ignition is attempted when the liquid reaches the flash point, a flare flame will form, but the flame will not continue. The cloud will burn and the fire will go out on its own because the energy released as a result of combustion is transferred to the remaining fuel and is not enough to produce enough steam in the remaining fuel. Since the flash point is the lowest temperature at which there is a risk of fire with a certain liquid, it is an important concept in fire

investigation and fire protection. It is very important in many cases to detect the presence of certain liquids during the investigation process and to know the flash points (40). The flash point is very important for fuels with a low carbon content. The JP-8's flash point (36 °C) is quite high and safe compared to the JP-4's flash point (-18 °C). As can be seen in Figure 8, the flash points of methanol (12 °C), ethanol (13 °C), and isopropanol (11.7 °C) are much lower than JP-8. Although the values indicated in the study are not very high when these alcohols are added to JP-8, it is observed that the flash points of the mixtures partially decrease. However, it is thought that this amount of decrease will not pose any problems in the transportation and processing of fuel. Since the flash point (96 °C) of the anti-icing additive we used in the study is much higher than JP-8, the flash points of the mixtures were measured as 47.4 °C, 50.1 °C, 53.3 °C and 55.4 °C, respectively when 2, 5, 7 and 10% were added to the fuel (JP-8). According to these obtained values, it is seen that the transportation and use of fuel mixtures have reached a more reliable point.

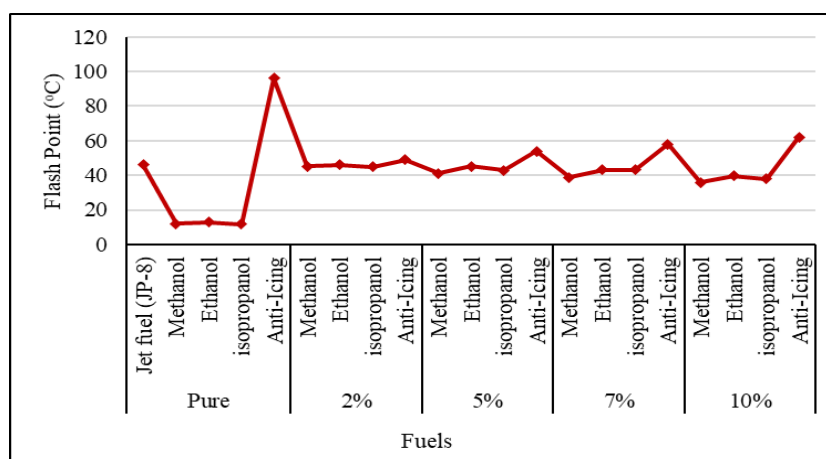


Figure 8: Changes in the flash point of additives used in pure form and the specified proportions

2.2.1. Freezing Point Change

The freezing point in jet fuels is defined as the temperature at which the last wax crystals contained in the test sample, which are cooled until wax crystals are formed, also melt when heated. In this case, the freezing point is a higher temperature than the solidification point of the fuel. One of the most important features of a fuel system is the performance of pumping the fuel contained in the tanks into the engine. The ability of the pump-to-pump fuel also depends on the fluidity of the fuel and the design of the system. When conducting tests related to fuels, the freezing point of the fuel is taken as the criterion for pumping at a low temperature. Jet fuels can be pumped even at temperatures 4°C-15 °C lower than the freezing point. It is the ability of the fuel to be used in cold weather. Fuel molecules that cool down to a certain temperature crystallize, and freeze when the temperature drops further. Crystallized fuel blocks the fuel system, preventing the flow of fuel. For these eight reasons, the freezing point of fuels should be between 5 and -10 °C lower

than the outside air temperature of the region. The freezing point is very important for the transfer of fuel from the tank to the engine while the engine is cold and during the first movement (41). Although there is no direct relationship between the freezing point and the viscosity, the freezing point increases or decreases with the viscosity. The high freezing point causes initial movement difficulties if the heating of the fuel is excluded. During the operation of the engines at temperatures near the freezing point, the fuel filters become clogged. Therefore, the required freezing point depends on the lowest operating temperature of the machine (42). As can be seen in Figure 9, the freezing points of the alcohols and anti-icing we used in the study are much lower than JP-8. Therefore, it has been found that when these additives are added to JP-8 at the specified rates (2, 5, 7, and 10%), the freezing points of the new fuels obtained gradually decrease. It is also believed that problems such as fuel freezing cannot occur by increasing the altitude of aircraft in this situation.

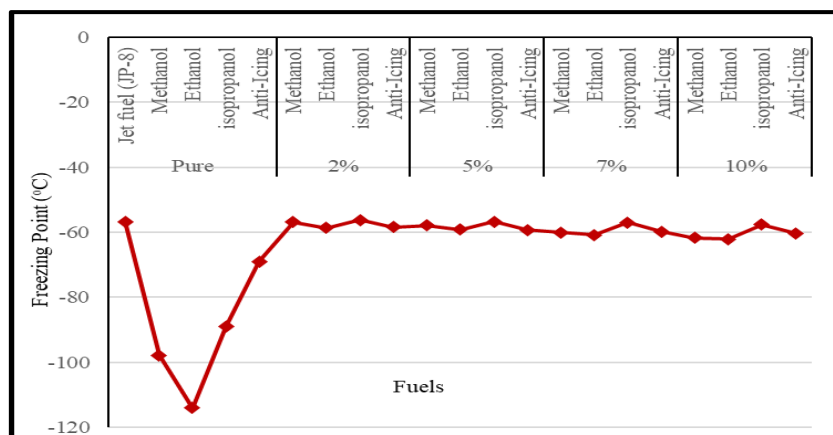


Figure 9: Changes in the freezing point of additives used in the pure state and the specified proportions.

3. DISCUSSION

1. Like many countries in the world, our country is a country with very low reserves in terms of fossil fuels. This situation leads to the export of domestic capital along with its dependence on foreign energy.

2. With its growing population, Turkey has become an important center in Europe, Central Asia, and the Middle East in the industry and defense industry, especially in the energy field.

3. In recent years, our country has reached a very important point in the production and use of renewable energy sources. According to the data for the last quarter of 2021, 55% of the total energy production was produced from domestic and renewable energy sources.

4. The importance of biofuels among renewable energy sources is quite high. In this sense, the importance of fuels such as bioethanol, biomethanol, biodiesel, bioisopropanol, biogas, and hydrogen is increasing day by day.

5. Ethanol, methanol, and isopropanol, which are used as additives in this study, can be used as fuel alone, or they can also be used by adding them to some fuels to improve certain properties.

6. The densities of the alcohols (ethanol, methanol, isopropanol) used in the study are lower than JP-8 fuel. When 2%, 5%, 7%, and 10% of these alcohols were added to JP-8 fuel, the densities of the mixtures formed decreased slightly compared to the density of JP-8 fuel. The decrease in the density of the fuel with the addition of these alcohols will also lead to a decrease in energy values. However, it is thought that this small amount of energy decrease that will occur will be at a tolerable level. In addition, apart from the above-mentioned alcohols, the density of the anti-icing agent added to the fuel is much higher compared to JP-8 fuel and pulls the density of the mixture up with an increase in the additional ratio. In this case, it is expected that the energy value of the fuel mixture will increase.

7. In particular, the viscosities of the fuels used in aircraft are of great importance. Since the viscosity of the methanol used in the study (0.597 mm²/s) is low compared to the viscosity of JP-8 fuel, it was also found that the viscosity of the mixture decreases as the proportion of methanol mixed into the fuel increases. In this way, it will be possible for the fuel to flow more easily from the tank to the engine. Since the viscosity value of ethanol is 1.10 and it is very close to our main fuel JP-8 fuel, it has been found that there is no significant change in the viscosity value of the mixture when mixed at 2%, 5%, or 7% and 10% rates. However, since the viscosity values of isopropanol and anti-icing additives (1.768 and 3.680) are very high compared to JP-8 fuel, it has been observed that there is a significant increase in the viscosity of the new blend fuels formed when added to the main fuel at the specified rates in the study. However, it is thought that these increases are at a level that will not pose a problem caused by viscosity during flight.

8. One of the important features of jet fuels is the flash point. Since the flash point values of the alcohols used in the study (12, 13, 11, 7) were much lower than JP-8, fuel, the flash point values of the fuel mixtures obtained when the specified amounts were added to the main fuel decreased relatively. However, it is thought that these reduced amounts will not carry a risk in the transportation and processing of fuel. The flash point (96 °C) value of the anti-icing used as an additive is quite high compared to JP-8. It is observed that the flash point values of fuel mixtures formed when added to the main fuel at the rates indicated in the study also gradually increase. With the increase in the flash point value, the transportation and use of fuel mixtures have become even more reliable.

9. One of the most important features sought in jet fuels is the freezing point of the fuel. The freezing point of JP-8 used in the study is -56.7 °C and is higher than all of the additives used. In this case, it has been observed that the freezing point values of fuel mixtures gradually decrease with additives added to the fuel at the rates of 2%, 5%, 7%, and 10%. Aircraft cruising at very high altitudes are exposed to low temperatures. These low temperatures bring with them the risk of freezing of

fuels. As mentioned above, it is believed that these risks will be reduced thanks to the freezing point, which is significantly reduced by additives added to jet fuel in various proportions.

4. REFERENCES

1. Çolakoğlu M, Aslan S, Kumdereli E. Biyokütle ve Biyoenerji Sektörlerine Genel Bakış [Internet]. 2021. Available from: [<URL>](#).
2. Acar A. Unlocking demand-side response in Turkey: A white paper [Internet]. 2020 [cited 2024 May 9]. Available from: [<URL>](#).
3. Cabrera E, de Sousa JMM. Use of Sustainable Fuels in Aviation—A Review. *Energies* [Internet]. 2022 Mar 26;15(7):2440. Available from: [<URL>](#).
4. IRENA (International Renewable Energy Agency). Renewable Power: Sharply falling generation costs [Internet]. 2017 [cited 2024 May 9]. Available from: [<URL>](#).
5. Graver B, Zheng XS, Daniel R, Mukhopadhaya J, Pronk E. Vision 2050 Aligning Aviation with The Paris Agreement [Internet]. 2022. Available from: [<URL>](#).
6. Aksoy T. Ups'in Biyodizel Yatırımı ve Havacılıkta Biyoyakıt Kullanımı [Internet]. 2015 [cited 2024 May 7]. Available from: [<URL>](#).
7. Yamik H, Calam A, Solmaz H, İçingür Y. Effects of Diesel and JP-8 Aviation Fuel Blends on Engine Performance and Exhaust Emissions in A Single Cylinder Diesel Engine. *J Fac Eng Archit Gazi Univ* [Internet]. 2013;28(4):787–93. Available from: [<URL>](#).
8. N. Yılmaz, A. Atmanli Investigation of Alternative Fuel Utilization in Aviation. *Journal of Sustainable Aviation Research*, (2016),1(1), 3-10.
9. Solmaz H, Yamik H, Uyumaz A, Polat S, Yılmaz E. An Experimental Study on The Effects of Diesel and Jet-A1 Fuel Blends on Combustion, Engine Performance and Exhaust Emissions in A Direct Injection Diesel Engine. *J Therm Sci Technol* [Internet]. 2016;36(2):51–60. Available from: [<URL>](#).
10. Pulyaeva VN, Kharitonova NA, Kharitonova EN. Advantages and Disadvantages of the Production and Using of Liquid Biofuels. *IOP Conf Ser Mater Sci Eng* [Internet]. 2020 Dec 1;976(1):012031. Available from: [<URL>](#).
11. Khan MAH, Bonifacio S, Clowes J, Foulds A, Holland R, Matthews JC, et al. Investigation of Biofuel as a Potential Renewable Energy Source. *Atmosphere* [Internet]. 2021 Oct 3;12(10):1289. Available from: [<URL>](#).
12. Datta A, Hossain A, Roy S. An Overview on Biofuels and Their Advantages and Disadvantages. *Asian J Chem* [Internet]. 2019 Jul 7;31(8):1851–8. Available from: [<URL>](#).
13. Perritano J. Top 10 Advantages of Biofuels [Internet]. [cited 2024 May 7]. Available from: [<URL>](#).
14. Torkashvand M, Hasan-Zadeh A, Torkashvand A. Mini Review on Importance, Application, Advantages and Disadvantages of Biofuels. *J Mater Environ Sci* [Internet]. 2022;13(6):612–30. Available from: [<URL>](#).
15. Jeswani HK, Chilvers A, Azapagic A. Environmental sustainability of biofuels: a review. *Proc R Soc A Math Phys Eng Sci* [Internet]. 2020 Nov 25;476(2243):20200351. Available from: [<URL>](#).
16. Gürçam S. Global commercial aviation policies in the context of the climate crisis and an analysis of these approaches from the perspective of Türkiye. *Environ Res Technol* [Internet]. 2022 Sep 30;5(3):227–40. Available from: [<URL>](#).
17. Peeters PM, Eijgelaar E. Tourism's climate mitigation dilemma: Flying between rich and poor countries. *Tour Manag* [Internet]. 2014 Feb 1;40:15–26. Available from: [<URL>](#).
18. Scott D, Peeters P, Gössling S. Can tourism deliver its "aspirational" greenhouse gas emission reduction targets? *J Sustain Tour* [Internet]. 2010 Apr 1;18(3):393–408. Available from: [<URL>](#).
19. Filimonau V, Mika M, Pawlusiński R. Public attitudes to biofuel use in aviation: Evidence from an emerging tourist market. *J Clean Prod* [Internet]. 2018 Jan 20;172:3102–10. Available from: [<URL>](#).
20. Prussi M, O'Connell A, Lonza L. Analysis of current aviation biofuel technical production potential in EU28. *Biomass and Bioenergy* [Internet]. 2019 Nov 1;130:105371. Available from: [<URL>](#).
21. Gegg P, Budd L, Ison S. The market development of aviation biofuel: Drivers and constraints. *J Air Transp Manag* [Internet]. 2014 Jul 1;39:34–40. Available from: [<URL>](#).
22. Mohsin R, Kumar T, Majid ZA, Kumar I, Manickam Wash A. Assessment of Usage of Biofuel in Aviation Industry in Malaysia. *Chem Eng Trans* [Internet]. 2017 Mar 20;56:277–82. Available from: [<URL>](#).
23. Kandaramath Hari T, Yaakob Z, Binitha NN. Aviation biofuel from renewable resources: Routes, opportunities and challenges. *Renew Sustain Energy Rev* [Internet]. 2015 Feb 1;42:1234–44. Available from: [<URL>](#).
24. Şen Y, Erdağ T. Evaluation of Air Transport Sector Development Stages with Pest Analysis: An Investigation in The Scope of 5 Periods+Covid-19 Pandemic Process Period. *TroyAcademy* [Internet]. 2021;6(2):422–61. Available from: [<URL>](#).
25. Bengisu G. Bioethanol as an Alternative Fuel Source. *Alinteri Zirai Bilim Derg* [Internet]. 2014;27(2):43–52.
26. Department of Defense Test Method Standard, Environmental Engineering Considerations and

Laboratory Tests, MIL-STD-810H. US Government Printing Office; 2003.

27. Çelebi AK, Uğur A. Fiscal Incentives for Biofuels: An Evaluation Turkey. Hacettepe Univ J Econ Adm Sci [Internet]. 2015 Aug 24;33(2):25–45. Available from: [<URL>](#).
28. Avcı M. Investigation of the Effect of Alcohol and Anti-Icing Additives on the Properties of Jet Fuel. Batman University Graduate School of Education; 2022.
29. Van Dyk S, Saddler J. Progress in Commercialization of Biojet /Sustainable Aviation Fuels (SAF): Technologies, potential and challenges [Internet]. 2021 [cited 2024 May 9]. Available from: [<URL>](#).
30. Drown DC, Harper K, Frame E. Screening vegetable oil alcohol esters as fuel lubricity enhancers. J Am Oil Chem Soc [Internet]. 2001 Jun 1;78(6):579–84. Available from: [<URL>](#).
31. Edwards T. "Kerosene" Fuels for Aerospace Propulsion - Composition and Properties. In: 38th AIAA/ASME/SAE/ASEE Joint Propulsion Conference & Exhibit [Internet]. Indianapolis: American Institute of Aeronautics and Astronautics; 2002. Available from: [<URL>](#).
32. Heath E. Air Force JP-8 Fuel Distribution System: A Statistical Analysis to Determine Where and When to Sample [Internet]. Theses and Dissertations. Air Force Institute of Technology; 2005. Available from: [<URL>](#).
33. ALS Türkiye. Petrol Ürünleri Kütüphanesi ve Diğer Organik Bileşikler [Internet]. [cited 2024 May 7]. Available from: [<URL>](#).
34. NATO. Turbine Fuels, Aviation, Kerosene Types, NATO F-34 (Jp-8), NATO F-35, And Jp-8+100 [Internet]. 1992. Available from: [<URL>](#).
35. ATSDR (Agency for Toxic Substances and Disease Registry). Toxicological Profile for JP-5, JP-8, and Jet a Fuels [Internet]. Available from: [<URL>](#).
36. Reşitoğlu İA, Keskin A. Exhaust Emission Characteristics of Gasoline Engine Fuelled Propane-Methanol. Karaelmas Sci Eng J [Internet]. 2018;8(2):505–9. Available from: [<URL>](#).
37. Keskin A. The Influence of Ethanol-Gasoline Blends on Spark Ignition Engine Vibration Characteristics and Noise Emissions. Energy Sources, Part A Recover Util Environ Eff [Internet]. 2010 Aug 13;32(20):1851–60. Available from: [<URL>](#).
38. Beşergil B. Fuels and Oils. İzmir: Ege University Press; 2009.
39. Viswanath DS, Ghosh TK, Prasad DHL, Dutt NVK, Rani KY. Theories of Viscosity. In: Viscosity of Liquids [Internet]. Dordrecht: Springer Netherlands; 2007. p. 109–33. Available from: [<URL>](#).
40. Stauffer E, Dolan JA, Newman R. Flammable and Combustible Liquids. In: Fire Debris Analysis [Internet]. Elsevier; 2008. p. 199–233. Available from: [<URL>](#).
41. Kabak N. Applications of Jp-8 Fuel on Diesel Engines. [Eskişehir]: Osmangazi University Institute of Science and Technology; 2005.
42. Care S. The usability of liquid fuel obtained by pyrolysis of coal and waste cotton oil together in diesel engines. Institute of Natural and Applied Sciences; 2014.



Study of The Amides Obtained by The Synthesis of Cottonseed Oil and Diethanolamine as Inhibitor to Prevent Atmospheric Corrosion

Teyub Ismayilov¹, Sevinj Suleymanova^{1*} , Parvana Movsumova¹ , Nurana Musayeva¹ , Sabahat Aslanova^{1*} 

¹Academician Y.H. Mammadaliyev Institute of Petrochemical Processes of the Ministry of Science and Education of the Republic of Azerbaijan.

Abstract: Amides of cottonseed oil and diethanolamine were synthesized in 1:1, 1:2 and 1:3 mole ratios and the structures of the substances were confirmed using infrared spectroscopy. Physicochemical properties were also studied. Conservative liquids were developed by adding 3, 5 and 10% of the obtained amides into T-30 oil. Corrosion tests involved immersing metal plates in conservative liquids within a hydrochamber, seawater, and 0.001% H₂SO₄ solution. The studies revealed that synthetic amides can be used to develop conservative liquids of high protective efficiency. The best results were obtained by 10% solutions. It was determined that metal plates immersed in a 10% solution of amide in a mole ratio of 1:2 were protected from corrosion during 205 days in "Г-4" hydrochamber, 165 days in seawater, and 160 days in a 0.001% H₂SO₄ solution. Taking into account that the optimum composition created as a result of research is more favorable from an economic point of view, turbine oil was used as a solvent medium, and the obtained results met the demand.

Keywords: Cottonseed oil, diethanolamine, amide, atmospheric corrosion, turbine oil.

Submitted: January 27, 2023. **Accepted:** March 21, 2024.

Cite this: Ismayilov T, Suleymanova S, Movsumova P, Musayeva N, Aslanova S. Study of The Amides Obtained by The Synthesis of Cottonseed Oil and Diethanolamine as Inhibitor to Prevent Atmospheric Corrosion. JOTCSA. 2024;11(3):959-66.

DOI: <https://doi.org/10.18596/jotcsa.1242271>

***Corresponding author's E-mail:** sss-seva@mail.ru

1. INTRODUCTION

Atmospheric corrosion, being one of the most common types of corrosion, has led to significant attention being focused on the development of protection tools and methods. The occurrence of atmospheric corrosion on steel surfaces causes great losses of material resources (1-3).

Atmospheric corrosion affects all metal structures operating outdoors (about 50% of the total existing metal stock), namely: overhead pipelines, capacity equipment, metal parts of buildings, piers, bridges, transport facilities. During operation, the surfaces of devices are inevitably exposed to moisture and pollution, and it's the main reason for the occurrence and increase of corrosion processes (4, 5).

Atmospheric corrosion can be classified into categories such as dry corrosion, damp corrosion, and wet corrosion according to surface humidity. Humid and wet flow refers to electrochemical mechanisms, but dry flow refers to chemical mechanisms (6, 7).

The main type of corrosion: is atmospheric corrosion (the cause of oxidation is the contact of the metal object with oxygen and water vapor in the air). Rust develops faster when there are pollutants in the air in the form of chemically active substances. Liquid corrosion (occurs on metal equipment in a water environment). If we are talking about seawater, oxidation on it is significantly accelerated due to the high salt content of the liquid. Soil corrosion (metal equipment located on the ground is affected by this type). Chemical reactions begin and continue under the influence of chemical elements that make up the soil, groundwater, various types of seepage. Corrosion in metal products can manifest itself in different ways (8, 9).

- a continuous rusty layer or its separate parts are formed;
- small areas of rust penetrating the part are formed;
- deep cracks are formed;
- one of the alloy components is oxidized;
- deep penetration occurs throughout the volume;
- several symptoms appear at the same time;

The reasons can be of two types (10): Chemically, i.e., the metal dissolves as a result of chemical reactions with active substances. Electrochemical is related to the generation of an electric current when in contact with electroly solutions, under its influence electron exchange occurs in metals. This causes damage to the crystal structure and the formation of rust (11).

There are several main ways to protect metal equipment from corrosion (27):

- metal alloy;
- protective coatings (metal, non-metal);
- electrochemical protection;
- changes in the properties of the corrosive medium;
- rational product structure;

This is one of the really effective ways to increase the rust resistance of metals. Chromium, nickel, molybdenum, etc. is added to the alloy or metal during the alloying process alloying elements such as. This is one of the really effective ways to increase the rust resistance of metals. They lead to passivation of the metal, that is, the corrosion protection of the metal or alloy increases due to the stopping of the anode process (12).

Additional layers are artificially formed on the surface of the metal product to protect it from corrosion. Such coatings can be metallic or non-metallic. However, regardless of their composition, they are subject to the same requirements: good adhesion properties, durability, the ability to maintain their properties in an aggressive environment (13). Protection of metal equipment with metal coatings differs from other methods in its unequivocal effect. Non-metallic protective coatings are divided into inorganic and organic. Inorganic coatings, metal oxides, chromium, phosphorus compounds, etc. are used to protect metal equipment from corrosion with non-metallic coatings (28). Organic coatings include paint coatings, resins, plastics, polymer coatings and rubbers (14). Atmospheric corrosion has taken a large place in the destruction of metal equipment, and much attention is paid to the development of protective means and methods. The essence of the protection of metals from atmospheric corrosion inhibitors consists of chemical and physical interaction with moisture, oxygen and other corrosive substances, as a result of which substances neutral in terms of corrosion are formed and passivation of metal surfaces, hydrophobization, or both occur together (15). At the beginning of the 20th century, it was determined that some gas-containing chemical compounds have the ability to precipitate on the surface of metals and protect them from the harmful effects of the environment. These

compounds are called volatile corrosion inhibitors or VCI - volatile corrosion inhibitors (16). Among the foreign samples, VIBATAN Metal Antiox 01792 can be distinguished. It is a universal concentrate of volatile corrosion inhibitors for ferrous and non-ferrous metals. Another volatile corrosion inhibitor with a high concentration of VIBATAN Metal Antiox 01801 can also be attributed here (17, 18). Its field of application is the creation of a protective coating against corrosion in the military industry and large machinery. The most domestically produced ЛИАК include derivatives and salts of aliphatic, aromatic, cyclic and heterocyclic amines (19, 20). These are mainly nitrites, nitrates, borates, phosphates, benzoate, nitrobenzoates. These are mainly nitrites, nitrates, borates, phosphates, benzoates, nitrobenzoates (21). In this regard, the issue of protection against atmospheric corrosion and reduction of losses during transportation and storage is very relevant. The application of inhibitors is one of the known methods of corrosion protection, as well as one of the most effective methods among the various methods of preventing the disintegration of a metal surface. The inhibitors synthesized by us are considered to be low-component, ecologically harmless and biodegradable, and especially "Green" inhibitors.

2. MATERIAL AND METHOD

2.1. Materials

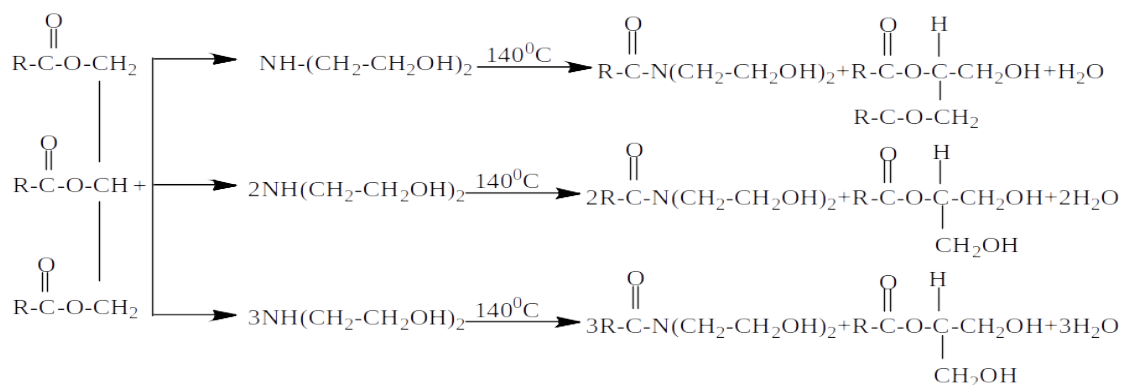
Cottonseed oil is obtained by cold pressing cotton seeds, after removing the fiber from them. This method makes it possible to preserve microelements and nutrients characteristic of natural cotton in the oil. Cotton seeds collected in the Republic of Azerbaijan. DEA (purity > 98.5% Merck®, Germany). Indicators of cotton seed: Approximate seed weight: about 1 gram, Approximate seed size: 1 cm, Seed germination percentage: 90%, Beginning of fruiting/flowering: in the year of planting, Estimated yield: usually 10-20 flowers per plant

2.2. Synthesis

Amides of cottonseed oil and diethanolamine (DEA) in different mole ratios were synthesized. The reactions were carried out in a three-necked flask equipped with a stirrer, a heater and a thermometer. The reaction begins by weighing the required amount of cottonseed oil and filling into the flask, and is followed by turning on the heater and stirrer. As the temperature reaches 60-70°C, the required amount of DEA is weighed and added to the flask. It is followed by raising the temperature to 140°C and stirring at this temperature for 4 hours and cooling after the end of the reaction.

3. RESULTS AND DISCUSSION

3.1. The course of The Reaction



3.2. Instrumental Characterization

The structure was studied by infrared spectroscopy method (IR spectroscopy) ALPHA IR-Fourier spectrophotometer of German BRUKER company.

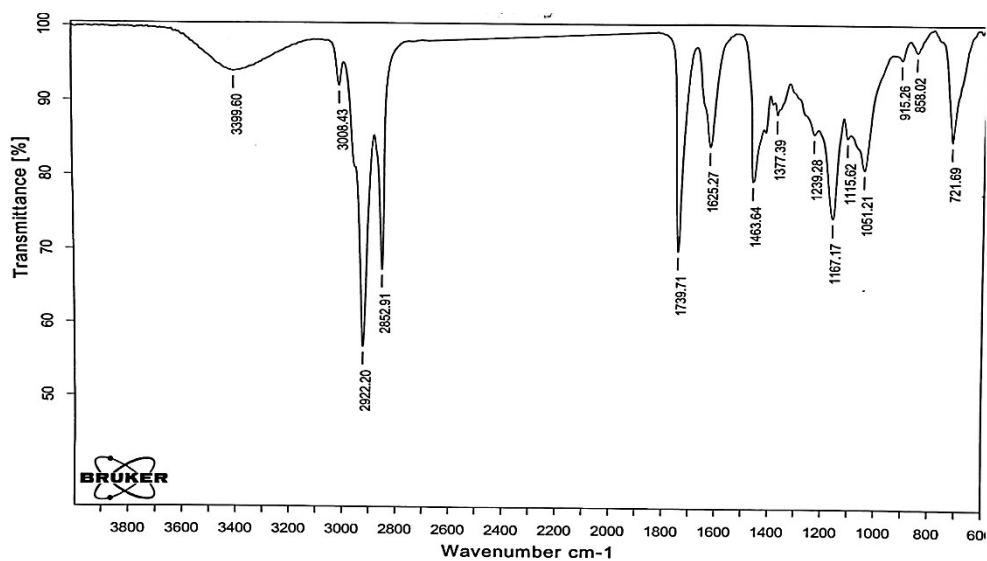


Figure 1: IR spectrum of the amide obtained in 1:1 mole ratio.

So, 250 g of cottonseed oil were taken for the purpose of obtaining amide in a 1:1 mole ratio. After the temperature reached 60-70°C, 30 g of DEA were added and the temperature was raised to 140°C. After stirring for 4 hours, the IR spectrum of the substance was plotted and determined (Figure 1).

The following absorption bands were observed in the spectrum:

- 721 cm^{-1} - mathematical vibration of C-H bond of CH_2 group;
- 1625 cm^{-1} - valence vibration of C-N bond of $-\text{CO}-\text{N}-$ group (tertiary amide);
- 1739 cm^{-1} - C=O bond of the ester;
- 1051, 1239 cm^{-1} - C-N bond C-NH group;
- 1115, 1167 cm^{-1} - C-O-C bond of the ester;
- 1377, 1463, 2852, 2922 cm^{-1} - valence vibration of C-H bond of CH_3 and CH_2 groups;
- 3008 cm^{-1} - C-H bond of cottonseed oil C=C group.
- 3399 cm^{-1} - N-H bond of DEA and O-H bond of C-OH group coincide.

IR spectrum of the sample reveals that the reaction didn't run to completion. Absorption bands are observed at 1739, 1115, 1167 cm^{-1} characteristic for cottonseed oil and the ester. Observation of the absorption band of tertiary amide at 1625 cm^{-1} confirms obtaining the tertiary amide. In the region of 3365 cm^{-1} , an absorption band characteristic for O-H bond of C-OH group also appears and coincides with the absorption band corresponding to N-H bond.

For the purpose of obtaining the amide of cottonseed oil with DEA in a 1:2 mole ratio, 250 g of cottonseed oil were taken and filled into a flask, heated to 60-70°C, and at this temperature, 60g of DEA were weighed and added to it and stirred at this temperature for 4 hours. After the completion of the reaction, IR spectrum was plotted (Figure 2) and determined.

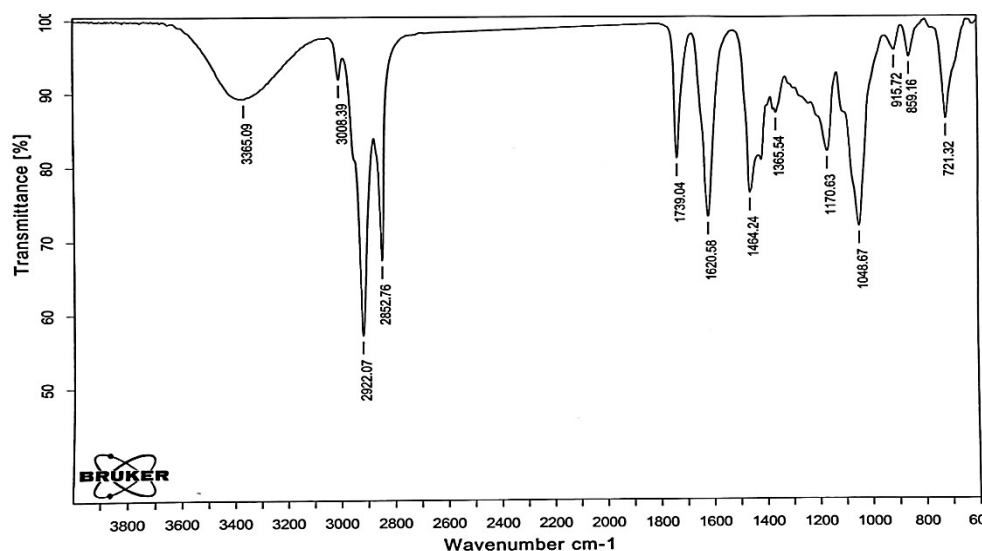


Figure 2: IR spectrum of the amide obtained in 1:2 mole ratio.

The following absorption bands were observed in the spectrum:

- 721 cm^{-1} - mathematical vibration of C-H bond of CH_2 group;
- 859, 915 cm^{-1} - deformation vibration of C-H bond of $\text{HC}=\text{C}$ -group;
- 1048 cm^{-1} - valence vibration of C-N bond;
- 1170 cm^{-1} - C-O-C bond of the ester;
- 1739 cm^{-1} - $\text{C}=\text{O}$ bond of the ester;
- 1620 cm^{-1} - valence vibration of C-N bond of $-\text{CO}-\text{N}$ -group (tertiary amide);
- 1365, 1464, 2852, 2922 cm^{-1} - deformation and valence vibrations of C-H bond of CH_3 and CH_2 groups;
- 3008 cm^{-1} - valence vibration of C-H bond of $\text{HC}=\text{CH}$ -group;
- 3356 cm^{-1} - valence vibration of O-H bond of COH group.

The reaction didn't run to complete even at 1:2 mole ratio. Absorption bands characteristic for the tertiary amide obtained at 1621 cm^{-1} proves the intensity of the absorption bands in comparison to 1:1 mole ratio. Absorption band intensity of $\text{C}=\text{O}$ group of the ester characteristic for cottonseed oil at 1739 cm^{-1} was also decreased.

In order to obtain the amide of cottonseed oil and DEA in 1:3 mole ratio, 250 g of cottonseed oil were taken and filled into a flask, heated to 60-70°C, then 90 g of DEA were added to it, mixed at 140°C for 4 hours. IR of the obtained substance was determined by plotting the spectrum (Figure 3).

The following absorption bands were observed in the spectrum:

- 720 cm^{-1} - mathematical vibration of C-H bond of CH_2 group;
- 858, 915 cm^{-1} - deformation vibration of C-H bond of $\text{CH}=\text{C}$ -group;
- 1047 cm^{-1} - valence vibration of C-N bond;
- 1185, 1209, 1257 cm^{-1} - C-O-C bond (a small amount) of the ester;
- 1364, 1421, 1464, 2852, 2922 cm^{-1} - deformation and valence vibrations of C-H bond of CH_3 and CH_2 groups;
- 1617 cm^{-1} - valence vibration of C-N bond of $-\text{CO}-\text{N}$ -group (tertiary amide);
- 1739 cm^{-1} - $\text{C}=\text{O}$ bond of the ester (a small amount)
- 3008 cm^{-1} - valence vibration of C-H bond of $\text{HC}=\text{C}$ group;
- 3358 cm^{-1} - valence vibration of O-H bond of COH group.

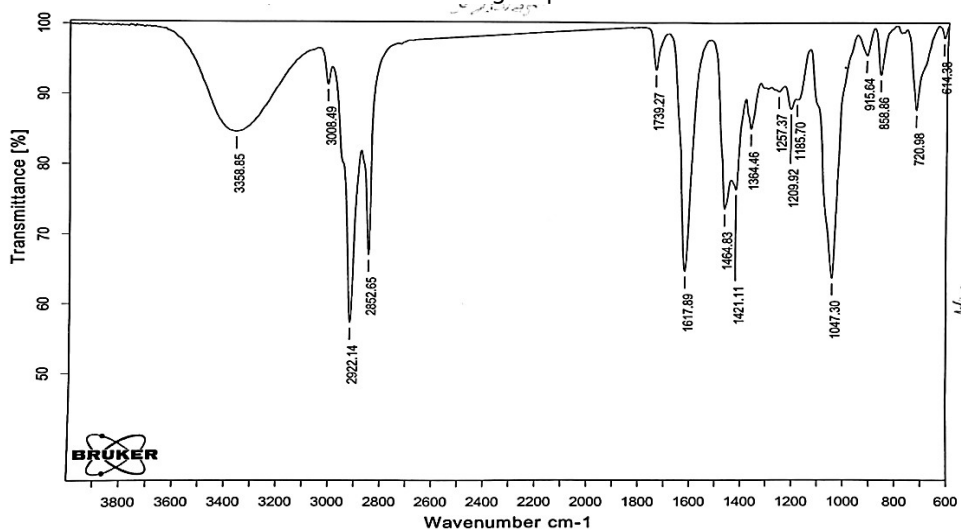


Figure 3: IR spectrum of the amide obtained in 1:3 mole ratio.

In the case of taking the initial substances in a 1:3 mole ratio, a small amount of cottonseed oil remained in the product obtained by the reaction. Intensity of the absorption band characteristic of

cottonseed oil (1739 cm^{-1}) was very low. This ratio provides high intensity of the absorption band (1617 cm^{-1}) of C-N bond of the tertiary amide. The analysis of the spectra proved that the amide yield was higher by taking of the initial substances in this ratio. A small amount of unreacted cottonseed oil remained in the system. Physicochemical parameters of the synthesized amides were determined. The results are given in Table 1.

3, 5, 7, and 10% of synthesized amides were added to T-30 oil and physicochemical properties of the solutions were determined. The results are set into Tab. 2. Protective ability of the developed conservative liquids was determined by the direct tests in different structural chambers. The tests were carried out as in the first section. Purified and dried metal plates were tested in a thermohumidity

chamber in a 0.001% H_2SO_4 solution in seawater. The obtained results are given in Table 2. As is evident from the table, the highest results were shown by the composition obtained by adding 1:2 mole ratio of 10% amide of cottonseed oil and DEA to T-30 oil. A metal plate immersed into a conservative liquid developed by this way was protected from corrosion for 205 days in "Г-4" hydrochamber, 165 days in seawater, and 160 days in a 0.001% sulfuric acid solution.

Also, the hydrochamber "Г-4" test results of the 10% solutions obtained are given in the form of a diagram (Fig. 4).

Test results of 10% solutions in the hydrochamber "Г-4" are given in the following diagram (Fig. 4).

Table 1: Physicochemical properties of the resulting amides.

Properties	Device	Method	Samples		
			Cottonseed oil+DEA (1:1 mole ratio)	Cottonseed oil+DEA (1:2 mole ratio)	Cottonseed oil+DEA (1:3 mole ratio)
Kinematic viscosity, mm^2/sec , 20°C	Stabinger SVM	ASTM D445	Impossibility of measuring	636.32	1350.4
Density, g/cm^3 , 20°C	DMA 4500M	ASTM D5002	Impossibility of measuring	0.9660	0.9792
Refractive index, 20°C	Abbemat 500	Device method	1.4778	1.4810	1.4821
Iodine number, $\text{gY}/100 \text{ g}$	Methodics	GOST 2070-82	51.11	47.84	54.75
Acid number, mgKOH/g	Methodics	GOST 11362	1.13	1.86	3.50
Freezing point, $^\circ\text{C}$	Stanhope seta	ASTMD 97	+3	0	+2

Table 2: Test results of the conservative liquids developed on the basis of the synthesized amides.

	Composition of conservative liquids		"Г-4" hydrochamber	Seawater	0.001% H_2SO_4
	T-30 oil, %	Amides, %			
1	97	Cott.oil+DEA 1:1,3	126	120	125
2	95	Cott.oil +DEA 1:1,5	152	140	147
3	93	Cott.oil +DEA 1:1,7	164	158	150
4	90	Cott.oil +DEA 1:1,10	185	160	157
5	97	Cott.oil +DEA 1:2,3	162	124	126
6	95	Cott.oil +DEA 1:2,5	136	132	130
7	97	Cott.oil +DEA 1:2,7	162	146	154
8	90	Cott.oil +DEA 1:2,10	205	165	160
9	97	Cott.oil +DEA 1:3,3	164	136	142
10	95	Cott.oil +DEA 1:3,5	165	148	146
11	97	Cott.oil +DEA 1:3,7	175	156	149
12	90	Cott.oil +DEA 1:3,10	184	165	154

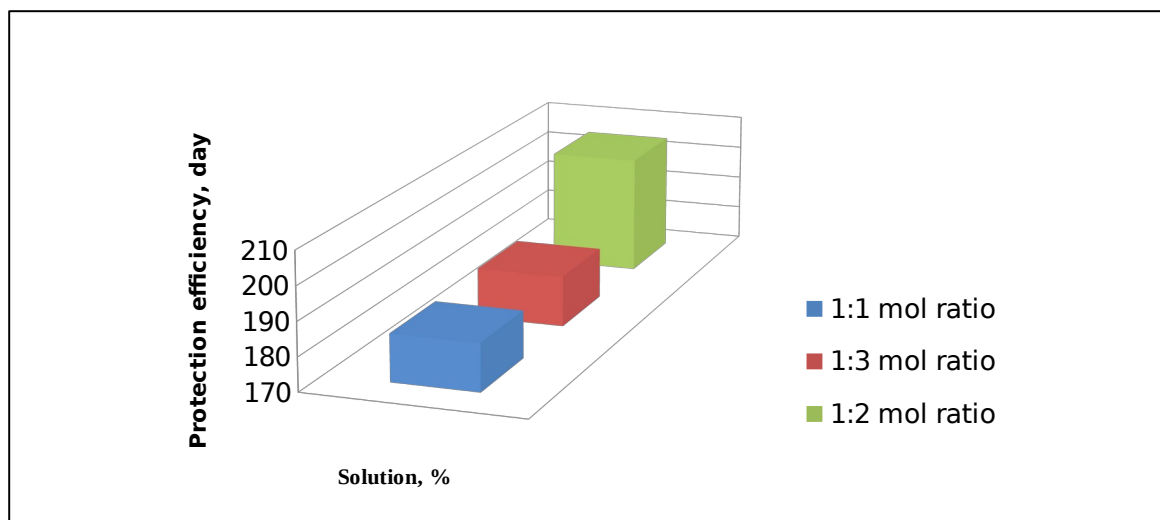


Figure 4: Test results diagram of the obtained amidines.

As is evident from the diagram, the solution of cottonseed oil and DEA shows the best results in 1:2 mole ratio.

If we look at the research works carried out in our country and abroad, tests were carried out in the "Г-4" hydrochamber by adding nitro compounds synthesized in the presence of nitric acid to T-30 turbine oil based on $C_{12}H_{24}$, $C_{14}H_{28}$ and $C_{16}H_{32}$ - $C_{18}H_{36}$ α -olefins. A nitro compound synthesized on the basis of $C_{14}H_{28}$ α -olefin was observed for 108 days of corrosion protection (22). For the first time, amidoamines synthesized by reacting diethylenetriamine (DETA), triethylenetetraamine (TETA) and polyethylene polyamines (PEPA) with technical or distilled petroleum acids (PA) in different molar ratios are added to T-30 turbine oils at different concentrations (3, 5, 7 and 10%) preservation fluids were prepared and tested in different harsh environments. Preservation fluid with a 2:1 molar ratio of PA to PEPA showed a preservation effect for 41 days (23). K-17, Mifol KM, HF-203P and Mayacor can be preserved in a hydrochamber for 70 days to 100 days, the protective effects of which have been observed (24).

In other works, compositions of obtaining nitrated oil with Mg, Co, and Ni salts of natural petroleum acids were prepared and their properties as conservation liquid were studied. The obtained results show that the corrosion protection of the Steel-3 metal plate in the "Г-4" hydrochamber is weak, either alone or in the presence of compositions with Co, Ni and Mg salts of petroleum acid. While nitrous oil protected the steel-3 metal plate from corrosion for 55 days, the protection index with petroleum acid salts was between 45-62 days (25). In other works, compositions of obtaining nitrated oil with Mg, Co, and Ni salts of natural petroleum acids were prepared and their properties as conservation liquid were studied. The obtained results show that the corrosion protection of the Steel-3 metal plate in the "Г-4" hydrochamber is weak, either alone or in the presence of compositions with Co, Ni and Mg salts of petroleum acid. While nitrous oil protected the steel-3 metal plate from corrosion for 55 days, the protection index with petroleum acid salts was between 45-62 days (26).

4. CONCLUSIONS

1. The structures of the synthesized substances were confirmed using IR spectroscopy method, and physicochemical properties were determined. 3, 5, 7 and 10% solutions of cottonseed oil were prepared in T-30 oil and studied as conservative liquids. The best result was shown by a 10% solution in 1:2 mole ratio. It was determined that metal plates immersed in a 10% solution exhibited corrosion protection efficiency lasting 205 days in a hydrochamber, 165 days in seawater, and 160 days in a 0.001% H_2SO_4 solution.

2. As a result, it can be noted that, unlike other researches, our test results showed a relatively high protection effect and, besides being and economically efficient, ecologically safe, it has a simple structure in the manufacturing technology.

5. REFERENCES

- Krätschmer A, Odnevall Wallinder I, Leygraf C. The evolution of outdoor copper patina. *Corros Sci* [Internet]. 2002 Mar 1;44(3):425-50. Available from: [<URL>](#).
- Aastrup T, Wadsak M, Schreiner M, Leygraf C. Experimental in situ studies of copper exposed to humidified air. *Corros Sci* [Internet]. 2000 Jun 1;42(6):957-67. Available from: [<URL>](#).
- Morcillo M, Chico B, Mariaca L, Otero E. Salinity in marine atmospheric corrosion: its dependence on the wind regime existing in the site. *Corros Sci* [Internet]. 2000 Jan 1;42(1):91-104. Available from: [<URL>](#).
- Rammelt U, Koehler S, Reinhard G. Use of vapour phase corrosion inhibitors in packages for protecting mild steel against corrosion. *Corros Sci* [Internet]. 2009 Apr 1;51(4):921-5. Available from: [<URL>](#).
- Sabir S, Ibrahim AA. Influence of atmospheric pollution on corrosion of materials in Saudi Arabia. *Corros Eng Sci Technol* [Internet]. 2017 May 19;52(4):276-82. Available from: [<URL>](#).

6. Andreev NN, Kuznetsov YI. Volatile Inhibitors of Metal Corrosion. I. Vaporization. *Int J Corros Scale Inhib* [Internet]. 2012;1(1):16-25. Available from: [<URL>](#).
7. Mikhailov AA, Panchenko YM, Kuznetsov YI. Atmospheric corrosion and protection of metals. Pershin's Publishing house; 2016. 554 p.
8. Ferreira KCR, Cordeiro RFB, Nunes JC, Orofino H, Magalhães M, Torres AG, et al. Corrosion Inhibition of Carbon Steel in HCl Solution by Aqueous Brown Onion Peel Extract. *Int J Electrochem Sci* [Internet]. 2016;11:406-18. Available from: [<URL>](#).
9. Aghazada YJ, Abbasov VM, Cafarov RP, Abdullayev SE, Hasanov EK. The Optimization of Process Forming Of Conservative Liquids Based On Theoxidized Liquid Rubber And Amidoamines. *Am J Eng Res* [Internet]. 2017;6(10):287-90. Available from: [<URL>](#).
10. Abbasov VM, Amiraslanova MN, Hasanov EK, Aliyeva LI, Aghazadeh YJ, Safarova SZ. Conservation liquids on the bases of turbine oil of grade T-30 and corrosion inhibitor. *J Adv Chem* [Internet]. 2016 Dec 17;11(7):3715-22. Available from: [<URL>](#).
11. Aghazada YJ. The research of the amidoamines in compositions with various contents as inhibitors. *Int Res J Eng Technol* [Internet]. 2016;3(5):6-9. Available from: [<URL>](#).
12. Umoren SA, Ebenso EE. Studies of the anti-corrosive effect of *Raphia hookeri* exudate gum-halide mixtures for aluminium corrosion in acidic medium. *Pigment Resin Technol* [Internet]. 2008 May 23;37(3):173-82. Available from: [<URL>](#).
13. Tupikov RA, Dragunov YG, Kharina IL, Zmienko DS. Protection of carbon steels against atmospheric corrosion in a wet tropical climate using gas-plasma metallization with aluminum. *Prot Met* [Internet]. 2008 Dec 8;44(7):673-82. Available from: [<URL>](#).
14. Abbasov VM, Aliyeva LI, Gasanov EK, Aghazade YJ, Rzayeva NS. Conservative liquids based on synthetic petroleum acids salts and aliphatic nitro-compounds. *J Adv Chem* [Internet]. 2014 Jun 17;10(2):2230-3. Available from: [<URL>](#).
15. Escalante-Perez ME, Porcayo-Calderon J, Vazquez-Velez E, Casales-Diaz M, Gonzalez-Rodriguez JG, Martinez-Gomez L. Effect of the Depth of the Solution Layer on the Atmospheric Corrosion of Carbon Steel. *Int J Electrochem Sci* [Internet]. 2016;11:374-84. Available from: [<URL>](#).
16. Abbasov VM, Abdullayev EŞ, Agazade YD, Gasanov EK. Sintez i issledovaniye konserviruyushchikh zhidkостей na osnove nitrosoedinenij i amidov. In: Scientific achievements of the third millennium [Internet]. 2012. p. 20-2. Available from: [<URL>](#).
17. Abbasov VM, Ağazadə YC, Həsənov EK, Ağakışiyeva HM, Abdullayev EŞ. Nitrobirləşmənin təbii neft turşularının duzları və amidlə kompozisiyasından yaradılmış konservasiya mayesinin tədgigi. *Azərbaycan Kim jurnalı* [Internet]. 2013;3:16-9. Available from: [<URL>](#).
18. Trusov VI, Krinskaya RS, Danilovskaya LP, Kuzinova TM. Ingibitor korrozii dlya konservachii vnutrennikh poverkhnostey. *Korroziya* [Internet]. 2019;50-1. Available from: [<URL>](#).
19. Abbasov VM, Kerimov NG, Meherremov RS, Gurbanov IH. Konservasiya yağları uchun olefinlerin və korroziya inhibitorlarının nitrolaşma məhsulları. *Neft kimyası və Neft emalı prosesləri*. 2001;1:13-9.
20. Abbasov VM, Alieva LI, Gasanov EK, Nazarov IG. Razrabotka i sozдание konservatsionnikh zhidkостей na osnove turbinnogo masla T-30 i nitroalkanov. *Neftepererab i Neft*. 2015;1:36-41.
21. Abbasov VM, Abdullayev YŞ, Agazade YC, Hesenov EK. Nitrobirləşmələr və amidoaminlər əsasında konservasiya sürtkülerinin hazırlanması. *Kim Probl*. 2012;4:437-43.
22. Babić-Samardžija K, Lupu C, Hackerman N, Barron AR, Luttge A. Inhibitive Properties and Surface Morphology of a Group of Heterocyclic Diazoles as Inhibitors for Acidic Iron Corrosion. *Langmuir* [Internet]. 2005 Dec 1;21(26):12187-96. Available from: [<URL>](#).
23. Abbasov VM, Abdullayev YŞ, Agazadeh YC, Hesenov EK. Nitrobirləşmə və amidoaminin kompozisiyası əsasında hazırlanmış konservasiya mayələrinin tədgigi. In: 1st International chemistry and chemical engineering conference. 2013. p. 17-21.
24. Kravchenko NG, Shchekin VK, Yefimova EA, Zherdev DV. Zashchitniye svoystva konserviruyushchikh masel. *Izv VIAM* [Internet]. 2023;4:122. Available from: [<URL>](#).
25. Gabelko NV, Vigdorovich VI. Vlagopronichaemost konserviruyushchikh materialov na osnove mineralnikh masel i mnogofunktsionalnikh prisadok ИФХАН-29А i geksadetsilamina. *Vestn TGU* [Internet]. 2002;7(3):360-4. Available from: [<URL>](#).
26. Gabelko NV, Vigdorovich VI. Effektivnost geksadetsilamina kak zagustitelya masla i maslorastvorimoy antikorroziynoj prisadki. *Vestnik*. 2002;7(2):268-71.
27. Timonin VA. Ekologicheskiye aspekty problemy korrozii. *Korroziya*. 2004;1:2-3.
28. Semenoba IV, Florianovich GM, Khoroshilov AV. Korroziya i zashchita ot korrozii. *Fizmatlit*. 2010;416.



A facile green synthesis of LDH nanosheets using sugar molecules

Ahmad Faiz Abdul Latip*¹ , Mineesha Sivakumar¹ , Faiz Bukhari Mohd Suah¹ ,
Mohd Hazwan Hussin¹  and Mohd Zobir Hussein² 

¹School of Chemical Sciences, Universiti Sains Malaysia, Penang, Malaysia

²Institute of Advanced Technology, Universiti Putra Malaysia, Selangor, Malaysia

Abstract: The exfoliation of LDH materials is highly favorable for the formation of single-layer layered double hydroxides (LDH) nanosheets due to their unique chemical, thermal, optics, and biological properties. The green method for the exfoliation of layered double hydroxides (LDH) offers several advantages compared to conventional methods because it is considered safe, cost-effective, and eco-friendly. This report focuses on the exfoliation of layered double hydroxides (LDH) using sugar molecules as a green exfoliating agent without having to first pre-intercalate the layered material. The exfoliation of LDH is confirmed by X-ray diffraction (XRD), Fourier transform infrared spectroscopy (FTIR), transmission electron microscopy (TEM), thermogravimetric (TGA), differential scanning calorimetry (DSC), and Brunauer-Emmett-Teller (BET) analyses. We also examined the crystalline phase of LDH in different stages of liquid exfoliation; suspension, semi-dry suspension, and dried solid samples using XRD. XRD data shows one broad peak for all the LDH exfoliated samples at $2\theta = 23.9^\circ, 22.4^\circ$, and 22.3° respectively, which correspond to the characteristic (006) basal reflection of LDH single layers. These single peaks indicate the formation of LDH nanosheets. The higher intensity peak at the region $1000\text{-}1020\text{ cm}^{-1}$ for LDH exfoliated samples indicates the successful exfoliation of sugar molecules in the interlayer of LDH. In BET, the wide hysteresis loop for the exfoliated LDHs proved the successful exfoliation of sugar molecules into LDH layers. TEM images show ultrathin sheets of LDH and spherical-like particles. This work shows that LDH nanosheets can be obtained by using green biomolecules through simple synthetic methods.

Keywords: Green synthesis, layered double hydroxide (LDH), exfoliation, sugar molecules, LDH nanosheets.

Submitted: March 26, 2024. **Accepted:** May 19, 2024.

Cite this: Abdul Latip AF, Sivakumar M, Mohd Suah FB, Hussin MH, Hussein MZ. A facile green synthesis of LDH nanosheets using sugar molecules. JOTCSA. 2024;11(3):967-80.

DOI: <https://doi.org/10.18596/jotcsa.1458997>.

*Corresponding author. E-mail: afaiz@usm.my.

1. INTRODUCTION

Layered double hydroxide (LDH) is a two-dimensional (2D) layered material that belongs to the hydrotalcite-like (HT) compound group. LDH is represented by the formula $[M_{1-x}^{2+}M_x^{3+}(\text{OH})_2]^{x+} \cdot [A_{x/n}]^{n-} \cdot m\text{H}_2\text{O}$, where M^{2+} and M^{3+} are divalent and trivalent cations and A^{n-} are inorganic or organic anions (1). The exchangeable interlayer anions, A^{n-} in the layered structure render the compounds such a unique material for intercalation chemistry (2). When these layers are exfoliated, nanosheets of LDH can be obtained, which are typically in the nanometer range (3). Over the past few decades, research into the exfoliation chemistry of LDH has seen a sharp increase (3).

The exfoliation of LDH is the process of breaking apart the LDH multilayers into single layers consisting of nanosheets (4, 5). The LDH nanosheets display unique mechanical, optical, and biological properties compared to their bulky counterparts. Interestingly, liquid-phase exfoliation is one of the promising routes for exfoliating layered materials (3). This top-down approach has several advantages since they are easy to operate, versatile, and easily scalable (3). Several reports have dealt with the exfoliation of LDH in different solvents. However, using organic solvents as exfoliating solvents can be harmful as it is likely to harm the health of humans, animals, and plants (6). Adachi-Pagano et al.(2000) reported the exfoliation of ZnAl-LDH in organic solvent using

dodecyl sulfate (DDS) and butanol (7). Hibino and Jones et al.(2001) employed glycinate-containing MgAl-LDH in formamide at room temperature (5). Jobbagy and Regazzoni et al.(2004) studied the exfoliation of Mg-Al-DDS in toluene and CCl_4 (8). Previously researchers used organic solvents which are more toxic therefore, it is essential to use less toxic and more sustainable solvents to minimize the impact on the environment and human health. In this work, we demonstrate the green synthesis of LDH nanosheets using sugar molecules to exfoliate LDH without having to first pre-intercalate the layered material in dimethyl sulphoxide (DMSO). DMSO is a highly potential solvent for exfoliation due to its higher dielectric constant and low toxicity profile. DMSO is also miscible with water and most organic liquids (9). Sugar molecules are readily available, renewable, and non-toxic carbohydrates (10). It contains a large number of hydroxyl groups which may greatly facilitate the exfoliation of layered materials (11). When sugar molecules are intercalated between LDH layers, the functional groups of the sugars may influence the hydrogen bonds between the hydroxyl groups of intercalated molecules and the hydroxyl groups of basal layers of LDH. This may further lead to breaking the layers apart (11). It has been previously reported that sugar crystals are used to exfoliate boron nitride lamellae in water due to covalent interactions (12). Chen and co-workers investigated the interactions of natural sugars with inorganic layered nanomaterials, using natural sugar as a green exfoliating agent to exfoliate transition-metal dichalcogenides (TMDs) (11). Furthermore, the reports on structural studies have been reported by Joensen et al. on XRD study on single-layer and restacked MoS_2 (13). The structural studies of a single layer of MoS_2 in aqueous suspension show that a single layer differs from a bulk single crystal. When single-layer MoS_2 suspension dries up, a new phase is obtained, whereas in dry restacked MoS_2 , bulk Mo-Mo distance starts to reappear. Sasaki et al. reported a stable colloidal suspension of an exfoliated titanate and the ensuing reassembling process (14). The layered protonic titanate was successfully exfoliated into single-layer nanosheets and the delaminated nanosheets were restacked upon drying; this reassembling process revealed the macromolecule aspects for the obtained individual nanosheets. XRD data showed that the amorphous halo changed into well well-order crystalline pattern upon drying. However, to our best knowledge, only limited studies have been reported on the structural information of the layered material in different sample phases using the X-ray diffraction (XRD) technique. This study demonstrates for the first time the crystalline phase of LDH in different stages of liquid exfoliation; suspension, semi-dry suspension, and dried solid samples.

2. EXPERIMENTAL SECTION

2.1. Reagents

Magnesium nitrate hexahydrate [$\text{Mg}(\text{NO}_3)_2 \cdot 6\text{H}_2\text{O}$] and aluminium nitrate nanohydrate [$\text{Al}(\text{NO}_3)_3 \cdot 9\text{H}_2\text{O}$] were purchased from Sigma-Aldrich. Sodium hydroxide (NaOH) and dimethyl sulfoxide (DMSO) were purchased from Merck. Sucrose, glucose, and lactose were purchased from R&M Chemicals Sdn. Bhd., Malaysia. All chemicals were used as received without purification.

2.2. Preparation of Mg-Al LDH

30 mmol magnesium nitrate hexahydrate [$\text{Mg}(\text{NO}_3)_2 \cdot 6\text{H}_2\text{O}$] and 15 mmol aluminium nitrate nanohydrate [$\text{Al}(\text{NO}_3)_3 \cdot 9\text{H}_2\text{O}$] were weighed separately in an analytical weighing balance. 50 ml of a solution containing 30 mmol magnesium nitrate hexahydrate and 15 mmol aluminum nitrate nanohydrate (Mg: Al = 2:1) were put together in a beaker.

2.3. Synthesis and exfoliation of Mg-Al LDH

Mg-Al LDH was prepared by following an established method (Co-precipitation) (15). The prepared Mg-Al LDH solution was added dropwise to 30 ml of distilled water mixed with 70 ml DMSO solution containing 1g of sucrose under stirring conditions. Throughout the mixing of the metal salt solutions, the pH of the reaction mixture was kept at 9 using 1 M of NaOH solution. The reaction was carried out under the nitrogen gas purge. The slurry product obtained was centrifuged for 3 minutes at 3500 rpm in 3 cycles. The resulting product was kept in a freezer dryer for 24 hours and the samples were mashed into a powder form for further characterization. The same procedure was repeated for 1g glucose and 1g lactose.

2.4. Characterizations

X-ray diffraction patterns of synthesized samples were recorded on a Bruker-D8 diffractometer using $\text{Cu-K}\alpha$ radiation. The Fourier transform infrared spectra were recorded on an FTIR spectrometer (Perkin Elmer, System 2000) while the morphologies of LDH samples were analyzed using transmission electron microscopy (FEI Tecnai G2 F20). Thermal analysis of samples was recorded using the Perkin Elmer SDTA 6000 Thermogravimetric analyzer and differential scanning calorimetry measurements were obtained using the Perkin Elmer DSC instrument. The surface area was measured using a Brunauer Emmett-Teller instrument (Micromeritic ASAP 2020). A graph of the cumulative particle size distribution of exfoliated LDH was plotted to determine the median diameter of the particle.

3. RESULTS AND DISCUSSION

3.1. XRD

Figure 1 shows the typical X-ray diffraction (XRD) patterns of the synthesized LDH and its exfoliated diffraction patterns. Figure 1a shows the first basal reflection for pristine LDH at $2\theta = 10.3^\circ$ corresponding to the basal spacing of $d_{003} = 8.6 \text{ \AA}$. (16). The d-spacing of pristine LDH calculated from the (003) peak was 8.6 \AA , which well matched with that of previously reported NO_3^- intercalated LDH

(17). Other basal reflections are observed at $2\theta = 20.2^\circ$ corresponding to the basal spacing of $d_{006} = 4.4 \text{ \AA}$ and $2\theta = 29.6^\circ$ corresponding to the basal spacing of $d_{006} = 3.0 \text{ \AA}$ (16). Figure 1b shows the XRD pattern for LDH exfoliated with sucrose. The diffraction pattern exhibits a sharp peak at $2\theta = 20.8^\circ$, corresponding to the basal spacing of $d_{006} = 4.3 \text{ \AA}$ (17). The basal spacing of d_{006} is observed in Figure 1c (LDH exfoliated with glucose) and Figure 1d (LDH exfoliated with lactose). These basal spacings of d_{006} in all the exfoliated samples may indicate the formation of single-layer LDH nanosheets (18). For comparison, Figure 1e exhibits the stacked spectrum of LDH pristine and each LDH exfoliated with sucrose, glucose, and lactose, where the latter patterns indicate the formation of single-layer nanosheets. Figure 1f

shows the XRD patterns for suspension samples (a)–(c). In all samples, single sharp peaks are observed at $2\theta = 23.9^\circ, 22.4^\circ$, and 22.3° respectively, which correspond to the characteristic (006) basal reflection of LDH single layers (18). Figure 1g shows the XRD patterns for semi-dry samples (a)–(c). Similarly, sharp peaks are observed at $2\theta = 20.4^\circ, 21.4^\circ$, and 20.1° at the basal reflection (006) indicating the formation of single-layer LDH. The 2θ values for the semi-dry samples differ from the suspension samples due to the different hydration states and drying techniques (14). A broad peak is observed for suspension samples, maybe due to water molecules, whereas for semi-dry samples, the shape of the water peak is narrower (14).

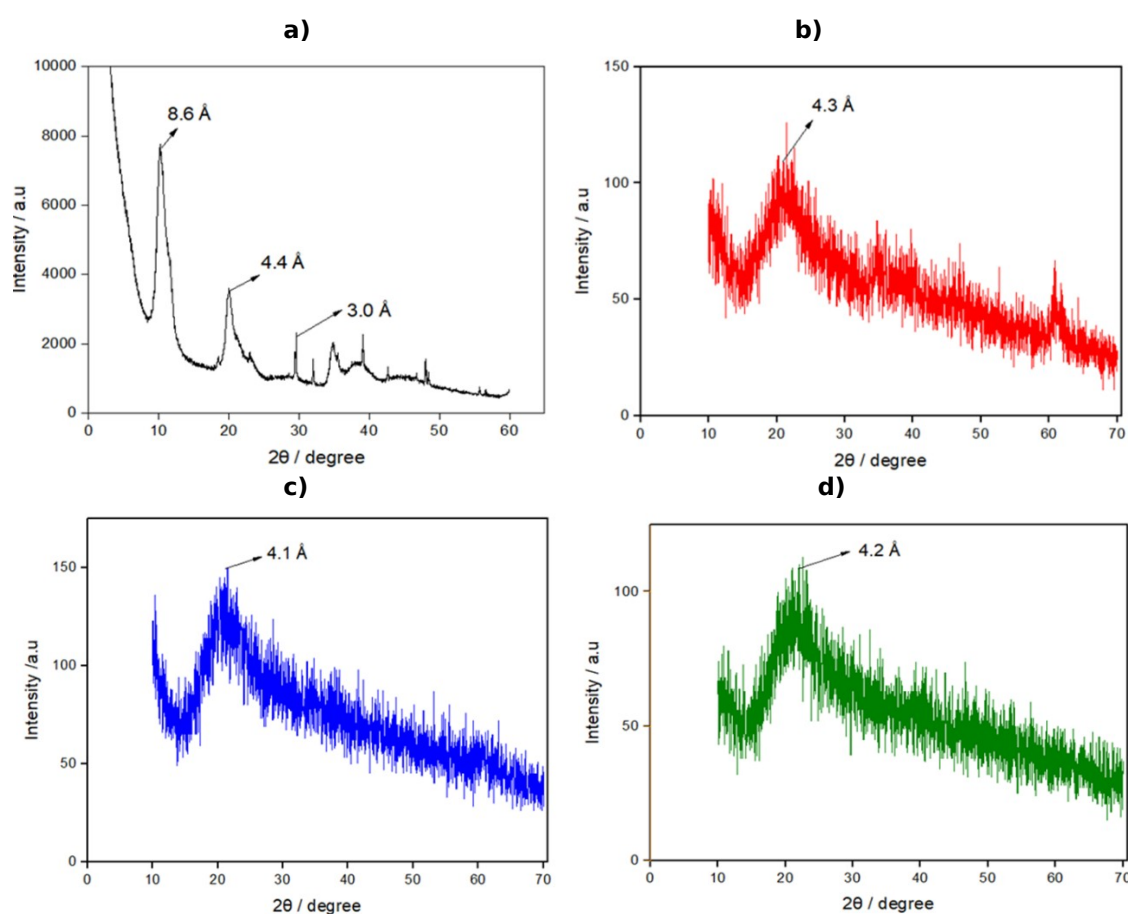


Figure 1: XRD pattern of a) LDH pristine b) LDH exfoliated with sucrose c) LDH exfoliated with glucose d) LDH exfoliated with lactose.

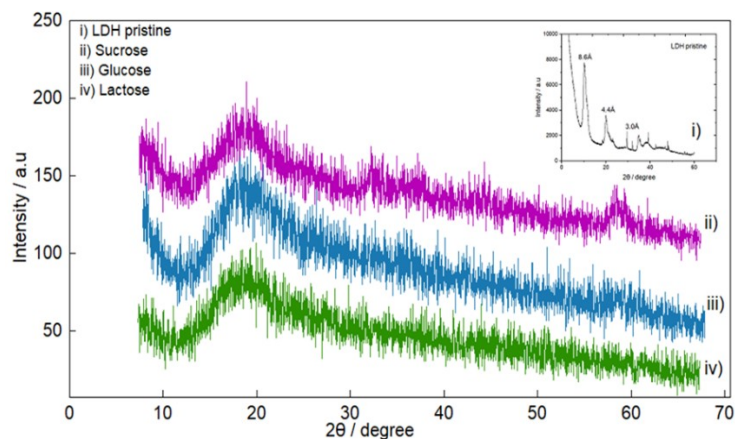


Figure 1e: Stacked XRD patterns of i) LDH pristine ii) LDH exfoliated with sucrose iii) LDH exfoliated with glucose iv) LDH exfoliated with lactose.

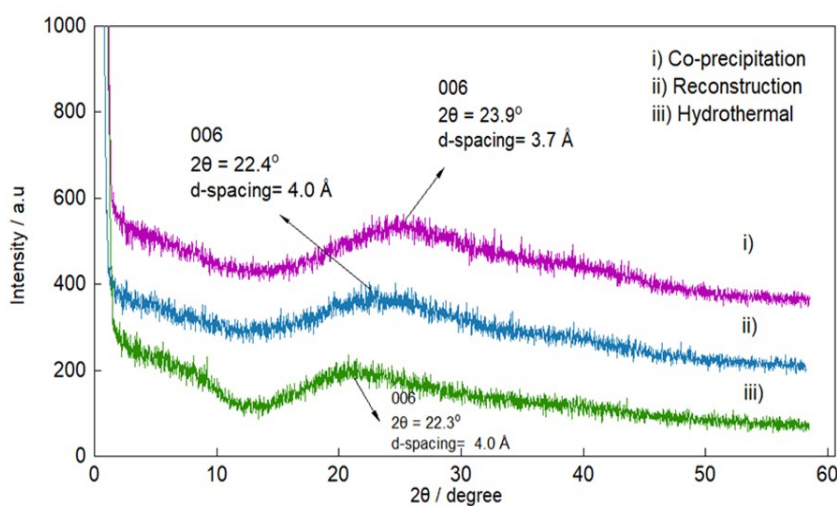


Figure 1f: X-ray diffraction pattern of suspension samples i) LDH exfoliated with sucrose (co-precipitation) ii) LDH exfoliated with sucrose (Reconstruction) iii) LDH exfoliated with sucrose (hydrothermal).

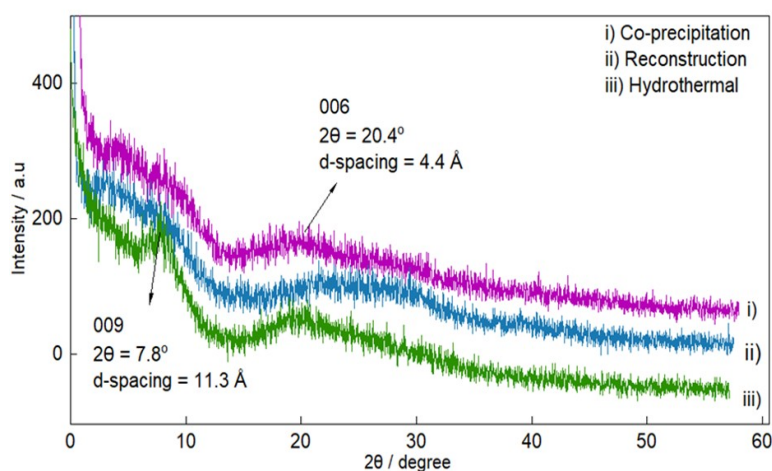


Figure 1g: X-ray diffraction pattern of semi-dry samples i) LDH exfoliated with sucrose (co-precipitation) ii) LDH exfoliated with sucrose (Reconstruction) iii) LDH exfoliated with sucrose (hydrothermal).

3.2. TGA

Figure 2 shows a thermogravimetric analysis of LDH pristine and LDH exfoliated with sucrose, glucose, and lactose. Figure 2a exhibits four decomposition stages of mass loss for the LDH pristine sample. The first mass loss of 10.9% at 210 °C was due to the loss of physically adsorbed water (19). The second mass loss of 8.1% at 365 °C was due to water loss in the LDH interlayer regions. The third mass loss of 9.9% at 521 °C was attributed to the decompositions of carbonate and the hydroxyl layers in between the LDH layers. The final mass loss of 16.1% at 690 °C is due to the decomposition of the organic compound (19). A similar pattern is observed in LDH exfoliated with sucrose (Figure 2b). Three thermal steps occurred at 42.6, 247, and 404 °C, registering the corresponding mass losses of 34.0, 24.7, and 5.3% respectively. The first mass loss is attributed to the loss of surface and interlayer water, whereas the second step might be due to the dehydroxylation of brucite sheets. The final step can be assigned to the decomposition of nitrate ions (20). Similarly, Figure 2c shows three thermal steps of mass losses which occurred at 39.6, 250.6, and 336.1 °C, registering the corresponding mass losses of 53.1, 10.3, and 9.8% respectively. The first mass loss is due to the loss of surface and interlayer water, while the second step is attributed to the dehydroxylation of the brucite sheets. The final mass loss is due to the decomposition of organic compounds or the rest residues of LDH (21). The mass loss pattern is also observed in Figure 2d. The first mass loss of 45.5% at 103.5 °C was due to the removal of weekly adsorbed water, followed by the second one at 268 °C (correspondingly 15.6%); this is ascribed to dehydroxylation of the LDH lattices. The third mass loss of 3.1% at 460 °C is due to the decomposition of nitrate ions (20). Figure 2e shows the stacked spectrum of the TGA/DTG graph of LDH pristine, LDH exfoliated with sucrose, glucose, and lactose for comparison. The first mass loss percentage for LDH pristine is less compared to exfoliated samples. This might be due to more water loss during the exfoliation process. In conclusion, the TGA data have significantly enhanced the thermal stability of exfoliated LDH compared to LDH pristine.

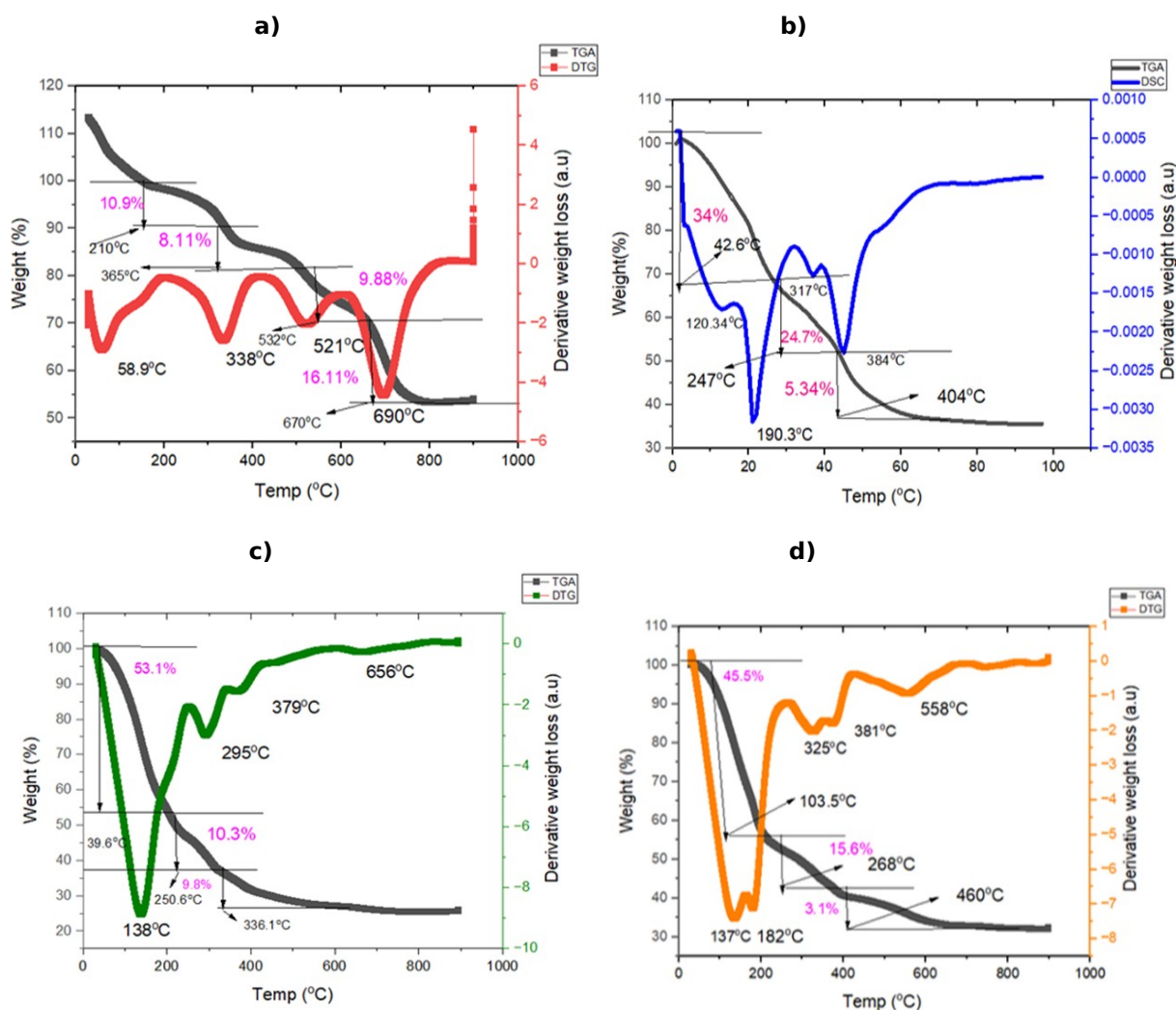


Figure 2: TGA/DTG graph of a) LDH pristine b) LDH exfoliated with sucrose c) LDH exfoliated with glucose c) LDH exfoliated with lactose.

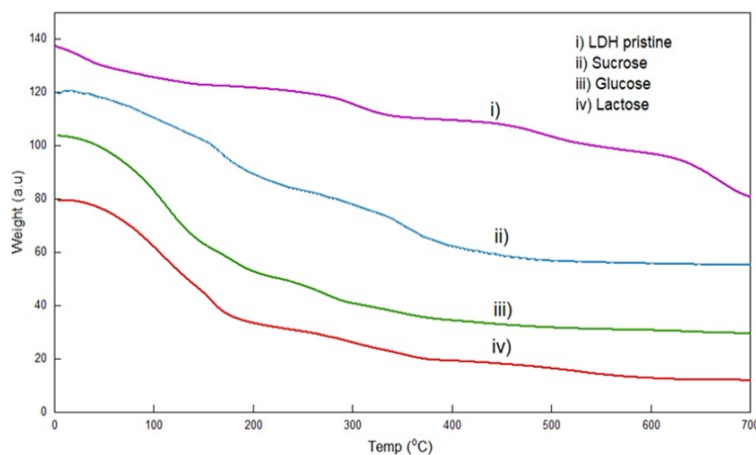


Figure 2e: Stack spectrum of TGA/DTG graph of i) LDH pristine ii) LDH exfoliated with sucrose iii) LDH exfoliated with glucose iv) LDH exfoliated with lactose.

3.3. DSC

Figure 3 shows differential scanning calorimetry (DSC) of LDH pristine and exfoliated LDH with sucrose, glucose, and lactose. Figure 3a exhibits three peaks at temperatures 276, 308, and 341 °C. These peaks are due to the endothermic reaction caused by the melting process (22). The sharp endothermic peak at 308 °C might be due to an initial LDH de-hydroxylation of the metal hydroxide layers (23). Figure 3b shows two peaks at 113 and 380 °C. These peaks are due to the endothermic reaction caused by the loss of adsorbed surface water (22). Figure 3c exhibits two peaks at 137 and 316 °C. The peak at 137 °C was due to an endothermic reaction caused by melting, while the peak at 316 °C was due to an exothermic reaction caused by crystallization (22). In contrast, Figure 3d exhibits one sharp peak at 139 °C due to an endothermic reaction caused by melting. Figure 3e compares the stacked spectrum of DSC spectra of LDH pristine and exfoliated LDH with sucrose, glucose, and lactose. Exfoliated LDH samples show lower endothermic temperatures compared to LDH pristine. This might be due to more surface and interlayer water loss during the formation of LDH nanosheets. The DSC data have significantly enhanced the thermal stability of exfoliated LDH compared to LDH pristine.

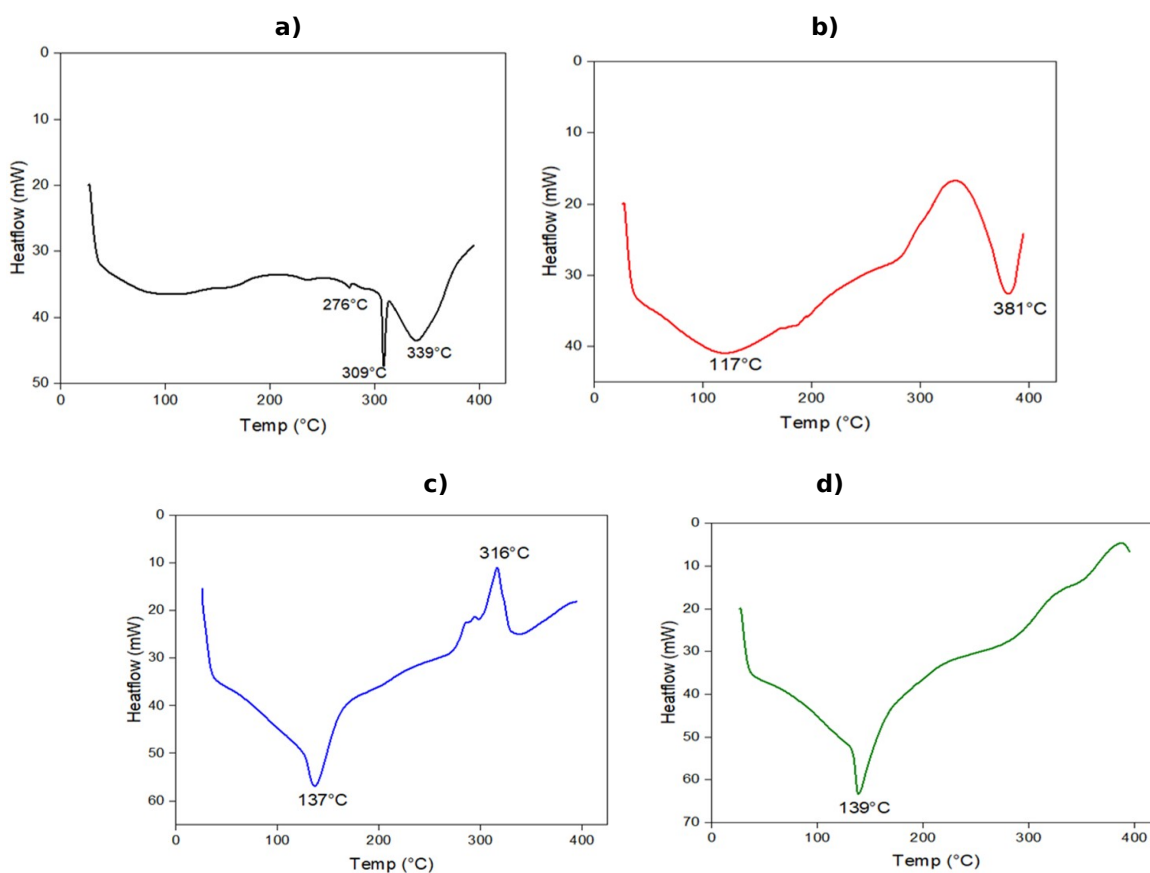


Figure 3: DSC graph of a) LDH pristine b) LDH exfoliated with sucrose c) LDH exfoliated with glucose d) LDH exfoliated with lactose.

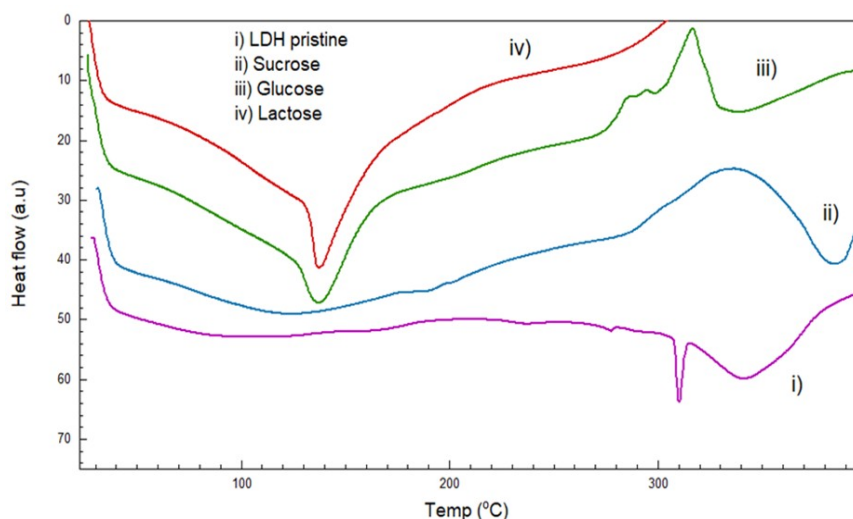
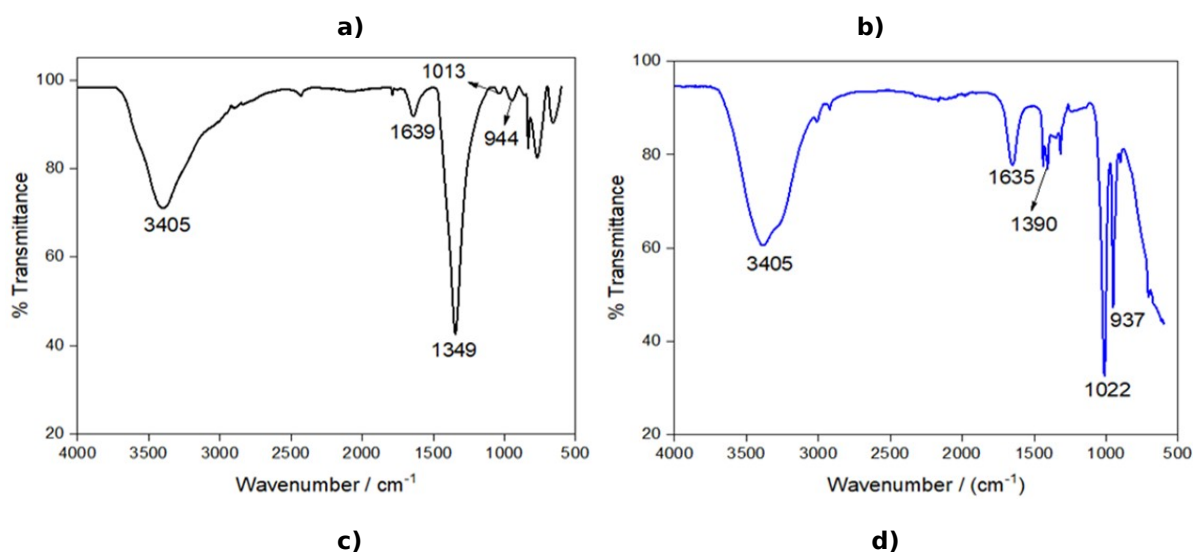


Figure 3e: Stack DSC graph of i) LDH pristine ii) LDH exfoliated with sucrose iii) LDH exfoliated with glucose iv) LDH exfoliated with lactose.

3.4. FTIR

Figures 4a, 4b, 4c, and 4d depict the FTIR spectra of LDH pristine and LDH exfoliated with glucose, lactose, and sucrose. Figures 4a, 4b, 4c, and 4d show absorption peaks in region 3400 cm^{-1} . These peaks were due to the O-H stretching of water molecules and hydroxyl groups in the lamellar structure (24). Figures 4a, 4b, 4c, and 4d also show absorption peaks at 1349 , 1344 , 1338 , and 1390 cm^{-1} , respectively which are attributed to the vibration of carbonate species. The bands in the region of $900\text{-}1000\text{ cm}^{-1}$ were ascribed to the stretching of Al-O and Mg-O bonds (25). The band that occurred around 1600 cm^{-1} was attributed to O-H of interlayer water molecules, while the absorption band of nitrate ions was observed at 1390 cm^{-1} . The absorption peaks at the region

$1000\text{-}1020\text{ cm}^{-1}$ in LDH pristine and exfoliated samples were due to C-H stretching (12). However, the intensity peak at the region $1000\text{-}1020\text{ cm}^{-1}$ for LDH exfoliated with sugar molecules is higher compared to LDH pristine due to the C-H stretching in sugar molecules which indicates the successful exfoliation of sugar molecules in the interlayer of LDH. All the bands that appeared in LDH pristine also appeared in exfoliated LDHs. This may indicate that LDH was successfully exfoliated into single-layer structures. Figure 4e demonstrates the stacked spectrum of LDH pristine and exfoliated LDH, where it shows the important bands of LDH. The bands present in LDH pristine in the region of 3400 , 1600 , and 1300 cm^{-1} are also present in exfoliated LDHs.



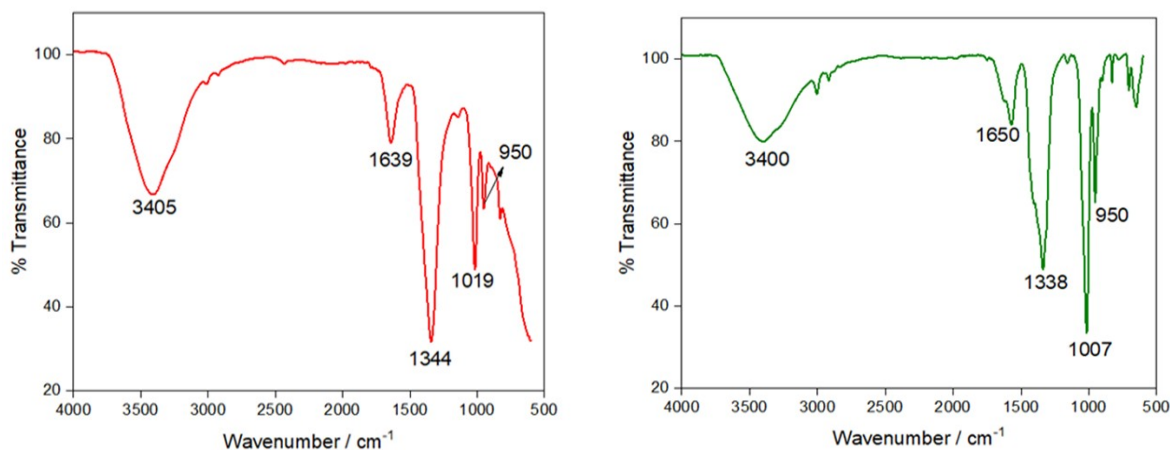


Figure 4: FTIR spectra of a) LDH pristine b) LDH exfoliated with sucrose c) LDH exfoliated with glucose c) LDH exfoliated with lactose.

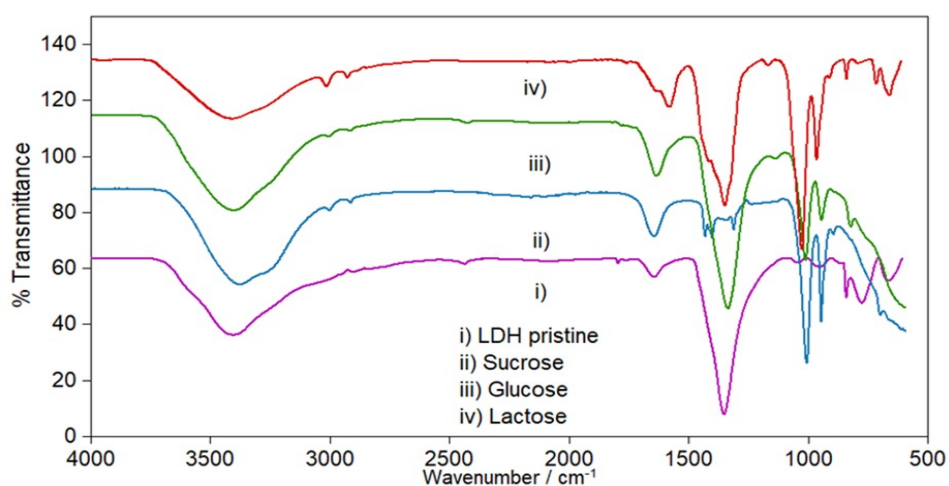


Figure 4e: Stacked FTIR spectra of i) LDH pristine ii) Exfoliated LDH with sucrose iii) Exfoliated LDH with glucose iv) Exfoliated LDH with lactose

3.5. Stack FTIR of suspension exfoliated LDH with sucrose by co-precipitation, hydrothermal, and reconstruction.

Figure 4f depicts the FTIR spectrum of suspension LDH exfoliated with sucrose. Three different preparation methods were employed for the suspension samples below, namely co-precipitation, reconstruction, and hydrothermal. All the suspension samples show absorption peaks in the region of 3400 cm^{-1} . These peaks were due to the O-H stretching of water molecules and hydroxyl groups in the lamellar structure (24). Besides, absorption peaks in the region of 1600 cm^{-1} are assigned to the stretching of the O-H of interlayer water molecules. The bands in the $900\text{-}1000\text{ cm}^{-1}$ region were ascribed to the stretching of Al-O and Mg-O bonds (24).

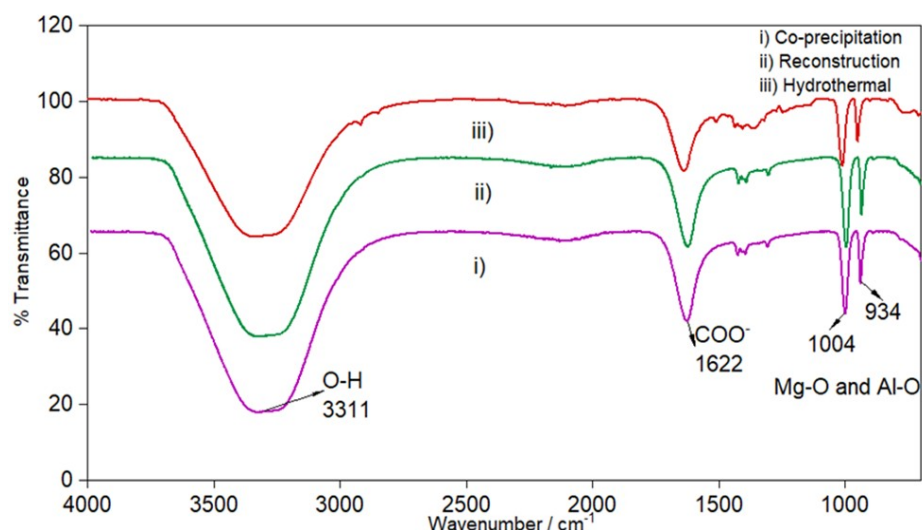


Figure 4f: Stacked FTIR spectra of suspension samples i) LDH exfoliated with sucrose (co-precipitation) ii) LDH exfoliated with sucrose (reconstruction) iii) LDH exfoliated with sucrose (hydrothermal).

3.6. Stack FTIR of semi-dry exfoliated LDH with sucrose by co-precipitation, hydrothermal, and reconstruction

Figure 4g shows FTIR spectroscopy analysis of semi-dry exfoliated LDH with sucrose. Different methods have been used for the semi-dry samples below such as co-precipitation, reconstruction, and hydrothermal. All the suspension samples show absorption peaks in the region 3400 cm^{-1} . These peaks are due to the O-H stretching of water

molecules and hydroxyl groups in the lamellar structure (25). Besides, absorption peaks at the region 1600 cm^{-1} due to O-H of interlayer water molecules. The bands in the $900\text{--}1000\text{ cm}^{-1}$ region are ascribed to the stretching of Al-O and Mg-O bonds (24). Absorption peaks at the region 1300 cm^{-1} due to the vibration of nitrate ions. FTIR makes it easy to determine the functional groups and possible interactions between intercalated anions and inorganic lamellae.

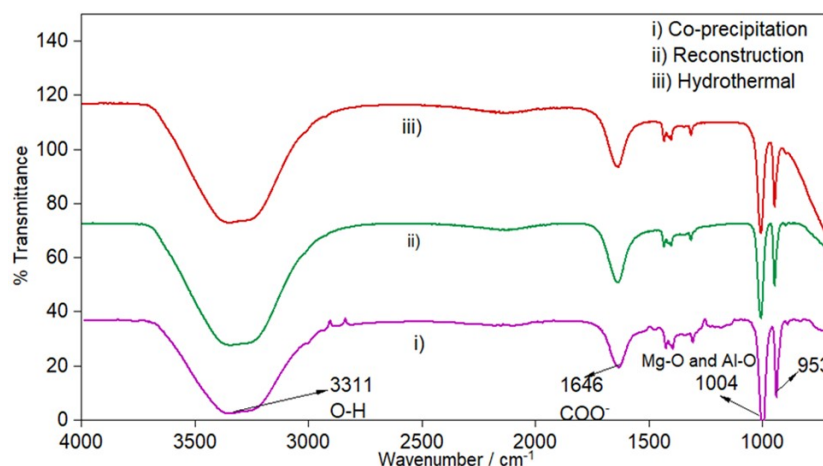


Figure 4g: Stacked FTIR spectra of semi-dry samples i) LDH exfoliated with sucrose (co-precipitation) ii) LDH exfoliated with sucrose (reconstruction) iii) LDH exfoliated with sucrose (hydrothermal).

3.7. BET

Figure 5 shows the nitrogen adsorption-desorption isotherms of LDH pristine and LDH exfoliated with sucrose, glucose, and lactose. Figure 5a shows the LDH pristine, where it displays type IV sorption isotherms with a H3 hysteresis loop. This loop belongs to mesoporous materials, composed of plate-like substances with agglomerating slit-shaped pores (26). Figures 5b, 5c, and 5d show LDH exfoliated with sucrose, glucose, and lactose.

They display H2-type loops where the distributions of pore size radius are wide (27). Compared to LDH pristine, LDH exfoliated with sucrose, glucose, and lactose shows a broad adsorption branch. This is due to the increase in basal spacing during the exchange of sugar molecules into the interlayer LDH (27). The adsorption and desorption curves of sucrose do not overlap in low relative pressure, indicating that sucrose molecules form strong chemical bonds with the adsorption sites, resulting

in a slow desorption rate and incomplete desorption (29). The wide hysteresis loop for the

exfoliated LDHs proved the successful exfoliation of sugar molecules into LDH layers.

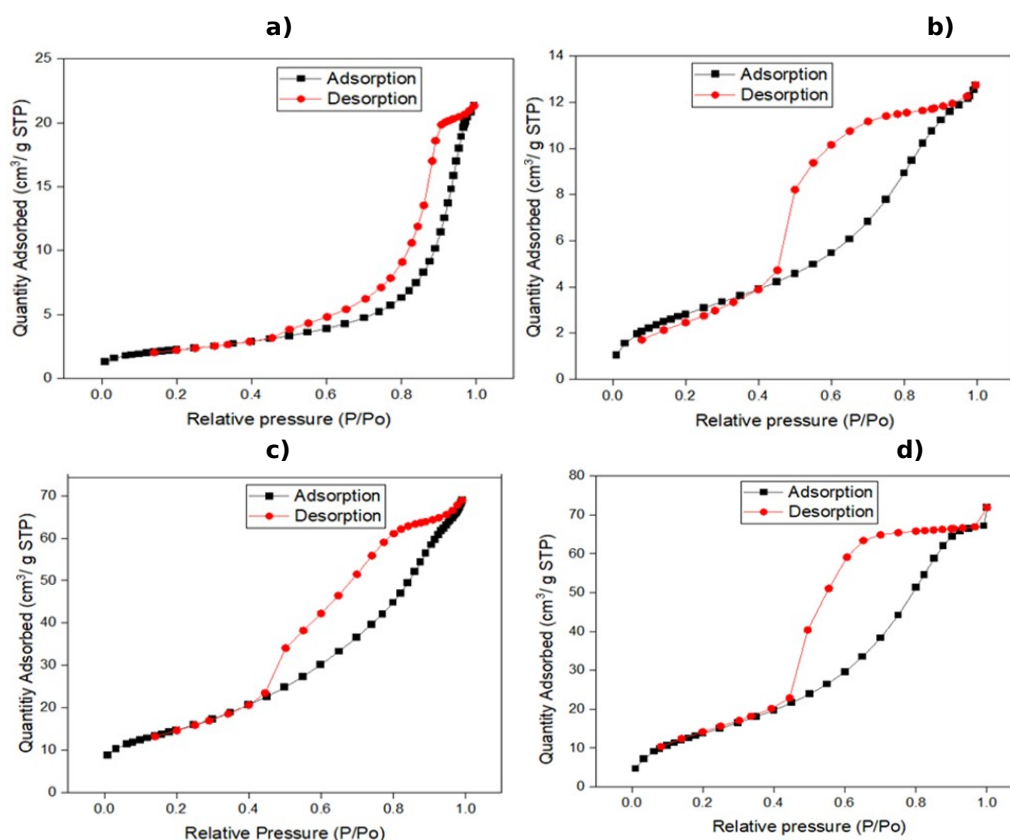
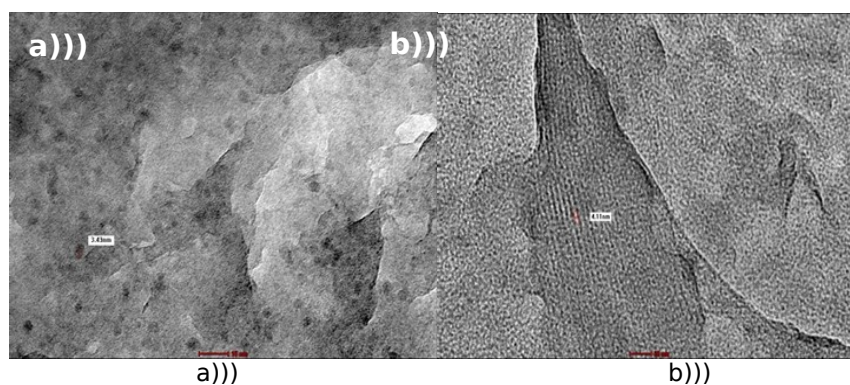


Figure 5: BET graph of a) LDH pristine b) LDH exfoliated with sucrose c) LDH exfoliated with glucose d) LDH exfoliated with lactose.

3.8. TEM

The formation of the LDH nanosheet was observed using transmission electron microscopy (TEM). Figure 6a reveals that LDH exfoliated with sucrose (co-precipitation suspension) has dark, agglomerated spherical-like particles (30). LDH nanosheets can be observed in Figure 6b (co-precipitation semi-dry) and in Figure 6c (co-precipitation fully dried) with a thickness of 4.35 nm and 3.98 nm respectively (31). Figure 6d shows agglomerated dark particles for LDH exfoliated with sucrose (reconstruction suspension). Both

Figure 6e (reconstruction semi-dry) and 6f (reconstruction fully dried) show spherical-like particles. TEM image of exfoliated LDH nanosheets can be observed with a thickness of 2.68 nm in Figure 6g (hydrothermal suspension). LDH exfoliated with sucrose (hydrothermal semi-dry) reveals a dark spherical-like particle with a diameter of 8.15 nm in Figure 6h while LDH exfoliated with sucrose (hydrothermal fully dried) reveals a spherical-like particle with a diameter of 3.01 nm in Figure 6i.



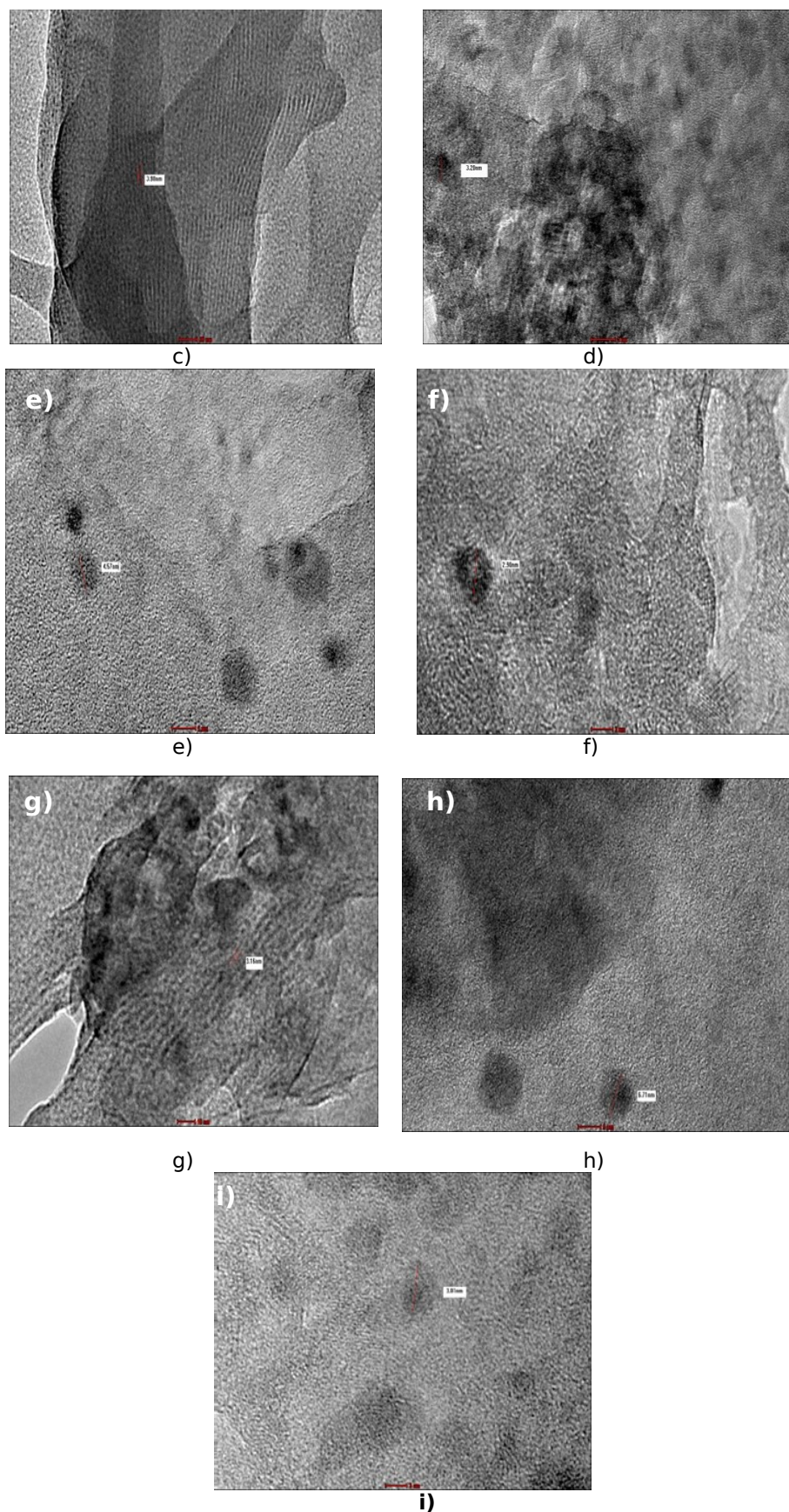


Figure 6: TEM images of exfoliated LDH with sucrose a) Co-precipitation suspension b) Co-precipitation semi-dried c) Co-precipitation fully dried d) Reconstruction suspension e) Reconstruction semi-dried f) Reconstruction fully dried g) Hydrothermal suspension h) Hydrothermal semi-dried i) Hydrothermal fully dried.

4. CONCLUSION

The exfoliation of LDH has emerged as a highly promising and rapidly advancing research area, primarily due to its extensive applications and potential in the field of material sciences. Sugar molecules have demonstrated their potential as an effective exfoliating agent for the exfoliation of layered double hydroxides (LDH) without the need for pre-intercalation of the layered material. The exfoliation of LDH has been successfully confirmed through a comprehensive analysis using various techniques including X-ray diffraction (XRD), Fourier transform infrared spectroscopy (FTIR), transmission electron microscopy (TEM), thermogravimetric analysis (TGA), differential scanning calorimetry analysis (DSC), and Brunauer-Emmett-Teller (BET) analysis. These techniques collectively provide strong evidence for the exfoliation of LDH. The presence of a singular peak in the X-ray diffraction (XRD) analysis indicates that the exfoliation process effectively produced individual layers of LDH nanosheets. Besides, a study is conducted on the crystalline state of layered double hydroxide (LDH) at various phases during the process of liquid exfoliation. This investigation encompassed the stages of suspension, semi-dry suspension, and dried solid samples. The X-ray diffraction (XRD) study indicates the presence of a distinct and prominent peak, suggesting the successful development of single-layer nanosheets. Fourier transform Infrared (FTIR) analysis also provides evidence of the effective exfoliation of multilayer materials. All the bands observed in LDH pristine samples were likewise observed in exfoliated LDHs and the intensity of the peaks for the exfoliated LDH is higher compared to pristine LDH. In addition, the thermal stability of LDH exfoliated samples is greatly enhanced through the utilization of TGA and DSC analysis. The mass loss percentage of exfoliated double hydroxide (LDH) is greater than pristine LDH. The broad hysteresis loops seen in the BET analysis of exfoliated LDHs provide evidence of the successful incorporation of sugar molecules into the LDH layers. The application of transmission electron microscopy (TEM) yielded significant findings about the formation of LDH nanosheets and pseudo-hexagonal particles in exfoliated LDHs. In summary, there is a pressing need for the development of environmentally friendly techniques for the exfoliation of layered double hydroxides (LDHs).

5. CONFLICT OF INTEREST

The authors declare no conflict of interest.

6. ACKNOWLEDGMENTS

This research was supported by the Ministry of Higher Education Malaysia under the Fundamental Research Grant Scheme (FRGS) with Grant no: 203/PKIMIA/6711925.

7. REFERENCES

1. Ghazali SA, Fatimah I, Bohari FL. Synthesis of Hybrid Organic-Inorganic Hydrotalcite-Like Materials Intercalated with Duplex Herbicides: The Characterization and Simultaneous Release Properties. Vol. 26, *Molecules*. 2021.
2. Gorrasi G, Sorrentino A. Layered double hydroxide polymer nanocomposites for food-packaging applications. *Layer Double Hydroxide Polym Nanocomposites*. 2020;743-79.
3. Zhang Y, Xu H, Lu S. Preparation and application of layered double hydroxide nanosheets. *RSC Adv* [Internet]. 2021;11(39):24254-81. Available from: <URL>.
4. Munonde TS, Zheng H, Nomngongo PN. Ultrasonic exfoliation of NiFe LDH/C nanosheets for enhanced oxygen evolution catalysis. *Ultrason Sonochem*. 2019;59:104716.
5. Karthikeyan J, Fjellvåg H, Bundli S, Sjøstad AO. Efficient Exfoliation of Layered Double Hydroxides; Effect of Cationic Ratio, Hydration State, Anions and Their Orientations. *Materials (Basel)* [Internet]. 2021 Jan 2 [cited 2022 Oct 12];14(2):1-11.
6. Joshi D, Adhikari N. An Overview on Common Organic Solvents and Their Toxicity. *J Pharm Res Int*. 2019 Jun 29;1-18.
7. Chen Z, Fan Q, Huang M, Cölfen H. Synthesis of two-dimensional layered double hydroxides: a systematic overview. *CrystEngComm* [Internet]. 2022;24(26):4639-55. Available from: <URL>.
8. Niu Y, Zheng C, Xie Y, Kang K, Song H, Bai S, et al. Efficient Adsorption of Ammonia by Surface-Modified Activated Carbon Fiber Mesh. Vol. 13, *Nanomaterials*. 2023.
9. Verheijen M, Lienhard M, Schrooders Y, Clayton O, Nudischer R, Boerno S, et al. DMSO induces drastic changes in human cellular processes and epigenetic landscape in vitro. *Sci Reports* 2019 91 [Internet]. 2019;9(1):1-12. Available from: <URL>.
10. Zhitova E, Krivovichev S, Yakovenchuk V, Ivanyuk G, Pakhomovsky Y, Mikhailova J. Crystal chemistry of natural layered double hydroxides. 4. Crystal structures and evolution of structural complexity of quintinite polytypes from the Kovdor alkaline massif, Kola peninsula, Russia. *Mineral Mag*. 2017 Jul 11;82.
11. Chen K, Zhang W, Pan X, Huang L, Wang J, Yang Q, et al. Natural Sugar: A Green Assistance to Efficiently Exfoliate Inorganic Layered Nanomaterials. *Inorg Chem*. 2018 May 7 ;57(9):5560-6. Available from: <URL>.
12. Chen S, Xu R, Liu J, Zou X, Qiu L, Kang F, et al. Simultaneous Production and Functionalization of Boron Nitride Nanosheets by Sugar-Assisted Mechanochemical Exfoliation. *AdvMater*. 2019 Mar 1;31(10):1804810. Available from: <URL>.
13. Hoenig E, Strong SE, Wang M, Radhakrishnan JM, Zaluzec NJ, Skinner JL, et al. Controlling the Structure of MoS₂ Membranes via Covalent Functionalization with Molecular Spacers. *Nano Lett* [Internet]. 2020 Nov 11;20(11):7844-51. Available from: <URL>.
14. Bae HJ, Goh Y, Yim H, Yoo SY, Choi J-W, Kwon D-K. Atomically thin, large area aluminosilicate nanosheets

- fabricated from layered clay minerals. *Mater Chem Phys* [Internet]. 2019;221:168-77. Available from: [<URL>](#).
15. Matusik J, Hyla J, Maziarz P, Rybka K, Leiviskä T. Performance of Halloysite-Mg/Al LDH Materials for Aqueous As(V) and Cr(VI) Removal. *Materials (Basel)* [Internet]. 2019;12(21).
16. Naik B, Arulraj J, Kolinjavadi M, Rajamathi M. Solvent-Mediated and Mechanochemical Methods for Anion Exchange of Carbonate from Layered Double Hydroxides Using Ammonium Salts. *ACS Omega*. 2019 Nov 12;XXXX.
17. Liang J, Ma R, Iyi N, Ebina Y, Takada K, Sasaki T. Topochemical Synthesis, Anion Exchange, and Exfoliation of Co–Ni Layered Double Hydroxides: A Route to Positively Charged Co–Ni Hydroxide Nanosheets with Tunable Composition. *Chem Mater*. 2010 Jan 26;22(2):371-8. Available from: [<URL>](#).
18. Kansal S, Singh P, Biswas S, Chowdhury A, Mandal D, Priya S, et al. Superior-catalytic performance of Ni-Co layered double hydroxide nanosheets for the reduction of p-nitrophenol. *Int J Hydrogen Energy* [Internet]. 2023;48(56):21372-82. Available from: [<URL>](#)
19. Magri VR, Duarte A, Perotti GF, Constantino VRL. Investigation of Thermal Behavior of Layered Double Hydroxides Intercalated with Carboxymethylcellulose Aiming Bio-Carbon Based Nanocomposites. Vol. 3, *ChemEngineering*. 2019.
20. Ebadi M, Buskaran K, Saifullah B, Fakurazi S, Hussein MZ. The Impact of Magnesium–Aluminum-Layered Double Hydroxide-Based Polyvinyl Alcohol Coated on Magnetite on the Preparation of Core-Shell Nanoparticles as a Drug Delivery Agent. *Int J Mol Sci* [Internet]. 2019;20(15). Available from: [<URL>](#).
21. Rosa-Guzmán M, Guzman A, Cayetano-Castro N, Del Rio J, Corea M, Martínez-Ortiz M. Thermal Stability Evaluation of Polystyrene-Mg/Zn/Al LDH Nanocomposites. *Nanomaterials*. 2019 Oct 27;9:1528.
22. Ghanbari E, Picken SJ, van Esch JH. Analysis of differential scanning calorimetry (DSC): determining the transition temperatures, and enthalpy and heat capacity changes in multicomponent systems by analytical model fitting. *J Therm Anal Calorim* [Internet]. 2023;148(22):12393-409. Available from: [<URL>](#).
23. Zhitova ES, Greenwell HC, Krzhizhanovskaya MG, Apperley DC, Pekov I V, Yakovenchuk VN. Thermal Evolution of Natural Layered Double Hydroxides: Insight from Quintinite, Hydrotalcite, Stichtite, and Iowaite as Reference Samples for CO₃- and Cl-Members of the Hydrotalcite Supergroup. Vol. 10, *Minerals*. 2020.
24. Hashim N, Sharif SNM, Isa IM, Ali NM, Damanhuri MIM. Synthesis and Characterisation of Zinc/Aluminium-Layered Double Hydroxide-L-Phenylalanate Nanocomposites Using Ion Exchange Method. *Educ J Sci Math Technol*. 2017 Jun 15 ;4(1):24-33. Available from: [<URL>](#).
25. Razak NIA, Yusoff NISM, Wahit MU. Characterization and Thermal Behaviour of Magnesium-Aluminium Layered Double Hydroxide. *J Adv Res Exp Fluid Mech Heat Transf*. 2021 Dec 23;5(1):1-9. Available from: [<URL>](#).
26. Szymaszek-Wawryca A, Díaz U, Samojeden B, Motak M. Synthesis, Characterization, and NH₃-SCR Catalytic Performance of Fe-Modified MCM-36 Intercalated with Various Pillars. Vol. 28, *Molecules*. 2023.
27. Zhang L-Y, Han Y-L, Liu M, Deng S-L. Ni-Al layered double hydroxide-coupled layered mesoporous titanium dioxide (Ni-Al LDH/LM-TiO₂) composites with integrated adsorption-photocatalysis performance. *RSC Adv* [Internet]. 2023;13(25):16797-814. Available from: [<URL>](#).
28. Bohari F, Noor N, Sheikh mohd ghazali S ahmad izaddin, Dzulkifli N, Fatimah I, Adam N. Synthesis and Characterization of 2,4-Dichlorophenoxypropanoic Acid (2,4-DP) Herbicide Interleaved into Calcium-Aluminium Layered Double Hydroxide and the Study of Controlled Release Formulation. *Indones J Chem*. 2022 Aug 9;22:1330.
29. Niu Y, Zheng C, Xie Y, Kang K, Song H, Bai S, et al. Efficient Adsorption of Ammonia by Surface-Modified Activated Carbon Fiber Mesh. Vol. 13, *Nanomaterials*. 2023.
30. Nagendra B, Rosely CVS, Leuteritz A, Reuter U, Gowd EB. Polypropylene/Layered Double Hydroxide Nanocomposites: Influence of LDH Intralayer Metal Constituents on the Properties of Polypropylene. *ACS Omega*. 2017 Jan 31;2(1):20-31. Available from: [<URL>](#).
31. Abinaya R, Archana J, Harish S, Navaneethan M, Ponnusamy S, Muthamizhchelvan C, et al. Ultrathin layered MoS₂ nanosheets with rich active sites for enhanced visible light photocatalytic activity. *RSC Adv*. 2018;8(47):26664-75. Available from: [<URL>](#).



Exploring the Antibacterial Efficacy of Silver Nanoparticles Synthesized through Abiotic Stress-Induced Germinated Seeds of *Vigna radiata*: A Comparative Analysis

Tissamol Abraham¹, K. P. Theertha¹, Sachin K. Ashok¹, Jebin Joseph², T. Sajini^{1*} 

¹Department of Chemistry, St. Berchmans College (Autonomous) Campus, Mahatma Gandhi University, Kottayam, India.

²Department of Botany, St. Berchmans College (Autonomous) Campus, Mahatma Gandhi University, Kottayam, India.

Abstract: The novel microwave-assisted green synthesis of silver nanoparticles (AgNPs) from stress-induced germinated seeds of *Vigna radiata* (VR) is explored in this research. AgNPs were successfully synthesized using abiotic stress-induced germinated seeds of VR, induced by salinity, drought, and heavy metals such as sodium chloride (NaCl), polyethylene glycol (PEG), and a chromium solution, respectively. The characterization of the synthesized AgNPs was performed using various techniques, including UV-visible spectrophotometer, dynamic light scattering (DLS), zeta potential, XRD, FT-IR, and FE-SEM. The concentration of AgNPs synthesized from Vr-NaCl, Vr-Cr, Vr-PEG, and Vr-DW followed the order Ag/Vr-DW > Ag/Vr-NaCl > Ag/Vr-PEG > Ag/Vr-Cr. Notably, the synthesized AgNPs exhibited significant antibacterial activity against *Staphylococcus aureus* bacteria. A comparative analysis of the antibacterial efficacy of AgNPs synthesized using different stress-induced VR seed extracts revealed that AgNPs from PEG stress-induced germinated seeds of VR displayed excellent antibacterial activity. These findings underscore the potential of stress-induced germinated seeds of VR as a promising resource for producing AgNPs with exceptional antibacterial properties, thereby opening avenues for the development of innovative antimicrobial agents.

Keywords: Silver nanoparticles, *Vigna radiata*, Microwave, Green synthesis, Stress-induced germination, Antibacterial.

Submitted: July 31, 2023. **Accepted:** May 7, 2024.

Cite this: Abraham T, Theertha KP, Ashok SK, Joseph J, Sajini T. Exploring the Antibacterial Efficacy of Silver Nanoparticles Synthesized through Abiotic Stress-Induced Germinated Seeds of *Vigna radiata*: A Comparative Analysis. JOTCSA. 2024;11(3): 984-94.

DOI: <https://doi.org/10.18596/jotcsa.1335103>

***Corresponding author's E-mail:** sajinijebin@sbcollge.ac.in

1. INTRODUCTION

Silver nanoparticles (AgNPs) have gained significant attention in recent years due to their unique physical and chemical properties, including excellent antibacterial activity against a broad range of microorganisms (1,2). The antibacterial properties of AgNPs have been widely utilized in various fields, including medicine, food packaging, water treatment, and cosmetics (3). The use of AgNPs in these fields has been facilitated by their small size, high surface area-to-volume ratio, and ability to penetrate bacterial cell walls and membranes, leading to the disruption of cell functions and eventual cell death (4,5).

For the production of AgNPs, a number of techniques have been devised, including chemical, physical, and biological methods (6,7). Chemical

methods are widely used due to their simplicity and reproducibility (8). However, they frequently include the usage of hazardous substances, which can be harmful to both the environment and human health. Physical methods, such as laser ablation, have also been used for the synthesis of AgNPs. However, they are often expensive, time-consuming, and require specialized equipment (9). Biological methods, including plant extracts and microorganisms, have emerged as a green and sustainable approach for synthesizing AgNPs, avoiding the use of toxic chemicals and reducing the environmental impact of AgNP synthesis (10-12). Among various green synthesis strategies, microwave-assisted synthesis offers a rapid and efficient method for producing AgNPs with precise control over their size and morphology (11,12). The use of microwave irradiation allows for a faster reaction rate and reduced synthesis time compared

to conventional methods, enabling high throughput production of AgNPs (15,16). Microwave-assisted synthesis also promotes uniform heating and improved particle size distribution, leading to enhanced stability and performance of AgNPs in various applications such as catalysis, sensing, and biomedical fields (17,18).

Using plant extracts to synthesize AgNPs has several advantages, including low cost, easy availability, and a wide range of phytochemicals that can act as reducing agents, capping agents, and stabilizers (19-22). Among various plant species, *Vigna radiata* (VR), also known as mung bean or green gram, has been widely used to synthesize AgNPs (23,24). Several studies have reported the synthesis of AgNPs using VR extracts, including stem, leaf, and seed extracts (23-26). Some studies showed the effect of AgNPs on the seed germination stages of VR (27,28). The phytochemicals present in VR are flavonoids, saponins, tannins, phytic acid, carotenoids, starch, proteins, fibre, and minerals (29). However, the use of stress-induced germinated seeds of VR for synthesizing AgNPs has not been explored in depth.

Stress-induced germination can occur through the activation of abiotic stress response pathways in the seeds, leading to changes in gene expression and metabolic activity (30-32). For example, exposure to high salinity levels can activate signalling pathways that regulate the release of seed dormancy and promote germination (33). Under stress conditions, the seeds release certain chemicals and hormones that initiate the growth of the embryonic axis and the shoot (34,35). Stress-induced germination process can enhance the synthesis of secondary metabolites, including phenolic compounds and flavonoids, which can act as reducing agents and stabilize the synthesized AgNPs (32). Therefore, stress-induced seed germination of VR can be a potential approach for enhancing the synthesis of AgNPs with improved antibacterial activity.

In this study, we aimed to explore the antibacterial efficacy of AgNPs synthesized from stress-induced germinated seeds of VR. The seeds were germinated in various extract media, including NaCl, PEG, distilled water, and chromium solution. The seed extract prepared from germinated seeds in distilled water was taken as the control. The AgNPs were synthesized using a green approach of microwave irradiation, which is a simple and efficient method for synthesizing AgNPs. The size, shape, and distribution of the AgNPs can be determined using various techniques such as field emission scanning electron microscopy (FE-SEM), UV-visible spectrophotometer, dynamic light scattering (DLS), zeta potential, and Fourier transform infrared spectroscopy (FT-IR). The antibacterial activity of the prepared AgNPs was evaluated against *Staphylococcus aureus* (*S. aureus*). A comparative analysis of the antibacterial efficacy of AgNPs synthesized using different seed extracts was also performed.

The environmental significance of the present work lies in the utilization of stress-induced germinated seeds of VR for the synthesis of AgNPs through a green approach (36). This approach offers the following environmental benefits: (a) Sustainable

resource utilization: VR seeds are commonly available and easily cultivated. By utilizing germinated seeds under stressful conditions, the research taps into a readily accessible and renewable resource. This reduces the reliance on scarce or non-renewable materials for AgNPs synthesis, making it more sustainable (9). (b) Eco-friendly synthesis: The green approach of microwave irradiation and the use of plant extracts as the reaction medium reduce the dependence on hazardous chemicals and solvents typically employed in conventional nanoparticle synthesis methods. This eco-friendly process minimizes the generation of toxic by-products and waste, contributing to the reduction of environmental pollution (37). (c) Reduced energy consumption: microwave irradiation is a rapid and energy-efficient method for AgNPs synthesis. Compared to traditional heating methods, it requires less time and energy to complete the reaction (38). This energy-saving aspect aligns with efforts to reduce the carbon footprint associated with scientific research and industrial processes. (d) Potential alternative to conventional antimicrobial agents: The synthesized AgNPs demonstrated significant antibacterial activity against *Staphylococcus aureus* bacteria (39). If further developed and optimized, these AgNPs derived from VR seeds could offer an environmentally friendly alternative to conventional antimicrobial agents. This could potentially contribute to reducing the widespread use of chemical-based antibiotics and antimicrobials, which can have negative impacts on ecosystems and promote the development of antibiotic-resistant bacteria.

The results of this study can provide insights into the potential use of stress-induced germinated seeds of VR as a novel and eco-friendly approach for synthesizing AgNPs with enhanced antibacterial activity. The utilization of stress-induced germinated seeds of VR for AgNP synthesis presents an environmentally significant approach that aligns with the principles of sustainability, eco-friendliness, and reduced energy consumption. By exploring greener alternatives, this research contributes to the development of environmentally benign strategies for nanoparticle synthesis and antimicrobial applications, which can have positive implications for both human health and the environment.

2. EXPERIMENTAL

2.1. Materials

VR seeds were obtained from the local market in Kottayam, India. Analytical grade chemicals such as AgNO₃, NaCl, PEG 6000, and K₂Cr₂O₇ were purchased from Merck, India. All the solutions were prepared in double distilled water.

2.2. Stress-induced Seed Germination of VR

Stress-induced germination of VR refers to the process of inducing germination in the seeds of this plant species under stress conditions such as high salt, drought, temperature fluctuations, or exposure to chemicals. Here we opted for exposure to chemicals such as salt, heavy metal ion solution, and PEG, keeping distilled water as control. For the culturing of VR under different stress conditions,

initially wash the VR seeds thoroughly with distilled water and dry them. Then place 50 seeds in four petri dishes and add 50 mL of stress-inducing 0.5 ppm solutions of NaCl, PEG, and chromate solution to three separate petri dishes and 50 mL of distilled water to the fourth petri dish. Wet a filter paper with distilled water and place it on top of the seeds in each petri dish. Close the petri dishes and incubate them in a dark place at room temperature for 48 hours. After 48 hours, carefully remove the filter paper using forceps and examine the germination rate of the seeds in each petri dish. Record the number of germinated seeds in each dish.

2.3. Extraction Procedure

Collect the stress-induced germinated seeds of VR in NaCl, PEG, distilled water, and chromium solution. Wash the seeds thoroughly with distilled water to remove any residual salt or chemicals. Dry the seeds separately in an oven at 50 °C. Place 6 g of dried seeds in RB flask with 50 mL of distilled water and reflux it for 30 minutes at 80 °C. The resultant extract in each case was filtered through Whatman 41 filter paper. The extracts obtained from NaCl, PEG, chromium solution, and distilled water are designated as Vr-NaCl, Vr-PEG, Vr-Cr, and Vr-DW, respectively.

2.4. Synthesis of Silver Nanoparticles

To reduce Ag (I) ions to Ag (0), the four extracts obtained from VR were used. To achieve this, 10 mL of the extract was mixed with 90 mL of a 1 mM aqueous silver nitrate solution, and the resulting mixture was exposed to microwave irradiation for 4 minutes in a domestic microwave oven [Sharp R219T (W)] operating at 800 W power and 2450 MHz frequency. The formation of AgNPs was monitored at 30-second intervals using a UV-vis spectrophotometer. The AgNPs obtained from Vr-NaCl, Vr-PEG, Vr-Cr, and Vr-DW were designated as

Ag/Vr-NaCl, Ag/Vr-PEG, Ag/Vr-Cr, and Ag/Vr-DW, respectively.

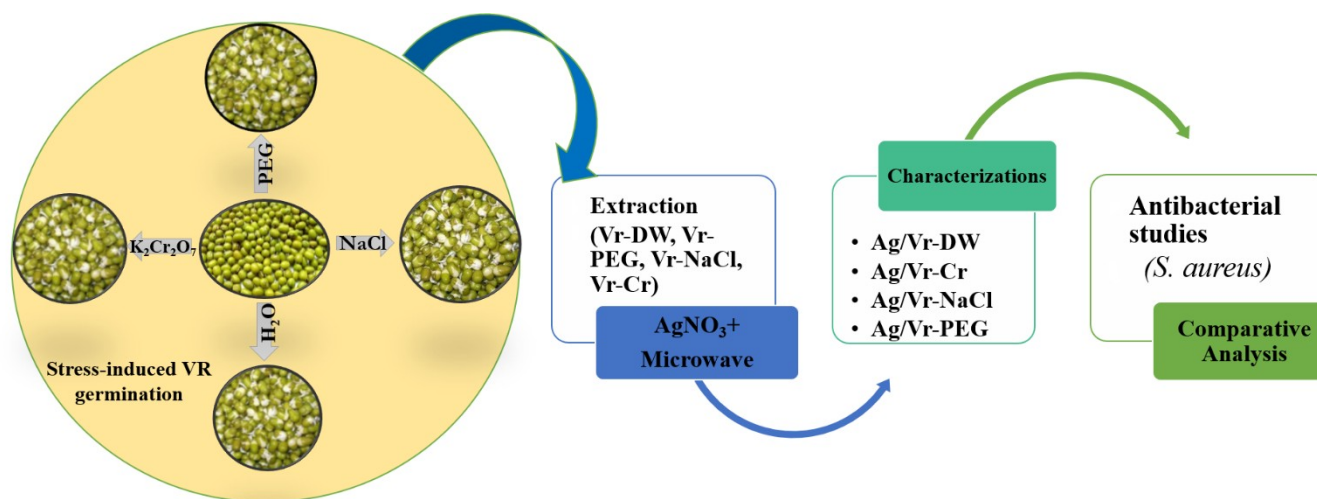
2.5. Characterization of Silver Nanoparticles

The surface plasmon resonance of synthesized AgNPs has been analyzed by UV-vis spectrophotometer. The AgNPs colloid was diluted with distilled water and loaded in a quartz cuvette. The UV-vis spectral range was set between 200-600 nm. The study was performed with the Shimadzu UV-2450 Spectrophotometer. FT-IR spectra of synthesized AgNPs were analyzed using the Perkin Elmer-400 spectrometer with ATR attachment. VR extracts and nanoparticles synthesized from different extracts of VR were scanned, and the scans were collected with resolution and 500-3500 cm^{-1} wavenumber.

FE-SEM is used to determine the particle size distribution and average size of particles in nanometer scale of the synthesized nanoparticles. For FE-SEM analysis, MAIA3 XMH FE-SEM was used. The hydrodynamic size of synthesized nanoparticles was measured with a dynamic light scattering detector (DLS). The surface charge and stability were also examined. The overall experimental procedure is depicted in Scheme 1.

2.6. Antibacterial Study

Antibacterial activity was determined using the standard agar well diffusion method against the human pathogenic bacteria *Staphylococcus aureus* (40-42). The cultures were swabbed on nutrient agar plate, wells were prepared on each plate using sterile Cork borer. 100 μL of samples were loaded into respective wells, and six replications were maintained for each sample using the respective VR extracts as control (C). The plates were incubated at 37 °C for 48 hours. After incubation, the zone of inhibition around the well was measured.



Scheme 1: Schematic representation of the synthesis and analysis.

3. RESULTS AND DISCUSSION

3.1. Germination Percentage

The germination percentage of VR under different chemical stress was recorded at 48 hours after incubating it in the respective solutions of NaCl, PEG, chromium solution, and distilled water. The

percentage of germination was determined using the equation (33) given below.

$$\text{Germination \%} = \frac{\text{Number of germinated seed}}{\text{Number of seeds kept for germination}} \times 100$$

The percentages of germination of VR in NaCl, PEG, chromium solution, and distilled water are found to be 96%, 100%, 90%, and 98%, respectively. Stress-induced germination in VR is a complex process involving multiple physiological, biochemical, and molecular changes such as water uptake, enzyme activation, respiration, oxidative stress, hormone levels, and gene expression. These changes enable the seed to cope with adverse conditions and promote germination.

Seed germination of VR can be affected by the presence of sodium chloride, chromium solution, and polyethylene glycol in the growth medium. The effects of VR seed germination in the presence of these solutions depend on the concentration of chemicals used and the duration of exposure (31,32). High concentrations and prolonged exposure can have detrimental effects on seed germination and seedling growth, while moderate stress can stimulate the synthesis of protective compounds and improve stress tolerance (31,43). NaCl is known to cause osmotic stress in plants, which can lead to various physiological and biochemical changes such as delayed germination, reduced growth, accumulation of proline, increased antioxidant activity, and changes in gene expression (30,34,43,44). PEG (polyethylene glycol) is a water-soluble polymer that is often used to induce osmotic stress in plants during germination

studies. When seeds of VR are germinated in the presence of PEG solution, it can affect their growth and development in various ways, such as delayed germination, reduced seedling growth, increased accumulation of osmoprotectants, and changes in gene expression (45). Chromium is a heavy metal that can have toxic effects on plant growth and development, such as inhibition of seed germination, reduction in seedling growth, chlorosis and leaf necrosis, accumulation of chromium in plant tissues, and activation of defense mechanism (46-48). Even if we are applying different kinds of stress, the plant has various adaptive mechanisms that help it to cope with the stress and continue to grow and develop under adverse conditions (30). Some of the secondary metabolites that have been identified in VR are flavonoids, alkaloids, tannins, saponins, and phenolic acids (49-50).

3.2. Synthesis of Silver Nanoparticles

AgNPs were produced through the application of microwave radiation to a mixture comprising 90 mL of a 1 mM silver nitrate aqueous solution and 10 mL of germinated VR extracts. During the process of microwave irradiation, the colourless reaction mixture gradually transformed into a yellowish-brown hue. Over time, the colour continued to evolve towards a consistent yellowish-brown shade, even with prolonged microwave irradiation, suggesting the successful formation of AgNPs. This colour change can be attributed to the presence of a metal surface containing free electrons in the conduction band, as well as positively charged nuclei, which collectively contribute to the observed coloration of the reaction mixture. The images of extracts and the respective AgNPs are depicted in Figure 1.

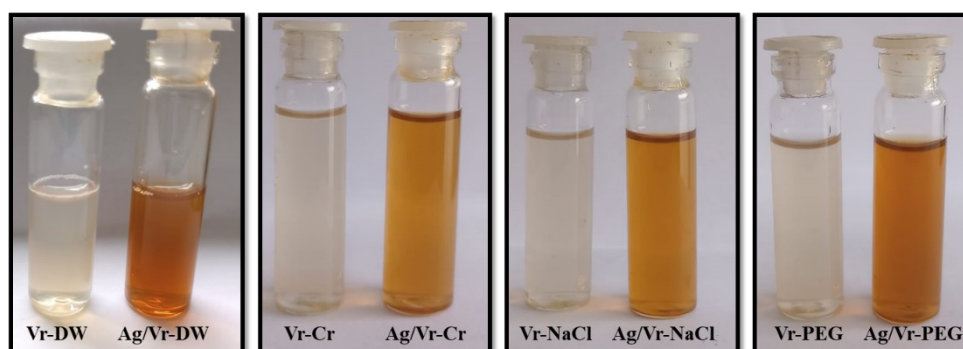


Figure 1: Images of VR-extracts and the respective AgNPs.

3.3. Characterization of silver nanoparticles

3.3.1. UV-visible spectrophotometer analysis

UV-vis. spectroscopy is a common analytical technique used to determine the optical properties of nanoparticles, including the size, shape, and concentration of the particles. The technique involves measuring the absorption of light by the nanoparticles at specific wavelengths in the UV-vis. range. Here, the four different AgNPs samples, Ag/Vr-DW, Ag/Vr-PEG, Ag/Vr-NaCl, and Ag/Vr-Cr, with 4 minute microwave irradiation were analyzed using UV-vis spectroscopy, and the obtained absorption peaks are depicted in Figure 2.

The absorption peak suggests that all four samples showed characteristic absorption peaks of AgNPs.

AgNPs exhibit a phenomenon called localized surface plasmon resonance (LSPR), which occurs due to the collective oscillation of conduction electrons in response to incident light (13,14,25). This results in a characteristic absorption peak in the UV-vis. spectrum. The position of this peak depends on the size, shape, and composition of the nanoparticles. Generally, spherical AgNPs exhibit a plasmon peak around 400-450 nm (visible range) (51,52). The intensity of the plasmon resonance peak is related to the concentration or density of AgNPs in the sample. Higher intensities indicate a greater number or higher concentration of nanoparticles. The intensity of the peak varied among the samples, with the highest peak observed in Ag/Vr-DW and the lowest peak observed in Ag/Vr-

Cr. The change in peak intensity implies the varying concentration of AgNPs formation. The shape of the peak can also provide information about the size distribution and uniformity of the nanoparticles. Here, a narrow, symmetric peak suggests a monodisperse population of nanoparticles (40,43,54). In addition to the plasmon resonance peak, AgNPs may exhibit additional absorption bands in the UV or visible region. These bands can arise from other electronic transitions or higher order plasmon modes.

The phytochemicals present in VR are responsible for the reduction process and stabilization of AgNPs (23,55). The stress-induced germination affected the formation of AgNPs compared to the control, Ag/Vr-DW. Chemical stress such as salinity, heavy metals, and PEG delayed the germination of seeds and, hence, the production of primary metabolites. Stress-induced process promote the synthesis of secondary metabolites in plants that could help the formation of AgNPs (30).

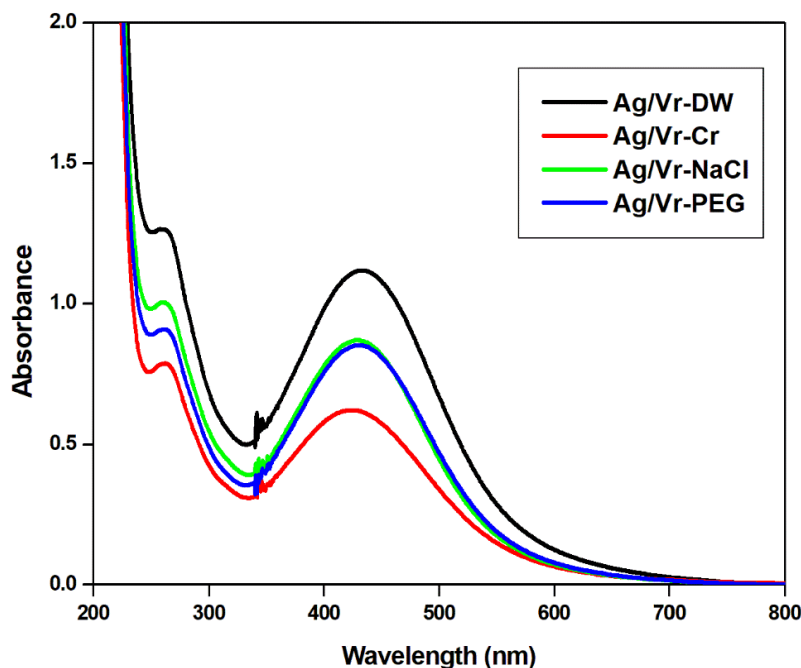


Figure 2: UV-vis. absorption spectrum of Ag/Vr-DW, Ag/Vr-Cr, Ag/Vr-NaCl and Ag/Vr-PEG.

3.3.2. FT-IR analysis

The method of using FT-IR (Fourier transform infrared) spectroscopy to pinpoint the functional groups present in a given sample. The vibrations of various functional groups in the sample are represented by the peaks seen in the spectrum. FT-IR spectra of Ag/Vr-DW, Ag/Vr-Cr, Ag/Vr-NaCl, and Ag/Vr-PEG and their respective extracts show four characteristic vibrational peaks at 3311cm^{-1} , 2074cm^{-1} , 1635cm^{-1} , and 576cm^{-1} (Figure 3). The peaks observed at 3311cm^{-1} and 1635cm^{-1} attributed to the stretching vibrations of O-H and N-H functional groups, respectively (56). The peak observed at 2074cm^{-1} is likely due to the presence of a $\text{C}\equiv\text{N}$ triple bond, which is indicative of a nitrile functional group. The vibrational peak at 576cm^{-1} indicates N-H bending vibrations (57). The extracts of VR contain various biomolecules such as carbohydrates, proteins, lipids, nucleic acids, and secondary metabolites. These peaks suggest that there may be some organic molecules present in the sample that are interacting with the AgNPs. The presence of the same peaks in both the extract and AgNPs samples indicates that the nanoparticles are likely coated or capped with the same organic molecules that are present in the extract. These

organic molecules may act as stabilizing agents for the nanoparticles, preventing them from agglomerating or undergoing further chemical reactions. This suggests that the extract may be a potential source of natural capping agents for the synthesis of AgNPs.

3.3.3. FE-SEM analysis

FE-SEM analysis is a type of electron microscopy that uses a focused beam of electrons to generate high-resolution images of the surface of a sample. The FE-SEM images of Ag/Vr-DW, Ag/Vr-Cr, Ag/Vr-NaCl, and Ag/Vr-PEG are depicted in Figure 4. All the FE-SEM images of the synthesized nanoparticles show a spherical shape. The spherical shape of the nanoparticles is a significant characteristic of AgNPs synthesized using plant extracts (58,59). The uniformity in shape suggests that the synthesis process is well controlled and reproducible (53). The average size of the nanoparticles can also be determined from the FE-SEM images by measuring the diameter of the spheres using ImageJ software. The mean areas of the AgNPs in Ag/Vr-DW, Ag/Vr-Cr, Ag/Vr-NaCl, and Ag/Vr-PEG are 6.7nm, 5.5nm, 924nm and 4.7nm, respectively.

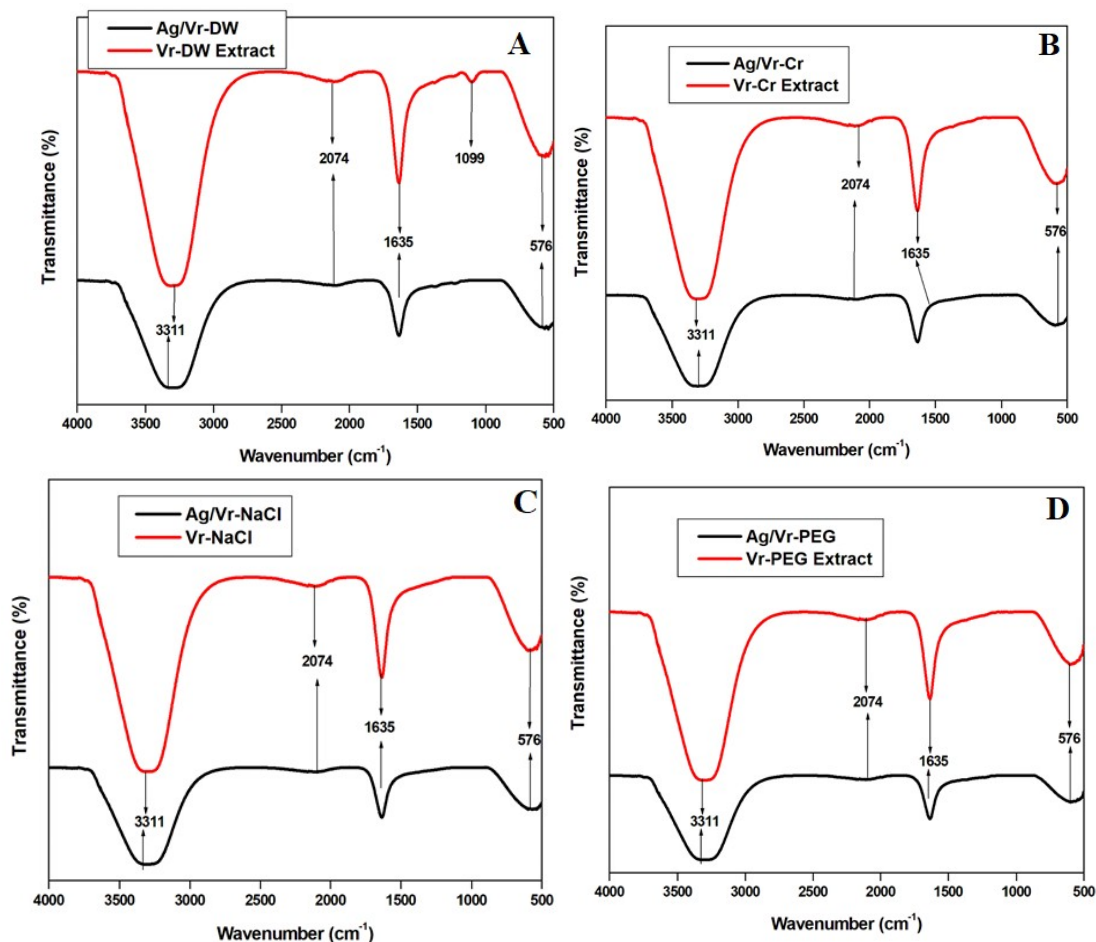


Figure 3: FT-IR spectra of (A) Ag/Vr-DW, (B) Ag/Vr-Cr, (C) Ag/Vr-NaCl and (D) Ag/Vr-PEG.

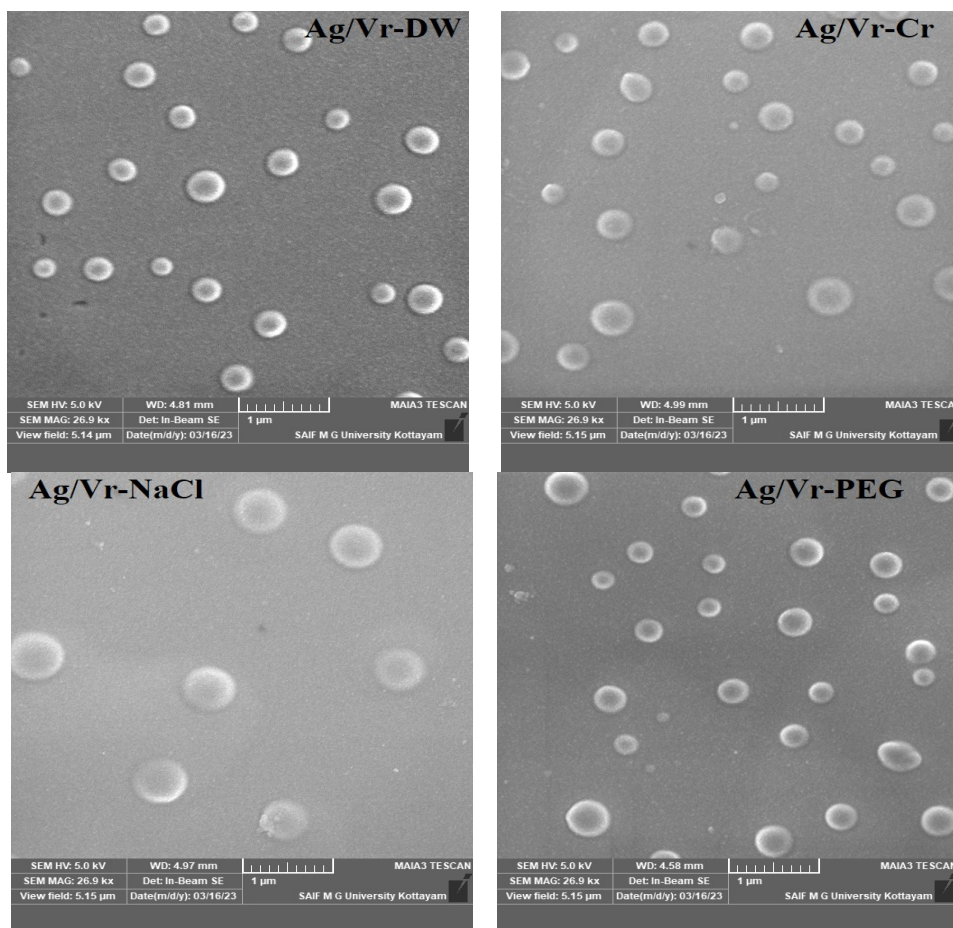


Figure 4: FE-SEM images of Ag/Vr-DW, Ag/Vr-Cr, Ag/Vr-NaCl and Ag/Vr-PEG.

3.3.4. Dynamic light scattering and zeta potential analysis

Dynamic light scattering (DLS) and zeta potential analysis are commonly used techniques to characterize the size distribution and surface charge of nanoparticles (60). Here, the DLS and zeta potential analyses were performed on four different

types of AgNPs synthesized from stress-induced germinated seeds of VR, with different chemical stresses applied: Ag/Vr-DW, Ag/Vr-Cr, Ag/Vr-NaCl, and Ag/Vr-PEG. The obtained data are depicted in Table 1 and the respective graphs are plotted in Figure 5.

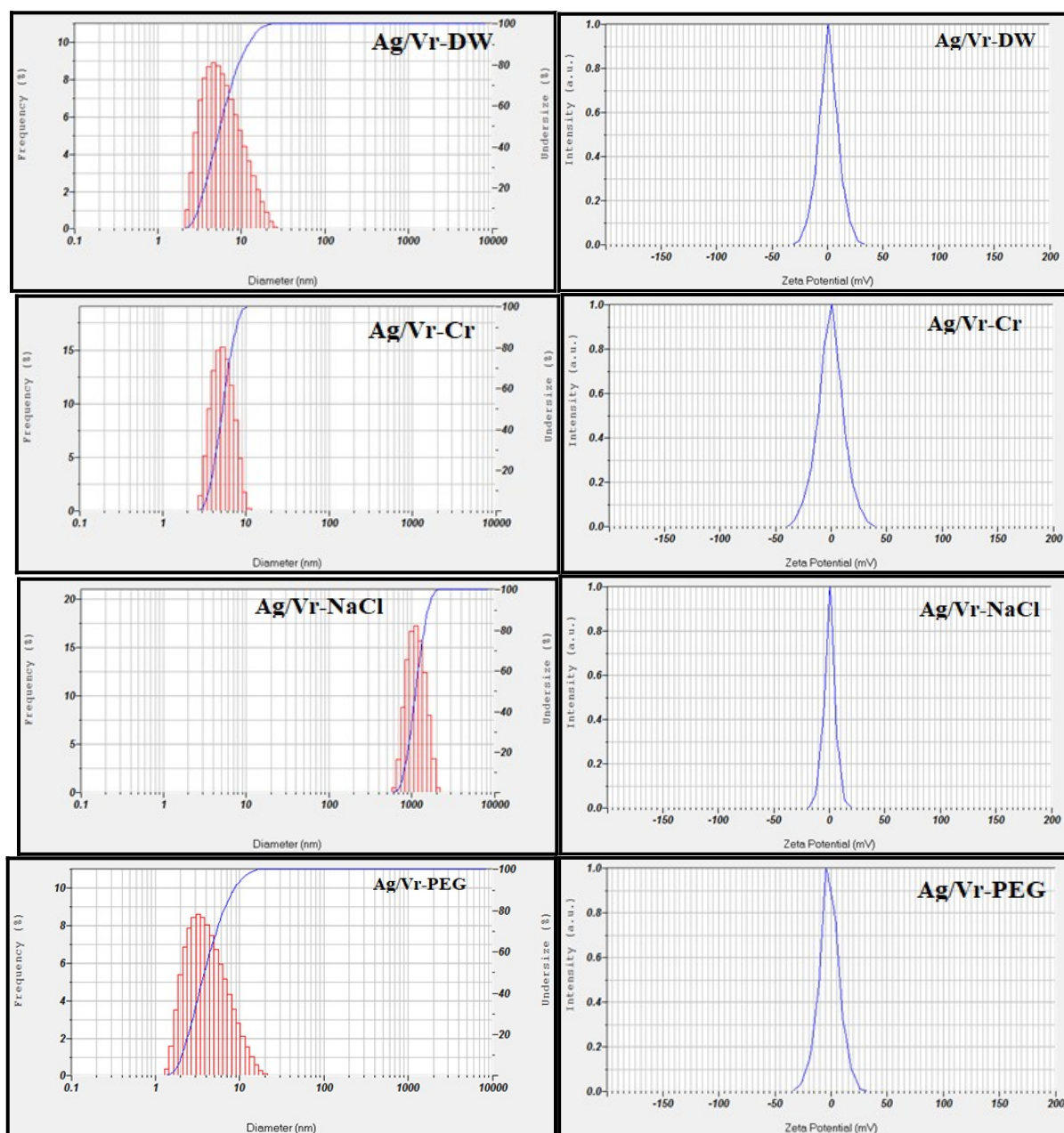


Figure 5: DLS and Zeta potential graphs of Ag/Vr-DW, Ag/Vr-Cr, Ag/Vr-NaCl and Ag/Vr-PEG.

The hydrodynamic particle size distribution of Ag/Vr-DW, Ag/Vr-Cr, Ag/Vr-NaCl, and Ag/Vr-PEG obtained from DLS analysis are 6.7nm, 5.5nm, 925nm, and 4.7nm, respectively. To minimize background scattering, the nanoparticle samples were diluted appropriately before conducting the analysis. The hydrodynamic size measurement of AgNPs takes into account the hydration layer present on the surface, resulting in a larger size compared to the size determined from FE-SEM images (61). The hydrodynamic size of AgNPs may be influenced by the presence of phytochemicals present in the VR extract.

The zeta potential value is a measure of the surface charge of the nanoparticles. A positive zeta potential value indicates that the surface of the nanoparticles is positively charged, whereas a negative value indicates a negative surface charge (62). In accordance with the results of the analysis, the zeta potential values for Ag/Vr-DW, Ag/Vr-Cr, Ag/Vr-NaCl, and Ag/Vr-PEG were 0.8, -0.5, 0.2, and -1.8, respectively. These values suggest that the surface of Ag/Vr-DW and Ag/Vr-NaCl nanoparticles is positively charged, whereas the surface of Ag/Vr-Cr and Ag/Vr-PEG nanoparticles is negatively charged. The zeta potential value is an essential factor that influences the stability of nanoparticles in

suspension (40). When the surface of nanoparticles is charged, they repel each other, which prevents them from agglomerating or settling. A high absolute value indicates that the nanoparticles are highly stable.

Table 1: Mean size and zeta potential values of AgNPs.

Nanoparticles	Mean Size (nm)	Zeta Potential (mV)
Ag/Vr-DW	6.7	0.8
Ag/Vr-Cr	5.5	-0.5
Ag/Vr-NaCl	925	0.2
Ag/Vr-PEG	4.7	-1.8

3.4. Antibacterial Studies

The antibacterial activity of the synthesized AgNPs against *Staphylococcus aureus* indicates their potential application as antimicrobial agents.

Several studies have reported the synthesis of AgNPs using *Vigna radiata* as a plant material and evaluated their antibacterial activity against different bacterial strains (23,24,63). The present study has tested four different types of AgNPs synthesized from stress-induced germinated seeds of VR, Ag/Vr-DW, Ag/Vr-Cr, Ag/Vr-NaCl, and Ag/Vr-PEG using the respective extracts as controls (C). The obtained results are depicted in Figures 6 and 7. According to the results, Ag/Vr-PEG exhibited the highest antibacterial activity against *S. aureus*, followed by Ag/Vr-NaCl, Ag/Vr-Cr, and Ag/Vr-DW, respectively. This trend is somewhat in the reverse order of the AgNPs concentration in the synthesized nanoparticles. The Ag/Vr-PEG exhibited higher antibacterial activity, likely due to the efficient reduction and stabilization facilitated by polyethylene glycol during synthesis. Moreover, the stress-induced germination process under PEG stress conditions may have led to the accumulation of bioactive compounds in the VR extract, enhancing the reduction efficiency of silver ions and promoting stronger interactions between AgNPs and bacterial cells.

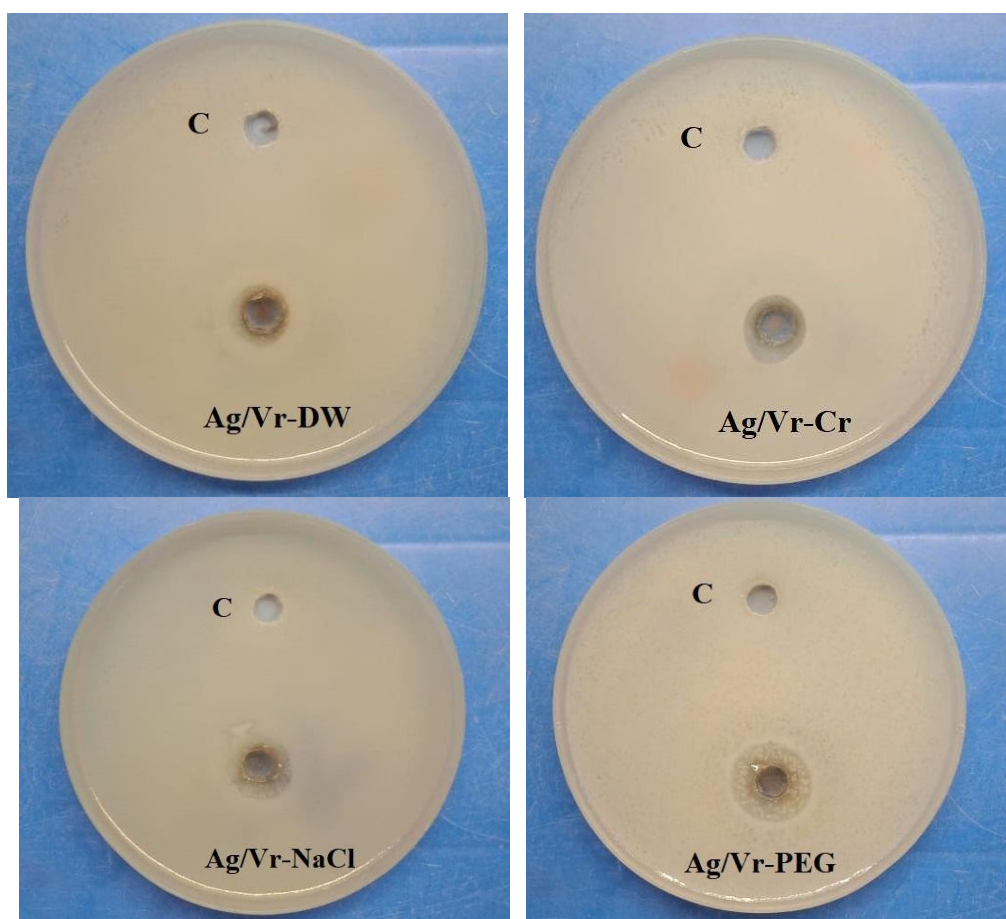


Figure 6: Antibacterial activity of Ag/Vr-DW, Ag/Vr-Cr, Ag/Vr-NaCl and Ag/Vr-PEG towards *Staphylococcus aureus*.

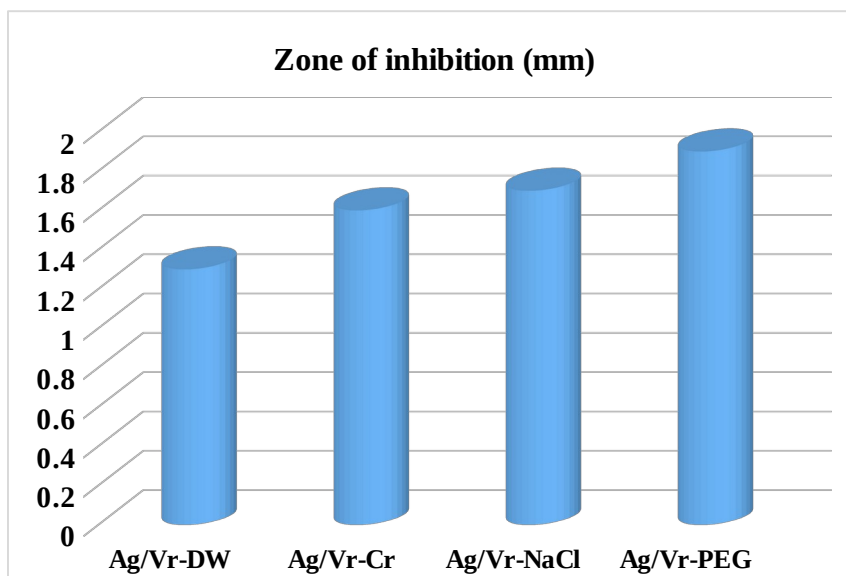


Figure 7: Zone of inhibition exhibited by different AgNPs.

The difference in antibacterial activity among the four types of synthesized nanoparticles could be due to variations in the size, morphology, or surface chemistry of the nanoparticles (64-66). For instance, the zeta potential analysis suggests that the surface charges of the nanoparticles differ, which can impact their interactions with bacterial cells. In addition, the chemical stresses applied during synthesis can also affect the antibacterial activity of the synthesized nanoparticles. For example, the presence of chromium ions may reduce the antibacterial activity of Ag/Vr-Cr nanoparticles, as chromium ions can interact with the silver ions and reduce their effectiveness.

It is also worth noting that the higher concentration of AgNPs in Ag/Vr-DW nanoparticles does not necessarily correlate with higher antibacterial activity. The antibacterial activity of the nanoparticles is influenced by a range of factors, including the concentration of silver ions, the size and morphology of the nanoparticles, and their surface chemistry (67,68).

The diverse phytochemical compositions of the extracts can also influence the reduction kinetics and stabilization of AgNPs during synthesis, leading to variations in size, shape, and surface properties (69). Factors such as pH, ionic strength, and the presence of biomolecules within the extracts may also impact AgNP characteristics and their interactions with bacterial cells (11). Moreover, the inherent antimicrobial properties of specific plant extracts could synergistically enhance the antibacterial efficacy of the synthesized AgNPs. This comparative analysis highlighted the importance of understanding extract-mediated effects on AgNP properties to optimize their antimicrobial activity for various applications. Figure 8 depicts a potential mechanism for the formation of AgNPs and their antibacterial activity.

To enhance the antibacterial efficacy of synthesized AgNPs, optimization strategies encompass controlled synthesis parameters such as reaction time and precursor concentration to tailor

nanoparticle size and surface characteristics (70). Surface functionalization techniques involving capping agents and ligands can enhance interactions with bacterial cells, while combination therapy with other antibacterial agents can exploit synergistic effects (71). Moreover, pH and ionic strength optimization, surface engineering for specificity, and biocompatibility enhancement are crucial considerations to improve AgNP efficacy and safety (67). Validation through rigorous in vitro and in vivo testing further ensures the efficacy and applicability of optimized AgNPs in various biomedical and environmental contexts.

4. CONCLUSION

The abiotic stress induced germinated VR seed through the microwave assisted method is a novel approach for the green synthesis of AgNPs. The abiotic stress was induced using sodium chloride, polyethylene glycol, distilled water, and chromium solution. The synthesized AgNPs were characterized using several techniques, including UV-vis, DLS, Zeta Potential, FT-IR, and FE-SEM. The AgNPs concentration synthesized from Vr-NaCl, Vr-Cr, Vr-PEG, and Vr-DW is of the order Ag/Vr-DW > Ag/Vr-NaCl > Ag/Vr-PEG > Ag/Vr-Cr. The study revealed that the prepared AgNPs exhibited a significant antibacterial activity against *Staphylococcus aureus* bacteria. Additionally, a comparative analysis of the antibacterial efficacy of AgNPs showed Ag/Vr-PEG > Ag/Vr-NaCl > Ag/Vr-Cr > Ag/Vr-DW. This research highlights the potential of stress-induced germinated seeds of VR as a sustainable and eco-friendly source for synthesizing AgNPs with excellent antibacterial properties. The findings contribute to the development of new antimicrobial agents that can be utilized in various applications, such as healthcare and biomedical fields, where combating bacterial infections is of utmost importance. Further investigations and optimizations can be followed to explore the full potential and applications of AgNPs derived from stress-induced germinated seeds of VR in antimicrobial research and development.

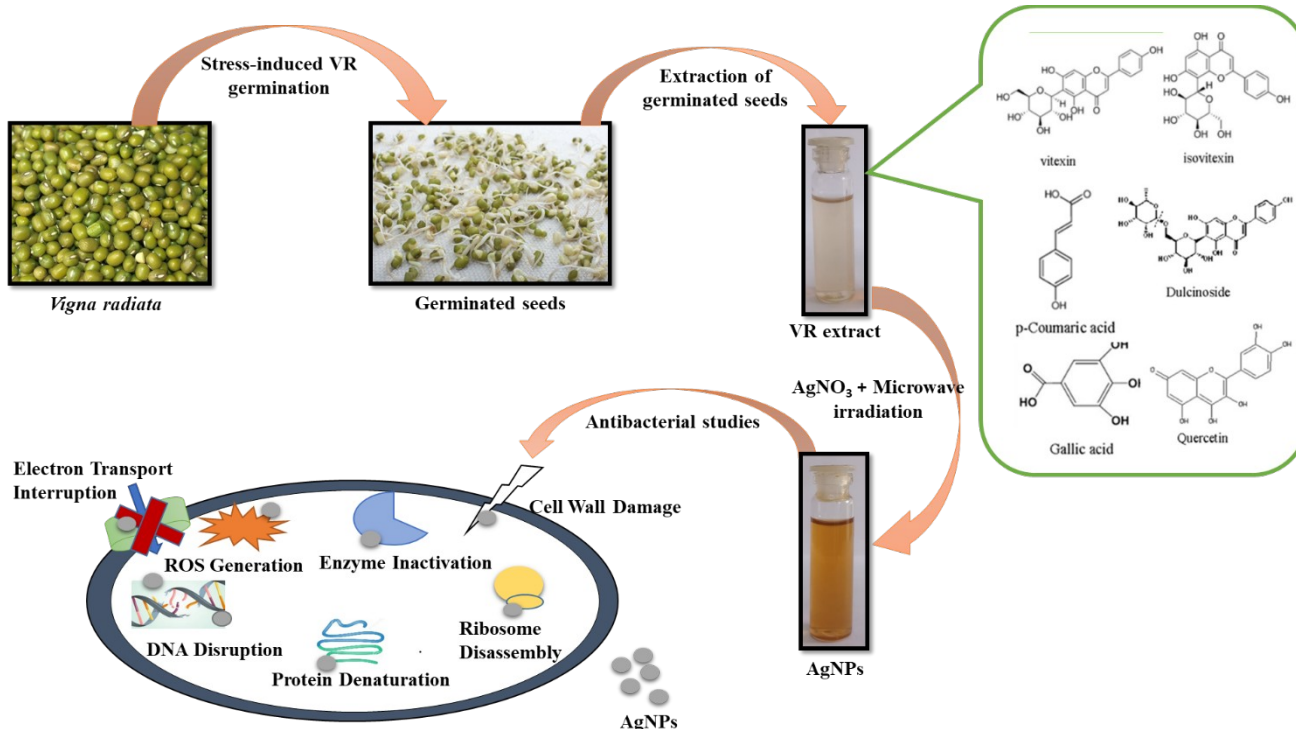


Figure 8: Potential mechanism for the formation of AgNPs and its antibacterial activity.

5. FUNDING

This research received no external funding.

6. CONFLICTS OF INTEREST

There are no conflicts to declare.

7. DATA AVAILABILITY STATEMENT

Data are available upon reasonable request.

8. ACKNOWLEDGEMENT

The authors thank Indian Science Technology and Engineering facilities Map (I-STEM), a Program supported by the Office of the Principal Scientific Adviser to the Govt. of India, for enabling access to the Field emission scanning electron microscopy (FESEM) with Energy Dispersive Spectroscopy (EDS), MAIA3 XMH at the Sophisticated Analytical Instrument Facility (DST-SAIF), Mahatma Gandhi University, Kottayam, India, to carry out this work.

9. REFERENCES

- Hasan KMF, Xiaoyi L, Shaoqin Z, Horváth PG, Bak M, Bej6 L, et al. Functional silver nanoparticles synthesis from sustainable point of view: 2000 to 2023 – A review on game changing materials. Heliyon [Internet]. 2022 Dec 1;8(12):e12322. Available from: [<URL>](#).
- Revathy R, Joseph J, Augustine C, Sajini T, Mathew B. Synthesis and catalytic applications of silver nanoparticles: a sustainable chemical approach using indigenous reducing and capping agents from Hyptis capitata. Environ Sci Adv [Internet]. 2022 Sep 27;1(4):491-505. Available from: [<URL>](#).
- Syafiuddin A, Salmiati, Salim MR, Beng Hong Kueh A, Hadibarata T, Nur H. A Review of Silver Nanoparticles: Research Trends, Global Consumption, Synthesis, Properties, and Future Challenges. J Chinese Chem Soc [Internet]. 2017 Jul 8;64(7):732-56. Available from: [<URL>](#).
- Yin IX, Zhang J, Zhao IS, Mei ML, Li Q, Chu CH. The Antibacterial Mechanism of Silver Nanoparticles and Its Application in Dentistry. Int J Nanomedicine [Internet]. 2020 Apr;Volume 15:2555-62. Available from: [<URL>](#).
- Khan A, Ahmad N, Fazal H, Ali M, Akbar F, Khan I, et al. Biogenic synthesis of silver nanoparticles using Rubus fruticosus extract and their antibacterial efficacy against Erwinia caratovora and Ralstonia solanacearum phytopathogens. RSC Adv [Internet]. 2024 Feb 14;14(9):5754-63. Available from: [<URL>](#).
- Nair GM, Sajini T, Mathew B. Advanced green approaches for metal and metal oxide nanoparticles synthesis and their environmental applications. Talanta Open [Internet]. 2022 Aug 1;5:100080. Available from: [<URL>](#).
- Raut S, Bhatavadekar A, Chougule R, Lekhak U. Silver nanoparticles synthesis from Crinum moorei: Optimization, characterization, kinetics and catalytic application. South African J Bot [Internet]. 2024 Feb 1;165:494-504. Available from: [<URL>](#).
- Suriati G, Mariatti M, Azizan A. Synthesis of Silver Nanoparticles by Chemical Reduction Method: Effect of Reducing Agent and Surfactant Concentration. Int J Automot Mech Eng [Internet]. 2014 Dec 30;10(1):1920-7. Available from: [<URL>](#).
- Ogundare SA, Adesetan TO, Muungani G, Moodley V, Amaku JF, Atewolara-Odule OC, et al. Catalytic degradation of methylene blue dye and antibacterial

- activity of biosynthesized silver nanoparticles using *Peltophorum pterocarpum* (DC.) leaves. *Environ Sci Adv* [Internet]. 2023 Feb 6;2(2):247-56. Available from: [<URL>](#).
10. Roy A, Bulut O, Some S, Mandal AK, Yilmaz MD. Green synthesis of silver nanoparticles: biomolecule-nanoparticle organizations targeting antimicrobial activity. *RSC Adv* [Internet]. 2019 Jan 21;9(5):2673-702. Available from: [<URL>](#).
11. Ahmed S, Ahmad M, Swami BL, Ikram S. A review on plants extract mediated synthesis of silver nanoparticles for antimicrobial applications: A green expertise. *J Adv Res* [Internet]. 2016 Jan 1;7(1):17-28. Available from: [<URL>](#).
12. Patra JK, Baek KH. Green Nanobiotechnology: Factors Affecting Synthesis and Characterization Techniques. *J Nanomater* [Internet]. 2014 Jan 1;2014(1):417305. Available from: [<URL>](#).
13. Saha S, Malik MM, Qureshi MS. Microwave Synthesis of Silver Nanoparticles. *Nano Hybrids* [Internet]. 2013 May;4:99-112. Available from: [<URL>](#).
14. Joseph S, Mathew B. Microwave-assisted facile synthesis of silver nanoparticles in aqueous medium and investigation of their catalytic and antibacterial activities. *J Mol Liq* [Internet]. 2014 Sep 1;197:346-52. Available from: [<URL>](#).
15. Joseph S, Mathew B. Microwave Assisted Biosynthesis of Silver Nanoparticles Using the Rhizome Extract of *Alpinia galanga* and Evaluation of Their Catalytic and Antimicrobial Activities. *J Nanoparticles* [Internet]. 2014 May 13;2014:967802. Available from: [<URL>](#).
16. Seku K, Gangapuram BR, Pejjai B, Kadimpati KK, Golla N. Microwave-assisted synthesis of silver nanoparticles and their application in catalytic, antibacterial and antioxidant activities. *J Nanostructure Chem* [Internet]. 2018 Jun 8;8(2):179-88. Available from: [<URL>](#).
17. Sreeram KJ, Nidhin M, Nair BU. Microwave assisted template synthesis of silver nanoparticles. *Bull Mater Sci* [Internet]. 2008 Dec 28;31(7):937-42. Available from: [<URL>](#).
18. Singh D, Rawat D, Isha. Microwave-assisted synthesis of silver nanoparticles from *Origanum majorana* and *Citrus sinensis* leaf and their antibacterial activity: a green chemistry approach. *Bioresour Bioprocess* [Internet]. 2016 Dec 16;3(1):14. Available from: [<URL>](#).
19. Chand K, Cao D, Eldin Fouad D, Hussain Shah A, Qadeer Dayo A, Zhu K, et al. Green synthesis, characterization and photocatalytic application of silver nanoparticles synthesized by various plant extracts. *Arab J Chem* [Internet]. 2020 Nov 1;13(11):8248-61. Available from: [<URL>](#).
20. Sorescu AA, Nuță A, Ion RM, Ioana-Raluca ȘB. Green synthesis of silver nanoparticles using plant extracts. In: *The 4th International Virtual Conference on Advanced Scientific Results*. 2016. p. 188-93.
21. Elia P, Zach R, Hazan S, Kolusheva S, Porat Z, Zeiri Y. Green synthesis of gold nanoparticles using plant extracts as reducing agents. *Int J Nanomedicine* [Internet]. 2014 Aug 20;9(1):4007-21. Available from: [<URL>](#).
22. Mittal AK, Chisti Y, Banerjee UC. Synthesis of metallic nanoparticles using plant extracts. *Biotechnol Adv* [Internet]. 2013 Mar 1;31(2):346-56. Available from: [<URL>](#).
23. Choudhary MK, Kataria J, Cameotra SS, Singh J. A facile biomimetic preparation of highly stabilized silver nanoparticles derived from seed extract of *Vigna radiata* and evaluation of their antibacterial activity. *Appl Nanosci* [Internet]. 2016 Jan 19;6(1):105-11. Available from: [<URL>](#).
24. Vazhacharickal PJ, Krishna GS. Green Synthesis of Silver, Copper and Zinc Nanoparticles from Mung bean (*Vigna radiata*) and Cowpea (*Vigna unguiculata*) Exudates and Evaluation of their Antibacterial Activity: An Overview. *Int J Curr Res Acad Rev* [Internet]. 2022;10(6):48-81. Available from: [<URL>](#).
25. Banerjee P, Satapathy M, Mukhopahayay A, Das P. Leaf extract mediated green synthesis of silver nanoparticles from widely available Indian plants: synthesis, characterization, antimicrobial property and toxicity analysis. *Bioresour Bioprocess* [Internet]. 2014 Dec 24;1(1):3. Available from: [<URL>](#).
26. Lourthuraj AA, Selvam MM, Hussain MS, Abdel-Warith AWA, Younis EMI, Al-Asgah NA. Dye degradation, antimicrobial and larvicidal activity of silver nanoparticles biosynthesized from *Cleistanthus collinus*. *Saudi J Biol Sci* [Internet]. 2020 Jul 1;27(7):1753-9. Available from: [<URL>](#).
27. Bahri S, Sharma Bhatia Sushma Moitra S, Sharma N, Bhatt R, Sinha Borthakur N, Agarwal R, et al. Influence of silver nanoparticles on seedlings of *Vigna radiata* (L.) R.Wilczek. *DU J Undergrad Res Innov* [Internet]. 2016;2(1):142-8. Available from: [<URL>](#).
28. Anju TR, Parvathy S, Sruthimol S, Jomol J, Mahi M. Assessment of Seed Germination and Growth of *Vigna radiata* L in the Presence of Green Synthesised and chemically Synthesised Nanoparticles. *Curr Trends Biotechnol Pharm* [Internet]. 2022 Jun 20;16:38-46. Available from: [<URL>](#).
29. Hou D, Yousaf L, Xue Y, Hu J, Wu J, Hu X, et al. Mung Bean (*Vigna radiata* L.): Bioactive Polyphenols, Polysaccharides, Peptides, and Health Benefits. *Nutrients* [Internet]. 2019 May 31;11(6):1238. Available from: [<URL>](#).
30. Ramakrishna A, Ravishankar GA. Influence of abiotic stress signals on secondary metabolites in plants. *Plant Signal Behav* [Internet]. 2011;6(11):1720-31. Available from: [<URL>](#).
31. Hasanuzzaman M, Nahar K, Alam M, Roychowdhury R, Fujita M. Physiological, Biochemical, and Molecular Mechanisms of Heat

- Stress Tolerance in Plants. *Int J Mol Sci* [Internet]. 2013 May 3;14(5):9643–84. Available from: [<URL>](#).
32. Ilyas M, Khan WA, Ali T, Ahmad N, Khan Z, Fazal H, et al. Cold Stress-induced Seed Germination and Biosynthesis of Polyphenolics Content in Medicinally Important *Brassica rapa*. *Phytomedicine Plus* [Internet]. 2022 Feb 1;2(1):100185. Available from: [<URL>](#).
33. Krishna Surendar K, Varshini S V., Deepa Sankari R, Susithra N, Kavitha S, Shankar M. Impact of Salt Stress (NaCl) on Seed Germination, Photosynthetic Pigments of Green Gram Cultivars of Co6 and Co8. *Plant Gene Trait* [Internet]. 2014;5(6):40–4. Available from: [<URL>](#).
34. Ghorbanpour A, Mami Y, Ashournezhad M, Abri F, Amani M. Effect of salinity and drought stress on germination of fenugreek. *African J Agric Res* [Internet]. 2011 Oct 26;6(24):5529–32. Available from: [<URL>](#).
35. Okçu G, Demir Kaya M, Atak M. Effects of Salt and Drought Stresses on Germination and Seedling Growth of Pea (*Pisum sativum* L.). *Turkish J Agric For* [Internet]. 2005 Jan 1;29(4):237–42. Available from: [<URL>](#).
36. Theertha KP, Ashok SK, Abraham T, Revathy R, Sajini T. Exploring the antibacterial potential of green synthesized silver nanoparticle decorated on functionalized multi-walled carbon nanotube: synthesis and analysis. *Chem Pap* [Internet]. 2024 Feb 16;78(3):1601–11. Available from: [<URL>](#).
37. Vidyasagar, Patel RR, Singh SK, Singh M. Green synthesis of silver nanoparticles: methods, biological applications, delivery and toxicity. *Mater Adv* [Internet]. 2023 Apr 24;4(8):1831–49. Available from: [<URL>](#).
38. Salem SS. A mini review on green nanotechnology and its development in biological effects. *Arch Microbiol* [Internet]. 2023 Apr 22;205(4):128. Available from: [<URL>](#).
39. Arshad F, Naikoo GA, Hassan IU, Chava SR, El-Tanani M, Aljabali AA, et al. Bioinspired and Green Synthesis of Silver Nanoparticles for Medical Applications: A Green Perspective. *Appl Biochem Biotechnol* [Internet]. 2023 Sep 5; Article in Press:1–34. Available from: [<URL>](#).
40. Liaqat N, Jahan N, Khalil-ur-Rahman, Anwar T, Qureshi H. Green synthesized silver nanoparticles: Optimization, characterization, antimicrobial activity, and cytotoxicity study by hemolysis assay. *Front Chem* [Internet]. 2022 Aug 29;10:952006. Available from: [<URL>](#).
41. Tippayawat P, Phromviyo N, Boueroy P, Chompoosor A. Green synthesis of silver nanoparticles in aloe vera plant extract prepared by a hydrothermal method and their synergistic antibacterial activity. *PeerJ* [Internet]. 2016 Oct 19;4(10):e2589. Available from: [<URL>](#).
42. Vijayan R, Joseph S, Mathew B. Green synthesis of silver nanoparticles using *Nerualia zeylanica* leaf extract and evaluation of their antioxidant, catalytic, and antimicrobial potentials. *Part Sci Technol* [Internet]. 2019 Oct 3;37(7):809–19. Available from: [<URL>](#).
43. Ma Y, Dias MC, Freitas H. Drought and Salinity Stress Responses and Microbe-Induced Tolerance in Plants. *Front Plant Sci* [Internet]. 2020 Nov 13;11(13):591911. Available from: [<URL>](#).
44. Benlioğlu B, Özkan U. Germination and Early Growth Performances of Mung Bean (*Vigna radiata* (L.) Wilczek) Genotypes Under Salinity Stress. *Tekirdağ Ziraat Fakültesi Derg* [Internet]. 2020 Sep 29;17(3):318–28. Available from: [<URL>](#).
45. Jincy M, Prasad VBR, Jeyakumara P, Senthila A, Manivannan N. Evaluation of green gram genotypes for drought tolerance by PEG (polyethylene glycol) induced drought stress at seedling stage. *Legum Res - An Int J* [Internet]. 2019 Sep 23;44(6):684–91. Available from: [<URL>](#).
46. Babu TN, Varaprasad D, Bindu YH, Kumari MK, Dakshayani L, Reddy MC, et al. Impact of Heavy Metals (Cr, Pb and Sn) on In Vitro Seed Germination and Seedling Growth of Green Gram (*Vigna radiata* (L.) R. Wilczek). *Curr Trends Biotechnol Pharm* [Internet]. 2014;8(2):160–5. Available from: [<URL>](#).
47. Singh D, Sharma NL. Effect of Chromium on Seed Germination and Seedling Growth of Green Gram (*Phaseolus aureus* L) and Chickpea (*Cicer arietinum* L). *Int J Appl Nat Sci* [Internet]. 2017;6(2):37–46. Available from: [<URL>](#).
48. Parayil SP, Praseetha KA, Abhilash ES. Study on Germination and Growth of Chromium Treated Green Gram, *Vigna radiata* (L.). *Nat Environ Pollut Technol* [Internet]. 2014;13(1):221–3. Available from: [<URL>](#).
49. Sharma KR, Giri G. Quantification of Phenolic and Flavonoid Content, Antioxidant Activity, and Proximate Composition of Some Legume Seeds Grown in Nepal. Salmerón I, editor. *Int J Food Sci* [Internet]. 2022 Aug 29;2022:4629290. Available from: [<URL>](#).
50. Kabré J d'Arc W, Dah-Nouvlessounon D, Hamba F, Agonkoun A, Guinin F, Sina H, et al. Mung Bean (*Vigna radiata* (L.) R. Wilczek) from Burkina Faso Used as Antidiabetic, Antioxidant and Antimicrobial Agent. *Plants* [Internet]. 2022 Dec 16;11(24):3556. Available from: [<URL>](#).
51. Moodley JS, Krishna SBN, Pillay K, Serphen, Govender P. Green synthesis of silver nanoparticles from *Moringa oleifera* leaf extracts and its antimicrobial potential. *Adv Nat Sci Nanosci Biotechnol* [Internet]. 2018 Mar 9;9(1):015011. Available from: [<URL>](#).
52. Calderón-Jiménez B, Johnson ME, Montoro Bustos AR, Murphy KE, Winchester MR, Vega Baudrit JR. Silver Nanoparticles: Technological Advances, Societal Impacts, and Metrological Challenges. *Front Chem* [Internet]. 2017 Feb 21;5:6. Available from: [<URL>](#).
53. Wei S, Wang Y, Tang Z, Hu J, Su R, Lin J, et al. A size-controlled green synthesis of silver

nanoparticles by using the berry extract of Sea Buckthorn and their biological activities. *New J Chem* [Internet]. 2020 Jun 8;44(22):9304-12. Available from: [<URL>](#).

54. Ibrahim HMM. Green synthesis and characterization of silver nanoparticles using banana peel extract and their antimicrobial activity against representative microorganisms. *J Radiat Res Appl Sci* [Internet]. 2015 Jul 1;8(3):265-75. Available from: [<URL>](#).

55. Kumari R, Singh JS, Singh DP. Biogenic synthesis and spatial distribution of silver nanoparticles in the legume mungbean plant (*Vigna radiata* L.). *Plant Physiol Biochem* [Internet]. 2017 Jan 1;110:158-66. Available from: [<URL>](#).

56. Hamouda RA, Hussein MH, Abo-elmagd RA, Bawazir SS. Synthesis and biological characterization of silver nanoparticles derived from the cyanobacterium *Oscillatoria limnetica*. *Sci Rep* [Internet]. 2019 Sep 10;9(1):13071. Available from: [<URL>](#).

57. Ragamathunnisa M, Jasmine Vasantha Rani E, Padmavathy R, Radha N. Spectroscopic study on Thiourea and Thiosemicarbazide in Nonaqueous media. *IOSR J Appl Phys* [Internet]. 2013;4(1):5-8. Available from: [<URL>](#).

58. He Y, Wei F, Ma Z, Zhang H, Yang Q, Yao B, et al. Green synthesis of silver nanoparticles using seed extract of *Alpinia katsumadai*, and their antioxidant, cytotoxicity, and antibacterial activities. *RSC Adv* [Internet]. 2017 Aug 15;7(63):39842-51. Available from: [<URL>](#).

59. Pirtarighat S, Ghannadnia M, Baghshahi S. Green synthesis of silver nanoparticles using the plant extract of *Salvia spinosa* grown in vitro and their antibacterial activity assessment. *J Nanostructure Chem* [Internet]. 2019 Mar 4;9(1):1-9. Available from: [<URL>](#).

60. Edison TNJI, Lee YR, Sethuraman MG. Green synthesis of silver nanoparticles using *Terminalia cuneata* and its catalytic action in reduction of direct yellow-12 dye. *Spectrochim Acta Part A Mol Biomol Spectrosc* [Internet]. 2016 May 15;161:122-9. Available from: [<URL>](#).

61. Hemlata, Meena PR, Singh AP, Tejavath KK. Biosynthesis of Silver Nanoparticles Using *Cucumis prophetarum* Aqueous Leaf Extract and Their Antibacterial and Antiproliferative Activity Against Cancer Cell Lines. *ACS Omega* [Internet]. 2020 Mar 17;5(10):5520-8. Available from: [<URL>](#).

62. Ashraf H, Anjum T, Riaz S, Naseem S. Microwave-Assisted Green Synthesis and

Characterization of Silver Nanoparticles Using *Melia azedarach* for the Management of *Fusarium* Wilt in Tomato. *Front Microbiol* [Internet]. 2020 Mar 10;11:238. Available from: [<URL>](#).

63. Nazrina Camalxaman S, Md Zain Z, Amom Z, Mustakim M, Mohamed E, Sham Rambely A. In vitro Antimicrobial Activity of *Vigna radiata* (L) Wilzeck Extracts Against Gram Negative Enteric Bacteria. *World Appl Sci J* [Internet]. 2013;21(10):1490-4. Available from: [<URL>](#).

64. Burduşel AC, Gherasim O, Grumezescu AM, Mogoantă L, Ficai A, Andronescu E. Biomedical Applications of Silver Nanoparticles: An Up-to-Date Overview. *Nanomaterials* [Internet]. 2018 Aug 31;8(9):681. Available from: [<URL>](#).

65. Castillo-Henríquez L, Alfaro-Aguilar K, Ugalde-Álvarez J, Vega-Fernández L, Montes de Oca-Vásquez G, Vega-Baudrit JR. Green Synthesis of Gold and Silver Nanoparticles from Plant Extracts and Their Possible Applications as Antimicrobial Agents in the Agricultural Area. *Nanomaterials* [Internet]. 2020 Sep 7;10(9):1763. Available from: [<URL>](#).

66. Abou El-Nour KMM, Eftaiha A, Al-Warthan A, Ammar RAA. Synthesis and applications of silver nanoparticles. *Arab J Chem* [Internet]. 2010 Jul 1;3(3):135-40. Available from: [<URL>](#).

67. Zhang Z, Shen W, Xue J, Liu Y, Liu Y, Yan P, et al. Recent advances in synthetic methods and applications of silver nanostructures. *Nanoscale Res Lett* [Internet]. 2018 Dec 18;13(1):54. Available from: [<URL>](#).

68. Siddiqi KS, Husen A, Rao RAK. A review on biosynthesis of silver nanoparticles and their biocidal properties. *J Nanobiotechnology* [Internet]. 2018 Dec 16;16(1):14. Available from: [<URL>](#).




69. Liao C, Li Y, Tjong S. Bactericidal and Cytotoxic Properties of Silver Nanoparticles. *Int J Mol Sci* [Internet]. 2019 Jan 21;20(2):449. Available from: [<URL>](#).

70. Vega-Baudrit J, Gamboa SM, Rojas ER, Martinez VV. Synthesis and characterization of silver nanoparticles and their application as an antibacterial agent. *Int J Biosens Bioelectron* [Internet]. 2019;5(5):166-73. Available from: [<URL>](#).

71. Garibo D, Borbón-Nuñez HA, de León JND, García Mendoza E, Estrada I, Toledano-Magaña Y, et al. Green synthesis of silver nanoparticles using *Lysiloma acapulcensis* exhibit high-antimicrobial activity. *Sci Rep* [Internet]. 2020 Jul 30;10(1):12805. Available from: [<URL>](#).



C/N/CeO₂/Alpha-Fe₂O₃ Doped Mesoporous Carbon as A Photocatalyst Material for Hydrogen Gas Production by Water Splitting Method

Nabilah Dita Anaqah¹ , Reza Ardiyanti Rahman¹ , Mintang Mulyanto¹ , Lioz Alexander¹ ,
Andi Fitri Ayu Lestari¹ , Riki Subagyo¹ , Yuly Kusumawati^{1*} 

¹Department of Chemistry, Faculty of Science and Data Analytics, Institut Teknologi Sepuluh Nopember, Kampus ITS Keputih, 60111, Sukolilo, Surabaya, Indonesia.

Abstract: This study focuses on hydrogen production through a water-splitting photocatalytic reaction using solar energy and an additional semiconductor material C/N/CeO₂/α-Fe₂O₃ as a photocatalyst. The semiconductor material C/N/CeO₂/α-Fe₂O₃ underwent thorough characterization via FTIR, FESEM-EDX, XRD, N₂ adsorption-desorption, and UV-Vis-DRS analysis. Subsequently, photocatalytic activity tests were conducted to measure hydrogen production levels for varying weight percentages of C/N/CeO₂/α-Fe₂O₃, including 0%, 10%, and 15 mass% of the C/N component. Results showed that the material with 0% variation produced 2.21 μmol/gram of hydrogen gas (1 hour) and 17.58 μmol/gram (after 3 hours), while the 10% variation yielded 4.52 μmol/gram (1 hour) and 19.08 μmol/gram (after 3 hours). These findings suggest that the C/N/CeO₂/α-Fe₂O₃ material containing 10% C/N may offer the most optimal performance as a photocatalyst for hydrogen production.

Keywords: Renewable Energy, Photocatalytic Water Splitting, Hydrogen Production, C/N/CeO₂/α-Fe₂O₃.

Submitted: November 25, 2023. **Accepted:** April 30, 2024.

Cite this: Anaqah ND, Rahman RA, Mulyanto M, Alexander L, Lestari AFA, Subagyo R, Kusumawati Y. C/N/CeO₂/Alpha-Fe₂O₃ Doped Mesoporous Carbon as A Photocatalyst Material for Hydrogen Gas Production by Water Splitting Method. JOTCSA. 2024;11(3): 995-1004.

DOI: <https://doi.org/10.18596/jotcsa.1395875>

***Corresponding author's E-mail:** y_kusumawati@chem.its.ac.id

1. INTRODUCTION

According to British Petroleum's statistical evaluation of the world energy in 2021, in 2020, 83%, 12.6%, and 6.3% of the world's energy consumption came from fossil fuels, nuclear energy, and renewable energy sources (mostly solar, wind, and water). Increased demand has led to increased use of fossil energy sources, which has led to the depletion of fossil energy reserves (1). Therefore, every country in the world must immediately initiate a significant energy transition to address future environmental and economic challenges (2).

Hydrogen is considered one of the primary candidates to meet future energy needs (3-5). Hydrogen is classified into three types: gray, green, and blue. Gray hydrogen, the most prevalent type currently, is derived from natural gas with high CO₂ emissions. Green hydrogen is produced from water using renewable energy sources, emitting no CO₂. Blue hydrogen is akin to gray hydrogen but incorporates CO₂ capture and storage (6). Green hydrogen as an alternative fuel for the shipping industry (7). One of the challenges in utilizing hydrogen (H₂) as future energy is to produce it from

clean sources (8). Hydrogen production is divided into conventional and renewable technologies, with conventional methods relying on fossil fuel processing like steam reforming, partial oxidation, and auto-thermal reforming, while renewable technologies focus on sources such as water or biomass (9).

Water splitting is a promising method for producing hydrogen from a clean source (10). This method offers both environmental and economic benefits over water electrolysis, utilizing solar energy to produce hydrogen with high conversion efficiency through a clean energy approach, thus avoiding greenhouse gas emissions (11). The process of water splitting involves harnessing one of the most abundant, clean, and limitless resources available. When the energy used to separate water is derived from renewable or low-carbon sources, the resulting hydrogen is known as green hydrogen (12).

The photocatalytic process of water splitting requires a semiconductor as the primary catalyst that uses light energy, particularly sunlight, to split water molecules into hydrogen and oxygen. Semiconductors as catalysts are essential in

capturing light energy, stimulating water degradation, and facilitating these chemical reactions (13). Therefore, the semiconductors are a must to synthesize for these reactions to work.

The semiconductor commonly used in photocatalytic applications is titanium dioxide (TiO_2) because of its excellent optical and electronic properties, high chemical stability, low cost, non-toxic, and environmentally friendly (14). However, one of the main weaknesses of TiO_2 is that the band gap is relatively large, 3.2 eV, which means that TiO_2 only absorbs ultraviolet (UV) light and a small fraction of visible light (15). In addition, the rapid recombination between electrons (e^-) and holes (hole, h^+) leads to the loss of energy that can be used to trigger the desired chemical reaction, thereby reducing the efficiency of photocatalysis (16).

The $\alpha\text{-Fe}_2\text{O}_3$ material (ferric oxide or hematite) is a material that has the potential as a photocatalytic semiconductor material (17). Hematite has a band gap width of 2.1 eV, which is smaller than TiO_2 , the ability to generate electron-hole pairs when exposed to light, and chemical stability suitable for various reaction environments (18). An Organic Structure-Directing Agent (OSDA) in synthesizing $\alpha\text{-Fe}_2\text{O}_3$ is an approach to align the alpha structure. Methylene blue acts as a template molecule in the synthesis of $\alpha\text{-Fe}_2\text{O}_3$ photocatalyst and as a target of aromatic compounds in photocatalytic degradation. However, $\alpha\text{-Fe}_2\text{O}_3$ has a high recombination rate because it has a concise hole diffusion path (around 2–4 nm) as well as a low oxidation ability, which leads to a reduction in the amount of hydrogen without reducing the coke rate (19). To solve the laxity of $\alpha\text{-Fe}_2\text{O}_3$, active materials with a large surface area are needed. One approach is to dope $\alpha\text{-Fe}_2\text{O}_3$ with other materials. Doping is one of the most crucial modification strategies to adjust the band gap of existing photocatalysts and reduce the carrier recombination rate (20).

Cerium oxide (CeO_2) is widely used in photocatalysis because it is an electron acceptor and can facilitate oxidation-reduction reactions (21). CeO_2 material exhibits chemical stability in various environments and energy conversion efficiency in various photocatalytic applications. Its advantage lies in cerium's ability to absorb oxygen, which allows it to release oxygen in reducing conditions and store it when it fills the oxygen space in oxidizing conditions (22). CeO_2 materials are commonly combined with other semiconductors and surface modifications to improve performance in solar energy conversion and photocatalytic reactions (23).

The presence of lattice oxygen, oxygen vacancies, or defects in the crystal lattice of a material such as CeO_2 can play an important role in photocatalytic performance (24). More oxygen vacancies in the CeO_2 lattice generally increase its ability to participate in redox reactions such as $\text{Ce}^{4+}/\text{Ce}^{3+}$ and $\text{Fe}^{2+}/\text{Fe}^{3+}$. This increases its reactivity and photocatalytic performance. However, care must be taken to ensure that chemical reactions do not lead to undesirable side effects (25). A practical approach to minimize the side effects caused by

lattice oxygen is to modify the photocatalyst material (26).

Nitrogen and carbon doping can help reduce side effects that can occur due to the presence of oxygen vacancies in materials such as CeO_2 . This can improve the control and stability of chemical reactions (27). Doping carbon with nitrogen has been shown to improve photocatalytic performance by promoting charge delocalization and surface modification of carbon. Combining these two dopants in CeO_2 makes properties more suitable for applications such as photocatalysis (28).

In this research, the $\alpha\text{-Fe}_2\text{O}_3$ photocatalyst material was modified with C/N/ CeO_2 , resulting from modifying CeO_2 with N-doped carbon. The materials C/N/ CeO_2 and C/N/ $\text{CeO}_2/\alpha\text{-Fe}_2\text{O}_3$ were synthesized via the hydrothermal method. The hydrothermal method has been chosen because this method can be conducted in mild operating conditions and the crystallite size and purity can be controlled (29-30). The resulting C/N/ $\text{CeO}_2/\alpha\text{-Fe}_2\text{O}_3$ composite was confirmed by a series of characterizations, including UV-Vis diffuse reflections measurement to determine band gap energy, X-Ray diffraction for knowing structure and crystal phase of the material, Fourier-Transform Infra-Red spectroscopy measurement find the functional groups of material, Field Emission Scanning Electron Microscopy for explain surface morphology dan atom distribution, GC-TCD to analyze the components of complex mixtures and detect all molecules including hydrogen, which is then followed by a photocatalytic effectiveness test, and N_2 adsorption-desorption isotherm to find out surface area and pore distribution. In addition to these characterizations, photocatalytic activity tests were also carried out to determine the evolution of the hydrogen produced. Modifying $\alpha\text{-Fe}_2\text{O}_3$ with C/N/ CeO_2 is expected to increase the photocatalytic activity, thermal and chemical stability, and surface area of the photocatalyst material. The large surface area of the photocatalyst material creates active centers, which also increases hydrogen production. Hopefully, this research can provide alternatives and scientific references to photocatalytic materials that are effectively used for hydrogen production through water splitting.

2. EXPERIMENTAL SECTION

2.1. Materials

The material used in this research was cerium(III) nitrate hexahydrate $\text{Ce}(\text{NO}_3)_3 \cdot 6\text{H}_2\text{O}$ (99.8% Sigma-Aldrich), iron (III) chloride FeCl_3 (99%, Merck), methylene blue (99 %, Merck), ethanol (99.9%, Merck), N_2 gas (>99.99%, UHP), glycine (99%, Sigma-Aldrich), ammonium hydroxide NH_4OH (25%, Merck), distilled water (H_2O), urea $\text{CO}(\text{NH}_2)_2$ (99%, Merck), 500 mesh commercial activated carbon, sodium hydroxide NaOH (99.9%, Merck) and methanol (99.9%, Merck).

2.2. Synthesis of Nitrogen-Doped Mesoporous Activated Carbon (C/N)

5.04 g of commercial activated carbon was purchased and used without any purification and was added to 250 mL of 2 M urea solution made from $\text{CO}(\text{NH}_2)_2$ and distilled water stirred with a

magnetic stirrer at 35 °C for 24 hours. The samples were then dried at 105 °C for 6 hours. After the sample was dried, it was activated in a tube furnace supplied with N₂ gas at a temperature of 450 °C for 50 minutes.

2.3. Synthesis of C/N-doped CeO₂ (C/N/CeO₂)

The synthesized N-doped mesoporous activated carbon was then grouped with weight percent variations of 10 and 15 mass%. Each was added to 10 mL of distilled water by ultrasonication for 30 minutes until a black suspension was obtained. Afterwards, 15 mL of a 0.1 M (Ce(NO₃)₃·6H₂O) was added to the suspension and stirred with a magnetic stirrer for 15 minutes. Then, 2 M NaOH was added dropwise to the mixture until the pH reached 10-12. The mixture was stirred with a magnetic stirrer for one hour. The sample was placed in a hydrothermal autoclave at 180 °C for 24 hours. The hydrothermal results were decanted, and then the precipitate was dried in an oven at 60 °C for 12 hours.

2.4. Synthesis of α-Fe₂O₃

The synthesis of the α-Fe₂O₃ material was carried out by dissolving 0.41 g of glycine, 0.025 g of methylene blue, and 5.04 g of FeCl₃·6H₂O in 10 mL of distilled water and stirring with a magnetic stirrer for 30 min. Add 5 mL of NH₄OH to the solution while stirring again. After adding NH₄OH, the solution was placed in a hydrothermal autoclave and heated at 160 °C for 10 hours. The mixture resulting from the hydrothermal process is left to stand at room temperature and then decanted to separate the filtrate and sediment. The resulting brick-red solid was then centrifuged using distilled water and ethanol as solvent to remove impurities. Then, the centrifugation results were decanted again to remove the precipitate and dried at 80 °C for six hours. The solid was then calcined under N₂ gas at 450 °C for three hours.

2.5. Synthesis of C/N/CeO₂/α-Fe₂O₃

After obtaining the C/N/CeO₂ and α-Fe₂O₃ materials, the synthesis of C/N/CeO₂/α-Fe₂O₃ was continued using a hydrothermal process with variations (0, 10, and 15 mass%). A total of 0.33 grams of N/CeO₂-doped mesoporous carbon composite was dissolved in 7.5 mL of distilled water and stirred for 30 minutes. Then, 0.65 grams of α-Fe₂O₃ was dissolved in 20.3 mL of distilled water and added to the N/CeO₂ mixture. The mixture was stirred for 1 hour. The obtained samples were placed in a hydrothermal autoclave and heated at 140 °C for five hours and then left at room temperature. The solid obtained at the end of the synthesis is C/N/CeO₂/α-Fe₂O₃ as the photocatalyst material with 0, 10, and 15 mass% compositions C/N. The higher the weight percentage of C/N added, the darker the product color obtained. The mass of products produced includes C/N/CeO₂/α-Fe₂O₃ 0 mass%, C/N/CeO₂/α-Fe₂O₃ 10 mass% and C/N/CeO₂/α-Fe₂O₃ 15 mass% in order are 0.4478; 0.4432; and 0.4452 grams.

2.6. Material Characterization

Several instruments were used to characterize C/N/CeO₂/α-Fe₂O₃ such as Fourier Transform Infrared Spectrophotometer (FTIR, Shimadzu, ν = 400-4000 cm⁻¹), Field Emission Scanning Electron Microscopy with Energy Dispersive X-ray Spectroscopy (FESEM-

EDX,) and X-Ray Diffraction (XRD, 2θ = 20-90°) where these three instruments are used to determine the structure properties of the material. Brunauer-Emmett-Teller (BET) and Barrett Joyner Halenda (BJH) are used to obtain the surface area and the pore size of the material, UV-Vis Diffuse Reflectance spectrophotometer (UV-DRS, Agilent Cary 60, λ = 200-800 nm) is used to analyze the band gap of the material.

2.7. Photocatalytic Activity Test

The photocatalytic activity test was conducted in the Centre of Advanced Material and Energy Sciences, Universiti Brunei Darussalam, Brunei Darussalam. Osram Powerstar lamp was employed as a light source. A 20 mg of catalyst was dispersed in a 25 mL aqueous solution containing 20% of methanol. To provide visible light, a UV filter was conducted during irradiation. An irradiation chamber, Opsytec BS-02, was used to have a stable temperature and light intensity. The temperature inside the irradiation chamber was measured during the photocatalytic reaction at ~40-50 °C. The light intensity was measured using LI-COR light meter Model LI-250A. The hydrogen production was collected by gas syringe after 1-hour and 3-hour irradiation. The collected gas was then analyzed via gas chromatography, Shimadzu GC-2014, with a thermal conductive detector (TCD).

3. RESULTS AND DISCUSSION

The FTIR spectrum of activated carbon and the synthesis results of nitrogen-doped activated carbon in Figure 1a show that the absorption peak at wave number 1078 cm⁻¹ is associated with the C=O group, and the peak at 1539 cm⁻¹ is associated with the stretching of the C-OH single bond. After nitrogen doping, the absorption peak shifted red to 1026 and 1537 cm⁻¹. This shows that the structure of the mesoporous carbon changed with the addition of nitrogen. The particular band peak still present after N-doped carbon indicates no damage from urea impregnation (24).

After the nitrogen-doped activated carbon material (C/N) was obtained, the material was doped with CeO₂ in variations of 0, 10, and 15 mass%. The addition of CeO₂ doping to C/N Figure 1b gives several absorption bands which are 450 cm⁻¹, 1360 cm⁻¹, 1640 cm⁻¹ and 3470 cm⁻¹. The absorption bands 474 and 484 cm⁻¹ indicate the presence of stretching vibrations in CeO₂, the absorption at 1643 cm⁻¹ indicates the presence of bending bonds (H-O-H), and the absorptions at 3475 and 3473 cm⁻¹ indicate the presence of -OH bonds caused by water absorption during the synthesis process. The specified variations affect the spectra results, as indicated by differences in peak sharpness in each spectrum. In Figure 1c, you can see the characterization results of the C/N/CeO₂/α-Fe₂O₃ material for variations of 0, 10, and 15 mass%. of the C/N weight. The absorption bands 484 and 580 cm⁻¹ show the characteristic properties of α-Fe₂O₃ and CeO₂ compounds. The absorption at 1637 cm⁻¹ indicates the presence of the C-N functional group. Based on the characterization results, the C/N/CeO₂/α-Fe₂O₃ material varies in 0, 10, and 15 mass%. was successfully synthesized.

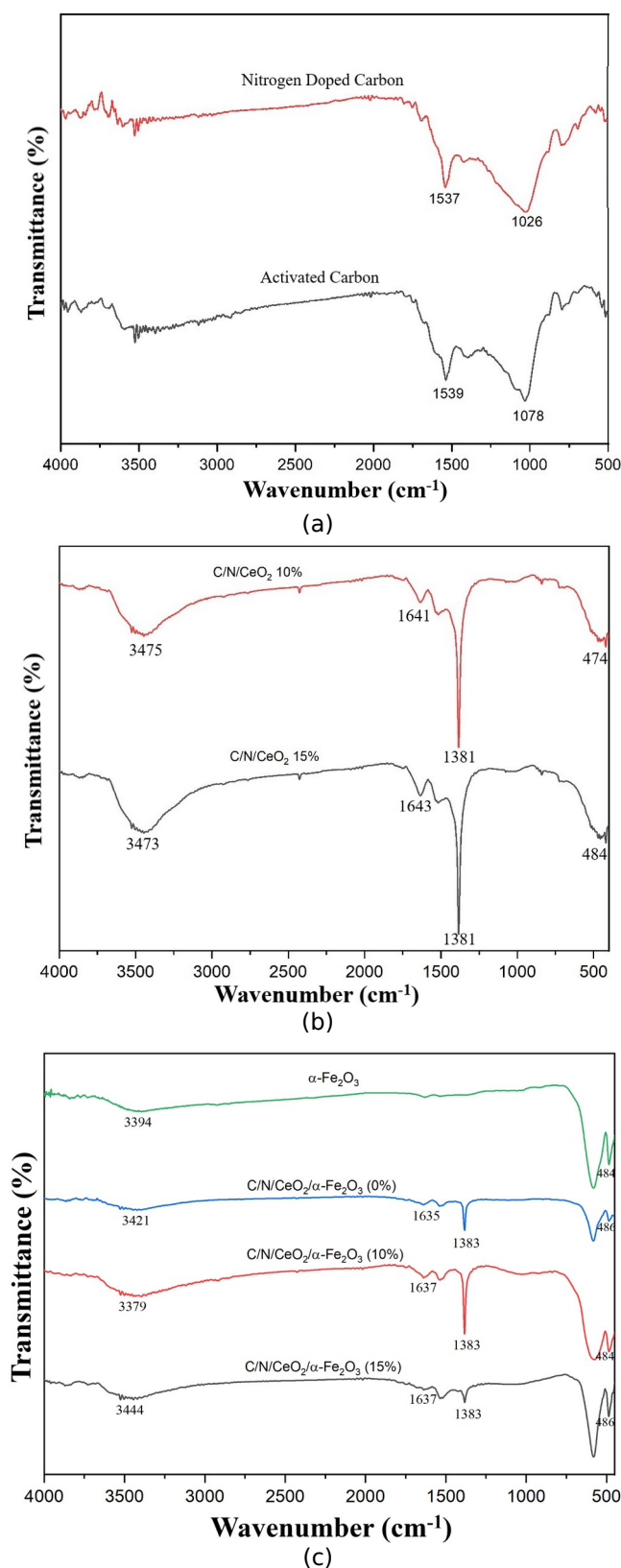


Figure 1: (a) FTIR results of activated carbon and nitrogen-doped activated carbon and (b) FTIR results of C/N/CeO₂ 10 and 15 mass%., and FTIR results of α -Fe₂O₃ and (c) C/N/CeO₂/ α -Fe₂O₃ (0, 10 and 15 mass%).

Results of FESEM-EDX characterization of C/N, α -Fe₂O₃, and C/N/CeO₂/ α -Fe₂O₃ materials at 10 mass% and its morphology can be observed in Figures 2a, b, and c. The FESEM results of the C/N material showed porous structural morphology and many small particles around the pores caused by the

carbonization process (29). The EDX results of C/N show the distribution of C atoms in red, O atoms in green, and N atoms in orange. The distribution of elements and morphology indicate that N-doped mesoporous carbon was successfully synthesized. The FESEM characterization results of α -Fe₂O₃ show

that the material's morphology is hollow and porous due to the addition of the structure-directing agent methylene blue. After doping, the FESEM results show C/N/CeO₂/α-Fe₂O₃ 10 mass%. Shows that the morphology of the initially porous material was covered by dopant material. This is because the

addition of C/N causes the pores to be closed by the catalyst. EDX results of α-Fe₂O₃ and C/N/CeO₂/α-Fe₂O₃ materials at 10 mass%. The difference in atom distribution lies in the blue Ce atoms and the red C atoms in C/N/CeO₂/α-Fe₂O₃ 10 mass%.

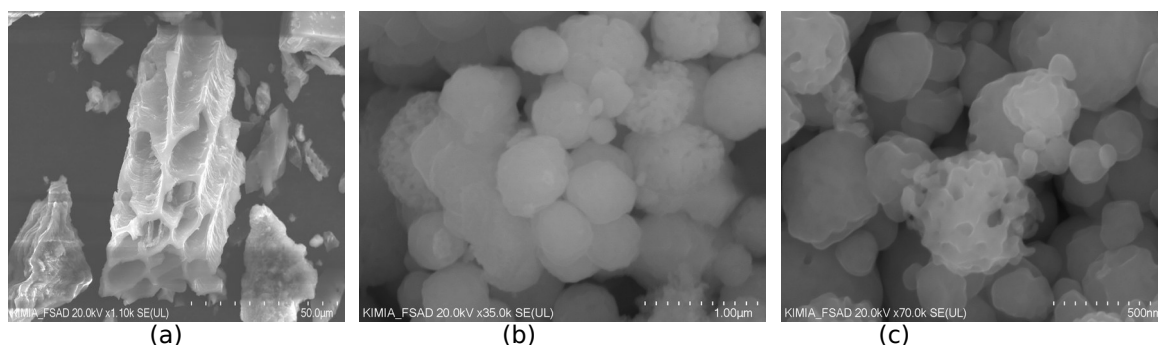


Figure 2: (a) FESEM-EDX C/N (b) Fesem-EDX α-Fe₂O₃ and (c) FESEM-EDX C/N/CeO₂/α-Fe₂O₃.

The sample diffractogram results were monitored at an angle of 2θ from the range (20–90) using a Cu Kα light source (λ = 1.54060 Å). The results of the diffractogram pattern of C/N/CeO₂/α-Fe₂O₃ (0, 10 and 15 mass%) shown in Figure 3 show that the sample results have a hematite phase with a diffraction peak of 2θ = 33.2; 35.7; 40.9; 49.7; 54.3; 62.4; and 64° with Miller indices (1 0 4), (1 1 0), (1 1 3), (0 2 4), (1 1 6), (2 1 4), (3 0 0) from the JCPDS database code (84-0311) (20). In addition, Figure 3 shows the crystalline phase diffraction peaks 2θ = 47.6 and 56.5°, which correspond to the Miller index

(2 2 0), (3 1 1) from the JCPDS database code (34-0394), indicating this, that the peak nano-large formations were formed from the pure cubic CeO₂ phase (30). The diffractogram results at diffraction peak 2θ = 28.6° showed that nitrogen-doped mesoporous carbon in the diffractograms of C/N/CeO₂/α-Fe₂O₃ (10 mass%) and C/N/CeO₂/α-Fe₂O₃ (15 mass%), while the diffractogram of C/N/CeO₂/α-Fe₂O₃ (0 mass%) does not contain a diffraction peak at 2θ = 28.6°. Based on the characterization results, the C/N/CeO₂/α-Fe₂O₃ material varies between 0, 10, and 15 mass%. was successfully synthesized.

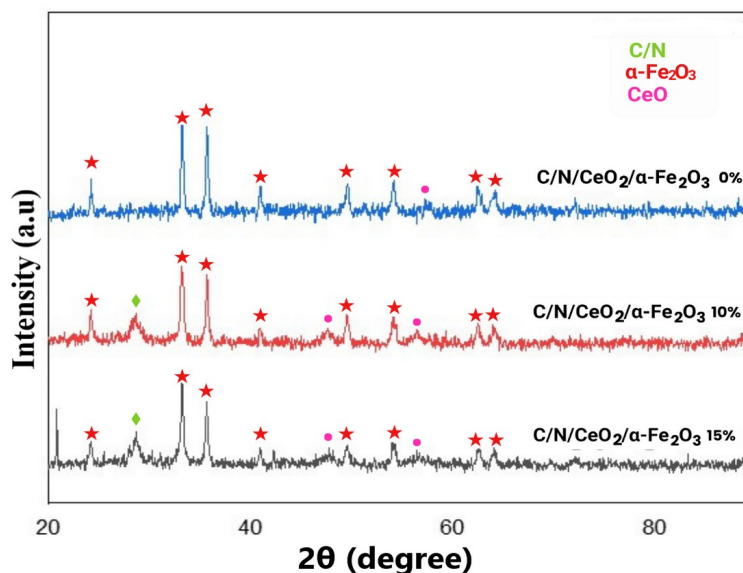


Figure 3: Diffractogram results of C/N/CeO₂/α-Fe₂O₃ (0, 10 and 15 mass%).

The nitrogen adsorption-desorption isotherm was measured at -195.85 °C. The samples were prepared under vacuum conditions (10⁻⁴ Torr) at a temperature of 150 °C. The surface area is calculated from the adsorption isotherm branch by applying the BET equation using a single point. The pore size distribution was estimated using the BJH method from the desorption branch. The results of C/N nitrogen adsorption-desorption characterization showed a BET surface area of 203.84 m² /g with a

pore size of 4.95 nm, as shown in Figure 4a. Figure 4b shows the C/N sample has an H₄ hysteresis-type loop. These results indicate that the C/N material has a mesoporous structure. The desorption branch for H₄ hysteresis-type pores at low P/P₀ 0.1 indicates that the desorption branch is not closed. This shows that the desorption process does not reach the same level as the adsorption process. The pores remain partially filled after the desorption process is complete (29).

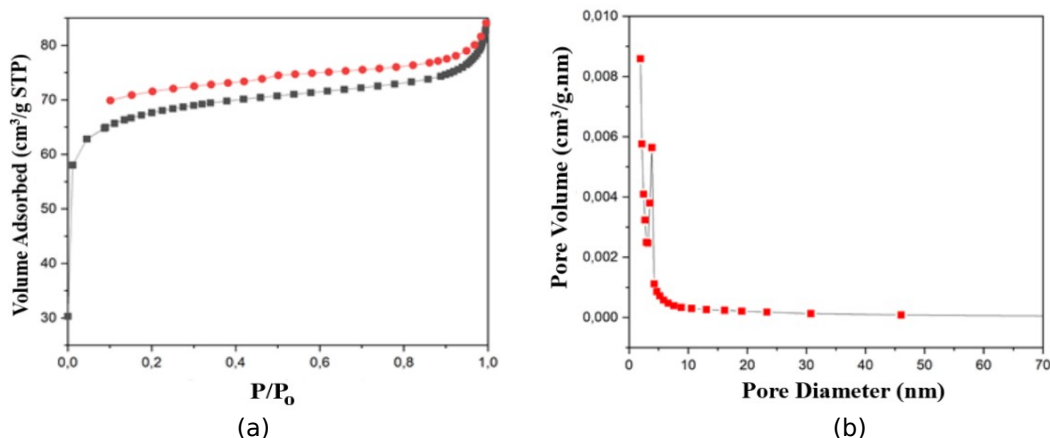


Figure 4: (a) C/N nitrogen adsorption-desorption isotherm and (b) pore size distribution.

UV-Vis DRS tests provide information in a wavelength spectrum versus R or reflectance (%). The band gap energy is obtained by converting the R% to the Kubelka-Munk factor (31). Materials exposed to photons partially absorb, reflect, and transmit bandgap energy. The results of the UV-Vis DRS test show that the more C/N present in the photocatalyst material, the less energy is required. Based on the Kabelka-Munk relationship with

energy, the photocatalyst material varies by 0 mass %. Figure 5a, C/N has a band gap energy of 1.98 eV and a variation of 10 mass%. Figure 5b has a band gap energy of 1.9 eV while at a variation of 15 mass %. Figure 5c produces a band gap energy of 1.69 eV. These results suggest that the variation ranges from 0 to 15 mass %. With the C/N composition, the resulting band gap energy decreases and moves into the visible light region (32).

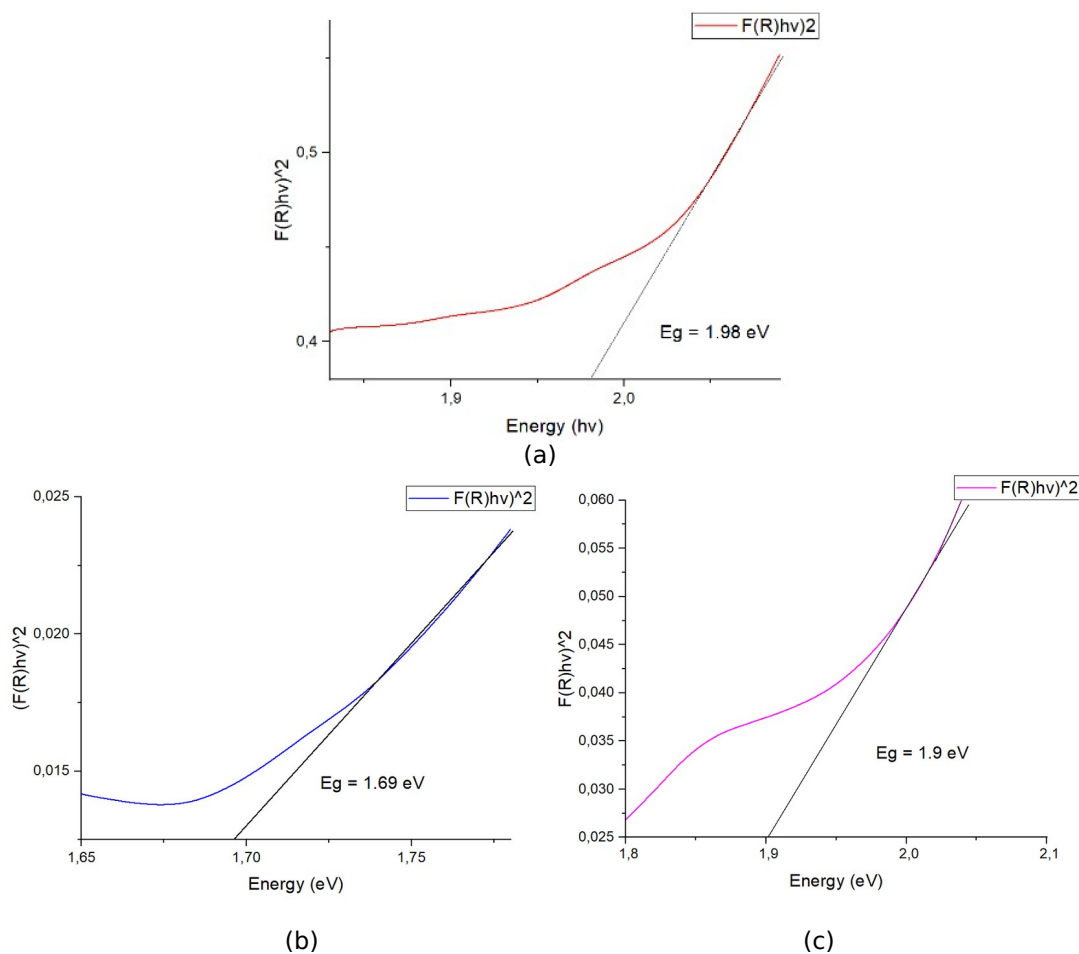


Figure 5: UV-Vis DRS (a) C/N 0 mass%, (b) C/N 10 mass%, (c) C/N 15 mass%.

The addition of C/N is used as an anionic dopant, which can reinforce the weakness of CeO₂ as an inhibitor of coke and recombination rates (33). The C/N material has active centers due to the presence of electron pairs from the N atom, which can

weaken the O-O bond. This increases the photocatalytic activity as an oxygen reduction reaction takes place. The dipole-dipole interaction formed by bonding carbon atoms to nitrogen shows a higher positive charge density and stronger

electron affinity. However, adding nitrogen-doped carbon in an excessive ratio can limit the catalytic activity. This is because the active N site is coated with carbon (34). Figure 6 shows that the more C/N

is added to the photocatalyst material, the higher the generated reflection intensity. It can be assumed that more light is absorbed with the higher reflected intensity.

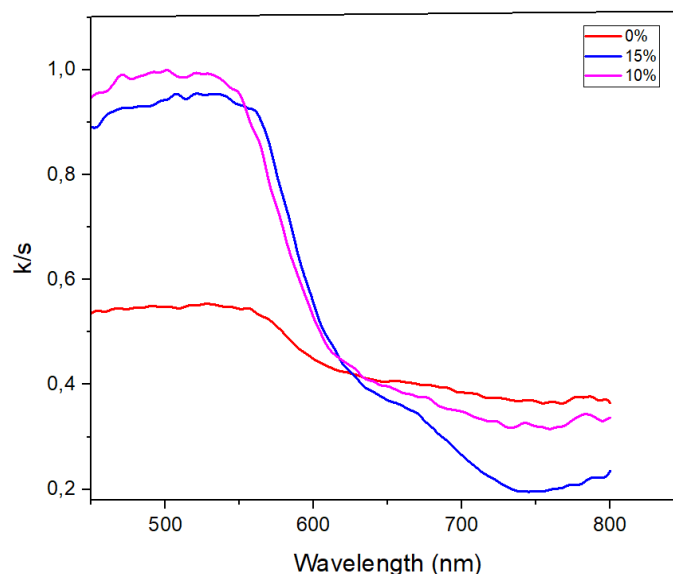


Figure 6: UV-Vis DRS spectra wavelength to reflectance (%) of C/N in every variation.

The photocatalytic activity test for hydrogen production was carried out using a GC-TCD device. The photocatalyst solid was weighed up to 50 mg and then dispersed in 25 mL of 20% methanol solution. The mixture was stirred for 10 minutes and

then ultrasonicated for 10 minutes. Argon gas was then flowed through the mixture for 5 minutes. The solution was placed in a photocatalytic reactor and irradiated with UV light for 3 hours (Figure 7).

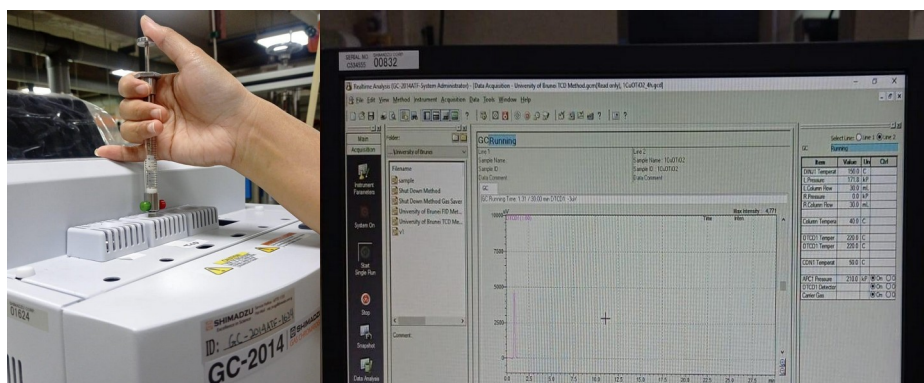


Figure 7: GC-TCD Device for measure the hydrogen gas formed in this experiment.

The hydrogen gas formed is then removed with a syringe and introduced into the GC-TCD device for the analysis process. The results of hydrogen gas amount obtained within 1 and 3 hours with

variations in C/N/CeO₂/α-Fe₂O₃ (C/N 0, 10 and 15 mass%). The equation used to measure the amount of hydrogen in the syringe is as follows

$$\text{Volume of } H_2 \text{ in reaction bottle} = \frac{\text{Volume of } H_2 \text{ in syringe} \times 33.5 \text{ mL of headspace}}{0.5 \text{ mL of extracted } H_2 \text{ gas}} \quad (\text{Eq. 1})$$

It is known that the Volume of Hydrogen in Syringe/mL comes from the peak divided by the hydrogen calibration results.

Photocatalyst material C/N/CeO₂/α-Fe₂O₃ variation 0 mass%. gives results for the amount of hydrogen production in 1 hour of 2.21 μmol/g and after 3 hours of 17.58 μmol/g (Figure 8). Photocatalyst material C/N/CeO₂/α-Fe₂O₃ variation 10 mass% gave

optimal results with an amount of hydrogen production in 1 hour of 4.2 μmol/g and after 3 hours of 19.08 μmol/g. Adding composition variations of 15 mass % material does not produce hydrogen gas in visible light. This may be caused by the surface and pore structure of C/N having covered the active site of the catalyst and the band gap energy is 1.69 eV, leading to the solar radiation-based infrared light region. According to research

data by Dao et al (2023) (35), hydrogen production with $\alpha\text{-Fe}_2\text{O}_3$ doped and undoped NGr material resulted in hydrogen production amounts of 1.95

$\mu\text{mol}/\text{mg}\cdot\text{h}$ and $0.39 \mu\text{mol}/\text{mg}\cdot\text{h}$. This indicates that the addition of C/N/ CeO_2 doping can increase the photocatalytic efficiency.

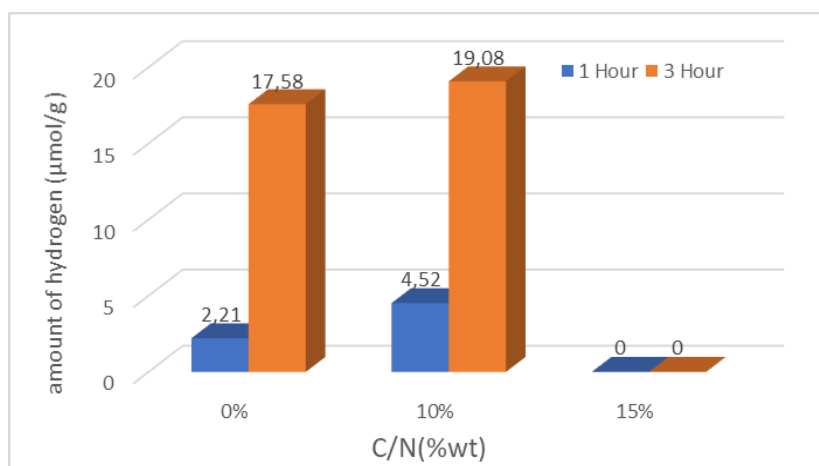


Figure 8: Hydrogen production by variation of C/N content within 1 and 3 hours.

The consideration of an optimal photocatalytic system for H_2 involves physical processes. The

entire chemical process is represented in the following figure.

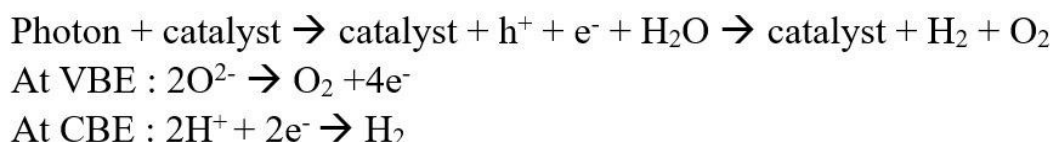


Figure 10: General mechanism of hydrogen gas production.

The development of electrical semiconductor settings has made a significant contribution to the operational efficiency of photocatalysis processes. Semiconductors are differentiated from conductors based on two main bands, namely the valence band (VB) and conduction band (CB), with an energy difference (E_g) that differentiates the two. The activation process ensures that electrons and holes are only found in the valence band. To excite a semiconductor, the incoming light energy must be equal to or higher than the band gap energy. When photons excite electrons from the valence band to the conduction band, holes are formed in their place. The mechanism of photocatalytic air mechanization of alpha semiconductor $\text{Fe}_2\text{O}_3/\text{CeO}_2/\text{C}/\text{N}$ involves certain steps. In the initial

stage, electrons and holes are created when light hits the semiconductor surface. The energy released can be in the form of heat or photons when electrons and holes recombine quickly on the semiconductor surface. Additionally, electrons and holes can also be involved in chemical reactions, as illustrated in the equation below. Additionally, the photoexcited pairs can initiate chemical reactions at the semiconductor surface, with the holes reacting with H_2O molecules to produce the desired reaction products. In the final stage, electrons and holes produced from the photoexcitation process will take part in the reaction that produces O_2 and H_2O . This is a simple overview of the photocatalytic air separation process.

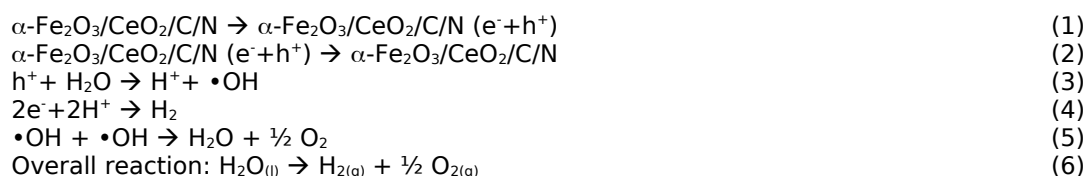


Figure 11: Mechanism of hydrogen gas production.

4. CONCLUSION

In this research, N-doped mesoporous carbon (pore size of 4.9260 nm and surface area 203,84 m^2/g) was successfully synthesized as a $\text{CeO}_2/\alpha\text{-Fe}_2\text{O}_3$ dopant via the hydrothermal method. The effect of doping composition variations N-doped mesoporous carbon 0, 10, and 15 mass% in photocatalytic

reactions for hydrogen gas production was investigated. Photocatalytic activity efficiency test results show that optimum C/N/CeO₂/α-Fe₂O₃ photocatalyst material with C/N variation 10 mass% for hydrogen production in 1 hour is 4.2 μmol/g and 19.08 μmol/g in 3 hours. After three hours, the hydrogen production fluctuation increased by 76.31%. In addition, the C/N mass percentage variation to the photocatalyst material affects the active catalytic sites and band gap energy. Based on the above description, it can be concluded that C/N/CeO₂/α-Fe₂O₃ has the potential to be used and developed as a photocatalyst for hydrogen production through the water-splitting reaction.

5. CONFLICT OF INTEREST

There is no conflict of interest.

6. ACKNOWLEDGEMENT

The authors gratefully acknowledge financial support from the Directorate General of Higher Education, Research and Technology, Ministry of Education, Research and Technology, Republic of Indonesia through the Student Creativity Program (PKM 2023). Dr. Hasliza Bahruzi from the Centre of Advanced Material and Energy Sciences, Universiti Brunei Darussalam, Brunei Darussalam is acknowledged for providing apparatus for photocatalytic activity.

7. REFERENCES

- Holechek JL, Geli HME, Sawalhah MN, Valdez R. A Global Assessment: Can Renewable Energy Replace Fossil Fuels by 2050? Sustainability [Internet]. 2022 Apr 16;14(8):4792. Available from: [<URL>](#).
- Welsby D, Price J, Pye S, Ekins P. Unextractable fossil fuels in a 1.5 °C world. Nature [Internet]. 2021 Sep 9;597(7875):230–4. Available from: [<URL>](#).
- Garzón Baquero JE, Bellon Monsalve D. From fossil fuel energy to hydrogen energy: Transformation of fossil fuel energy economies into hydrogen economies through social entrepreneurship. Int J Hydrogen Energy [Internet]. 2024 Feb 7;54:574–85. Available from: [<URL>](#).
- Marouani I, Guesmi T, Alshammari BM, Alqunun K, Alzamil A, Alturki M, et al. Integration of Renewable-Energy-Based Green Hydrogen into the Energy Future. Processes [Internet]. 2023 Sep 7;11(9):2685. Available from: [<URL>](#).
- Bilgic G, Bendes E, Ozturk B, Atasever S. Recent advances in artificial neural network research for modeling hydrogen production processes. Int J Hydr En. 2023; 48:18947–18977. Available from: [<URL>](#).
- Atilhan, S., Park, S., El-Halwagi, M. M., Atilhan, M., Moore, M., & Nielsen, R. B. (2021). Green hydrogen as an alternative fuel for the shipping industry. Current Opinion in Chemical Engineering, 31, 100668. <https://doi.org/10.1016/j.COCHE.2020.100668>.
- Marouani I, Guesmi T, Alshammari BM, Alqunun K, Alzamil A, Alturki M, et al. Integration of Renewable-

Energy-Based Green Hydrogen into the Energy Future. Processes. 2023 Sep 7;11(9):2685.

- Kaplan H, Şahin M, Bilgiç G. The Influence of Magnetic Field on Newly Designed Oxyhydrogen and Hydrogen Production by Water Electrolysis. Energy Technol [Internet]. 2021 Dec 10;9(12):2100617. Available from: [<URL>](#).
- Bilgiç G, Öztürk B. Modeling of Artificial Neural Networks for Hydrogen Production via Water Electrolysis. El-Cezeri J Sci Eng [Internet]. 2023 Jan 11;10(1):137–46. Available from: [<URL>](#).
- Hota P, Das A, Maiti DK. A short review on generation of green fuel hydrogen through water splitting. Int J Hydrogen Energy [Internet]. 2023 Jan 5;48(2):523–41. Available from: [<URL>](#).
- Ravi P, Noh J. Photocatalytic Water Splitting: How Far Away Are We from Being Able to Industrially Produce Solar Hydrogen? Molecules [Internet]. 2022 Oct 23;27(21):7176. Available from: [<URL>](#).
- Arsad AZ, Hannan MA, Al-Shetwi AQ, Begum RA, Hossain MJ, Ker PJ, et al. Hydrogen electrolyser technologies and their modelling for sustainable energy production: A comprehensive review and suggestions. Int J Hydrogen Energy [Internet]. 2023 Aug 22;48(72):27841–71. Available from: [<URL>](#).
- Hakki A, AlSalka Y, Mendive CB, Ubogui J, dos Santos Claro PC, Bahnemann D. Hydrogen Production by Heterogeneous Photocatalysis. In: Wandelt K, editor. Encyclopedia of Interfacial Chemistry [Internet]. Elsevier; 2018. p. 413–9. Available from: [<URL>](#).
- Dharma HNC, Jaafar J, Widiastuti N, Matsuyama H, Rajabsadeh S, Othman MHD, et al. A Review of Titanium Dioxide (TiO₂)-Based Photocatalyst for Oilfield-Produced Water Treatment. Membranes (Basel) [Internet]. 2022 Mar 19;12(3):345. Available from: [<URL>](#).
- Sharma PK, Cortes MALRM, Hamilton JWJ, Han Y, Byrne JA, Nolan M. Surface modification of TiO₂ with copper clusters for band gap narrowing. Catal Today [Internet]. 2019 Feb 1;321–322:9–17. Available from: [<URL>](#).
- Wei Y, Wu Q, Meng H, Zhang Y, Cao C. Recent advances in photocatalytic self-cleaning performances of TiO₂-based building materials. RSC Adv [Internet]. 2023 Jul 11;13(30):20584–97. Available from: [<URL>](#).
- Mimouni I, Bouziani A, Naciri Y, Boujnah M, El Belghiti MA, El Azzouzi M. Effect of heat treatment on the photocatalytic activity of α-Fe₂O₃ nanoparticles: towards diclofenac elimination. Environ Sci Pollut Res [Internet]. 2022 Jan 5;29(5):7984–96. Available from: [<URL>](#).
- Zhang H, Liu J, Xu T, Ji W, Zong X. Recent Advances on Small Band Gap Semiconductor Materials (≤2.1 eV) for Solar Water Splitting. Catalysts [Internet]. 2023 Apr 12;13(4):728. Available from: [<URL>](#).

19. Parthasarathy P, Vivekanandan S. Biocompatible TiO₂-CeO₂ Nano-composite synthesis, characterization and analysis on electrochemical performance for uric acid determination. *Ain Shams Eng J* [Internet]. 2020 Sep 1;11(3):777-85. Available from: [<URL>](#).
20. Cheng R, Xia J, Wen J, Xu P, Zheng X. Nano Metal-Containing Photocatalysts for the Removal of Volatile Organic Compounds: Doping, Performance, and Mechanisms. *Nanomaterials* [Internet]. 2022 Apr 13;12(8):1335. Available from: [<URL>](#).
21. Kusmierek E. A CeO₂ Semiconductor as a Photocatalytic and Photoelectrocatalytic Material for the Remediation of Pollutants in Industrial Wastewater: A Review. *Catalysts* [Internet]. 2020 Dec 8;10(12):1435. Available from: [<URL>](#).
22. Wang X, Wang J, Sun Y, Li K, Shang T, Wan Y. Recent advances and perspectives of CeO₂-based catalysts: Electronic properties and applications for energy storage and conversion. *Front Chem* [Internet]. 2022 Dec 8;10:1089708. Available from: [<URL>](#).
23. Tran DPH, Pham MT, Bui XT, Wang YF, You SJ. CeO₂ as a photocatalytic material for CO₂ conversion: A review. *Sol Energy* [Internet]. 2022 Jul 1;240:443-66. Available from: [<URL>](#).
24. Yang M, Shen G, Wang Q, Deng K, Liu M, Chen Y, et al. Roles of Oxygen Vacancies of CeO₂ and Mn-Doped CeO₂ with the Same Morphology in Benzene Catalytic Oxidation. *Molecules* [Internet]. 2021 Oct 21;26(21):6363. Available from: [<URL>](#).
25. Suman, Singh S, Ankita, Kumar A, Kataria N, Kumar S, et al. Photocatalytic activity of α -Fe₂O₃@CeO₂ and CeO₂@ α -Fe₂O₃ core-shell nanoparticles for degradation of Rose Bengal dye. *J Environ Chem Eng* [Internet]. 2021 Oct 1;9(5):106266. Available from: [<URL>](#).
26. Ranjbari A, Demeestere K, Kim KH, Heynderickx PM. Oxygen vacancy modification of commercial ZnO by hydrogen reduction for the removal of thiabendazole: Characterization and kinetic study. *Appl Catal B Environ* [Internet]. 2023 May 5;324:122265. Available from: [<URL>](#).
27. Paick J, Hong S, Bae JY, Jyoung JY, Lee ES, Lee D. Effective Atomic N Doping on CeO₂ Nanoparticles by Environmentally Benign Urea Thermolysis and Its Significant Effects on the Scavenging of Reactive Oxygen Radicals. *ACS Omega* [Internet]. 2023 Jun 27;8(25):22646-55. Available from: [<URL>](#).
28. Ishak N, Jeyalakshmi V, Setka M, Grandcolas M, Devadas B, Šoóš M. Upgrading of g-C₃N₄ semiconductor by a Nitrogen-doped carbon material: A photocatalytic degradation application. *J Environ Chem Eng* [Internet]. 2023 Apr 1;11(2):109381. Available from: [<URL>](#).
29. Yao C, Wang M, Jiang W, Chen Y. Study on a novel N-doped mesoporous carbon for the efficient removal of methylene blue from aqueous solution. *Environ Eng Res* [Internet]. 2020 Oct 27 [cited 2024 Jun 5];26(5):200339. Available from: [<URL>](#).
30. Jayakumar G, Irudayaraj A, Raj AD, Irudayaraj AA. Particle Size Effect on the Properties of Cerium Oxide (CeO₂) Nanoparticles Synthesized by Hydrothermal Method. *Mech Mater Sci Eng J* [Internet]. 2017;9(1). Available from: [<URL>](#).
31. Landi S, Segundo IR, Freitas E, Vasilevskiy M, Carneiro J, Tavares CJ. Use and misuse of the Kubelka-Munk function to obtain the band gap energy from diffuse reflectance measurements. *Solid State Commun* [Internet]. 2022 Jan 1;341:114573. Available from: [<URL>](#).
32. Yuan D, Liu Q. Photon energy and photon behavior discussions. *Energy Reports* [Internet]. 2022 May 1;8:22-42. Available from: [<URL>](#).
33. Ayyub MM, Rao CNR. Design of efficient photocatalysts through band gap engineering. In: Boukherroub R, Ogale SB, Robertson N, editors. *Nanostructured Photocatalysts* [Internet]. Elsevier; 2020. p. 1-18. Available from: [<URL>](#).
34. Wu B, Meng H, Morales DM, Zeng F, Zhu J, Wang B, et al. Nitrogen-Rich Carbonaceous Materials for Advanced Oxygen Electrocatalysis: Synthesis, Characterization, and Activity of Nitrogen Sites. *Adv Funct Mater* [Internet]. 2022 Aug 31;32(31):2204137. Available from: [<URL>](#).
35. Dao V, Cipriano LA, Ki SW, Yadav S, Wang W, Di Liberto G, et al. 2D/2D Z-scheme-based α -Fe₂O₃@NGr heterojunction implanted with Pt single-atoms for remarkable photocatalytic hydrogen evolution. *Appl Catal B Environ* [Internet]. 2023 Aug 5;330:122586. Available from: [<URL>](#).
36. Khani H, Khandan N, Eikani MH, Eliassi A. Investigation of synthesized Fe₂O₃ and CuO-Fe₂O₃ for pure hydrogen production by chemical-loop reforming of methanol in a micro-channel reactor. *Int J Hydrogen Energy* [Internet]. 2023 Feb 22;48(16):6436-50. Available from: [<URL>](#).



Biogenic Copper Oxide Nanoparticles Synthesized from Whole Plant Extract of *Nicotiana plumbaginifolia* Viv.: Characterization, Antibacterial, and Antioxidant Properties

Abhimanyu Pawar^{1*} , Arvind Mungole² , Kishor Naktode¹ 

¹Department of Chemistry, Nevjabai Hitkarini College, Bramhapuri, Maharashtra 441 206, India.

²Department of Botany, Nevjabai Hitkarini College, Bramhapuri, Maharashtra 441 206, India.

Abstract: Nanoparticles crafted through biological processes show potential for advancing medicine. Plant-derived compounds, produced through environmentally friendly green synthesis, present distinctive and beneficial applications in the field of nanomedicine. This study describes an easy, sustainable, environmentally friendly, and cost-efficient method to create copper oxide nanoparticles (CuO NPs) using whole part of *Nicotiana plumbaginifolia* Viv. extract. The characterization involved various techniques like solid UV-Visible-DR analysis, Fourier transform infrared (FTIR), EDAX analysis, X-ray diffraction (XRD), transmitted electron microscopy (TEM), and scanning electron microscopy (SEM). The copper oxide nanoparticles (CuO NPs) were found to be quasi-spherical pattern, with sizes ranging from 12 to 14 nm, and exhibited a crystal structure identified as monoclinic. The resulting copper oxide nanoparticles (CuO NPs) were examined for antimicrobial and antioxidant properties. It showed suppressing bacterial growth against tested human pathogenic bacteria, emphasizing their potential as antimicrobial agents. Results revealed that the maximum zone of inhibition was observed when the concentrations (25, 50, and 100 μL .) of NPs is increased against *S. aureus* i.e. 17 mm, 20 mm and 22 mm respectively. Whereas findings also reveal potent antioxidant activity, with escalating CuO nanoparticle concentrations correlating to increased percentage inhibition 50 $\mu\text{g/mL}$ - 1.68%, 100 $\mu\text{g/mL}$ - 10.45%, 150 $\mu\text{g/mL}$ - 18.54%, 200 $\mu\text{g/mL}$ - 37.83%, and 250 $\mu\text{g/mL}$ - 51.72%. The highest activity, at 51.72%, occurs at 250 $\mu\text{g/mL}$.

Keywords: Biogenic synthesis, CuO nanoparticles, Antimicrobial activity, Antioxidant activity.

Submitted: January 20, 2024. **Accepted:** May 13, 2024.

Cite this: Pawar A, Mungole A, Naktode K. Biogenic Copper Oxide Nanoparticles Synthesized from Whole Plant Extract of *Nicotiana plumbaginifolia* Viv.: Characterization, Antibacterial, and Antioxidant Properties. JOTCSA. 2024;11(3): 1005-16.

DOI: <https://doi.org/10.18596/jotcsa.1422924>

***Corresponding author's E-mail:** abhaypawar1988@gmail.com

1. INTRODUCTION

In contemporary times, Nano biotechnology has evolved as a fundamental domain of modern science, representing a novel era in material science. Its myriad applications have garnered global attention. This interdisciplinary field, at the intersection of nanotechnology and biology, holds immense promise for advancements in various scientific disciplines. Crucial research in this field centers on synthesizing nanoparticles with varied shapes, sizes, chemical compositions, and controlled dispersions for exploration (1,2). Nanomaterials, or nanoparticles, serve as crucial building blocks, attracting considerable attention for their positive impact across diverse domains such as detergents, catalysis, energy, shampoos, polymers, soaps, cosmetics, toothpaste, food and agriculture, medicine, soaps, antimicrobial agents, paints, footwear, textiles, and electronics. This has

spurred research interest in nanoparticle synthesis (3,4).

Metal oxide nanoparticles have emerged as a focal point in scientific research, owing to their diverse applications that captivate the attention of investigators keen on exploring their unique properties. Notably, copper oxide nanoparticles have garnered particular interest among transition metal oxides due to their efficacy in various domains, such as antimicrobial applications, sensors, nanofluids, energy storage systems, antioxidant activity, anticancer agents, and catalysis (5-11). The distinctive capability of copper oxide nanoparticles to modulate the physical, optical, and electronic properties of compounds further accentuates their significance in contemporary research. Numerous methods have been employed for the synthesis of copper oxide nanoparticles, encompassing physical, biological,

and chemical approaches (12). However, conventional methods often entail the use of expensive and toxic chemicals, rendering them unsuitable for biomedical applications (13). Consequently, there is a growing impetus to explore synthetic methods rooted in naturally occurring biomaterials, presenting an alternative avenue for obtaining copper oxide nanoparticles tailored for biological applications. This shift towards biocompatible synthesis methods not only aligns with the principles of sustainability but also underscores the importance of developing nanoparticle formulations suitable for integration into biomedical contexts (14,15).

The biosynthesis or green synthesis of copper oxide nanoparticles utilizing various plant extracts, such as *Ephedra alata*, *Rubia cordifolia* bark, *Spinacia oleracea* leaf, *Eichhornia Crassipes* leaf, *Abelmoschus esculentus*, *Berberis vulgaris* leaf, *Sesbania grandiflora* leaf, *Bombax ceiba* plant, *Rumex nepalensis* (16-26) etc. has been extensively documented in scientific literature. This approach harnesses the inherent properties of plant extracts to facilitate the reduction and stabilization of copper ions, ultimately yielding nanoparticles with tailored characteristics. Notably, the utilization of plant extracts in copper oxide nanoparticle synthesis offers several key advantages. First and foremost, these extracts are readily accessible, contributing to the economic feasibility of the synthesis process. Additionally, the use of plant extracts is generally considered safe and non-toxic, aligning with the principles of green chemistry (27-30). The avoidance of harmful chemicals in the synthesis process is pivotal, especially in the context of biomedical applications. *Nicotiana plumbaginifolia* Viv. is an erect annual plant up to 1 m tall. It belongs to Solanaceae family, which is generally known as night shade family, native to the west Indies and Mexico and is usually found in waste places near water. The antimicrobial and antioxidant potential of plants is due to the presence of several secondary metabolites that have different mechanisms of action; some are proteins and enzymes, while others are vitamins, anthocyanins, alkaloids, flavonoids, carotenoids, and other phenolic compounds. Solanaceae family is the rich source of alkaloid content as the Nicotine is reported from *Nicotiana tobacum*. There no work has been reported from this plant material in the field of green synthesis of copper oxide nanoparticles.

Copper oxide nanoparticles, synthesized through biogenic or green methods, have demonstrated superior microbial toxicity related to other metal oxides (31). This heightened antimicrobial activity renders them particularly attractive for applications in areas such as healthcare and biomedical research. The specific mechanisms underlying the enhanced microbial toxicity of copper oxide nanoparticles warrant further investigation, opening avenues for elucidating their potential in combating microbial threats.

This study represents a pioneering synthesis of copper oxide nanoparticles utilizing the *Nicotiana plumbaginifolia* Viv. The methodology employed underscores an environmentally conscious approach, emphasizing the adoption of greener

protocols. We introduce a clean, cost-effective, non-toxic chemical, less time and eco-friendly technique for the fabrication of copper oxide nanoparticles, with *Nicotiana plumbaginifolia* Viv. serving as a key component in the synthesis process. The synthesized nanoparticles were comprehensively characterized through X-ray Diffraction (XRD), Fourier Transform Infrared Spectroscopy (FTIR), Energy Dispersive X-ray Spectroscopy (EDX), UV-Visible spectroscopy, Transmission Electron Microscopy (TEM), and Scanning Electron Microscopy (SEM). These biocompatible nanoparticles demonstrated notable antimicrobial and antioxidant activities.

2. EXPERIMENTAL SECTION (All capitals, one space before and after the heading)

2.1. Materials and Methods

The selected botanical specimen, *Nicotiana plumbaginifolia* Viv. was sourced from the proximate Bramhapuri region in the Chandrapur district of Maharashtra state, India. The plant material was meticulously collected and utilized in extract preparation. The following chemicals have been used under study, ensuring high-grade chemical standards for the experiments:

1. Sigma-Aldrich supplied Cupric nitrate trihydrate
2. 1,1-Diphenyl-2-picrylhydrazyl (DPPH)
3. Butylated Hydroxytoluene (BHT).

2.2. Preparation of Aqueous Extracts from Whole Plant Material

The harvested *Nicotiana plumbaginifolia* Viv. plant was meticulously cleansed with de-ionized water, eliminating debris and extraneous material. Subsequently, the plant material was sliced into small fragments and air-dried under shade. The entirety of the plant components were pulverized into a fine powder using a mortar and pestle. A measured quantity (20 g) of the plant powder was introduced into a 200 mL distilled water-filled, clean, and dry round-bottom flask. The resultant mixture underwent boiling at 60–70 °C for a minimum of 30 minutes, followed by natural cooling to room temperature. The solution was then meticulously filtered using Whatman number 41 filter paper. The resulting filtrate was refrigerated and earmarked for subsequent utilization in the synthesis of CuO NPs.

2.3. Biogenic Synthesis of CuO NPs

The synthesis of CuO NPs followed the established method by Sharma et al. (32). A round-bottom flask (RBF) containing 100 mL of *Nicotiana plumbaginifolia* Viv. plant extract underwent heating at 70-80 °C using a magnetic stirrer. Subsequently, a 30 mL aqueous solution containing 3 g of cupric nitrate trihydrate was gradually introduced with continuous stirring. The resulting mixture was boiled until a greenish-colored gel formed. This gel was collected, transferred into a ceramic crucible, and subjected to calcination in a furnace at 400 °C for 3 hours. The culmination of this process yielded finely dispersed black-colored CuO NPs, which were then utilized for subsequent characterization.

2.4. Characterizations

The nanoparticles underwent a comprehensive

characterization employing methodologies outlined in the literature review (33). Scanning electron microscopy (34) was employed for size and morphology analysis. Fourier transmission infrared spectroscopy (35) was utilized for optical characterization, functional group analysis, and identification. Transmission electron microscopy (36) enabled size analysis. Energy dispersive X-ray elemental analysis (37) assessed chemical composition and purity. UV-visible spectroscopy (38) was employed to investigate nanoparticle formation and confirm synthesis. X-ray absorption spectrometry (39) facilitated the determination of elemental analysis, electronic structure, and elemental composition. The copper oxide nanoparticles, derived from the reduction of copper salt using an extract of plant materials, underwent meticulous characterization through diverse analytical techniques. UV-visible diffuse reflectance spectra were acquired using the Thermo Scientific Evolution 300 UV-visible spectrophotometer. FT-IR analysis within the 4000-100 cm^{-1} range was executed with the Thermo Nicolet iS50 FTIR Spectrometer. Crystallographic and structural analyses were conducted using the Bruker AXS D8 X-ray diffraction technique with copper as the X-ray source. For size, morphology, and composition analysis, TEM (Jeol/JEM, 2100, at 200 kV) and SEM-EDX (Jeol 6390la/OXFORD XMX N) were employed. All analyses were performed by SAIF, Kochi (India).

2.5. Antimicrobial Activity

The antimicrobial efficacy of synthesized CuO nanoparticles was examined at concentrations of 25, 50, and 100 μL against *E. coli*, *S. aureus*, *P. aeruginosa*, and *K. pneumonia*, employing the well diffusion method. The assessment centered on zones of inhibition observed in Figure 9 and summarized in Table 1. Comparative analysis with the standard antibiotic, amikacin (30 μg), depicted in figure 10, offered contextual insights. The observed zones of inhibition serve as indicators of CuO nanoparticles effectiveness in suppressing bacterial growth, emphasizing their potential as antimicrobial agents.

2.6. Anti-Oxidant Activity

The antioxidant efficacy of the synthesized CuO

nanoparticles was evaluated through the assessment of 1,1-Diphenyl-2-picrylhydrazyl (DPPH) free radical scavenging activity. Varied concentrations (20, 40, 60, 80, and 100 $\mu\text{g/mL}$) of the prepared CuO nanoparticles from *Nicotiana plumbaginifolia* Viv. were formulated by combining 3 mL of methanol and 1 mL of 4% DPPH solution equally at room temperature. The mixture was left undisturbed in a dark environment for 30 minutes before measuring absorbance at 517 nm using a visible spectrophotometer, with butylated hydroxytoluene (BHT) serving as the standard. The percentage of radical scavenging activity (% RSA) was calculated using the formula:

$$\% \text{ RSA} = [(\text{abs}_{517 \text{ nm of control}} - \text{abs}_{517 \text{ nm of sample}}) / \text{abs}_{517 \text{ nm of control}}] \times 100 \text{ (Eq.1)}$$

(% RSA- percentage radical scavenging activity, Abs -absorbance) (Eq.2)

3. RESULTS AND DISCUSSION

Solid UV-Visible-DR analysis is a technique employed to discern the optical absorption properties and energy structure of nanoscale substances. This method involves measuring the diffuse reflectance of a solid material across the ultraviolet and visible spectra, allowing for the characterization of its electronic transitions and absorption features. The analysis provides valuable insights into the optical behavior and energy band structure of the nanomaterial under investigation. Figure 1 presents the solid UV-Visible spectrum of synthesized CuO nanoparticles through *Nicotiana plumbaginifolia* Viv. as manifested by the diffuse reflectance (DR) analysis. The spectrum reveals a broad absorption band edge scanning the range of 200 to 730 nm (40). The Kubelka-Munk (K-M) function, utilized for analyzing diffuse reflectance spectra (DRS) from weakly absorbing materials, is employed to convert DRS values into absorbance (41,42). The bandgap energy assessment involved plotting $(F(R)_{h\nu})^2$ against $h\nu$ (energy in eV) for the biosynthesized CuO nanoparticles from *Nicotiana plumbaginifolia* Viv. as depicted in Figure 2. The determined bandgap energy for the biosynthesized CuO nanoparticles was 5.16 eV.

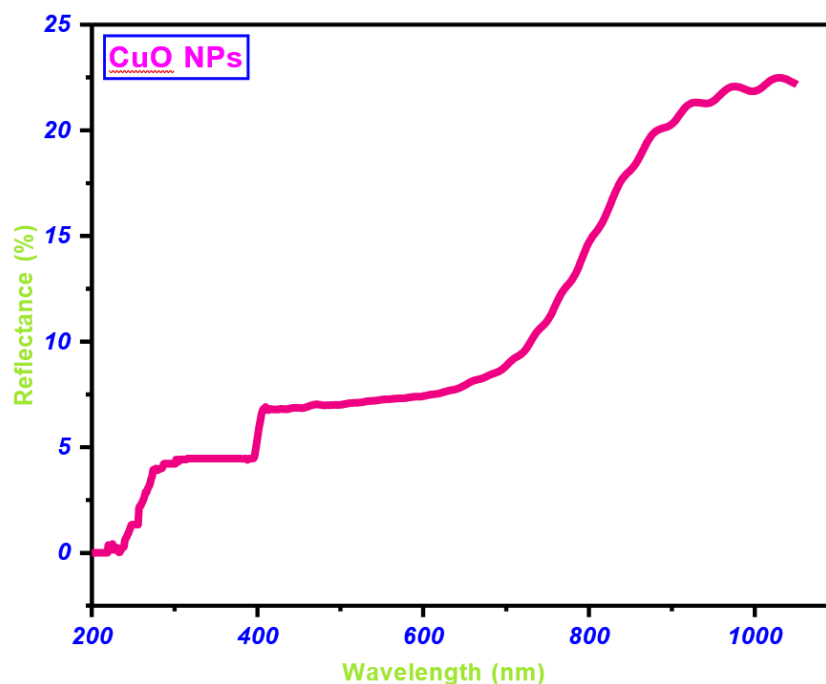


Figure 1: Diffuse reflectance spectrum of CuO NPs synthesized.

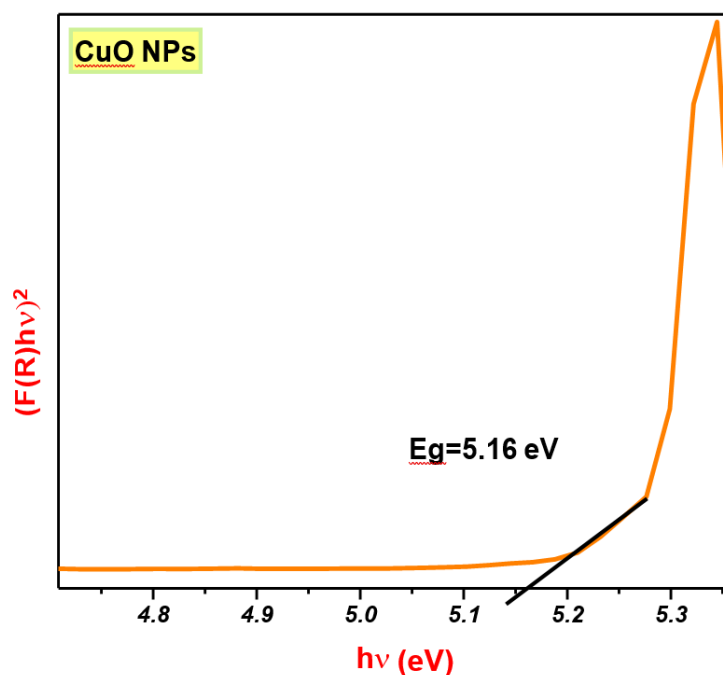


Figure 2: Plot of $(F(R)/h\nu)^2$ versus $h\nu$ (eV) for CuO NPs synthesized.

Figure 3 displays the FTIR measurements of the synthesized copper oxide nanoparticles, facilitating the identification of potential biomolecules serving as both reducing and capping agents in the synthesis process. The FTIR spectrum exhibits distinctive peaks at various wavenumbers, offering valuable insights into the molecular composition of the synthesized copper oxide nanoparticles. At 3432.67 cm^{-1} , the presence of O-H (hydroxyl group) is indicated, while the peak at 1629.55 cm^{-1} corresponds to -C=O (carbonyl) vibrations. Notably, peaks at 1382.71 , 1141.65 , and 1029.8 cm^{-1} signify

CN group, C-O, and $\text{CH}_2\text{-O}$ bending or stretching vibrations, respectively, shedding light on specific molecular functionalities. The presence of C-Cl (halo compound) is indicated by the peak at 827.31 cm^{-1} (43-44). Furthermore, distinctive peaks at 673.03 and 518.75 cm^{-1} are attributed to the Cu-O vibration in the copper oxide nanoparticles (45,46). These observations collectively unravel the intricate molecular details of the synthesized nanoparticles, providing a comprehensive understanding of their composition and functional groups.

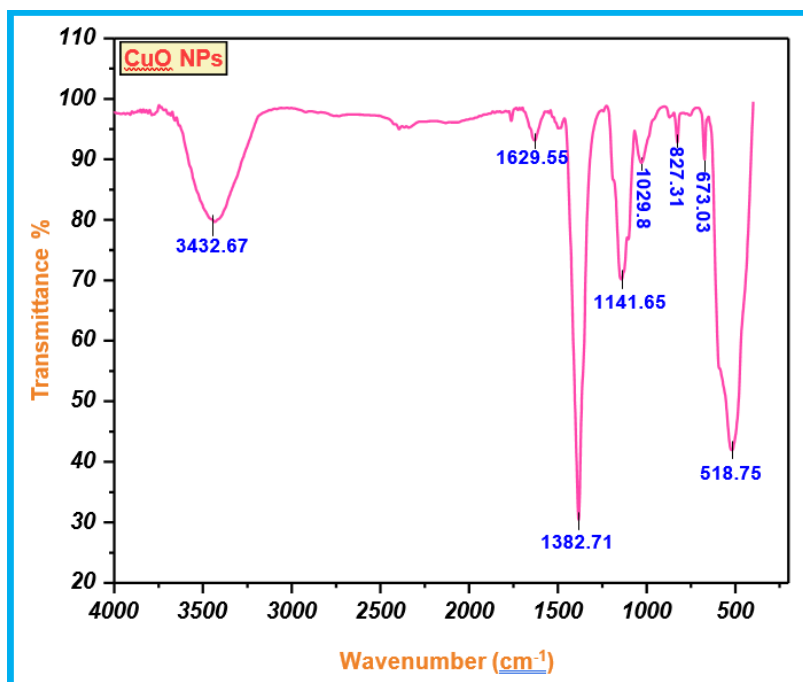


Figure 3: FTIR spectra of CuO NPs formed.

Figure 4 depicts the X-ray diffraction (XRD) pattern of CuO nanoparticles synthesized via *Nicotiana glumbaginifolia* Viv. The identified XRD peaks at 2-theta values of 32.615°, 35.655°, 38.872°, 48.792°, 53.803°, 58.609°, 61.718°, 66.394°, 68.344°, 72.28847°, and 75.278° precisely correspond to the (110), (002), (111), (202), (020), (202), (113), (311), (220), (311), and (004) hkl planes,

respectively. This pattern aligns with standard values from JCPDS file No. 89-5895 (47), confirming the monoclinic crystal structure of the synthesized CuO nanoparticles (48,49). The observed peaks signify the high degree of crystallinity and structural consistency of the prepared nanoparticles.

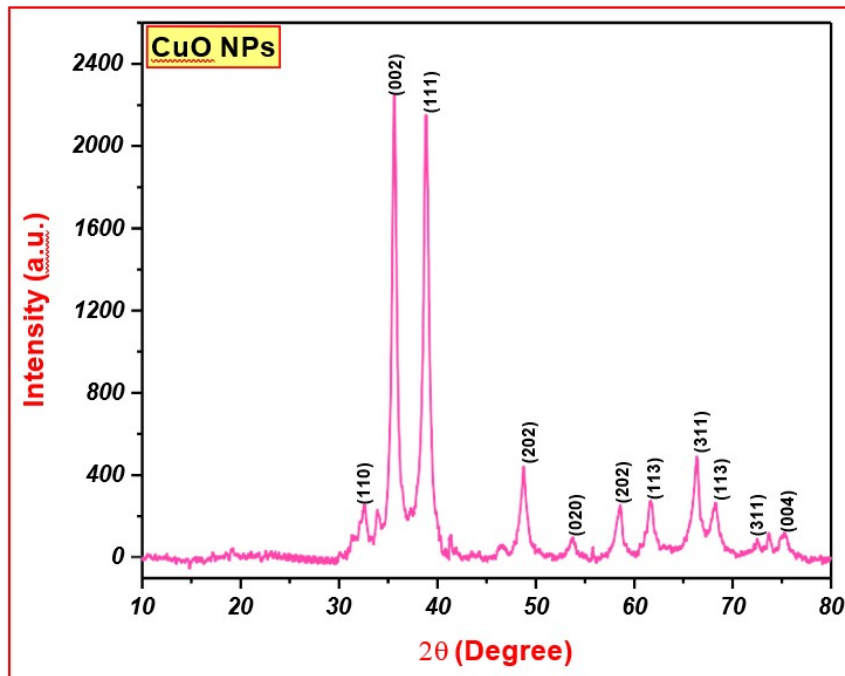


Figure 4: XRD pattern of CuO NPs formed.

Scanning electron microscopy (SEM) was employed to assess the surface morphology of CuO nanoparticles synthesized from *Nicotiana glumbaginifolia*. In Figure 5, SEM images reveal uniform shapes with varying sizes and occasional surface aggregation. The observed size variations

are attributed to synthesis parameters influenced by phytochemical constituents in the plant (50). Surface aggregations suggest localized influences of diverse plant-derived species on nanoparticle assembly.

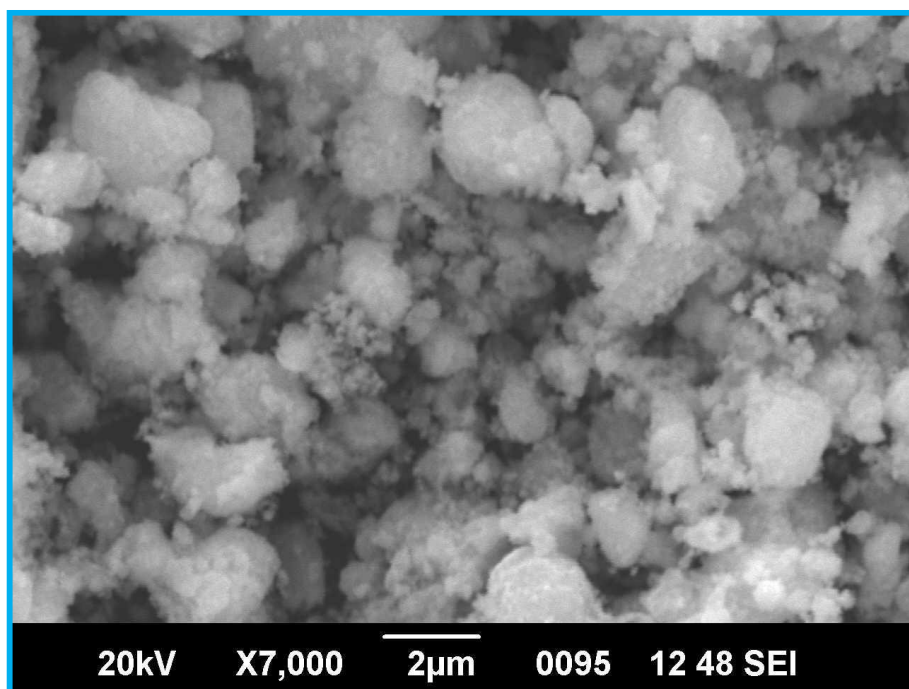


Figure 5: SEM figure of CuO NPs prepared.

Energy dispersive X-ray analysis (EDAX) stands as a highly valuable technique for elucidating the chemical composition and elemental constitution of nanomaterials. In Figure 6, the EDAX spectrum corresponding to the CuO nanoparticles synthesized through the utilization of *Nicotiana plumbaginifolia* Viv. is presented. The spectrum prominently exhibits distinctive signals indicative of copper and oxygen. These discernible signals unequivocally authenticate the existence of copper and oxygen in the CuO nanoparticle form, as visually represented in Figure 6.

The copper signals in the spectrum are notably characterized by a weight percentage of 53.62% and an atomic percentage of 28.5%. Concurrently, the oxygen signals manifest a weight percentage of 24.46% with an atomic percentage of 51.63%. This

quantitative analysis attests to the precise elemental makeup of the synthesized CuO nanoparticles. The discerned weight and atomic percentages offer quantitative insights into the proportional contribution of each element, underscoring the composition of the nanomaterial.

Furthermore, the EDAX spectrum reveals additional peaks, which are attributed to photochemical constituents inherent in the *Nicotiana plumbaginifolia* Viv. plant. These supplementary peaks underscore the presence of diverse elements associated with the plant-derived synthesis process. The comprehensive analysis not only validates the synthesis of CuO nanoparticles but also provides a nuanced understanding of the elemental composition, thereby contributing to the in-depth characterization of the nanomaterial.

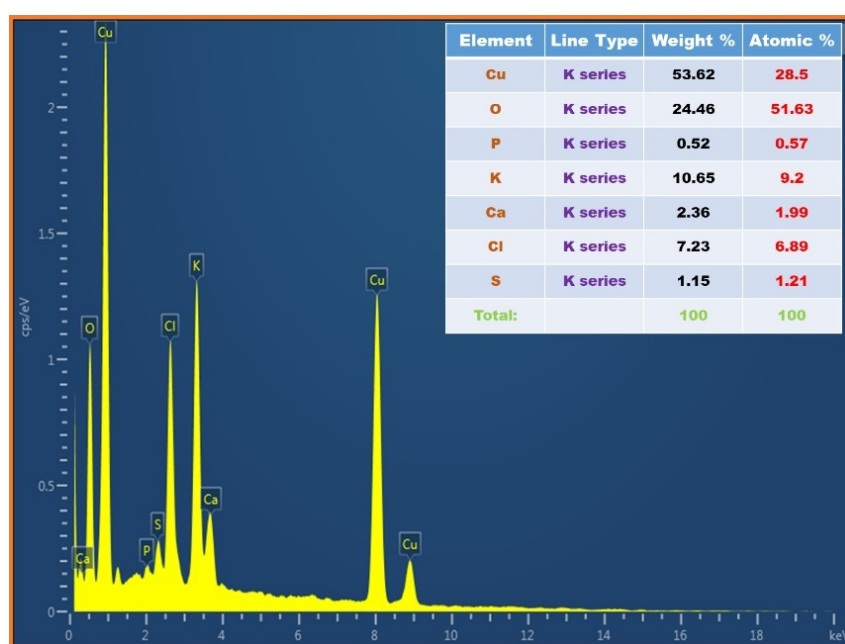


Figure 6: EDAX spectra of CuO NPs synthesized.

Transmission electron microscopy (TEM) stands as an indispensable tool for the detailed examination of materials, facilitating the elucidation of their morphology, size, and structural arrangement. In figure 7, distinctive images of the synthesized CuO nanoparticles are presented, offering valuable insights into their physical characteristics. The observations derived from these images reveal that the designed CuO nanoparticles exhibit quasi-spherical morphology, with an average size distribution spanning from 12 to 14 nm. The observed size variation is ascribed to surface agglomeration phenomena, influenced by the concentration of the plant extract employed during the nanoparticle synthesis process. The interplay of these parameters contributes to the nuanced size distribution of the CuO nanoparticles, reflecting the dynamic nature of their formation. The utilization of Selected Area Electron Diffraction (SAED) further substantiates the crystalline nature of the synthesized CuO nanoparticles derived from *Nicotiana plumbaginifolia* Viv. The SAED pattern, as depicted in figure 8, manifests a distinctive quasi-spherical pattern, affirming the ordered atomic arrangement within the nanoparticles. This crystalline pattern serves as compelling evidence of the high structural integrity and regularity of the CuO nanoparticles at the nanoscale.

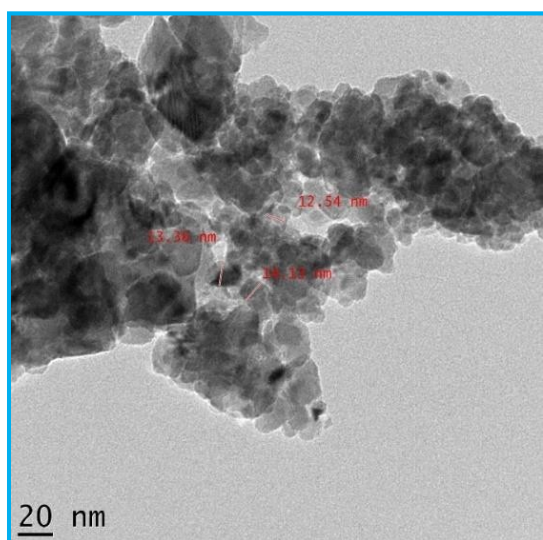


Figure 7: TEM image of CuO NPs formed.

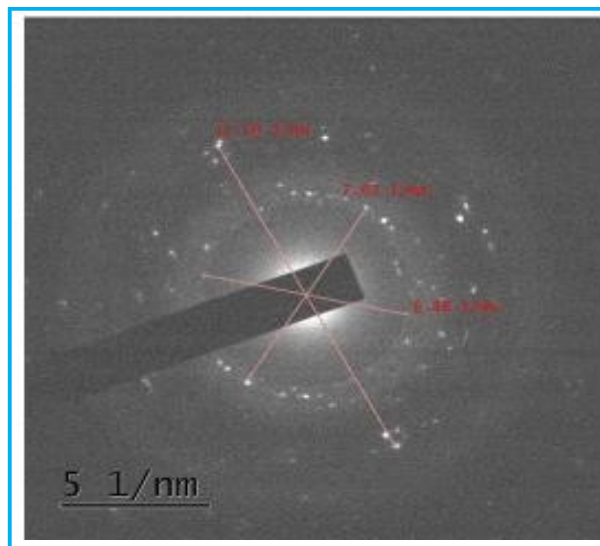


Figure 8: SAED pattern image of synthesized CuO NPs.

In figure 9, amikacin at 30 μg demonstrates sensitivity in *E. coli*, yielding a 19 mm inhibition zone. In contrast, CuO NPs exhibit no inhibition at 25 μL and 50 μL , with a 15 mm zone observed at 100 μL . For *S. aureus* and *P. aeruginosa*, amikacin (30 μg) elicits 25 mm and 10 mm inhibition zones, respectively. CuO NPs produce inhibition zones of 17 mm, 20 mm, and 22 mm for *S. aureus* (at 25 μL , 50 μL , and 100 μL) and show no inhibition for *P. aeruginosa* (25 μL , 50 μL , and 100 μL). *K. pneumoniae* displays sensitivity to amikacin (30 μg) with a 22 mm inhibition zone, while CuO NPs exhibit no inhibition at all concentrations. Remarkably, at a 100 μL concentration of CuO NPs, robust antimicrobial activity is evident only against *E. coli* and *S. aureus*, with *S. aureus* demonstrating significant activity even at 25 μL and 50 μL concentrations (Table 1). In the past, many workers have carried out the antimicrobial activities from different plant-mediated extract-based synthesized copper oxide nanoparticles (51-55).

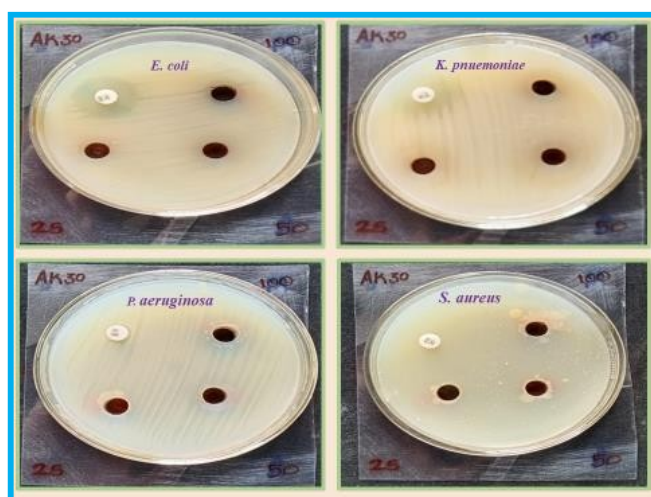


Figure 9: Synthesized CuO NPs exhibit antibacterial activity comparable to standard Amikacin (AK30 μg).

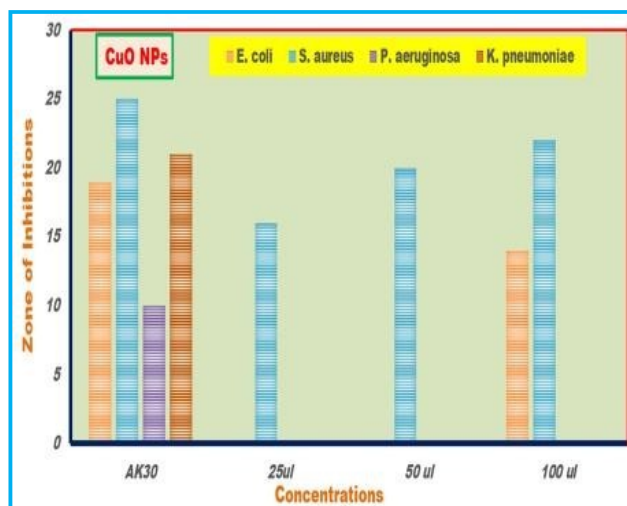


Figure 10: Antimicrobial activity of formed CuO NPs against a) *E. coli* b) *S. aureus* c) *P. aeruginosa* d) *K. Pneumoniae*.

Table 1: ZOI (Zone of inhibition) of organisms at different concentrations.

ZOI (mm) Organisms	Concentrations			
	AK30	25 uL	50 uL	100 uL
<i>E. coli</i>	19	NI	NI	15
<i>K. pneumoniae</i>	22	NI	NI	NI
<i>S. aureus</i>	25	17	20	22
<i>P. aeruginosa</i>	10	NI	NI	NI

Note: *E. coli* = *Escherichia coli*, *S. aureus* = *Staphylococcus aureus*, *P. aeruginosa* = *Pseudomonas aeruginosa*, *K. pneumoniae* = *Klebsiella pneumoniae*, NI = No Inhibition. AK30 = Amikacin 30 mcg.

The antioxidant efficacy of CuO nanoparticles on 1,1-Diphenyl-2-picrylhydrazyl (DPPH) is depicted in figure 11. The findings reveal potent antioxidant activity, with escalating CuO nanoparticle concentrations correlating to increased percentage inhibition: 50 µg/mL - 1.68%, 100 µg/mL - 10.45%, 150 µg/mL - 18.54%, 200 µg/mL - 37.83%, and 250 µg/mL - 51.72%. The highest activity, at 51.72%, occurs at 250 µg/ml. This heightened antioxidative

capability is attributed to bioactive compounds, including alkaloids, phenolic compounds, and flavonoids, in *Nicotiana plumbaginifolia*. Similar studies have also been carried out, showing enhancement of the antioxidant properties of the material (56-57). The synergistic interaction with nanomaterials enhances CuO nanoparticle antioxidant properties, showcasing potential for addressing diverse diseases.

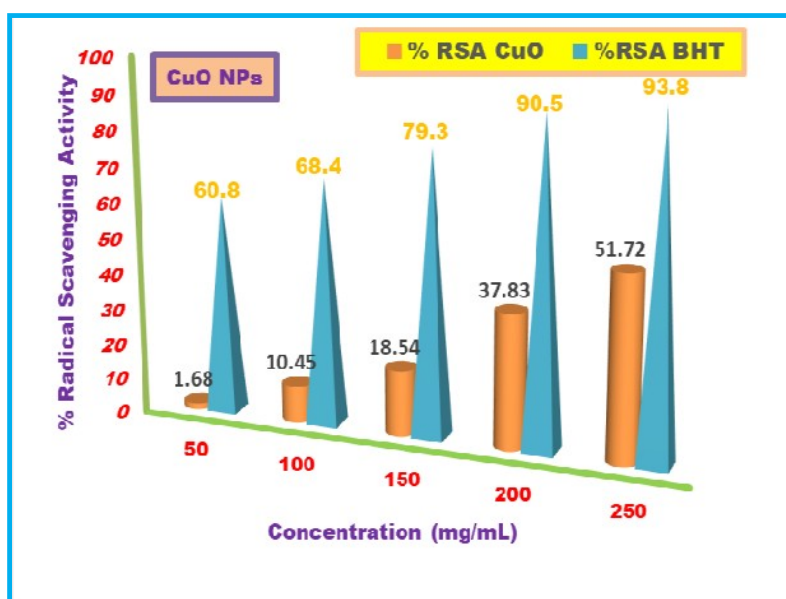


Figure 11: Antioxidant activity of CuO NPs biosynthesized.

4. CONCLUSION

This study presents a cost-effective and benign approach for the synthesis of copper oxide nanoparticles (CuO NPs) utilizing the entire *Nicotiana plumbaginifolia* Viv. plant. The plant's abundance of diverse phytochemicals serves a dual purpose by reducing metal ions and stabilizing the resulting nanoparticles. Structural characteristics of the CuO NPs were systematically analyzed using spectroscopic techniques. Furthermore, the antimicrobial and antioxidant properties of the synthesized nanoparticles were investigated. The band gap of the biogenically synthesized CuO NPs was quantified at 5.16 eV, demonstrating notable antimicrobial efficacy against pathogenic bacteria and significant antioxidant activity.

5. CONFLICT OF INTEREST

All authors declare no conflicts of interest.

6. ACKNOWLEDGMENTS

We extend heartfelt appreciation to the principal of Nevjabai Hitkarini College, Bramhapuri, Maharashtra (India), for steadfast support, encouragement, and providing research facilities. Our gratitude also extends to the Sophisticated Test and Instrumentation Centre (STIC) at Cochin University of Science and Technology, Cochin, Kerala, India, for their invaluable assistance in characterizing the samples.

7. REFERENCES

1. Akhtar MS, Panwar J, Yun YS. Biogenic Synthesis of Metallic Nanoparticles by Plant Extracts. ACS Sustain Chem Eng [Internet]. 2013 Jun 3;1(6):591-602. Available from: [<URL>](#).
2. Roco MC. The long view of nanotechnology development: The National Nanotechnology Initiative at 10 years. J Nanoparticle Res [Internet]. 2011 Feb 12;13(2):427-45. Available from: [<URL>](#).
3. Kim BS, Song JY. Biological synthesis of gold and silver nanoparticles using plant leaf extracts and antimicrobial applications. In: Hou CT, Shaw JF, editors. Biocatalysis and biomolecular engineering. USA: Wiley & Sons; 2010. p. 447-57.
4. Buzea C, Pacheco II, Robbie K. Nanomaterials and nanoparticles: Sources and toxicity. Biointerphases [Internet]. 2007 Dec 1;2(4):MR17-71. Available from: [<URL>](#).
5. Singh P, Ali SW, Kale RD. Antimicrobial Nanomaterials as Advanced Coatings for Self-Sanitizing of Textile Clothing and Personal Protective Equipment. ACS Omega [Internet]. 2023 Mar 7;8(9):8159-71. Available from: [<URL>](#).
6. Černík M, Thekkae Padil VV. Green synthesis of copper oxide nanoparticles using gum karaya as a biotemplate and their antibacterial application. Int J Nanomedicine [Internet]. 2013 Feb;8:889-98. Available from: [<URL>](#).
7. Chaudhary S, Rohilla D, Umar A, Kaur N, Shanavas A. Synthesis and characterizations of luminescent copper oxide nanoparticles: Toxicological profiling and sensing applications.

Ceram Int [Internet]. 2019 Aug;45(12):15025-35. Available from: [<URL>](#).

8. Chang MH, Liu HS, Tai CY. Preparation of copper oxide nanoparticles and its application in nanofluid. Powder Technol [Internet]. 2011 Feb;207(1-3):378-86. Available from: [<URL>](#).
9. Ikhiyoa IL, Onoh EU, Nkele AC, Abor BC, Obitte BCN, Maaza M, et al. The Green Synthesis of Copper Oxide Nanoparticles Using the Moringa Oleifera Plant and its Subsequent Characterization for Use in Energy Storage Applications. East Eur J Phys [Internet]. 2023 Mar 2;(1):162-72. Available from: [<URL>](#).
10. Ganesan K, Jothi VK, Natarajan A, Rajaram A, Ravichandran S, Ramalingam S. Green synthesis of Copper oxide nanoparticles decorated with graphene oxide for anticancer activity and catalytic applications. Arab J Chem [Internet]. 2020 Aug;13(8):6802-14. Available from: [<URL>](#).
11. Rehana D, Mahendiran D, Kumar RS, Rahiman AK. Evaluation of antioxidant and anticancer activity of copper oxide nanoparticles synthesized using medicinally important plant extracts. Biomed Pharmacother [Internet]. 2017 May;89:1067-77. Available from: [<URL>](#).
12. Singh A, Singh NB, Hussain I, Singh H. Effect of biologically synthesized copper oxide nanoparticles on metabolism and antioxidant activity to the crop plants Solanum lycopersicum and Brassica oleracea var. botrytis. J Biotechnol [Internet]. 2017 Nov;262:11-27. Available from: [<URL>](#).
13. Khatoon UT, Mohan Mantravadi K, Nageswara Rao GVS. Strategies to synthesise copper oxide nanoparticles and their bio applications - a review. Mater Sci Technol [Internet]. 2018 Dec 1;34(18):2214-22. Available from: [<URL>](#).
14. El Bialy BE, Hamouda RA, Abd Eldaim MA, El Ballal SS, Heikal HS, Khalifa HK, et al. Comparative Toxicological Effects of Biologically and Chemically Synthesized Copper Oxide Nanoparticles on Mice. Int J Nanomedicine [Internet]. 2020 May;15:3827-42. Available from: [<URL>](#).
15. Chakraborty N, Banerjee J, Chakraborty P, Banerjee A, Chanda S, Ray K, et al. Green synthesis of copper/copper oxide nanoparticles and their applications: a review. Green Chem Lett Rev [Internet]. 2022 Jan 2;15(1):187-215. Available from: [<URL>](#).
16. Vincent J, Lau KS, Evyan YCY, Chin SX, Sillanpää M, Chia CH. Biogenic Synthesis of Copper-Based Nanomaterials Using Plant Extracts and Their Applications: Current and Future Directions. Nanomaterials [Internet]. 2022 Sep 23;12(19):3312. Available from: [<URL>](#).
17. Eid AM, Fouda A, Hassan SED, Hamza MF, Alharbi NK, Elkelish A, et al. Plant-Based Copper Oxide Nanoparticles; Biosynthesis, Characterization, Antibacterial Activity, Tanning Wastewater Treatment, and Heavy Metals Sorption. Catalysts [Internet]. 2023 Feb 3;13(2):348. Available from: [<URL>](#).

18. Atri A, Echabaane M, Bouzidi A, Harabi I, Soucase BM, Ben Chaâbane R. Green synthesis of copper oxide nanoparticles using Ephedra Alata plant extract and a study of their antifungal, antibacterial activity and photocatalytic performance under sunlight. *Heliyon* [Internet]. 2023 Feb 1;9(2):e13484. Available from: [<URL>](#).
19. Vinothkanna A, Mathivanan K, Ananth S, Ma Y, Sekar S. Biosynthesis of copper oxide nanoparticles using *Rubia cordifolia* bark extract: characterization, antibacterial, antioxidant, larvicidal and photocatalytic activities. *Environ Sci Pollut Res* [Internet]. 2022 Feb 17;30(15):42563–74. Available from: [<URL>](#).
20. Thandapani G, Arthi K, Pazhanisamy P, John JJ, Vinothini C, Rekha V, et al. Green synthesis of copper oxide nanoparticles using *Spinacia oleracea* leaf extract and evaluation of biological applications: Antioxidant, antibacterial, larvicidal and biosafety assay. *Mater Today Commun* [Internet]. 2023 Mar;34:105248. Available from: [<URL>](#).
21. Saligedo TS, Muleta GG, Tsega TW, Tadele KT. Green Synthesis of Copper Oxide Nanoparticles Using *Eichhornia Crassipes* Leaf Extract, its Antibacterial and Photocatalytic Activities. *Curr Nanomater* [Internet]. 2023 Apr;8(1):58–68. Available from: [<URL>](#).
22. Javid-Naderi MJ, Sabouri Z, Jalili A, Zarrinfar H, Samarghandian S, Darroudi M. Green synthesis of copper oxide nanoparticles using okra (*Abelmoschus esculentus*) fruit extract and assessment of their cytotoxicity and photocatalytic applications. *Environ Technol Innov* [Internet]. 2023 Nov;32:103300. Available from: [<URL>](#).
23. Derakhshani E, Asri M, Naghizadeh A. Plant-Based Green Synthesis of Copper Oxide Nanoparticles Using *Berberis vulgaris* Leaf Extract: an Update on Their Applications in Antibacterial Activity. *Bionanoscience* [Internet]. 2023 Mar 30;13(1):212–8. Available from: [<URL>](#).
24. Ramasubbu K, Padmanabhan S, Al-Ghanim KA, Nicoletti M, Govindarajan M, Sachivkina N, et al. Green Synthesis of Copper Oxide Nanoparticles Using *Sesbania grandiflora* Leaf Extract and Their Evaluation of Anti-Diabetic, Cytotoxic, Anti-Microbial, and Anti-Inflammatory Properties in an In-Vitro Approach. *Fermentation* [Internet]. 2023 Mar 27;9(4):332. Available from: [<URL>](#).
25. Arun S., Karthik B., Yatish K., Prashanth K., Balakrishna GR. Green synthesis of copper oxide nanoparticles using the *Bombax ceiba* plant: Biodiesel production and nano-additive to investigate diesel engine performance-emission characteristics. *Energy* [Internet]. 2023 Jul;274:127345. Available from: [<URL>](#).
26. Abhimanyu P, Arvind M, Kishor N. Biosynthesis of CuO Nanoparticles Using Plant Extract as a Precursor: Characterization, Antibacterial, and Antioxidant Activity. *Nano Biomed Eng* [Internet]. 2023 Dec;15(4):369–77. Available from: [<URL>](#).
27. Hano C, Abbasi BH. Plant-Based Green Synthesis of Nanoparticles: Production, Characterization and Applications. *Biomolecules* [Internet]. 2021 Dec 25;12(1):31. Available from: [<URL>](#).
28. Shafey AM El. Green synthesis of metal and metal oxide nanoparticles from plant leaf extracts and their applications: A review. *Green Process Synth* [Internet]. 2020 Jun 18;9(1):304–39. Available from: [<URL>](#).
29. Nande A, Raut S, Michalska-Domanska M, Dhoble SJ. Green Synthesis of Nanomaterials Using Plant Extract: A Review. *Curr Pharm Biotechnol* [Internet]. 2021 Sep 20;22(13):1794–811. Available from: [<URL>](#).
30. Soni V, Raizada P, Singh P, Cuong HN, S R, Saini A, et al. Sustainable and green trends in using plant extracts for the synthesis of biogenic metal nanoparticles toward environmental and pharmaceutical advances: A review. *Environ Res* [Internet]. 2021 Nov;202:111622. Available from: [<URL>](#).
31. Baek YW, An YJ. Microbial toxicity of metal oxide nanoparticles (CuO, NiO, ZnO, and Sb₂O₃) to *Escherichia coli*, *Bacillus subtilis*, and *Streptococcus aureus*. *Sci Total Environ* [Internet]. 2011 Mar;409(8):1603–8. Available from: [<URL>](#).
32. Sharma JK, Srivastava P, Singh G, Akhtar MS, Ameen S. Catalytic thermal decomposition of ammonium perchlorate and combustion of composite solid propellants over green synthesized CuO nanoparticles. *Thermochim Acta* [Internet]. 2015 Aug;614:110–5. Available from: [<URL>](#).
33. Akintelu SA, Folorunso AS, Folorunso FA, Oyebamiji AK. Green synthesis of copper oxide nanoparticles for biomedical application and environmental remediation. *Heliyon* [Internet]. 2020 Jul;6(7):e04508. Available from: [<URL>](#).
34. Pawar AP, Naktode KS, Mungole AJ. Green synthesis of silver nanoparticles from whole plant extract analyzed for characterization, antioxidant, and antibacterial properties. *Phys Chem Solid State* [Internet]. 2023 Nov 21;24(4):640–9. Available from: [<URL>](#).
35. Manasa DJ, Chandrashekar KR, Madhu Kumar DJ, Niranjana M, Navada KM. Mussaenda frondosa L. mediated facile green synthesis of Copper oxide nanoparticles - Characterization, photocatalytic and their biological investigations. *Arab J Chem* [Internet]. 2021 Jun;14(6):103184. Available from: [<URL>](#).
36. Aziz WJ, Jassim HA. A new paradigm shift to prepare copper nanoparticles using biological synthesis and evaluation of antimicrobial activity. *Plant Arch* [Internet]. 2018;18(2):2020–4. Available from: [<URL>](#).
37. Kuppusamy P, Ilavenil S, Sriganesh S, Maniam GP, Yusoff MM, Govindan N, et al. Treating of palm oil mill effluent using *Commelina nudiflora* mediated copper nanoparticles as a novel bio-control agent. *J Clean Prod* [Internet]. 2017 Jan;141:1023–9. Available from: [<URL>](#).

38. Maruthupandy M, Zuo Y, Chen JS, Song JM, Niu HL, Mao CJ, et al. Synthesis of metal oxide nanoparticles (CuO and ZnO NPs) via biological template and their optical sensor applications. *Appl Surf Sci* [Internet]. 2017 Mar;397:167-74. Available from: [<URL>](#).
39. Sriranjani R, Srinithya B, Vellingiri V, Brindha P, Anthony SP, Sivasubramanian A, et al. Silver nanoparticle synthesis using *Clerodendrum phlomidis* leaf extract and preliminary investigation of its antioxidant and anticancer activities. *J Mol Liq* [Internet]. 2016 Aug;220:926-30. Available from: [<URL>](#).
40. Kasatkov S, Fantin A, Manzoni AM, Sakhonenkov S, Makarova A, Smirnov D, et al. Chemical interaction and electronic structure in a compositionally complex alloy: A case study by means of X-ray absorption and X-ray photoelectron spectroscopy. *J Alloys Compd* [Internet]. 2021 Mar;857:157597. Available from: [<URL>](#).
41. Parthibavarman M, Sharmila V, Sathishkumar P, Gaikwad SA. A Rapid One-Pot Synthesis of CuO Rice-Like Nanostructure and Its Structural, Optical and Electrochemical Performance. *J Electron Mater* [Internet]. 2018 Sep 18;47(9):5443-51. Available from: [<URL>](#).
42. Landi S, Segundo IR, Freitas E, Vasilevskiy M, Carneiro J, Tavares CJ. Use and misuse of the Kubelka-Munk function to obtain the band gap energy from diffuse reflectance measurements. *Solid State Commun* [Internet]. 2022 Jan 1;341:114573. Available from: [<URL>](#).
43. Berger T, Trunschke A. Optical Properties: UV/Vis Diffuse Reflectance Spectroscopy and Photoluminescence. In: *Metal Oxide Nanoparticles* [Internet]. Wiley; 2021. p. 435-82. Available from: [<URL>](#).
44. Renuga D, Jeyasundari J, Shakthi Athithan AS, Brightson Arul Jacob Y. Synthesis and characterization of copper oxide nanoparticles using *Brassica oleracea* var. *italica* extract for its antifungal application. *Mater Res Express* [Internet]. 2020 Apr 1;7(4):045007. Available from: [<URL>](#).
45. Vidovix TB, Quesada HB, Januário EFD, Bergamasco R, Vieira AMS. Green synthesis of copper oxide nanoparticles using *Punica granatum* leaf extract applied to the removal of methylene blue. *Mater Lett* [Internet]. 2019 Dec;257:126685. Available from: [<URL>](#).
46. Antonoglou O, Lafazanis K, Mourdikoudis S, Vourlias G, Lialiaris T, Pantazaki A, et al. Biological relevance of CuFeO₂ nanoparticles: Antibacterial and anti-inflammatory activity, genotoxicity, DNA and protein interactions. *Mater Sci Eng C* [Internet]. 2019 Jun;99:264-74. Available from: [<URL>](#).
47. Anto Feradrick Samson V, Mohamed Racik K, Prathap S, Madhavan J, Victor Antony Raj M. Investigations of Structural, Optical and dielectric studies of Copper Oxide nanoparticles. *Mater Today Proc* [Internet]. 2019;8:386-92. Available from: [<URL>](#).
48. Vetrimani A, Geetha K, Angel Jemima E, Arulnathan N, Kim HS, Kathalingam A. Effect of the green synthesis of CuO plate-like nanoparticles on their photodegradation and antibacterial activities. *Phys Chem Chem Phys* [Internet]. 2022;24(47):28923-33. Available from: [<URL>](#).
49. Ganga BG, Varma MR, Santhosh PN. Evidence of reduced antiferromagnetic transition in mesocrystals of CuO synthesized by a surfactant-free solution phase method. *CrystEngComm* [Internet]. 2015;17(37):7086-93. Available from: [<URL>](#).
50. Mittal AK, Chisti Y, Banerjee UC. Synthesis of metallic nanoparticles using plant extracts. *Biotechnol Adv* [Internet]. 2013 Mar 1;31(2):346-56. Available from: [<URL>](#).
51. Singh P, Singh KR, Singh J, Das SN, Singh RP. Tunable electrochemistry and efficient antibacterial activity of plant-mediated copper oxide nanoparticles synthesized by *Annona squamosa* seed extract for agricultural utility. *RSC Adv* [Internet]. 2021;11(29):18050-60. Available from: [<URL>](#).
52. Achamo T, Zereffa EA, Murthy HCA, Ramachandran VP, Balachandran R. Phyto-mediated synthesis of copper oxide nanoparticles using *Artemisia abyssinica* leaf extract and its antioxidant, antimicrobial and DNA binding activities. *Green Chem Lett Rev* [Internet]. 2022 Jul 3;15(3):598-614. Available from: [<URL>](#).
53. Bhatia N, Kumari A, Chauhan N, Thakur N, Sharma R. *Duchsnea indica* plant extract mediated synthesis of copper oxide nanomaterials for antimicrobial activity and free-radical scavenging assay. *Biocatal Agric Biotechnol* [Internet]. 2023 Jan;47:102574. Available from: [<URL>](#).
54. Maheo AR, B. SMV, T. AAP. Biosynthesis and characterization of *Eupatorium adenophorum* and chitosan mediated Copper oxide nanoparticles and their antibacterial activity. *Results in Surfaces and Interfaces* [Internet]. 2022 Feb;6:100048. Available from: [<URL>](#).
55. Kamçı H, Taş R, Çelebioğlu HU. Antibacterial Activity of Copper Nanoparticles Synthesized by Using *Peumus boldus* Leaf Extract. *Eur J Sci Technol* [Internet]. 2022 May 2;5(36):139-42. Available from: [<URL>](#).
56. Peddi P, PTSRK PR, Rani NU, Tulasi SL. Green synthesis, characterization, antioxidant, antibacterial, and photocatalytic activity of *Suaeda maritima* (L.) Dumort aqueous extract-mediated copper oxide nanoparticles. *J Genet Eng Biotechnol* [Internet]. 2021 Dec;19(1):131. Available from: [<URL>](#).
57. Sarkar J, Chakraborty N, Chatterjee A, Bhattacharjee A, Dasgupta D, Acharya K. Green Synthesized Copper Oxide Nanoparticles Ameliorate Defence and Antioxidant Enzymes in *Lens culinaris*. *Nanomaterials* [Internet]. 2020 Feb 12;10(2):312. Available from: [<URL>](#).



Molecular Interaction Studies on Physicochemical and Derived Properties of Binary Mixtures at Atmospheric Pressure

Aishwarya V. Navarkhele¹ , Vaijanath V. Navarkhele^{2*} 

¹Research Scholar, Dr. Babasaheb Ambedkar Marathwada University, Aurangabad - 431 004, India.

²Department of Physics, Dr. Babasaheb Ambedkar Marathwada University, Aurangabad - 431 004, India.

Abstract: The physicochemical properties like refractive indices, densities, and static dielectric constants of binary mixtures were measured over the entire concentration range. Refractive index and densities were measured at 293.15 K, and dielectric constants at (293.15, 298.15, and 303.15 K) temperatures for the n-propanol-formamide binary system. From dielectric data, the related and excess properties were calculated and reported in this work. From experimental refractive indices and densities, various related and excess properties were estimated and reported in this study. Static dielectric constants, densities, and refractive index of the binary system increase with the increase in the mole fraction of formamide. The results obtained were discussed in terms of intermolecular interactions, structural effects, hydrogen bonding, and other possible interactions between like and unlike molecules of the binary system.

Keywords: Physicochemical properties; Related properties; Excess properties; Binary system.

Submitted: August 28, 2023. **Accepted:** May 19, 2024.

Cite this: Navarkhele AV, Navarkhele VV. Molecular Interaction Studies on Physicochemical and Derived Properties of Binary Mixtures at Atmospheric Pressure. JOTCSA. 2024;11(3): 1017-24.

DOI: <https://doi.org/10.18596/jotcsa.1349140>

***Corresponding author's E-mail:** vv_namam@yahoo.co.in

1. INTRODUCTION

The physicochemical properties like refractive index, densities, and dielectric constants of pure liquids and their mixtures are very important for accurate design and proper development in many industrial processes (1). Variation in these physical properties with temperature, composition, and frequency gives important information about molecular structure, intermolecular interactions, hydrogen bonding, molecular associations, charge transfer, dipole-dipole, and dipole-induced dipole interactions (2).

Formamide is an amide derived from formic acid, which is used as a solvent in various chemical processes. It is used in the agrochemical and pharmaceutical industries and as a solvent in the polymer and resin industry. N-propanol is a primary alcohol and a clear, colorless, transparent liquid soluble in water. It is used as a solvent in the manufacturing of the pharmaceutical industry and as a chemical intermediate. The knowledge of the physicochemical properties of the corresponding liquids and their mixtures plays an important role in analytical sciences and pharmaceutical processes like synthesis, design, extraction, purification, and the processes involved (3). Limited information is available on the physicochemical properties of n-propanol with formamide. Only some reports are

available on binary interaction studies of n-propanol and formamide with other polar liquids using different techniques and instruments. The dielectric study of formamide-butylene glycol at various temperatures was reported by Navarkhele et al. (4). Kabir et al. (5) reported densities and excess molar volumes of ethanol, methanol, and n-propanol with pure water at various temperatures. Static permittivity, refractive index, density, and related properties of pyridine with 1-propanol have been reported by Trivedi et al. (6).

In this study, authors reported refractive indices (n), densities (ρ) at 293.15 K, and static dielectric constants at 293.15, 298.15, and 303.15 K temperatures over the entire composition range. The related properties like excess dielectric constant (ϵ^E), effective Kirkwood correlation factor (g^{eff}), atomic polarization, electronic polarization, permittivity at a higher frequency, molar volume, molar refraction, polarizability, solvated radii, molar polarization, deviation in molar refraction and the excess properties like excess density (d^E), excess refractive index (n^E), excess molar polarization (P_m^E) and excess molar volume (V^E) were estimated from the experimental data using appropriate equations to confirm molecular interaction, hydrogen bonding, and other possible interactions between the components of mixtures.

2. EXPERIMENTAL SECTIONS

2.1. Chemicals

Chemicals formamide and n-propanol were obtained from a pharmaceutical company –Aurangabad – Maharashtra, with 99.9% purity and used without extra purification. The final compositions were prepared by adding formamide in n-propanol at eleven different stages. All mixtures were ready just before the experimental use.

2.2. Equipments

The refractive indices of the mixtures were measured using a digital pocket refractometer PAL-RI, made by Atago-Japan. The apparatus measures the refractive index in the range of 1.3306 to 1.5284. The refractive indices of pure liquids and their mixtures were measured only at 293.15 K temperature. The accuracy in the measurement of the refractive index given by the manufacturer is ± 0.0003 at 20 °C.

A wet sensor was used to measure static dielectric constants made by Delta-T Devices Ltd. UK that is based on the frequency domain reflectometry technique. Five to six readings were recorded for the mixture, and the average value of that was taken as a dielectric constant. The working detail of the wet sensor was explained in our earlier publication (7). The uncertainty in the dielectric constant given by the manufacturer is about $\pm 3\%$. The temperature controller arrangement with a water bath was used to sustain a constant temperature within the correctness limit of ± 1 °C.

Anton Paar oscillation U-tube densitometer (model DMA- 35, Austria) was used to measure the densities of the mixtures. The densitometer is calibrated with double-distilled water and air. The densities of pure liquids and their mixtures were measured only at 293.15 K temperature. The uncertainty in density given by the firm is ± 0.001 g·cm⁻³ at 20 °C.

2.3. Excess Dielectric Constants (ϵ^E)

The formation of a new structure in the binary mixtures can be confirmed from the knowledge of excess dielectric constants (ϵ^E). The excess dielectric constant is calculated using the equation (8):

$$\epsilon^E = (\epsilon_{sm}) - [\epsilon_1 \cdot \Phi_1 + \epsilon_2 \cdot \Phi_2] \quad (1)$$

Where (ϵ_{sm} is the static dielectric constants of mixtures, $\epsilon_1, \epsilon_2, \Phi_1$ and Φ_2 are the static dielectric constants and mole fractions of liquid 1 (n-propanol) and liquids 2 (formamide) respectively.

2.4. Kirkwood Factor (g)

The orientation of the electric dipoles in polar mixtures can be confirmed by the nature of Kirkwood correlation factor (9) values. The modified Kirkwood correlation factor, that is, effective Kirkwood correlation factor (g^{eff}) given by (10,11), is estimated by the equation:

$$\frac{4 \Pi N \left(\frac{\mu_1^2 \cdot \rho_1 \cdot \Phi_1}{M_1} + \frac{\mu_2^2 \cdot \rho_2 \cdot \Phi_2}{M_2} \right) g^{eff}}{9 K T} = \frac{(\epsilon_{sm} - \epsilon_{\infty m})(2 \epsilon_{sm} + \epsilon_{\infty m})}{\epsilon_{sm}(\epsilon_{\infty m} + 2)^2} \quad (2)$$

where “ g^{eff} ” is the effective Kirkwood correlation factor for the binary mixtures.

In above equation, N, K, T, $\mu_1^2, \mu_2^2, \rho_1, \rho_2, M_1, M_2, \Phi_1, \Phi_2, \epsilon_{sm}$ and $\epsilon_{\infty m}$ represent Avogadro's number, Boltzmann constant, temperature, the squared dipole moment of liquid 1-2, the density of liquid 1-2, the molecular weight of liquid 1-2, the mole fraction of liquid 1-2, static dielectric constant of the mixture and dielectric constant at a higher frequency, respectively.

2.5. Molar Refraction, Solvated Radii, Polarizability, Molecular Polarization, Atomic Polarization, Permittivity at Higher Frequency, and Deviation in Molar Refraction

From experimental refractive indices, densities, and dielectric constants data of pure liquids and mixtures, the authors have estimated molar refraction (R_m), atomic polarization (P_A), polarizability (α), solvated radii (r) and molecular polarization (P_m) by the following equations (12-16):

$$R_m = \left(\frac{n^2 - 1}{n^2 + 2} \right) V_m = P_A + P_E = P_T = P_D \quad (3)$$

$$P_A = 1.05 n^2 \quad (4)$$

$$\left(\frac{n^2 - 1}{n^2 + 2} \right) = \left(\frac{4}{3} \right) \Pi n' \alpha \quad (5)$$

$$V_m = \left(\frac{4}{3} \right) \Pi r^3 \quad (6)$$

$$P_m = V_m \left(\frac{\epsilon_s - 1}{\epsilon_s + 2} \right) \quad (7)$$

The right-hand side of equation (3) is equal to the summation of both atomic polarization (P_A) and electronic polarization (P_E), and that is equal to total polarization (P_T) or distortion polarization (P_D). In the

above equations “n” is the refractive index, $n' = \frac{N}{V_m}$,

N is Avogadro's number “ ϵ_s ” static dielectric constant and $V_m = (M/d)$ is molar volume; in this, ‘M’ is molecular weight and ‘d’ is the density of the liquids, respectively.

The permittivity at higher frequency ϵ_{∞} is the square of the refractive index, and the equation calculated it:

$$\epsilon_{\infty} = n^2 \quad (8)$$

2.6. Excess Refractive Index (n^E), Excess Density (d^E), Excess Molar Polarization (P_m^E), Excess Molar Volume (V^E) and Deviation in Molar Refraction

By using experimental values of refractive indices and densities, the excess refractive index (n^E) and

excess density were determined by the following equations:

$$n^E = n_{mix} - (\Phi_1 \cdot n_1 - \Phi_2 \cdot n_2) \quad (9)$$

$$d^E = d_{mix} - (\Phi_1 \cdot d_1 - \Phi_2 \cdot d_2) \quad (10)$$

where n_{mix} and d_{mix} are the values of refractive indices and densities of the mixtures and Φ_1 , Φ_2 , n_1 , n_2 , d_1 , and d_2 are the mole fractions, refractive indices, and densities of the first and second liquids, respectively.

From calculated molar polarization, the $(P_m)^E$ of the mixtures was determined by the equation:

$$P_m^E = P_{mix} - [P_{m1} \cdot \Phi_1 + P_{m2} \cdot \Phi_2] \quad (11)$$

In the above equation, P_{mix} and Φ_1 , Φ_2 , P_{m1} , P_{m2} , are the polarization of mixtures and mole fraction, molar polarization of liquid 1 and 2, respectively.

Excess molar volume $(V)^E$ was determined using the following equation (17):

$$V^E = V_{mix} - (\Phi_1 \cdot V_{m1} - \Phi_2 \cdot V_{m2}) \quad (12)$$

Where V_{mix} is the molar volume of the mixtures Φ_1 , Φ_2 represents mole fraction, V_{m1} and V_{m2} are the molar volume of the components 1 and 2, respectively.

From the knowledge of refractive indices and densities, the deviation in molar refraction was determined by the well-known equation (18):

$$Rm^E/\Delta_R = Rm_{mix} - (\Phi_1 \cdot Rm_1 - \Phi_2 \cdot Rm_2) \quad (13)$$

In the above equation (Rm_{mix}) is the molar refractivity of the mixtures Φ_1 , Φ_2 represents mole fraction and Rm_1 and Rm_2 are the molar refractivity of pure liquids 1 and 2, respectively.

3. RESULTS AND DISCUSSION

3.1. Static Dielectric Constant

Table 1 lists the experimental dielectric constants of the studied binary system. The dielectric constants of the mixtures decrease with an increase in temperature. The decrease in dielectric constants with an increase in temperature is due to orientation polarization. When the thermal motion of the mixture is increased, there is a fall in orientation polarization that reduces the alignment of the permanent dipoles; therefore, there is a decrease in dielectric constants (19). From the same Table, it is also noticed that the dielectric constant increases with an increase in mole fraction. This may be due to a decrease in the size and shape of the complex molecules after hydrogen bonding. This may increase the number of dipoles in the binary mixtures and increase the mobility as well as the volume of the rotating molecules. The experimental results are in agreement with the earlier results given by (20,21).

Table 1: Values of static dielectric constants for binary mixture of n-propanol + formamide at various molar fractions at different temperatures.

Mole fraction of formamide	Static dielectric constant T=293.15K	Static dielectric constant T=298.15K	Static dielectric constant T=303.15K
0.00	21.55	19.88	18.53
0.07	29.92	28.22	26.75
0.15	37.77	35.91	34.58
0.23	45.60	43.56	42.15
0.32	54.01	51.58	50.32
0.41	63.68	60.94	59.12
0.51	74.02	71.15	69.24
0.62	84.18	81.28	79.30
0.73	93.80	90.78	88.76
0.86	103.37	100.17	98.19
1.00	112.79	109.52	107.35

Figure 1 illustrates the variation in static dielectric constants against mole fraction. From Figure 1, it is observed that the variation in ϵ' with mole fraction is non-linear. In polar mixtures, if the molecular association is happening, a non-linear variation in the dielectric constants with concentration is expected, and the same is noticed in the Figure. This shows that an intermolecular association is occurring in the studied binary system (22,23).

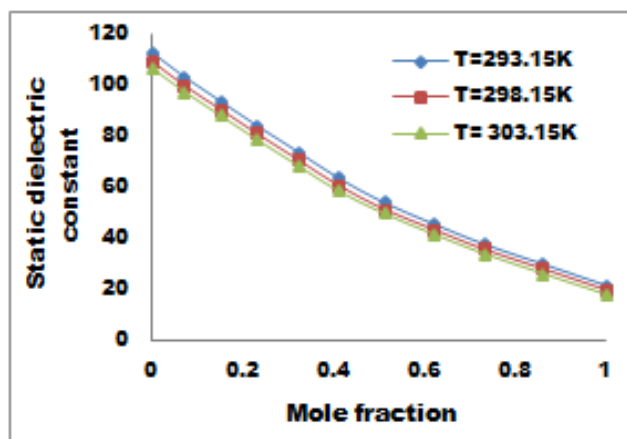


Figure 1: Variation in static dielectric constants (ϵ_s) against mole fraction at different temperatures.

Table 2 gives experimental densities and refractive indices of the binary system at 293.15 K. The density values of the mixtures increase with an increase in the mole fraction of formamide. When the concentration of formamide increases, that may create intermolecular bonds, and new bonds may form between similar and dissimilar molecules that may decrease the volume of the mixtures, increasing density. Similar results have been recorded by Farid (12).

Table 2: Values of densities and refractive indices for a binary mixture of n-propanol + formamide at various mole fractions at 293.15 K temperature.

Mole fraction of formamide	Density ($\text{g}\cdot\text{cm}^{-3}$)	Refractive index
0.00	0.8032	1.3874
0.07	0.8362	1.3933
0.15	0.8690	1.3994
0.23	0.9021	1.4056
0.32	0.9350	1.4119
0.41	0.9680	1.4181
0.51	1.0011	1.4244
0.62	1.0341	1.4307
0.73	1.0671	1.4367
0.86	1.1001	1.4431
1.00	1.1333	1.4495

From Table 2, it is also noticed that refractive indices of the studied binary system increase with increasing mole fraction of formamide over the entire composition range.

3.2. Excess Dielectric Constant (ϵ^E)

The estimated (ϵ^E) values are presented in Figure 2. From Figure 2, it is observed that the excess dielectric constants are positive over the entire mole fraction range for the studied temperatures. This confirms that in the mixtures, the two liquids relate together in such a way that the effective dipole moment increases. In addition, the number of dipoles in the mixture may be more than the corresponding average number in the pure liquids, which may be due to the formation of a new structure leading to a higher macroscopic permittivity. Similar results are reported by Hosmani et al. and Navarkhele et al. (24,25).

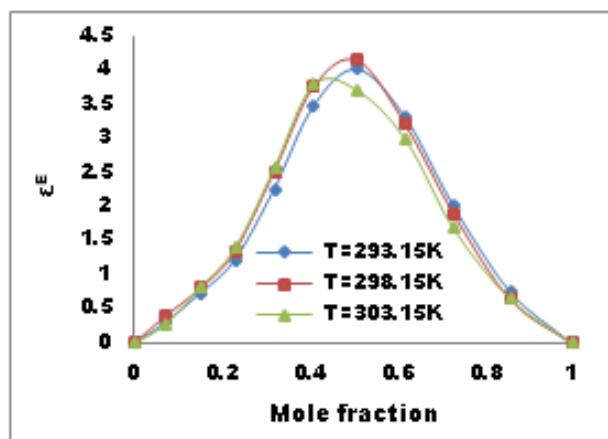


Figure 2: Variation in excess dielectric constant against mole fraction at different temperatures.

3.3. Kirkwood Factor (g)

The orientation of electric dipoles in polar mixtures may be confirmed by Kirkwood factor (g). If the values of (g^{eff}) are greater than 1 ($g^{\text{eff}} > 1$), it shows parallel orientation, and if (g^{eff}) is less than 1 ($g^{\text{eff}} < 1$), it shows anti-parallel orientation of electrical dipoles. The effective Kirkwood correlation factor (g^{eff}) of the binary system was calculated using equation 2 and graphically illustrated in Figure 3. Figure 3 noted that the g^{eff} values are greater than 1 ($g^{\text{eff}} > 1$) over the entire mole fraction range. This is a sign of the parallel orientation of electric dipoles in n-propanol molecules. From Figure 3, it is also observed that the variation in g^{eff} with mole fraction is non-linear at the studied temperatures, confirming the net increase in dipole ordering due to H-bond complexation. The results are in agreement with the earlier results of Trivedi et al. and Hosamani et al. (6,24).

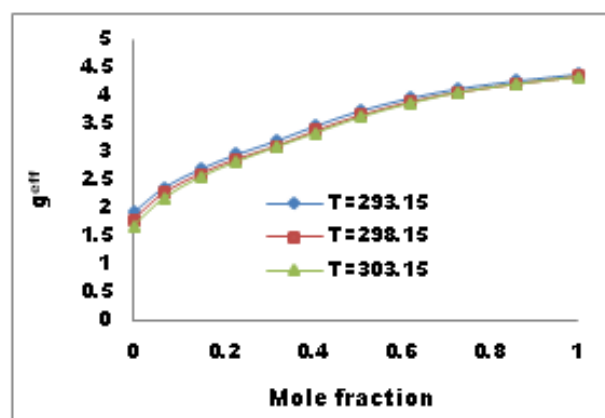


Figure 3: Variation in effective Kirkwood correlation factors against mole fraction at different temperatures.

3.4. Molar Volume (V_m), Molar Refractions (R_m), Polarizability (α), Solvated Radii (r), Molar Polarization (P_m), Atomic Polarization (P_A), Electronic Polarization (P_E) and

Permittivity at Higher Frequency (ϵ_∞)

The estimated values of the molar volume (V_m), molar refractions (R_m), polarizability (α), solvated radii (r), molar polarization (P_m), atomic polarization (P_A), electronic polarization (P_E), and permittivity at

higher frequency (ϵ_∞) of the studied binary mixtures are illustrated in Table 3. From Table 3, it is noticed that all the above parameters are decreasing over the entire mole fraction range

except (ϵ_∞) and (P_A). Since permittivity at higher frequency and atomic polarization depends on the refractive indices of the mixtures. Since the refractive index of the studied binary system

increases, these parameters also increase with the mole fraction of formamide.

Table 3: Values of molar volume (V_m), molar refraction (R_m), polarizability (α), solvated radii (r), molar polarization (P_m), atomic polarization (P_A), electronic polarization (P_E), and permittivity at higher frequency (ϵ_∞) for a binary mixture of n-propanol + formamide at various mole fractions at 293.15 K temperature.

Mole fraction of formamide	V_m (cm ³ /mol)	R_m (cm ³ /mol)	α (10 ²⁴) cm ³ /mole	(r) Å ⁰	(P_m) cm ³ /mole	(P_A)	(P_E)	ϵ_∞
0.00	77.292	18.204	7.22	2.65	67.444	2.02	19.19	1.93
0.07	72.222	17.248	6.83	2.58	65.432	2.03	15.21	1.94
0.15	67.525	16.348	6.48	2.52	62.432	2.05	14.29	1.95
0.23	63.158	15.500	6.14	2.47	59.177	2.07	13.42	1.97
0.32	59.112	14.705	5.83	2.41	55.946	2.09	12.61	1.99
0.41	55.335	13.947	5.53	2.36	52.808	2.11	11.83	2.01
0.51	51.803	13.229	5.24	2.31	49.758	2.13	11.09	2.02
0.62	45.501	12.546	4.97	2.26	46.812	2.14	10.39	2.04
0.73	45.407	11.889	4.71	2.21	43.985	2.16	9.72	2.06
0.86	42.491	11.264	4.46	2.16	41.281	2.18	9.07	2.08
1.00	39.744	10.667	4.24	2.12	38.708	2.21	8.47	2.11

3.5. Excess Density (d^E), Excess Refractive Index (n^E), Excess Molar Polarization (P_m^E), Excess Molar Volume (V^E), and Deviation in Molar Refraction (Δ_R)

Table 4 gives estimated excess density (d^E), excess refractive index (n^E), excess molar polarization (P_m^E),

excess molar volume (V^E), and deviation in molar refraction with mole fraction of formamide. As Table 4 shows, the (d^E) values of the binary mixtures are negative over the entire composition range at the studied temperature. This may be due to a decrease in the molar volume of the binary mixtures.

Table 4: Values of excess density, excess refractive index, excess molar polarization, excess molar volume, and deviation in molar refractivity for binary mixture of n-propanol + formamide at various mole fractions at 293.15 K temperature.

Mole fraction of formamide	Excess density (D) ^E	Excess Refractive index (n) ^E	Excess molar polarization (P_m) ^E	Excess molar volume (V^E)	Δ_R cm ³ .mol ⁻¹
0.00	0.00000	0.00000	0.000	0.00	0.00
0.07	-0.00018	-0.00013	0.86	-1.25	-0.19
0.15	-0.00028	-0.00024	0.73	-2.12	-0.33
0.23	-0.00017	-0.00027	0.35	-2.69	-0.41
0.32	-0.00026	-0.00018	-0.0026	-2.96	-0.45
0.41	-0.00025	-0.00020	-0.26	-2.99	-0.46
0.51	-0.00014	-0.00012	-0.44	-2.77	-0.42
0.62	-0.00013	-0.00004	-0.51	-2.35	-0.35
0.73	-0.00023	-0.00026	-0.46	-1.74	-0.27
0.86	-0.00012	-0.00019	-0.29	-0.95	-0.15
1.00	0.00000	0.00000	0.000	0.00	0.00

From Table 4, it is also observed that the excess refractive indices values of the binary mixtures are negative over the entire composition range. The (n^E) give a signal of maximum solvent-solvent interaction that depends mainly on different physical properties of the solvents, such as dipole moment, dielectric constant, donor number, chemical structure, basicity, and polarizability (12).

The estimated values of (P_m^E) of the binary mixture are given in Table 4. From the values, it is observed that the excess molar polarization is positive in the n-propanol-rich region and negative in the formamide-rich region at the studied temperature.

The (V^E) of the binary mixtures is given in Table 4 and graphically illustrated in Figure 4. From Figure 4, it is noticed that the excess molar volume values are negative over the entire mole fraction range at

the studied temperature. The negative values of excess molar volumes may be due to the volume contraction after mixing. Knowledge of (V^E) values can confirm the non-ideal behavior of real mixtures. Negative values of excess molar volumes show strong intermolecular interaction, hydrogen bonding, charge transfer complexes, and other complex-forming interactions, including strong dipole-dipole interactions between the components of molecules in the mixture (26).

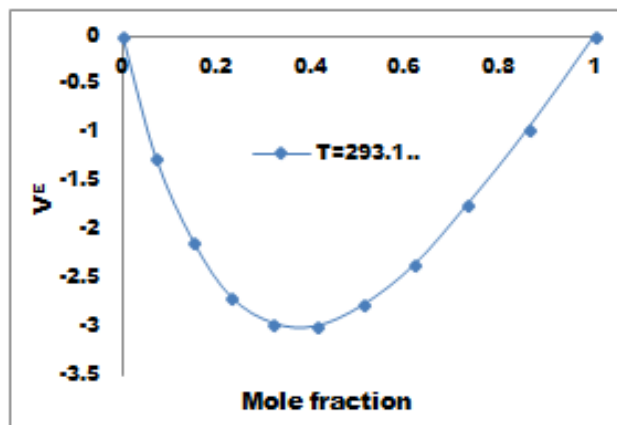


Figure 4: Variation in excess molar volume against molar fraction at 293.15 K temperature.

The deviation in molar refraction (Δ_R) is given in Table 4 and graphically illustrated in Figure 5. The (Δ_R) values are negative over the entire mole fraction range for the studied temperature. From Figure 5, it is seen that the variation in (Δ_R) with mole fraction exhibits a parabolic shape with a minimum value located between 0.3 and 0.4 mole fraction. The negative deviation in molar refraction signifies electronic perturbation due to the orbital mixing of the components of the mixtures. The negative (Δ_R) can be used as a measure of the strength of the interaction between the elements of the mixtures and is strongly dependent on composition and temperature (27,28). Negative values of (Δ_R) also point out greater dispersive forces in the mixtures than in pure components (29).

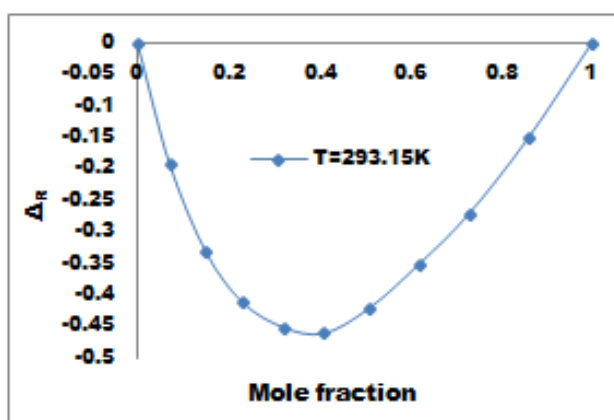


Figure 5: Variation in deviation in molar refraction against mole fraction at 293.15 K temperature.

4. CONCLUSION

This study provides fundamental physicochemical properties and their related and excess properties of a binary system. Variation in these properties with mole fraction is explained in terms of molecular interactions, hydrogen bonding, and other possible interactions. It was found that the dielectric constants decrease with an increase in temperature and increase with the increase in the mole fraction of the solute. The densities and refractive indices of the binary mixtures increase with an increase in the mole fraction of solute at the studied temperature. For the studied temperatures, the dielectric data shows an excellent non-linear behavior supporting an intermolecular association and hydrogen bonding in the binary system.

The excess dielectric constants of the binary mixture are found to be positive and show a more polar structure, leading to higher macroscopic permittivity. The non-linear variation in (g^{eff}) values confirms the presence of molecular interactions, hydrogen bonding, and other possible interactions in the binary mixtures.

The estimated parameters of molar volume, molar refraction, polarizability, solvated radii, molar polarization, and electronic polarization of the binary system decrease, whereas permittivity at a higher frequency and atomic polarization increase with an increase in mole fraction.

The excess densities (d^E), excess refractive indices (n^E), excess molar volumes (V^E), and deviation in molar refraction of the binary mixtures are found to be negative over the entire composition range and at the studied temperature. The negative excess molar volumes (V^E) confirm volume contraction after mixing of the binary mixtures. The values of (Δ_R) are negative and show greater dispersive forces in the mixtures than in pure components from a molecular interaction perspective; we suggest that the contributors to (V^E) are most likely from the hydrogen bonding formation interactions, charge transfer complexes and other complex-forming interactions in the binary system.

5. ACKNOWLEDGMENTS

The authors are thankful to the Head of the Department of Physics, Dr. Babasaheb Ambedkar Marathwada University-Aurangabad (M.S.) India for providing the experimental facility for the said work.

6. AUTHOR CONTRIBUTIONS

The manuscript was written with contributions from all listed authors. All authors have approved of the manuscript.

7. FUNDING

There is no funding from any agency for this work.

8. CONFLICT OF INTEREST

The authors declare no competing financial interest.

9. REFERENCES

1. Long B, Wang Z, Yang H, Ding Y. Intermolecular interactions of 1,2-diethoxyethane with toluene: An insight from surface and volumetric properties at different temperatures. *J Mol Liq* [Internet]. 2018 Jan 1;249:1-8. Available from: [<URL>](#).
2. Yilmaz H, Güler S. Excess properties of methanol-water binary system at various temperatures. *Nuovo Cim D* [Internet]. 1998 Dec;20(12):1853-61. Available from: [<URL>](#).
3. Jouyban A, Soltanpour S, Chan HK. A simple relationship between dielectric constant of mixed solvents with solvent composition and temperature. *Int J Pharm* [Internet]. 2004 Jan 28;269(2):353-60. Available from: [<URL>](#).
4. Navarkhele VV, Bhanarkar MK. High-frequency dielectric response of the binary mixture formamide-butylene glycol. *Phys Chem Liq* [Internet]. 2010 Feb 11;48(1):89-98. Available from: [<URL>](#).
5. Kabir MH, Motin MA, Huque ME. Densities and excess molar volumes of Methanol, Ethanol and N-Propanol in pure Water and in Water + Surf Excel solutions at different temperatures. *Phys Chem Liq* [Internet]. 2004 Jun 16;42(3):279-90. Available from: [<URL>](#).
6. Trivedi CM, Rana VA. Static permittivity, refractive index, density and related properties of binary mixtures of pyridine and 1-propanol at different temperatures. *Indian J Pure Appl Phys* [Internet]. 2014;52:183-91. Available from: [<URL>](#).
7. Navarkhele V V. Dielectric and Excess Properties of Glycols with Formamide Binary Mixtures at Different Temperatures. *Russ J Phys Chem A* [Internet]. 2018 Jul 8;92(7):1417-22. Available from: [<URL>](#).
8. Sengwa RJ, Sankhla S, Shinyashiki N. Dielectric Parameters and Hydrogen Bond Interaction Study of Binary Alcohol Mixtures. *J Solution Chem* [Internet]. 2008 Feb 14;37(2):137-53. Available from: [<URL>](#).
9. Kirkwood JG. The dielectric polarization of polar liquids. *J Chem Phys* [Internet]. 1939 Oct 1;7(10):911-9. Available from: [<URL>](#).
10. Kumbharkhane AC, Puranik SM, Mehrotra SC. Dielectric relaxation of tert-butyl alcohol-water mixtures using a time-domain technique. *J Chem Soc, Faraday Trans* [Internet]. 1991 Jan 1;87(10):1569-73. Available from: [<URL>](#).
11. Kumbharkhane AC, Puranik SM, Mehrotra SC. Dielectric relaxation studies of aqueous N,N-dimethylformamide using a picosecond time domain technique. *J Solution Chem* [Internet]. 1993 Mar;22(3):219-29. Available from: [<URL>](#).
12. El-Dossoki FI. Refractive index and density measurements for selected binary protic-protic, aprotic-protic, and aprotic-protic systems at temperatures from 298.15 K to 308.15 K. *J Chinese Chem Soc* [Internet]. 2007 Oct 25;54(5):1129-37. Available from: [<URL>](#).
13. Mognaschi ER, Laboranti LM. Association of pure polar liquids: dielectric properties of docosanoic acid. *J Chem Soc Faraday Trans* [Internet]. 1996 Jan 1;92(18):3367-9. Available from: [<URL>](#).
14. Ray SK, Rath J, Dwivedi C. Excess Molar Polarization in Binary Mixtures of Polar Liquids. *Phys Chem Liq* [Internet]. 2001 Mar;39(2):227-37. Available from: [<URL>](#).
15. Kim JI. A Critical Study of the Ph 4 AsPh 4 B Assumption for single ion thermodynamics in amphiprotic and dipolar-protic solvents; evaluation of physical parameters relevant to theoretical consideration. *Zeitschrift für Phys Chemie* [Internet]. 1978 Feb 1;113(2):129-50. Available from: [<URL>](#).
16. Oswal S. Studies on density, viscosity, dielectric constant, and refractive index of binary mixtures of esters in benzene and carbon tetrachloride. *Can J Chem* [Internet]. 1988 Jan 1;66(1):111-6. Available from: [<URL>](#).
17. González EJ, Requejo PF, Maia FM, Domínguez Á, Macedo EA. Solubility, density and excess molar volume of binary mixtures of aromatic compounds and common ionic liquids at T= 283.15 K and atmospheric pressure. *Phys Chem Liq* [Internet]. 2015 Jul 4;53(4):419-28. Available from: [<URL>](#).
18. Aliaj F, Syla N, Kurtishaj A, Elezaj N, Tolaj Z, Arbnesi T, et al. Densities, refractive indices, and derived properties of binary mixtures of ethanol with benzene and pyridine at various temperatures under atmospheric pressure. *Int J Thermophys* [Internet]. 2020 Apr 3;41(4):49. Available from: [<URL>](#).
19. Pottel R. N. E. Hill, W. E. Vaughan, A. H. Price und M. Davies: Dielectric properties and molecular behaviour D. Van Nostrand. In: *Berichte der Bunsengesellschaft für physikalische Chemie* [Internet]. John Wiley & Sons, Ltd; 1970. p. 176-7. Available from: [<URL>](#).
20. Navarkhele VV, Bhanarkar MK. Microwave dielectric response of binary mixture of N,N-dimethylformamide with propylene glycol using TDR method. *Mol Phys* [Internet]. 2009 Sep 10;107(17):1823-30. Available from: [<URL>](#).
21. Kumbharkhane AC, Puranik SM, Mehrotra SC. Structural study of amide-water mixtures using dielectric relaxation technique. *J Mol Liq* [Internet]. 1992 Mar 1;51(3-4):261-77. Available from: [<URL>](#).
22. Navarkhele V, Navarkhele A. Static Dielectric Constants, Densities, Refractive Indices and Related Properties of Binary Mixtures at Various Temperatures Under Atmospheric Pressure. *Int J Thermodyn* [Internet]. 2022 Sep 1;25(3):1-10. Available from: [<URL>](#).
23. Lone BG, Undre PB, Patil SS, Khirade PW, Mehrotra SC. Dielectric study of methanol-ethanol mixtures using TDR method. *J Mol Liq* [Internet]. 2008 May 30;141(1-2):47-53. Available from: [<URL>](#).
24. Hosamani MT, Fattepur RH, Deshpande DK, Mehrotra SC. Temperature- and frequency-dependent dielectric studies of p-fluorophenylacetone-methanol mixtures using time-domain reflectometry. *J Chem Soc, Faraday Trans* [Internet]. 1995 Jan 1;91(4):623-6. Available from: [<URL>](#).
25. Navarkhele VV, Bhanarkar MK. Dielectric relaxation study of formamide-propylene glycol using time domain reflectometry. *Phys Chem Liq* [Internet]. 2011 Jul;49(4):550-9. Available from: [<URL>](#).
26. Navarkhele A V., Sakhare RS, Vijayendraswamy SM, Navarkhele V V. Dielectric constant, density, and refractive index in binary mixtures of ethanol with N,N-Dimethylformamide at 293.15 K. *Russ J Phys Chem A* [Internet]. 2022 May 25;96(5):945-53. Available from: [<URL>](#).
27. Noh HJ, Park SJ, In SJ. Excess molar volumes and deviations of refractive indices at 298.15K for binary and ternary mixtures with pyridine or aniline or quinoline. *J Ind Eng Chem* [Internet]. 2010 Mar 25;16(2):200-6. Available from: [<URL>](#).
28. Singh S, Parveen S, Shukla D, Gupta M, Shukla JP. Volumetric, optical, acoustical and viscometric study of molecular association in binary mixtures of butylamine

with 1-butanol and tert-butanol. Acta Phys Pol A [Internet]. 2007;111(6):847-58. Available from: [<URL>](#).

29. Aniya V, Kumari A, Reddy R, Satyavathi B. Measurement and modeling of phase equilibrium,

volumetric properties and molar refractivity of 2-methylpropan-2-ol + ethane-1,2-diol. J Solution Chem [Internet]. 2017 Jun 6;46(6):1177-201. Available from: [<URL>](#).



Investigation of Rapid Chemical Recycling of Waste Polyethylene Terephthalate Under Microwave Effect Using Calcined Dolomite as Catalyst

Mehmet Ali Boz¹ , Vedat Arda Küçük¹ , Muhammed Bora Akın^{1*} 

¹Çankırı Karatekin University, Department of Chemical Engineering, Çankırı, 18100, Türkiye.

Abstract: According to the United Nations, our planet produces an average of 430 million tons of plastic annually. A significant portion of the environmental pollution caused by the use of plastics is due to polyethylene terephthalate (PET) used in short-lived packaging products. Various studies have been conducted with the aim of recycling or converting PET waste into useful products. In addressing the dual environmental challenges posed by waste PET and dolomite, this study innovates in the realm of sustainable recycling practices. We explore the efficiency of a solid catalyst derived from waste dolomite in catalyzing the hydrolysis of waste PET. This research not only showcases the catalytic prowess of waste-derived dolomite in breaking down PET into its constituent monomers but also highlights the process's optimization for maximum efficiency. Through careful analysis and optimization of various parameters, including Temperature, reaction time, and catalyst concentration, we achieve an unprecedented conversion rate, illustrating the potential of this method in contributing to the circular economy. Our findings offer a groundbreaking approach to PET waste management, emphasizing the importance of sustainability and innovation in tackling environmental pollution. Dolomite is a widely available ore with a composition of $\text{CaCO}_3 \cdot \text{MgCO}_3$. After calcination, the obtained $\text{CaO} \cdot \text{MgO}$ mixture can be used to recycle PET via hydrolysis. In this study, Temperature (140 °C, 150 °C, 160 °C), ethanol concentration (0%, 5%, 10%), potassium hydroxide concentration (0%, 5%, and 10%), and the amount of calcined dolomite (0 g/100 mL, 0.03 g/100 mL, and 0.06 g/100 mL) parameters were selected for the PET hydrolysis process conducted in a short time using a microwave digestion system. The Taguchi L_9 experimental design was applied, and all experiments were repeated four times.

Keywords: Hydrolysis, PET, Waste, Catalyst, Dolomite.

Submitted: April 1, 2024. **Accepted:** May 18, 2024.

Cite this: Boz MA, Küçük VA, Akın MB. Investigation of Rapid Chemical Recycling of Waste Polyethylene Terephthalate Under Microwave Effect Using Calcined Dolomite as Catalyst. JOTCSA. 2024;11(3): 1025-36.

DOI: <https://doi.org/10.18596/jotcsa.1462797>

***Corresponding author's E-mail:** mboraakin@gmail.com

1. INTRODUCTION

In the process of natural stone production, the cutting operations carried out in both quarries and manufacturing plants result in significant amounts of waste material, which can represent between 50% and 60% of the total stone processed (1). The variability in waste generation is influenced by several factors, including the stone's inherent mineralogical properties, the presence and pattern of discontinuities and cracks, and the specific methodologies employed in the production and processing stages. The waste produced within these settings is predominantly categorized based on its

size: into coarse or large fragments and fine particulates (2).

The coarse or large waste fragments, which make up about 40% of the quarry's output, vary significantly in size (from a few centimeters to several meters) and can adopt a variety of shapes. This diversity in size and shape underscores the complexity of managing such waste efficiently (3). On the other hand, the fine waste generated, particularly from the processing of natural stones in factories, is mainly comprised of powder-like substances with particle sizes falling below 150 micrometers. This fine waste is mechanically

collected and transported to disposal sites, often necessitating the use of loaders for loading onto trucks, followed by transport to designated dumping areas (4).

The management and disposal of natural stone waste pose logistical and environmental challenges. Unused agricultural lands, often located at considerable distances from natural stone operations and deposits, are frequently repurposed as sites for waste disposal. This practice, however, raises concerns regarding the optimal and sustainable use of land resources. Agricultural lands, even if currently unutilized, should ideally be preserved for agricultural purposes or land conservation efforts rather than being transformed into waste disposal sites. Moreover, the practice of utilizing operational sites as disposal areas can significantly hinder operational efficiency by reducing maneuverability within these spaces. Additionally, opting for waste disposal in alternative locations introduces extra logistical burdens, primarily due to the transportation costs involved.

Environmental concerns associated with natural stone waste are multifaceted, encompassing issues such as landscape alteration, soil displacement, deterioration of water quality in both surface and underground sources, and contributions to air and visual pollution. These impacts underscore the urgency of adopting more sustainable waste management practices within the natural stone industry (5).

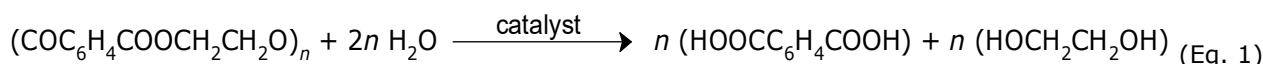
Recognizing the substantial environmental footprint and economic implications of such waste, there's a growing emphasis on repurposing natural stone waste into valuable secondary products (6). This waste is increasingly being utilized in various applications, including but not limited to the creation of building materials, the construction of roads (7,8), the production of concrete (9), as abrasives (10), the erection of flood prevention barriers (11), for soil neutralization purposes (12), and in the manufacturing of cement (9), and composites (13). Moreover, its use in filtration processes and the feed industry represents innovative approaches to waste valorization, contributing to a more circular economy where

waste is transformed into resources, thus alleviating environmental impacts while simultaneously enhancing production sustainability in the natural stone sector (14).

The escalating production and disposal of PET pose a dual challenge of environmental pollution and resource wastage, with millions of tons of PET waste accumulating in landfills and natural habitats each year. This situation is exacerbated by the durable nature of PET, which resists biodegradation, leading to prolonged environmental persistence (15). Given these concerns, there is an urgent need for more effective recycling methods that not only mitigate environmental harm but also reclaim the value embedded in waste PET.

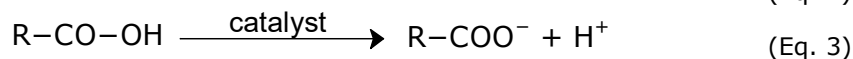
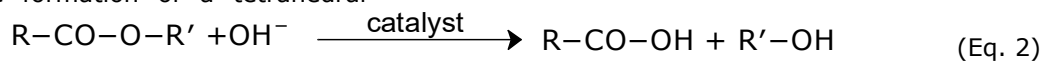
Chemical recycling, particularly hydrolysis, presents a viable alternative to mechanical recycling, offering the potential to break down PET into its constituent monomers, which can be reused to produce new PET or other valuable products. This process not only diverts PET from landfills but also reduces the reliance on virgin materials, aligning with the principles of a circular economy. However, conventional hydrolysis processes often rely on expensive and environmentally harmful catalysts, which can limit their sustainability and economic viability (16).

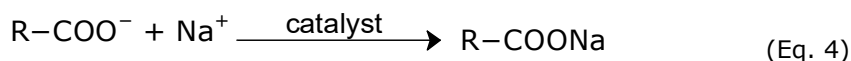
PET hydrolysis is a chemical process in which the PET polymer interacts with water molecules to break down into its fundamental monomers. This process occurs at high temperatures and pressure under acid, base, or neutral catalysis (17). In acidic hydrolysis, the ester bonds in PET react with a strong acid, such as sulfuric acid (H_2SO_4), to release terephthalic acid ($HOOC_6H_4COOH$ - TPA) and ethylene glycol ($HOCH_2CH_2OH$ - EG) monomers. In basic hydrolysis, the use of a base like sodium hydroxide (NaOH) causes the breakdown of PET into sodium salts and EG. The TPA derivatives and EG obtained from these reactions are essential components that can be reused in new PET production or other chemical processes. PET hydrolysis is a crucial step in the recycling of polymer waste (18). The equation for the general hydrolysis reaction is given in Equation (1).



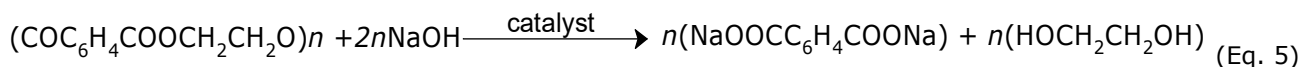
Equations 2-4 show the mechanism of how PET breaks down into TPA and EG via basic hydrolysis in the presence of NaOH. The OH^- ion from NaOH acts as a nucleophile and attacks the carbonyl carbon in the ester group of the PET polymer chain. This attack results in the formation of a tetrahedral

intermediate. The tetrahedral intermediate breaks down, resulting in the cleavage of the ester bond. This forms EG and a carboxylate ion ($R-COO^-$). The carboxylate ion ($R-COO^-$) reacts with Na^+ from the NaOH solution to form sodium terephthalate (19).





In the overall reaction, the PET polymer chain is fully broken down into sodium TPA and EG:



In response to these challenges, this study explores the use of waste dolomite as a novel, eco-friendly catalyst for the hydrolysis of waste PET. Dolomite, a sedimentary carbonate rock, is abundant in nature and often regarded as a waste byproduct in various industrial processes (20). In PET recycling, the use of CaCO_3 and MgCO_3 , the chemicals that make up dolomite, is commonly considered a filler to enhance the mechanical properties of plastics, reduce processing time, and decrease costs (21). Additionally, these substances can improve the thermal stability and heat resistance of PET, thereby expanding the application areas of recycled PET (22). By repurposing this readily available material, the study not only seeks to enhance the environmental and economic efficiency of PET hydrolysis but also to promote the valorization of waste materials as resources for sustainable development.

The hydrolysis of PET is a well-studied process with applications in recycling and waste management. Both acid and base can catalyze the hydrolysis of PET, resulting in the production of TPA and EG (23). Research has demonstrated that incorporating metal hydroxides like sodium or potassium hydroxide through melt mixing can enhance the hydrolysis of PET (24). Studies have also explored the kinetics of PET hydrolysis using acids such as nitric acid and sulfuric acid, emphasizing the significance of temperature and catalysts in the process (25).

Various factors, including the presence of cellulose and polypropylene, can influence the efficiency of PET hydrolysis (26). Enzymatic hydrolysis of PET, utilizing enzymes like cutinase, has been investigated for waste stream management (27). Additionally, the use of ionic liquids as solvents and catalysts has shown promise in improving the conversion and yield of TPA during PET hydrolysis (28).

The depolymerization of PET through hydrolysis has been studied under different temperatures and conditions to optimize the process for industrial applications (29). Research has also delved into hydrolyzing PET below its melting range to understand the impact of factors like diffusion and crystallinity on reaction kinetics (30). Alkaline hydrolysis and neutral hydrolysis have been explored as methods to break down PET into its monomers, such as TPA and EG (31,32).

In conclusion, the hydrolysis of PET is a multifaceted process influenced by parameters like temperature, catalysts, and reaction conditions.

Understanding these mechanisms and factors is crucial for the development of effective recycling and waste management strategies.

The research methodology in this study involves a comprehensive experimental design to evaluate the catalytic performance of calcined dolomite in the hydrolysis of PET, examining factors such as temperature, catalyst loading, and reaction time. The study also employs statistical analysis to optimize the hydrolysis conditions, aiming to maximize the yield of TPA, a key monomer derived from PET. Through this rigorous analysis, the study endeavors to establish a scalable and sustainable model for chemical recycling, contributing valuable insights to the fields of waste management and green chemistry.

By addressing the environmental impact of PET waste and demonstrating the feasibility of using waste dolomite as an effective catalyst, this research not only advances the scientific understanding of chemical recycling but also highlights the broader potential for integrating waste valorization into environmental sustainability strategies. Ultimately, this study underscores the importance of innovative approaches to waste management, encouraging further exploration of waste-to-resource technologies that can contribute to the transition toward a more sustainable and circular economy.

2. MATERIALS AND METHODS

2.1. Materials

The used KOH ($\geq 85\%$ KOH basis, pellets, white) was obtained from Sigma-Aldrich, and ethanol (absolute) from Isolab. The conductivity value of the used pure water was at most $10 \mu\text{S}$, produced using a Merck Millipore Essential pure water device. The dolomite used in the experiment was procured from Doltaş Mining Co. located in İzmir. Crushed, ground, and sieved dolomite has been calcined by burning in a furnace at $1000 \text{ }^\circ\text{C}$ for 5 hours to be used as a catalyst. Waste PET was obtained by collecting PET used in daily life. After being washed with pure water, the waste PET was dried, then crushed, divided into pieces, and sieved. Pieces in the range of 2-3 mm were used in the experiments. Hydrolysis experiments were conducted using a Microwave Digestion System, speedwave XPERT.

2.2. Methods

In the study, temperature ($140 \text{ }^\circ\text{C}$, $150 \text{ }^\circ\text{C}$, $160 \text{ }^\circ\text{C}$), ethanol (0 mL, 5 mL, 10 mL), KOH (0 g, 5 g, 10 g), and catalyst (0 g, 5 g, 10 g) were selected as parameters (Table 1).

During the experiment, solutions prepared were taken and placed into PET, and a catalyst was added. The reactor, sealed to prevent leakage, was placed in a microwave heating setup and heated to

the temperature specified in the experiment design. Once the desired temperature was reached, it was maintained for 15 minutes and then allowed to cool down.

Table 1: Factors and levels used in the Taguchi L₉ design experiments.

Factors	Level 1	Level 2	Level 3
Temperature (°C)	140	150	160
Ethanol (mL/100 mL)	0	5	10
KOH (g/100 mL)	0	5	10
Catalyst (g/100 mL)	0	0.03	0.06

The Taguchi L₉ experimental design method was employed in the experiments, serving as a strategic framework for the systematic analysis of multiple variables simultaneously. This approach is particularly beneficial in reducing the complexity and resource requirements of experimental studies, as it allows for the efficient identification of the most influential factors and their optimal settings. In the context of this study, the Taguchi L₉ design was meticulously chosen to investigate the impact of four distinct factors, each varied across three different levels, thereby ensuring a comprehensive exploration of the experimental space with a limited number of runs. Specifically, the design encompassed 4 factors, which were temperature, ethanol concentration, KOH quantity, and the

amount of catalyst, all considered critical to the process under study. Each of these factors was tested at three levels to ascertain their individual and combined effects on the experimental outcomes. To enhance the reliability and validity of the results, every experimental condition specified within the Taguchi L₉ design was replicated at least four times. This rigorous repetition serves to mitigate the potential influence of experimental errors and variability, providing a robust dataset for analysis. The structure and specific assignments of these factors and levels within the Taguchi L₉ experimental design are detailed in Table 2, offering a clear roadmap for the execution and analysis of the experiments.

Table 2: Taguchi L₉ experimental design of hydrolysis reaction with waste PET.

Run	Temperature (°C)	Ethanol (mL/100 mL)	KOH (g/100 mL)	Catalyst (g/100 mL)
1	140	0	0	0
2	140	5	5	0.03
3	140	10	10	0.06
4	150	0	5	0.06
5	150	5	10	0
6	150	10	0	0.03
7	160	0	10	0.03
8	160	5	0	0.06
9	160	10	5	0

3. RESULTS AND DISCUSSION

As a result of the experiment, the amounts of PET that did not react were measured, and the conversion rates were calculated using the formula

given in Equation 6. The calculation results based on the data from the experiments are summarized in Table 3. Since four repetitions were performed, the obtained conversion percentages are reported in four separate columns as: R1, R2, R3, and R4

$$\text{Conversion \%} = \frac{\text{Initial PET amount} - \text{Remaining PET amount}}{\text{Initial PET amount}} \times 100 \quad (\text{Eq. 6})$$

Table 3: The conversion percentages obtained from the experiments.

Exp. Number	Temperature (°C)	Ethanol (mL/100 mL)	KOH (g/100 mL)	Cat. (mg/L)	R1 (X%)	R2 (X%)	R3 (X%)	R4 (X%)
1	140	0	0	0	3.75	4.28	4.02	4.06
2	140	5	5	0.03	15.55	16.01	15.91	15.41

3	140	10	10	0.06	61.55	57.44	59.31	60.43
4	150	0	5	0.06	21.46	20.67	19.75	21.85
5	150	5	10	0	62.16	62.59	67.31	61.70
6	150	10	0	0.03	3.62	3.97	4.50	5.31
7	160	0	10	0.03	66.94	66.41	69.27	68.13
8	160	5	0	0.06	3.43	4.95	4.74	4.40
9	160	10	5	0	32.33	36.00	36.21	34.51

The signal-to-noise (S/N) ratios were calculated from the obtained conversion rates using the "larger is better" approach and are provided in Table 4.

Table 4 presents the average effect of each parameter's variation on the signal-to-noise (S/N) ratio. The data reveals insightful trends about the factors influencing process efficiency and outcome quality. Temperature demonstrates a steady increase in the S/N ratio from 23.84 at Level 1 to 26.65 at Level 3, signifying that elevated

temperatures positively affect the outcome, with a moderate difference of 2.82 indicating its impact. Similarly, Ethanol shows an increase in S/N ratio from 25.03 to 26.27, marking a subtle yet positive influence of increased ethanol concentration, albeit with a smaller difference of 2.10. Notably, KOH stands out for its significant impact, with the S/N ratio soaring from 12.38 to 36.05 between the extreme levels, underscoring a robust effect of KOH concentration on the process, evidenced by a substantial difference of 23.67.

Table 4: Response table for signal to noise ratios*.

Level	Average S/N Ratios			
	Temperature	Ethanol	KOH	Catalyst
1	23.84	25.03	12.38	26.30
2	24.98	24.17	27.04	24.35
3	26.65	26.27	36.05	24.82
Difference	2.82	2.10	23.67	1.95
Ranking	2	4	1	3

*Larger is better.

In contrast, Catalyst's influence is more moderate, with S/N ratios ranging from 26.30 to 24.82 and a difference of 1.95, indicating a beneficial yet comparatively lesser impact than temperature and much less than KOH. The ranking of factors by their influence on the S/N ratio places KOH at the pinnacle, followed by temperature, catalyst, and ethanol, in descending order of impact. This meticulous analysis aids in pinpointing the critical

factors that markedly influence the desired outcome. Concentrating on the highest-ranked factors enables process optimization to attain superior performance. Employing a statistical methodology furnishes a structured evaluation, offering definitive guidance for ameliorating process efficiency or enhancing the quality of outcomes. For a clearer understanding of Table 4, the data are graphically represented in Figure 1.

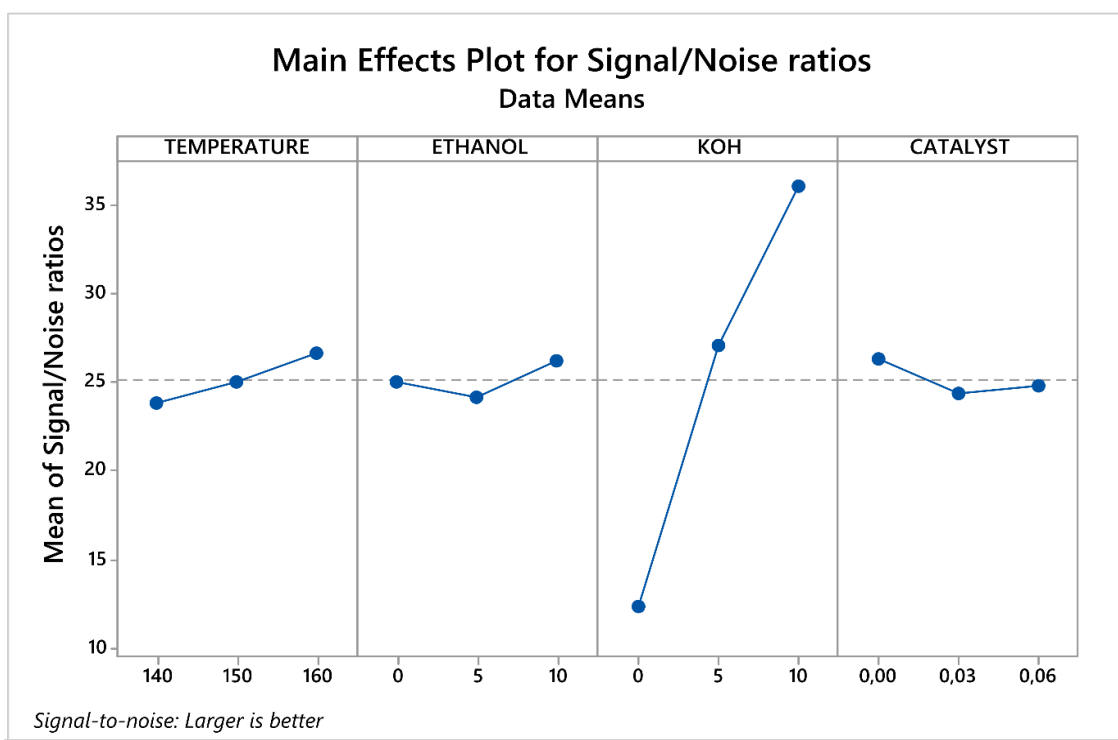


Figure 1: Main effects plot for S/N ratios.

Due to the difficulty in interpreting S/N ratios, parameter level can be calculated using the S/N average conversion rates corresponding to each ratios (Table 5).

Table 5: Response Table for Means*.

Level	Average Conversion Percentages (%)			
	Temperature	Ethanol	KOH	Catalyst
1	26.477	30.883	4.253	34.077
2	29.574	27.847	23.805	29.252
3	35.610	32.932	63.603	28.332
Difference	9.133	5.085	59.351	5.745
Ranking	2	4	1	3

*Larger is better.

The analysis for Table 5 reveals how each parameter distinctly influences the conversion rate, illustrating the complexity of the process and the importance of precise control over conditions. Temperature demonstrates a clear trend of increasing conversion percentages with rising levels, illustrating a substantial effect on the process's efficiency. The leap from 26.477% at the lowest level to over 35% at the highest signifies the critical role temperature plays, positioning it as a pivotal factor for optimizing outcomes.

The efficiency of the PET hydrolysis process is indeed significantly influenced by temperature. Several studies have demonstrated the impact of temperature on the hydrolysis of PET. In one study, the temperature had a significant impact on the hydrolysis of PET. The degradation follows an Arrhenius equation, which relates the degradation

rate to temperature and relative humidity. Hydrolysis of PET is accelerated at higher temperatures, leading to increased chain scission and crystallinity changes. The model presented in the paper suggests that the combination of temperature and RH directly affects the rate of PET degradation (33).

Similarly, in a review by Geyer and others (2016), while discussing chemical methods for PET recycling, the dependence of these processes on temperature is emphasized. According to this study, researchers working with different methods reported that increasing temperatures improved the efficiency of PET hydrolysis. Only in enzymatic reactions was it shown that deviations from the optimal temperature range reduced the efficiency of the hydrolysis reaction (34). Moreover, a study by Conroy and Zhang (2024) (35) confirms the

continued interest in PET hydrolysis, emphasizing that the effect of temperature on PET hydrolysis is a critical factor for efficient polymer breakdown. According to the study, increasing temperatures significantly improve reaction kinetics, lower activation energies, and lead to rapid PET decomposition. As a result, Temperature stands out as one of the most important factors for effective hydrolysis in PET recycling (35).

KOH, on the other hand, showcases an even more pronounced impact, with its conversion percentage soaring at the highest level, emphasizing its paramount importance in the reaction mechanism. This dramatic increase points to KOH's efficacy in facilitating the conversion process, highlighting it as a primary lever for enhancing performance.

KOH has been recognized for its effectiveness in facilitating the PET hydrolysis conversion process. Studies have shown that KOH plays a crucial role in enhancing the hydrolysis of PET waste. Karayannidis et al. (2002) investigated the recycling of PET through alkaline hydrolysis and highlighted the use of KOH in the process, demonstrating its efficacy in promoting the conversion of PET into valuable products like TPA (36).

Moreover, Adibfar et al. (2014) (37) found that KOH-activated PET showed superior adsorption properties for molecules of varying sizes, indicating the effectiveness of KOH in modifying PET for enhanced performance (37). Additionally, Yoshioka et al. (2003) (38) conducted a study on the conversion of PET into oxalic acid and TPA using alkaline solutions, showcasing the role of KOH in the

hydrolysis process (38). Furthermore, Rubio Arias et al. (2022) (39) developed a KOH-in-methanol hydrolysis process for the selective depolymerization of PET and polycarbonate, emphasizing the efficiency of KOH in achieving instantaneous PET hydrolysis (39). These findings collectively underscore the significance of KOH in promoting the hydrolysis and conversion of PET waste into valuable products, highlighting its role as an effective catalyst in the PET recycling industry.

Ethanol and Catalyst, while contributing to variations in conversion rates, exhibit a more nuanced influence compared to the stark effects of Temperature and KOH. Ethanol's moderate variation suggests its role is significant but secondary in optimizing the process. The effect of ethanol on PET hydrolysis is already known in the literature (24). The Catalyst's impact, being the least pronounced, indicates its supportive but less critical role in the conversion process.

Overall, this analysis not only ranks the parameters by their influence on conversion rates but also underscores the importance of a balanced approach in managing these variables to achieve optimal results. Adjustments in KOH concentration and temperature management emerge as key strategies for improving conversion efficiencies, with considerations for Ethanol and Catalyst providing additional fine-tuning capabilities. This statistical insight forms a foundation for targeted optimizations, guiding efforts towards achieving the most efficient and effective conversion process. To facilitate a better understanding of this table, the data are presented graphically in Figure 2.

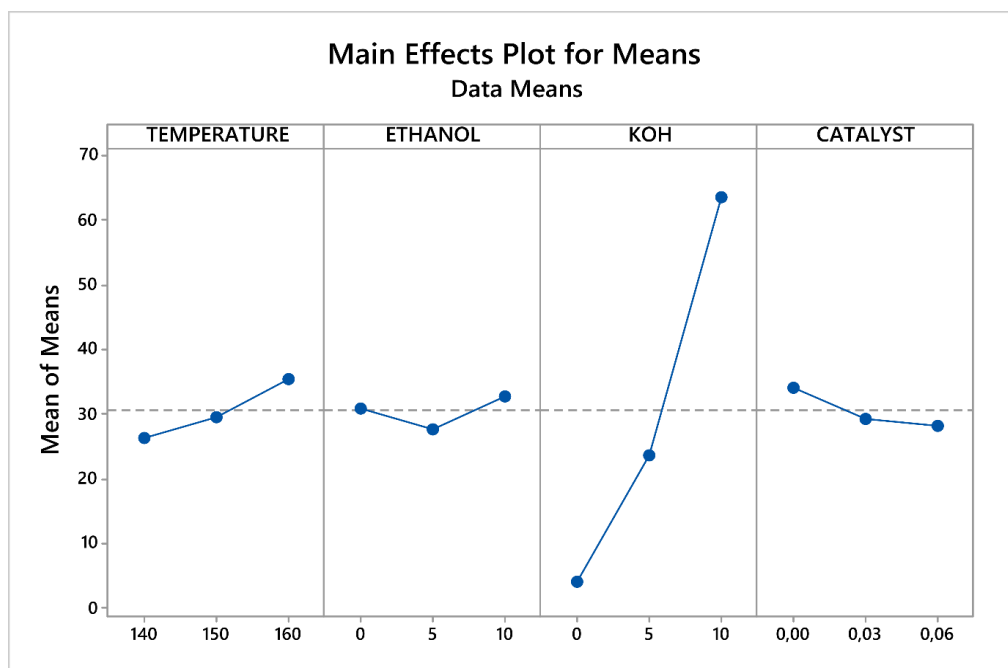


Figure 2: Main effects plot for Means.

In Figure 2, the average conversion percentages corresponding to the actual levels of the parameters can be observed.

A hypothesis test and analysis of variance (ANOVA) were conducted to understand whether the parameters used in the experiment had a significant effect on the response (Table 6). In hypothesis testing, the null hypothesis assumes that all means are equal, meaning the factors do not significantly affect the response. The null hypothesis is accepted if the p-value calculated at a 95% confidence interval is greater than 0.05, and it is rejected if the p-value is less than 0.05 (the H_1 hypothesis cannot be dismissed).

$H_0: \mu_1 = \mu_2 = \mu_3 \dots = \mu_k$

H_1 : The means are not equal

Table 6, detailed here, offers a profound insight into the statistical underpinnings of an experiment aimed at deciphering the effects of various factors (Temperature, Ethanol, KOH, and Catalyst) on a specified outcome. This statistical examination, coupled with an overarching regression model, endeavors to unravel the intricacies of data variability, providing a systematic approach to quantify the influence of each factor.

Table 6: Analysis of Variance (ANOVA) results.

	Degrees of Freedom	Adjusted Sum of Squares	Adjusted Mean Squares	F-value	P-value
Regression	4	21858.9	5454.7	161.42	0.000
Temperature	1	500.5	500.5	14.78	0.001
Ethanol	1	25.2	25.2	0.74	0.395
KOH	1	21135.1	21135.1	624.31	0.000
Catalyst	1	198.0	198.0	5.85	0.022
Error	31	1049.5	33.9		
Residual	4	999.4	249.9	134.84	0.000
Pure Error	27	50	1.9		
Total	35	22908.3			

The Degrees of Freedom (DF) serves as a foundational metric, delineating the scope within which the data can fluctuate. With the regression model boasting 4 degrees of freedom, mirroring the quartet of examined factors, and the error manifesting 31 degrees, this delineation underscores the residual variance unaccounted for by the model, thus spotlighting areas of further investigation or model refinement.

The Adjusted Sum of Squares, a critical statistical measure, quantifies the total variance attributable to each factor, meticulously adjusted for their respective degrees of freedom. KOH's notably high value in this metric signifies its predominant role in dictating the data's variance, suggesting its paramount importance in the experimental outcome.

Further dissecting this variance, the Adjusted Mean Squares metric offers an average variance per factor, with KOH again emerging as the pivotal influence, showcasing its substantial impact on the experimental results. This is further corroborated by the F-value, a statistical test for assessing the null hypothesis' viability—that a factor bears no impact. KOH's exceptional F-value not only refutes this

hypothesis but also heralds its critical role in the dependent variable's variation.

The P-value metric, reflecting the likelihood of observing the data under the null hypothesis, fortifies the statistical argument with its threshold significance. Both the overall regression and the exceptionally low p-values for KOH solidify their undeniable effects on the outcome, while the higher p-value for Ethanol suggests a statistically insignificant effect.

This statistical narrative is further enriched by the analysis of "Error" and "Total" variance, with "Residual" and "Pure Error" finely parsing the unexplained variance into components of model fit and randomness, respectively. This granularity aids in identifying the fidelity of the model to the observed data and the inherent variability unexplained by the examined factors.

In essence, this ANOVA table meticulously maps out the impacts of various factors on an experimental outcome, highlighting KOH, Temperature, and Catalyst as the primary influencers, while Ethanol lags behind in significance. This detailed statistical analysis illuminates the pathways through which each factor interplays within the experimental

framework, guiding strategic decisions for resource allocation and adjustments aimed at optimizing outcomes, thereby advancing our comprehension of the underlying data dynamics.

To elucidate the relationship between experimental parameters and the response, regression analysis has been conducted using experimental data. The calculated regression coefficients are provided in Table 7.

Table 7: Calculated regression coefficients.

Term	Coefficient	Standard Error of Coefficient	T-value	P-value
Constant	-65.8	18.0	-3.66	0.001
Temperature	0.457	0.119	3.85	0.001
Ethanol	0.205	0.238	0.86	0.395
KOH	5.935	0.238	24.99	0.000
Catalyst	-95.7	39.6	-2.42	0.022

This regression analysis table meticulously delineates the intricate dynamics between several experimental variables—Temperature, Ethanol, KOH, and Catalyst—and their impact on a specified response, providing a comprehensive quantitative assessment of their roles. Through the precise calculation of regression coefficients, alongside their standard errors, and the statistical rigor of T-values and P-values, the analysis offers a profound understanding of each parameter's statistical weight and its consequent influence on the experimental outcome.

The significant negative coefficient of the constant term underscores the intrinsic baseline of the response, asserting that, even in the absence of variable influences, the response deviates significantly from zero. This finding is pivotal, highlighting the inherent response characteristics before considering the effects of the experimental parameters.

Temperature emerges as a significant modifier of the response, with its positive coefficient revealing a direct proportional relationship. This parameter's statistical significance is validated by both its T-value and P-value, emphasizing its critical role in modulating the response, thereby suggesting a targeted avenue for experimental manipulation to achieve desired outcomes.

In contrast, the role of Ethanol is ambiguous; its coefficient, combined with a high standard error and a T-value that could be considered statistically insignificant, along with a statistically insignificant P-value, indicates that its effect on the response is negligible. This shows that changes in Ethanol concentration will not lead to meaningful changes in the response, thus directing experimental focus away from this parameter.

KOH stands out with its pronounced coefficient, signifying a robust positive correlation with the response. This parameter's overwhelming statistical

significance is incontrovertible, heralding it as a paramount factor in influencing the response. The substantial magnitude of KOH's effect underscores its potential as a primary lever in optimizing experimental outcomes.

The catalyst's coefficient, despite suggesting a possible negative relationship with the response, is enveloped in uncertainty due to its significant standard error and significant P-value. This ambiguity renders the catalyst a less reliable factor for influencing the response, indicating a lower priority in experimental adjustments.

In essence, this rigorous statistical analysis systematically uncovers the differential impact of each experimental parameter on the response, with Temperature and KOH identified as pivotal influencers—offering clear pathways for experimental optimization. Meanwhile, Ethanol and Catalyst, owing to their less pronounced effects, delineate areas where experimental resources might be more judiciously allocated. This nuanced understanding facilitates a strategic approach to experimental design, aiming for enhanced efficiency and targeted outcomes. The regression equation derived from Table 7 is provided in Equation 7:

$$\text{Conversion\%} = -65.8 + 0.457 \cdot \text{Temperature} + 0.205 \cdot \text{Ethanol} + 5.935 \cdot \text{KOH} - 95.7 \cdot \text{Catalyst} \quad (7)$$

The calculated R^2 (regression coefficient) indicates that the regression equation can explain more than 90% of the variance in the data.

4. CONCLUSION

The efficient management and repurposing of industrial waste stand as pivotal challenges. This study addresses these challenges head-on by transforming Dolomite waste, a byproduct of its high production volumes, into a commercially viable and applicable product. Through a rigorous examination and demonstration of the calcination

process, we've unlocked the potential of waste Dolomite, converting it into a valuable CaO-MgO mixture. This mixture, characterized by its calcination, has found application as a catalyst in subsequent processes, showcasing the innovative repurposing of waste materials.

One of the standout achievements of this research is the depolymerization of waste PET utilizing the catalysts derived from Dolomite waste calcination. This process not only exemplifies a sustainable approach to waste management but also results in the production of TPA, a fundamental raw material in PET manufacturing. Such an outcome not only contributes to the circular economy but also adds value to what would otherwise be considered waste.

Furthermore, the study leverages a systematic experimental design to delve into the hydrolysis of waste PET, meticulously analyzing the influence of individual parameters on the process. This systematic approach enables a deeper understanding of the chemical interactions at play and identifies optimal conditions for maximizing efficiency and output. By integrating waste management with the production of valuable chemical precursors, this research embodies the principles of green chemistry and sustainability, paving the way for innovative solutions in chemical engineering.

In conclusion, the comprehensive analysis presented through the regression model and ANOVA table provides an insightful understanding of the effects of various experimental parameters (Temperature, Ethanol, KOH, and Catalyst) on the conversion process. The derived regression equation, $Conversion\% = -65.8 + 0.457 \cdot Temperature + 0.205 \cdot Ethanol + 5.935 \cdot KOH - 95.7 \cdot Catalyst$, with an R^2 value of 94.83, underscores the model's robust ability to explain a significant portion of the variance observed in the conversion rates.

The statistical significance of each parameter, as delineated by the regression analysis, highlights the varying degrees of influence they exert on the conversion outcome. Temperature and KOH emerge as the most impactful factors, with KOH showing a particularly strong positive relationship with conversion, indicating its critical role in the chemical process. On the other hand, Ethanol's influence is minimal, and its parameter's high P-value suggests that changes in ethanol concentration may not substantially affect the conversion rate within the scope of this experimental setup. The Catalyst, despite a suggested negative relationship with the conversion rate, is enveloped in uncertainty due to its considerable standard error and significant P-value, indicating a less deterministic influence on the process.

The significant negative coefficient of the constant term in the regression equation indicates a

meaningful baseline from which the effects of the variables are measured, suggesting that even in the absence of these experimental parameters, the response level is notably different from zero.

Overall, the regression and ANOVA analyses together offer a nuanced view of how each parameter contributes to the conversion process, guiding future experimental designs and optimizations. With KOH identified as the most significant contributor to conversion efficiency, followed by temperature, strategic adjustments in these parameters can be leveraged to optimize conversion outcomes. Meanwhile, the lesser impact of Ethanol and the ambiguous role of the Catalyst provide valuable insights into areas where experimental efforts and resources might be more judiciously applied or conserved.

In the future, the feasibility of conducting studies on the use of catalysts derived from waste materials in the hydrolysis of PET by evaluating the wastes of other ores is observed.

5. CONFLICT OF INTEREST

The authors declare that they have no conflict of interest with anyone in this study.

6. ACKNOWLEDGEMENTS

The authors would like to thank the Department of Chemical Engineering, Çankırı Karatekin University, for the use of laboratories and equipment in their studies.

7. REFERENCES

1. Mashaly AO, El-Kaliouby BA, Shalaby BN, El-Gohary AM, Rashwan MA. Effects of marble sludge incorporation on the properties of cement composites and concrete paving blocks. *J Clean Prod* [Internet]. 2016 Jan;112:731-41. Available from: [<URL>](#).
2. Singh M, Saini B, Chalak HD. Influence of stone processing waste on mechanical, durability, and ecological performance of hybrid fiber-reinforced engineered cementitious composite. *Transp Res Rec J Transp Res Board* [Internet]. 2023 May 9;2677(5):260-78. Available from: [<URL>](#).
3. Khan K, Ahmad W, Amin MN, Ahmad A, Nazar S, Alabdullah AA, et al. Exploring the use of waste marble powder in concrete and predicting its strength with different advanced algorithms. *Materials* (Basel) [Internet]. 2022 Jun 9;15(12):4108. Available from: [<URL>](#).
4. Richetti F, Grings KJO, Ribeiro FRC, de Lima CJF, Kulakowski MP. Production of granilite concrete plates with recycled aggregates and ornamental rock processing sludge. *Matéria* (Rio Janeiro) [Internet]. 2022;27(3). Available from: [<URL>](#).

5. Al-Zboon K, Masoud T. Recycling of stone cutting waste in the construction sector: A review. *J Solid Waste Technol Manag* [Internet]. 2021 Feb 1;47(1):56–60. Available from: [<URL>](#).
6. Turuallo G, Mallisa H, Rupang N. Sustainable development: Using stone dust to replace a part of sand in concrete mixture. Woods R, Yoshida M, Miyajima M, Alauddin K, Arifin S, Fadjari A, et al., editors. *MATEC Web Conf* [Internet]. 2020 Dec 9;331:05001. Available from: [<URL>](#).
7. Benjeddou O, Mashaan N. Experimental study of the usability of recycling marble waste as aggregate for road construction. *Sustainability* [Internet]. 2022 Mar 9;14(6):3195. Available from: [<URL>](#).
8. Ural N, Kahveci AN. Use of marble waste as a road base material in different size ranges. *Balt J Road Bridg Eng* [Internet]. 2023 Mar 30;18(1):18–46. Available from: [<URL>](#).
9. Aliabdo AA, Abd Elmoaty AEM, Auda EM. Re-use of waste marble dust in the production of cement and concrete. *Constr Build Mater* [Internet]. 2014 Jan;50:28–41. Available from: [<URL>](#).
10. Elaissi A, Alibi H, Ghith A. Effect of pumice stone and perlite abrasives characteristics on denim abrasion. *J Compos Mater* [Internet]. 2022 Jun 22;56(13):2107–16. Available from: [<URL>](#).
11. Pilecka E, Morman J. Utilization of fine-grained mining waste strengthened cement for the modernization of flood embankments. *Bull Miner Energy Econ Res Inst Polish Acad Sci* [Internet]. 2017;101:347–60. Available from: [<URL>](#).
12. Abdelkader HAM, Hussein MMA, Ye H. Influence of waste marble dust on the improvement of expansive clay soils. Colangelo F, editor. *Adv Civ Eng* [Internet]. 2021 Sep 21;2021:1–13. Available from: [<URL>](#).
13. Bakshi P, Pappu A, Patidar R, Gupta MK, Thakur VK. Transforming marble waste into high-performance, water-resistant, and thermally insulative hybrid polymer composites for environmental sustainability. *Polymers (Basel)* [Internet]. 2020 Aug 9;12(8):1781. Available from: [<URL>](#).
14. Valentini L, Mascarini L, Ez-zaki H, Bediako M, Marangu JM, Bellotto M. Use of waste calcium carbonate in sustainable cement. In 2021. p. 11–9. Available from: [<URL>](#).
15. Bonfim DPF, Cruz FGS, Bretas RES, Guerra VG, Aguiar ML. A sustainable recycling alternative: Electrospun PET-membranes for air nanofiltration. *Polymers (Basel)* [Internet]. 2021 Apr 5;13(7):1166. Available from: [<URL>](#).
16. Bartolome L, Imran M, Gyoo B, A. W, Hyun D. Recent developments in the chemical recycling of PET. In: *Material Recycling - Trends and Perspectives* [Internet]. InTech; 2012. Available from: [<URL>](#).
17. Stanica-Ezeanu D, Matei D. Natural depolymerization of waste poly(ethylene terephthalate) by neutral hydrolysis in marine water. *Sci Rep* [Internet]. 2021 Feb 24;11(1):4431. Available from: [<URL>](#).
18. Zhang L. Kinetics of hydrolysis of poly(ethylene terephthalate) wastes catalyzed by dual functional phase transfer catalyst: A mechanism of chain-end scission. *Eur Polym J* [Internet]. 2014 Nov;50:1–5. Available from: [<URL>](#).
19. Ghasemi MH, Neekzad N, Ajdari FB, Kowsari E, Ramakrishna S. Mechanistic aspects of poly(ethylene terephthalate) recycling-toward enabling high quality sustainability decisions in waste management. *Environ Sci Pollut Res* [Internet]. 2021 Aug 19;28(32):43074–101. Available from: [<URL>](#).
20. Pina CM, Pimentel C, Crespo Á. The dolomite problem: A matter of time. *ACS Earth Sp Chem* [Internet]. 2022 Jun 16;6(6):1468–71. Available from: [<URL>](#).
21. Yan X, Qian X, Lu R, Miyakoshi T. Synergistic effect of addition of fillers on properties of interior waterborne UV-curing wood coatings. *Coatings* [Internet]. 2017 Dec 23;8(1):9. Available from: [<URL>](#).
22. Gao W, Ding L, Zhu Y. Effect of surface modification on the dispersion, thermal stability and crystallization properties of PET/CaCO₃ nanocomposites. *Tenside Surfactants Deterg* [Internet]. 2017 May 15;54(3):230–7. Available from: [<URL>](#).
23. Rosmaninho MG, Jardim E, Moura FCC, Ferreira GL, Thom V, Yoshida MI, et al. Surface hydrolysis of postconsumer polyethylene terephthalate to produce adsorbents for cationic contaminants. *J Appl Polym Sci* [Internet]. 2006 Dec 15;102(6):5284–91. Available from: [<URL>](#).
24. Li Y, Chen J, Han W, Yi H, Wang J, Xing P, et al. Toward Making Poly(ethylene terephthalate) Degradable in Aqueous Environment. *Macromol Mater Eng* [Internet]. 2022 Apr 2;307(4):2100832. Available from: [<URL>](#).
25. Yoshioka T, Okayama N, Okuwaki A. Kinetics of hydrolysis of PET powder in nitric acid by a modified shrinking-core model. *Ind Eng Chem Res* [Internet]. 1998 Feb 1;37(2):336–40. Available from: [<URL>](#).
26. Mahadevan Subramanya S, Mu Y, Savage PE. Effect of cellulose and polypropylene on hydrolysis of polyethylene terephthalate for chemical recycling. *ACS Eng Au* [Internet]. 2022 Dec 21;2(6):507–14. Available from: [<URL>](#).
27. Kawai F, Kawabata T, Oda M. Current knowledge on enzymatic PET degradation and its possible application to waste stream management and other fields. *Appl Microbiol Biotechnol* [Internet]. 2019 Jun 8;103(11):4253–68. Available from: [<URL>](#).
28. Liu F, Cui X, Yu S, Li Z, Ge X. Hydrolysis reaction of poly(ethylene terephthalate) using ionic liquids as solvent and catalyst. *J Appl Polym Sci* [Internet]. 2009 Dec 15;114(6):3561–5. Available from: [<URL>](#).
29. Onwucha CN, Ehi-Eromosele CO, Ajayi SO, Schaefer M, Indris S, Ehrenberg H. Uncatalyzed neutral hydrolysis of waste PET bottles into pure terephthalic acid. *Ind Eng Chem Res* [Internet]. 2023 Apr 26;62(16):6378–85. Available from: [<URL>](#).
30. Goje AS, Thakur SA, Diware VR, Patil SA, Dalwale PS, Mishra S. Hydrolytic depolymerization of poly(ethylene terephthalate) waste at high temperature under autogenous pressure. *Polym Plast Technol Eng* [Internet]. 2004 Jan 10;43(4):1093–113. Available from: [<URL>](#).

31. Kao CY, Cheng WH, Wan BZ. Investigation of alkaline hydrolysis of polyethylene terephthalate by differential scanning calorimetry and thermogravimetric analysis. *J Appl Polym Sci* [Internet]. 1998 Dec 5;70(10):1939–45. Available from: [<URL>](#).
32. Pereira P, Savage PE, Pester CW. Neutral hydrolysis of post-consumer polyethylene terephthalate waste in different phases. *ACS Sustain Chem Eng* [Internet]. 2023 May 8;11(18):7203–9. Available from: [<URL>](#).
33. Dubelley F, Planes E, Bas C, Pons E, Yrieix B, Flandin L. Predictive durability of polyethylene terephthalate toward hydrolysis over large temperature and relative humidity ranges. *Polymer (Guildf)* [Internet]. 2018 Apr;142:285–92. Available from: [<URL>](#).
34. Geyer B, Lorenz G, Kandelbauer A. Recycling of poly(ethylene terephthalate) – A review focusing on chemical methods. *Express Polym Lett* [Internet]. 2016;10(7):559–86. Available from: [<URL>](#).
35. Conroy S, Zhang X. Theoretical insights into chemical recycling of polyethylene terephthalate (PET). *Polym Degrad Stab* [Internet]. 2024 May;223:110729. Available from: [<URL>](#).
36. Karayannidis GP, Chatziavgoustis AP, Achilias DS. Poly(ethylene terephthalate) recycling and recovery of pure terephthalic acid by alkaline hydrolysis. *Adv Polym Technol* [Internet]. 2002 Dec 2;21(4):250–9. Available from: [<URL>](#).
37. Adibfar M, Kaghazchi T, Asasian N, Soleimani M. Conversion of poly(ethylene terephthalate) waste into activated carbon: Chemical activation and characterization. *Chem Eng Technol* [Internet]. 2014 Jun 8;37(6):979–86. Available from: [<URL>](#).
38. Yoshioka T, Ota M, Okuwaki A. Conversion of a used poly(ethylene terephthalate) bottle into oxalic acid and terephthalic acid by oxygen oxidation in alkaline solutions at elevated temperatures. *Ind Eng Chem Res* [Internet]. 2003 Feb 1;42(4):675–9. Available from: [<URL>](#).
39. Rubio Arias JJ, Barnard E, Thielemans W. Ultrafast simultaneous and selective depolymerization of heterogeneous streams of polyethylene terephthalate and polycarbonate: Towards industrially feasible chemical recycling. *ChemSusChem* [Internet]. 2022 Aug 5;15(15):e202200625. Available from: [<URL>](#).



Optimizing Experimental Parameters for Rietveld Refinement of Powder X-ray Diffraction from Small Gold Nanocrystals

Hamidreza Hekmatjou¹, Hande Öztürk^{1*} 

¹Özyegin University, Department of Mechanical Engineering, İstanbul, 34794, Turkey.

Abstract: Lattice parameters, average crystal sizes and apparent microstrains obtained from Rietveld refinement of powder diffraction data from gold nanopowders of 5-30 nm size are systematically investigated. A computational workflow is introduced where atomistic models of gold nanocrystals are created, and corresponding analytical diffraction data are computed and refined. The effect of nanocrystal size, nanocrystal shape, step size of the diffraction data and refinement range on the refined parameters are separately discussed for developing an optimized Rietveld refinement strategy for accurate sample characterization. Results show that a step size no greater than 0.2° ensures stable refined lattice parameters, crystal sizes and microstrains for gold nanocrystals smaller than 30 nm. For larger nanocrystals, smaller step sizes are necessary. Accuracy of refined lattice parameters are dependent on the refinement range more strongly for smaller nanocrystals than larger ones. Depending on the shape of the nanocrystal, limited refinement range may result in over or underestimations of the lattice parameter, hence extended refinement ranges are suggested for highest accuracy. Refined crystal sizes are underestimated for ideal crystalline nanospheres while they are overestimated for ideal crystalline nanocubes. This behavior stems from the incompatible Scherrer shape constant assumed in the refinement software. Finally, microstrains refined from energy-minimized gold nanospheres are significantly overestimated for smaller nanocrystals than larger ones for limited refinement range. However, if the refinement range includes four to five high-intensity Bragg peaks, then the refined microstrains stabilize irrespective of the nanocrystal size.

Keywords: Rietveld refinement, powder X-ray diffraction, nanocrystals, crystallographic analysis.

Submitted: September 14, 2023. **Accepted:** May 3, 2024.

Cite this: Hekmatjou H, Öztürk H. Optimizing Experimental Parameters for Rietveld Refinement of Powder X-ray Diffraction from Small Gold Nanocrystals. JOTCSA. 2024;11(3): 1037-54.

DOI: <https://doi.org/10.18596/jotcsa.1358713>

***Corresponding author's E-mail:** hande.ozturk@ozyegin.edu.tr

1. INTRODUCTION

The relation between internal structure and material property is a key area in materials science since several properties are determined by the particular way atoms arrange themselves inside the material. Hence, developing reliable, robust and non-invasive methods to characterize internal structure of materials is critical to understand and engineer their properties. For crystalline materials, X-ray diffraction is a popular method with non-destructive, high throughput, non-invasive properties, capability to achieve structural information with sub-Ångström level resolution with a wide range of application modalities. The analytical theory behind X-ray diffraction is well established and successfully implemented in experimental analysis routines for regular crystalline materials with single crystalline or

powder forms. Rietveld refinement(1), one of the most used crystallographic solution algorithms named after its developer, is a powerful method that allows for solving for the crystallographic properties of a sample from its powder diffraction (neutron or X-ray) data. This is accomplished by following three steps: **1)** Building an initial unit cell model assumed to be representative of the atomic configuration in the sample, **2)** calculating its corresponding theoretical diffraction data, and **3)** refining the theoretical data by iteratively adjusting the unit cell parameters and recalculating until it fits to the measured diffraction data with a predetermined tolerance. Once completed successfully, this iterative optimization procedure results in the crystallographic solution of the sample which contains detailed description of the crystal structure, including atomic positions, thermal vibrations of the atoms around lattice positions, the

size of the crystalline domain, etc. This crystallographic solution is not unique however, because while the structural information sought for is 3D in real space, the data that is analyzed is 1D, forbidding a one-to-one mapping of number of unknowns to number of measurements. Hence, it is not uncommon that the optimization algorithm gets stuck at a local minimum in the solution space or does not converge to a solution at all. But currently there are improved mathematical algorithms and experimental procedures which help avoid these local minima to an extent, making novel Rietveld refinement software to be more robust compared to their initial versions. Nonetheless, one must be aware of the uniqueness problem of the obtained crystallographic solution and validate it with complementary measurements techniques. This is critical especially for crystallographic analysis of multi-phase material samples, unknown crystals and nanocrystalline powders.

Nanocrystals may seem like nanoscale versions of classical crystalline materials; however, they do not satisfy some of the critical assumptions behind the theory of diffraction, which is atomic periodicity over long ranges. This brings several complications into their diffraction analysis procedures. First, diffraction peaks of nanocrystalline powders are extremely broad compared to their bulk counterparts causing significant overlap between neighboring Bragg peaks. This causes peak finding and peak fitting algorithms to fail to correctly identify all peaks. Since the number of atomic planes in a nanocrystal diffracting at a particular Bragg angle is much less than that of a regular crystal, complete destructive interference between Bragg angles is impossible(2) leading to a significant amount of diffuse scattering between Bragg angles(3). This makes background removal during data analysis challenging. Finally, the intensities of Bragg peaks measured from nanocrystalline powders of small particles are relatively weak and may easily be lost under the background signal causing misidentification of the phase of the powder.

In addition to the numerical challenges of analyzing diffraction patterns of nanocrystalline powders, an accurate formulation to relate the diffraction intensity distribution to structural parameters of nanocrystals is also lacking. This is a problem for step 2 of the Rietveld refinement algorithm: The cif files of nanocrystals are particle size dependent and are not available in databases. Hence, the initial information about the atomic stacking of the analyzed nano-powder is accessed from the cif files of bulk counterparts which do not necessarily reflect the nano-characteristic features of the sample and cause incompatibility between the theoretical and the actual measured diffraction signal. This incompatibility leads to the resulting Rietveld refinement to be biased, leading to incorrect characterization of the studied sample. Our past work confirmed such inaccuracies in the refinement of small nanocrystalline powders: for example, we found that due to the extreme peak broadening phenomenon, the scattering probability of an

irradiated monodispersed particle ensemble was not correctly predicted by the classical Klug and Alexander formulation(4) suggesting that the multiplicity of reflection for small nanocrystals was different than their bulk counterparts. This caused the one-to-one relation between the particle and intensity statistics to break down for nanocrystals smaller than 30 nm or so(5). Similar conclusions were drawn by other researchers as well(6). We observed that even when the nanocrystal was modeled identical to a bulk crystal with nanometric dimensions, its analytical diffraction data resulted in inaccurate lattice parameters from Rietveld analysis(7). These inaccuracies decayed with increasing crystal size confirming that the small sizes of nanocrystals were to blame for the large deviations in peak intensity positions from analytically obtained Bragg angles.

These examples point to the great care to be exercised while interpreting diffraction analysis results of nanocrystalline powders performed by algorithms based on classical diffraction theory. Moreover, they motivate systematic investigations to evaluate the performance of Rietveld refinement on the diffraction data of nanocrystalline powders since powder diffraction is still the first method to confirm appropriate synthesis of such materials. Ultimately these efforts would lead to a set of best practices for performing diffraction experiments and analyzing measurements appropriately for reliable structural analysis of nanocrystalline powders with quantified errors. With this goal, here we investigated how the results of Rietveld refinement performed on powder diffraction data from gold nanocrystalline particles vary with the step size of collected diffraction data and refinement range selected in Rietveld analysis. To alleviate ambiguities such as noise and statistical uncertainties which may prevent us from drawing clear conclusions, we performed our investigation on computer simulated diffraction data. Ideal crystalline, spherical and cubic gold nanocrystals and energy-minimized spherical gold nanocrystals at 0 K were used as the diffracting samples since these models were structurally simple and served to isolate sources of sample-specific error and accurately quantify them in the Rietveld analysis. Particle size was limited from 5 to 30 nm because the 5 nm crystal size was small enough to enhance nano-specific features in the diffraction data and 30 nm size was large enough to observe bulk-size features in the diffraction data. Finally, using these models, three crystallographic parameters namely, lattice parameters, average crystal sizes and average microstrains obtained from Rietveld refinement were systematically analyzed.

2. FUNDAMENTAL FORMULATION OF RIETVELD REFINEMENT

The theoretical basis of Rietveld refinement lies in the calculation of expected diffraction pattern from an investigated sample based on combining **a)** sample related parameters such as the assumed crystal structure model with **b)** instrumental parameters of the experimental setup used to

measure diffraction data such as the wavelength of X-rays, the profile of the incoming beam, polarization of the X-rays, etc. Then this theoretical pattern is refined against measured diffraction data until a predetermined extent of agreement is achieved.

The assumed crystal structure is built from the cif (crystallographic information file) file of the sample which contains average crystallographic information about the unit cell such as its dimensions and shape, the relative positions (u,v,w) and types of atoms in the cell, their thermal vibration parameters etc. To associate the diffracting sample with its expected diffracted intensity distribution, one must start from this unit cell. Hence, the expected scattering amplitude from a single unit cell oriented at a given hkl Bragg condition is formulated as the total scattering amplitude of its constituent atoms and called the structure factor F_{hkl} . For a monatomic unit cell consisting of a single atom type, F_{hkl} is given as(8):

$$F_{hkl} = \sum_{j=1}^{N_c} f_j \exp(2\pi i [hu_j + kv_j + lw_j]) \quad (\text{Eq.1})$$

Here N_c is the number of atoms in the unit cell, f is the atomic scattering amplitude for a single atom that depends on the energy of X-rays and the scattering direction, and $[u_j, v_j, w_j]$ is the fractional coordinate of atom j with respect to the unit cell dimensions along x , y and z axes. The diffraction intensity, which is the measurable quantity, is proportional to the squared magnitude of F_{hkl} . To obtain the full diffraction pattern, we multiply the intensity formula of the unit cell with terms taking care of diffraction probability of an irradiated crystal as well as instrumental parameters. The effect of instrumental parameters on the expected diffraction profile is formulated by convolving the sample profile by the instrument profile. Hence, an empirical form of Bragg intensity distribution can be written as¹:

$$I_{hkl}(2\theta) \propto I_0 |F_{hkl}|^2 m_{hkl} T(2\theta) LP(2\theta) A(2\theta) \quad (\text{Eq.2})$$

In Eq.2, I_0 is the incoming X-ray intensity which corresponds to a normalized form of the incoming photon count on the sample, m_{hkl} is the multiplicity of the hkl reflection which is the number of equivalent planes with the same interplanar distance characteristic of the unit cell, $T(2\theta)$ is the temperature factor also known as the Debye-Waller factor that models the temperature-dependent decay in the diffraction intensity resulting from dynamic motion of atoms inside the crystal, $A(2\theta)$ is the absorption factor modeling the decay in the diffraction intensity as a result of incoming photon absorption within the crystal as the X-rays travel inside and finally $LP(2\theta)$ is the Lorentz-polarization factor. LP takes care of the geometry-dependent diffraction probability variation from one Bragg peak to another and the polarization of the incoming X-

ray beam. As seen, Eq.2 can easily generate the first estimate of the diffraction intensity distribution if initial crystal properties and the instrumental parameters including X-ray wavelength are provided about the investigated sample: first the Bragg angles are computed based on the Bragg's law, $2d_{hkl} \sin\theta_{hkl} = \lambda$, using the type and lattice parameter of the sample's unit cell and the wavelength of the X-rays, next an analytical peak function which is usually a Gaussian, or a Lorentzian or a bifunctional combination of those is centered at each Bragg angle within the measurement space and each one of the peaks is assigned a maximum value computed by Eq.2, finally these peak profiles are convoluted by the instrument profile function. The later steps involve using a least square error minimization algorithm to minimize the discrepancy between this calculated intensity profile I_{calc} and measured or observed profile I_{obs} iteratively by adjusting/refining the model parameters resulting in a new estimate of I_{calc} . The minimized function takes the following form(9):

$$R_{wp} = \left\{ \frac{\sum_i w_i [I_{(obs)i} - I_{(calc)i}]^2}{\sum_i w_i [I_{(obs)i}]^2} \right\}^{1/2} \quad (\text{Eq.3})$$

where R_{wp} is the weighted residual, I_{obs} is the observed or measured diffraction data which is analyzed, i is the dummy index referring to the angular step and w_i is the weighting factor at step i . The weighting factor is typically determined by considering the uncertainties associated with the experimental data, such as counting statistics and instrument-related factors(10, 11).

3. METHODOLOGY

In this section, the steps followed for simulation of the nanocrystal powders as well as their corresponding diffraction data and the Rietveld refinement strategy are explained.

3.1. Simulation of Nanocrystalline Powders

We studied three sets of monodispersed and ideally random powder ensembles: one consisting of ideal crystalline nanospheres, one of ideal crystalline nanocubes and one of non-ideal nanospheres resulting from minimum-energy atomic configurations obtained from Molecular Dynamics simulations at 0 K. While the first two nanocrystal models were used to obtain the performance and sensitivity of Rietveld analysis with minimized uncertainties in the investigated sample and refinable parameters, the third model was used to study the capability and robustness of Rietveld refinement to capture particle-wide fluctuations in the atomic stacking on the corresponding diffraction data. For both the spherical and cubic ideal nanocrystals, particle dimensions were set to 5, 15, 20, and 30 nm. These ideal crystalline particles had their atoms situated at repeating FCC unit cells having a lattice parameter of 4.0626 Å belonging to gold at 0 K. The energy-minimized spherical nanoparticles were obtained by equilibration of ideal crystalline spherical nanoparticles at 0 K and these experienced static atomic displacements due to surface relaxation/reconstruction(12) compared

¹ These functions differ in the way they model the angular dependence of particle size and microstrain related broadening in the observed Bragg profiles.

with ideal crystalline nanospheres. Further detail on the energy minimization step is provided in our previous works(13, 14). Once the atomistic models of all nanocrystals were built, lattice parameters and particle dimensions were evaluated following the methodology described in a previous work(12). Particle sizes were calculated by considering undercoordinated surface atoms having a coordination number smaller than 12. These atoms each had a pairing atom located in opposite direction such that the line connecting them passed through the particle center and was considered one diameter line. Average particle size was obtained from the mean of all diameter lines connecting paired surface atoms. Next, the average lattice parameters were calculated by decomposing an

ideal crystalline particle into repeating unit cells where each unit cell was built by one origin atom and three corner atoms positioned at <110> directions. These 4-atom groups were mapped in the corresponding equilibrated particle to calculate the lattice parameter of the energy-minimized nanospheres. For ideal crystalline spherical and cubic nanoparticles, the lattice parameters were constant within the particle. However, for the energy-minimized spherical nanocrystal, the lattice parameter varied from particle core to particle surface due to the surface relaxation/reconstruction. The crystallographic parameters of the created nanocrystal models are reported in Table 1.

Table 1: Nominal size, average size (D_{RS} , t_{RS}) and lattice parameters (a_{RS}) and total number of atoms of the nanocrystal models from real space (RS) calculations. Uncertainties reported are standard deviations from the mean.

Size	Spherical particles					Cubic particles		
	# of atoms	Ideal Crystalline		Energy minimized		# of atoms	Ideal Crystalline	
		D_{RS} (nm)	a_{RS} (Å)	D_{RS} (nm)	a_{RS} (Å)		t_{RS} (nm)	a_{RS} (Å)
5	3589	4.606±0.155	4.0626	4.589±0.138	4.0499±0.03446	7814	4.875	4.0626
10	28897	9.486±0.149	4.0626	9.470±0.132	4.0567±0.0242	66327	10.156	4.0626
15	106114	14.773±0.152	4.0626	14.760±0.1351	4.0594±0.0191	210939	15.032	4.0626
20	231477	19.235±0.152	4.0626	19.224±0.1358	4.0608±0.0158	485151	19.907	4.0626
30	781145	28.981±0.153	4.0626	28.973±0.137	4.0617±0.0118	1721477	30.470	4.0626

3.2. Computation of Diffraction Datasets

Analytical powder diffraction data was computed by the Debye scattering equation(15). This equation is derived by formulating the expected diffraction intensity from a single particle, and then integrating the diffracted intensity distribution over the surface of a unit sphere(16) in reciprocal space. This last step results in the orientational average of the expected diffraction signal from the particle, which corresponds to the normalized intensity distribution from a monodispersed particle ensemble (powder) with infinitely many identical particles of independent orientations. The Debye equation takes the following form:

$$\langle I(2\theta) \rangle = \sum_{n=1}^N \sum_{m=1}^N f_n f_m \frac{\sin(qr_{nm})}{qr_{nm}} \quad (\text{Eq.4})$$

Here N is the number of atoms in a single particle making up the powder, q is the magnitude of the momentum transfer vector given as $q = |\vec{q}| = \frac{4\pi \sin\theta}{\lambda}$ where θ is half the scattering angle and $r_{nm} = |\vec{r}_n - \vec{r}_m|$ is the magnitude of the interatomic distance vector connecting the n'th and m'th atoms. As seen, the Debye scattering equation is a general formulation of average diffraction intensity from a

group of atoms, irrespective of whether the particle is crystalline or amorphous. Secondly, the orientational average of the intensity distribution is computed analytically, therefore the resulting intensities are free of statistical uncertainties from finite scattering probability of the irradiated crystals(4, 17) or uncertainty due to the photon counting processes. Hence, we selected this formulation and evaluated Eq.4 for our nanocrystalline powder models to obtain our diffraction datasets. However, instead of directly evaluating Eq.4, we used the optimized Debyer(18) algorithm to compute the diffraction data to reduce the computation time. An X-ray wavelength of 1 Å was selected and the diffraction data was computed over an angular range of [5°-180°] for all nanocrystal models. To investigate the effect of step size of the diffraction data on the refined parameters, all datasets were computed with 4 different step sizes: 0.01°, 0.05°, 0.1° and 0.2°. Figure 1 demonstrates the computed intensities from ideal crystalline spherical, ideal crystalline cubic and energy-minimized spherical nanocrystals of 5 nm nominal size.

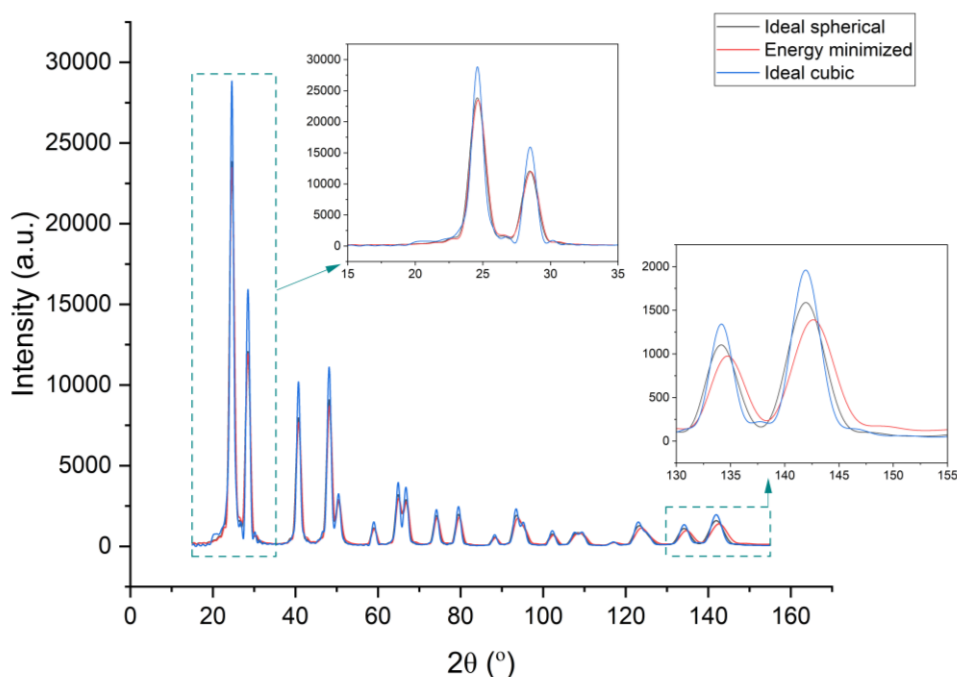


Figure 1: The computed powder diffraction profiles of the studied nanocrystal powders ($\lambda = 1 \text{ \AA}$). The differences between the computed profiles are enhanced at higher diffraction angles.

3.3. Rietveld Refinement of the Diffraction Data

We used the open source software GSAS II(19) to perform Rietveld refinement on our diffraction data. Before each refinement, we uploaded the computed diffraction data as well as the cif file of gold, which included the unit cell properties of bulk crystalline gold tabulated in standard databases. Next, an instrument file which had hypothetical parameters corresponding to an ideal diffractometer assumed in our diffraction calculations was provided. Using the instrument and sample related parameters, a diffraction pattern was modeled by GSAS II using Eq.2 and this pattern was modified at each refinement cycle until it matched with the observed (computed) diffraction data. At the end of the refinement, three crystallographic properties were

extracted: average lattice parameter was obtained from the peak centers while average crystal size and apparent microstrain (if present) were computed from peak broadening. For crystal size and microstrain calculations, Williamson-Hall method(20) was used such that the total broadening of a given Bragg peak was modeled as a combination of broadening associated with limited crystal size and local variation of the lattice parameter within the individual crystal. In this case, size-related peak broadening was modeled by the Scherrer equation(21) and microstrain was assumed to be isotropic and was allowed to vary smoothly over the diffraction angles with a $\tan \theta$ dependence(22) where θ was half the scattering angle.

Table 2: Initial parameters in Rietveld refinement. Parameters indicated by an asterisk (*) are refined and those without are fixed at their initial values.

Size	Spherical particles										Cubic particles				
	Ideal Crystalline					Energy minimized					Ideal Crystalline				
	D_R^* (μm)	a_R^* (\AA)	$\mu\epsilon$	MS D (\AA^2)	LGmix *	D_R^* (μm)	a_R^* (\AA)	μ^*	MS D (\AA^2)	LGmix *	D_R^* (μm)	a_R^* (\AA)	$\mu\epsilon$	MS D (\AA^2)	LGmix *
5	0.00	4.0782	0	0	1.0	0.00	4.0782	100	0	1.0	0.00	4.0782	0	0	1.0
10	0.01	4.0782	0	0	1.0	0.01	4.0782	100	0	1.0	0.01	4.0782	0	0	1.0
15	0.01	4.0782	0	0	1.0	0.01	4.0782	100	0	1.0	0.01	4.0782	0	0	1.0
20	0.02	4.0782	0	0	1.0	0.02	4.0782	100	0	1.0	0.02	4.0782	0	0	1.0
30	0.03	4.0782	0	0	1.0	0.03	4.0782	100	0	1.0	0.03	4.0782	0	0	1.0

Depending on the type of the sample, different refinement strategies were followed: for ideal crystalline gold nanocrystals, lattice parameter, profile shape factor (LGmix, mixing parameter of Gaussian and Lorentzian peak profile functions), average crystal size and an arbitrary scale factor was initialized and refined. For energy-minimized

gold nanospheres, microstrain was added to the refinement parameters to account for surface atom displacements resulting from energy minimization. Since the refined data were free of instrumental errors or statistical uncertainties, we did not subtract any background scattering before the refinement. This refinement scheme was consistent

with previous literature(7). Table 2 summarizes the initial values of the refinement parameters used for each nanocrystal model where D_{R_i} , a_{R_i} , $\mu\epsilon$, MSD, and LGmix represent initial particle size, lattice parameter, microstrain, mean-square atom displacement, and Lorentzian-Gaussian mixing parameter, respectively. Moreover, the refined parameters are indicated by * in Table 2 whereas parameters without * were fixed at their initial values during the refinement.

Following each successful refinement, the updated values of the refined parameters were collected and systematically analyzed. Figure 2 shows how a

successful refined model looks like for a 5 nm spherical (left) and cubic (right) nanocrystal. In this figure, observed intensities are the analytically computed intensities, whereas calculated intensities are the best fitted Rietveld models. The difference between the two intensities shown in turquoise color is called the residual. The lack of large variations in the residuals indicates that the fit is successful. Additionally, the blue ticks are well aligned with the centers of the computed and fitted diffraction peaks indicating that the crystal unit cell of the nanoparticles is correctly represented by the refined cif file of bulk gold.

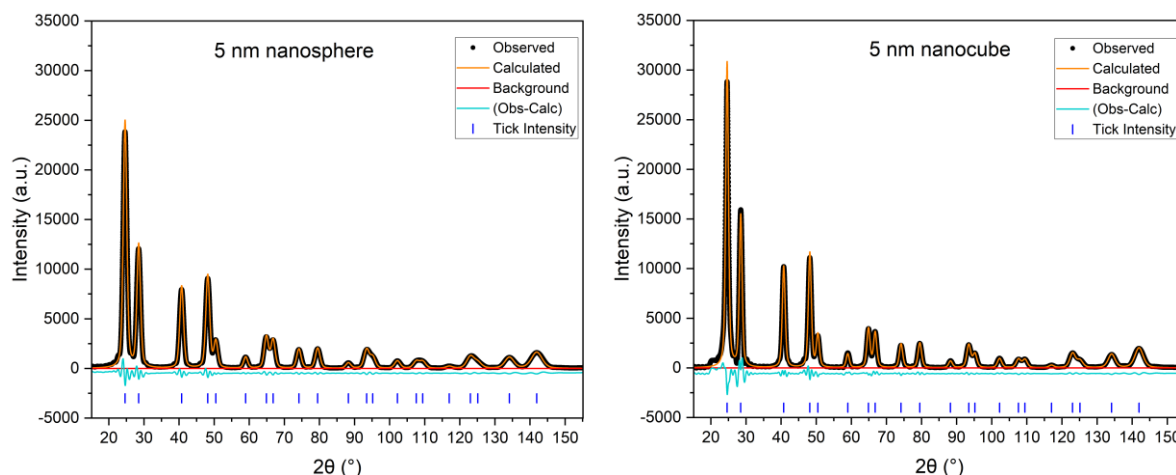


Figure 2: A successful Rietveld refinement of the diffraction data from a 5 nm ideal crystalline nanosphere (left) and a 5 nm ideal crystalline nanocube. Calculated refers to the diffraction data modeled by GSAS II, whereas Observed refers to the analytical diffraction data computed by the Debye equation. The blue tick marks show the expected positions of the Bragg peaks predicted by Bragg's law.

4. RESULTS

In this section, we investigate the variation of the refined lattice parameters, crystallite sizes and microstrains with respect to the step size of the investigated diffraction data, angular range of refinement, nanocrystal size and shape.

4.1. Accuracy of Refined Lattice Parameters

The figure 3 shows the effect of refinement range and step size of the diffraction data on the refined lattice parameters for powders consisting of ideal crystalline gold nanospheres with different diameters. In each subplot, 4 different Rietveld

analysis results are seen, where the diffraction data in each was computed with a different angular step size ($d\theta$) ranging from 0.01° to 0.2° . The purple horizontal lines in the subplots show the true lattice parameter of the gold nanocrystals which was equal to 4.0626 \AA . The horizontal axis indicates the refinement range selected. As seen, the refinement range is not evenly distributed along the horizontal axis, but rather it was extended gradually by adding each new Bragg peak one by one except when there were overlapping peaks in the diffraction profile. Overlapping peaks were added to the refinement range together for better fitting quality.

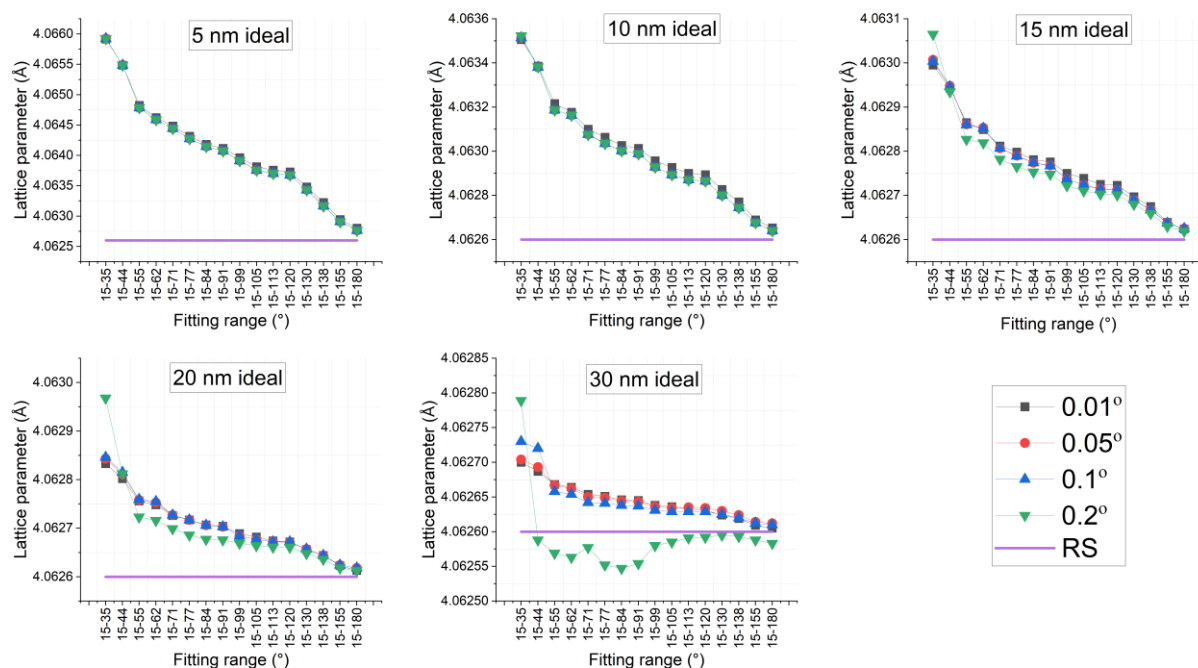


Figure 3: The variations of Rietveld-refined lattice parameter using different angular ranges for ideal crystalline gold nanospheres. RS stands for real-space calculations.

Multiple conclusions can be drawn from the figure: first, for all nanocrystal sizes, increasing the refinement range causes the extracted lattice parameters to decrease and converge to their true values. This is expected since with increasing the fitting range, we included more Bragg peaks in the Rietveld analysis which contributed to the accuracy of refined average lattice parameters(23). This trend seems to repeat for all step sizes selected in the diffraction data except for the case with $d\theta = 0.2^\circ$. Here significant fluctuations in the refined lattice parameter are visible especially for the largest nanocrystal, i.e., 30 nm. This can be explained on the basis of the crystal size and peak broadening relationship in the diffraction data: as formulated by Scherrer(21), an inverse relationship exists between the Bragg peak breadth and the crystal size of the diffracting object. This means that the sharpest Bragg peaks belong to the largest nanocrystal. Hence, when $d\theta$ was set to a relatively large value such as 0.2° , the peak profile was effectively sampled with too few points and the probability of missing the exact peak center increased. This directly translated to increased fluctuations in the refined lattice parameters. Secondly, in all nanocrystals, limiting the refinement range to lower angle Bragg peaks seems to cause significant overestimations in the extracted lattice parameters. Similar observations were made in a past study(7) for the same gold nanocrystal system where lattice parameters from lower-angle Bragg peaks were overestimated and higher-angle ones were underestimated, and it was mentioned that the root cause for lower-angle Bragg peaks to overestimate the true lattice parameter was the limited number of atoms in the diffracting crystallite. Here we confirm this observation as well as its particle size variation since with increasing nanocrystal size, the amount of overestimation in the refined lattice parameter for a particular refinement range decrease. The only exception is

the case with $d\theta=0.2^\circ$ for 30 nm nanocrystals where lower angle Bragg peaks first overestimated and then underestimated the true lattice parameters. Not surprisingly, this particle size also happened to result in the lowest quality of fit from Rietveld refinement when $d\theta=0.2^\circ$ as seen in Figure 4. Here wR is the weighted residual reported by GSAS II and normalization is performed with respect to the length of the diffraction data. For 30 nm nanocrystals, the reported weighted residual was $\sim 13\%$, higher than that of smaller nanocrystals with the same step size which may explain the unexpected underestimations of the lattice parameters. In fact, the normalized weighted residual plots in Figure 4 confirm the degrading quality of fit with increasing step size for all nanospheres. This shows that, the value of angular step size while collecting diffraction data is more critical for larger nanocrystals than smaller ones.

Repeating the above analysis on the diffraction data from energy-minimized spherical gold nanocrystals yields some common and some slightly different results which are summarized in Figure 5. Note that here the real-space-computed lattice parameters (RS) vary with the size of the nanocrystals and they increase with increasing size as shown in Table 1 and our previous work(7). This size dependence of lattice parameters of nanospheres is a consequence of surface reconstruction which causes the atoms in the surface region of the nanocrystals to be displaced radially inward due to the energy-minimization process resulting in smaller lattice parameters within the surface layer. However, this phenomenon is less appreciable for larger nanocrystals with smaller surface to volume ratio leading to larger average lattice parameters. Looking at the refined lattice parameters we see that they are again overestimated especially for lower angle Bragg peaks but converge to their true average values with increasing fitting range. Unlike

ideal crystalline nanospheres, here the refined lattice parameters are never underestimated even for the largest nanocrystal with the highest step size in the diffraction data. Between ideal crystalline and energy-minimized nanospheres, the former shows much smaller deviations of refined lattice parameters from the true value than the latter: for the 5 nm energy-minimized gold nanosphere with $d\theta=0.01^\circ$, Rietveld-refined lattice parameters are overestimated by $\approx 0.004 \text{ \AA}$ at most, which decay to

$\approx 0.001 \text{ \AA}$ over the widest refinement range. The corresponding values for the ideal crystalline nanosphere are less than 0.0005 \AA over all refinement ranges. These deviations decrease with increasing nanocrystal size for both particle systems. Finally, the value of the step size has negligible effect on the refined lattice parameters for all particles except for 20 and 30 nm nanocrystals.

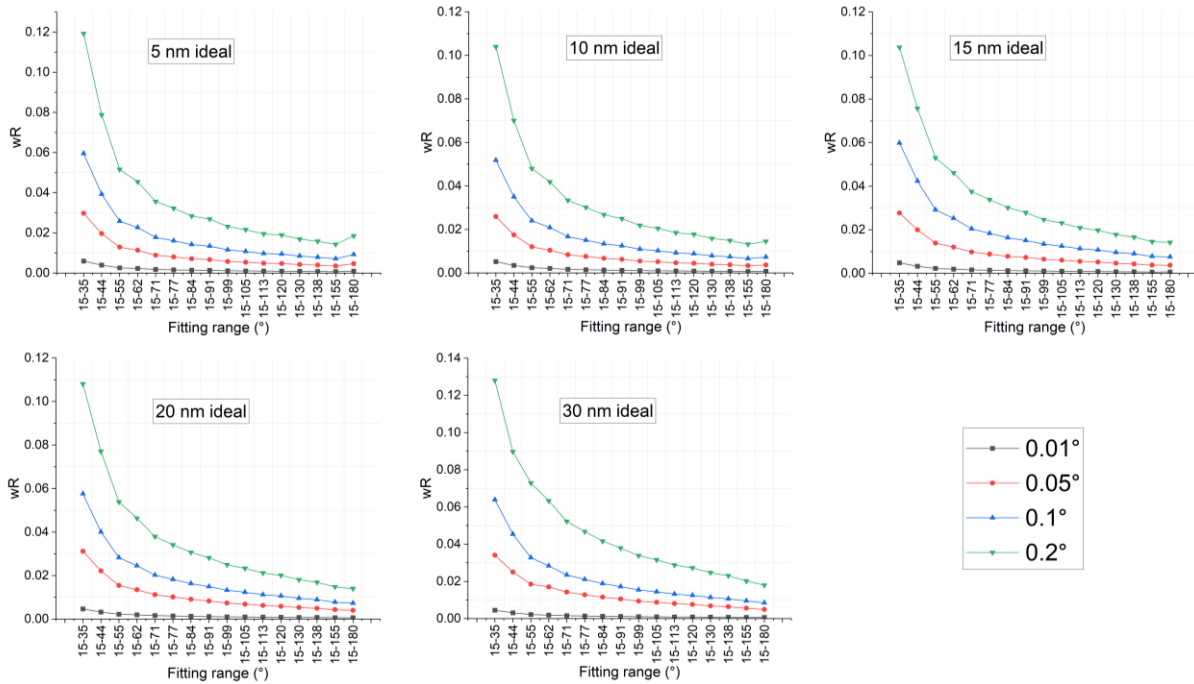


Figure 4: The weighted residuals (wR) normalized by the number of measurement points from Rietveld refinement of diffraction data computed with different step sizes of ideal crystalline gold nanospheres.

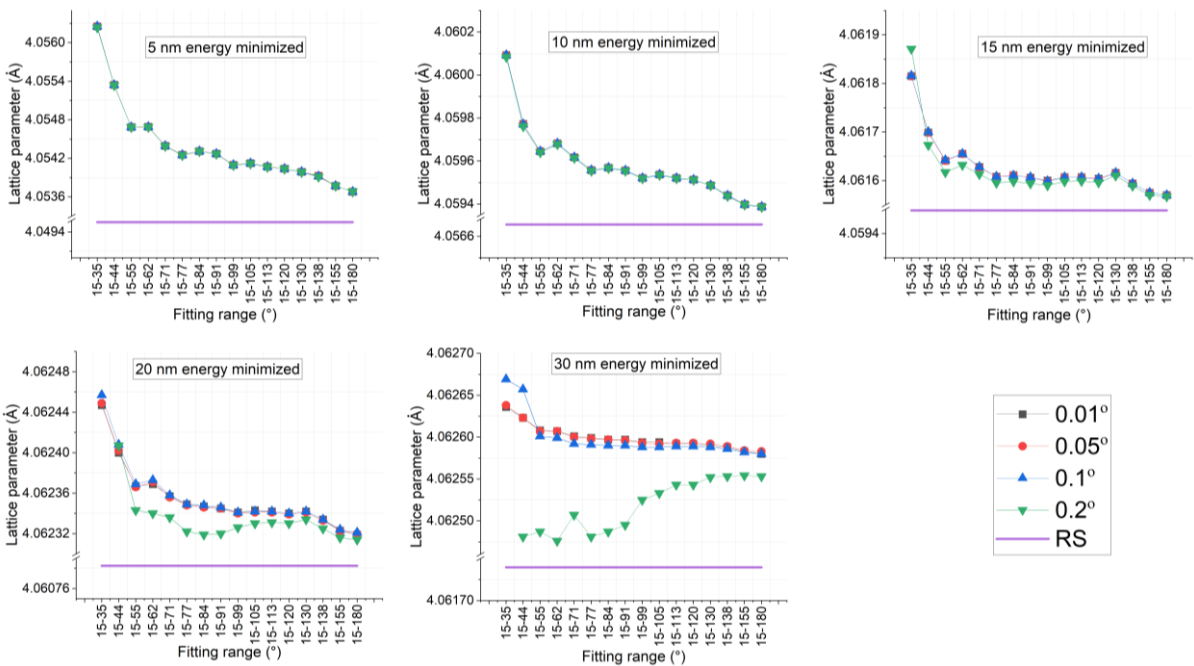


Figure 5: The variations of Rietveld refined lattice parameters using different angular ranges for energy-minimized gold nanospheres. Axis breaks on the vertical axis were used to enhance the readability of the figure.

To investigate whether the shape of the nanocrystals affects the accuracy of the Rietveld-refined lattice parameters, we repeated our analysis on the diffraction data from ideal crystalline gold nanocubes as well. Figure 6 summarizes our findings. First, we observe that except for the 5 nm nanocrystal, all other nanocubes show similar features as their spherical counterparts: 1) the refined lattice parameters approach their true values with increasing fitting range, 2) the selection of the angular step size has almost negligible effect for the smaller nanocrystals, but it causes some fluctuations in the lattice parameters of the larger nanocrystals. This can be explained by the significant peak broadening associated with the profiles of smaller nanocrystals. Unlike

nanospheres, however, the refined lattice parameters of nanocubes are always underestimated except for the 5 nm nanocube. To understand the root cause of this difference, we also performed Line Profile Analysis (LPA) on both spherical and cubic ideal nanocrystals. Unlike Rietveld refinement which imposes a unique crystal unit cell and assigns relative intensities to all Bragg peaks based on Eq.2, LPA treats all Bragg peaks independently. This makes it possible to obtain better fits and higher accuracy in individual peak profile parameters, such as peak centers and maxima, at the expense of a unique crystallographic unit cell parameter. Therefore, LPA was used to investigate angle-dependent variations of lattice parameters.

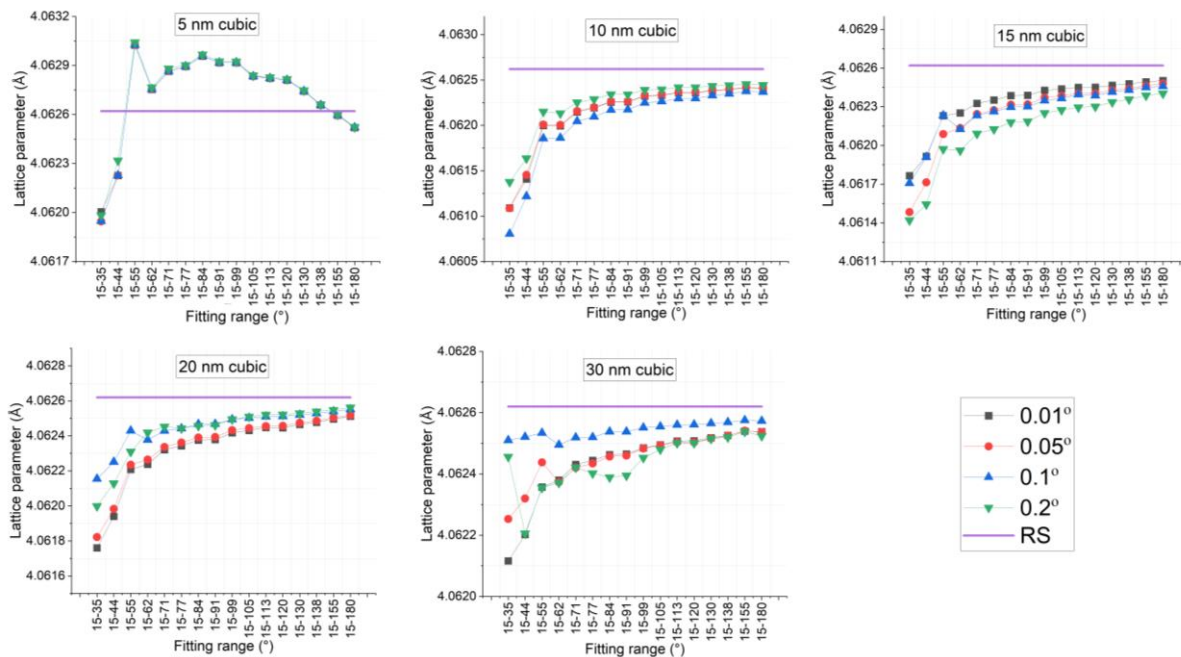


Figure 6: The variations of lattice parameter using different angular ranges for cubic ideal nanoparticles.

For all our datasets, LPA was implemented by fitting a separate Gaussian profile function to each Bragg peak and refining the sum of all functions against the computed diffraction data with a least square error minimization scheme. The Gaussian peak profiles were justified since our hypothetical samples did not include any microstructural defects affecting the Bragg peak profiles(24), there was no additional peak profile modifications due to the incoming X-ray beam(25) and the mixing parameters (LGMix) we obtained from Rietveld refinement of the diffraction datasets were smaller

than 0.5 indicating that our Bragg peaks resembled more to Gaussian rather than Lorentzian profiles. For consistency with Rietveld refinement, no background was subtracted during fitting. Once all peaks converged, their peak centers were collected and converted to the corresponding lattice parameters by Bragg’s law and the interplanar spacing relation valid for cubic crystals, $2d_{hkl} \sin\theta_{hkl} = \lambda$ and $d_{hkl} = \frac{a}{\sqrt{h^2+k^2+l^2}}$. Table 3 summarizes the results of this analysis.

Table 3: Lattice parameters obtained by LPA from the diffraction data of ideal crystalline gold nanospheres and nanocubes ($d\theta=0.01^\circ$).

Peaks	5nm sphere ideal (Å)	5nm cubic ideal (Å)	10nm sphere ideal (Å)	10nm cubic ideal (Å)	15nm sphere ideal (Å)	15nm cubic ideal (Å)	20nm sphere ideal (Å)	20nm cubic ideal (Å)	30nm sphere ideal (Å)	30nm cubic ideal (Å)
1 1 1	4.065797	4.065816	4.063491	4.06339	4.062977	4.06298	4.062826	4.062824	4.062701	4.062702
2 0 0	4.066810	4.061720	4.063396	4.062009	4.062923	4.06222	4.062791	4.062331	4.062686	4.062444
2 2 0	4.064353	4.062726	4.063052	4.06253	4.062791	4.062535	4.062714	4.06255	4.062651	4.062568
3 1 1	4.064332	4.063807	4.062917	4.062879	4.062745	4.062747	4.062689	4.062696	4.062641	4.062652
2 2 2	4.063548	4.066964	4.063564	4.063265	4.062833	4.062856	4.062717	4.062739	4.062644	4.062655
4 0 0	4.063111	4.061855	4.062848	4.062414	4.062708	4.062482	4.062662	4.062515	4.062625	4.062552
3 3 1	4.064982	4.063775	4.062565	4.062708	4.062653	4.062687	4.062644	4.062669	4.062624	4.062641
4 2 0	4.062124	4.062939	4.063127	4.062671	4.062744	4.062583	4.062672	4.062581	4.062628	4.062593
4 2 2	4.063207	4.063064	4.062778	4.06268	4.062675	4.062629	4.062645	4.062619	4.062621	4.062618
3 3 3	4.063355	4.063201	4.062753	4.062724	4.06266	4.062667	4.062635	4.062646	4.062615	4.062633
4 4 0	4.061254	4.061619	4.062625	4.062453	4.062625	4.06254	4.062616	4.062558	4.062608	4.062577
5 3 1	4.062840	4.062840	4.062639	4.062556	4.062574	4.062622	4.0626	4.062628	4.062605	4.062625
4 4 2	4.062210	4.062210	4.062912	4.063026	4.062787	4.062693	4.062667	4.062639	4.062616	4.062623
6 2 0	4.062621	4.062237	4.062624	4.062547	4.062614	4.062597	4.062609	4.062613	4.062603	4.06262
5 3 3	4.063275	4.063308	4.062683	4.062393	4.062492	4.062519	4.062564	4.062575	4.062594	4.062606
6 2 2	4.062301	4.062300	4.062579	4.062847	4.062717	4.06266	4.06264	4.062607	4.062608	4.062604
4 4 4	4.061247	4.061811	4.062394	4.062607	4.062558	4.062629	4.062583	4.06264	4.062598	4.062659
5 5 1	4.062514	4.063091	4.062683	4.062508	4.06252	4.062551	4.06256	4.062584	4.062589	4.062608
6 4 0	4.062989	4.062069	4.062379	4.062824	4.06284	4.062646	4.062684	4.062579	4.062609	4.062581
6 4 2	4.061839	4.062021	4.062451	4.062553	4.062546	4.062596	4.06257	4.062603	4.062587	4.062602
5 5 3	4.062105	4.062489	4.062444	4.062548	4.062531	4.062584	4.062558	4.062597	4.062581	4.062609
Mean	4.063182	4.062946	4.062805	4.062673	4.062691	4.062620	4.062649	4.062609	4.062621	4.06261
Std	0.001419	0.001325	0.000348	0.000303	0.000135	0.000146	7.19747E-05	9.32339E-05	3.05669E-05	5.08219E-05
%dev	-0.01432	-0.00851	-0.00504	-0.0018	-0.00224	-0.0005	-0.00123	-0.00023	-0.00051	-0.0002

The first column of Table 3 shows the Miller indices of the Bragg peaks, and the remaining columns report the corresponding lattice parameters. As seen, the lattice parameters of cubic and spherical nanocrystals vary from one reflection to another, in general they decrease as the Miller indices increase but there is no clear trend as to which particle shape has a larger or smaller lattice parameter. However, comparing lattice parameters of nanospheres and nanocubes of the same size, we see that for the first 4 Bragg peaks having the highest intensities (see Figure 2), the lattice parameter of the spherical nanocrystal is always overpredicted whereas that of the cubic nanoparticle is underpredicted from the second and the third Bragg reflections. Since Rietveld-refined lattice parameters are a complicated average biased towards lattice parameters from higher intensity Bragg peaks, including these two Bragg peaks in the refinement range may cause the overall refined lattice parameter to be underpredicted for the cubic particle. An exception seems to be the 5 nm nanocube, however unlike larger nanocubes, here the third Bragg peak deviates positively from the true lattice parameter shifting the Rietveld-refined lattice parameter upwards from 4.0626 Å. This concept was mentioned in our previous study(7) as well: while insufficient number of scatters causes positive or negative shifts in the diffraction peak centers from predictions of the Bragg's law, the sign

and amount of shift depends also on the X-ray wavelength selected and the shape of the nanocrystal. Hence, it is not surprising to see difference between the Rietveld-refined lattice parameters of spherical and cubic crystallites as well as how closely they agree with the true lattice parameters of the system. Finally, the last three rows of Table 3 report Mean, std and %dev which are the average lattice parameter, standard deviation and percent deviation of the mean lattice parameters from the true value, i.e., 4.0626 Å, respectively. Looking at the arithmetic mean and standard deviations of LPA-based values for each nanocrystal, we notice that although both the lattice parameters of spherical and cubic nanocrystals are greater than their true value, the lattice parameter of the spherical nanocrystal has higher deviations from the true lattice parameter compared to the cubic nanocrystal with the same size. This conclusion also holds for the deviations of Rietveld-refined lattice parameters from their true values seen in Figures 3 and 6 and it can again be explained by the greater number of atoms contained in a cubic nanocrystal compared to a spherical nanocrystal of the same size: the higher the number of scatters, the better the convergence of the refined lattice parameter to its true value.

4.2. Accuracy of Refined Crystal Sizes

The second crystallographic parameter we discuss is the average crystal sizes from Rietveld refinement of diffraction data. Figure 7 demonstrates the variation of refined crystal size for ideal crystalline gold nanospheres for different fitting ranges. Note that here the particle size and crystal size refer to the same physical quantity which is the linear dimension of one nanoparticle since all nanocrystal models were built as single crystalline particles. As seen in all nanoparticles studied, Rietveld-refined average particle sizes are less than the true average diameter (D_{RS}) of the nanocrystals shown by horizontal lines (also see Table 1). Unlike the case for lattice parameters, the refined sizes are

stable with some random fluctuation for all fitting ranges selected. This is expected since the studied particles had isotropic shapes which did not depend on the crystallographic direction. Looking at the step sizes of the diffraction data, no generalizable trend between the step size and refined particle size is detected. This indicates that if there is no local variation in the lattice parameters of the nanocrystals which was the case for our ideal crystalline nanopowders, the angular dependence of the peak broadening, $\beta(2\theta)$, is accurately predicted by the Scherrer relation(21) which predicts a variation proportional to $1/\cos\theta$.

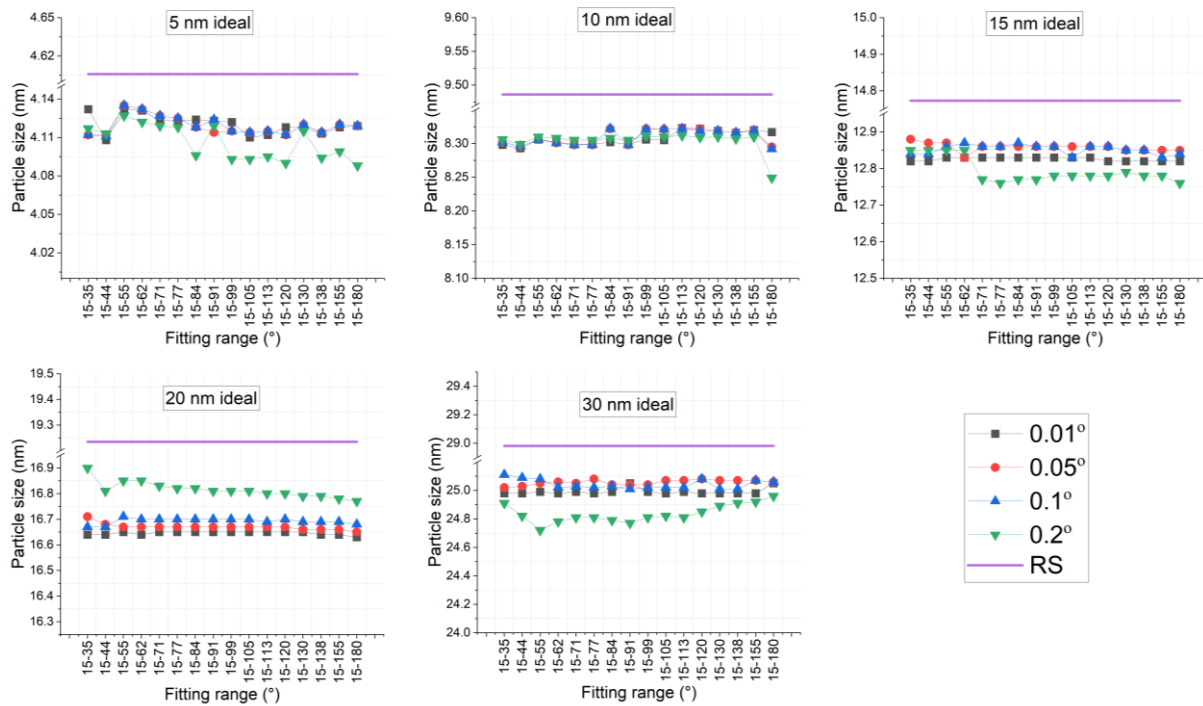


Figure 7: The variations of particle size using different angular ranges for ideal crystalline gold nanospheres. Axis breaks are used to enhance the readability of particle sizes.

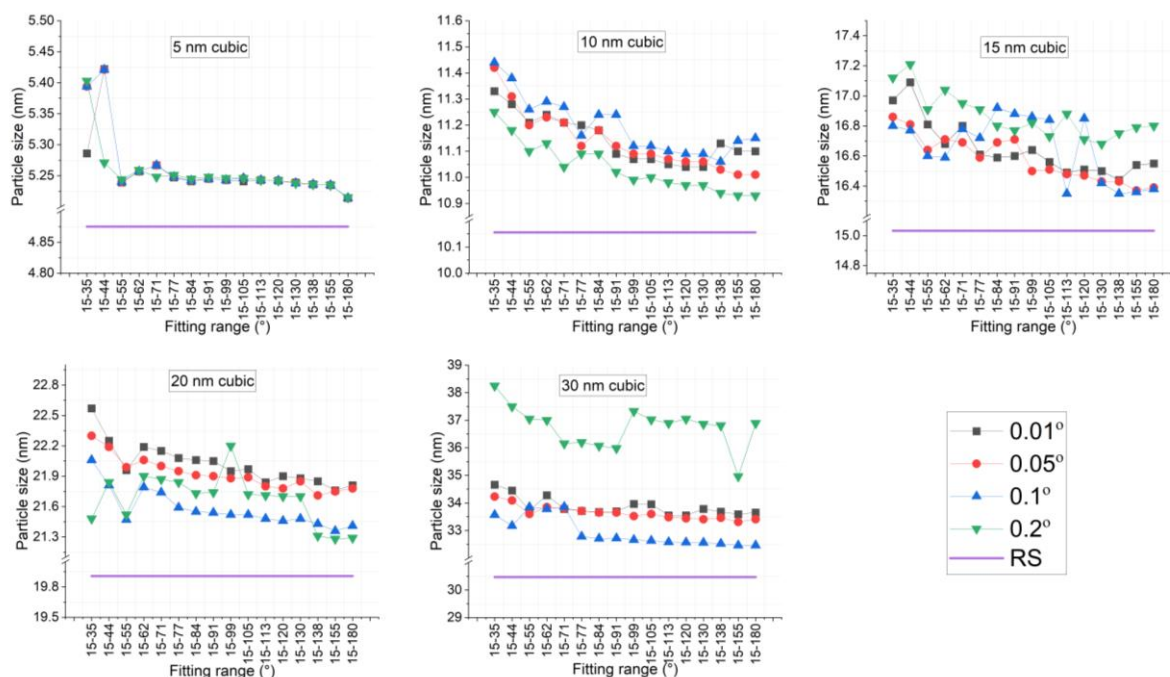


Figure 8: The variations of particle size using different angular ranges for ideal crystalline gold nanocubes. Repeating this analysis on the diffraction profiles of ideal nanocubes resulted in the data presented in Figure 8. In contrast to spherical nanocrystals, here all Rietveld-refined particle sizes are larger than the true linear dimensions (t_{RS}). Similar to spherical nanocrystals, a smaller step size does not necessarily improve the accuracy of the refined sizes except for the 30 nm nanocrystal: for this particle the peak broadening due to limited crystal size is minimum and Bragg peaks are sharper than smaller cubic crystals. Hence a larger step size causes enhanced inaccuracies in the peak broadening estimations. In addition, a cubic crystal contains a larger number of atoms than a spherical crystal of the same size as seen in Table 1. Therefore, the intensities of cubic crystals are much sharper than those of spherical crystals of the same shape as shown in Figure 1. This enlarged peak sharpness causes further challenges in peak broadening estimation in diffraction data of cubic nanocrystals computed with large step sizes. Overall, these factors explain the worst performance of the particle size refinement with large step size in the 30 nm cubic nanocrystals. In other nanocrystal sizes, the refined sizes seem to fluctuate randomly around a mean and they are almost independent of the step size for the smallest nanocrystal with the broadest Bragg peaks. However, unlike ideal crystalline gold nanospheres, a slight decay in the refined sizes with increasing refinement range is detected. We believe this may be a consequence of the anisotropy in the linear dimensions of the nanocubes which causes slightly different peak broadening terms for different family of hkl reflections and is neglected in modeling the peak-breadth variations over the angular range by GSAS II.

A second factor that may explain the increased fluctuations of refined sizes of nanocubes compared to nanospheres is the difference in the fitting qualities. Note that unlike lattice parameters which only depend on the center of the Bragg peaks, crystallite sizes which depend on the peak breadth are much more dependent on how well the Bragg peak shapes are modeled by the selected analytical functions. One may see in Figure 2 that a mixture of Gaussian-Lorentzian peak profile function captures the main features of Bragg peaks from spherical nanocrystals well, but it is not as successful for Bragg peaks from cubic nanocrystals. This phenomenon is especially visible in the first Bragg peak of the 5 nm nanocube where relatively high residuals are visible around the tail of the peak. It shows that, even though the Rietveld refinements from both cubic and spherical nanocrystals converged successfully, they did not approximate the measured diffraction data equally well as confirmed by the higher normalized weighted residuals of cubic nanocrystals shown in Figure 9. We emphasize that the weighted residuals alone are not the best criterion to judge the goodness of the fitted model; however, visual inspection also confirms that the assumed peak profiles resulted in poorer fit quality for cubic crystals.

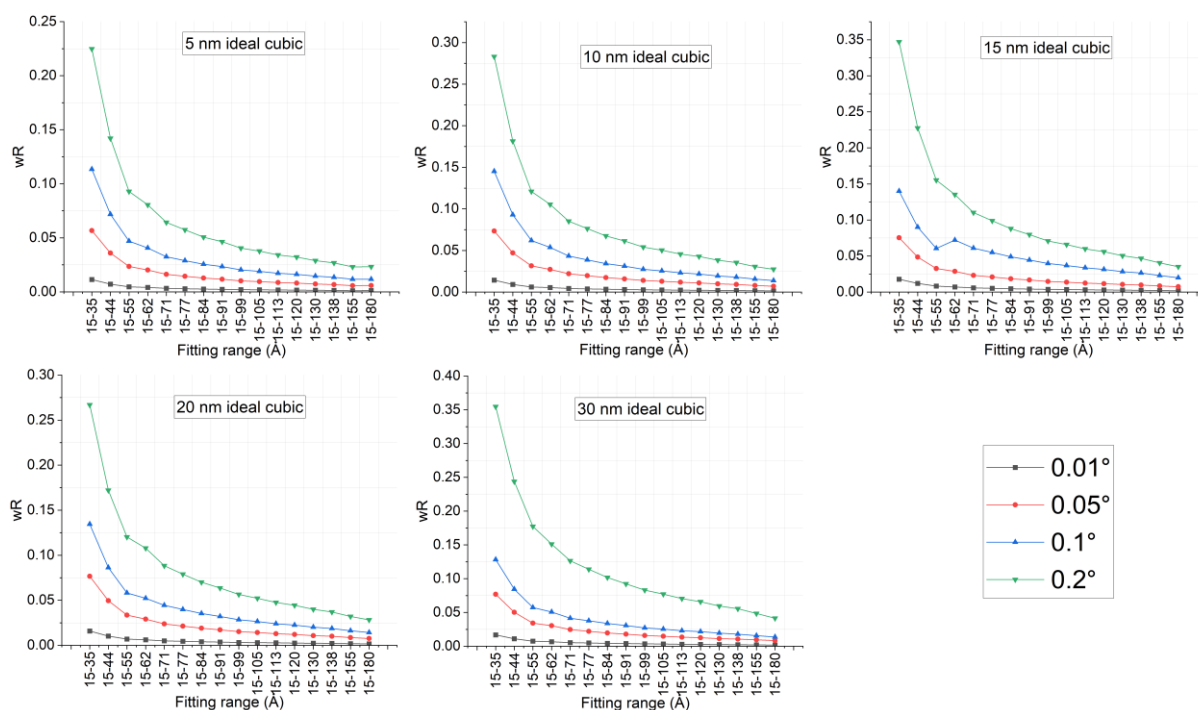


Figure 9: The weighted residuals (wR) normalized by the number of measurement points from Rietveld refinement of diffraction data computed with different step sizes of ideal cubic crystalline gold nanospheres.

Finally, the fact that refined particle sizes from cubic nanocrystals are overestimated while they are underestimated from spherical nanocrystals intimates that the prefactor multiplying the inverse of the peak breadth to the crystal size in the Scherrer equation, i.e. $D_{hkl} = \frac{C\lambda}{\beta_{hkl} \cos\theta_{hkl}}$, may have an effect in the size errors. To confirm this, we checked the value of the shape constant C assumed in GSAS II and found it was equal to one. In the literature, it is a common practice to set the value of C close to unity(26-28). However, this prefactor has been a source of confusion in the past literature of powder diffraction analysis since the concepts such as peak breadth, integral breadth and the meaning of crystal size were not rigorously explained or interpreted. One publication that addressed this issue was written by Patterson(29) where Scherrer constants for spherical crystals were derived by two approaches, one exact and one approximate, for

two different breadth definitions: full width at half maximum and integral breadth. According to this study, different definitions of the peak breadth resulted in different values for the prefactor in the Scherrer equation. Recently we worked out the derivation of these Scherrer constants and tested their validity on computer-generated diffraction profiles of spherical crystals formulated by Patterson function(30). We found that the full-width-at-half-maximum based Scherrer constant for cubes were less than 1 (ranging from 0.886 to 0.907 depending on the hkl reflection(31)) while those of spheres were greater than 1 (1.16 for all reflections). This difference in the Scherrer constants of cubic and spherical nanocrystals therefore explains why Rietveld-refined crystal sizes are $\approx 10\%$ greater than the true sizes for cubic nanocrystals and $\approx 12\%$ less than those of spherical nanocrystals.

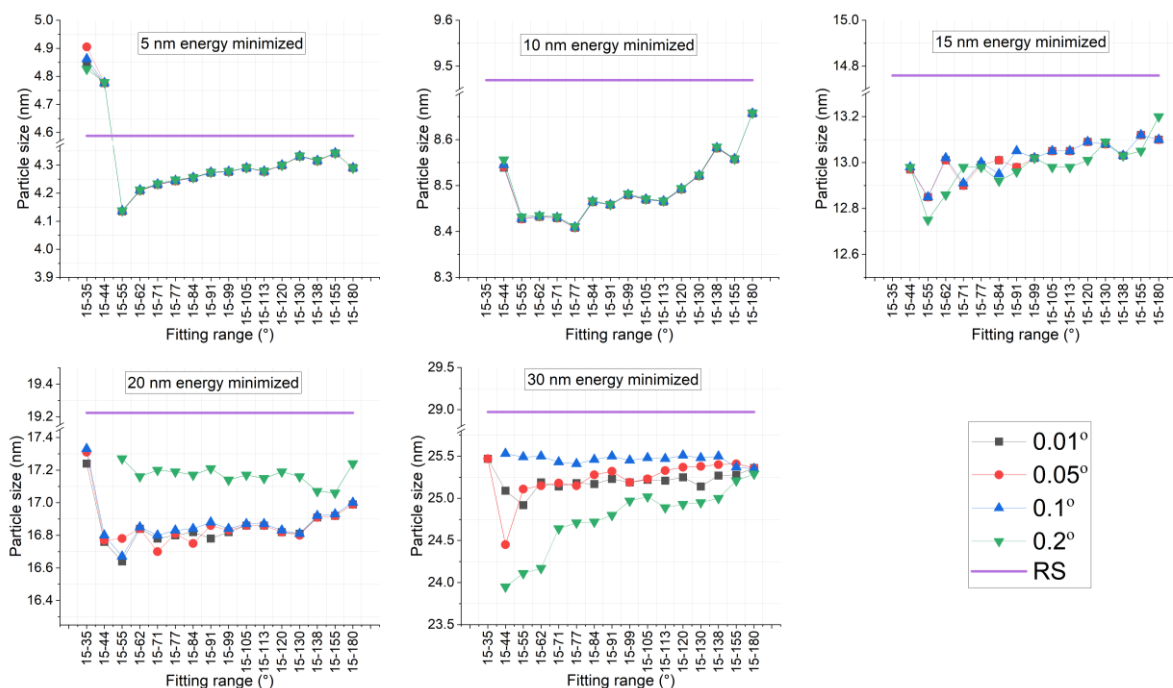


Figure 10: The variations of refined particle size using different angular ranges for energy-minimized nanospheres.

Switching our attention to the crystal sizes refined from diffraction profiles of energy-minimized gold nanospheres, we see similar trends in Figure 10 with ideal crystalline nanospheres shown in Figure 7. For all nanocrystals, the refined particle sizes are smaller than their true mean diameters shown by horizontal lines (see Table 1). For the smallest nanospheres, the angular step size has negligible effect on the refined crystal sizes irrespective of the selected fitting range. Unlike ideal crystalline nanospheres, however, the fitting range has a greater influence on the refined crystal sizes of energy-minimized nanospheres since for these particles the atoms were allowed to relax and were slightly displaced towards particle center compared to their ideal lattice points. This caused slight distortions in particle shape and variations of diameters along different crystallographic directions. Because each Bragg peak yields the crystal size along a different direction, variations of refined size over the fitting range are justified due to the atomic displacements within the surface layer. Comparing average sizes of gold nanospheres before and after the energy minimization process by real space calculations (see Table 1), we find that the true mean diameters decreased slightly with the highest diameter reduction occurring in the smallest nanocrystal due to significant surface relaxation process. Interestingly, refined crystal sizes from energy-minimized nanospheres turned out to be slightly higher than those of ideal crystalline counterparts. Although it is hard to identify the reason behind these slightly larger crystal sizes - since the refinement scheme applied on the diffraction data of ideal crystalline and energy minimized gold nanospheres were different- a chain of events during the refinement of diffraction data seems to be the cause: the Bragg peaks computed from energy-minimized models of nanospheres were slightly broader than those of ideal crystalline

nanospheres as seen in Figure 1. However, the refinement scheme applied on the diffraction data of energy-minimized nanospheres included both microstrain and crystal size refinements unlike ideal crystalline nanospheres where only crystal size contributed to peak breadth. Hence a portion of the enhanced peak broadening of energy-minimized nanospheres was attributed to the apparent microstrains. Consequently, not all but a portion of the peak broadening was treated as resulting from limited crystal size which possibly led to slightly larger crystal sizes in energy minimized nanospheres. In conclusion, the refined crystal sizes from energy-minimized nanospheres were approximately 12% less than their true mean diameters.

4.3. Variation of the Refined Microstrains

For classical crystalline powders with particle sizes above 100 nm, a single unit cell is enough to represent the full atomic configuration inside individual particles since for such particles the surface to volume ratio is negligibly small. For nanocrystalline powders, however, surface atoms make up a significantly large proportion of all atoms in the particle and therefore the atomic configuration cannot be represented by a unique rule even at 0 K temperature at which all atoms are frozen at their designated positions(7). This results from the undercoordinated surface atoms in nanocrystals which get displaced towards the particle center to minimize the overall energy of the particle. Once the minimum energy configuration is established, a single unit cell no longer represents the positioning of atoms in the nanocrystal; a significant variation in interplanar spacings between atomic planes from the particle core to the particle surface occurs. In this section we analyze how these static atomic displacements of surface atoms show as broadening of Bragg peaks, therefore

treated as apparent microstrains in Rietveld refinement of the diffraction data, and how refined microstrains vary with refinement range and step size of the diffraction data.

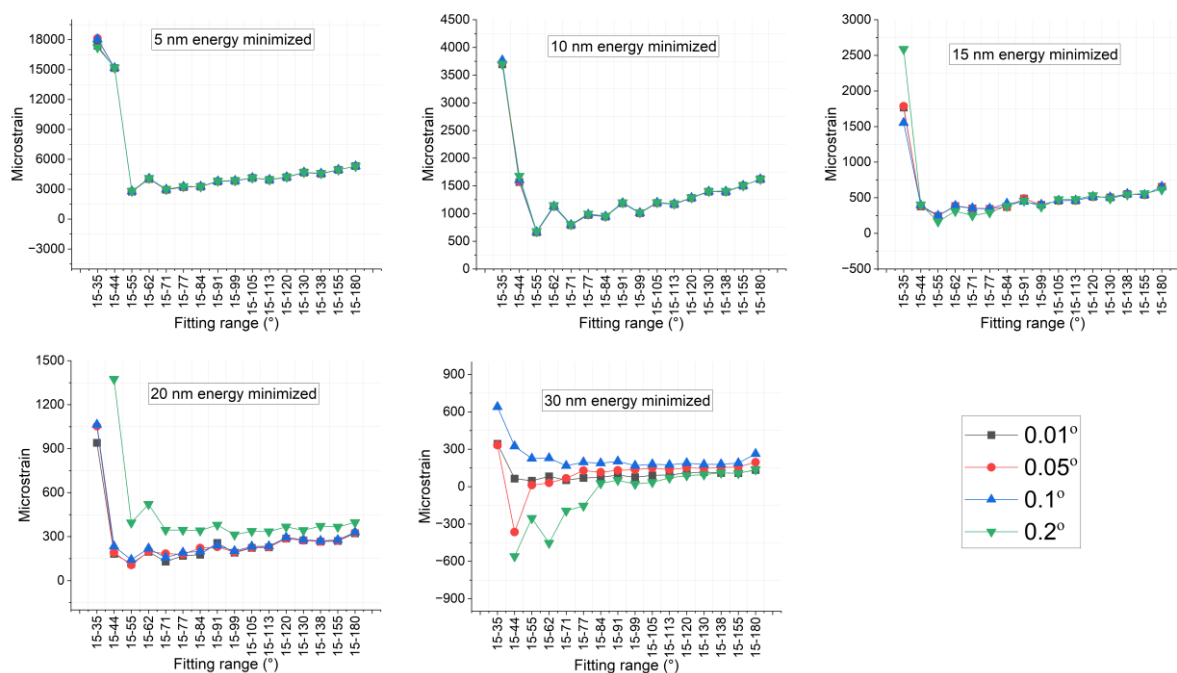


Figure 11: The variations of apparent microstrain from Rietveld refinement using different angular ranges for energy-minimized gold nanospheres.

Figure 11 presents the refined (apparent) microstrains from diffraction data of energy minimized gold nanospheres. These are isotropic microstrains which are assumed to be independent of the crystallographic direction, so a single value is computed and treated as a measure of the average microstrain in the powder. Unlike previous sections, these graphs do not include a true value, since an appropriate real space computation compatible with the microstrain definition in X-ray diffraction analysis is not available in the literature(12). We see that for all nanocrystals, the refined microstrains are maximized for limited refinement range and decay down to stable values as the refinement range increases and includes more Bragg peaks. Among different nanocrystals, the highest values at limited refinement range as well as the ultimate values at extended refinement range are observed for 5 nm nanocrystals for all step sizes. This is because the atomic configuration in the smallest nanocrystal suffers from the greatest amount of surface reconstruction and interplanar spacing variations in the nanocrystal surface contribute to significant peak broadening. In all nanocrystals, the high initial refined microstrains decay and stabilize beyond 55° , which corresponds to the angular range containing the first five Bragg peaks (see Figure 1). The fact that refined microstrains stabilize around the same refinement

range for all nanocrystal sizes indicates that refined microstructural parameters are predominantly determined by the Bragg peaks with the highest intensity, which are the first four Bragg peaks in gold crystals. Among different particle sizes, the amount of over- or under-prediction from the ultimate refined microstrains is also much higher for smaller nanocrystals than larger ones. This probably stems from the greater effect of surface atoms and their large atomic displacements on the diffraction profiles which cause their refinement to be more challenging and harder to converge to a unique crystallographic solution especially when the refinement range is limited. Normalized weighted residuals shown in Figure 12 also support this conclusion where the highest residuals are observed from the smallest nanospheres with the largest step sizes of diffraction data. Finally, similar to the refined lattice parameters and average crystal sizes, the step size has an increasing effect on the refined microstrains for larger nanocrystals than smaller ones. This is because estimating the broadening of sharper peaks is more challenging and prone to errors which causes variations in the refined microstrains of larger nanocrystals. An improper selection of step size while measuring diffraction data may result in even negative and unphysical refined microstrains such as those observed in 30 nm gold nanospheres at $d\theta=0.2^\circ$.

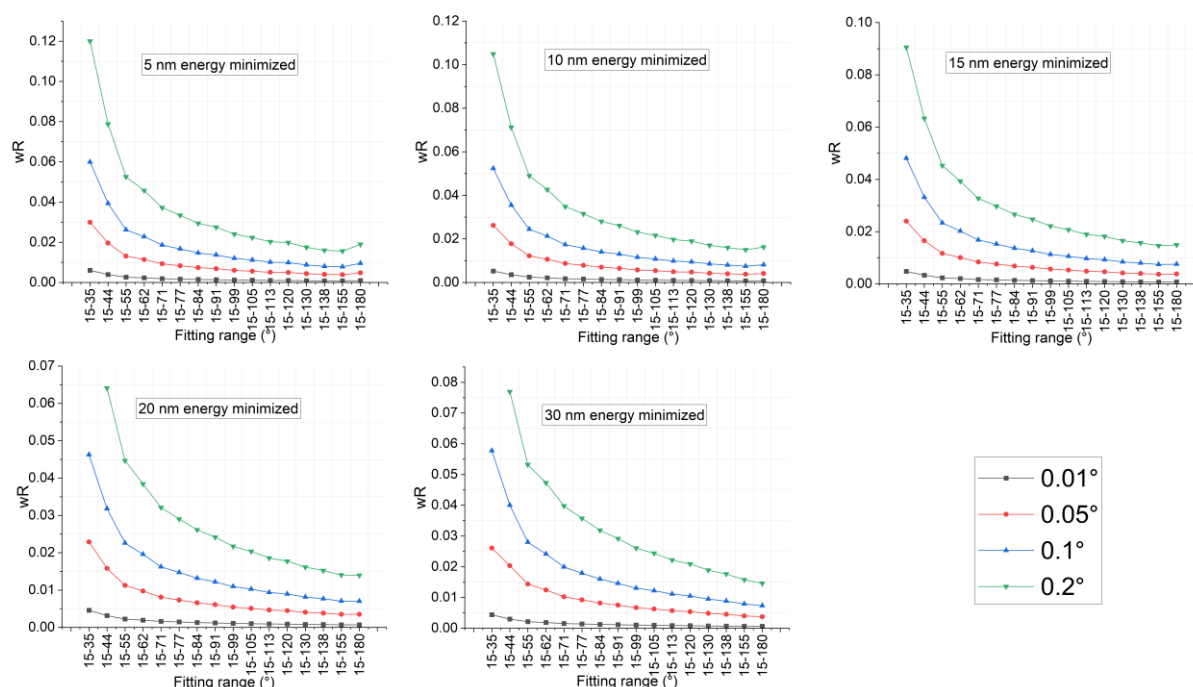


Figure 12: The weighted residuals (wR) normalized by the number of measurement points from Rietveld refinement of diffraction data computed with different step sizes of energy minimized crystalline gold nanospheres.

These results demonstrate that apparent microstrains refined from diffraction data of nanocrystalline powders are never zero even at 0 K. As the crystal size increases to 30 nm, the extended-range refined microstrains approach a value of ≈ 200 which can be considered almost zero since a microstrain value of 1000 is considered typical for bulk crystalline powders measured at room temperature(32).

5. CONCLUSIONS

In this work, we presented a systematic analysis of Rietveld refinement performed on analytical X-ray diffraction profiles from small gold nanocrystals ranging from 5 to 30 nm in size. The variation of refined average lattice parameters, average crystallite sizes and apparent microstrains with respect to 1) step size of the diffraction data, 2) crystal shape and 3) refinement range was investigated. Three model systems were studied for this purpose: ideal crystalline nanospheres, ideal crystalline nanocubes and energy-minimized nanospheres by Molecular Dynamics simulations. Our analysis showed the following:

Lattice parameters obtained from Rietveld refinement improved with increasing refinement range for all nanocrystal systems. Limited refinement range caused overestimations of lattice parameters in spherical ideal and energy-minimized nanocrystals whereas it caused underestimations in the case of cubic nanocrystals. The opposite trend in spherical and cubic nanocrystals was explained to stem from opposite shifts of refined Bragg peak centers for some of the most intense Bragg peaks in cubic gold nanocrystals which were the first four peaks within the diffraction spectra. Comparing energy-minimized and ideal crystalline

nanospheres, the former system resulted in larger deviations from the true lattice parameters than the latter which indicated that static atom displacements in small nanocrystals affected the accuracy of refined lattice parameters from their diffraction data. The step size of the diffraction data had negligible effect on the refined lattice parameters of the smallest nanocrystals whereas it became more important for larger nanocrystals which had much sharper Bragg peaks. However, no clear relation was detected between smaller step size in the diffraction data and higher accuracy in the Rietveld-refined lattice parameters as long as the step size was not too wide. For a step size of 0.2° , large fluctuations were detected, and these were attributed to increased fitting errors in Rietveld refinement resulting from the number of measurement points over the Bragg peak range being too few. Our results were consistent with past work from the literature(33).

2) Crystallite sizes obtained from Rietveld refinement were stable over the refinement range for ideal crystalline gold nanospheres. This indicated that the Scherrer-predicted $1/\cos\theta$ variation of size-related peak broadening accurately represented the variation of breadth over different reflections. This was not the case for ideal crystalline nanocubes where much higher fluctuations than those in ideal crystalline nanospheres were present over the refinement range. These fluctuations were attributed to the anisotropic linear dimensions of cubic nanocrystals and higher residuals of the refined profiles. The refined crystal sizes for ideal spheres were $\approx 10\%$ lower than the true mean diameters whereas they were $\approx 12\%$ higher than the thicknesses of ideal cubes. Incompatible Scherrer shape constant was found to cause this difference between the Rietveld-refined and true

dimensions of spherical and cubic nanoparticles. Smaller step size of the diffraction data helped better modeling of the peak profile, but its effect was negligible for the smallest nanocrystals. Although larger nanocrystals having much sharper Bragg peaks required much smaller step size for accurate profile modelling, we could not correlate smaller step size with higher accuracy in the refined crystallite sizes. Finally, for energy-minimized gold nanospheres, Rietveld-refined average diameters were more dependent on the refinement range. This was because peak broadening was contributed by two factors in these systems: static atomic displacements acting like apparent strains in the particle and limited crystal size. Modelling peak breadth and separating different broadening contributions to each Bragg peak necessitated several Bragg peaks increasing the refinement range.

3) Rietveld refinement of static displacements in the form of apparent microstrains for energy-minimized gold nanospheres were strongly dependent on the refinement range. Short refinement range including only 2-3 Bragg peaks resulted in large apparent microstrains which decreased with increasing refinement range. Refinement range was especially critical for the smallest nanocrystal which was affected by the largest amount of surface reconstruction and associated static atom displacements. Unfortunately, we did not have analytical formulations to predict the true values of static displacements hence we could not infer the accuracy of the values obtained from Rietveld refinement in this case. However, for 30 nm nanocrystals, the refined microstrains approached a value which was 20% of what was considered typical for unstressed regular crystalline powders measured at room temperature. For all nanocrystal sizes, a refinement range beyond 55° was found sufficient to obtain stabilized values for refined microstrains.

These results show that for gold nanocrystals having an average size of 30 nm and above, the diffraction data must be collected with a step size less than $\approx 0.2^\circ$ to avoid large fluctuations in the Rietveld-refined crystallographic parameters. This step size is consistent with past work as well(33). For smaller nanocrystals, the largest step size resulting in stable crystallographic parameters from Rietveld refinement is expected to be larger than 0.2° . For highest accuracy in refined lattice parameters and crystal sizes, selecting as wide of a refinement range as possible is suggested. Although this sounds somewhat contrary to the claims by Uvarov reporting no appreciable difference in refined lattice parameters and crystal sizes (23) with increased refinement range, the minimum refinement range selected in that work was 60° , the smallest particle size of samples measured was 10 nm, most of the studied samples were of mixed phase and the Rietveld analysis was performed on measured diffraction data necessitating several more parameters to be simultaneously refined, including background scattering. Therefore, it is unclear whether some of the nanoscale features we observed in our analytical diffraction data were observable in their measurements. Finally, nanocrystal shape has a significant effect on the performance of Rietveld refinement of nanocrystalline powders. However, these effects are expected to be less severe in the analysis of diffraction data measured from realistic powders consisting of a distribution of particle sizes and shape. In that case, the results would be more biased towards the larger particle and its shape.

6. ACKNOWLEDGMENTS

We thank to Mr. Merdan Batyrow for performing Molecular Dynamics simulations to generate energy-minimized models of gold nanospheres and reviewing our manuscript. This research was funded by the Turkish Scientific and Technological Research Council (TUBİTAK) under the BİDEB 2232 program (Project no: 118C268).

7. SUPPORTING INFORMATION

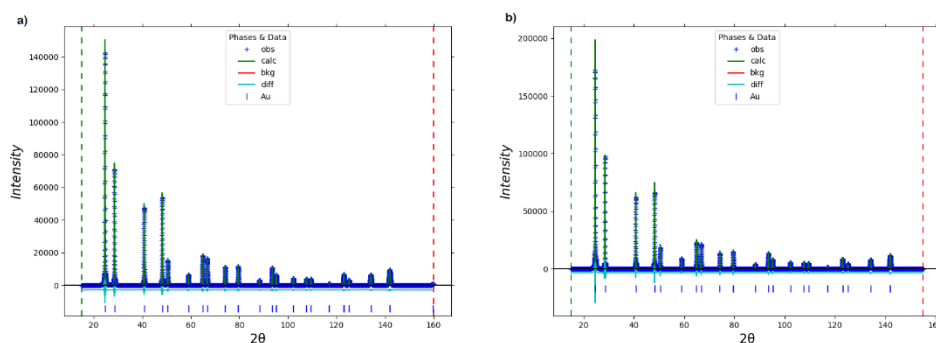


Figure S1: A successful Rietveld refinement of the diffraction data from a 30 nm ideal crystalline nanosphere (left) and a 30 nm ideal crystalline nanocube. The blue tick marks show the expected positions of the Bragg peaks predicted by Bragg's law.

REFERENCES

1. Rietveld HM. A profile refinement method for nuclear and magnetic structures. *J Appl Crystallogr* [Internet]. 1969 Jun 2;2(2):65–71. Available from: [<URL>](#).
2. Cullity BD. *Elements of X-ray Diffraction*. Addison-Wesley Publishing Company; 1978.
3. Ingham B. X-ray scattering characterisation of nanoparticles. *Crystallogr Rev* [Internet]. 2015 Oct 2;21(4):229–303. Available from: [<URL>](#).

4. Öztürk H, Yan H, Hill JP, Noyan IC. Sampling statistics of diffraction from nanoparticle powder aggregates. *J Appl Crystallogr* [Internet]. 2014 Jun 1;47(3):1016–25. Available from: [<URL>](#).
5. Öztürk H, Yan H, Hill JP, Noyan IC. Correlating sampling and intensity statistics in nanoparticle diffraction experiments. *J Appl Crystallogr* [Internet]. 2015 Aug 1;48(4):1212–27. Available from: [<URL>](#).
6. Fewster PF. A new theory for X-ray diffraction. *Acta Crystallogr Sect A Found Adv* [Internet]. 2014 May 1;70(3):257–82. Available from: [<URL>](#).
7. Xiong S, Öztürk H, Lee SY, Mooney PM, Noyan IC. The nanodiffraction problem. *J Appl Crystallogr* [Internet]. 2018 Aug 1;51(4):1102–15. Available from: [<URL>](#).
8. Warren BE. *X-ray Diffraction*. New York: Dover Publications; 1990.
9. Larson AC, Von Dreele RB. GSAS General Structure Analysis System [Internet]. Available from: [<URL>](#).
10. McCusker LB, Von Dreele RB, Cox DE, Louër D, Scardi P. Rietveld refinement guidelines. *J Appl Crystallogr* [Internet]. 1999 Feb 1;32(1):36–50. Available from: <https://scripts.iucr.org/cgi-bin/paper?S0021889898009856>
11. Young RA. The Rietveld Method. *Powder Diffraction* [Internet]. 1993 Dec 10;8(4):252–4. Available from: [<URL>](#).
12. Xiong S, Lee SY, Noyan IC. Average and local strain fields in nanocrystals. *J Appl Crystallogr* [Internet]. 2019 Apr 1;52(2):262–73. Available from: [<URL>](#).
13. Baloochiyan A, Batyrow M, Öztürk H. Accuracy Limits of Pair Distribution Function Analysis in Structural Characterization of Nanocrystalline Powders by X-ray Diffraction. *J Turkish Chem Soc Sect A Chem* [Internet]. 2022 May 31;9(2):527–44. Available from: [<URL>](#).
14. Batyrow M, Eruçar İ, Öztürk H. Size dependent change of mean square displacement in gold nanocrystals: A molecular dynamics simulation. *Concurr Comput Pract Exp* [Internet]. 2023 Nov 12;35(24):e7566. Available from: [<URL>](#).
15. Debye P. Zerstreung von Röntgenstrahlen. *Ann Phys* [Internet]. 1915 Jan 14;351(6):809–23. Available from: [<URL>](#).
16. Warren BE. *X-Ray Diffraction*. Dover Publications; 2012.
17. Alexander L, Klug HP, Kummer E. Statistical Factors Affecting the Intensity of X-Rays Diffracted by Crystalline Powders. *J Appl Phys* [Internet]. 1948 Aug 1;19(8):742–53. Available from: [<URL>](#).
18. Debyer. Debyer documentation [Internet]. [cited 2024 Jun 10]. Available from: [<URL>](#).
19. Toby BH, Von Dreele RB. GSAS-II: the genesis of a modern open-source all purpose crystallography software package. *J Appl Crystallogr* [Internet]. 2013 Apr 1;46(2):544–9. Available from: [<URL>](#).
20. Williamson G., Hall W. X-ray line broadening from filed aluminium and wolfram. *Acta Metall* [Internet]. 1953 Jan;1(1):22–31. Available from: [<URL>](#).
21. Scherrer P. Bestimmung der inneren Struktur und der Größe von Kolloidteilchen mittels Röntgenstrahlen. In: *Kolloidchemie Ein Lehrbuch* [Internet]. Berlin, Heidelberg: Springer Berlin Heidelberg; 1912. p. 387–409. Available from: [<URL>](#).
22. Stephens PW. Phenomenological model of anisotropic peak broadening in powder diffraction. *J Appl Crystallogr* [Internet]. 1999 Apr 1;32(2):281–9. Available from: [<URL>](#).
23. Uvarov V. The influence of X-ray diffraction pattern angular range on Rietveld refinement results used for quantitative analysis, crystallite size calculation and unit-cell parameter refinement. *J Appl Crystallogr* [Internet]. 2019 Apr 1;52(2):252–61. Available from: [<URL>](#).
24. Ungár T. Microstructural parameters from X-ray diffraction peak broadening. *Scr Mater* [Internet]. 2004 Oct;51(8):777–81. Available from: [<URL>](#).
25. Rebuffi L, Sánchez del Río M, Busetto E, Scardi P. Understanding the instrumental profile of synchrotron radiation X-ray powder diffraction beamlines. *J Synchrotron Radiat* [Internet]. 2017 May 1;24(3):622–35. Available from: [<URL>](#).
26. Yager KG, Majewski PW. Metrics of graininess: robust quantification of grain count from the non-uniformity of scattering rings. *J Appl Crystallogr* [Internet]. 2014 Dec 1;47(6):1855–65. Available from: [<URL>](#).
27. Herklotz M, Scheiba F, Hinterstein M, Nikolowski K, Knapp M, Dippel AC, et al. Advances in in situ powder diffraction of battery materials: a case study of the new beamline P02.1 at DESY, Hamburg. *J Appl Crystallogr* [Internet]. 2013 Aug 1;46(4):1117–27. Available from: [<URL>](#).
28. Smilgies DM. Scherrer grain-size analysis adapted to grazing-incidence scattering with area detectors. *J Appl Crystallogr* [Internet]. 2009 Dec 1;42(6):1030–4. Available from: [<URL>](#).
29. Patterson AL. The Scherrer Formula for X-Ray Particle Size Determination. *Phys Rev* [Internet]. 1939 Nov 15;56(10):978–82. Available from: [<URL>](#).
30. Noyan İC, Öztürk H. Lower uncertainty bounds of diffraction-based nanoparticle sizes. *J Appl Crystallogr* [Internet]. 2022 Jun 1;55(3):455–70. Available from: [<URL>](#).



Residues from The Mishraq Sulfur Mine and The Nano-Sulfur Derived from Them as Modifiers for The Mechanical and Thermal Properties of Iraqi Asphalt

Saad Salih Ahmed^{1*} , Ammar Ahmed Hamdoon² , Mote`a O. Abdulla³ 

¹Nineveh Education Direstorate Ministry of Education, Mosul, 41001, Iraq.

²Department of Chemistry, College of Education for Pure Sciences, University of Mosul, 41001, Mosul, Iraq.

³Mishraq Sulfur State Company, Ministry of Industry and Minerals-Iraq, 41001, Mosul, Iraq.

Abstract: This study included the modification of asphalt using sulfur waste (foam) resulting from the purification of sulfur from the Al-Mishraq field through a chemical oxidation method. In addition, it utilized nano sulfur prepared from these wastes in the modification of asphalt. The study initiated with a comprehensive analysis of foam composition and employed various diagnostic techniques. It then proceeded to prepare calcium polysulfide, sodium polysulfide and potassium polysulfide from the foam, followed by the preparation of nano_sulfur from these salts. The sulfur's nano-sized particles were characterized using scanning electron microscopy (SEM) and energy-dispersive X-ray spectroscopy (EDX) to determine sulfur content, and the particle size range was (83.40nm), (45.13nm) and (38.51nm). The prepared nano-sulfur was used to modify the properties of Iraqi asphalt. The original and modified asphalt's rheological properties were determined by measuring properties such as Ductility, softening point, penetration, penetration index, Marshall stability, chemical immersion, and aging. The modified asphalt showed rheological properties that qualified it for use in paving operations, especially in terms of resistance to acid rain and stability.

Keywords: Asphalt, Nano_sulfur, Foam, Polysulfide.

Submitted: November 4, 2023. **Accepted:** May 19, 2024.

Cite this: Ahmed SS, Hamdoon AA, Abdulla MO. Residues from The Mishraq Sulfur Mine and The Nano_Sulfur Derived from Them as Modifiers for The Mechanical and Thermal Properties of Iraqi Asphalt. JOTCSA. 2024;11(3): 1055-64.

DOI: <https://doi.org/10.18596/jotcsa.1386031>

***Corresponding author's E-mail:** saad.21esp4@student.uomosul.edu.iq

1. INTRODUCTION

Asphalt is a complex mixture of various hydrocarbon compounds with high molecular weights, in addition to containing atoms of sulfur, oxygen, and nitrogen (1,2). Asphalt is widely used in road paving due to its high adhesion to different metals and its viscosity property, in addition to its low cost (3). Traditional asphalt mixtures can perform well in paving operations. However, in recent years with the growth of traffic volume, heavy loads, harsh weather conditions and economic cost, all of this has led to an increased demand to improve the mechanical properties of traditional asphalt materials by modification using various high-quality and more reliable additives (4-7). Referring to previous studies, there have been many recent studies that focused on modifying asphalt and improving its specifications using

various additives, including sulfur, by increasing the viscosity of asphalt binders, thus improving the adhesion of asphalt to aggregates and crushing. And resistance to aging (8-11).

(Al-Hadidy, 2023) (13) was able to use sulfur waste in asphalt mixtures, as the resulting binders were subjected to tests of penetration, ductility, softening point, absolute viscosity, modulus of elasticity, and durability. The study showed, in general, good results conforming to the standard specifications for Iraqi asphalt (12).

Abass and Hamdoon (2021) (12) used a mixture of synthetic polymer (EVA) and natural polymer (wood) to modify asphalt with the addition of 1% by weight of sulfur at a temperature of 180 degrees Celsius for one hour. The rheological properties of the modified samples were measured. The study

gave good results in the field of asphalt resistance to deformation processes (13).

Nguyen & Le studied the effect of sulfur on the performance of asphalt mixtures by investigating the engineering and morphological properties of sulfur-modified asphalt using various tests, scanning electron microscopy (SEM) was also used in addition to conducting Marshall stability testing and indirect tensile (IDT) testing to evaluate the resistance of sulfur-modified asphalt mixtures. This study found that sulfur-modified asphalt leads to significant improvements in the mechanical properties of asphalt and crack and fatigue resistance (14).

(Zhang, J., & Tan, Y) (15) studied the rheological properties of asphalt by adding sulfur and styrene-butadiene-styrene (SBS), The results showed an increase in compatibility between the additives and asphalt in addition to improved performance of asphalt after adding sulfur to SBS-modified asphalt (15).

Zhang et al, 2022 were able to use four percentages of sulfur (0%, 15%, 30%, 45%) by weight of the asphalt binder. It was noted from the results that adding sulfur at a low percentage, such as 15%, leads to softening of the asphalt binder (16).

Singh et al. (2020) (17) and his team were able to improve asphalt properties represented by penetration, viscosity, Ductility and increased aging resistance, as well as Marshall stability through the addition of sulfur to asphalt and its use in asphalt modification (17).

This study attempted to benefit from the wastes from sulfur refining in Al_Mishraq mine (Nineveh, Iraq) resulting from chemical treatment represented as (foam) in an attempt to produce asphalt with rheological properties suitable for the environmental conditions in our country Iraq – Nineveh.

2. EXPERIMENTAL SECTION

2.1. Preparing The Raw Material

The raw material used in this study, which consists of the foam material, was obtained from the Mishraq Sulfur mine (Mishraq Sulfur Company) in the form of gray powdered pellets.

2.2. Chemical Analysis

Numerous chemical analyses were conducted to determine the components of the Foam. The elemental sulfur content in sulfur wastes was estimated. Additionally, the sulfate ion percentage was determined in a solution containing calcium sulfate, sodium sulfate, and potassium sulfate according to standard methods (18,19).

2.3. Foam as Asphalt Modifier

A weight of 100 grams of asphalt with the specified properties in Table (1) was placed in an asphalt processing device. Various proportions of foam were added with continuous mixing, and the temperature

was gradually raised to the range of 170-180 °C. Mixing continued at this temperature for 60 minutes. Afterward, necessary measurements were conducted to determine the properties of the modified asphalt, including ductility (20), penetration (21), softening point (22), penetration index (23), Marshall test (24), stripping (25) and aging (26).

2.4. Preparing Calcium, Potassium, and Sodium Polysulfide Solutions from Foam

Given the high sulfur content in sulfur waste (Foam) according to the analyses conducted in section 2-2, these solutions can be prepared from it according to standard methods (27).

2.5. Preparing Nano-Sized Sulfur Powder

Nano sulfur powder was prepared in three ways as follows (27):

25 mL of sodium polysulfide solution was placed first, 25 mL of potassium polysulfide solution second, and 25 mL of potassium polysulfide solution third, Each addition alone in a beaker, and diluted hydrochloric acid was added with continuous stirring until the solution turned light yellow, The solution was then centrifuged at 4000 revolutions per minute for 30 minutes and washed thoroughly with distilled water to remove any sulfide ions. The resulting precipitate was dried and weighed. The models were then analyzed using (SEM), (EDX) and (XRD), and this precipitate represents nanoscale sulfur.

2.6. Nano-Sulfur as A Modifiers Materials for The Rheological Properties of Asphalt

The prepared nanosized sulfur was utilized in the asphalt modification process by taking 100 grams of asphalt. Various proportions of nanosized sulfur, obtained from the previous sections were added to the asphalt. The mixture was gradually heated with continuous stirring to a temperature range of 170-180 °C. It was then kept at this temperature for 60 minutes, Subsequently, the rheological properties were measured as outlined in section 2-3.

3. RESULTS AND DISCUSSION

The Mishraq mine is located 45 kilometers south of the city of Mosul on the western bank of the Tigris River. Sulfur is extracted from this field using the well-known Frasch method. Due to its geological nature, the sulfur contains approximately 1% of hydrocarbon materials, which are removed through chemical oxidation using concentrated sulfuric acid. This method produces solid sulfur compounds with a sulfur content of around 88%. To obtain asphalt with specifications suitable for road paving, resistance to various environmental conditions, and the ability to withstand heavy and repetitive loads, numerous researchers have explored the use of various additives to improve asphalt properties. Our study focused on utilizing locally available byproducts from the Sulfur Mashreq (foam) and its derived materials to modify asphalt and enhance its rheological characteristics. This was achieved through several steps.

3.1. Rheological Properties of Original Asphalt and The Paving Asphalt

The rheological properties of original asphalt and the paving asphalt were measured. Table 1 and 2 below shows the rheological properties for these two types of asphalt.

Table 1: Rheological properties of original asphalt.

Properties	Result
Ductility (cm)	+150
Penetration (100gm.5sec.25°C)	46.1
Softening point (°C)	50
Penetration index (PI)	-1.376

The rheological properties of the asphalt suitable for use in paving operations, in a way that suits the climate conditions of our country Iraq, were also determined according to the standard specifications shown in Table 2:

Table 2: Rheological Properties of paving Asphalt (23).

Properties	Range ASTM (23)
Ductility (cm)	≥100
Penetration (100gm.5sec.25°C)	40-50
Softening point (°C)	50-58
Penetration index (PI)	-2 _+2

3.2. Foam Components and Their Use in Improving Asphalt Properties

To know the components of the foam resulting from the purification of Mishraq sulfur in Iraq using the chemical oxidation method, we carried out chemical analyzes of this material and Table 3 shows the components of these residues (foam) according to the analyzes conducted.

Table 3: Components of the foam.

Parameters	Wt (%)
Free Sulfur	88.15
Bonded sulfur	2.58
Carbon	1.86
Acidity	1.53
Ash	2.23
Moisture	3.65

Also, energy dispersive X-ray spectroscopy (EDX) was used, which enables obtaining the composition or chemical analysis of the material as (EDX) technique provides the nature of the elements contained in the material and their percentages (28). Figure 1 shows the main elements in the foam.

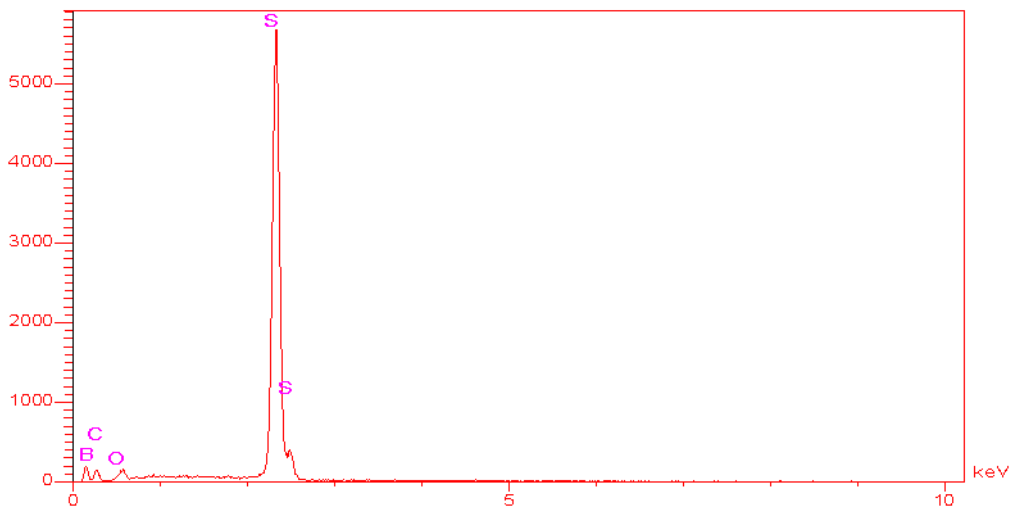


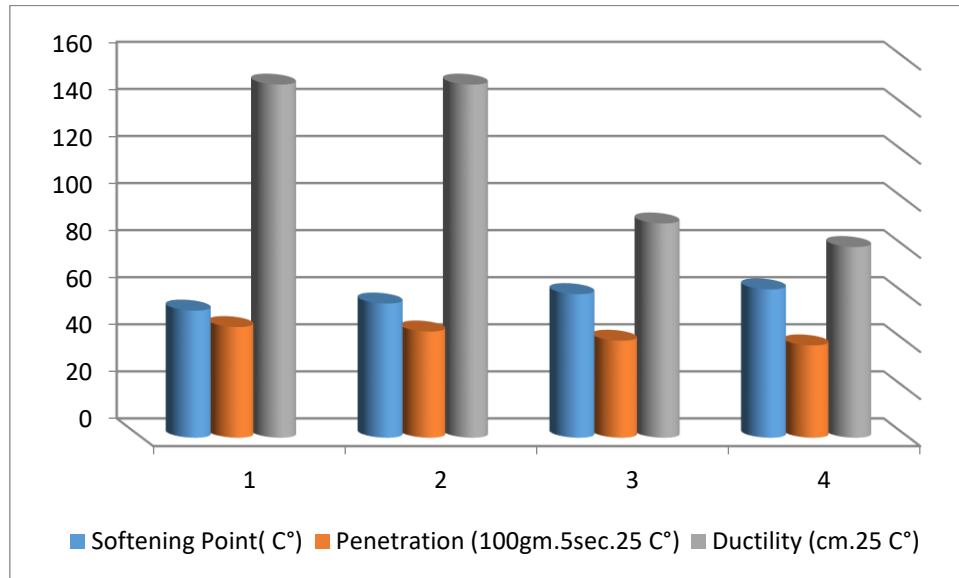
Figure 1: Energy dispersive X-ray spectroscopy (EDX) spectrum of the (foam).

Table 3 shows the results of the chemical analysis of the foam. Figure 1 represents the analysis using the energy dispersive X-ray spectrum (EDX) of the foam. Through the analyzes it is clear that the foam material consists mainly of sulfur with minor amounts of other elements. On this basis, this

material was used to modify asphalt at a temperature ranging between 170-180 °C for 60 minutes after determining the optimal conditions of temperature and time used in the modification process. Table 4 and Figure 2 illustrate the results obtained.

Table 4: The rheological properties of the asphalt modified by the foam.

Sample	Foam ratio %	Ductility (cm.25 °C)	Penetration (100gm.5sec.25°C)	Softening Point (°C)	Penetration index (PI)
AS1	0.5	+150	47	54	-0.391
AS2	1	+150	45.1	57	0.165+
AS3	1.5	91	41.2	61	+0.756
AS4	2	81	39.2	63	+1.016

**Figure 2:** The rheological properties of asphalt modified by the foam.

We note from Table 4 and Figure 2 that the rheological properties represented by Ductility, penetration and softening point were all within the standard Iraqi specifications at additions of 0.5% and 0.1% of the added material. The table also shows that the best addition ratio is 1%. At 1.5% addition, Ductility and softening point were observed to be outside the required specifications. At 2% percentage, all these properties were observed to be outside the standard specifications. Therefore, foam material can be used to improve the specifications of asphalt at the identified ratios and under the conditions identified for reaction temperature and specific time.

3.3. Prepared the Nano-Sulfur

Nano sulfur was prepared from the foam using three methods as outlined in section (2-5) of the experimental part. The prepared nano sulfur was then characterized using scanning electron microscopy (SEM) to determine the nanoscale sizes. Energy dispersive X-ray spectroscopy (EDX) was also used to determine the sulfur content.

3.3.1. Nano-Sulfur prepared from calcium polysulfide

Nano-sulfur was prepared from calcium polysulfide (CaS_x), as shown through (SEM) and (EDX) measurements.

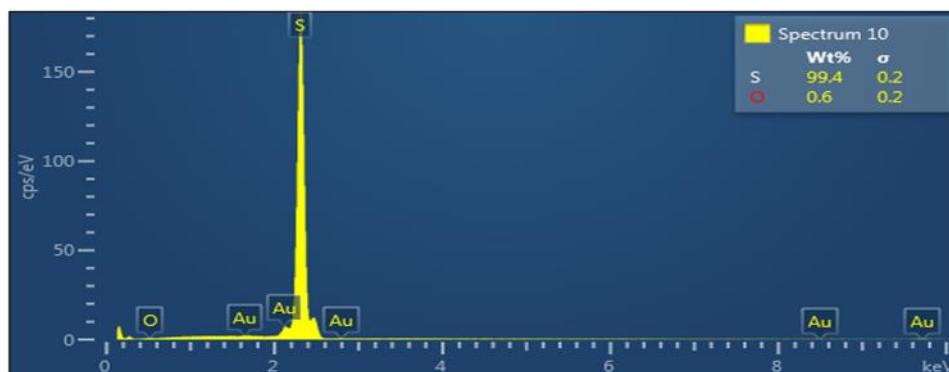
**Figure 3:** (EDX) spectrum for the nano-sulfur prepared from CaS_x.



Figure 4: (SEM) of the nano-sulfur prepared from CaSx.

We note from Figure 3, which represents the energy dispersive X-ray spectroscopy spectrum, and Figure 4, which represents the scanning electron microscope examination, that the nano sulfur prepared from potassium polysulfide was 99.4%, which is a high percentage indicating the purity of the prepared sulfur. The remaining 0.6% of oxygen represents moisture since hydrogen is not shown in this measurement (29). We also note from the

(SEM) measurement that the nanoscale size of sulfur was 83.40nm. To utilize the prepared nano sulfur in one of the industrial fields, it was used to modify asphalt under the same optimal conditions used to modify asphalt using the main material foam at a temperature of 170-180 °C for 60 minutes. Table 5 and Figure 5 illustrate the results obtained.

Table 5: The rheological properties of asphalt modified by nano-sulfur (83.40nm).

Sample	S-NP%	Ductility (cm.25 °C)	Penetration (100gm.5sec.25°C)	Softening Point (°C)	Tenetration index (PI)
AS5	0.5	+150	46.4	54	-0.421
AS6	1	+150	45.6	55	-0.238
AS7	1.5	+150	44.3	57	+0.190
AS8	2	135	39.3	61	+0.647

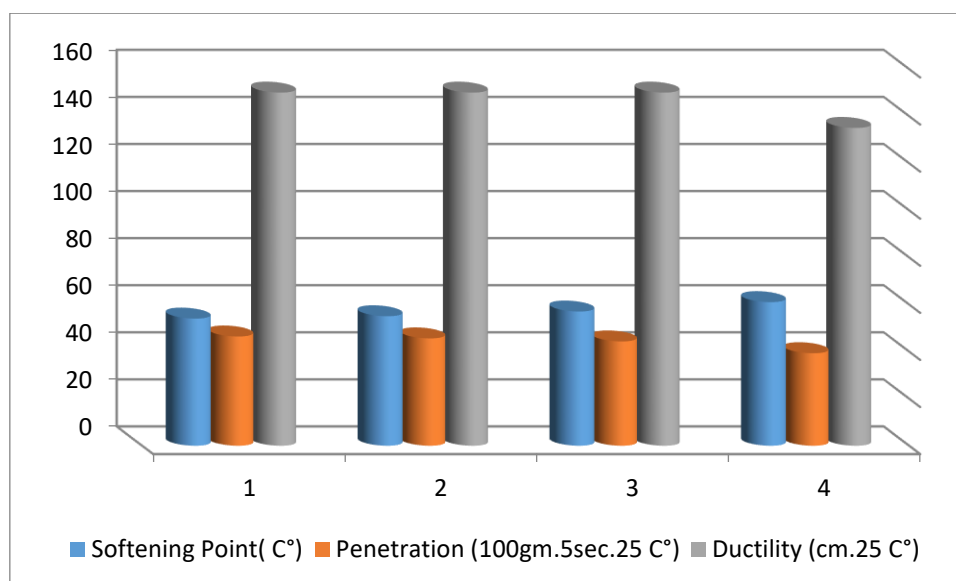


Figure 5: The rheological properties of asphalt modified by nano-sulfur (83.40nm).

From Table 5 and Figure 5, it can be observed that the ratios were satisfactory, except at the percentages of 2%, where the softening point was outside the desired specifications

3.3.2. Nano-Sulfur prepared from potassium polysulfide

Nano-sulfur was prepared from potassium polysulfide (K₂S_x), as indicated by (SEM) and (EDX) measurements shown in the following figures.

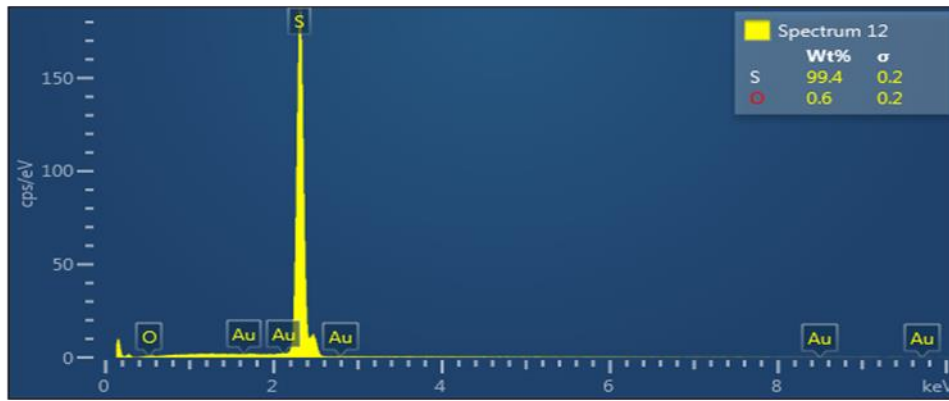


Figure 6: % (EDX) spectrum for the nano-sulfur prepared from K2SX.



Figure 7: (SEM) of the nano-sulfur prepared from K2SX.

From these measurements, it can be observed that the sulfur content is 99.4% and the size of the nano-sulfur is 45.13nm. Table 6 and Figure 8

illustrate the results of using this type of sulfur in asphalt modification.

Table 6: The rheological properties of asphalt modified with nano-sulfur (45.13nm).

Sample	S-NP%	Ductility (cm.25 °C)	Penetration (100gm.5sec.25 °C)	Softening Point (°C)	Penetration index (PI)
AS9	0.5	+150	47.1	53	-0.614
AS10	1	+150	45.8	55	-0.228
AS11	1.5	+150	43.4	57	+0.076
AS12	2	141	40.1	60	+0.501

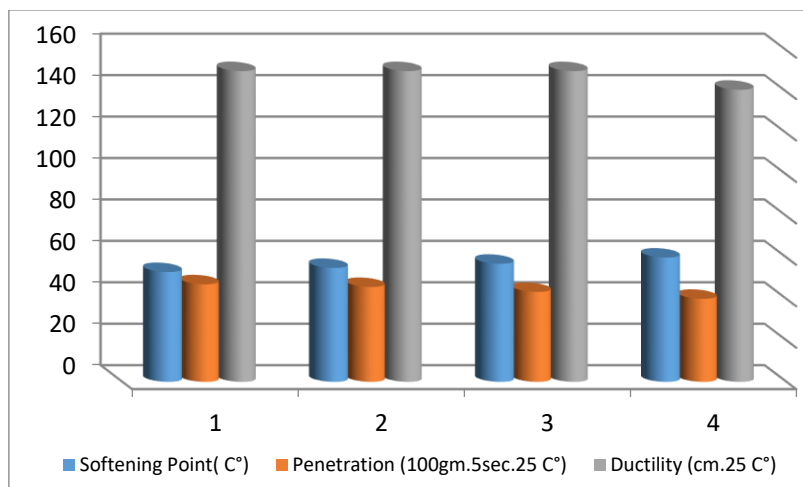


Figure 8: The rheological properties of asphalt modified by nano-sulfur (45.13nm).

3.3.3. Nano-Sulfur prepared from sodium polysulfide

Nano-sulfur was prepared from sodium polysulfide (NaS_x), as indicated by SEM and EDX measurements shown in the following figures.

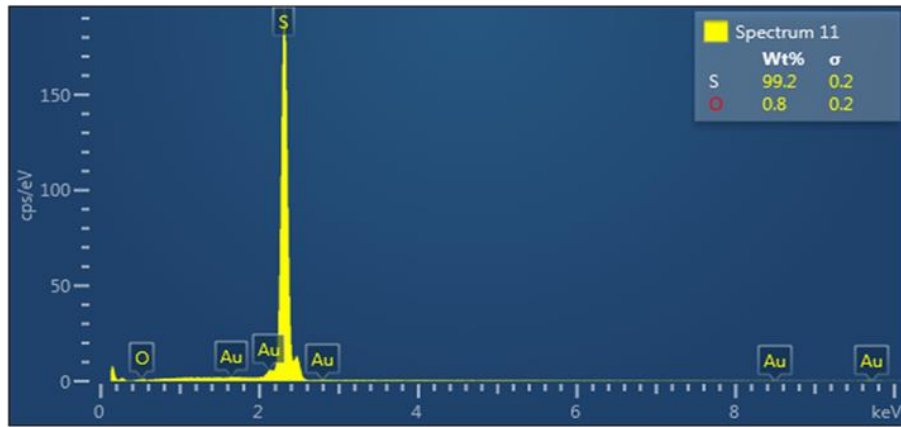


Figure 9: (EDX) spectrum for the nano-sulfur prepared from Na₂S_x.



Figure 10: (SEM) examination of the nano-sulfur prepared from Na₂S_x.

Through these figures, it can be observed that the nano-sulfur prepared from sodium polysulfide has a sulfur content ratio of 99.2%, indicating high purity of the prepared sulfur. Additionally, the nano-sulfur has a size of 38.51nm for the purpose of comparing

the effects of different nano-sized particles, this prepared nano-sulfur was used in asphalt modification. Table 7 and Figure 11 illustrate the results obtained.

Table 7: The rheological properties of asphalt modified with nano-sulfur (38.51nm).

Sample	S-NP%	Ductility (cm.25 °C)	Penetration (100gm.5sec.25 °C)	Softening Point (°C)	Penetration index (PI)
AS13	0.5	+150	47.3	53	-0.604
AS14	1	+150	46.6	54	-0.411
AS15	1.5	+150	45.3	56	-0.036
AS16	2	145	42.6	59	+0.442

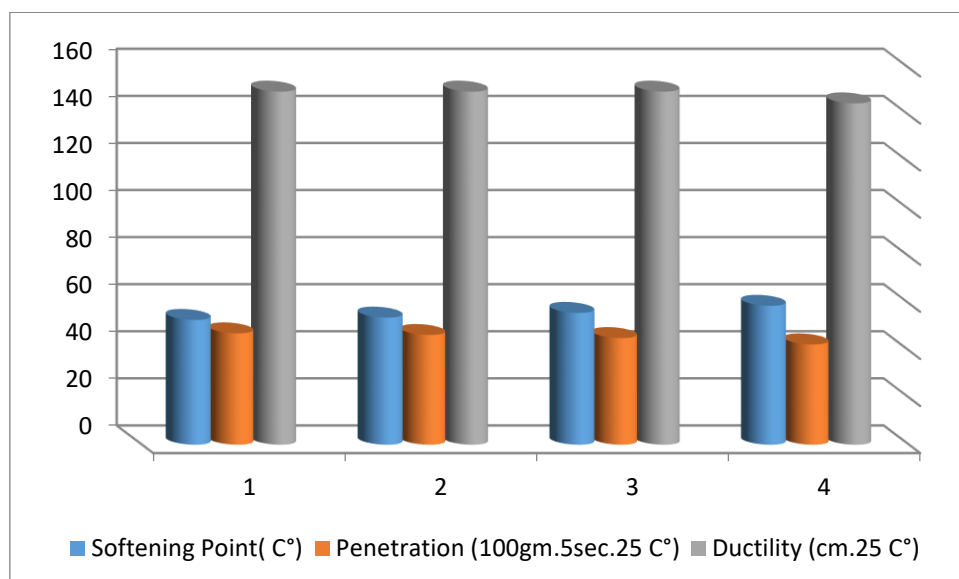


Figure 11: The rheological properties of asphalt modified by nano-sulfur (38.51nm).

We note from the results obtained from asphalt modification using different nanoscale sizes that good models were obtained that can be used in asphalt paving according to the rheological properties measured. We also note that nano sulfur of 38.51nm gave the best results, as it was observed from the results that all ratios of the additive (0.5, 1, 1.5, 2)% were within the standard specifications for asphalt used in paving. Next was nano sulfur of 45.13nm, although at a 2% additive ratio, the softening point and penetration were at the minimum properties As for nano sulfur of 83.40nm, the results showed that at a 2% additive ratio, the softening point and penetration were outside the standard specifications, along with a decrease in Ductility. By observing the results, it can be said that the smaller the nanoscale size of sulfur, the better results it gives for modifying asphalt properties. The ratio of the additive with the smaller size can also be increased as a result of greater dispersion and interaction of nanoscale particles with the asphalt.

To confirm the success of these asphalt models in paving roads and withstanding repeated traffic loads as well as resisting environmental conditions, acid rain and time degradation, four well-modified model samples represented by AS14, AS2, AS6, and AS11 were selected and subjected to Marshall testing, chemical immersion testing, and aging testing in addition to measuring the properties of the original asphalt to determine the suitability of these models for road paving works.

The Marshall Stability and Flow values are determined from this test and the Marshall Quotient is calculated by dividing the Marshall Stability by the Flow value (30). Table 8 illustrates the stability and flow values for the tested samples compared to the original model and according to the specifications of the Iraqi Public Works Department (S.C.R.B) inimum limit of the standard specifications for asphalt used in paving.

Table 8: The stability and flow values for the original asphalt, modified asphalt, and the specifications of the Iraqi Roads and Bridges Authority (S.C.R.B).

Sample No	Asphalt (%)	Marshall Test		
		Stability (KN)	Flow (mm)	MQ
AS0		10.7	5.2	2.05
AS2	4.5	14.3	2.9	4.93
AS6		15.2	3.0	5.06
AS10		16.2	3.1	5.22
AS15		16.6	3.0	5.53
AS**		7 Minm.	2-4	3.5 Minm.

AS* the specifications of the Iraqi Roads and Bridges Authority

It is evident from Table 8 above that all the modified models are better than the original model if used as paving asphalt. The MQ value of the modified models can also be observed to be higher than the MQ value of the original asphalt. We also note that asphalt modified with nano sulfur of 38.51 nm has the best stability value. Therefore, the modified models would be more resistant to permanent deformation and repeated loads than the original asphalt.

To determine the resistance of the asphalt after mixing with aggregates to acid rain and high temperatures, the same samples that underwent Marshall testing were subjected to chemical immersion (stripping) testing and compared to the basic model. Table 9 illustrates the stripping results of the original asphalt (AS0) and the modified models from aggregates after chemical immersion.

Table 9: Chemical Immersion.

No. of modified sample	Percentage of Na ₂ CO _{3gm}	R&WNO	R&WNO for the original asphalt	R&WNO for the modified samples
	0.025	1		
	0.041	2		
AS0	0.082	3	3	
	0.164	4		
AS2, AS6	0.328	5		5
AS10	0.656	6		6
AS15	1.312	7		7
	2.624	8		

We note from Table 9 and the stripping values (the amount of sodium carbonate at which asphalt began to strip or separate from aggregates), that the modified models began stripping at a higher amount of sodium carbonate compared to the original

asphalt. Number (1) refers to the amount of sodium carbonate which is 0.025 grams in 50 mL of distilled water, and number (8) refers to the highest amount of sodium carbonate which is 2.624 grams. Possessing higher stripping values enables the

modified asphalt to better adhere to aggregates compared to the original asphalt, providing greater resistance to acid rain and high temperatures.

To determine the resistance of the prepared asphalt models to environmental conditions and aging over time, aging testing was conducted on both the original model (AS0) and the well-selected modified models chosen for testing. The testing was conducted according to standard specifications as shown in Table 10.

We note from Table 10, which represents aging test results, that the effect of aging conditions such as

heat and oxidation on the rheological properties of the modified asphalt models was less than the effect on the original asphalt. This indicates that the modified asphalt models are characterized by great resistance to environmental conditions, aging over time and stress processes. This is a positive aspect of modification. The modified asphalt models showed less change and degradation of rheological properties compared to the original asphalt when subjected to aging testing, indicating higher resistance to aging factors such as heat and oxidation.

Table 10: Aging testing.

Sample no.	Rheological properties	Before test	After test
AS0	Ductility cm. 25 °C	+150	+150
	Penetration (100gm.5sec.25°C)	46.1	42.2
	Softening point (°C)	50	53
AS2	Ductility cm. 25°C	+150	+150
	Penetration (100gm.5sec.25°C)	45	44.6
	Softening point (°C)	57	58
AS6	Ductility cm. 25 °C	+150	+150
	Penetration (100gm.5sec.25°C)	45.6	45.1
	Softening point (°C)	55	53
AS10	Ductility cm. 25 °C	+150	+150
	Penetration (100gm.5sec.25°C)	45.8	45.4
	Softening point (°C)	55	54
AS15	Ductility cm. 25°C	+150	+150
	Penetration (100gm.5sec.25°C)	45.3	45.1
	Softening point (°C)	56	55

4. CONCLUSION

- 1- The solid sulfur materials (Foam) resulting from the chemical purification method of sulfur in the General Company for Sulfur in Al-Mishraq contain a high percentage of elemental sulfur that can be utilized in various fields
- 2- The possibility of preparing calcium sulfide, potassium polysulfide, and calcium polysulfide solutions from sulfur waste materials as a raw material.
- 3- Preparation of nano-sized sulfur powder with varying nano-scale dimensions.
- 4- Using sulfur wastes materials (Foam) and the nano sulfur prepared from these wastes materials in modifying asphalt and improving its rheological properties.
- 5- Improvement of the rheological properties of asphalt is more pronounced as the nano-sulfur particle size decreases.
- 6- Obtaining good asphalt samples that can be used in road paving due to their ability to resist various environmental conditions, including repeated loads, acid rain, and aging, as evidenced by Marshall testing, chemical immersion, and aging tests.

5. CONFLICT OF INTEREST

There are no conflicts of interest.

6. ACKNOWLEDGMENTS

Upon the completion of this work, we express our sincere gratitude to both the University of Mosul, College of Education for Pure Sciences, Department of Chemistry, and the General Company for Sulfur in Al-Mishraq for their invaluable assistance and support throughout the research process.

7. REFERENCES

1. Redelius P, Soenen H. Relation between bitumen chemistry and performance. Fuel [Internet]. 2015 Jan;140:34–43. Available from: [<URL>](#).
2. Read J, Whiteoak D. The shell bitumen handbook [Internet]. Thomas Telford Publishing; 2003. Available from: [<URL>](#).
3. Vargas X, Afanasjeva N, Alvarez M, Marchal P, Choplin L. Asphalt rheology evolution through thermo-oxidation (aging) in a rheo-reactor. Fuel [Internet]. 2008 Oct;87(13–14):3018–23. Available from: [<URL>](#).
4. Mohammed M, Parry T, Thom N, Grenfell J. Microstructure and mechanical properties of fibre reinforced asphalt mixtures. Constr Build Mater [Internet]. 2020 Apr;240:117932. Available from: [<URL>](#).
5. Shen J, Amirhanian S, Xiao F, Tang B. Influence of surface area and size of crumb rubber on high temperature properties of crumb rubber modified binders.

- Constr Build Mater [Internet]. 2009 Jan;23(1):304–10. Available from: [<URL>](#).
6. Allam A, Elfateh A, Shafeq M, Abdo M. Effects of different additives on the behavior of asphalt. In: The International Undergraduate Research Conference [Internet]. The Military Technical College; 2022. p. 1–4. Available from: [<URL>](#).
7. Owaid K, Hamdoon A, Matti R, Saleh M, Abdelzaher M. Waste Polymer and Lubricating Oil Used as Asphalt Rheological Modifiers. *Materials (Basel)* [Internet]. 2022 May 24;15(11):3744. Available from: [<URL>](#).
8. Li R, Xiao F, Amirkhanian S, You Z, Huang J. Developments of nano materials and technologies on asphalt materials – A review. *Constr Build Mater* [Internet]. 2017 Jul;143:633–48. Available from: [<URL>](#).
9. Shah PM, Mir MS. Application of nanotechnology in pavement engineering: a review. *Can J Civ Eng* [Internet]. 2020 Sep;47(9):1037–45. Available from: [<URL>](#).
10. Fang C, Yu R, Liu S, Li Y. Nanomaterials Applied in Asphalt Modification: A Review. *J Mater Sci Technol* [Internet]. 2013 Jul;29(7):589–94. Available from: [<URL>](#).
11. Zeng L, Xiao L, Zhang J, Fu H. The Role of Nanotechnology in Subgrade and Pavement Engineering: A Review. *J Nanosci Nanotechnol* [Internet]. 2020 Aug 1;20(8):4607–18. Available from: [<URL>](#).
12. Abass MF, Hamdoon AA. Studying the effect of using a mixture (synthetic polymer: natural polymer) on the rheological properties of asphalt. *J Phys Conf Ser* [Internet]. 2021 Sep 1;1999(1):012143. Available from: [<URL>](#).
13. Al-Hadidy AI. Sustainable Recycling of Sulfur Waste Through Utilization in Asphalt Paving Applications. *Int J Pavement Res Technol* [Internet]. 2023 Mar 2;16(2):474–86. Available from: [<URL>](#).
14. Nguyen VH, Le VP. Performance evaluation of sulfur as alternative binder additive for asphalt mixtures. *Int J Pavement Res Technol* [Internet]. 2019 Jul 19;12(4):380–7. Available from: [<URL>](#).
15. Zhang J, Tan Y. Rheology, morphology and phase behavior of SBS/sulfur modified asphalt based on experimental assessment and molecular dynamics. *Int J Pavement Eng* [Internet]. 2023 Jan 28;24(2):2159029. Available from: [<URL>](#).
16. Hatif Z, Al-Hdabi A, Nageim H Al. Effect of adding nano clay on asphalt characteristics. In 2023. p. 060020. Available from: [<URL>](#).
17. Singh M, Jain K, Kahlon SS. Use of Sulphur as an Additive in Bitumen: A Review. *Int Res J Eng Technol* [Internet]. 2020;7(10):36–43. Available from: [<URL>](#).
18. Williams WJ. *Handbook of Anion Determination* [Internet]. Butterworth & Co(publisher) Ltd.; 1979. Available from: [<URL>](#).
19. Shareef SS, Halo TA, Abdulla MO. Recovery of Sulfur from the Residues of the Chemical Method for the Purification of Sulfur from the Farsch Mine in the Al-Mishraq Mine. *Iraqi J Ind Res* [Internet]. 2023 Jun 14;10(1):15–25. Available from: [<URL>](#).
20. Hussein A, Hamdoon A, Ahmed S, Mubarak H, Saleh M. Study of the effect of adding a blend of (ethylene vinyl acetate: styrene butadiene rubber) on the rheological properties of asphaltic materials. *Egypt J Chem* [Internet]. 2022 Mar 6;65(11):395–406. Available from: [<URL>](#).
21. Bustillo Revuelta M. *Construction Materials* [Internet]. Cham: Springer International Publishing; 2021. (Springer Textbooks in Earth Sciences, Geography and Environment). Available from: [<URL>](#).
22. Al-Mohammed M, Al-Hadidy A. Durability and Rutting Resistance of SBS-Modified Asphalt Mixtures Containing Blowdown as a Sustainable Filler. *Al-Rafidain Eng J* [Internet]. 2023 Sep 1;28(2):48–57. Available from: [<URL>](#).
23. Çetin M. Pavement design with porous asphalt [Internet]. 2013. Available from: [<URL>](#).
24. ASTM. D1559-89 - Test method for resistance of plastic flow of bituminous mixtures using Marshall apparatus. *Annual Book of Astm Standards*. Philadelphia PA: American Society for Testing and Materials, America [Internet]. 1998. Available from: [<URL>](#).
25. Speight JG. *Asphalt Materials Science and Technology* [Internet]. 2016. Available from: [<URL>](#).
26. ASTM. D 1754–97 Standard Test Method for Effects of Heat and Air on Asphaltic Materials (Thin-Film Oven Test) 1 [Internet]. 2002. Available from: [<URL>](#).
27. Brauer G, editor. *Handbook of Preparative Inorganic Chemistry* [Internet]. London: Academic Press Inc.; 1963. Available from: [<URL>](#).
28. Scimeca M, Bischetti S, Lamsira HK, Bonfiglio R, Bonanno E. Energy Dispersive X-ray (EDX) microanalysis: A powerful tool in biomedical research and diagnosis. *Eur J Histochem* [Internet]. 2018 Mar 15;62(1):89–99. Available from: [<URL>](#).
29. Lyman CE, Newbury DE, Goldstein JI, Williams DB, Romig AD, Armstrong JT, et al. *Scanning Electron Microscopy and X-Ray Microanalysis* [Internet]. Microscopy and Microanalysis. Plenum Press; 1990. Available from: [<URL>](#).
30. Zoorob SE, Suparma LB. Laboratory design and investigation of the properties of continuously graded Asphaltic concrete containing recycled plastics aggregate replacement (Plastiphalt). *Cem Concr Compos* [Internet]. 2000 Jan;22(4):233–42. Available from: [<URL>](#).



Isolation of Bioactive Compounds in *Allanblackia floribunda* Fruit and The Molecular Docking of The Compounds Against SARS-CoV-2 Variants

Abimbola Deola Olanipekun^{1*} , Francis Jide Faleye², Ibiyinka Ogunlade², O. I. Akinwumi², T. Esan¹

¹Bamidele Olumilua University of Education, Science and Technology, Ikere Ekiti, Nigeria.

²Department of Chemistry, Ekiti State University, Ekiti State University, Ado-Ekiti, Nigeria.

Abstract: Compounds were isolated from the seed of *Allanblackia floribunda* using biologically guided chromatographic methods. Garcinia bioflavonoid (GB-1a and GB-2a), microdiplosone, and malic acid were isolated from the seed, pulp, and peel of the fruit. These compounds, even though they are known compounds previously isolated from another member of the Clusiaceae family, have not been isolated from *Allanblackia floribunda*. The structural elucidation of isolated compounds was done using IR, ¹HNMR, ¹³C NMR, and MS spectroscopy. The molecular docking studies of compounds with SARS-CoV-2 variants (6M0J), omicron 2 (7T9L), and 6LU7 and subsequent comparison with molnupiravir and remdesivir known medications for SARS-CoV-2 showed that GB1a and GB2a had docking scores of -8.3 and -8.6 respectively which was close to that of molnupiravir (-8.3) but greater than that of remdesivir (-7.6). At the same time, that of microdiplodiasone and malic acid were lower than that of the two drugs. Also, GB1a and GB2a had better docking scores when docked with omicron 2 (7T9L) and 6LU7 than the reference ligands. These suggest that the compounds can be investigated further for the development of active drugs against SARS-CoV-2.

Keywords: *Allanblackia floribunda*, Garcinia bioflavonoids, SARS-CoV-2.

Submitted: November 20, 2023. **Accepted:** June 3, 2024.

Cite this: Olanipekun AD, Faleye FJ, Ogunlade I, Akinwumi OI, Esan T. Isolation of Bioactive Compounds in *Allanblackia floribunda* Fruit and The Molecular Docking of The Compounds Against SARS-CoV-2 Variants. JOTCSA. 2024;11(3): 1065-72.

DOI: <https://doi.org/10.18596/jotcsa.1393491>

***Corresponding author's E-mail:** olanipekun.abimbola@bouesti.edu.ng

1. INTRODUCTION

Allanblackia, a genus of flowering plants in the Clusiaceae family, is predominantly found in tropical regions. This family has 14 genera and trees of about 600 species that belong to this family have been identified (1). The *Clusiaceae* family is a known source of important secondary metabolites, which includes xanthenes, coumarins, bioactive bioflavonoids, and some benzophenones, which are produced by the plants primarily for defense purposes are useful for several medicinal purposes in human (2-4).

Different parts of the plants have been investigated for their medicinal benefits, which were prompted by their local therapeutic uses. The bark is locally used against cough, dysentery, diarrhea, and toothache as an aphrodisiac and pain reliever. They are also known to have antihypertensive, anti-inflammatory, and hypoglycemic activities (5). The extracts are used to relieve smallpox, chicken pox, measles,

scrotal elephantiasis, asthma, and bronchitis (1, 6). To alleviate painful joints, the body can also be rubbed with the pounded bark of *Allanblackia floribunda* (7,8). The fruit components have high antioxidant activities, which has encouraged its use as nutraceuticals (9). The seed has high fat and carbohydrate content, which plays an important role in body metabolism; it is also rich in essential minerals, especially calcium and magnesium (10,11).

Chemical constituents previously isolated from *Allanblackia* include Garcinol, cambogin, guttiferone F, and allanxanthone A, which were obtained from *Allanblackia monticola* fruits (12). Xanthenedione (Allanxanthone C), garciniafuran, tovophyllin A, rubraxanthone, norcowin, mangostin, and stigmaterol were also isolated from its stem bark (13). Xanthone derivative named allanxanthone E was isolated and characterized through phytochemical investigations performed on the seeds together with seven known compounds: 1,7-

dihydroxy-3-methoxy-2-(3-methylbut-2-enyl)xanthone, α -mangostin, garciniafuran, allanxanthone C, and 1,6-dihydroxy-2,4-diprenylxanthone, friedelin and lupeol (13,14).

Benzophenones (hydrocotin, guttiferone F) and xanthones (1,3,5-trihydroxyxanthone and 4,5-dihydro-1,6,7-trihydroxy-4',4',5-trimethoxyfurano-[2,3;3,4] xanthone) were identified in the heartwood of *A. floribunda* and *A. stuhlmanni* as well as bioflavonoids such as Moreflavone and Volkensiflavone (15). Allanxanthone A, 1,5-dihydroxyxanthone, 1,5,6-trihydroxy-3,7-dimethoxyxanthone, stigmaterol and stigmasteryl-3-O- β -D-glucopyranoside were isolated from the stem bark of *A. floribunda* (16). Funkugiside, morelloflavone, volkensiflavone I, 7-dihydroxyxanthone, morelloflavone, and spicataside were also isolated from the stem bark and root (8).

Compounds useful as drugs to cure SARS-CoV-2, which posed a major challenge all over the world in the year 2020, have been investigated by scientists, especially because of the discovery of different variants. Molnupiravir and remdesivir are potential drugs that can be used to inhibit SARS-CoV-2. In-vivo and in-silico approaches have been used to ascertain its effectiveness as potential drugs (17-19). Their use as drugs has reduced hospitalization of patients (19).

Trials conducted using 304 cases showed that molnupiravir has the potential to effectively decrease the mortality rate in patients diagnosed with COVID-19 within the moderate limit (20).

Also, research to find out drugs that are potent targets of specific diseases has recently been enhanced using molecular docking studies against possible target proteins (21). Rutin, ritonavir, emetine, and some other compounds have been investigated for their possible potency against SARS-CoV-2 protease (PDB: 6Y84 using molecular docking study (22-23)). Some of these studies have provided positive outcomes that have brought about major advances in medicine and drug research.

The seed of *A. floribunda* is of great importance because of its seed oil, and no isolation has been reported from it. Therefore, in this work, the isolation and structural elucidation of four compounds were reported from the seed and their docking against different variants of SARS-CoV-2.

2. EXPERIMENTAL SECTION

2.1. Plant Material

A substantial amount of mature fruit from *Allanblackia floribunda* was harvested in a forest located at Igbara Odo Ekiti, situated in Ekiti State, Nigeria. Subsequently, this plant was authenticated and documented at the Department of Plant Science's herbarium unit at Ekiti State University with voucher number UHAE EPH 2:001.

2.2. Extraction and Isolation

The seeds, pulp, and the peel of the fruit were carefully separated, and the moisture content was removed by drying at room temperature for two weeks. The dried seed (3.60 kg) was milled using an electric blender (Marlex AC9829) and extracted with chloroform for three days in order to extract the oil content of the seed. The residue was further extracted using methanol for three days; the methanol extract was also decanted, filtered, and concentrated.

The methanol extracts of the seeds, due to their high antioxidant and microbial activity deduced from previous work, were fractionated using the column chromatography method. 80 g of the methanol extract of the seed was dissolved in methanol and adsorbed on silica gel (230-400 mesh), and the constituents were separated by column chromatography using 300 mL of the following solvents or solvent mixture in a step-wise gradient. In each case, the preceding solvent/solvent mixture was gradually enriched with the next solvents in the gradient. The solvent gradient was in the following order: *n*-hexane (100%), ethyl acetate in *n*-hexane (5, 10, 15, 20, 25...95%), ethyl acetate (100%), methanol in ethyl acetate (5, 10, 15, 20, 25...95%), and methanol (100%).

After being collected into test tubes, the fractions were evaluated using TLC analysis by spraying with vanillin-sulphuric acid. Those exhibiting similar R_f values were combined and resulted in a total of 32 dried fractions (labeled F1-F32). After passing through a mixture of EtOAc-*n*-hexane (90:10), F15 was subjected to column chromatography using silica gel and solvents, including *n*-hexane, ethyl acetate, and methanol, in the same manner. Similar fractions were combined, resulting in five (5) bulked fractions. TLC analysis revealed that some of these contained only one compound. Here, Compound I and compound II were obtained. F₂₁ eluted with the mixture of EtOAc-methanol (75:25) was further separated using *n*-hexane, ethyl acetate, and methanol. The eluent was collected in test tubes, after which similar fractions were combined and evaporated, from which Compound 3 was isolated.

The chromatographic purification process used for the seed was repeated to purify 80 g of the crude methanol extract obtained from *A. floribunda* fruit pulp. 368 fractions were collected, which were later combined based on the TLC analysis into 17 fractions. Subsequent column chromatography was carried out until the desired pure compounds were obtained. A white crystal (compound IV) was discovered from fractions 8 and 9, which was properly filtered out and washed using ethyl acetate.

2.3. Spectroscopic Analysis

The spectroscopic details of the isolated compounds were investigated using Bruker Platinum ATR mounted onto a Bruker Tensor 27 FT-IR spectrometer, Agilent technologies 1620 infinity series/Agilent quadrupole LCMS and the samples were run on Bruker 400MHz NMR spectrometer.

2.4. Plant Material *In silico* Analysis

2.4.1 Ligand preparation

The PubChem ID of the ligands (compounds 1- 4), molnupiravir, and remdesivir were obtained from PubChem. Chimera 1.14 was used to retrieve the structures based on their ID and subsequently save them in PDB format while minimizing optimal docking energy. Minimized compounds were uploaded to AutoDockTools-1.5.6 software, where the OpenBabel plugin was used for conversion into the PDBQT format.

2.4.2 Protein preparation

The crystal structures of required protein, SARS-CoV-2 main protease (Mpro: 6LU7), SARS-CoV-2 spike receptor-binding domain bound with ACE2 (6MOJ) and Cryo-EM structure of SARS-CoV-2 Omicron spike protein in complex with human ACE2 (7T9L) were obtained from the RCSB protein data bank (www.rcsb.org) in PDB format.

To prepare the structures, the PDB format of the proteins was uploaded to Chimera 1.14 workspace; after eliminating non-standard residues like ions, water, and bounded ligands from the protein structure, it underwent structural minimization via Chimera 1.14's editing wizard. The process involved taking 100 steepest descent steps with a size of Å=0.02 and then undergoing 10 conjugate gradient steps at a step size of Å=0.02 as well with an additional interval update every ten times; this was carried out in total. The Gasteiger force field was used to assign charges and Polar hydrogen bonds was incorporated. Then, the protonation state of histidine was set with AutoDockTools-1.5.6 software. Upon completion, PDB files of the modified protein were saved in PDBQT format before being uploaded for molecular docking analysis using PyRx software.

2.4.3 Molecular Docking

To conduct the molecular docking of proteins and ligands, AutoDock Vina in the PyRx were used. The grid space was established by focusing on significant amino acid residues that were chosen from UniProtKB. Grid box size, center (29.7237, 11.7994, 42.1527)Å and size (38.2112, 26.7617, 36.1823) Å, x, y and z respectively were set for Mpro 6LU7. Also, Grid box size, center (x -51.8334 Å, y -35.9153 Å and z 4.4678 Å) and size (x 69.4516, y 62.4510 and z 69.1699) were set for SARS-CoV-2 spike RBD (6MOJ) and SARS-CoV-2 spike RBD omicron variant (7TqL) Grid box size was set at center (x 226.1996 Å, y 176.1916 Å and z 236.6954 Å) and size (x 35.0793, y 42.4635 and z 67.3292).

3. RESULTS AND DISCUSSION

3.1. Structural Elucidation

3.1.1. Compound I

Compound I (GB-1a) is an amorphous yellow solid with a melting point of 200 °C. The IR showed absorption bands at 3187 cm⁻¹ and 1733 cm⁻¹ for a carbonyl group. The mass as revealed by the LC-MS is m/z 542 with molecular formula C₃₀H₂₂O₁₁, the fragmentation at m/z 541 [M⁺ - H], 415, 288, 261, 141, 113, 112. The H NMR spectrum showed C-5 (OH) signal at δ 2.01 (s, 1H) and other OH at 0.89 (

d, J = 7.0 Hz, 1H), also, there was a presence of doublets at δ 7.38 (d, J = 2.2 Hz, 1H), 7.09 (d, J = 8.6 Hz, 1H), 5.62 (d, J = 11.9 Hz, 1H), 5.49 (d, J = 9.8 Hz, 1H), 5.15 (d, J = 13.0 Hz, 1H), 4.59 (d, J = 11.1 Hz, 1H). This result is in close agreement with those reported by Jackson et al. (1971) (24) for GB-1a (Table 1). The ¹³C NMR (100 MHz, MeOD) showed signal at δ 197.52, 196.44, 166.56, 164.13, 163.42, 161.16, 157.24, 145.00, 130.42, 128.52, 121.69, 117.93, 115.61, 115.05, 114.39, 113.23, 112.79, 101.83, 101.24, 95.95, 94.88, 81.78, 79.16, 42.67 which is in agreement with those reported by Agrawal (1989) (25) (Table 2). Although this compound has been previously isolated from *Garcinia bsrchananir* and *Clusia columnaris* Engl, the isolation of GB-1a [(2S,2'R,3R)-5,5',7,7'-tetrahydroxy-2,2'-bis(4-hydroxyphenyl)-[3,8'-bichroman]-4,4'-dione] (1) from *A. floribunda* seed for the first time has been reported here.

3.1.2. Compound II

Compound II is an amorphous yellow solid with a melting point of 200 °C. The IR showed absorption bands of OH at 3185 and 1633 cm⁻¹ for a carbonyl group. The Mass, as revealed by the LC-MS, is m/z 298 with molecular formula C₁₄H₁₄O₆, the fragmentation at m/z, 261, 142, and 141. The ¹H NMR (400 MHz, MeOD) showed signal at δ 7.31 (s, 1H), 7.26 (d, J = 8.4 Hz, 1H), 7.11 (d, J = 8.3 Hz, 2H), 6.87 (d, J = 8.4 Hz, 1H), 6.65 (d, J = 7.4 Hz, 1H), 6.58 (d, J = 7.7 Hz, 1H), 6.52 (s, 1H), 6.43 (d, J = 8.3 Hz, 1H), 6.36 (s, 1H), 6.27 (s, 1H), 6.08 (s, 1H), 5.99 (d, J = 11.7 Hz, 1H), 5.74 (d, J = 11.9 Hz, 1H), 5.65 (d, J = 12.0 Hz, 1H), 4.09 (q, J = 7.1 Hz, 1H), 2.01 (s, 1H), 1.25 - 1.17 (m, 1H) (Table 3). The ¹³C NMR (100 MHz, MeOD) showed signal at δ 13C NMR (101 MHz, MeOD) δ 196.77, 182.44, 166.78, 164.31, 163.45, 149.47, 145.28, 127.89, 119.32, 114.25, 102.02, 98.56, 81.41, 13.09 (Table 4). The compound isolated was elucidated as microdiplodiasone[(R)-2-ethyl-5,7-dihydroxy-2-((R)-5-oxotetrahydrofuran-2-yl)chroman-4-one] (2) when compared with those reported by Siddiqui et al. (2011) (26).

3.1.3. Compound III

Compound III (GB-2a) is an amorphous yellow solid with a melting point of 210 °C. The IR showed an OH absorption band at 3222 and 1643cm⁻¹ for a carbonyl group. The Mass as revealed by the LC-MS is m/z 558 with molecular formula C₃₀H₂₂O₁₁, the fragmentation at m/z 599 [M⁺ + 1], 421, 295, 268, 153, 141, 113, 112. The ¹H NMR spectrum showed C-5 (OH) signal at 2.16 (s, 1H) and other OH at 1.27 (s, 1H); also, there was a presence of doublets at 3.41 (d, J = 9.0 Hz, 5H), 5.16 (d, J = 7.6 Hz, 1H), 5.34 (d, J = 13.6 Hz, 1H), 6.86 (d, J = 6.5 Hz, 1H), 7.30 (s, 2H). This result is in close agreement with those reported by Jackson et al (1971) (24) (Table 1). The ¹³C NMR (101 MHz, MeOD) showed a signal at δ 81.5, 49.6, 196.5, 163.4, 95.9, 164.3, 94.6, 161.2, 102.7, 105.1, 129.4, 128.5, 156.9, 114.1 and 128.5 which is in agreement with those reported by Agrawal (1989) (25) (Table 2) for GB-2a [2'-(3,4-dihydroxyphenyl)-5,7,7'-trihydroxy-2-(4-hydroxyphenyl)-[3,8'-bichroman]-4,4'-dione] (3). Although this compound has been previously isolated

from *Garcinia bsrchananir* and *Clusia columnaris* Engl, the isolation of GB-2a (Figure 1) from *A.floribunda* seed for the first time is been reported

here, but (27) had earlier confirmed the presence of GB-2a in an investigation carried out on the seed extract of *A. floribunda* using HPLC-PDA-ESI/MS.

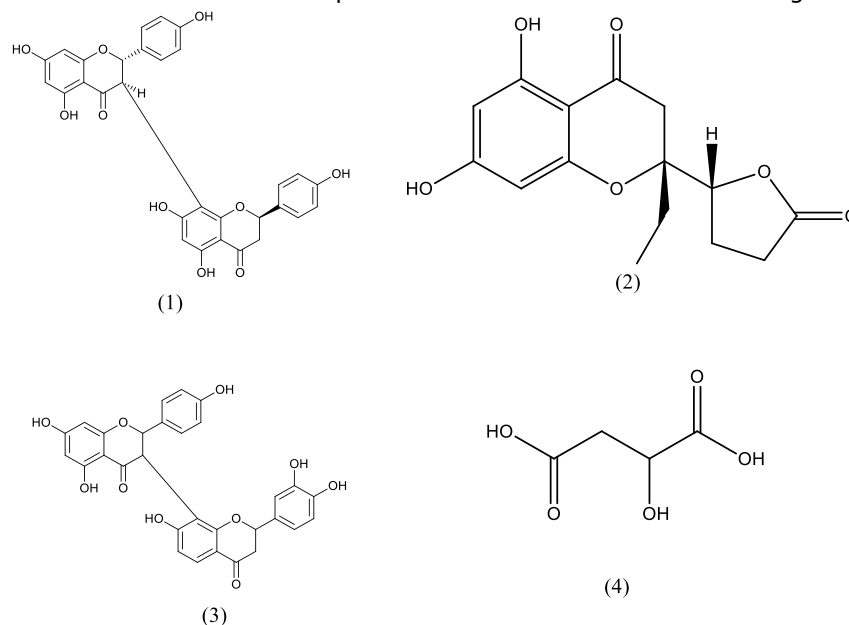


Figure 1: Isolated Compounds from *A. floribunda*.

3.1.4. Compound IV

Compound IV is a white powder with a melting point of 130 °C. The IR showed OH absorption bands at 3397 and 1713 cm^{-1} for a carbonyl group. The molecular weight is 134 with the molecular formula $\text{C}_4\text{H}_6\text{O}_5$. The NMR showed ^1H NMR (600 MHz, MeOD)

δ 4.83 (s, 1H), 2.93 (d, $J = 15.4$ Hz, 1H), 2.81 (d, $J = 15.4$ Hz, 2H) and ^{13}C NMR (150 MHz, MeOD) δ 175.04 (-COOH), 170.67 (-COOH), 50.76 (-CH), 42.62 (-CH₂) which is in agreement with results reported by Kosir et al. (1998) (28) for malic acid (4) (Table 5).

Table 1: ^1H Nuclear Magnetic Resonance results obtained for of Compound I and III.

^1H	Compound I	GB-1a Jackson et al (1971) (24)	Compound III	GB-2a Jackson et al (1971) (24)
C-5 OH	2.01 (s, 1H)	2.05 (s, 1H)	2.16 (s, 1H)	2.31 (s, 1H)
2.44 (s, 1H)				
Other OH	0.89 (t, $J = 7.0$ Hz, 1H)	0.90 (s, 1H)	1.27 (s, 1H)	1.44 (s, 4H)
C ₆ ring	4.59 (d, $J = 11.1$ Hz, 1H)	4.27	3.95 (d, $J = 11.6$ Hz, 3H)	4.10 (s, 3H)
C ₂ /C ₆	2.53 (d, $J = 17.5$ Hz, 1H)	2.98 (d, 2H $J=9.0$)		
3.05 (d, 2H $J=9.0$)	3.53 (d, $J = 8.7$ Hz, 2H), 2.82 (d, $J = 11.1$ Hz, 2H)			
C ₃ /C ₅	4.59 (d, $J = 11.1$ Hz, 1H)			
	3.39 (d 2H $J=9.0$)			
3.48 (d 2H $J=9.0$)	3.41 (d, $J = 9.0$ Hz, 5H)	3.08-3.20 (d, 5H)		
C ₂ /C ₃ (Ring 1-C)	5.62 (d, $J = 11.9$ Hz, 1H)	4.54 (d 1H $J=12.0$)	5.16 (d, $J = 7.6$ Hz, 1H)	4.71 (d, $J = 12$ Hz, 1H)
(Ring I-C)	5.62 (d, $J = 11.9$ Hz, 1H)	5.55 (d 1H $J=12.0$)	5.34 (d, $J = 13.6$ Hz, 1H)	5.32 (d, $J = 12$ Hz, 1H)
C ₂ (Ring II-C)	5.49 (d, $J = 11.8$ Hz, 1H)	4.75 (d 1H $J=12.0$)	6.86 (d, $J = 6.5$ Hz, 1H)	4.30 (d, $J = 12$ Hz, 1H)
C ₃ (Ring II-C)	7.38 (d, $J = 11.6$ Hz, 1H)			
7.09 (d, $J = 11.6$ Hz, 1H)	7.10 (d 1H $J=12.0$)			
7.59 (d 1H $J=12.0$)	7.30 (s, 2H)	6.91 (d, $J = 12$ Hz, 1H)		
7.35 (d, $J = 12$ Hz, 1H)				

Table 2: The data obtained from the ^{13}C NMR analysis of Compound I and III.

^{13}C NMR	Compound I	GB-1a Agrawal (1989) (25)	Compound III	GB-2a Agrawal (1989) (25)
C-2	81.8	81.4	81.5	81.7
C-3	42.7	47.7	49.6	51.0
C-4	196.4	195.2	196.5	197.2
C-5	164.1	163.4	163.4	164.6
C-6	95.9	96.0	95.9	93.3
C-7	166.6	165.9	164.3	164.9
C-8	94.9	95.0	94.6	93.1
C-9	163.4	162.3	161.2	162.1
C-10	101.2	101.0	102.7	162.1
C-1'	128.5	127.9	105.1	105.8
C-2'	130.4	128.5	129.4	130.3
C-3'	114.4	114.5	128.5	128.2
C-4'	157.2	157.1	156.9	159.2
C-5'	113.2	114.5	114.1	113.2
C-6'	128.5	128.5	128.5	128.2

Table 3: ^1H NMR spectral assignments of Compound II.

^1H Assignment	Compound II	Siddiqui et al. (2011) (26)
5-OH	7.31 (s, 1H)	11.57 (s, 1H)
7-OH	7.26 (d, J=8.4 Hz, 1H)	11.45 (s, 1H)
H-8	7.11 (d, J=8.4 Hz, 1H)	7.21 (brs, 1H)
H-6	6.87 (d, J=8.4 Hz, 1H)	7.11 (brs, 1H)
H-9	5.99 (d, J=11.7 Hz, 1H)	4.58 (t, 1H)
H-3 α	5.74 (d, J=11.9 Hz, 1H)	2.98 (d, J=17.1Hz, 1H)
H-3 β	5.65 (d, J=12.0 Hz, 1H)	2.61 (d, J=17.1Hz, 1H)
H-11	4.09 (m, 2H)	2.60 (m, 2H)
H-10	2.01 (m, 2H)	2.32 (m, 2H)
H-13	1.25 (s, 3H)	1.43 (s, 3H)

Table 4: ^{13}C Nuclear Magnetic Resonance analysis result for compound II.

^{13}C NMR	Compound II	Siddiqui et al. (2011) (26)
C-4	196.77	196.6
C-12	182.44	176.6
C-5	166.78	166.0
C-7	164.31	161.2
C-8a	163.45	158.2
C-4a	149.47	109.3
C-6	145.28	110.6
C-8	127.39	108.9
C-9	81.77	82.7
C-2	81.41	81.1
C-3	42.67	42.8
C-11	29.38	28.1
C-10	22.44	22.2
C-13	18.09	18.8

Table 5: The compound IV ^{13}C NMR result.

^{13}C NMR	Compound IV	Kosit et al. (1998) (28)
-COOH	175.04	178.0
-COOH	170.67	178.0
-CH	50.76	69.9
-CH	42.62	41.3

3.2. Molecular Docking

The molecular docking studies of ligands (Table 6) with the omicron Variant (6M0J) and subsequent comparison with molnupiravir and remdesivir, a known medication for SARS-CoV-2 (Figure 2), showed that GB1a and GB2a had docking scores of -8.6 and -8.3 Kcal mol⁻¹ respectively which was close to that of molnupiravir (-8.3 Kcal mol⁻¹) but greater

than that of remdesivir (-7.6 Kcal mol⁻¹), while that of microdiplodiasone and malic acid were lower than that of the two drugs. Also, GB1a and GB2a revealed better docking scores when docked with omicron 2 (7T9L) and 6LU7 than the reference ligands. Microdiplodiasone had docking scores similar to the reference ligands in the target proteins (-6.1 and -6.8 Kcal mol⁻¹), and malic acid had a lower value

compared to other ligands. The binding of the ligands with the omicron Variant (6M0J) had the best binding energy as the ligand formed a firm bond with it. The binding with GB1a formed hydrogen bond interaction with ALA 43, GLU 42, TYR 53, ASN 147, GLU 24, MET 138, ASP 101, ARG 108, PRO 107, pi-pi interaction with ALA 136, ALA 146, ALA 105. Van der Waal's interaction with ARG 113, ASN 103 (Table 7) which was closely related to the binding of 6M0J with molnupiravir and remdesivir. GB2a had hydrogen bond interaction with ARG 113 and TYR 53, pi-pi

interaction with ALA 146 and Van der Waal's interaction with GLU 24 and ARG 108. Malic acid only formed hydrogen bond interaction with THR 72, ARG 99 and HIS 110 when it was docked with omicron variant (6M0J).

Therefore, GB1a and GB2a with better docking scores than the reference ligands and similar target sites can be useful ligands in the design of anti-COVID drugs and vaccines.

Table 6: The molecular docking result of isolated compounds with different variant of COVID-19.

	Ligand	Binding Energy (Kcal mol ⁻¹)		
		6LU7	6M0J	7T9L
A	GB-1a	-6.6	-8.6	-7.3
B	GB-2a	-6.7	-8.3	-7.4
C	Malic acid	-4.3	-4.9	-4.7
D	Microdiplodiasone	-6.1	-6.8	-6.8
E	Molnupiravir	-6.1	-8.3	-6.5
F	Remdesivir	-6.2	-6.8	-7.6

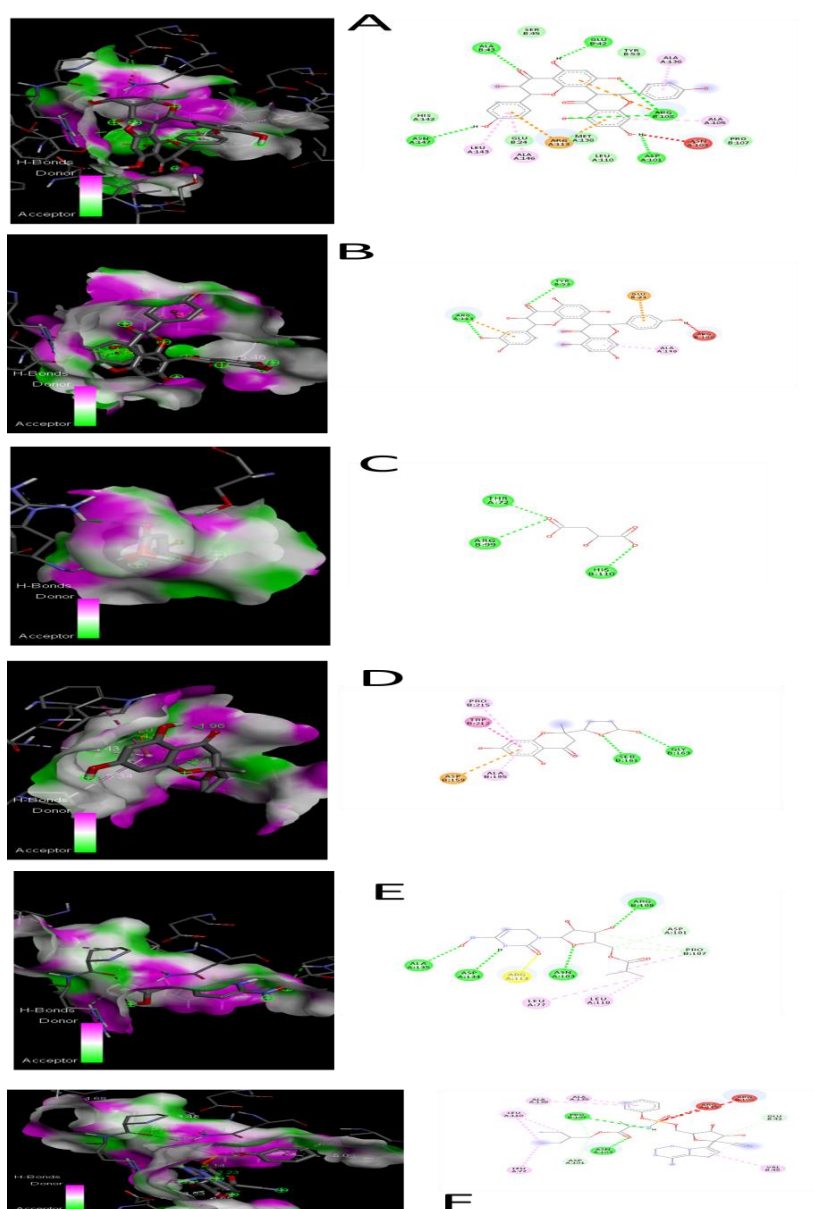


Figure 2: Molecular docking result of Isolated compounds (A-C), molnupiravir (D), and remdesivir (F) against SARS-CoV-2 spike receptor-binding domain bound with ACE2 (6M0J).

Table 7: Molecular docking result of Isolated compounds (A-C), molnupiravir (D), and remdesivir (F) against SARS-CoV-2 spike receptor-binding domain bound with ACE2 (6M0J).

Compounds	Binding Affinity	H-Bonds	Amino acid interaction	
			Hydrophobic/Pi-cation/Pi-anion/Pi-alkyl interactions	Van der Waals interactions
GB-1	-8.6	ALA 43, GLU 42, TYR 53, ASN 147, GLU 24, MET 138, ASP 101, ARG 108, PRO 107	ALA 136, ALA 146, ALA 105.	ARG 113, ASN 103.
GB-2	-8.3	ARG 113, TYR 53	ALA 146	GLU 24, ARG 108
Malic acid	-4.9	THR 72, ARG 99, HIS 110		
Microdiplodiasone	-6.8			
Molnupiravir	-8.3	ALA 135, ASP 134, ARG 113, ASN 103, ARG 108	LEU 77, LEU 110	ASP 101, PRO 107
Remdesivir	-6.8	PRO 107, ASN 103, ASP 101, GLU 42	LEU 110, ALA136, ALA 135, LEU 77, VAL 48	ARG 113, AER 108

4. CONCLUSION

The extraction and isolation of the chemical component of *Allanblackia floribunda* fruit led to the isolation of four known compounds: GB-1a, GB-2a, Malic acid, and Microdiplodiasone. The molecular docking of these compounds with SARS-CoV-2 (6LU7), Omicron 1 (6M0J), and Omicron 2 (7T9L) showed good docking scores when compared to molnupiravir and remdesivir as reference drugs. Hence, these compounds can be investigated further for their drug ability and toxicity against human cells.

5. CONFLICT OF INTEREST

There are no conflicts to declare.

6. REFERENCES

- Orwa C, Mutua A, Kindt R, Jamnadass R, Simons A. Agroforestry database: a tree reference and selection guide, version 4.0. 2009; Available from: [<URL>](#).
- Acuna U, Jancovski N, Kennelly E. Polyisoprenylated Benzophenones from Clusiaceae: Potential Drugs and Lead Compounds. *Curr Top Med Chem* [Internet]. 2009 Nov 1;9(16):1560–80. Available from: [<URL>](#).
- Kuete V, Tangmouo JG, Penlap Beng V, Ngounou FN, Lontsi D. Antimicrobial activity of the methanolic extract from the stem bark of tridesmostemon omphalocarpoides (Sapotaceae). *J Ethnopharmacol* [Internet]. 2006 Mar 8;104(1–2):5–11. Available from: [<URL>](#).
- Minami H, Takahashi E, Kodama M, Fukuyama Y. Three xanthenes from *Garcinia subelliptica*. *Phytochemistry* [Internet]. 1996 Feb 1;41(2):629–33. Available from: [<URL>](#).
- Ayoola GA, Ngene IE, Awobajo FO, Olatunji-Bello II, Odugbemi TO. Hypoglycaemic effect of the aqueous extract of the leaves of *Allanblackia floribunda* Oliv.(Guttiferae). *J Phytol* [Internet]. 2009;1(4):260–6. Available from: [<URL>](#).
- Betti JL. An ethnobotanical study of medicinal plants among the Baka pygmies in the Dja biosphere reserve, Cameroon. *Afr Study Monogr* [Internet]. 2004;25(1):1–27. Available from: [<URL>](#).
- Laird SA, Howe S, Sidwell K. Medicinal plants of the Limbe botanic garden. Mount Cameroon Project; 1996.
- Brusotti G, Papetti A, Serra M, Temporini C, Marini E, Orlandini S, et al. *Allanblackia floribunda* Oliv.: An aphrodisiac plant with vasorelaxant properties. *J Ethnopharmacol* [Internet]. 2016 Nov 4;192:480–5. Available from: [<URL>](#).
- Olanipekun AD, Faleye FJ, Ogunlade I, Popoola O. Antimicrobial and the total antioxidant activities of the methanolic extract of *allanblackia floribunda* fruit. *Int J Curr Res* [Internet]. 2018;10(7):71669–73. Available from: [<URL>](#).
- Olanipekun AD, Faleye FJ, Ogunlade I. The Chemical and Anti-Nutrient Composition of *Allanblackia Floribunda* Oliv Fruit. *Eksu J Sci Technol* [Internet]. 2017;3(1):32–7. Available from: [<URL>](#).
- Dike MC, Asuquo ME. Proximate, phytochemical and mineral compositions of seeds of *Allanblackia floribunda*, *Garcinia kola* and *Poga oleosa* from Nigerian rainforest.

- African J Biotechnol [Internet]. 2012 Jun 21;11(50):11096–8. Available from: [<URL>](#).
12. Lenta BN, Vonthron-Sénécheau C, Weniger B, Devkota KP, Ngoupayo J, Kaiser M, et al. Leishmanicidal and Cholinesterase Inhibiting Activities of Phenolic Compounds from *Allanblackia monticola* and *Symphonia globulifera*. *Molecules* [Internet]. 2007 Jul 20;12(8):1548–57. Available from: [<URL>](#).
13. Azebaze AGB, Meyer M, Valentin A, Nguemfo EL, Fomum ZT, Nkengfack AE. Prenylated Xanthone Derivatives with Antiplasmodial Activity from *Allanblackia monticola* STANER L.C. *Chem Pharm Bull* [Internet]. 2006 Jan;54(1):111–3. Available from: [<URL>](#).
14. Nguemaving JR, Azebaze AGB, Kuete V, Eric Carly NN, Beng VP, Meyer M, et al. Laurentixanthonones A and B, antimicrobial xanthonones from *Vismia laurentii*. *Phytochemistry* [Internet]. 2006 Jul 1;67(13):1341–6. Available from: [<URL>](#).
15. Locksley HD, Murray IG. Extractives from Guttiferae. Part XIX. The isolation and structure of two benzophenones, six xanthonones and two biflavonoids from the heartwood of *Allanblackia floribunda* Oliver. *J Chem Soc C Org* [Internet]. 1971 Jan 1;(0):1332. Available from: [<URL>](#).
16. Nkengfack AE, Azebaze GA, Vardamides JC, Fomum ZT, van Heerden FR. A prenylated xanthone from *Allanblackia floribunda*. *Phytochemistry* [Internet]. 2002 Jun 1;60(4):381–4. Available from: [<URL>](#).
17. Vangeel L, Chiu W, De Jonghe S, Maes P, Slechten B, Raymenants J, et al. Remdesivir, Molnupiravir and Nirmatrelvir remain active against SARS-CoV-2 Omicron and other variants of concern. *Antiviral Res* [Internet]. 2022 Feb 1;198:105252. Available from: [<URL>](#).
18. Patil SM, Maruthi KR, Bajpe SN, Vyshali VM, Sushmitha S, Akhila C, et al. Comparative molecular docking and simulation analysis of molnupiravir and remdesivir with SARS-CoV-2 RNA dependent RNA polymerase (RdRp). *Bioinformatics* [Internet]. 2021 Nov 30;17(11):932–9. Available from: [<URL>](#).
19. Ashour NA, Abo Elmaaty A, Sarhan AA, Elkaeed EB, Moussa AM, Erfan IA, et al. A Systematic Review of the Global Intervention for SARS-CoV-2 Combating: From Drugs Repurposing to Molnupiravir Approval. *Drug Des Devel Ther* [Internet]. 2022 Mar;Volume 16:685–715. Available from: [<URL>](#).
20. Lee CC, Hsieh CC, Ko WC. Molnupiravir—A Novel Oral Anti-SARS-CoV-2 Agent. *Antibiotics* [Internet]. 2021 Oct 23;10(11):1294. Available from: [<URL>](#).
21. Tripathi A, Misra K. Molecular Docking: A Structure-Based Drug Designing Approach. *JSM Chem* [Internet]. 2017;5(2):1042. Available from: [<URL>](#).
22. Das S, Sarmah S, Lyndem S, Singha Roy A. An investigation into the identification of potential inhibitors of SARS-CoV-2 main protease using molecular docking study. *J Biomol Struct Dyn* [Internet]. 2020 May 13;39(9):3347–57. Available from: [<URL>](#).
23. Hosseini M, Chen W, Xiao D, Wang C. Computational molecular docking and virtual screening revealed promising SARS-CoV-2 drugs. *Precis Clin Med* [Internet]. 2021 Apr 3;4(1):1–16. Available from: [<URL>](#).
24. Jackson B, Locksley HD, Scheinmann F, Wolstenholme WA. Extractives from Guttiferae. Part XXII. The isolation and structure of four novel biflavanones from the heartwoods of *Garcinia buchananii* Baker and *G. eugeniifolia* Wall. *J Chem Soc C Org* [Internet]. 1971 Jan 1;3791–804. Available from: [<URL>](#).
25. Agrawal PK. Studies in Organic Chemistry. 39. Carbon-13 NMR of Flavonoids [Internet]. Agrawal PK, editor. Carbon-13 NMR of Flavonoids. New York: Elsevier; 1989. Available from: [<URL>](#).
26. Siddiqui IN, Zahoor A, Hussain H, Ahmed I, Ahmad VU, Padula D, et al. Diversonol and Blennolide Derivatives from the Endophytic Fungus *Microdiplodia* sp.: Absolute Configuration of Diversonol. *J Nat Prod* [Internet]. 2011 Mar 25;74(3):365–73. Available from: [<URL>](#).
27. Akpanika GA, Winters A, Wilson T, Ayoola GA, Adepoju-Bello AA, Hauck B. Polyphenols from *Allanblackia floribunda* seeds: Identification, quantification and antioxidant activity. *Food Chem* [Internet]. 2017 May 1;222:35–42. Available from: [<URL>](#).
28. Kosir I, Kocjancic M, Kidric J. Wine analysis by 1D and 2D NMR spectroscopy. *Analisis* [Internet]. 1998 Mar 1;26(2):97–101. Available from: [<URL>](#).



A Method Optimization Study for Atomic Absorption Spectrometric Determination of Nickel Content in Meclizine Hydrochloride

Pridhvi Krishna Gaddey¹ , Raja Sundararajan^{1*} 

¹Department of Pharmaceutical Analysis, GITAM School of Pharmacy, GITAM (Deemed to be University), Visakhapatnam, Pin code: 530 045, Andhra Pradesh (State), India.

Abstract: Heavy metals are naturally occurring elements. Their widespread distribution in the environment has raised questions about their possible consequences on both human health and the environment. So, the toxicological and safety assessment of these heavy metals is one of the major issues in recent days. An accurate method for the determination of nickel in bulk drugs was required due to its high toxicity risk. The aim of the current study was to develop a validated analytical technique for the determination of nickel content in bulk drugs using an atomic absorption spectrometer. The wavelength was 232 nm, and the integration duration was 5.0 seconds. It was determined that the detection and quantification limits were 0.051 mg/L and 0.15 mg/L, respectively. The recovery rates for nickel concentrations spiked by 50%, 100%, and 150% in meclizine hydrochloride were determined to be 109.33%, 96.5%, and 97.55%, respectively. The status of heavy metals and trace elements in bulk drugs were discussed in this article, along with an easy-to-use AAS approach that can be applied at the industrial level to ensure the quality and uniformity of bulk medications and other related products.

Keywords: Atomic absorption, Catalyst, Flame atomization, Heavy metal toxicity, Nickel.

Submitted: December 10, 2023. **Accepted:** May 15, 2024.

Cite this: Gaddey PK, Sundararajan R. A Method Optimization Study for Atomic Absorption Spectrometric Determination of Nickel Content in Meclizine Hydrochloride. JOTCSA. 2024;11(3): 1073-80.

DOI: <https://doi.org/10.18596/jotcsa.1402767>

***Corresponding author's E-mail:** sraja61@gmail.com

1. INTRODUCTION

Potential contaminants must be recognized at various stages of the pharmaceutical manufacturing process, particularly in the final product, to avoid potential health risks. Metals can enter active pharmaceutical ingredients through a variety of sources (raw materials generated from plants or minerals, catalysts, reactors, pipelines, and other manufacturing equipment), and their presence is regularly monitored (1). The quick measurement of numerous elements that are metallic and non-metallic in crude and animal fats and refined vegetable oils, many of which are present in parts per million, has been accomplished using atomic absorption spectrophotometry. Ca, Cu, Fe, Mg, Mn, P, and Zn were measured in various refined and crude vegetable oils (2). Nickel (Ni) as raney nickel was used as a catalyst in the process of synthesis of meclizine hydrochloride. According to Zhao et al. (3), meclizine hydrochloride was designed and synthesized by the following method. The initial constituents for the synthesis of 1-[(3-methyl phenyl) methyl] piperazine dihydrochloride was 1-

(chloromethyl)-3-methylbenzene and piperazine. The title chemical meclizine hydrochloride was created by acidifying with (4-chlorophenyl) phenylmethyl chloride. Humans are continually exposed to Ni due to the quantity of Ni in the earth's crust. Natural nickel shortage is uncommon because of its abundance, and a Ni-deficient diet is tough to sustain due to its prevalence in food. Human contact with Ni-polluted surroundings has been linked to a number of diseases. Chronic nickel and nickel compound exposure in the body has been linked to a number of human health consequences, which include lung fibrosis, renal failure, cardiovascular illness, and respiratory tract cancer (4). Nickel's hazardous and carcinogenic effects are linked to how it is absorbed into the body. Nickel and nickel compounds' potential toxicity was determined by their physicochemical properties, as well as the amount, duration, and route of exposure. Ni can enter the body through inhalation, food consumption, and skin absorption, though the chemical form of the element determines how it enters cells. Inhalation is the most dangerous method of nickel exposure (5).

Meclizine hydrochloride is an antihistaminic medicine used to prevent and cure nausea and vomiting caused by various illnesses, including motion sickness, ménière's disease, and hypersensitivity reactions (6). Meclizine is an antihistamine of the 1st generation (non-selective H¹ antagonist). It also possesses anticholinergic properties in the central nervous system. Meclizine's antiemetic and antivertigo activities are due to its blockade of these receptors. In the medulla, this inhibiting impact occurs in the vomiting center and the chemoreceptor trigger zone (CTZ). Signals from the solitary tract nucleus and the vestibular nuclei to the vomiting and chemoreceptor trigger zone center in the medulla are inhibited as a result of these actions via histamine neurotransmission. Vestibular incitation and labyrinth excitability are also reduced as a result of this action (7). Atomic absorption spectroscopy (AAS) is a spectroscopy analytical technique that uses free atoms in their gaseous state to absorb optical radiation (light) in order to quantitatively determine the chemical components. AAS is utilized in pharmacology, biophysics, archeology, and toxicological research. It can determine over 70 distinct elements in solution or directly in solid samples via electrothermal vaporization. The clinical study of metals in biological fluids and tissues, including whole blood, plasma, urine, saliva, brain tissue, liver, hair, and muscle tissue, is one of the many applications of atomic absorption spectrometry in chemistry. The applications of atomic absorption spectrometry include both quantitative and qualitative examination (8). Various analytical techniques for determining meclizine hydrochloride in single- and combined-dosage form were found by the literature review like UV spectrophotometer (9-13), CE (14), HPLC (15-25), LC-MS (26-27), HPTLC (28). From the literature review, it was discovered that there was no verified method for determining nickel in meclizine hydrochloride by atomic absorption spectrometry. There were many methods for the estimation of meclizine hydrochloride in bulk drugs and marketed formulations. However, there was no single method for determining nickel content in meclizine hydrochloride. Compared to all the existing methods for meclizine hydrochloride, the present method was novel because of its ability to determine nickel in meclizine hydrochloride.

Compared to other methods with instruments like ICP-OES and ICP-MS, this method was preferable because it's feasible and cost-effective. Hence, the aim of the current study was to develop a validated analytical technique for the determination of nickel content in bulk drugs using an atomic absorption spectrometer according to ICH guidelines.

2. EXPERIMENTAL

2.1. Reagents and Chemicals

Meclizine hydrochloride (Figure 1) was obtained as a gift sample from Symbio Labs, India. Merck supplied the nickel standard for the study. Nitric acid, perchloric acid, and hydrochloric acid of AR grade from Fisher Scientific were used. The water used was MilliQ water.

2.2. Instrumentation

A Shimadzu Corporation AA-6300 atomic absorption spectrometer with fully integrated atomizers was used for the experiment. The system was managed by a computer with an interface. The ideal operating circumstances for nickel flame atomization were shown in Table 1. An LC/GC analytical balance was used.

2.3. Preparation of Solutions

2.3.1. Nickel standard stock solution preparation

Nickel standard (1000 mg/L) solution of 10.0 mL was transferred into a 100 mL volumetric flask and diluted up to mark with the Milli Q water. This solution consisted of 100 mg/L of nickel. Transferring 5.0 mL of this solution into a 100 mL volumetric flask, it was diluted with Milli Q water to the appropriate concentration. This solution contained 5 mg/L of nickel.

2.3.2. Preparation of blank solution

Nitric acid (HNO₃) was concentrated in 10 mL, and ten milliliters of perchloric acid (HClO₄) were transferred to a hundred-milliliter beaker. The solution was heated until the amount was decreased to between 6 and 7.0 mL, and white vapors were released on a hot plate. Then, the solution was cooled and transferred to a ten-millilitre volumetric flask and diluted to the mark with the milli Q water.

Table 1: Optimal operating conditions for flame atomization of nickel.

Parameter	Setting
Lamp	Nickel hollow cathode lamp
Wavelength	232.0 nm
Slit Width	0.2 nm
Lamp current	7 mA
Lamp mode	BGC-D2
Prespray Time	5.0 Sec
Integration Time	5.0 Sec
Oxidant Flow (L / min)	15.0 L / min
Acetylene Flow (L / min)	1.6 L / min
Recommended Flame	Air-Acetylene
Burner height	7 mm

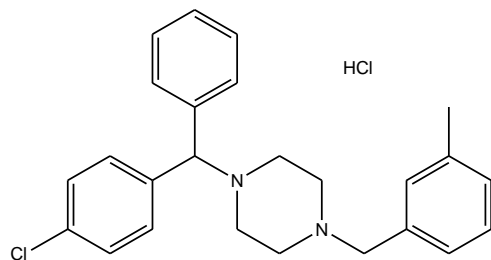


Figure 1: Structure of meclizine hydrochloride.

2.3.3. Preparation of sample solution

Precisely weighed, one gram of sample was transferred into a 100 mL beaker. 10.0 mL of concentrated HNO_3 and 10.0 mL of HClO_4 were added. The solution was heated until the amount was decreased to between 6 and 7.0 mL, and white vapors were released on a hot plate. Then, the solution was cooled, put into a 10.0 mL clean and dry volumetric flask, and diluted to the proper concentration with Milli Q water.

2.4. Analytical Validation Parameters

2.4.1. System suitability

With concentrations of 0.50, 1.0, 1.5, 2.0, and 2.5 mg/L, five standard nickel solutions were made and aspirated into the atomic absorption spectroscopy burner. To evaluate the applicability of the system, averages for triplicate absorbance readings at each standard nickel concentration level were established, and the correlation coefficient was verified.

2.4.2. Specificity

The specificity of the method was tested using blank, 1.0 mg/L nickel standard, and drug samples.

2.4.3. Linearity

Through the study of standard nickel concentrations ranging from 0.5, 1.0, 1.5, 2.0, and 2.5 mg/L, the suggested method's linearity was assessed. After this, a calibration curve is built, and linear regression analysis is used to calculate the r^2 value.

2.4.4. Limit of detection (LOD) and limit of quantitation (LOQ)

LOD and LOQ are used to assess an instrument's or analytical procedure's performance. The limits of detection (LOD) and quantification (LOQ) were computed using 3 and 10 SD/b , respectively, where b is the slope of the analytical curve, and SD is the standard deviation of successive observations.

2.4.5. Accuracy

The sample was spiked in three levels: 50, 100, and 150%. Three replicates were done for each concentration. The amount of nickel in each trial was computed, along with the nickel content % recovery for each method.

2.4.6. Precision at LOQ level

Six analyses of the LOQ level standard stock solution were performed in the precision. As a result, the system's consistency was shown, and the % RSD for six replicates was determined.

2.4.7. Method precision

Six separate preparations of a 100% spike sample solution of meclizine hydrochloride were made, and each was aspirated. Six preparations' nickel contents and nickel content's percent RSD were calculated.

2.5. Batch Analysis

Batch analysis was performed on any one batch of meclizine hydrochloride. 1.0033 g of sample was transferred into a 100 mL beaker. 10 mL of concentrated nitric acid and 10 mL of perchloric acid were added (Perchloric acid and perchlorates are dangerous if heated. Use extreme caution while heating). The solution was heated on a hot plate until the volume was reduced to about 6 - 7 mL and white fumes evolved. Then, the solution was cooled and transferred to a 10 mL volumetric flask and diluted up to the mark with Milli Q water.

3. RESULTS AND DISCUSSION

3.1. System Suitability

The purpose of the system suitability test was to ensure that the entire testing system, including the instrument, reagents, and analyst, was suitable for the intended application. The measure that showed the instrument was responding at its best was the correlation coefficient. Standard solutions (0.5–2.5 mg/L) were made using a nickel working standard and aspirated into an atomic absorption spectrophotometer. A total of 5 concentrations were analyzed for system suitability. The correlation coefficient obtained for concentration versus absorbance in the calibration solution was found to be 0.9985. The system suitability results were tabulated in Table 2. The parameters of system suitability were assessed and determined to be within the limitations in accordance with ICH guidelines (28). Hence, the method was observed to be system suitable.

3.2. Specificity

The capacity to separate the nickel signal from the background signal and the matrix signals was the definition of parameter specificity. The 100% standard solution, sample solution, and blank solution were all used to test the method. The absorbance measured using the blank solution was discovered to be only 5% of the absorbance measured using the standard solution at 100%. The results were shown in Table 3. The specificity results meet the acceptance criteria according to ICH guidelines (29). Both matrices had no effect on the results. Thus, it was determined that the procedure was specific.

Table 2: System suitability.

S. No	Name	Absorbance	Correlation coefficient
1	Standard-1 (0.5 mg/L)	0.0405	
2	Standard-2 (1.0 mg/L)	0.0810	
3	Standard-3 (1.5 mg/L)	0.1230	0.9985
4	Standard-4 (2.0 mg/L)	0.1571	
5	Standard-5 (2.5 mg/L)	0.1295	

Table 3: Specificity.

S. No	Name	Absorbance
1	Blank	0.0025
2	100% Standard Solution	0.0748
3	Sample	-0.0201

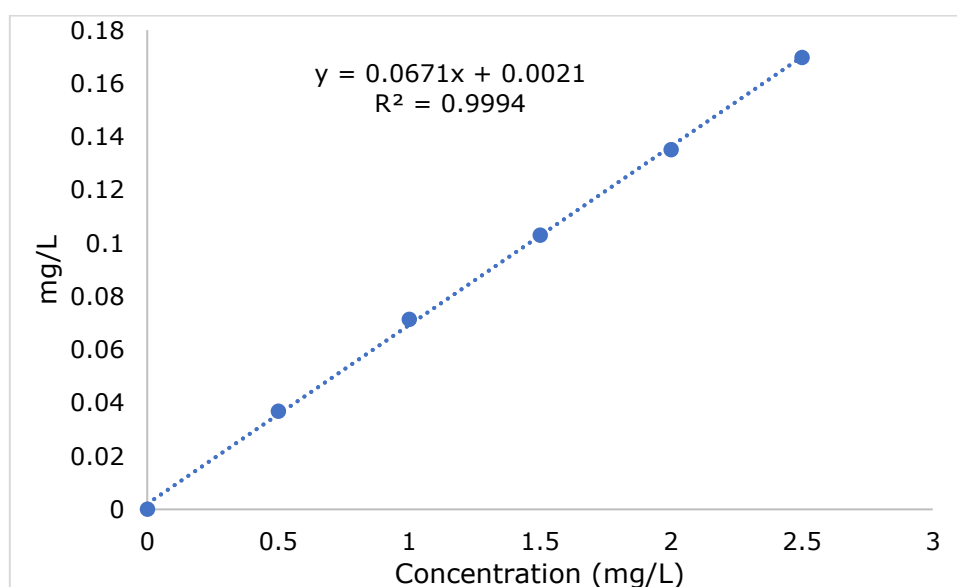
3.3. Linearity

The range of the approach was defined using linearity studies. Examining numerous distinct concentrations of the investigated element allowed for the determination of the linearity of nickel. Aqueous standard solutions with concentrations ranging from 0.5, 1.0, 1.5, 2.0, and 2.5 mg/L were used to produce the calibration curves. The concentration of the nickel standard solution correlated with

absorbance at a 0.9994 correlation coefficient. Table 4 presents the linearity results in tabular form. The calibration curve for meclizine hydrochloride is displayed in Figure 2. The linearity range of 0.5-2.5 mg/L demonstrated good linearity. The results were within the limits in accordance with ICH guidelines (29). Hence, the developed method was found to be linear.

Table 4: Linearity of nickel.

S. No	Name	Absorbance	Correlation coefficient
1	Standard-1 (0.5 mg/)	0.0368	
2	Standard-2 (1.0 mg/L)	0.0714	
3	Standard-3 (1.5 mg/L)	0.1030	0.9994
4	Standard-4 (2.0 mg/L)	0.1351	
5	Standard-5 (2.5 mg/L)	0.1697	

**Figure 2:** Linearity of nickel.

3.4. LOD and LOQ

The detection limit of a certain analytical procedure was the lowest concentration of analyte in a sample

that can be detected but not always quantitated as an exact value. The quantitation limit of a certain analytical procedure was the lowest amount of

analyte in a sample that can be quantitatively quantified with sufficient precision and accuracy. The method's limit of detection and limit of quantitation parameters demonstrate its sensitivity. The calibration curve was used to calculate the LOD and LOQ of the technique. The detection and quantification limits, LOD and LOQ, were derived using the well-known 3 and 10 criteria, respectively, using the standard deviation of samples. The results of LOD and LOQ were achieved as 0.051 mg/L and 0.15 mg/L respectively. These values denote the sensitivity of the method.

3.5. Precision at LOQ Level

The precision of an analytical method was defined as the variation between a set of measurements acquired from multiple sampling of the same homogenous sample under the given conditions. The limit of the quantification level solution in six replicates was aspirated, and the relative standard deviation for a limit of the quantification solution was computed. The relative standard deviation for absorbance of nickel standard solution at the limit of quantification level from six replicates was found to be 6.24 %, less than 15.0%. Table 5 lists the results of the precision at the limit of quantification level.

Table 5: Precision at LOQ level.

S. No	LOQ solution	Absorbance
1	Aspiration-1	0.0169
2	Aspiration-2	0.0183
3	Aspiration-3	0.0165
4	Aspiration-4	0.0154
5	Aspiration-5	0.0163
6	Aspiration-6	0.0178
	Average	0.0169
	S. D	0.011
	% RSD	6.24

3.6. Method Precision

The precision of the procedure was examined to demonstrate whether the instrument response to the nickel standard solution was consistently reproducible. Method precision was measured in percentage relative standard deviation. Six replicates of the 100% spike sample solution were used for the precision test. The experimental results showed that

the approach was reliable, with an RSD of 1.67 percent. The estimated findings for nickel determination in the working standard solution were shown in Table 6, together with the relative standard deviation. It was found that the results were within acceptance criteria according to ICH guidelines (29). Hence, the technique was determined to be precise.

Table 6: Method precision.

S. No	Name	Concentration (mg/L)	Sample weight (g)	Nickel content (mg/L)
1	Preparation-1	0.9463	1.0021	9.4
2	Preparation-2	0.9463	1.0018	9.4
3	Preparation-3	0.9590	1.0038	9.6
4	Preparation-4	0.9632	1.0042	9.6
5	Preparation-5	0.9802	1.0022	9.8
6	Preparation-6	0.9700	1.0025	9.7
	Average			9.6
	SD			0.1602
	% RSD			1.67

3.7. Accuracy

The closeness of the test results achieved by that method to the true value was the accuracy of the analytical procedure. Adding known amounts of standard nickel concentrations 10, 20, and 30 mg/L to three different meclizine hydrochloride standard sample solutions, the accuracy of the procedure was determined. These samples were aspirated in triplicate for each class and represented three increment levels of 50%, 100%, and 150%. The nickel content in each trail was calculated in order to

determine its percentage recovery. The outcomes were summarised in Table 7. The data showed a best recovery of 93.33 % - 112.00%. Since recovery is more important in a method involving sample preparation steps like extraction or digestion, the % recovery of the sample should be of more importance while validating the method. This recovery range shows the method's accuracy. It was found to be within acceptance criteria in accordance with ICH guidelines (29). Hence, the technique was found to be accurate.

Table 7: Accuracy.

S. No	Name	Concentration (mg/L)	Sample Weight (g)	Result (mg/L)	Spiked Concentration (mg/L)	% Recovery	% RSD	
1	Sample	Preparation-1	BDL	1.0004				
		Preparation-2	BDL	0.9996	BDL	-	-	-
		Preparation-3	BDL	1.0005				
2	Spiked at LOQ level	Preparation-1	0.1536	1.0005	1.5		100.00	
		Preparation-2	0.1447	0.9993	1.4	1.5	93.33	4.03
		Preparation-3	0.1388	1.0004	1.4		93.33	
3	Spiked at 50% level	Preparation-1	0.5652	1.0030	5.6		112.00	
		Preparation-2	0.5652	1.0010	5.6	5.0	112.00	4.22
		Preparation-3	0.5209	1.0001	5.2		104.00	
4	Spiked at 100% level	Preparation-1	0.9581	1.0068	9.5		95.00	
		Preparation-2	0.9620	1.0072	9.6	10.0	96.00	1.04
		Preparation-3	0.9768	1.0028	9.7		97.00	
5	Spiked at 150% level	Preparation-1	1.4691	1.0030	14.6		97.33	
		Preparation-2	1.4671	1.0028	14.6	15.0	97.33	0.40
		Preparation-3	1.4691	1.0026	14.7		98.00	

3.8. Batch Analysis

Batch analysis was performed and obtained results are reported in Table 8. The nickel content was to be less than 10 ppm. In the batch analysis, the nickel

concentration was found to be below the quantification limit. The nickel concentration was found to be within the acceptance criteria. This method can be used for regular analysis.

Table 8. Batch analysis.

S. No	Batch	Nickel Content
1	Batch 1	Below quantification limit

4. CONCLUSION

Meclizine hydrochloride is a medicine that is frequently recommended to alleviate nausea, vomiting, and dizziness. Nickel, a catalyst used in the production of meclizine hydrochloride, needs to be measured because it can be dangerous to people. There were several methods reported for the estimation of meclizine hydrochloride in pharmaceutical formulations but no method was reported for estimation of nickel in meclizine hydrochloride bulk drug. The analytical atomic absorption spectrometry method for the assessment of nickel content in bulk drugs was developed and validated. This work evaluated nickel as an elemental contaminant in meclizine hydrochloride using a verified simple, exact, and accurate atomic absorption spectroscopy technique. The dissolution of samples with nitric acid and perchloric acid provided simple sample preparation without adverse effects. USP General Chapter 232 specifies a 20-ppm maximum allowed nickel concentration. The nickel content of meclizine hydrochloride can be ascertained using this quick, affordable, and accurate approach.

5. CONFLICT OF INTEREST

The authors declare no conflict of interest, financial or otherwise.

6. ACKNOWLEDGEMENT

The authors are thankful to the management of GITAM (Deemed to be University), Visakhapatnam, Andhra Pradesh, India, for providing the necessary facilities and M.V.V.S Murthi fellowship grants to carry out the research work.

7. REFERENCES

- Margu  E, Font s C, Buend a A, Hidalgo M, Queral  I. Determination of metal residues in active pharmaceutical ingredients according to European current legislation by using X-ray fluorescence spectrometry. *J Anal At Spectrom* [Internet]. 2009 Aug 18;24(9):1253–7. Available from: [<URL>](#).
- Piccolo B, O'Connor RT. Atomic absorption spectroscopy. *J Am Oil Chem Soc* [Internet]. 1968 Nov;45(11):789–92. Available from: [<URL>](#).
- Zhao ZR, Tang W, Yang DC, Fan L. Synthesis of meclizine hydrochloride. *Chinese J New Drugs* [Internet]. 2008;17(13):1139–44. Available from: [<URL>](#).
- Zambelli B, Ciurli S. Nickel and human health. In: Sigel A, Sigel H, Sigel RKO, editors. *Interrelations between Essential Metal Ions and Human Diseases*

- [Internet]. Springer Dordrecht; 2013. p. 321–57. Available from: [<URL>](#).
5. Genchi G, Carocci A, Lauria G, Sinicropi MS, Catalano A. Nickel: Human health and environmental toxicology. *Int J Environ Res Public Health* [Internet]. 2020 Jan 21;17(3):679. Available from: [<URL>](#).
6. Ghareeb MM, Mohammedways TM. Development and evaluation of orodispersible tablets of meclizine hydrochloride. *Int J Pharm Sci Res* [Internet]. 2012;3(12):5101–10. Available from: [<URL>](#).
7. Wibble T, Engström J, Verrecchia L, Pansell T. The effects of meclizine on motion sickness revisited. *Br J Clin Pharmacol* [Internet]. 2020 Aug 3;86(8):1510–8. Available from: [<URL>](#).
8. Paudel S, Kumar S, Mallik A. Atomic absorption spectroscopy: a short review. *EPRA Int J Res Dev*. 2021;6(9):322–7.
9. Shinde P, Rai C, Daswadkar S, Chaudhari P, Kasture P V. Development of UV spectrophotometric method of meclizine hydrochloride in bulk and pharmaceutical formulation. *Res J Pharm Technol* [Internet]. 2012;5(6):857–9. Available from: [<URL>](#).
10. Naveen KGS, Srinivas U, Joshi H. Development and validation of spectrophotometric method for simultaneous estimation of meclizine and folic acid in bulk and pharmaceutical dosage forms. *PharmaTutor*. 2017;5(6):29–34.
11. Shinde SA, Sayyed ZM, Chaudhari BP, Chaware VJ, Biyani KR. Development and validation of spectrophotometric method for simultaneous estimation of meclizine hydrochloride and pyridoxine hydrochloride in tablet dosage form. *J Pharm Sci Biosci Res* [Internet]. 2016;6(1):137–43. Available from: [<URL>](#).
12. Bkhaitan MM, Mirza AZ. Spectrophotometric method for determination of meclizine in pure and dosage form via ion pair complex formation using eosin Y. *Curr Pharm Anal* [Internet]. 2018 Jan 23;14(2):95–100. Available from: [<URL>](#).
13. Ibrahim MM, Elzanfaly ES, El-Zeiny MB, Ramadan NK, Kelani KM. Spectrophotometric determination of meclizine hydrochloride and pyridoxine hydrochloride in laboratory prepared mixtures and in their pharmaceutical preparation. *Spectrochim Acta Part A Mol Biomol Spectrosc* [Internet]. 2017 May 5;178:234–8. Available from: [<URL>](#).
14. Ho YH, Wu HL, Wu SM, Chen SH, Kou HS. Quantitative enantiomeric analysis of chlorcyclizine, hydroxyzine, and meclizine by capillary electrophoresis. *Anal Bioanal Chem* [Internet]. 2003 Jul 1;376(6):859–63. Available from: [<URL>](#).
15. Peraman R, Manikala M, Kondreddy VK, Yiragamreddy PR. A Stability-indicating RP-HPLC method for the quantitative analysis of meclizine hydrochloride in tablet dosage form. *J Chromatogr Sci* [Internet]. 2015 May 1;53(5):793–9. Available from: [<URL>](#).
16. Nawaz MS. A new validated stability indicating RP-HPLC method for simultaneous estimation of pyridoxine hydrochloride and meclizine hydrochloride in pharmaceutical solid dosage forms. *Chromatogr Res Int* [Internet]. 2013 May 7;2013(1):747060. Available from: [<URL>](#).
17. Shinde G, Ganesh Shashikant S. Development and validation of RP-HPLC method for simultaneous estimation of meclizine hydrochloride and caffeine in bulk and tablet dosage form. *Eur J Pharm Med Res* [Internet]. 2019;6(6):433–41. Available from: [<URL>](#).
18. Foda NH, Jun HW, McCall JW. Quantitative analysis of meclizine in tablet formulations by HPLC. *Anal Lett* [Internet]. 1988 Jul;21(7):1177–88. Available from: [<URL>](#).
19. Gowramma B, Kumar RS, Lakshmanan K, Kalirajan R, Meyyanathan SN. A new stability-indicating chiral RP-HPLC method for the determination of degradation products in meclizine hydrochloride. *Curr Pharm Anal* [Internet]. 2021 Sep 30;17(8):1075–87. Available from: [<URL>](#).
20. Ubale M, Shioorkar M, Choudhari V. A validated stability-indicating HPLC assay method for meclizine HCl in bulk drug. *Int J Adv Pharm Anal* [Internet]. 2016;6(3):16–20. Available from: [<URL>](#).
21. Naveen Kumar GS, Srinivasa U. Development and validation of HPLC method for simultaneous estimation of meclizine and folic acid in bulk drug and pharmaceutical formulations. *Int J Curr Res* [Internet]. 2017;9(6):51934–9. Available from: [<URL>](#).
22. Reddy MS, Karthik PK, Kumar KV. Simultaneous estimation of meclizine hydrochloride and nicotinic acid in pharmaceutical dosage form by RP-HPLC method. *Asian J Pharm Res Heal Care* [Internet]. 2013;5(2):73–80. Available from: [<URL>](#).
23. Gowramma B, Kumar RS, Kalirajan R, Lakshmanan K, Meyyanathan SN. Enantiomeric separation of meclizine hydrochloride in pharmaceutical dosage form by HPLC method. *Curr Drug Res Rev* [Internet]. 2020 Jun 19;12(1):63–71. Available from: [<URL>](#).
24. Imai T, Kimura S, Imamura Y, Uchiyama K, Iijima T, Underberg WJ, et al. Quantitation of meclizine dihydrochloride in serum by reversed phase ion pair high performance liquid chromatography. *J Liq Chromatogr* [Internet]. 1987 Sep 1;10(11):2505–12. Available from: [<URL>](#).
25. Mary L, Srinivasan R, Mary KL, Kumar DR, Aswini P. Simultaneous estimation of meclizine and nicotinic acid by using RP-HPLC. *J Pharm Anal Res* [Internet]. 2014;3(4):426–33. Available from: [<URL>](#).
26. Wang Z, Qian S, Zhang Q, Chow MSS. Quantification of meclizine in human plasma by high performance liquid chromatography–mass spectrometry. *J Chromatogr B* [Internet]. 2011 Jan 1;879(1):95–9. Available from: [<URL>](#).

27. Byran G, Ramachandran SK, Lakshmanan K, Rajagopal K, Subramania Nainar M. Development and validation of LC/MS method for the determination of meclizine enantiomers in pharmaceutical formulations. Drug Dev Ind Pharm [Internet]. 2021 Mar 4;47(3):361–6. Available from: [<URL>](#).
28. Westgate E, Sherma J. Analysis of the active ingredient, meclizine, in motion sickness tablets by high performance thin layer chromatography with densitometric measurement of fluorescence quenching. J Liq Chromatogr Relat Technol [Internet]. 2001 Nov 30;24(18):2873–8. Available from: [<URL>](#).
29. Borman P, Elder D. Q2(R1) Validation of analytical procedures. In: Teasdale A, Elder D, Nims RW, editors. ICH Quality Guidelines: An Implementation Guide [Internet]. Wiley; 2017. p. 127–66. Available from: [<URL>](#).



Determination of Irbesartan in Pharmaceutical Preparations by Polarographic Methods

Bilal Yilmaz^{1*}, Aytekin Korkmaz¹, Semih Yilmaz², Yucel Kadioglu¹

¹Department of Analytical Chemistry, Faculty of Pharmacy, University of Ataturk, 25240, Erzurum, Türkiye

²Faculty of Medicine, University of Ankara, 06100, Ankara, Türkiye.

Abstract: In this study, the polarographic behavior of irbesartan was investigated using the cyclic polarographic method. A mercury drop electrode was used to quantify the peak currents in comparison to Ag/AgCl at 0.10 V/s. Additionally, quick and easy square wave and differential pulse polarographic methods were developed and validated to determine irbesartan in pharmaceutical preparations. For both methods, the calibration curves were linear at concentrations between 5 and 70 µg/mL. The precision was given by relative standard deviation and was less than 2.61%. Accuracy was given with relative error and did not exceed 1.24%. The suggested methods are extremely accurate and precise. No interference was found under the chosen experimental conditions. In pharmaceutical preparations, irbesartan had an average recovery of 99.8%. Therefore, the methods are applicable to the determination of irbesartan in pharmaceutical preparations.

Keywords: Irbesartan, Polarography, Validation, Tablet.

Submitted: November 8, 2023. **Accepted:** June 8, 2024.

Cite this: Yilmaz B, Korkmaz A, Yilmaz S, Kadioglu Y. Determination of Irbesartan in Pharmaceutical Preparations by Polarographic Methods. JOTCSA. 2024;11(3): 1080-90.

DOI: <https://doi.org/10.18596/jotcsa.1387493>

***Corresponding author's E-mail:** yilmazb@atauni.edu.tr

1. INTRODUCTION

Cardiovascular disease is responsible for 17.9 million annual deaths, or about 30% of all fatalities globally (1). At least 45% of heart disease deaths can be attributed to hypertension. Numerous medications, such as beta-blockers, diuretics, angiotensin-converting enzyme inhibitors, angiotensin-receptor blockers, and calcium channel blockers, have been used to treat hypertension (2). Irbesartan (Figure 1) is a medication that lowers blood pressure (3). In the past, it was also used to treat chronic renal failure, congestive heart failure, and hypertension.

Several analytical techniques, such as UV-spectrophotometry (4-10), spectrofluorimetry (11), capillary electrophoresis (12), LC-MS (13-16), and HPLC (17-25), have been reported for the detection of irbesartan.

When using these techniques, various issues arise. Methods for measuring spectrum have poor sensitivity. Chromatographic techniques necessitate derivatization or drawn-out extraction processes, and they are generally sluggish and expensive.

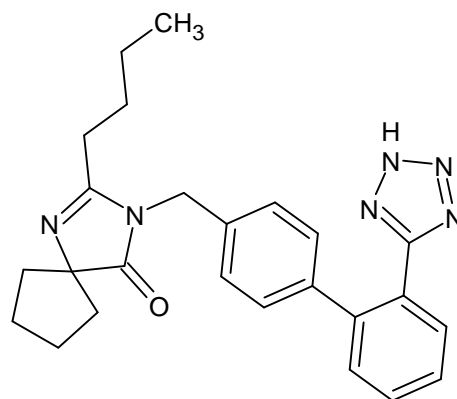


Figure 1: Chemical structure of irbesartan.

Bozal et al. (26) has reported voltammetric methods with differential pulse (DP) and square wave (SW) for the analysis of irbesartan in the pharmaceutical tablet formulations and in human serum samples. The calibration curve of voltammetric methods was linear for irbesartan in the range 8×10^{-6} - 1×10^{-4} M. Intra- and inter-day precision values were lower than 1.72%. The minimum and maximum recovery of irbesartan was 95.02 and 99.21%, respectively.

The LOQ values of methods were found as 2.56×10^{-6} and 2.01×10^{-6} . In addition, validation parameters, such as accuracy, reproducibility and recovery were evaluated.

As a result, using simpler, quicker, and less expensive electrochemical techniques that are nonetheless sensitive can be thought of as a beneficial alternative. Comparing the polarographic approaches to many other analytical methods, several advantages are apparent. The spectrum of viable applications for polarography has expanded thanks to advancements in pulse techniques that make it possible to identify electroactive substances even at low concentrations. The polarographic processes have a number of benefits over chromatography, including low cost and a quick turnaround time for analysis. As opposed to HPLC, which frequently can disturb equilibria in the reaction mixture, electroanalytical approaches are significantly more useful for kinetic and equilibria research.

It is crucial to develop a new technique for figuring out how much medication is present in pharmaceutical solutions or biological fluids. With the advantages that, in the majority of cases, derivatization is not required and that these techniques are less sensitive to matrix effects than other analytical techniques, a wide range of pharmacological compounds have been determined using electroanalytical techniques. The identification of electrode mechanism is another electrochemistry application. Drugs' redox characteristics can provide information about their pharmacological efficacy, in vivo redox activities, or metabolic destiny. Despite the analytical significance of irbesartan's electrochemical behavior and reduction process, no research on the polarographic analysis of its electrochemical reduction in pharmaceuticals has been published.

Therefore, this work introduced novel polarographic techniques that allow for the direct detection of irbesartan in pharmaceutical preparations without the need for time-consuming extraction or evaporation steps before drug analysis. This article covers square wave (SW) and differential pulse (DP) polarography at mercury drop electrode as

completely proven, quick, simple, and effective methods for irbesartan detection.

2. EXPERIMENTAL SECTION

2.1. Chemicals

Irbesartan was purchased from Sigma-Aldrich in Germany. We bought Karvea tablets at the neighborhood pharmacy in Erzurum, Turkey.

2.2. Electrochemical Instrumentation

On a Gamry Potentiostat Interface 1000, electrochemical experiments were conducted. A platinum-wire auxiliary electrode, a mercury drop working electrode (area of HMDE 0.026 cm^2) and an Ag/AgCl (KCl, 3M) electrode acting as the reference electrode were selected for the three electrode cell arrangement. The pulse width is 50 ms, the scan rate is 20 mV/s, drop size 0.38 mm^2 , the amplitude of the square wave pulse is 25 mV, and the amplitude of the differential pulse is 50 mV. These parameters are used for analytical applications.

2.3. Preparation of Standard Solutions

Irbesartan (100 $\mu\text{g/mL}$) stock standard solution was made in 0.5 M sulfuric acid. This stock solution was used to build working standard solutions. The concentration of the standard solutions was 5, 10, 20, 30, 40, 50, 60 and 70 $\mu\text{g/mL}$. 7.5, 37.5, and 67.5 $\mu\text{g/mL}$ were the concentrations at which the QC solutions were obtained.

2.4. Statistical Analysis

With the use of a computer program, SPSS 15.0 was used for the statistical analyses. The irbesartan standard line and calculations were made using regression analyses. The results' mean and standard deviation were given.

3. RESULTS AND DISCUSSION

3.1. Development and Optimization of the Method

At the mercury drop electrode, the electrochemical behavior of irbesartan was studied. The supporting electrolyte for the cyclic voltammetric technique was 0.5 M sulfuric acid. A typical cyclic voltammograms for 100 $\mu\text{g/mL}$ irbesartan at 0.1 V/s scan rate are shown in Figure 2. At -1.055 V, the decrease peak was observed in the cathodic sweep.

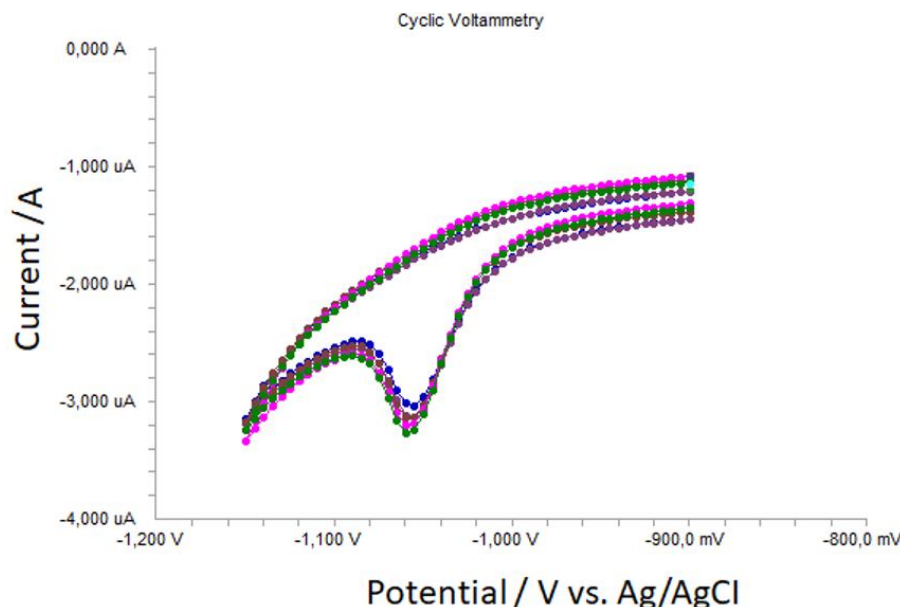


Figure 2: Cyclic voltammograms of 100 µg/mL irbesartan solution.

Moreover, research was done on how scan rate affected cathodic peak currents and peak potentials within the potential scan rate range of 0.005-1.0 V/s.

Figure 3 shows the 20 µg/mL irbesartan linear sweep voltammograms as a function of scan rate.

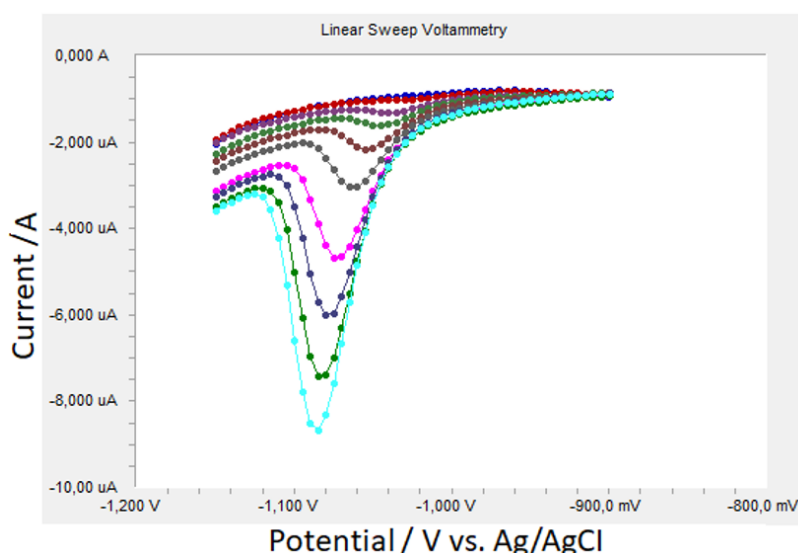


Figure 3: Linear sweep voltammograms of 20 µg/mL irbesartan as a function of scan rate.

The linear sweep voltammograms for irbesartan as a function of scan rate are displayed in Figures 4a, 4b. The logarithm of peak currents against the logarithm of scan rates graphs, however, show straight lines with a slope of 0.56 at irbesartan concentrations of 20 µg/mL (Figure 4c). This value is near to the projected value of 0.5 expected for a perfect diffusion-controlled electrode process (23).

A diffusional process for the peak should be taken into account since this should be done utilizing the log I-log v curve. According to these results, the redox species rapidly diffuse from the solution rather than precipitate onto the electrode surface. The solubility of the intermediate species in 0.5 M sulfuric acid or a lack of product adherence to the electrode surface, respectively, can cause this phenomena (24,25).

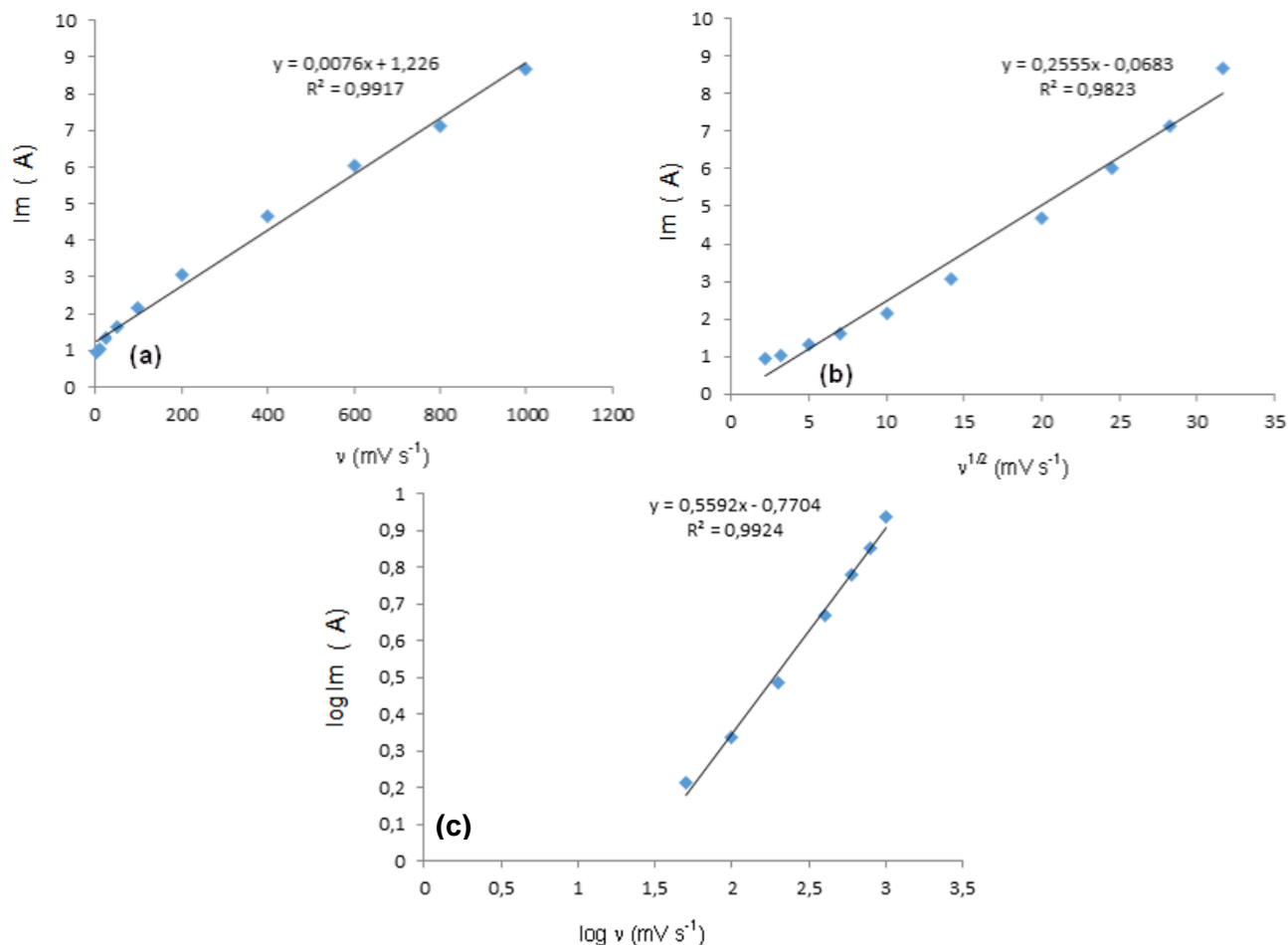


Figure 4(a-c): Dependence of peak current on scan rate (20 $\mu\text{g/mL}$).

3.2. Validation of the Method

While establishing the validation parameters, ICH Q2B guidelines were adhered to. Stability, ruggedness, limit of detection (LOD), limit of quantification (LOQ), specificity, linearity, precision, accuracy, and recovery are some of these requirements (27).

3.2.1. Specificity

In this study, common excipients and additives were investigated for potential interferences. After preparation, the QC samples were inspected. There is no indication that these substances are interfering at the amounts found in dose formulations. This formulation used an excipient that is most commonly used in the pharmaceutical sector. The specificity of the method was examined by keeping an eye out for

any interference from common tablet ingredients such as titanium dioxide, cellulose, silicon dioxide and magnesium stearate. The recommended approach was unaffected negatively by these deviations. Depending on the analysis's conclusions, the process may be particular.

3.2.2. Linearity

Standard solutions were prepared as 5-70 $\mu\text{g/mL}$ for both SWP and DPP. The development of calibration curves for the irbesartan standard was made possible by plotting the compound concentration vs peak current responses (Figures 5 and 6). The calibration curves' correlation coefficients were utilized to evaluate them. The linear regression equations were obtained and are presented in Table 1 using the Microsoft Excel® tool and the least squares method.

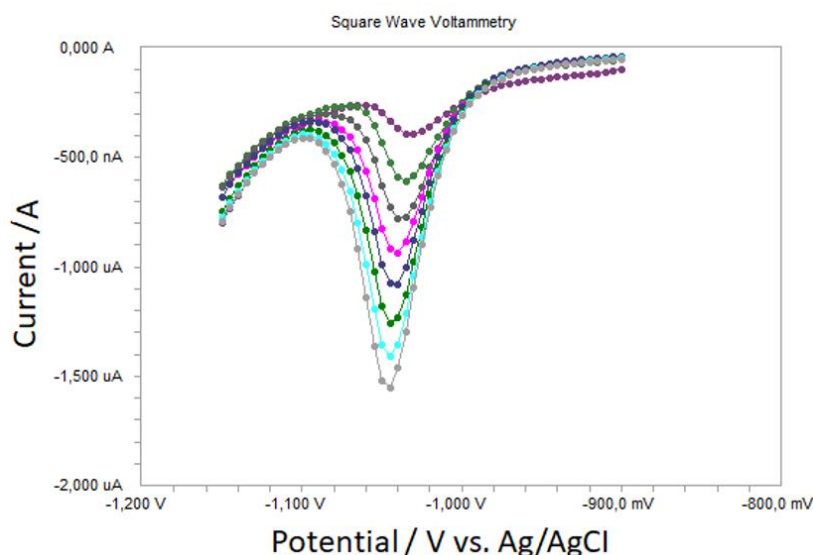


Figure 5: SW voltammograms of irbesartan (5-70 $\mu\text{g/mL}$).

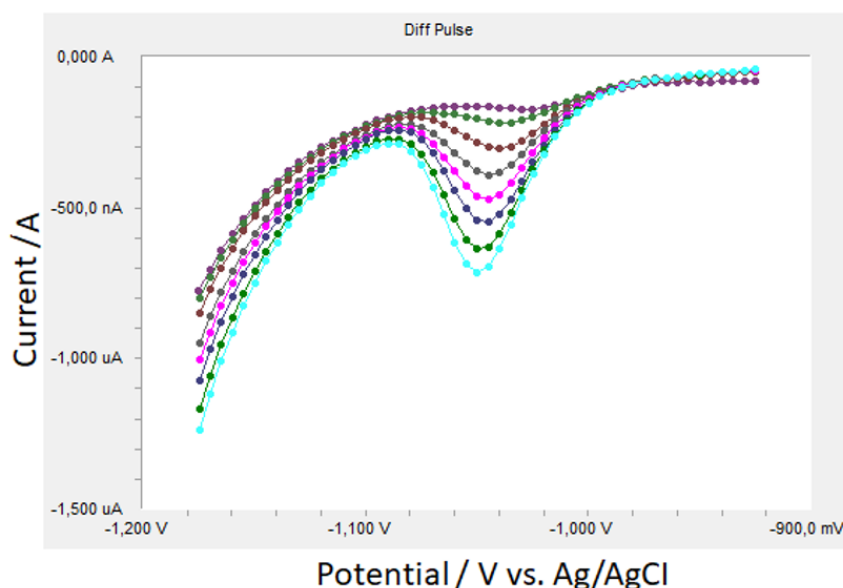


Figure 6: DP voltammograms of irbesartan (5-70 $\mu\text{g/mL}$).

Table 1: Regression information for the irbesartan calibration lines (n=6).

Parameters	SWP	DPP
Linearity ($\mu\text{g/mL}$)	5-70	5-70
Slope	0.0172	0.0083
Intercept	0.3849	0.1355
Coefficient of correlation	0.992	0.999
LOD ($\mu\text{g/mL}$)	0.50	0.40
LOQ ($\mu\text{g/mL}$)	1.50	1.20
Precision (RSD%)	2.61	2.34
Accuracy (% relative error)	-1.24	1.17
Precision of peak current (RSD%)	1.12	1.07
Accuracy of peak potential (RSD%)	1.24	1.31

3.2.3. Accuracy and precision

Using the QC samples, the SWV and DPV techniques' precision and accuracy were assessed for intra-day and inter-day use. The QC samples' same-day analysis was used to evaluate the accuracy and

precision of intra-day measurements. By comparing the assays conducted on two different days, it was able to evaluate the precision and accuracy between those dates. The precision ranged from 0.87% to 2.61%, whereas the intra-day accuracy ranged from

1.09% to 1.24% (Table 1). The data clearly show that this procedure has good precision and accuracy.

3.2.4. Limits of detection (LOD) and quantification (LOQ)

Using calibration standards, the LOD and LOQ values of the recommended techniques were calculated. LOD and LOQ values were calculated as $3.3 \sigma/S$ and $10 \sigma/S$, respectively, where S is the slope of the calibration curve and σ is the standard deviation of y -intercept of regression equation ($n=6$) (30). Table 1 provides a summary of the findings.

3.2.5. Ruggedness

In this experiment, a different analyst used the same instrument and standard to calculate the SW and DP voltammograms of irbesartan. The results showed no statistically significant differences across the operators, demonstrating the resilience of the suggested method.

3.2.6. Stability

For a minimum of 72 hours, the stability of the irbesartan stock solution was investigated. Additionally, at both room temperature and refrigeration temperatures of 4 and -20 °C, irbesartan standard solutions demonstrated 72-hour stability. The recommended range for irbesartan accuracy is 90-110%. In these cases, there are no significant irbesartan breakdown products.

3.2.7. Recovery

To evaluate the effects of formulation interference, the recovery was investigated at three different concentrations. The recoveries were done by combining irbesartan tablet samples that had already undergone analysis with a known quantity of pure medications. The amounts recovered from the spiked samples were compared to the actual added concentrations to determine the recoveries. The results are presented in Table 2.

Table 2: Recovery of irbesartan in tablet ($n=6$).

Pharmaceutical preparation	Added ($\mu\text{g/mL}$)	SWP			DPP		
		Found \pm SD	Recovery (%)	RSD ^a (%)	Found \pm SD	Recovery (%)	RSD ^a (%)
Karvea (25 $\mu\text{g/mL}$)	5	4.9 \pm 0.17	98.0	3.46	5.1 \pm 0.13	102.0	2.54
	15	14.5 \pm 0.29	96.7	2.00	14.8 \pm 0.25	98.7	1.69
	35	35.6 \pm 1.12	101.7	3.14	35.2 \pm 1.67	100.6	4.74

^aRSD: Relative standard deviation

3.3. Procedure for Pharmaceutical Preparations

The 300 mg irbesartan-containing Karvea tablet was carefully weighed and finely ground. The right amount of powder was dissolved in 50 milliliters of 0.5 M sulfuric acid. Next, a balloon flask was filled to the ultimate capacity of 100 mL. After the tablet

solutions were appropriately diluted, a Whatman filter was employed to filter them in order to provide a final concentration that fell between the linearity limitations of the SWP and DPP procedures (Figures 7 and 8). The calibration curve was used to determine the drug concentration for irbesartan.

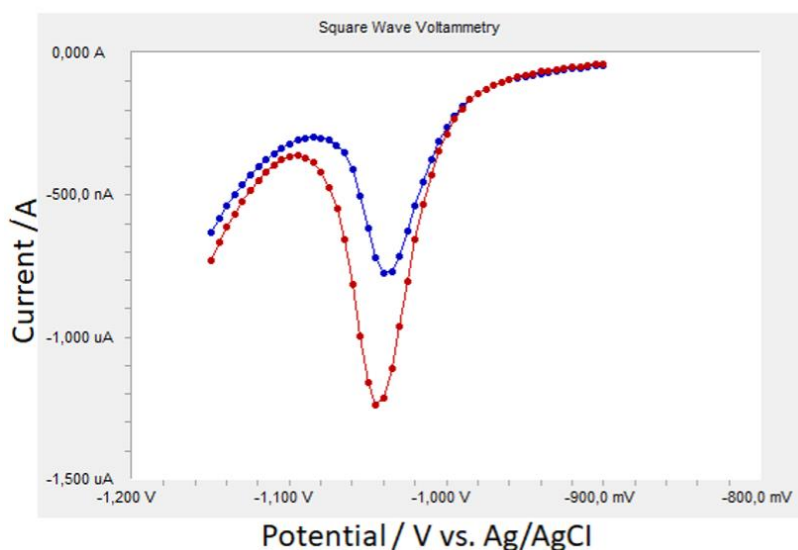


Figure 7: The SW voltammograms of Karvea tablet containing irbesartan (30 and 60 $\mu\text{g/mL}$).

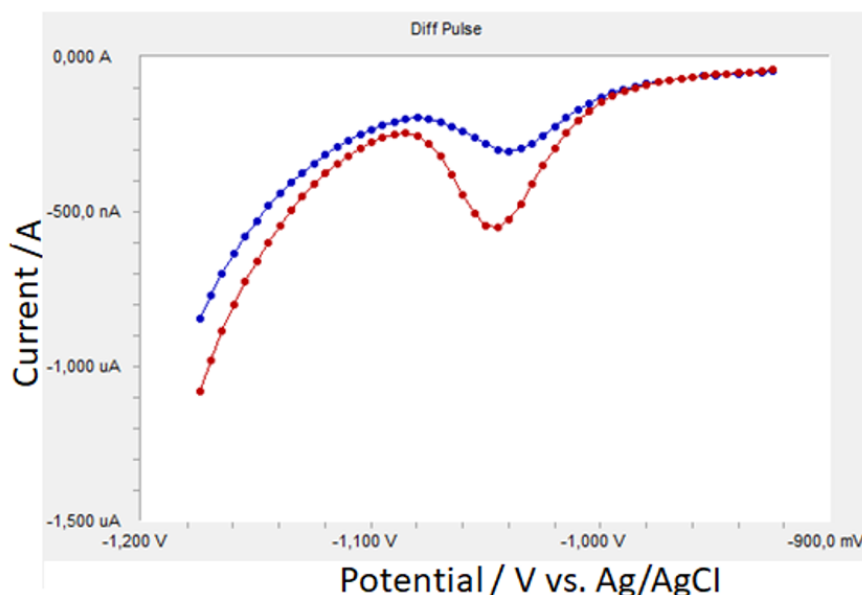


Figure 8: The DP voltammograms of Karvea tablet containing irbesartan (30 and 60 µg/mL).

3.4. Comparison of the Methods

Voltammetry is a potentially novel analytical method that has been proposed recently for the electrochemical detection of pharmaceuticals. Because of their exceptional price, user-friendliness, and quick analysis durations, voltammetric techniques are essential for pharmaceutical analysis (28,29).

The commercial tablets were identified using SW and DP techniques (Table 2). The findings demonstrate the excellent reproducibility and dependability of the two techniques. The t-test was used to compare the best outcomes statistically. The calculated t-values do not surpass the theoretical values at a 95% confidence level (Table 3).

Consequently, the differences between SW and DP voltammetric techniques are minimal. Using the suggested procedures, the %RSD for the polarographic analysis of irbesartan tablets was 1.07%. The recovery of standard additives further confirmed the validity of the proposed methods used on irbesartan tablet. A mean recovery rate of 99.8% was attained. The outcomes of the drug analysis obtained using the suggested techniques closely match the value asserted.

The proposed methods' results were contrasted with those of the official (30) and reference methods (8). The student t- and F-values, which were calculated with a 95% level of confidence, revealed no appreciable variations in performance between the official or reference procedures and the recommended methods (Table 3).

Table 3: Comparison of the proposed and reported methods of irbesartan.

Parameters	SWP	DPP	Official method (30)	Reported method (8)
Mean (recovery %)	99.2	100.4	100.04	99.63
SD	0.621	1.074	-	-
% RSD	0.626	1.069	0.260	0.362
Variance	0.386	1.153	-	-
SE	0.253	0.438	-	-
t-test (2.228) ^a	0.897	-	-	-
F- test (5.1) ^a	3.74	-	-	-

SE: Standard error, No statistically significant difference between the four approaches exists, $F_t > F_c$: H_0 hypothesis is accepted ($P > 0.05$), ^aTheoretical values, Theoretical values at $P=0.05$.

4. CONCLUSION

There are two new electro-analytical techniques that combine DP and SW to estimate the irbesartan content in pharmaceutical formulations. The efficacy and simplicity of the SW and DP procedures for the quantitative determination of irbesartan were shown. The main advantage of this method is that the concentration of the active ingredient may be

measured directly from the irbesartan formulations without any additional processing, such as time-consuming or derivatization. The methodologies mentioned above can be effectively used to perform routine analyses of irbesartan in both its pure form and its formulations.

5. CONFLICT OF INTEREST

According to the writers, there was no conflict of interest.

6. REFERENCES

1. Foley R, Parfrey P, Sarnak M. Clinical epidemiology of cardiovascular disease in chronic renal disease. *Am J Kidney Dis* [Internet]. 1998 Nov;32(5):S112–9. Available from: [<URL>](#).
2. Nguyen Q, Dominguez J, Nguyen L, Gullapalli N. Hypertension management: an update. *Am Heal drug benefits* [Internet]. 2010 Jan;3(1):47–56. Available from: [<URL>](#).
3. Kurbanoglu S, Yarman A. Simultaneous Determination of Hydrochlorothiazide and Irbesartan from Pharmaceutical Dosage Forms with RP-HPLC. *Turkish J Pharm Sci* [Internet]. 2020 Oct 1;17(5):523–7. Available from: [<URL>](#).
4. Ramakrishna S, SudhaLakshmi PB, Rambabu C. Visible spectrophotometric methods for the determination of irbesartan in pharmaceutical formulations. *Int J Pharm Pharm Sci*. 2012;4(3):86–7.
5. Albero I, Ródenas V, García S, Sánchez-Pedreño C. Determination of irbesartan in the presence of hydrochlorothiazide by derivative spectrophotometry. *J Pharm Biomed Anal* [Internet]. 2002 Jun 20;29(1–2):299–305. Available from: [<URL>](#).
6. Ganesh K, Balraj C, Elango KP. Spectroscopic and spectrofluorimetric studies on the interaction of irbesartan with 2,3-dichloro-5,6-dicyano-1,4-benzoquinone and iodine. *Spectrochim Acta Part A Mol Biomol Spectrosc* [Internet]. 2011 Sep 1;79(5):1621–9. Available from: [<URL>](#).
7. Abdellatef HE. Extractive-spectrophotometric determination of disopyramide and irbesartan in their pharmaceutical formulation. *Spectrochim Acta Part A Mol Biomol Spectrosc* [Internet]. 2007 Apr 1;66(4–5):1248–54. Available from: [<URL>](#).
8. Erk N. Three new spectrophotometric methods applied to the simultaneous determination of hydrochlorothiazide and irbesartan. *Pharmazie* [Internet]. 2003;58(8):543–8. Available from: [<URL>](#).
9. Sivasubramanian L, Lakshmi KS. H-point standard addition method for simultaneous spectrophotometric determination of irbesartan, hydrochlorothiazide and telmisartan in tablets. *International J Res Pharm Chemistry* [Internet]. 2014;4(2):373–80. Available from: [<URL>](#).
10. Pradhan KK, Pradhan KK, Mishra US, Pattnaik S, Mishra D, Panigrahi G, et al. Method Development, Validation and Stability Study of Irbesartan in Bulk and Pharmaceutical Dosage Form by UV-Spectrophotometric Method. *Int J Pharm Biol Arch* [Internet]. 2011;2(4):1114–22. Available from: [<URL>](#).
11. Omar MA, Abdelmageed OH, Abdel-Gaber AA, Abdel-Megied AM. Spectrophotometric and spectrofluorimetric determination of certain angiotensin receptor blockers through complex formation. *J Pharm Sci Res* [Internet]. 2011 Oct 1;3(10):1499–510. Available from: [<URL>](#).
12. Hillaert S, Van den Bossche W. Optimization and validation of a capillary zone electrophoretic method for the analysis of several angiotensin-II-receptor antagonists. *J Chromatogr A* [Internet]. 2002 Dec 6;979(1–2):323–33. Available from: [<URL>](#).
13. Ferreirós N, Dresen S, Alonso RM, Weinmann W. Validated Quantitation of Angiotensin II Receptor Antagonists (ARA-II) in Human Plasma by Liquid-Chromatography-Tandem Mass Spectrometry Using Minimum Sample Clean-up and Investigation of Ion Suppression. *Ther Drug Monit* [Internet]. 2007 Dec;29(6):824–34. Available from: [<URL>](#).
14. Gonzalez O, Alonso RM, Ferreirós N, Weinmann W, Zimmermann R, Dresen S. Development of an LC-MS/MS method for the quantitation of 55 compounds prescribed in combined cardiovascular therapy. *J Chromatogr B* [Internet]. 2011 Feb 1;879(3–4):243–52. Available from: [<URL>](#).
15. Qiu X, Wang Z, Wang B, Zhan H, Pan X, Xu R ai. Simultaneous determination of irbesartan and hydrochlorothiazide in human plasma by ultra high performance liquid chromatography tandem mass spectrometry and its application to a bioequivalence study. *J Chromatogr B* [Internet]. 2014 Apr 15;957:110–5. Available from: [<URL>](#).
16. Lu CY, Feng CH. Quantitation of irbesartan and major proteins in human plasma by mass spectrometry with time-of-flight analyzer. *J Pharm Biomed Anal* [Internet]. 2011 Jan 5;54(1):100–5. Available from: [<URL>](#).
17. Bae SK, Kim M, Shim E, Cho D, Shon J, Liu K, et al. HPLC determination of irbesartan in human plasma: its application to pharmacokinetic studies. *Biomed Chromatogr* [Internet]. 2009 Jun 10;23(6):568–72. Available from: [<URL>](#).
18. Rao RN, Bompelli S, Maurya PK. High-performance liquid chromatographic determination of anti-hypertensive drugs on dried blood spots using a fluorescence detector – method development and validation. *Biomed Chromatogr* [Internet]. 2011 Nov 10;25(11):1252–9. Available from: [<URL>](#).
19. Ferreiros N, Iriarte G, Alonso R, Jimenez R. Development of a solid phase extraction procedure for HPLC-DAD determination of several angiotensin II receptor antagonists in human urine using mixture design. *Talanta* [Internet]. 2007 Oct 15;73(4):748–56. Available from: [<URL>](#).
20. Hafez HM, Elshanawane AA, Abdelaziz LM, Kamal MM. Quantitative Determination of three Angiotensin-II-receptor Antagonists in Presence of Hydrochlorothiazide by RP-HPLC in their Tablet Preparations. *Iran J Pharm Res IJPR* [Internet]. 2013;12(4):635–43. Available from: [<URL>](#).

21. Shakya AK, Al-Hiari YM, Alhamami OMO. Liquid chromatographic determination of irbesartan in human plasma. *J Chromatogr B* [Internet]. 2007 Apr 1;848(2):245–50. Available from: [<URL>](#).
22. Koyuturk S, Can NO, Atkosar Z, Arli G. A novel dilute and shoot HPLC assay method for quantification of irbesartan and hydrochlorothiazide in combination tablets and urine using second generation C18-bonded monolithic silica column with double gradient elution. *J Pharm Biomed Anal* [Internet]. 2014 Aug 25;97:103–10. Available from: [<URL>](#).
23. Laviron E, Roullier L, Degrand C. A multilayer model for the study of space distributed redox modified electrodes. *J Electroanal Chem Interfacial Electrochem* [Internet]. 1980 Sep 10;112(1):11–23. Available from: [<URL>](#).
24. Wang J. *Electroanalytical techniques in clinical chemistry and laboratory medicine* [Internet]. New York: VCH Publishers; 1988. Available from: [<URL>](#).
25. Kissinger PT, Heineman WR. *Laboratory Techniques in Electroanalytical Chemistry* [Internet]. Journal of the American Chemical Society. New York: Marcel Dekker, Inc.; 1996. Available from: [<URL>](#).
26. Bozal B, Doğan-Topal B, Uslu B, Özkan SA, Aboul-Enein HY. Quantitative Analysis of Irbesartan in Pharmaceuticals and Human Biological Fluids by Voltammetry. *Anal Lett* [Internet]. 2009 Sep 23;42(14):2322–38. Available from: [<URL>](#).
27. The European Agency for the Evaluation of Medicinal Products. ICH Topic Q2B Note for Guideline on Validation of Analytical Procedures: Methodology GPMP/ICH/281/95 [Internet]. 1996. Available from: [<URL>](#).
28. El-Hefnawey G., El-Hallag I., Ghoneim E., Ghoneim M. Voltammetric behavior and quantification of the sedative-hypnotic drug chlordiazepoxide in bulk form, pharmaceutical formulation and human serum at a mercury electrode. *J Pharm Biomed Anal* [Internet]. 2004 Jan 27;34(1):75–86. Available from: [<URL>](#).
29. Corti P, Corbini G, Gratterer P, Furlanetto S, Pinzauti S. Determination of some quinolones in tablets, human plasma and urine by differential-pulse polarography. *Int J Pharm* [Internet]. 1994 Oct 6;111(1):83–7. Available from: [<URL>](#).
30. *British Pharmacopoeia*, The Stationary Office, London, 2003. Available from: [<URL>](#).



Synthesis and Characterization of N₂O₂ Type Schiff Base Ligand with Salicylaldehyde Derivate and Its Metal Complexes

Sümeysra Tuna Yıldırım^{1*} 

¹Erzincan Binali Yıldırım University, Faculty of Pharmacy, Department of Analytical Chemistry, Erzincan, 24002, Türkiye.

Abstract: Schiff bases and their metal complexes, which play a role in various biological processes, are one of the most important classes of organic and inorganic compounds. Due to their high use in the field of health, it is important to introduce these compounds into the literature through synthesis and research studies. In this study a new Schiff base ligand was synthesized by the reaction of 4-diethylamino-2-hydroxybenzaldehyde with o-aminophenol. This ligand was used to prepare Co(II), Ni(II), Cu(II) and Zn(II) complexes. The structural characterization of the synthesized ligand and metal complexes was elucidated by various spectroscopic and thermal analysis methods such as FT-IR, ¹H-NMR, ¹³C-NMR, UV-Vis., XRD, SEM and TGA. As a result of these characterization studies, it was determined that the synthesized Schiff base acted as an N₂O₂ type tetradentate ligand and that the metal ions were bound to the ligand via phenolic oxygen and azomethine nitrogen.

Keywords: Imine, Ligand, Metal Complex, Schiff Base, Structural Characterization.

Submitted: December 15, 2023. **Accepted:** May 27, 2024.

Cite this: Tuna Yıldırım S. Synthesis and Characterization of N₂O₂ Type Schiff Base Ligand with Salicylaldehyde Derivate and Its Metal Complexes. JOTCSA. 2024;11(3): 1091-8.

DOI: <https://doi.org/10.18596/jotcsa.1405238>

***Corresponding author's E-mail:** stuna@erzincan.edu.tr

1. INTRODUCTION

Schiff bases or azomethines, which contain an imine group (-HC=N-) in their structure, are among the most preferred compounds today due to their biological activities. They are synthesized by the reaction with a compound containing carbonyl group and an active amine under appropriate conditions, are among the widely used ligands owing to structural, biological, and pharmacological properties (1-3). These are precious ligands due to their ability to coordinate different metals and play a role in the formation of metal complexes due to the coordinator feature of the nitrogen atom in their structure. Metal complex formation from the ligands is important for effective and specific catalysts for oxidation, reduction, hydrolysis, and other transformations of organic and inorganic chemistry (4, 5). In addition, they are in the class of compounds that have been studied extensively due to their flexibility and selectivity properties.

Schiff base ligands and complexes are increasingly used in various fields such as medicine and pharmacy, preparation of some drugs, analytical chemistry, biological systems, agriculture, dyestuff

production, cosmetics, polymer production, plastic industry, electronics industry, aircraft industry and liquid crystal technology (6, 7). In recent studies, it has been determined that they have a lot of biological and pharmacological activities such as antibacterial, antimicrobial, anti-inflammatory, anti-HIV, antioxidant, antitumor, anticancer, antiulcer, diuretic, and antipyretic activities (8-10).

2. EXPERIMENTAL SECTION

2.1. Materials and Instruments

In the synthesis of ligand and metal complexes, 4-diethylamino-2-hydroxybenzaldehyde (98%, Sigma-Aldrich), o-aminophenol (99%, Sigma-Aldrich), cobalt(II) acetate tetrahydrate (99%, Merck), nickel(II) acetate tetrahydrate (%99.9, Sigma-Aldrich), copper(II) acetate monohydrate (99%, Merck), zinc(II) acetate dihydrate (99.5%, Merck), p-toluenesulfonic acid (98%, Merck) as precursors and acetone, ethanol, methanol, diethyl ether, dimethyl sulfoxide as solvents at analytical reagent grade were used.

The infrared spectrum of the synthesized compounds was taken with Thermo Scientific Nicolet 6700 FT-IR

Spectrophotometer and their thermogravimetric analyses were performed using the Shimadzu model TGA-50 device. Elemental analyses were taken with LECO-932 CHNSO model elemental analyzer. $^1\text{H-NMR}$ and $^{13}\text{C-NMR}$ spectra were taken on Bruker DPX-400, 400 MHz high performance digital NMR spectrometer. UV spectra were recorded with Shimadzu 1240 model UV-Vis Spectrophotometer. Magnetic susceptibilities were measured by a modified Gouy method. In addition, the FEI QUANTA FEG 450 model Scanning Electron Microscope (SEM) the Panalytical was used to determine the morphology of ligand, and Empyrean X-Ray Diffraction (XRD) Device (using $\text{CuK}\alpha_1$ $\lambda=1.5405\text{\AA}$ radiation with 2θ of $10\text{--}100^\circ$, operated at 45 kV and 40 mA) was used for XRD patterns of the ligand.

2.2. Synthesis of Compounds

2.2.1. Synthesis of Ligand

4-Diethylamino-2-hydroxybenzaldehyde (1.93 g, 10 mmol) in 20 mL hot ethyl alcohol was dripped to 20 mL ethyl alcohol solution of *o*-aminophenol (1.09 g, 10 mmol) and (0.01 g) *p*-toluenesulfonic acid. The solution was refluxed for 4 h. The dark yellow compound obtained as a result of the reaction (Figure 1) was filtered off, washed several times with hot distilled water and diethyl ether, recrystallized from

ethanol, and dried at room temperature (11, 12). FT-IR (ν cm^{-1} , KBr); 3430 (phenolic, O-H), 3050 (aromatic, C-H), 2975-2930 (aliphatic, C-H), 1618 (C=N), 1568-1435 (C=C) and 1287 (C-O). $^1\text{H-NMR}$ (δ , DMSO-d_6); 14.20 (s, 1H), 9.62 (s, 1H), 8.64 (s, 1H), 7.29 (d, 1H), 7.04 (s, 1H), 7.00 (s, 1H), 6.91 (s, 1H), 6.84 (d, 1H), 6.28 (s, 1H), 5.98 (s, 1H), 2.52 (q, 4H), 1.27 (t, 6H). $^{13}\text{C-NMR}$ (DMSO-d_6); δ 166.19 (C=N), 159.14 (s), 152.10 (s), 150.56 (s), 135.11 (s), 134.43 (s), 126.64 (s), 120.05 (Aromatic-C), 119.01 (s), 116.65 (s), 109.50 (s), 104.14 (s), 97.69 (s), 44.35 (-CH₂), 13.08 (-CH₃).

2.2.2. Synthesis of metal complexes

The ligand (0.57 g, 1.00 mmol) was dissolved in 20 mL ethyl alcohol and then metal salts [$\text{Co}(\text{CH}_3\text{COO})_2 \cdot 4\text{H}_2\text{O}$ (0.125 g, 0.50 mmol), $\text{Ni}(\text{CH}_3\text{COO})_2 \cdot 4\text{H}_2\text{O}$ (0.124 g, 0.50 mmol), $\text{Cu}(\text{CH}_3\text{COO})_2 \cdot \text{H}_2\text{O}$ (0.10 g, 0.50 mmol), $\text{Zn}(\text{CH}_3\text{COO})_2 \cdot 2\text{H}_2\text{O}$ (0.110 g, 0.50 mmol)] in 20 mL ethyl alcohol were dripped to ligand solutions separately. These solutions were heated under reflux for 2-4 h (Figure 1). The compounds were filtered off, washed several times using hot distilled water and diethyl ether, and dried at room temperature (13, 14).

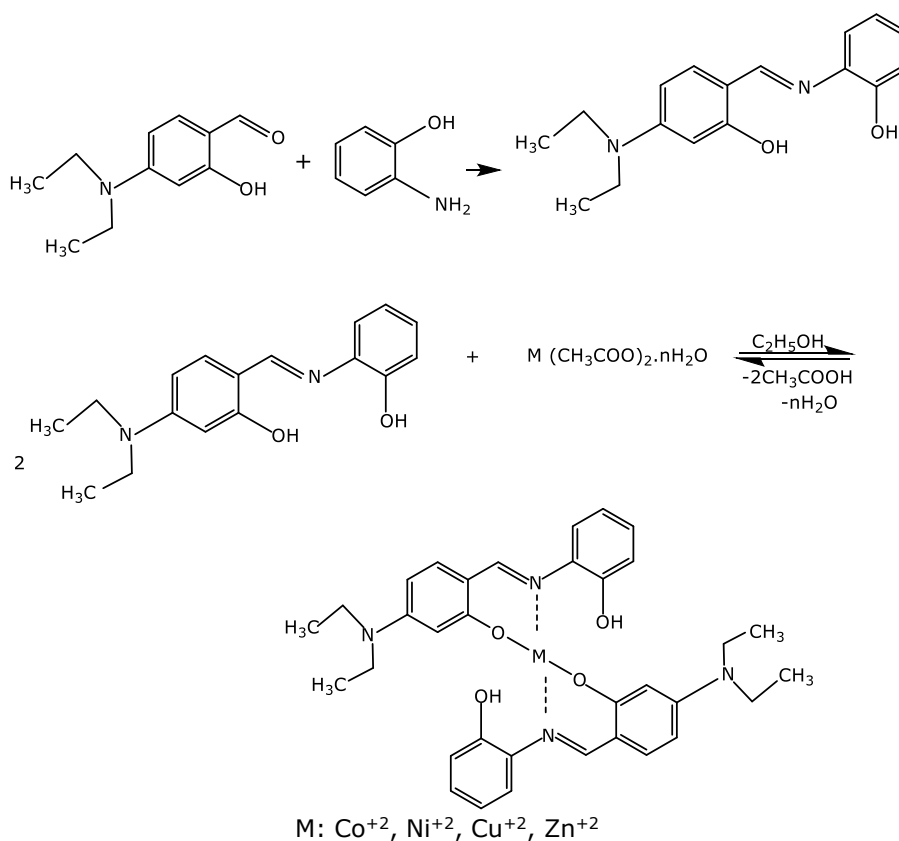


Figure 1: Synthesis of 2-[(4-(diethylamino)-2-hydroxybenzylidene)amino]phenol and metal complexes (C₁₋₄).

3. RESULTS AND DISCUSSION

3.1. Structural Characterization

The elemental, spectral, and thermal analyses were used to investigate the structure of the synthesized compounds (15, 16). No mass loss was observed in the thermograms of the synthesized compounds

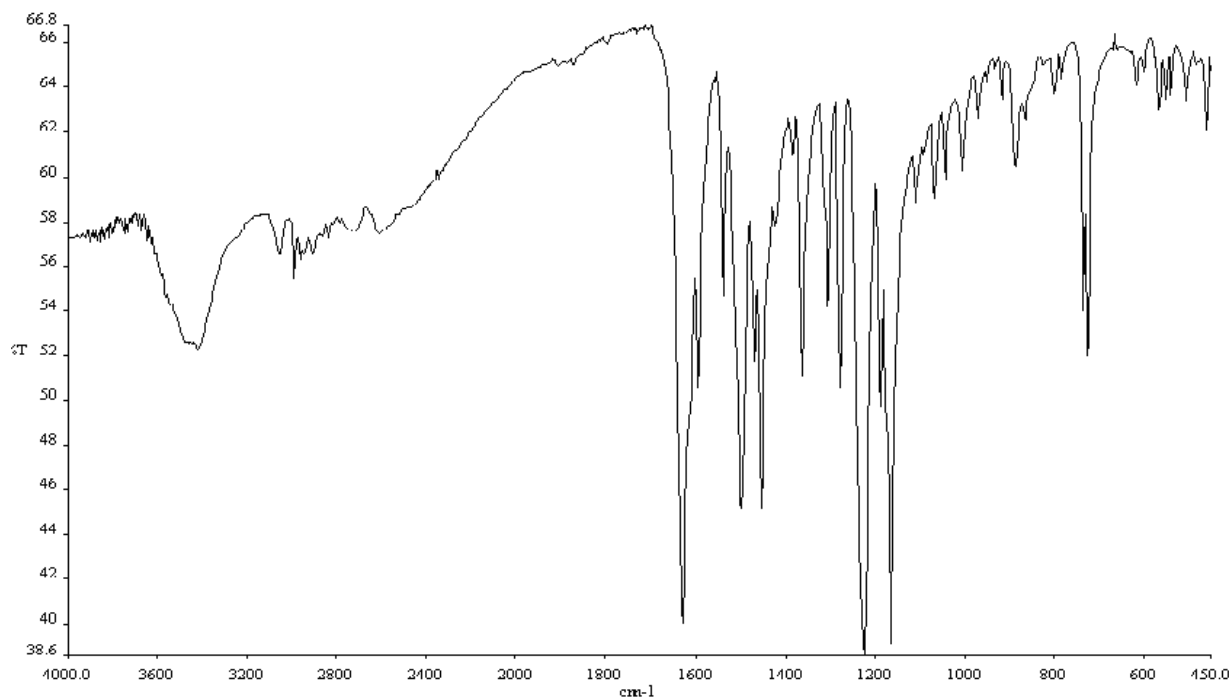
from 25 °C to 270 °C. This means that there was no crystal water at the compounds (17, 18). As seen in Table 1, elemental analysis showed that the ligand:metal ratio was 2:1 at the compounds. That is, the data obtained from the thermogram supports the results of the elemental analysis.

Table 1: Some analytical and physical data of ligand and metal complexes.

Compound	Formula	W (g/mol)	Color	m.p (°C)	μ_{eff}	Yield (%)	Elemental Analysis, % Calculated (Found)		
							C	H	N
Ligand	$\text{C}_{17}\text{H}_{20}\text{N}_2\text{O}_2$	284.359	Dark Yellow	132-134	-	84.00	71.81 (71.79)	7.09 (7.04)	9.85 (9.78)
[Co(L)₂]	$\text{CoC}_{34}\text{H}_{38}\text{N}_4\text{O}_4$	625.635	Dark Brown	>300	4.09	68.00	65.27 (65.19)	6.12 (6.07)	8.95 (8.91)
[Ni(L)₂]	$\text{NiC}_{34}\text{H}_{38}\text{N}_4\text{O}_4$	625.395	Light Brown	>300	2.68	62.00	65.30 (65.28)	6.12 (6.06)	8.96 (8.81)
[Cu(L)₂]	$\text{CuC}_{34}\text{H}_{38}\text{N}_4\text{O}_4$	630.248	Dark Green	>300	1.73	66.00	64.80 (64.76)	6.08 (6.02)	8.89 (8.78)
[Zn(L)₂]	$\text{ZnC}_{34}\text{H}_{38}\text{N}_4\text{O}_4$	632.092	Dark Yellow	>300	Dia.	69.00	64.61 (64.59)	6.06 (6.01)	8.86 (8.79)

As seen in Figure 2, a wide band was observed at 3430 cm^{-1} assignable to the phenolic O-H group. Characteristic band of imine group (-CH=N-) was observed at 1618 cm^{-1} as a sharp peak. The other bands at 3050 cm^{-1} , $2975\text{-}2930\text{ cm}^{-1}$, $1568\text{-}1435\text{ cm}^{-1}$, and 1287 cm^{-1} were assigned to the aromatic C-H, the aliphatic C-H, the C=C stretching vibration, and

the phenolic C-O group, respectively (19, 20). In addition, the absence of the -C=O stretching vibration of 4-diethylamino-2-hydroxybenzaldehyde at 1637 cm^{-1} and the -NH₂ stretching vibration of aromatic amine at 3440 cm^{-1} in the spectrum showed that the reaction was completed. Instead of the two bands, -CH=N- stretching vibration was formed.

**Figure 2:** Infrared spectrum of ligand.

The -CH=N- stretching vibration of ligand, which was observed at 1618 cm^{-1} , showing the existence of imine group, shifted to the low-frequency region to $1602\text{-}1609\text{ cm}^{-1}$ in metal complexes (Figure 3). The observed shift indicates that N atom at the imine group plays a role in the formation of M-N bond. The nitrogen atom donated its unpaired electrons to metal ions (21, 22). In addition, the shifts in the peak observed at 1287 cm^{-1} support that deprotonated oxygen forms coordinated bonds with metal ions in complex formation.

The ¹H-NMR spectrum showed that the integral ratios were consistent with the expected number of protons

in each group (23, 24). At the spectrum of the ligand (Figure 4), a proton singlet was observed at 14.20 ppm, which regard to the phenolic OH group. The other singlet was observed at 9.62 ppm belongs to the proton of the -OH group which is adjacent to diethylamino group. The chemical shift of H proton of the imine group at ligand was observed as a singlet at 8.64 ppm. Protons belonging to aromatic ring were observed as multiples in the range of 7.29-5.98 ppm. While the chemical shift of the H proton of -CH₂ group was observed at 2.52 ppm, the chemical shift of group -CH₃ was observed at 1.27 ppm.

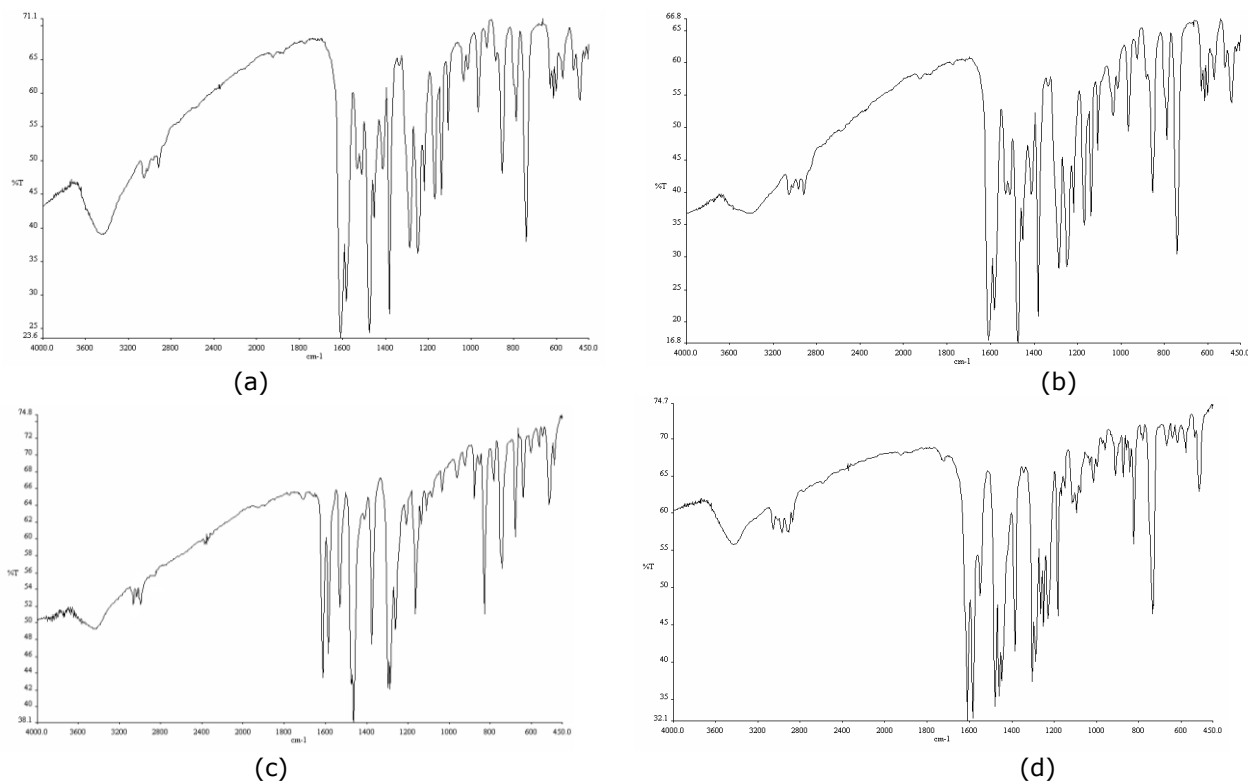


Figure 3: Infrared spectra of metal complexes [(a) $[\text{Co}(\text{L})_2]$, (b) $[\text{Ni}(\text{L})_2]$, (c) $[\text{Cu}(\text{L})_2]$, (d) $[\text{Zn}(\text{L})_2]$].

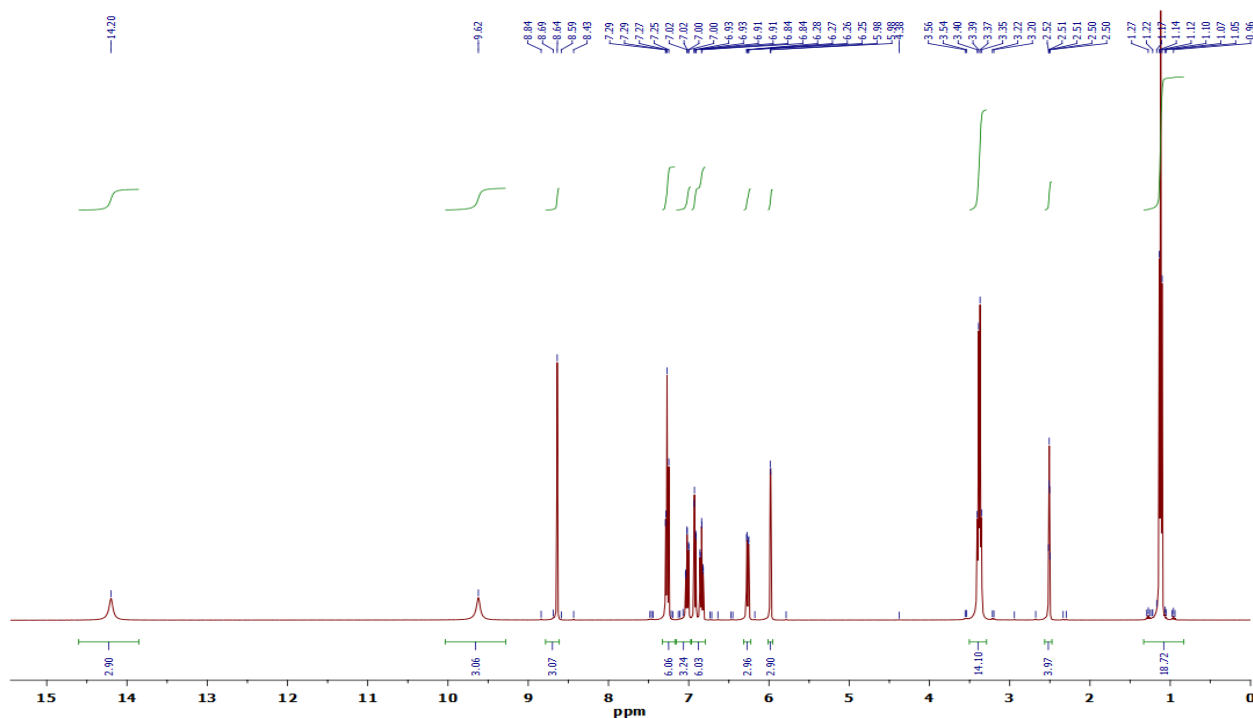


Figure 4: ^1H -NMR spectrum of ligand.

In the ^{13}C -NMR spectrum of ligand (Figure 5), chemical shift of the C atom of the $-\text{OH}$ group which is adjacent to the diethylamino group, was observed at 152.10 ppm. The chemical shift of carbon atom of the other $-\text{OH}$ group was observed at 150.56 ppm (25, 26). The chemical shift observed at 166.19 ppm belongs to the imine group carbon atom. The

chemical shift of C-N group C was observed at 159.14 ppm and C atoms of the aromatic ring were observed in the range of 135.11-97.69 ppm. The chemical shifts of the C proton of $-\text{CH}_2$ group and $-\text{CH}_3$ group were observed at 44.35 ppm and 13.08 ppm, respectively (27).

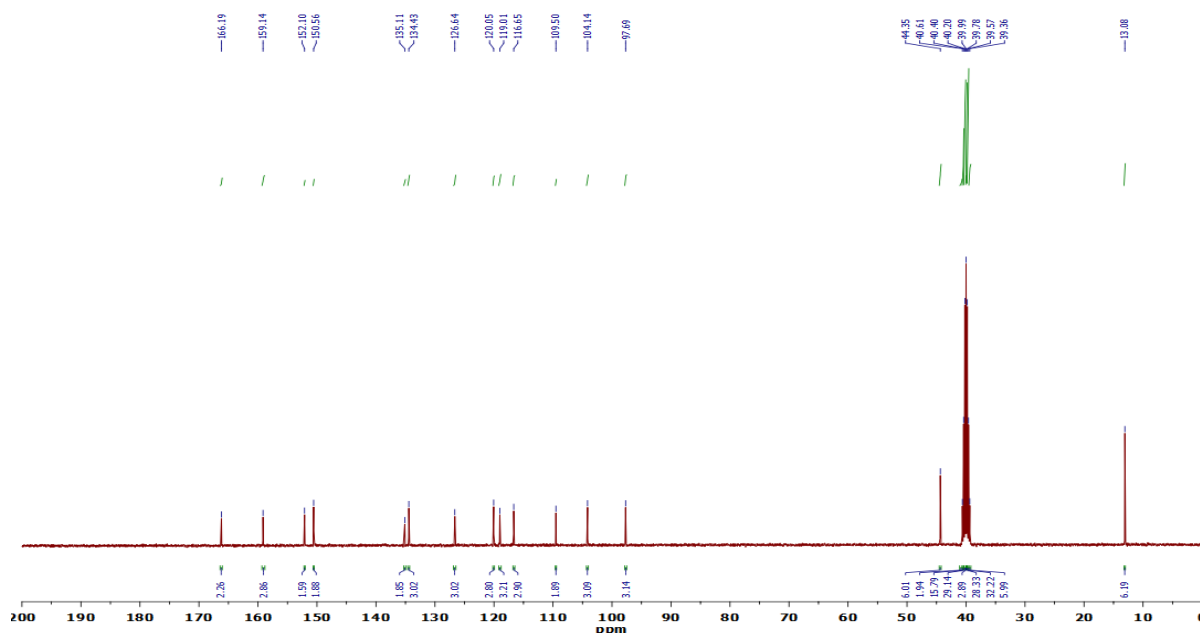


Figure 5: ^{13}C -NMR spectrum of ligand.

The structural characterization of the metal complexes was supported by magnetic susceptibility (μ_{eff}) values. μ_{eff} of Co(II) complex was 4.09 B.M., corresponding to 3 electrons and μ_{eff} of Ni(II) complex was 2.68 B.M., corresponding to 2 electrons. For Cu(II) complex, μ_{eff} value was 1.73 B.M., corresponding to 1 electron. These paramagnetic complexes preferred tetrahedral geometry and the diamagnetic Zn(II) complex preferred tetrahedral structure because of d_{10} configurations (28, 29).

Detailed information about the electronic structures of the compounds can be obtained from UV-Vis. spectra. UV-Vis. measurements of compounds were taken with ethanol. The absorption band of the ligand was at 332 nm involving the $n \rightarrow \pi^*$ electronic

transition (30, 31). The $n \rightarrow \pi^*$ transition of the unpaired electrons of the nitrogen atoms of the imine group was observed as a broad peak at 412 nm (Figure 6). Considering the peak intensities, a decrease was observed in the peak intensities of the metal complexes compared to the ligand. Otherwise, the band of the ligand obtained from $n \rightarrow \pi^*$ shifted to 390-415 nm at the complexes. This caused a wavelength shift during the formation of the $n \rightarrow \pi^*$ transition complexes of unpaired electrons of the nitrogen atom of imine group. This shift showed interaction between $-\text{CH}=\text{N}-$ group and metal ions. The absorption bands appearing in the 425-450 nm range at the complexes indicated charge transfer transitions.

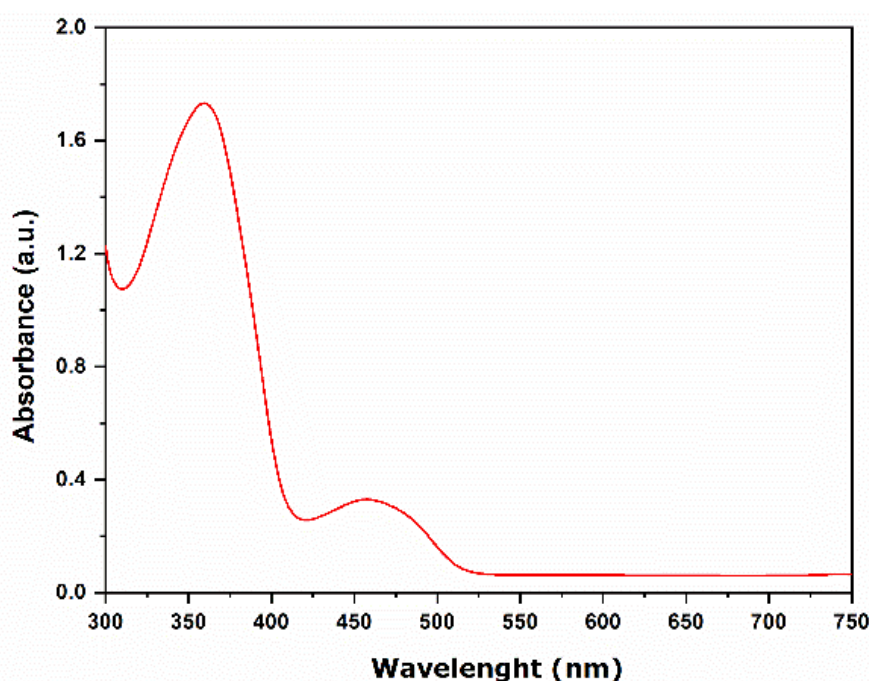


Figure 6: UV-Vis. spectrum of ligand.

The surface morphology of the ligand was examined with Scanning Electron Microscope analysis (Figure 7). As seen in Figure 6, surface morphology of the

ligand was determined to contain compact, dense nanoparticles and localized clusters (32, 33).

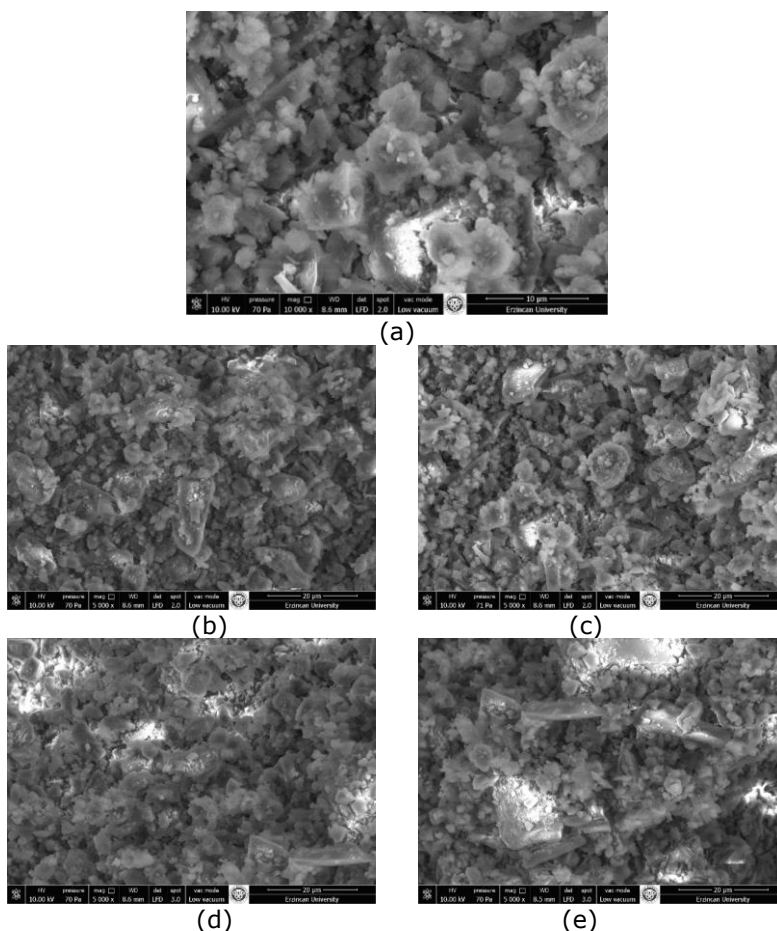


Figure 7: SEM image of ligand (a) and metal complexes [(b) $[\text{Co}(\text{L})_2]$, (c) $[\text{Ni}(\text{L})_2]$, (d) $[\text{Cu}(\text{L})_2]$, (e) $[\text{Zn}(\text{L})_2]$].

The structural analysis of the ligand was carried out by using XRD varying the diffraction angle, 2θ from 10 to 100° (Figure 8). As seen in XRD pattern, the ligand has sharp crystalline peaks. Also, XRD analysis

showed the presence of two important characteristic peaks at $2\theta=18.54^\circ$ and $2\theta=21.28^\circ$ of imine group of the ligand (34, 35).

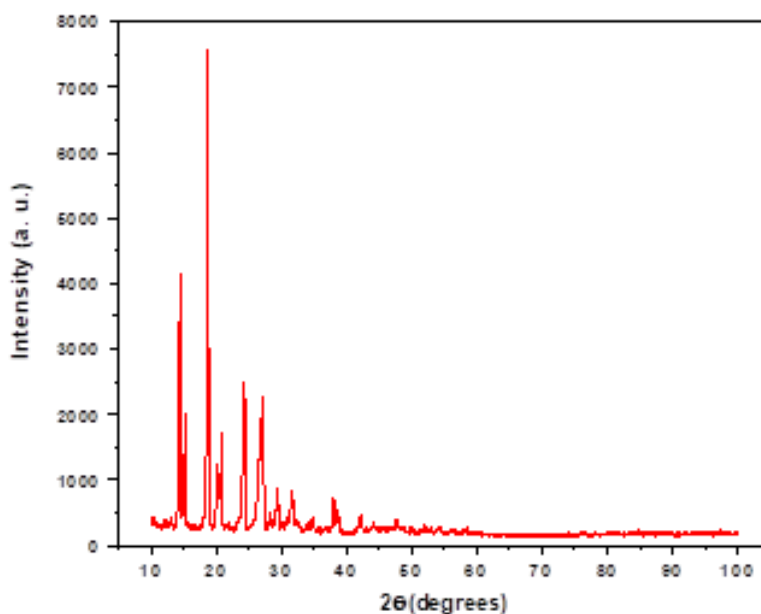


Figure 8: XRD pattern of ligand.

4. CONCLUSION

N_2O_2 type ligand, 2-[(4-(diethylamino)-2-hydroxybenzylidene)amino]phenol, was synthesized from the reaction of an aromatic aldehyde with *o*-aminophenol. The four metal complexes were synthesized from the reaction with metal acetates and synthesized ligand. The characterization studies were completed by using instrumental analysis methods such as FT-IR, 1H -NMR, ^{13}C -NMR, UV-Vis, XRD, SEM, TGA, and magnetic susceptibility. It was determined that in all complexes, the ligand acted as a bidentate chelate by binding to metal ion through imine nitrogen and phenolic oxygen, and M:L ratio for all complexes was 1:2 and the ligand existed as a tetradentate ligand.

5. REFERENCES

- Kajal A, Bala S, Kamboj S, Sharma N, Saini V. Schiff Bases: A Versatile Pharmacophore. *J Catal* [Internet]. 2013 Aug 27;2013:93512. Available from: [<URL>](#).
- Ashraf T, Ali B, Qayyum H, Haroone MS, Shabbir G. Pharmacological aspects of schiff base metal complexes: A critical review. *Inorg Chem Commun* [Internet]. 2023 Apr 1;150:110449. Available from: [<URL>](#).
- Kanagavalli A, Jayachitra R, Thilagavathi G, Padmavathy M, Elangovan N, Sowrirajan S, et al. Synthesis, structural, spectral, computational, docking and biological activities of Schiff base (E)-4-bromo-2-hydroxybenzylidene amino)-N-(pyrimidin-2-yl) benzenesulfonamide from 5-bromosalicylaldehyde and sulfadiazine. *J Indian Chem Soc* [Internet]. 2023 Jan 1;100(1):100823. Available from: [<URL>](#).
- Juyal VK, Pathak A, Panwar M, Thakuri SC, Prakash O, Agrwal A, et al. Schiff base metal complexes as a versatile catalyst: A review. *J Organomet Chem* [Internet]. 2023 Oct 15;999:122825. Available from: [<URL>](#).
- Berhanu AL, Gaurav, Mohiuddin I, Malik AK, Aulakh JS, Kumar V, et al. A review of the applications of Schiff bases as optical chemical sensors. *TrAC Trends Anal Chem* [Internet]. 2019 Jul 1;116:74–91. Available from: [<URL>](#).
- Antony R, Arun T, Manickam STD. A review on applications of chitosan-based Schiff bases. *Int J Biol Macromol* [Internet]. 2019 May 15;129:615–33. Available from: [<URL>](#).
- Kamel RM, Shahat A, Anwar ZM, El-Kady HA, Kilany EM. A novel sensitive and selective chemosensor for fluorescent detection of Zn^{2+} in cosmetics creams based on a covalent post functionalized Al-MOF. *New J Chem* [Internet]. 2021;45(18):8054–63. Available from: [<URL>](#).
- Pervaiz M, Sadiq S, Sadiq A, Younas U, Ashraf A, Saeed Z, et al. Azo-Schiff base derivatives of transition metal complexes as antimicrobial agents. *Coord Chem Rev* [Internet]. 2021 Nov 15;447:214128. Available from: [<URL>](#).
- Jarrahpour AA, Motamedifar M, Pakshir K, Hadi N, Zarei M. Synthesis of Novel Azo Schiff Bases and Their Antibacterial and Antifungal Activities. *Molecules* [Internet]. 2004 Sep 30;9(10):815–24. Available from: [<URL>](#).
- Talebi A, Salehi M, Khaleghian A, Kubicki M. Evaluation of anticancer activities, apoptosis, molecular docking, and antioxidant studies of new Ni(II), VO(IV), Cu(II) and Co(III) Schiff base complexes. *Inorganica Chim Acta* [Internet]. 2023 Feb 1;546:121296. Available from: [<URL>](#).
- Kursunlu AN, Guler E, Sevgi F, Ozkalp B. Synthesis, spectroscopic characterization and antimicrobial studies of Co(II), Ni(II), Cu(II) and Zn(II) complexes with Schiff bases derived from 5-bromo-salicylaldehyde. *J Mol Struct* [Internet]. 2013 Sep 24;1048:476–81. Available from: [<URL>](#).
- Bhagat S, Sharma N, Chundawat TS. Synthesis of Some Salicylaldehyde-Based Schiff Bases in Aqueous Media. *J Chem* [Internet]. 2013 Jan 1;2013:909217. Available from: [<URL>](#).
- Maxim C, Pasatoiu TD, Kravtsov VC, Shova S, Muryn CA, Winpenny REP, et al. Copper(II) and zinc(II) complexes with Schiff-base ligands derived from salicylaldehyde and 3-methoxysalicylaldehyde: Synthesis, crystal structures, magnetic and luminescence properties. *Inorganica Chim Acta* [Internet]. 2008 Oct 1;361(14–15):3903–11. Available from: [<URL>](#).
- Naeimi H, Moradian M. Synthesis and characterization of nitro-Schiff bases derived from 5-nitro-salicylaldehyde and various diamines and their complexes of Co(II). *J Coord Chem* [Internet]. 2010 Jan 10;63(1):156–62. Available from: [<URL>](#).
- Maity D, Drew MGB, Godsell JF, Roy S, Mukhopadhyay G. Synthesis and characterization of Cu(II) complexes of tetradentate and tridentate symmetrical Schiff base ligands involving *o*-phenylenediamine, salicylaldehyde and diacetylmonoxime. *Transit Met Chem* [Internet]. 2010 Mar 9;35(2):197–204. Available from: [<URL>](#).
- dos Santos JE, Dockal ER, Cavalheiro ÉTG. Synthesis and characterization of Schiff bases from chitosan and salicylaldehyde derivatives. *Carbohydr Polym* [Internet]. 2005 May 25;60(3):277–82. Available from: [<URL>](#).
- Avsar G, Altinel H, Yılmaz MK, Guzel B. Synthesis, characterization, and thermal decomposition of fluorinated salicylaldehyde Schiff base derivatives (salen) and their complexes with copper(II). *J Therm Anal Calorim* [Internet]. 2010 Jul 11;101(1):199–203. Available from: [<URL>](#).
- Bouzerafa B, Aggoun D, Ouennoughi Y, Ourari A, Ruiz-Rosas R, Morallon E, et al. Synthesis, spectral characterization and study of thermal behavior kinetics by thermogravimetric analysis of metal complexes derived from salicylaldehyde and

- alkylamine. *J Mol Struct* [Internet]. 2017 Aug 15;1142:48–57. Available from: [<URL>](#).
19. Shi L, Ge HM, Tan SH, Li HQ, Song YC, Zhu HL, et al. Synthesis and antimicrobial activities of Schiff bases derived from 5-chloro-salicylaldehyde. *Eur J Med Chem* [Internet]. 2007 Apr 1;42(4):558–64. Available from: [<URL>](#).
20. Adesibikan AA, Emmanuel SS. Synthesis and Characterization of Co (ii) Complex with a Schiff Base Ligand Derived from Salicylaldehyde and 4-chloroaniline. *Int J Nov Res Phys Chem Math* [Internet]. 2023;10(2):12–7. Available from: [<URL>](#).
21. Meenukuty MS, Mohan AP, Vidya VG, Vijay Kumar VG. Synthesis, characterization, DFT analysis and docking studies of a novel Schiff base using 5-bromo salicylaldehyde and β -alanine. *Heliyon* [Internet]. 2022 Jun 1;8(6):e09600. Available from: [<URL>](#).
22. Abdel-Latif SA, Hassib HB, Issa YM. Studies on some salicylaldehyde Schiff base derivatives and their complexes with Cr(III), Mn(II), Fe(III), Ni(II) and Cu(II). *Spectrochim Acta Part A Mol Biomol Spectrosc* [Internet]. 2007 Jul 1;67(3–4):950–7. Available from: [<URL>](#).
23. Cimerman Z, Galešić N, Bosner B. Structure and spectroscopic characteristics of Schiff bases of salicylaldehyde with 2,3-diaminopyridine. *J Mol Struct* [Internet]. 1992 Nov 26;274(C):131–44. Available from: [<URL>](#).
24. Singh VP, Singh S, Singh DP, Tiwari K, Mishra M. Synthesis, spectroscopic (electronic, IR, NMR and ESR) and theoretical studies of transition metal complexes with some unsymmetrical Schiff bases. *J Mol Struct* [Internet]. 2014 Jan 24;1058(1):71–8. Available from: [<URL>](#).
25. Yousif E, Majeed A, Al-Sammarrae K, Salih N, Salimon J, Abdullah B. Metal complexes of Schiff base: Preparation, characterization and antibacterial activity. *Arab J Chem* [Internet]. 2017 May;10:S1639–44. Available from: [<URL>](#).
26. Iftikhar B, Javed K, Khan MSU, Akhter Z, Mirza B, Mckee V. Synthesis, characterization and biological assay of Salicylaldehyde Schiff base Cu(II) complexes and their precursors. *J Mol Struct* [Internet]. 2018 Mar 5;1155:337–48. Available from: [<URL>](#).
27. Rajasekar M, Sreedaran S, Prabu R, Narayanan V, Jegadeesh R, Raaman N, et al. Synthesis, characterization, and antimicrobial activities of nickel(II) and copper(II) Schiff-base complexes. *J Coord Chem* [Internet]. 2010 Jan 10;63(1):136–46. Available from: [<URL>](#).
28. Cristóvão B. Spectral, thermal and magnetic properties of Cu(II) and Ni(II) complexes with Schiff base ligands. *J Serbian Chem Soc* [Internet]. 2011;76(12):1639–48. Available from: [<URL>](#).
29. Chandra S, Kumar U. Spectral and magnetic studies on manganese(II), cobalt(II) and nickel(II) complexes with Schiff bases. *Spectrochim Acta Part A Mol Biomol Spectrosc* [Internet]. 2005 Jan 1;61(1–2):219–24. Available from: [<URL>](#).
30. Liu J, Wu BW, Zhang B, Liu Y. Synthesis and Characterization of Metal Complexes of Cu(II), Ni(II), Zn(II), Co(II), Mn(II) and Cd(II) with Tetradentate Schiff Bases. *Turkish J Chem* [Internet]. 2006 Jan 1;30(1):41–8. Available from: [<URL>](#).
31. Taha ZA, Ajlouni AM, Al-Hassan KA, Hijazi AK, Faiq AB. Syntheses, characterization, biological activity and fluorescence properties of bis-(salicylaldehyde)-1,3-propylenediimine Schiff base ligand and its lanthanide complexes. *Spectrochim Acta Part A Mol Biomol Spectrosc* [Internet]. 2011 Oct 15;81(1):317–23. Available from: [<URL>](#).
32. Neelakantan MA, Marriappan SS, Dharmaraja J, Jeyakumar T, Muthukumaran K. Spectral, XRD, SEM and biological activities of transition metal complexes of polydentate ligands containing thiazole moiety. *Spectrochim Acta Part A Mol Biomol Spectrosc* [Internet]. 2008 Nov 15;71(2):628–35. Available from: [<URL>](#).
33. Deswal Y, Asija S, Dubey A, Deswal L, Kumar D, Kumar Jindal D, et al. Cobalt(II), nickel(II), copper(II) and zinc(II) complexes of thiadiazole based Schiff base ligands: Synthesis, structural characterization, DFT, antidiabetic and molecular docking studies. *J Mol Struct* [Internet]. 2022 Apr 5;1253:132266. Available from: [<URL>](#).
34. Khan MI, Khan A, Hussain I, Khan MA, Gul S, Iqbal M, et al. Spectral, XRD, SEM and biological properties of new mononuclear Schiff base transition metal complexes. *Inorg Chem Commun* [Internet]. 2013 Sep 1;35:104–9. Available from: [<URL>](#).
35. Shakir M, Hanif S, Sherwani MA, Mohammad O, Al-Resayes SI. Pharmacologically significant complexes of Mn(II), Co(II), Ni(II), Cu(II) and Zn(II) of novel Schiff base ligand, (E)-N-(furan-2-yl methylene) quinolin-8-amine: Synthesis, spectral, XRD, SEM, antimicrobial, antioxidant and in vitro cytotoxic studies. *J Mol Struct* [Internet]. 2015 Jul 15;1092:143–59. Available from: [<URL>](#).



Evaluation of Structural and Dielectric Properties of Eu^{3+} , B^{3+} co-doped Ba_2GdMO_6 ($\text{M}=\text{Nb}$, Ta) Double Perovskite Ceramics

Mustafa İlhan^{1*}, Lütfiye Feray Güleriyüz²

¹Department of Environmental Engineering, Faculty of Engineering, Marmara University, Maltepe, 34854, İstanbul, Türkiye.

²Department of Tobacco Technology Engineering, Manisa Celal Bayar University, Akhisar 45200, Manisa, Türkiye.

Abstract: In the study, the structural and dielectric properties of Ba_2GdMO_6 ($\text{M}=\text{Nb}$, Ta) double perovskite ceramics produced with solid-state method were examined by co-doping $x\text{Eu}^{3+}$ and $y\text{B}^{3+}$ ($x=10$ mol%, $y=0, 5, 15, 30, 50, 70$ and 100 mol%). XRD (X-ray diffraction) results of the ceramic samples exhibited a single-phase structure with cubic symmetry $Fm-3m$ space group, while increasing B^{3+} concentration led to an increase in crystallite sizes and lattice parameters up to 50 mol% in both series. SEM (scanning electron microscopy) examinations revealed the presence of boron-supported grain growth and agglomeration in the grains of both series, and also a slight angularity occurred in grain shape at high B^{3+} concentrations. The dielectric constant (ϵ') of the ceramic samples in both series increased with increasing boron concentration up to 50 mol%, and it was approximately 33.5 and 35.4 at 20 Hz for the $\text{Ba}_2\text{Gd}_{1-x}\text{NbO}_6:x\text{Eu}^{3+}$, $y\text{B}^{3+}$ and $\text{Ba}_2\text{Gd}_{1-x}\text{TaO}_6:x\text{Eu}^{3+}$, $y\text{B}^{3+}$, respectively. The decrease in the dielectric constant after 50 mol% may be attributed to the presence of increased strain in the structure, as shown by the decrease in crystallite size. The increasing B^{3+} concentration caused a decrease in dielectric loss ($\tan \delta$) in both series, which was attributed to the suppression of oxygen vacancies due to the increased presence of B^{3+} and hence to a decrease in ionic conductivity and dielectric loss.

Keywords: $\text{Ba}_2\text{GdNbO}_6$; $\text{Ba}_2\text{GdTaO}_6$; Eu^{3+} , B^{3+} co-doping; dielectric properties.

Submitted: February 28, 2024. **Accepted:** May 20, 2024.

Cite this: İlhan M, Güleriyüz LF. Evaluation of Structural and Dielectric Properties of Eu^{3+} , B^{3+} co-doped Ba_2GdMO_6 ($\text{M}=\text{Nb}$, Ta) Double Perovskite Ceramics. JOTCSA. 2024;11(3): 1099-110.

DOI: <https://doi.org/10.18596/jotcsa.1444484>

***Corresponding author's E-mail:** mustafa.ilhan@marmara.edu.tr

1. INTRODUCTION

The $\text{A}_2\text{BB}'\text{O}_6$ type double perovskite structure attracts the attention of material scientists and solid-state chemists. This interest stems from their dielectric properties, such as low dielectric loss, and low chemical reactivity, as well as their potential applications, such as their compatibility with some of the commonly used superconductors as a result of having a suitable coefficient of thermal expansion (1-6). The double perovskites with the general formula $\text{A}_2\text{B}'\text{B}''\text{O}_6$ are formed when the B site of ABO_3 is occupied by two different cations (B' = rare earth elements, B'' = transition metal, d-block metals, such as Nb, Ta, Mo, Sb) in the disordered state (7,8). Perovskite oxides with the structure ABO_3 , which contain two different cations represented as A and B, are structurally stable due to the balanced arrangement of the constituent atoms and valences. Moreover, when the B site is occupied by a transition

metal, $\text{B}'\text{O}_6$ and $\text{B}''\text{O}_6$ in $\text{A}_2\text{B}'\text{B}''\text{O}_6$ perovskite can reduce the symmetry of the A sites and become suitable hosts for doping rare earth ions to obtain luminescent ferroelectrics (9-16). On the other hand, investigating the electrical properties of ferroelectric materials doped with trivalent europium ion (Eu^{3+}) is important for the development of versatile optoelectronic devices (17-19). The Eu^{3+} is known for its strong luminescence in the red spectral region. It exhibits interesting spectral properties with ${}^5\text{D}_0 \rightarrow {}^7\text{F}_J$ ($J=0, 1, 2, 3, 4, 5, 6$) transitions, as well as having non-degenerate ($J=0$) first levels of transitions in both the absorption and luminescence spectrum, and has a great advantage over other RE ions (20-25). Boron is extensively employed as a flux in traditional solid-state reactions due to its relatively low melting point. Additionally, it's utilized to enhance optical and dielectric properties, alongside influencing structural aspects like morphology and crystallinity (26-29). Additionally, there are studies on the effect of boron

on grain morphology and its improvement in dielectric properties in which the doping of boron has the effect of increasing the bulk properties to some extent and can reduce the grain boundaries in the structure (30-32).

In the study, the structural and dielectric properties of Eu^{3+} doped Ba_2GdMO_6 ($M=\text{Nb, Ta}$) ceramics were studied by B^{3+} co-doping. The structural and dielectric characterizations of ceramic samples were carried out by XRD, SEM, and impedance analyses.

2. EXPERIMENTAL

$\text{Ba}_2\text{Gd}_{1-x}\text{NbO}_6:\text{xEu}^{3+}$, yB^{3+} ($x=10$ mol%, $y=0, 5, 15, 30, 50, 70$ and 100 mol%) and $\text{Ba}_2\text{Gd}_{1-x}\text{TaO}_6:\text{xEu}^{3+}$, yB^{3+} ($x=10$ mol%, $y=0, 5, 15, 30, 50, 70$ and 100 mol%) ceramic samples were fabricated by solid-state reaction. Barium carbonate BaCO_3 (Sigma-Aldrich, 99%), niobium oxide (Nb_2O_5 : Alpha Aesar, 99.9%), tantalum oxide (Ta_2O_5 : Alpha Aesar, 99.9%) powders and gadolinium oxide (Gd_2O_3 : Alpha Aesar, 99.9%) were used as starting materials in calculated stoichiometric amounts. Europium oxide (Eu_2O_3 : Alpha Aesar, 99.9%) and boric acid (H_3BO_3 : Kimyalab, %99.9) were used as dopant materials. The stoichiometric amounts of $\text{Ba}_2\text{Gd}_{0.9}\text{NbO}_6:0.1\text{Eu}^{3+}$ and $\text{Ba}_2\text{Gd}_{0.9}\text{TaO}_6:0.1\text{Eu}^{3+}$ starting materials were weighed and mixed in an agate mortar to provide homogeneity. Then, by adding different amounts of boric acid (H_3BO_3), the final mixture of the powders was thoroughly mixed and ground in an agate mortar for the last time to provide more homogeneity. For sintering process, the sufficient amount of mixture was taken and calcined in an alumina crucible at 1250 °C for 6 h after pelleting.

The phase structure of the samples were examined by XRD (X-ray diffractometer; D2 PHASER, Bruker Corp., Germany) using Cu-K_α (1.5406 Å) radiation in between $2\theta=15-80$ °C with scan speed 2 °C/min. The grain morphology of the samples was investigated by scanning electron microscopy (FEG-SEM; XL 30S, Philips Corp., Netherlands). The crystal structure was visualized via VESTA software. The average crystallite sizes of the samples were determined from the Scherrer Eq. (1) (33):

$$D = \frac{k \cdot \lambda}{B \cdot \cos \theta} \quad (1)$$

where D stands for particle size in nanometers, with k is a constant (usually taken as 0.9). $\text{CuK}\alpha$ represents the wavelength ($\lambda = 0.15406$ Å), and B is the full width at half maximum in radians. Frequency-dependent changes of real and imaginary permittivity and loss factor were defined using dielectric Eq. (2) and Eq. (3) respectively:

$$\varepsilon' = \frac{C}{C_0}, \quad \varepsilon'' = \frac{G}{\omega C_0}, \quad C_0 = \varepsilon_0 \frac{A}{d} \quad (2)$$

$$\tan \delta = \frac{\varepsilon''}{\varepsilon'} \quad (3)$$

where C_0 is vacuum capacitance, C is capacitance, w is angular frequency and G is conductance. The dielectric properties of the ceramic samples were carried out using an impedance analyzer (HIOKI, LCR Hitester 3532-50; between frequency 20 Hz– 10^6 Hz, UK) at room temperature.

3. RESULTS AND DISCUSSION

3.1. XRD-SEM Results of $\text{Ba}_2\text{Gd}_{1-x}\text{NbO}_6:\text{xEu}^{3+}$, yB^{3+} and $\text{Ba}_2\text{Gd}_{1-x}\text{TaO}_6:\text{xEu}^{3+}$, yB^{3+}

Figure 1a and Figure 2a show the XRD results for $\text{Ba}_2\text{Gd}_{1-x}\text{MO}_6:\text{xEu}^{3+}$, yB^{3+} ($M=\text{Nb, Ta}$), ($x=10$ mol%, $y=0, 5, 15, 30, 50, 70, 100$ mol%) samples, respectively. X-ray diffractions of all the sintered samples from 0 to 100 mol% B^{3+} showed the single-phase of Ba_2GdMO_6 ($M=\text{Nb, Ta}$). The crystal structure of $\text{Ba}_2\text{GdNbO}_6$ (JCPDS card no. 47-0378) and $\text{Ba}_2\text{GdTao}_6$ (JCPDS card no. 49-1900) was indexed with space group $Fm\bar{3}m$ (225) and cubic symmetry. Figure 3 shows the schematic representation of Ba_2GdMO_6 ($M=\text{Nb, Ta}$) crystal structure consisting of edge-shared $\text{B}'\text{O}_6$ (GdO_6) and $\text{B}''\text{O}_6$ (MO_6) octahedral, where the formation of the single-phase or the absence of any minor phase may be explained to the substitution of Eu^{3+} ions with ionic radius 0.947 Å (for 6 CN) by Gd^{3+} ions ($r=0.938$ Å, for 6 CN), and the dissolution of the boron co-doped at different concentrations in double perovskite host. Figure 1b and Figure 2b shows XRD two theta angles (400) for $\text{Ba}_2\text{Gd}_{1-x}\text{NbO}_6:\text{xEu}^{3+}$, yB^{3+} and $\text{Ba}_2\text{Gd}_{1-x}\text{TaO}_6:\text{xEu}^{3+}$, yB^{3+} , respectively, where the XRD two theta peaks shifted towards smaller angles. Considering the slightly larger ionic radius of Eu^{3+} , the substitution of Gd^{3+} with Eu^{3+} would contribute to lattice expansion. In addition, B^{3+} ions, which are characterized by a small ionic radius and are likely to occupy the structure as interstitial atoms, can lead to the expansion of the lattice. Table 1 summarizes the variation of lattice data and crystallite size. The shift is related to the increase in the lattice constant which elevates up to 100 mol% B^{3+} concentration in both series. The cell data (a , V) for 0 and 100 mol% B^{3+} concentrations were 8.4729 Å, 608.27 Å³ and 8.5029 Å, 614.75 Å³ respectively, for $\text{Ba}_2\text{Gd}_{1-x}\text{NbO}_6:\text{xEu}^{3+}$, yB^{3+} , while they were 8.4680 Å, 607.22 Å³ and 8.4942 Å, 612.87 Å³, respectively, for $\text{Ba}_2\text{Gd}_{1-x}\text{TaO}_6:\text{xEu}^{3+}$, yB^{3+} . The lattice parameters $\text{Ba}_2\text{GdNbO}_6$ (34) and $\text{Ba}_2\text{GdTao}_6$ (35) compounds are $a=8.4900$ Å, $V=611.96$ Å³ and $a=8.4780$ Å, $V=609.37$ Å³, respectively. The cell data had values close to the literature data, where the lattice volume increased by about 1% in both series.

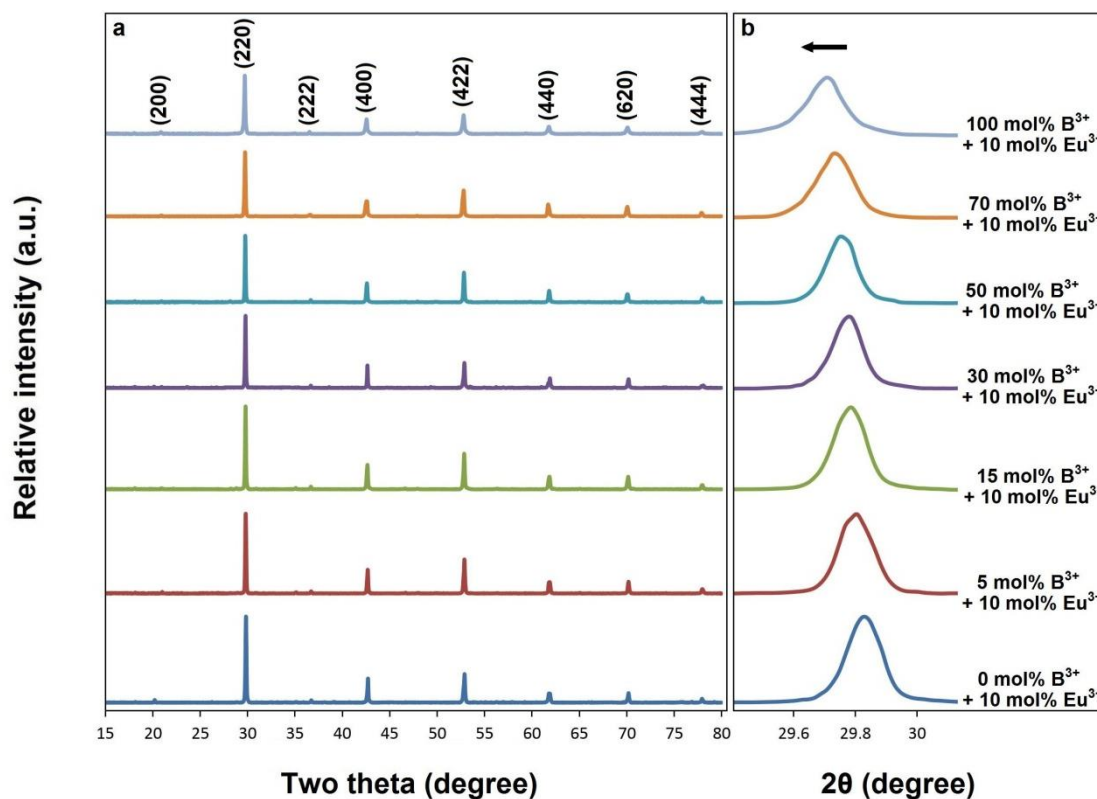


Figure 1: (a) X-ray diffractions of $\text{Ba}_2\text{Gd}_{1-x}\text{NbO}_6:x\text{Eu}^{3+}$, $y\text{B}^{3+}$ co-doped ceramics ($x=10$ mol%, and $y= 0, 5, 15, 30, 50, 70$ and 100 mol%), (b) XRD two theta peak (400) shifted to lower angles with B^{3+} concentration.

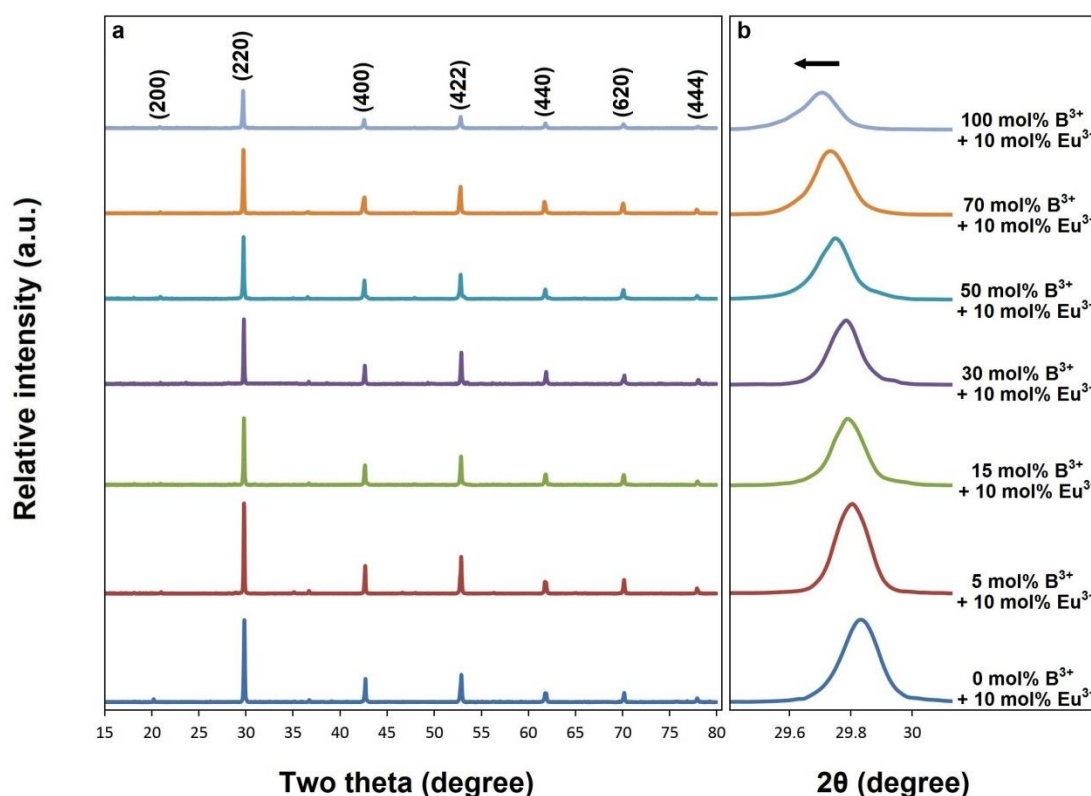


Figure 2: (a) X-ray diffractions of $\text{Ba}_2\text{Gd}_{1-x}\text{TaO}_6:x\text{Eu}^{3+}$, $y\text{B}^{3+}$ co-doped ceramics ($x=10$ mol%, and $y= 0, 5, 15, 30, 50, 70$ and 100 mol%), (b) XRD two theta peak (400) shifted to lower angles with B^{3+} concentration.

The average crystallite sizes of the samples determined from the Scherrer equation using two theta reflection peaks (220), (400) and (422) are summarized in Table 1. The increasing B^{3+}

concentration led to an increase in crystallite size in both series up to range of 30-50 mol%, and then a decrease occurred at 70 and 100 mol% concentrations. As seen in Table 1, the crystallite

sizes from 0 to 50 mol% B^{3+} varied to 42.36-49.14 nm for $Ba_2Gd_{1-x}NbO_6:xEu^{3+}, yB^{3+}$, while the sizes changed in the same range as 47.07-55.61 nm for $Ba_2Gd_{1-x}TaO_6:xEu^{3+}, yB^{3+}$, respectively. However, increasing boron concentration caused a decrease in crystallinity size at 70 and 100 mol% levels, where the crystallite sizes for 70 and 100 mol% B^{3+} concentrations were 45.79 and 43.38 nm (for $Ba_2Gd_{1-x}NbO_6:xEu^{3+}, yB^{3+}$) and 49.72 and 46.28 nm (for $Ba_2Gd_{1-x}TaO_6:xEu^{3+}, yB^{3+}$), respectively. Since

the temperature effect will increase with increasing boron, the nucleation rate will slow down, which is related to the increasing crystallite size in the 0-50 mol% range. On the other hand, the decrease in crystallite size at 70 and 100 mol% can be linked to elevated boron concentration, leading to heightened nucleation, lattice deformation, and disruption of the charge balance within the structure, particularly at higher levels of doping (36-38).

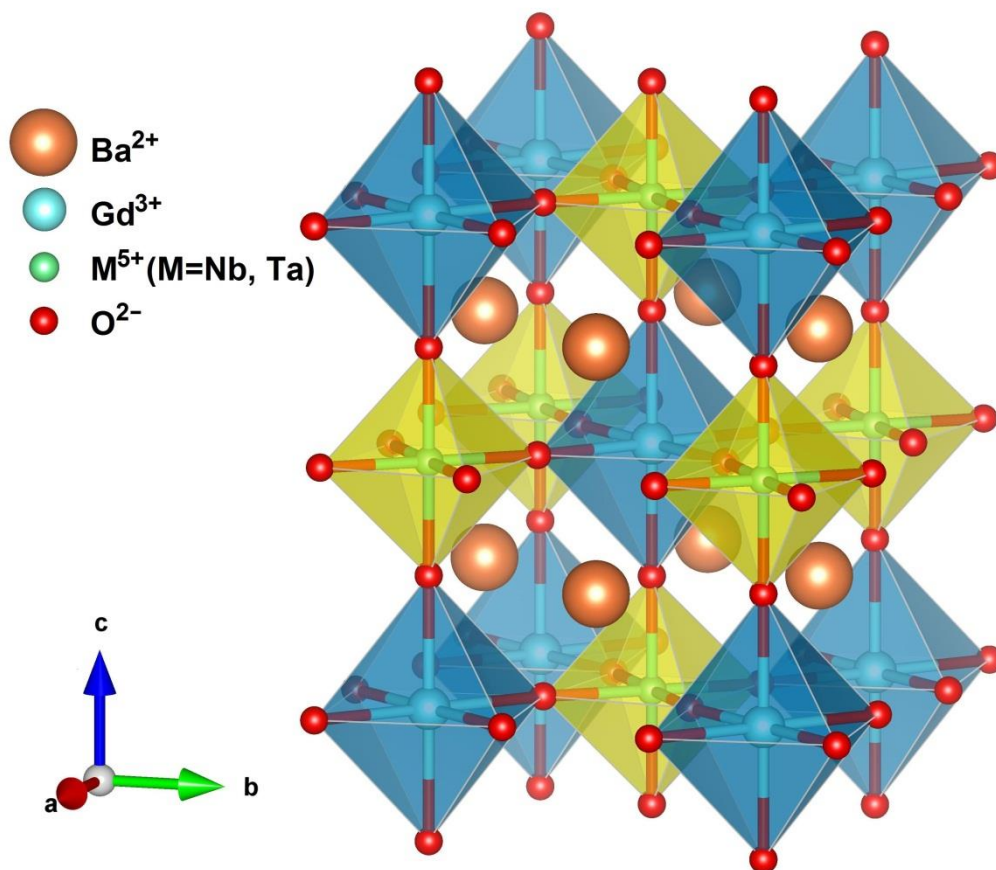


Figure 3: Crystal structure visualization of Ba_2GdMO_6 ($M=Nb, Ta$).

Table 1: Lattice parameters (a , V) and average crystallite sizes (D) for xEu^{3+}, yB^{3+} co-doped $Ba_2Gd_{1-x}NbO_6$ and $Ba_2Gd_{1-x}TaO_6$ ceramics.

Sample concentration (mol%)	$Ba_2Gd_{1-x}NbO_6:xEu^{3+}, yB^{3+}$			$Ba_2Gd_{1-x}TaO_6:xEu^{3+}, yB^{3+}$		
	a (Å)	V (Å ³)	D (nm)	a (Å)	V (Å ³)	D (nm)
0 B^{3+} , 10 Eu^{3+}	8.4729	608.27	42.36	8.4680	607.22	47.07
5 B^{3+} , 10 Eu^{3+}	8.4804	609.88	43.78	8.4717	608.02	48.08
15 B^{3+} , 10 Eu^{3+}	8.4841	610.69	46.57	8.4792	609.63	51.79
30 B^{3+} , 10 Eu^{3+}	8.4879	611.50	49.11	8.4830	610.44	55.92
50 B^{3+} , 10 Eu^{3+}	8.4954	613.12	49.14	8.4904	612.06	55.61
70 B^{3+} , 10 Eu^{3+}	8.4991	613.93	45.79	8.4867	611.25	49.72
100 B^{3+} , 10 Eu^{3+}	8.5029	614.75	43.38	8.4942	612.87	46.28

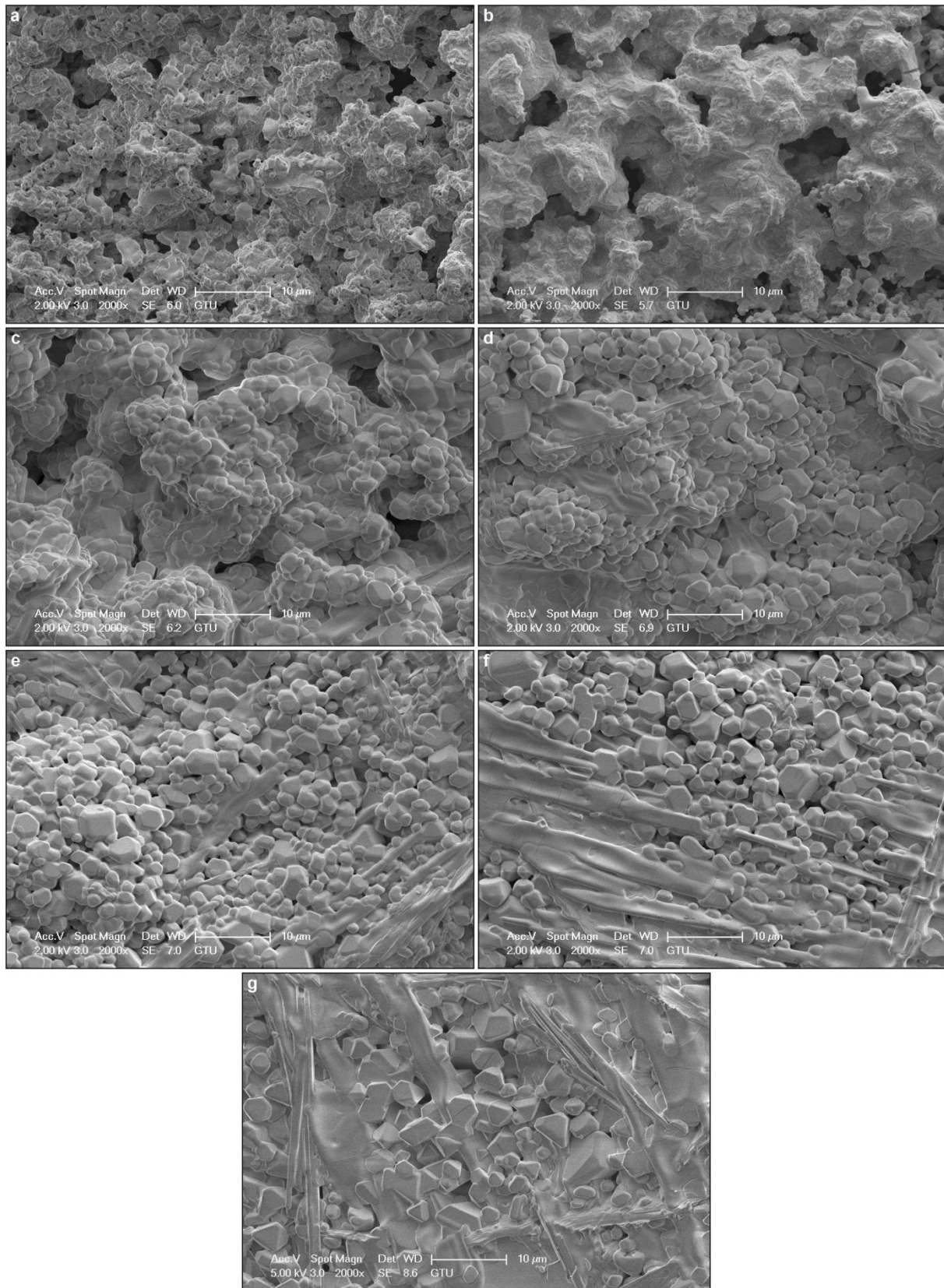


Figure 4: SEM micrographs of 10 mol% Eu^{3+} and (a) 0, (b) 5, (c) 15, (d) 30, (e) 50, (f) 70 and (g) 100 mol% B^{3+} co-doped $\text{Ba}_2\text{GdNbO}_6$ ceramics, at 2000 \times magnification and 2 kV acceleration voltage.

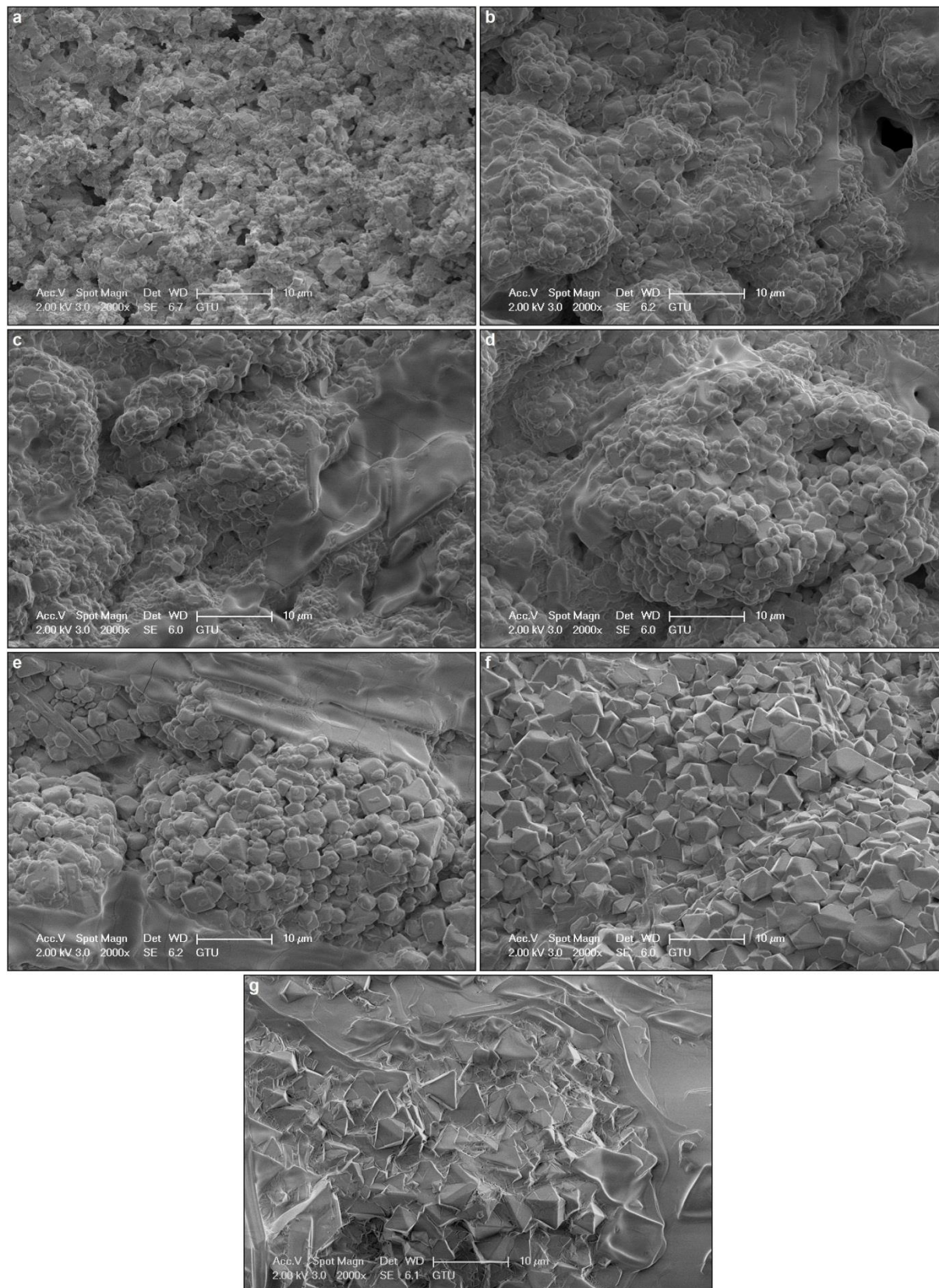


Figure 5: SEM micrographs of 10 mol% Eu^{3+} and (a) 0, (b) 5, (c) 15, (d) 30, (e) 50, (f) 70 and (g) 100 mol% B^{3+} co-doped $\text{Ba}_2\text{GdTao}_6$ ceramics, at 2000 \times magnification and 2 kV acceleration voltage.

Figure 4(a-g) and Figure 5(a-g) show the SEM micrographs of $\text{Ba}_2\text{Gd}_{1-x}\text{NbO}_6:x\text{Eu}^{3+}$, $y\text{B}^{3+}$ and $\text{Ba}_2\text{Gd}_{1-x}\text{TaO}_6:x\text{Eu}^{3+}$, $y\text{B}^{3+}$ ($x=10$ mol%, $y=0, 5, 30, 50, 70$ and 100 mol%) samples, respectively, at 2000 \times magnifications under 2 kV accelerating voltage. SEM micrographs of both series have an irregular shape and the grains are rounded, while the

increasing B^{3+} concentration led to grain growth and agglomeration. As well-known boron's flux effect reduces sintering temperature. Consequently, the increase in grain size may be attributed to the elevated temperatures resulting from boron addition. This higher temperature facilitates the release of stored energy within the grains, leading to an

increase in grain size (39,40). In addition, as seen in Figure 4(f,g) and Figure 5(f,g), the grain shape showed a slight angular trend at high B^{3+} concentrations. Moreover, at a concentration of 100 mol% B^{3+} , the agglomeration and flux effect is evident in the grains (Figure 4g and Figure 5g). The grain size of $Ba_2Gd_{1-x}NbO_6:xEu^{3+}$, yB^{3+} samples varied mostly in the range of 0.5-2 μm at 0 mol% concentration and there are also some grains reaching 3-4 μm , while the size of large grains ranging from 3 to 6 μm , while the grain size can exceed 10 μm , at 100 mol% concentration (Figure 4(f,g)). The grain sizes of $Ba_2Gd_{1-x}TaO_6:xEu^{3+}$, yB^{3+} samples are round-like and/or shapeless grains varied between 0.5-3 μm at 0 mol%, whilst the sizes of the angular grains at 100 mol% ranged between 4-10 μm (Figure 5(f,g)).

3.2. Dielectric Properties of $Ba_2Gd_{1-x}MO_6:xEu^{3+}$, yB^{3+} ($M=Nb, Ta$), ($x=10$ mol%, $y=0, 5, 15, 30, 50, 70$ and 100 mol%) Ceramics

Figure 6(a,b) show the dielectric constants (ϵ') with frequency for $Ba_2Gd_{1-x}NbO_6:xEu^{3+}$, yB^{3+} and $Ba_2Gd_{1-x}TaO_6:xEu^{3+}$, yB^{3+} ($x=10$ mol%, $y=0, 5, 15, 30, 50, 70$ and 100 mol%) samples, respectively. In Figure 6a, the dielectric constants of $Ba_2Gd_{1-x}NbO_6:xEu^{3+}$, yB^{3+} from 0 to 100 mol% B^{3+} changed approximately 21.3 and 33.5 at 20 Hz, respectively. In Figure 6b, at the same range and 20 Hz, the ϵ' values for the $Ba_2Gd_{1-x}TaO_6:xEu^{3+}$, yB^{3+} ceramics were 21.3 and 35.4, respectively. However, the dielectric constant did not change in the high frequency or over 10^3 Hz. As the frequency rises, the electron exchange's capability to align with the applied field diminishes, leading to a reduction in the dielectric constant. At extremely high frequencies, the field reverses before the space charge carriers can respond, thereby preventing them from contributing to polarization (41-47), so the dielectric constant almost stayed unchanged at the high-frequency range. Moreover, as seen in Figure 6(a,b) there is an increase in polarization or dielectric constant from 0 to 50 mol% B^{3+} . The increase can be accounted for by the Maxwell-Wagner theory of external factors. According to this principle, the dielectric constant correlates directly with the grain size of the sample. The larger grain sizes result in greater atom polarizability, leading to an uptick in the dielectric constant (48-52). In the SEM micrographs in Figure 4(a-g) and Figure 5(a-g), it was previously noted that there is an increase in grain size with increasing B^{3+} concentration. Hence, this circumstance may be ascribed to the declining occurrence of grain boundaries in both series, coupled with the rise in polarizability and the value of ϵ' within the atomic structure. Additionally, although there was a slight increase in grain size at 70 and 100 mol% B^{3+} concentrations in both series, there was a decrease in dielectric constant. Caruntu et al (53) stated that there is a direct correlation between the change of dielectric constant and crystallite size/microstrain, in which the crystallite size increases uniformly from 32

to 94 nm with the increase of sintering temperature from 600 to 1000 °C. On the other hand, Kim et al (54), in their study on $BaTiO_3$ and $SrTiO_3$, found that the presence of an optimal amount of lattice distortion or strain increases the dielectric constant. However, there is no information about crystallite size change in the study. As seen in Table 1, a decrease in crystallite size occurs at 70 and 100 mol% B^{3+} concentrations. Furthermore, while there is a noticeable rise in both crystallite size and dielectric constant as the concentration increases from 0 to 50 mol%, the augmented cell constant can be attributed to alterations in charge equilibrium and the existence of strain. In this context, the decrease in dielectric constant at 70 and 100 mol% could be linked to heightened strain due to an increased cell constant and deteriorated charge balance, as evidenced by the reduction in crystallite size.

Figure 7(a,b) show the dielectric losses ($\tan \delta$) with frequency for $Ba_2Gd_{1-x}NbO_6:xEu^{3+}$, yB^{3+} and $Ba_2Gd_{1-x}TaO_6:xEu^{3+}$, yB^{3+} ($x=10$ mol%, $y=0, 5, 15, 30, 50, 70$ and 100 mol%) samples, respectively. As seen in Figure 7(a,b), dielectric loss continuously decreases with the increase in frequency. In the low-frequency range where resistance is high, polarization necessitates more energy because of the grain boundary. Conversely, in the high-frequency range where resistance is low, electron transfer across the grain boundary requires minimal energy, resulting in reduced energy loss (54-57). On the other hand, the dielectric loss factor for both sample series decreased with increasing B^{3+} concentration up to 50 mol% and then showed a slight increase at 70 and 100 mol%. Various studies in the literature connect the $\tan \delta$ in ferroelectrics to oxygen vacancies, which contribute to the dielectric loss or leakage current (58-61). Liu et al (62) studied the dielectric loss and oxygen vacancy relation by fabricating $TTB-Ba_4Nd_2Fe_2Nb_8O_{30}$ ceramics at different annealing and sintering temperatures as well as in O_2 and N_2 atmospheres, where the increase in temperature reduces oxygen vacancies and electrical conductivity. Similarly, in the study reported by Iqbal et al (57) on $CuFe_2O_4$, an increase in crystallite size and dielectric constant occurred due to the increase in annealing temperature. The results of the flux effect of boron, as seen in the XRD-SEM section, the temperature effect on the structure will increase with increasing boron concentration. Thus, the higher concentration of boron will not only intensify the material's sensitivity to temperature but also impact the presence of oxygen vacancies. Therefore, the decrease in the dielectric loss factor in both series may be attributed to the suppression of oxygen vacancies by the temperature effect that increases with the increase in B^{3+} . In addition, the slightly increased dielectric loss at the 70 and 100 mol% levels is likely due to the high B^{3+} concentration leading to some increase in the mobility of oxygen vacancies in the structure.

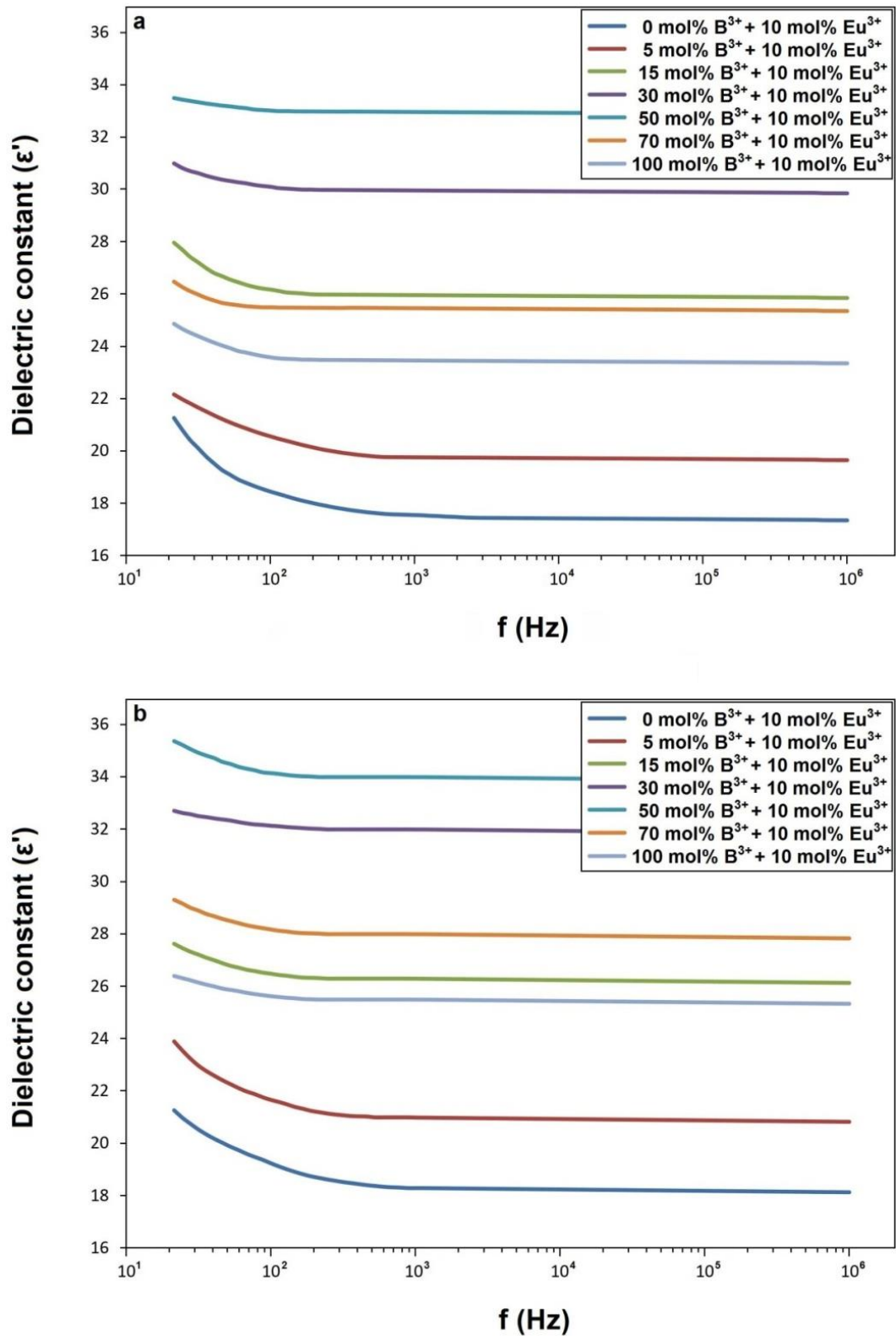


Figure 6: Dielectric constants for (a) $Ba_2Gd_{1-x}NbO_6 \cdot xEu^{3+}$, yB^{3+} ($x=10$ mol%, $y=0, 5, 15, 30, 50, 70, 100$ mol%), and (b) $Ba_2Gd_{1-x}TaO_6 \cdot xEu^{3+}$, yB^{3+} ($x=10$ mol%, $y=0, 5, 15, 30, 50, 70, 100$ mol%) ceramics.

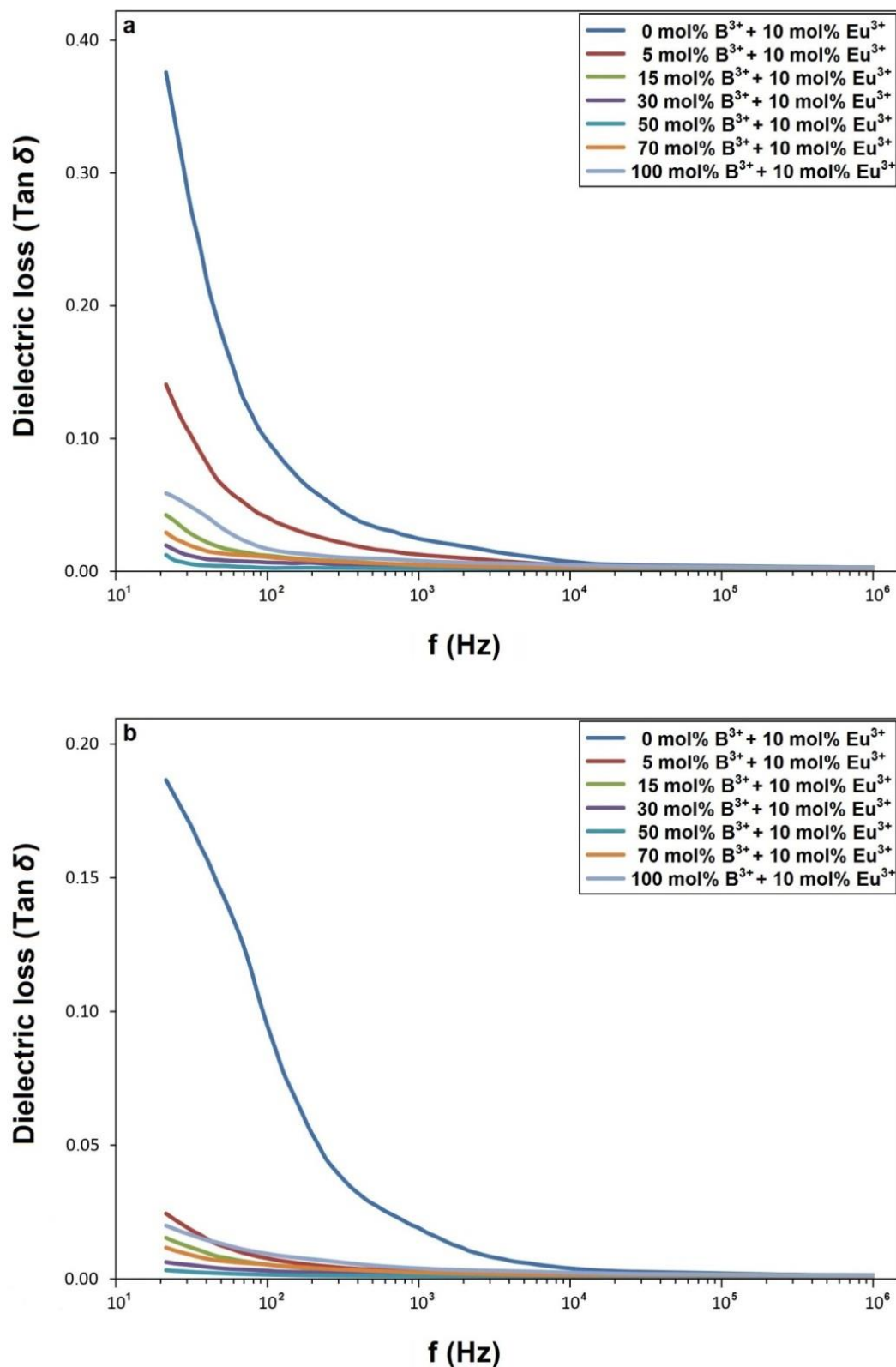


Figure 7: Dielectric losses ($\tan \delta$) for (a) $Ba_2Gd_{1-x}NbO_6:xEu^{3+}, yB^{3+}$ ($x=10$ mol%, $y=0, 5, 15, 30, 50, 70, 100$ mol%), and (b) $Ba_2Gd_{1-x}TaO_6:xEu^{3+}, yB^{3+}$ ($x=10$ mol%, $y=0, 5, 15, 30, 50, 70, 100$ mol%) ceramics.

4. CONCLUSION

The effect of boron on the structural and dielectric properties was studied by using Eu^{3+} , B^{3+} co-doped double perovskite $Ba_2Gd_{1-x}MO_6:xEu^{3+}, yB^{3+}$ ($M=Nb, Ta$), ($x=10$ mol%, $y=0, 5, 15, 30, 50, 70$ and 100 mol%) ceramics, in which XRD results of the ceramics showed a single-phase structure. $Ba_2Gd_{1-x}TaO_6:xEu^{3+}, yB^{3+}$ samples had slightly better

crystallite sizes than $Ba_2Gd_{1-x}NbO_6:xEu^{3+}, yB^{3+}$ ones, while the crystallinity of both sample series increased up to about 50 mol% B^{3+} , and then decreased at 70 and 100 mol%. SEM micrographs of Eu^{3+} , B^{3+} co-doped samples showed that boron in both series supported aggregation and growth in grains, and a slight angularity in grain shape occurred at high B^{3+} concentrations. The ϵ' values of $Ba_2Gd_{1-x}NbO_6:xEu^{3+}, yB^{3+}$, and $Ba_2Gd_{1-x}NbO_6:xEu^{3+}, yB^{3+}$ were measured

in the range of 21.3-33.5 and 21.3 and 35.4 at 20 Hz, respectively. For both series, the increasing dielectric constant up to 50 mol% B³⁺ concentration was associated with the developing grain size and crystallinity, while its decrease at 70 and 100 mol% was associated with the reduction in crystallite size. The dielectric loss factor for both series decreased with increasing B³⁺ concentration, whilst Ba₂Gd_{1-x}TaO₆:xEu³⁺, yB³⁺ series exhibited a lower loss factor. The decline in dielectric loss in both series as B³⁺ concentration rises was linked to the reduction of oxygen vacancies. The heightened presence of B³⁺ resulted in diminished ionic conductivity and consequently decreased dielectric loss. The study may be useful in evaluating the dielectric properties of double perovskite ceramics, in terms of controlling the grain morphology and crystallite size.

5. CONFLICT OF INTEREST

There is no conflict of interest

6. REFERENCES

- Luo Y, Chen Y, Li L, Chen J, Pang T, Chen L, et al. Three-mode fluorescence thermometers based on double perovskite Ba₂GdNbO₆:Eu³⁺,Mn⁴⁺ phosphors. *Ceram Int* [Internet]. 2023 Dec;49(23):38007–14. Available from: [<URL>](#).
- Li J, Wang X, Cui R, Deng C. Synthesis and photoluminescence studies of novel double-perovskite phosphors, Ba₂GdTao₆:Eu³⁺ for WLEDs. *Optik (Stuttg)* [Internet]. 2020 Jan;201:163536. Available from: [<URL>](#).
- Sun Q, Wang S, Devakumar B, Sun L, Liang J, Huang X. Synthesis, Crystal Structure, and Photoluminescence Characteristics of High-Efficiency Deep-Red Emitting Ba₂GdTao₆:Mn⁴⁺ Phosphors. *ACS Omega* [Internet]. 2019 Aug 20;4(8):13474–80. Available from: [<URL>](#).
- Han B, Zhu J, Chu C, Yang X, Wang Y, Li K, et al. Sm³⁺-Mn⁴⁺ activated Sr₂GdTao₆ red phosphor for plant growth lighting and optical temperature sensing. *Sensors Actuators A Phys* [Internet]. 2023 Jan;349:114089. Available from: [<URL>](#).
- Sun J, Sun Z, Li Y, Jin Z, Ma L, Lu R, et al. Realization of plant growth lighting and temperature detecting based on novel Bi³⁺, Sm³⁺ and Mn⁴⁺ doped Ca₂GdNbO₆ double perovskite phosphors. *Opt Mater (Amst)* [Internet]. 2023 Nov;145:114394. Available from: [<URL>](#).
- Wang L, Zhang Y, Gao D, Sha X, Chen X, Zhang Y, et al. Concentration- and temperature- dependent luminescence quenching and optical transition of Sr₂GdTao₆: Eu³⁺ phosphor for potential applications in white LEDs. *Results Phys* [Internet]. 2024 Jan;56:107238. Available from: [<URL>](#).
- Han Y jie, Wang S, Liu H, Shi L, Zhang J ying, Zhang Z ni, et al. Synthesis and luminescent properties of a novel deep-red phosphor Sr₂GdNbO₆:Mn⁴⁺ for indoor plant growth lighting. *J Lumin* [Internet]. 2020 Apr;220:116968. Available from: [<URL>](#).
- Ranjbar B, Pavan A, Kennedy BJ, Zhang Z. Structural and magnetic properties of the ruthenium double perovskites Ba_{2-x}Sr_xYRuO₆. *Dalt Trans* [Internet]. 2015;44(23):10689–99. Available from: [<URL>](#).
- Shimizu Y, Sakagami S, Goto K, Nakachi Y, Ueda K. Tricolor luminescence in rare earth doped CaZrO₃ perovskite oxides. *Mater Sci Eng B* [Internet]. 2009 Apr;161(1-3):100–3. Available from: [<URL>](#).
- Wang S, Sun Q, Devakumar B, Liang J, Sun L, Huang X. Novel highly efficient and thermally stable Ca₂GdTao₆:Eu³⁺ red-emitting phosphors with high color purity for UV/blue-excited WLEDs. *J Alloys Compd* [Internet]. 2019 Oct;804:93–9. Available from: [<URL>](#).
- Yin X, Wang Y, Huang F, Xia Y, Wan D, Yao J. Excellent red phosphors of double perovskite Ca₂LaMO₆:Eu (M=Sb, Nb, Ta) with distorted coordination environment. *J Solid State Chem* [Internet]. 2011 Dec;184(12):3324–8. Available from: [<URL>](#).
- Chen J, Zhao S, Zhao Z, Liao M, Pan S, Feng J, et al. The structure and luminescence properties of blue-green-emitting Sr₂YNbO₆: Bi³⁺ phosphors. *J Lumin* [Internet]. 2021 Nov;239:118336. Available from: [<URL>](#).
- Baral SC, Maneesha P, Rini EG, Sen S. Recent advances in LaNiMnO double perovskites for various applications; challenges and opportunities. *Prog Solid State Chem* [Internet]. 2023 Dec;72:100429. Available from: [<URL>](#).
- Wang CF, Shi C, Zheng A, Wu Y, Ye L, Wang N, et al. Achieving circularly polarized luminescence and large piezoelectric response in hybrid rare-earth double perovskite by a chirality induction strategy. *Mater Horizons* [Internet]. 2022;9(9):2450–9. Available from: [<URL>](#).
- Mishra S, Choudhary RNP, Parida SK. A multifunctional transition metal based double perovskite Ba₂(FeW)O₆: Structural, microstructural, optical, electrical and ferroelectric properties. *Ceram Int* [Internet]. 2023 Jul;49(14):22702–17. Available from: [<URL>](#).
- Parida BN, Panda N, Padhee R, Parida RK. Ferroelectric and optical behavior of Pb_{0.5}Ba_{1.5}BiNbO₆ double perovskite. *Ferroelectrics* [Internet]. 2019 Feb 17;540(1):18–28. Available from: [<URL>](#).
- Bendahhou A, Marchet P, El-Houssaine A, El Barkany S, Abou-Salama M. Relationship between structural and dielectric properties of Zn-substituted Ba₅CaTi_{2-x}Zn_xNb₈O₃₀ tetragonal tungsten bronze. *CrystEngComm* [Internet]. 2021;23(1):163–73. Available from: [<URL>](#).
- Jindal S, Vasishth A, Devi S, Anand G. A review on tungsten bronze ferroelectric ceramics as electrically tunable devices. *Integr Ferroelectr* [Internet]. 2018 Jan 2;186(1):1–9. Available from: [<URL>](#).

[<URL>](#).

19. Shimizu K, Kato H, Kobayashi M, Kakihana M. Synthesis and photocatalytic properties of tetragonal tungsten bronze type oxynitrides. *Appl Catal B Environ* [Internet]. 2017 Jun;206:444–8. Available from: [<URL>](#).

20. İlhan M, Keskin İÇ. Evaluation of structural behaviour, radioluminescence, Judd-Ofelt analysis and thermoluminescence kinetic parameters of Eu^{3+} doped TTB-type lead metaniobate phosphor. *Phys B Condens Matter* [Internet]. 2020 May;585:412106. Available from: [<URL>](#).

21. İlhan M, Ekmekçi MK, Mergen A, Yaman C. Synthesis and Optical Characterization of Red-Emitting $\text{BaTa}_2\text{O}_6:\text{Eu}^{3+}$ Phosphors. *J Fluoresc* [Internet]. 2016 Sep 21;26(5):1671–8. Available from: [<URL>](#).

22. İlhan M, Ekmekçi MK, Demir A, Demirer H. Synthesis and Optical Properties of Novel Red-Emitting $\text{PbNb}_2\text{O}_6:\text{Eu}^{3+}$ Phosphors. *J Fluoresc* [Internet]. 2016 Sep 20;26(5):1637–43. Available from: [<URL>](#).

23. İlhan M. Synthesis, structural characterization, and photoluminescence properties of TTB-type $\text{PbTa}_2\text{O}_6:\text{Eu}^{3+}$ phosphor. *Int J Appl Ceram Technol* [Internet]. 2017 Nov 30;14(6):1144–50. Available from: [<URL>](#).

24. İlhan M, Güleriyüz LF, Ekmekçi MK. Structural Properties, Photoluminescence, and Judd-Ofelt Parameters of Eu^{3+} -Doped CoNb_2O_6 Phosphor. *J Turkish Chem Soc Sect A Chem* [Internet]. 2023 Aug 30;10(3):745–56. Available from: [<URL>](#).

25. İlhan M, Ekmekçi MK, Keskin İÇ. Judd-Ofelt parameters and X-ray irradiation results of $\text{MNb}_2\text{O}_6:\text{Eu}^{3+}$ ($M = \text{Sr}, \text{Cd}, \text{Ni}$) phosphors synthesized via a molten salt method. *RSC Adv* [Internet]. 2021;11(18):10451–62. Available from: [<URL>](#).

26. Başak AS, Ekmekçi MK, Erdem M, İlhan M, Mergen A. Investigation of Boron-doping Effect on Photoluminescence Properties of $\text{CdNb}_2\text{O}_6:\text{Eu}^{3+}$ Phosphors. *J Fluoresc* [Internet]. 2016 Mar 11;26(2):719–24. Available from: [<URL>](#).

27. İlhan M, Katı Mİ, Keskin İÇ, Güleriyüz LF. Evaluation of structural and spectroscopic results of tetragonal tungsten bronze $\text{MTa}_2\text{O}_6:\text{Eu}^{3+}$ ($M = \text{Sr}, \text{Ba}, \text{Pb}$) phosphors and comparison on the basis of Judd-Ofelt parameters. *J Alloys Compd* [Internet]. 2022 Apr;901:163626. Available from: [<URL>](#).

28. İlhan M, Güleriyüz LF. Boron doping effect on the structural, spectral properties and charge transfer mechanism of orthorhombic tungsten bronze $\beta\text{-SrTa}_2\text{O}_6:\text{Eu}^{3+}$ phosphor. *RSC Adv* [Internet]. 2023;13(18):12375–85. Available from: [<URL>](#).

29. İlhan M, Güleriyüz LF, Katı Mİ. Exploring the effect of boron on the grain morphology change and spectral properties of Eu^{3+} activated barium tantalate phosphor. *RSC Adv* [Internet]. 2024;14(4):2687–96. Available from: [<URL>](#).

30. Li Z, Zhou W, Su X, Luo F, Huang Y, Wang C. Effect of boron doping on microwave dielectric properties of SiC powder synthesized by combustion synthesis. *J Alloys Compd* [Internet]. 2011 Jan;509(3):973–6. Available from: [<URL>](#).

31. Mazumder R, Seal A, Sen A, Maiti HS. Effect of Boron Addition on the Dielectric Properties of Giant Dielectric $\text{CaCu}_3\text{Ti}_4\text{O}_{12}$ Ferroelectrics [Internet]. 2005 Oct;326(1):103–8. Available from: [<URL>](#).

32. Zhang X, Wang B, Huang W, Chen Y, Wang G, Zeng L, et al. Synergistic Boron Doping of Semiconductor and Dielectric Layers for High-Performance Metal Oxide Transistors: Interplay of Experiment and Theory. *J Am Chem Soc* [Internet]. 2018 Oct 3;140(39):12501–10. Available from: [<URL>](#).

33. Cullity BD, Stock SR. *Elements of X-ray Diffraction*. USA: Prentice Hall; 2001.

34. Koshy J, Thomas JK, Kurian J, Yadava YP, Damodaran AD. Development and characterization of $\text{GdBa}_2\text{NbO}_6$, a new ceramic substrate for YBCO thick films. *Mater Lett* [Internet]. 1993 Oct;17(6):393–7. Available from: [<URL>](#).

35. Babu TGN, Koshy J. $\text{Ba}_2\text{GdTao}_6$, a ceramic substrate for $\text{YBa}_2\text{Cu}_3\text{O}_7\text{-gd}$ films. *Mater Lett* [Internet]. 1997 Nov;33(1–2):7–11. Available from: [<URL>](#).

36. Tahar RBH, Tahar NBH. Boron-doped zinc oxide thin films prepared by sol-gel technique. *J Mater Sci* [Internet]. 2005 Oct;40(19):5285–9. Available from: [<URL>](#).

37. Addonizio ML, Diletto C. Doping influence on intrinsic stress and carrier mobility of LP-MOCVD-deposited $\text{ZnO}:\text{B}$ thin films. *Sol Energy Mater Sol Cells* [Internet]. 2008 Nov;92(11):1488–94. Available from: [<URL>](#).

38. İlhan M, Ekmekçi MK, Güleriyüz LF. Effect of boron incorporation on the structural, morphological, and spectral properties of $\text{CdNb}_2\text{O}_6:\text{Dy}^{3+}$ phosphor synthesized by molten salt process. *Mater Sci Eng B* [Internet]. 2023 Dec;298:116858. Available from: [<URL>](#).

39. Polyxeni V, Nikolaos D P, Nikos S, Sotirios X, Evangelos H. Temperature effects on grain growth phenomena and magnetic properties of silicon steels used in marine applications. *Ann Mar Sci* [Internet]. 2023 Jun 21;7(1):40–4. Available from: [<URL>](#).

40. Güleriyüz LF, İlhan M. Structural, morphological, spectral properties and high quantum efficiency of Eu^{3+} , B^{3+} co-activated double perovskite Ba_2GdMO_6 ($M = \text{Nb}, \text{Ta}$) phosphors. *Mater Sci Eng B* [Internet]. 2024 Jun;304:117373. Available from: [<URL>](#).

41. Mahapatro J, Agrawal S. Effect of Eu^{3+} ions on electrical and dielectric properties of barium hexaferrites prepared by solution combustion method. *Ceram Int* [Internet]. 2021 Jul;47(14):20529–43. Available from: [<URL>](#).

42. Evangeline T G, Annamalai A R, Ctibor P. Effect of Europium Addition on the Microstructure and Dielectric Properties of CCTO Ceramic Prepared Using Conventional and Microwave Sintering. *Molecules* [Internet]. 2023 Feb 8;28(4):1649. Available from: [<URL>](#).
43. Rayssi C, El.Kossi S, Dhahri J, Khirouni K. Frequency and temperature-dependence of dielectric permittivity and electric modulus studies of the solid solution $\text{Ca}_{0.85}\text{Er}_{0.1}\text{Ti}_{1-x}\text{Co}_{4x/3}\text{O}_3$ ($0 \leq x \leq 0.1$). *RSC Adv* [Internet]. 2018;8(31):17139–50. Available from: [<URL>](#).
44. Kadam AA, Shinde SS, Yadav SP, Patil PS, Rajpure KY. Structural, morphological, electrical and magnetic properties of Dy doped Ni–Co substitutional spinel ferrite. *J Magn Magn Mater* [Internet]. 2013 Mar;329:59–64. Available from: [<URL>](#).
45. Tan YQ, Yu Y, Hao YM, Dong SY, Yang YW. Structure and dielectric properties of $\text{Ba}_5\text{NdCu}_{1.5}\text{Nb}_{8.5}\text{O}_{30-\delta}$ tungsten bronze ceramics. *Mater Res Bull* [Internet]. 2013 May;48(5):1934–8. Available from: [<URL>](#).
46. Esha IN, Al-Amin M, Toma FTZ, Hossain E, Khan MNI, Maria KH. Synthesis and analysis of the influence of Eu^{3+} on the structural, ferromagnetic, dielectric and conductive characteristics of $\text{Ni}_{0.4}\text{Zn}_{0.45}\text{Cu}_{0.15}\text{Fe}_{(2-x)}\text{Eu}_x\text{O}_4$ composites using conventional double sintering ceramic method. *J Ceram Process Res* [Internet]. 2019 Oct;20(5):530–9. Available from: [<URL>](#).
47. Shah MR, Akther Hossain AKM. Structural and dielectric properties of La substituted polycrystalline $\text{Ca}(\text{Ti}_{0.5}\text{Fe}_{0.5})\text{O}_3$. *Mater Sci* [Internet]. 2013 Jan 25;31(1):80–7. Available from: [<URL>](#).
48. Wagner KW. Zur Theorie der unvollkommenen Dielektrika. *Ann Phys* [Internet]. 1913 Jan 14;345(5):817–55. Available from: [<URL>](#).
49. Maxwell JC. A treatise on electricity and magnetism. London: Caleredon press, Oxford University; 1873.
50. Samet M, Kallel A, Serghei A. Maxwell-Wagner-Sillars interfacial polarization in dielectric spectra of composite materials: Scaling laws and applications. *J Compos Mater* [Internet]. 2022 Aug 28;56(20):3197–217. Available from: [<URL>](#).
51. Saengvong P, Chanlek N, Srepusharawoot P, Harnchana V, Thongbai P. Enhancing giant dielectric properties of Ta^{5+} -doped $\text{Na}_{1/2}\text{Y}_{1/2}\text{Cu}_3\text{Ti}_4\text{O}_{12}$ ceramics by engineering grain and grain boundary. *J Am Ceram Soc* [Internet]. 2022 May 15;105(5):3447–55. Available from: [<URL>](#).
52. Karmakar S, Mohanty HS, Behera D. Exploration of alternating current conduction mechanism and dielectric relaxation with Maxwell–Wagner effect in $\text{NiO–CdO–Gd}_2\text{O}_3$ nanocomposites. *Eur Phys J Plus* [Internet]. 2021 Oct 15;136(10):1038. Available from: [<URL>](#).
53. Caruntu G, Rarig Jr R, Dumitru I, O’Connor CJ. Annealing effects on the crystallite size and dielectric properties of ultrafine $\text{Ba}_{1-x}\text{Sr}_x\text{TiO}_3$ ($0 < x < 1$) powders synthesized through an oxalate-complex precursor. *J Mater Chem* [Internet]. 2006;16(8):752–8. Available from: [<URL>](#).
54. Kim L, Jung D, Kim J, Kim YS, Lee J. Strain manipulation in $\text{BaTiO}_3/\text{SrTiO}_3$ artificial lattice toward high dielectric constant and its nonlinearity. *Appl Phys Lett* [Internet]. 2003 Mar 31;82(13):2118–20. Available from: [<URL>](#).
55. Sati PC, Kumar M, Chhoker S, Jewariya M. Influence of Eu substitution on structural, magnetic, optical and dielectric properties of BiFeO_3 multiferroic ceramics. *Ceram Int* [Internet]. 2015 Mar;41(2):2389–98. Available from: [<URL>](#).
56. Ganguly P, Jha AK. Enhanced characteristics of $\text{Ba}_5\text{SmTi}_3\text{Nb}_7\text{O}_{30}$ ferroelectric nanocrystalline ceramic prepared by mechanical activation process: A comparative study. *Mater Res Bull* [Internet]. 2011 May;46(5):692–7. Available from: [<URL>](#).
57. Iqbal MJ, Yaqub N, Sepiol B, Ismail B. A study of the influence of crystallite size on the electrical and magnetic properties of CuFe_2O_4 . *Mater Res Bull* [Internet]. 2011 Nov;46(11):1837–42. Available from: [<URL>](#).
58. Chakrabarti A, Bera J. Effect of La-substitution on the structure and dielectric properties of $\text{BaBi}_4\text{Ti}_4\text{O}_{15}$ ceramics. *J Alloys Compd* [Internet]. 2010 Sep;505(2):668–74. Available from: [<URL>](#).
59. Kumar P, Kar M. Effect of structural transition on magnetic and optical properties of Ca and Ti co-substituted BiFeO_3 ceramics. *J Alloys Compd* [Internet]. 2014 Jan;584:566–72. Available from: [<URL>](#).
60. İlhan M, Ekmekci MK, Esmer K. Structural and dielectric properties of $\text{Eu}^{3+}, \text{B}^{3+}$ co-doped CoNb_2O_6 ceramic. *J Turkish Chem Soc Sect A Chem* [Internet]. 2024 May 15;11(2):765–74. Available from: [<URL>](#).
61. Kendall KR, Thomas JK, Loye HC. Synthesis and ionic conductivity of a new series of modified Aurivillius phases. *Chem Mater* [Internet]. 1995 Jan 1;7(1):50–7. Available from: [<URL>](#).
62. Fei Liu S, Jun Wu Y, Li J, Ming Chen X. Effects of oxygen vacancies on dielectric, electrical, and ferroelectric properties of $\text{Ba}_4\text{Nd}_2\text{Fe}_2\text{Nb}_8\text{O}_{30}$ ceramics. *Appl Phys Lett* [Internet]. 2014 Feb 24;104(8):082912. Available from: [<URL>](#).



Structural and Dielectric Properties of RE³⁺, B³⁺ co-doped (RE³⁺=Sm³⁺, Dy³⁺) BaTa₂O₆ Tetragonal Tungsten Bronze-Type Ceramics

Mustafa İlhan^{1*}, Mehmet İsmail Katı², Lütfiye Feray Güteryüz³

¹Department of Environmental Engineering, Faculty of Engineering, Marmara University, Maltepe, 34854, İstanbul, Türkiye.

²Department of Medical Imaging Techniques, Vocational School of Health Sciences, Manisa Celal Bayar University, 45030, Manisa, Türkiye.

³Department of Tobacco Technology Engineering, Manisa Celal Bayar University, Akhisar 45200, Manisa, Türkiye.

Abstract: In this paper, the effect of boron doping on dielectric properties was investigated using BaTa₂O₆:xSm³⁺, yB³⁺ (x=5 mol%, y= 0, 5, 15, 30, 50, 70, 100 mol%) and BaTa₂O₆:xDy³⁺, yB³⁺ (x=10 mol%, y= 0, 5, 15, 30, 50, 70, 100 mol%) tungsten bronze ceramics fabricated by the conventional solid-state synthesis. XRD (X-ray diffraction) results revealed a single BaTa₂O₆ phase with space group *P4/mbm* (127) for both series. Additionally, in both series, there was an increase in crystallite sizes and cell parameters with increasing B³⁺ concentration. SEM (scanning electron microscopy) examinations indicated that the increase of boron promoted grain growth and grain elongation. In impedance results, in both series, increasing boron concentration up to 100 mol% increased the dielectric constant. Moreover, the presence of boron was associated with a relaxing transition in the B-site substitution of RE³⁺ (RE=Sm, Dy) ions and a contribution to the dielectric permittivity, while the increase in tetragonality or c/a ratio for both series was ascribed to the increase in the ferroelectric Curie temperature. In both series, a decrease in dielectric loss (tan δ) occurred, which was explained by the increasing sintering temperature effect with increasing boron, reducing the mobility of oxygen vacancies.

Keywords: XRD, SEM, RE³⁺ B³⁺ co-doping, Dielectric properties.

Submitted: March 16, 2024. **Accepted:** May 27, 2024.

Cite this: İlhan M, Katı MI, Güteryüz LF. Structural and Dielectric Properties of RE³⁺, B³⁺ co-doped (RE³⁺=Sm³⁺, Dy³⁺) BaTa₂O₆ Tetragonal Tungsten Bronze-Type Ceramics. JOTCSA. 2024;11(3): 1111-24.

DOI: <https://doi.org/10.18596/jotcsa.1453941>

***Corresponding author's E-mail:** mustafa.ilhan@marmara.edu.tr

1. INTRODUCTION

Tetragonal tungsten bronze (TTB) oxides compose the largest dielectric family just next to the perovskites (AMO₃), and they exhibit chemical and magnetic stability with excellent crystal structure (1-4). TTB structures can generally have very important and advantageous electrical, magnetic, optical and photocatalytic properties with various applications in the electronics, chemistry and energy conversion areas. Therefore, research on the electrical properties of TTB materials will contribute significantly to the development of multifunctional optoelectronic devices in the future (5-8). Luminescent-ferroelectrics can be obtained from ferroelectric host materials doped with RE ions. Among trivalent rare earths (RE³⁺), when doped into various inorganic hosts, Sm³⁺ ions exhibit 4f-4f transitions mainly from the ⁴G_{5/2} excited state to ⁶H_{5/2}, ⁶H_{7/2}, ⁶H_{9/2}, and ⁶H_{11/2} energy levels, leading to the orange-red emission (9,10), while Dy³⁺ ions

show energy levels of ⁶H_{15/2}, ⁶H_{13/2}, ⁶H_{11/2}, and ⁶H_{9/2} mainly resulting from ⁴F_{9/2} excitation, leading to blue-yellow-red emission (11-13).

TTB crystal symmetry can be derived from an A-cationic deficient perovskite structure by cylindrical rotation of a square group consisting of four corner-sharing octahedra through 45°, and they may exhibit large spontaneous polarization and high dielectric constants due to its structure consisting of corner-sharing MO₆ (M=Ta, Nb etc) octahedra arrays and three different tunnels (or sites) for cation filling (14-16). BaTa₂O₆ exhibits excellent ferroelectric properties, and it has orthorhombic, tetragonal and hexagonal polymorphs, in which the tetragonal polymorph has TTB-type structure (17,18). BaTa₂O₆ is reported due to luminescence, dielectric, thermodynamic, and photocatalytic properties (19-22). Boron is widely used to reduce the sintering temperature of ceramics and to improve optical and dielectric properties as well as structural features

such as morphology and crystallinity (23-26). Moreover, there are studies on the effect of boron on grain morphology and its improvement in dielectric properties in which the doping of boron has the effect of increasing the bulk properties to some extent and can reduce the grain boundaries in the structure (27-29).

In the study, the structural and dielectric properties of Sm^{3+} , B^{3+} co-doped BaTa_2O_6 and Dy^{3+} , B^{3+} co-doped BaTa_2O_6 ceramics were investigated. The structural and dielectric characterizations of the samples were carried out by XRD, SEM, and impedance analyses.

2. EXPERIMENTAL

$\text{BaTa}_2\text{O}_6:x\text{Sm}^{3+}, y\text{B}^{3+}$ ($x=5$ mol%, $y=0, 5, 15, 30, 50, 70$ and 100 mol%) and $\text{BaTa}_2\text{O}_6:x\text{Dy}^{3+}, y\text{B}^{3+}$ ($x=10$ mol%, $y=0, 5, 15, 30, 50, 70$ and 100 mol%) ceramic samples were fabricated by solid-state reaction. Barium carbonate BaCO_3 (Sigma-Aldrich, 99%), niobium oxide (Nb_2O_5 : Alfa Aesar, 99.9%), and tantalum oxide (Ta_2O_5 : Alfa Aesar, 99.9%) powders were used as starting materials in calculated stoichiometric amounts. Dysprosium oxide (Dy_2O_3 : Alfa Aesar, 99.9%) samarium oxide (Sm_2O_3 : Alfa Aesar, 99.9%) and boric acid (H_3BO_3 : Kimyalab, %99.9) were used as dopant materials. The stoichiometric amounts of $\text{BaTa}_2\text{O}_6:0.05\text{Sm}^{3+}$ and $\text{BaTa}_2\text{O}_6:0.10\text{Dy}^{3+}$ starting materials were weighed and mixed in an agate mortar to provide more homogeneity. Then, by adding different amounts of boric acid (H_3BO_3), the final mixture of the powders was thoroughly mixed and ground in an agate mortar for the last time to provide more homogeneity. For sintering process, the sufficient amount of mixture was taken an alumina crucible at 1425°C for 10 h after pelleting.

The phase structure of the ceramic samples were examined by (X-ray diffractometer; Panalytical Emperial, Malvern Panalytical Ltd., United Kingdom) using Cu-K_α (1.5406 Å) radiation in between $2\theta=20-65^\circ\text{C}$ with scan speed $2^\circ\text{C}/\text{min}$. The grain morphology of the ceramic samples was investigated by scanning electron microscopy (FE-

SEM; Gemini 500, Zeiss Corp., Germany). The lattice parameters were found from (001) and (400) reflections. The average crystallite sizes were calculated using (101), (210), and (311) reflections from Scherrer Eq. (1) (30):

$$D = \frac{k \cdot \lambda}{B \cdot \cos \theta} \quad (2)$$

where D stands for particle size in nanometers, with k assumed to be a constant (usually taken as 0.9). $\text{CuK}\alpha$ represents the wavelength ($\lambda = 0.15406 \text{ \AA}$), and B is the full width at half maximum in radians. Frequency-dependent changes of real and imaginary permittivity and loss factor were defined using dielectric Eq. (2) and Eq. (3) respectively:

$$\epsilon' = \frac{C}{C_0}, \epsilon'' = \frac{G}{\omega C_0}, C_0 = \epsilon_0 \frac{A}{d} \quad (2)$$

$$\tan \delta = \frac{\epsilon''}{\epsilon'} \quad (3)$$

where C_0 is vacuum capacitance, C is capacitance, ω is angular frequency and G is conductance. The dielectric properties of the ceramic samples were carried out using an impedance analyzer (HIOKI, LCR Hitester 3532-50; between frequency $20 \text{ Hz}-10^6 \text{ Hz}$, UK) at room temperature.

3. RESULTS AND DISCUSSION

3.1. XRD-SEM Results of $\text{BaTa}_2\text{O}_6:x\text{Sm}^{3+}, y\text{B}^{3+}$ and $\text{BaTa}_2\text{O}_6:x\text{Dy}^{3+}, y\text{B}^{3+}$ Ceramics

Figure 1 and Figure 2 show the XRD results for $\text{BaTa}_2\text{O}_6:x\text{Sm}^{3+}, y\text{B}^{3+}$ ($x=5$ mol%, $y=0, 5, 15, 30, 50, 70$ and 100 mol%) and $\text{BaTa}_2\text{O}_6:x\text{Dy}^{3+}, y\text{B}^{3+}$ ($x=10$ mol%, $y=0, 5, 15, 30, 50, 70$ and 100 mol%) series, respectively. In both series, X-ray diffractions of all the sintered samples from 0 to 100 mol% B^{3+} have BaTa_2O_6 pattern. The single-phase TTb (tetragonal tungsten bronze) type structure of BaTa_2O_6 identified by XRD peaks JCPDS card no. 17-0793 and $P4/mbm$ (127) space group (9,10).

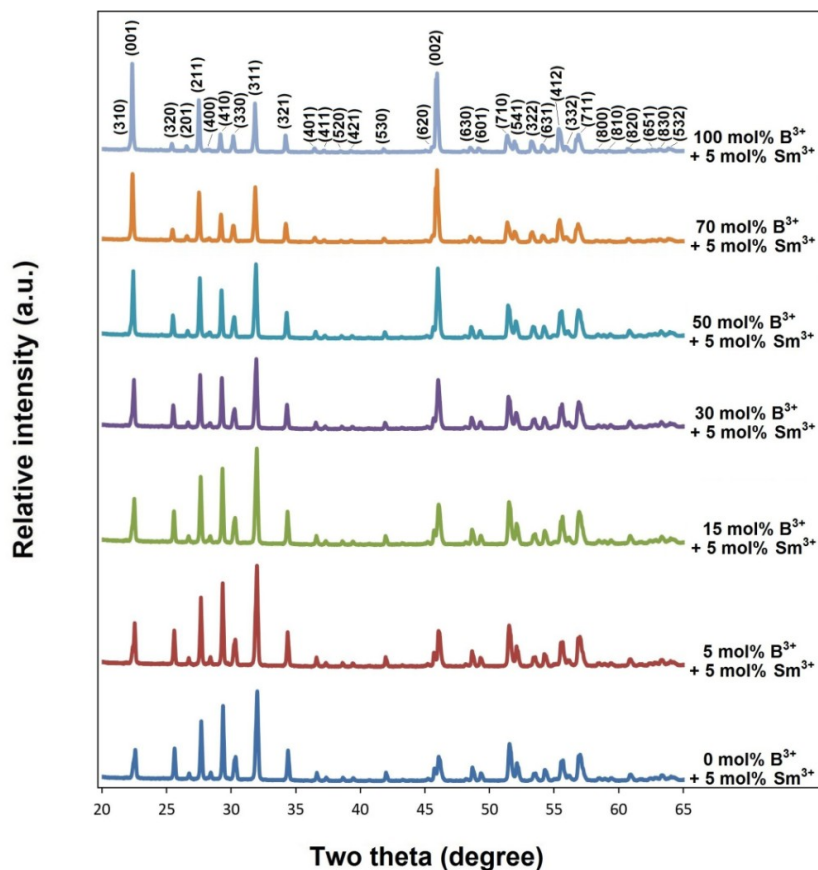


Figure 1: X-ray diffractions of $\text{BaTa}_2\text{O}_6:xB^{3+}, y\text{Sm}^{3+}$ ($x=5$ mol%, $y=0, 5, 15, 30, 50, 70$ and 100 mol%) ceramic series.

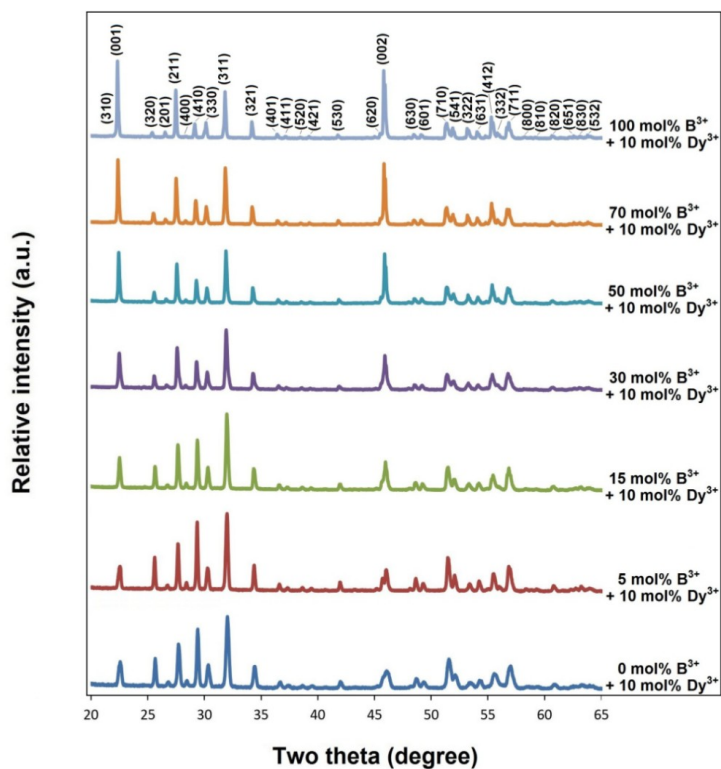


Figure 2: X-ray diffractions of $\text{BaTa}_2\text{O}_6:xDy^{3+}, yB^{3+}$ ($x=10$ mol%, $y=0, 5, 15, 30, 50, 70$ and 100 mol%) ceramic series.

Figure 3 shows the schematic view of TTB-BaTa₂O₆ structure expressed with the formula A₄B₂C₄M₁₀O₃₀. Accordingly, A tunnels are pentagonal with a coordination number (CN) of 15, the B tunnels are square with a CN of 12, and the C tunnels are triangular with a CN of 9, while the octahedral Ta sites in the structure have a CN of 6 (19,24). In addition, as seen in Figure 3, the BaTa₂O₆ is composed of a structure of adjacent octahedral-sharing corners where the pentagonal A sites are occupied by Ba²⁺, the square B sites by Ba²⁺ or empty, and the small triangular (C) sites are empty, where Ba²⁺ cations have ionic radii of 1.61 Å for 12 CN, and 1.47 Å for 9 CN. Based on the suitability of sites A and B for RE³⁺ (RE=Sm, Dy) occupation, for Sm³⁺ ions ($r=1.24$ Å for CN 12 and $r=1.132$ Å for CN 9) and Dy³⁺ ($r=1.083$ Å for CN 9) ions will be able to occupy the A and B sites, respectively. Consequently, the absence of a secondary phase in the XRD peaks for the 5 mol% Sm³⁺ doped series and the 10 mol% Dy³⁺ doped series showed that RE³⁺ ions were incorporated in the A and B sites as interstitial atoms in the structure. Moreover, the absence of a secondary phase indicated that B³⁺ ions were dissolved in the three-tunnel structure of BaTa₂O₆. Similar results have been reported in the study on the luminescence of β-SrTa₂O₆:Eu³⁺, B³⁺, and XPS results confirm that boron is incorporated in the tungsten bronze structure (23). On the other hand, as seen in Figure 1 and Figure 2, increasing B³⁺ concentration caused an increase in (001) and (002) peaks. In the study reported by Gardner and Morrison (31), the increased splitting in (001) reflections and the B-site cation size RE (RE = La, Nd, Sm, Gd, Dy, Y) decreases. Additionally, in luminescence on BaTa₂O₆:Eu³⁺, B³⁺ phosphor

conducted by İlhan et al (24), the (001) reflection increases with the increase in B³⁺, while the asymmetry ratio, which is related to increased Eu³⁺ activation in B sites, decreases. This issue will be discussed in detail in the dielectric section.

The cell data and crystallite sizes of BaTa₂O₆:xSm³⁺, yB³⁺ and BaTa₂O₆:xDy³⁺, yB³⁺ series are tabulated in Table 1 and Table 2, respectively. The lattice parameters from 0 to 100 mol% B³⁺ changed to $a=12.5544$ Å, $c=3.9377$ Å, $V=620.64$ Å³, and $a=12.6151$ Å, $c=3.9799$ Å, $V=633.37$ Å³ (for BaTa₂O₆:xSm³⁺, yB³⁺); $a=12.5427$ Å, $c=3.9377$ Å, $V=619.48$ Å³, and $a=12.6049$ Å, $c=3.9798$ Å, $V=632.33$ Å³ (for BaTa₂O₆:xDy³⁺, yB³⁺) respectively. The cell parameters of tetragonal BaTa₂O₆ are reported as $a=12.52$ Å, $b=3.956$ Å, $V=620.10$ Å³ by Layden (18), and it appears the lattice data in the study are compatible with the literature. In addition, the c/a ratio, which expresses tetragonality, decreased with increasing B³⁺ concentration in both series. In Table 1 and Table 2, the c/a ratios for the BaTa₂O₆:xSm³⁺, yB³⁺ and BaTa₂O₆:xDy³⁺, yB³⁺ series were found 0.3137-0.3155 and 0.3139-0.3157 for 0 and 100 mol% B³⁺, respectively. The increase in boron led to an increase in crystallite size, while the sizes changed to 33.54-50.30 nm (for BaTa₂O₆:xSm³⁺, yB³⁺) and 30.05-48.71 nm (for BaTa₂O₆:xDy³⁺, yB³⁺) from 0 to 100 mol% B³⁺, respectively. Since the temperature effect will increase with the increase of boron and the nucleation rate will slow down, therefore the increase in crystal size can be attributed to the decrease in nucleation and also the change in the charge balance of cell.

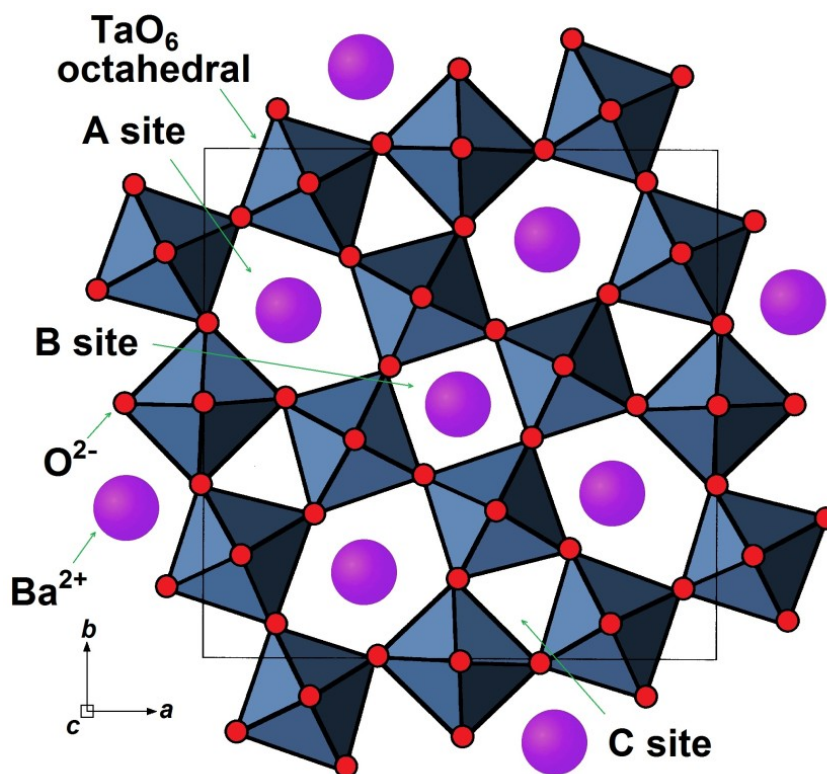


Figure 3: Schematic illustration of TTB-BaTa₂O₆ crystal structure.

Table 1: Cell parameters and average crystallite sizes for BaTa₂O₆: xSm³⁺, yB³⁺ ceramics.

Sample (mol%)	Lattice parameters				Crystallite size (<i>D</i>) (nm)
	<i>a</i> (Å)	<i>c</i> (Å)	<i>V</i> (Å ³)	<i>c/a</i>	
0 B ³⁺ , 5 Sm ³⁺	12.5544	3.9377	620.64	0.3137	33.54
5 B ³⁺ , 5 Sm ³⁺	12.5654	3.9445	622.79	0.3139	35.41
15 B ³⁺ , 5 Sm ³⁺	12.5711	3.9491	624.08	0.3141	37.49
30 B ³⁺ , 5 Sm ³⁺	12.5825	3.9536	625.93	0.3142	39.83
50 B ³⁺ , 5 Sm ³⁺	12.5939	3.9627	628.52	0.3147	42.48
70 B ³⁺ , 5 Sm ³⁺	12.6111	3.9745	632.10	0.3152	45.51
100 B ³⁺ , 5 Sm ³⁺	12.6151	3.9799	633.37	0.3155	50.30

Table 2: Cell parameters and average crystallite sizes for BaTa₂O₆: xDy³⁺, yB³⁺ ceramics.

Sample (mol%)	Lattice parameters				Crystallite size (<i>D</i>) (nm)
	<i>a</i> (Å)	<i>c</i> (Å)	<i>V</i> (Å ³)	<i>c/a</i>	
0 B ³⁺ , 10 Dy ³⁺	12.5427	3.9377	619.48	0.3139	30.05
5 B ³⁺ , 10 Dy ³⁺	12.5540	3.9402	620.98	0.3139	31.82
15 B ³⁺ , 10 Dy ³⁺	12.5654	3.9468	623.15	0.3141	34.65
30 B ³⁺ , 10 Dy ³⁺	12.5825	3.9513	625.57	0.3140	39.97
50 B ³⁺ , 10 Dy ³⁺	12.5882	3.9605	627.58	0.3146	42.13
70 B ³⁺ , 10 Dy ³⁺	12.5996	3.9719	630.54	0.3152	44.54
100 B ³⁺ , 10 Dy ³⁺	12.6049	3.9798	632.33	0.3157	48.71

Figure 4(a-g) and Figure 5(a-g) show the SEM micrographs of BaTa₂O₆:xSm³⁺, yB³⁺ (x=5 mol%, y=0, 5, 30, 50, 70, 100 mol%) and BaTa₂O₆:xDy³⁺, yB³⁺ (x=10 mol%, y=0, 5, 30, 50, 70, 100 mol%) samples, respectively, at 2000× magnifications under 2 kV accelerating voltage. In the SEM micrographs of both series, grains were shapeless and roundish at low B³⁺ concentration, while increasing boron concentration caused grain growth and rod-like shape in grains. As is well known, boron has a reducing effect on the sintering temperature due to the flux effect. Therefore, the increase in grain size can be explained by the increasing temperature effect of boron addition, which releases the energy stored in the grains and thus causes the grain size to increase (32,33). In Figure 4a and Figure 5a, the undoped B³⁺ samples have a small grain size and a round-like irregular grain-shaped morphology in both series. For BaTa₂O₆:xSm³⁺, yB³⁺ series, in Figure 4b, the grains to grow and elongate began to occur in the sample co-doped with 5 mol%

B³⁺, and it became more pronounced at 15 mol% B³⁺ (Figure 4c). In Figure 4d, the grain shape of the 30 mol% B³⁺ doped sample had almost rod-like, and showing thick-grain formations while the growth and elongation trend in the grains continued as seen in Figure 4(e-g). In Figure 4e, the fine grain morphology was considerably decreased at 50 mol% B³⁺, and it completely disappeared at 70 (Figure 4f) and 100 mol% (Figure 4g) B³⁺ concentrations. For BaTa₂O₆:xDy³⁺, yB³⁺ series, similar to the BaTa₂O₆:xSm³⁺, yB³⁺ series in Figure 5b, grain growth occurred in the sample doped with 5 mol% B³⁺, while it continued at 15 (Figure 5c), 30 (Figure 5d), 50 (Figure 5e), 70 (Figure 5f), and 100 (Figure 5g) mol%. Also, thickening was evident in the BaTa₂O₆:xDy³⁺, yB³⁺ series. The grain sizes for the undoped B³⁺ sample usually range of 0.2-1.5 μm (for BaTa₂O₆:xSm³⁺, yB³⁺) and 0.3-3 μm (for BaTa₂O₆:xDy³⁺, yB³⁺). The thicknesses and lengths at 100 mol% reached the range of 2-15 μm and 5-40

μm (for $\text{BaTa}_2\text{O}_6:\text{xSm}^{3+}, \text{yB}^{3+}$) and 2.5-30 μm and 6- 50 μm (for $\text{BaTa}_2\text{O}_6:\text{xDy}^{3+}, \text{yB}^{3+}$), respectively.

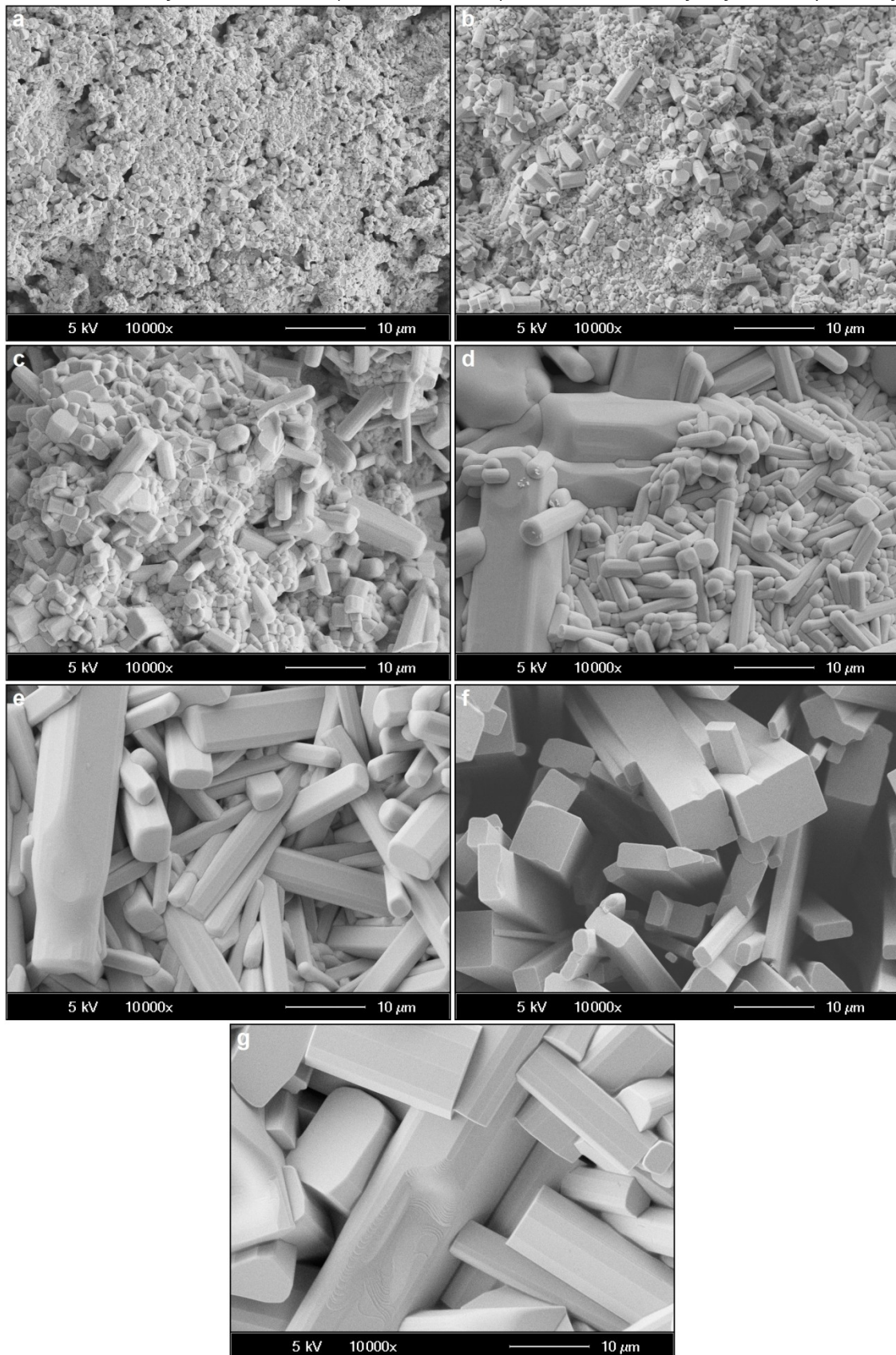


Figure 4: SEM micrographs of 5 mol% Sm^{3+} and (a) 0, (b) 5, (c) 15, (d) 30, (e) 50, (f) 70 and (g) 100 mol% B^{3+} co-doped BaTa_2O_6 ceramics, at 10000 \times magnification and 5 kV acceleration voltage.

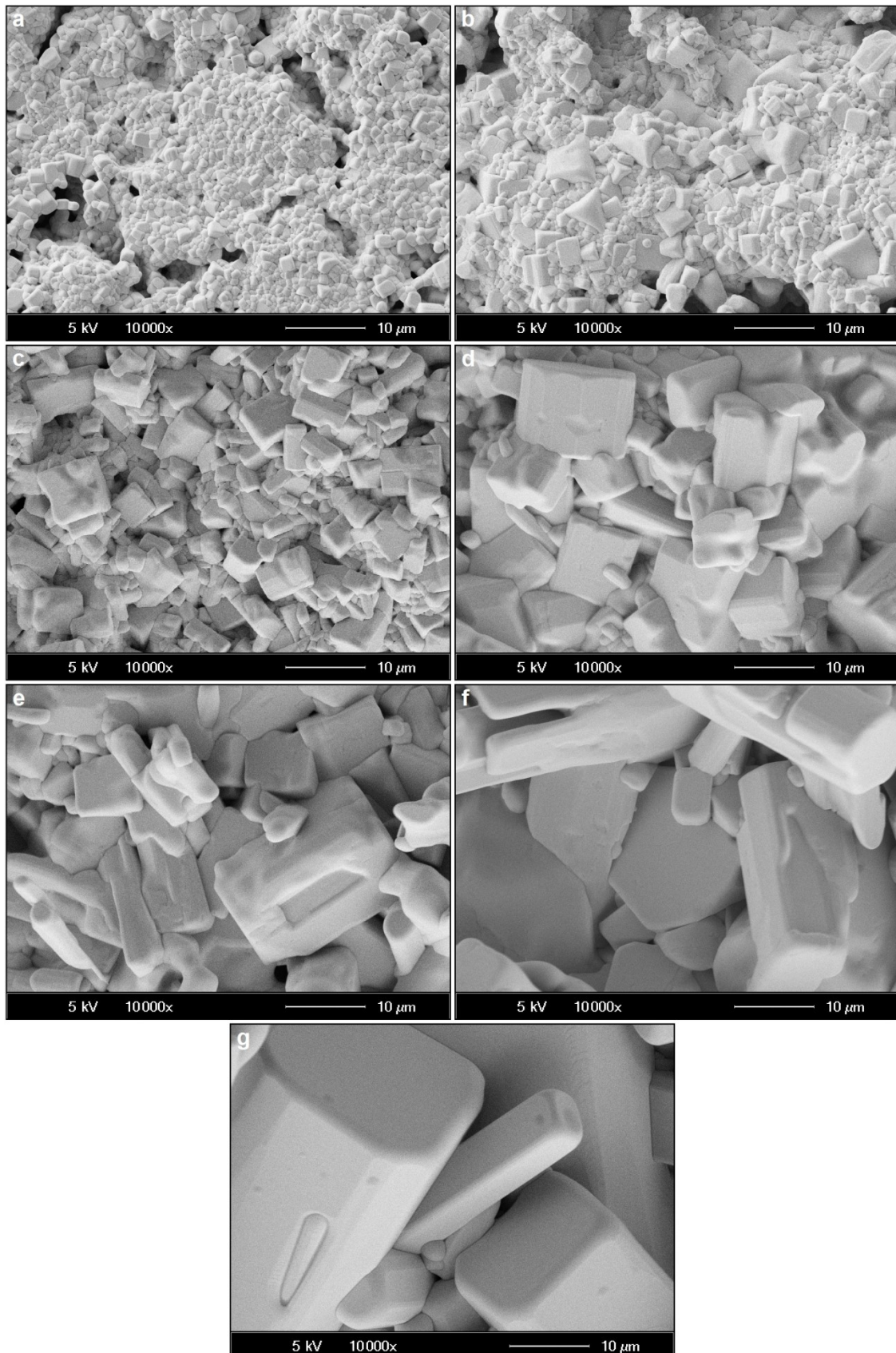


Figure 5: SEM micrographs of 10 mol% Dy³⁺ and (a) 0, (b) 5, (c) 15, (d) 30, (e) 50, (f) 70 and (g) 100 mol% B³⁺ co-doped BaTa₂O₆ ceramics, at 10000x magnification and 5 kV acceleration voltage.

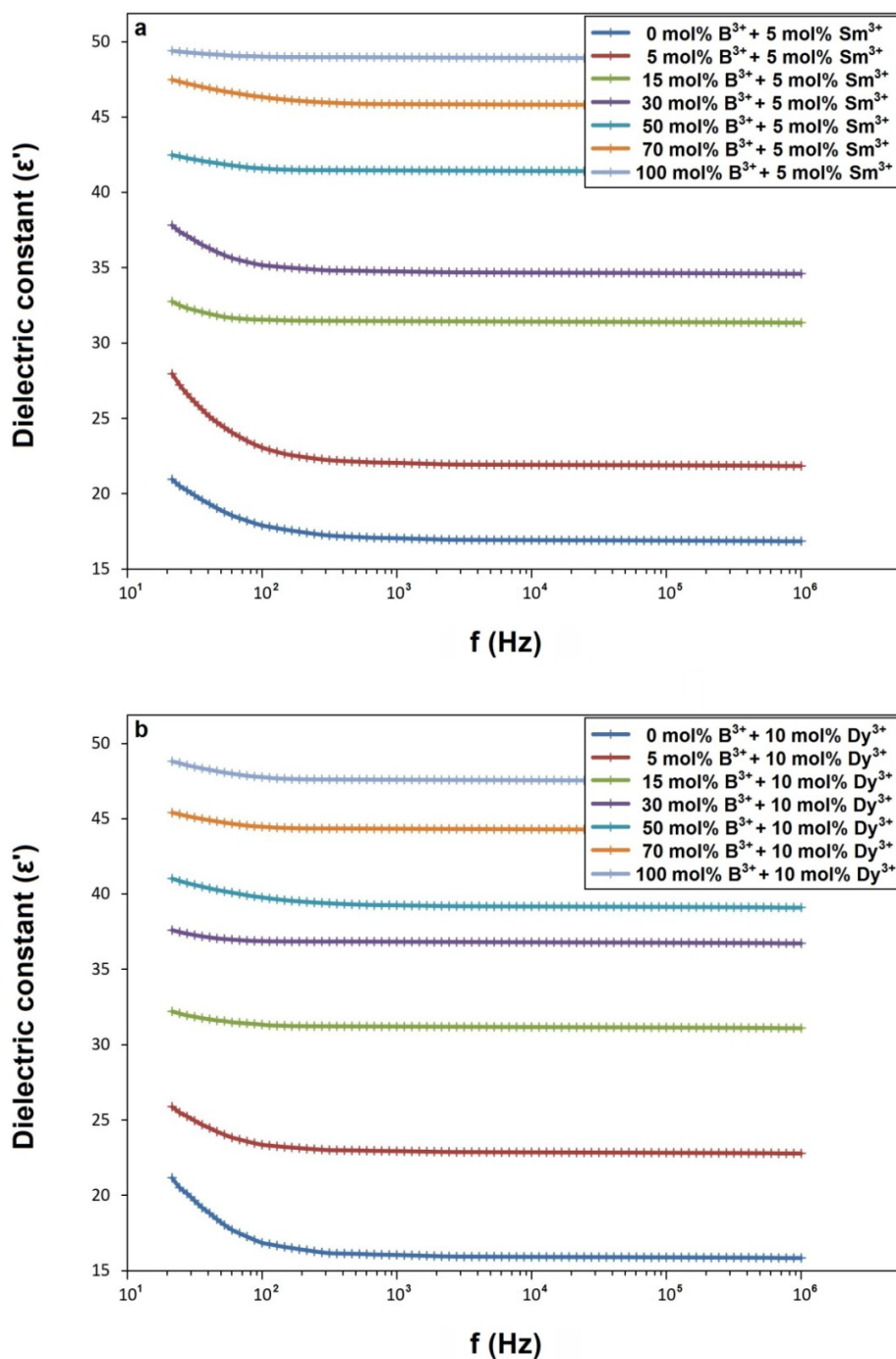


Figure 6: Dielectric constants (ϵ') for (a) $\text{BaTa}_2\text{O}_6:x\text{Sm}^{3+}, y\text{B}^{3+}$ ($x=5$ mol%, $y=0, 5, 15, 30, 50, 70, 100$ mol %), and (b) $\text{BaTa}_2\text{O}_6:x\text{Dy}^{3+}, y\text{B}^{3+}$ ($x=10$ mol%, $y=0, 5, 15, 30, 50, 70, 100$ mol%) ceramics.

3.2. Dielectric Properties of $\text{BaTa}_2\text{O}_6:x\text{Sm}^{3+}, y\text{B}^{3+}$ and $\text{BaTa}_2\text{O}_6:x\text{Dy}^{3+}, y\text{B}^{3+}$ Series

Figure 6(a,b) show the dielectric constants (ϵ') with frequency for $\text{BaTa}_2\text{O}_6:x\text{Sm}^{3+}, y\text{B}^{3+}$ ($x=5$ mol%, $y=0, 5, 15, 30, 50, 70$ and 100 mol%) and $\text{BaTa}_2\text{O}_6:x\text{Dy}^{3+}, y\text{B}^{3+}$ ($x=10$ mol%, $y=0, 5, 15, 30, 50, 70$ and 100 mol%) samples, respectively. In Figure 6a, the dielectric constants of $\text{BaTa}_2\text{O}_6:x\text{Sm}^{3+}, y\text{B}^{3+}$ series from 0 to 100 mol% B^{3+} changed approximately 21.1 and 49.4 at 20 Hz, respectively. In Figure 6b, at the same range and 20 Hz, the ϵ' values for the $\text{BaTa}_2\text{O}_6:x\text{Dy}^{3+}, y\text{B}^{3+}$ series were 21.3 and 48.9 , respectively. However, the dielectric constant did

not change in the high frequency or over 10^3 Hz. As the frequency increases, the ability of electron exchange to follow the applied field decreases, and thus the dielectric constant decreases. At very high frequencies, the field reverses before the movement of space charge carriers, and as a result, it does not contribute to polarization (34-40), so the dielectric constant almost stayed unchanged at the high-frequency range. Moreover, as seen in Figure 6(a,b) there is an increase in polarization or dielectric constant from 0 to 100 mol% B^{3+} in both series. This increase may be explained based on Maxwell-Wagner external factors theory (41,42). According

to this theory, the dielectric constant is directly proportional to the grain size of the sample, where an increase in grain size leads to an increase in the polarizability of the atoms, and causes an increase in dielectric constant (41-45). In the SEM micrographs in Figure 4(a-g) and Figure 5(a-g), it was previously noted that there is an increase in grain size with increasing B³⁺ concentration. Therefore, this situation may be explained by the decreasing presence of the grain boundaries in both series, and thus the increase in the polarizability and ϵ' value of the atoms in the structure. Moreover, in Table 1 and Table 2, the enhancing crystalline sizes support the improvement in bulk property and increase in dielectric constant (46,47). On the other hand, as highlighted in many studies, TTB-type compounds can be expected to contribute to paraelectric behavior due to their ferroelectric properties. In the studies, it has been shown that centrosymmetric B-site substitution affects the ferroelectric properties of TTB compounds where the A-site size is fixed (48-50). The B-site substitution can lead to a relaxor transition and improve the dielectric permittivity, indicating that B-site substitution is an excellent method to improve the dielectric properties of TTB (31,51). As is well known, the $^5D_0 \rightarrow ^7F_2$ transition in Eu³⁺ luminescence is a "hypersensitive transition" and provides information about the environmental symmetry of the Eu³⁺ ion. In this context, the non-centrosymmetric A-sites and centrosymmetric B-sites in TTB structure are related to the $^5D_0 \rightarrow ^7F_2$ and $^5D_0 \rightarrow ^7F_1$ transitions of Eu³⁺, respectively. So, the $^5D_0 \rightarrow ^7F_2 / ^5D_0 \rightarrow ^7F_1$ ratio or asymmetry ratio indicates the occupancy of A and B sites where decreasing ratio is associated with the B-site (24,52). Relatedly, the structural, morphological and luminescence properties BaTa₂O₆:xEu³⁺, yB³⁺ (x=10 mol%, y=0, 5, 15, 30, 50, 70, and 100 mol%) phosphors are studied, in which the asymmetry ratio decreased approximately 70% up to 100 mol% boron concentration, indicating Eu³⁺ activation in B sites (24). Moreover, the structural and morphological results of BaTa₂O₆:xEu³⁺, yB³⁺ show close similarities to the Sm³⁺ and Dy³⁺ ions examined in this study. Consequently, it is possible that boron concentration shows a similar behavior for Sm³⁺ and Dy³⁺ ions in tungsten bronze structure, causing a relaxing transition in B site substitution and contributing to the dielectric permeability. Furthermore, regarding TTB structures in relation to B-site occupation, there are some papers on Curie temperature (T_C) and c/a ratio (tetragonality). Gardner and Morrison (31) highlighted the ferroelectric Curie temperature (T_C) for the TTB-Ba₄R_{0.67}Nb₁₀O₃₀ (R = La, Nd, Sm, Gd, Dy, Y) increases with the increase in tetragonality, and RE cation size is decreasing. Similarly, Stennett et al (51) reported an increase in Curie temperature with decreasing ionic radius M in the B-site of TTB-Ba₂MTi₂Nb₃O₁₅ (M=Bi, La, Pr, Nd, Sm, Eu, Gd, Dy), in which tetragonality increases. As seen in Table 1 and Table 2, the c/a ratio of both series increased up to 100 mol% B³⁺ concentration. According to these findings, the increase in B³⁺ availability resulting in an increase in tetragonality may be linked to an increase in the ferroelectric Curie temperature. Moreover, in Table 1 and Table 2, when the c/a ratios are compared, the c/a ratios of the Dy³⁺ cation with a smaller ionic radius are relatively high.

Thus, a decreasing radius indicates increasing tetragonality and Curie temperature, which is in agreement with References (31) and (51).

Figure 7(a,b) show the dielectric losses (tan δ) with frequency for BaTa₂O₆:xSm³⁺, yB³⁺ (x=5 mol%, y=0, 5, 15, 30, 50, 70 and 100 mol%) and BaTa₂O₆:xDy³⁺, yB³⁺ (x=10 mol%, y=0, 5, 15, 30, 50, 70 and 100 mol%) samples, respectively. In Figure 7a, the dielectric loss of BaTa₂O₆:xSm³⁺, yB³⁺ series from 0 to 100 mol% B³⁺ changed approximately 0.40 and 0.02 at 20 Hz, respectively. In Figure 7b, at the same range and 20 Hz, the ϵ' values for the BaTa₂O₆:xDy³⁺, yB³⁺ series were 0.45 and 0.01, respectively. Additionally, both series exhibited a dielectric loss below approximately 0.10 in the range of 5-100 mol% and at 20 Hz. In Figure 7(a,b), the dielectric loss decreases continuously as the frequency increases. In the low frequency range corresponding to high resistance, more energy is required for polarization due to the grain boundary, whereas in the high frequency range corresponding to low resistance, very little energy will be needed for electron transfer due to the grain boundary, and the energy loss will be less (53,54). Moreover, the dielectric loss factor for both sample series decreases with increasing B³⁺. In the literature, different studies highlight oxygen vacancies as responsible for dielectric loss or leakage current in ferroelectrics (55-61). In the study of Kumar and Kar (55), the substitution of Ti⁴⁺ into BiFeO₃ significantly reduces oxygen vacancies and leakage current for tan δ . Similarly, Sati et al (56) attributed the decreased dielectric loss with Eu substitution to BiFeO₃ to the decrease in oxygen vacancies. Liu et al (57) investigated the dielectric loss and oxygen vacancy relation by fabricating TTB-Ba₄Nd₂Fe₂Nb₈O₃₀ ceramics at different annealing and sintering temperatures as well as in O₂ and N₂ atmospheres, in which the increase in temperature reduces oxygen vacancies and electrical conductivity. The consequences of the temperature effect resulting from the increase in boron were mentioned in the structural section. In this context, the increased boron concentration will not only cause a greater temperature effect on the material, but also have an effect on oxygen vacancies. Consequently, the decrease in the dielectric loss factor in both series may be attributed to the suppression of oxygen vacancies by the temperature effect that increases with the increase in B³⁺.

4. CONCLUSION

The effect of boron on the structural and dielectric properties was studied by using Eu³⁺, B³⁺ co-doped tetragonal tungsten bronze BaTa₂O₆:xSm³⁺, yB³⁺ (x=5 mol%, y=0, 5, 15, 30, 50, 70, 100 mol%) and BaTa₂O₆:xDy³⁺, yB³⁺ (x=10 mol%, y=0, 5, 15, 30, 50, 70, 100 mol%) ceramics. The single-phase structure was preserved in XRD results of both series, while the crystallinity of the samples increased with boron concentration. SEM micrographs of Sm³⁺, B³⁺ co-doped and Dy³⁺, B³⁺ co-doped samples showed that boron supported grain growth and elongation. The dielectric constants (ϵ') for BaTa₂O₆:xSm³⁺, yB³⁺, and BaTa₂O₆:xDy³⁺, yB³⁺ series were measured in the range of 21.1-49.4 and 21.3-48.9 at 20 Hz, respectively. For both series, the increasing dielectric constant up to 100 mol% B³⁺

concentration was associated with the improving grain size and crystallinity. The dielectric loss factor for both series decreased with increasing B^{3+} concentration, while the $\tan \delta$ for $BaTa_2O_6:xSm^{3+}$, yB^{3+} and $BaTa_2O_6:xDy^{3+}$, yB^{3+} changed as 0.40-0.02 and 0.45-0.01 at 20 Hz, respectively. The dielectric loss decrease in both series with the increasing B^{3+}

concentration was attributed to the suppression of oxygen vacancies with the increased presence of B^{3+} . The study may be useful in evaluating the dielectric properties of tetragonal tungsten bronze ceramics, in terms of controlling the grain morphology and crystallite size.

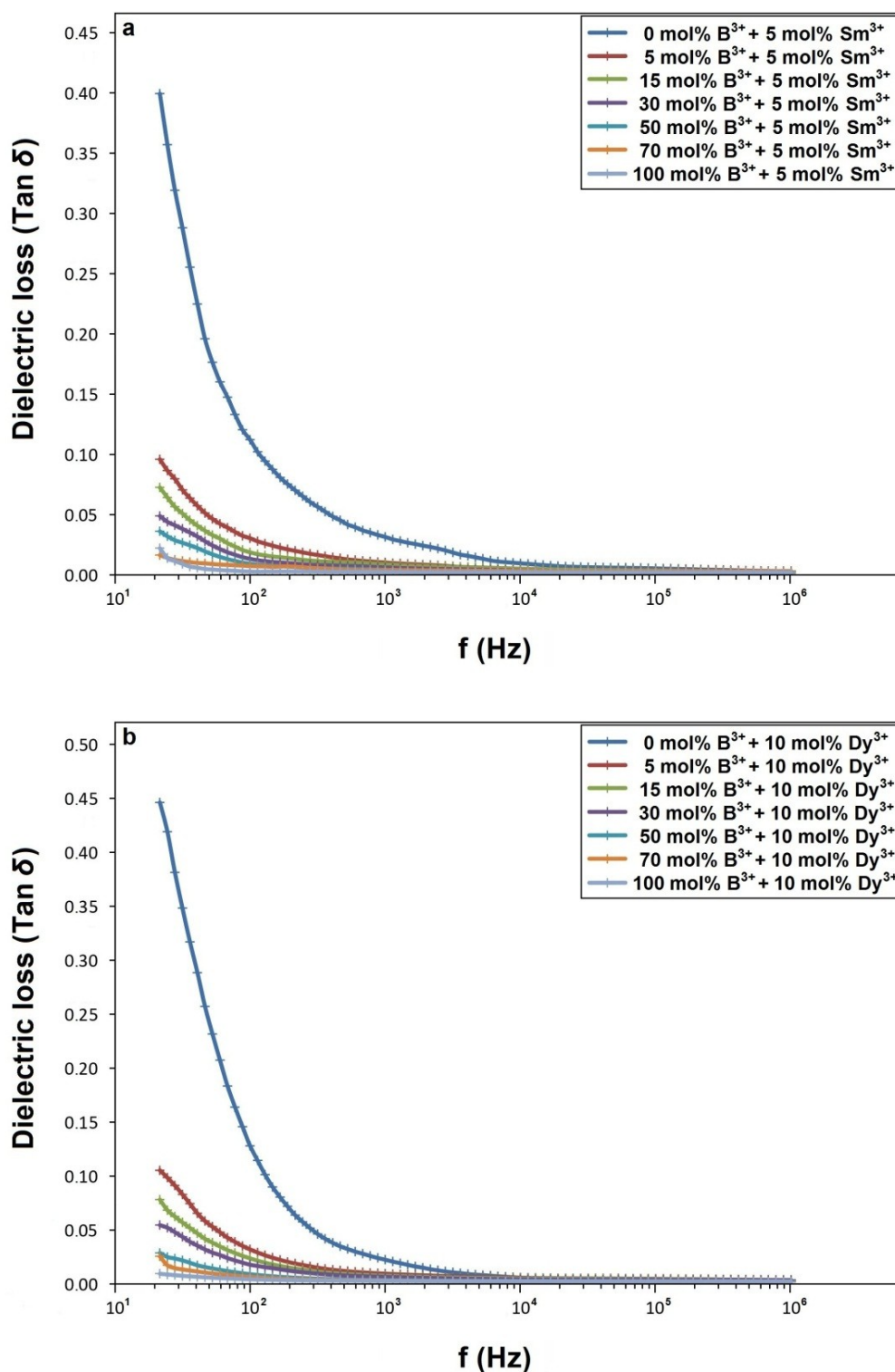


Figure 7: Dielectric losses ($\tan \delta$) for (a) $BaTa_2O_6:xSm^{3+}$, yB^{3+} ($x=5$ mol%, $y=0, 5, 15, 30, 50, 70, 100$ mol %), and (b) $BaTa_2O_6:xDy^{3+}$, yB^{3+} ($x=10$ mol%, $y=0, 5, 15, 30, 50, 70, 100$ mol%) ceramics.

5. CONFLICT OF INTEREST

There is no conflict of interest

6. REFERENCES

- Feng W Bin, Zhu XL, Liu XQ, Fu M Sen, Ma X, Jia SJ, et al. Relaxor nature in $Ba_5RZr_3Nb_7O_{30}$ (R= La, Nd, Sm) tetragonal tungsten bronze new system. *J Am Ceram Soc* [Internet]. 2018 Apr 24;101(4):1623-31. Available from: [<URL>](#).
- Zhu XL, Liu XQ, Chen XM. Crystal Structure and Dielectric Properties of $Sr_5RTi_3Nb_7O_{30}$ (R=La, Nd, Sm, and Eu) Tungsten Bronze Ceramics. *J Am Ceram Soc* [Internet]. 2011 Jun;94(6):1829-36. Available from: [<URL>](#).
- Roulland F, Josse M, Castel E, Maglione M. Influence of ceramic process and Eu content on the composite multiferroic properties of the $Ba_{6-2x}Ln_{2x}Fe_{1+x}Nb_{9-x}O_{30}$ TTB system. *Solid State Sci* [Internet]. 2009 Sep;11(9):1709-16. Available from: [<URL>](#).
- Fang L, Peng X, Li C, Hu C, Wu B, Zhou H. Dielectric Properties of $Ba_4Sm_2Fe_2M_8O_{30}$ (M=Nb, Ta) with Tetragonal Bronze Structure. *J Am Ceram Soc* [Internet]. 2010 Sep 12;93(9):2430-3. Available from: [<URL>](#).
- Bendahhou A, Marchet P, El-Houssaine A, El Barkany S, Abou-Salama M. Relationship between structural and dielectric properties of Zn-substituted $Ba_5CaTi_{2-x}Zn_xNb_8O_{30}$ tetragonal tungsten bronze. *CrystEngComm* [Internet]. 2021;23(1):163-73. Available from: [<URL>](#).
- Botella P, Solsona B, García-González E, González-Calbet JM, López Nieto JM. The hydrothermal synthesis of tetragonal tungsten bronze-based catalysts for the selective oxidation of hydrocarbons. *Chem Commun* [Internet]. 2007; (47):5040-2. Available from: [<URL>](#).
- Jindal S, Vasishth A, Devi S, Anand G. A review on tungsten bronze ferroelectric ceramics as electrically tunable devices. *Integr Ferroelectr* [Internet]. 2018 Jan 2;186(1):1-9. Available from: [<URL>](#).
- Shimizu K, Kato H, Kobayashi M, Kakihana M. Synthesis and photocatalytic properties of tetragonal tungsten bronze type oxynitrides. *Appl Catal B Environ* [Internet]. 2017 Jun;206:444-8. Available from: [<URL>](#).
- İlhan M, Güteryüz LF. Cathodoluminescence and photoluminescence of $BaTa_2O_6:Sm^{3+}$ phosphor depending on the sintering temperature. *Chem Pap* [Internet]. 2022 Nov;76(11):6963-74. Available from: [<URL>](#).
- Ekmekçi MK, İlhan M, Başak AS, Deniz S. Structural and Luminescence Properties of Sm^{3+} Doped TTB -Type $BaTa_2O_6$ Ceramic Phosphors. *J Fluoresc* [Internet]. 2015 Nov 26;25(6):1757-62. Available from: [<URL>](#).
- İlhan M, Keskin İÇ, Gültekin S. Assessing of Photoluminescence and Thermoluminescence Properties of Dy^{3+} Doped White Light Emitter TTB-Lead Metatantalate Phosphor. *J Electron Mater* [Internet]. 2020 Apr 17;49(4):2436-49. Available from: [<URL>](#).
- İlhan M, Keskin İÇ. Analysis of Judd-Ofelt parameters and radioluminescence results of $SrNb_2O_6:Dy^{3+}$ phosphors synthesized via molten salt method. *Phys Chem Chem Phys* [Internet]. 2020;22(35):19769-78. Available from: [<URL>](#).
- Ekmekçi MK, İlhan M, Güteryüz LF, Mergen A. Study on molten salt synthesis, microstructural determination and white light emitting properties of $CoNb_2O_6:Dy^{3+}$ phosphor. *Optik (Stuttg)* [Internet]. 2017 Jan;128:26-33. Available from: [<URL>](#).
- Tressaud A. Structural architecture and physical properties of some inorganic fluoride series: a review. *J Fluor Chem* [Internet]. 2011 Oct;132(10):651-9. Available from: [<URL>](#).
- İlhan M, Ekmekçi MK, Mergen A, Yaman C. Photoluminescence characterization and heat treatment effect on luminescence behavior of $BaTa_2O_6:Dy^{3+}$ phosphor. *Int J Appl Ceram Technol* [Internet]. 2017 Nov 13;14(6):1134-43. Available from: [<URL>](#).
- İlhan M, Keskin İÇ. Evaluation of the Structural, Near-Infrared Luminescence, and Radioluminescence Properties of Nd^{3+} Activated TTB-Lead Metatantalate Phosphors. *J Turkish Chem Soc Sect A Chem* [Internet]. 2023 May 31;10(2):453-64. Available from: [<URL>](#).
- Xu T, Zhao X, Zhu Y. Synthesis of Hexagonal $BaTa_2O_6$ Nanorods and Influence of Defects on the Photocatalytic Activity. *J Phys Chem B* [Internet]. 2006 Dec 1;110(51):25825-32. Available from: [<URL>](#).
- Layden GK. Polymorphism of $BaTa_2O_6$. *Mater Res Bull* [Internet]. 1967 May;2(5):533-9. Available from: [<URL>](#).
- Keskin İÇ, İlhan M. Thermoluminescence Kinetic Parameters and Radioluminescence of RE^{3+} (RE = Pr, Sm, Tb, Ho, Er)-Doped Barium Tantalate Phosphors. *J Electron Mater* [Internet]. 2023 Aug 31;52(8):5614-30. Available from: [<URL>](#).
- Layden GK. Dielectric and structure studies of hexagonal $BaTa_2O_6$. *Mater Res Bull* [Internet]. 1968 Apr;3(4):349-59. Available from: [<URL>](#).
- İlhan M, Mergen A, Sarioğlu C, Yaman C. Heat capacity measurements on $BaTa_2O_6$ and derivation of its thermodynamic functions. *J Therm Anal Calorim* [Internet]. 2017 May 29;128(2):707-11. Available from: [<URL>](#).
- Kato H, Kudo A. New tantalate photocatalysts for water decomposition into H_2 and O_2 . *Chem Phys Lett* [Internet]. 1998 Oct;295(5-6):487-92. Available from: [<URL>](#).
- İlhan M, Güteryüz LF. Boron doping effect on the structural, spectral properties and charge transfer mechanism of orthorhombic tungsten bronze β -

- SrTa₂O₆:Eu³⁺ phosphor. RSC Adv [Internet]. 2023;13(18):12375-85. Available from: [<URL>](#).
24. İlhan M, Güteryüz LF, Katı Mİ. Exploring the effect of boron on the grain morphology change and spectral properties of Eu³⁺ activated barium tantalate phosphor. RSC Adv [Internet]. 2024;14(4):2687-96. Available from: [<URL>](#).
25. Başak AS, Ekmekçi MK, Erdem M, İlhan M, Mergen A. Investigation of Boron-doping Effect on Photoluminescence Properties of CdNb₂O₆: Eu³⁺ Phosphors. J Fluoresc [Internet]. 2016 Mar 11;26(2):719-24. Available from: [<URL>](#).
26. İlhan M, Ekmekçi MK, Güteryüz LF. Effect of boron incorporation on the structural, morphological, and spectral properties of CdNb₂O₆:Dy³⁺ phosphor synthesized by molten salt process. Mater Sci Eng B [Internet]. 2023 Dec;298:116858. Available from: [<URL>](#).
27. Zhang X, Wang B, Huang W, Chen Y, Wang G, Zeng L, et al. Synergistic Boron Doping of Semiconductor and Dielectric Layers for High-Performance Metal Oxide Transistors: Interplay of Experiment and Theory. J Am Chem Soc [Internet]. 2018 Oct 3;140(39):12501-10. Available from: [<URL>](#).
28. Mazumder R, Seal A, Sen A, Maiti HS. Effect of Boron Addition on the Dielectric Properties of Giant Dielectric CaCu₃Ti₄O₁₂. Ferroelectrics [Internet]. 2005 Oct;326(1):103-8. Available from: [<URL>](#).
29. Li Z, Zhou W, Su X, Luo F, Huang Y, Wang C. Effect of boron doping on microwave dielectric properties of SiC powder synthesized by combustion synthesis. J Alloys Compd [Internet]. 2011 Jan;509(3):973-6. Available from: [<URL>](#).
30. Cullity BD, Stock SR. Elements of X-ray Diffraction. USA: Prentice Hall; 2001.
31. Gardner J, Morrison FD. A-site size effect in a family of unfilled ferroelectric tetragonal tungsten bronzes: Ba₄R_{0.67}Nb₁₀O₃₀ (R= La, Nd, Sm, Gd, Dy and Y). Dalton Trans [Internet]. 2014;43(30):11687-95. Available from: [<URL>](#).
32. Polyxeni V, Nikolaos D P, Nikos S, Sotirios X, Evangelos H. Temperature effects on grain growth phenomena and magnetic properties of silicon steels used in marine applications. Ann Mar Sci [Internet]. 2023 Jun 21;7(1):40-4. Available from: [<URL>](#).
33. Güteryüz LF, İlhan M. Structural, morphological, spectral properties and high quantum efficiency of Eu³⁺, B³⁺ co-activated double perovskite Ba₂GdMO₆ (M= Nb, Ta) phosphors. Mater Sci Eng B [Internet]. 2024 Jun;304:117373. Available from: [<URL>](#).
34. Mahapatro J, Agrawal S. Effect of Eu³⁺ ions on electrical and dielectric properties of barium hexaferrites prepared by solution combustion method. Ceram Int [Internet]. 2021 Jul;47(14):20529-43. Available from: [<URL>](#).
35. Evangeline T G, Annamalai A R, Ctibor P. Effect of Europium Addition on the Microstructure and Dielectric Properties of CCTO Ceramic Prepared Using Conventional and Microwave Sintering. Molecules [Internet]. 2023 Feb 8;28(4):1649. Available from: [<URL>](#).
36. Esha IN, Al-Amin M, Toma FTZ, Hossain E, Khan MNI, Maria KH. Synthesis and analysis of the influence of Eu³⁺ on the structural, ferromagnetic, dielectric and conductive characteristics of Ni_{0.4}Zn_{0.45}Cu_{0.15}Fe_(2-x)Eu_xO₄ composites using conventional double sintering ceramic method. J Ceram Process Res [Internet]. 2019 Oct;20(5):530-9. Available from: [<URL>](#).
37. Shah MR, Akther Hossain AKM. Structural and dielectric properties of La substituted polycrystalline Ca(Ti_{0.5}Fe_{0.5})O₃. Mater Sci [Internet]. 2013 Jan 25;31(1):80-7. Available from: [<URL>](#).
38. Kadam AA, Shinde SS, Yadav SP, Patil PS, Rajpure KY. Structural, morphological, electrical and magnetic properties of Dy doped Ni-Co substitutional spinel ferrite. J Magn Mater [Internet]. 2013 Mar;329:59-64. Available from: [<URL>](#).
39. Tan YQ, Yu Y, Hao YM, Dong SY, Yang YW. Structure and dielectric properties of Ba₅NdCu_{1.5}Nb_{8.5}O₃₀₋₆ tungsten bronze ceramics. Mater Res Bull [Internet]. 2013 May;48(5):1934-8. Available from: [<URL>](#).
40. Rayssi C, El.Kossi S, Dhahri J, Khirouni K. Frequency and temperature-dependence of dielectric permittivity and electric modulus studies of the solid solution Ca_{0.85}Er_{0.1}Ti_{1-x}Co_{4x/3}O₃ (0≤x≤0.1). RSC Adv [Internet]. 2018;8(31):17139-50. Available from: [<URL>](#).
41. Wagner KW. Zur Theorie der unvollkommenen Dielektrika. Ann Phys [Internet]. 1913 Jan 14;345(5):817-55. Available from: [<URL>](#).
42. Maxwell JC. A treatise on electricity and magnetism. London: Caleredon press, Oxford University; 1873.
43. Saengvong P, Chanlek N, Srepusharawoot P, Harnchana V, Thongbai P. Enhancing giant dielectric properties of Ta⁵⁺-doped Na_{1/2}Y_{1/2}Cu₃Ti₄O₁₂ ceramics by engineering grain and grain boundary. J Am Ceram Soc [Internet]. 2022 May 15;105(5):3447-55. Available from: [<URL>](#).
44. Karmakar S, Mohanty HS, Behera D. Exploration of alternating current conduction mechanism and dielectric relaxation with Maxwell-Wagner effect in NiO-CdO-Gd₂O₃ nanocomposites. Eur Phys J Plus [Internet]. 2021 Oct 15;136(10):1038. Available from: [<URL>](#).
45. Samet M, Kallel A, Serghei A. Maxwell-Wagner-Sillars interfacial polarization in dielectric spectra of composite materials: Scaling laws and applications. J Compos Mater [Internet]. 2022 Aug 28;56(20):3197-217. Available from: [<URL>](#).
46. Mach TP, Ding Y, Binder JR. Impact of Particle and Crystallite Size of Ba_{0.6}Sr_{0.4}TiO₃ on the Dielectric Properties of BST/P(VDF-TrFE) Composites in Fully

- Printed Varactors. Polymers (Basel) [Internet]. 2022 Nov 19;14(22):5027. Available from: [<URL>](#).
47. Kurnia, Heriansyah, Suharyadi E. Study on The Influence of Crystal Structure and Grain Size on Dielectric Properties of Manganese Ferrite (MnFe_2O_4) Nanoparticles. IOP Conf Ser Mater Sci Eng [Internet]. 2017 May;202:012046. Available from: [<URL>](#).
48. Chi EO, Gandini A, Ok KM, Zhang L, Halasyamani PS. Syntheses, Structures, Second-Harmonic Generating, and Ferroelectric Properties of Tungsten Bronzes: $\text{A}_6\text{M}_2\text{M}'_8\text{O}_{30}$ ($\text{A} = \text{Sr}^{2+}, \text{Ba}^{2+}, \text{or Pb}^{2+}$; $\text{M} = \text{Ti}^{4+}, \text{Zr}^{4+}, \text{or Hf}^{4+}$; $\text{M}' = \text{Nb}^{5+} \text{ or Ta}^{5+}$). Chem Mater [Internet]. 2004 Sep 1;16(19):3616–22. Available from: [<URL>](#).
49. Rotaru A, Arnold DC, Daoud-Aladine A, Morrison FD. Origin and stability of the dipolar response in a family of tetragonal tungsten bronze relaxors. Phys Rev B [Internet]. 2011 May 31;83(18):184302. Available from: [<URL>](#).
50. Neurgaonkar RR, Nelson JG, Oliver JR. Ferroelectric properties of the tungsten bronze $\text{M}^{2+}_6\text{M}^{4+}_2\text{Nb}_8\text{O}_{30}$ solid solution systems. Mater Res Bull [Internet]. 1992 Jun;27(6):677–84. Available from: [<URL>](#).
51. Stennett MC, Reaney IM, Miles GC, Woodward DI, West AR, Kirk CA, et al. Dielectric and structural studies of $\text{Ba}_2\text{MTi}_2\text{Nb}_3\text{O}_{15}$ (BMTNO_{15} , $\text{M} = \text{Bi}^{3+}, \text{La}^{3+}, \text{Nd}^{3+}, \text{Sm}^{3+}, \text{Gd}^{3+}$) tetragonal tungsten bronze-structured ceramics. J Appl Phys [Internet]. 2007 May 15;101(10):104114. Available from: [<URL>](#).
52. Li G, Cheng L, Liao F, Tian S, Jing X, Lin J. Luminescent and structural properties of the series $\text{Ba}_{8-x}\text{Eu}_x\text{Ti}_{2+x}\text{Ta}_{8-x}\text{O}_{30}$ and $\text{Ba}_{4-y}\text{K}_y\text{Eu}_2\text{Ti}_{4-y}\text{Ta}_{6+y}\text{O}_{30}$. J Solid State Chem [Internet]. 2004 Mar;177(3):875–82. Available from: [<URL>](#).
53. Sati PC, Kumar M, Chhoker S, Jewariya M. Influence of Eu substitution on structural, magnetic, optical and dielectric properties of BiFeO_3 multiferroic ceramics. Ceram Int [Internet]. 2015 Mar;41(2):2389–98. Available from: [<URL>](#).
54. Ganguly P, Jha AK. Enhanced characteristics of $\text{Ba}_5\text{SmTi}_3\text{Nb}_7\text{O}_{30}$ ferroelectric nanocrystalline ceramic prepared by mechanical activation process: A comparative study. Mater Res Bull [Internet]. 2011 May;46(5):692–7. Available from: [<URL>](#).
55. Kumar P, Kar M. Effect of structural transition on magnetic and optical properties of Ca and Ti co-substituted BiFeO_3 ceramics. J Alloys Compd [Internet]. 2014 Jan;584:566–72. Available from: [<URL>](#).
56. Chakrabarti A, Bera J. Effect of La-substitution on the structure and dielectric properties of $\text{BaBi}_4\text{Ti}_4\text{O}_{15}$ ceramics. J Alloys Compd [Internet]. 2010 Sep;505(2):668–74. Available from: [<URL>](#).
57. Fei Liu S, Jun Wu Y, Li J, Ming Chen X. Effects of oxygen vacancies on dielectric, electrical, and ferroelectric properties of $\text{Ba}_4\text{Nd}_2\text{Fe}_2\text{Nb}_8\text{O}_{30}$ ceramics. Appl Phys Lett [Internet]. 2014 Feb 24;104(8):082912. Available from: [<URL>](#).
58. Kendall KR, Thomas JK, Loye HC. Synthesis and ionic conductivity of a new series of modified Aurivillius phases. Chem Mater [Internet]. 1995 Jan 1;7(1):50–7. Available from: [<URL>](#).
59. İlhan M, Ekmekci MK, Esmer K. Structural and dielectric properties of $\text{Eu}^{3+}, \text{B}^{3+}$ co-doped CoNb_2O_6 ceramic. J Turkish Chem Soc Sect A Chem [Internet]. 2024 May 15;11(2):765–74. Available from: [<URL>](#).
60. Chandra Sati P, Arora M, Chauhan S, Kumar M, Chhoker S. Effect of Dy substitution on structural, magnetic and optical properties of BiFeO_3 ceramics. J Phys Chem Solids [Internet]. 2014 Jan;75(1):105–8. Available from: [<URL>](#).
61. Nadeem M, Khan W, Khan S, Husain S, Ansari A. Tailoring dielectric properties and multiferroic behavior of nanocrystalline BiFeO_3 via Ni doping. J Appl Phys [Internet]. 2018 Oct 28;124(16):164105. Available from: [<URL>](#).



Biogeochemical Exploration for Gold Mineralization Using Wild Plants

Osama Abd-Elmoniem Ebyan^{1*} 

¹Nuclear Materials Authority, P.O.Box 530 El Maadi, Cairo, Egypt.

Abstract: *Lotus hebranicus* and *Zilla spinosa* were selected for gold biogeochemical exploration in Wadi El-Missikat. Their soil associations were examined using Inductively Coupled Plasma, Emission & Mass spectrometry, ICPEs spectrometry, and Mass Spectrometry. The significant levels of gold in plants and soil, along with the consistent link between gold and its markers, plus the relationship between gold in plants and soil, suggest the presence of gold mineralization in nearby rocks in the area under investigation. *Lotus hebranicus* has a greater ability to accumulate Au compared to *Zilla spinosa*. Both of these species can be utilized for exploring and phytoremediating silver. Additionally, *Lotus hebranicus* is more effective in uptaking and storing Sb than *Zilla spinosa*, making it valuable for treating Sb contamination. *Lotus hebranicus* and *Zilla spinosa* are beneficial for both exploration and remediation tasks.

Keywords: Biogeochemical exploration; Phytoremediation; Gold, Silver; Antimony, Arsenic.

Submitted: January 18, 2024. **Accepted:** June 6, 2024.

Cite this: Ebyan OAE. Biogeochemical Exploration for Gold Mineralization Using Wild Plants. JOTCSA. 2024;11(3): 1125-40.

DOI: <https://doi.org/10.18596/jotcsa.1421730>

***Corresponding author's E-mail:** osama_ishere@hotmail.com

1. INTRODUCTION

Exploration and processing of minerals are significant parts of the global industry. Several plants can absorb gold from the soil and store it within their tissues. Progress has been achieved in comprehending these mechanisms, making the use of plants in gold prospecting a viable option (1). The initial study on gold accumulation in vegetation dates back to 1900 (2) and has since been followed by research on its biogeochemistry and the utilization of plants as a tool for exploring gold-rich ore deposits (1-11).

The presence of trace elements in plants is a result of their transfer from rocks and soil to plants (12). In their natural environment, trace elements are found in low concentrations without causing any significant harm to biodiversity (13,14). Plants show a variety of behaviors when it comes to absorbing trace elements. Biogeochemical prospecting is a cost-effective method for exploration (15,16). Three main uptake patterns are accumulation, indication, and exclusion, which vary among plant species due to their unique abilities (17). Research on the absorption of gold is abundant, with a focus on how gold is transported from soil to plants (1, 17-24). Plants tend to absorb chemicals from the soil, making

them useful for metal exploration and soil remediation purposes (25).

Gold levels in wild plants typically stay below 10 $\mu\text{g}\cdot\text{kg}^{-1}$ dry weight, even when found near gold deposits (26). Higher reported values may result from wind-carried substrate contamination. Gold, Au, is commonly found in plants like *Phacelia sericea* near gold mines, aiding in the detection of soil gold deposits by geologists (15). Geologists have utilized these plants to find gold in the soil. *Brassica juncea*, a quick-growing member of the mustard family, is a hyperaccumulator of gold and has been grown in soil with small amounts of gold to yield almost 1 milligram of gold per gram of dry plant tissue. Researchers aim to improve this gold yield for potential gold mining purposes.

Studies have shown that plants can be used to explore gold in its biogeochemistry. Various plant species, such as *Pseudotsuga menziesii*, *Pinus banksiana*, *Picea mariana*, *Hordeum vulgare*, and *Phacelia sericea*, have the ability to accumulate detectable amounts of gold (27). Gold can be absorbed by plants in soluble form and easily transported to different parts of the plant through the root vascular systems (23).

Aljahdali and Alhassan (28) defined the biological absorption coefficient (BAC) as the measure of absorption intensity of chemical elements by plants

from their substrate, which can be calculated using the provided equation.

$$BAC = \frac{\text{Concentration of Elements in Plants: } C_p}{\text{Concentration of Elements in Soil: } C_s} \quad (\text{Eq. 1})$$

where C_p is the concentration of an element in a plant and C_s is the concentration of the same element in soil. BAC tells if a plant species is an accumulator or hyperaccumulator of trace elements or a specific trace element from the soil into the plants (12,13,28).

BAC levels differ greatly based on weight, with most elements below one. Plants were grouped into five categories based on BAC values: 1) Intensive; 10-100, 2) Strong; 1.0-10, 3) Intermediate; 0.1-1.0, 4) Weak; 0.01-0.1, 5) Very weak; 0.001-0.01 (29,30).

Numerous wild plants found in the Eastern Desert of Egypt include *Glinus lotoides*, *Aerva javanica*, *Astragalus vogelli*, *Tamarix nilotica*, *Zygophyllum*

coccineum, *Zilla spinosa*, *Fagonia boveana*, *Moringa peregrina*, *Trichodesma africanum*, *Lotus hebranicus*, *Pergularia tomentosa*, and *Citrullus colocynthis* (31, 32). Most of these plants are considered short-lived compared to grazing plants (33). The perennial plants *Zilla spinosa* and *Lotus hebranicus* were selected for this study. Perennial plant cover serves as a lasting element of the desert vegetation, reflecting the habitat conditions. The locations of soil and plant samples in Wadi El-Missikat, Eastern Desert, Egypt, are indicated on a Landsat image of the area (Figure 1).

The present study briefs the ability of the gold uptake by plants, *Lotus hebranicus* and *Zilla spinosa*, for further exploration of gold.

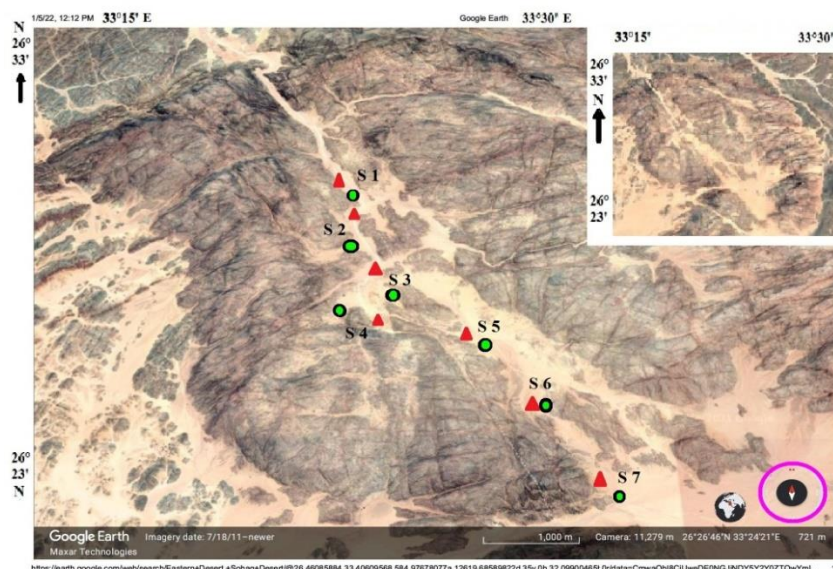


Figure 1: Landsat image showing samples location of the studied soil and plants in Wadi El-Missikat area.

2. MATERIAL AND METHODS

2.1 Plant Samples Collection

The plant species studied are *Lotus hebranicus*, *Lotus* sp., (Figure 2), and *Zilla spinosa*, *Zilla* sp., (Figure 3) from the Fabaceae and Zygophyllaceae families, respectively. These plants are highly prevalent in the research location and are thus ideal for this investigation. The collection of these species was done manually, with a minimum of 140 g of plant material prepared for each sample. Samples were promptly sent for analysis to prevent degradation of the collection bags, which can disintegrate if stored for long periods.

Every time, healthy plants were carefully selected for sampling, free of soil deposits. They were cleansed with tap and distilled water, then deionized water, and finally dried in an electric furnace at 105 °C for 12 hours. Afterward, the whole herba was blended

and powdered using stainless-steel and mechanical agate mortar, respectively. The resulting powder was stored in clean polyethylene bottles.



Figure 2: *Lotus hebranicus* plant.

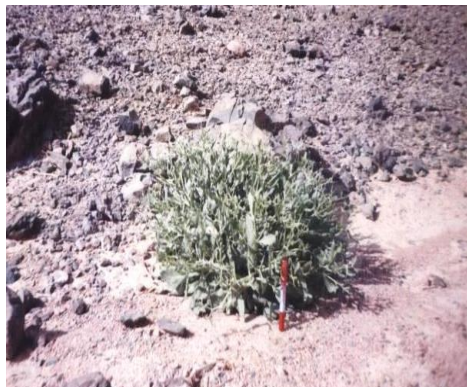


Figure 3: *Zilla spinosa* plant.

2.2. Plant Analysis

1.0 g of dried plant samples were for analysis by digestion in HNO₃ then in modified aqua regia (hot 1:1:1 HCl, HNO₃, H₂O) with an ICP-AES or ICP-MS finish (Acme Labs, Vancouver, Method 1VE) for 37 elements. Quality control (blanks, duplicates, and CRMs) constituted 10.8% of the samples analyzed. Many of the elements reported by this method were at or below detection.

2.3. Soil Samples Collection

Composite soil samples were gathered from the top 30 cm of soil depth, often in conjunction with plant samples. The soil samples were placed in bags and quartered before being crushed and pulverized with a mechanical agate mortar. Next, they were dried in an oven at 100 °C for 5 hours and stored in polyethylene bags for analysis.

2.4. Soil Analysis

0.5 g of finely powdered soil was precisely weighed and sent for analysis (Acme Labs, Vancouver) by ICP-AES and ICP-MS following a multiacid digestion involving heating in HNO₃-HClO₄- HF to fuming and taken to dryness, with the residue dissolved in HCl (Acme Method 1EX). For soil samples' concentrations above the upper detection levels for some elements, Acme's assay method STD DST6 was used.

Chemical analysis of plant and soil samples was carried out at ACME Analytical Laboratories in Vancouver, Canada. Detection limits for trace elements were 0.01–0.5 ppm. The analytical

precision, as calculated from replicate analyses, varied from 2% to 20% for trace elements.

3. RESULTS

Gold, silver, antimony, and arsenic found in plants can identify areas with gold deposits based on the plant's capacity to absorb and store these elements. Plants unable to absorb gold will be disregarded. Silver, antimony, arsenic, bismuth, copper, lead, selenium, tellurium, and zinc are key elements linked to gold (34, 35). Among these, silver, antimony, and arsenic were chosen due to their strong connection with gold.

3.1. Distribution of Gold, Silver, Antimony and Arsenic in The Studied Soil Samples

The primary origin of the soil samples is closely linked to the predominant granitic rocks in the surveyed region. Exploration typically focuses on indicators of gold mineralization such as Te, Bi, As, Ag, Cu, and Sb, among others (36-42). Tables 1 and 2 displayed the concentration mean of Au and its pathfinder in the studied plants and its associating soil. Firstly, these elemental distributions will be discussed in El-Missikat soil.

3.2. Gold and Its Pathfinders in Soil

The amount of gold in soil samples beneath the wild plants studied varies from 91.0 to 160.0 µg.kg⁻¹, averaging 106.0 µg.kg⁻¹. This is greater than the levels found in granitic rocks as reported by Kabata-Pendias and Pendias (17), which ranged from 1.2 to 1.8 µg.kg⁻¹. The soil analyzed contains gold levels approximately 100 times greater than those documented by Kabata-Pendias and Pendias (17). Abyan (18) found that the gold concentration in comparable soil, such as that in Gebel Qattar in the North Eastern Desert of Egypt, ranged from 1 to 3 µg.kg⁻¹, revealing a presence of gold enrichment in El-Missikat soil.

Williams et al. (21) observed that soil in an Au mining area in New Zealand has gold levels ranging from 3-48 µg.kg⁻¹. The average gold concentration in the soil studied was 106.0 µg.kg⁻¹, which is double the previously recorded values. This implies the possibility of gold mineralization in the studied area or nearby locations.

Table 1: Concentration of elements; Au, Ag, Sb, and As µg.kg⁻¹ in dry weight of *Lotus* sp. and soil samples and the biological absorption coefficients; BAC.

Samples	Au			Ag			Sb			As		
	<i>Lotus</i> sp	Soil	BAC	<i>Lotus</i> sp	Soil	BAC	<i>Lotus</i> sp	Soil	BAC	<i>Lotus</i> sp	Soil	BAC
1	10.5	94	0.11	59	164	0.36	66	198	0.33	1050	2070	0.51
2	9.98	91	0.11	57	180	0.32	65	202	0.32	1000	2005	0.50
3	10.7	100	0.11	62	173	0.36	69	205	0.34	985	2000	0.49
4	10.3	100	0.10	62	200	0.31	70	209	0.33	1030	1960	0.52
5	10.9	110	0.10	64	223	0.29	71	211	0.34	1100	1980	0.55
6	11.2	130	0.10	65	230	0.28	73	225	0.32	970	2040	0.48
7	11.5	160	0.10	68	236	0.29	76	240	0.31	940	1990	0.47
Average	10.71	112	0.10	62	201	0.32	70	213	0.33	1011	2006	0.50

Table 2: Concentration of elements; Au, Ag, Sb, and As $\mu\text{g.kg}^{-1}$ in dry weight of *Zilla* sp. and soil samples and the biological absorption coefficients; BAC.

Samples	Au			Ag			Sb			As		
	<i>Zilla</i> sp	Soil	BAC	<i>Zilla</i> sp	Soil	BAC	<i>Zilla</i> sp	Soil	BAC	<i>Zilla</i> sp	Soil	BAC
1	1.12	99	0.01	90	193	0.46	28	195	0.14	590	2000	0.30
2	1.19	91	0.01	95	199	0.47	27	196	0.14	610	2013	0.30
3	1.15	93	0.01	96	195	0.49	31	198	0.16	640	2030	0.32
4	1.35	101	0.01	98	203	0.48	31	201	0.15	600	2008	0.30
5	1.26	104	0.01	97	201	0.48	30	205	0.15	575	1980	0.29
6	1.54	101	0.02	102	210	0.51	33	200	0.17	560	1970	0.28
7	1.48	108	0.01	98	200	0.46	32	208	0.15	630	2018	0.31
Average	1.30	100	0.01	97	200	0.48	30	200	0.15	601	2003	0.30

Silver concentrations in the soil samples fell between 164 and 236 $\mu\text{g.kg}^{-1}$ on average, at 200.1 $\mu\text{g.kg}^{-1}$ (Tables 1 and 2). These levels were notably higher than those reported by Jones et al. (43), who found that typical soil silver concentrations were under 100 $\mu\text{g.kg}^{-1}$, but aligned with Mukherjee (44), who noted that typical silver concentrations in soil ranged from 30 to 400 $\mu\text{g.kg}^{-1}$.

Antimony; Sb, like arsenic; As, is considered a priority pollutant (19,45,46). On average, Sb concentration in the Earth's crust is 200-300 $\mu\text{g.kg}^{-1}$ (47) while uncontaminated soils have around 1000 $\mu\text{g.kg}^{-1}$ (48,49). Soil samples showed Sb levels ranging from 195 to 240 $\mu\text{g.kg}^{-1}$, averaging at 206.5 $\mu\text{g.kg}^{-1}$ (Tables 1 and 2), which is double Ebyan's finding of 100 $\mu\text{g.kg}^{-1}$ (18) but aligns with Rish's (50) statement that Sb's presence in the Earth's crust is between 200 and 300 $\mu\text{g.kg}^{-1}$. Kabata-Pendias and Pendias (17) noted that Sb in surface soil ranges from 50 to 4000 $\mu\text{g.kg}^{-1}$. Smith and Huyck (51) mentioned that the average Sb abundance in the crust is 200 $\mu\text{g.kg}^{-1}$, in line with our results.

Depending on the soil's parent material, background concentrations of arsenic can differ among soils. Typically, soil contains around 5000 $\mu\text{g.kg}^{-1}$; 5 mg.kg^{-1} of arsenic (52). The average As concentration in European topsoil is around 7000 $\mu\text{g.kg}^{-1}$ (53, 54). Arsenic and gold are often found together in gold deposits, as they are both hosted in Fe-sulfide minerals like pyrite, marcasite, and arsenopyrite, with As geochemistry influencing Au accumulation (55). Many countries have exceeded the USEPA's recommended soil As concentration of 24 $\mu\text{g.kg}^{-1}$ due to human activities (56, 57).

The levels of As in the soil samples varied from 1960 to 2070 $\mu\text{g.kg}^{-1}$ with an average of 2004.5 $\mu\text{g.kg}^{-1}$ as shown in Tables 1 and 2, exceeding the findings of Eyban (18), who documented a range of 1200 to 1400 $\mu\text{g.kg}^{-1}$ for arsenic in soil. Arsenic is distributed rather uniformly in major types of rocks, and its common concentrations in most rocks ranged between 500 and 2500 $\mu\text{g.kg}^{-1}$. All values of As in the present study are in agreement with values mentioned by Kabata-Pendias and Pendias (17) and

the United States Environmental Protection Agency (USEPA).

Figure 4a exhibited the same even distribution of Au and its associated elements, Ag, Sb, and As, in soil samples beneath *Lotus* sp. and *Zilla* sp., despite differing concentrations. Figures 4b and 4c displayed moderate positive links between Au-Ag and Ag-Sb, while a strong positive relationship between Au-Sb and Au-As indicated a solid correlation between gold and its indicators in Figures 4d and 4e.

3.3. Uptake of Gold, Silver, Antimony and Arsenic by The Studied Plant Samples

Lotus sp. had an average Au concentration of 10.7 $\mu\text{g.kg}^{-1}$, while *Zilla* sp. had a concentration of 1.3 $\mu\text{g.kg}^{-1}$ (Tables 1 and 2). The highest uptake levels for *Lotus* sp. were 11.5 $\mu\text{g.kg}^{-1}$ and 1.54 $\mu\text{g.kg}^{-1}$ for *Zilla* sp., with the lowest at 9.98 $\mu\text{g.kg}^{-1}$ and 1.12 $\mu\text{g.kg}^{-1}$. The average biological absorption coefficients (BAC) for Au were 0.1 for *Lotus* sp. and 0.01 for *Zilla* sp., suggesting they are moderate to weak hyperaccumulator plants (30).

According to Girling et al. (58), the amount of Au in plants is usually below 1.0 $\mu\text{g.kg}^{-1}$, so *Lotus* sp. may increase Au levels by eleven times and *Zilla* sp. may also increase levels by two times compared to the background level.

Oakes (59) indicated that the levels of Au in fruits and vegetables range from 0.01 to 0.4 $\mu\text{g.kg}^{-1}$, where *Lotus* sp. and *Zilla* sp. can concentrate Au by 1071 and 130 times greater than the reported values, respectively. *Helichrysum arenarium* has Au concentrations ranging from 0.4 to 5.8 $\mu\text{g.kg}^{-1}$, with *Lotus* sp. capable of concentrating Au more than *Helichrysum arenarium*.

Rashed (60) discovered that *Cyamopsis tetragonolobus* in the east of Aswan, Eastern Desert, Egypt, can absorb Au elements up to 4.6 $\mu\text{g.kg}^{-1}$. Ebyan (18) found that in the Gattar area, Eastern desert, Egypt, *Zygophyllum coccineum*, *Zilla spinosa*, *Fagonia boveana*, *Aerva javanica*, and *Moringa peregrine* can accumulate Au with average amounts of 1, 3, 2, 4, and 4 $\mu\text{g.kg}^{-1}$. Furthermore, *Lotus* sp. has even higher Au concentration values.

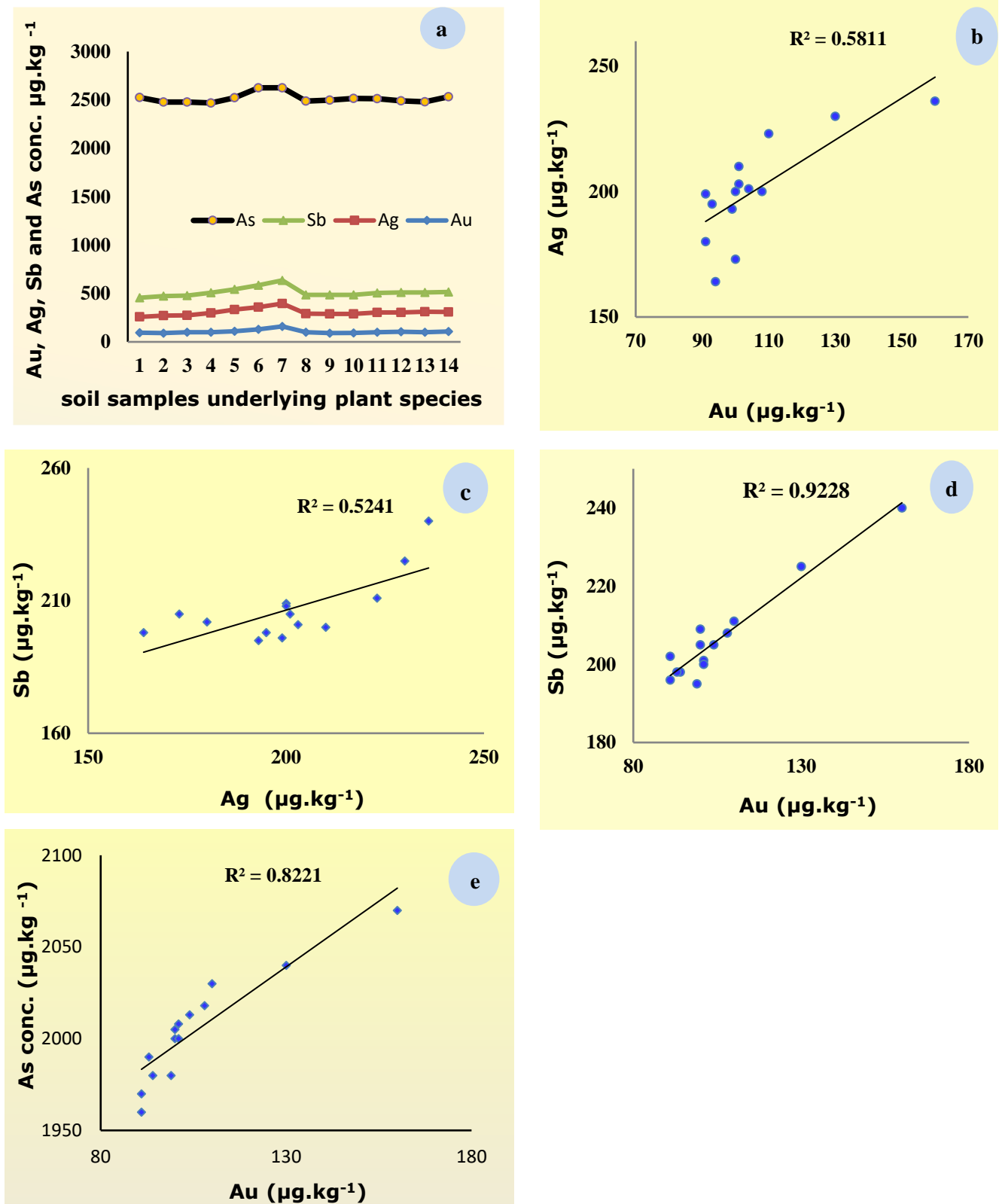


Figure 4: Correlation between Au, Ag, Sb, and As elements in soil samples underlying two plants.

Busche (9), Ebyan (18), and Rashed (60) found that the average concentration of Au in plant samples was $0.4 \mu\text{g.kg}^{-1}$. They also suggested that Au anomalies in plants could signal the presence of gold veins in the area where the anomalies were discovered.

Hacklette et al. (61) found that *Lotus* sp. can absorb and store higher levels of Au compared to previous studies (9,18,58,61). The high Au content in plants

may indicate gold mineralization in the area. Analysis of *Lotus* species and soil suggests that Au uptake in plants increases with higher soil Au levels. This is supported by a positive correlation between Au levels in plants and soil (Figure 5). *Lotus* sp. can concentrate more Au than *Zilla* sp. (Figure 6).

In the plant samples examined, Figure 7 displayed the same consistent absorption as Au. Ahmed et al.

(62) confirmed the presence of gold mineralization in El-Missikat area in Jasper and quartz veins.

The upper and lower limits of Ag absorption in *Lotus* and *Zilla* were 57-68 $\mu\text{g.kg}^{-1}$ and 90-102 $\mu\text{g.kg}^{-1}$, as shown in Tables 1 and 2. On average, the uptake of Ag in these species was measured at 62 $\mu\text{g.kg}^{-1}$ and 97 $\mu\text{g.kg}^{-1}$, respectively.

Vural (15) found that Ag concentration in *Helichrysum arenarium* ranged from 4-47 $\mu\text{g.kg}^{-1}$. *Lotus* and *Zilla* plants can absorb higher levels of Ag than this. Reimann et al (63) stated that *Betula pubescens* and *Pinus syluestris* in Northern Europe can absorb Ag at 7.0 and 8.0 $\mu\text{g.kg}^{-1}$. He also noted that *Hylocomium splendens* and *Pleurozium schreberi* can absorb Ag at 25 $\mu\text{g.kg}^{-1}$ in dry weight. *Lotus* and *Zilla* plants can absorb more Ag than these plants, according to Reimann et al. (63).

Ebyan (18) stated that *Lotus* sp. and *Zilla* sp. plants showed greater uptake and accumulation of Ag, with levels of 26, 44, 40, and 15 $\mu\text{g.kg}^{-1}$ in *Fagonia*, *Moringa*, *Aerva*, and *Zygophillum* plants, indicating their superior ability for Ag absorption and concentration compared to the other plants.

Ebyan (18) found that *Fagonia*, *Moringa*, *Aerva*, and *Zygophillum* plants accumulated 26, 44, 40, and 15 $\mu\text{g.kg}^{-1}$ of Ag, indicating that *Lotus* sp. and *Zilla* sp. have a greater capacity for Ag absorption than *Fagonia* and *Moringa*. Rashed (64) reported that *Aerva javanica* in Wadi Allaqi, Egypt, can absorb 70 $\mu\text{g.kg}^{-1}$ of Ag in dry samples. *Zilla* sp. had an average of 97 $\mu\text{g.kg}^{-1}$ Ag, higher than the value in Wadi Allaqi, while *Lotus* sp. values were similar. Bonanno (65) stated that *Phragmites australis* sp. absorbs <50 $\mu\text{g.kg}^{-1}$ Ag, whereas *Zilla* sp. and *Lotus* sp. recorded 102 and 68 $\mu\text{g.kg}^{-1}$ Ag, respectively, which is relatively higher.

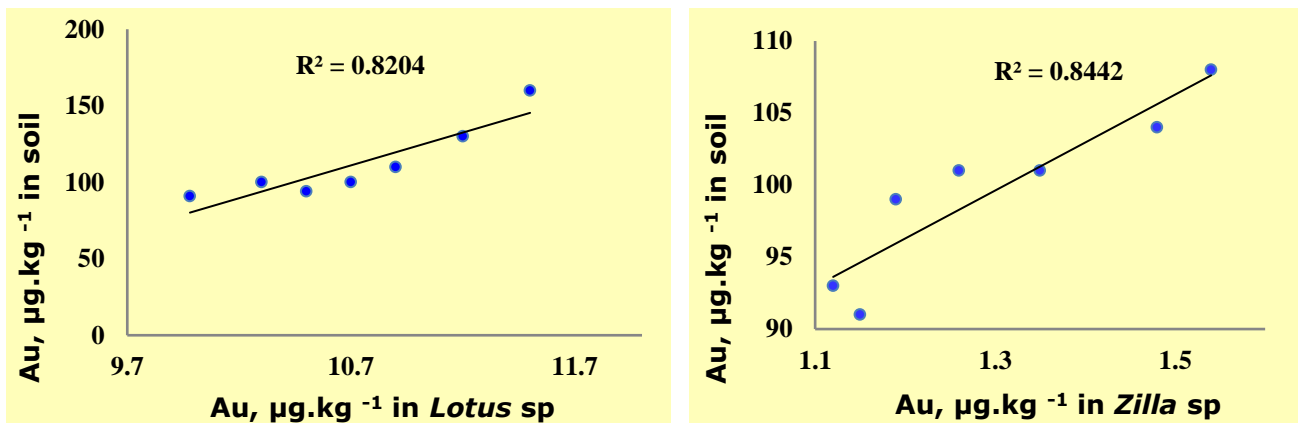


Figure 5: Correlation of Au concentration in plant species and their underlying soil.

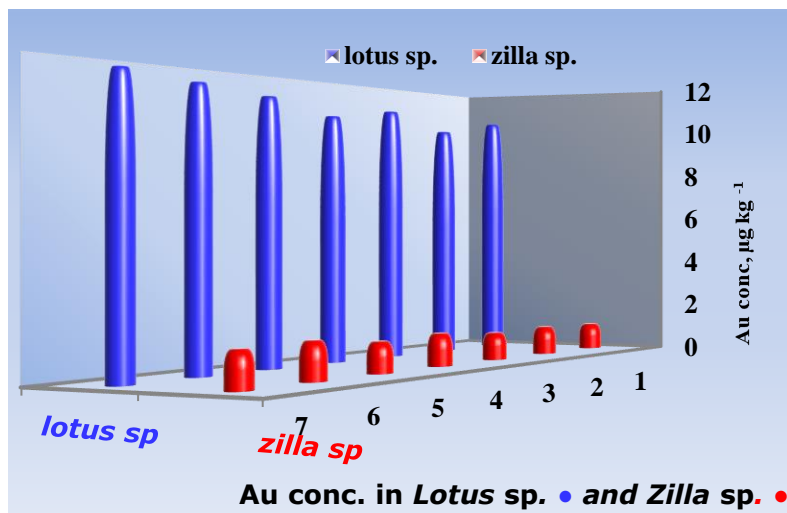


Figure 6: Histogram showing Au accumulation in *Lotus* sp. and *Zilla* sp. plant samples.

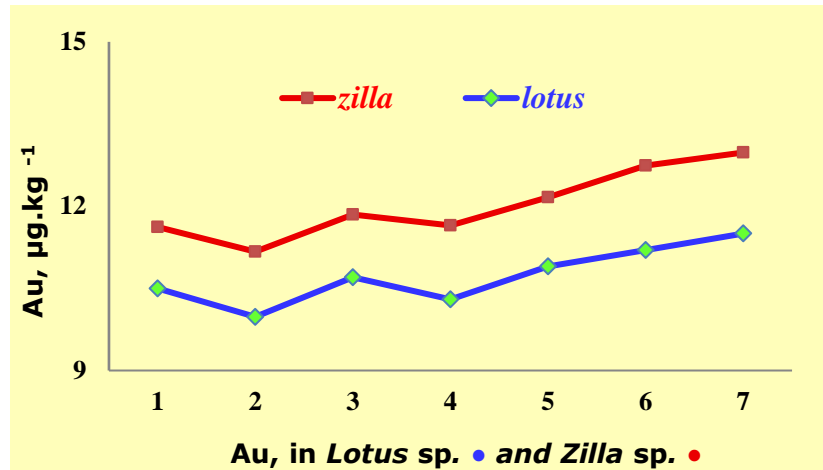


Figure 7: Histogram showing Au accumulation in *Lotus sp.* and *Zilla sp.* plant samples.

Khadija et al (66) found that *Rhazya stricta* plant can accumulate an average of nearly 70 $\mu\text{g.kg}^{-1}$ of Ag. This falls within the range of 68 to 102 $\mu\text{g.kg}^{-1}$ Ag in the current study. Reimann et al (63) demonstrated that *Lotus sp.* and *Zilla sp.* can uptake and retain Ag element at levels nine and thirteen times higher than the global average of 8 $\mu\text{g.kg}^{-1}$ for silver in plants.

According to Chaney et al (67), hyperaccumulator plants have the ability to gather ten to 500 times the

amount of an element compared to regular plants, making them ideal for phytoremediation. Therefore, *Lotus* and *Zilla* plants are ideal for studying and cleaning up silver using phytoremediation. The positive correlation between the concentration of Ag element in *Lotus sp.* and *Zilla sp.* and the soil beneath them implies that the source rocks may also contain minerals (Figure 8).

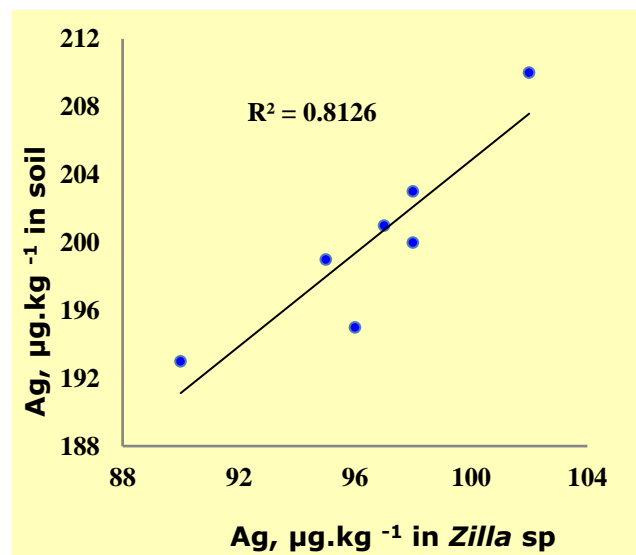
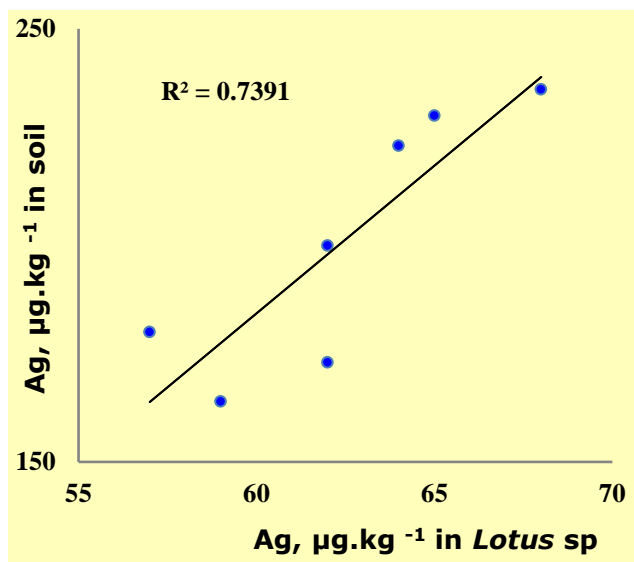


Figure 8: Correlation of Ag concentration in plants species and their underlying soil.

Figure 9 shows the concentration of Ag in two species, *Lotus* and *Zilla*, indicating that they can uptake and accumulate the silver element with nearly equal values, whereas Figure 10 shows the identical and homogenous absorption of Ag in the studied plant samples.

Several studies have investigated the transfer of Sb from soil to plants under natural or controlled conditions, finding that the absorption and retention of Sb by plants are greatly influenced by the oxidation states of Sb, type of soil, and species of plant (68-70).

Antimony is recognized as a significant toxic element by the European Union and global experts (71,72). Recent years have seen a rise in Sb pollution globally (73,74). *Lotus sp.* was found to have Sb concentrations ranging from 65 to 76 $\mu\text{g.kg}^{-1}$ with an average of 70 $\mu\text{g.kg}^{-1}$ (Table 1), higher than values reported in wild plants in the Eastern desert of Egypt (18). Reimann et al. (63) discovered that certain plants in Northern Europe, *Hylocomium splendens* and *Pleurozium schreberi*, can accumulate up to 0.06 $\mu\text{g.kg}^{-1}$ of Sb in dry samples.

According to Bonanno (65), *Phragmites australis* can uptake Sb at a rate of 0.05 $\mu\text{g.kg}^{-1}$. *Hylocomium splendens*, *Pleurozium schreberi*, and *Phragmites*

australis are able to store Sb levels ranging from 50 $\mu\text{g.kg}^{-1}$ to 60 $\mu\text{g.kg}^{-1}$ (63,65). Additionally, various edible plants have been detected with Sb content

between 30-220 $\mu\text{g.kg}^{-1}$ when grown in contaminated soils (75-79).

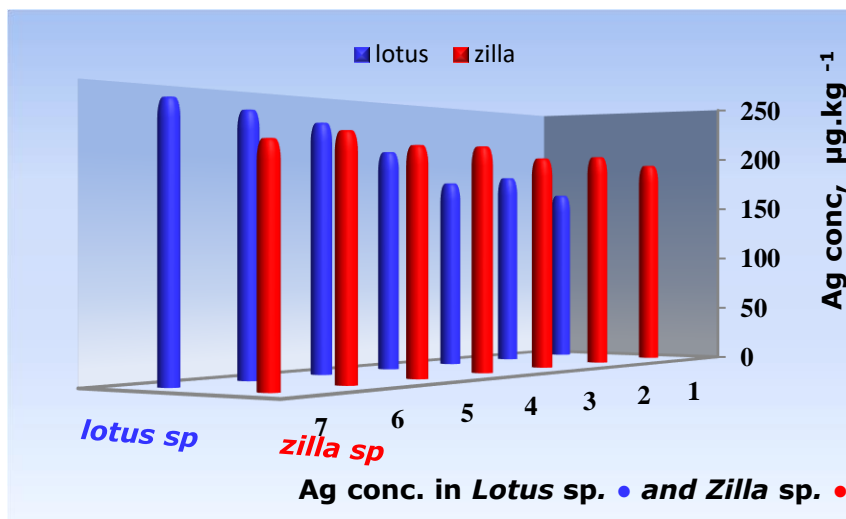


Figure 9: Histogram showing Ag accumulation in *Lotus sp.* and *Zilla sp.* plant samples.

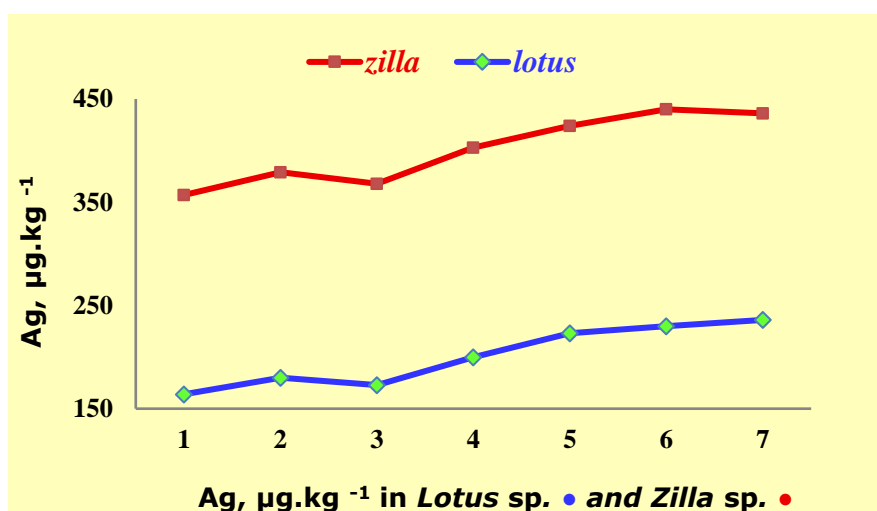


Figure 10: Histogram showing Ag accumulation in *Lotus sp.* and *Zilla sp.* plant samples.

Hockmann et al. (80) found *Lotus sp.* can accumulate Sb levels up to fifteen times higher than *L. perenne*, which had a concentration of 5 $\mu\text{g.kg}^{-1}$. Background Sb levels in plants range from 0.2 to 50 $\mu\text{g.kg}^{-1}$ (47,48,82). In Losacio mine soil in Spain, various plant species had Sb concentrations: *Quercus rotundifolia* (13 $\mu\text{g.kg}^{-1}$), *Agrostis castellana* (60 $\mu\text{g.kg}^{-1}$), *Agrostis delicatula* (6 $\mu\text{g.kg}^{-1}$), *Anthoxanthum odoratum* (2 $\mu\text{g.kg}^{-1}$), *Carlina corymbosa* (30 $\mu\text{g.kg}^{-1}$), *Dactylis glomerata* (7 $\mu\text{g.kg}^{-1}$), *Daphne gnidium* (2 $\mu\text{g.kg}^{-1}$), *Daucus carota* (80 $\mu\text{g.kg}^{-1}$), *Lavandula stoechas* (46 $\mu\text{g.kg}^{-1}$), *Marrubium vulgare* (15 $\mu\text{g.kg}^{-1}$), *Rubus idaeus* (60 $\mu\text{g.kg}^{-1}$), *Santolina rosmarinifolia* (80 $\mu\text{g.kg}^{-1}$), and *Centaurea paniculata* (49 $\mu\text{g.kg}^{-1}$). These values are consistent with those reported by Casado et al. (47).

Reimann et al. (63) reported a WAP uptake of 10 $\mu\text{g.kg}^{-1}$ for Sb. *Lotus sp.* can absorb and accumulate Sb seven times higher than the average uptake in

plants worldwide. Both *Lotus sp.* and *Zilla sp.* have biological absorption coefficients (*BAC*) for Sb (*Sbp/Sbs*) of 0.33 and 0.15, respectively. Tschan et al. (83) noted that *BAC* is below 0.03. Leduc and Gardou (82) found similar *BAC* rates in plants from Sb-rich ore deposits in Vendée, France. High *BAC* values were recorded for *Lotus sp.* and *Zilla sp.* (82,83).

Behzad et al. (30) found that plant samples fall into the moderate category of hyperaccumulator plants. Their study (Figure 11) revealed a correlation for Sb between *Lotus sp.* and *Zilla sp.* and their corresponding soils. *Lotus sp.* showed a positive correlation with their underlying soil, while *Zilla sp.* exhibited a negative correlation. Casado et al. (47) noted that Sb levels in plants did not correlate with concentrations in soils. *Lotus sp.* was able to uptake and accumulate more Sb compared to *Zilla sp.* (Figure 12).

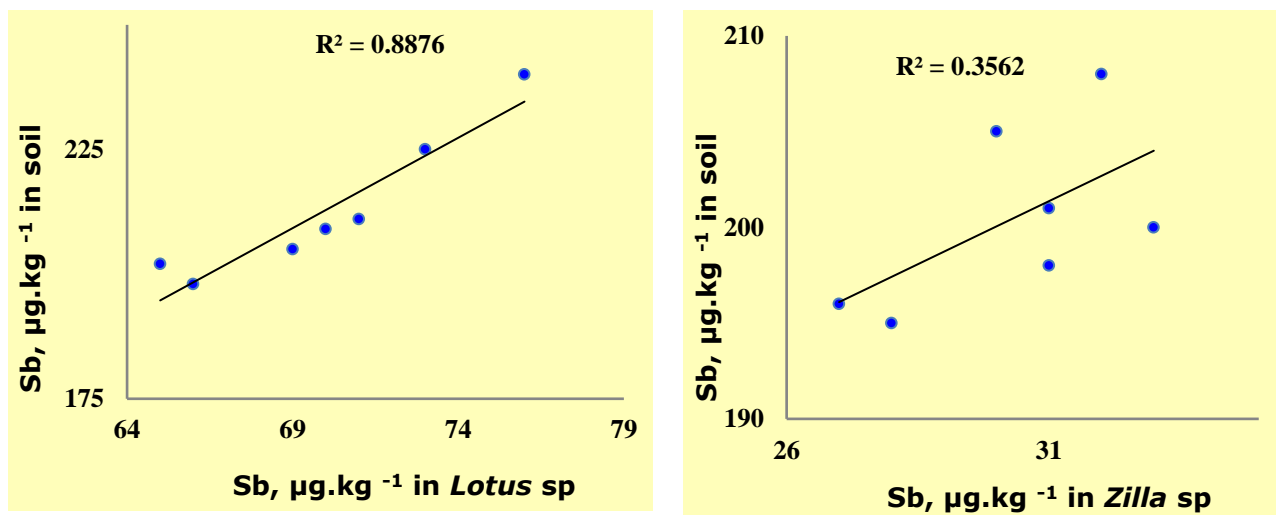


Figure 11: Correlation of Sb concentration in plant species and their underlying soils.

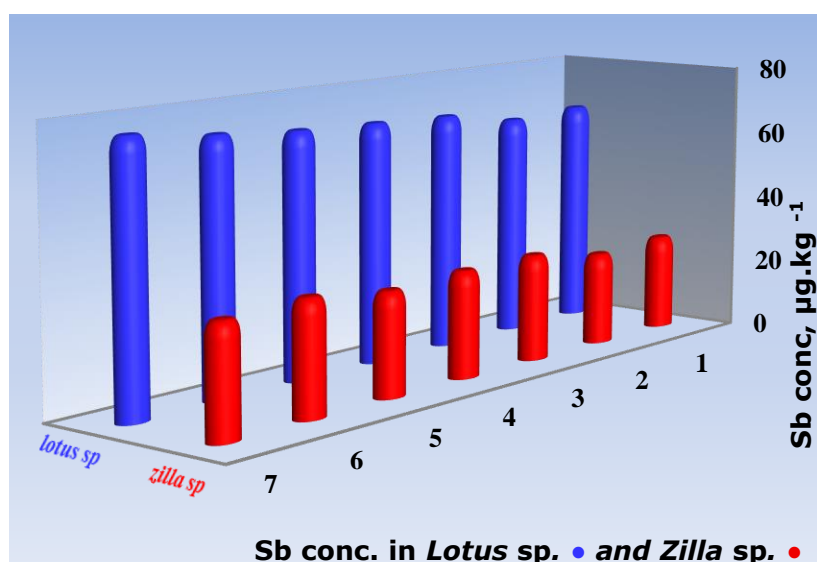


Figure 12: Histogram showing Sb accumulation in *Lotus sp.* and *Zilla sp.* plant samples.

Chemical analysis of As in *Lotus sp.* showed a range of 1100-940 $\mu\text{g.kg}^{-1}$ (Table 1) with an average of 1011 $\mu\text{g.kg}^{-1}$. The As ratio (As p/As s) in *Lotus sp.* ranged from 0.55 to 0.47, with an average of 0.5. In *Zilla sp.*, As contents ranged from 640 to 560 $\mu\text{g.kg}^{-1}$ with an average of 601 $\mu\text{g.kg}^{-1}$ (Table 2). The As

ratio in *Zilla sp.* ranged from 0.32 to 0.28. Ebyan (18) reported a maximum As concentration of 300 $\mu\text{g.kg}^{-1}$ in *Zilla sp.* in the Gattar area, while the present study found levels twice as high. The data suggest that *Lotus sp.* absorbs and concentrates As more efficiently than *Zilla sp.* (Figure 13).

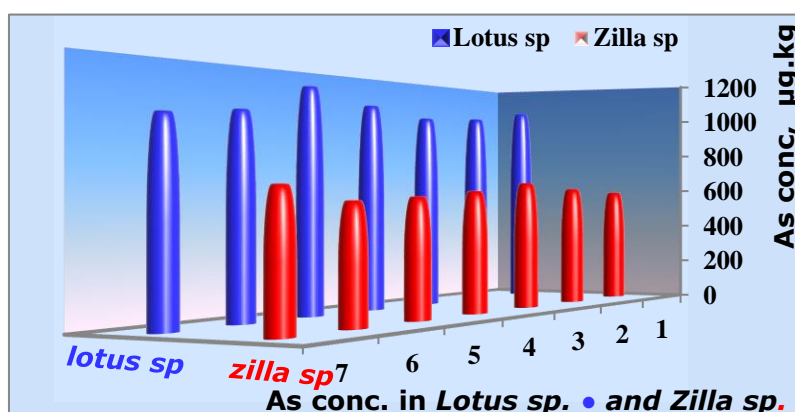


Figure 13: Histogram showing As accumulation in *Lotus sp.* and *Zilla sp.* plant samples.

Rashed (64) found that *Aerva* sp. near the gold mine at wadi Allaqi, Eastern Desert, Egypt, has the ability to absorb As at 400 $\mu\text{g.kg}^{-1}$ and far from the mine with 150 $\mu\text{g.kg}^{-1}$. Both plant species in the present study showed one- and two-times higher values than those recorded by Rashed (64). The concentration of As in plants is usually lower than 1000 $\mu\text{g.kg}^{-1}$ dry weight in different plant species growing on As-contaminated soil (84,85). Wild plant species that naturally inhabit arsenic-contaminated areas could likely show high potential for arsenic uptake (86). Plants can be classified for arsenic uptake into three

basic groups: excluders, indicators, and accumulators (86,87). Accumulator plants for arsenic element have a threshold arsenic content above 1,000 $\mu\text{g.kg}^{-1}$ (Dw). Prasad (88) mentioned that the most arsenic accumulator species were *Amaranthus billitoides*; 800-120000 $\mu\text{g.kg}^{-1}$, *Chamaemelum fuscatum*, 7000-23000 $\mu\text{g.kg}^{-1}$, *Convolvulus arvensis*, 100-26000 $\mu\text{g.kg}^{-1}$, *Cynodon dactylon*, 200-40000 $\mu\text{g.kg}^{-1}$, and *Malva nicaensis*, 1000-28000 $\mu\text{g.kg}^{-1}$. The *Lotus* sp. in the present study is considered an accumulator plant for arsenic, according to the Prasad report.

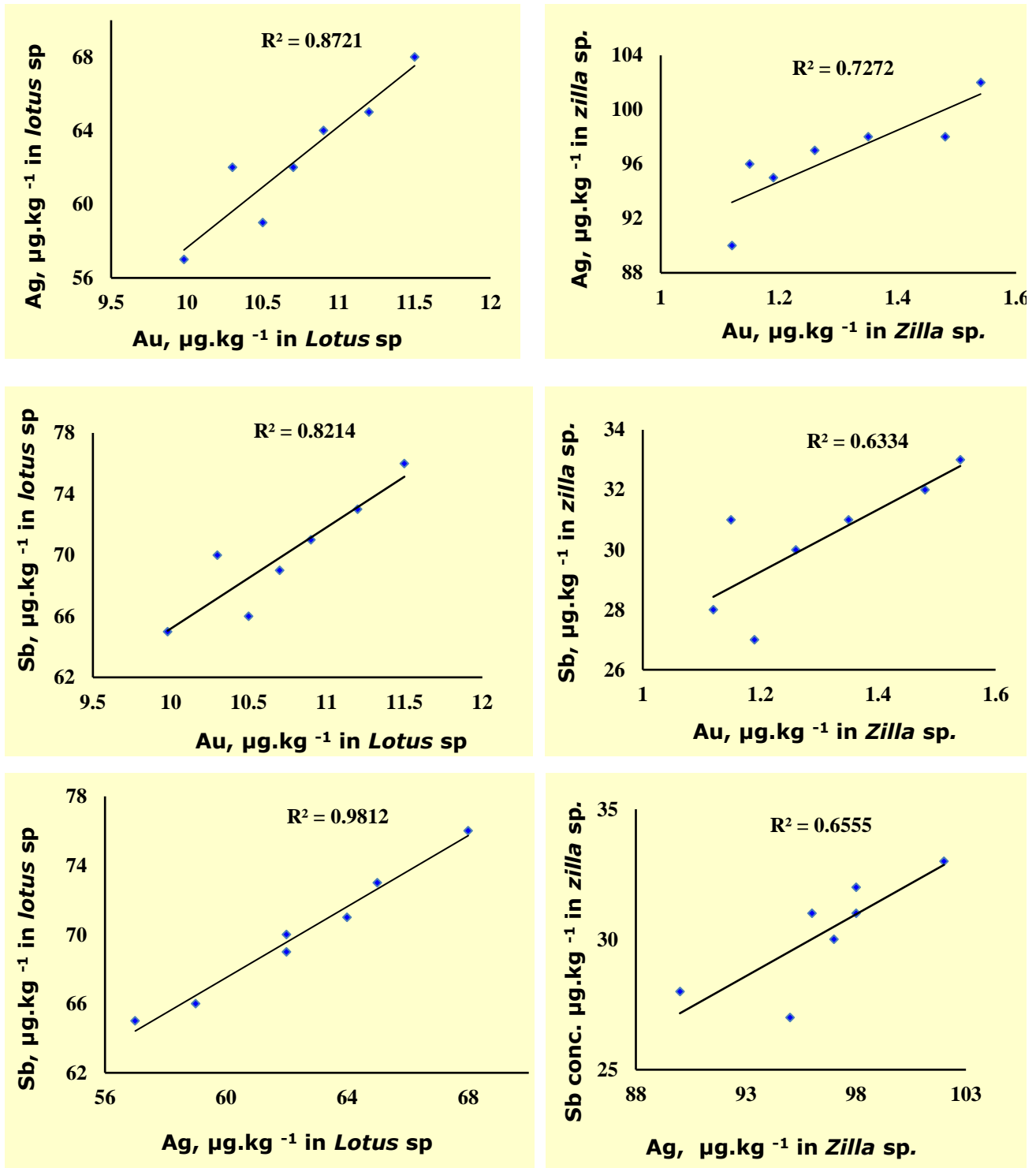


Figure 14: Strong positive and positive correlation between Au, Ag, and Sb in *Lotus* sp. and *Zilla* sp. samples.

3.4. The Relationship Between Gold and Its Pathfinder

In the present study, there is a clear correlation between Au, Ag and Sb in *Lotus* and *Zilla* species, as indicated in Figure 14. The presence of strong positive correlation between Au and Ag, Au and Sb and Ag and Sb, in *Lotus* plants. Also, there is a

positive correlation between Au and Ag, Au and Sb, and Ag and Sb, in *Zilla* plant. It can be concluded from the previous discussion that *Lotus* sp. can uptake and accumulate Au, Sb and As elements higher than *Zilla* sp. On the other hand, *Zilla* sp. can uptake and accumulate Ag elements more than *Lotus* sp. (Figure 15).

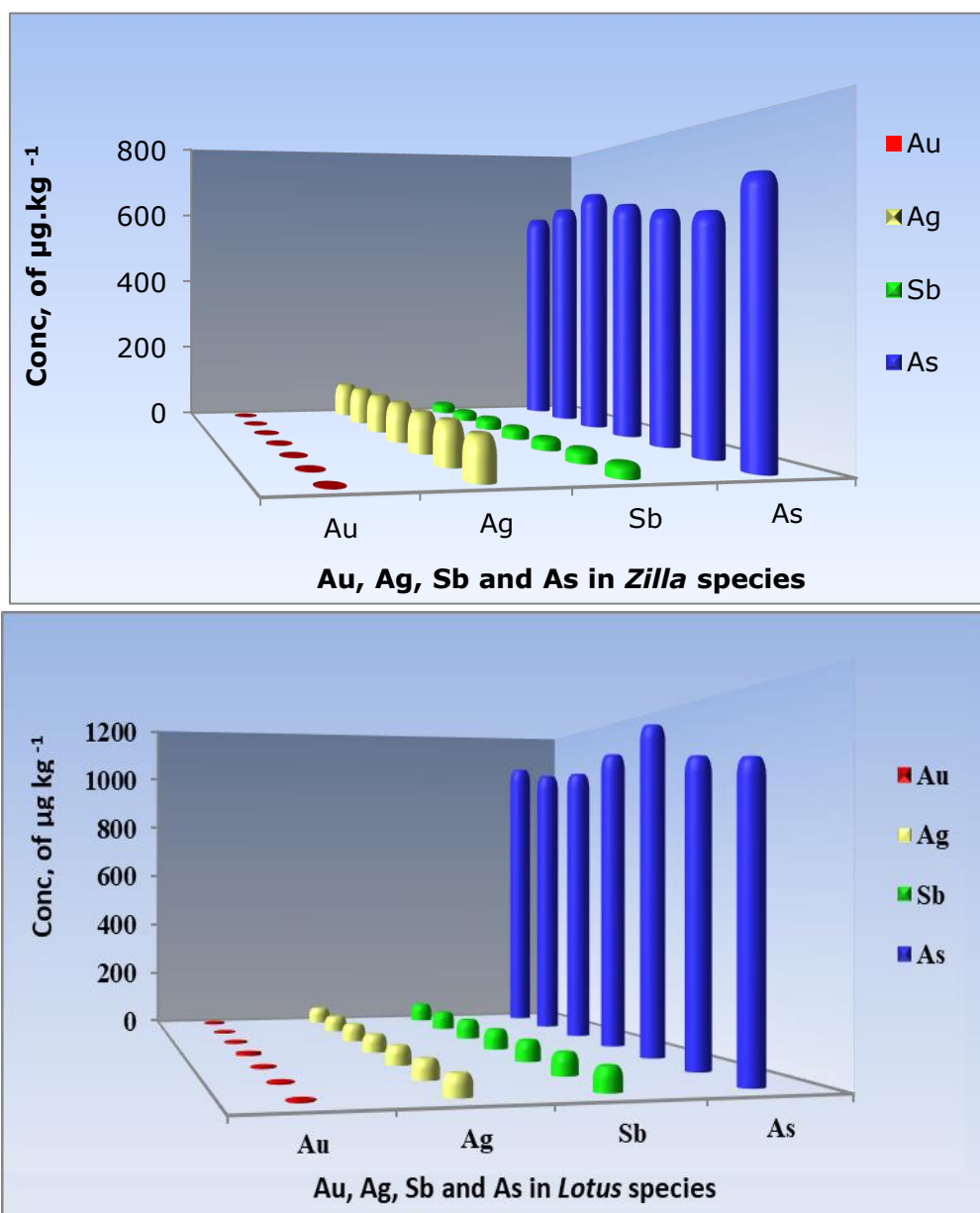


Figure 15: Frequency curves of Au, Ag, Sb, and As elements; $\mu\text{g.kg}^{-1}$ in two plants species.

4. CONCLUSIONS

The high Au content in plants and its associating soil, in addition to the moderate to strong correlation between gold and its pathfinders, could be considered an indication for the presence of gold mineralization in the adjacent rocks of El-Missikat area, which may be confirmed by the positive correlation between Au in the plants and in the underlying soil. Also, *Lotus* sp. can concentrate Au more than *Zilla* sp. For silver exploration and phytoremediation, researchers can use *Lotus* and *Zilla* plants. The *Lotus* sp. can uptake and accumulate Sb element more than the *Zilla* sp., so, it is useful for

remediation processes of Sb as a toxic element. We conclude that we can utilize these plants for both exploration and remediation procedures.

Availability of data and materials

I clarify the availability of data and materials after receiving the acceptance from the journal.

Consent to participate

I declare our agreement to participate in this work.

Consent to publish

I declare our agreement to publish this work.

Funding

The author report there is no funding associated with the work featured in this article.

Data availability statement

The authors confirm that the data supporting the findings of this study are available within the article.

Disclosure statement

No potential conflict of interest was reported by the author(s).

Ethical approval statement

All authors attest to the uniqueness of this paper, its non-publication in any form or language (in part or in whole), and its simultaneous submission to multiple publications for consideration. I also assert unequivocally that I have presented the results accurately, honestly, and without any fabrication, falsification, or data modification (including image-based manipulation).

5. REFERENCES

- Girling CA, Peterson PJ. Gold in plants. *Gold Bull* [Internet]. 1980 Dec;13(4):151-7. Available from: [<URL>](#).
- Lungwitz EE. The Lixiviation of Gold Deposits by Vegetation. *J Eng Min.* 1900;69:500-2.
- Shacklette H, Lakin H, Hubert A, Curtin G. Absorption of gold by plants [Internet]. 1970. Available from: [<URL>](#).
- Dekate YG. Absorption of Gold by Sorghum Saccharatum Pers. *J Indian Geosci Assoc.* 1971;13:75-8.
- Kovalevskii AL, Kovalevskaya OM. Biogeochemical haloes of gold in various species and parts of plants. *Appl Geochemistry* [Internet]. 1989 Jul;4(4):369-74. Available from: [<URL>](#).
- Brooks RR. Biological methods of prospecting for gold. *J Geochemical Explor* [Internet]. 1982 Nov;17(2):109-22. Available from: [<URL>](#).
- Dunn CE. Biogeochemistry as an aid to exploration for gold, platinum and palladium in the northern forests of Saskatchewan, Canada. *J Geochemical Explor* [Internet]. 1986 Mar;25(1-2):21-40. Available from: [<URL>](#).
- Erdman JA, Olson JC. The use of plants in prospecting for gold: A brief overview with a selected bibliography and topic index. *J Geochemical Explor* [Internet]. 1985 Dec;24(3):281-304. Available from: [<URL>](#).
- Busche FD. Using plants as an exploration tool for gold. *J Geochemical Explor* [Internet]. 1989 Apr;32(1-3):199-209. Available from: [<URL>](#).
- Raskin I, Ensley BD. *Phytoremediation of Toxic Metals: Using Plants to Clean up the Environment* [Internet]. New York: John Wiley and Sons; Available from: [<URL>](#).
- Jafarirad S, Mehrabi M, Divband B, Kosari-Nasab M. Biofabrication of zinc oxide nanoparticles using fruit extract of *Rosa canina* and their toxic potential against bacteria: A mechanistic approach. *Mater Sci Eng C* [Internet]. 2016 Feb;59:296-302. Available from: [<URL>](#).
- Aljahdali MO, Alhassan AB. The efficiency of trace element uptake by seagrass *Cymodocea serrulata* in Rabigh lagoon, Red Sea. *Environ Sci Pollut Res* [Internet]. 2022 Feb 8;29(10):14948-60. Available from: [<URL>](#).
- Aljahdali MO, Alhassan AB. Metallic Pollution and the Use of Antioxidant Enzymes as Biomarkers in *Bellamyia unicolor* (Olivier, 1804) (Gastropoda: Bellamyinae). *Water* [Internet]. 2020 Jan 10;12(1):202. Available from: [<URL>](#).
- Boutahar L, Espinosa F, Sempere-Valverde J, Selfati M, Bazairi H. Trace element bioaccumulation in the seagrass *Cymodocea nodosa* from a polluted coastal lagoon: Biomonitoring implications. *Mar Pollut Bull* [Internet]. 2021 May;166:112209. Available from: [<URL>](#).
- Vural A. Gold and Silver Content of Plant *Helichrysum Arenarium*, Popularly Known as the Golden Flower, Growing in Gümüşhane, NE Turkey. *Acta Phys Pol A* [Internet]. 2017 Sep;132(3-II):978-80. Available from: [<URL>](#).
- El Tokhi M, Mahmoud B, Alaabed S. Distribution of Heavy Metals in the Bottom Sediments of the Arabian Gulf, United Arab Emirates. *Acta Phys Pol A* [Internet]. 2015 Aug;128(2B):B-103-B-107. Available from: [<URL>](#).
- Kabata-Pendias A. *Trace Elements in Soils and Plants* [Internet]. CRC Press; 2000. Available from: [<URL>](#).
- Ebyan OA. The Environmental Influence of Presence of Some Trace and Rare Elements in Some Soils Plants in Egypt and Namibia. [Egypt]; 2014.
- EPA U. Method 3050b. Acid Digestion of Sediments, Sludges, and Soils [Internet]. [cited 2023 Mar 16]. Available from: [<URL>](#).
- Jones KC, Lepp NW, Obbard JP. Other metals and metalloids. *Heavy Met soils.* 1990;280-321.
- Williams CA. *The Analysis of Gold in Plants and Soils by Inductively Coupled Plasma Mass Spectrometry.* [Guildford]; 1996.
- Rodríguez E, Peralta-Videa JR, Israr M, Sahi S V., Pelayo H, Sánchez-Salcido B, et al. Effect of mercury and gold on growth, nutrient uptake, and anatomical changes in *Chilopsis linearis*. *Environ Exp Bot* [Internet]. 2009 Mar;65(2-3):253-62. Available from: [<URL>](#).
- Bali R, Siegele R, Harris AT. Phytoextraction of Au: Uptake, accumulation and cellular distribution in *Medicago sativa* and *Brassica juncea*. *Chem Eng J* [Internet]. 2010 Jan 15;156(2):286-97. Available from: [<URL>](#).
- Gagnon V, Rodrigue-Morin M, Migneault M, Tardif A, Garneau L, Lalonde S, et al. Survival, growth and element translocation by 4 plant species growing on acidogenic gold mine tailings in Québec. *Ecol Eng* [Internet]. 2020 May;151:105855. Available from: [<URL>](#).

25. Pullagurala VLR, Rawat S, Adisa IO, Hernandez-Viezcas JA, Peralta-Videa JR, Gardea-Torresdey JL. Plant uptake and translocation of contaminants of emerging concern in soil. *Sci Total Environ* [Internet]. 2018 Sep;636:1585–96. Available from: [<URL>](#).
26. Anderson CWN, Brooks RR, Stewart RB, Simcock R. Gold Uptake by Plants. *Gold Bull* [Internet]. 1999 Jun;32(2):48–52. Available from: [<URL>](#).
27. El Tokhi M, Amin BM, Alaabed S. Trace Metals Contamination of Bottom Sediments of Abu Dhabi Area, UAE. *Acta Phys Pol A* [Internet]. 2016 Jul;130(1):138–41. Available from: [<URL>](#).
28. Aljahdali MO, Alhassan AB. Ecological risk assessment of heavy metal contamination in mangrove habitats, using biochemical markers and pollution indices: A case study of *Avicennia marina* L. in the Rabigh lagoon, Red Sea. *Saudi J Biol Sci* [Internet]. 2020 Apr;27(4):1174–84. Available from: [<URL>](#).
29. Perel'man AI. Landscape geochemistry; Department of the Secretary of State, Translation Bureau, Multilingual Services. Department of the Secretary of State, Translation Bureau, Multilingual Services; 1972.
30. Mehrabi B, Alimohamdai H, Farhadian Babadi M, Ghahremani Nejad F. Biogeochemical Exploration in Sari Gunay Gold Deposit, Northwestern Iran. *Geopersia* [Internet]. 2016;6(2):223–32. Available from: [<URL>](#).
31. Boulos L. Flora and Vegetation of the Deserts of Egypt. *Flora Mediterr* [Internet]. 2008;18:341–59. Available from: [<URL>](#).
32. Zahran M, Willis A. The Vegetation of Egypt [Internet]. Dordrecht: Springer Netherlands; 2009. (Plant and Vegetation; vol. 2). Available from: [<URL>](#).
33. El-Amier YA, Abdulkader OM. Vegetation and Species Diversity in the Northern Sector of Eastern Desert, Egypt. *West African J Appl Ecol* [Internet]. 2015 Sep 10;23(1):75–95. Available from: [<URL>](#).
34. Boyle RW, Jonasson IR. The geochemistry of arsenic and its use as an indicator element in geochemical prospecting. *J Geochemical Explor* [Internet]. 1973 Oct;2(3):251–96. Available from: [<URL>](#).
35. Boyle RW. The geochemistry of gold and its deposits (together with a chapter on geochemical prospecting for the element). *Can Geol Surv Bull* [Internet]. 1979;280:584. Available from: [<URL>](#).
36. Hartikainen A. Soil geochemical studies in gold exploration at three targets in Haapoluoma, Seinäjoki, W-Finland. *Geol Surv Finl*. 2012;52:149–75.
37. Nude PM, Asigri JM, Yidana SM, Arhin E, Foli G, Kutu JM. Identifying Pathfinder Elements for Gold in Multi-Element Soil Geochemical Data from the Wa-Lawra Belt, Northwest Ghana: A Multivariate Statistical Approach. *Int J Geosci* [Internet]. 2012;3(1):62–70. Available from: [<URL>](#).
38. Carlos AS. Geokhemicheskie Poiskovye Priznaki Zolotorudnoi Mineralizatsii Vistochnoi Chasti Baltiskogo Schita. [Russia]; 2002.
39. Reis A., Sousa A., Cardoso Fonseca E. Soil geochemical prospecting for gold at Marrancos (Northern Portugal). *J Geochemical Explor* [Internet]. 2001 Sep;73(1):1–10. Available from: [<URL>](#).
40. McClenaghan M., Thorleifson L., DiLabio RN. Till geochemical and indicator mineral methods in mineral exploration. *Ore Geol Rev* [Internet]. 2000 Jun;16(3–4):145–66. Available from: [<URL>](#).
41. Korshunova VA, Charykova MV. Mobile Forms of Gold and Pathfinder Elements in Surface Sediments at the Novye Peski Gold Deposit and in the Piilola Prospecting Area (Karelia Region). *Minerals* [Internet]. 2019 Jan 11;9(1):34. Available from: [<URL>](#).
42. Nzulu GK, Bakhit B, Högberg H, Hultman L, Magnuson M. Elucidating Pathfinding Elements from the Kubi Gold Mine in Ghana. *Minerals* [Internet]. 2021 Aug 24;11(9):912. Available from: [<URL>](#).
43. Jones KC, Davies BE, Peterson PJ. Silver in Welsh soils: Physical and chemical distribution studies. *Geoderma* [Internet]. 1986 Mar;37(2):157–74. Available from: [<URL>](#).
44. Mukherjee AB. The Use and Release of Silver in Finland. [Helsinki]: The Finnish environment; Finnish Environment Institute; 1997.
45. Council Directive 76/464/EEC of 4 May 1976 on Pollution Caused by Certain Dangerous Substances Discharged into the Aquatic Environment of the Community [Internet]. 1976 [cited 2023 Feb 23]. Available from: [<URL>](#).
46. Cui XD, Wang YJ, Hockmann K, Zhou DM. Effect of iron plaque on antimony uptake by rice (*Oryza sativa* L.). *Environ Pollut* [Internet]. 2015 Sep;204:133–40. Available from: [<URL>](#).
47. Casado M, Anawar HM, Garcia-Sanchez, A, Santa Regina I. Antimony and Arsenic Uptake by Plants in an Abandoned Mining Area. *Commun Soil Sci Plant Anal* [Internet]. 2007 May;38(9–10):1255–75. Available from: [<URL>](#).
48. Bowen HJ. Environmental Chemistry of the Elements. New York: Academic Press: London; 1979.
49. Hans Wedepohl K. The composition of the continental crust. *Geochim Cosmochim Acta* [Internet]. 1995 Apr;59(7):1217–32. Available from: [<URL>](#).
50. Rish MA. Antimony. In: Merian E, Anke M, Ihnat M, Stoeppler M, editors. Elements and Their Compounds in the Environment [Internet]. Wiley; 2004. p. 659–70. Available from: [<URL>](#).
51. Smith KS, Huyck HLO. An Overview of the Abundance, Relative Mobility, Bioavailability, and Human Toxicity of Metals. In: The Environmental Geochemistry of Mineral Deposits [Internet]. Society of Economic Geologists; 1997. p. 29–70. Available from: [<URL>](#).
52. Basu A, Saha D, Saha R, Ghosh T, Saha B. A review on sources, toxicity and remediation technologies for removing arsenic from drinking water. *Res Chem Intermed* [Internet]. 2014 Feb 9;40(2):447–85. Available from: [<URL>](#).
53. Karczewska A, Bogda A, Krysiak A. Arsenic in soils in the areas of former mining and mineral processing in

- Lower Silesia, southwestern Poland. In 2007. p. 411–40. Available from: [<URL>](#).
54. Stafilov T, Aliu M, Sajin R. Arsenic in Surface Soils Affected by Mining and Metallurgical Processing in K. Mitrovica Region, Kosovo. *Int J Environ Res Public Health* [Internet]. 2010 Nov 18;7(11):4050–61. Available from: [<URL>](#).
55. Xing Y, Brugger J, Tomkins A, Shvarov Y. Arsenic evolution as a tool for understanding formation of pyritic gold ores. *Geology* [Internet]. 2019 Apr 1;47(4):335–8. Available from: [<URL>](#).
56. Hossain MA, Begum A, Akhtar K. Study on Knowledge about Arsenic Contamination in Drinking Water among the People Living in Selected Villages of Bangladesh. *J Shaheed Suhrawardy Med Coll* [Internet]. 2017 Mar 7;6(2):57–9. Available from: [<URL>](#).
57. Mondal P, Bhowmick S, Chatterjee D, Figoli A, Van der Bruggen B. Remediation of inorganic arsenic in groundwater for safe water supply: A critical assessment of technological solutions. *Chemosphere* [Internet]. 2013 Jun;92(2):157–70. Available from: [<URL>](#).
58. Girling CA, Peterson PJ, Warren H V. Plants as indicators of gold mineralization at Watson Bar, British Columbia, Canada. *Econ Geol* [Internet]. 1979 Jul 1;74(4):902–7. Available from: [<URL>](#).
59. Oakes TW, Shank KE. Concentrations of radionuclides and selected stable elements in fruits and vegetables [Internet]. Oak Ridge, TN (United States); 1977 Jan. Available from: [<URL>](#).
60. Rashed MN. Trace element determination in warm-climate plants by Atomic Absorption Spectroscopy and Ion Selective Electrodes. *J Arid Environ* [Internet]. 1995 Aug;30(4):463–78. Available from: [<URL>](#).
61. Shacklette HT, Erdman JA, Harms TF, Papp CSE. Trace elements in plant foodstuffs. In: Harms TF. New York; 1978. p. 25–42.
62. Ahmed MR, Mohammed HS, El-Feky MG, Abdel-Monem YK. Gold Leaching Using Thiourea from Uranium Tailing Material, Gabal El-Missikat, Central Eastern Desert, Egypt. *J Sustain Metall* [Internet]. 2020 Dec 8;6(4):599–611. Available from: [<URL>](#).
63. Reimann C, Koller F, Frengstad B, Kashulina G, Niskavaara H, Englmaier P. Comparison of the element composition in several plant species and their substrate from a 1 500 000-km² area in Northern Europe. *Sci Total Environ* [Internet]. 2001 Oct 20;278(1–3):87–112. Available from: [<URL>](#).
64. Rashed MN. Monitoring of contaminated toxic and heavy metals, from mine tailings through age accumulation, in soil and some wild plants at Southeast Egypt. *J Hazard Mater* [Internet]. 2010 Jun;178(1–3):739–46. Available from: [<URL>](#).
65. Bonanno G. Trace element accumulation and distribution in the organs of *Phragmites australis* (common reed) and biomonitoring applications. *Ecotoxicol Environ Saf* [Internet]. 2011 May;74(4):1057–64. Available from: [<URL>](#).
66. Semhi K, Abdalla OAE, Al Khirbash S, Khan T, Asaidi S, Farooq S. Mobility of rare earth elements in the system soils–plants–groundwaters: a case study of an arid area (Oman). *Arab J Geosci* [Internet]. 2009 Apr 6;2(2):143–50. Available from: [<URL>](#).
67. Chaney RL, Malik M, Li YM, Brown SL, Brewer EP, Angle JS, et al. Phytoremediation of soil metals. *Curr Opin Biotechnol* [Internet]. 1997 Jun;8(3):279–84. Available from: [<URL>](#).
68. Nakamaru YM, Altansuvd J. Speciation and bioavailability of selenium and antimony in non-flooded and wetland soils: A review. *Chemosphere* [Internet]. 2014 Sep;111:366–71. Available from: [<URL>](#).
69. Natasha, Shahid M, Khalid S, Dumat C, Pierart A, Niazi NK. Biogeochemistry of antimony in soil-plant system: Ecotoxicology and human health. *Appl Geochemistry* [Internet]. 2019 Jul;106:45–59. Available from: [<URL>](#).
70. Wan X, Yang J, Lei M. Speciation and uptake of antimony and arsenic by two populations of *Pteris vittata* L. and *Holcus lanatus* L. from co-contaminated soil. *Environ Sci Pollut Res* [Internet]. 2018 Nov 19;25(32):32447–57. Available from: [<URL>](#).
71. Callahan MA, Slimak MW, Gabel NW, May IP, Fowler CF. Water-Related Environmental Fate of 129 Priority Pollutants. Volume I: Introduction and Technical Background, Metals and Inorganics, Pesticides and PCBs. [Internet]. Available from: [<URL>](#).
72. Council of the European, Directive–Pollution caused by certain dangerous substances discharged into the aquatic environment of the community. 2006.
73. He M, Wang X, Wu F, Fu Z. Antimony pollution in China. *Sci Total Environ* [Internet]. 2012 Apr;421–422:41–50. Available from: [<URL>](#).
74. Herath I, Vithanage M, Bundschuh J. Antimony as a global dilemma: Geochemistry, mobility, fate and transport. *Environ Pollut* [Internet]. 2017 Apr;223:545–59. Available from: [<URL>](#).
75. Feng R, Wei C, Tu S, Ding Y, Wang R, Guo J. The uptake and detoxification of antimony by plants: A review. *Environ Exp Bot* [Internet]. 2013 Dec;96:28–34. Available from: [<URL>](#).
76. He M. Distribution and phytoavailability of antimony at an antimony mining and smelting area, Hunan, China. *Environ Geochem Health* [Internet]. 2007 Jun 10;29(3):209–19. Available from: [<URL>](#).
77. He M, Wang N, Long X, Zhang C, Ma C, Zhong Q, et al. Antimony speciation in the environment: Recent advances in understanding the biogeochemical processes and ecological effects. *J Environ Sci* [Internet]. 2019 Jan;75:14–39. Available from: [<URL>](#).
78. Shtangeeva I, Niemelä M, Perämäki P. Effects of soil amendments on antimony uptake by wheat. *J Soils Sediments* [Internet]. 2014 Apr 13;14(4):679–86. Available from: [<URL>](#).
79. Tschan M, Robinson B, Johnson CA, Bürgi A, Schulin R. Antimony uptake and toxicity in sunflower and maize growing in SbIII and SbV contaminated soil. *Plant Soil* [Internet]. 2010 Sep 16;334(1–2):235–45. Available from: [<URL>](#).

80. Hockmann K, Tandy S, Studer B, Evangelou MWH, Schulin R. Plant uptake and availability of antimony, lead, copper and zinc in oxic and reduced shooting range soil. *Environ Pollut* [Internet]. 2018 Jul;238:255–62. Available from: [<URL>](#).
81. Brooks RR. *Geobotany and Biogeochemistry in Mineral Exploration*; Harper's geoscience series. New York: Harper & Row; 1972.
82. Leduc C. DE, Gardou C. Biogeochemical prospecting for antimony: results of an orientation study on the Brouzils deposit (Vendee, France). *Bull la Soc Bot Fr Actual Bot* [Internet]. 1992;139(1):123–31. Available from: [<URL>](#).
83. Tschan M, Robinson BH, Schulin R. Antimony in the soil - plant system - a review. *Environ Chem* [Internet]. 2009;6(2):106. Available from: [<URL>](#).
84. Adriano DC. Arsenic. In: *Trace Elements in Terrestrial Environments* [Internet]. New York, NY: Springer New York; 2001. p. 219–61. Available from: [<URL>](#).
85. Austruy A, Wanat N, Moussard C, Vernay P, Joussein E, Ledoigt G, et al. Physiological impacts of soil pollution and arsenic uptake in three plant species: *Agrostis capillaris*, *Solanum nigrum* and *Vicia faba*. *Ecotoxicol Environ Saf* [Internet]. 2013 Apr;90:28–34. Available from: [<URL>](#).
86. Mateo C, Navarro M, Navarro C, Leyva A. Arsenic Phytoremediation: Finally a Feasible Approach in the Near Future. In: *Environmental Chemistry and Recent Pollution Control Approaches* [Internet]. IntechOpen; 2019. Available from: [<URL>](#).
87. Baker AJM. Accumulators and excluders -strategies in the response of plants to heavy metals. *J Plant Nutr* [Internet]. 1981 Jan 21;3(1–4):643–54. Available from: [<URL>](#).
88. Prasad MN V. Trace Elements in Traditional Healing Plants—Remedies or Risks. In: *Trace Elements as Contaminants and Nutrients* [Internet]. Wiley; 2008. p. 137–60. Available from: [<URL>](#).



Recycling of Waste Polymethyl-Methacrylate as an Optical Transparent Host

Erkan Aksoy^{1*} 

¹Project and Technology Office, Rectorate, Bartın University, 74100, Bartın, Türkiye.

Abstract: Reusing waste or otherwise discarded polymethyl methacrylate (wPMMA) as a host matrix for optical photonic applications such as down-conversion or luminescence solar concentrators can spare the use of pristine materials, with strong implications for sustainability. Here, a homogeneous emissive film was produced using wPMMA by dissolving in toluene and adding a fluorescent perylene dye (perylene-3,4,9,10-tetracarboxylic hexyl ester, PTHE) followed by spin coating casting. This resulting film is optically transparent and green-emissive with a high photoluminescence quantum yield (PLQY of 84%). It has been investigated by various spectroscopic techniques such as absorption, photoluminescence, emission lifetime, and dye photostability. While this film exhibited some excimer PL at longer wavelengths compared to the solution phase, it also increased its emission lifetime by approximately 3 times. Moreover, while the CIE coordinates (x, y) of the blue-green PL in the solution phase was 0.21, 0.56, the PL spectrum of the wPMMA:PTHE film instead had (CIE, x, y) of 0.30, 0.60. Recycling these and similar suitable waste polymers and transforming them into value-added products such as down-conversion or luminescent solar concentrator films can contribute to sustainable development goals within the scope of clean energy, energy efficiency, and waste utilization.

Keywords: Waste polymethyl methacrylate, optical host, recovery of waste polymer, solid-state lighting, luminescence solar concentrator, perylene dye.

Submitted: December 30, 2023. **Accepted:** June 21, 2024.

Cite this: Aksoy E. Recycling of Waste Polymethyl-Methacrylate as an Optical Transparent Host. JOTCSA. 2024;11(3): 1141-50.

DOI: <https://doi.org/10.18596/jotcsa.1412323>

***Corresponding author's E-mail:** eaksoy@bartin.edu.tr

1. INTRODUCTION

Plastics are a wide category of synthetic materials composed of chains or networks (polymers) of repeating smaller building blocks (monomers). Plastics typically possess exceptional versatility, allowing them to be shaped into various forms without compromising on durability, flexibility, lightweight nature, or affordability. They also enable composite production with adjustable structural and physical properties depending on different synthetic substitutions or blending with other materials (1-4). This remarkable adaptability has supported plastics finding applications in a wide range of industries since the mid-20th century, spanning from automotive and packaging to electronics and medical device manufacturing (5-8). While plastic production and usage have grown exponentially in recent decades - estimated to reach approximately 400 million tons per year - the product lifecycle of these materials is not fully developed. Approximately 12% of plastic production is disposed

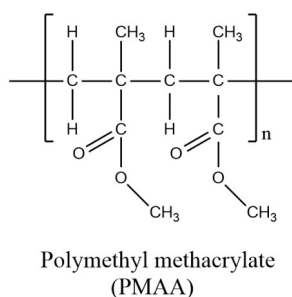
of by incineration, and only approximately 9% is recycled despite their chemical suitability for reuse (9). Hence, while plastics serve numerous useful purposes in modern society, most of the plastics produced remain discarded in nature for hundreds of years following use (a result of their chemical stability). This pollution contaminating environments and water resources is now an urgent environmental problem that must be addressed (10-12). Hence, efforts to recycle rather than discard plastics not only contribute to the protection of environmental and human health but also contribute to a sustainable future in terms of protecting natural resources, saving energy, combating climate change, and managing economic outputs and waste (4,13,14).

Polymethyl methacrylate (PMMA), also known as acrylic glass, is a thermoplastic polymer obtained by polymerization of methyl methacrylate (MMA) monomer (5). PMMA is used in many different areas, such as furniture, building facades, lighting

fixtures, automobiles, contact lenses, chemical tanks, and optics and photonic technologies (15). In photonic technologies specifically, PMMA is used extensively in roles such as light transport in optical fibres, eyeglasses, and telescope lenses, LCD (liquid crystal display) and LED (light emitting diode) screen protectors, dye hosts for light conversion layers in blue LEDs, and optical filter production (5,7,16-24). All these features and application areas make PMMA an important plastic group in this technological field. However, PMMA has low biodegradability in waste environments, and its production processes have several environmental impacts to consider - such as the necessity of using water in its production, the production of MMA from oil and natural gas, and energy consumption - which establish the importance of PMMA recycling and (re)use.

Perylene derivatives are known for their strong light absorption in the visible region and high fluorescence quantum yields. In addition, since they exhibit high optical, electrochemical, and thermal stability, perylene dyes are used in many optical or optoelectronic technologies such as (organic) light emitting diodes (LEDs and OLEDs), organic solar cells (OSCs), luminescent solar concentrators (LSC), lasers, ion sensing, and phototherapy (25-34). Perylene tetra esters contain the same planar polycyclic aromatic core but typically suffer significant aggregation caused by quenching (ACQ) of their emission in the film phase (35,36). Two basic approaches to eliminate or alleviate ACQ are to synthesize perylene derivatives with steric functional groups that reduce the aggregation effect (35,37,38), or by doping and isolating low concentrations of perylene derivatives into optically transparent host materials, in both cases increasing the intermolecular distance (34,37). This second approach, in particular, allows these ACQ-prone dyes to be used in high-efficiency applications such as wavelength-converting lighting technologies and solar concentrators (34,39).

In this study, we show that waste/discarded PMMA polymer (wPMMA) can be reclaimed as an optically transparent host for Perylene-3,4,9,10-



tetracarboxylic hexyl ester (PTHE), doped at 1 wt% and with optoelectronic applications as outlined above. Due to the environmental and economic impacts of waste polymers, this technique can contribute to the Sustainable Development Goals (40) and reduce the need for additional PMMA production from petrochemicals. PTHE and the dye-loaded films were characterized by FTIR, ¹H-NMR, ¹³C-NMR, HRMS, TGA, XRD, and optical spectroscopy. PTHE exhibited extremely high PL intensity and PLQY when homogeneously dispersed in the organic-compatible wPMMA, with excellent stability towards photoexcitation. The PTHE:wPMMA film (or others like it) can hence be used as an environmentally friendly material feedstock in the production of white light-emitting (O)LEDs or other photonics applications.

2. EXPERIMENTAL SECTION

2.1. Materials and Instruments

Perylene tetracarboxylic dianhydride (PTCDA), 1-hexanol, 1-bromohexane, 1,8-diazabicyclo[5.4.0]undec-7-ene (DBU), N,N-dimethylformamide, chloroform, toluene, silica gel and thin layer chromatography (TLC) were obtained from Sigma and Merck. The waste polymethyl methacrylate (wPMMA) used in this study (Figure 1, picture on the right) was obtained as waste from a laser-cutting stationery shop. PTHE was synthesized (Figure 2) according to the literature (21,41). The synthetic details are provided below, together with its structural, thermal, and optical characterizations.

FTIR-ATR, ¹H, and ¹³C NMR spectra were obtained using IRaffinity-1 SHIMADZU-FTIR and Bruker (400 MHz and 100 MHz) spectrometers, respectively. TGA analysis was carried out with a Hitachi STA 7300 Model device with an increase of 10 °C per minute in a nitrogen atmosphere. Absorption and photoluminescence (PL), absolute PL quantum yield (Φ_{PL}) (with an integrated sphere), time-correlated single photon count (τ, ns) (EPL-470 nm excitation) studies and photostability testing were performed with the Analytical Jena S600 UV-Vis spectrophotometer and Edinburgh FLS920P and FS5 Instruments.



Figure 1: Molecular structure of polymethyl methacrylate (left) and available waste polymethyl methacrylate (wPMMA) (right).

2.2. Synthesis and Characterization of Perylene-3,4,9,10-tetracarboxylic hexyl ester (PTHE)

Perylene tetra esters emit with very high fluorescence efficiency in the solution phase (PLQY ≥ 90%) (42). Therefore, in this study, PTHE was chosen as a reference fluorophore. Detailed information on the synthesis methods and

characterization of PTHE (Figure 1) and wPMMA:PTHE film (Figure 2) are given below (Figure 1-10).

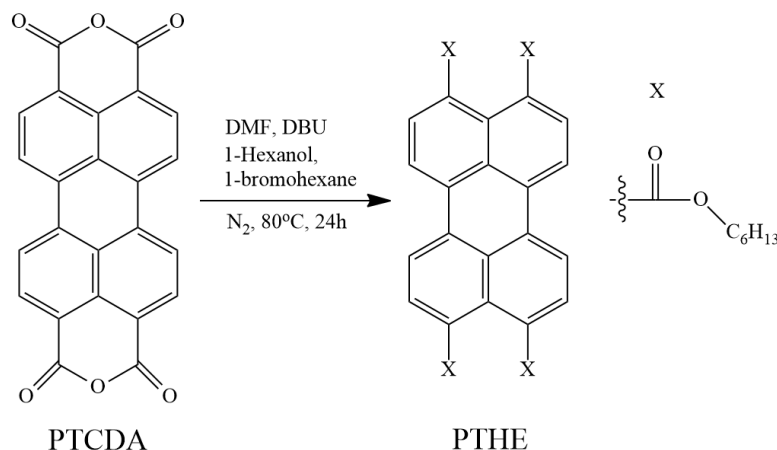


Figure 2: Reaction scheme of PTHE.

Perylene-3,4,9,10-tetracarboxylic dianhydride (PTCDA) (1 g, 2.55 mmol), *N,N*-dimethylformamide (DMF), 1-bromohexane (4.2 g, 25.5 mmol) and 1-hexanol (2.6 g, 25.5 mmol) were added into a two-necked round-bottomed flask. After it was stirred for 20 minutes in a magnetic stirrer, the DBU (1.5 mL) catalyst was added and stirred at 80 °C under reflux in N_2 for 24 hours. After the flask was brought to room temperature, it was poured into distilled water, and the precipitate was filtered through vacuum filter paper and washed with methanol. After drying the solid at 60 °C, it was dissolved in chloroform and purified by column chromatography over silica gel. Yield (79%) 1.54 g.

FTIR (ATR) (Figure 3): ν_{max} = ($C_{Ar}-H$): 2951, 2928 cm^{-1} , ($C-H$): 2864, 2848 cm^{-1} , ($C=O$): 1726, 1710 cm^{-1} , ($C-O$): 1263 and 746 cm^{-1} . ^1H-NMR (400 MHz, Chloroform- d , TMS/ppm) δ (Figure 4): 8.25-8.23 (d, J : 8.0 Hz, 4H), 8.01-7.99 (d, J : 8.0 Hz, 4H), 4.30 (t, J : 8.0 Hz, 8H), 1.77 (m, J : 8.0 Hz, 8H), 1.43 (m, J : 8.0 Hz, 8H), 1.34 (m-overlap, J : 4.0 Hz, 16H), 0.89 ppm. (m, J : 8.0 Hz, 12H). $^{13}C-NMR$ (100 MHz, Chloroform- d , TMS/ppm) δ (Figure 5): 168.48, 133.01, 130.42, 130.38, 121.35, 65.62, 31.49, 28.53, 25.65, 22.54, 14.01 ppm. HRMS (Figure 6): (Molecular mass; 764.4) Found: 764.4 M. The first temperature at which PTHE begins to degrade is 349 °C (TGA) (Figure 7).

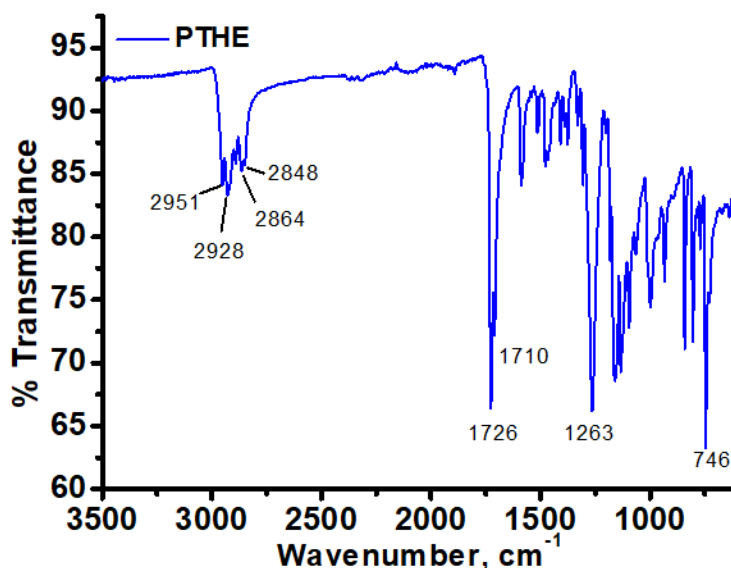
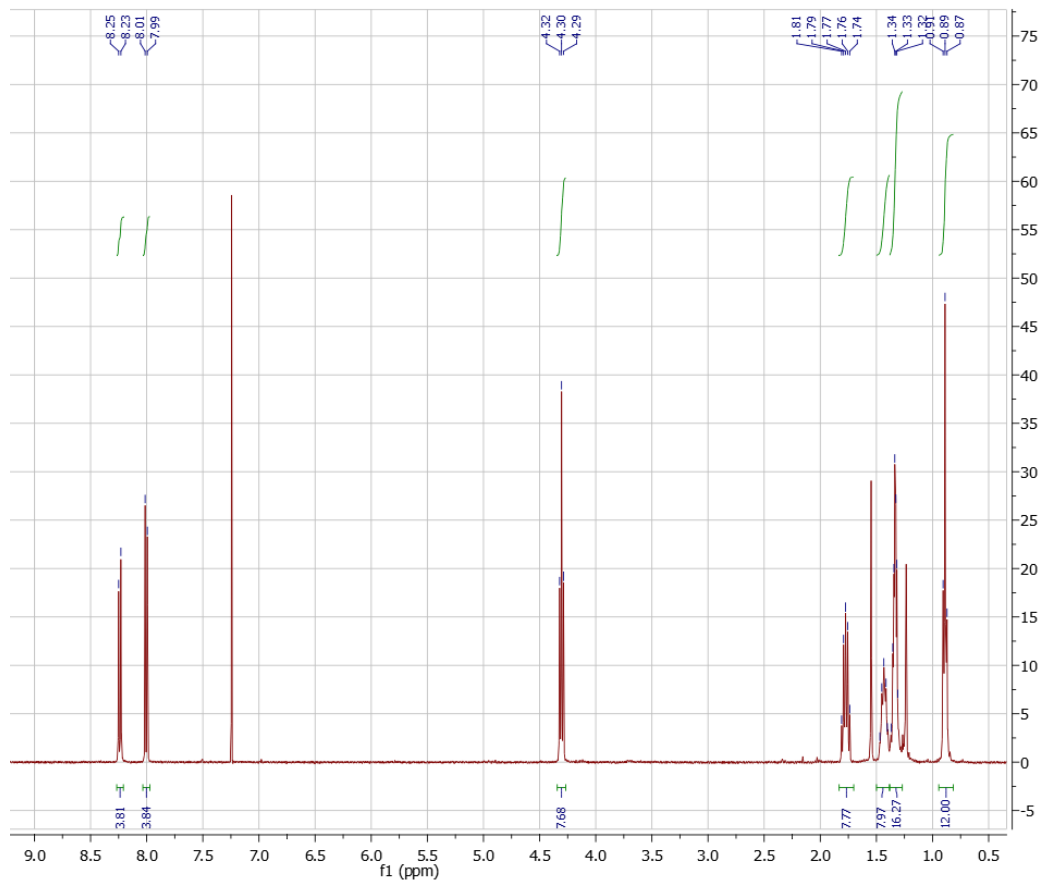
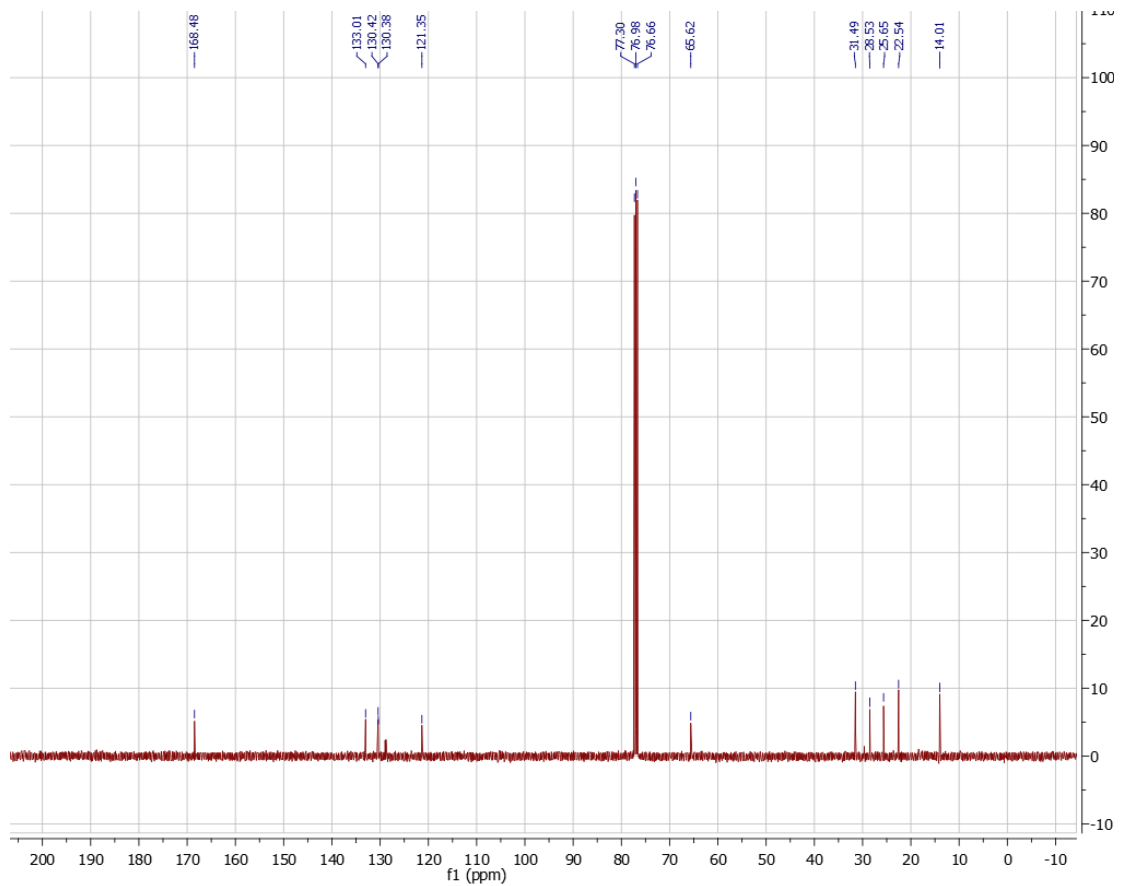


Figure 3: FTIR spectrum of PTHE.

**Figure 4:** $^1\text{H-NMR}$ of PTHE.**Figure 5:** $^{13}\text{C-NMR}$ of PTHE.

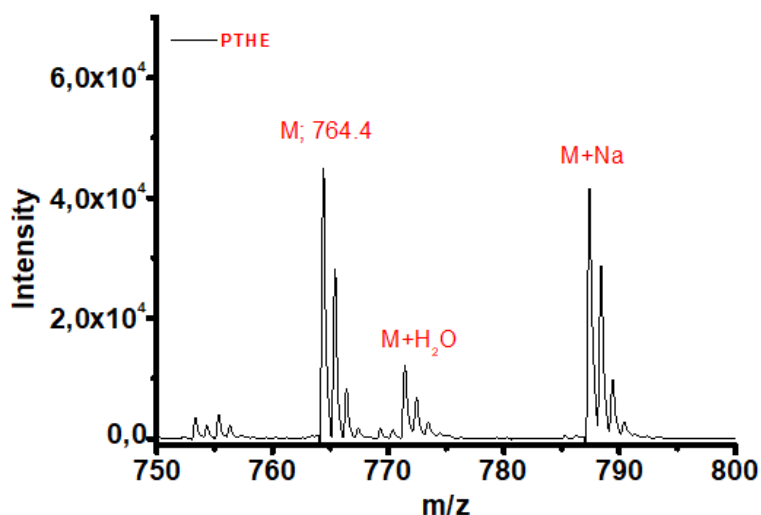


Figure 6: HRMS of PTHE.

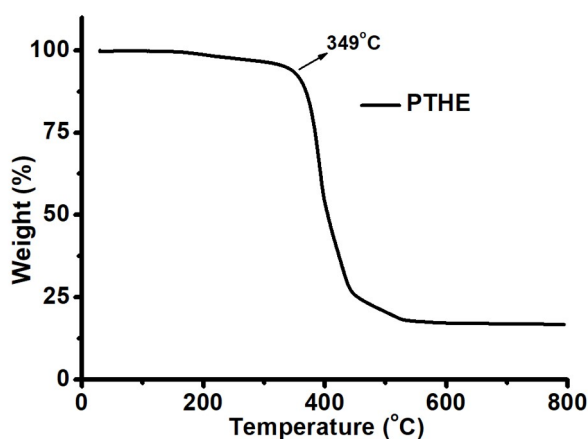


Figure 7: TGA analysis of PTHE.

2.3. Preparation and Characterization of wPMMA-PTHE Solution and Film

150 mg of wPMMA was added to a capped bottle, then 10 mL of toluene was added and stirred at 50 °C for 24 hours with a magnetic stirrer. A clear solution of wPMMA was obtained, and 1% by mass of PTHE was added to it. A homogeneous solution of wPMMA:PTHE was obtained by stirring for a further 2 hours.

100 mL of the wPMMA:PTHE toluene solution was dropped on a clean 2.5 x 2.5 cm glass tile, rotating at 2000 rpm. After this film dried, the process was repeated 10 times to build thickness, and the film was left to dry at room temperature. Pictures of the prepared transparent and green-emissive wPMMA:PTHE film under daylight and UV light are given in Figure 8.

The Fourier transform infrared (FTIR-ATR) characterization study of wPMMA:PTHE film, in comparison with PTHE and wPMMA, is given in Figure 9. Aromatic C-H peaks of PTHE are seen at 2951 cm^{-1} and 2928 cm^{-1} . C=O, which belongs to ester bonds, exhibited strong peaks at 1726 cm^{-1} and 1710 cm^{-1} . Additionally, a strong peak of C-O is

observed at 1263 cm^{-1} and is compatible with the literature (42). The aliphatic C-H peak of wPMMA shows itself weakly at 2949 cm^{-1} . C=O and C-O peaks belonging to the ester structure are seen as sharp and intense at 1724 cm^{-1} and 1143 cm^{-1} , respectively. In the wPMMA:PTHE film, it has the characteristic peaks of the two materials. Due to the high PMMA ratio, wPMMA characteristic peaks are dominant. However, the presence of two new intense peaks observed at 796 cm^{-1} and 1016 cm^{-1} indicates that there is an interaction between the wPMMA and PTHE (Figure 9).

The X-ray diffractions (XRD) of PTHE powder, wPMMA, and wPMMA:PTHE are given in Figure 10. PTHE powder showed peaks at $2\theta = 8,6, 10.76, 13.0, 15.36, 16.72, 17.56, 18.16, 18.44, 21.48$ (intense), 23.8, 24.88, 25.56, 42.56 and 43.48. The values of the broad 2θ peaks of wPMMA and wPMMA:PTHE films are approximately 13.68 (intense), 25.0, and 42.56, respectively. It exhibited broadness, which is characteristic of wPMMA and belongs to the amorphous structure. In the wPMMA:PTHE film, 2θ peaks belonging to PTHE were not observed due to the low PTHE doping rate (Figure 10) (43).



Figure 8: Images of PTHE film (in wPMMA) under daylight and UV light.

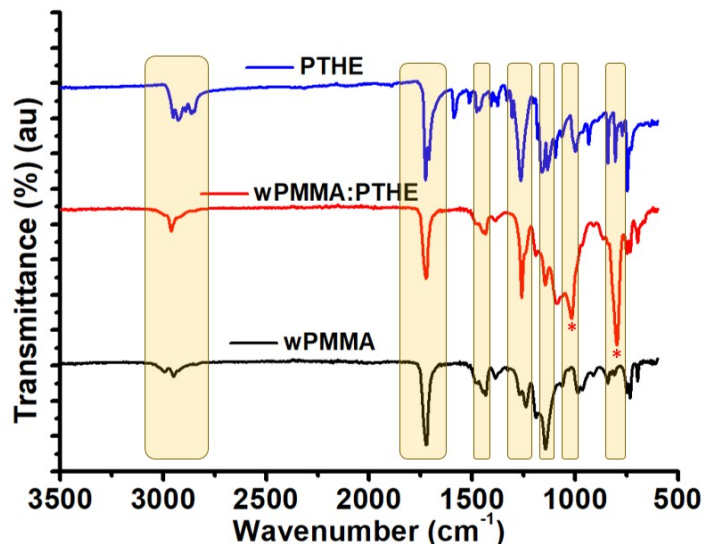


Figure 9: FTIR spectrum of PTHE powder, wPMMA and wPMMA:PTHE (99:1, wt%) films.

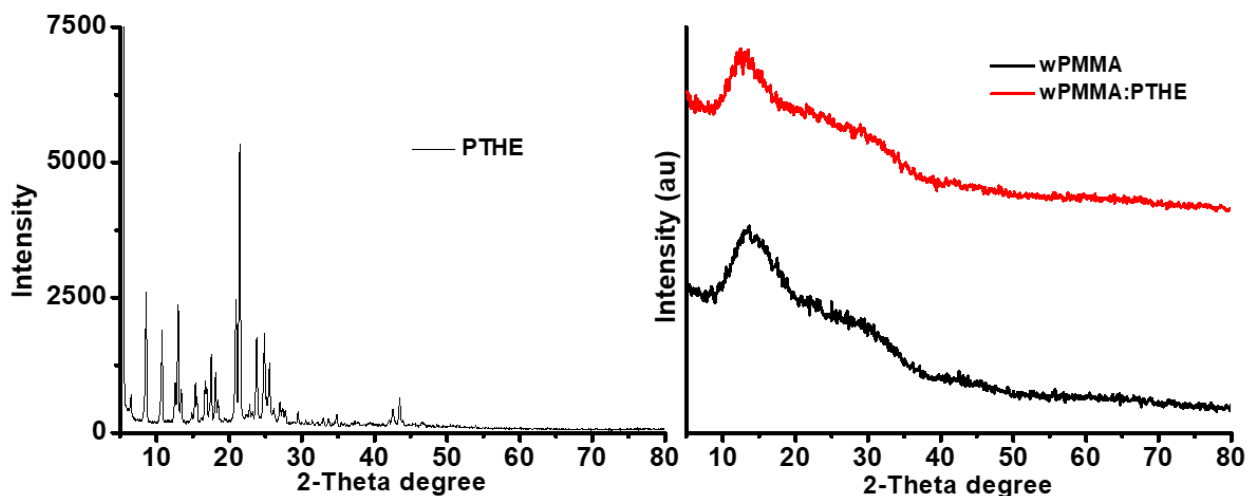


Figure 10: XRD spectrum of PTHE powder (left) and XRD spectra (au) of film phase of wPMMA and wPMMA:PTHE (99:1, wt%) (right).

3. RESULTS AND DISCUSSION

The absorption and photoluminescence spectra of PTHE in toluene [1×10^{-6} M] and in wPMMA (1 wt%) are given in Figure 11a. Dilute PTHE in toluene exhibits absorbance peaks at 474 and 445 nm belonging to the $n-\pi^*$ transitions associated with its extended aromatic pi system (38,42). Compared to a previously reported study (41), the absorption of PTHE is almost the same as in chloroform solution (λ_{absmax} : 472 nm). For the preparation of solid films, 1 wt% doping of PTHE into wPMMA was chosen to control aggregation of the PTHE. In the wPMMA:PTHE film the absorption peaks (λ_{absmax}) of

PTHE were found to be nearly identical to the toluene solution, at 472 and 443 nm.

In the PL spectrum of PTHE, it was found that the λ_{PLmax} shifted from 492 to 525 nm on changing from solution to film measurements. PTHE is proposed to exhibit excimer behavior in wPMMA that gives rise to this wavelength shift, motivated by fact that there was no significant difference in the absorption spectrum (that might indicate ground-state aggregate formation) and that the PL spectrum exhibited only a single peak at longer wavelengths. Emission lifetime measurements of the solution and wPMMA:PTHE film were also performed, it was

determined that the average lifetime of the PL at 525 nm in the film was extended from 3.8 to 12.1 ns (Figure 11b and Table 1). When examined in more detail, while PTHE had a single exponential state in solution, it exhibited a double exponential state in the film phase (at 525 nm). The first exponential state is similar to the situation in solution, with an exciton lifetime of 3.77 ns and a relative contribution of 61.71% to the total emission (Table 1). The second decay component instead has a lifetime of 15.38 ns, and a relative contribution of 38.38%. This second emission component with increased lifetime indicates the existence of excimeric states, with no impact on the absorption spectrum. When reported neat-film emission spectra of similar PTE derivatives of different chain lengths are examined, the presence of PL from aggregates leads to shifting to much longer wavelengths (≈ 600 nm) (44).

The longer wavelength excimer emission in the film phase also increases the Stokes shift compared to the monomeric behaviour in dilute solution (shifts of 772 and 2139 cm^{-1}), significantly reducing reabsorption of PTHE in the film phase. Indeed, the absolute PLQY (Φ) in the film is quite high, as in solution: 98 and 84% in solution and film, respectively (Table 1). Commission Internationale de l'éclairage (CIE) chromaticity coordinates of the PL spectra are shown in Figure 11c, with the excimer emission providing a slightly different emission colour point for the film. The PL_{max} intensity of the film, which was exposed to the excitation wavelength at its maximum absorption in the kinetic mode of the Edinburgh FS5 fluorometer for 90 minutes, was measured at 525 nm every second and exhibited a highly photostable behavior (Figure 11d).

Table 1: Average lifetime value (τ) of wPTHE in toluene (1×10^{-6} M) and at film phase (%1 doped in wPTHE).

PTHE	τ_1 (ns)	%	τ_2 (ns)	%
In toluene	3.80	100	-	-
In wPMMA	3.77	61.71	15.38	38.29

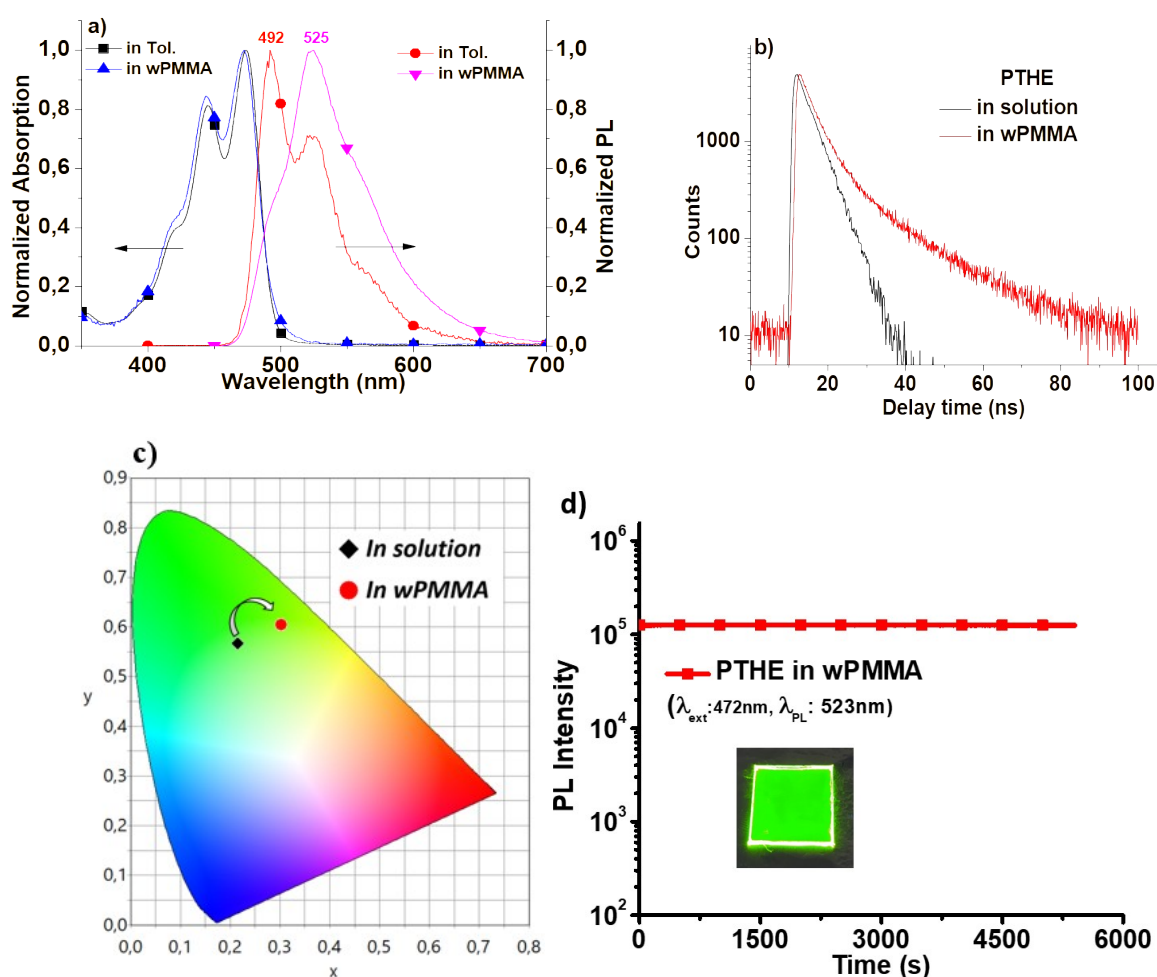


Figure 11: a) Absorption and PL spectra of PTHE in solution and film phase. b) Lifetime decay of PTHE in solution and wPMMA (%1 doped PTHE). c) CIE diagrams of PL spectra of PTHE in toluene (1×10^{-6} M) and in wPMMA. d) Optical stability test of PTHE.

Table 2: Photophysical properties of PTHE in toluene [1×10^{-6} M] and film (in wPMMA) [maximum absorption, $\lambda_{\text{abs}}^{\text{max}}$ and maximum PL, $\lambda_{\text{PL}}^{\text{max}}$ peaks (nm); Stokes shift, $\Delta\lambda$ (nm and cm^{-1}); PLQY, ($\Phi\%$).

	In toluene [1×10^{-6}]				In wPMMA (1%)			
	$\lambda_{\text{abs}}^{\text{max}}$	$\lambda_{\text{PL}}^{\text{max}}$	$\Delta\lambda$ (nm) or (cm^{-1})	Φ %	$\lambda_{\text{abs}}^{\text{max}}$	$\lambda_{\text{PL}}^{\text{max}}$	$\Delta\lambda$ (nm) or (cm^{-1})	$\Phi\%$
PTHE	474	492	18 nm or 772 cm^{-1}	98	472	525	53 nm or 2139 cm^{-1}	84

4. CONCLUSION

The increasing use of plastics and the resulting serious environmental threat they pose must be addressed by all means available. In this study, solutions of waste PMMA were combined with an organic dye to produce green-emissive films suitable for photonics applications. Reprocessing such waste into high-value products may contribute to SDG goals and services within the scope of a sustainable future, clean energy, and energy efficiency (40).

PTHE, which is homogeneously dispersed in waste PMMA, absorbs blue light in the range of 400-500 nm when only 1% is added while also exhibiting a very high fluorescence quantum yield. Reusing waste PMMA with different combinations of fluorophores in this way could open the door to its use in many photonic technologies that absorb, transform, or emit wavelengths.

5. ACKNOWLEDGMENTS

The author would like to thank Dr. Andrew Danos for his support of this work and suggestions.

6. REFERENCES

- Fan LT, Retzloff DG, Vanderpool WO. Solid waste-plastics composites. Physical properties and feasibility for production. *Environ Sci Technol* [Internet]. 1972 Dec 1;6(13):1085–91. Available from: [<URL>](#).
- Bossa N, Sipe JM, Berger W, Scott K, Kennedy A, Thomas T, et al. Quantifying mechanical abrasion of mwcnt nanocomposites used in 3d printing: Influence of cnt content on abrasion products and rate of microplastic production. *Environ Sci Technol* [Internet]. 2021 Aug 3;55(15):10332–42. Available from: [<URL>](#).
- Jiang H, Zhang Y, Wang H. Surface reactions in selective modification: The prerequisite for plastic flotation. *Environ Sci Technol* [Internet]. 2020 Aug 18;54(16):9742–56. Available from: [<URL>](#).
- Shamsuyeva M, Endres HJ. Plastics in the context of the circular economy and sustainable plastics recycling: Comprehensive review on research development, standardization and market. *Compos Part C Open Access* [Internet]. 2021 Oct;6:100168. Available from: [<URL>](#).
- Ali U, Karim KJBA, Buang NA. A Review of the properties and applications of poly (methyl methacrylate) (PMMA). *Polym Rev* [Internet]. 2015 Oct 2;55(4):678–705. Available from: [<URL>](#).

- Yaqoob L, Noor T, Iqbal N. Conversion of plastic waste to carbon-based compounds and application in energy storage devices. *ACS Omega* [Internet]. 2022 Apr 26;7(16):13403–35. Available from: [<URL>](#).

- Santidrián A, Sanahuja O, Villacampa B, Diez JL, Benito AM, Maser WK, et al. Chemical postdeposition treatments to improve the adhesion of carbon nanotube films on plastic substrates. *ACS Omega* [Internet]. 2019 Feb 28;4(2):2804–11. Available from: [<URL>](#).

- Wang Y, Wang H, Li S, Sun S. Waste PET Plastic-derived CoNi-based metal-organic framework as an anode for lithium-ion batteries. *ACS Omega* [Internet]. 2022 Oct 4;7(39):35180–90. Available from: [<URL>](#).

- Tsakona M, Baker E, Rucevska I, Maes T, Appelquist R, Macmillan-Lawler M, et al. Drowning In plastics – marine litter and plastic waste vital graphics [Internet]. United Nations Environment Programme. 2021. 6–77 p. Available from: [<URL>](#).

- Jambeck JR, Geyer R, Wilcox C, Siegler TR, Perryman M, Andrady A, et al. Plastic waste inputs from land into the ocean. *Science* (80-) [Internet]. 2015 Feb 13;347(6223):768–71. Available from: [<URL>](#).

- Barnes DKA, Galgani F, Thompson RC, Barlaz M. Accumulation and fragmentation of plastic debris in global environments. *Philos Trans R Soc B Biol Sci* [Internet]. 2009 Jul 27;364(1526):1985–98. Available from: [<URL>](#).

- Authors R, Brighty:, Jones GC, V4 RJ. High-level science review for "A Plastic Oceans" film contents section [Internet]. 2016. Available from: [<URL>](#).

- Al-Salem SM, Lettieri P, Baeyens J. Recycling and recovery routes of plastic solid waste (PSW): A review. *Waste Manag* [Internet]. 2009 Oct;29(10):2625–43. Available from: [<URL>](#).

- Naderi Kalali E, Lotfian S, Entezar Shabestari M, Khayatzadeh S, Zhao C, Yazdani Nezhad H. A critical review of the current progress of plastic waste recycling technology in structural materials. *Curr Opin Green Sustain Chem* [Internet]. 2023 Apr;40:100763. Available from: [<URL>](#).

- Manoukian OS, Sardashti N, Stedman T, Gailunas K, Ojha A, Penalosa A, et al. Biomaterials for tissue engineering and regenerative medicine. In: *Encyclopedia of Biomedical Engineering* [Internet]. Elsevier; 2019. p. 462–82. Available from: [<URL>](#).

16. Deka N, Bera A, Roy D, De P. Methyl methacrylate-based copolymers: Recent developments in the areas of transparent and stretchable active matrices. *ACS Omega* [Internet]. 2022 Oct 25;7(42):36929–44. Available from: [<URL>](#).
17. Li Y, Wang YQ, Liu D, Gao Y, Wang SN, Qiu H. Dual-emission ratiometric fluorescent probe based on lanthanide-functionalized carbon quantum dots for white light emission and chemical sensing. *ACS Omega* [Internet]. 2021 Jun 8;6(22):14629–38. Available from: [<URL>](#).
18. El-Bashir SM. Enhanced fluorescence polarization of fluorescent polycarbonate/zirconia nanocomposites for second generation luminescent solar concentrators. *Renew Energy* [Internet]. 2018 Jan;115:269–75. Available from: [<URL>](#).
19. El-Bashir SM. Coumarin-doped PC/CdSSe/ZnS nanocomposite films: A reduced self-absorption effect for luminescent solar concentrators. *J Lumin* [Internet]. 2019 Feb;206:426–31. Available from: [<URL>](#).
20. Al-Mahdouri A, Gonome H, Okajima J, Maruyama S. Theoretical and experimental study of solar thermal performance of different greenhouse cladding materials. *Sol Energy* [Internet]. 2014 Sep;107:314–27. Available from: [<URL>](#).
21. Aksoy E, Demir N, Varlikli C. White LED light production using dibromoperylene derivatives in down conversion of energy. *Can J Phys* [Internet]. 2018 Jul;96(7):734–9. Available from: [<URL>](#).
22. Coffey B, Clough L, Bartkus DD, McClellan IC, Greenberg MW, LaFratta CN, et al. Photophysical properties of cyclometalated platinum(II) diphosphine compounds in the solid state and in pmma films. *ACS Omega* [Internet]. 2021 Oct 26;6(42):28316–25. Available from: [<URL>](#).
23. Langhals H, Schlücker T, Reiners F, Karaghiosoff K. Terminal terthiophenediones: fast-decay fluorescent dyes and their efficient syntheses. *ACS Omega* [Internet]. 2021 Sep 28;6(38):24973–80. Available from: [<URL>](#).
24. Sengottuvelu D, Shaik AK, Mishra S, Ahmad H, Abbaszadeh M, Hammer NI, et al. Multicolor nitrogen-doped carbon quantum dots for environment-dependent emission tuning. *ACS Omega* [Internet]. 2022 Aug 9;7(31):27742–54. Available from: [<URL>](#).
25. Fang H, Xia D, Zhao C, Zhou S, Wang R, Zang Y, et al. Perylene bisimides-based molecular dyads with different alkyl linkers for single-component organic solar cells. *Dye Pigment* [Internet]. 2022 Jul;203:110355. Available from: [<URL>](#).
26. Zheng X, Wei Q, Shan T, Zhang Y, Zhong H. The halogen effect of perylene diimide-based non-fullerene acceptors on photovoltaic properties. *Dye Pigment* [Internet]. 2022 May;201:110232. Available from: [<URL>](#).
27. Keum C, Becker D, Archer E, Bock H, Kitzerow H, Gather MC, et al. Organic light-emitting diodes based on a columnar liquid-crystalline perylene emitter. *Adv Opt Mater* [Internet]. 2020 Sep 15;8(17):2000414. Available from: [<URL>](#).
28. Ostos FJ, Iasilli G, Carlotti M, Pucci A. High-Performance luminescent solar concentrators based on poly(cyclohexylmethacrylate) (PCHMA) films. *Polymers (Basel)* [Internet]. 2020 Dec 3;12(12):2898. Available from: [<URL>](#).
29. Schiphorst J ter, Kendhale AM, Debije MG, Menelaou C, Herz LM, Schenning APHJ. Dichroic perylene bisimide triad displaying energy transfer in switchable luminescent solar concentrators. *Chem Mater* [Internet]. 2014 Jul 8;26(13):3876–8. Available from: [<URL>](#).
30. Szukalska A, Szukalski A, Stachera J, Zajac D, Chrzumnicka E, Martynski T, et al. Perylene-based chromophore as a versatile dye for light amplification. *Materials (Basel)* [Internet]. 2022 Jan 27;15(3):980. Available from: [<URL>](#).
31. Liu Y, Wang K, Guo D, Jiang B. Supramolecular assembly of perylene bisimide with β -cyclodextrin grafts as a solid-state fluorescence sensor for vapor detection. *Adv Funct Mater* [Internet]. 2009 Jul 24;19(14):2230–5. Available from: [<URL>](#).
32. Yang N, Song S, Ren J, Liu C, Li Z, Qi H, et al. Controlled aggregation of a perylene-derived probe for near-infrared fluorescence imaging and phototherapy. *ACS Appl Bio Mater* [Internet]. 2021 Jun 21;4(6):5008–15. Available from: [<URL>](#).
33. Guner T, Aksoy E, Demir MM, Varlikli C. Perylene-embedded electrospun PS fibers for white light generation. *Dye Pigment* [Internet]. 2019 Jan;160:501–8. Available from: [<URL>](#).
34. Aksoy E, Danos A, Varlikli C, Monkman AP. Navigating CIE space for efficient TADF downconversion WOLEDs. *Dye Pigment* [Internet]. 2020 Dec;183:108707. Available from: [<URL>](#).
35. Zhang B, Lyskov I, Wilson LJ, Sabatini RP, Manian A, Soleimaninejad H, et al. FRET-enhanced photoluminescence of perylene diimides by combining molecular aggregation and insulation. *J Mater Chem C* [Internet]. 2020;8(26):8953–61. Available from: [<URL>](#).
36. Kozma E, Mróz W, Villafiorita-Monteleone F, Galeotti F, Andicsová-Eckstein A, Catellani M, et al. Perylene diimide derivatives as red and deep red-emitters for fully solution processable OLEDs. *RSC Adv* [Internet]. 2016;6(66):61175–9. Available from: [<URL>](#).
37. Aksoy E, Danos A, Li C, Monkman A, Varlikli C. The Effect of imide substituents on the excited state properties of perylene diimide derivatives. *Turkish J Sci Technol* [Internet]. 2022 Mar 20;17(1):11–21. Available from: [<URL>](#).
38. Aksoy E, Danos A, Li C, Monkman AP, Varlikli C. Silylethynyl substitution for preventing aggregate

- formation in perylene diimides. *J Phys Chem C* [Internet]. 2021 Jun 17;125(23):13041–9. Available from: [<URL>](#).
39. Davis NJLK, MacQueen RW, Roberts DA, Danos A, Dehn S, Perrier S, et al. Energy transfer in pendant perylene diimide copolymers. *J Mater Chem C* [Internet]. 2016;4(35):8270–5. Available from: [<URL>](#).
40. de Sousa FDB. The role of plastic concerning the sustainable development goals: The literature point of view. *Clean Responsible Consum* [Internet]. 2021 Dec;3:100020. Available from: [<URL>](#).
41. Benning S, Kitzrow HS, Bock H, Achard MF. Fluorescent columnar liquid crystalline 3,4,9,10-tetra-(n-alkoxycarbonyl)-perylene. *Liq Cryst* [Internet]. 2000 Jul;27(7):901–6. Available from: [<URL>](#).
42. Aksoy E, Bozkus V, Varlikli C. Tuning the colour of solution processed perylene tetraester based OLEDs from yellowish-green to greenish-white: A molecular engineering approach. *Dye Pigment* [Internet]. 2023 Mar;211:111050. Available from: [<URL>](#).
43. Hashem M, Rez MF, Fouad H, Elsarnagawy T, Elsharawy M, Umar A, et al. Influence of titanium oxide nanoparticles on the physical and thermomechanical behavior of poly methyl methacrylate (PMMA): A Denture Base Resin. *Sci Adv Mater* [Internet]. 2017 Jun 1;9(6):938–44. Available from: [<URL>](#).
44. Piosik E, Synak A, Paluszkiewicz J, Martyński T. Concentration dependent evolution of aggregates formed by chlorinated and non-chlorinated perylene tetracarboxylic acid esters in pure spin-coated films and in a PMMA matrix. *J Lumin* [Internet]. 2019 Feb;206:132–45. Available from: [<URL>](#).



Intrinsically Disordered Proteins by Homology Modeling and Replica Exchange Molecular Dynamics Simulations: A Case Study of Amyloid- β 42

Orkid Coskuner-Weber^{1*} 

¹Turkish-German University, Molecular Biotechnology, Sahinkaya Caddesi, No. 106, Istanbul 34820 Turkey.

Abstract: Homology modeling emerges as a potent tool unveiling the structural enigma of intrinsically disordered proteins (IDPs), with recent advancements such as AlphaFold2 enhancing the precision of these analyses. The process usually involves identifying homologous proteins with known structures and utilizing their templates to predict the three-dimensional architecture of the target IDP. However, IDPs lack a well-defined three-dimensional structure, and their flexibility makes it difficult to predict their conformations accurately. On the other hand, special sampling molecular dynamics simulations have been shown to be useful in defining the distinct structural properties of IDPs. Here, the structural properties of the disordered amyloid- β 42 peptide were predicted using various homology modeling tools, including C-I-TASSER, I-TASSER, Phyre2, SwissModel, and AlphaFold2. In parallel, extensive replica exchange molecular dynamics simulations of A β 42 were conducted. Results from homology modeling were compared to our replica exchange molecular dynamics simulations and experiments to gain insights into the accuracy of homology modeling tools for IDPs used in this work. Based on our findings, none of the homology modeling tools used in this work can fully capture the structural properties of A β 42. However, C-I-TASSER yields a radius of gyration and tertiary structure properties that are more in accord with the simulations and experimental data rather than I-TASSER, Phyre2, SwissModel, and AlphaFold2.

Keywords: Intrinsically disordered proteins, Amyloid- β 42, Homology modeling, Replica exchange molecular dynamics simulations.

Submitted: March 22, 2024. **Accepted:** June 22, 2024.

Cite this: Coskuner Weber O. Intrinsically Disordered Proteins by Homology Modeling and Replica Exchange Molecular Dynamics Simulations: A Case Study of Amyloid- β 42. JOTCSA. 2024;11(3): 1151-64.

DOI: <https://doi.org/10.18596/jotcsa.1457169>

***Corresponding author's E-mail:** weber@tau.edu.tr

1. INTRODUCTION

The history of homology modeling of IDPs is relatively recent compared to the longer history of homology modeling for well-folded proteins (1,2). In fact, the field of IDPs has gained attention over the past two decades as the prevalence and functional importance of IDPs that lack a stable, well-defined three-dimensional structure have been recognized more and more (3-6). Homology modeling, initially developed for structured proteins, saw an expansion of its application to IDPs in the mid-2000s (7). However, we should note that the lack of well-defined templates and the dynamic nature of IDPs pose significant hurdles. Advances in computational methods, such as machine learning and deep learning, have played a crucial role in improving the accuracy of predicting the structures of IDPs (8). AlphaFold2, developed by DeepMind, made headlines

with its success in predicting the structures of both structured and disordered proteins (9-14). Current research continues to focus on refining methods for homology modeling for IDPs. The incorporation of experimental data, such as NMR and cryo-electron microscopy, along with improved algorithms, contributes to the ongoing development of accurate predictive models.

Replica exchange molecular dynamics (REMD) simulations offer a valuable computational approach for studying the structures and dynamics of IDPs (see, for example 15-19). REMD simulations involve running multiple replicas of a system at different temperatures and periodically exchanging their conformations (20). This exchange allows for enhanced conformational sampling, particularly in regions of the energy landscape that may be challenging to explore with conventional molecular

dynamics simulations (21). IDPs often exist as dynamic ensembles, sampling a wide conformational space. REMD simulations facilitate the exploration of this space, enabling the observation of the distribution of different conformations and transitions between them (21).

Amyloid- β 42 (A β 42) is an intrinsically disordered protein with 42 amino acid residues and is at the center of Alzheimer's disease (5,22). It has been studied experimentally and computationally extensively (see, for example 23-28). However, a comparative study of A β 42 using the most widely used homology modeling tools and REMD simulations is currently lacking in the literature. Such a comparative study is crucial for cross-validation of structural models related to IDPs. REMD simulations and experiments can be used to refine and validate the homology-based models for IDPs. Therefore, in this study, different homology modeling tools used widely for the structural prediction of IDPs (C-I-TASSER, I-TASSER, Phyre2, SwissModel, and AlphaFold2) were utilized to obtain the three-dimensional structures of A β 42. Furthermore, REMD simulations of A β 42 were conducted. The obtained structural properties were compared to each other and experiments.

2. MATERIALS AND METHODS

The three-dimensional structures of A β 42 were predicted using its amino acid sequence by C-I-TASSER, I-TASSER, Phyre2, SwissModel, and AlphaFold2. C-I-TASSER (Contact-guided Iterative threading ASSEMBLY Refinement) is a new method extended from I-TASSER (29). Starting from an amino acid sequence, C-I-TASSER generates inter-residue contact maps using various deep neural network predictors (29). Next, it identifies the structural templates from the PDB by multiple threading approaches with full-length atomic models assembled by contact map-guided replica exchange Monte Carlo simulations (29). The large-scale benchmark tests showed that C-I-TASSER generates significantly more accurate models than I-TASSER, especially for proteins that do not have homologous templates in the PDB (29).

I-TASSER (Iterative Threading ASSEMBLY Refinement) is a homology modeling method that combines threading, ab initio modeling, and iterative refinement process to generate three-dimensional models for proteins (30). Threading is the initial step where I-TASSER searches for homologous protein structures in a structural database. It identifies template structures that are similar to the target protein sequence. Threading involves aligning the target sequence onto these templates to create a preliminary three-dimensional model. After threading, I-TASSER generates additional models using ab initio modeling techniques. This consists of predicting the protein's structure based on its amino acid sequence without relying on template structures. The threaded and ab initio models are then assembled into a pool of candidate models. These models are ranked based on their energy and structural compatibility with the input sequence and

experimental constraints, if available. The algorithm employs an iterative optimization process to refine the models. This involves simulation and optimization steps to improve the accuracy of the models. The final step consists of selecting the best model from the refined pool of candidates. The model is chosen based on its energy score, structural quality, and compatibility with experimental data, if available (31).

Phyre2 (Protein Homology/analogy Recognition Engine) is a homology modeling tool that is used for protein structure prediction (32). It utilizes a combination of homology modeling, profile-profile matching, and ab initio methods to generate three-dimensional structural models for a given amino acid sequence. Phyre2 initially attempts to find homologous proteins with known structures in sequence databases. If a homologous protein is found, it uses the structural information from that template to predict the structure of the target protein. Homology modeling is effective when there is a significant similarity between the target sequence and the template. In cases where conventional homology modeling may not be applicable due to low sequence similarity, Phyre2 employs profile-profile matching techniques. This involves comparing the target sequence's profile with profiles of known protein structures. If homology modeling and profile-profile matching do not yield suitable templates, Phyre2 resorts to ab initio modeling. This involves predicting the protein structure without relying on known templates. The models undergo refinement to improve their accuracy and quality. This step may include energy minimization and optimization processes. The algorithm then evaluates the quality of generated models using different metrics, such as energy scores and structural consistency.

The SwissModel generates protein structures, and it operates on the principle of homology modeling, where the structure of a target protein is predicted based on the known structures of homologous proteins (33). It begins by searching a database of experimentally determined protein structures, such as PDB, to find homologous proteins with known structures that are similar to the target protein. Then, it performs a sequence alignment, which aids in establishing the correspondence between amino acids in the target sequence and the templates. It builds a three-dimensional model using the known three-dimensional structure of a homologous template as a starting point. This step involves aligning the target sequence onto the template structure and adjusting the backbone and side-chain conformations to fit the target sequence. The homology model is subjected to energy minimization and refinement steps to improve the geometry and overall quality of the model. It assesses the quality of generated models using various criteria, including stereochemical properties, bond lengths, and angles (33).

AlphaFold2 is an advanced artificial intelligence system designed for protein folding prediction (12,34,35). It gained significant attention for its

exceptional performance in the Critical Assessment of Structure Prediction (CASP) competition. It employs deep learning to predict protein structures. It involves a deep neural network that is trained on a large dataset of protein structures. This model is trained on a diverse set of known protein structures from PDB. The model learns to recognize patterns and relationships between amino acid sequences and corresponding three-dimensional structures. It uses an attention mechanism inspired by the Transformer architecture, which is a kind of neural network architecture usually used in natural language processing tasks. This attention mechanism enables the model to capture long-range interactions between amino acids in the sequence. It incorporates information from multiple sequence alignments, which considers evolutionary relationships between related proteins. This helps to improve the accuracy, especially for regions where the sequence similarity is low. It predicts inter-residue distances between pairs of amino acids in the sequence. This distance prediction provides important information about the spatial relationships between different parts of the protein. It assembles the three-dimensional structure of the protein and generates a probability distribution for each atom's position in the structure. The refinement process involves iterative optimization processes to enhance the geometry and overall quality of the predicted structures. It uses an ensemble approach by generating multiple models for a given protein.

These homology modeling and structure prediction tools were chosen because these are heavily used in the studies of IDPs in commercial and academic settings. See, for example, references (7,36-40).

All-atom REMD simulations of the A β 42 monomer in an aqueous solution environment were performed with the AMBER22 software package (41). An extended structure was used initially for A β 42. T-REMD simulations were conducted using the Amber ff99SB parameters for the protein, and the Onufriev-Bashford-Case generalized Born implicit water model (42). These models were chosen to avoid confined aqueous volume effects using an explicit water model, and we recently showed that these parameters yield results in excellent agreement with experiments for A β (42,43). Specifically, T-REMD simulations using the Amber ff99SB parameters for A β along with the Onufriev-Bashford-Case generalized Born implicit model for water were shown to yield structural properties in excellent

agreement with NMR experiments (42,43). Langevin dynamics was used to control the temperature with a collision frequency of 2 ps⁻¹ (21). The particle mesh Ewald method was used for treating the long-range interactions with a cutoff value of 25 Å (44). The temperatures of each replica for A β 42 were exponentially distributed between 280 K and 400 K, yielding an exchange ratio of 0.74 for A β 42. After energy minimization of the initial structure with the steepest descent method, the initial conformation was equilibrated for 200 ps for each replica (21). The peptide was then simulated using an integration timestep of 2 fs for each replica, and trajectories were saved every 500 steps. Exchanges between replicas were attempted every five ps. The system was simulated for 100 ns for each replica with a total simulation time of 2.4 μ s. 60 ns are required to reach convergence, which is in agreement with earlier studies (45). The structural properties were then calculated for A β 42 obtained after convergence from the replica closest to 310 K. The end-to-end distance values, the radius of gyration, secondary structure properties per residue, and intra-molecular contact map, as well as salt bridges, were calculated and compared to those obtained using I-TASSER, C-I-TASSER, Phyre2, SwissModel, and AlphaFold2 as well as to experiments. Following our earlier studies, intramolecular peptide interactions occur when the centers of mass of two residues are within 9.0 Å of each other (45). An interaction is considered to be a salt bridge when a hydrogen bond exists between the two residues and the hydrogen-bonded residues possess opposite electrostatic charges. If the distance between the donor and acceptor atoms of the hydrogen bond is ≤ 2.5 Å and the hydrogen bond angle is larger than 113°, then a hydrogen bond exists (45).

3. RESULTS AND DISCUSSION

The top-ranked three-dimensional structures of A β 42 obtained from C-I-TASSER, I-TASSER, Phyre2, SwissModel, and AlphaFold2 are depicted in Figure 1. As seen in Figure 1, different homology modeling methods yield varying three-dimensional structures for A β 42. Selected A β 42 structures obtained from REMD simulations are illustrated in Figure 2.

To gain deeper insights into the structural properties of these three-dimensional model structures for A β 42, the end-to-end (R_{EE}) and radius of gyration (R_g) values were calculated and compared to experiments (Table 1) (46-48).

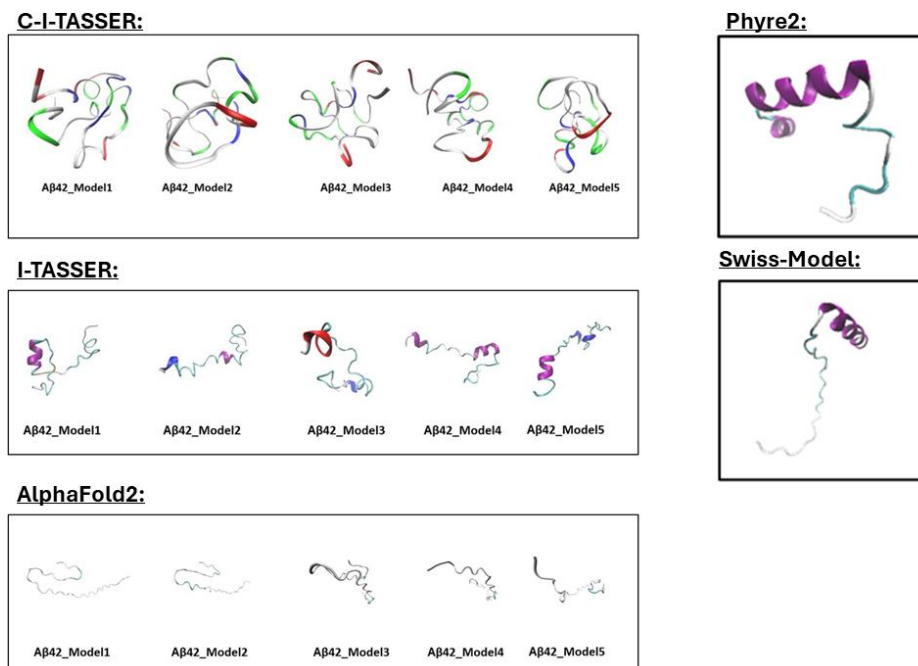


Figure 1: Top-ranked three-dimensional structures from C-I-TASSER, I-TASSER, Phyre2, SwissModel, and AlphaFold2 for A β 42.

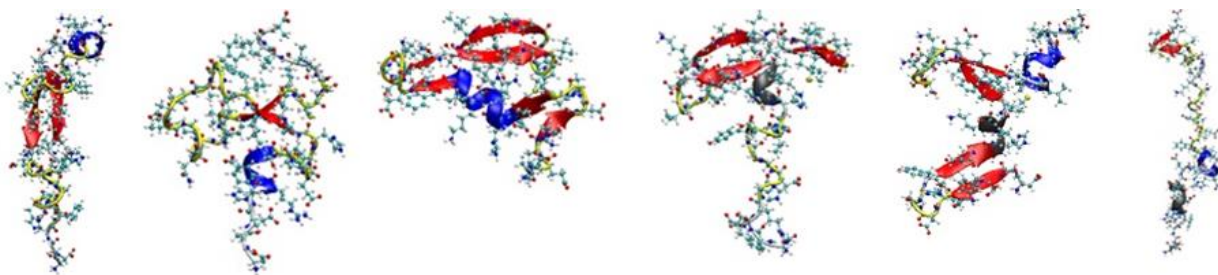


Figure 2: Selected three-dimensional structures for A β 42 from REMD simulations.

Table 1: Calculated R_{EE} and R_g values for A β 42 and their comparison to experiments.

	R_{EE} (Å)	R_g (Å)
C-I-TASSER		
Model 1	9.64	8.53
Model 2	8.17	8.41
Model 3	7.93	8.47
Model 4	7.85	8.34
Model 5	4.58	8.53
I-TASSER		
Model 1	33.57	12.53
Model 2	35.23	14.49
Model 3	18.91	10.74
Model 4	39.72	14.96
Model 5	37.43	14.58
Phyre2		
Model	39.91	14.96
SwissModel		
Model	47.47	17.96
AlphaFold2		
Model 1	50.77	19.82
Model 2	47.48	18.11
Model 3	41.84	16.84
Model 4	45.93	17.08
Model 5	39.20	17.03
REMD Simulations		
Average Values	37.73 \pm 8.69	10.81 \pm 1.83
Experiments (47,48)		
	35.66 \pm 8.51	9.00 \pm 1.00

REMD simulations yield R_{EE} and R_g values that are in agreement with the experiments. The R_g values obtained for the three-dimensional models for A β 42 using C-I-TASSER show excellent agreement with the results obtained from REMD simulations and experiments. However, the R_{EE} values for A β 42 using C-I-TASSER do not agree with those values obtained from REMD simulations or experiments. Instead, the R_{EE} values obtained using I-TASSER and Phyre2 show more agreement with REMD simulations and experiments. Interestingly, AlphaFold2, which is widely used for IDPs, cannot capture the experimental R_{EE} and R_g values for A β 42. To gain even more insights, the potential of mean force (PMF) surfaces based on R_{EE} and R_g values were computed using the trajectories obtained from REMD simulations (Figure 3). Figure 3 shows that there are

two most energetically stable basins for A β 42 (basin IA and basin IB). These most preferred basins are located at R_g values ranging from 10.6 Å to 11.4 Å and 10.3 Å to 10.7 Å. The first basin has A β 42 structures that have 10% α -helix and 6% β -sheet structures. The second most preferred basin has structures with about 22% α -helix and only 1% β -sheet structures. Energetically preferred structures are located in the basin with R_{EE} and R_g values closer to experimental data, as seen in Figure 3 (see also Table 1), indicating that most homology modeling methods used in this work yield for A β 42 three-dimensional structures that are not preferred energetically. Incorporating constraints related to R_{EE} and R_g experimental values could help improve the outcome of homology modeling tools for IDPs.

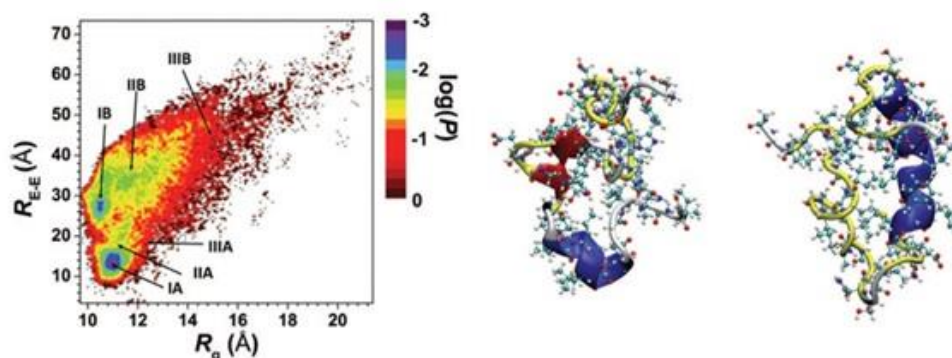


Figure 3: The potential of mean force surface area based on R_g and R_{EE} values of A β 42 using the trajectories obtained from REMD simulations.

The secondary structure elements per residue, along with their abundances using the trajectories obtained from REMD simulations, were calculated. REMD simulations yield overall 11.0% α -helix, 10.9% 3_{10} -helix, 0.4% π -helix, 3.4% β -sheet, 25.1% turn and 49.2% random coil structure for A β 42. To gain a

deeper insight into the distinct structuring – given the crucial roles of α -helix and β -sheet structure adopting residues in Alzheimer's disease – the probabilities per residue of these secondary structure elements were calculated (Figure 4).

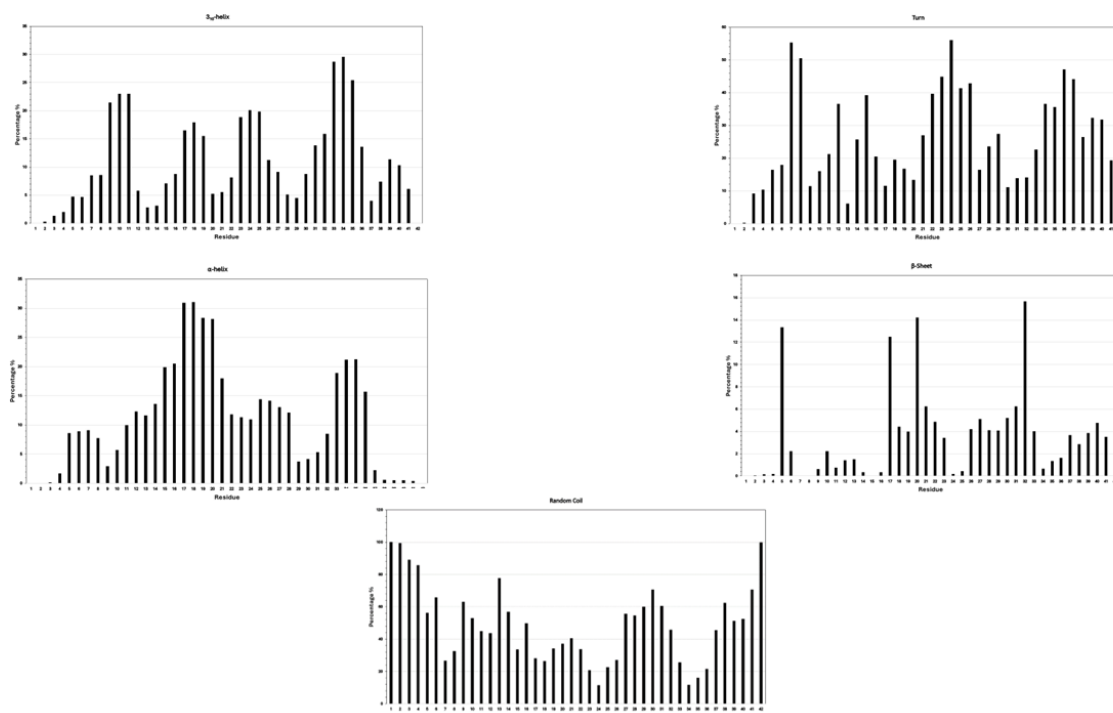


Figure 4: The calculated secondary structure elements, along with their probabilities for A β 42, using the trajectories obtained from REMD simulations.

The most abundantly formed secondary structure elements are the turn and random coil structures. β -sheet structure formation in A β 42 is crucial due to its involvement in oligomer, fibril, and aggregate formation processes in Alzheimer's disease. Therefore, it is crucial to adapt tools that can detect the residues forming β -sheet structure. Based on REMD simulations, β -sheet formation occurs at Arg5, Glu11, Val12, Phe19-Glu22, Gly25-Asn27, Gly33, Met35, Val36, Val40 and Ile41 with probabilities up to 23%. α -helix formation is detected at Arg5-Gln15, Lys16-Asp23, and Gly29-Val36. Turn structure formation is detected at Arg5-Val12 and Glu22-Lys28, with the largest abundance occurring in the Ala21-Ala30 region. These findings support the NMR

measurements that reported bend-like and turn conformations for the Asp7-Glu11 and Phe20-Ser26 regions (48). Experiments also demonstrated turn structure formation for the Ala21-Ala30 region (49). α -helix formation occurs in the N-terminal, mid-domain, and C-terminal regions. Still, residues in the mid-domain region form a more abundant α -helix structure than those in the N-terminal and C-terminal regions. Experiments and computational studies also detected the abundant β -sheet structure formation in the C-terminal region and showed an agreement with the findings reported herein (48,50). The calculated secondary structure abundances of A β 42 conformations located in different basins on the PMF surface (Figure 2) are listed in Table 2.

Table 2: The calculated secondary structures, along with their probabilities for A β 42 structures located in each basin on the PMF surface.

	Basin IA	Basin IIA	Basin IIIA	Basin IB	Basin IIB	Basin IIIB
α-helix (%)	10.0	14.5	15.3	21.5	15.8	15.2
3_{10}-helix (%)	9.1	9.5	11.0	9.5	11.4	11.1
β-sheet (%)	6.2	3.6	2.4	1.1	2.6	2.9
Turn (%)	32.4	29.5	28.1	28.2	30.3	29.5
Coil (%)	41.6	42.5	42.7	39.6	39.7	41.0

Overall, REMD simulations show an in-depth representation of secondary structure properties of intrinsically disordered proteins and agree with experiments overall. Additionally, the secondary structure components of the three-dimensional models for A β 42 obtained from C-I-TASSER, I-TASSER, Phyre2, SwissModel, and AlphaFold2 were calculated. The obtained results are presented in Scheme 1. C-I-TASSER, I-TASSER, and AlphaFold2 yield bend and turn structures for the Ala21-Ala30 region of A β 42 in agreement with experiments (49). None of the homology modeling tools studied in this work can capture the distinct β -sheet structuring in the C-terminal region of the peptide. We should note

here that the detection of amino acid residues forming β -sheet structure is crucial because these residues play a role in the oligomerization, fibrillation, and aggregation processes of A β 42 in Alzheimer's disease (5). In addition, the prominent distinct α -helix formation in the mid-domain region can be obtained using Phyre2 and I-TASSER homology modeling tools. All in all, these homology modeling tools cannot fully capture the distinct structuring of the intrinsically disordered A β 42 peptide. The incorporation of dynamic effects in homology modeling methods may improve the outcome of homology modeling tools for inherently disordered proteins.

Sequence:

D1A2E3F4R5H6D7S8G9Y10E11V12H13H14Q15K16L17V18F19F20A21E22D23V24G25S26N27K28G29A30I31I32G33L34M35V36G37G38V39V40I41A42

C-I-TASSER:

Model 1: CCSCSGGGGTSSSSCCCTTTTTSCBTCTTCSBSSCSSSSCCC

Model 2: CCSSCSTTTTTSSCCCCSSSTTSCBTCTTCSBSSCSSSSCCC

Model 3: CTBCCGGGTCCCCCSTTSSSCSCTTTSCSCCTTTTCBC

Model 4: CCSCCCTGGGTSCBCSSSTTSCCCTTCCBCSSSSCCC

Model 5: CCSSCSTTTTTSSCCCCSSSSSSCCSCSSCCCCSSSSCCC

I-TASSER:

Model 1: CCSTTTSBTTBCCCCCBTHHHHHHTTTSCCBSCCSTTBCC

Model 2: CCTTTTTSSSCTTCTTTTTHHHHTTSTTSCSSBTBTBCC

Model 3: CCIIIITTTCCSSCCTTTTTTTTTGGGGCSCBTBSCC

Model 4: CHHHHTBTBCCCCCCHHHHHHHSSCSCSCTTTTCCC

Model 5: CTTTTHHHSTTSCCBTBTTTTTTSCGGCSTTSTTCCC

Phyre2:

Model: CCCCCSSSCSHHHHHHHHHHHHCCTTHHHHHHHHHHHHC

Swiss-Model:

Model: CCCCCCCCCCCCCCCCCCCCCSHHHHHHHHHHHHHHC

AlphaFold2:

Model 1: CCCCCCCCCCCCCCCCCCCCCSSSCCCCCCTTSCCCC

Model 2: CCCCCCCCCCTTCCCCSSSCSSCCCCCCCCSSSSCCC

Model 3: CCCCCCCCCCCCCCCCCCCCCSSSCCCCCCCCCSSSSCCC

Model 4: CCCCCCCCCCCCCCCCCCCCCSCTTCCCCSSSSCCC

Model 5: CCCCCSCCCCCCCCCCCCCSSSCCCCCCTTSCCCC

Scheme 1: The calculated secondary structure elements per residue of A β 42 using the three-dimensional structures obtained from C-I-TASSER, I-TASSER, Phyre2, SwissModel, and AlphaFold2. H is for α -helix, B for isolated β -bridge, G for 3_{10} -helix, I for n-helix, T for turn, and S for bend structure.

The tertiary structure properties were studied by means of intra-molecular interactions. Figure 5 shows the calculated tertiary structure properties for A β 42 using the trajectories obtained from REMD simulations. We note stark interactions between the

central hydrophobic core (CHC) region and the N-terminal region, the N- and C-terminal regions, and the CHC region and the C-terminal region. These findings are in agreement with those of Yang and Teplow for A β 42 (50).

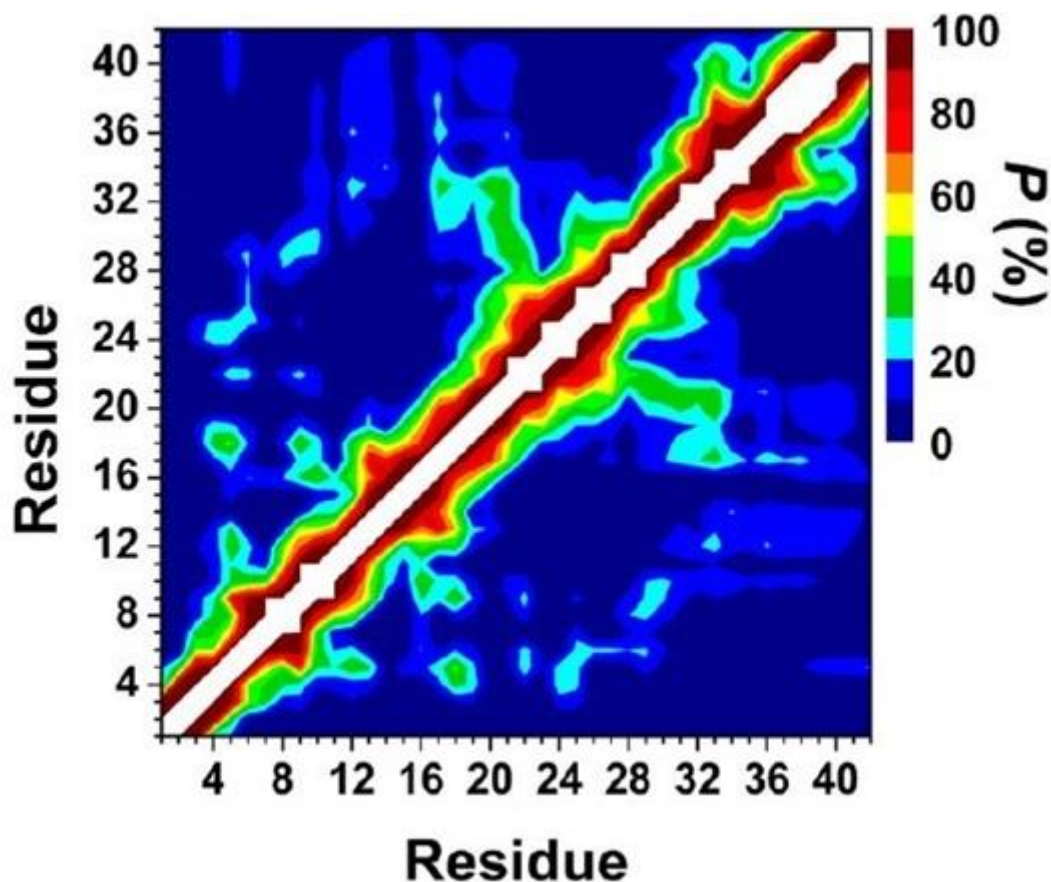


Figure 5: The calculated intra-molecular contact map for A β 42 using the trajectories obtained from REMD simulations.

The intra-molecular contact maps for the three-dimensional A β 42 models obtained from C-I-TASSER, I-TASSER, Phyre2, SwissModel, and

AlphaFold2 were calculated as well. Figures 6-10 present the findings from these calculations.

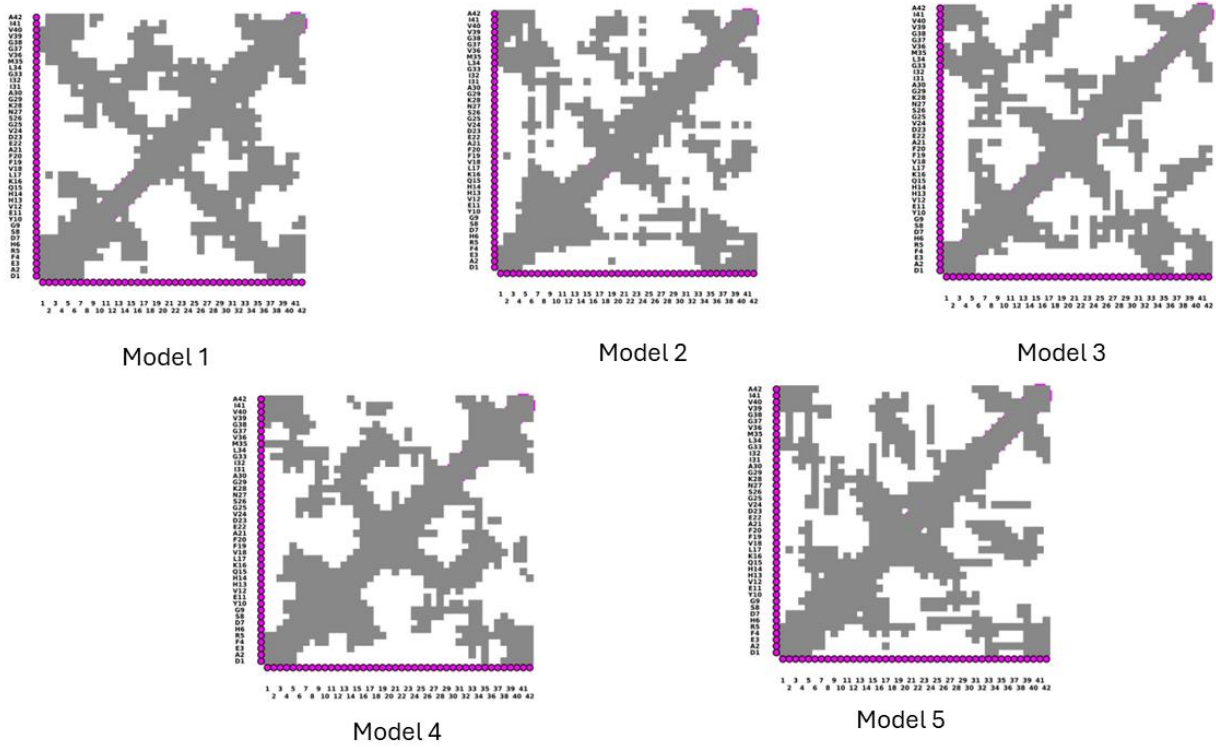


Figure 6: The calculated intra-molecular interaction maps for Aβ42 using the three-dimensional models obtained from C-I-TASSER.

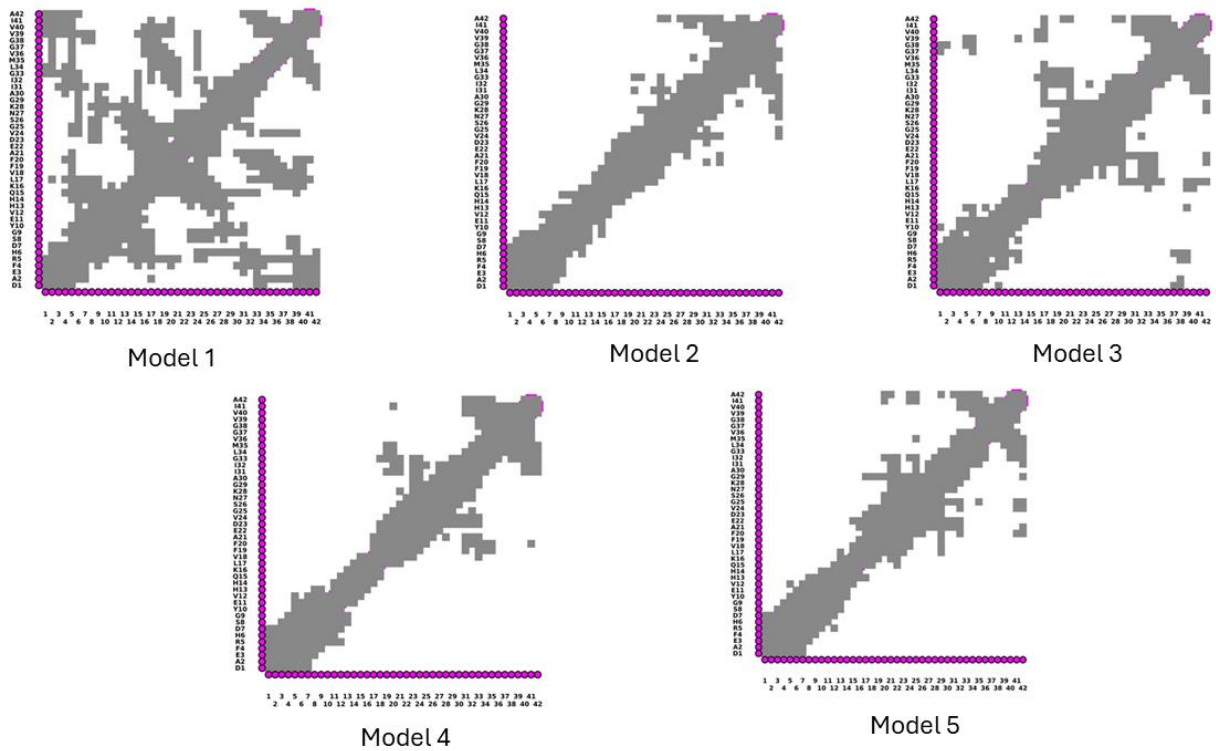


Figure 7: The calculated intra-molecular interaction maps for Aβ42 using the three-dimensional models obtained from I-TASSER.

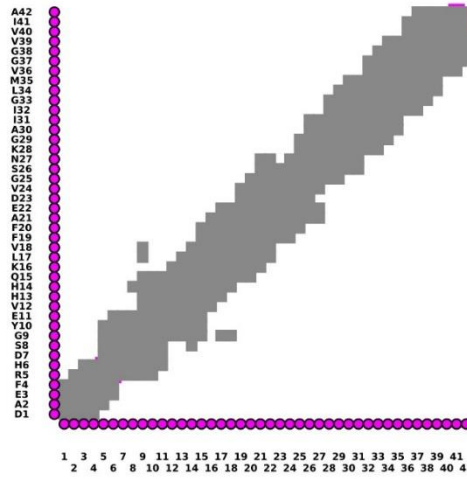


Figure 8: The calculated intra-molecular interactions map for Aβ42 using the three-dimensional models obtained from Phyre2.

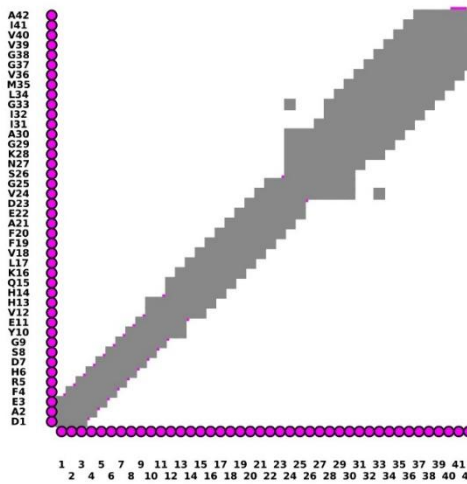


Figure 9: The calculated intra-molecular interactions map for Aβ42 using the three-dimensional models obtained from Swiss-Model.

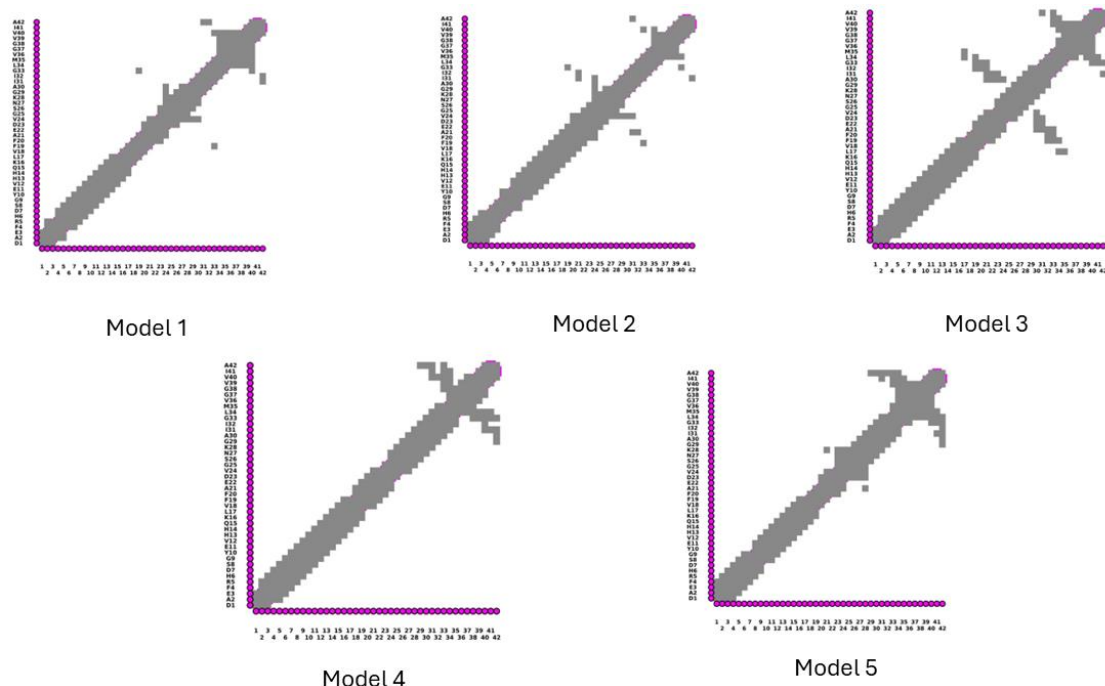


Figure 10: The calculated intra-molecular interaction maps for Aβ42 using the three-dimensional models obtained from AlphaFold2.

As seen in Figure 6, C-I-TASSER can capture even the weak interactions between the N-terminal and C-terminal regions, CHC region and C-terminal region, N-terminal and mid-domain regions, as well as mid-domain and C-terminal regions of A β 42. On the other hand, such interactions could be obtained using Model 1 for A β 42 from I-TASSER (Figure 7). Furthermore, Model 3 for A β 42 from I-TASSER represents the CHC region and C-terminal interactions as well. Interestingly, intra-molecular interaction maps calculated using the three-dimensional models from Phyre2, Swiss-Model, and AlphaFold2 cannot reproduce the data obtained from REMD simulations. Given the wide usage of

AlphaFold2 in the studies of A β and IDPs in general, including its implementation in databases of IDPs (51), these findings indicate that caution has to be given to such studies since AlphaFold2 is not capable of fully reproducing the structural properties of A β .

Table 4 lists the calculated salt bridges for A β 42 using the trajectories obtained from REMD simulations.

Table 5 lists the salt bridges calculated using the three-dimensional models from C-I-TASSER, I-TASSER, Phyre2, Swiss-Model, and AlphaFold2.

Table 4: The salt bridges of A β 42 from REMD simulations.

Residue	Residue	Probability (%) R(C-N) \leq 6.0 Å
Arg5	Glu3	59.6
Arg5	Glu22	26.7
Arg5	Asp1	15.0
Arg5	Glu11	14.1
Arg5	Ala42	21.3
Lys16	Glu11	8.0
Lys28	Glu22	13.2
Lys28	Asp23	7.1
Asp1	Glu3	5.3
Arg5	Asp7	1.2
Lys16	Asp7	11.1
Lys16	Glu3	1.8

Table 5: The calculated salt bridges for A β 42 using the three-dimensional structures obtained from C-I-TASSER.

C-I-TASSER		
Model 1		
Residue	Residue	Distance (Å)
Arg5	Asp1	2.9
Arg5	Asp7	4.9
Asp7	His14	5.0
Glu11	His14	5.8
Model 2		
Residue	Residue	Distance (Å)
Arg5	Glu11	2.6
Lys16	Asp23	2.5
Model 3		
Residue	Residue	Distance (Å)
Arg5	Glu3	3.5
Asp7	His6	5.6
Glu11	His13	3.8
Lys28	Glu11	2.4
Lys16	Asp23	2.4
Model 4		
Residue	Residue	Distance (Å)
Arg5	Asp1	5.9
Lys16	Asp7	5.6
Glu11	His13	5.8
Glu11	Lys28	2.5
Lys16	Asp23	2.5
Model 5		
Residue	Residue	Distance (Å)
Arg5	Asp7	2.8
Asp23	His14	5.6
Lys16	Asp23	3.2

Table 6: The calculated salt bridges for A β 42 using the three-dimensional structures obtained from I-TASSER, Phyre2, and Swiss-Model.

I-TASSER		
Model 1		
Residue	Residue	Distance (Å)
Arg5	Glu3	2.7
Glu3	His6	5.5
Glu11	His14	4.7
Model 2		
Residue	Residue	Distance (Å)
Arg5	Asp1	2.7
Asp1	His6	5.3
Glu11	His14	5.8
Glu22	Lys28	2.5
Model 3		
Residue	Residue	Distance (Å)
Asp1	His6	5.0
Arg5	Glu11	5.7
Glu11	His13	3.7
Lys16	Glu22	2.5
Model 4		
Residue	Residue	Distance (Å)
Arg5	Asp1	3.8
Asp1	His6	5.6
Asp7	His13	5.3
Glu11	His13	5.7
Glu11	His14	2.8
Lys16	Glu22	3.3
Model 5		
Residue	Residue	Distance (Å)
Arg5	Asp1	2.7
Glu11	His14	5.0
Phyre2		
Residue	Residue	Distance (Å)
Arg5	Glu3	5.0
Swiss-Model		
Residue	Residue	Distance (Å)
Glu11	His13	4.9

Table 7: The calculated salt bridges for A β 42 using the three-dimensional structures obtained from AlphaFold2.

AlphaFold2		
Model 1		
Residue	Residue	Distance (Å)
Glu11	His13	5.3
Model 2		
Residue	Residue	Distance (Å)
Glu11	His13	5.5
Model 3		
Residue	Residue	Distance (Å)
Arg5	Glu3	4.7
Glu11	His13	4.5
Model 4		
Residue	Residue	Distance (Å)
Glu11	His13	3.4
Model 5		
Residue	Residue	Distance (Å)
Glu11	His13	5.4

As seen in Tables 4-7, none of the homology modeling methods used in this work can fully capture the salt bridges obtained from REMD simulations. We should note that C-I-TASSER yields results closer to REMD simulations. However, the results are still not

fully captured for the full spectrum of the salt bridges. AlphaFold2 performs poorly in detecting the salt bridges of A β 42.

All in all, the structural properties for the intrinsically disordered A β 42 peptide reported by experiments or REMD simulations cannot be fully captured by C-I-TASSER, I-TASSER, Phyre2, Swiss-Model, and AlphaFold2.

We should mention here that I-TASSER relies heavily on existing protein structures (templates) in the Protein Data Bank (PDB). If there are no suitable templates for the target protein, the predictions can be less accurate. On the other hand, the accuracy of C-I-TASSER heavily depends on the quality and correctness of the constraints provided. AlphaFold2's performance is influenced by the quality and quantity of existing protein structures in its training dataset. Proteins with novel folds or those not well-represented in the training data may have lower prediction accuracy. Furthermore, AlphaFold2 predicts static structures and does not inherently provide insights into protein function and dynamics, which are critical for understanding biological processes. Moreover, Phyre2 relies heavily on template-based modeling, which means it can only be as accurate as the template it uses. Like AlphaFold2, Phyre2 provides only static structures and does not account for the dynamic nature of proteins. Proteins often undergo conformational changes that are crucial for their functions, which a single static model cannot capture. Swiss-Model relies on the availability of suitable templates. Swiss-Model generates static structures as well, but these do not capture the dynamic nature of proteins. Errors or discrepancies in template annotation or structural data can propagate into the model, leading to inaccurate predictions. Despite this, REMD simulations are computationally expensive because they require running multiple replicas in parallel, each at different temperatures. The accuracy of the results depends on the quality of the force field parameters and the chosen boundary conditions. Inaccurate force fields can lead to erroneous interpretations of the conformational space.

We also should mention here that C-I-TASSER utilizes predicted residue-residue contact maps from deep learning algorithms. These contact maps provide additional structural constraints that can significantly improve the accuracy of the model based on our findings, especially for regions or proteins where threading templates are less reliable.

4. CONCLUSION

Homology modeling methods, including C-I-TASSER, I-TASSER, Phyre2, SwissModel, and AlphaFold2, are used in the studies of IDPs, including A β . In this work, C-I-TASSER, I-TASSER, Phyre2, Swiss-Model, and AlphaFold2 were used to generate the three-dimensional models for A β 42, which is at the center of Alzheimer's disease. In parallel, extensive REMD simulations of A β 42 were conducted. Results obtained from different homology modeling methods were compared to the results obtained from REMD simulations and available experimental data. None of the homology modeling methods used in this study can fully reproduce the REMD simulation results or available experimental data. Given the wide usage of

these homology modeling methods in the studies of IDPs, these findings show that outermost care must be provided to such studies.

Specifically, C-I-TASSER performs better than I-TASSER, Phyre2, Swiss-Model, and AlphaFold2 in terms of the radius of gyration, parts of secondary structure, parts of salt bridges, and tertiary structure properties. However, the end-to-end distance and obtained full spectrum of salt bridges, as well as the full spectrum of the secondary structure properties, cannot be reproduced accurately using C-I-TASSER either. Surprisingly, AlphaFold2 performs poorly for A β 42. Given the significant usage of AlphaFold2 in the studies of IDPs, our findings show that the incorporation of end-to-end distance and radius of gyration constraints in further development of AlphaFold2 could improve the outcomes for IDPs.

5. CONFLICT OF INTEREST

The author declares no conflict of interest.

6. REFERENCES

1. Hameduh T, Haddad Y, Adam V, Heger Z. Homology modeling in the time of collective and artificial intelligence. *Comput Struct Biotechnol J* [Internet]. 2020 Jan 1;18:3494–506. Available from: [<URL>](#).
2. Coskuner-Weber O, Uversky VN. Current stage and future perspectives for homology modeling, molecular dynamics simulations, machine learning with molecular dynamics, and quantum computing for intrinsically disordered proteins and proteins with intrinsically disordered regions. *Curr Protein Pept Sci* [Internet]. 2024 Feb 17;25(2):163–71. Available from: [<URL>](#).
3. Uversky VN. Introduction to Intrinsically disordered proteins (IDPs). *Chem Rev* [Internet]. 2014 Jul 9;114(13):6557–60. Available from: [<URL>](#).
4. Uversky VN. Dancing protein clouds: The strange biology and chaotic physics of intrinsically disordered proteins. *J Biol Chem* [Internet]. 2016 Mar 25;291(13):6681–8. Available from: [<URL>](#).
5. Coskuner-Weber O, Mirzanli O, Uversky VN. Intrinsically disordered proteins and proteins with intrinsically disordered regions in neurodegenerative diseases. *Biophys Rev* [Internet]. 2022 Jun 8;14(3):679–707. Available from: [<URL>](#).
6. Dunker AK, Obradovic Z. The protein trinity—linking function and disorder. *Nat Biotechnol* [Internet]. 2001 Sep;19(9):805–6. Available from: [<URL>](#).
7. Trivedi R, Nagarajaram HA. Intrinsically disordered proteins: An overview. *Int J Mol Sci* [Internet]. 2022 Nov 14;23(22):14050. Available from: [<URL>](#).
8. Liu Y, Wang X, Liu B. A comprehensive review and comparison of existing computational methods for

- intrinsically disordered protein and region prediction. *Brief Bioinform* [Internet]. 2019 Jan 18;20(1):330–46. Available from: [<URL>](#).
9. Cramer P. AlphaFold2 and the future of structural biology. *Nat Struct Mol Biol* [Internet]. 2021 Sep 10;28(9):704–5. Available from: [<URL>](#).
10. Bryant P, Pozzati G, Elofsson A. Improved prediction of protein-protein interactions using AlphaFold2. *Nat Commun* [Internet]. 2022 Mar 10;13(1):1265. Available from: [<URL>](#).
11. Jones DT, Thornton JM. The impact of AlphaFold2 one year on. *Nat Methods* [Internet]. 2022 Jan 11;19(1):15–20. Available from: [<URL>](#).
12. Jumper J, Evans R, Pritzel A, Green T, Figurnov M, Ronneberger O, et al. Highly accurate protein structure prediction with AlphaFold. *Nature* [Internet]. 2021 Aug 26;596(7873):583–9. Available from: [<URL>](#).
13. Ruff KM, Pappu R V. AlphaFold and implications for intrinsically disordered proteins. *J Mol Biol* [Internet]. 2021 Oct 1;433(20):167208. Available from: [<URL>](#).
14. Yang Z, Zeng X, Zhao Y, Chen R. AlphaFold2 and its applications in the fields of biology and medicine. *Signal Transduct Target Ther* [Internet]. 2023 Mar 14;8(1):115. Available from: [<URL>](#).
15. Cecchini M, Rao F, Seeber M, Cafilisch A. Replica exchange molecular dynamics simulations of amyloid peptide aggregation. *J Chem Phys* [Internet]. 2004 Dec 1;121(21):10748–56. Available from: [<URL>](#).
16. Nguyen PH, Ramamoorthy A, Sahoo BR, Zheng J, Faller P, Straub JE, et al. Amyloid Oligomers: A joint experimental/computational perspective on Alzheimer's disease, Parkinson's disease, type II diabetes, and amyotrophic lateral sclerosis. *Chem Rev* [Internet]. 2021 Feb 24;121(4):2545–647. Available from: [<URL>](#).
17. Nguyen P, Derreumaux P. Understanding amyloid fibril nucleation and A β oligomer/drug interactions from computer simulations. *Acc Chem Res* [Internet]. 2014 Feb 18;47(2):603–11. Available from: [<URL>](#).
18. Coskuner-Weber O, Uversky V. Insights into the molecular mechanisms of Alzheimer's and Parkinson's diseases with molecular simulations: Understanding the roles of artificial and pathological missense mutations in intrinsically disordered proteins related to pathology. *Int J Mol Sci* [Internet]. 2018 Jan 24;19(2):336. Available from: [<URL>](#).
19. Coskuner-Weber O, Uversky VN. Alanine scanning effects on the biochemical and biophysical properties of intrinsically disordered proteins: A case study of the histidine to alanine mutations in amyloid- β 42. *J Chem Inf Model* [Internet]. 2019 Feb 25;59(2):871–84. Available from: [<URL>](#).
20. Zhou R. Replica exchange molecular dynamics method for protein folding simulation. In: *Protein Folding Protocols* [Internet]. New Jersey: Humana Press; 2007. p. 205–24. Available from: [<URL>](#).
21. Allison TC, Coskuner O, Gonzalez CA. *Metallic systems: A quantum chemist's perspective* [Internet]. Allison TC, Coskuner O, Gonzalez CA, editors. CRC Press; 2011. Available from: [<URL>](#).
22. Coskuner-Weber O, Habiboglu MG, Teplow D, Uversky VN. From quantum mechanics, classical mechanics, and bioinformatics to artificial intelligence studies in neurodegenerative diseases. In: *Methods in Molecular Biology* [Internet]. Humana, New York, NY; 2022. p. 139–73. Available from: [<URL>](#).
23. Tycko R. Solid-State NMR studies of amyloid fibril structure. *Annu Rev Phys Chem* [Internet]. 2011 May 5;62(1):279–99. Available from: [<URL>](#).
24. Karamanos TK, Kalverda AP, Thompson GS, Radford SE. Mechanisms of amyloid formation revealed by solution NMR. *Prog Nucl Magn Reson Spectrosc* [Internet]. 2015 Aug 1;88–89:86–104. Available from: [<URL>](#).
25. Fawzi NL, Ying J, Ghirlando R, Torchia DA, Clore GM. Atomic-resolution dynamics on the surface of amyloid- β protofibrils probed by solution NMR. *Nature* [Internet]. 2011 Dec 8;480(7376):268–72. Available from: [<URL>](#).
26. Ma B, Nussinov R. Simulations as analytical tools to understand protein aggregation and predict amyloid conformation. *Curr Opin Chem Biol* [Internet]. 2006 Oct 1;10(5):445–52. Available from: [<URL>](#).
27. Buchete NV, Tycko R, Hummer G. Molecular dynamics simulations of Alzheimer's β -amyloid protofilaments. *J Mol Biol* [Internet]. 2005 Nov 4;353(4):804–21. Available from: [<URL>](#).
28. Zhang M, Ren B, Chen H, Sun Y, Ma J, Jiang B, et al. Molecular simulations of amyloid structures, toxicity, and inhibition. *Isr J Chem* [Internet]. 2017 Jul 16;57(7–8):586–601. Available from: [<URL>](#).
29. Zheng W, Zhang C, Li Y, Pearce R, Bell EW, Zhang Y. Folding non-homologous proteins by coupling deep-learning contact maps with I-TASSER assembly simulations. *Cell Reports Methods* [Internet]. 2021 Jul 26;1(3):100014. Available from: [<URL>](#).
30. Yang J, Zhang Y. I-TASSER server: New development for protein structure and function predictions. *Nucleic Acids Res* [Internet]. 2015 Jul 1;43(W1):W174–81. Available from: [<URL>](#).
31. Roy A, Kucukural A, Zhang Y. I-TASSER: a unified platform for automated protein structure and function prediction. *Nat Protoc* [Internet]. 2010 Apr 25;5(4):725–38. Available from: [<URL>](#).
32. Kelley LA, Mezulis S, Yates CM, Wass MN, Sternberg MJE. The Phyre2 web portal for protein modeling, prediction and analysis. *Nat Protoc*

- [Internet]. 2015 Jun 7;10(6):845–58. Available from: [<URL>](#).
33. Waterhouse A, Bertoni M, Bienert S, Studer G, Tauriello G, Gumienny R, et al. SWISS-MODEL: homology modelling of protein structures and complexes. *Nucleic Acids Res* [Internet]. 2018 Jul 2;46(W1):W296–303. Available from: [<URL>](#).
34. Akdel M, Pires DE V., Pardo EP, Jänes J, Zalevsky AO, Mészáros B, et al. A structural biology community assessment of AlphaFold2 applications. *Nat Struct Mol Biol* [Internet]. 2022 Nov 7;29(11):1056–67. Available from: [<URL>](#).
35. Mirdita M, Schütze K, Moriwaki Y, Heo L, Ovchinnikov S, Steinegger M. ColabFold: Making protein folding accessible to all. *Nat Methods* [Internet]. 2022 Jun 30;19(6):679–82. Available from: [<URL>](#).
36. Shafat Z, Ahmed A, Parvez MK, Parveen S. Intrinsic disorder in the open reading frame 2 of hepatitis E virus: A protein with multiple functions beyond viral capsid. *J Genet Eng Biotechnol* [Internet]. 2023 Dec 1;21(1):33. Available from: [<URL>](#).
37. O'Brien DP, Hernandez B, Durand D, Hourdel V, Sotomayor-Pérez AC, Vachette P, et al. Structural models of intrinsically disordered and calcium-bound folded states of a protein adapted for secretion. *Sci Rep* [Internet]. 2015 Sep 16;5(1):14223. Available from: [<URL>](#).
38. Kheirabadi M, Taghdir M. Is unphosphorylated Rex, as multifunctional protein of HTLV-1, a fully intrinsically disordered protein? An in silico study. *Biochem Biophys Reports* [Internet]. 2016 Dec 1;8:14–22. Available from: [<URL>](#).
39. Yang J, Zhang Y. Protein structure and function prediction using I-TASSER. *Curr Protoc Bioinforma* [Internet]. 2015 Dec 17;52(1):5.8.1–5.8.15. Available from: [<URL>](#).
40. Lee YT, Ayoub A, Park SH, Sha L, Xu J, Mao F, et al. Mechanism for DPY30 and ASH2L intrinsically disordered regions to modulate the MLL/SET1 activity on chromatin. *Nat Commun* [Internet]. 2021 May 19;12(1):2953. Available from: [<URL>](#).
41. Case DA, Aktulga HM, Belfon K, Cerutti DS, Cisneros GA, Cruzeiro VWD, et al. AmberTools. *J Chem Inf Model* [Internet]. 2023 Oct 23;63(20):6183–91. Available from: [<URL>](#).
42. Caliskan M, Mandaci SY, Uversky VN, Coskuner-Weber O. Secondary structure dependence of amyloid- β (1–40) on simulation techniques and force field parameters. *Chem Biol Drug Des* [Internet]. 2021 May 22;97(5):1100–8. Available from: [<URL>](#).
43. Weber OC, Uversky VN. How accurate are your simulations? Effects of confined aqueous volume and AMBER FF99SB and CHARMM22/CMAP force field parameters on structural ensembles of intrinsically disordered proteins: Amyloid- β 42 in water. *Intrinsically Disord Proteins* [Internet]. 2017 Jan 30;5(1):e1377813. Available from: [<URL>](#).
44. Darden T, York D, Pedersen L. Particle mesh Ewald: An $N \cdot \log(N)$ method for Ewald sums in large systems. *J Chem Phys* [Internet]. 1993 Jun 15;98(12):10089–92. Available from: [<URL>](#).
45. Wise-Scira O, Xu L, Kitahara T, Perry G, Coskuner O. Amyloid- β peptide structure in aqueous solution varies with fragment size. *J Chem Phys* [Internet]. 2011 Nov 28;135(20):1448–57. Available from: [<URL>](#).
46. Sgourakis NG, Yan Y, McCallum SA, Wang C, Garcia AE. The Alzheimer's Peptides A β 40 and 42 Adopt Distinct Conformations in Water: A Combined MD / NMR Study. *J Mol Biol* [Internet]. 2007 May 18;368(5):1448–57. Available from: [<URL>](#).
47. Tomaselli S, Esposito V, Vangone P, van Nuland NAJ, Bonvin AMJJ, Guerrini R, et al. The α -to- β Conformational Transition of Alzheimer's A β -(1–42) Peptide in Aqueous Media is Reversible: A Step by Step Conformational Analysis Suggests the Location of β Conformation Seeding. *ChemBioChem* [Internet]. 2006 Feb 6;7(2):257–67. Available from: [<URL>](#).
48. Nag S, Sarkar B, Banerjee A, Sahoo B, Varun KAS, Maiti S. The Nature of the Amyloid- β Monomer and the Monomer-Oligomer Equilibrium. *Biophys J* [Internet]. 2011 Feb 2;100(3):202a. Available from: [<URL>](#).
49. Murray MM, Krone MG, Bernstein SL, Baumketner A, Condron MM, Lazo ND, et al. Amyloid β -protein: Experiment and theory on the 21–30 fragment. *J Phys Chem B* [Internet]. 2009 Apr 30;113(17):6041–6. Available from: [<URL>](#).
50. Yang M, Teplow DB. Amyloid β -protein monomer folding: Free-energy surfaces reveal alloform-specific differences. *J Mol Biol* [Internet]. 2008 Dec 12;384(2):450–64. Available from: [<URL>](#).
51. Piovesan D, Del Conte A, Clementel D, Monzon AM, Bevilacqua M, Aspromonte MC, et al. MobiDB: 10 years of intrinsically disordered proteins. *Nucleic Acids Res* [Internet]. 2023 Jan 6;51(D1):D438–44. Available from: [<URL>](#).



Surfactant Micelles as Catalysts: Kinetic Modelling and Key Models

Karri Lavanya¹ , R S S Srikanth Vemuri^{1*} , Shyamala Pulipaka² ,
Venkata Nagalakshmi Kilana³ , Ravi Vital Kandisa⁴ 

¹Department of Basic Sciences and Humanities, Vignan's Institute of Engineering for Women (Autonomous), Visakhapatnam, Andhra Pradesh, India-530049.

²Department of Chemistry, Andhra University, Visakhapatnam, Andhra Pradesh, India-53003.

³Department of Chemistry, Gayatri Vidya parishad College of Engineering (Autonomous), Madhurawada, Visakhapatnam, Andhra Pradesh, India-530048.

⁴Kalam Institute of Technology - WHO Collaborating Centre, Visakhapatnam, India-530031.

Abstract: Surfactant molecules possess both hydrophilic and hydrophobic properties, featuring a hydrophilic head and a hydrophobic tail. When surfactants reach a critical micellar concentration, they assemble into stable molecular aggregates called micelles. These micelles serve as effective catalysts for a range of chemical reactions. To elucidate and make sense of experimental data related to micelle-catalyzed reactions, researchers often employ kinetic modeling as a valuable tool. Several kinetic models have been introduced to describe the reaction rates within micellar environments. In this discussion, we will provide a concise overview of four widely utilized models: The Berezin model, the pseudophase model, the ion exchange model, and the Piskiewicz model.

Keywords: Micellar catalysis, Kinetic modeling, Berezin model, Pseudophase model, Ion exchange model, Piskiewicz model.

Submitted: December 3, 2023. **Accepted:** June 24, 2024.

Cite this: Lavanya K, Vemuri R S S, Pulipaka S, Kilana V N, Kandisa R V. Surfactant Micelles as Catalysts: Kinetic Modelling and Key Models. JOTCSA. 2024;11(3): 1165-80.

DOI: <https://doi.org/10.18596/jotcsa.1399457>

***Corresponding author's E-mail:** vrsssrikanth@gmail.com

1. INTRODUCTION

Surfactant molecules exhibit amphiphilic properties, with a hydrophilic head and a hydrophobic tail, making them soluble in both aqueous and non-aqueous oil phases (1,2). Below the Critical Micellar Concentration (CMC), surfactant molecules are generally believed to exist as individual molecules in the solution. However, as the concentration surpasses the CMC, these surfactant molecules start to aggregate, forming structures known as micelles (1,2). These micelles play a crucial role in altering the rates of chemical reactions. The arrangement of reactants and products within the micellar environment significantly influences the transition states of reactions, thereby impacting their reaction rates (3-24). To gain a deeper understanding of the underlying mechanisms of these catalyzed reactions within micelles, it is most effective to employ appropriate kinetic models.

In the early 1980s, significant efforts were made to establish this field of chemistry as a distinct discipline, with researchers like Berezin (25-27), Romsted, and Bunton (28-32) contributing to its

development. Mittal and Lindman's *Surfactants in Solution* explores the formation of micelles and the impact of surfactants on reaction kinetics. Mittal's *Solution Chemistry of Surfactants* delves into the chemical and physical interactions of surfactants in various environments (33,34). Bunton and Romsted's contribution in *Solution Behavior of Surfactants*, edited by Mittal and Fendler, focuses on the role of reactive counter ions in surfactant systems, examining their interactions and catalytic effects. These works collectively offer valuable knowledge for understanding micellar catalysis and the underlying mechanisms of surfactant behavior in solutions (35).

The most widely accepted models for explaining the effects of micelles on reaction rates include the pseudophase model (29,30), the Berezin model (25), the Piskiewicz model (36,37), and the pseudophase ion exchange model (38). These models aid in providing a better understanding of the intricate processes involved in reactions occurring within micellar environments.

The purpose of this review article on kinetic models for micellar-catalyzed reactions is to consolidate and critically evaluate the various theoretical frameworks that explain how micelles impact the kinetics of response. By examining models such as the pseudophase, Berezin, Piskiewicz, and pseudophase ion exchange models, we aim to clarify the mechanistic pathways and provide a comparative analysis to guide researchers in selecting appropriate models for various catalytic systems. Ultimately, this comprehensive analysis will advance our understanding and utilization of micellar systems in chemical reactions.

2. MICELLAR CATALYSIS

Micelles, the organized assemblies of surfactant molecules, serve as remarkable catalysts for specific chemical reactions by creating an ideal microenvironment (39). The application of the Gouy-Chapman model assists in comprehending the electrical double layer formed around charged surfactant molecules. When surfactant molecules possess charged groups, such as ionic head groups or ionized hydrophilic regions, an electric double layer takes shape around each micelle. In this model, the electric double layer comprises two distinct areas: the Stern layer, which is the innermost layer characterized by a compact arrangement of ions strongly associated with the charged surface, and the diffuse layer, extending outward from the Stern layer, where ions exhibit a more diffuse distribution and a weaker association with the surface. Within the confines of the micelle, the concentration of reactant molecules exceeds that in the surrounding bulk solution. This localized increase in concentration significantly elevates the likelihood of reactant molecules colliding and initiating chemical reactions, resulting in an accelerated reaction rate. Furthermore, micelles have a unique capability to solubilize hydrophobic reactant molecules within their hydrophobic core. By solubilizing these reactants, micelles effectively elevate their effective concentration, rendering them more accessible to other reactant molecules, thus enhancing their participation in the reaction.

Micelles also excel in stabilizing reaction intermediates or transition states that are energetically unfavorable or unstable. By encapsulating these species within their structure, micelles create a favorable environment for the response to advance, reducing activation energy and boosting reaction rates. The well-defined surface of micelles further contributes to their catalytic activity. Reactant molecules can interact with the micelle's surface, promoting adsorption and subsequent reactions at the interface. This surface reaction mechanism significantly augments the overall reaction rate.

Essentially, micellar catalysis employs a multifaceted approach to accelerate reaction rates by concentrating reactants, dissolving hydrophobic compounds, stabilizing intermediates, and providing a structured surface for interactions. These qualities make micelles an indispensable tool for numerous chemical processes.

Micellar catalysis, with its ability to catalyze reactions by creating a favorable environment, has sparked interest among researchers eager to explore its potential. To delve deeper into the mechanisms driving these catalyzed reactions within micelles, scientists have embraced kinetic modeling. This approach offers a systematic framework for describing and predicting the behavior of reactions in this distinctive setting. Several kinetic models have been proposed to elucidate the intricate details of micellar catalysis. These models, such as the Berezin model and the pseudophase model, the ion exchange model, and the Piskiewicz model, offer valuable insights into how micelles influence reaction rates, providing researchers with the tools to interpret and predict the outcomes of reactions catalyzed by these molecular assemblies. By combining kinetic models with micellar catalysis, scientists are effectively advancing their understanding of these systems and their practical applications in diverse fields such as medicine and wastewater treatment.

3. KINETIC MODELS

The majority of kinetic data have been analyzed using the following kinetic models, providing a quantitative or semi-quantitative discussion.

3.1. Pseudophase Model

The pseudophase model, first formulated by Menger and Portnoy (29,30), provides a structured approach for rationalizing kinetic data in micellar systems. According to this model, chemical reactions can occur in one or both two pseudophases found in the micellar system, namely the aqueous pseudophase and the micellar pseudophase. It postulates that reactants partition between the bulk solution and the micellar phase, with the actual reaction exclusively taking place within the micelles. The concentration of reactants within the micellar phase is treated as a pseudo concentration, giving the model a distinctive name.

A widely accepted scheme for an unimolecular, micellar-catalyzed reaction is as follows (Figure 1)

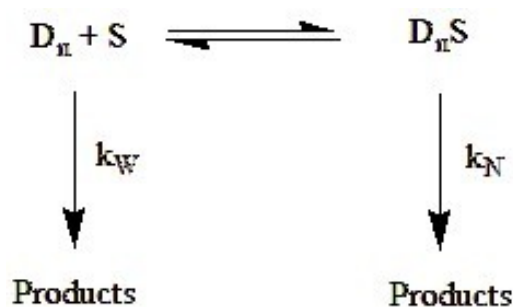


Figure 1: Scheme for an unimolecular micellar-catalyzed reaction.

Where K is the micelle-substrate binding constant, k_{W} and k_{M} are rate constants for the water and micellar phases, respectively, and S is a neutral substrate. K_{p} is the observed rate constant. The formula for micelle concentration $[D_{\text{n}}]$ is $[D_{\text{n}}] = ([C] - \text{CMC})/N$. Where CMC stands for the critical micellar concentration, N is the aggregation number, and C

is the surfactant's stoichiometric concentration. Model outputs the rate-law

$$k_{\psi} = \frac{k_w + k_M K[D_n]}{(1 + K[D_n])} \quad (1)$$

This rate law adjusts to

$$\frac{1}{k_w - k_{\psi}} = \frac{1}{k_w - k_M} + \frac{1}{k_w - k_M} \left(\frac{N}{K([C] - CMC)} \right) \quad (2)$$

The relationship between reaction rates and micellar effects can be effectively studied by

analyzing the slope and intercept of a plot, where $1/(k_w - k_M)$ is plotted against $1/([C] - CMC)$. These calculations yield the rate constants k_M and K .

The pseudophase model has proven to be a successful tool for explaining how micelles influence rates of various reactions, as summarized in Table 1. However, there are instances, such as the acid hydrolysis of p-nitrobenzaldehyde acetals and p-nitrophenyl diphenyl phosphate with fluoride ion in cetyltrimethylammonium fluoride (CTAF) (31), where the model falls short. In these cases, where the only counterions present are OH^- or F^- , it is postulated that the reaction occurs not only in the aqueous and micellar pseudo phases but also at the interface where the micelle meets the surrounding water.

Table 1: Reactions in micellar medium interpreted by Pseudophase model.

Reaction	Micellar medium	Remarks	Ref
P - Nitrophenyl Acetate with Benzo hydroxamate ion	Alkyl dimethyl and diethyl ethanol ammonium bromides.	The pseudophase model provided the quantitative explanation of the kinetic micellar effect for this reaction.	40
1,3- dipolar cycloadditions of benzonitrile oxide with a series of N-substituted maleimides	SDS CTAB Alkyl poly (ethylene oxide) surfactants	Micellar accelerations have been observed, and the kinetic data obtained has been analyzed using the pseudophase model for bimolecular reactions.	41
Ninhydrin with Chromium - glycyglycine Complex.	16-s-16 gemini	The quantitative analysis of reaction rate variations in the presence of gemini surfactants was conducted successfully using the pseudophase model.	42
Ninhydrin with Glycine-Leucine dipeptide.	16-s-16 gemini	In gemini surfactants, the reaction exhibits a greater acceleration. The catalytic effects and rate increment brought about by gemini surfactants have been quantitatively explained by a pseudophase model of the micellar solution.	43
Ninhydrin with Chromium (III) amino acid in acetate buffer.	Dimeric gemini	The study utilized the pseudophase model of micellar catalysis to investigate the impact of gemini on the rate constant.	44
Ninhydrin with Zn (II)-Gly-Leu Complex.	CTAB	The relationship between the rate constant (k_{ψ}) and the concentration of CTAB was thoroughly discussed and described. The kinetic data were analyzed based on the pseudophase model of surfactant micelles. Various parameters, including thermodynamic and binding constants, were also calculated.	45
Ninhydrin with (Cr (III) - Gly-Tyr) 2+ Complex.	CTAB, gemini	The results obtained in the micellar medium were interpreted using the pseudophase model of micelles. Furthermore, the micellar binding constants K_S for the $[Cr(III)-Gly-Tyr]^{2+}$ complex and K_N for ninhydrin were determined using the kinetic data.	46
Ninhydrin with Copper (II) - Glycyl phenyl alanine complex.	CTAB	The pseudophase model interpreted the effect of CTAB on reaction rate.	47
Ninhydrin with (Cu (II) - Gly-L-Ala) + complex.	TTABr	The reaction follows first- and fractional-order kinetics with respect to $[Cu(II)-Gly-L-Ala]T^+$ and $[ninhydrin]T$ in aqueous and TTABr micelles. The applied pseudophase model successfully	48
Ninhydrin with Glycine in Sodium acetate- Acetic Buffer.	gemini	The pseudophase model was utilized to analyze the experimental data of the rate constant (k_{ψ}) for [gemini]. The observed catalytic effect is ascribed to the combined influence of hydrophobic and electrostatic interactions between gemini surfactant molecules and the reactive species.	49
Ninhydrin with Glycyl phenylalanine (Dipeptide).	CTAB gemini	It was found that the surfactants had a catalytic effect on the reaction. Similar to conventional gemini surfactants, they exhibited the usual pattern of increasing and then stabilizing rate constants.	50

Reaction	Micellar medium	Remarks	Ref
Ninhydrin with Methionine Amino Acids.	gemini	The ninhydrin-methionine reaction exhibited a characteristic influence commonly associated with surfactants, which was elucidated through the application of a pseudophase model of micelles. Furthermore, additional factors, such as reaction rates and binding constants, were determined through calculations.	51
Reaction between dyes and mixed Surfactants in aqueous medium.	DTAB SDS	The quantitative analysis of reaction rate variations in the presence of DTAB and SDS surfactants was conducted successfully using the pseudophase model.	52
Ninhydrin with Tyrosine Aminoacid.	gemini	A detailed analysis of the relationship between the rate constant (k_p) and surfactant concentration was conducted using the pseudophase model. Through this quantitative approach, the micellar binding parameters and thermodynamic parameters were calculated.	53
Ninhydrin with Arginine Amino acid	gemini	A detailed analysis of the relationship between the rate constant (k_p) and surfactant concentration was conducted using the pseudophase model.	54
Hydrolysis of phenyl chloroformate	SDS, Brj35 , TTAB	A simple pseudophase model was applied. The trend of the reaction is $SDS < Brj_{35} < TTAB < SB3 - 14$	55
Kinetic study in water-ethylene glycol cationic, zwitterionic, nonionic, and anionic micellar solutions	TDAB, SDS	The researchers observed that the effects of the micellar medium could be explained by considering various factors, such as charge-charge interactions, polarity, ionic strength, and water content in the micellar interfacial region.	56
The reaction between $[Ru(NH_3)_5pz]^{2+} + S_2O_8^{2-}$	CTACI AOT	The results are interpreted by taking the pseudophase model, modified in some cases, as a general basis in order to take into account the specificity of the reaction medium.	57
Picolinic acid promoted hexavalent chromium oxidation of glycerol	SDS CPC	Reaction inhibits in CPC, whereas it accelerates in SDS.	58
Oxidation of methyl blue by Ce(IV)	TX-100	The rate decreases when there is an increase in TX-10 concentration.	59
Oxidation of aspartic acid with molybdenum-oxime-ligand	SDS	The interfacial active species proves useful in catalyzing aspartic acid oxidation.	60
Persulfate oxidation of methylene blue	SDS TX-100	The rate of reaction decreases with respect to the increase in [SDS] and is not affected by TX-100.	61

The pseudophase model offers a simplified representation of complex systems, making it more accessible for understanding and analysis. It enables researchers to make predictions about how the system behaves under various conditions, which is crucial for exploring and optimizing its properties.

However, the model has limitations. It assumes that reactions exclusively occur within the micellar phase, overlooking the possibility of alternative reaction pathways. In certain situations, reactions may take place at the interface between the micelle and the solvent or involve species not integrated into the micelles. These scenarios are not adequately addressed by the pseudophase model, highlighting the need for alternative models to account for these complexities.

3.2. Piszkiwicz Model

Combining elements from both the Berezin and pseudophase models, the Piszkiwicz model introduces a fresh perspective on micellar catalysis (36,37). This model says that the reaction primarily takes place within a distinct reaction layer situated at the surface of the micelle. The rate of the response is governed by the concentration of

reactants within this reaction layer, which acts as a critical zone for the reaction to occur. Importantly, the Piszkiwicz model takes into account the distribution of reactants between the bulk solution and the micellar surface, recognizing the dynamic interplay between these two regions.

Visualizing the Piszkiwicz model (Figure 2), one can envision a scenario where the micelle's surface plays a pivotal role in mediating the reaction. It is within this reaction layer that reactants interact and transform, guided by their proximity to the micellar surface. This unique model bridges the gap between the traditional Berezin and pseudophase models, offering a more comprehensive insight into the micellar catalysis process. It provides insights into the crucial role of the micellar surface and the interplay between the bulk solution and the micellar environment in catalyzing chemical reactions.

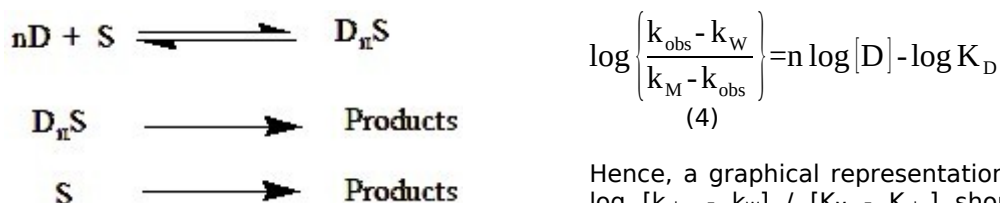


Figure 2: Visualization of the Piszkievicz model.

Here, the rate constants for the reaction in the micelle and water, respectively, are k_M and k_W . K_D is the dissociation constant of the micelle-substrate complex. The equation yields the rate law.

$$k_{\text{obs}} = \frac{k_M [D]^n + k_W K_D}{K_D + [D]^n} \quad (3)$$

The equation (3) can also be modified to adopt the following form:

Hence, a graphical representation of $\log[D]$ against $\log [k_{\text{obs}} - k_W] / [K_M - K_{\text{obs}}]$ should yield a linear relationship. The slope of this plot corresponds to the value of 'n,' often referred to as the cooperativity index, which characterizes the system's behavior. When $\log [k_{\text{obs}} - k_W] / [K_M - K_{\text{obs}}]$ equals zero, the value of $n \log[D]$ becomes equivalent to $\log K_D$.

The Piszkievicz model offers a quantitative framework to understand the enhanced rates observed in micellar-catalyzed reactions (as summarized in Table 2). It equips researchers with the mathematical tools to calculate rate constants and predict reaction rates under varying conditions. This model takes into consideration how reactants are organized within micelles, the role played by micellar interfaces, and the influence of micellar properties on reaction rates. This knowledge is instrumental in the design and optimization of catalytic systems.

Table 2: Reactions in micellar medium interpreted by Piszkievicz model.

Reaction	Micellar medium	Remarks	Ref
Picolinic acid promoted hexavalent chromium oxidation of glycerol	SDS CPC	Reaction inhibits in CPC, whereas it accelerates in SDS.	58
Oxidation of L-leucine by N-bromo naphthalimide	CTAB	The results were elucidated by utilizing the models developed by Piszkievicz, Raghavan, and Srinivasan.	62
Alkaline fading of malachite green	DTAB TX-100 SDS	The researchers utilized both Piszkievicz's pseudophase ion exchange model and traditional/classical models in their study.	63
Reaction of dithionite ion and bis-(2-pyridinealoximate) di oxomolybdate (IV) complex	SDS	The quantitative analysis of the impact of anionic surfactants on the reaction medium was determined using the Piszkievicz model, which describes the intricate sequence of complex interactions	64
Oxidation of L-lysine by permanganate ion in perchloric acid medium	SLS and PEG	The reaction has been found to possess positive activation entropy, indicating the dissociative nature of the transition state and outer-sphere electron transfer mechanism.	65
Interaction of malachite green and brilliant green with water	Brij 35, sodium dodecyl sulfate, cetyltrimethylammonium bromide, and 3-(dimethyl dodecyl ammonium)-propane sulfonate	Spectrophotometric measurements were utilized to establish the relationship between the concentration of different surfactants, and the rate constants governing the interaction of malachite green (MG) and brilliant green (BG) dyes with water. The medium effect and the concentration effect characterized the impact of surfactant micelles on the rate constants of the reactions.	66
Oxidation of paracetamol by water-soluble colloidal MnO_2 in the presence of an anionic surfactant	SDS	The influence of SDS as a catalyst in water-based solutions has been extensively studied using Piszkievicz. Several important parameters have been determined, including the binding constant ($7.59 \times 10^{-2} \text{ mol}^{-1} \text{ dm}^3$), dissociation constant potential reaction mechanism, and rate law have been proposed.	67
Oxidative degradation of acridine orange by acidic chlorite	CTAB	The results were elucidated by utilizing the models developed by Piszkievicz, Raghavan, and Srinivasan.	68
Oxidation of hydroxylamine hydrochloride by Vanadium (V)	SDS	The results were elucidated by utilizing the models developed by Piszkievicz, Raghavan, and Srinivasan.	69
Hydrolysis of di-2-methoxy-4-nitroaniline phosphate	SDS Brij-35	The binding constants between the reactants and surfactants evaluated from the Piszkievicz model.	70
Thioglycolic acid oxidation by N,N'-phenylene	SDS CTAB	SDS and CTAB catalyzed the reaction.	71

Reaction	Micellar medium	Remarks	Ref
bis(salicylideneiminato)manganese(III)			
Redox reaction of bis-(2-pyridinealdoximate)dioxomolybdate(IV) complex with thiosulphate	CTAB	A slow rate characterizes the aqueous acidic medium compared with the surfactant (CTAB) medium and with the second order rate constant of 0.1299 ± 0.004 and $0.294 \pm 0.02 \text{ dm}^3 \text{ mol}^{-1} \text{ s}^{-1}$, respectively.	72
Oxidation of glutamic acid by bis-(2-pyridinealdoximate)dioxomolybdate(IV) complex	CTAB	Cetyltrimethylammonium bromide in the system increased the oxidation rate of the GTA due to the high impact of hydrophobic and ion interaction between the micelle and substrates.	73

Numerous experimental studies have validated the Piszkiwicz model. By comparing predicted rate constants and reaction rates with actual experimental data, a strong agreement has been observed in many instances.

However, it's important to note that the Piszkiwicz model relies on simplifying assumptions. For instance, it assumes the existence of a single reactive species within micelles and disregards interactions between micelles. While these simplifications make the model mathematically manageable, they may oversimplify the complexities of real systems. Consequently, there can be deviations between model predictions and experimental observations in certain cases, underscoring the necessity for a detailed comprehension of the system's complexity.

3.3. Ion Exchange Model

The ion exchange model, focused on reactions involving charged reactants (38), provides a unique perspective on micellar catalysis. It views micellar aggregates as similar to ion exchange resins, possessing the capability to bind and exchange ions. The essence of the model lies in the concept that the rate of the reaction is profoundly influenced by the exchange of ions between these micellar aggregates and the surrounding bulk solution.

The Ion-Exchange Model provides a detailed understanding of how charged reactants and catalysts interact within micellar catalysis. It emphasizes the significance of ion exchange equilibrium, which plays a crucial role in determining the reaction rate. This model is particularly useful for reactions involving ionic reactants or catalysts, where the exchange of ions between the micelles and the bulk solution significantly impacts the catalytic process.

To work effectively, the model makes two key assumptions:

1. The micellar surface is either saturated with counterions, or the binding constant (β) remains constant.
2. The selectivity of the surface for various counterions can be expressed through a straightforward ion exchange constant.

The value of β , typically falling in the range of 0.6 to 0.9 (74), is independent of surfactant concentration in the presence of counterions. This model allows researchers to predict the effects of various parameters, such as surfactant concentration, temperature, and pH, on the reaction rate. By understanding the factors influencing the ion exchange equilibrium, reaction conditions can be strategically manipulated to enhance catalytic

performance. The exchange between the micelle (M) and the aqueous phase (W) is described by the ion-exchange constant, K_N^X .

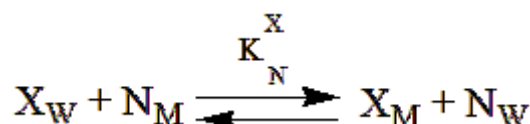


Figure 3: Ion-Exchange model.

$$K_N^X = \frac{[N_W][X_M]}{[X_W][N_M]} \quad (5)$$

N is the reactive ion, and X is the counterion of the surfactant.

$$M_N^S = [N_M]/[D_N], \quad M_X^S = [X_M]/[D_N] \quad \text{and} \quad M_N^S + M_X^S = \beta$$

According to Romsted (10) M_N^S represents the concentration of the reactive ion in moles per liter of Stern layer volume.

$[D_N] = [C - \text{CMC}]$, where C is the concentration of surfactant. S is the neutral substrate bound along with X.

However, directly validating this model experimentally poses challenges. The small scales involved in observing and measuring the ion exchange process within micelles make it complex. Consequently, some assumptions and predictions of the model may require further experimental validation.

While the ion exchange model provides a comprehensive understanding of the interaction between reactants and catalysts within micellar catalysis, it is essential to recognize its limitations. One significant limitation is the difficulty in direct experimental validation due to the small scales involved in observing and measuring the ion exchange process within micelles. This can lead to discrepancies between theoretical predictions and experimental observations. Furthermore, the model assumes a constant level of counterion binding (β) and a straightforward ion exchange constant, which might oversimplify the actual complexities of micellar systems. The model's accuracy is primarily contingent upon these assumptions holding under various experimental conditions. Consequently, some aspects of the model's predictions may require further experimental scrutiny to ensure

reliability. Additionally, the ion exchange model is particularly suited for reactions involving ionic reactants or catalysts. For reactions involving non-ionic species or those predominantly occurring at the micellar interface, alternative models might offer more precise representations. Addressing these limitations is crucial for refining the model and enhancing its applicability to a broader range of catalytic processes.

The ion exchange model is particularly suitable for reactions involving ionic micelles. In this model, the micellar surface acts similarly to an ion-exchange resin, selectively binding and exchanging ions. This model considers the micelle as a charged entity with counterions bound to its surface. The rate of reaction is influenced by the exchange of reactive ions with the micellar-bound counterions, described by the ion-exchange constant, K_N^X (equation 5).

For ionic micelles, the ion exchange model is suitable, whereas the pseudophase model is more fitting for non-ionic micelles. The first-order rate constants exhibit an increasing trend with rising surfactant concentration, reaching stability when the substrate is fully micellar-bound. This pattern is particularly observed when the reactive ion serves as the sole counterion in the solution, aligning with the ion-exchange pseudophase model of micellar catalysis in aqueous systems (35). This behavior has been noted in reactions like nucleophilic addition or substitution by cyanide or bromide ions and in acetal hydrolysis within micellized alkane sulfonic acids.

The practical interpretation of the equilibria (PIE) model extends its utility beyond measuring the intrinsic pK and surface pH of micelles. It can also be effectively employed to determine the surface pH in microemulsions, vesicles, and biological membranes. Furthermore, Romsted and Zanetti have demonstrated that the model remains applicable to micellar solutions containing buffers, even in the presence of added counterions, provided that the exchangeable counterion amounts in the aqueous pseudophase are expressed as activities. The buffer is hydrophilic and carries the same charge as the micelle surface, remaining exclusively in the aqueous phase (75).

The ion exchange model delivers a comprehensive mechanistic understanding of how reactants and catalysts interact within micellar catalysis. It elucidates the transport of reactants into micelles, their interaction with catalysts, and their subsequent exit from the micelles. This comprehension proves invaluable for optimizing reaction conditions and designing more efficient catalytic systems.

By understanding the factors influencing the ion exchange equilibrium, researchers can strategically manipulate reaction conditions to enhance catalytic performance. However, directly observing and measuring the ion exchange process within micelles can be complex due to the small length scales involved, necessitating further experimental validation of some model assumptions and predictions (as summarized in Table 3).

Table 3: Reactions in micellar medium interpreted by ionic exchange model.

REACTION	Micellar medium	Remarks	Ref
Acid hydrolysis of vinyl ethers	SDS CTAB Brij35	In the cases of cationic and non-ionic micelles, minimal effects on rate were observed. However, anionic micelles exhibited an increase in the reaction velocity, and the rate constants reached their maximum values as the concentration of SDS (sodium dodecyl sulfate) increased.	38
Picolinic acid promoted hexavalent chromium oxidation of glycerol	SDS CPC	Reaction inhibits in CPC, whereas it accelerates in SDS.	58
Alkaline fading of malachite green (MG ⁺)	DTAB TX-100 SDS	Piszkiwicz's pseudophase ion exchange model and classical models were used.	63
Hydrophobic n-diazeniumdiolates and the aqueous interface of sodium dodecyl sulfate (SDS) micelles.	SDS	The quantitative analysis of the reaction is achieved successfully through the utilization of the ion exchange model.	76
Application of the pseudophase ion exchange model to a micellar-catalyzed reaction in water-glycerol solutions	CTAB	The hydrolysis of p-nitrophenyl diphenyl phosphate (NPDPP) in the presence of sodium hydroxide (NaOH), micelles of CTAB, and aqueous solutions of glycerol was studied experimentally. The findings were interpreted using the pseudophase ion exchange model (PPIE). The effect of glycerol on micelle formation and its influence on the reaction medium were investigated. The obtained results suggest that the PPIE model can effectively describe micellar catalysis in water-glycerol solutions.	77
Acid-catalyzed hydrolysis of hydrophobic ketals in aqueous cationic micelles: partial failure of the pseudophase ion exchange model	CTAB CTACI	The objective of the study was to investigate the effects of aqueous CTAX, with and without added salt (NaX), on the rate of acid hydrolysis of two hydrophobic micellar-bound ketals. The experiments were conducted at temperatures of 30°C and 40°C. The main purpose was to assess the accuracy of the Pseudophase Ion Exchange (PIE) model in predicting the reactions of neutral organic substrates with co-ions.	78
Reaction between malachite green and	CBDAC HTAAB	The cationic surfactants show catalytic effect, whereas anionic surfactants show inhibitory effect.	79

REACTION	Micellar medium	Remarks	Ref
sodium hydroxide	SDS		
Reduction of ketones by sodium borohydride	CTAB CTAC	Micellar inhibition. A pseudophase ionic exchange model was applied for kinetic analysis.	80
Oxidation of propane-2-ol to acetone by pentavalent vanadium	CPC SDS TX-100	Inhibits in CPC and accelerates in SDS & TX-100.	81
Oxidation of D-Sorbitol by pentavalent vanadium ion	CPC SDS TX-100	SDS and TX-00 can be used as catalysts for obtaining D-glucose from oxidation D-sorbitol.	82

Despite its wide acceptance, experimental verification of the ion exchange model can present challenges. Directly observing and measuring the ion exchange process within micelles can be complex due to the small length scales involved. Consequently, some aspects of the model's assumptions and predictions may necessitate further experimental validation.

It's important to note that the ion exchange model finds its most suitable application in reactions involving charged reactants or catalysts, where the ion exchange equilibrium plays a significant role. For reactions primarily involving non-ionic species or those occurring predominantly at the micellar interface, alternative models or frameworks may offer a more accurate representation of the catalytic process.

3.4. Berezin Model

The Berezin model (25) operates on the premise that the reaction predominantly unfolds within the aqueous core of the micelle. In this model, the reactants are considered to exist in an equilibrium state with the micellar surface, and the surface concentration of these reactants significantly influences the rate of the reaction.

A key assumption of the Berezin model is the existence of a swift equilibrium between the reactants within the bulk solution and those that have been adsorbed onto the micellar surface. This equilibrium signifies that reactants readily interact with the micelle, and this interaction plays a crucial role in governing the overall reaction rate. The Berezin model provides a simplified yet insightful representation of micellar catalysis, shedding light on the interplay between reactants and the micellar environment in these catalytic processes.

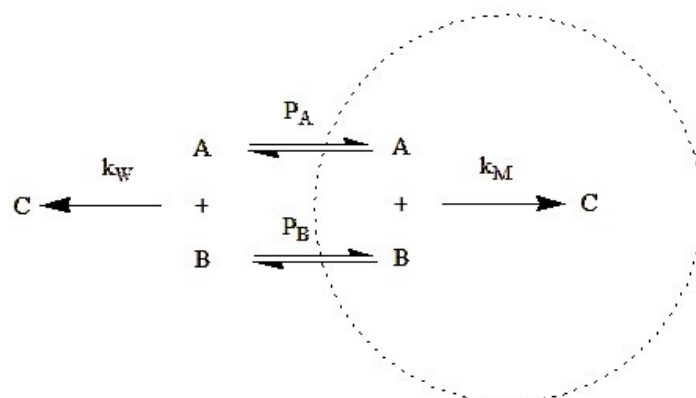


Figure 4: Berezin model.

When examining a surfactant solution above the critical micelle concentration (CMC), we can view it as a two-phase system. In this scenario, we can describe the observed reaction velocity, denoted as V , as an average over the entire system's volume. This means we take into account the contributions from both the micellar phase (V_M) and the aqueous phase (V_w) to calculate the overall reaction rate. This approach allows us to consider how reactions occur within both phases, with their respective reaction velocities, to understand the system's behavior better. In essence, it provides a comprehensive view of the reaction dynamics in surfactant solutions above the CMC.

$$V = V_M C \bar{V} + V_w (1 - C \bar{V}) = k_{\text{exp}} [A]_0 [B]_0 \quad (7)$$

\bar{V} Represents the molar volume of the surfactant, while C denotes the surfactant concentration (expressed in molarity) that is below the critical

micelle concentration (CMC). Under the assumption that the situation adheres to the law of mass action, we derive the following...

$$V_M = k_M [A]_M [B]_M \quad \text{and} \quad V_w = k_w [A]_w [B]_w \quad (8)$$

Equations are employed to establish concentration between the initial total concentrations of reactants, denoted as $[A]_0$ and $[B]_0$, and their actual concentrations within their respective phases.

$$\frac{[A]_M}{[A]_w} = P_A \quad (\text{Partition coefficient}) \quad (9)$$

$$[A]_0 = [A]_M C \bar{V} + [A]_w (1 - C \bar{V}) \quad (10)$$

Equations 5, 6, and 7 collectively lead to the following conclusion:

$$k_{\text{exp}} = \frac{k_M p_A p_B C \bar{V} + k_W (1-C \bar{V})}{(1+K_A C)(1+K_B C)} \quad (11)$$

In the given context, the equation $K_A = (P_A - 1) \bar{V}$ Defines the parameters K_A and K_B . Here, k_W and k_M represent the rate constants for the water and micellar phases, respectively, while k_{exp} signifies the experimentally determined effective reaction rate constant.

Now, as a limiting scenario, if the measured reaction velocity encompasses not only the rates occurring in the micellar and aqueous phases but also the rate of a reaction involving solubilized and unsolubilized reactants, we can express it in the following manner:

$$V = k_M [A]_M [B]_M C \bar{V} + k'_M [A]_M [B]_W C \bar{V} + k''_M [A] \quad (12)$$

In this scenario, various rate constants apply to different phases. For the water and micellar phases, the rate constants are represented as k_W and k_M , respectively. Additionally, there are rate constants k'_M and k''_M for the solubilized and insolubilized phases.

Within the micellar phases, $[A]_W$ and $[B]_W$ are used.

The terms \bar{V} and $(1-C \bar{V})$ correspond to the volume fractions of the micellar and aqueous phases, respectively.

Combining all these factors, the resulting equation captures the complex interplay of reactions in different places of the system.

$$k_{\text{exp}} = \dots \quad (13)$$

The Berezin model offers a successful framework for understanding how micelles impact the rates of bimolecular reactions and provides a means to determine binding constants, as summarized in Table 4. This model simplifies the complex micellar environment, making it more accessible for analysis and comprehension of reaction kinetics with the micelle.

In the Berezin model, the micelle is treated as an effective medium with distinctive properties, such as different dielectric constant solvation characteristics compared to surrounding bulk solvents. This unique perspective enables the model to make quantitative predictions about reaction rates and other kinetic parameters within the micellar system. These predictions can then be compared with experimental data, enhancing our ability to understand and predict reaction behavior in micelles.

Table 4: Reactions in micellar medium interpreted by Berezin model.

REACTION	Micellar medium	Remarks	Ref
Oxidation of dextrose by <i>N</i> -bromo phthalimide	SDS Triton X - 100	In SDS, the rate decreases, and in TX-100, the rate increases. Mechanism explains with Berezin's model.	83
Oxidation of tris (2,2'-bipyridyl) cobalt (iii) by parabenzquinone	SDS	SDS accelerates the reaction and kinetic analysis carried out by using Berezin's model.	84
Hydrolysis of mono- <i>n</i> -ethyl- <i>o</i> -toluidine phosphate	CTAB	The rate of hydrolysis by micelles was examined using the Menger-Portnoy, Piszkiwicz, and Berezin kinetic models. Various thermodynamic parameters were assessed. The rate (surfactant) profile allowed for the determination of kinetic parameters, namely the micellar phase (k_w) and binding constant (K_s).	85
Hydrophobic <i>n</i> -diazoniumdiolates and the aqueous interface of sodium dodecyl sulfate (SDS) micelles	SDS	The rate of NO release from micellar-bound diazeniumdiolates is determined by the surface charge of the micelles.	86
Kinetics of nitrophenol violet anion reaction with OH ⁻ ion:	CTAB, CTAOH	Compared to Piszkiwicz's, Terezin's, and pseudophase ion-exchange models.	87
Kinetics of alkaline fading of methyl violet in micellar solutions of surfactants: comparing	Brij 35, 3-(dimethyldodecylammonio)-propane sulfonate SDS	Each of the kinetic models used for the treatment of experimental data has certain inner assumptions and consequently gives results that are somewhat different in their physical meaning. The comparison of the applicability of the models can be made on the basis of values of standard deviations of model parameters calculated as unknown during the fitting. In this respect, Berezin's and PIE models give better results than application of Piszkiwicz's model	88
Reaction rate of cationic triphenylmethane dyes with water according to Berezin's model	non-ionic cationic anionic zwitterionic	Berezin's model performed well when applied to the description of the micellar effect on the reaction of dye with the hydroxide ion. However, it was revealed that this model does not take into account the change in the local concentration of the HO ⁻ ions due to a compression of the double electric layer upon the addition of reacting ions to the system, as well as the constant of association of the HO ⁻ ions with cationic head groups of surfactant.	89

REACTION	Micellar medium	Remarks	Ref
Oxidation of lactic acid by chromic acid	SDS	Catalysis by SDS. Berezin's model and Piszkievicz's model were applied.	90
The redox reaction of allylthiourea and bis-(2-pyridinealdoximate)dioxomolybdate(IV) complex in an aqueous acidic medium	CTAB, SDS	Piszkievicz and Berezin models are utilized to analyze and interpret the redox properties of allylthiourea when interacting with a Mo(IV) complex in the presence of surfactants. These models' parameters are employed to explain the observed behavior.	91
Analysis of kinetic data for ionic micellar mediated semi-ionic bimolecular reaction	CTAB	The least-squares values obtained from both models show a similar fit to the observed data; the reliability of the calculated K_s values from the Berezin model appears to be higher than those from the Ion Exchange model. This conclusion is drawn from the fact that the K_s values obtained from the BPP model closely match the corresponding K_s values determined through spectrophotometric methods.	92
Oxidation of methanol to formaldehyde	SDS	Rate enhanced by 324-fold times in the presence of SDS.	93
Oxidation of dextrose by N-Bromosuccinimide	SDS TX-100	The catalytic ability is greater for TX-100 than for SDS.	94
Base catalyzed hydrolysis of 4-nitrophenyl esters of phosphoric, phosphoric, and toluene sulfonic acids	Dicationic and mono-cationic surfactants	In micellar pseudophase, the α -effect of the hydroperoxide ion in the peroxyhydrolysis reaction is retained and reaches 100 times.	95
Catalytic oxidation of benzyl alcohol (BA), p-chlorobenzyl alcohol (p-CIBA), and p-anisyl alcohol (p-OMeBA)	Cetylpyridium chloride (CPCI) Dodecylpyridinium chloride (DPCI)	12-fold catalytic enhancement for the oxidation of p-anisyl alcohol in the CPCI micellar environment	96
Reaction of cyanide and picrate ions	TX-100	The reaction mixture was found to enhance the rate of the reaction at the CMC below TX-100.	97
Oxidation of racemic tartaric acid by Ce(IV)	SDS	Plots of pseudo-first-order rate constants in the presence of surfactant (sodium dodecyl sulfate, SDS) against the [SDS] abruptly rise in the concentration range below CMC (critical micelle concentration), after which the rate exponentially falls.	98

However, it's important to reorganize the limitations of the Berezin model. This model assumes a uniform and homogeneous micellar structure, which simplifies the real-world complexity and heterogeneity of micelles. Consequently, the Berezin model is most suitable for reactions that occur within the micelle's core or at the micelle-solvent interface. It may not be well-suited for reactions involving reactants that do not strongly interact with the micellar environment, where more intricate models might be necessary for a precise representation of the catalytic process.

4. CONCLUSION

In conclusion, the exploration of micellar catalysis and kinetic modeling offers invaluable insights into the intricate world of chemical reactions within micelles. Through our examination of various kinetic models, including the Berezin, Piszkievicz, ion exchange, and pseudophase models, we have gained a deeper understanding of the mechanisms governing these reactions and the influence of micelles on their rates. While each model presents its advantages and limitations, their collective contribution has significantly enhanced our comprehension of micellar catalysis. Moving forward, continued research in this field holds great potential for unlocking new avenues for sustainable chemical synthesis and industrial applications. By refining existing models and developing innovative approaches, we can further elucidate the complex interplay between reactants, catalysts, and micellar

environments, paving the way for enhanced efficiency and selectivity in catalytic processes.

4.1. Future Aspects

Future research in micellar catalysis and kinetic modeling holds significant promise for advancing our understanding of complex chemical reactions in heterogeneous environments. By integrating cutting-edge computational techniques with experimental data, researchers can elucidate sophisticated reaction mechanisms and design more efficient catalysts. Additionally, exploring the influence of various parameters such as temperature, pH, and surfactant concentration on reaction kinetics will provide valuable insights for optimizing catalytic processes. Moreover, the development of predictive models capable of accurately simulating micellar systems will facilitate the design of novel catalytic materials with tailored properties. Continued exploration of micellar catalysis and kinetic modeling is poised to unlock new avenues for sustainable chemical synthesis and industrial applications, driving innovation in diverse fields ranging from pharmaceuticals to renewable energy.

5. CONFLICT OF INTEREST

The authors declare that they have no known competing financial interests or personal relationships that could have appeared to influence the work reported in this paper.

6. REFERENCES

1. Kaatze U. Kinetics of Micelle Formation and Concentration Fluctuations in Solutions of Short-Chain Surfactants. *J Phys Chem B* [Internet]. 2011 Sep 8;115(35):10470–7. Available from: [<URL>](#).
2. Perinelli DR, Cespi M, Lorusso N, Palmieri GF, Bonacucina G, Blasi P. Surfactant Self-Assembling and Critical Micelle Concentration: One Approach Fits All? *Langmuir* [Internet]. 2020 Jun 2;36(21):5745–53. Available from: [<URL>](#).
3. Ghosh KK, Sinha D, Satnami ML, Dubey DK, Rodriguez-Dafonte P, Mundhara GL. Nucleophilic Dephosphorylation of p -Nitrophenyl Diphenyl Phosphate in Cationic Micellar Media. *Langmuir* [Internet]. 2005 Sep 1;21(19):8664–9. Available from: [<URL>](#).
4. Kolay S, Ghosh KK, MacDonald A, Moulins J, Palepu RM. Micellization of Alkyltriphenylphosphonium Bromides in Ethylene Glycol and Diethylene Glycol + Water Mixtures: Thermodynamic and Kinetic Investigation. *J Solution Chem* [Internet]. 2008 Jan 29;37(1):59–72. Available from: [<URL>](#).
5. Ghosh KK, Verma SK. Kinetics of α -chymotrypsin catalyzed hydrolysis of 4-nitrophenyl acetate in ethanolamine surfactants. *Indian J Biochem Biophys* [Internet]. 2008;45(5):350–3. Available from: [<URL>](#).
6. Ghosh KK, Verma SK. Effects of head group of cationic surfactants on the hydrolysis of p -nitrophenyl acetate catalyzed by α -chymotrypsin. *Int J Chem Kinet* [Internet]. 2009 Jun 25;41(6):377–81. Available from: [<URL>](#).
7. Ghosh KK, Sinha D, Satnami ML, Dubey DK, Shrivastava A, Palepu RM, et al. Enhanced nucleophilic reactivity of hydroxamate ions in some novel micellar systems for the cleavage of Parathion. *J Colloid Interface Sci* [Internet]. 2006 Sep;301(2):564–8. Available from: [<URL>](#).
8. Saha R, Ghosh A, Saha B. Kinetics of micellar catalysis on oxidation of p-anisaldehyde to p-anisic acid in aqueous medium at room temperature. *Chem Eng Sci* [Internet]. 2013 Aug;99:23–7. Available from: [<URL>](#).
9. Saha R, Ghosh A, Saha B. Micellar catalysis on 1,10-phenanthroline promoted hexavalent chromium oxidation of ethanol. *J Coord Chem* [Internet]. 2011 Nov 10;64(21):3729–39. Available from: [<URL>](#).
10. Ghosh A, Saha R, Saha B. Suitable combination of promoter and micellar catalyst for kilo fold rate acceleration on propanol to propionaldehyde conversion in aqueous media. *J Ind Eng Chem* [Internet]. 2014 Jan;20(1):345–55. Available from: [<URL>](#).
11. Saha R, Ghosh A, Sar P, Saha I, Ghosh SK, Mukherjee K, et al. Combination of best promoter and micellar catalyst for more than kilo-fold rate acceleration in favor of chromic acid oxidation of d-galactose to d-galactonic acid in aqueous media at room temperature. *Spectrochim Acta Part A Mol Biomol Spectrosc* [Internet]. 2013 Dec;116:524–31. Available from: [<URL>](#).
12. Acharjee A, Rakshit A, Chowdhury S, Malik S, Barman MK, Ali MA, et al. Micellar catalyzed and heteroaromatic base promoted rate enhancement of oxidation of an alicyclic alcohol in aqueous medium. *J Mol Liq* [Internet]. 2019 Mar;277:360–71. Available from: [<URL>](#).
13. Ghosh A, Saha R, Mukherjee K, Ghosh SK, Bhattacharyya SS, Laskar S, et al. Selection of Suitable Combination of Nonfunctional Micellar Catalyst and Heteroaromatic Nitrogen Base as Promoter for Chromic Acid Oxidation of Ethanol to Acetaldehyde in Aqueous Medium at Room Temperature. *Int J Chem Kinet* [Internet]. 2013 Mar 22;45(3):175–86. Available from: [<URL>](#).
14. Chowdhury KM, Mandal J, Saha B. Micellar catalysis of chromium(VI) oxidation of ethane-1,2-diol in the presence and absence of 2,2'-bipyridine in aqueous acid media. *J Coord Chem* [Internet]. 2009 Jun 1;62(11):1871–8. Available from: [<URL>](#).
15. Mukherjee K, Ghosh A, Saha R, Sar P, Malik S, Saha B. Best combination of promoter and micellar catalyst for the rapid conversion of sorbitol to glucose. *Spectrochim Acta Part A Mol Biomol Spectrosc* [Internet]. 2014 Mar;122:204–8. Available from: [<URL>](#).
16. Acharjee A, Rakshit A, Chowdhury S, Ali MA, Singh B, Saha B. Mixed anionic-nonionic micelle catalyzed oxidation of aliphatic alcohol in aqueous medium. *J Mol Liq* [Internet]. 2020 Apr;303:112655. Available from: [<URL>](#).
17. Saha R, Ghosh A, Saha B. Combination of best promoter and micellar catalyst for chromic acid oxidation of 1-butanol to 1-butanal in aqueous media at room temperature. *Spectrochim Acta Part A Mol Biomol Spectrosc* [Internet]. 2014 Apr;124:130–7. Available from: [<URL>](#).
18. Ghosh SK, Saha R, Mukherjee K, Ghosh A, Bhattacharyya SS, Saha B. Micellar Catalysis on 1,10-Phenanthroline Promoted Chromic Acid Oxidation of Propanol in Aqueous Media. *J Korean Chem Soc* [Internet]. 2012 Feb 20;56(1):164–8. Available from: [<URL>](#).
19. Ghosh SK, Ghosh A, Saha R, Saha B. Suitable combination of promoter and micellar catalyst for chromic acid oxidation of formaldehyde to formic acid in aqueous acid media at room temperature. *Phys Chem Liq* [Internet]. 2015 Jan 2;53(1):146–61. Available from: [<URL>](#).
20. Chowdhury S, Rakshit A, Acharjee A, Mahali K, Saha B. Surface phenomenon in micellar media: An excellent controlling factor for oxidation of fatty aldehyde in aqueous medium. *J Mol Liq* [Internet]. 2020 Jul;310:113224. Available from: [<URL>](#).
21. Chowdhury S, Rakshit A, Acharjee A, Kumar D, Saha B. Anionic micelles and their ideal binary mixture: Worth media for sustainable oxidation of hydrophobic alcohol. *J Mol Liq* [Internet]. 2022 Jan;346:117118. Available from: [<URL>](#).

22. Ansari TN, Xu G, Preston A, Gao P. Recent Highlights in Micellar Catalysis: An Industrial Outlook. *Org Process Res Dev* [Internet]. 2024 Apr 19;28(4):816–30. Available from: [<URL>](#).
23. Senchukova AS, Fetin PA, Perevyazko I, Lezov AA, Fetina VI, Vaitusionak AA, et al. Water-Soluble Copolymers of Styrene and a Surfactant Monomer in Micellar Catalysis. *J Polym Res* [Internet]. 2024 Mar 27;31(3):80. Available from: [<URL>](#).
24. Acharjee A, Rakshit A, Chowdhury S, Saha B. Micelle catalysed conversion of 'on water' reactions into 'in water' one. *J Mol Liq* [Internet]. 2021 Jan;321:114897. Available from: [<URL>](#).
25. Berezin I V, Martinek K, Yatsimirskii AK. Physicochemical Foundations of Micellar Catalysis. *Russ Chem Rev* [Internet]. 1973 Oct 31;42(10):787–802. Available from: [<URL>](#).
26. Osipov AP, Martinek K, Yatsimirskii AK, Berezin I V. Micellar effects in the acylation of N-substituted imidazoles by p-nitrophenyl esters of carboxylic acids. *Bull Acad Sci USSR Div Chem Sci* [Internet]. 1974 Sep;23(9):1905–9. Available from: [<URL>](#).
27. Martinek K, Osipov AP, Yatsimirski AK, Berezin IV. Mechanism of micellar effects in imidazole catalysis. *Tetrahedron* [Internet]. 1975 Jan;31(7):709–18. Available from: [<URL>](#).
28. Bunton CA, Romsted LS, Smith HJ. Quantitative treatment of micellar catalysis of reactions involving hydrogen ions. *J Org Chem* [Internet]. 1978 Oct 1;43(22):4299–303. Available from: [<URL>](#).
29. Bunton CA, Romsted LS, Savelli G. Tests of the pseudophase model of micellar catalysis: its partial failure. *J Am Chem Soc* [Internet]. 1979 Feb 1;101(5):1253–9. Available from: [<URL>](#).
30. Bunton CA, Romsted LS, Thamavit C. The pseudophase model of micellar catalysis. Addition of cyanide ion to N-alkylpyridinium ions. *J Am Chem Soc* [Internet]. 1980 May 1;102(11):3900–3. Available from: [<URL>](#).
31. Bunton CA, Frankson J, Romsted LS. Reaction of p-nitrophenyldiphenyl phosphate in cetyltrimethylammonium fluoride. *J Phys Chem* [Internet]. 1980 Oct 1;84(20):2607–11. Available from: [<URL>](#).
32. Romsted LS. A General Kinetic Theory of Rate Enhancements for Reactions between Organic Substrates and Hydrophilic Ions in Micellar Systems. In: *Micellization, Solubilization, and Microemulsions* [Internet]. Boston, MA: Springer US; 1977. p. 509–30. Available from: [<URL>](#).
33. Mittal KL, Lindman B. *Surfactants in Solution* [Internet]. Mittal KL, Lindman B, editors. Boston, MA: Springer US; 1984. Available from: [<URL>](#).
34. Mittal KL. *Solution Chemistry of Surfactants* [Internet]. Mittal KL, editor. Boston, MA: Springer New York; 1979. Available from: [<URL>](#).
35. Bunton CA, Romsted LS. Reactive Counterion Surfactants. In: *Solution Behavior of Surfactants* [Internet]. Boston, MA: Springer US; 1982. p. 975–91. Available from: [<URL>](#).
36. Piszkiwicz D. Micelle catalyzed reactions are models of enzyme catalyzed reactions which show positive homotropic interactions. *J Am Chem Soc* [Internet]. 1976 May 1;98(10):3053–5. Available from: [<URL>](#).
37. Piszkiwicz D. Positive cooperativity in micelle-catalyzed reactions. *J Am Chem Soc* [Internet]. 1977 Mar 1;99(5):1550–7. Available from: [<URL>](#).
38. Velázquez MM, García-Mateos I, Herraes MA, Rodríguez LJ. Pseudo-phase ion-exchange model for micellar catalysis in the acid hydrolysis of vinyl ethers. *Int J Chem Kinet* [Internet]. 1984 Mar 19;16(3):269–76. Available from: [<URL>](#).
39. Menger FM, Portnoy CE. Chemistry of reactions proceeding inside molecular aggregates. *J Am Chem Soc* [Internet]. 1967 Aug 1;89(18):4698–703. Available from: [<URL>](#).
40. Bal S, Satnami ML, Kolay S, Palepu RM, Dafonte PR, Ghosh KK. Kinetic Studies of Micelle - Assisted Reaction of p-Nitrophenyl Acetate with Benzo-Hydroxamate Ion in Water-Ethylene Glycol Mixtures. *J Surf Sci Technol* [Internet]. 2007;23(1-2):33–48. Available from: [<URL>](#).
41. Rispens T, Engberts JBFN. A Kinetic Study of 1,3-Dipolar Cycloadditions in Micellar Media. *J Org Chem* [Internet]. 2003 Oct 1;68(22):8520–8. Available from: [<URL>](#).
42. Kumar D, Rub MA. Interaction of ninhydrin with chromium-glycylglycine complex in the presence of dimeric gemini surfactants. *J Mol Liq* [Internet]. 2018 Jan;250:329–34. Available from: [<URL>](#).
43. Kumar D, Rub MA. Studies of interaction between ninhydrin and Gly-Leu dipeptide: Influence of cationic surfactants (m-s-m type Gemini). *J Mol Liq* [Internet]. 2018 Nov;269:1–7. Available from: [<URL>](#).
44. Kumar D, Rub MA. Study of the interaction between ninhydrin and chromium(III)-amino acid in an aqueous-micellar system: Influence of gemini surfactant micelles. *J Mol Liq* [Internet]. 2020 Mar;301:112373. Available from: [<URL>](#).
45. Kumar D, Rub MA. Role of cetyltrimethylammonium bromide (CTAB) surfactant micelles on kinetics of $[Zn(II)-Gly-Leu]^+$ and ninhydrin. *J Mol Liq* [Internet]. 2019 Jan;274:639–45. Available from: [<URL>](#).
46. Akram M, Kumar D, Kabir-ud-Din. Influence of cationic gemini and conventional CTAB on the interaction of $[Cr(III)-Gly-Tyr]^{2+}$ complex with ninhydrin. *Colloids Surfaces A Physicochem Eng Asp* [Internet]. 2013 Jul;428:92–9. Available from: [<URL>](#).

47. Kumar D, Neo KE, Rub MA, Tan ZL, Beh WL, Wong HL. Study of copper(II)-glycylphenylalanine complex with ninhydrin in aqueous and cationic CTAB micellar media: A kinetic and mechanistic approach. *J Mol Liq* [Internet]. 2015 Mar;203:204-9. Available from: [<URL>](#).
48. Akram M, Saeed AAM, Kabir-ud-Din. Micellar, salt, and organic solvent effects on the rate of [Cu(II)-Gly-I-Ala]⁺ complex-ninhydrin reaction. *J Mol Liq* [Internet]. 2015 Sep;209:367-73. Available from: [<URL>](#).
49. Bhattarai A, Abdul Rub M, Posa M, Saha B, Kumar D. Catalytic impacts of cationic twin headed and tailed gemini surfactants toward study of glycine and ninhydrin in sodium acetate-acetic acid buffer system. *J Mol Liq* [Internet]. 2022 Aug;360:119442. Available from: [<URL>](#).
50. Kumar D, Rub MA, Akram M, Kabir-ud-Din. Interaction between dipeptide (glycyl-phenylalanine) and ninhydrin: Role of CTAB and gemini (16-s-16, s=4, 5, 6) surfactant micelles. *J Colloid Interface Sci* [Internet]. 2014 Mar;418:324-9. Available from: [<URL>](#).
51. Alghamdi YG, Rub MA, Kumar D. Influence of twin-headed gemini micellar system on the study of methionine amino acid with ninhydrin in buffer solution. *R Soc Open Sci* [Internet]. 2023 Feb 15;10(2):221229. Available from: [<URL>](#).
52. Sachin KM, Karpe SA, Singh M, Bhattarai A. Study on surface properties of sodiumdodecyl sulfate and dodecyltrimethylammonium bromide mixed surfactants and their interaction with dyes. *Heliyon* [Internet]. 2019 Apr;5(4):e01510. Available from: [<URL>](#).
53. Kumar D, Rub MA. Study of the reaction of ninhydrin with tyrosine in gemini micellar media. *RSC Adv* [Internet]. 2019;9(38):22129-36. Available from: [<URL>](#).
54. Rub MA, Bhattarai A, Saha B, Jaffari ZH, Thu HT, Kumar D, et al. Effect of dicationic gemini surfactants on the rate of reaction between ninhydrin and arginine. *Chem Pap* [Internet]. 2022 May 20;76(5):2865-74. Available from: [<URL>](#).
55. Muñoz M, Rodríguez A, Del Mar Graciani M, Luisa Moyá M. Micellar medium effects on the hydrolysis of phenyl chloroformate in ionic, zwitterionic, nonionic, and mixed micellar solutions. *Int J Chem Kinet* [Internet]. 2002 Jan 28;34(7):445-51. Available from: [<URL>](#).
56. Rodríguez A, Muñoz M, Graciani M del M, Fernández Chacón S, Moyá ML. Kinetic Study in Water-Ethylene Glycol Cationic, Zwitterionic, Nonionic, and Anionic Micellar Solutions. *Langmuir* [Internet]. 2004 Nov 1;20(23):9945-52. Available from: [<URL>](#).
57. López-Cornejo P, Pérez P, García F, de la Vega R, Sánchez F. Use of the Pseudophase Model in the Interpretation of Reactivity under Restricted Geometry Conditions. An Application to the Study of the [Ru(NH₃)₅pz]²⁺+S₂O₈²⁻ Electron-Transfer Reaction in Different Microheterogeneous Systems. *J Am Chem Soc* [Internet]. 2002 May 1;124(18):5154-64. Available from: [<URL>](#).
58. Ghosh SK, Basu A, Saha R, Ghosh A, Mukherjee K, Saha B. Micellar catalysis on picolinic acid promoted hexavalent chromium oxidation of glycerol. *J Coord Chem* [Internet]. 2012 Apr 10;65(7):1158-77. Available from: [<URL>](#).
59. Hassan M, AlAhmadi MD, Mosaid M. Micellar effect on the kinetics of oxidation of methyl blue by Ce(IV) in sulfuric acid medium. *Arab J Chem* [Internet]. 2015 Jan;8(1):72-7. Available from: [<URL>](#).
60. Ugbaga Nkole I, Ola Idris S, Abdulkadir I, David Onu A. Oxidation of aspartic acid with molybdenum-oxime-ligand framework in acidified-aqua and interfacial active media: Menger-Portnoy kinetic model. *Inorg Chem Commun* [Internet]. 2024 Mar;161:111979. Available from: [<URL>](#).
61. Ewais HA, Basaleh AS, Al Angari YM. Kinetic studies on the persulfate oxidation of methylene blue in the absence and presence of silver(I) as a catalyst in aqueous and micellar media. *Int J Chem Kinet* [Internet]. 2023 Jun 20;55(6):271-80. Available from: [<URL>](#).
62. Katre Y, Goyal N, Singh AK. Effect of CTAB Micelle on the Oxidation of L-Leucine by N-Bromophthalimide: a Kinetic Study. *Zeitschrift für Phys Chemie* [Internet]. 2011 Jan 1;225(1):107-24. Available from: [<URL>](#).
63. Samley B, Toosi AR. Kinetics Study of Malachite Green Fading in the Presence of TX-100, DTAB and SDS. *Bull Korean Chem Soc* [Internet]. 2009 Sep 20;30(9):2051-6. Available from: [<URL>](#).
64. Nkole IU, Idris SO, Abdulkadir I, Onu AD. Application of Piszkievicz model on the electron transfer reaction of dithionite ion and bis-(2-pyridinealdoximate)dioxomolybdate(IV) complex. *Sci Rep* [Internet]. 2022 Dec 22;12(1):22125. Available from: [<URL>](#).
65. Hassan M, Al-Dhoun M, Batineh Y, Najjar AA, Dahadha A, Ibrahim QA. Micellar and Polymer Catalysis in the Kinetics of Oxidation of L-lysine by Permanganate Ion in Perchloric Acid Medium. *South African J Chem* [Internet]. 2021;75:73-9. Available from: [<URL>](#).
66. Laguta AN, Eltsov SV. Micellar effects in kinetics of interaction of malachite green and brilliant green with water. *Kharkov Univ Bull Chem Ser* [Internet]. 2017;28(51):96-103. Available from: [<URL>](#).
67. Kumar Singh A, Sen N, Kumar Chatterjee S, Susan MABH. Kinetic study of oxidation of paracetamol by water-soluble colloidal MnO₂ in the presence of an anionic surfactant. *Colloid Polym Sci* [Internet]. 2016 Oct 28;294(10):1611-22. Available from: [<URL>](#).
68. Pare B, Vijay R, Bhagwat VW, Fogliani C. Catalytic effect of pre-micellar aggregates on oxidative degradation of acridine orange by acidic chlorite. *J Indian Chem Soc* [Internet]. 2007;85:443-7. Available from: [<URL>](#).

69. Swain R, Panigrahi GP. Kinetics and mechanism of oxidation of hydroxylaminehydrochloride by vanadium (V) in the presence of sodium lauryl sulphate. *Indian J Chem* [Internet]. 2001;40(11):1191-5. Available from: [<URL>](#).
70. Yadav H, Bhoite SA, Singh AK. Kinetic and mechanistic study of micellar effect of hydrolytic reaction of Di-2-methoxy-4-nitroaniline phosphate. *J Dispers Sci Technol* [Internet]. 2017 Jan 2;38(1):121-31. Available from: [<URL>](#).
71. Ibrahim I, Idris SO, Abdulkadir I, Onu DA. Thioglycolic acid oxidation by N, N'-phenylenebis(salicylideneiminato)manganese(III) in DMSO/H₂O: Effects of sodium dodecylsulfate and cetyltrimethylammonium bromide. *Results Chem* [Internet]. 2022 Jan;4:100541. Available from: [<URL>](#).
72. Nkole IU, Idris SO, Abdulkadir I, Onu AD. Redox reaction of bis-(2-pyridinealdoximate)dioxomolybdate(IV) complex with thiosulphate ion in aqueous acidic and surfactant media. *Inorg Chem Commun* [Internet]. 2022 Jun;140:109468. Available from: [<URL>](#).
73. Nkole IU, Idris SO, Abdulkadir I, Onu AD. Cationic Surfactant-Based Catalysis on the Oxidation of Glutamic Acid by Bis-(2-pyridinealdoximate)dioxomolybdate(IV) Complex. *Catal Letters* [Internet]. 2023 Dec 17;153(12):3581-90. Available from: [<URL>](#).
74. Bunton CA. Reaction Kinetics in Aqueous Surfactant Solutions. *Catal Rev* [Internet]. 1979 Jan 5;20(1):1-56. Available from: [<URL>](#).
75. Romsted LS, Zanette D. Quantitative treatment of indicator equilibria in micellar solutions of sodium decyl phosphate and sodium lauryl sulfate. *J Phys Chem* [Internet]. 1988 Aug 1;92(16):4690-8. Available from: [<URL>](#).
76. Mohr A, Pozo Vila T, Korth H, Rehage H, Sustmann R. Hydrophobic N -Diazeniumdiolates and the Aqueous Interface of Sodium Dodecyl Sulfate (SDS) Micelles. *ChemPhysChem* [Internet]. 2008 Nov 10;9(16):2397-405. Available from: [<URL>](#).
77. Ionescu LG, Trindade VL, de Souza EF. Application of the Pseudophase Ion Exchange Model to a Micellar Catalyzed Reaction in Water-Glycerol Solutions. *Langmuir* [Internet]. 2000 Feb 1;16(3):988-92. Available from: [<URL>](#).
78. Armstrong C, Gotham W, Jennings P, Nikles J, Romsted LS, Versace M, et al. Acid Catalyzed Hydrolysis of Hydrophobic Ketals in Aqueous Cationic Micelles: Partial Failure of The Pseudophase Ion Exchange Model. In: *Surfactants in Solution* [Internet]. Boston, MA: Springer US; 1989. p. 197-209. Available from: [<URL>](#).
79. Raducan A, Olteanu A, Puiu M, Oancea D. Influence of surfactants on the fading of malachite green. *Open Chem* [Internet]. 2008 Mar 1;6(1):89-92. Available from: [<URL>](#).
80. Cerichelli G, Coreno M, Mancini G. Reduction of Ketones by Sodium Borohydride in the Presence of Cationic Surfactants. *J Colloid Interface Sci* [Internet]. 1993 Jun;158(1):33-9. Available from: [<URL>](#).
81. Ghosh SK, Basu A, Paul KK, Saha B. Micelle catalyzed oxidation of propan-2-ol to acetone by penta-valent vanadium in aqueous acid media. *Mol Phys* [Internet]. 2009 Apr 10;107(7):615-9. Available from: [<URL>](#).
82. Saha B, Chowdhury KM, Mandal J. Micellar Catalysis on Pentavalent Vanadium Ion Oxidation of D-Sorbitol in Aqueous Acid Media: A Kinetic Study. *J Solution Chem* [Internet]. 2008 Sep 10;37(9):1321-8. Available from: [<URL>](#).
83. Singh M. Mechanistic aspects of oxidation of dextrose by N-bromophthalimide in acidic medium: a micellar kinetic study. *Res Chem Intermed* [Internet]. 2013 Feb;39(2):469-84. Available from: [<URL>](#).
84. Subba Rao P V., Krishna GS., Ramakrishna K. Kinetics and mechanism of oxidation of tris(2,2'-bipyridyl-cobalt(II) by p-benzoquinone-Micellar effect of sodium dodecyl sulphate. *Indian J Chem* [Internet]. 1991;30A:136-9. Available from: [<URL>](#).
85. Yadav H, Boite SA. Hydrolysis of mono-n-ethyl-toluidine phosphate. *Chem Rev Lett* [Internet]. 2014;3(11):628-35. Available from: [<URL>](#).
86. Mohr PC, Mohr A, Vila TP, Korth HG. Localization of Hydrophobic N -Diazeniumdiolates in Aqueous Micellar Solution. *Langmuir* [Internet]. 2010 Aug 3;26(15):12785-93. Available from: [<URL>](#).
87. Laguta AN, Eltsov S V., Mchedlov-Petrosyan NO. Micellar rate effects on the kinetics of nitrophenol violet anion reaction with HO⁻ ion: Comparing Piszkievicz's, Berezin's, and Pseudophase Ion-Exchange models. *J Mol Liq* [Internet]. 2019 Mar;277:70-7. Available from: [<URL>](#).
88. Laguta AN, Eltsov S V., Mchedlov-Petrosyan NO. Kinetics of alkaline fading of methyl violet in micellar solutions of surfactants: Comparing Piszkievicz's, Berezin's, and pseudophase ion-exchange models. *Int J Chem Kinet* [Internet]. 2019 Feb 14;51(2):83-94. Available from: [<URL>](#).
89. Laguta A. Quantitative analysis of micellar effect on the reaction rate of cationic triphenylmethine dyes with water according to Berezin's model. *Kharkov Univ Bull Chem Ser* [Internet]. 2020;35(58):37-44. Available from: [<URL>](#).
90. Panigrahi GP, Mishra SK. Micellar-catalysis: Effect of sodium lauryl sulphate in the oxidation of lactic acid by chromic acid. *J Mol Catal* [Internet]. 1993 May;81(3):349-62. Available from: [<URL>](#).
91. Nkole IU, Idris SO, Onu AD, Abdulkadir I. The study of Piszkievicz's and Berezin's models on the redox reaction of allylthiourea and bis-(2-pyridinealdoximate)dioxomolybdate(IV) complex in an aqueous acidic medium. *Beni-Suef Univ J Basic Appl Sci* [Internet]. 2022 Dec 16;11(1):68. Available from: [<URL>](#).

92. Cheong MY, Ariffin A, Niyaz Khan M. A Comparative Analysis of Pseudophase Ion-Exchange (PIE) Model and Berezin Pseudophase (BPP) Model: Analysis of Kinetic Data for Ionic Micellar-mediated Semi-ionic Bimolecular Reaction. Bull Korean Chem Soc [Internet]. 2007 Jul 20;28(7):1135-40. Available from: [<URL>](#).
93. Sar P, Ghosh A, Ghosh D, Saha B. Micellar catalysis of quinquivalent vanadium oxidation of methanol to formaldehyde in aqueous medium. Res Chem Intermed [Internet]. 2015 Aug 5;41(8):5565-86. Available from: [<URL>](#).
94. Singh M. Kinetics and Mechanism of Micellar Catalyzed Oxidation of Dextrose by N-Bromosuccinimide in H₂SO₄ Medium. Int J Carbohydr Chem [Internet]. 2014 Dec 1;2014:783521. Available from: [<URL>](#).
95. Turovskaya MK, Belousova IA, Razumova NG, Gaidash TS, Prokop'eva TM, Kotenko AA, et al. Reactivity of Inorganic α -Nucleophiles in Acyl Transfer in Aqueous and Micellar Media: IV. Peroxyhydrolysis of Acyl Derivatives in Organized Microheterogeneous Systems¹. Russ J Org Chem [Internet]. 2024 Feb 29;60(2):252-8. Available from: [<URL>](#).
96. Layek M, Karmakar P, Pal P, Rahaman SM, Kundu S, Mitra M, et al. Influence of Chain Length and Concentration-Dependent Morphological Switching on Oxidation of Aromatic Alcohols in a Micellar Environment. Ind Eng Chem Res [Internet]. 2024 Jan 24;63(3):1334-48. Available from: [<URL>](#).
97. Albadani A, Hassan M, Obayed FA. Kinetic study of factor affecting the reaction of cyanide and picrate ions in the presence of micellar catalyst. Chem Int [Internet]. 2022;8(4):136-43. Available from: [<URL>](#).
98. Sahu S, Kumar Padhy R, Prasad Nanda S. Surfactant catalyzed electron transfer mechanism in the oxidation of racemic tartaric acid by Ce(IV). Mater Today Proc [Internet]. 2023;78:786-91. Available from: [<URL>](#).



Development of the Nanoemulsion Formulation Containing Ylang Ylang Essential Oil for Topical Applications, and Evaluation of Its *In Vitro* Cytotoxicity as well as ADMET Profile

Nesrin Karabatak^{1†}, Bahar Gok^{2†}, Yasemin Budama Kilinc^{2,3*}

¹Graduate School of Natural and Applied Science, Yildiz Technical University, 34220 Istanbul, Turkey.

²Faculty of Chemical and Metallurgical Engineering, Department of Bioengineering, Yildiz Technical University, 34220 Istanbul, Turkey.

³Health Biotechnology Joint Research and Application Center of Excellence, 34220 Istanbul, Turkey.

[†]The authors contributed equally.

Abstract: Ultraviolet (UV) rays damage DNA, causing adverse effects such as photoaging and cancer on the skin. For the well-being of individuals, there is a need to develop innovative skin products with high effectiveness using protective and therapeutic agents. In our study, a nanoemulsion (NE) formulation containing Ylang-ylang essential oil (YO), which has many biological active properties such as antimicrobial, antioxidant, anti-inflammatory, and anticancer, was produced by the ultrasonic emulsification method and characterized. The thermodynamic stability was evaluated, and its release profile determined the dialysis membrane technique. The cytotoxic effect of YO-NE was examined with the *in vitro* method on the HacaT cell line using the MTT method and *in silico* method using the ADMET profile. Dynamic light scattering (DLS) results showed that the average droplet size of the YO-NE formulation was 184.1 ± 2.307 nm, the polydispersity index (PdI) was 0.151 ± 0.006 , and the Zeta potential (ζ) -10.8 ± 0.400 mV. As a result of release studies, it was observed that $99.98 \pm 1.00\%$ of YO release from NE occurred within 5 hours. Based on the thermodynamic stability test results, it was determined that the developed formulation did not show sedimentation or phase separation. Cytotoxicity results revealed that the YO-NE formulation was safe. All the results indicated that the YO-NE formulation might be considered a non-toxic product candidate with physicochemical properties suitable for topical use.

Keywords: Nanoemulsion (NE), Ylang-ylang essential oil (YO), Cytotoxicity, Topical application.

Submitted: January 13, 2024. **Accepted:** June 23, 2024.

Cite this: Karabatak N, Gok B, Budama Kilinc Y. Development of the Nanoemulsion Formulation Containing Ylang Ylang Essential Oil for Topical Applications, and Evaluation of Its *In Vitro* Cytotoxicity as well as ADMET Profile. JOTCSA. 2024;11(3): 1181-96.

DOI: <https://doi.org/10.18596/jotcsa.1418645>

***Corresponding author's E-mail:** yaseminbudama@gmail.com

1. INTRODUCTION

Skin, the largest body organ, plays a critical role in maintaining homeostasis and creates a protective barrier between the environment and the body (1). However, exposure of this barrier to excessive sunlight may disrupt the barrier function of the skin (2). Exposure to ultraviolet (UV) radiation can lead to the overproduction of reactive oxygen species (ROS) in skin cells, DNA damage, lipid peroxidation, protein modification, and cell apoptosis (3). These factors can lead to skin problems such as photoaging, wrinkles, inflammation, and even skin cancer (4). Plants or bioactive components obtained from plants can be used to overcome these problems (5-7).

Plants and active substances derived from plants are widely used in producing cosmetic materials for protection from UV rays, antioxidants, cell renewal and minimizing the effects of photoaging (8). Essential oils (EOs) from plants, their usage in the plant defence mechanisms against different parasite species and infections is used in various medical approaches with biochemical effects such as antiviral, anticancer, antibacterial, and anti-inflammatory activities (9). Ylang-ylang, also commonly known as *Cananga odorata*, is a fast-growing tree commonly found in tropical Asian countries such as Malaysia, Philippines, Indonesia and some islands of the Indian Ocean. Ylang-ylang EOs are currently widely used in the food, perfume,

cosmetics industry and aromatherapy to treat many diseases such as asthma, fever, inflammation, wounds, microbial infections, colds, etc (10,11). The Ylang-ylang plant and especially the EOs obtained from it contain antioxidant components. The antioxidant effects of EO obtained from ylang-ylang help to reduce oxidative stress and positively support body health by fighting free radicals that cause cellular damage (12).

Although EOs have many biological activities, their clinical applications are limited due to their hydrophobic structure and poor stability in different environmental conditions such as air, light, humidity, and high temperature. To overcome the limitations in the clinical use of EOs, they are prepared in nano-sized and suitable dosage forms for the application method (13). The development of innovative formulations in the field of nanomedicine has enabled increasing the therapeutic efficacy and reducing the toxicity of natural compounds and their bioactive components (14-16).

Among nanoformulations as nanoemulsions (NEs), frequently preferred for topical use, are translucent and/or transparent emulsions characterized by nano-sized droplets (17). When used as a topical carrier, small droplets have a large surface-to-volume ratio, allowing the activated compound to spread easily into the skin and provide high absorption. In addition, nanoemulsions can increase the solubility of lipophilic compounds and change the skin's diffusion barrier depending on the nanoemulsion's composition. Thus, they may enable the drug to penetrate better into the skin layers (18,19). The nanometer size of NE improves its transmission target and specificity, making it more perfect and effective than pure EO (20). NE formulations are safe for human health. They increase the solubility, bioabsorption, biomembrane permeability, and bioavailability of poorly soluble active substances. Additionally, NEs are biocompatible, biodegradable, and do not have mutagenic effects. Thanks to their controlled release properties, NEs minimize the toxicity of the active ingredient and contribute to a better therapeutic effect (21,22). Additionally, NEs contain fewer surfactants than microemulsions, and these surfactants are environmentally friendly, cost-effective, and economically viable (20).

In this study, YO-NE nanoformulation was prepared using the ultrasonic emulsification method and then characterized by different techniques. DLS was used to determine parameters such as average droplet size, ζ potential, and PdI. The thermodynamic (centrifugation and thermal stress test) and physicochemical stability of the YO-NE formulation were evaluated. The release profile of the YO-NE formulation was determined with a UV-Vis spectrophotometer using the dialysis membrane method. The cytotoxic activity of YO-NE was evaluated by the MTT method using the HacaT cell line. Finally, the ADMET profile of YO was considered.

2. EXPERIMENTAL SECTION

2.1. Material

Ylang-ylang oil was purchased from Aksuvital, Ethanol, Kolliphore® P-188, DL-alpha tocopherol acetate from Sigma-Aldrich; undecyl alcohol and isodecyl neopentanoate were purchased from Schülke. Caprylic/capric triglyceride was purchased from Gattefosse. The HaCaT cell line used in the MTT assay was purchased from Thermo Fisher Scientific, MTT from Biomaterials, and trypsin/EDTA (0.25%) was purchased from Gibco. Fetal Bovine Serum (FBS) and penicillin-streptomycin Solution were purchased from Biological Industries.

2.2. Method

2.2.1. Development of the YO-NE

YO-NE formulation, in which the aqueous phase is a continuous phase (O/W), was prepared using the ultrasonic emulsification method (23). The water phase of NE was obtained by dissolving 7.5% Kolliphore® P-188 in water. The oil phase was formed by the addition of 1% undecyl alcohol, 1.25% transcutool, 1.5% isodecyl neopentanoate, 10% caprylic capric triglyceride, 0.2% DL-alpha tocopherol acetate, 3% Labrafil and 0.5% YO. These phases were prepared separately, and then the water phase was added to the oil phase. The premixing step was performed using a homogenizer (Witeg, Germany) at 8100 rpm for 5 minutes. After pre-mixing, the emulsion was ultrasonicated at 50% amplitude for 20 minutes using a 20 kHz and 750 W sonicator (Ultrasonics, USA).

2.2.2. Analysis of droplet size, PdI and ζ potential of YO-NE

The parameters such as PdI, average droplet size, and Zeta potential (ζ) values of YO-NE were measured using Zeta Sizer Nano ZS (Malvern Instruments, UK). All measurements were performed at 25°C. Specimens were diluted as 1:100 in sterile water and carried out in triplicate (24).

2.2.3. Analysis of pH and electrical conductivity of YO-NE

A pH meter (Ohaus® STARTER 3100M) with a conductivity probe was used to determine the electrical conductivity and pH of the YO-NE formulation. All analyses were performed in triplicate at 25°C.

2.2.4. Active ingredient content analysis

Active ingredient content analysis is used to assess the stability of drugs in pharmaceutical formulation. In this experiment, the YO-NE formulation (250 μ L) was dissolved in 10 mL ethanol and sonicated in an ultrasonic bath for 30 min (25). The YO content in the sample was then determined using the equation for the spectrophotometric analysis curve of YO.

2.2.5. Morphology analysis

The morphology of YO-NEs was examined by transmission electron microscopy (TEM) (JEOL TEM 1400 Plus). A carbon-coated grid was used in the analyses. A sufficient amount of the formulation was placed on the grid, and images were displayed under a voltage of 80 kV (26).

2.2.6. YO-NE accelerated stability tests

Following the preparation of the YO-NE formulation accelerated thermodynamic stability tests consisting of centrifugation and thermal stress tests were carried out within 24 hours. 0.5 g of the YO-NE formulation was centrifuged at 4500 rpm for 30 minutes at $25 \pm 1^\circ\text{C}$. Macroscopically, it was evaluated for any phase separation or turbidity (27). For thermal stability testing, 0.5 g of YO-NE formulation was carried out in a water bath at $40\text{--}80^\circ\text{C}$ with temperature increments of 5°C each. The thermal stability test of the YO-NE formulation was evaluated in terms of organoleptic features organoleptic aspects such as color, odor, texture and phase separation.

2.2.7. Calibration curve

Seven different YO concentrations (2.34, 4.68, 9.36, 18.75, 37.5, 75 and 150 $\mu\text{g}/\text{mL}$) were prepared in ethanol. Then, the absorbance values of these samples were measured with a UV-Vis Spectrophotometer (Shimadzu, Japan) at 283.2 nm, and the calibration curve was drawn (28). This curve was used to determine the amount of YO in the release study of YO-NEs.

2.2.8. Release study

Since the YO-NE formulation is intended for topical application, the release study was performed at skin pH 5.5 and temperature (32°C) (29,30). 1 g of YO-NE was added to the dialysis capsule, and 1 mL of release medium was taken at specified time intervals from a water bath shaking at 120 rpm and added with an equal volume of fresh release medium. The amount of YO released was determined by analyzing the absorbance of the samples with a UV-Vis spectrometer at 283.2 nm. YO release (%) was calculated using Equation (1).

$$\text{Release\%} = \frac{\text{Released YO}}{\text{Total YO}} \cdot 100 \quad (1)$$

2.2.9. Preparation of cell culture

The cytotoxic effect of YO and YO-NE on HaCaT cells was evaluated using MTT assay. HaCaT cell line was incubated in Dulbecco's Modified Eagle's Medium (DMEM) medium containing 100 U/mL penicillin-100 g/mL streptomycin antibiotic and 10% Fetal Bovine Serum (FBS) in a 5% CO_2 incubator at 37°C until 80% confluent. The proliferating cells were washed with 5 mL sterile phosphate buffer solution (PBS). To lift off the cells from the flask, 1 mL of trypsin-EDTA was added and incubated for 5 minutes. To neutralize the effect of trypsin, 5 mL of culture medium was added to the cells and the cells were centrifuged at 123 g for 5 minutes. The supernatant was discarded, and the pellet was dissolved in 1 mL of medium and counted on a thoma slide (31).

2.2.10. Cell viability test (MTT)

The *in vitro* safety of YO and YO-NE was evaluated by MTT test using the HaCaT cell line. In this method, cells were seeded in a 96-well plate ($1 \times 10^4/\text{well}$) and incubated for 24 hours at 37°C in a humidified incubator with 5% CO_2 . After incubation, five different concentrations of YO and YO-NE (0.25, 0.5, 1, 3 and 5 mg/mL) were added to the wells and

incubated for 24 hours. In this test system, 0.1% DMSO was used to prepare concentrations of YO. DMEM was used to prepare the concentrations of NEs. For YO, DMEM containing 0.1% DMSO was used as a control, while for YO-NE, only DMEM was used. Ten μL of MTT solution was added to each well and incubated for 4 hours. The medium was carefully removed, and the colored formazan crystals were dissolved in 100 μL of dimethyl sulfoxide (DMSO). The absorbance given by the cells in the plates was measured at 570 nm using a microplate reader. YO and YO-NE untreated control value was expressed as 100% cell viability. Equation (2) was used to determine cell viability.

$$\text{Cell viability} = \left(\frac{\text{OD}_{570} \text{ of sample}}{\text{OD}_{570} \text{ of control}} \right) \times 100 \quad (2)$$

2.2.11. Physicochemical and pharmacokinetic analyses of linalool and germacrene-D

Linalool is found in many aromatic plant families, such as Rutaceae and Lamiaceae. Linalool is a naturally occurring acyclic monoterpene alcohol. Numerous traditional and edible plants, including coriander, peppermint and cinnamon, produce essential oils containing linalool (32). The Food and Drug Administration (FDA) has deemed linalool as GRAS safe (GRAS) as a synthetic flavoring agent as well as an excipient in foods for humans (21 CFR 182.60) and as an ingredient in animal drugs and foods (21 CFR 582.60) (33). The chiral hydrocarbon germacrene-D is a widely available plant component that is recognized as a critical intermediate in the biosynthesis of many sesquiterpenes (34). These sesquiterpene hydrocarbons are biosynthetic precursors of various (often oxidized) structures from which humans have exploited many compounds with significant medicinal and other bioactivities (35).

Kalagatur et al. (2018) (11) characterised ylang-ylang oil by GC-MS and reported that the main compounds in the oil were linalool (29.15%), germacrene-D (11.82%) and thymol (8.45%). In this study, physicochemical and pharmacokinetic analyses were carried out due to the high amounts of linalool and germacrene-D compounds in ylang-ylang oil.

Drug susceptibility characteristics were analyzed using SwissADME (absorption, distribution, metabolism and excretion) and the PkCSM tool to predict crucial pharmacokinetic properties such as drug candidate molecules' absorption, distribution, metabolism, excretion, and toxicity (ADMET). The canonical simplified molecular input line entry system (SMILES) format of the compound was retrieved from PubChem (<https://pubchem.ncbi.nlm.nih.gov/>) and entered into SwissADME and PkCSM (<http://www.swissadme.ch/>) (<https://biosig.lab.uq.edu.au/pkcsM/>) has been sent (36,37). Drug susceptibility is determined by Lipinski's rule of five (RO5) (38).

2.2.12. Estimation of biological activity

The evaluation of the overall biological potential of the compounds was performed using PASS (<http://195.178.207.233/PASS/index.html>). This software estimates the predicted activity spectrum of a compound with probability (P_a = probability of 'activity' and P_i = probability of 'inactivity'). The cut-off value was set as $P_a \geq 0.7$ (39). This method is based on the training set's structural activity relationship (SAR) analysis, which contains more than 205,000 compounds exhibiting more than 3750 biological activities. Compounds that show a probability that the P_a value is higher than the P_i value are those considered to be possible for a specific pharmacological activity (40).

3. RESULTS AND DISCUSSION

3.1. Characterization of YO-NE

The ultrasonic homogenization method is a fast and effective method to create stable NEs with appropriate droplet sizes and low PdI (41,42). In this study, NE formulation was synthesized with ultrasonic homogenization, followed by characterization and stability studies.

DLS, one of the most preferred methods, was employed to determine the hydrodynamic size, PdI, and ζ potential value of the synthesized NE (43,44). The results were given in Figure 1 and Figure 2. The average droplet size of the empty NE was 183.2 ± 1.498 nm. However, the average droplet size of YO-NE was 187 ± 2.307 nm. The most important advantage of NEs over emulsions is that they are nanosystems with small droplet sizes of 20-200 nm (45). The small droplet size of NEs provides many advantages, such as overcoming difficulties, separation, flocculation and coalescence due to gravity (46,47). Many studies have reported that droplet sizes between 100-200 nm may benefit NEs in topical applications due to their excellent penetrability and controlled release capabilities (48,49). Based on the average droplet size data, the

YO-NE formulation was considered suitable for topical administration.

PdI value is essential for the homogeneity of droplet sizes in NE and the stability of the formulation. A PdI value of <0.1 means a narrow size distribution of droplets, and this is the indication of the formulation homogeneity. A PdI value of >0.2 indicates a wide dimensional distribution of droplets, i.e., heterogeneity of the formulation (50). It was determined that the PdI value of empty NE was 0.190 ± 0.020 and the PdI value of YO-NE was 0.151 ± 0.006 . The results showed that the droplets formed have a tight size range, i.e., homogeneous.

Ozdemir et al. (2023) (51) found that the average droplet size of the NE formulation (F2) containing etodolac was 163.5 ± 2.2 , PdI 0.141 ± 0.02 , zeta potential -33.1 ± 1.7 . Gündel et al. (2020) (52) found the average droplet size of NE formulation containing eucalyptus as 68 ± 0.15 , PdI 0.18 ± 0.01 , zeta potential -9.09 ± 0.65 . Our results coincided with those presented in previous studies in the literature.

ζ potential is used to calculate the charge on the surface of NE droplets and to indirectly determine the electric charge of particles in a heterogeneous system (53). The minus charge in the ζ potential value is due to the carboxylic acid groups of fatty acids used in the formulation of fatty acids (54). The ζ potential of empty NE was found to be -10.7 ± 0.252 mV and the ζ potential of YO-NE was found to be -10.8 ± 0.400 mV.

Kildaci et al. (2021) (55) obtained a stable LSO-NE for topical application, an acceptable mean droplet size of 90.61 ± 0.94 , a PdI value of 0.15 ± 0.008 and a zeta potential value of 9.64 ± 0.55 mV. Kilinc et al. (2022) (56) obtained a stable CA-NE for topical application and found an average droplet size of 120.4 ± 6.39 nm, PdI value of 0.180 ± 0.018 , and zeta value of 11.5 ± 1.15 mV. This study's results were similar to those presented in previous studies in the literature.

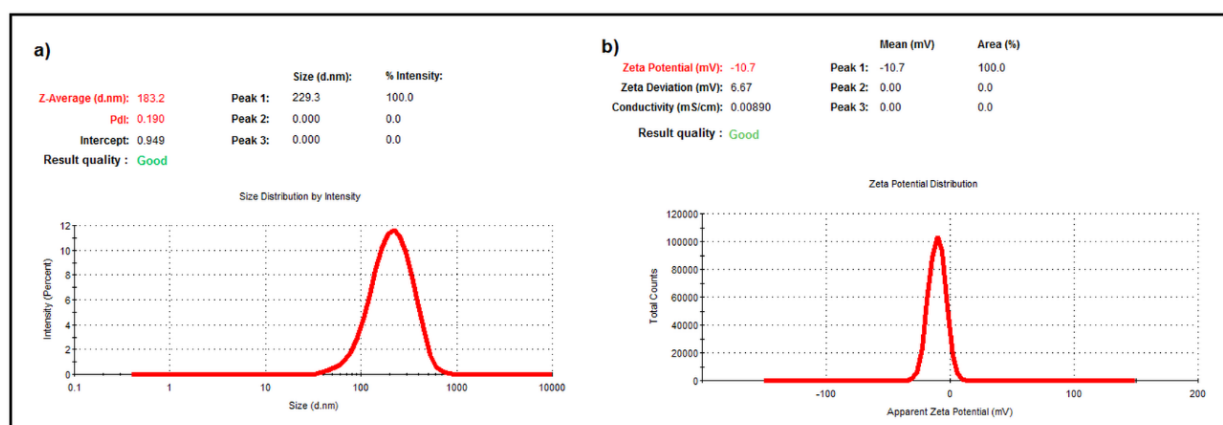


Figure 1: DLS analyses of the empty NE. (a) Average droplet size plot and PdI, (b) ζ potential graph.

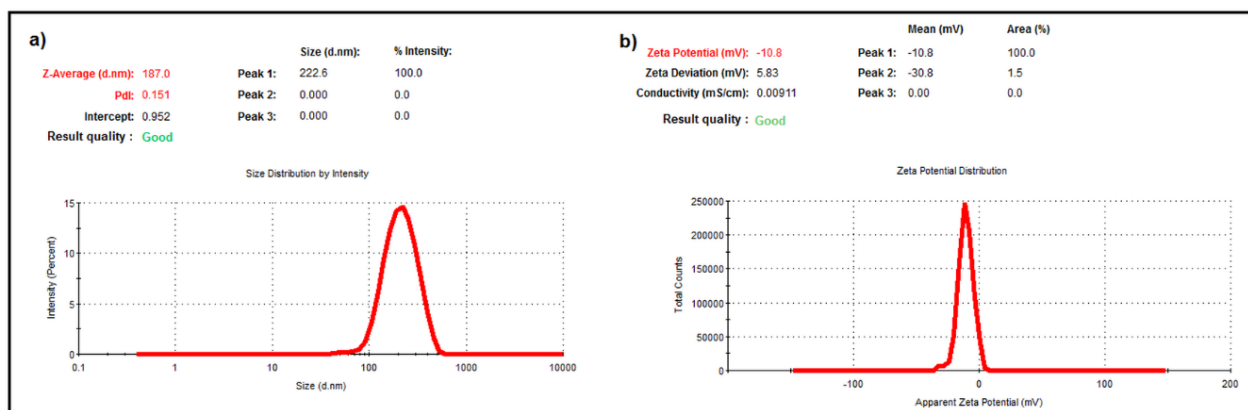


Figure 2: DLS analyses of YO-NE (a) Average droplet size plot and PdI, (b) ζ potential graph.

3.2. pH and Conductivity

The pH value is crucial for assessing the stability of nanoemulsions. pH changes in the formulation suggest the possibility of chemical reactions leading to problems in the stability and quality of the final product (57). The pH value of the skin is approximately 5.5 and generally a pH in the range of 4.0 to 7.0 is appropriate for topical applications. In conclusion, according to the data obtained from our study, the pH value of YO-NE is 5.83, which makes it appropriate for topical application (Table 1). Rashid et al. (2021) (58) determined the pH value of methotrexate-loaded nanoemulsion as 5.81 ± 0.22 , which is an acceptable value for application as transdermal systems since it is within the specified range scale of the physiological pH of the skin. Hammodi et al. (2020) (59) found the pH value (5.96 ± 0.025) of letrozole loaded NE formulation to be in the acceptable range for topical use. Our results are similar to those results presented in previous studies in the literature.

Conductivity is the measurement of the amount of free ions and water present in the solution and the determination of its response. The O/W formulation is suitable for use in the cosmetic industry as its structure is less oily after topical application (60). This parameter allows the determination of the kind of NE prepared. The high conductivity of YO-NE ($92.63 \mu\text{S}/\text{cm}$) indicates that the aqueous phase is a continuous phase and the nanoemulsion formed is an oil-in-water nanoemulsion (O/W). In this study, YO-NE formulations' pH and conductivity values are higher than empty-NE (Table 1). Wang et al., (2020) (61) reported the effect of pH on both the hydrodynamic diameter of droplets and the conductivity of NEs. In this effect, the hydrodynamic diameter of the droplets gradually increases with increasing pH. Regulation of pH changes the ionic strength and, therefore, affects the droplet size of NEs. As the pH value increases, the conductivity of NEs gradually increases, which means that the ionic strength increases simultaneously. These results explain why YO-NEs have higher pH and conductivity values than empty-NEs.

Table 1: The pH and conductivity values of NEs. (Data are presented as mean \pm SD).

Formulation	pH	Conductivity ($\mu\text{S}/\text{cm}$)
Empty-NE	4.48 ± 0.02	87.33 ± 0.65
YO-NE	5.83 ± 0.02	92.63 ± 5.90

3.3. Active Ingredient Content Analysis

Active substance content analysis is critical for any dosage form. The amount of active ingredient in the product should not deviate from the amount specified on the label beyond certain limits during the shelf life of the formulation (62). In this study, NE content (%) was determined as $90.00 \pm 0.01\%$ on the day of production. This result shows that it is able to protect the YO loaded in the final NE formulation against degradation.

3.4. Morphology Analysis

Electron microscopy provides high-resolution images for structural examination of droplets in nanoemulsion formulations. Figure 3 shows the TEM image of the YO-NE formulation. TEM analysis supported characterization studies of the synthesized nanoemulsion formulation. The image showed that the formulation had a spherical morphology and a homogeneous and monodisperse distribution, supporting the PdI results obtained from DLS analyses.

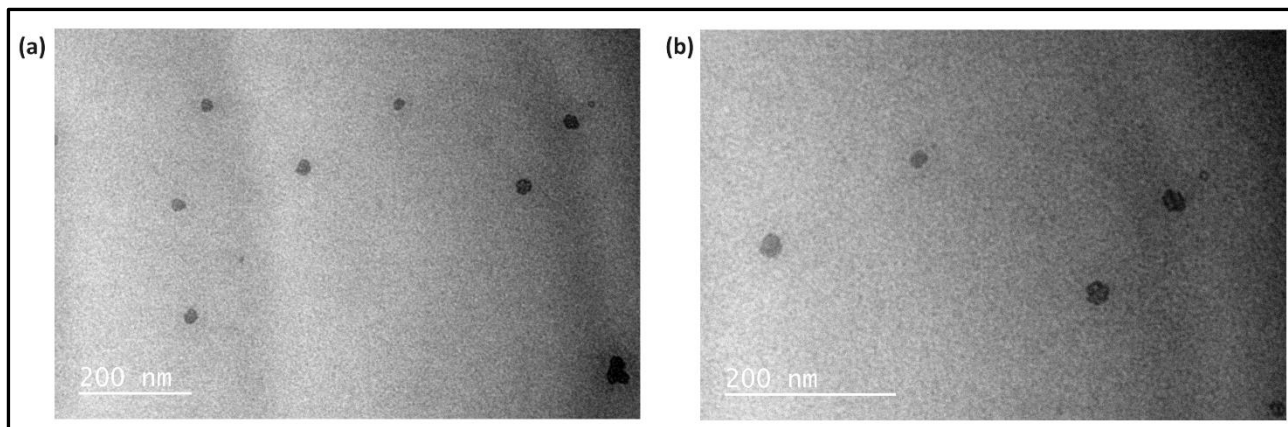


Figure 3: TEM image of YO-NE.

3.5. Accelerated Stability Tests

Stability is essential for formulations developed as product candidates. It provides information about the shelf life of the product candidate. A nanoemulsion formulation must remain physically stable with little or no change in droplet size throughout its shelf life. The creaming and phase separation rate of NEs (regarding shelf life) can be evaluated by gravitational force (63) and thermal stability (64). In the literature, emulsions have been assessed for any phase separation or turbidity as a result of centrifuge testing (27,60,65) and analyzed for organoleptic properties such as colour, odour, texture and phase separation as a result of thermal

stress testing (26,66). YO-NEs showed no physical changes or phase separation following 4,500 rpm gravitational force and thermal stability tests for 30 min (Table 2). In addition DLS results were given in Table 3.

3.6. Calibration Curve of YO

YO solutions were prepared in ethanol at different concentrations (2.34, 4.68, 9.36, 18.75, 37.5, 75 and 150 µg/mL). Then, the absorbance values of these samples were measured at 283.2 nm with a UV-Vis spectrophotometer, and the calibration curve shown in Figure 4 was drawn.

Table 2: Accelerated stability test data of the NEs.

Formulation	Organoleptic properties
Empty NE	Milky aspect
YO-NE	Milky aspect

Table 3: DLS results before and after preliminary stability tests.

Results	Average Droplet Size(nm)	Polydispersity Index (PdI)	Zeta potential (mV)
Before Stability Tests	184.1±2.307	0.151±0.006	-10.8±0.400
After Thermal Test	192.1±5.524	0.143±0.015	-9.31±0.792
After Centrifuge Test	172.5±5.374	0.163±0.042	-11.3±0.070

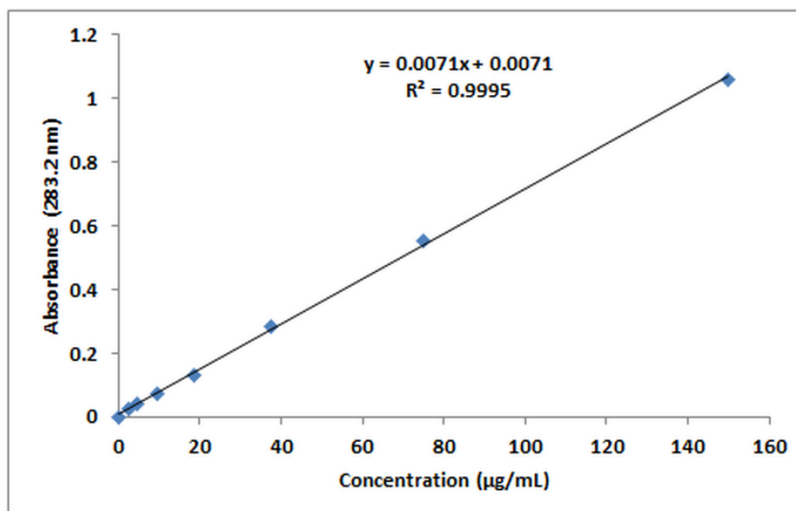


Figure 4: Calibration curve of YO (n=3).

3.7. Release Study Results of YO-NE

Oil-in-water (O/W) type NEs are unique systems that offer higher transparency, stability, biological activity, better physical and chemical properties, and better-controlled release (67). In this study, a release study of YO-NE formulation was carried out by comparing it with YO by diffusion membrane method under simulated skin pH and temperature conditions.

Figure 5 presents the % release of YO as a function of time. As seen in Figure 5, free YO was observed to be released from the membrane very quickly. While 98.84% of YO was released in the first 45 minutes, 99.98±1.00% of YO was released from YO-NE within 5 hours.

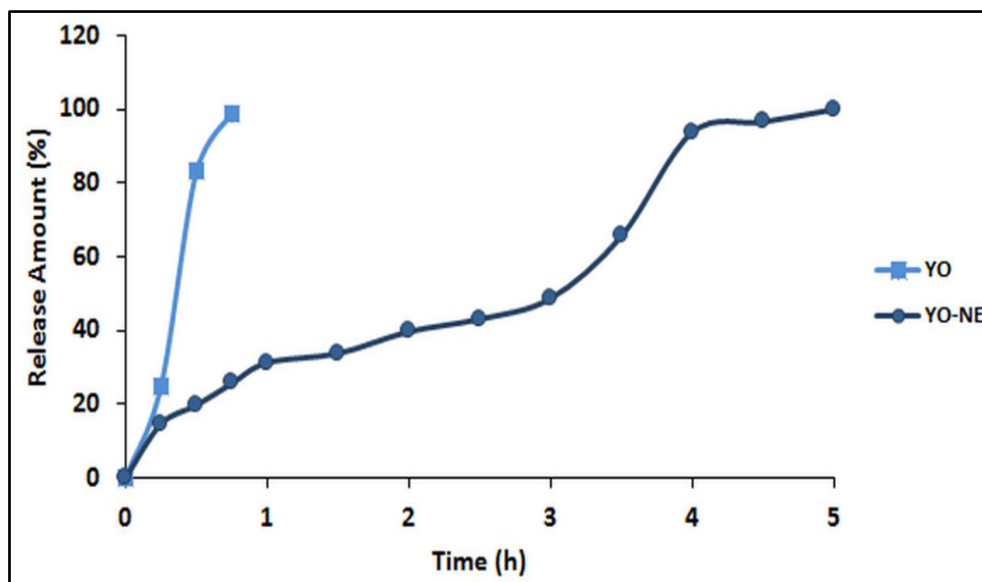


Figure 5: Release profile of YO-NEs.

While free YO molecules are released quickly, the release profile obtained by formulating YO as nanoemulsion ensures continuous release and long-term maintenance of a constant amount of oil (68,69).

The release of active ingredients from the nanoemulsion is controlled by interactions between the drug and surfactant or by partitioning the drug between the oil and water phases. Small droplet size and higher surface area in nanoemulsions will allow adequate release of the loaded drug. The release occurs in a controlled manner (70). Surfactant content is an essential factor affecting the release rate from the oil-containing nanoemulsion system. High surfactant ratio formulations have a slower release rate than low surfactant ratio formulations (71).

Shah et al (2019) (72) developed seven different NE formulations containing moxifloxacin, showing that these formulations released more than 90% of the drug content within 3 hours. Botros et al. (2020) (73) reported that almost all active ingredients were released from the formulation within 4.5 hours. These results are quite suitable for a topical preparation whose skin contact time is generally around 6 hours. Moreover, this short-term release indicates that its active ingredient is suitable for absorption and also provides good bioavailability (73). Our findings are similar to the literature.

3.8. Cytotoxicity Analysis of YO-NE

MTT assay was performed to determine the cytotoxic effect of YO and YO-NE formulation. This assay is

based on the metabolic activity of living cells by reducing MTT to formazan crystals. Since the overall mitochondrial activity of the cell population is related to the number of viable cells, the MTT assay is commonly used to evaluate the cytotoxic effects on cell lines or primary diseased tissues *in vitro* (74,75).

The cytotoxic activity of YO and YO-NE formulation was determined using HaCaT cells. HaCaT cells are easily used in skin toxicity studies due to being the first cell line subjected to cosmetic agents applied to the skin, high experimental reproducibility, ease of use, rapid proliferation and low cost (31). According to ISO standards, cell viability above 80% does not have a cytotoxic effect; 80% to 60% is low; 60% to 40% is medium; and below 40% is cytotoxic (76). The results showed that all concentrations of YO (0.25, 0.5, 1, 3, 5 mg/mL) reduced cell viability in HaCaT cells by 55.75 ± 3.25 %, 41.10 ± 3.64%, 40.70 ± 3.65 %, 39.66 ± 4.02%, and 31.34 ± 2.04%, respectively (p<0.05). All concentrations of YO-NE (0.25, 0.5, 1, 3, 5 mg/mL) were found to have 96.62±1.44%, 83.29±2.52%, 82.30±2.64%, 81.69±1.24%, 67.95±0.80% cell viability in HaCaT cells, respectively (p<0.05). However, the concentrations of YO-NE tested (except 5 mg/mL: low cytotoxicity) did not show any cytotoxic effect on HaCaT cells. As shown in Figure 6, concentrations of 0.25 mg/mL, 0.5 mg/mL, 1 mg/mL, and 3 mg/mL YO-NE formulation had over 80% cell viability compared to the control group. This result indicates that the encapsulation of YO with NE makes it more cytocompatible compared to YO. Similar results were reported in literature (70,77,78).

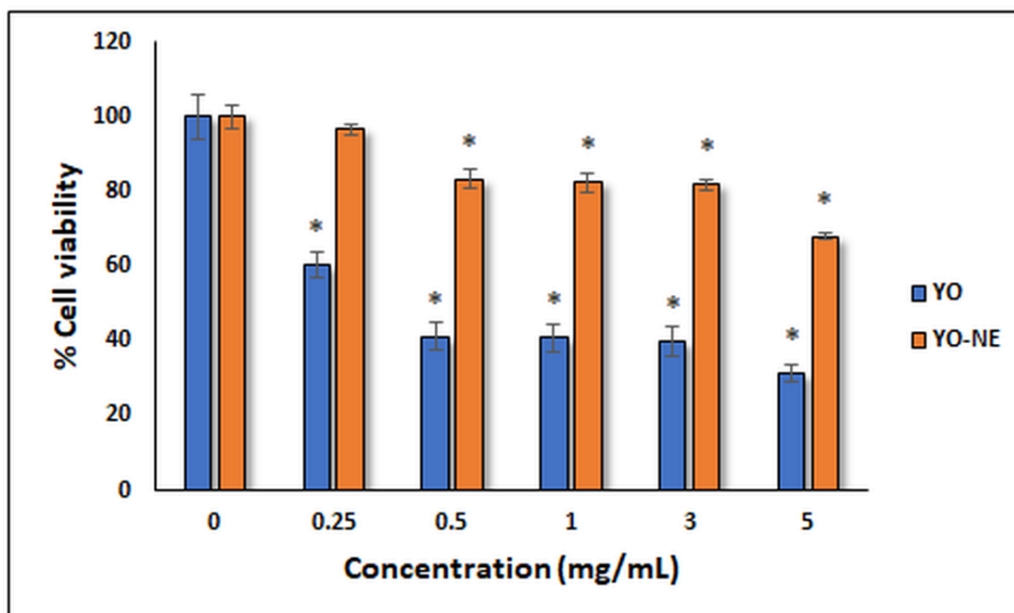


Figure 6: Cytotoxicity data of YO and YO-NE on HaCaT cells. The asterisk (*) indicates that the difference between the control group and the treatment groups is significant at the $p < 0.05$ level.

Solubility, instability and toxicity of lipophilic drugs pose problems. One of the most effective solutions to target these drugs is the formulation of NEs of lipophilic nutraceuticals. The solubility of lipophilic compounds increases as they disperse in the aqueous phase of the emulsion, preventing them from coming into direct contact with body fluids and tissues, thus reducing toxicity. Moreover, NEs provide high bioavailability of small amounts of encapsulated lipophilic substance to cells. They can, therefore, be used to study the uptake of encapsulated drug-active substance in cell cultures, improve the growth conditions and viability of cells, and conduct *in vitro* toxicity studies of lipophilic drugs (79). MTT results showed lower cytotoxicity of YO-NE compared to YO, indicating the nanoemulsion's controlled release properties and that YO's encapsulation is a suitable strategy to reduce its cytotoxicity towards HaCaT cells. Compared to YO, YO-NE still showed high biocompatibility even at higher concentrations and did not significantly affect HaCaT cell viability (80).

3.9. Analysis of Physicochemical and Pharmacokinetic Properties of Linalool and Germacrene-D

Kalagatur et al. (2018) (11) characterized ylang-ylang oil by GC-MS and reported that the main compounds in the oil's structure were linalool (29.15%), germacrene-D (11.82%), and thymol (8.45%). Physicochemical and pharmacokinetic analyses were performed to determine whether linalool and germacrene-D compounds in ylang-ylang oil are drugs (33). Various molecular properties such as absorption, distribution, metabolism, excretion, and structural properties such as molecular weight, number of hydrogen bond acceptors or donors, lipophilicity, and molar refractivity were investigated (39).

The physicochemical and pharmacokinetic properties of the compounds (Linalool, Germacrene-D) are

shown in Table 4 and Table 5. The Bioavailability Radar was displayed when predicting physicochemical properties such as lipophilicity, size, polarity, solubility, flexibility, and saturation (Figure 7). The radar plot shows that the selected compounds linalool and germacrene-D are within the pink area. This indicates a good bioavailability profile for the compounds and better drug similarity of the compounds alone. The pink area, the radar plot of molecules following Lipinski's rule of five, means that it is drug-like. According to Lipinski's rule of five, in order for a chemical compound to be orally active in humans, it must fulfill at least three of the following criteria: molecular weight ≤ 500 , XLOGP3 < 3.5 , hydrogen bond acceptor ≤ 10 , hydrogen bond donor ≤ 5 and molar refractivity = 40-130 (36). In our study, Linalool complies with the rule of five. Germacrene-D violated the rule of one since MLOGP > 4.15 . These two chemical compounds were accepted as drug analogs as drug as they met the Lipinski's rules. Therefore, ylang-ylang oil containing these chemical compounds has a high potential to be drug analogs (55).

The bioavailability of a drug depends on the absorption processes and first-pass metabolism in the liver, which depends on the solubility and permeability of the compound. Drugs with optimum log P and low molecular mass (< 500) also have high permeability (81). In our study, these two compounds have high Caco-2 cell permeability as the permeability (nm/sec) > 0.90 . The selected linalool and germacrene-D compounds exhibited negative Log Kp values (skin permeability) of -1.737 and -1.429, indicating that they may be suitable as promising compounds for transdermal delivery.

James et al. (2023) (82) found the log Kp value of the linalool compound to be -1.43. Drioiche et al. (2023) (83) found the log Kp value of Germacrene-D compound to be -1.429. In estimating skin permeability, the log Kp value should be in the range

of -8.0 to -1.0. In this study, the Log Kp values of linalool and germacrene-D compounds were found in the recommended range and similar to the studies in

the literature. These results ensure good dermal penetration of these compounds.

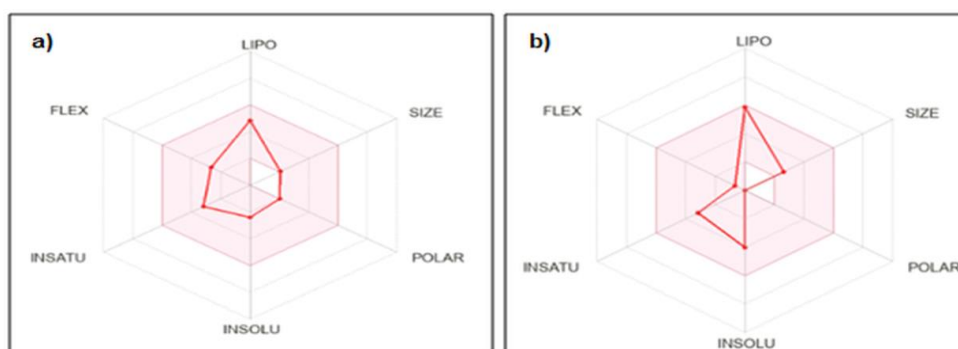


Figure 7: Bioavailability radar showing and signaling drug susceptibility to Linalool (a) and Germacrene-D (b)

CYP450 and its isoforms belong to the hemoprotein family and play an important role in drug metabolism and clearance. Inhibition of isoforms leads to lower clearance and accumulation of the drug or its metabolism. Gastrointestinal (GI) absorption indicates the capacity of the drug to be absorbed and pass into the bloodstream. A compound without CYP450 inhibition and with high GI absorption properties implies that the compound has a good capacity for metabolization and absorption (39). In our study, Linalool and Germacrene-D compounds did not cause CYP450 inhibition and showed high GI

absorption of over 90%. The ability of a drug to cross the blood-brain barrier and enter the brain is a parameter that must be taken into account to help reduce or ameliorate side effects and toxicity (37). These two compounds provided values above $\log BB > 0.3$ and were found to be easily and well distributed into the brain and thus, able to bind to specific receptors. These two compounds showed good drug clearance values, and neither was a substrate for organic cation transporter 2 (OCT2). Furthermore, no hERG 1 channel inhibition or toxicity was predicted from the compounds.

Table 4: Linalool and Germacrene-D ADMET Properties.

Property	Physicochemical properties	Linalool	Germacrene-D
Absorption	Water solubility (log mol/L)	-2.612	-5.682
	Caco-2 permeability (log Papp in 10^{-6} cm/s)	1.493	1.436
	Intestinal absorption (human) (% Absorbed)	93.163	95.59
	Skin Permeability (log Kp)	-1.737	-1.429
	P-glycoprotein substrate (Yes/No)	No	No
	P-glycoprotein I inhibitor (Yes/No)	No	No
	P-glycoprotein II inhibitor (Yes/No)	No	No
Distribution	VDss (human) (log L/kg)	0.152	0.544
	Fraction unbound (human) (Fu)	0.484	0.261
	BBB permeability (log BB)	0.598	0.723
	CNS permeability (log PS)	-2.339	-2.138
Metabolism	CYP2D6 substrate (Yes/No)	No	No
	CYP3A4 substrate (Yes/No)	No	No
	CYP1A2 inhibitor (Yes/No)	No	No
	CYP2C19 inhibitor (Yes/No)	No	No
	CYP2C9 inhibitor (Yes/No)	No	No
	CYP2D6 inhibitor (Yes/No)	No	No
	CYP3A4 inhibitor (Yes/No)	No	No
Excretion	Total Clearance (log ml/min/kg)	0.446	1.42
	Renal OCT2 substrate (Yes/No)	No	No
Toxicity	AMES toxicity (Yes/No)	No	No
	Max. tolerated dose (human) (log mg/kg/day)	0.774	0.497
	hERG I inhibitor (Yes/No)	No	No
	hERG II inhibitor (Yes/No)	No	No
	Oral Rat Acute Toxicity (LD50)	1.704	1.634
	Oral Rat Chronic Toxicity (LOAEL)	2.024	1.413
	Hepatotoxicity (Yes/No)	No	No
	Skin Sensitisation (Yes/No)	Yes	Yes
	<i>T. pyriformis</i> toxicity (log ug/L)	0.515	1.671
	Minnow toxicity (log mM)	1.277	0.257

Table 5: Physicochemical properties of Linalool and Germacrene-D.

Physicochemical properties	Linalool	Germacrene-D
Formula	C ₁₀ H ₁₈ O	C ₁₅ H ₂₄
Molecular weight	154.25 g/mol	204.357 g/mol
Number of heavy atoms	11	15
Number of aromatic heavy atoms	0	0
Fraction Csp ³	0.60	0.60
Number of rotatable bonds	4	1
Number of H-bond acceptors	1	0
Number of H-bond donors	1	0
Log P	2.6698	4.8913
Molar Refractivity	50.44	70.68
TPSA	20.23 Å ²	0.00 Å ²
Lipophilicity		
Log Po/w (XLOGP3)	2.97	4.74
Water solubility		
Log S (ESOL)	-2.40 6.09x10 ⁻¹ mg/mL; 3.95x10 ⁻³ mol/L Soluble	-4.03 1.92x10 ⁻² mg/mL; 9.39x10 ⁻⁵ mol/L Moderately soluble

3.10. Biological Activity Analysis of Linalool and Germacrene-D

The biological activity properties of Linalool and Germacrene-D compounds are presented in Table 6. Possible biological activities of Linalool and Germacrene-D compounds were obtained by the PASS server. Additionally, the set of pharmacological effects, mechanisms of action, and specific toxicities that may be exhibited by a compound in its interaction with biological entities were predicted by the PASS server (84). The software estimates the

predicted activity spectrum of a compound into probable activity (Pa) and probable inactivity (Pi). Only activities where Pa > Pi are considered possible for a given compound. If Pa > 0.7, the probability of experimental pharmacological effect is high, if 0.5 < Pa < 0.7, the probability of experimental pharmacological effect is less, when Pa < 0.5, the chance of finding the activity experimentally is less, but it may indicate the chance of finding a new compound (40).

Table 6: Biological activities of Linalool and Germacrene.

Components	Pa	Pi	Activity
Linalool	0.978	0.002	Mucomembranous protector
	0.913	0.003	Cell adhesion molecule inhibitor
	0.896	0.009	Aspulvinone dimethylallyltransferase inhibitor
	0.868	0.003	Fatty-acyl-CoA synthase inhibitor
	0.860	0.007	Beta-adrenergic receptor kinase inhibitor
	0.860	0.007	G-protein-coupled receptor kinase inhibitor
	0.836	0.002	Ecdysone 20-monooxygenase inhibitor
	0.832	0.002	BRAF expression inhibitor
	0.803	0.005	Lipid metabolism regulator
	0.798	0.004	Antisecretoric
	0.808	0.017	Antieczematic
	0.781	0.004	Undecaprenyl-phosphate mannosyltransferase inhibitor
	0.711	0.002	Antiviral (Rhinovirus)
0.719	0.022	TP53 expression enhancer	
Germacrene-D	0.915	0.004	Antieczematic
	0.885	0.002	Carminative
	0.817	0.010	Antineoplastic
	0.732	0.002	Testosterone agonist
	0.712	0.011	Phosphatase inhibitor
0.714	0.064	Ubiquinol-cytochrome-c reductase inhibitor	

Linalool contributes to topical anti-inflammatory and analgesic activities by inhibiting COX-2 protein expression in inflammatory tissues and reducing oxidative stress (85). Germacrene D reduces inflammation by preventing the release of inflammatory mediators by inactivating the enzymes that cause inflammation. One of the main mechanisms of Germacrene D is the inhibition of

prostaglandin synthesis. Prostaglandins are compounds that affect the inflammatory response and pain generation. This inhibition both alleviates inflammation and reduces pain generation (86). Linalool and Germacrene-D compounds play an essential role in the pathogenesis of inflammatory diseases. These compounds inhibit cell adhesion molecules involved in leukocyte traffic to provide

therapeutic intervention for leukocytes. With these properties, it is known to have therapeutic potential in human inflammatory disorders (87). These compounds exhibit various biological activities such as mucomembranous protector, cell adhesion molecule inhibitor, antisecretory, and antieczematic. It is understood that these compounds may be involved in the regulation of dermatological diseases caused by inflammation, with their remarkable anti-inflammatory activities, as they have high pharmacological activity values ($Pa > 0.7$).

4. CONCLUSION

UV rays can cause various damage to the skin, such as erythema, pigment change, photoaging and skin cancer. Essential oils can contribute to the prevention or treatment of damage to the skin caused by UV rays due to their UV protective properties. In our study, YO essential oil was used to protect against UV damage with its anti-inflammatory and antioxidant properties. YO was formulated in the NE dosage form to provide features such as increased skin permeability, bioavailability, solubility, therapeutic activity, stability, and controlled release. YO-NE was obtained with suitable average droplet size, PdI, and the ζ potential values, highly thermodynamically stable without sedimentation or phase separation, pH, and conductivity values suitable for topical application. It was determined that almost all the YO in the NE formulation was released within five hours. Cytotoxicity results showed that NE reduced the cytotoxicity of YO, and the YO-NE formulation had no toxicity. In conclusion, YO could be a formulation candidate that can be applied topically in treating dermatological diseases due to its controlled release feature, formulated in NE dosage form, non-toxicity, and the unique biological activities of Linalool and Germacrene-D compounds.

5. CONFLICT OF INTEREST

No conflict of interest.

6. ACKNOWLEDGMENTS

This work was supported by Yildiz Technical University Scientific Research Foundation [FCD-2021-4509]. In this study, the infrastructure of the Applied Nanotechnology and Antibody Production Laboratory established with TUBITAK support (project numbers: 115S132, 117S097 and 5200110) was used. The authors would also like to thank TUBITAK for their support.

7. REFERENCES

1. Kammeyer A, Luiten RM. Oxidation events and skin aging. *Ageing Res Rev* [Internet]. 2015 May;21:16–29. Available from: [<URL>](#).
2. Nanni V, Canuti L, Gismondi A, Canini A. Hydroalcoholic extract of *Spartium junceum* L. flowers inhibits growth and melanogenesis in B16-F10 cells by inducing senescence. *Phytomedicine*

[Internet]. 2018 Jul;46:1–10. Available from: [<URL>](#).

3. Rabe JH, Mamelak AJ, McElgunn PJS, Morison WL, Sauder DN. Photoaging: Mechanisms and repair. *J Am Acad Dermatol* [Internet]. 2006 Jul;55(1):1–19. Available from: [<URL>](#).

4. Zhu S, Zhao Z, Qin W, Liu T, Yang Y, Wang Z, et al. The Nanostructured lipid carrier gel of Oroxylin A reduced UV-induced skin oxidative stress damage. *Colloids Surfaces B Biointerfaces* [Internet]. 2022 Aug;216:112578. Available from: [<URL>](#).

5. González S, Fernández-Lorente M, Gilaberte-Calzada Y. The latest on skin photoprotection. *Clin Dermatol* [Internet]. 2008 Nov;26(6):614–26. Available from: [<URL>](#).

6. Mukherjee S, Date A, Patravale V, Korting HC, Roeder A, Weindl G. Retinoids in the treatment of skin aging: an overview of clinical efficacy and safety. *Clin Interv Aging* [Internet]. 2006 Dec;1(4):327–48. Available from: [<URL>](#).

7. Pacheco MT, Silva ACG, Nascimento TL, Diniz DGA, Valadares MC, Lima EM. Protective effect of sucupira oil nanoemulsion against oxidative stress in UVA-irradiated HaCaT cells. *J Pharm Pharmacol* [Internet]. 2019 Sep 3;71(10):1532–43. Available from: [<URL>](#).

8. Guzmán E, Lucia A. Essential Oils and Their Individual Components in Cosmetic Products. *Cosmetics* [Internet]. 2021 Dec 3;8(4):114. Available from: [<URL>](#).

9. Sedky NK, Abdel-Kader NM, Issa MY, Abdelhady MMM, Shamma SN, Bakowsky U, et al. Co-Delivery of Ylang Ylang Oil of *Cananga odorata* and Oxaliplatin Using Intelligent pH-Sensitive Lipid-Based Nanovesicles for the Effective Treatment of Triple-Negative Breast Cancer. *Int J Mol Sci* [Internet]. 2023 May 7;24(9):8392. Available from: [<URL>](#).

10. Goodrich KR. Floral scent in Annonaceae. *Bot J Linn Soc* [Internet]. 2012 May;169(1):262–79. Available from: [<URL>](#).

11. Kalagatur NK, Mudili V, Kamasani JR, Siddaiah C. Discrete and combined effects of Ylang-Ylang (*Cananga odorata*) essential oil and gamma irradiation on growth and mycotoxins production by *Fusarium graminearum* in maize. *Food Control* [Internet]. 2018 Dec;94:276–83. Available from: [<URL>](#).

12. Upadhyay N, Singh VK, Dwivedy AK, Chaudhari AK, Dubey NK. Assessment of nanoencapsulated *Cananga odorata* essential oil in chitosan nanopolymer as a green approach to boost the antifungal, antioxidant and in situ efficacy. *Int J Biol Macromol* [Internet]. 2021 Feb;171:480–90. Available from: [<URL>](#).

13. Youness RA, Al-Mahallawi AM, Mahmoud FH, Atta H, Braoudaki M, Fahmy SA. Oral Delivery of Psoralidin by Mucoadhesive Surface-Modified Bilosomes Showed Boosted Apoptotic and Necrotic

- Effects against Breast and Lung Cancer Cells. *Polymers (Basel)* [Internet]. 2023 Mar 15;15(6):1464. Available from: [<URL>](#).
14. Fahmy SA, Ponte F, Fawzy IM, Sicilia E, Azzazy HMES. Betaine host-guest complexation with a calixarene receptor: enhanced in vitro anticancer effect. *RSC Adv* [Internet]. 2021;11(40):24673–80. Available from: [<URL>](#).
15. Azzazy HMES, Sawy AM, Abdelnaser A, Meselhy MR, Shoeib T, Fahmy SA. Peganum harmala Alkaloids and Tannic Acid Encapsulated in PAMAM Dendrimers: Improved Anticancer Activities as Compared to Doxorubicin. *ACS Appl Polym Mater* [Internet]. 2022 Oct 14;4(10):7228–39. Available from: [<URL>](#).
16. Fahmy SA, Mahdy NK, Al Mulla H, ElMeshad AN, Issa MY, Azzazy HMES. PLGA/PEG Nanoparticles Loaded with Cyclodextrin-Peganum harmala Alkaloid Complex and Ascorbic Acid with Promising Antimicrobial Activities. *Pharmaceutics* [Internet]. 2022 Jan 7;14(1):142. Available from: [<URL>](#).
17. Kong M, Park HJ. Stability investigation of hyaluronic acid based nanoemulsion and its potential as transdermal carrier. *Carbohydr Polym* [Internet]. 2011 Jan 30;83(3):1303–10. Available from: [<URL>](#).
18. Soriano-Ruiz JL, Calpena-Capmany AC, Cañadas-Enrich C, Febrer NB de, Suñer-Carbó J, Souto EB, et al. Biopharmaceutical profile of a clotrimazole nanoemulsion: Evaluation on skin and mucosae as anticandidal agent. *Int J Pharm* [Internet]. 2019 Jan;554:105–15. Available from: [<URL>](#).
19. Thomas L, Zakir F, Mirza MA, Anwer MK, Ahmad FJ, Iqbal Z. Development of Curcumin loaded chitosan polymer based nanoemulsion gel: In vitro, ex vivo evaluation and in vivo wound healing studies. *Int J Biol Macromol* [Internet]. 2017 Aug;101:569–79. Available from: [<URL>](#).
20. Echeverría J, Albuquerque R. Nanoemulsions of Essential Oils: New Tool for Control of Vector-Borne Diseases and In Vitro Effects on Some Parasitic Agents. *Medicines* [Internet]. 2019 Mar 27;6(2):42. Available from: [<URL>](#).
21. Jaiswal M, Dudhe R, Sharma PK. Nanoemulsion: an advanced mode of drug delivery system. *3 Biotech* [Internet]. 2015 Apr 8;5(2):123–7. Available from: [<URL>](#).
22. Sharadha M, Gowda D V, Vishal Gupta N, Akhila AR. An overview on topical drug delivery system—updated review. *Int J Res Pharm Sci* [Internet]. 2020;11(1):368–85. Available from: [<URL>](#).
23. Ghosh V, Saranya S, Mukherjee A, Chandrasekaran N. Cinnamon Oil Nanoemulsion Formulation by Ultrasonic Emulsification: Investigation of Its Bactericidal Activity. *J Nanosci Nanotechnol* [Internet]. 2013 Jan 1;13(1):114–22. Available from: [<URL>](#).
24. Gul U, Khan MI, Madni A, Sohail MF, Rehman M, Rasul A, et al. Olive oil and clove oil-based nanoemulsion for topical delivery of terbinafine hydrochloride: in vitro and ex vivo evaluation. *Drug Deliv* [Internet]. 2022 Dec 31;29(1):600–12. Available from: [<URL>](#).
25. Ozkan B, Altuntas E, Cakir Koc R, Budama-Kilinc Y. Development of piperine nanoemulsions: an alternative topical application for hypopigmentation. *Drug Dev Ind Pharm* [Internet]. 2022 Mar 4;48(3):117–27. Available from: [<URL>](#).
26. Budama-Kilinc Y, Gok B, Kecel-Gunduz S, Altuntas E. Development of nanoformulation for hyperpigmentation disorders: Experimental evaluations, in vitro efficacy and in silico molecular docking studies. *Arab J Chem* [Internet]. 2022 Dec;15(12):104362. Available from: [<URL>](#).
27. Gaba B, Khan T, Haider MF, Alam T, Baboota S, Parvez S, et al. Vitamin E Loaded Naringenin Nanoemulsion via Intranasal Delivery for the Management of Oxidative Stress in a 6-OHDA Parkinson's Disease Model. *Biomed Res Int* [Internet]. 2019 Apr 14;2019:2382563. Available from: [<URL>](#).
28. Ercin E, Kecel-Gunduz S, Gok B, Aydin T, Budama-Kilinc Y, Kartal M. Laurus nobilis L. Essential Oil-Loaded PLGA as a Nanoformulation Candidate for Cancer Treatment. *Molecules* [Internet]. 2022 Mar 15;27(6):1899. Available from: [<URL>](#).
29. Rashid SA, Bashir S, Naseem F, Farid A, Rather IA, Hakeem KR. Olive Oil Based Methotrexate Loaded Topical Nanoemulsion Gel for the Treatment of Imiquimod Induced Psoriasis-like Skin Inflammation in an Animal Model. *Biology (Basel)* [Internet]. 2021 Oct 31;10(11):1121. Available from: [<URL>](#).
30. Budama-Kilinc Y, Kecel-Gunduz S, Ozdemir B, Bicak B, Akman G, Arvas B, et al. New nanodrug design for cancer therapy: Its synthesis, formulation, in vitro and in silico evaluations. *Arch Pharm (Weinheim)* [Internet]. 2020 Nov 5;353(11):2000137. Available from: [<URL>](#).
31. Gok B, Budama-Kilinc Y, Kecel-Gunduz S. Anti-aging activity of Syn-Ake peptide by in silico approaches and in vitro tests. *J Biomol Struct Dyn* [Internet]. 2024 Jul 2;42(10):5015–29. Available from: [<URL>](#).
32. Gunaseelan S, Balupillai A, Govindasamy K, Ramasamy K, Muthusamy G, Shanmugam M, et al. Linalool prevents oxidative stress activated protein kinases in single UVB-exposed human skin cells. Slominski AT, editor. *PLoS One* [Internet]. 2017 May 3;12(5):e0176699. Available from: [<URL>](#).
33. Haque MI, Khalipha ABR, Sakib MR, Prottay AAS, Islam MA, Zannat R, et al. In-Silico Molecular Docking Study of Linalool Against 3ELJ for Cell Cycle Arrest and Apoptosis in HEPG2 Cells. *Int J Evergr Sci Res* [Internet]. 2021;3(2):105–18. Available from: [<URL>](#).
34. Steliopoulos P, Wüst M, Adam KP, Mosandl A. Biosynthesis of the sesquiterpene germacrene D in *Solidago canadensis*: 13C and 2H labeling studies.

- Phytochemistry [Internet]. 2002 May;60(1):13–20. Available from: [<URL>](#).
35. Prosser I, Altug IG, Phillips AL, König WA, Bouwmeester HJ, Beale MH. Enantiospecific (+)- and (–)-germacrene D synthases, cloned from goldenrod, reveal a functionally active variant of the universal isoprenoid-biosynthesis aspartate-rich motif. *Arch Biochem Biophys* [Internet]. 2004 Dec;432(2):136–44. Available from: [<URL>](#).
36. Daina A, Michielin O, Zoete V. SwissADME: a free web tool to evaluate pharmacokinetics, drug-likeness and medicinal chemistry friendliness of small molecules. *Sci Rep* [Internet]. 2017 Mar 3;7(1):42717. Available from: [<URL>](#).
37. Pires DE V, Blundell TL, Ascher DB. pkCSM: Predicting Small-Molecule Pharmacokinetic and Toxicity Properties Using Graph-Based Signatures. *J Med Chem* [Internet]. 2015 May 14;58(9):4066–72. Available from: [<URL>](#).
38. Lipinski CA, Lombardo F, Dominy BW, Feeney PJ. Experimental and computational approaches to estimate solubility and permeability in drug discovery and development settings. *Adv Drug Deliv Rev* [Internet]. 2001 Mar;46(1–3):3–26. Available from: [<URL>](#).
39. Rakhecha B, Agnihotri P, Dakal TC, Saquib M, Monu, Biswas S. Anti-inflammatory activity of nicotine isolated from *Brassica oleracea* in rheumatoid arthritis. *Biosci Rep* [Internet]. 2022 Apr 29;42(4):BSR20211392. Available from: [<URL>](#).
40. Mojumdar M, Kabir MSH, Hasan MS, Ahmed T, Rahman MR, Akter Y, et al. Molecular docking and pass prediction for analgesic activity of some isolated compounds from *Acalypha indica* L. and ADME/T property analysis of the compounds. *World J Pharm Res* [Internet]. 2016;5(7):1761–70. Available from: [<URL>](#).
41. Zhao D, Ge Y, Xiang X, Dong H, Qin W, Zhang Q. Structure and stability characterization of pea protein isolate-xylan conjugate-stabilized nanoemulsions prepared using ultrasound homogenization. *Ultrason Sonochem* [Internet]. 2022 Nov;90:106195. Available from: [<URL>](#).
42. Manzoor M, Sharma P, Murtaza M, Jaiswal AK, Jaglan S. Fabrication, characterization, and interventions of protein, polysaccharide and lipid-based nanoemulsions in food and nutraceutical delivery applications: A review. *Int J Biol Macromol* [Internet]. 2023 Jun;241:124485. Available from: [<URL>](#).
43. Kapoor A, Preet S. Evaluation of Acaricidal Activity of Cinnamomum camphora (F. Lauraceae) Essential Oil Nanoemulsion Against Cattle Tick *Rhipicephalus microplus*. *Adv Zool Bot* [Internet]. 2023 Apr;11(2):121–8. Available from: [<URL>](#).
44. Rupa E, Li J, Arif M, Yaxi H, Puja A, Chan A, et al. *Cordyceps militaris* Fungus Extracts-Mediated Nanoemulsion for Improvement Antioxidant, Antimicrobial, and Anti-Inflammatory Activities. *Molecules* [Internet]. 2020 Dec 4;25(23):5733. Available from: [<URL>](#).
45. Ayllón-Gutiérrez R, López-Maldonado EA, Macías-Alonso M, González Marrero J, Díaz-Rubio L, Córdova-Guerrero I. Evaluation of the Stability of a 1,8-Cineole Nanoemulsion and Its Fumigant Toxicity Effect against the Pests *Tetranychus urticae*, *Rhopalosiphum maidis* and *Bemisia tabaci*. *Insects* [Internet]. 2023 Jul 24;14(7):663. Available from: [<URL>](#).
46. Liu Q, Huang H, Chen H, Lin J, Wang Q. Food-Grade Nanoemulsions: Preparation, Stability and Application in Encapsulation of Bioactive Compounds. *Molecules* [Internet]. 2019 Nov 21;24(23):4242. Available from: [<URL>](#).
47. Gorjian H, Mihankhah P, Khaligh NG. Influence of tween nature and type on physicochemical properties and stability of spearmint essential oil (*Mentha spicata* L.) stabilized with basil seed mucilage nanoemulsion. *J Mol Liq* [Internet]. 2022 Aug;359:119379. Available from: [<URL>](#).
48. Mohammed NK, Muhiadin BJ, Meor Hussin AS. Characterization of nanoemulsion of *Nigella sativa* oil and its application in ice cream. *Food Sci Nutr* [Internet]. 2020 Jun 21;8(6):2608–18. Available from: [<URL>](#).
49. Kampa J, Frazier R, Rodriguez-Garcia J. Physical and Chemical Characterisation of Conventional and Nano/Emulsions: Influence of Vegetable Oils from Different Origins. *Foods* [Internet]. 2022 Feb 25;11(5):681. Available from: [<URL>](#).
50. Lima TS, Silva MFS, Nunes XP, Colombo A V, Oliveira HP, Goto PL, et al. Cineole-containing nanoemulsion: Development, stability, and antibacterial activity. *Chem Phys Lipids* [Internet]. 2021 Sep;239:105113. Available from: [<URL>](#).
51. Özdemir S, Üner B, Karaküçük A, Çelik B, Sümer E, Taş Ç. Nanoemulsions as a Promising Carrier for Topical Delivery of Etodolac: Formulation Development and Characterization. *Pharmaceutics* [Internet]. 2023 Oct 23;15(10):2510. Available from: [<URL>](#).
52. Gündel S da S, de Godoi SN, Santos RCV, da Silva JT, Leite LB de M, Amaral AC, et al. In vivo antifungal activity of nanoemulsions containing eucalyptus or lemongrass essential oils in murine model of vulvovaginal candidiasis. *J Drug Deliv Sci Technol* [Internet]. 2020 Jun;57:101762. Available from: [<URL>](#).
53. Lunardi CN, Gomes AJ, Rocha FS, De Tommaso J, Patience GS. Experimental methods in chemical engineering: Zeta potential. *Can J Chem Eng* [Internet]. 2021 Mar 12;99(3):627–39. Available from: [<URL>](#).
54. Dheyab MA, Aziz AA, Jameel MS, Noqta OA, Khaniabadi PM, Mehrdel B. Simple rapid stabilization method through citric acid modification for magnetite nanoparticles. *Sci Rep* [Internet]. 2020 Jul 1;10(1):10793. Available from: [<URL>](#).

55. Kildaci I, Budama-Kilinc Y, Kecel-Gunduz S, Altuntas E. Linseed Oil Nanoemulsions for treatment of Atopic Dermatitis disease: Formulation, characterization, in vitro and in silico evaluations. *J Drug Deliv Sci Technol* [Internet]. 2021 Aug;64:102652. Available from: [<URL>](#).
56. Gok B, Budama Kilinc Y. Chlorogenic acid nanoemulsion for staphylococcus aureus causing skin infection: Synthesis, characterization and evaluation of antibacterial efficacy. *Sigma J Eng Nat Sci* [Internet]. 2022 Aug;41(2):322–30. Available from: [<URL>](#).
57. Marhamati M, Ranjbar G, Rezaie M. Effects of emulsifiers on the physicochemical stability of Oil-in-water Nanoemulsions: A critical review. *J Mol Liq* [Internet]. 2021 Oct;340:117218. Available from: [<URL>](#).
58. Rashid SA, Bashir S, Ullah H, Khan DH, Shah PA, Danish MZ, et al. Development, characterization and optimization of methotrexate-olive oil nano-emulsion for topical application. *Pak J Pharm Sci* [Internet]. 2021;34. Available from: [<URL>](#).
59. Hammadi ID, N. Abd Alhammid S. Preparation and Characterization of Topical Letrozole Nanoemulsion for Breast Cancer. *Iraqi J Pharm Sci* [Internet]. 2020 Jun 25;29(1):195–206. Available from: [<URL>](#).
60. Roselan MA, Ashari SE, Faujan NH, Mohd Faudzi SM, Mohamad R. An Improved Nanoemulsion Formulation Containing Kojic Monooleate: Optimization, Characterization and In Vitro Studies. *Molecules* [Internet]. 2020 Jun 4;25(11):2616. Available from: [<URL>](#).
61. Wang L, Guan X, Zheng C, Wang N, Lu H, Huang Z. New Low-Energy Method for Nanoemulsion Formation: pH Regulation Based on Fatty Acid/Amine Complexes. *Langmuir* [Internet]. 2020 Sep 1;36(34):10082–90. Available from: [<URL>](#).
62. Altuntaş E, Yener G. Formulation and Evaluation of Thermoreversible In Situ Nasal Gels Containing Mometasone Furoate for Allergic Rhinitis. *AAPS PharmSciTech* [Internet]. 2017 Oct 9;18(7):2673–82. Available from: [<URL>](#).
63. Mat Hadzir N, Basri M, Abdul Rahman MB, Salleh AB, Raja Abdul Rahman RNZ, Basri H. Phase Behaviour and Formation of Fatty Acid Esters Nanoemulsions Containing Piroxicam. *AAPS PharmSciTech* [Internet]. 2013 Mar 6;14(1):456–63. Available from: [<URL>](#).
64. Guttoff M, Saberi AH, McClements DJ. Formation of vitamin D nanoemulsion-based delivery systems by spontaneous emulsification: Factors affecting particle size and stability. *Food Chem* [Internet]. 2015 Mar;171:117–22. Available from: [<URL>](#).
65. Bernardi DS, Pereira TA, Maciel NR, Bortoloto J, Viera GS, Oliveira GC, et al. Formation and stability of oil-in-water nanoemulsions containing rice bran oil: in vitro and in vivo assessments. *J Nanobiotechnology* [Internet]. 2011;9(1):44. Available from: [<URL>](#).
66. Altuntaş E, Yener G. Anti-aging potential of a cream containing herbal oils and honey: Formulation and in vivo evaluation of effectiveness using non-invasive biophysical techniques. *IOSR J Pharm Biol Sci* [Internet]. 2015;10(6):51–60. Available from: [<URL>](#).
67. Shen Y, Ni ZJ, Thakur K, Zhang JG, Hu F, Wei ZJ. Preparation and characterization of clove essential oil loaded nanoemulsion and pickering emulsion activated pullulan-gelatin based edible film. *Int J Biol Macromol* [Internet]. 2021 Jun;181:528–39. Available from: [<URL>](#).
68. Jerobin J, Sureshkumar RS, Anjali CH, Mukherjee A, Chandrasekaran N. Biodegradable polymer based encapsulation of neem oil nanoemulsion for controlled release of Aza-A. *Carbohydr Polym* [Internet]. 2012 Nov;90(4):1750–6. Available from: [<URL>](#).
69. Fopase R, Pathode SR, Sharma S, Datta P, Pandey LM. Lipopeptide and essential oil based nanoemulsion for controlled drug delivery. *Polym Technol Mater* [Internet]. 2020 Dec 11;59(18):2076–86. Available from: [<URL>](#).
70. Rajitha P, Shammika P, Aiswarya S, Gopikrishnan A, Jayakumar R, Sabitha M. Chaulmoogra oil based methotrexate loaded topical nanoemulsion for the treatment of psoriasis. *J Drug Deliv Sci Technol* [Internet]. 2019 Feb;49:463–76. Available from: [<URL>](#).
71. Mohd Narawi M, Chiu HI, Yong YK, Mohamad Zain NN, Ramachandran MR, Tham CL, et al. Biocompatible Nutmeg Oil-Loaded Nanoemulsion as Phyto-Repellent. *Front Pharmacol* [Internet]. 2020 Mar 17;11:214. Available from: [<URL>](#).
72. Shah J, Nair AB, Jacob S, Patel RK, Shah H, Shehata TM, et al. Nanoemulsion Based Vehicle for Effective Ocular Delivery of Moxifloxacin Using Experimental Design and Pharmacokinetic Study in Rabbits. *Pharmaceutics* [Internet]. 2019 May 11;11(5):230. Available from: [<URL>](#).
73. Botros SR, Hussein AK, Mansour HF. A Novel Nanoemulsion Intermediate Gel as a Promising Approach for Delivery of Itraconazole: Design, In Vitro and Ex Vivo Appraisal. *AAPS PharmSciTech* [Internet]. 2020 Oct 6;21(7):272. Available from: [<URL>](#).
74. Roggia I, Gomes P, Dalcin AJF, Ourique AF, Mânica da Cruz IB, Ribeiro EE, et al. Profiling and Evaluation of the Effect of Guarana-Loaded Liposomes on Different Skin Cell Lines: An In Vitro Study. *Cosmetics* [Internet]. 2023 May 12;10(3):79. Available from: [<URL>](#).
75. Serrano I, Alinho B, Cunha E, Tavares L, Trindade A, Oliveira M. Bacteriostatic and Antibiofilm Efficacy of a Nisin Z Solution against Co-Cultures of *Staphylococcus aureus* and *Pseudomonas aeruginosa*

- from Diabetic Foot Infections. *Life* [Internet]. 2023 Feb 11;13(2):504. Available from: [<URL>](#).
76. Standard I. Biological evaluation of medical devices—Part 5: Tests for in vitro cytotoxicity. Geneva, Switz Int Organ Stand. 2009;
77. Caldeira LR, Fernandes FR, Costa DF, Frézard F, Afonso LCC, Ferreira LAM. Nanoemulsions loaded with amphotericin B: A new approach for the treatment of leishmaniasis. *Eur J Pharm Sci* [Internet]. 2015 Apr;70:125–31. Available from: [<URL>](#).
78. Musa SH, Razali FN, Shamsudin N, Salim N, Basri M. Novel topical nano-colloidal carrier loaded with cyclosporine: Biological evaluation potentially for psoriasis treatment. *J Drug Deliv Sci Technol* [Internet]. 2021 Jun;63:102440. Available from: [<URL>](#).
79. Meghani N, Patel P, Kansara K, Ranjan S, Dasgupta N, Ramalingam C, et al. Formulation of vitamin D encapsulated cinnamon oil nanoemulsion: Its potential anti-cancerous activity in human alveolar carcinoma cells. *Colloids Surfaces B Biointerfaces* [Internet]. 2018 Jun;166:349–57. Available from: [<URL>](#).
80. Liao S, Yang G, Wang Z, Ou Y, Huang S, Li B, et al. Ultrasonic preparation of Tween-essential oil (*Zanthoxylum schinifolium* Sieb. et Zucc) oil/water nanoemulsion: Improved stability and alleviation of *Staphylococcus epidermidis* biofilm. *Ind Crops Prod* [Internet]. 2022 Nov;188:115654. Available from: [<URL>](#).
81. Singh I, Morris A. Performance of transdermal therapeutic systems: Effects of biological factors. *Int J Pharm Investig* [Internet]. 2011;1(1):4. Available from: [<URL>](#).
82. James JP, Ail PD, Crasta L, Kamath RS, Shura MH, T.J S. In Silico ADMET and Molecular Interaction Profiles of Phytochemicals from Medicinal Plants in Dakshina Kannada. *J Heal Allied Sci NU* [Internet]. 2024 Apr 19;14(2):190–201. Available from: [<URL>](#).
83. Drioiche A, Ailli A, Remok F, Saidi S, Gourich AA, Asbabou A, et al. Analysis of the Chemical Composition and Evaluation of the Antioxidant, Antimicrobial, Anticoagulant, and Antidiabetic Properties of *Pistacia lentiscus* from Boulemane as a Natural Nutraceutical Preservative. *Biomedicines* [Internet]. 2023 Aug 24;11(9):2372. Available from: [<URL>](#).
84. Jamuna S, Rathinavel A, Mohammed Sadullah S, Devaraj S. In silico approach to study the metabolism and biological activities of oligomeric proanthocyanidin complexes. *Indian J Pharmacol* [Internet]. 2018;50(5):242–50. Available from: [<URL>](#).
85. Li XJ, Yang YJ, Li YS, Zhang WK, Tang HB. α -Pinene, linalool, and 1-octanol contribute to the topical anti-inflammatory and analgesic activities of frankincense by inhibiting COX-2. *J Ethnopharmacol* [Internet]. 2016 Feb;179:22–6. Available from: [<URL>](#).
86. Amanpour A, Çelebi F, Kahraman IG, Çelik F. Diyet İnflamatuvar İndeksi, İnflamasyon ve Beslenme. *Türkiye Sağlık Bilim ve Araştırmaları Derg* [Internet]. 2022 Dec 29;5(3):59–80. Available from: [<URL>](#).
87. Ulbrich H, Eriksson EE, Lindbom L. Leukocyte and endothelial cell adhesion molecules as targets for therapeutic interventions in inflammatory disease. *Trends Pharmacol Sci* [Internet]. 2003 Dec;24(12):640–7. Available from: [<URL>](#).



Modulation of Human Acetylthiocholine Esterase Activity by Novel Fused Pyrimidine Derivatives: *In vitro*, Theoretical and ADMET Studies

Zaizafoone N. Nasif^{1,*} , Zahraa S. Al-Garawi¹ , Füreya Elif Öztürkkan² 

¹Mustansiriyah University, Department of Chemistry, Baghdad, 10001, Iraq.

²Kafkas University, Department of Chemical Engineering, Kars, 36100, Turkey.

Abstract: Pyrimidine compounds have medicinal and biological activities as previously reported. In this work, two novel fused pyrimidine compounds were synthesized, fused pyrazolo-pyrimidine compound was synthesized by cyclization of 5-amino-4-cyano-1-phenyl pyrazole with propionic acid in the presence of POCl₃, and the other fused pyrrole-pyrano-pyrimidine compound was synthesized by cyclization of ethyl(*E*)-N-(3-cyano-4-(4-(dimethylamino)phenyl)-7-methyl-4,5,6,7-tetrahydropyrano[2,3-*b*] pyrrole-2-yl) formimidate with hydrazine hydrate, in methanol. These fused pyrimidine compounds were characterized by FT-IR and ¹H NMR. The effect of these compounds was studied on the activity of the human neurotransmission enzyme acetylthiocholine esterase AChE. Results indicated that these compounds significantly inhibited AChE activity at concentrations of 10⁻¹¹ M. Michalis-Menton showed mixed noncompetitive inhibition of AChE activity. In conclusion, newly synthesized compounds could be promising derivatives for enhancing cholinergic neurotransmission. Among the other derivatives, derivative 4 formed H-bond interactions with key amino acid residues Tyr334, and Asp72, whereas the other electrostatic interactions formed with Tyr334, Phe330, Ile287, Tyr121, Arg289, Trp279, Gly335, and Phe288. In the case of derivatives 9, similar binding interactions with active pockets of 2ACE were observed due to the high homology of the binding site residues. In addition, we examined ADMET properties with the help of online databases to search for possible drug similarity of synthesized compounds 4 and 9 and revealed that both molecules were compatible with Lipinski's five rules.

Keywords: Fused pyrazolo-pyrimidine, AChE activity, Molecular docking, Noncompetitive inhibition, ADMET.

Submitted: July 15, 2023. **Accepted:** June 27, 2024.

Cite this: Nasif ZN, Al-Garawi ZS, Öztürkhan FE. Modulation of Human Acetylthiocholine Esterase Activity by Novel Fused Pyrimidine Derivatives: *In vitro*, Theoretical and ADMET Studies. JOTCSA. 2024;11(3):1197-210.

DOI: <https://doi.org/10.18596/jotcsa.1327285>

***Corresponding author's E-mail:** z.mohsin@uomustansiriyah.edu.iq

1. INTRODUCTION

Acetylcholinesterase is known to be distributed in nervous tissue such as the brainstem, cerebellum, and peripheral and autonomic nervous systems. Skeletal muscle also contains AChE with distribution patterns seemingly related to the type of muscle (fast versus slow twitch) and their specific function. The presence and function of AChE on red blood cells are less commonly known. Blood group antigens reside on the outer lipid bilayer of red blood cells for convenient antibody recognition. In the same regard, AChE is also present in red blood cell membranes (1).

Alzheimer's disease (AD) is associated with memory and thinking impairment, behavioral problems, and disturbance in daily living activities. AD is common in old people due to irreversible neuronal loss. The deficiency of acetylcholine (ACh) in synapses of the

cerebral cortex is one of the important sufferers of AD and can be treated by the inhibition of AChE that hydrolyzes ACh into choline and acetate (2).

Fused pyrimidine rings are among a wide range of nitrogen heterocyclics that have been studied due to their pharmaceutical activities to produce biologically important molecules (3-5). The pyrimidine ring is fused into different heterocyclic (6,7) and exhibits several activities such as antimicrobial, antitumor, antimalarial, antihypertensive, vasodilator, and anti-allergic (8,9). The observed activity may be due to the presence of fused pyrimidine moiety. The chloro, amine, fluorine, bromine, amino-pyrimidine, 4-methoxyphenylpyridine, hydroxynaphthalene, coumarin ring, pyrazolo-pyrimidine, thino-pyrimidine, phenyl-pyrimidine scaffold presence in various positions of the aromatic ring may enhanced biological potential (10).

On the other hand, naphthyridine also represents one of the important fused nitrogen compounds with diverse biological activities, such as antibacterial, anticancer, anti-inflammatory, and anti-ureolytic activity (11-14). During the last decade, there was a large interest in fused nitrogen heterocycles to synthesize novel pyridopyrimidine and naphthyridine derivatives. Those novel compounds were

characterized using *IR Candida albicans*. Most fused pyrimidine has been used and licensed by the FDA (15) to treat some cancer types. Pazopanib (A) 'trade name vortient and methotrexate (B) has a pyrimidine core that is considered a cancer therapy drug (16) leading to the synthesis of new fused bicyclic and tricyclic pyrimidine analogs and their effect on cancer cells (17).

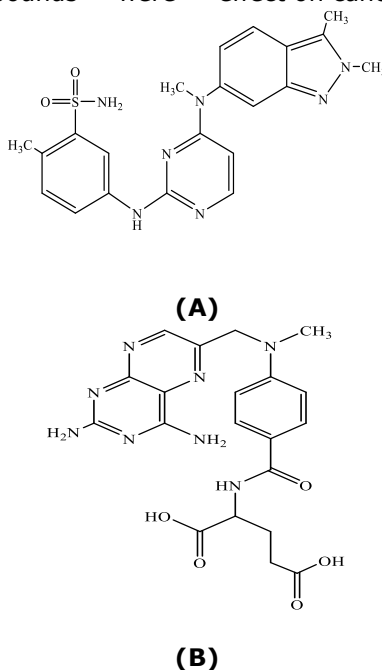


Figure 1: Fused pyrimidine compounds licensed by FDA. (A) Pazopanib and (B) methotrexate.

Herein, we synthesized new pyrimidine derivatives to explore their potential as inhibitors of human AChE activity. These compounds were characterized using Fourier transform infrared FT-IR and proton nuclear magnetic resonance ^1H NMR. The inhibition activity of the compounds was studied *in vitro* in human serum.

2. EXPERIMENTAL SECTION

2.1. Materials

All chemicals were purchased from Sigma-Aldrich and Fluka companies. ^1H NMR spectra were recorded on a Bruker, Ultra Shield 400 Mhz, spectrometer (Switzerland) using DMSO- d_6 and CDCl_3 as a solvent with tetramethylsilane (TMS) as an internal standard (Iran Polymer & Petrochemical Institute). All reactions were carried out with the thin layer chromatography technique (TLC) and revealed by a mixture of n-hexane and ethyl acetate (3: 2) as pure eluents.

2.2. Synthesis of Fused Pyrimidines

In this study, we used previously prepared compound 2 listed in Table 4 to synthesize compounds 3 and 4. The previously synthesized compound 7 was used to prepare compound 9, see Table 1.

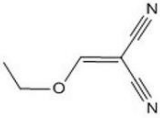
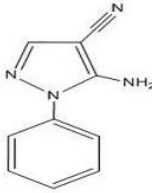
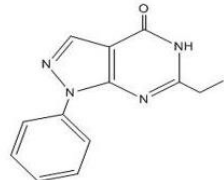
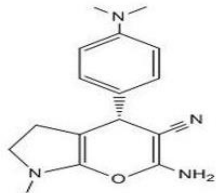
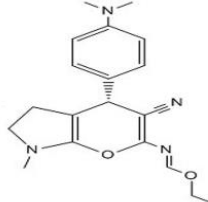
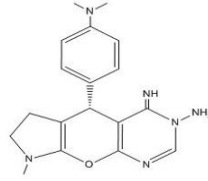
2.2.1. Synthesis of compound 2: 2-(Ethoxy methylene) malononitrile (20)

A weight of 0.66 g, 0.01 mole of redistilled malononitrile, 1.48 g, 0.01 mol of triethyl orthoformate, and 2.04 g, 0.02 mole of acetic anhydride was stirred and heated to 110 °C until the reaction had subsided and the temperature dropped to 95 °C. Distillation was used to remove impurities from the clear yellow reaction mixture until the temperature reached 115 °C. Then a vacuum distillation (100 °C, 15 mm) was used to remove the rest of the solvent. The product was cooled down to 80 °C and then refluxed 1.0 g of charcoal and 35 mL of absolute ethanol for 5 minutes. After filtering and washing with 3 mL of hot absolute ethanol, the filtrate was cooled on ice until crystallization was completed and recrystallized from ethanol to purify the white crystalline material and then dried to constant weight *in vacuo* to obtain the compound 2, with a yield: 89% (1.8 g) and mp: 55-57 °C.

2.2.2. Preparation of compound 3: 5-Amino-4-cyano-1-phenyl pyrazole (21)

A mixture of compound 2 (1.22 g, 0.01 mole) and phenylhydrazine (1.08 g, 0.01 mole) in ethanol (40 mL) was refluxed for 1 h. The precipitate was separated by cooling, filtered, and purified by recrystallization from ethanol/water to give a light yellow compound 3, with a yield of 88% (1.75 g) and mp: 134-136 °C.

Table 1: A library of synthesized compounds.

No.	Chemical structure	Name of the compound
2		2-(ethoxymethylene)malononitrile (18)
3		5-Amino-4-cyano-1-phenyl pyrazole
4		6-ethyl-1-phenyl-1,5-dihydro-4H-pyrazolo[3,4-d] pyrimidin-4-one
7		2-amino-4-(4-(dimethylamino)phenyl)-7-methyl-4,5,6,7-tetrahydropyrano[2,3-b]pyrrole-3-carbonitrile (19)
8		ethyl(<i>E</i>)-N-(3-cyano-4-(4-(dimethylamino)phenyl)-7-methyl-4,5,6,7-tetrahydropyrano[2,3-b]pyrrol-2-yl)formimidate
9		5-(4-(dimethylamino)phenyl)-4-imino-8-methyl-5,6,7,8-tetrahydropyrrolo[3',2':5,6]pyrano[2,3-d]pyrimidin-3(4 <i>H</i>)-amine

2.2.3. Synthesis of compound 4: 6-Ethyl-1-phenyl-1,5-dihydro-4H-pyrazolo[3,4-d] pyrimidine-4-one

A mixture of compound **3** (2.67 g, 0.01 mole) was dissolved in propionic acid (5 mL), then quickly added 0.2 mL of POCl₃ and refluxed for 12 h. After the mixture cooled, a mass of white precipitate was observed. To neutralize the acid, fused K₂CO₃ was added until no bubble occurred. The mixture was filtered and washed with ethanol, dried, and then recrystallized from ethanol to give a pale-yellow compound **4** with a yield of 68% (1.35 g) and mp: 101-103 °C.

2.2.4. Synthesis of compound 7: 2-Amino-4-(4-(dimethylamino) phenyl)-7-methyl-4,5,6,7-tetrahydropyrano[2,3-b] pyrrole-3-carbonitrile

In a typical procedure, equimolar amounts of 4-(dimethylamino) benzaldehyde (1.49 g, 0.01mole), malononitrile (0.66 g, 0.01 mole) and N-methyl-2-pyrrolidinone (0.99 g, 0.01 mole) were mixed with

tetraethyl ammonium bromide (10 mole %) in 15 mL, 90 % of ethanol and refluxed with stirring for 95 minutes. After the reaction was completed, the mixture was cooled to room temperature and poured into ice to obtain the crude products. The products were recrystallized as 1,4-dioxane to give compound **7** with a yield of 92% (1.85 g) and mp: 178-180 °C.

2.2.5. Synthesis of compounds 8: Ethyl(*E*)-N-(3-cyano-4-(4-(dimethylamino) phenyl)-7-methyl-4,5,6,7-tetrahydropyrano [2,3-b]pyrrol-2-yl) formimidate

A mixture of compound **7** (2.96 g, 0.01 mole), triethyl orthoformate (1.48 g, 0.01 mole), and 16 mL of acetic anhydride was refluxed for 5 h. Under vacuum, the solvent was removed and the product was recrystallized from benzene to give brown-colored compound **8** with a yield of 77% (1.46 g) and mp: 162-164 °C.

2.2.6. Synthesis of compound 9: 5-(4-(dimethylamino) phenyl)-4-imino-8-methyl-5,6,7,8 tetrahydro pyrrolo [3',2':5,6] pyrano [2,3-d] pyrimidine-3(4H)-amine

A mixture of the compound **8** (3.52 g, 0.01 mole) in 25 mL methanol, a solution of hydrazine hydrate (0.50g, 0.01mole), or ethylene diamine (0.60 g, 0.01 mole), or phenyl hydrazine (1.08 g, 0.01 mole) was stirred for 1 hour and left overnight. The next day, the mixture was filtered, dried, and recrystallized from 1,4-dioxane to give yellow-colored compound **9** with a yield of 80% (1.63 g) and mp: 261-263 °C.

2.3. The Activity of Human AChE

2.3.1. Acetylcholinesterase (AChE) assay

The activity of acetylcholine esterase (AChE) was studied according to Ellman et al method (22) with a slight modification. Acetylthiocholine iodide (ASChI, 34 µL, 0.06 M) was added to 50 µL of 5,5-dithiobis [2-nitrobenzoic acid] (DTNB) and 2.25 mL of sodium phosphate buffer (pH=7.3, 0.2 M) and finally, 10 µL of human serum was added to the mixture and vortexed well. The changes in absorbency were

assayed before and after adding the substrate at 430 nm for 2 minutes.

$$\text{AChE activity } (\mu\text{mole}/ 2 \text{ min/mL}) = \Delta A / 2 * d.f$$

2.3.2. Effect of pyrimidine derivatives (Compounds **4** and **9**) on AChE activity

The effect of each derivative (compounds **4** and **9**) on the AChE was also studied according to the modified Ellman method. Briefly, a stock of the synthesized compounds (0.01M) was freshly prepared and used to prepare a series of different concentrations (10^{-2} , 10^{-3} , 10^{-5} , 10^{-7} , 10^{-9} and 10^{-11} M) of dimethylsulfoxide (DMSO). A volume of 0.25 mL of pyrimidine derivatives was added to 50 µL DTNB (0.001 M), followed by the addition of 10 µL of human serum, mixed well, and 2 mL of the mixture was withdrawn to be mixed with 34 µL of ASChI substrate (0.06 M). The absorbance was assessed before and after adding the substrate at 430 nm for 2 minutes.

The inhibition percentage % of the enzyme activity was determined according to the equation:

$$\% \text{ Inhibition} = 100 - \frac{\text{The activity in the presence of an inhibitor}}{\text{The activity in the absence of an inhibitor}} \times 100 \quad (\text{Eq. 1})$$

2.3.3. Type of inhibition (23)

To study the type of inhibition, different concentrations of AChTI (substrate) (0.02, 0.04, 0.06, and 0.08 M) were used against a constant concentration of inhibitors. The enzyme activity was assayed using the Lineweaver-Burk equation in the presence and absence of the compounds, and then the type of inhibition, inhibitor constant K_i , maximum velocity V_{max} , and Michalis-Menton constant K_m were determined.

2.4. Docking Study

A molecular docking study was carried out using the Autodock 4.2 program (24), while Discovery Studio Visualizer (25) was used to select the best binding mode with the receptor and 3D interaction poses. The 3D structures of AChE (PDB ID: 2ACE) were obtained from the Protein Data Bank (www.rcsb.org), followed by separating the co-crystallized ligands and water molecules. Then polar hydrogens were added. Finally, the 3D structures of the tested compounds were optimized using Gaussian 03 software with the semi-empirical AM1 method.

2.5. Estimation of Pharmacokinetic and Toxicological Properties

Absorption, distribution, metabolism, excretion, and toxicity (ADMET) refers to the characteristic properties of a drug that express its pharmacokinetics in the human body. Lipinski's rule of 5 states (26) that absorption or permeability is more likely when there are no more than five hydrogen bond donors and acceptors, no molecular weight greater than 500 g/mol, and octanol/water partition coefficient greater than five. In this study, we evaluated the absorption, distribution, metabolism, and excretion properties of two

synthesized molecules using the SwissADME online database (27) and screened them according to the Lipinski 5 rule. We also examined the toxicity risk assessment properties of the compounds with the help of the ProTOX-II online database (28) and OSIRIS Property Explorer (29).

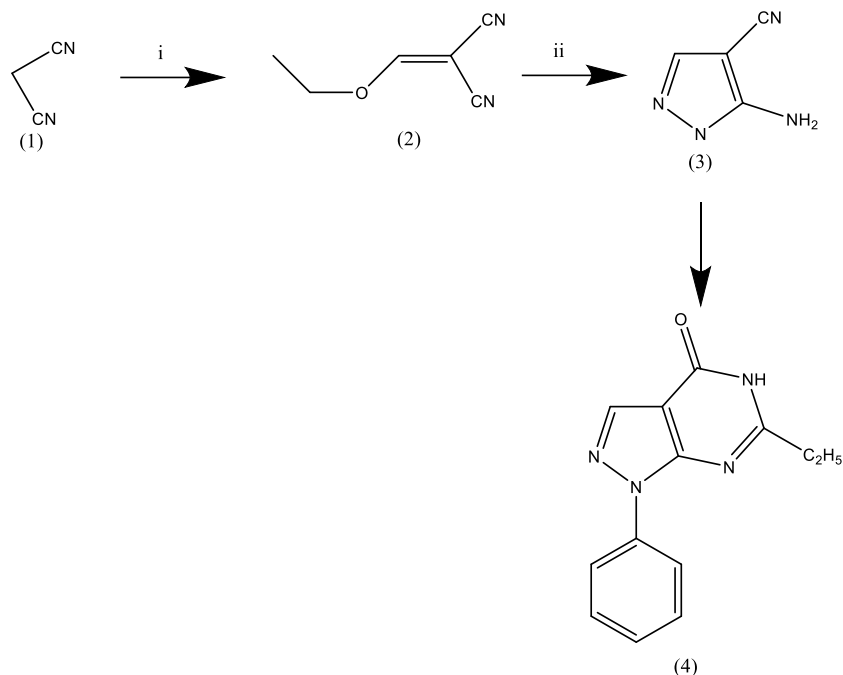
3. RESULTS AND DISCUSSION

3.1. Synthesis of Compounds **4** and **9**

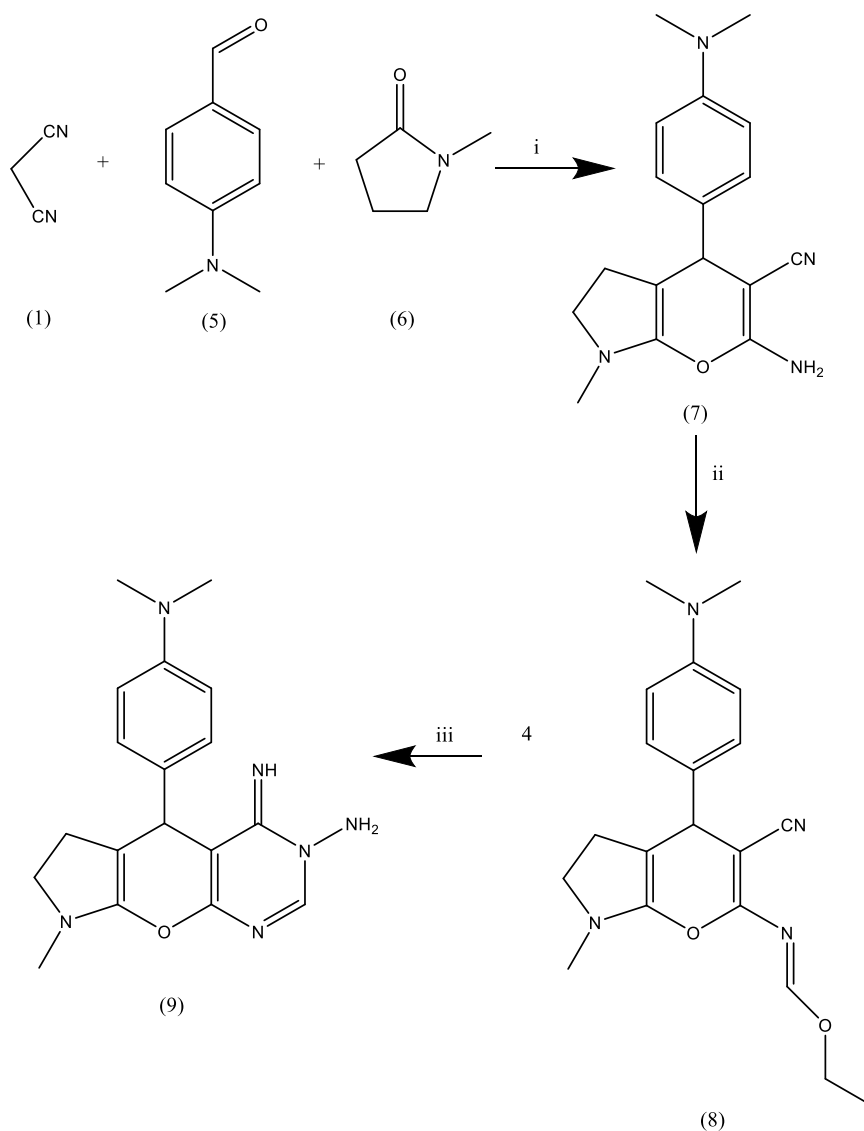
Previous studies mentioned that a good yield of compound **3** 5-amino-4-cyano pyrazole (30,31) could be obtained by the standard addition of phenylhydrazine to an unsaturated ethoxymethylene compound **2**. Compound **4** was synthesized by treating compound **3** with some aliphatic carboxylic acids such as acetic acid, formic acid, and propionic acid respectively in the presence POCl_3 as shown in Scheme (1).

3.2. Characterization by FT-IR and ^1H NMR

The intermediate compounds **3** and **7** were well characterized using FT-IR and ^1H NMR. The FT-IR spectra of the compound **3** in Figure (1a), showed stretching bands at 3329 and 3431 cm^{-1} for symmetrical and unsymmetrical (NH_2), 3109 cm^{-1} for ($\text{C-H}_{\text{arom.}}$), 2931-3061 cm^{-1} for ($\text{C-H}_{\text{aliph.}}$), 2222 cm^{-1} for (CN), 1637 cm^{-1} for ($\text{C} = \text{N}$) and 1599 cm^{-1} for ($\text{C}=\text{C}$) with the disappearance of stretching bands from the ether group. The FT-IR spectra of **4** in Figure (1b) showed bands of (NH_2) stretching at 3329 cm^{-1} . Although 3431 cm^{-1} and ($\text{C}\equiv\text{N}$) at 2222 cm^{-1} were not recognized, the (NH) stretching at 3155 cm^{-1} , ($\text{CH}_{\text{arom.}}$) at 3103 cm^{-1} , ($\text{CH}_{\text{aliph.}}$) at 2816-2943 cm^{-1} , ($\text{C}=\text{O}$) at 1685 cm^{-1} , ($\text{C}=\text{N}$) at 1604 cm^{-1} , and ($\text{C}=\text{C}$) at 1554 cm^{-1} were observed.



Scheme 1: Synthesis of compound 4. The conditions used were (i) Triethylorthoformate/acetic anhydride, 140 °C, 4 h. (ii) Phenyl hydrazine/EtOH, 78 °C, 2 h. (iii) Propionic acid/ POCl₃ / K₂CO₃, 120 °C, 18 h.



Scheme 2: Synthesis of compound 9. The reaction conditions were (i) (C₂H₅)₄N⁺ Br⁻ /EtOH, 78 °C, 1h. (ii) Triethylorthoformate/acetic anhydride, 140 °C, 5h. (iii) NH₂NH₂.H₂O/ MeOH, room temperature for 2h.

Compound **7** was added to triethylorthoformate in acetic anhydride to form an imidoformate derivative **8**, then compound **8** was added to hydrazine hydrate for 1 hr 2° to form fused pyrimidine derivative [9], Scheme (2). The FTIR spectra of the compound **7** in Figure 1c showed stretching bands symmetrical and asymmetrical at 3335 and 3433 cm^{-1} for NH_2 , 3213 cm^{-1} for aromatic C-H stretching, 2860 - 3076 cm^{-1} for aliphatic C-H stretching, 2208 cm^{-1} for $\text{C}\equiv\text{N}$ stretching, 1610 cm^{-1} for N-H bending, 1562 cm^{-1} for C=C, band at 1234 cm^{-1} for asymmetrical C-O-C and band at 1072 cm^{-1} for asymmetrical C-O-C. For compound **9**, a band of $\text{C}\equiv\text{N}$, but bands of NH_2 stretching at 3319 and 3416 cm^{-1} , N-H at 3192 cm^{-1} , aromatic C-H at 3122 cm^{-1} , aliphatic C-H at 2810-

3072 cm^{-1} , C=N at 1602 cm^{-1} , and a band C=C at 1550 cm^{-1} , Figure 1d.

The ^1H NMR spectrum of compound **3** in Figure (2e) showed signals at $\delta = 6.69$ ppm (s, 2H, NH_2), $\delta = 7.42$ -7.54 ppm (m, 5H, ArH) and $\delta = 7.78$ ppm (s, 1H, N=CH). For compound **4**, signals at $\delta = 2.14$ ppm (s, 3H, CH_3), $\delta = 7.36$ -8.05 ppm (m, 5H, ArH), $\delta = 8.27$ ppm (s, 1H, N=CH) and $\delta = 12.34$ ppm (s, 1H, NH). The ^1H NMR spectrum of compound **7** in Figure 2f showed signals at $\delta = 2.28$ ppm (s, 3H, NCH_3), $\delta = 2.40$ ppm (t, 2H, CH_2), $\delta = 2.59$ ppm (t, 2H, NCH_2), $\delta = 2.82$ ppm (s, 6H, $\text{N}(\text{CH}_3)_2$), $\delta = 4.45$ ppm (s, 1H, CH), $\delta = 6.34$ ppm (s, 2H, NH_2), $\delta = 6.58$ -7.24 ppm (m, 4H, ArH).

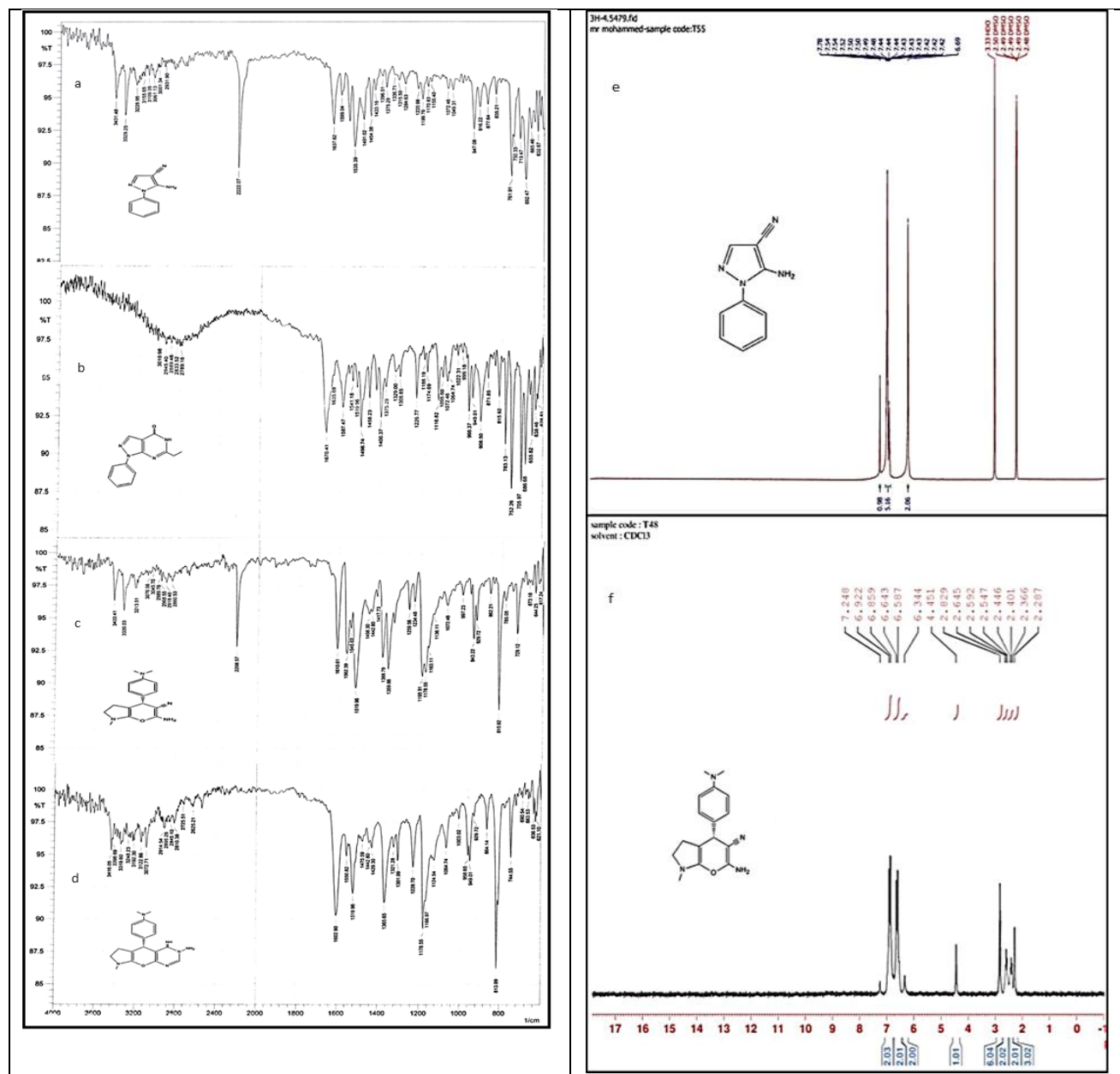


Figure 2: Characterization of the prepared compounds. The FTIR spectra of compounds **3**, **4**, **7**, and **9** are shown in a-d. The ^1H NMR of compounds **3** and **7** are shown in e and f.

3.3. Effect of Pyrimidine Derivatives (Compound 4 and 9) on AChE Activity

Clinically, acetylcholinesterase inhibitors (AChEI) are used to treat various diseases, including Myasthenia

gravis, Glaucoma, Lewy body dementia, and Alzheimer's disease (32).

Treatment is believed to reduce symptoms by improving cholinergic function and increasing the

amount of acetylcholine in cholinergic synapses. The active site must be reversibly bound to the active site of the enzyme to be a successful inhibitor, as irreversible binding can result in severe consequences, including death (33). In this regard, in many nations, the synthesis of fused pyrimidine compounds and investigating microbiological and toxicity tests are commonly useful.

The activity of AChE was estimated before and after adding the compounds **4** and **9** using a series of

concentrations (10^{-2} , 10^{-3} , 10^{-5} , 10^{-7} , 10^{-9} , 10^{-11}) M of and different concentrations of ASChI (0.02, 0.04, 0.06 and 0.08) M) Figure 2a. In this paper, the effect of compounds **4** and **9** on human AChE activity against DMSO as a blank solution was analyzed, Figure 2b. Pyrimidine derivatives **4** and **9** showed inhibitory effects on enzyme activity compared with the normal values of AChE ($2.63 \mu\text{mol}/2 \text{ min}/\text{mL}$), Figure 2b, Table 2.

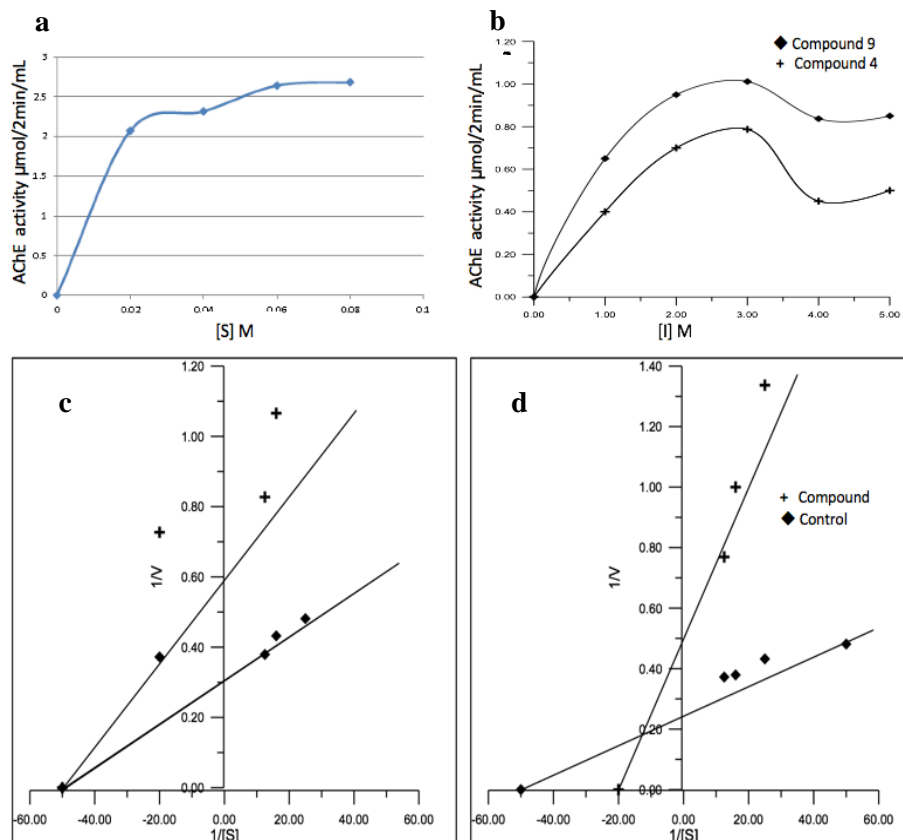


Figure 3: The activity of human AChE at different concentrations of ASChI before and after adding compounds **4** and **9**. a) The enzymatic activity of free AChE, b) The enzymatic activity of AChE after adding compounds **4** and **9**. The Lineweaver-Burk plots of AChE in the presence of the maximum concentration of compounds **4** and **9** are shown in c and d.

Table 2: Effect of pyrimidine (compounds **4** and **9**) on AChE activity.

Compounds	Inhibitor (M)	AChE $\mu\text{mol}/2\text{min}/\text{ml}$	% inhibition
Control	zero	2.630	-
Compound 4	10^{-3}	0.500	80.98
	10^{-5}	0.450	82.88
	10^{-7}	0.780	70.07
	10^{-9}	0.700	73.38
	10^{-11}	0.400	84.79*
Compound 9	10^{-3}	0.850	67.68
	10^{-5}	0.837	68.18
	10^{-7}	1.012	61.60
	10^{-9}	0.950	63.88
	10^{-11}	0.650	75.29*

* Maximum inhibition concentration in each compound.

Table 2 indicated that the highest significant inhibition% of compound **4** (84.79%) and compound **9** (75.29%) were at (10^{-11}) M concentrations, which could be attributed to the presence of more than one

nucleophile side in both compounds. Compound **9** has (NH_2), dimethyl aniline group linked to anthracenyl showed good inhibition of AChE activity, whereas the phenyl ring attached to imidazole [1,2-

a] pyridine in the compound **4** may compete with the substrate ASChI and cause properly orient to fit the active site of the enzyme. The type of inhibition and kinetic parameters (K_m , V_{max} , and K_i) at different substrate concentrations were determined using the Lineweaver-Burk plot, Figure 2c and 2d), and Table 3.

Table 3: Kinetic properties of AChE with and without pyrimidine compounds.

Sample	Inhibitor (M)	K_m (M)	V_{max} ($\mu\text{mol/mL/2min}$)	K_i (M)	Inhibition type
Control	Zero	0.02	5	-	-
	10^{-7}	0.02	2.5	3×10^{-8}	Non-competitive
Compound 4	10^{-11}	0.02	2.22	2.1×10^{-12}	Non-competitive
	10^{-7}	0.05	1.92	9.2×10^{-8}	Mix
Compound 9	10^{-11}	0.05	1.81	8.3×10^{-12}	Mix

Results in Table 3 showed that K_m values varied depending on the type of inhibition. The higher K_m value and the lower K_i value refer to the highest affinity of the inhibitor to fit into the active site cleft of the enzyme. Accordingly, compounds **4** and **9** have the highest affinity to bind the enzyme at 10^{-11} M, where the lowest K_i values. This assumes the kinetics of a tight-binding inhibitor. The results also showed that compound **9** have mixed-type inhibition, which can be attributed to the structure of the inhibitor that makes a conformational change after binding to -SH, -COOH, imidazole group of Ser, His, Glu in AChE, which located in the active center of the enzyme or essential in determining the active conformation of the enzyme molecule. On the other hand, the non-competitive inhibition of compound **4** is a classical model of inhibitor that binds to another site at enzyme molecule and causes conformational change locking the enzymatic activity.

The amide group in the pyrimidine ring and the hetero aromatic ring contributed to the inhibition of acetyl and butyl cholinesterase. Compared to the unsubstituted pyrazole compounds, the substitution of pyrazole with the aryl ring increases the inhibition potency of the compounds. Now, it has been shown that a large number of Sp^2 carbons, and therefore the n orbitals, increases molecular recognition by the AChE enzyme, as the active site of AChE is composed of many aromatic amino acids (34). Importantly, the affinity toward the active site could be affected by several factors, such as size, three-dimensional structure, the existence of groups that easily bind noncovalently to groups within or near the active site, etc. The position in space could be attributed as a result of such a good-fit orientation such as the covalent bonding and hydrogen bonding with the serine residue. A previous study (35) reported a rational design of 5H-thiazolo[3,2-a] pyrimidine derivatives that acted as AChE inhibitors binding to the active site of the human AChE substratum domain. Studies of molecular analysis led to the discovery of some pyrimidine derivatives, such as 3H-thiazole substituted with 3H [3,2-a], where their biological activity was fully in line with the proposed binding. The replaced 5H-thiazole [3,2-a] pyrimidine derivatives could improve the structure of enzyme inhibitors into novel therapeutic agents for serious neurodegenerative diseases.

Another study (36) developed a sequence of 6H-benzo[c]chromen-6-one and 7,8,9,10-tetrahydrobenzo[c]chromen-6-one derivatives in a variety of plant-derived nutritional products. The biological activity was tested as a potential inhibitor of acetylcholine esterase and butyrylcholine esterase. However, it did not show an inhibitory effect on cholinesterase enzymes and suggested that compounds based on the inhibition of cholinesterase enzymes should be generated with benzo [c] chromene-6-one.

A new series of some novel 1,2,3,4-tetrahydropyrimidine condensed pyrazinamide has been developed and evaluated as inhibitors of acetyl and butyl cholinesterase (AChE and BuChE) (37,38) reported a straightforward two-stage synthesis and biological evaluation of novel racemic benzochromene pyrimidinones as non-hepatotoxic, acetylcholine esterase inhibitors and found significantly lower inhibition of hAChE compared to EeAChE, IC₅₀ values ranging from 1279 to 3657 nM. Compound 3Bb was the most effective inhibitor.

The kinetic mechanism of inhibition of hAChE by compound 3Bb was investigated using classical double reciprocal plots of Lineweaver-Burk to gain insight into the mode of inhibition. Analysis of this graph revealed the interception of the lines above the x-axis, suggesting that 3Bb is capable of interacting with both the free and the acylated enzyme, thus acting as a mixed-type hAChE inhibitor. The constants of inhibitor dissociation K_i (the constant of complex dissociation enzyme-inhibitor) and K_i' (the constant of complex dissociation enzyme-inhibitor-substrate) are calculated at 0.38 and 1.12 μM , respectively.

A sequence of novel 1,2,3,4-tetrahydropyrimidines of biological interest has been synthesized (37). Compound libraries were prepared using *p*-toluenesulfonic acid as an active catalyst compared to Lewis acid. The results showed that all synthesized compounds were active against acetyl and butylcholinesterase enzyme activities. Anis et al (39) prepared a new hybrid molecule type pyrazolo[4,3-e]-1,2,4-triazole [1,5-c] pyrimidines derivatives. The anti-acetylcholine esterase activity of compounds was evaluated, and results indicated significant activities (IC₅₀= 1.73–39.86 μM). The

dihydrobenzimidazopyrimidine derivatives were analyzed against acetylcholinesterase (AChE) and exhibited effective inhibitory activity at 46.8 nM and 42.5 nM IC₅₀ (40).

3.4. Molecular Docking

In the present work, an in silico study was performed using molecular docking simulation to test the capability of some synthesized compounds as potential AChE inhibitors. Target compounds **4** and **9** and Donepezil were docked as ligands with the active pocket of AChE (PDB ID: 2ACE) to achieve favorable conformation, with the maximum number of interactions and minimal free energy, as shown in Figs. 4, 5, and 6. The study findings including binding energies and types of interactions are shown in Table 4.

Figure 4 shows 2D and 3D Donepezil interactions as a ligand with target 2ACE, including H-bond, π - π , and van der Waals interactions with residues of

Tyr121, Trp279, Tyr334, Phe284, and Leu282 amino acids at the active site of AChE with a binding energy -8.6 kcal/mol and distances ranging from 2.68 to 3.23. The docking simulation of compounds **4** and **9** demonstrated stronger electrostatic interactions (van der Waal's, π - π stacking, and H-bond) with lower docking energies -11.4, -10.6 kcal/mol respectively as shown in Fig. 4, 5 & 6. Among the other derivatives, derivative **4** formed H-bond interactions with key amino acids residues Tyr334, and Asp72, whereas the other electrostatic interactions formed with Tyr334, Phe330, Ile287, Tyr121, Arg289, Trp279, Gly335, and Phe288. In the case of derivative **9**, similar binding interactions with the active pockets of 2ACE were observed due to the high homology of the binding site residues. The considerable number of various binding interactions with amino acid residues of the active pocket in the target protein, as well as favorable binding energies, suggests that these compounds could be used as clinically effective inhibitors for the AChE enzyme.

Table 4: Docking results obtained for synthesized coumarin derivatives with acetylcholinesterase (PDB ID: 2ACE).

Compound	Ligand moiety	Site	Interaction	E (kcal/mol)
4	NH ₂	N TYR 334 (A)	H-bond acceptor	-12.4
	NH	O ASP 72 (A)	H- bond acceptor	
	C=O	N GLY 335 (A)	H- bond donor	
	6-ring	TYR 334 (A)	Pi-Pi	
	C=C	ILE 287 (A)	Pi-Alkyl	
	NH ₂	N ASP 72 (A)	H- bond acceptor	
9	NH	O PHE 330 (A)	H- bond acceptor	-11.6
	C=C	N ASP 72 (A)	Pi- Anion	
	6-ring	TYR 334 (A)	Pi-Alkyl	
		TRP 279 (A)	Pi-Alkyl	
	-OCH ₃	NH TYR 121 (A)	H- bond acceptor	
Donepezil	6-ring	O PHE 330 (A)	H- bond acceptor	-8.6
		N PHE 284 (A)	H- donor	
		TRP 279 (A)	Pi-H bond	
	C=C	ASP 285 (A)	Pi-Pi	
		LEU 282 (A)	Pi-Alkyl	

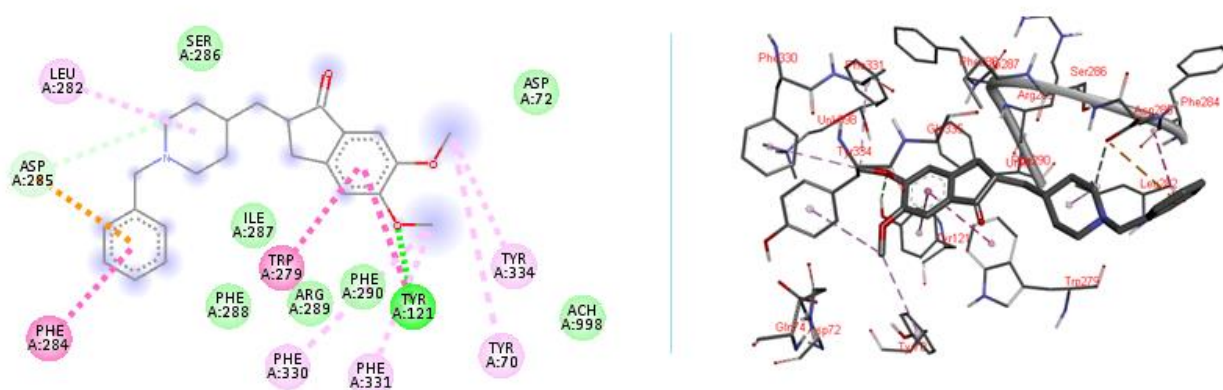


Figure 4: The receptor-ligand interactions on 2D and 3D-Diagram of Donepezil on the catalytic site of AChE enzyme.

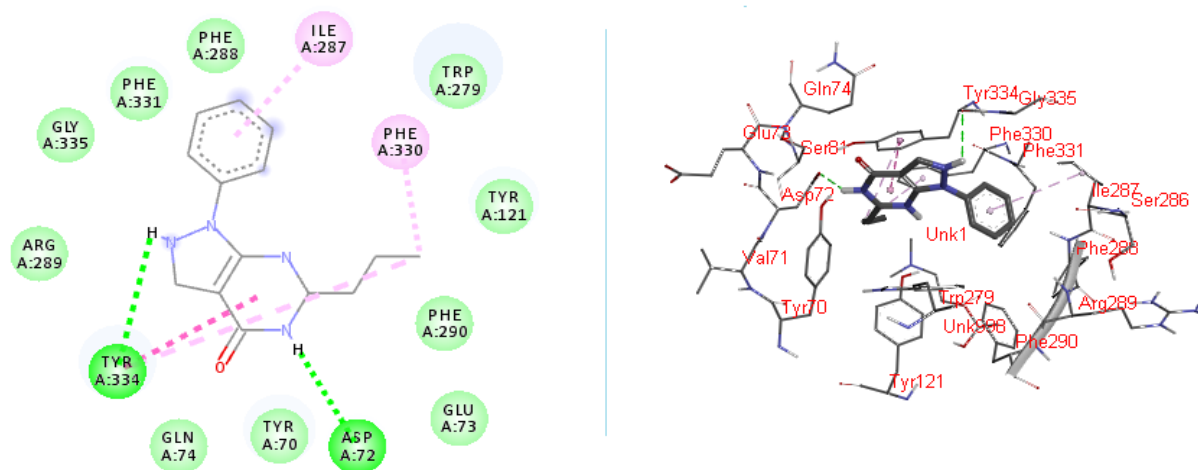


Figure 5: The receptor-ligand interactions on 2D and 3D-Diagram of compound **4** with the catalytic site of AChE enzyme.

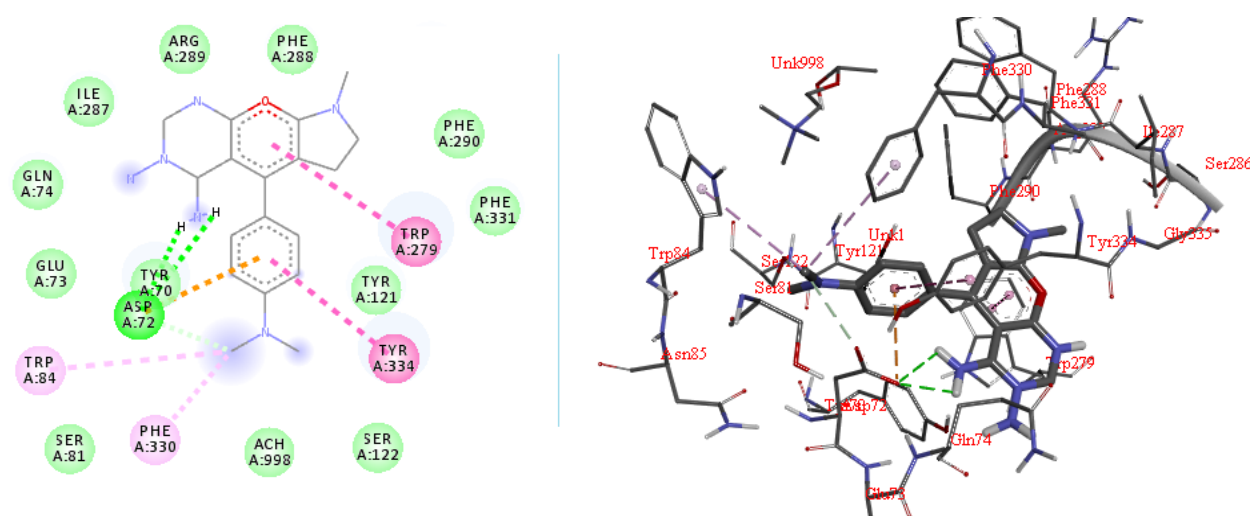


Figure 6: The receptor-ligand interactions on 2D and 3D-Diagram of compound **9** with the catalytic site of AChE enzyme.

3.5. Pharmacokinetic and Toxicological Properties

Both compounds have high gastrointestinal absorption. It shows that these compounds can be easily consumed in the gastrointestinal tract when taken by oral administration. Both compounds can cross the blood-brain barrier and cannot be used as substrates of P-glycoprotein. The red dot in the yolk area indicates that compounds **4** and **9** may remain in the brain unaffected by P-glycoprotein. According to the BOILED-Egg data model, compounds **4** and **9** have excellent drug capability for both blood-brain barrier penetration and gastrointestinal absorption, Figure 7. Although compound **4** is an inhibitor of CYP1A2, it is a non-inhibitor of the enzymes CYP2C19, CYP2C9, CYP2D6, and CYP3A4 enzymes. While Compound **9** is the non-inhibitor of CYP1A2, it is the

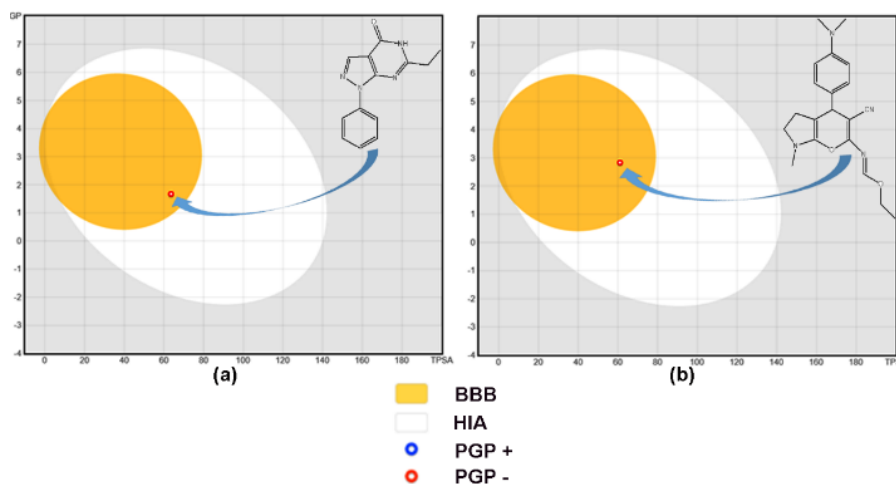
inhibitor of CYP2C19, CYP2C9, CYP2D6, and CYP3A4 enzymes. A cytochrome P450 non-inhibitor indicates that the molecule will not interfere with the biotransformation of the substance (drug) metabolized by cytochrome P450. Both compounds comply with Lipinski's rule of 5, see Table 5. When the toxic properties of the compounds were evaluated, it was determined that Compound **4** had hepatotoxic and carcinogenic properties but was mutagenic, immunotoxic, cytotoxic, irritant, and inactive. Compound **9** is inactive in terms of hepatotoxic and carcinogenic, mutagenic, immunotoxic, cytotoxic, and irritant. When all these properties are evaluated, it is recommended to carry out further research on the drug properties of compounds **4** and **9**.

Table 5: The pharmacokinetic properties of compounds **4** and **9**.

Properties	4	9
Molecular weight ^a	240.26	352.43
	g/mol	g/mol
Number of atoms	30	50
Heavy atoms	18	26
Rotatable bonds	2	5
H-Bond acceptors	3	4
H-Bond donors	1	0
Molar refractivity	69.26	105.73
TPSA (Å ²)	63.57	61.09
Log <i>P</i> _{o/w}	2.20	2.83
GI absorption	High	High
BBB permeant	Yes	Yes
<i>P</i> -gp substrate	No	No
CYP1A2 inhibitor	Yes	No
CYP2C19 inhibitor	No	Yes
CYP2C9 inhibitor	No	Yes
CYP2D6 inhibitor	No	Yes
CYP3A4 inhibitor	No	Yes
Log <i>K</i> _p (cm/s)	-6.72	-6.50
Lipinski	Yes, 0 violation	Yes, 0 violation
Toxicity class ^a	4	4
Predicted LD ₅₀	1000	1200
	mg/kg	mg/kg
Hepatotoxicity	Active	Inactive
Carcinogenicity	Active	Inactive
Immunotoxicity	Inactive	Inactive
Mutagenicity	Inactive	Inactive
Cytotoxicity	Inactive	Inactive
MMP ^b	Inactive	Inactive
Irritant	Inactive	Inactive

^aThe toxicity class consists of six numbers. (Number 1 means toxic; number 6 means non-toxic.)

^bMMP: Mitochondrial Membrane Potential

**Figure 7:** The BOILED-Egg models of compounds **4** (a) and **9** (b).

4. CONCLUSION

In the present study, a new family of multitarget molecules has been designed to be able to interact with AChE. These compounds were well characterized and showed significant substitutions predominantly at (NH₂) and dimethyl aniline group linked to anthracenyl. These substituted molecules showed a good inhibitory effect on AChE activity, whereas a phenyl ring attached to imidazole [1,2-a]

pyridine was studied to improve the inhibitory of AChE activity. The data of this research suggest that these molecules are promising leads for the development of novel multitarget-directed ligands of MTDL with good inhibitory potency of AChE, which is presently missing in the therapeutic arsenal. The strong interactions with amino acid residues of the active pocket in the target protein as well as favorable binding energies suggest that these compounds could be used as clinically effective

inhibitors for the AChE enzyme. When the predicted pharmacokinetic and toxicological properties (ADMET) of the synthesized compounds are evaluated, it is suggested that they may be good drug candidates due to their low toxicity class and compatibility with the Lipinski rules, and further *in vivo/in vitro* studies are recommended.

5. CONFLICT OF INTEREST

The authors have nothing to declare.

6. ACKNOWLEDGMENTS

This research was registered in the annual plan of the Department of Chemistry at Mustansiriya University, on January 11, 2021. The authors thank Mustansiriya University for supporting this research <https://uomustansiriya.edu.iq/>. The authors are also grateful to Dr. Hamed Hashim for his useful decisions regarding FT-IR.

7. ETHICS APPROVAL AND CONSENT TO PARTICIPATE

7.1. Ethical Approval

Research ethics was approved by the ethics committee of Mustansiriya University (Iraq).

7.2. Human and Animal Rights

Animals were not used in this investigation. The procedures were in accordance with the standard ethical statement authorized by Mustansiriya University. The authors have obtained permission from the participants to do the *in vitro* study.

8. AUTHOR CONTRIBUTION

The authors have contributed equally to this manuscript.

9. REFERENCES

- Sher N, Alkhalifah DHM, Ahmed M, Mushtaq N, Shah F, Fozia F, et al. Comparative Study of Antimicrobial Activity of Silver, Gold, and Silver/Gold Bimetallic Nanoparticles Synthesized by Green Approach. *Molecules* [Internet]. 2022 Nov 15;27(22):7895. Available from: [<URL>](#).
- Sher N, Ahmed M, Mushtaq N, Khan RA. Calligonum polygonoides reduced nanosilver: A new generation of nanoparticle for medical applications. *Eur J Integr Med* [Internet]. 2020 Jan 1;33:101042. Available from: [<URL>](#).
- Hussein AM, Ahmed OM. Regioselective one-pot synthesis and anti-proliferative and apoptotic effects of some novel tetrazolo[1,5-a]pyrimidine derivatives. *Bioorg Med Chem* [Internet]. 2010 Apr;18(7):2639–44. Available from: [<URL>](#).
- Khobragade CN, Bodade RG, Konda SG, Dawane BS, Manwar A V. Synthesis and antimicrobial activity of novel pyrazolo[3,4-d]pyrimidin derivatives. *Eur J Med Chem* [Internet]. 2010 Apr;45(4):1635–8. Available from: [<URL>](#).
- Abd El-Latif NA, Amr AEGE, Ibrahim AA. Synthesis, Reactions, and Pharmacological Screening of Heterocyclic Derivatives Using Nicotinic Acid as a Natural Synthone.

Monatshefte für Chemie - Chem Mon [Internet]. 2007 Jun 12;138(6):559–67. Available from: [<URL>](#).

6. Prakash O, Kumar R, Kumar R, tyagi P, Kuhad RC. Organiodine(III) mediated synthesis of 3,9-diaryl- and 3,9-difuryl-bis-1,2,4-triazolo[4,3-a][4,3-c]pyrimidines as antibacterial agents. *Eur J Med Chem* [Internet]. 2007 Jun;42(6):868–72. Available from: [<URL>](#).

7. Guetzoyan LJ, Spooner RA, Lord JM, Roberts LM, Clarkson GJ. Simple oxidation of pyrimidinylhydrazones to triazolopyrimidines and their inhibition of Shiga toxin trafficking. *Eur J Med Chem* [Internet]. 2010 Jan;45(1):275–83. Available from: [<URL>](#).

8. Chen Q, Zhu XL, Jiang LL, Liu ZM, Yang GF. Synthesis, antifungal activity and CoMFA analysis of novel 1,2,4-triazolo[1,5-a]pyrimidine derivatives. *Eur J Med Chem* [Internet]. 2008 Mar;43(3):595–603. Available from: [<URL>](#).

9. Mahmoud MR, El-Ziaty AK, Ismail MF, Shiba SA. Synthesis of novel pyrimidine and fused pyrimidine derivatives. *Eur J Chem* [Internet]. 2011 Sep 30;2(3):347–55. Available from: [<URL>](#).

10. Patil SB. Recent medicinal approaches of novel pyrimidine analogs: A review. *Heliyon* [Internet]. 2023 Jun 1;9(6):e16773. Available from: [<URL>](#).

11. Raghunath BT, Balasaheb PP, Satish MC, Pratiksha G, Vasant MP. Synthesis and Antimicrobial Activity of Benzo[H][1,6]Naphthyridine Derivatives. *J Org Inorg Chem* [Internet]. 2016;2(1):2. Available from: [<URL>](#).

12. Deady LW, Rodemann T, Zhuang L, Baguley BC, Denny WA. Synthesis and Cytotoxic Activity of Carboxamide Derivatives of Benzo[b][1,6]naphthyridines. *J Med Chem* [Internet]. 2003 Mar 1;46(6):1049–54. Available from: [<URL>](#).

13. Madaan A, Verma R, Kumar V, Singh AT, Jain SK, Jaggi M. 1,8-Naphthyridine Derivatives: A Review of Multiple Biological Activities. *Arch Pharm (Weinheim)* [Internet]. 2015 Dec 9;348(12):837–60. Available from: [<URL>](#).

14. Al-Qaisi ZHJ, Al-Garawi ZS, Al-Karawi AJM, Hammood AJ, Abdallah AM, Clegg W, et al. Corrigendum to "Antiureolytic activity of new water-soluble thiazazole derivatives: Spectroscopic, DFT, and molecular docking studies" *Spectrochimica Acta Part A: Molecular and Biomolecular Spectroscopy* 272 (2022) 120971. *Spectrochim Acta Part A Mol Biomol Spectrosc* [Internet]. 2022 Jun;274:121102. Available from: [<URL>](#).

15. Vijesh AM, Isloor AM, Shetty P, Sundershan S, Fun HK. New pyrazole derivatives containing 1,2,4-triazoles and benzoxazoles as potent antimicrobial and analgesic agents. *Eur J Med Chem* [Internet]. 2013 Apr;62:410–5. Available from: [<URL>](#).

16. Aggarwal R, Kumar V, Gupta GK, Kumar V. Synthesis of some new 3,5-diamino-4-(4'-fluorophenylazo)-1-aryl/heteroarylpyrazoles as antimicrobial agents. *Med Chem Res* [Internet]. 2013 Aug 27;22(8):3566–73. Available from: [<URL>](#).

17. Vicentini CB, Romagnoli C, Andreotti E, Mares D. Synthetic Pyrazole Derivatives as Growth Inhibitors of Some Phytopathogenic Fungi. *J Agric Food Chem* [Internet]. 2007 Dec 1;55(25):10331–8. Available from: [<URL>](#).

18. Nabi Mohammed M, Ahmed Mutanabbi A, Mohammed HH. Synthesis, Antibacterial Evaluation and Docking Study of Some New Fused Pyrido-Pyrimidine and Naphthyridine Cycles. *J Glob Pharma Technol*. 2019;11(5).

19. Al Nabi MHA, Mohammed HH, Abdellah AM, Mageed ZN, Salman GA. Synthesis and Biological Evaluation of Fused Pyrrolo-Pyrano-Pyrimidine and Pyrrolo-Pyrano-Pyridine Derivatives. *J Pharm Sci Res* [Internet]. 2019;11(4):1589-94. Available from: [<URL>](#).
20. Huber W. 2,4-Diamino-5-(4-methyl-5- β -hydroxyethylthiazolium chloride)-methylpyrimidine Hydrochloride, a New Analog of Thiamin. *J Am Chem Soc* [Internet]. 1943 Nov 1;65(11):2222-6. Available from: [<URL>](#).
21. Aggarwal R, Kumar V, Singh SP. Synthesis and NMR spectral studies of some new 1-heteroaryl-5-amino-3-alkyl/aryl-4-cyanopyrazoles. *Indian J Chem* [Internet]. 2006 [cited 2024 Jul 4];45B:1426-30. Available from: [<URL>](#).
22. Ellman GL, Courtney KD, Andres V, Featherstone RM. A new and rapid colorimetric determination of acetylcholinesterase activity. *Biochem Pharmacol* [Internet]. 1961 Jul 1;7(2):88-95. Available from: [<URL>](#).
23. Zaifafoon N. Kinetics for the Inhibition of Serum Acetylthiocholin Esterase Activity by Some Prepared Phenobarbital Derivatives. *Int J Biochem Res Rev* [Internet]. 2015 Jan 10;7(2):100-11. Available from: [<URL>](#).
24. Trott O, Olson AJ. AutoDock Vina: Improving the speed and accuracy of docking with a new scoring function, efficient optimization, and multithreading. *J Comput Chem* [Internet]. 2010 Jan 30;31(2):455-61. Available from: [<URL>](#).
25. BIOVIA. Dassault Systèmes, BIOVA Discovery Studio Visualizer 2021, v21.1.0.20298, San Diego: Dassault Systèmes. 2021.
26. Lipinski CA, Lombardo F, Dominy BW, Feeney PJ. Experimental and computational approaches to estimate solubility and permeability in drug discovery and development settings. *Adv Drug Deliv Rev* [Internet]. 2001 Mar;46(1-3):3-26. Available from: [<URL>](#).
27. Daina A, Michielin O, Zoete V. SwissADME: a free web tool to evaluate pharmacokinetics, drug-likeness and medicinal chemistry friendliness of small molecules. *Sci Rep* [Internet]. 2017 Mar 3;7(1):42717. Available from: [<URL>](#).
28. Banerjee P, Eckert AO, Schrey AK, Preissner R. ProTox-II: a webserver for the prediction of toxicity of chemicals. *Nucleic Acids Res* [Internet]. 2018 Jul 2;46(W1):W257-63. Available from: [<URL>](#).
29. Sander T. Molecular Properties Prediction - OSIRIS Property Explorer [Internet]. [cited 2022 Dec 30]. Available from: [<URL>](#).
30. Anderson JD, Cottam HB, Larson SB, Dee Nord L, Revankar GR, Robins RK. Synthesis of certain pyrazolo[3,4-d]pyrimidin-3-one nucleosides. *J Heterocycl Chem* [Internet]. 1990 Feb 11;27(2):439-53. Available from: [<URL>](#).
31. Karoui A, Allouche F, Deghrigue M, Agrebi A, Bouraoui A, Chabchoub F. Synthesis and pharmacological evaluation of pyrazolopyrimidopyrimidine derivatives: anti-inflammatory agents with gastroprotective effect in rats. *Med Chem Res* [Internet]. 2014 Mar 4;23(3):1591-8. Available from: [<URL>](#).
32. Thakurathi N, Vincenzi B, Henderson DC. Assessing the prospect of donepezil in improving cognitive impairment in patients with schizophrenia. *Expert Opin Investig Drugs* [Internet]. 2013 Feb 9;22(2):259-65. Available from: [<URL>](#).
33. Brown SS, Kalow W, Pilz W, Whittaker M, Woronic CL. The Plasma Cholinesterases: A New Perspective. 1981;1-123. Available from: [<URL>](#).
34. Trujillo-Ferrara J, Montoya Cano L, Espinoza-Fonseca M. Synthesis, anticholinesterase activity and structure-Activity relationships of m-Aminobenzoic acid derivatives. *Bioorg Med Chem Lett* [Internet]. 2003 May;13(10):1825-7. Available from: [<URL>](#).
35. Zhi H, Chen L mei, Zhang L lin, Liu S jie, Chi Cheong Wan D, Lin H quan, et al. Design, synthesis, and biological evaluation of 5H-thiazolo[3,2-a]pyrimidine derivatives as a new type of acetylcholinesterase inhibitors. *ARKIVOC* [Internet]. 2008;266-77. Available from: [<URL>](#).
36. Gulcan HO, Unlu S, Esiringu İ, Ercetin T, Sahin Y, Oz D, et al. Design, synthesis and biological evaluation of novel 6H-benzo[c]chromen-6-one, and 7,8,9,10-tetrahydrobenzo[c]chromen-6-one derivatives as potential cholinesterase inhibitors. *Bioorg Med Chem* [Internet]. 2014 Oct;22(19):5141-54. Available from: [<URL>](#).
37. Elumalai K, Ali MA, Elumalai M, Eluri K, Srinivasan S. Acetylcholinesterase enzyme inhibitor activity of some novel pyrazinamide condensed 1,2,3,4-tetrahydropyrimidines. *Biotechnol Reports* [Internet]. 2015 Mar;5:1-6. Available from: [<URL>](#).
38. Dgachi Y, Bautista-Aguilera O, Benchekroun M, Martin H, Bonet A, Knez D, et al. Synthesis and Biological Evaluation of Benzochromenopyrimidinones as Cholinesterase Inhibitors and Potent Antioxidant, Non-Hepatotoxic Agents for Alzheimer's Disease. *Molecules* [Internet]. 2016 May 14;21(5):634. Available from: [<URL>](#).
39. Romdhane A, Said A Ben, Cherif M, Jannet H Ben. Design, synthesis and anti-acetylcholinesterase evaluation of some new pyrazolo[4,3-e]-1,2,4-triazolo[1,5-c]pyrimidine derivatives. *Med Chem Res* [Internet]. 2016 Jul 18;25(7):1358-68. Available from: [<URL>](#).
40. Koti Reddy E, C. R, Sajith AM, K. V. D, C. S, Anwar S. Functionalised dihydroazo pyrimidine derivatives from Morita-Baylis-Hillman acetates: synthesis and studies against acetylcholinesterase as its inhibitors. *RSC Adv* [Internet]. 2016;6(81):77431-9. Available from: [<URL>](#).



Curing Kinetic Analysis and Isothermal Prediction of DBTL Catalyzed Polyurethane Reaction by Differential Scanning Calorimetry

Seçil Sevim Ünlütürk*  and Necati Güdümcüoğlu 

Kansai Altan Paint Industry and Trade Inc.

Abstract: Kinetic analysis is generally carried out to clarify the reaction mechanism with kinetic parameters and to predict the kinetic properties of materials under different reaction parameters. The kinetics of the polyurethane polymerization reaction between acrylic polyol and isocyanate was investigated by Differential Scanning Calorimetry (DSC) in terms of catalyst amounts and sampling times. Single and multiple heating analyses were used to obtain DSC curves for each sample. The simple kinetic model and Multilinear Regression Fit (MRF) were used to calculate the kinetic parameters and simulate the isotherm prediction curves. The kinetic calculations showed that the glass transition temperatures (up to 44 °C) and activation energy (E_a) values increased with the degree of conversion for all cases. The reduction in the rate constant for partially cured samples was greater than the initial sampling time of the same sample. This observation indicates that the diffusion controlled reaction dominates and E_a increases due to the highly cross-linked and dense medium in partially cured samples. Isothermal prediction curves provide an understanding of different curing conditions at different reaction temperatures and times. Prediction curves show slower conversion even for final samples, confirming that final samples may remain uncured. Applying the results of this study, especially for real-world applications, where fully cured samples are required, additional annealing procedures can be easily established.

Keywords: Polyurethane, Curing Kinetic, Differential Scanning Calorimetry

Submitted: March 22, 2024. Accepted: June 12, 2024.

Cite this: Ünlütürk SS, Güdümcüoğlu N. Curing Kinetic Analysis and Isothermal Prediction of DBTL Catalyzed Polyurethane Reaction by Differential Scanning Calorimetry. JOTCSA. 2024;11(3):1211–24.

DOI: <https://doi.org/10.18596/jotcsa.1441231>.

*Corresponding author. E-mail: sclsvm@gmail.com.

1. INTRODUCTION

Polyurethanes are widely used polymeric materials in foams, coatings, adhesives, insulators, etc. They are very popular especially in automobile coatings due to their advantages in terms of weathering, appearance, chemical and mechanical resistance, etc.(1) All these advantages are provided by controlling the reaction kinetics of the polymeric matrix. In other words, understanding the rate of the chemical reaction is critical in terms of deciding the desired outcomes of the chemical reaction.

Kinetic analysis is very popular in terms of both understanding the reaction mechanism by describing the kinetic process and the kinetic prediction of the reaction in different reaction parameters. Generally, the kinetic process can be defined with the kinetic triplet which are the activation energy (E_a), the pre-exponential factor (A), and the reaction model ($f(a)$). The activation energy is the energy barrier for the

reaction. It is valuable to evaluate the reaction parameters like reaction temperature, time, etc., and accordingly the desired product yield. While the pre-exponential factor can be described as the vibrational frequency of the activated complex, the reaction model is directly relevant to the reaction mechanism (2). The reaction model can be autocatalyzing or nth order depending on the reaction mechanism. An autocatalytic process due to the formation of hydroxyl groups in an epoxy system was studied by Yi et al. to understand the solvent effect of the system(3). On the other hand nth order curing reaction model is accepted as the simplest way to describe the curing kinetic reactions of thermosetting plastics(4) like polyurethanes.

Several techniques can be used to evaluate the reaction kinetics. Viscosity measurements were preferred to estimate the reaction kinetics by Manu et al. but they work only below the gel point of the materials(5) which limits to study of other materials.

Techniques like gel permeation chromatography (GPC) and nuclear magnetic resonance (NMR) spectroscopy are also tools to study the reaction kinetics. However, the insolubility of materials in organic solvents restricts the usage of these techniques(6). Epoxy amine reactants can be considered as an example of this case that the recently cured products are insoluble in the organic solvent that is used in these methods. Additionally, these kinds of techniques require critical expertise it is difficult to analyze the spectra. The presence of numerous methyl and methylene groups makes the NMR spectrum very complex. Similarly, GPC, may not be very realistic or indicative due to the highly branched polymer structure(7). Apart from these thermal analysis like thermal gravimetric analysis (TGA) or differential thermal analysis (DTA) and mostly differential scanning calorimetry (DSC), can be used for the determination of the curing reactions. (8, 9)

In this study, the reaction between an isocyanate and acrylic polyol curing reaction was investigated by the non-isothermal method of DSC. The isothermal method was not preferred because there is an inconsistency caused by the fact that a significant part of the cure reaction occurs before the set isothermal temperature is reached. The non-isothermal method includes single and multiple heating rate procedures. In this study, mainly a single heating rate was used because of its advantage of being fast and valuable in comparative studies such as evaluating the relative efficiencies of various catalysts. (7) Dibutyltin dilaurate catalyst which is one of the popular organo-tin catalysts in the

production of polyurethanes because of its strong catalytic activity towards diisocyanates and polyols(10) was used. Different amounts of DBTL were added to understand its effect on the kinetic reaction of PUR. Since it is known that PUR reactions have second-order reaction kinetic(11), nth-order reaction kinetics were applied for the samples with 0, 0.01, 0.1, and 0.5 phr (per hundred resin) catalyst amounts in different curing periods. Results were investigated by the calculations according to the simple kinetic model and Multilinear Regression fit (MRF). The isoconventional predictions were evaluated in terms of % conversion concerning reaction time and temperature for different isothermal temperatures and reaction times, respectively. The curing results were also proved by Dynamic Mechanical Analysis, DMA too.

2. EXPERIMENTAL SECTION

2.1. Materials and Preparation

The polyurethane polymer matrix in which commercially available acrylic polyol and modified isocyanate were reacted was used in this study. Butyl acetate was chosen as the solvent. Dibutyltin dilaurate (DBTL) which is a highly reactive solvent-free tin catalyst was added in different amounts to study the effect of catalyst amount on the curing kinetics of the PUR system. Four different samples, C1, C2, C3, and C4 were studied as the catalyst amounts were 0, 0.01, 0.1, and 0.5 phr, respectively. The NCO:OH molar ratio was arranged as 1:1 for all samples. The representative structure of the PUR reaction between polyol and isocyanate is given in Figure 1.

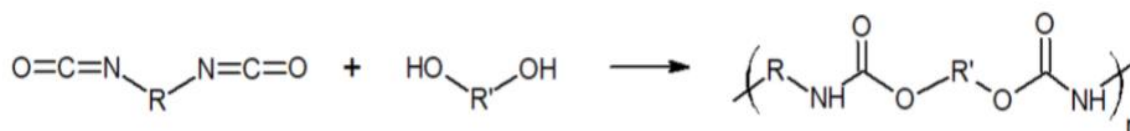


Figure 1. The representative structure of PUR reaction between polyol and isocyanate

Reactants were mixed with Cowles type mixer for 15 minutes at 350 rpm to have a homogenous mixture. The samples were applied to tinplate by 50 μm applicators to have uniform films. Different periods were selected for DSC analysis. For each sample, t_0 (after flash-off time at room temperature - 15 minutes after application), $t_{30\text{min}-80^\circ\text{C}}$ (30 minutes at 80°C annealing after 15 minutes flash-off time), and t_{final} (1 week after 30 minutes at 80°C annealing process and 15 minutes flash-off time) sampling periods were chosen and analyzed in DSC separately. Flash-off time is the necessary waiting time to coat/recoat on a freshly coated surface. DMA analysis for each sample was also applied for Day 1 and Day 7 to understand and compare the effect of catalyst amount on the curing mechanism. Since free films are required for DMA analysis, the same samples were applied to Polypropylene (PP) substrates. Free films of the samples cannot be obtained before Day 1 because of not curing sufficiently.

2.2. Differential Scanning Calorimetry (DSC) Kinetic Measurements

The glass transition temperatures (T_g) and curing kinetics of PUR systems with and without dibutyltin dilaurate catalyst were investigated by DSC 8000, Perkin Elmer. Non-isothermal, also called as isoconventional method was used under different heating rates between -20°C and 200°C temperature ranges. The non-isothermal method was preferred instead of the isothermal method because of obtained relatively more reliable information according to the Kinetics Committee of the International Confederation for Thermal Analysis and Calorimetry (ICTAC) recommendations (12). As mentioned before, inconsistent results may be obtained since a significant part of the material cured during the heat rise to the set isothermal temperature

For the multiple heating methods, the heating rates of 2.5, 5, 10, 20, and 50 K/min were considered. A nitrogen atmosphere was arranged as a constant flow of 50 mL/min. The thermal data obtained from heat

flow as a function of temperature was used to determine both T_g and curing enthalpy of the system. The calibration of DSC was checked by melting temperature and the melting enthalpy of the Indium standard. The curing curves were subtracted from the background curves which were obtained by the same procedure, the same pan (Image S1) but without the sample in it. Isothermal predictive curves are also obtained in terms of % conversion variation concerning time and reaction temperature at different isothermal temperatures and reaction times, respectively.

2.2.1 Theoretical Approach

Theoretically, the reaction rate "n", depends on two variables; temperature "T", and the conversion degree "a". If the reactants and/or products are in the gas form, pressure is also needed as a required term(12). However, there is no reactant or product in gas form in the PUR reaction mechanism. Also, there is an external gas flow in thermal analysis as 50 mL/K. Consequently, the pressure is forced to be constant and neglected in the rate equation that is considered.

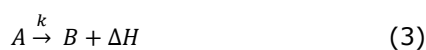
$$v = \frac{d\alpha}{dt} = k(T)f(\alpha) \quad (1)$$

In the equation above, $k(T)$ is the specific rate constant at temperature T and $f(\alpha)$ is the reaction model. The equation is used to describe the rate of a single-step process. If the process is accompanied by the releasing/absorption of heat as measured in DSC, the conversion degree "a" is evaluated by a ratio of curing enthalpy at time t (ΔH_t) to the total curing enthalpy (ΔH_T). Total curing enthalpy can be found experimentally by calculating the area under the curing peak of the uncured sample. Representative image was shown in Figure S1.

$$\alpha = \frac{\Delta H_t}{\Delta H_T} \quad (2)$$

In this case, the conversion degree changes between 0 and 1 as the progress of the process. It can also be named as % Conversion with a variation between 0 and 100. The important point that should be in mind is that the physical properties measured by thermal analysis like DSC can not be related to a specific reaction. As mentioned before, it only gives information about the overall transformation of the reaction. (12)

In the PUR case, the reaction obeys the second-order reaction kinetics. (11, 13, 14) That is the reason nth order reaction model was accepted. The kinetic calculations were done by the scanning kinetics model which assumes the simple kinetic model and uses Multilinear Regression fit (MRF) to curve fit. Whenever a peak is detected on a DSC curve when the sample is subjected to a controlled temperature ramp, it can be assumed that there has been a transformation. This can be represented as the following chemical reaction;



Where, A and B are the materials before and after the conversion, respectively. k is the reaction rate as mentioned before and ΔH is the enthalpy (heat) of the chemical reactions or the physical transition. For the kinetic calculations, the rate of the reaction, the change of reactants to products, and related time/temperature were the concerned terms. The combination of the Eq.1 and 2 give the following which shows the nth-order reaction kinetic with respect to time.

$$\frac{d\alpha}{dt} = k(1 - \alpha)^n \quad (4)$$

Combining the Arrhenius equation (Eq.5) which is used to define rate constant and Eq.4, the final equation is obtained as Eq.6.

$$k(T) = A \exp\left(-\frac{E_a}{RT}\right) \quad (5)$$

$$\frac{d\alpha}{dt} = A \exp\left(-\frac{E_a}{RT}\right) (1 - \alpha)^n \quad (6)$$

where A and E_a are the pre-exponential factor and the activation energy, respectively. R is the universal gas constant (15). The activation energy, pre-exponential factor, and the reaction model, which are named as kinetic triplet, should be described to understand the overall kinetic process of the reaction mechanism. While the activation energy can be defined as the barrier to the reaction starts, the pre-exponential factor is the vibrational frequency of the activated complex. The reaction model is directly linked to the reaction mechanism(2). In this equation, there is one independent variable t, two dependent variables α and T, three unknown constants A , E_a , and n , and the universal gas constant, R .

In DSC, temperature varies with time linearly as shown below;

$$T - T(0) = \beta \cdot t \quad (7)$$

$$\beta = \frac{dT}{dt} \quad (8)$$

Where t is the time, β is the scanning rate, and T and T(0) are the current and initial temperatures, respectively. s time, and β is the scanning rate. All the calculations in this study were done by the following equation which represents the theoretical shape of the DSC curve and obtained by the combination of the eq.8 and 6.

$$\beta \frac{d\alpha}{dt} = A \exp\left(-\frac{E_a}{RT}\right) (1 - \alpha)^n \quad (9)$$

The obtained DSC curves were fitted by the equation 9 or 6 in which the only difference is the unit as dt or dT. A , E_a and n values can be calculated by single DSC curve by having ΔH_t as mentioned in Eq.2. Since there are three unknown parameters, multilinear regression is used by reducing the linear form of equation above (Eq.9). A multilinear regression is performed to solve these three unknown variables by using $\ln \beta \frac{d\alpha}{dt}$, $-\frac{1}{RT}$, and $\ln(1 - \alpha)$ as variables evaluated from DSC data.

On the other hand, the model-free approach was also discussed. Different approximations exist to solve the temperature integral, but Ozawa and Kissinger's equations are very popular in terms of the relationship between activation energy and heating rate, temperature as given below.

Ozawa equation (16);

$$-\ln(\beta) = 1.0516 \left(\frac{E_a}{RT_p} \right) - A \quad (10)$$

Kissinger equation (17);

$$-\ln\left(\frac{\beta}{T_p^2}\right) = \left(\frac{E_a}{RT_p}\right) - \ln\left(\frac{AR}{E_a}\right) \quad (11)$$

In the equations above, β is the heating rate. From the first equation, Ozawa, a plot of $-\ln(\beta)$ vs. $\left(\frac{1}{T_p}\right)$ gives a straight line as a slope that the activation energy can be calculated. Similarly, from the second equation, Kissinger, a plot of $-\ln\left(\frac{\beta}{T_p^2}\right)$ vs. $\left(\frac{1}{T_p}\right)$, the slope can be used to calculate the activation energy.

2.3. Dynamic Mechanical Analysis (DMA)

Dynamic mechanical analysis (DMA) is a thermal analysis technique that measures the deformation of materials under periodic stress. The sinusoidal strain is measured depending on a variable applied sinusoidal stress. As a result, a phase difference occurs between the stress and strain waves that are used to determine storage modulus, loss modulus, and tan delta values (18). Storage modulus (E') is directly linked to the stiffness of a viscoelastic material. It is proportional to the stored energy. On the other hand, loss modulus (E'') represents the molecular motion of the material as the energy dissipation. The loss factor, also known as tan delta ($\tan \delta$) can be obtained by the ratio of loss and storage modulus values as shown below. As a result, it is a dimensionless parameter. It measures the damping behavior in a viscoelastic system(19).

$$\tan \delta = \frac{E''}{E'}$$

Materials do not have a single value as glass transition temperature is generally defined with a range of temperatures. The glass transition temperature (T_g) can be obtained from all these terms. T_g from the storage modulus is calculated from the onset of the storage modulus curve which is the lowest measured T_g . Storage modulus also generally informs about the mechanical strength of the material where begins to fail in terms of temperature. T_g values from loss modulus and $\tan \delta$ are calculated from the maximum peak points. All these make DMA probably the most sensitive thermal technique for T_g determinations(20).

2.4. Fourier Transform Infrared Spectroscopy (FTIR)

The Fourier Transform Infra-Red Spectrometry (FTIR) is considered one of the most valuable analytical techniques to characterize and evaluate organic materials. In this study, FTIR spectroscopy was utilized to monitor the reaction of the polyurethane (21) and investigate the curing process as DSC and DMA.

FTIR has advantages over dispersive methods, including increased signal-to-noise ratio and the ability to obtain spectra of low energy, such as absorption bands with weak intensity. ATR was originally developed and commercialized for analyzing samples that are difficult to prepare or insoluble, such as rubbers and cured resins. The sample is placed in contact with an ATR crystal, one of the most used accessories for FTIR measurements, which absorbs near-infrared radiation and has a high refractive index. While some parts of the radiation penetrate the sample, and some parts are reflected. The depth of penetration of the beam depends on several parameters like the wavelength, angle of incidence, and refractive index of the crystal. Due to the requirement for close contact between the sample surface and the crystal, this method is not suitable for analyzing heterogeneous surfaces, such as many coatings. Additionally, weakly transparent and highly pigmented coatings are difficult to analyze using this technique. Since these kinds of disadvantages are not the subjects in our case, FTIR-ATR measurements for the samples are chosen as an alternative to being proof of DSC experimental and simulation results.

3. RESULTS AND DISCUSSION

3.1. DSC Results

Non-isothermal, isoconventional DSC method was used to investigate the curing process of a polyurethane system in the absence and the presence of dibutyltin dilaurate catalyst with different amounts. The typical DSC thermographs at different curing periods for different catalyst amounts were presented in Figure 2 from a to d as 0, 0.01, 0.1, and 0.5 phr (from C1 to C4), respectively. Due to the exothermic reaction of polyurethane, the curing peak exists in the exothermic area(22). While the black line represents the T_0 as just after the flash-off time (15 minutes later from the application), the red line shows the curing curve of the sample after 30 minutes at 80°C. The significant decrease in the exothermic curing peak is shown in the blue line that represents the DSC thermographs of significantly cured PUR samples. A decrease or total loss of the exothermic curing peaks means that the curing process is almost done at t_{final} . As shown in **Figure 2**, the endothermic peak areas decrease from a to d graphs and disappear for t_{final} curves. Especially for the maximum catalyst amounts it is more obvious. For example, for t_0 curves the dHc which is determined by the integrated area of the endothermic curing curve, decreases as 113, 102, 88, and 84 with increasing catalyst amount.

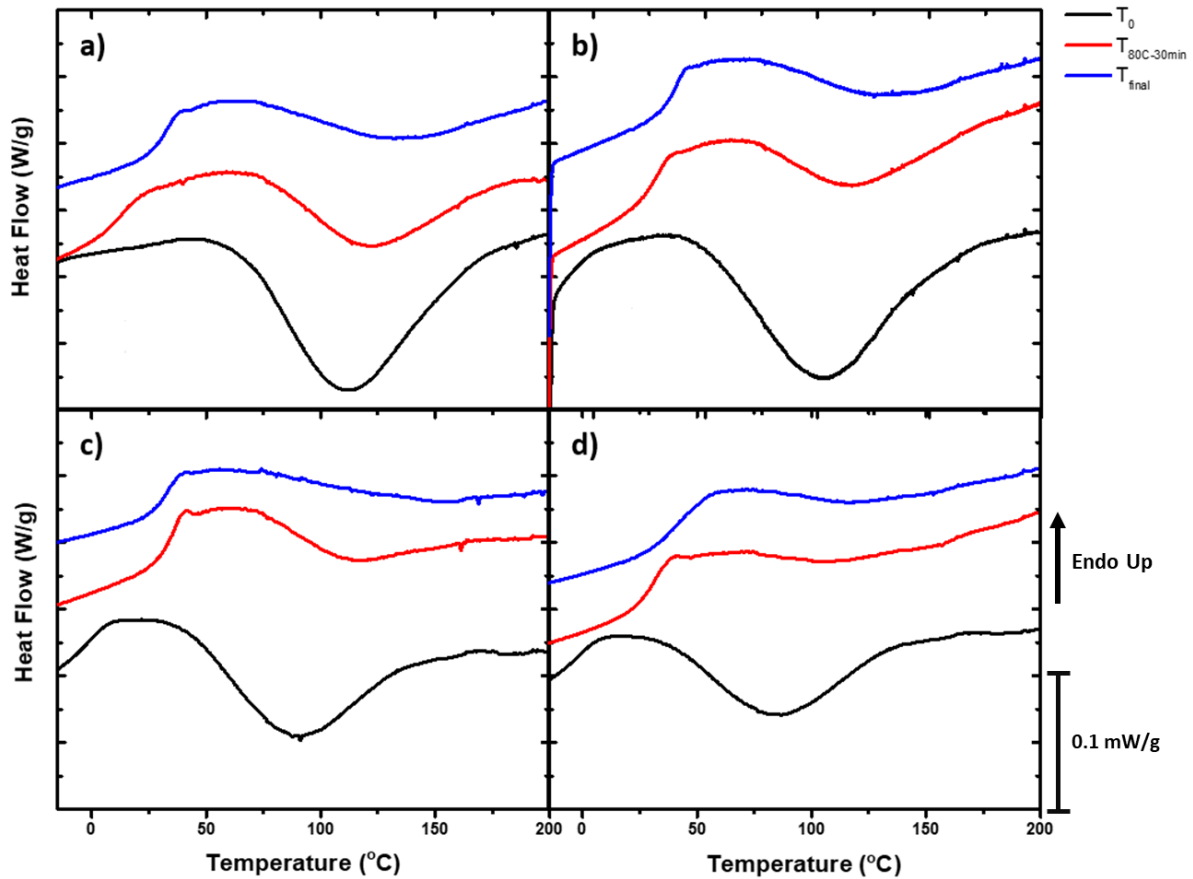


Figure 2. Typical endo up DSC curves for polyurethane coating with a) no catalyst, b) 0.01 phr, c) 0.1 phr, and d) 0.5 phr dibutyltin dilaurate catalyst amounts at different curing processes as T_0 (black), $T_{80C-30min}$ (red) and T_{final} (1 week after 30 minutes at 80°C annealing process and 15 minutes flash-off time) (blue).

Table 1. Kinetic parameters obtained regarding the 2nd order reaction kinetic according to the MRF for different catalyst amounts and curing times. The heating rate is 5°C/min.

Sample	Catalyst Amount	Curing Time	$T_{initial}$ (°C)	T_{peak} (°C)	ΔH_c (J/g)	T_g (°C)	E_a (kJ/mol)	a
C1	0	T_0	60	113	90.5	-	72.1	0.00
		$T_{80C-30min}$	73	122	36.9	15	84.0	0.57
		T_{final}	75	134	25.5	32	88.0	0.81
C2	0.01 phr	T_0	48	102	87.0	-	65.0	0.02
		$T_{80C-30min}$	70	117	30.4	28	81.4	0.66
		T_{final}	78	127	23.6	36	97.0	0.84
C3	0.1 phr	T_0	39	88	54.0	-1	70.8	0.40
		$T_{80C-30min}$	71	114	18.5	35	89.1	0.79
		T_{final}	-	-	-	33	81.0	0.88
C4	0.5 phr	T_0	38	84	39.6	2	73.0	0.53
		$T_{80C-30min}$	-	-	-	31	110.1	0.94
		T_{final}	-	-	-	44	155.2	0.96

As shown in Table 1, the important characteristic parameters such as initial curing temperature (T_i), peak curing temperature (T_p), and the enthalpy of curing reaction (ΔH_c) can be obtained by DSC thermographs. T_i and T_p values shift to the higher temperature values concerning conversion degree.

ΔH_c was obtained by the simple kinetic model and Multilinear Regression fit (MRF). Similarly, the activation energies of the samples were directly obtained by MRF, too. Activation energies obtained from the whole samples increase for conversion degree (Figure 3a). Activation energy variation

concerning conversion may help to understand the type of process or reaction in different systems. Besides, a constant E_a value throughout the reaction process indicates that the single reaction type (addition reaction) dominates the curing in the polyurethane system(23). In epoxy systems, relatively stable E_a value may reduce at higher

conversions which indicates the occurrence of autocatalytic effects (24). As in our case, increasing E_a with respect to conversion shows that the curing reaction is controlled mostly by diffusion rather than chemical reactions (3). The increasing trend of E_a with conversion is also correlated with similar studies that applied different modeling methods (15).

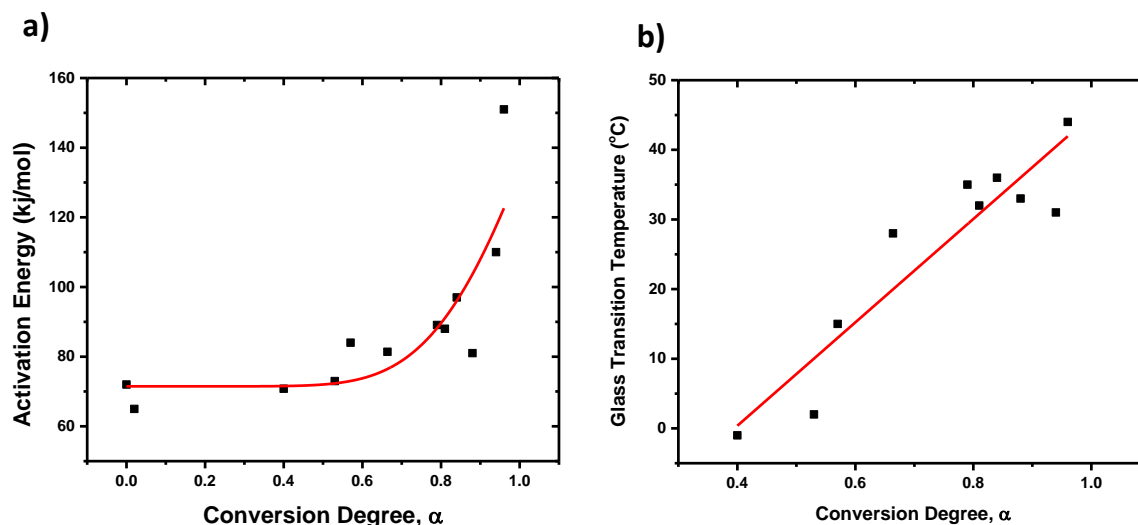


Figure 3. Variation of a) the activation energy and b) glass transition temperature with respect to the degree of conversion for all the studied samples.

The glass transition temperature of the samples is generally obtained from the second heat of DSC curves (25-27) to clear the history of the polymeric sample and smooth away the relaxation enthalpy. However, in our case, since a curing reaction exists in a DSC furnace only in one heating process, T_g was calculated from the first heating. It can be assumed that it is still reliable in terms of the accuracy T_g values in first and second heating do not change (unless heating and cooling temperatures exceed $\pm 50K$ and change the structural composition of the polymeric chain). Commonly it is not possible to see the T_g for the samples at T_0 , since the curing reaction does not start, and the polymeric structure is not formed. Increasing the curing time as $T_{80C-30min}$ and T_{final} samples, T_g becomes computable (Table 1). T_g increases with crosslinking density which also increases by the curing reaction of polyurethane system. Consequently, the direct relationship between T_g and conversion degree is observed as expected (Figure 3b). While the T_g of half-cured samples is $15^\circ C$, the cured samples have $44^\circ C$ as the T_g value. The effect of the catalyst is also seen clearly that increasing the catalyst amount results in totally cured samples even in the samples with curing times 30 minutes at $80^\circ C$ (C4). With the highest catalyst amount, half of the curing reaction was complete at

T_0 that the curing exothermic peaks could not be observed for other sampling times. On the other hand, the samples without any catalyst did not completely cure even after 1 week. Similar phenomena were also observed in DMA analysis. The general trend and tan delta curves of the samples at Day 1 and 7 are shown in Figure 4a and b.

3.2 DMA Results

DMA analysis was performed on Day 1 and Day 7 for the samples without catalyst and with 0.01 and 0.5 phr catalyst. Because of the requirement of the free films for DMA analysis, it was not possible to analyze before Day 1 for each sample. Free films cannot be obtained for uncured samples. The significant change in T_g values between Day 1 and Day 7 obtained from storage modulus, loss modulus, and tan delta values are also shown in Figure 4a, clearly. Tan delta curves are also shown in Figure 4b. In the sample with the maximum catalyst used (C4), even on the first day, the samples have larger T_g values than the seventh day of the non-catalyzed sample (C1). These results which are comparable with DSC, show the significant effect of catalyst amount and the curing time on the total curing of the samples.

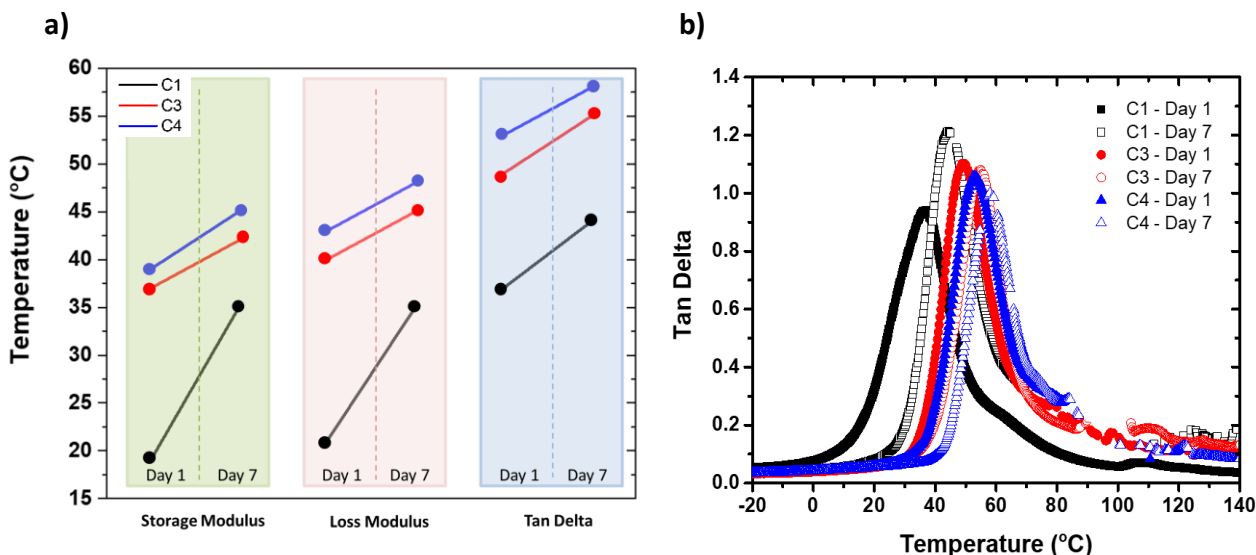


Figure 4. a) The difference in glass transition temperature (T_g) obtained from the onset of storage modulus, peak maximum of loss modulus, and tan delta values are given. b) Tan Delta values obtained by DMA for day 1 (filled) and 7 (holes) of the samples with different catalyst amounts 0, 0.01, and 0.5 phr as black, red, and blue, respectively. The shift in tan delta value between the first and the seventh days is more significant in the C1 sample.

3.3. FTIR Measurements

FTIR measurements were carried out for the samples for both unreacted reagents and the cured ones with different curing times as done in DSC measurements. FTIR has advantages over DMA measurements because all the samples can be measured without any limitations of the sample form.

Results showed the polyurethane structure with the typical carbonyl absorption band of the ester bond located at 1720 cm^{-1} , and another peak close to it at

1680 cm^{-1} , which is attributed to the urethane and urea carbonyl groups. The absorbance at around $3330 - 3380\text{ cm}^{-1}$ is consistent with the stretching of the NH bond and is characteristic of the urethane and urea groups. The other characteristic bands is 2940 cm^{-1} due to the alkane -CH stretching vibration (28). The main concerned peaks are the absorbance at 2270 cm^{-1} indicating unreacted isocyanate groups and 1680 cm^{-1} for the urethane peak. During the curing process, it is expected and monitored the absence of NCO peaks and the formation of urethane peaks.

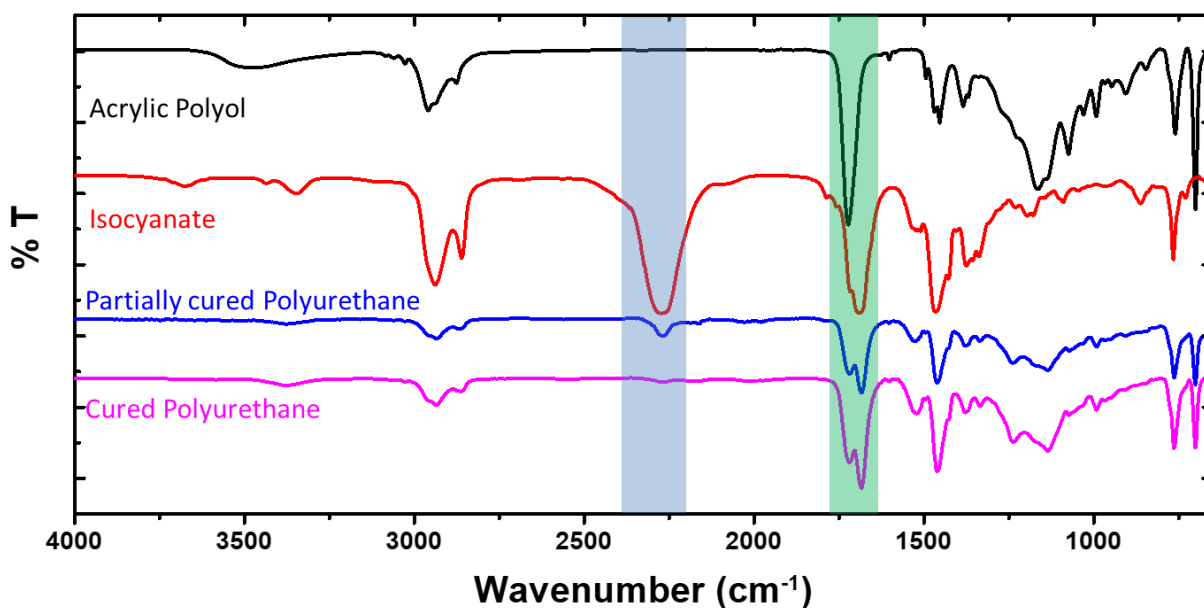


Figure 5. FTIR spectra of acrylic polyol, isocyanate, partially cured polyurethane, and fully cured polyurethane samples from up to down. While the blue region shows the NCO peak at 2270 cm^{-1} , green region shows C=O bond from both urethane and isocyanate molecule.

As mentioned before, the FTIR analysis was applied to prove both the experimental and simulation results of DSC measurements. For this purpose, samples were applied on glasses to obtain FTIR spectra. However, while the NCO peak at 2270 cm^{-1} was decreasing, we could not observe an increase in the 1680 cm^{-1} urethane peak (Figure S2) because of the matrix itself. In **Figure 5** the reference FTIR spectra are also shown that isocyanate also has an intense peak at 1680 cm^{-1} which comes from C=O bond of

isocyanate chemical structure (Figure 6). As a result, it would not be possible to monitor the kinetic reaction of the polyurethanes because of the unobservable urethane peak in the same area. The curing reaction of polyurethane can be observed by monitoring the reduction of the NCO peak (Figure S2) by assuming all the NCO is converted to polyurethane and does not form urea by reacting with any water/humidity (29) in the environment, that may not be realistic.

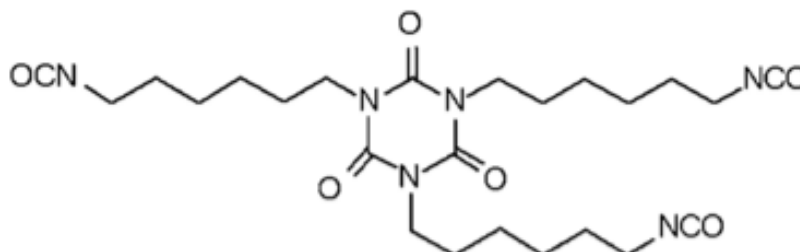


Figure 6. Chemical structure of HDI based isocyanate. C=O group in the cyclic structure results signal at 1680 cm^{-1} in FTIR spectra.

These limitations show that FTIR may not be a suitable measurement, as DMA. That is the reason DSC techniques was discussed for the further study.

3.4 Model-Free Kinetic Calculations

In this study, Multiple Regression Fit (MRF) was used essentially in terms of easy handling of kinetic parameters and fast results due to the sufficiency of single-rate heating curves. However, Ozawa and Kissinger's methods were also distinguished to investigate the possible differences between the results obtained from single-rate and multi-rate heating curves. For this purpose, curing analysis was applied to the samples with different heating rates as 2.5, 5, 10, and 20 K/min. Two different samples (C1-C2) were studied with two methods to compare the kinetic parameters. As shown in Figure S3 the kinetic parameters like T_i and T_p shift to the higher temperatures with the increase in the heating rate. Similarly, the signal intensity of the whole curve increases, and T_g and curing peaks become more visible with higher heating rates. The reason for this phenomenon can be explained by the fact that the curing reaction is not only a thermodynamic process but also a dynamic process. In the case of using lower

heating rates, the reactants find sufficient time to react with each other. So, relatively lower curing initial and peak temperature values are obtained at lower heating rates(30). Since the thermal effect per unit time increases, the enthalpy of the system also increases(31). The data obtained from Figure S3 were used to obtain E_a values from Ozawa and Kissinger equations.

The plots that were mentioned before for Ozawa and Kissinger methods are shown in Figure 7, and the obtained kinetic parameters are given in Table S1. The straight line of the slope was obtained for both models to calculate the kinetic parameters. Calculated activated energies were very close to Ozawa and Kissinger's methods. The activation energies for the C1 sample are 24.1 kJ/mol and 23.3 kJ/mol obtained from the Ozawa and Kissinger methods, respectively with a 0.9997 correlation factor. For the other sample, activation energies were 19.5 and 19.2 kJ/mol for the Ozawa and Kissinger methods, respectively with relatively the same correlation coefficients. The results also showed that the E_a of the curing system decreases after the addition of catalyst which proves that the reaction system is more rapid with the catalyst. (31)

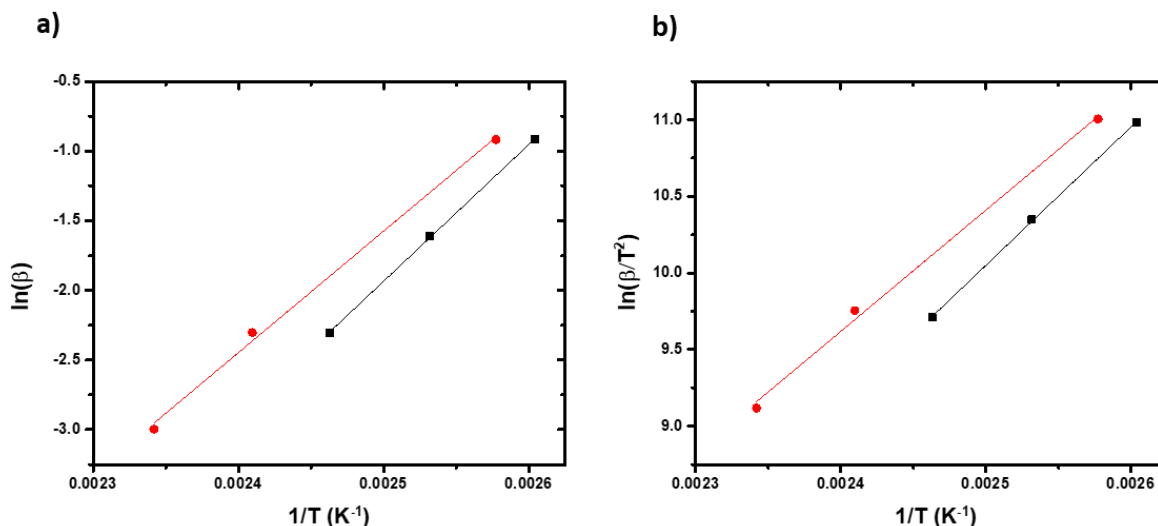


Figure 7. a) Ozawa and b) Kissinger plot of C1 (black) and C2 (red) samples with curing time 30 minutes at 80°C. The slope of the graphs is linear, and the activation energies obtained from both methods gave similar values with high correlation coefficients.

3.5. Isothermal Prediction Calculations

As mentioned before, MRF results were applied for all samples because of the easy and fast availability of the curing results. The isothermal prediction curves in terms of % conversion with respect to reaction time or isothermal temperature were also obtained from MRF simulations. As with all other similar simulation software, the results do not give certain values but comparable approximations. In Figure 8 the isothermal conversion predictive curves for the samples without a catalyst at different sampling times, t_0 and t_{final} are shown. The effect of curing time in terms of curing reaction kinetic is seen in this simulation.

As shown in Figure 8a, 5 minutes under 100 °C isothermal reaction temperature is enough for a 40% conversion degree for the t_0 sampling. On the other hand, approximately 125 °C isothermal reaction temperature or 20 minutes at the same temperature is necessary for the same conversion degree when a significantly (81% of cured, Table 1) cured sample (t_{final} sampling). Similarly, to achieve 90% conversion for t_0 sampling, 100 minutes at almost 65 °C is required. However, for the same reaction time, the reaction temperature should be increased up to 110 °C to achieve the same conversion degree in the 81% cured samples. At first sight, the expectation can be vice versa that one expects that the almost cured sample should require minimum reaction time or lower isothermal reaction temperatures. However as mentioned before, in our system diffusion-controlled reaction mechanism is more dominant than the chemical reaction (3). In other words, it decreases the ion mobility, increases the crosslinking density of the matrix, and reduces the reaction rate.

Figure 8b explains this phenomenon from different aspects that the relatively low reaction rate in 81% cured sample can be understood clearly. While for the cured sample 70% conversion can only be achieved in 60 minutes at 100 °C, the same conversion can be achieved in 15 minutes at the same reaction temperature.

The effect of catalyst amount on the curing kinetic is shown in Figure 9. For all samples, t_0 sampling was considered to ignore the effect of diffusion-reaction related to the reaction time. As shown in Figure 9a, increasing the catalyst amount % conversion increases. As an example, the % conversion of the samples with 0, 0.01, and 0.5 phr catalyst amounts increases as 10%, 20%, and 40%, respectively for 5 minutes of reaction time at 75 °C isothermal reaction temperature. Similarly, at 100 °C, for an 80% conversion degree, 5 minutes is enough for the sample with the maximum catalyst amount. For 0.01 phr and no catalyst samples, the required reaction times for the same circumstances are 20 minutes and 30 minutes, respectively. Figure 9b, % conversion with respect to reaction time under isothermal reaction temperatures are shown for the same samples. The catalyst effect is deducible when reaction times for 90% conversion degrees at 100 °C isothermal reaction temperatures are considered. While 10 minutes reaction time is enough with the maximum amount of catalyst existing, required reaction times increase to 30 minutes and 60 minutes for the 0.01 phr and no catalyst samples, respectively. Figure S4 can give a similar idea about the curing kinetics by the graphs of isothermal reaction temperatures vs reaction time curves in different conversion degrees for the samples with different catalyst amounts.

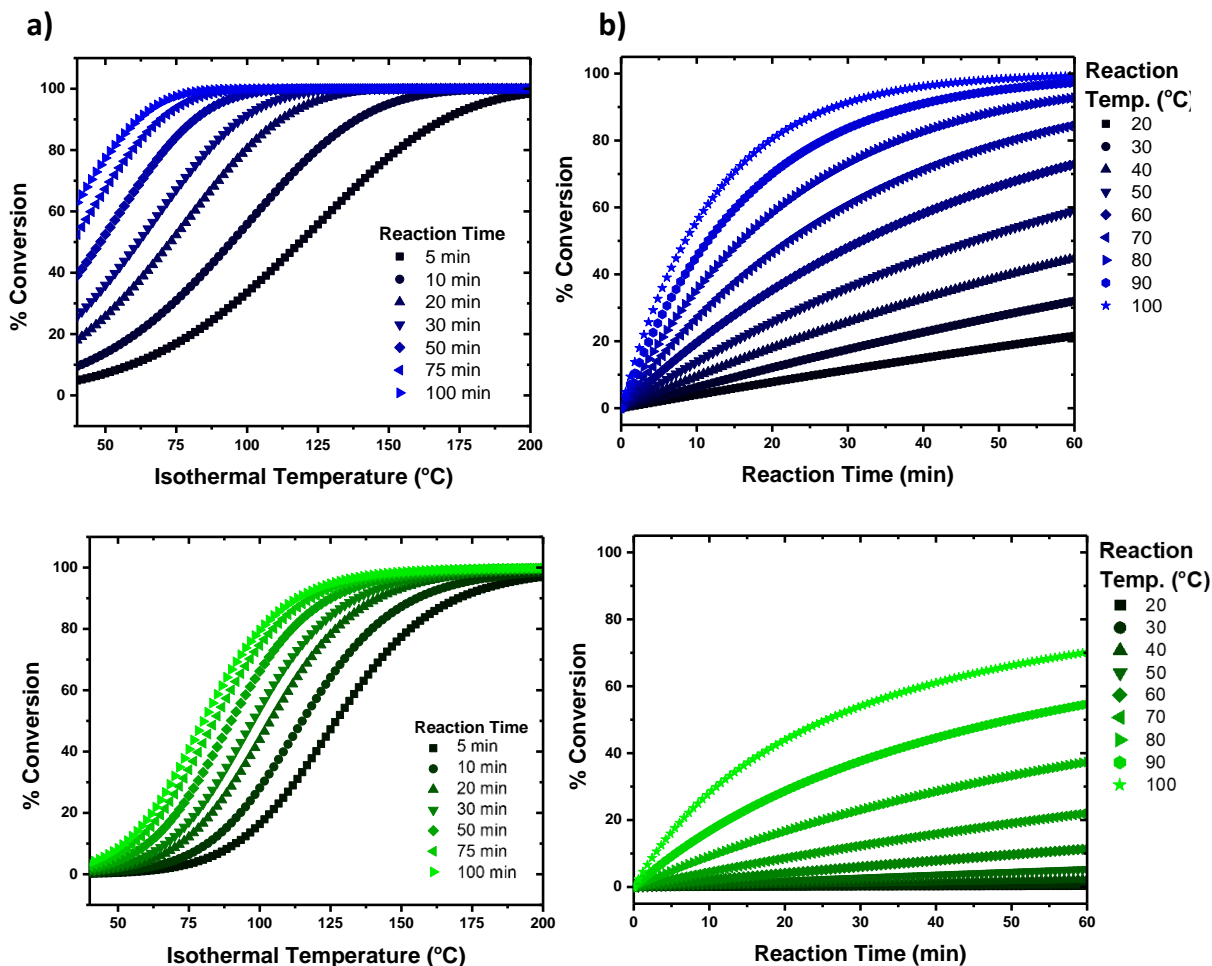


Figure 8. Isothermal conversion predictive curves for the sample without catalyst (C1) at t_0 sampling (blue) and t_{final} sampling (green) to show the effect of curing time. a) % Conversion vs. isothermal temperature for different reaction times and b) % conversion vs reaction time for different isothermal reaction temperatures were shown.

The basic idea obtained from all the isothermal prediction curves gives information about the reaction rate of the samples with dependence on the curing time and the catalyst amount. Figure 10 summarizes both explanations in one graph in which the rate constant of two samples (C1, without any catalyst, and C4 with the maximum amount of catalyst) are given with respect to reaction temperature at different curing times. The existence of the catalyst increases the rate of the reaction

which is more significant after 75 °C. However, the rate constant variation at room temperature (25 °C) also obey the trend that the catalyst amount increases the rate of reaction significantly and the degree of curing effects it, too. The curing temperature is directly linked to the diffusion reaction, in other words, the ion mobility and the crosslink density of the system result decrease in the rate constant, as expected.

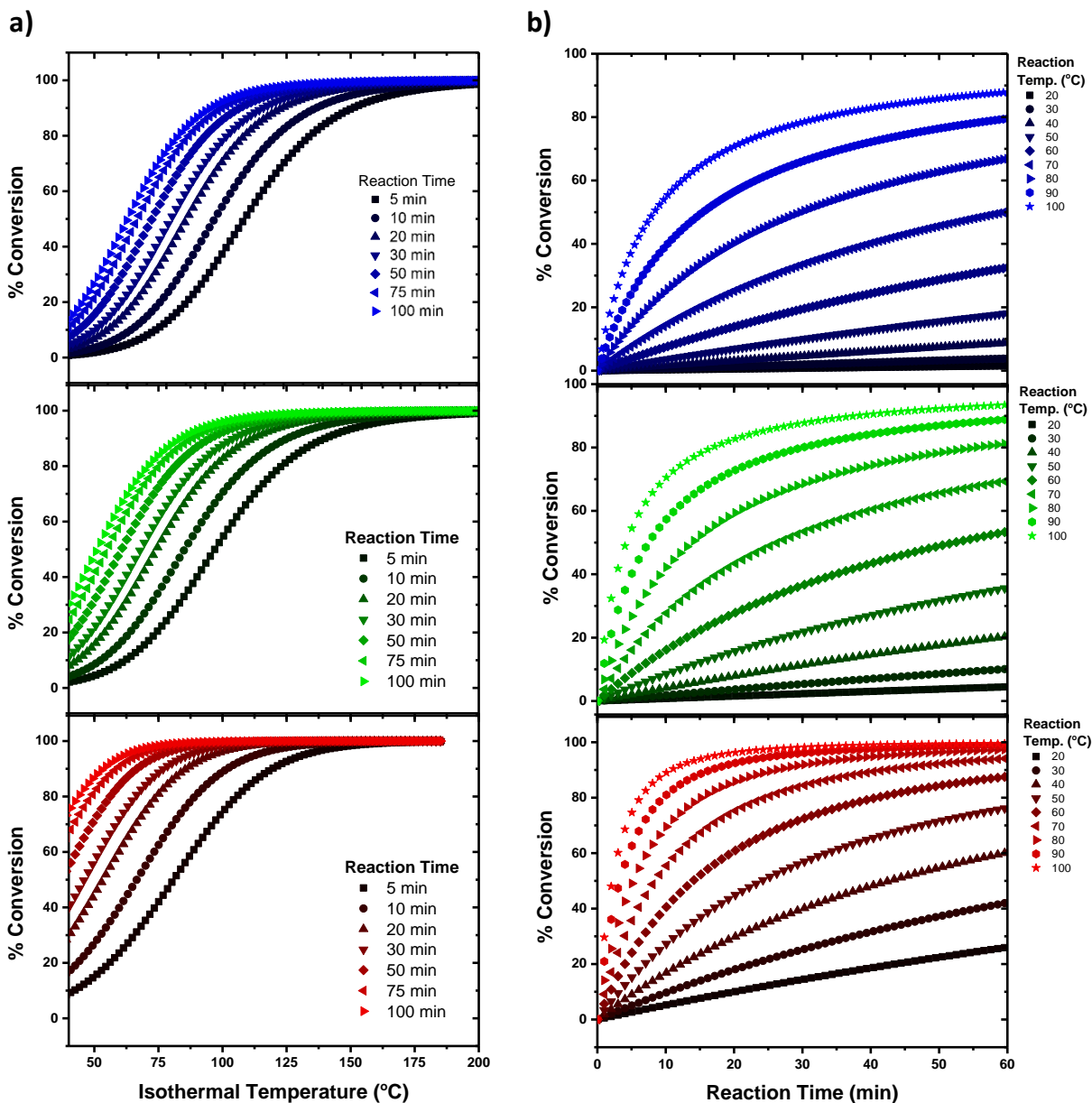


Figure 9. Isothermal conversion predictive curves for C1 (Blue), C2 (green), and C4 (red) samples to understand the effect of catalyst amount. Conversion vs. a) isothermal temperature and b) time curves are shown for different reaction times and reaction temperatures, respectively.

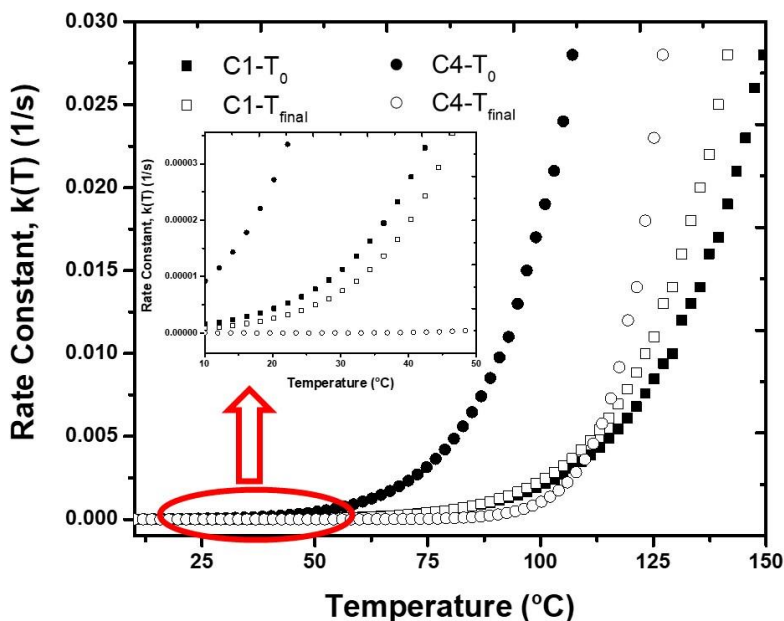


Figure 10. The rate constant of the sample without catalyst (C1) and the maximum amount of catalyst (C4) for t_0 and T_{final} curing times. For each case, the final samples have lower reaction rates for all reaction temperatures.

All these prediction curves simulate valuable results to estimate the curing kinetics of any system under different reaction conditions like catalyst amounts, reaction time temperatures, etc. Especially for industrial-scale production cases, kinetic estimations are more critical.

4. CONCLUSION

In this study, the two major aims of kinetic analysis, to clarify the reaction mechanism with kinetic parameters and to predict the kinetic characteristic of the materials under different reaction parameters were aimed and achieved by both DSC and DMA analysis. Both thermal analysis results confirm each other however, the restrictions of the sample preparation in DMA limit understanding of the kinetic mechanism in lower reaction times. That is the reason, DSC analysis was preferred in terms of its ability to obtain lots of kinetic information. The effect of the curing time and the amount of DBTL catalyst on polyurethane reaction kinetics were investigated by single and multi-heating methods to understand the kinetic characteristic of the reaction. The simple kinetic model and Multilinear Regression fit (MRF) were used to calculate the kinetic parameters and simulate the isothermal prediction curves.

The results showed that the curing time and the catalyst amount affect the kinetic process of polyurethane reactions regarding the specific reactants and the catalyst. T_g values of the samplings of the same curing times increase with respect to catalyst amounts. Undeterminable T_g values for t_0 sampling with no and lower catalyst amounts became detectable with the increase of catalyst. Similarly, the maximum T_g value was obtained by the maximum catalyst amount as 44 °C.

The conversion degrees confirm the T_g values in which there is a direct relation between each other. The activation energy of any case in our system increases with the increase in conversion degree. Diffusion-controlled reaction mechanism results in a decrease in the reaction rate due to the increased crosslinked matrix. A decrease in the number of reactants and less reactive reagents because of the high-dense medium makes it difficult to continue the reaction, so the activation energy increases.

Isothermal prediction curves were studied to simulate the curing behavior of the polyurethane matrix under different isothermal temperatures and reaction times. Curves showed that final samples have lower conversion than the initial samples for the same reaction conditions, due to the diffusion controlled mechanism. In the case of different catalyst amounts, for the initial sampling time, the higher catalyst amount sample has significantly higher conversion. Since there is no high-dense medium because of the consideration of the initial samplings, the diffusion-controlled mechanism does not affect the reaction kinetics.

The kinetic calculations and the isothermal prediction curve are critical in terms of real-life applications, especially in the coating industry. The optimization of the curing conditions for a specific system may require lots of experimental procedures unless kinetic approximations are applied. On the other hand, the information obtained from these calculations can be used to provide the required conditions to obtain fully cured samples even after the first curing procedures. Current study also prove simple and effective way to understand the optimization of organic coating indication different systems with different catalyst.

5. CONFLICT OF INTEREST

There is no conflict of interest in this study.

7. REFERENCES

- Groenewolt M. Polyurethane coatings: a perfect product class for the design of modern automotive clearcoats. *Polymer International*. 2019;68(5):843-7. Available from: [<URL>](#).
- Li K, Gan C, Zhang W, Li C, Li G. Validity of isothermal kinetic prediction by advanced isoconversional method. *Chemical Physics*. 2023;567:111801. Available from: [<URL>](#).
- Yi C, Rostron P, Vahdati N, Gunister E, Alfantazi A. Curing kinetics and mechanical properties of epoxy based coatings: The influence of added solvent. *Progress in Organic Coatings*. 2018;124:165-74. Available from: [<URL>](#).
- Liu S, Li X, Ge M, Du X, Zou M. Curing Kinetics of Methylene Diphenyl Diisocyanate-Based Polyurethane Elastomers. *Polymers*. 2022;14(17):3525. Available from: [<URL>](#).
- Manu SK, Sekkar V, Scariah KJ, Varghese TL, Mathew S. Kinetics of glycidyl azide polymer-based urethane network formation. *Journal of Applied Polymer Science*. 2008;110(2):908-14. Available from: [<URL>](#).
- Shundo A, Yamamoto S, Tanaka K. Network Formation and Physical Properties of Epoxy Resins for Future Practical Applications. *JACS Au*. 2022;2(7):1522-42. Available from: [<URL>](#).
- Balakrishnan R, Nallaperumal AM, Manu SKP, Varghese LA, Sekkar V. DSC assisted kinetic analysis on the urethane network formation between castor oil based ester polyol and poly(methylene di phenyl isocyanate) (pMDI). *International Journal of Polymer Analysis and Characterization*. 2022;27(2):132-46. Available from: [<URL>](#).
- Balakrishnan R, Soumyamol PB, Vijayalakshmi KP, Alen Varghese L, Rajeev R, Manu SK, et al. Kinetic analysis of urethane formation between castor oil-based ester polyol and 4,4'-diphenyl methane diisocyanate. *Indian Chemical Engineer*. 2021;63(5):491-500. Available from: [<URL>](#).
- Hui M, Yu-Cun L, Tao C, Tuo-Ping H, Jia-Hu G, Yan-Wu Y, et al. Kinetic studies on the cure reaction of hydroxyl-terminated polybutadiene based polyurethane with variable catalysts by differential scanning calorimetry. *e-Polymers*. 2017;17(1):89-94. Available from: [<URL>](#).
- Schuster F, Ngako Ngamgoue F, Goetz T, Hirth T, Weber A, Bach M. Investigations of a catalyst system regarding the foamability of polyurethanes for reactive inkjet printing. *Journal of Materials Chemistry C*. 2017;5(27):6738-44. Available from: [<URL>](#).
- Kaushik A, Singh P. Kinetic Study of Polyurethane Reaction between Castor Oil/TMP Polyol and Diphenyl Methane Diisocyanate in Bulk. *International Journal of Polymeric Materials and Polymeric Biomaterials*. 2006;55(8):549-61. Available from: [<URL>](#).
- Vyazovkin S, Burnham AK, Criado JM, Pérez-Maqueda LA, Popescu C, Sbirrazzuoli N. ICTAC Kinetics Committee recommendations for performing kinetic computations on thermal analysis data. *Thermochimica Acta*. 2011;520(1):1-19. Available from: [<URL>](#).
- Keskin S, Özkar S. Kinetics of polyurethane formation between glycidyl azide polymer and a triisocyanate. *Journal of Applied Polymer Science*. 2001;81(4):918-23. Available from: [<URL>](#).
- Kilivnik YN, Lipatova TE. The kinetics of formation of a crosslinked polyurethane in the presence of magnesium ions. *Polymer Science USSR*. 1976;18(12):3017-23. Available from: [<URL>](#).
- Stanko M, Stommel M. Kinetic Prediction of Fast Curing Polyurethane Resins by Model-Free Isoconversional Methods. *Polymers*. 2018;10(7):698. Available from: [<URL>](#).
- Cui H-W, Suganuma K, Uchida H. Using the Ozawa method to study the thermally initiated curing kinetics of vinyl ester resin. *RSC Advances*. 2015;5(4):2677-83. Available from: [<URL>](#).
- Vyazovkin S. Kissinger Method in Kinetics of Materials: Things to Beware and Be Aware of. *Molecules*. 2020;25(12). Available from: [<URL>](#).
- Shamsi R, Mir Mohamad Sadeghi G, Asghari GH. Dynamic mechanical analysis of polyurethanes and carbon nanotube based composites obtained from PET waste. *Polymer Composites*. 2018;39(S2):E754-E64. Available from: [<URL>](#).
- Shen Y, Tan J, Fernandes L, Qu Z, Li Y. Dynamic Mechanical Analysis on Delaminated Flax Fiber Reinforced Composites. *Materials*. 2019;12(16):2559. Available from: [<URL>](#).
- Bertotto MM, Gastón A, Rodríguez Batiller MJ, Calello P. Comparison of mathematical models to predict glass transition temperature of rice (cultivar IRGA 424) measured by dynamic mechanical analysis. *Food Sci Nutr*. 2018;6(8):2199-209. Available from: [<URL>](#).
- Dias RCM, Góes AM, Serakides R, Ayres E, Oréface RL. Porous biodegradable polyurethane nanocomposites: preparation, characterization, and biocompatibility tests. *Materials Research*. 2010;13. Available from: [<URL>](#).
- Zhang B, Wang B, Zhong Y, Wang S, Li X, Wang L. Experimental Study on Reducing the Heat of Curing Reaction of Polyurethane Polymer Grouting

Material. *Advances in Polymer Technology*. 2021;2021:9954498. Available from: [<URL>](#).

23. Remya Balakrishnan LAV, K Manu. Cure kinetics and thermodynamics of polyurethane network formation based on castor oil based polyester polyol and 4,4'-diphenyl methane diisocyanate. *Indian Journal of Chemical Technology*. 2021;28(3):7. Available from: [<URL>](#).

24. Tziamtzi CK, Chrissafis K. Optimization of a commercial epoxy curing cycle via DSC data kinetics modelling and TTT plot construction. *Polymer*. 2021;230:124091. Available from: [<URL>](#).

25. Hong JU, Lee TH, Oh D, Paik H-j, Noh SM. Scratch-healable automotive clearcoats based on disulfide polyacrylate urethane networks. *Progress in Organic Coatings*. 2021;161:106472. Available from: [<URL>](#).

26. Sáenz-Pérez M, Lizundia E, Laza JM, García-Barrasa J, Vilas JL, León LM. Methylene diphenyl diisocyanate (MDI) and toluene diisocyanate (TDI) based polyurethanes: thermal, shape-memory and mechanical behavior. *RSC Advances*. 2016;6(73):69094-102. Available from: [<URL>](#).

27. Cuevas JM, Cobos R, Germán L, Sierra B, Laza JM, Vilas-Vilela JL. Enhanced mar/scratch resistance in automotive clear coatings by modifying crosslinked polyurethane network with branched flexible oligomers. *Progress in Organic Coatings*. 2022;163:106668. Available from: [<URL>](#).

28. Lee H-T, Lin L-H. Waterborne Polyurethane/Clay Nanocomposites: Novel Effects of the Clay and Its Interlayer Ions on the Morphology and Physical and Electrical Properties. *Macromolecules*. 2006;39(18):6133-41. Available from: [<URL>](#).

29. Shi Y, Zhan X, Luo Z, Zhang Q, Chen F. Quantitative IR characterization of urea groups in waterborne polyurethanes. *Journal of Polymer Science Part A: Polymer Chemistry*. 2008;46(7):2433-44. Available from: [<URL>](#).

30. Yin H, Sun DW, Li B, Liu YT, Ran QP, Liu JP. DSC and curing kinetics study of epoxy grouting diluted with furfural -acetone slurry. *IOP Conference Series: Materials Science and Engineering*. 2016;137(1):012001. Available from: [<URL>](#).

31. Ma H, Zhang X, Ju F, Tsai S-B. A Study on Curing Kinetics of Nano-Phase Modified Epoxy Resin. *Scientific Reports*. 2018;8(1):3045. Available from: [<URL>](#).



Characterization, Antioxidant and Anticholinesterase Activity of Compounds Isolated from Alkaloid Extracts of *Citrus aurantifolia* Root Bark

Djélé Alette Edwige Zialé^{1,2,*} , Demel Axel Adou^{1,3} , Kohué Christelle Chantal N'gaman-Kouassi¹ , Julia Deschamp² , Nadia Bouchemal² , Tony Lionel Palama² , Marc Lecouvey² , Janat Akhanovna Mamyrbekova-Békro¹ , Yves-Alain Békro¹ 

¹Laboratory of Bio-Organic Chemistry and Natural Substances, Nangui Abrogoua University, 02 BP 801 Abidjan 02, Ivory Coast.

²Sorbonne Paris Nord University, CSPBAT Laboratory, CNRS UMR 7244, F-93017 Bobigny Cedex, France.

³Department of Science and Technology, Alassane Ouattara University, 01 BP 18 Bouaké 01, Ivory Coast.

Abstract: Xanthyletin (1), edulinin (2), 1-methyl-2-[(E)-(prop-1-enyl)]quinolin-4-one (3), 1,2-dimethylquinolin-4-one (4), lonchocarpol A (5), grandisinin (6), citracridone-I (7) and 5-hydroxynoracronycin (8) were isolated from alkaloid extracts of the root bark of *Citrus aurantifolia*. Their structures were characterized using spectral data (NMR, HRMS, and IR). Furthermore, compounds 2, 3, 4, and 6 known in the literature have been isolated for the first time in *Citrus aurantifolia*. However, compounds 1, 5, 7 and 8 are already known from the plant studied. The concentration required to reduce 50% of free radicals (RC_{50}) was carried out. Compounds 3 ($RC_{50} = 185.836 \mu\text{mol/L}$) and 4 ($RC_{50} = 218.277 \mu\text{mol/L}$) compared with vitamin C ($RC_{50} = 17.033 \mu\text{mol/L}$) showed antioxidant efficacy. The highest anticholinesterase activity was observed for compound 6 at $21.129 \mu\text{M}$ followed by compounds 3 and 4 at $251.130, 287.208 \mu\text{M}$, respectively.

Keywords: *Citrus aurantifolia*, Alkaloids, Isolation, Antioxidant, Anticholinesterase.

Submitted: December 4, 2023. **Accepted:** May 19, 2024.

Cite this: Zialé DAE, Adou DA, N'gaman-Kouassi KCC, Deschamp J, Bouchemal N, Palama TL, Lecouvey M, Mamyrbekova-Békro JA, Békro YA. Characterization, Antioxidant and Anticholinesterase Activity of Compounds Isolated from Alkaloid Extracts of *Citrus aurantifolia* Root Bark. JOTCSA. 2024;11(3): 1227-36.

DOI: <https://doi.org/10.18596/jotcsa.1395690>

***Corresponding author's E-mail:** aletteziale22@gmail.com

1. INTRODUCTION

Alzheimer's disease (AD) is a neurodegenerative brain disorder and is considered the most common form of dementia in the elderly. According to a recent study, the number of patients with AD is on the rise, currently estimated at 26.6 million. This number is projected to quadruple by 2050 (1,2). However, it's important to note that brain aging appears to be a significant risk factor for developing AD (3). In fact, the first signs of Alzheimer's disease, which account for 75% of cases, typically manifest as problems with memory and cognitive function (3). Unfortunately, conventional therapies for Alzheimer's disease have shown limited effectiveness, largely due to the imprecise understanding of its underlying causes (2).

Free radicals (FR) and reactive oxygen species (ROS) are from metabolic processes or external sources. They generally come from oxygenated, nitrogenous, and sulfurous substances. The presence of unpaired electrons renders these chemical compounds unstable, and their reactivity plays crucial roles in cell signaling, gene expression, and ion transport (4). However, an excess of free radicals (FR) is highly detrimental to normal biological processes, affecting proteins, lipids, RNA, DNA, and carbohydrates in living matter. This is why the research for new natural antioxidants from plants is receiving particular attention due to their exceptional contribution to the fight against disease. Among these phytochemicals of interest, alkaloids could contribute to managing cellular damage due to oxidative stress and reducing the risk of chronic diseases due to their antioxidant potential (4,5).

Several studies have demonstrated the involvement of free radicals (FR) in Alzheimer's disease (AD). Indeed, AD is characterized by the accumulation of senile plaques, which generate free radicals, leading to damage to nerve cells (6). Neuronal death occurs mainly in basal forebrain areas, which are the main sources of cholinergic innervation, leading to acetylcholine deficiency in patients (7). Some plant extracts are known to improve cognitive faculties by protecting nerve cells. That's why it's important to intensify the research to provide more effective and inexpensive palliative care (8).

Citrus aurantifolia (Christm) Swingle belongs to the Rutaceae family. It can grow up to about 5 meters in height and thrive in warm subtropical or tropical regions. Widely utilized in West Africa, particularly in Côte d'Ivoire, it is esteemed for its nutritional qualities. Various parts of the plant are traditionally used for medicinal purposes: the leaves have antiseptic, antiviral, antifungal, and antimalarial properties; the fruit serves as a diuretic, anti-mosquito agent, and antimalarial remedy; and the root bark is utilized for addressing conditions such as diabetes, atherosclerosis, constipation, arthralgia, and indigestion. (9,10). The health benefits of *C. aurantifolia* are associated with a high content of biologically active compounds such as flavonoids, coumarins, limonoids, phenols, alkaloids, carotenoids, minerals, and vitamins (10,11).

The present study focuses on the phytochemical, anticholinesterase, and free radical scavenging of constituents isolated from the total alkaloid extracts of *C. aurantifolia* root barks.

2. MATERIAL AND METHODS

2.1. Biological Material

Acetylcholinesterase (AChE) from *Electrophorus electricus* (electric eel) (C3389-2KU), acetylthiocholine iodide (ATCI), 5,5'-dithiobis-(2-nitrobenzoic acid) (DTNB), galantamine hydrobromide ($C_{17}H_{21}NO_3$, HBr; 368.27 g/mol), stable 2,2-diphenyl-1-picrylhydrazyl radical (DPPH), and ascorbic acid (vitamin C) were purchased from Sigma Aldrich (Poole, UK).

2.2. Plant Material

The root barks from *C. aurantifolia* were collected in Adiopodoumé (5° 20' 28" North, 4° 7' 54" West) in the south of Côte d'Ivoire. They were identified and authenticated by Professor Malan Djah François of Nangui Abrogoua University, Ivory Coast. A voucher specimen was deposited in the herbarium of laboratory of Bio-Organic Chemistry and Natural Substances of Nangui Abrogoua University, Côte d'Ivoire. After cleaning and air-drying, the root barks were ground.

2.3. Extracts Preparation

320 g of sample were extracted by maceration three times in methanol (3 x 1700 mL) for 72 hours under continuous stirring. The extracts were

combined and evaporated under reduced pressure (218 mbar) at 40 °C. Then, 150 mL of H_2SO_4 (2% v/v, pH = 2) was added. The solution obtained was extracted with diethyl ether (4 x 100 mL), followed by the addition of NaOH (m/v, 25%) to adjust the pH to 9. The mixture was then successively extracted with chloroform, ethyl acetate (5 x 100 mL), and an ethyl acetate/methanol mixture (3/1). The extract was dried with anhydrous Na_2SO_4 , and the filtrate was concentrated using a rotary evaporator (Büchi Rotavapor R-300 at 40 °C) to provide the CA1 (chloroform) and CA2 (ethyl acetate) extracts (12,13).

2.4. Fractionation and Isolation

2.4.1. Compounds isolated from chloroform extract

The chloroform extract (CA1, 754.7 mg) was subject to column chromatography (CC), (length 45 cm, diameter 4 cm, height 14 cm), containing 40 g of silica gel 60 GF₂₅₄ (Merck) with a gradient of petroleum ether (PE)/dichloromethane (DCM)/EtOH solvents by varying their proportions (7: 3: 0 to 0: 8: 2). Six fractions (F1 - F6) were collected according to their chromatographic profiles. After solvent removal from fractions F2 (46.7mg) and F4 (157.6 mg), respectively, two compounds **1** (20.7 mg) and **2** (56.7 mg) were obtained. Fraction F5 (68.2 mg) was fractionated on CC with a gradient of DCM/EtOH to give three subfractions (F5.1 - F5.3). Compound **3** (2.2 mg) was isolated from F5.2 on a preparative plate (PP) with DCM/MeOH (90:10). Fraction F6 (197.7 mg) was fractionated on CC with DCM/AcOEt (10 : 0 - 30 :70) to give two subfractions F6.1 and F6.2 (80.2 mg), F6.2 was further purified on CC to give compound **4** (3.4 mg).

2.4.2. Compounds isolated from ethyl acetate extract

The extract (CA2, 729 mg) was fractionated on CC with DCM/AcOEt (100: 0: to 0:100) to give 6 fractions (F1 - F6), F4 (160.6 mg) was purified on CC with a DCM/EtOH (100- 0 to 0-100) to give three subfractions (F4.1 - F4.3). Using HPLC-Prep, subfraction F4.2 (68 mg) yielded 2 fractions F4.2-1 and F4.2-2 (12.8 mg). Two compounds, **5** (2.6 mg) and **6** (3.4 mg) were isolated from F4.2-2 by PP (DCM/EtOH 10:0.5). The crystallization of F5 (250 mg) allowed the isolation of compound **7** (36.7 mg). Finally, fraction F6 (80.2 mg) was fractionated over CC (DCM/AcOEt) to give a single compound **8** (10.7 mg).

2.5. Structural Determination of the Isolated Compounds

The NMR spectra (1H , ^{13}C , JMOD, DEPT, COSY, HSQC, HMBC, and NOESY) were performed in $CDCl_3$ (compounds **1-7**) and $DMSO-d_4$ (compound **8**) on a BRUKER AVANCE III spectrometer (400 MHz). HPLC-MS was performed on 1260_InfinityII with a reverse phase C18-AGILENT column at 30 °C. The Bruker maXis mass spectrometer in negative (ESI⁻) or positive (ESI⁺) mode was used for the high resolution mass spectrometry (HRMS) data. IR spectra were performed on the IR spectrometer (380 FT Nicolet from Thermo Fischer scientific). The

melting points of the compounds were determined with Stuart® SMP30.

2.6. Determination of Antioxidant Potential Against DPPH Radicals

The antioxidant power of compounds **1-8** was carried out using the method described by Blois (14). The extracts were diluted to final concentrations of 0.5; 0.25; 0.125; 0.0625; 0.03125; 0.0156; 0.0078 mg/mL in methanol. To 1 mL of each extract, 1.5 mL of DPPH solution (0.03 mg/mL) was added. The homogeneous mixture was incubated in the dark for 30 minutes. The absorbance (Abs) of the mixture obtained was measured at 517 nm. The blank consisted of 1.5 mL of DPPH solution, to which 1 mL of MeOH was added. A solution of ascorbic acid prepared in the same conditions as the tested samples was used as a reference. The tests were repeated three times for each sample. Equation (I) was used to determine the percentage reduction (PR) of the DPPH radical:

$$PR (\%) = [(A_b - A_e) / A_b] \times 100 \quad (I)$$

A_b : Absorbance of the blank (1.5 mL of DPPH + 1 mL of MeOH)

A_e : Absorbance of the sample

The concentration required to reduce the DPPH radical by 50% (RC_{50}) was determined (8,15).

2.7. Anticholinesterase Activity

The percentage inhibition of acetylcholine (AChE) was determined according to the method described by Ellman et al (1961) (16). 50 μ L of sample methanolic solution (0.5; 0.25; 0.125; 0.0625; 0.03125; 0.0156; 0.0078 mg/mL) was diluted to 1/4 with the buffer solution in 96 well plates. For 30 min at 37°C, 10 μ L of AChE enzyme (0.22 U/mL in Tris-HCl buffer) was incubated, after which 20 μ L of DTNB (3 mM in buffer) and 10 μ L of ATCI (15 mM, H₂O millipore) were added. The resulting mixture was incubated at 18°C for 5 min in plates. Prepared under the same conditions, galanthamin and methanol were used as control and blank, respectively. The different absorbances were measured at 405 nm every 90 seconds for 6 minutes. The readings were taken three times. The anticholinesterase activity assays were performed three times for each sample. Equation (II) was used to determine the percentage inhibition (PI) of the enzyme.

$$PI (\%) = 100 - [(Ab \text{ extract} / Ab \text{ control}) \times 100] \quad (II)$$

Ab = Absorbance

3. RESULTS AND DISCUSSION

3.1. Extraction Yields

The extraction yields are 0.812% (CA1) and 0.522% (CA2) with chloroform and ethyl acetate, respectively.

3.2. Structures of the Isolated Compounds

Eight compounds were isolated; compounds **1** to **4** are from chloroform extract, and compounds **5** to **8** are from ethyl acetate extract. The molecular

structures of the isolated phytoconstituents were elucidated from spectral data (¹H, ¹³C NMR, HRMS) and by comparison with those in the literature.

3.2.1. Nuclear magnetic resonance and IR data

Xanthyletin (1): white crystals; yield: 2.75%, melting point (m.p). 132 °C. The HRSM spectrum showed a molecular ion at m/z 251.0684 [M + Na]⁺ giving the molecular weight at m/z 228 [M]. The ¹H NMR (400 MHz, CDCl₃, δ , ppm) showed the presence of doublets at 7.57 (1H, d, J = 9.5 Hz, H -4) and 6.22 (1H, d, J = 9.5 Hz, H -3) corresponding to the protons that can be attributed to the double bond conjugated to the carbonyl group. Two doublets at 6.34 (1H d, J = 9.9 Hz, H -6), 5.68 (1H, d, J = 9.9 Hz, H -7) and two singlets at 7.04 (1H, s, Ar- H) and 6.72 (1H, s, Ar- H) are in para position of dimethyl chromene. At 1.46 (6H, s, CH₃) two methyl groups resonate. The ¹³C NMR (100 MHz, CDCl₃, δ , ppm) (Jmod) highlights 14 carbons including 6 quaternary carbons at 161.33 (C-2), 155.57 (Ar-CH), 143.47 (C-4), 118.64 (Ar-CH), 112.85 (Ar-C) and 77.86 (C-8). 6 tertiary carbons at 143.47 (C-4), 131.36 (C-7), 124.89 (Ar-C), 120.91 (C-6), 113.18 (C-3) and 104.55 (C-9) 77.86 (C-8), 104.55 (Ar-C). The two primary carbons which correspond to the carbons of the CH₃- groups resonate at 28.48 (CH₃). IR spectrum at (CH₂Cl₂, cm⁻¹): 1719 cm⁻¹ reveals the carbonyl group (C=O). Anal. Calcd for C₁₄H₁₂O₃: C, 73.67; H, 5.30; O, 21.03. HRMS (m/z) C₁₄H₁₂O₃ (228 g/mol). The data acquired compared to those in the literature allow to determine the structure of the **Compound 1** (Figure 1) (17).

Edulinin (2): white crystals; yield: 7.51%, m.p. 135°C. The HRSM spectrum ¹H NMR (400 MHz, CDCl₃, δ , ppm) in positive mode indicates a peak corresponding to m/z 314.1364 [M + Na]⁺ which allow to determine the molecular weight at 291 [M]. The ¹H NMR (400 MHz, CDCl₃, δ , ppm) spectrum of phytocompound showed different signals at 7.85 (1H, d, J = 8.0 Hz, Ar- H), 7.60 (1H, dd, J = 8.6 and 7.1 Hz, Ar- H), 7.43 (1H, d, J = 8.5 Hz, Ar- H), 7.31 (1H, t, J = 7.6 Hz, Ar- H) indicating the protons of the aromatic ring. At 5.10 (1H, d, J = 3.4 Hz, OH) and 2.65 (1H, s, OH) spectrum showed OH groups. O-methyl and N-methyl resonate at 3.97 (3H, s, OCH₃) and 3.75 (3H, s, NCH₃). In addition, methylene and methyl protons resonated between 3.12-1.31 (1H, d, J = 13.7 Hz, H -a). The COSY spectrum showed a coupling between the protons H -5 (7.85 ppm) and H -6 (7.31 ppm); H -7 (7.60 ppm) pairs with H -8 (7.43 ppm) and H -6 (7.31 ppm). The protons H (OH1) at 5.10 ppm and H (OH2) at 3.59 ppm correlate with H -2' (3.59 ppm) and 6H (2Me) at 1.31 ppm, respectively. ¹³C NMR (100 MHz, CDCl₃, δ , ppm): 166.32 (C-2), 161.81 (C-4), 139.08 (Ar-C8a); 121.34 (C3), 117.88 (C4a), 73.11 (C3'), 130.91 (Ar-C7), 123.79 (Ar-C5), 122.76 (Ar-C6), 114.68 (Ar-C8), 79.48 (C2'), 62.40 (NCH₃), 30.24 (OCH₃), 27.87 (C1'), 25.84 (C3a)', 24.06 (C3' and C4'). The IR spectrum indicates the presence of an absorption band at 3415 cm⁻¹ reflecting the existence of hydroxyl groups (OH). The band observed at 2919 cm⁻¹ indicates an

aliphatic C-H valence vibration of the ethyl group (CH_3CH_2 -). The absorption band at 1624 cm^{-1} corresponds to a deformation vibration characteristic of the carbonyl function ($\text{C}=\text{O}$). Anal. Calcd for $\text{C}_{16}\text{H}_{21}\text{NO}_4$: C, 65.96; H, 7.27; N, 4.81; O, 21.97. HRMS (m/z) $\text{C}_{16}\text{H}_{21}\text{NO}_4$ (291 g/mol); **Compound 2** (Figure 1) (18,19).

1-methyl-2-[(E)-(prop-1-enyl)]quinolin-4-one (3): yellow solid; yield: 0.29%, m.p. $125\text{ }^\circ\text{C}$. The mass spectrum (HRMS) showed a molecular weight at m/z 199.10 corresponding to the chemical formula $\text{C}_{13}\text{H}_{13}\text{NO}$. The ^1H NMR (400 MHz, CDCl_3 , δ , ppm) spectrum showed different signals, at 8.45 (1H, d, $J = 7.9$ Hz, $H-5$), 7.66 (1H, dd, $J = 7.9, 1.6$ Hz, $H-7$), 7.49 ppm (1H, d, $J = 8.6$ Hz, $H-8$), 7.38 ppm (1H, t, $J = 7.6$ Hz, $H-6$) which define the presence of an aromatic ring. Three olefin protons at 6.37 (1H, s, $H-3$); 6.47 (1H, d, $J = 15.3$ Hz, $H-1'$) and 6.40 (1H, m, $H-2'$). The protons at 1.97 (3H, d, $J = 6.3$ Hz, $H-3$) and 3.75 (3H, s, NMe) correspond to the CH_3 and N-methyl groups, respectively. ^{13}C NMR (100 MHz, CDCl_3 , δ , ppm): 178.22 ($\text{C}=\text{O}$), 152.26 ($\text{C}-2$), 141.65 ($\text{C}8\text{a}$), 126.95 ($\text{C}5\text{a}$), 132.26 ($\text{C}7$), 126.80 ($\text{C}5$), 123.46 ($\text{C}6$), 115.55 ($\text{C}8$), 136.38 ($\text{C}2'$), 125.46 ($\text{C}1'$), 108.91 ($\text{C}3$), 35.56 (NCH_3), 19.04 (CH_3). IR (CH_2Cl_2 , cm^{-1}): 1595 ($\text{C}=\text{O}$), 1056 (NCH_3). Anal. Calcd for $\text{C}_{13}\text{H}_{13}\text{NO}$: C, 78.36; H, 6.58; N, 7.03; O, 8.03. HRMS $\text{C}_{13}\text{H}_{13}\text{NO}$ (199.10 g/mol); **Compound 3** (Figure 1) (20,21).

1,2-dimethylquinolin-4-one (4): brown solid; yield: 0.45%, m. p. $123\text{ }^\circ\text{C}$. ^1H and ^{13}C NMR (400 MHz, CDCl_3 , δ , ppm) spectrums of Compound 4 are similar to those of compound 3 with the substitution of the (E)-prop-1-enyl group by methyl at 2.48 (3H, s, CH_3) and 22.36 (CH_3). IR 1622 ($\text{C}=\text{O}$), 1141 (NCH_3). Anal. Calcd for $\text{C}_{11}\text{H}_{11}\text{NO}$: C, 76.28; H, 6.40; N, 8.09; O, 9.24. HRMS $\text{C}_{11}\text{H}_{11}\text{NO}$ (174.09 g/mol); **Compound 4** (Figure 1) (20,22).

5,7-dihydroxy-2-(4'-hydroxyphenyl)-6,8-bis(3-methylbut-2-enyl)chroman-4-one (5): Yellow-green amorphous solid; yield: 0.1%, m.p. $216\text{ }^\circ\text{C}$. The mass spectrum produced in Q-TOF MS ESI in negative mode showed a molecular ion at m/z 407.1860 $[\text{M}+\text{H}]^-$. The ^1H NMR (400 MHz, CDCl_3 , δ) spectrum of the phytocompound (5) showed at 12.33 ppm (1H, s, $\text{OH}-5$) and 6.38 ppm (1H, s, $\text{OH}-7$) the characteristic signals of the OH groups. The protons at 7.32 ppm (2H, d, $J = 8.5$ Hz, $H-2'$ and $H-6'$) and at 6.87 ppm (2H, d, $J = 8.6$ Hz, $H-3'$ and $H-5'$) correspond respectively to the protons in the ortho and meta position of the aromatic ring. A signal at 5.32 ppm (1H, dd, $J = 12.5, 2.7$ Hz, $H-2$); a singlet at 3.04 ppm (1H, dd, $J = 17.1, 12.8$ Hz, $\text{H}3\text{a}$) and at 2.79 ppm (1H, dd, $J = 17.1, 3.1$ Hz, $\text{H}-3\text{b}$). Signals resonating at 5.27 – 5.22 ppm (1H, m, $H-2''$) and 5.22 – 5.17 ppm (1H, m, $H-2'''$) then at 3.34 ppm (2H, d, $J = 6.9$ Hz, $H-1''$) and 3.29 ppm (2H, d, $J = 7.1$ Hz, $H-1'''$). Furthermore, protons resonating at 1.71 ppm (s, $3\text{H}-3\text{a}''$), 1.81 ppm (s, $3\text{H}-4''$), 1.70 ppm (s, $3\text{H}-4'''$) and 1.75 ppm (s, $3\text{H}-3\text{a}'''$) are the methyl (CH_3 -) and prenyl ($(\text{CH}_3)_2\text{-C}=\text{CH}-\text{CH}_2$ -) groups. ^{13}C NMR

(100 MHz, CDCl_3 , δ , ppm): 196.70 ($\text{C}=\text{O}$), 162.48, 159.45, 157.88, 107.39, 106.56, 102.94 (Ar-C), 43.43 ($\text{C}-3$), 22.03 ($\text{C}-1''$), 21.39 ($\text{C}-1'''$), 155.99 (Ar-C-4'), 131.26 (Ar-C-1'), 134.90 ($\text{C}-3''$), 134.13 ($\text{C}-3'''$), 127.85 (Ar-CH-2' and Ar-CH-6'), 115.64 (Ar-CH-3' and Ar-CH-5'), 78.65 ($\text{C}-2$), 122.11 ($\text{C}-2''$), 121.89 ($\text{C}-2'''$), 26.00 ($\text{CH}_3-3\text{a}''$ and $3\text{a}'''$), 18.01 (CH_3-4'' and $4'''$). IR (CH_2Cl_2 , cm^{-1}): 3368 (OH), 2918 (Ar-CH), 1627 ($\text{C}=\text{O}$). Anal. Calcd for $\text{C}_{25}\text{H}_{28}\text{O}_5$: C, 73.51; H, 6.91; N, 8.09; O, 19.58. HRMS $\text{C}_{25}\text{H}_{28}\text{O}_5$ (408.17 g/mol); **Compound 5** (Figure 1) (23,24).

1,6-dihydroxy-3,5-dimethoxy-10-methyl-4-(3'-methylbut-2'-enyl)acridin-9-one

(Grandisinin) (6): amorphous solid yellow-green; yield: 0.22%, m.p. $224.3\text{ }^\circ\text{C}$. The ^1H NMR spectrum of compound (6) showed different signal clusters. Two doublets, which integrate for one proton each were observed, one at 8.02 ppm (1H, d, $J = 8.8$ Hz, $H-8$) and the other at 6.95 (1H, d, $J = 8.7$ Hz, $H-7$) correspond to aromatic protons. An isolated aromatic signal proton at 6.38 ppm (1H, s, $H-2$); signals at 14.29 ppm (s, 1H, $H-1'$) and 12.34 ppm (s, 1H, $H-6'$) reveal the presence of two phenolic hydroxyl groups. The spectrum showed three singlets of 3H one at 3.56 ppm (3H, s, $N\text{-Me}$), and the other two at 3.92 ppm (3H, s, $O\text{-Me}5$), 3.90 ppm (3H, s, $O\text{-Me}3$) which each correspond to a methoxy group ($-O\text{-Me}$). Furthermore, the signals observed at 1.69 ppm (3H, s, $H-13\text{a}$), 1.79 ppm (3H, s, $H-14$) corresponding to methyl groups and protons at 3.46 (2H, d, $J = 6.1$ Hz, $H-11$), 5.23 ppm (t, $J = 1.5$ Hz, 1H, $H-12$) indicate the presence of a prenyl group ($(\text{CH}_3)_2\text{-C}=\text{CH}-\text{CH}_2$ -). ^{13}C NMR (100 MHz, CDCl_3 , δ , ppm): 182.38 ($\text{C}=\text{O}$), 164.96, 163.42, 149.76, 109.30, 106.90 (Ar-C), 94.56 (Ar-CH), 154.54, 142.79, 135.9, 118.49 (Ar-C), 123.36, 111.60 (Ar-CH), 59.94, 56.14 (OCH_3), 47.66 (NCH_3), 131.98 ($\text{C}-13$), 123.96 ($\text{C}-12$), 26.33 ($\text{C}-11$), 25.85 (CH_3), 18.20 (CH_3-13a). IR (CH_2Cl_2 , cm^{-1}): 1401 ($\text{C}=\text{C}$), 1627 (OH), 1020 (NCH_3), 1627 ($\text{C}=\text{O}$). Anal. Calcd for $\text{C}_{21}\text{H}_{23}\text{O}_5$: C, 68.28; H, 6.28; N, 3.78; O, 21.65. HRMS $\text{C}_{21}\text{H}_{23}\text{NO}_5$ (369.16 g/mol); **Compound 6** (Figure 1) (25).

6,10-dihydroxy-11-methoxy-3,3,12-trimethyl-3,12-dihydropyrano[2,3-c]acridin-7-one

(citracridone) (7): Yellow solid; yield: 2.32%, m.p. $243\text{ }^\circ\text{C}$. The ^1H NMR spectrum indicated signals from benzene nuclei at 8.07 ppm (1H, d, $J = 8.8$ Hz, $H-8$); 6.99 ppm (1H, d, $J = 8.8$ Hz, $H-9$) and 6.27 ppm (1H, s, $H-5$). A signal at 14.25 ppm (s, 1H, $-OH$) revealed the presence of a phenolic hydroxyl group. The signals at 6.54 ppm (1H, d, $J = 9.6$ Hz, $H-1$) and 5.58 ppm (1H, d, $J = 9.7$ Hz, $H-2$) correspond to 2 H which can be attributed to a double bond conjugated to a carbonyl group ($\text{C}=\text{O}$). The singlets at 3.91 ppm (3H, s, $O\text{-Me}$) and 3.70 ppm (3H, s, $N\text{-Me}$) correspond respectively to the $-O\text{Me}$ and NMe group, and finally two methyl groups (CH_3 -) resonating at 1, 52 ppm (6H s, $-\text{CH}_3$). ^{13}C NMR (100 MHz, CDCl_3 , δ , ppm): 181.63 ($\text{C}=\text{O}$), 154.50, 141.62, 135.88, 118.66 (Ar-C), 112.09, 123.58 (Ar-CH), 164.81, 161.22, 147.40, 106.94, 102.64 (Ar-C), 98.84 (Ar-CH), 90, 53 ($\text{C}-3$), $\text{C}2$

(124.84 ppm), 120.54 (C-1), 60.19 (OCH₃), 48.08 (NCH₃), 27.34 (CH₃). IR (CH₂Cl₂, cm⁻¹): 1401 (C=C), 1627 (C=O), 3407 (OH), 1096 (NCH₃). Anal. Calcd for C₂₀H₁₉O₅: C, 67.98; H, 5.42; N, 3.96; O, 22.64. HRMS C₂₀H₁₉O₅ (353.13 g/mol); **Compound 7** (Figure 1) (26).

6,11-dihydroxy-3,3,12-trimethylpyrano[2,3-c]acridin-7-one (8): Red solide; yield: 1.42%, m.p. 256 °C. The ¹H NMR spectrum showed signals from a benzene ring at 7.67 ppm (1H, dd, *J* = 7.7, 1.7 Hz, *H*-8); 7.28 ppm (1H, dd, *J* = 7.7, 1.8 Hz, *H*-9); 7.23 (1H, t, *J* = 7.7 Hz, *H*-10). A signal from another benzene ring appears at 6.14 ppm (1H, s, *H*-5). A signal at 14.49 ppm (1H, s, -OH) revealed

the presence of a phenolic hydroxyl group; the signals at 6.69 ppm (1H, d, *J* = 9.7 Hz, *H*-1) and 5.67 ppm (1H, d, *J* = 9.7 Hz, *H*-2) correspond to the 2 H of the double bond conjugated with the carbonyl group (C=O). A singlet at 3.75 ppm (3H, s, *N*-Me) and finally 2 (CH₃-) resonating at 1.47 ppm (6H s, 2CH₃). ¹³C NMR (DMSO-*d*₆): 181.37 (C=O), 163.71, 160.70, 148.74, 106.30, 101.99 (Ar-C), 97.00 (Ar-CH-5), 147.29, 136.69, 124.16 (Ar-C), 124.15, 115.25, 120.15 (Ar-CH), 124.16 (C-2), 120.55 (C-1), 76.75 (C-3), 48.08 (NCH₃), 26.78 (2CH₃). Anal. Calcd for C₁₉H₁₇O₄: C, 70.58; H, 5.30; N, 4.33; O, 19.79. HRMS C₁₉H₁₇O₄ (324.12 g/mol); **Compound 8** (Figure 1) (27).

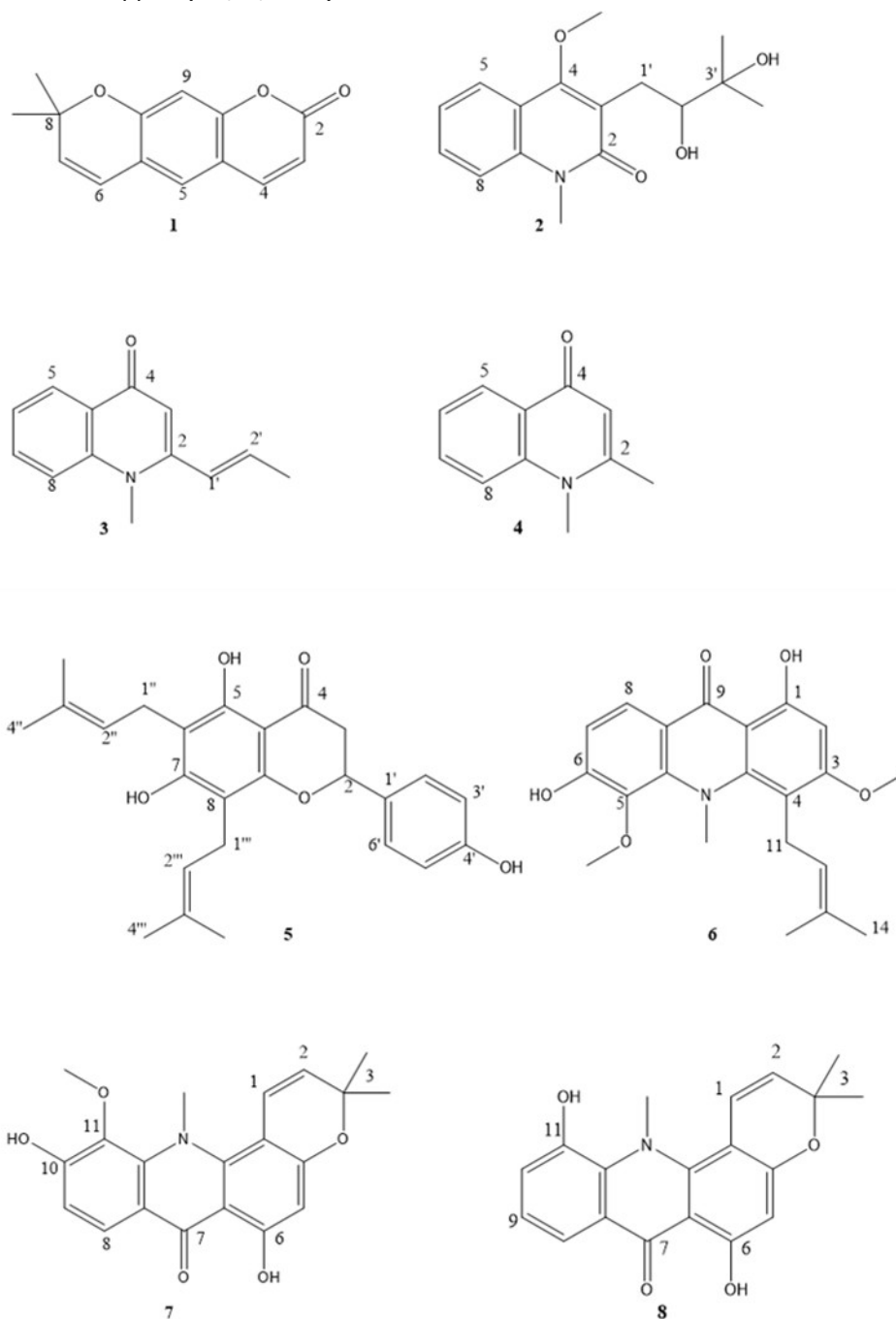


Figure 1: Structure of the compounds **1-8**.

3.3. DPPH Free Radicals Scavenging and Anticholinesterase Activity

The antioxidant potential against DPPH radicals and the anticholinesterase activity of compounds **1** to **8** were evaluated.

3.3.1. Antioxidant activity (DPPH radicals)

Figures 2 and 3 show overall that all the compounds present a reducing character of the DPPH radical.

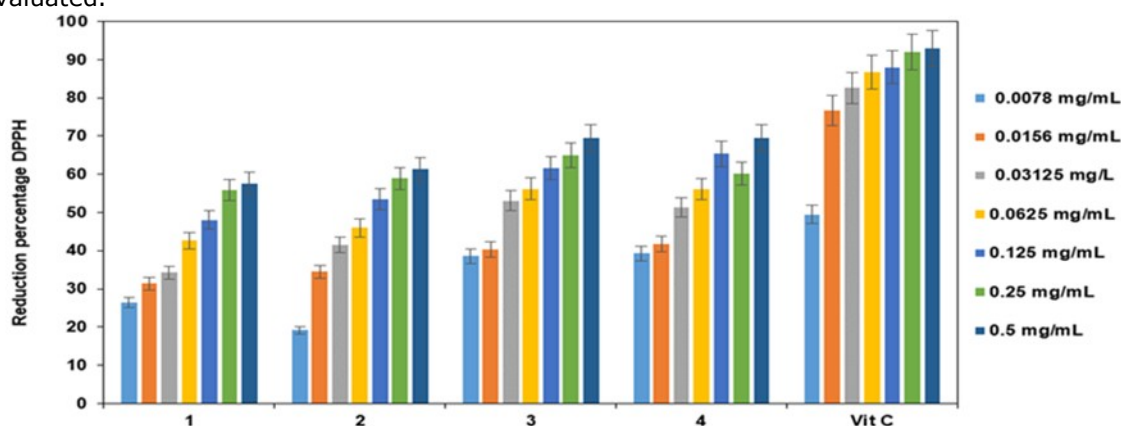


Figure 2: Reduction Percentage of the DPPH radical of the isolated compounds **1-4** and vitamin C.

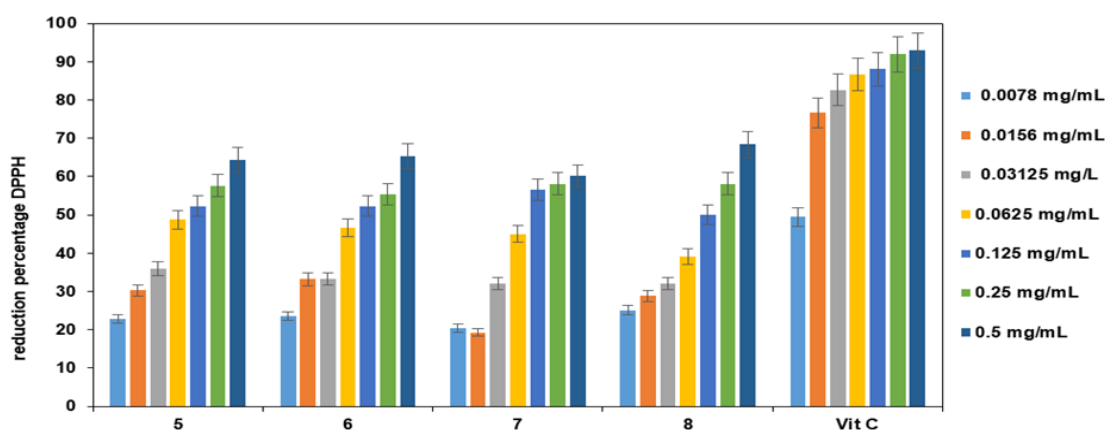


Figure 3: Reduction Percentage of the DPPH radical of the isolated compounds **5-8** and vitamin C.

The reduction percentages (RP) of the compounds **1-4** from CA1 showed a good antioxidant profile (Figure 2). On the other hand, compound **1** reduces DPPH radical at 1096.49 μM with RP (55.86%), and at 2192.98 μM (57.55%). Compound **2** has reduction ability at the different concentrations tested with RP at 429.55 μM (53.50%), 859.11 μM (58.84%), and 1718.21 μM (69.45%). Compounds **3** and **4** possess better ability to reduce DPPH radical with RP (53.08-69.45%) and (51.28 - 69.44%) at concentrations of 157.03 to 2512.56 μM .

The RP of compounds **5-8** from CA2 (Figure 9), showed RP > 50% at 306.24 to 1224.98 μM , with RP (52.31, 57.65 and 64.33%), (52.29, 55.44 and

65.30%), (56.57, 58.06 and 60.12%) and (54.07, 58.08 and 68.358%), respectively. The RP of vitamin C (49.49 - 88.49%), are higher than those of the isolated compounds at the tested concentrations. Thus, vitamin C is more effective than the samples tested at different concentrations against the DPPH radical. Therefore, we can admit that not only the presence of alkaloids but also coumarin and flavonoid contained in the extract of *C. aurantifolia* root bark would be at the origin of their antioxidant activity. In order to evaluate their antioxidant efficiency in scavenging the DPPH radical, the median reduction concentrations required to reduce DPPH radicals by up to 50% (RC_{50}) were defined (Table 1) (8,15).

Table 1: RC_{50} of compounds and vitamin C.

Compound s	1	2	3	4	5	6	7	8	Vit C
RC_{50} (μM)	271.93 6 \pm 0.001	1336.76 9 \pm 0.010	185.836 1 \pm 0.0001	218.27 7 \pm 0.002	205.81 1 \pm 0.007	306.642 1 \pm 0.0002	263.35 9 \pm 0.011	478.21 7 \pm 0.002	17.033 1 \pm 0.0002

Vit C: vitamin C; **1:** Xanthyletin; **2:** Edulinin; **3:** 1-methyl-2-[(E)-(prop-1-enyl)quinolin-4-one]; **4:** 1-methyl-2-[(E)-(prop-1-enyl)quinolin-4-one]; **5:** Lonchocarpol A; **6:** Grandisinin; **7:** Citracridone I; **8:** 5-hydroxynoracronycin

Table 1 shows that compounds **1**, **3**, **4**, **6**, and **7** have good antioxidant activity in a dose-dependent manner (28,29). Furthermore, compounds **3** and **4** show the highest antioxidant activity. The principle of antioxidant activity assessment is based on the ability of the compounds to give off hydrogen atoms. In fact, compounds 3 and 4 in Figure 1 show in positions 2' and 2, respectively, labile protons able to reduce the DPPH radical, which could justify their antioxidant capacity. The antioxidant potential compared to vitamin C shows the interest of the isolated compounds tested, since the oxidative phenomenon would be at the origin of oxidative stress, which is suspected to be responsible for

pathologies (15,30). Therefore, the anticholinesterase potential of the isolated compounds was evaluated.

3.3.2. Evaluation of acetylcholinesterase (AChE) inhibitory activity

The acetylcholinesterase (AChE) inhibitory activity of compounds (**1-8**) was evaluated during 360 s according to the Ellman method (16). Variable percentages of inhibition (PI) were obtained (Figures 4 and 5).

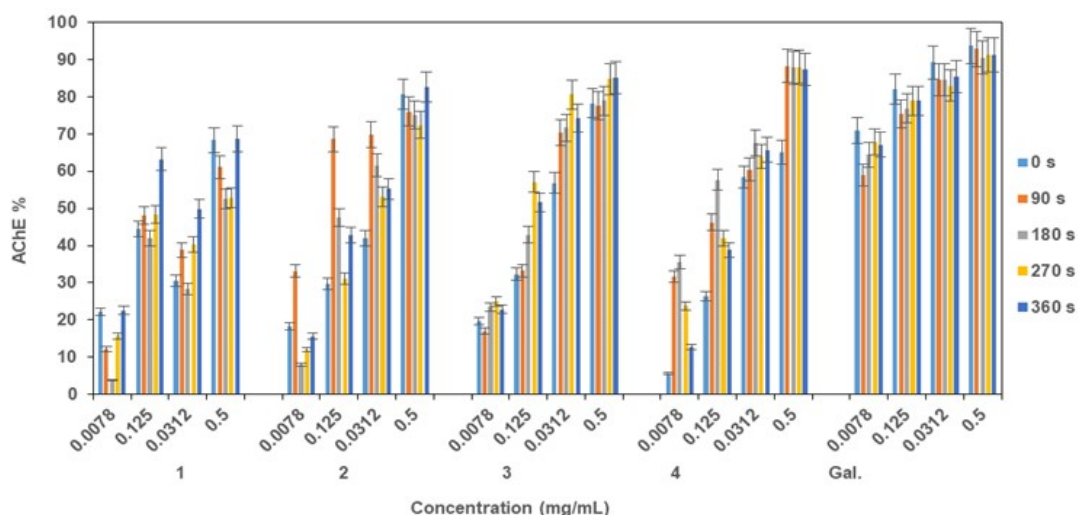


Figure 4: Anticholinesterase activity of compounds 1-4 and Galantamin.

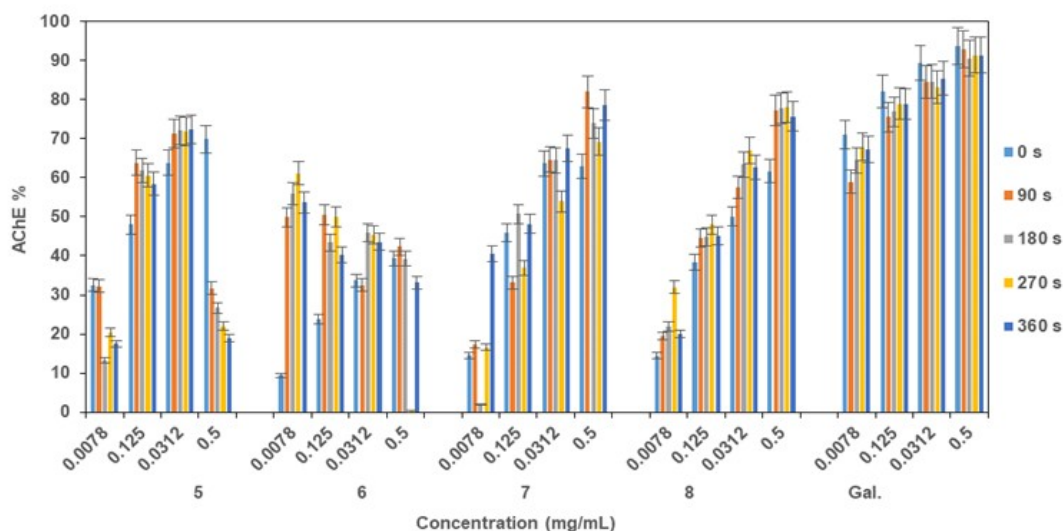


Figure 5: Anticholinesterase activity of compounds 5-8 and Galantamin.

Compounds 1-4 from CA1 showed acetylcholinesterase (AChE) inhibitory activity (Figure 4). Indeed, compound 1 recorded percentages of inhibition (PI) ranging from 52.448% to 68.797% at 548.245 μ M during 360 seconds. Compound 2 showed a PI of 72.366% to 82.61% at 1718.21 μ M during 360 seconds; at 429.553 μ M, the PI was greater than 55%. This result differs from that reported in the literature (19), which showed the low inhibitory capacity of 3-

(2',3'-dihydroxy-3'-methylbutyl)-4-methoxy-1-methylquinolin-2-one (Edulinin) on AChE, with a percentage of 19.4% at a concentration of 0.1 mg/mL. Compounds 3 and 4 showed respective PIs of 85.088% and 87.273% at 2511.3 μ M at 360 seconds; at 270 seconds, PIs of 84.727% and 87.998%; at 180 seconds, PIs of 78.917% and 87.850%; and at 90 seconds, PIs of 77.621% and 88.291%. In addition, this study was the first to

show the anticholinesterase activity of compounds **3** and **4**.

Compounds **5-8** from CA2, have also recorded acetylcholinesterase (AChE) inhibitory activity (Figure 5). On the other hand, compound **5** showed AChE inhibition at 1224.97 μM (PI = 69.849%) at 0 s; 306.244 μM PI (63.847 - 72.457%) during the 360 s and 76.5612 μM PI (58.417 - 63.776%) from 90 to 360 s. Regarding compound **6**, it inhibits the enzyme at 21.129 μM with PI > 50%. As to compounds **7** and **8**, they have higher potential with PI (81.950, 77.210%) at 1415.9 μM , (67.470 and 66.927%) at 353.977 μM , respectively. In view of all the above, we noted that all the isolated compounds have good abilities to inhibit the enzyme (AChE). The compounds **3**, **4**, and **6** showed PI close to that of galanthamin, used as a standard (PI > 60%).

To show of the structure-activity relationships of the compounds, several structural features were identified in the general structure of the compounds studied: a) the alkaloids (**2**, **3**, **4**, **6**, **7** and **8**), b) coumarins (**1**) and c) flavonoid (**5**).

Compounds **2,3,4,6,7**, and **8** from Citrus all feature an alkyl substituent on the nitrogen of the ring, which could justify the higher inhibition percentages (PI > 50) observed by these compounds. Indeed, Berkov et al. (2008), showed that the alkaloids N-allyl-nor-galanthamine and N-(14-methylallyl)-nor-galanthamin isolated from the leaves of *Leucojum aestivum* L demonstrated good inhibition of AChE. The presence of the substitution of the N-methyl derivative would be at the origin of the inhibitory activity of the two compounds (31). The best activity has been observed in sanguinin isolated from *Galanthus woronowii*. It is substituted at the N atom, but with a methyl group (32,33).

The results of a study carried out by Ryu et al (2012) on 20 flavonoids suggest that inhibitory flavonoids form a complex with AChE. The presence of a hydroxyl group, particularly in the A-ring of the flavonoid, as well as the double bond between C-2 and C-3, increases the enzyme's affinity (hydrogen bonds) and also enhances the AChE-inhibiting properties of flavonoids (34).

The traditional use of *Citrus aurantifolia* in the treatment of mental disorders could be justified by its antioxidant and anticholinesterase potential (11,35).

4. CONCLUSION

Chemical and biological studies of the root bark extracts from *C. aurantifolia* were performed. The structures of compounds were elucidated according to their spectral data (NMR, MS, and IR). The melting points were also determined. Additionally, this study identified eight known phytochemicals (**1-8**); among which compounds **2**, **3**, **4**, and **6** were isolated for the first time from the root bark of *C. aurantifolia*. The highest anticholinesterase activity was observed for compound **6**. The

combined antiradical and anticholinesterase activities of compounds **3** and **4** could explain the various therapeutic properties attributed to *Citrus aurantifolia* root barks in traditional medicine.

5. CONFLICT OF INTEREST

The authors declare that they have no conflicts of interest.

6. ACKNOWLEDGEMENTS

The authors thank the "Ministère de l'Enseignement Supérieur et de la Recherche Scientifique de Côte d'Ivoire (MESRSCI) for the financial support given to Djélé Alette Edwige Zialé for her PhD training at the Laboratoire CSPBAT of the Université Sorbonne Paris Nord, Bobigny (France). They also express their gratitude to the USPN for the access to the NMR Platform and to Professor Malan Djah François for the identification of the plant species studied.

7. REFERENCES

1. Brookmeyer R, Johnson E, Ziegler-Graham K, Arrighi HM. Forecasting the global burden of Alzheimer's disease. *Alzheimer's Dement* [Internet]. 2007 Jul 1;3(3):186–91. Available from: [<URL>](#).
2. Ahue MK, Bekro JAM, Maurice T, Virieux D, Pirat JL, Bekro YA. Preliminary phytochemical screening and protective effect of *Erythrina Senegalensis* in an in vivo mouse model of Alzheimer's disease. *J Med Pharm Allied Sci* [Internet]. 2017 Mar 1;630–44. Available from: [<URL>](#).
3. Ferri CP, Prince M, Brayne C, Brodaty H, Fratiglioni L, Ganguli M, et al. Global prevalence of dementia: a Delphi consensus study. *Lancet* [Internet]. 2005 Dec 17;366(9503):2112–7. Available from: [<URL>](#).
4. Adou DA, guessan AHON, -Békro JAM, Békro YA. Evaluation of the antioxidant potential and aglycone contents of ethereal extracts of 4 medicinal plants from Côte d'Ivoire. *J Pharmacogn Phytochem* [Internet]. 2022 Nov 1;11(6):46–9. Available from: [<URL>](#).
5. Aisa ER, Tukiran T. Comparison on Total Phenolics and Flavonoids and Antioxidant Activities of Methanol Extract of Horseshoe Crab (*Tachypleus gigas*) Eggs. *J Turkish Chem Soc Sect A Chem* [Internet]. 2023 Aug 30;10(3):787–96. Available from: [<URL>](#).
6. El Kadmiri N, Hamzi K, El Moutawakil B, Slassi I, Nadifi S. Les aspects génétiques de la maladie d'Alzheimer (Revue). *Pathol Biol* [Internet]. 2013 Dec 1;61(6):228–38. Available from: [<URL>](#).
7. Schliebs R, Arendt T. The significance of the cholinergic system in the brain during aging and in Alzheimer's disease. *J Neural Transm* [Internet]. 2006 Nov 9;113(11):1625–44. Available from: [<URL>](#).

8. Ziale DAE, Ngaman Kouassi KCC, Deschamp J, Bouchemal N, Palama TL, Lecouvey M, et al. Structural characterization and in vitro biological exploration of phytoconstituents isolated from a chloroform extract of *Rauvolfia vomitoria* (Apocynaceae) root bark from Côte d'Ivoire. *J Pharmacogn Phytochem* [Internet]. 2023 Jan 1;12(1):06–14. Available from: [<URL>](#).
9. Etebong E, Ubulom P, Etuk A. Antiplasmodial activity of methanol leaf extract of *Citrus aurantifolia* (Christm) Swingle. *J Herbmed Pharmacol* [Internet]. 2019 Sep 1;8(4):274–80. Available from: [<URL>](#).
10. Sunday Enejoh O, Oladejo Ogunyemi I, Smart Bala M, Sotonye Oruene I, Musa Suleiman M, Folorunsho Ambali S. Ethnomedical Importance of *Citrus Aurantifolia* (Christm) Swingle. *Pharma Innov J* [Internet]. 2015;4(8):1–6. Available from: [<URL>](#).
11. Amat-ur-Rasool H, Symes F, Tooth D, Schaffert LN, Elmorsy E, Ahmed M, et al. Potential Nutraceutical Properties of Leaves from Several Commonly Cultivated Plants. *Biomolecules* [Internet]. 2020 Nov 15;10(11):1556. Available from: [<URL>](#).
12. de Andrade JP, Giordani RB, Torras-Claveria L, Pigni NB, Berkov S, Font-Bardia M, et al. The Brazilian *Amaryllidaceae* as a source of acetylcholinesterase inhibitory alkaloids. *Phytochem Rev* [Internet]. 2016 Feb 22;15(1):147–60. Available from: [<URL>](#).
13. Assohoun K, Kabran GRM, Bekro JAM, Virieux D, Pirat JL, Bekro YA. Total alkaloids and in vitro antioxidant activity of *Crinum jagus* L. (*Amaryllidaceae*) organs from Côte d'Ivoire. *Int J Green Herb Chem* [Internet]. 2020 Oct 31;9(4):451–63. Available from: [<URL>](#).
14. Blois MS. Antioxidant Determinations by the Use of a Stable Free Radical. *Nature* [Internet]. 1958 Apr;181(4617):1199–200. Available from: [<URL>](#).
15. Eteko SD, N'Gaman-Kouassi K, Yao T, Mamyrbekova-Bekro J, Bekro Y. Phytochemical, Antioxidant and pharmacological study of (SM.) JACQ.- FEL. (*Melastomataceae*). *J Pharm Biol Sci* [Internet]. 2022 Jul 28;10(1):37–43. Available from: [<URL>](#).
16. Ellman GL, Courtney KD, Andres V, Featherstone RM. A new and rapid colorimetric determination of acetylcholinesterase activity. *Biochem Pharmacol* [Internet]. 1961 Jul 1;7(2):88–95. Available from: [<URL>](#).
17. Amaral JC, da Silva MM, da Silva MFGF, Alves TC, Ferreira AG, Forim MR, et al. Advances in the Biosynthesis of Pyranocoumarins: Isolation and ¹³C-Incorporation Analysis by High-Performance Liquid Chromatography–Ultraviolet–Solid-Phase Extraction–Nuclear Magnetic Resonance Data. *J Nat Prod* [Internet]. 2020 May 22;83(5):1409–15. Available from: [<URL>](#).
18. Noulala CGT, Ouete JLN, Atangana AF, Mbahbou GTB, Fotso GW, Stammler HG, et al. Soyauxinine, a New Indolopyridoquinazoline Alkaloid from the Stem Bark of *Araliopsis soyauxii* Engl. (*Rutaceae*). *Molecules* [Internet]. 2022 Feb 7;27(3):1104. Available from: [<URL>](#).
19. Yang Z duo, Zhang D bo, Ren J, Yang M jun. Skimmianine, a furoquinoline alkaloid from *Zanthoxylum nitidum* as a potential acetylcholinesterase inhibitor. *Med Chem Res* [Internet]. 2012 Jun 4;21(6):722–5. Available from: [<URL>](#).
20. Nguyen NT, Dang PH, Vu NXT, Le TH, Nguyen MTT. Quinoliniumolate and 2 H⁻1,2,3-Triazole Derivatives from the Stems of *Paramignya trimera* and Their α -Glucosidase Inhibitory Activities: In Vitro and in Silico Studies. *J Nat Prod* [Internet]. 2017 Jul 28;80(7):2151–5. Available from: [<URL>](#).
21. Yasir M, Tripathi MK, Singh P, Shrivastava R. The Genus *Glycosmis* [*Rutaceae*]: A Comprehensive Review on its Phytochemical and Pharmacological Perspectives. *Nat Prod J* [Internet]. 2019 Mar 18;9(2):98–124. Available from: [<URL>](#).
22. Rádľ S, Obadalová I. Utilization of Aromatic Denitrocyclization Reaction for the Synthesis of 3-Unsubstituted 1,4-Dihydroquinolin-4-one Derivatives. *Collect Czechoslov Chem Commun* [Internet]. 2004 Apr;69(4):822–32. Available from: [<URL>](#).
23. Ribeiro AB, Abdelnur PV, Garcia CF, Belini A, Severino VGP, da Silva MF das GF, et al. Chemical Characterization of *Citrus sinensis* Grafted on *C. limonia* and the Effect of Some Isolated Compounds on the Growth of *Xylella fastidiosa*. *J Agric Food Chem* [Internet]. 2008 Sep 10;56(17):7815–22. Available from: [<URL>](#).
24. Tahara S, Katagiri Y, Ingham JL, Mizutani J. Prenylated flavonoids in the roots of yellow lupin. *Phytochemistry* [Internet]. 1994 Aug 10;36(5):1261–71. Available from: [<URL>](#).
25. Tian-Shung W, Chang-Sheng K, Furukawa H. Acridone alkaloids and a coumarin from *Citrus grandis*. *Phytochemistry* [Internet]. 1983 Jan 1;22(6):1493–7. Available from: [<URL>](#).
26. Ye Y, Xu G, Li DL. Acridone alkaloids and flavones from the leaves of *Citrus reticulata*. *Nat Prod Res* [Internet]. 2022 Jul 18;36(14):3644–50. Available from: [<URL>](#).
27. Segun PA, Ismail FMD, Ogbale OO, Nahar L, Evans AR, Ajaiyeoba EO, et al. Acridone alkaloids from the stem bark of *Citrus aurantium* display selective cytotoxicity against breast, liver, lung and prostate human carcinoma cells. *J Ethnopharmacol* [Internet]. 2018 Dec 5;227:131–8. Available from: [<URL>](#).
28. Bissim SM, Kenmogne SB, Tcho AT, Lateef M, Ahmed A, Ngeufa Happi E, et al. Bioactive acridone alkaloids and their derivatives from *Citrus*

- aurantium (Rutaceae). *Phytochem Lett* [Internet]. 2019 Feb 1;29:148–53. Available from: [<URL>](#).
29. Tjahjandarie TS, Pudjiastuti P, Saputri RD, Tanjung M. Antimalarial and antioxidant activity of phenolic compounds isolated from *Erythrina cristagalli* L. *J Chem Pharm Res* [Internet]. 2014;6(4):786–90. Available from: [<URL>](#).
30. Favier A. Intérêt conceptuel et expérimental dans la compréhension des mécanismes des maladies et potentiel thérapeutique.
31. Berkov S, Codina C, Viladomat F, Bastida J. N-Alkylated galanthamine derivatives: Potent acetylcholinesterase inhibitors from *Leucojum aestivum*. *Bioorg Med Chem Lett* [Internet]. 2008 Apr 1;18(7):2263–6. Available from: [<URL>](#).
32. Sarikaya BB, Kaya GI, Onur MA, Bastida J, Somer NU. Phytochemical investigation of *Galanthus woronowii*. *Biochem Syst Ecol* [Internet]. 2013 Dec;51:276–9. Available from: [<URL>](#).
33. Ortiz JE, Garro A, Pigni NB, Agüero MB, Roitman G, Slanis A, et al. Cholinesterase-inhibitory effect and in silico analysis of alkaloids from bulbs of *Hieronymiella* species. *Phytomedicine* [Internet]. 2018 Jan 15;39:66–74. Available from: [<URL>](#).
34. Ryu HW, Curtis-Long MJ, Jung S, Jeong IY, Kim DS, Kang KY, et al. Anticholinesterase potential of flavonols from paper mulberry (*Broussonetia papyrifera*) and their kinetic studies. *Food Chem* [Internet]. 2012 Jun 1;132(3):1244–50. Available from: [<URL>](#).
35. Loizzo MR, Tundis R, Bonesi M, Menichini F, De Luca D, Colica C, et al. Evaluation of *Citrus aurantifolia* peel and leaves extracts for their chemical composition, antioxidant and anti-cholinesterase activities. *J Sci Food Agric* [Internet]. 2012 Dec 16;92(15):2960–7. Available from: [<URL>](#).



Chemical Strengthening of Soda-Lime Glasses via Ion Exchange Method

Simay YANİK¹, Mehtap ARSLAN-KABA¹, Guldem KARTAL SİRELİ^{1*}

¹Istanbul Technical University, Department of Metallurgical and Materials Engineering, Istanbul, 34398, Turkey

Abstract: The aim of this study is to improve the mechanical properties of glasses by the chemical strengthening method via the ion-exchange technique. For this purpose, KNO₃ salt baths were utilized for commercial soda-lime glasses. The diffusion-controlled strengthening mechanism is based on creating the compressive stress on the surface of glass by displacing the larger potassium ions with sodium ions. SEM-EDS line scan and XRF analysis, four-point bending, and Vickers hardness tests were performed for the structural and mechanical characterization of ion-exchanged glasses. The optimization of parameters led to a treatment duration of 24 hours at 400°C, resulting in a penetration depth of K⁺ ions reaching 85 μm. After ion exchange process, the improvement in the hardness, fracture toughness as well as bending strength values of the glasses was observed. The strengthened glasses exhibited notable enhancements in mechanical properties, specifically, hardness increased from 517 HV to 612 HV, and the fracture toughness increased to 3.14 MPa.m^{1/2} compared to the untreated glass, which displayed the fracture toughness of 1.09 MPa.m^{1/2}. Furthermore, the bending strength of treated specimens significantly improved to 421.6 MPa, representing a five-fold increase over the untreated sample's bending strength of 79 MPa.

Keywords: Chemical tempering, ion exchange, mechanical properties, soda-lime glass, strength

Submitted: October 19, 2023. **Accepted:** May 28, 2024.

Cite this: Yanik S, Arslan-Kaba M, Kartal Sireli G. Chemical Strengthening of Soda-Lime Glasses via Ion Exchange Method. JOTCSA. 2024;11(3):1237-44.

DOI: <https://doi.org/10.18596/jotcsa.1378346>.

***Corresponding Author. E-mail:** kartalqu@itu.edu.tr.

1. INTRODUCTION

The concept of glass describes in everyday life, as a material that is transparent solids having a hard and brittle structure. With a more technical definition, glass is a high-viscosity, inorganic liquid that does not have a crystalline structure or a definite melting point (1). Compared to other types of materials, glasses have features that meet the needs both technically and decoratively in many areas for centuries. However, its hard and brittle structure limits these usage areas. Today, glass is strengthened in many industries via different thermal and chemical strengthening methods to overcome its natural weakness and bring out its inherent superior properties (2-6).

Compared to the traditional thermal and chemical procedures (i.e., etching, flame polishing, tempering, etc.) the ion exchange, principally in the category of chemical strengthening method, provides many practical advantages especially diverse shape applicability including thin cross-sectional applications such as 2 mm and less (7-9). The ion exchange process, as stated in Equation 1, is based on the ion movement-diffusion mechanism occurring between the glass and salt bath where the process is performed (10). These ions are primarily monovalent alkali metals situated within the Si-O network structure of the glass and the molten salt bath (11-13).



Monovalent ions embedded in the glass networks embody the mechanical weak points in the glass and have the tendency of moving through an electric potential difference or concentration gradient with the help of thermal driving forces. Therefore, the monovalent ions located at the

interface of the glass surface and molten salt bath displace their locations mutually. When ions with larger diameters settle in the gaps of glass networks, the compressive stresses form at the surface and accordingly tensile stresses occur in the inner parts to balance forces. In addition to the

compressive stress formations, the surface chemistry of glass changes depending on penetration depth and amounts which causes the alteration of its refractive index value (14–16).

The main scope of the study is to improve the mechanical properties of soda-lime glasses by applying the ion exchange process and to examine the effects of process parameters on strength of soda-lime glasses systematically. The ion exchange method was applied in molten KNO_3 salt at various temperatures and times. The process temperatures were selected based on the glass transition temperature (T_g) of the samples and the melting temperature of KNO_3 salt and three different values were investigated. Likewise, considering routine process duration applications, four different time parameters were determined and examined. SEM-EDS line scan and XRF analysis techniques were utilized for the structural characterizations. The mechanical performance investigations were carried out via 4-point bending tests and Vickers hardness measurements. Moreover, the fracture toughness values of processed samples were determined.

2. EXPERIMENTAL SECTION

Experimental studies were carried out with commercial soda-lime glasses with the thickness of 2.1 mm and 2 cm x 6 cm dimensions, supplied by Kutaş (Tamcam) Group. The chemical structure of the samples is stated as (% wt.) 71.9 SiO_2 , 14.3 Na_2O , 7.9 CaO , 4 MgO , 0.4 K_2O , 1.2 Al_2O_3 and 0.3 others. Soda-lime glass samples with the thickness of 2.1 mm and 2 cm x 6 cm dimensions were used for experimental studies. In order to minimize the surface pollution and increase the efficiency of the ion exchange process, the glasses were cleaned in an ultrasonic cleaner using acetone and then dried using distilled water and alcohol.

Before the ion-exchange process, DSC/TGA of the glass samples was performed using a NETZSCH STA449 F3, from 30 °C to 650 °C with a heating rate of 10 °C /min under 50 mL/min flowing argon gas. As given in Figure1, the glass transition onset temperature was determined as 582.1 °C from the DSC curve. T_g value was used in the determination of the maximum applicable process temperature so 450 °C was determined as the highest temperature for this study.

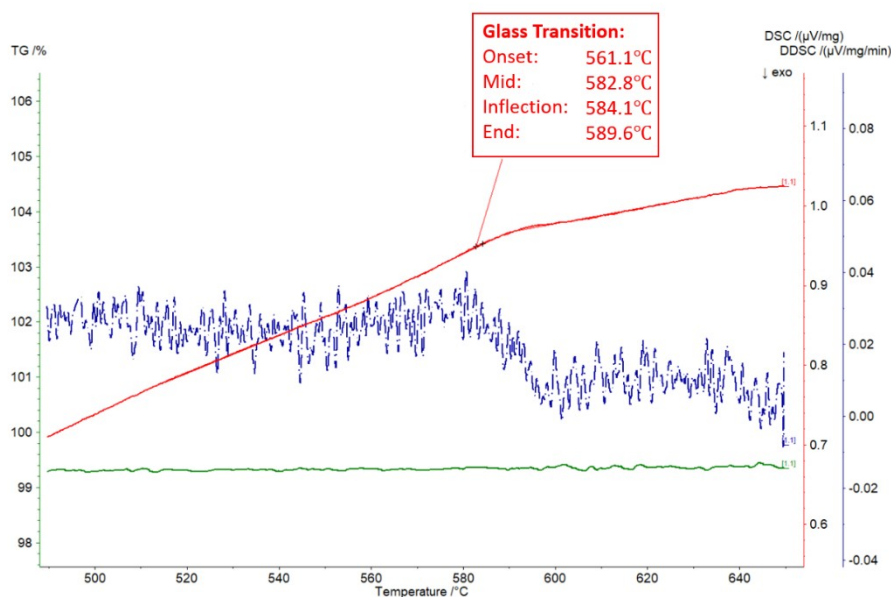


Figure 1. DSC Analysis Result of Samples.

Glass samples were subjected to an ion exchange process in a potassium nitrate salt bath (KNO_3) in the Nabertherm Controller B170 muffle furnace. The melting point of KNO_3 is 334 °C, so the experiments were carried out at 350 °C, 400 °C, and 450 °C for 4, 8, 12, and 24 hours. After the process, the surfaces of glass samples were cleaned with distilled water in order to remove the salt bath residues.

The cross-sectional structural characterizations were carried out via SEM-EDS analyses (Scanning electron microscopy - Energy Dispersive X-ray spectroscopy- using JEOL™ JSM 5410 microscope) to determine the amounts of potassium-sodium replacements, and so the diffusion depth profile

alterations. Likewise, relevant element amounts were determined and compared with Thermo Scientific – Niton XL3t GOLDD XRF analyzer before and after processing of glass samples.

The mechanical properties of processed samples were determined via a four-point bending test (AUTOGRAPH SHIMADZU AGS-J) to examine the bending strength variations and Vickers hardness instrument (TUKON™ 1102 instrument) under 500 g, 1000 g, and 2000 g loads for 10 seconds to measure the surface hardness alterations. Moreover, the fracture toughness values of processed samples were calculated according to Palmqvist Model.

3. RESULTS AND DISCUSSION

The XRF results of processed samples at different times and temperatures revealed that with increasing temperature K-Na replacements took place due to the thermal driving forces and concentration gradient effects. These substitutions became more obvious at longer process durations (16). For the treated samples for 12 hours and 24 hours, the potassium concentration in the samples increases steadily with increasing temperature which is consistent with REF (17).

Since longer process treatments at higher temperatures caused more potassium penetrations, the cross-sectional SEM-EDS line scan analyses of processed samples at 350 °C- 450 °C for 12-24 hours were further investigated to see the diffusion profile as presented in Figure 3 and given in Figure 4. With increasing temperature K^+ - Na^+ replacements became more deeper and the highest diffusing depth was observed at approximately 132 μm at the sample treated 450 °C for 24 hours.

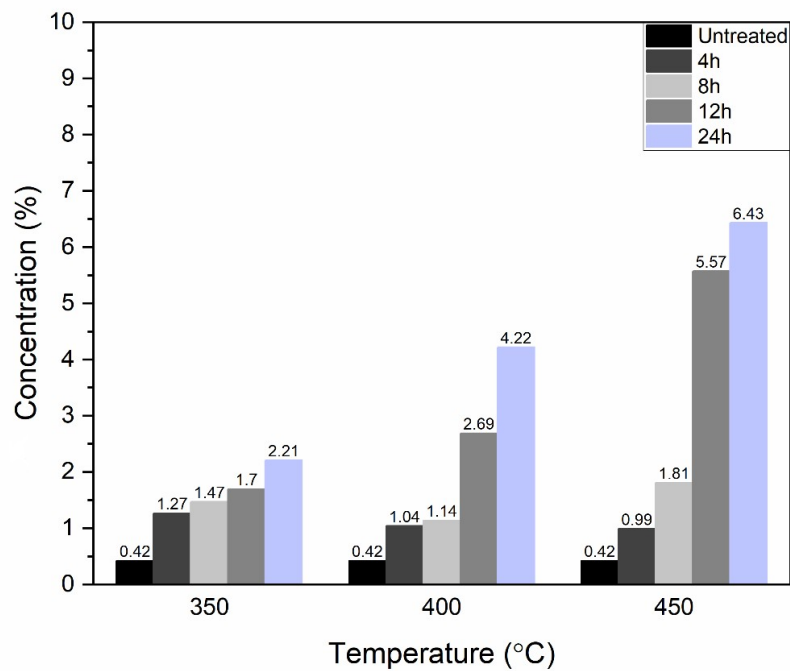


Figure 2. Concentration change of potassium in the sample.

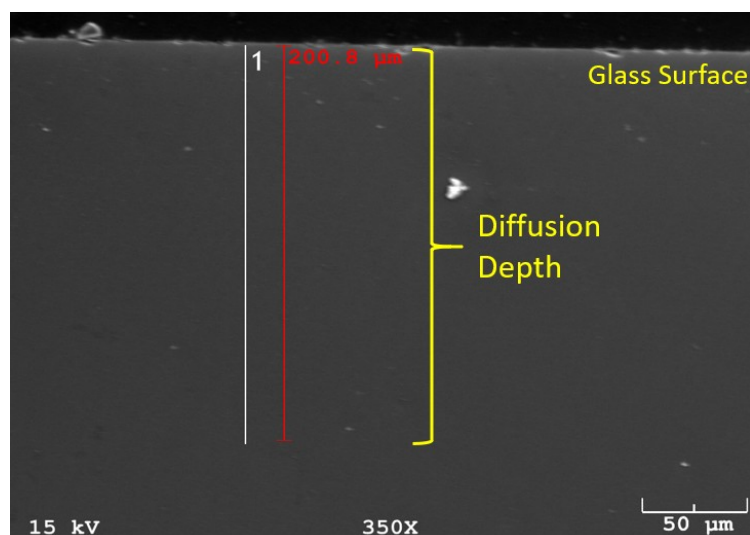


Figure 3. EDS line scan analysis image of sample treated at 350 °C for 12 hours.

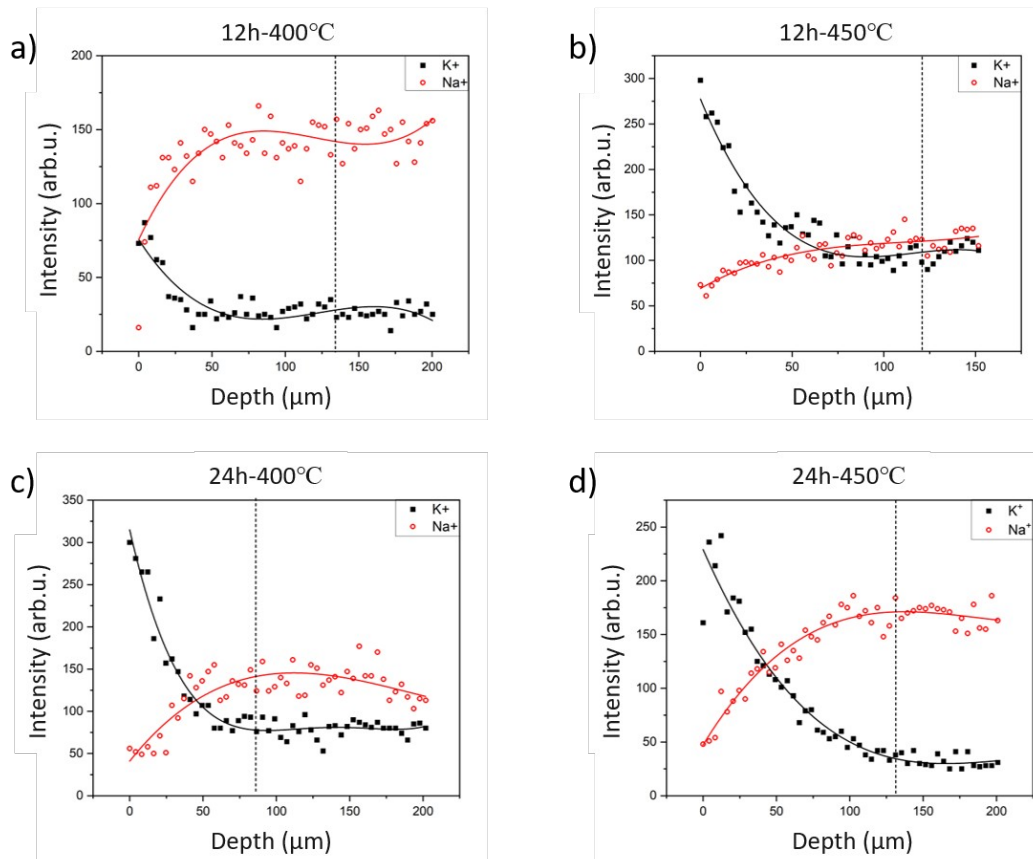


Figure 4. After a) 400 °C -12h, b) 450 °C -12h c) 400 °C -24h d) 450 °C -24h treatment, change of potassium composition according to depth after ion exchange.

For mechanical performance measurements, 4-point bending tests were performed to observe the change in bending strengths of treated samples for 12- 24 hours (Figure 5). The bending strength of the untreated sample is 79.5 MPa. So, after the treatment at 400 °C for 24 hours, the value increased to 421 MPa. Erdem et al. conducted ion exchange process for soda lime glasses and reported an increase in bending strength of soda-lime glasses from ~80 MPa to ~360 by ion-exchange method at 425 °C for 16 hours (16). The strength of the processed samples was improved with temperature until 450 °C then decreased which is probably because of that 450 °C is close to the strain point of this glass type. As mentioned in many literature studies, the effect of stress relaxation on the chemical strengthening of glasses

is quite large. In a study by Macrelli (15), stress relaxation can become an effective parameter if the difference between the strain point of the glass and the temperature at which the ion exchange process is performed is less than 100 °C. In this case, in soda lime glasses where the strain point value is assumed to be around 514 °C, the 450 °C process temperature is a critical value for stress relaxation. According to literature, the specified temperature values may also be important after certain processing times such as 8 hours. As a result, the reason why no increase in strength and fracture toughness was observed at processing times of more than 12 hours and at processing temperatures higher than 400 °C can be interpreted as the stress relaxation becoming an effective parameter at the specified time and temperature values (15).

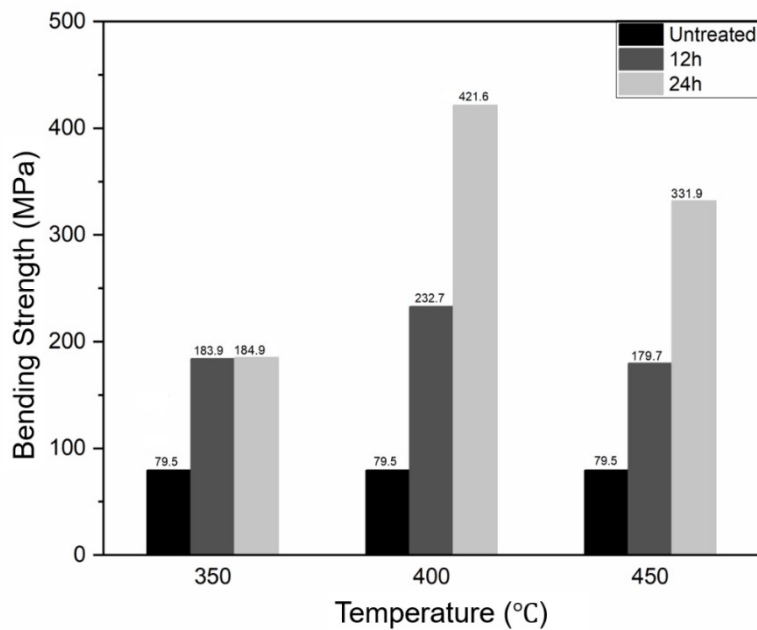


Figure 5. Bending strength values of glass samples that untreated and treated for 12 and 24 hours at 350 °C, 400 °C, 450 °C temperature values.

Figure 6 gives the Force-Displacement graphs were generated for the samples processed at 350 °C to 450 °C for 12 and 24 hours to compare with the untreated one. Apparently, the force and displacement values of untreated glasses are lower than treated glasses. Considering the process time effect, the strength values that the samples can withstand were higher at the sample treated longer. Glasses processed for 24 hours had the highest stress values for all temperature parameters (i.e., 826.3 N and 456 N for the sample treated at 400 °C

for 24 hours and 12 hours, respectively. Likewise, 650.5 N and 352.3 N for the sample treated at 450 °C for 24 hours and 12 hours, respectively). Considering the effects of process temperatures, the strengths increased up to 400 °C, then the values decreased as a result of the softening of the glass samples treated close to the strain point (e.g., 362.5 N, 826.3 N, 650.5 N for the sample treated for 24 hours at 350 °C, 400 °C and 450 °C, respectively).

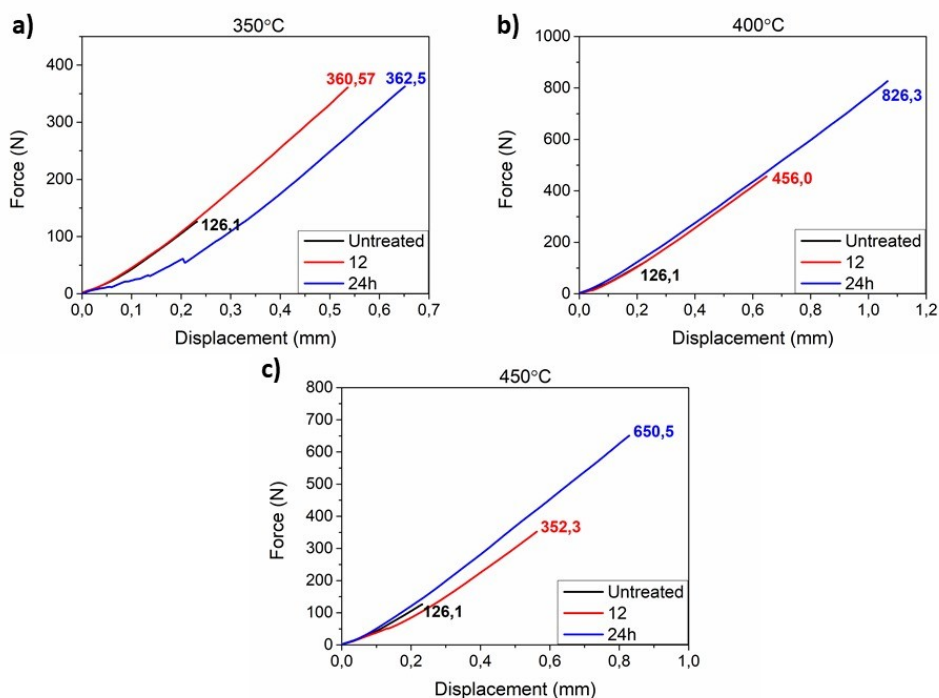


Figure 6. Force-displacement graph of untreated and ion-exchanged glasses at a) 350 °C b) 400 °C c) 450 °C for 12 and 24 hours.

Vickers hardness measurements were carried out at 500 g, 1000 g and 2000 g loads to evaluate the cracking resistances of processed glasses. The sample treated at 350 °C, 400 °C for 12 h had

resisted up to 1000 g (Figure 6). However, the sample treated for 24 hours at 400 °C did not fail to 1000 g (Figure 7). All samples had severe crack formations at higher loads namely 2000 g.

	500g	1000g	2000g
Untreated (517 HV)			
12 hours			
350 °C (656 HV)			
400 °C (638 HV)			
450 °C (601 HV)			

Figure 7. Optical microscope images of untreated and treated glasses at 350 °C, 400 °C, 450 °C for 12 hours.

	500g	1000g	2000g
Untreated (517 HV)			
400 °C			
12 hours (638 HV)			
24 hours (612 HV)			

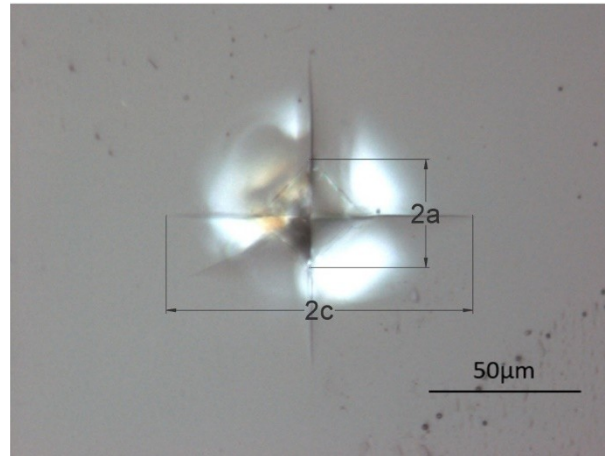
Figure 8. Optical microscope images of untreated and treated glass at 400 °C for 12 and 24 hours.

In the hardness values obtained as a result of the analysis, the glass samples belonging to the 400 °C parameters show higher results than the 450 °C (i.e., 638 HV for the sample treated at 400 °C for 12 hours and 601 HV for the sample treated at 450 °C for 12 hours, respectively) (Figure 7), which is consistent with the 4-point bending test in terms of temperature, while the samples belonging to the 12 hour processing time show higher values in terms of time at 400 °C (i.e., Likewise, 638 HV for the sample treated at 400 °C for 12 hours and 612 HV for the sample treated at 400 °C for 24 hours,

respectively) (Figure 8). These findings are consistent with REF 16 in which the highest hardness was obtained 620 HV at 425 °C for 16 hours. Moreover, the fracture toughness values were calculated for the treated samples (Table 1). For these calculations, the Palmqvist model and equation (2) were utilized due to the c/a ratio (see Figure 8) where the Vickers indentation and crack length were a and c respectively (i.e., the Palmqvist model is used at $c/a < 2.5$, whereas the Half-Penny model is preferred when $c/a \geq 2.5$) (18).

Table 1. Fracture toughness values of glass samples.

Sample	Fracture Toughness (MPa.m ^{1/2})	Applied Load (g)
Untreated	1.09	500
12h – 350 °C	1.78	2000
12h – 400 °C	2.60	2000
12h – 450 °C	2.70	1000
24h – 400 °C	3.14	1000

**Figure 9.** Vickers indentation and crack size

$$K_c = 0.079 \frac{P}{a^{3/2}} \log \left(4.5 \frac{a}{c} \right) \quad (2)$$

In general, fracture toughness of the untreated soda-lime glass (1.09 MPa.m^{1/2}) increased with temperature up to 450 °C, however increase in treatment time to 24 hours at 400 °C yielded the highest fracture toughness of 3.14 MPa.m^{1/2}. Similarly, the rise in fracture toughness of soda-lime glasses (reported as 0.66-2.22 MPa.m^{1/2} in REF 19) was stated at 425 °C for 16 hours treatment in REF 16, but increasing treatment temperature demonstrated a negative effect on crack formation probability. Considering bending strengths and fracture toughness values, the optimum condition was found as 400 °C and 24 hours for ion exchange treatment of soda lime glass in KNO₃ bath.

4. CONCLUSION

The soda-lime glasses were strengthened via ion exchanged based chemical strengthening method. The process parameters were optimized as 24 hours and 400 °C. After the strengthening treatment with optimized parameters, the penetration depth of K ions was obtained as 85 μm. The mechanical properties were noticeably improved by means of this economical, green and fast process. The hardness value was increased from 517 HV to 612 HV, and the fracture toughness was reached to 3.14 MPa.m^{1/2}, while the untreated one shows 1.09 MPa.m^{1/2}. The bending strength of the treated specimens were enhanced to 421.6 MPa which is 5-fold higher than the bending strength of the untreated sample (79 MPa).

5. CONFLICT OF INTEREST

Authors declare that there is no conflict of interest with any person, institute, company, etc.

6. ACKNOWLEDGMENTS

The authors would like to thank Prof. Dr. Murat Baydoğan and MSc. Mertcan Kaba for the mechanical tests, and to BSc. İlham Canan İlhan and BSc. Berkay Türkan for their assistance in the experimental procedure.

7. REFERENCES

- Zanotto ED, Mauro JC. The glassy state of matter: Its definition and ultimate fate. *J Non Cryst Solids*; 2017;471:490-5.
- Hasanuzzaman M, Rafferty A, Sajjia M, Olabi A-G. Properties of Glass Materials. Reference Module in Materials Science and Materials Engineering. Elsevier Ltd.; 2016. 1-12.
- Scalet BM, Garcia Muñoz M, Sissa Aivi Q, Roudier S, Luis DS. Best Available Techniques (BAT) Reference Document for the Manufacture of Glass. Joint Research Centre Reference Report. 2013. P.485.
- Nordberg ME, Mochel EL, Garfinkel HM, Olcott JS. Strengthening by ion exchange. *J Am Ceram Soc*. 1964;47(5):215-9.
- Bartholomew RF, Garfinkel HM. Chemical Strengthening of Glass. In: *Glass: Science And Technology: Volume 5*. Academic Press, Inc.; 1980. p.217-70.
- Leboeuf V, Blondeau JP, De Sousa Meneses D,

- Véron O. Potassium ionic exchange in glasses for mechanical property improvement. *J Non Cryst Solids*. 2013;377:60–5.
7. Garza-Méndez FJ, Hinojosa-Rivera M, Gómez I, Sánchez EM. Scaling properties of fracture surfaces on glass strengthened by ionic exchange. *Appl Surf Sci*. 2007;254(5):1471–4.
 8. West BR. Ion-exchanged glass waveguide technology: a review. *Opt Eng*. 2011;50(7):071107.
 9. Sglavo VM. Chemical strengthening of soda lime silicate float glass: effect of small differences in the KNO_3 bath. *Int J Appl Glass Sci*. 2015;6(1):72-82.
 10. Tang Z, Mauro YZ, Gee C, Duffy DL, Meyer TE, Abrams MB, Walker KA, Mauro JC. Methods for measurement and statistical analysis of the frangibility of strengthened glass. *Front. Mater*. 2015;2:50.
 11. Tailony R. Ion exchange glass strengthening using microwave processing. [MSc Thesis]. [Toledo]: The University of Toledo; 2015.
 12. Kistler SS. Stresses in Glass Produced by Nonuniform Exchange of Monovalent Ions. *J Am Ceram Soc*. 1962;45(2):59–68.
 13. Sglavo VM. Influence of KNO_3 bath composition on ion exchange process of commercial soda lime silicate float glass. In: *Ion exchange technologies*. 1st ed. InTech; 2012. p.305-14.
 14. Varshneya AK. Chemical Strengthening of Glass: Lessons Learned and Yet To Be Learned. *Int J Appl Glas Sci*. 2010;1(2):131–42.
 15. Gross TM. *Chemical Strengthening of Glass*. Springer Handbooks; 2019 p.273–96.
 16. Erdem İ, Guldiren D, Aydin S. Chemical tempering of soda lime silicate glasses by ion exchange process for the improvement of surface and bulk mechanical strength. *J Non Cryst Solids*. 2017;473:170–8.
 17. Gy R. Ion exchange for glass strengthening. *Mater Sci Eng B*. 2008;149(2):159–65.
 18. Külcü HK. İndentasyon Tekniği ile Temperli ve Tempersiz Soda-Silika Cam Kırılma Tokluğunun Belirlenmesi. [MSc Thesis]. [İstanbul]: Istanbul Technical University; 2015.
 19. Wright JC. Dynamic Fracture toughness of soda-lime glass. [MSc Thesis]. [West Lafayette]: Purdue University; 2010.



Microdetermination of Piroxicam in Pharmaceutical Formulations by Complexation with Fe(III) and Image Scanning Densitometry

Jamil Anwar¹ , Amara Dar² , Ramna Mumtaz² , Jesus M. Anzano^{3*} ,
Ayesha Mohyuddin¹ 

¹Department of Chemistry, School of Science, University of Management and Technology, Lahore, Pakistan.

²Center for Analytical Chemistry, School of Chemistry, University of the Punjab, Lahore, Pakistan.

³Department of Analytical Chemistry, University of Zaragoza, Zaragoza, Spain.

Abstract: Piroxicam is a nonsteroidal anti-inflammatory drug (NSAID) that is used to relieve pain or inflammation due to osteoarthritis or rheumatoid arthritis. Assay of piroxicam in pharmaceutical formulations can be performed by using a number of analytical techniques. This work estimates the drug in commercial samples using a novel method, Computational Image Scanning Densitometry (CISD). Micro-volumes of the aqueous solution of piroxicam were reacted with iron(III) sulfate solution under optimum conditions on a white Teflon well plate to form a pink-colored mononuclear complex. By using a smartphone, the picture of the colored complex in the well plate was taken and transferred to an attached computer. The overall optical density resulting from red, green, and blue (RGB) components from a specific area of the colored image was measured and digitalized with the help of custom-made software. A standard curve was prepared by plotting optical density against piroxicam concentration. The method was simple, fast, adequately precise, and accurate for the assay of the drug in commercial samples. The validity of the new method was checked by comparing the results with those obtained by a standard spectrophotometric method of Piroxicam estimation.

Keywords: Piroxicam assay, Image scanning densitometry, Pharmaceutical analysis, Piroxicam estimation, Drug assay.

Submitted: December 14, 2023. **Accepted:** July 3, 2024.

Cite this: Anwar J, Dar A, Mumtaz R, Anzano, JM, Mohyuddin A. Microdetermination of Piroxicam in Pharmaceutical Formulations by Complexation with Fe (III) and Image Scanning Densitometry. JOTCSA. 2024;11(3): 1245-54.

DOI: <https://doi.org/10.18596/jotcsa.1391053>

***Corresponding author's E-mail:** janzano@unizar.es

1. INTRODUCTION

Piroxicam belongs to the oxycam class of nonsteroidal anti-inflammatory drugs (NSAIDs) usually employed to treat pain, fever, and inflammation in the body. Its structure is related to the enolic acid class of 4-hydroxy-1,2-benzothiazine carboxamides (1). As it belongs to a non-narcotic group of drugs, it can safely be used to relieve mild to moderate pains such as fractures, dental, postpartum, postoperative pain, arthritis, acute gout, and musculoskeletal disorders (2). Several merits of piroxicam, such as its long half-life, high efficiency, potency, and fewer side effects, have encouraged its use in various ailments (3). It is proven as a suitable alternative to diclofenac, aspirin, ibuprofen, phenylbutazone, indomethacin, ketoprofen, naproxen, and sulindac (4).

Besides numerous positive points, piroxicam may cause certain side effects. It involves about 83 destructive reactions, and 73 of these are related to the gastrointestinal tract such as peptic ulcer, hemorrhages, perforation, and bleeding (5). Therefore, an assay of piroxicam is important to achieve optimum therapeutic quantity and for a better quality of pharmaceutical preparations (6). Although several analytical techniques have been reported in the literature for the determination of piroxicam in pharmaceutical preparations such as HPLC (7,8), capillary electrophoresis (9), solid-phase extraction (10), flow injection method (11), voltammetry (12) potentiometric methods (13) and several electro-analytical and spectroscopic methods (6,14-20), yet most of them suffer from certain drawbacks and limitations, such as complicated procedures and sophisticated instrumentation for analysis. To overcome these problems, the present

work describes a novel method based on image scanning densitometry (ISD) for estimating piroxicam in commercial formulations.

During the last two decades, a number of workers have employed computers and smartphones for image scanning and developed new analytical methods (21-23). These methods are relatively fast, simple, environment-friendly, and cost-effective compared to classical spectrophotometric methods. Verma and his students used image processing to determine the turbidity in water samples (24). Lyra and colleagues assayed a number of drugs by using a digital image-based flame emission spectrometric method (25). The total amino acid contents of food samples have been determined by computational image scanning densitometry (26).

Computational Scanning Image Densitometry (CSID) is a new technique that our group developed for chemical analysis (27). CSID is as precise and accurate as spectrophotometry but faster and simpler and does not require a spectrophotometer. It is based on measuring the optical density of a colored spot resulting from the reaction of the analyte and the coloring reagent. Our group has employed this technique successfully for the quantification of several metal ions (28), sulfides (29), formaldehyde (30), mercury (31), arsenic (32), nickel and chromium (33). The present work is based on the complexation of piroxicam with Fe (III). Piroxicam forms a stable pink color complex with Fe (III), which absorbs maximum around 504 nm (6).

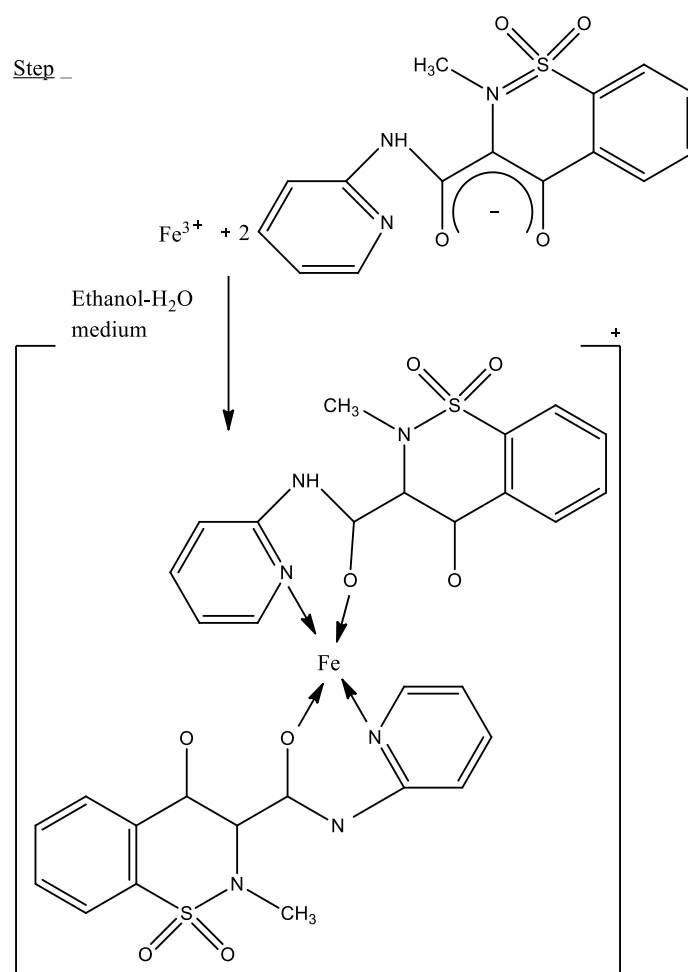


Figure 1: Chelation of Fe (III) with Piroxicam in water-ethanol media.

In the present work, micro-quantities of piroxicam in samples (in methanol-water) were mixed with a drop of iron (III) solution in a small well of Teflon well plate. A picture of colored solutions was taken with the help of a smartphone and transferred to an attached computer. Then, the optical density of each colored spot was measured with the help of customized software loaded on the computer. A calibration graph was prepared by plotting optical density against piroxicam concentration. To check the procedure's validity, a number of commercial samples containing piroxicam were analyzed using the proposed method and a standard spectrophotometric method, and the results obtained

from both methods were compared. The proposed method has proved itself fast, simple, accurate, and precise.

2. EXPERIMENTAL

2.1. Apparatus

For Image Scanning Densitometry, a 1 mL pipette (Pipetteman) and the well plate were used to develop colored spots. Cellphone cameras and ISD software (VB6-based graphical application with picture box, selection marquee, and flex grid) were used to measure the color density of digital images. A double-beam UV-visible spectrophotometer (Ultra-

3000 Rittun) with two quartz cells of 1 cm path length was used for spectrophotometric measurements.

2.2. Chemicals and Reagents

All reagents and organic solvents, including methanol and ethanol were of AnalaR Grade and were used in this work as such without further purification. Ferric sulfate (M.W. 399.88, Fluka Chemie AG, Switzerland) was purchased from the local market. Piroxicam reference standard drug (CAS No. 36322-90-4, M.W.= 331.4) was obtained from Sigma Chemical Company (St. Louis, USA) local agent. Capsules and tablets (Pfizer Ltd., Surrey, USA) of piroxicam were purchased from Scientific Pharmacy, Al-Khuwair, Muscat, Oman. For pH adjustment, Standard Buffers of pH 4, 7, and 10 were obtained from Hanna Instruments Inc. USA.

2.3. Preparation of Solutions

0.005 M Fe(III) solution was prepared by taking 0.2 g of $\text{Fe}_2(\text{SO}_4)_3$ in a 100 mL flask, and distilled water was used for the required dilution.

As Piroxicam was sparingly soluble in water hence, its 1000 ppm stock solution was prepared by dissolving 0.1 g of the drug in 10 mL of methanol and, after a little warming, filtered through the Whatman No. 42 filter paper. Then, the contents were diluted up to 100 mL with ethanol. Working solutions of piroxicam were prepared by diluting the 1000 ppm stock solution with ethanol.

Sample solutions of commercial dosage forms of Piroxicam (Feldene tablet, Pcam injection, Brexin tablet, Riacen capsule, Feldene capsules, Pcam tablet, Painza tablet, Pytex tablet, and Cyclodex tablet) were prepared in methanol. The powder contents of commercially available tablets and capsules (each 8 in number) of 10 mg strength of Piroxicam were taken in 25 mL methanol and, after a little warming, kept for 15 min for complete dissolution of the drug. The mixture was then filtered through Whatman No. 42 filter paper into 100 mL standard volumetric flasks. The residue was washed well with 4 to 5 mL portions of methanol for complete recovery of the drug, and each flask was diluted up to the mark with ethanol (as done for standards).

2.4. Optimization of Variables

All the possible variables, such as time, temperature, pH, volume of Fe(III) solution, and order of adding the reagents, were checked by reacting 5 mL of 1000 ppm solution of Piroxicam with different volumes of 0.005 M Fe(III) in a 100 mL flask under different experimental conditions. The volume was made up to the mark with ethanol. The absorbance of the final solution measured at 505 nm was taken as the measure of optimization.

2.4.1. Effect of concentration of Fe (III) solution

To check the effect of the concentrations of the Fe(III) solution, a 5 mL stock solution (1000 ppm) of piroxicam was made to react with different concentrations of a 0.005 M solution of Fe (III) in a series of 100 mL volumetric flasks. After 10 min, the red complex was diluted up to the mark with ethanol, and absorbance was measured against a

compensatory blank. The absorbance was plotted against the volume of the Fe(III) solution.

2.4.2. Effect of pH

To check the pH effect, the pH of the 5 mL solution of Piroxicam was adjusted to 4, 7, and 10 with the help of standard buffers in three 100 mL volumetric flasks. In each flask, 5 mL of 0.005 M Fe(III) solution was added, and after ten min, the volume was made up to the mark with ethanol. The absorbance of the red solution was measured against a compensatory blank.

2.4.3. Effect of time

To check the effect of time on the reaction of Piroxicam with Fe(III), 5 mL of stock solution (1000 ppm) of Piroxicam was reacted with 5 mL of 0.005M solution of Fe(III). After adjusting the pH at 4 of each solution, the contents were kept at room temperature for different intervals of time (5 to 50 min) before diluting the solution with ethanol and measuring the absorbance at 505 nm.

2.4.4. Effect of temperature

The effect of temperature was investigated by keeping the flasks at elevated temperatures (40, 60, and 80 °C) after adding 5 mL stock solution (1000 ppm) of Piroxicam with 5 mL of 0.005 M solution of Fe(III) in each flask. After heating for 10 min in a water bath, the contents of each flask were diluted up to the mark with ethanol, and the absorbance of each solution was measured at 505 nm against a compensatory blank.

2.4.5. Effect of order of reagents addition

To check the order of addition of reagents, the order between Piroxicam, Fe(III), and buffer was changed in the following sequence: a) Piroxicam + Fe(III) + pH-4 Buffer; b) Piroxicam + pH-4 Buffer + Fe(III); c) Fe(III) + pH-4 Buffer + Piroxicam. After mixing the reagents in different orders, the flasks were kept for 10 min and then diluted up to the mark with ethanol, and absorbance was measured at 505 nm.

2.4.6. Effect of organic solvents

To check the effect of various organic solvents, the contents of different flasks containing the reactants (Piroxicam + pH-4 Buffer + Fe (III)) were diluted with methanol, ethanol, acetone, ethyl acetate, and water after mixing them. In the case of dilution with water, the solution became significantly turbid.

2.5. Image Scanning Densitometric Method

Image Scanning Densitometry (ISD) was performed on a custom-made white Teflon plate with a series of wells of different capacities (0.25 to 1 mL). Piroxicam stock solution aliquots containing 10 to 100 ppm of the drug were transferred with the help of a micro-pipette into ten adjacent wells of 1 mL capacity into the plate. 0.2 mL buffer was added to each well, followed by 0.5 mL of 0.005 M solution of Fe(III). The contents were slightly mixed to allow the red color of varying intensity to develop in each well in the next ten min. Sample solutions of commercial formulations of Piroxicam were similarly treated in the next series of wells on the same Teflon plate. The image of the plate was captured with the help of a

smartphone or a camera and transferred to the computer, which was already loaded with custom-made image-scanning software. The color depth of each red-colored spot due to standard Piroxicam solution was measured with the help of the bespoke software (27). The calibration curve was obtained when the software plotted color intensity against Piroxicam concentration. The color intensity (optical density) of each spot of the commercial drug sample was also measured, and the quantity of the drug was calculated using the standard curve.

2.6. Reference (spectrophotometric) Method

Aliquots of 1000 ppm Piroxicam stock solution (1 to 10 mL) were transferred into ten clean and dry 100mL volumetric flasks. To adjust the pH at 4, 2 mL of standard pH 4 buffer was added to each flask. After thorough shaking, 5 mL of 0.005 M solution of Fe(III) was added to each flask and incubated for 10 min for complete complexation. The red complex was diluted up to the mark with ethanol. The absorbance of each homogeneous solution was measured against a compensatory blank at 505 nm. The Standard Curve was obtained by plotting the absorbance values against the concentration of Piroxicam. Then, the sample solutions of Piroxicam (pharmaceutical formulations) were treated similarly, and the absorbance of each solution was measured. The concentration of the drug in sample solutions was calculated from the Standard Curve.

3. RESULTS AND DISCUSSION

In this work, a novel method based on Image Scanning Densitometry (ISD) was developed for the assay of Piroxicam in commercial formulations. Our group has reported a number of techniques based on ISD (27-33). The method was optimized by analyzing the effect of different parameters such as solvent, pH, concentration of Fe(III), time, temperature and order of mixing the reagents and the results were compared with spectrophotometric method. The effect of all three colors (Red, Green Blue) of RGB channel were studied.

3.1. Effect of Organic Solvent

Piroxicam was sparingly soluble in water. Hence, some organic solvents had to be used to dissolve the drug. In addition, experimentation revealed that Piroxicam dissolved in methanol could not be diluted with water because the solution became significantly turbid and unfit for use in spectrophotometry. In this work, piroxicam solution prepared in methanol was diluted with ethanol, which gave the best results in terms of complete solubility and absorbance. In addition to ethanol, a few other polar solvents like acetone, methanol, and ethyl acetate were also employed for dilution. Still, as shown in Figure 2, maximum absorbance was obtained when ethanol was used as a diluting solvent.

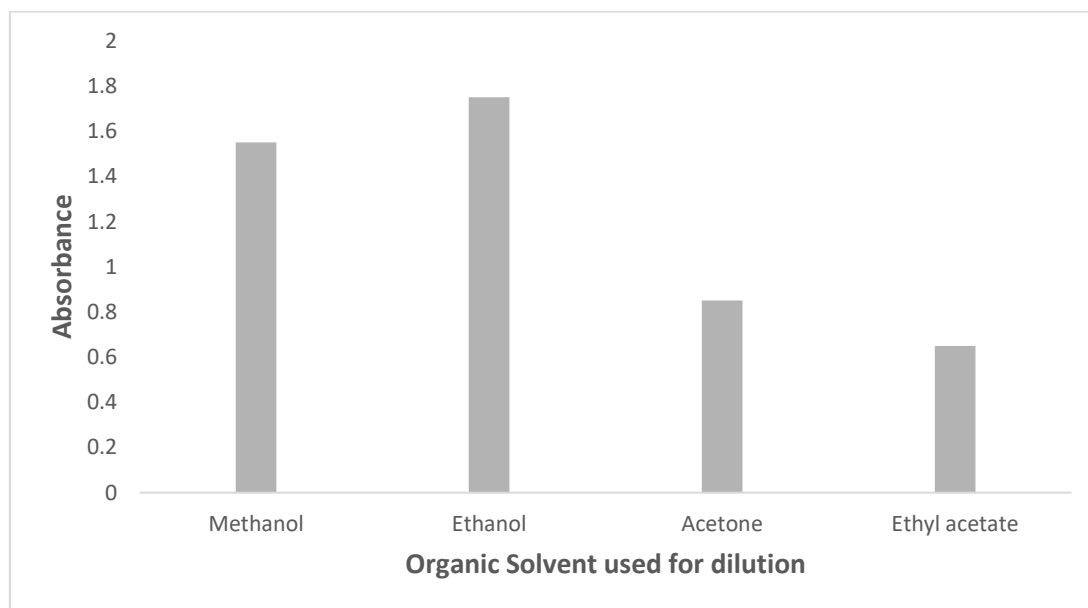


Figure 2: Effect of Organic Solvents on Complexation of Piroxicam with Fe(III).

3.2. Effect of pH

The effect of pH on the complexation of Piroxicam with Fe(III) and, ultimately, on the final absorbance at 505 nm was checked at acidic (pH=4), neutral (pH=7), and basic (pH=10) media. Piroxicam is a nonsteroidal anti-inflammatory drug (NSAID) that contains a carboxylic acid functional group (-COOH), which can act as a potential ligand for metal chelation. As shown in Figure 3, in the present work, the maximum absorbance was obtained at pH 4. This

was probably due to the fact that at low pH (acidic conditions), the carboxylic acid group in Piroxicam is more likely to be protonated, resulting in a negatively charged species. Fe(III) ions may have a higher affinity for the negatively charged ligand since the opposite charges can attract each other more strongly. Chelation can occur more readily at low pH due to the increased availability of negatively charged ligands.

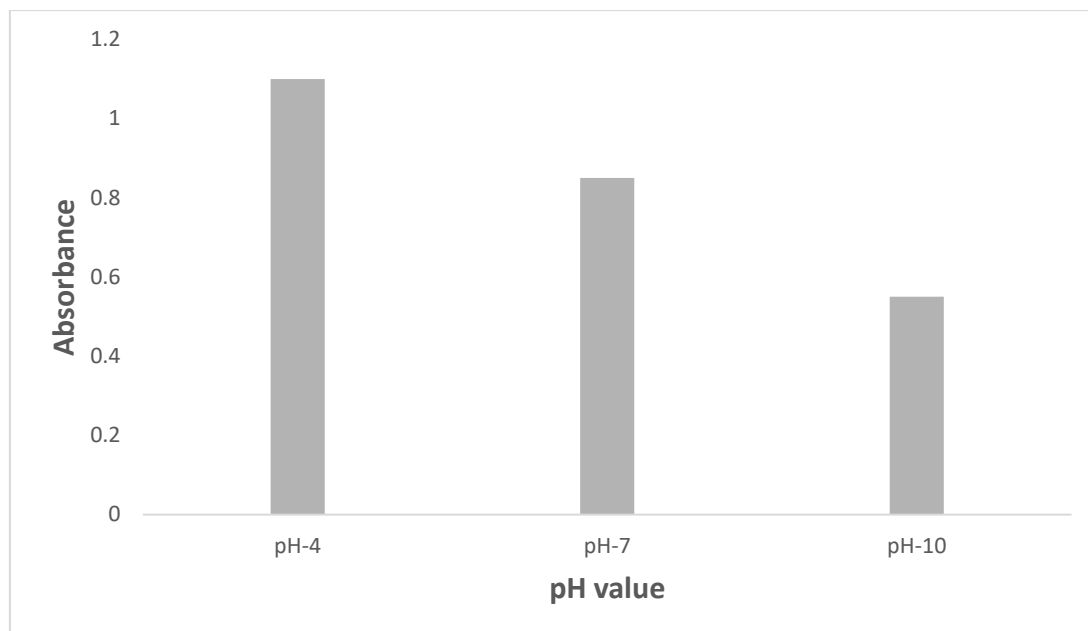


Figure 3: Effect of pH on Complexation of Piroxicam with Fe(III).

3.3. Effect of Concentration of Fe(III) Solution

The effect of the concentration of the iron(III) solution was checked by adding different volumes (1 to 10 mL) having concentrations 0.05 mM, 0.1 mM, 0.15 mM, 0.20 mM, 0.25 mM, 0.3 mM, 0.35 mM, 0.4 mM, 0.45 mM and 0.5 mM of ferric sulfate in a certain quantity of Piroxicam. As shown in Figure 4, the

absorbance reached a maximum when 4 mL of iron solution was added to 100 ppm of Piroxicam. Further addition of Fe(III) did not affect the final absorbance. Therefore, throughout this work, 5 mL of iron(III) solution was used to develop the red complex of Iron-Piroxicam.

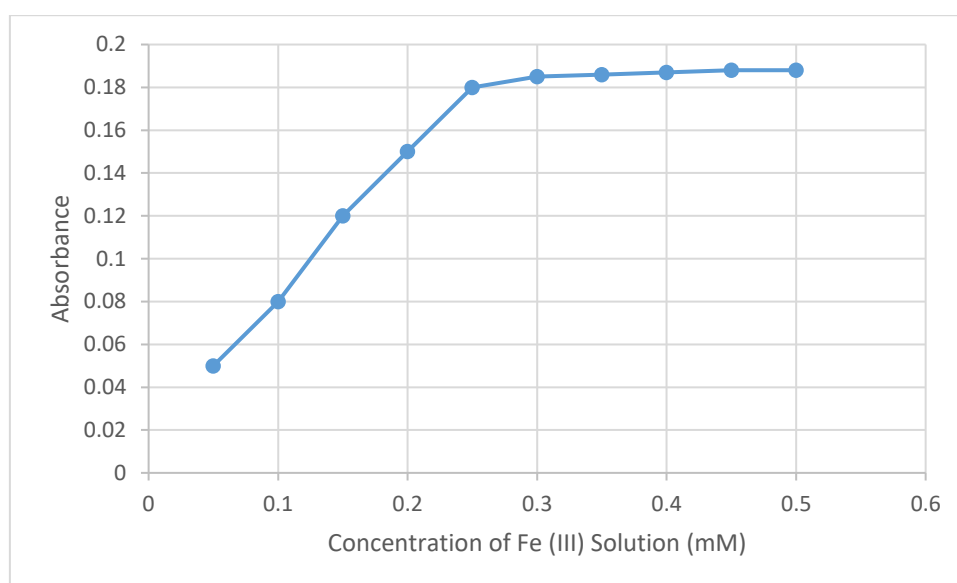


Figure 4: Effect of Concentration of Fe (III) Solution on Complexation.

3.4. Effect of Time and Temperature

The effect of temperature was checked by reacting the Piroxicam with iron(III) solution in the presence of pH-4 buffer and heating the contents at elevated temperature in a water bath before diluting with ethanol. It was observed that high temperature did not affect the final absorbance. Almost the same absorbance was monitored at 40 °C and 60 °C as was obtained at room temperature (25 °C). This reveals that the complexation between iron(III) and Piroxicam is completed at room temperature. The effect of time was checked by mixing the Piroxicam,

buffer, and Fe(III) solution in five different flasks and keeping them for various intervals of time before diluting with ethanol.

In all the flasks, the red color of the Piroxicam-iron (III) complex developed in the first five min, and then no change in absorbance was observed in the next hour. However, in this work, absorbance in all experiments was measured after 10 min of incubation with the reagents. The effect of time is shown in Figure 5.

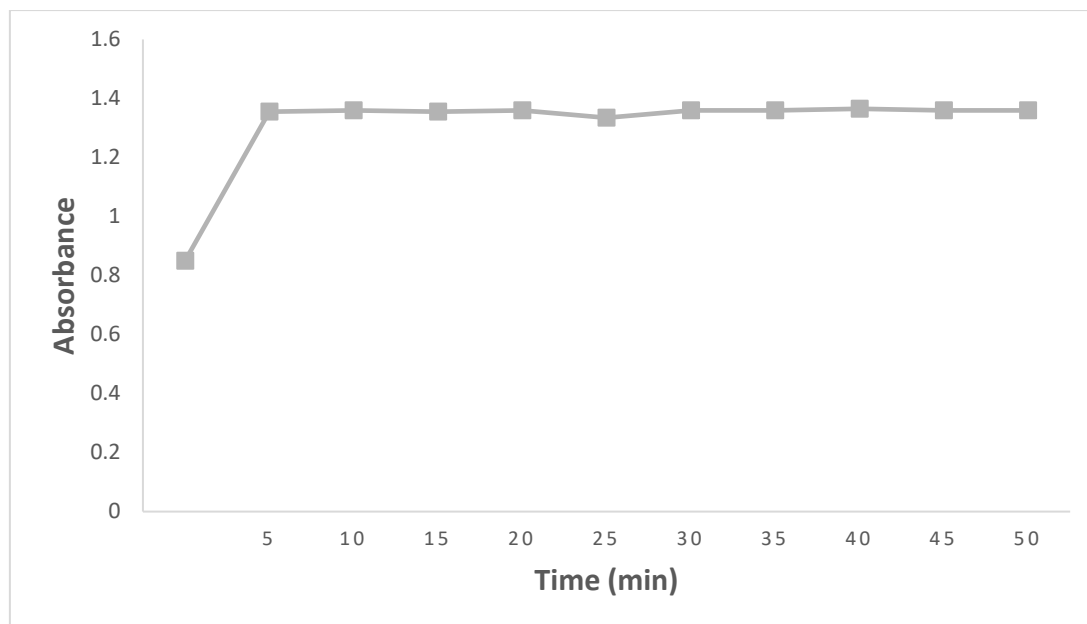


Figure 5: Effect of Time on Complexation of Piroxicam with Fe(III).

3.5. Effect of Order of Mixing the Reagents

This effect was checked by mixing Piroxicam, buffer, and Fe(III) solutions in different orders. Slightly better absorbance was observed when Piroxicam solution was taken first, and buffer was mixed with it. Lastly, an iron(III) solution was added to develop the red color of the complex. The slight enhancement

observed in absorbance in this order of mixing the reagents could be attributed to the fact that the addition of buffer may facilitate the protonation of Piroxicam prior to the addition of Fe(III) solution for complexation. The effect of the order of mixing the reagents is shown in Figure 6.



Figure 6: Effect of Order of Mixing the Reagents on Complexation.

3.6. Statistical Data

To validate the proposed method, ten samples of Piroxicam (50 ppm) were analyzed using the Image Scanning Densitometric method and the spectrophotometric method. The results obtained by both methods were used to calculate the analytical data, which are shown in Table 1. The analytical data show that in terms of accuracy and precision, the proposed method is almost comparable with the classical spectrophotometric method. In addition, the proposed method does not require a spectrophotometer and is thus free from instrumental errors.

3.7. Results of Commercial Formulations

The average results of Piroxicam content obtained by Image Scanning Densitometry and by Spectrophotometry with percentage errors are shown in Table 2. A close comparison has been found in the results obtained by both methods (Figure 7). Secondly, most of the results are close enough to the reported values given for the packing of various companies. Calibration curves with standard Piroxicam were plotted by both methods (Figures 8 and 9). The colored standard and sample solutions in the well plate are given in Figure 10.

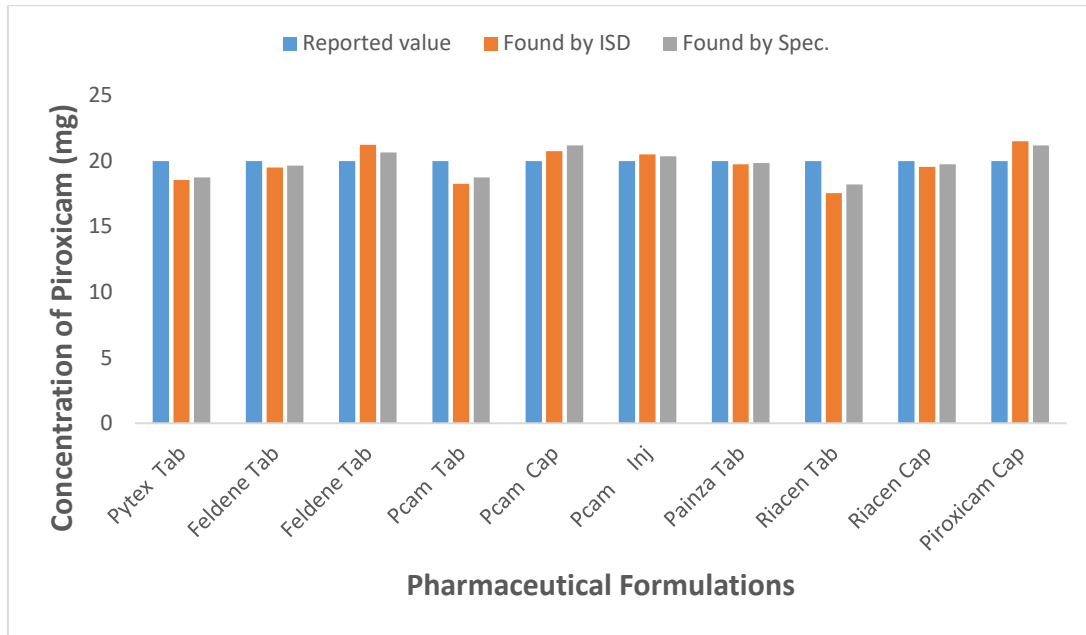


Figure 7: Piroxicam Quantities Reported and Found by ISD and Spectrophotometry.

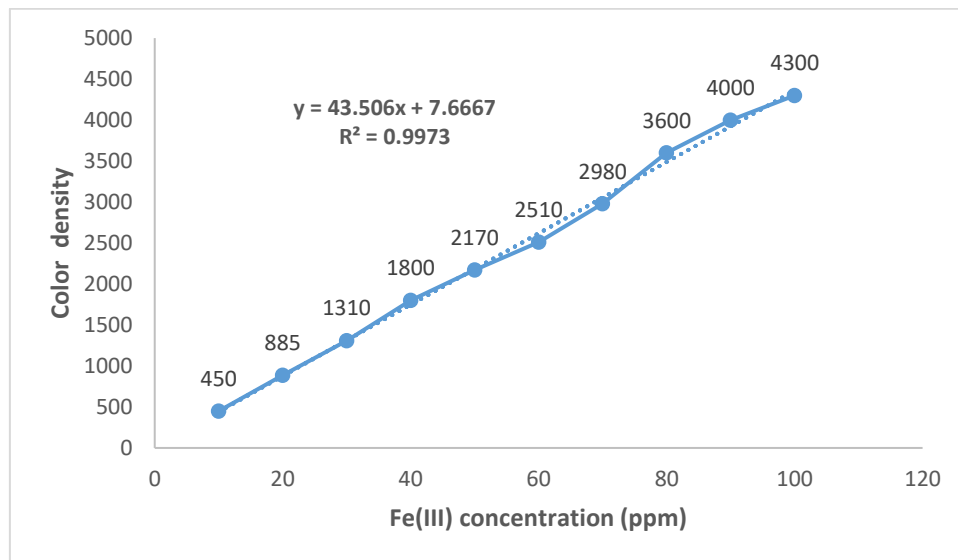


Figure 8: Calibration Curve for Piroxicam by image scanning densitometry.

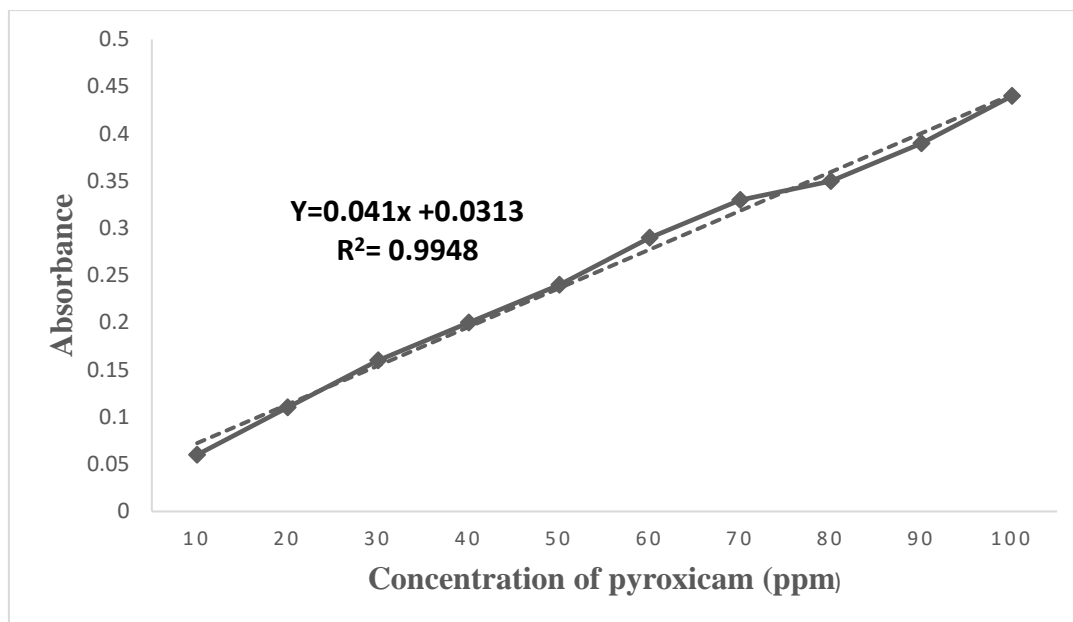


Figure 9: Calibration Curve for Piroxicam by Spectrophotometry.

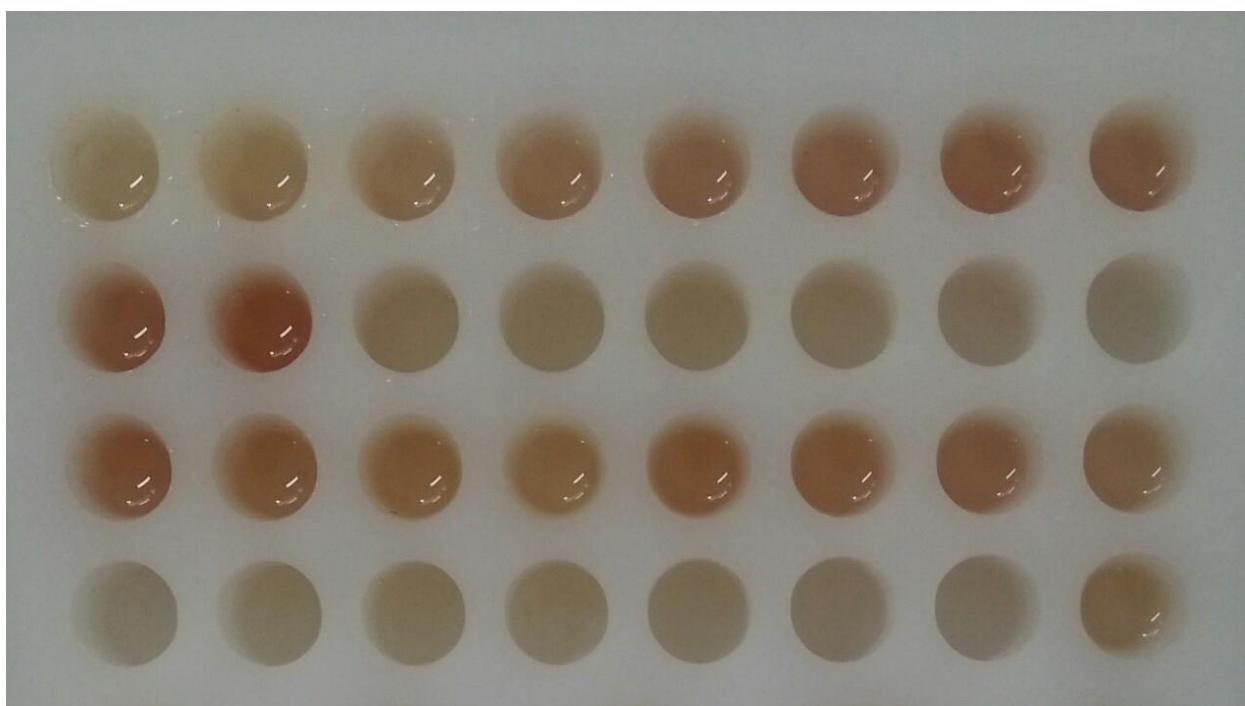


Figure 10: Standard and sample solutions in the Teflon well plate.

Interestingly, all the tablet formulations showed negative deviation from the reported value, whereas capsules and injection samples gave positive percentage error. This minute difference can be attributed to the presence of some fillers, which may

cause the extraction of the drug to not be 100% from the tablets. The analytical data given in Tables 1 and 2 showed the compatibility of the ISD method with the classical spectrophotometric method.

Table 1: Comparison of analytical data obtained by ISD and reference method.

No.	Parameter	Value Obtained by ISD method	Value Obtained by Ref. (Spec.) method
1.	Correlation Coefficient	0.9996	0.9952
2.	Standard Deviation	0.558	0.540
3.	Relative Standard Deviation	3.3644	3.3275
4.	Precision	3.28045	3.14582
5.	Accuracy	0.82684	0.80578

6.	LOD ($\mu\text{g/mL}$)	0.9570	0.9858
7.	LOQ ($\mu\text{g/mL}$)	2.9210	2.9578
8.	Confidence Level	1.865	1.758
9.	Multiple R	0.999468	0.995280
10.	R Square	0.9994	0.9948
11.	Adjusted R Square	0.996592	0.993680
12.	Standard Error	3.458210	3.584012
13.	Number of replicate samples	10	10

Table 2: Results of Commercial Formulations of Piroxicam by ISD and Reference Method.

No.	Commercial Formulation	Piroxicam Reported	Piroxicam found by ISD method (% error)	Piroxicam found by Spec. method (% error)
1.	Pytex Tablet	20 mg/tablet	18.55 (-7.25%)	18.75 (-6.25%)
2.	Feldene Tablet	20 mg/tablet	19.50 (-2.50%)	19.65 (-1.75%)
3.	Feldene Capsule # 323	20 mg/capsule	21.25 (+6.25%)	20.65 (+3.25%)
4.	Pcam Tablet	20 mg/tablet	18.25 (-8.75%)	18.75 (-6.25%)
5.	Pcam Capsule	20 mg/capsule	20.75 (+3.75%)	21.20 (+6.00%)
6.	Pcam Injection	20 mg/Injection	20.50 (+2.50%)	20.35 (+1.75%)
7.	Painza Tablet	20 mg/tablet	19.75 (-1.25%)	19.85 (-0.75%)
8.	Riacen Tablet	20 mg/tablet	17.55 (-12.25%)	18.20 (-9.00%)
9.	Riacen Capsule	20 mg/capsule	19.55 (-2.25%)	19.75 (-4.25%)
10.	Piroxicam Capsule	20 mg/capsule	21.50 (+7.50%)	21.20 (+6.00%)

4. CONCLUSION

Ten commercial formulations of various companies collected from the local market were analyzed for Piroxicam content by Image Scanning Densitometry (ISD) and by a reference spectrophotometric method. The statistical data and analytical results obtained by both methods, as shown in the Tables, revealed that ISD is a reliable and accurate method for the assay of drugs. In addition, this technique is fast, simple, cost-effective, and environment friendly and can be employed without any sophisticated spectrophotometer.

5. REFERENCES

- Xu S, Rouzer CA, Marnett LJ. Oxycams, a class of nonsteroidal anti-inflammatory drugs and beyond. IUBMB Life [Internet]. 2014 Dec 23;66(12):803–11. Available from: [<URL>](#).
- Shojaee SA, Rajaei H, Hezave AZ, Lashkarbolooki M, Esmailzadeh F. Experimental measurement and correlation for solubility of piroxicam (a non-steroidal anti-inflammatory drugs (NSAIDs)) in supercritical carbon dioxide. J Supercrit Fluids [Internet]. 2013 Aug 1;80:38–43. Available from: [<URL>](#).
- Wiseman EH, Cchang YH, Lombardino JG. Piroxicam, a novel anti-inflammatory agent. Chem Informationsd [Internet]. 1976 Oct 12;7(41):1300–3. Available from: [<URL>](#).
- Brogden RN, Heel RC, Speight TM, Avery GS. Piroxicam A reappraisal of its pharmacology and therapeutic efficacy. Drugs [Internet]. 1984 Oct 15;28(4):292–323. Available from: [<URL>](#).
- Laake K, Kjeldaas L, Borchgrevink CF. Side-effects of piroxicam (Feldene®). Acta Med Scand [Internet]. 1984 Jan 12;215(1):81–3. Available from: [<URL>](#).
- Azmi SNH, Iqbal B, Jaboob MAM, Al Shahari WAS, Rahman N. Spectrophotometric determination of piroxicam via chelation with Fe(III) in commercial dosage forms. J Chinese Chem Soc [Internet]. 2009 Dec 25;56(6):1083–91. Available from: [<URL>](#).
- Dragomiroiu ABGT, Cimpoiesu A, Ginghină O, Baloescu C, Bârcă M, Popa DE, et al. The development and validation of a rapid HPLC method for the determination of piroxicam. Farmacia [Internet]. 2015;63(1):123–31. Available from: [<URL>](#).
- Dikram SB, Mahmood RM. High performance liquid chromatographic method for the determination of Piroxicam, Naproxen, Diclofenac Sodium, and Mefenamic Acid in Bulk Drug and Pharmaceutical Preparations. Pure Appl Sci [Internet]. 2018;26(5):387–99. Available from: [<URL>](#).
- Dal AG, Oktayer Z, Doğrukol-Ak D. Validated method for the determination of Piroxicam by capillary zone electrophoresis and its application to tablets. J Anal Methods Chem [Internet]. 2014 Jan 1;2014(1):1–7. Available from: [<URL>](#).
- Rezaei B, Mallakpour S, Rahmanian O. A selective solid-phase extraction and preconcentration method with using molecularly imprinted polymer for Piroxicam in pharmaceutical sample. Anal Lett [Internet]. 2008 Jul 16;41(10):1818–31. Available from: [<URL>](#).
- Abed RI, Hadi H. Direct determination of piroxicam in pharmaceutical forms using flow injection-spectrophotometry. Bull Chem Soc Ethiop [Internet]. 2020 Apr 24;34(1):13–23. Available from: [<URL>](#).
- Ghobadpour G, Farjami F, Fasihi F. Sensitive electrochemical monitoring of Piroxicam in pharmaceuticals using carbon ionic liquid electrode. Curr Pharm Anal [Internet]. 2018 Nov 28;15(1):45–50. Available from: [<URL>](#).
- Rajendraprasad N, Basavaiah K. Potentiometric determination of piroxicam and oxfendazole in

- pharmaceuticals. *Curr Chem Lett* [Internet]. 2016;5(1):33–46. Available from: [<URL>](#).
14. Singh S, Patel JR, Kare S. Estimation of Piroxicam in tablet dosage form by using UV-Vis. spectrophotometer. *Asian J Res Chem* [Internet]. 2016;9(2):82–4. Available from: [<URL>](#).
15. Kormosh ZA, Hunka IP, Bazel YR. Spectrophotometric determination of piroxicam. *J Anal Chem* [Internet]. 2011 Apr 9;66(4):378–83. Available from: [<URL>](#).
16. El-Didamony AM, Amin AS. Adaptation of a color reaction for spectrophotometric determination of Diclofenac Sodium and Piroxicam in pure form and in pharmaceutical formulations. *Anal Lett* [Internet]. 2004 Dec 28;37(6):1151–62. Available from: [<URL>](#).
17. El-Ries MA, Mohamed G, Khalil S, El-Shall M. Spectrophotometric and potentiometric determination of Piroxicam and Tenoxicam in pharmaceutical preparations. *Chem Pharm Bull* [Internet]. 2003 Jan;51(1):6–10. Available from: [<URL>](#).
18. Amin AS. Spectrophotometric determination of piroxicam and tenoxicam in pharmaceutical formulations using alizarin. *J Pharm Biomed Anal* [Internet]. 2002 Jul 20;29(4):729–36. Available from: [<URL>](#).
19. Gowda BG, Seetharamappa J, Melwanki MB. Indirect spectrophotometric determination of Propranolol Hydrochloride and Piroxicam in pure and pharmaceutical formulations. *Anal Sci* [Internet]. 2002 Jun 19;18(6):671–4. Available from: [<URL>](#).
20. Hackmann ERM, dos Santos Gianotto EA, Santoro MIRM. Determination of Piroxicam in pharmaceutical preparations by ultraviolet direct spectrophotometry, ultraviolet difference spectrophotometry and high performance liquid chromatography. *Anal Lett* [Internet]. 1993 Feb;26(2):259–69. Available from: [<URL>](#).
21. Paciornik S, Yallouz A V., Campos RC, Gannerman D. Scanner image analysis in the quantification of mercury using spot-tests. *J Braz Chem Soc* [Internet]. 2006 Feb;17(1):156–61. Available from: [<URL>](#).
22. da Silva RS, Borges EM. Quantitative analysis using a flatbed scanner: Aspirin quantification in pharmaceutical tablets. *J Chem Educ* [Internet]. 2019 Jul 9;96(7):1519–26. Available from: [<URL>](#).
23. Islam MN, Ahmed I, Anik MI, Ferdous MS, Khan MS. Developing paper based diagnostic technique to detect uric acid in urine. *Front Chem* [Internet]. 2018 Oct 17;6:496. Available from: [<URL>](#).
24. Inderdeep Verma AS, Khushi Upadhyay M. Turbidity detection using image processing. *Int J Eng Sci Emerg Technol* [Internet]. 2021;10(6):154–60. Available from: [<URL>](#).
25. da Silva Lyra W, Castriani Sanches FA, Antônio da Silva Cunha F, Gonçalves Dias Diniz PH, Lemos SG, Cirino da Silva E, et al. Indirect determination of sodium diclofenac, sodium dipyrrone and calcium gluconate in injection drugs using digital image-based (webcam) flame emission spectrometric method. *Anal Methods* [Internet]. 2011;3(9):1975–80. Available from: [<URL>](#).
26. Uz-Zaman W, Rehman R, Zafar J. A novel approach to analyze total amino acids contents of food samples by computational image scanning densitometry. *Bulg Chem Commun* [Internet]. 2019;51(3):332–6. Available from: [<URL>](#).
27. Anwar J, Waheed-uz-Zaman, Shafique MU, Salman M. Computational Quantification of Spot Tests by Image Scanning-A New Analytical Technique for Micro Samples. *Anal Lett* [Internet]. 2010 Jan 12;43(2):367–71. Available from: [<URL>](#).
28. Uz-Zaman W, Anwar J, Rehman R, Iqbal T. Determination of iodide, iodate, dichromate, bismuth(III) and hydrogen peroxide through spot tests quantification by computational image scanning densitometry. *Asian J Chem* [Internet]. 2015;27(1):195–8. Available from: [<URL>](#).
29. Shafique U, Anwar J, Salman M, Waheed-uz-Zaman, Dar A, Rehman R, et al. Novel methods to determine sulfide in aqueous samples by quantification of lead sulfide spots. *J Sulfur Chem* [Internet]. 2011 Apr;32(2):151–7. Available from: [<URL>](#).
30. Dar A, Shafique U, Anwar J, Waheed-uz-Zaman, Naseer A. A simple spot test quantification method to determine formaldehyde in aqueous samples. *J Saudi Chem Soc* [Internet]. 2016 Sep;20:S352–6. Available from: [<URL>](#).
31. Salman M, Rehman R, Uz-Zaman W, Anwar J, Airam S, Rehman K. Microanalysis of mercury in fish and root vegetable samples by image scanning densitometry using computationally quantified spot tests. *Electron J Environ Agric Food Chem* [Internet]. 2012;11(4):279–85. Available from: [<URL>](#).
32. Salman M, Athar M, Waheed-uz-Zaman, Shafique U, Anwar J, Rehman R, et al. Micro-determination of arsenic in aqueous samples by image scanning and computational quantification. *Anal Methods* [Internet]. 2012;4(1):242–6. Available from: [<URL>](#).
33. Salman M, Shafique U, Zaman W uz, Rehman R, Yousaf A, Azhar F, et al. A rapid method for measurement of nickel and chromium at trace level in aqueous samples. *J Mex Chem Soc* [Internet]. 2011;55(4):214–7. Available from: [<URL>](#).



Synthesis, Biological Evaluation, and Molecular Docking Studies of New Nitro Vanillin Analogues as Anti-glycating Agents

Sajjad Anjum¹ , Priya Tufail² , Sajjad Haider² , Taibi Ben Hadda³ , Asad Ullah¹ , Sabira Begum¹ , Humera Jahan² , Zaheer Ul-Haq² , Bina Shaheen Siddiqui^{1*} 

¹H.E.J Research Institute of Chemistry, International Center for Chemical and Biological Sciences, University of Karachi, Karachi 75270, Pakistan.

²Dr. Panjawani Center for Molecular Medicine and Drug Development, International Center for Chemical and Biological Sciences, University of Karachi, Karachi 75270, Pakistan.

³Laboratoire de Chimie des Matériaux, Faculté des Sciences, Université Mohammed Premier, 60000 Oujda, Morocco.

Abstract: Persistent hyperglycemia is linked to a range of chronic complications in diabetes, such as neuropathy, retinopathy, nephropathy, and atherosclerosis. The underlying cause is the highly stable advanced glycation end products (AGEs) resulting from prolonged exposure to high glucose level. Hence the present study was undertaken on the anti-glycation activity of a series of synthetic analogues (Schiff bases) **4a-4o** of nitrovanillin synthesized by its coupling with different amino reagents. Nitrovanillin was obtained by the nitration of vanillin. Vanillin is a natural product that was obtained by the reduction of vanillic acid. Vanillic acid is another natural product which was isolated from ethanol extract of plant species *Tamarix aphylla* during the current study. These analogues were screened for *in-vitro* anti-glycation activity using rutin ($IC_{50} = 180 \pm 0.8 \mu M$) as a reference molecule. The best potent analogues **4a** ($IC_{50} = 121 \pm 1.0 \mu M$), **4f** ($IC_{50} = 95.0 \pm 0.7 \mu M$), and **4h** ($IC_{50} = 183 \pm 3.8 \mu M$) were subjected to computational study that revealed they were not only anti-glycation active, but also having well in ligand-protein interaction profile. While, all others analogues were found moderate to highly active. When the safety profile of these analogues **4a-4o** was evaluated by MTT assay using HepG2 cells against doxorubicin as a reference drug, the analogues **4a, 4e, 4f, 4i, 4l, 4m, and 4o** were found nontoxic, while analogues **4d, 4h, 4k, and 4n** showed insignificant toxicity.

Keywords: AGEs, Amadori product, anti-glycation, Column chromatography, Docking study, *Tamarix aphylla*.

Submitted: January 4, 2024. **Accepted:** June 3, 2024.

Cite this: Anjum S, Tufail P, Haider S, Ben Hadda T, Ullah A, Begum S, Jahan H, Ul-Haq Z, Siddiqui BS. Synthesis, Biological Evaluation, and Molecular Docking Studies of New Nitro Vanillin Analogues as Anti-glycating Agents. JOTCSA. 2024;11(3): 1255-66.

DOI: <https://doi.org/10.18596/jotcsa.1402128>

***Corresponding author's E-mail:** siddiqui_bina@yahoo.com

1 INTRODUCTION

Glycation is a non-enzymatic spontaneous process initiated when reducing sugars react with biological molecules such as amino acids, lipids, and nucleic acids. Glycation results in the formation of unstable Schiff bases when an excess amount of free blood sugars i.e., glucose, ribose, and fructose react with the free amino group proteins in the living system which then undergoes (1) several modifications through Amadori rearrangement and ends up with the generation of very stable advanced glycation end products (AGEs) (2, 3). In hyperglycemic conditions, excessive formation of AGEs causes various chronic

complications of diabetes mellitus (4), a very frequent heterogeneous disorder that affected almost 415 million people worldwide. The situation is so alarming that, by the end of 2040 the number will be increased to 642 million (5). Other diabetes-linked complications due to AGEs are tumor malignancy (6), nephropathy, neuropathy, retinopathy, atherosclerosis, and stroke (7). Certain structural distortions and malfunctions were also observed due to the glycation of blood albumins which trigger the formation of reactive oxygen species as well as prevent their scavenging capability for free radicals and create oxidative stress (8). The formation of AGEs is a normal process of body

metabolism (9) but an accelerated rate under hyperglycemia in tissues and circulation level promotes pathogenic complications and inflammatory response (10-12). Glycation of biological molecules in the living system not only involves AGEs generation but, dietary food items also act as a source of these species. They naturally exist in uncooked animal-derived foods and their contamination further increased during cooking at high temperatures to enhance flavor, color, and appearance. The fact that modern food items are the richest sources of AGEs is now well-documented since it was previously assumed that foods born AGE are poorly absorbed and their adverse health effects were ignored (13, 14). The destructive effects of AGEs paid great attention to the prevention of the formation of these species and the execution of these effects. The discovery of synthetic as well as natural anti-glycation agents with minimum side effects and high efficiencies such as flavonoid, phenol derivatives, imidazole, thiazolidine, and sulfonate were employed to control AGEs-linked complications (15). Although numerous anti-glycation agents have been developed in the past few years they have not gained attraction to prevent the process of glycation and manage the effects of AGEs such as aminoguanidine, which was not approved for clinical use due to toxicity and its adverse effects (16, 17). Similarly some safe drugs approved by FDA (USA) such as metformin, aspirin, diclofenac etc., but not so effective to prevent glycation during hyperglycemic conditions. However, some anti-glycating agents ie, ALT-711, benfotiamine, etc are under investigation for this aspect (18). Hence, there is a need to investigate safe and effective anti-glycation agents to treat glycation-associated disorders. Schiff bases have gained the overwhelming attraction of researchers due to their ubiquitous behavior in the field of medicine and pharmaceuticals due to anti-bacterial (19, 20) anti-tumor (21), anti-fungal (22), and anti-proliferative activities (23). Through our continuous effort to search the Schiff bases as anti-glycation agents, we reported the substituted synthesized benzenediol Schiff bases which were significantly active as AGEs inhibitors to cure diabetes-associated complications (24). With this motivation during the current study, a series of analogues **4a-4o** (Schiff bases) of nitro vanillin (Scheme-2) were synthesized and evaluated against the non-enzymatic glycation of protein using methylglyoxal-bovine serum albumin (MGO-BSA) glycation model. Their cytotoxicity evaluation was also conducted by employing an MTT assay using HepG2 (a human liver cancer cell line) cells. The analogues which showed the best anti-glycation activity were subjected to computational study to identify the possible binding sites of legend and protein targets by selecting the acarbose as a reference legend. Nitrovanillin was prepared by nitration (25) of vanillin **2** (Scheme-1): which was obtained by conversion of vanillic acid **1** (26) (Scheme-1). Vanillic acid was isolated during the present study from the ethanol extract of aerial parts of the plant *Tamarix aphylla*. The synthesis of these nitro vanillin derivatives, their *in-vitro* anti-glycation study, and molecular docking was conducted for the first time. The analogues reported in this

communication were new except **4a** (27) and showed significant anti-glycation effects without any cytotoxicity on the MTT assay.

2. EXPERIMENTAL SECTION

2.1. General Consideration

All analytical grade reagents were purchased from Sigma Aldrich USA *Jahan et., al.* Protocol (US9387198) (28) and were used to prepare AGEs. Phosphate buffer reagents were purchased from Duksan Pure Chemicals Co. Ltd. (NMR spectra at 400 MHz) and were recorded on a Bruker AM spectrometer in DMSO-*d*₆ with a residual peak of dimethyl sulfoxide ($\delta = 2.50$ ppm ¹H, 39.5 ppm, ¹³C). Chemical shifts were reported in parts per million (ppm) relative to TMS (δ). Coupling constants were recorded to the nearest 0.1 Hz. Signal multiplicity was reported as singlet (s), doublet (d), triplet (t) quartet (q), double doublet (dd), and multiplet (m). ¹³C spectra were recorded on an advanced Bruker 75 MHz spectrometer chemical shift recorded in parts per million (ppm). EI-MS spectra were recorded on MAT113D and MAT 312 mass spectrometers; Melting points were recorded on Buchi melting points-560 apparatus. The pre-coated silica gell-254 Merck Germany plates were used for thin-layer chromatography to monitor the reaction progress UV lights at 366 and 254 nm were used to visualize the spots. Normal phase column chromatography was conducted for the isolation of vanillic acid.

2.2. Isolation of Vanillic Acid 1

Chromatographic techniques were employed on silica gel to isolate the sufficient amount of compound **1** (vanillic acid) from aerial parts extract of plant species *Tamarix aphylla*. The compound **1** was then converted into nitro vanillin **4**. The nitro vanillin was used to synthesize the series of Schiff bases **4a-4o**.

2.3. General Procedure for Synthesis of Compounds 2-4

Compound **1**, 10 mmol was treated with an equal amount of DIBEL-H followed by cooling at -10 °C and stringing for 1 hour in THF to afford compound **2** with 93% yield (26) (scheme-1). The compound **2**, 8 mmol was, reflux, with anequal amount of MnO₂, in THF for 3 hour and compound **3** was obtained with 93% yield (26) (Scheme-1). Compound **3**, 7.2 mmol was refluxed with fuming HNO₃ at 60 °C for 1hour in MeCN and afforded compound **4** (nitro vanillin) with a 95% yield (25) (Scheme-1).

2.3.1. General procedure for synthesis of analogues 4a-4o

The analogues **4a-4o** is derivatives of compound **4**. Compound **4** was refluxed with different amino reagents in 10 mL anhydrous ethanol at 70-80 °C for 4-5 hours in the presence of the catalytic amount of glacial acetic acid followed by the reported protocol (29). Tabel-1 (Scheme-2). When each reaction was completed the precipitate appeared which was filtered, washed with distilled water, and recrystallized with ethanol. The percent yield of all analogues was calculated.

2.3.2. (E)-2-(4-Hydroxy-3-methoxy-5-nitrobenzylidene)hydrazine-1-carbothioamide (**4a**)

Yellow solid, yield 55%, m.p.: 179-180 °C, ¹H NMR (DMSO-*d*₆, 400 MHz): δ_H 10.95(s, 1H, OH), 7.86 (1H, brs, NH₂), 7.78 (1H, s, H-1'), 7.71 (1H, brs, NH₂), 7.39 (1H, d, *J* = 2.0 Hz, H-6), 7.07 (1H, d, *J* = 2.0 Hz, H-2), 3.89 (s, 3H, OCH₃). EI-MS *m/z* (% rel. abund.): 270 (M⁺), 253 (8), 236 (8), 194 (100), 177 (81), 164 (17), 121 (21), 104 (16), 90 (22), 59 (21), 44 (17). HREI-MS calcd for C₉H₁₀N₄O₄S: *m/z* = 270.0423 found 270.0427

2.3.3. (E)-2-(4-Hydroxy-3-methoxy-5-nitrobenzylidene) hydrazine-1-carboxamide (**4b**)

Yellow solid, yield 54 %, m.p.: 134-137 °C ¹H NMR (DMSO-*d*₆, 400 MHz): δ_H 7.76 (1H, s, H-1'), 7.67 (1H, s, H-2), 7.66.9 (1H, s, H-6), 7.50 (s, 1H, NH), 6.58 (s, 2H, NH₂), 23.92 (3H, s, OCH₃). ¹³C NMR (DMSO-*d*₆, 100 MHz): δ_C 159.7 (C), 150.5 (C), 144.2 (CH), 136.9 (C), 130.3 (C) 125.7 (C), 121.76 (C), 123.1 (CH), 111.2 (CH), 55.8 (CH₃). EI-MS *m/z* (% rel. abund.): 254 (M⁺, 85), 237 (19), 211 (11), 194 (100), 181 (22), 135 (83), 120 (30), 105 (10), 78 (12), 61 (52), 53 (18), 44 (7). HREI-MS calcd C₉H₁₀N₄O₅: *m/z* = 254.0651 found 254.0657

2.3.4. (2,4-Dinitrophenyl)hydrazineylidene)methyl)-2-methoxy-6-nitrophenol (**4c**)

Yellow powder, yield 55 %, m.p.: 185-188 °C, ¹H NMR (DMSO-*d*₆, 400 MHz): δ_H 8.87 (1H, d, *J* = 2.4 Hz, H-2), 8.50 (1H, s, H-1'), 8.35 (1H, dd, *J* = 9.0 and 2.0, Hz, H-5"), 8.10 (1H, d, *J* = 9.0 Hz, H-6"), 7.71 (1H, s, H-3"), 7.29 (1H, brs, H-6), 3.76 (3H, s, OCH₃). ¹³C NMR (DMSO-*d*₆, 100 MHz): δ_C 153.9 (C), 150.0 (C), 149.2 (C), 144.0 (C), 136.2 (C), 135.3 (C) 129.5 (C), 128.7 (CH), 123.1 (CH), 121.2 (CH), 116.7 (CH), 107.7 (CH), 106.7 (CH), 55.8 (CH₃). EI-MS *m/z* (% rel. abund.): 377 (M⁺, 100), 347 (14), 315 (14), 296 (8), 285 (5), 269 (9), 253 (4), 239 (4), 223 (4) 197 (35), 180 (19), 152 (14), 122 (12), 106 (6), 79 (11), 63 (13), 44 (10). HREI-MS calcd C₉H₁₀N₄O₅: *m/z* = 254.0651 found 254.0657

2.3.5. (E)-2-Methoxy-6-nitro-4-((2-phenylhydrazineylidene) methyl)phenol (**4d**)

Yellow solid, yield 55%, m.p.: 39-41 °C, ¹H NMR (DMSO-*d*₆, 400 MHz): δ_H 7.79 (1H, s, H-1'), 7.62 (1H, s, *J* = 2.0 Hz, H-2), 7.55 (d, 1H, *J* = 2.0 Hz, H-6), 7.22 (2H, t, *J* = 8.0 Hz, H-3"and H-5"), 7.07 (2H, d, *J* = 7.6 Hz, H-6"and, H-2"), 6.75 (1H, t, *J* = 7.2 Hz, H-4"), 3.93 (3H s, , OCH₃). ¹³C NMR (DMSO-*d*₆, 100 MHz): δ_C 149.7 (CH), 147.3 (C), 145.1 (C), 142.4 (C), 137.2 (C), 134.5 (C), 129.0 (CH) 126.8 (CH), 118.8 (CH), 115.0 (CH), 113.5 (CH). 112.0 (CH), 111.5 (CH), 56.5(CH₃), 121.2, 116.7, 107.6, 55.8; EI-MS EI-MS *m/z* (% rel. abund.): 287 (M⁺, 100), 252 (7), 238 (2), 225 (6), 209 (4), 184 (2), 169 (2), 143 (3), 133 (2) 107 (1), 92 (38), 77 (9), 65 (9), 50(2) HREI-MS calcd r C₉H₁₀N₄O₅: *m/z* = 254.0651 found 254.0657.

2.3.6. (E)-2-Methoxy-6-nitr(((4(trifluoromethyl)phenyl)imino)methyl)phenol (**4e**)

Yellow solid, yield 50%, m.p.: 90-93 °C, ¹H NMR (400 MHz, DMSO-*d*₆): δ_H 7.98 (1H, s, H-1'), 7.80 (2H, d, *J* = 8.2 Hz, H-5" and H-3), 7.69 (2H, d, *J* = 2.0

Hz, H-6 and H-2), 7.59 (2H, d, *J* = 8.0 Hz, H-6" and H-2"), 3.94 (3H, s, OCH₃). ¹³C NMR (DMSO-*d*₆, 100 MHz): δ_C 159.4 (C), 149.7 (C), 146.4 (C), 145.1 (C), 142.3 (C), 137.2 (C) 134.5 (CH), 129.0 (CH), 126.8 (CH). 118.8 (CH), 113.5(CH), 112.0 (CH), 111.5(CH), 56.5 (CH₃), EI-MS *m/z* (% rel. abund.): 340 (M⁺, 100), 321 (7), 310 (3), 293 (30), 279 (3), 264 (12), 251 (9), 248 (6), 235 (2) 222 (7), 202 (1), 196 (2), 172 (7), 153 (2), 145 (17), 125 (2), 107 (1), 95 (3), 79 (1), 75 (2), 63 (1), 53 (1), 51(1). HREI-MS calcd C₁₅H₁₁F₃N₂O₄: *m/z* = 340.0908 Found 340.0904.

2.3.7. (E)-2-Methoxy-6-nitro-4-(((2-(trifluoromethyl)phenyl) imino)methyl)phenol (**4f**)

Yellow solid, yield 55 %, m.p.: 103-106 °C, ¹H NMR (DMSO-*d*₆ 400 MHz): δ_H 8.64 (1H, s, H-1'), 8.08 (1H, s, H-2), 7.92 (1H, brs, H-6), 7.26 (1H, d, *J* = 6.0 Hz, H-3"), 7.11 (1H, t, *J* = 6.0 Hz, H-4"), 6.91 (1H, d, *J* = 6.0 Hz, H-6"), 6.85(1H, t, *J* = 6.0 Hz, H-5"), 3.98 (3H, s, OCH₃); ¹³C NMR (DMSO-*d*₆, 100 MHz): δ_C 160.2(CH), 157.3 (C), 155.0 (C), 150.2 (C),147.0 (C), 144.0 (C), 136.3 (C),135.3 (C), 129.5 (CH), 128.7 (CH), 123.1 (CH), 121.2 (CH), 116.7 (CH), 107.6 (CH), 55.8 (CH₃): EI-MS *m/z* (% rel. abund.): 340 (M⁺), 293 (1), 197 (100), 180 (53), 152 (7), 149 (20), 135 (24), 248 (6), 235 (2) 222 (7), 202 (1), 196 (2), 172 (7), 122 (9), 108 (3), 93 (3), 79,(14), 65 (11), 51 (10), 41 (1). HREI-MS calcd C₁₅H₁₁F₃ N₂O₄: *m/z* = 340.0671 Found 340.0677.

2.3.8. (E)-2-Methoxy-6-nitro-4-(((3-(trifluoromethyl)phenyl)imino)methyl)phenol (**4g**)

Yellow solid, yield 52%, m.p.: 91-94 °C, ¹H NMR (DMSO-*d*₆, 400 MHz): δ_H 8.68 (1H, s, H-1'), 8.08(2H, d, *J* = 2.0 Hz, H-6 and H-2), 7.68 (1H, t, *J* = 8.0 Hz, H-5"), 7.60(2H, d, *J* = 8.0 Hz, H-6"and, H-4"), 7.56 (1H, s, H-2"), 3.92 (3H, s, OCH₃). ¹³C NMR (DMSO-*d*₆, 100 MHz): δ_C 154.4 (CH), 151.7 (C), 150.4 (C), 144.0 (C), 140.8 (C), 136.2 (C) 135.3 (CH), 129.5 (C), 128.8 (C). 1124.8 (CH), 124.9 (CH), 123.1 (CH), 121.2(CH), 116.7 (CH), 56.5 (CH₃), EI-MS *m/z* (% rel. abund.): 340 (M⁺, 100), 321 (6), 293 (26), 264 (10), 251 (5), 222 (7), 200 (2), 172 (7), 145 (19), 95 (2), 75 (2), 51 (2). HREI-MS calcd for C₁₅H₁₁F₃N₂O₄: *m/z* = 340.0671 Found 340.0675.

2.3.7. (1E, 1'E)-Hydrazine-1,2-diylidenebis(methaneylylidene))bis(2-methoxy-6-nitrophenol) (**4h**)

Red solid, yield 56%, m.p.: 177-179 °C, ¹H NMR (DMSO-*d*₆, 400 MHz): δ_H 8.48 (2H, s, H-1', H-1") 7.79 (2H, s, H-2, H-2"), 7.35 (2H, s, H-6, H-6"), 3.80 (6H, s, OCH₃). ¹³C NMR (DMSO-*d*₆, 100 MHz): δ_C 190.1 (CH), 150.5(C), 149.2(C), 136.9 (C), 125.7 (C), 121.6 (CH), 111.7 (CH), 56.2(CH₃). EI-MS *m/z* (% rel.abund.): 390 (M⁺, 100), 373 (7), 360 (9), 312 (3), 295 (1), 267 (2), 239 (1), 225 (1), 222 (31) 196 (4), 17 (5), 176 (6), 164 (2), 149 (4), 135 (8), 106 (2.5), 92 (2), 78 (2), 53 (2), 44 (2). HREI-MS calcd for C₁₆H₁₄N₄O₈: *m/z* = 390.0812 Found 390.0818.

2.3.9. (E)-2-methoxy-6-nitro-4-((phenylimino) methyl) phenol (**4i**)

Yellow solid, yield 55%, m.p.: 42-45 °C, ¹H NMR (DMSO-*d*₆, 100 MHz.): δ_H 8.60 (1H, s, H-1'), 8.02

(1H, s, H-2), 7.75 (1H, s, H-6), 7.43 (2H, d, $J = 7.0$ Hz, H-1", H-6"), 7.30 (3H, t, $J = 8.0$ Hz, H-3", H-4" H-5"), 3.92 (3H, s, OCH₃). ¹³C NMR (DMSO-*d*₆, 400 MHz): δ_c 158.6 (CH), 149.7 (C), 145.1 (C), 142.0 (C), 133.6 (C), 129.0 (C), 125.3 (C), 118.8 (CH), 128.8 (CH), 113.5 (CH), 112.9 (CH), 111.7 (CH), 111.5 (CH), 111.2 (CH), 56.8 (CH₃), EI-MS *m/z* (% rel, abund): 272 (M⁺, 100), 242 (3), 196 (9), 183 (8), 154 (5), 127 (3), 77 (13), 51 (3). HREI-MS calcd for C₁₄H₁₂N₂O₄: *m/z* = 272.0797 Found 272.0793.

2.3.10. (E)-2-(4-Hydroxy-5-methoxy-3-nitrobenzylideneamino)benzoic acid (**4j**)

White solid, yield 51 %, mp.: 175-178 °C, ¹HNMR (DMSO-*d*₆, 400 MHz): δ_H 8.69 (1H, s, H-1'), 8.08 (2H, d, $J = 1.2$ Hz, H-2 and H-6), 7.83 (1H, t, $J = 6.0$ Hz, H-5"), 7.15 (1H, brs, H-2"), 7.11 (1H, m, H-4"), 6.76 (1H, dd, $J = 8.0, 2.0$ Hz, H-6") 3.92 (3H, s, OCH₃). ¹³C NMR (DMSO-*d*₆, 100 MHz): δ_c 163.45 (CH), 160.1 (CH), 149.7 (C), 145.1 (C), 142.4 (C), 137.2 (C), 134.5 (C), 129.0 (C), 126.8 (C), 123.4 (CH), 118.8 (CH), 113.5 (CH), 112.0 (CH), 111.5 (CH), 56.5 (CH₃), EI-MS *m/z* (% rel. abund.): 316 (M⁺, 100), 286 (74), 242 (5), 225 (8), 197 (18), 167 (8), 111 (11), 97 (21), 92 (40), 77 (14), 69 (19), 44 (37). HREI-MS calcd C₁₅H₁₂N₂O₆: *m/z* = 316.0695. Found 316.0692.

2.3.11. (E)-4-(((2-Hydroxyphenyl)imino)methyl)-2-methoxy-6-nitrophenol (**4k**)

White solid, yield 54%, m.p.: 173-176 °C, ¹HNMR (DMSO-*d*₆, 400 MHz): δ_H 8.79 (1H, s, H-1'), 8.23 (1H, s, H-2), 8.13 (1H, s, H-6), 7.42 (1H, d, $J = 6.0$ Hz, H-6"), 7.25 (1H, t, $J = 7.5$ Hz, H-4"), 7.07 (1H, d, $J = 8.0$ Hz, H-6"), 7.02 (1H, t, $J = 6.0$ Hz, H-5"), 4.09 (3H, s, OCH₃). ¹³C NMR (DMSO-*d*₆, 100 MHz): δ_c 159.2 (CH), 154.5 (C), 150.0 (C), 144.0 (C), 140.5 (C), 136.2 (C), 135.3 (C), 129.5 (CH), 128.7 (CH), 123.1 (CH), 121.28 (CH), 116.7 (CH), 107.6.0 (CH), 55.8 (CH₃), EI-MS *m/z* (% rel. abund.): 288 (M⁺, 100) 241 (12), 225 (5), 212 (3), 195 (2), 169 (2), 154 (1), 144 (2), 127 (1), 93 (3), 85 (1), 65 (5), 43 (1). HREI-MS calcd C₁₄H₁₂N₂O₅: *m/z* = 288.0746 Found: 288.0740.

2.3.12. (E)-2-Methoxy-4-(((5-(methylthio)-2-(trifluoromethyl)phenyl)imino)methyl)-6-nitrophenol (**4l**)

White solid, yield 51%, m.p.: 139-14 °C, ¹HNMR (DMSO-*d*₆, 400 MHz): δ_H 8.75 (1H, s, H-1'), 8.20 (2H, d, $J = 2.0$ Hz, H-2 and H-6), 7.87 (1H, s, H-6"), 7.71 (2H, d, $J = 8.0$ Hz, H-4" and H-3"), 4.07 (s, 3H, OCH₃), 3.98 (s, 3H, SCH₃). ¹³C NMR (DMSO-*d*₆, 100 MHz): δ_c 159.2 (CH), 154.5.1 (C), 150.0 (C), 144.0 (C), 140.5 (C), 136.2 (C), 135.3 (C), 129.5 (C), 128.7 (C), 123.1 (C), 121.2 (CH), 116.7 (CH), 107.6 (CH), 111.5 (CH), 55.8 (CH₃), 14.6 (CH₃). EI-MS *m/z* (% rel. abund.): 386 (M⁺ 100) 371 (17), 353 (52), 307 (13), 290 (1), 278.2 (2), 25 (1), 222 (1), 218 (9), 185 (2), 157 (2) 133 (1), 63 (1). HREI-MS calcd C₁₆H₁₃ F₃N₂O₄S: *m/z* = 386.0548 Found 386.0542.

2.3.13. (E)-4-Hydroxy-3-methoxy-5-nitrobenzaldehyde oxime (**4m**)

White powder, yield 55%, m.p.: 102-104 °C, ¹HNMR (DMSO-*d*₆, 400 MHz): δ_H 8.13 (1H, s, H-1'), 7.66 (d,

1H, $J = 2.0$ Hz, H-2), 7.45 (d, 1H, $J = 2.0$ Hz, H-6), 3.88 (s, 3H, OCH₃). ¹³C NMR (DMSO-*d*₆, 100 MHz): δ_c 149.6 (CH), 146.5 (C), 143.4 (C), 136.9 (C), 123.7 (C), 114.8 (CH), 112.0 (CH), 56.4 (CH₃). EI-MS *m/z* (% rel, abund): 212 (M⁺, 100), 195 (22), 177 (6), 152 (6), 139 (11), 108 (7), 96 (4), 77 (7), 63 (4), 53 (8). HREI-MS calcd for C₈H₈N₂O₅: *m/z* = 212.0433 Found 212.0437

2.3.14. (E)-4-(((3,4-Dichlorophenyl)imino)methyl)-2-methoxy-6-nitrophenol (**4n**)

White powder, yield 55%, m.p.: 102-104 °C, ¹HNMR (DMSO-*d*₆, 400 MHz): δ_H 8.13 (1H, s, H-1'), 7.66 (d, 1H, $J = 2.0$ Hz, H-2), 7.45 (d, 1H, $J = 2.0$ Hz, H-6), 3.88 (s, 3H, OCH₃). ¹³C NMR (DMSO-*d*₆, 100 MHz): δ_c 149.6 (CH), 146.5 (C), 143.4 (C), 136.9 (C), 123.7 (C), 114.8 (CH), 112.0 (CH), 56.4 (CH₃). EI-MS *m/z* (% rel, abund): 212 (M⁺, 100) 195 (22), 177 (6), 152 (6), 139 (11), 108 (7), 96 (4), 77 (7), 63 (4), 53 (8). EI-MS *m/z* (% rel. abund.): 240 (M⁺, 100), 242 (M⁺, 64), 244 (M⁺, 11), 323 (4), 310 (15), 293 (17), 280 (3), 268 (6), 266 (5), 251 (5), 222 (2), 187 (3), 172 (4), 145 (7), 109 (4), 79 (1), 63 (1), 51 (1), HREI-MS calcd C₁₄H₁₀ Cl₂N₂O₄: *m/z* = 340.0018 Found 340.0012.

2.3.15. (E)-2-Hydroxy-5-((4-hydroxy-3-methoxy-5-nitrobenzylidene)amino) acid (**4o**)

White solid: yield: 54%, m.p.: 196-199 °C, ¹HNMR (DMSO-*d*₆, 400 MHz): δ_H 8.67 (1H, s, H-1'), 8.08 (2H, d, $J = 2.0$ Hz, H-2 and H-6), 7.77 (1H, d, $J = 6.0$ Hz, H-6"), 7.56 (1H, d, $J = 6.0$ Hz, H-5"), 6.92 (1H, d, $J = 8.0$ Hz, H-6"), 7.18 (1H, brs, H-2") 3.90 (3H, s, OCH₃). ¹³C NMR (DMSO-*d*₆, 100 MHz): δ_c 160.1 (CH), 154.5 (C), 152.6 (C), 150.0 (C), 144.0 (C), 136.2 (C), 135.3 (C), 129.5 (C), 128.7 (CH), 123.1 (CH), 121.2 (CH), 116.7 (CH), 107.6 (CH), 56.4 (CH₃). ¹³C NMR (DMSO-*d*₆, 100 MHz): δ_c 168.5 (C), 160.1 (CH), 149.7 (C), 145.1 (C), 142.4 (C), 137.2 (C), 134.5 (C), 129.0 (C), 126.8 (CH), 123.4 (CH), 118.8 (CH), 116.7 (CH), 113.5 (CH), 112.0 (CH), 111.5 (CH) 56.5 (CH₃). EI-MS *m/z* (% rel. abund.): 332 (M⁺, 36), 288 (100), 258 (57), 241 (16), 197 (10), 153 (7), 135 (12), 109 (18), 93 (7), 79 (10), 65 (10), 53 (7). HREI-MS calcd C₁₅H₁₂N₂O₇: *m/z* = 332.0645 Found 332.0649.

2.4. Anti-glycation Study

2.4.1. Assay for anti-glycation study

The AGES were prepared according to the optimized protocol (US9387198) (27) briefly, disodium hydrogen phosphate (Na₂HPO₄) and sodium dihydrogen phosphate (NaH₂PO₄) (Duksan Pure Chemicals Co. Ltd.) were used to prepare a 100 mM phosphate buffer solution. Bovine serum albumin (BSA= 10 mg/mL) (Sigma Aldrich) and methylglyoxal (MGO 500 mM) (Thermo Fisher Scientific) were mixed with azide buffer (0.1 mM). All the working dilutions were prepared using deionized water. All the compounds were dissolved in dimethyl sulfoxide (DMSO) (Amresco LLC). The assay was performed in a flat-bottom 96-well black fluorescence plate (Corning Inc.). Initially, the nitro vanillin analogues were evaluated at 1mM concentration. Each compound was tested in triplicates. Rutin hydrate (1 mM) (Sigma Aldrich) was used as a reference glycation agent. BSA mixed with

sodium phosphate buffer was used as a negative control. The reaction plate was kept at 37 °C for 24 hours for incubation. The anti-glycation potential of all analogues was analyzed by measuring AGEs specific fluorescence (355 nm excitation and 460 nm emission) against blank by using Varioskan Lux microtitre plate reader (Thermo Fisher Scientific). Percent (%) inhibition of AGEs was calculated by using the formula given below

$$\text{Inhibition of fluorescence \%} = (1 - \text{Fluorescence of test derivative} / \text{Fluorescence of glycated BSA}) \times 100$$

The compounds exhibiting anti-glycation potential at 1 mM (> 50% inhibition) were further diluted 2 fold and their IC₅₀ values were determined by using the EZ-FIT Enzyme Kinetics protocol (Perrella Scientific Inc).

2.4.2. Cytotoxicity assay

HepG2 a human liver cancer cell line was purchased from ATCC (USA) and maintained in a sterile environment. Initially, the cells were cultivated in a 25 cm² cell-culture flask (Nest Co.Ltd.). The cell culture medium was prepared with Dulbecco's Modified Eagle Medium-high glucose (DMEM), fetal bovine serum (FBS), sodium pyruvate, sodium bicarbonate, and L-Glutamine (Gibco). The cells were kept in an incubator at 37 °C providing 5% CO₂ until they become 80% confluent. Later, the cells were trypsinized using 1X trypsin-EDTA (0.25%) and viability was determined using trypan blue. HepG2, 8x10⁴ cells / mL, were seeded in a 96-well flat-bottom sterile cell culture plate and incubated at 37 °C for 24 hours for adherent. The cells were treated with the analogues at 50 μM concentration in triplicates for 24 hours. The medium was aspirated and 100 μL MTT dye (5 mg/mL) was added to the cells. After 3 hours, the dye was removed, and 10% DMSO was added to each well to dissolve the formazan crystals. Colorimetric analysis was performed at 570 nm, using a spectrophotometer (Varioskan micro plate reader Thermo Fisher). The toxic effect of analogues on cell viability was measured by the formula given below.

$$\text{Inhibition \%} = 100 - [(\text{Absorbance of test Compound} - \text{Absorbance of blank}) / (\text{Absorbance of control} - \text{Absorbance of blank})]$$

2.4.3. Structure activity relationship of analogues 4a-4o

A series of nitro vanillin analogues **4a-4o** were prepared and tested for anti-glycation assay. All analogues have a common parent methoxy nitro phenol ring and variable region. The analogues were classified into three categories based on the basis of presences of different functional groups in the variable region for the study of the structure-activity relationship. Category "A" included analogues **4a** and **4b**, which bear the carbamide functional group, category "B" include analogues **4c** and **4d** which bear the hydrazinylidene functional group, and category "C" **4e-4o** included imino functional group other than the parent ring in their structure as shown in Table.1 The compounds exhibited excellent to moderate anti-

glycation potential against the *in-vitro* MGO-modified BSA model. The IC₅₀ values were found in the range of 95 to 465 μM. Rutin was used as standard which showed 62% inhibition in MGO-BSA glycation assay with IC₅₀ = 180±0.8 μM). Nitro vanillin analogues showed weak (glycation inhibition percentage < 50%), moderate (glycation inhibition percentage >50% and <70%), good (glycation inhibition percentage >70%), and excellent (glycation inhibition percentage >80%) anti-glycation activity. Analogue **4a** (81.83% inhibition, IC₅₀ = 121±1.0 μM) showed excellent anti-glycation activity compared to the reference rutin (62% inhibition, IC₅₀ = 180±0.8 μM). Rutin is a flavonoid, known for inhibiting early steps in the glycation process and hence modulates the formation of AGEs. The activity of analogue **4a** may be attributed to hydrazine thiocarbamide moiety in its structure. Analogue **4b** (48.33% inhibition) is structurally similar to analogue **4a** but it contains hydrazine carboxamide moiety and showed poor anti-glycation activity less than 50% inhibition compared to rutin and considered inactive. From the results, it is inferred that the replacement of thiocarbamide with carbamide moiety caused a compound inactive.

The analogues **4c** and **4d** contain phenyl hydrazine group and exhibited poor to good anti-glycation activity. analogue **4c** (44.31% inhibition) bears two nitro groups at *ortho* and *para* positions of phenyl hydrazinylidene ring in its structure resulting in less than 50 % inhibition and ranked as anti-glycation in active. The presence of the unsubstituted phenylhydrazinylidene group in analogue **4d** (69.71% inhibition, IC₅₀ = 220±0.15 μM), showed good anti-glycation activity. The comparison between these two analogues reveals that either presence of two nitro groups at *ortho* or *para* position compromise analogue **4c** inactive or the presence of an un-substituted phenyl hydrazine ring boosts up the potency of analogue **4d** against the glycation process. The analogues **4a-4o** bears phenyl imino moieties with substituted or unsubstituted phenyl amino ring in their structures and showed variation in activity from compound to compound. Thus, the presence of the tri-fluoromethane group at different positions of the phenylamino ring in some of these analogues revealed excellent to weak anti-glycation activity. The presence of this group at the *para* position resulted in moderate activity in analogue **4e** (80.82% inhibition, IC₅₀ = 336±2.9 μM), but the presence of this group at the *ortho* position in analogue **4f** (79.62% inhibition, IC₅₀ = 95.0 ± 0.7 μM) boosts up the activity and so that it behaves as a strongest anti-glycation candidate than all the synthetic analogues of series as it exhibited excellent anti-glycation activity.

On the other hand, the presence of the tri-fluoro methane group at the *meta* position of the phenylamino ring turns down the activity of analogue **4g** (45.30% inhibition) towards the weakest candidate so that, it showed less than 50% inhibition and stands as an inactive anti-glycating agent. Analogue **4h** (74.24% inhibition, IC₅₀ = 183±3.8 μM), a dimer of the parent compound showed

excellent anti-glycation activity comparable with that of rutin. The anti-glycation activity of this compound may be attributed to the presence of either a dimethylidene hydrazine group or two aromatic rings. Analogue **4i** (56.92% inhibition, $IC_{50} = 331 \pm 1.1 \mu M$) is without substitution on its phenylimino ring and showed moderate anti-glycation activity. Its activity could be compared with analogue **4j** and **4k**. Analogue **4i** is more active than analogue **4j** (42.10% inhibition) which showed less than 50% inhibition and which bears the acidic group at the *meta* position of its phenyl imino ring in its structure and is biologically inactive while analogue **4i** is less active than analogue **4k** (59.89 % inhibition, $IC_{50} = 237.0 \pm 2.2 \mu M$) which bears hydroxy group at the *ortho* position of phenylimino ring and showed moderate anti-glycation activity compared to standard rutin. These results indicated that the presence of a hydroxy group at the *ortho* position of the phenylimino ring enhances the activity while the presence of an acidic group at the *meta* position causes the analogue to be inactive. Analogue **4l** (70.64% inhibition, $IC_{50} = 187 \pm 0.6 \mu M$) bears a trifluoro methane group at the *ortho* position and thiomethane group at the *meta* position of phenylamino ring, when the activity of this analogue is compared with the activity of the analogue **4f**, which has only a trifluoromethane group at *ortho* position and which is a most potent compound of series, it is observed that presence of thiomethane group at *meta* position reduces the activity of analogue **4l** however its activity is still greater than analogue **9** which have tri-fluoro methane group at the *para* position and analogue **4g** which have trifluoro methane group at *meta* position respectively.

These results also revealed that the presence of thiomethane at the *meta* position along with trifluoromethane at the *ortho* position of the phenyl imino ring reduces the anti-glycation activity. The analogue **4m** (61.16% inhibition and $IC_{50} = 361 \pm 10.0 \mu M$) bears an oxime moiety and exhibited moderate anti-glycation activity compared to rutin. This analogue differs from other members of the series as it bears only the parent phenyl ring that is common to all analogs, so its activity cannot be compared with any other analogue in the series. The analogue **4n** (71.18% inhibition $IC_{50} = 214 \pm 2.4 \mu M$), bears two chlorine groups at *meta* and *para* positions of the phenylimino ring and showed good anti-glycation activity. The activity of this analogue is compared to the activity of analogue **4o** (55.64% inhibition, $IC_{50} = 245 \pm 2.4 \mu M$) which bears a hydroxy group at *meta* and acidic group at *para* positions and also showed good anti-glycation activity compared to rutin but less active than analogue **4n**. These results indicated that the substitution of phenyl imino ring at *ortho* and *meta* positions with chlorine groups enhances the activity while activity decreases when these positions are substituted with an acidic group at *ortho* and a hydroxy group at the *meta* position. The results are shown in Table 1. The safety profile of the analogue was evaluated by MTT assay using HepG2 cells. The analogue found with weak anti-glycation activity was not assessed for cytotoxicity. Analogue **4a**, **4e**, **4f**, **4i**, **4l**, **4m**, and **4o** were found nontoxic at 50 μM concentration when compared to the standard drug, doxorubicin, whereas analogue **4d**, **4h**, **4k**, and **4n** were fairly toxic as compared to standard doxorubicin at 50 μM . The results are shown in Table 1.

Table 1: *In-vitro* anti-glycation study and cytotoxicity evaluation of nitro vanillin analogues **4a-4o**.

Analogues	Anti-glycation Inhibition %	Anti-glycation IC_{50} ($\mu M \pm SEM$)	Cytotoxic Inhibition % 50 μM
4a	81.83	121 \pm 1.0	16.49
4b	NA	NA	NA
4c	NA	NA	NA
4d	69.71	220 \pm 1.5	47.88
4e	82.82	336 \pm 2.9	21.13
4f	79.62	95 \pm 0.7	0.10
4g	NA	NA	NA
4h	74.24	183 \pm 3.8	57.32
4i	56.92	331 \pm 1.1	2.39
4j	NA	NA	NA
4k	59.89	237 \pm 2.2	46.67
4l	70.64	187 \pm 0.6	16.8
4m	61.16	361 \pm 1.0	7.34
4n	71.18	214 \pm 2.4	32.32
4o	55.64	245 \pm 2.4	0.20
Doxorubicin	62.23	180 \pm 0.8	
Rutin			45.98 \pm 2.42

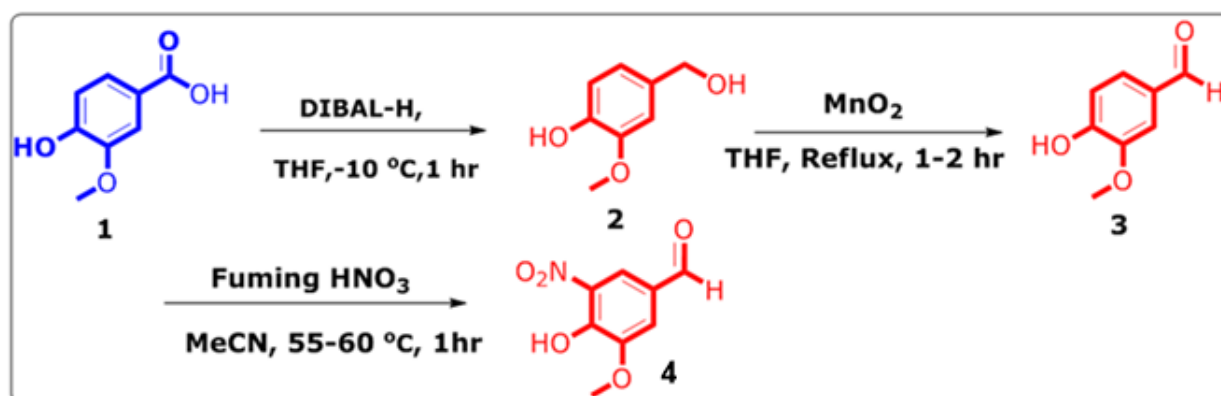
NA = INACTIVE

3. RESULTS AND DISCUSSION

3.1. Chemistry

The primary approach in our study was rested to select the smaller non-toxic, and biological active nucleus so that its new activity is investigated by the preparation of its synthetic analogues. Since natural products are less or non toxic and possess several biological activities so our study rounds about natural products. To fulfill our approach, we conducted column chromatography on the methanolic extract of aerial parts of the plant species *Tamarix aphylla* and isolated a non-toxic natural product vanillic acid **1** which is ubiquitous in several biological activities. To make this molecule more versatile it was

transformed *via* three steps reactions into an aldehyde motif nitro vanillin. The first step of transformation was a reduction of vanillic acid **1** into alcoholic moiety **2** which by oxidation in the second step converted into vanillin **3**. Vanillin **3** bears the aldehyde functional group susceptible to amino moiety for hydrazone synthesis. Since its *para* position is covered by the methoxy group which due to the positive mesomeric effect pretends the carbonyl group towards less susceptible to incoming moiety and yield was not so good. To enhance the yield vanillin was subjected to nitration and converted into nitro vanillin compound **4** (Scheme-1).



Scheme 1: Conversion of vanillic acid **1** into nitro vanillin **4**.

Compound **4** was utilized as an intermediate for the generation of a series of Schiff bases **4a-4o**, with excellent yield, Table-2 (Scheme-2). Our second approach was to evaluate the anti-glycation activity and bio-safety and establish the structure-activity relationship of these analogues (Table-1). Our third approach was a molecular docking study of the most potent analogues (Figure-2) and (Figure-3).

3.2. Structure Elucidation of Most Active Analog **4f**

3.2.1. ^1H and ^{13}C -NMR of analog **4f**

The ^1H NMR of most potent analogue **4f** was recorded on a Bruker AM (DMSO- d_6 , 400 MHz). In the spectrum of this compound the most down field signal was the signal of proton H-1' resonating at δ 8.64 as a singlet. The proton H-2 resonated as a singlet at δ 8.08 was the second down filed proton.

Then there was a singlet signal of proton H-6 resonated at δ 7.29 Proton H-3'' showed up as a doublet at δ 7.26 with a coupling constant ($J = 6.0$ Hz). Furthermore, there was a triplet of proton H-4'' resonating at δ 7.33. A doublet signal of proton H-6'' appeared at δ 6.91 ($J = 6.0$ Hz). The proton H-5'' resonated at δ 6.85 as triplet. The most up field signal was the signal of methoxy protons resonating as a singlet at δ 3.98.

^{13}C -NMR spectrum of the analog **4f** showed signals including seven quaternary signals resonating at δ_c 157.3, 155.0, 150.2, 147.0, 144.0, 136.3 and 135.3, while seven methene carbons were resonating at δ_c 160.2, 129.5 128.7, 123.1, 121.2, 116.7 and 107.6. A most upfield methyl carbon signal appeared at δ_c 55.8. This profile confirms the expected structure of analogue **4f** Figure-1.

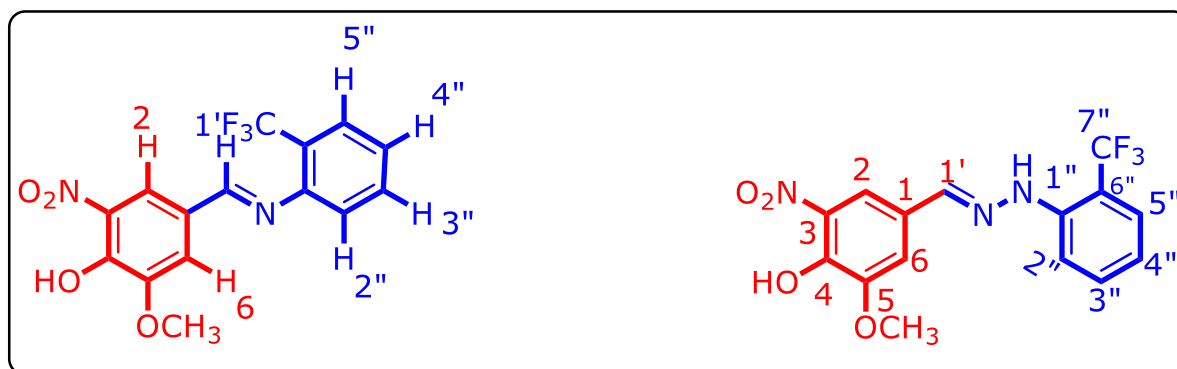


Figure 1: ^1H and ^{13}C -NMR of analogue **4f**.

Table 2: Synthesized nitro vanillin analogues **4a-4o**.

Entry	R	Analogues	Entry	R	Analogues
Category "A"					
1		4a	2		4b
Category "B"					
3		4c	4		4d
Category "C"					
5		4e	11		4k
6		4f	12		4l
7		4g	13		4m
8		4h	14		4n
9		4i	15		4o
10		4j			

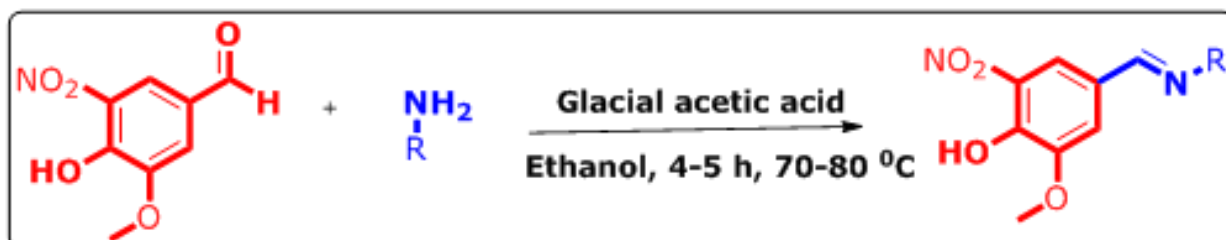
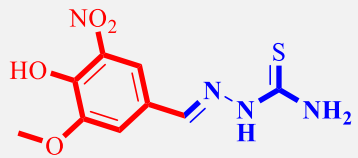
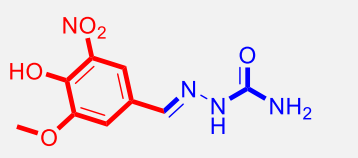
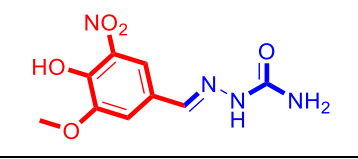
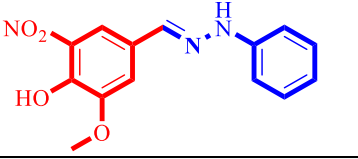
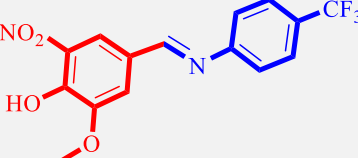
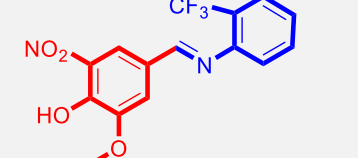
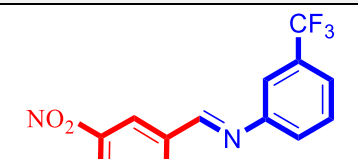
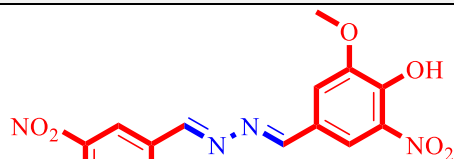
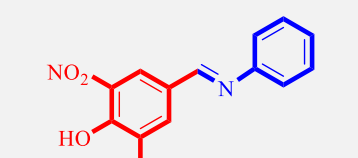
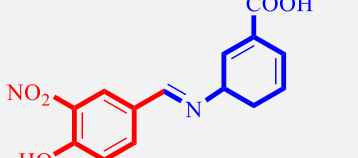
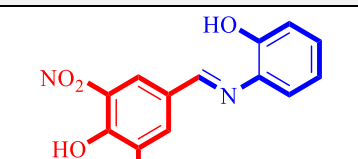
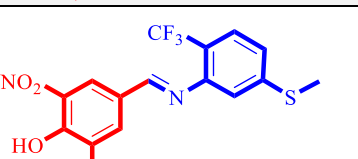
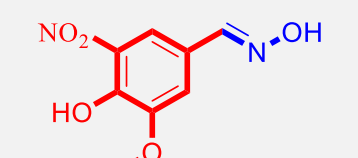
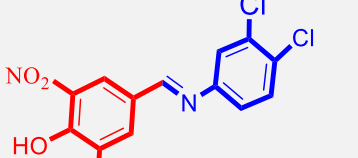
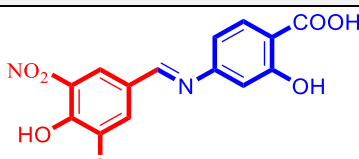
**Scheme 2:** Synthetic analogues of nitro vanillin **4a-4o**

Table 3: Synthetic analogs **4a-4o**.

Analog	Structure	Analog	Structure
4a		4b	
4c		4d	
4e		4f	
4g		4h	
4i		4j	
4k		4l	
4m		4n	
4o			

4. MOLECULAR DOCKING STUDY

Molecular docking is a computational and standard technique for identifying a binding mechanism of ligands and protein targets (30). The docking program implemented in the Molecular Operating Environment 2019.01 was used with default parameters to explore the binding mode of the

synthesized vanillin derivatives. The 3D structures of all the synthetic compounds were model, protonated and energy minimized using the MMFF94 force field implemented in MOE 2019.01(31, 32) conformations were generated for each compound and the best-ranked pose was selected for further study. Furthermore, all the docking poses were visualized

and all the images of the docked poses were prepared through the UCSF Chimera program (33).

4.1. Results and Discussion

Molecular docking is a well-known and most promising tool that provides the possible binding mechanisms between protein and ligand. In this study, docking protocol was applied on a series of vanillin derivatives to explore interactive mechanism with *Saccharomyces cerevisiae*. Previously reported α -glucosidase homology model template (PDB ID: 3A, 4A) has been used (34). The vanillin derivatives and comparative antagonist acarbose were docked into the binding pocket of the receptor by using the

default operating system of MOE. The protein ligand interactions of the docked pose of each complex were visualized manually. The highest ranked dock score conformer of vanillin derivatives and reference ligand (acarbose) were selected. The Docking score of the synthetic compounds having the best anti-glycation activity such as analogues **4a**, **4f**, **4h** and reference ligand was -6.91, -6.99, -7.96 and -4.382 kcal/mol respectively. The docking result revealed that acarbose as well as all the synthetic compounds binds in the binding pocket of the α -glucosidase (Table-4). Assemble binding pose of all the analogs along with reference ligand in α -glucosidase are illustrated in (Figure-3).

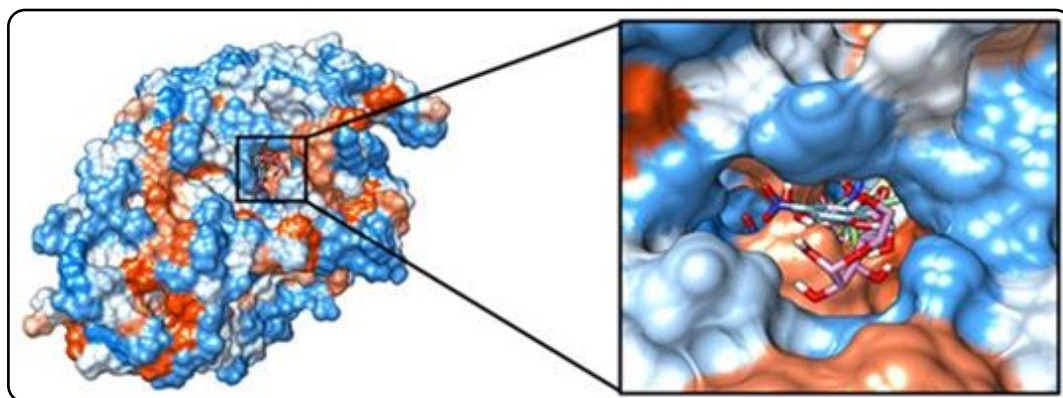


Figure 2: The assemble dock pose of Vanillin analogues **4a**, **4f**, **4h**, and reference ligand (acarbose) against the binding pocket of α -glucosidase are depicted in the 3D format.

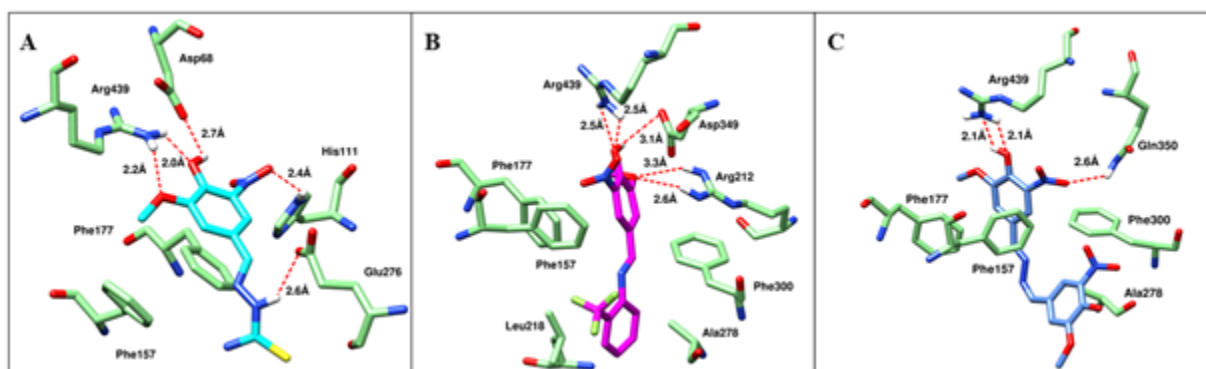


Figure 3: 3D graphical structure representing the binding interaction of analogous **4a**, **4f**, and **4h** (A, B, C) in the active pocket of α -glucosidase.

Table 4: Molecular interactions residue and binding energy of docked compounds in the binding pocket of α -glucosidase.

Compound ID	Binding Energy Kcal/mol	H-Bond	Hydrophobic	Pi-Stacking
Reference compound	-4.382	Arg212, His111, Arg439	Glu276, Glu304, Asp349	Phe177, His239, Pro309
analog 4a	-6.91	Arg439, His111, Glu276	Phe157	Arg439, Phe177
analog 4f	-6.99	Arg439, Asp349, Arg212	Phe157, Phe177, Leu218, Ala278, Phe300	----
analog 4h	-7.96	Arg439, Gln350	Phe157, Phe177, Ala278, Phe300	----

5. CONCLUSION

In the current study, the analogues **4a-4o** were synthesized on the core nucleolus of nitro vanillin by coupling reaction of different amino reagents on the carbonyl group of nitro vanillin in an acid medium followed by a Schiff base mechanism. The analogues were subjected to *in-vitro* screening against AGES through an *in-vitro* MGO-modified BSA model by using rutin as a standard compound. Besides analogues **4b**, **4c**, **4g**, and **4j** which were inactive, other analogues were moderate to highly active. Among potent analogues, the best active analogue was analogue **4f** which bears the trifluoromethyl group at the phenyl imino ring in its structure. The other highly active analogs were analogue **4a**, which bears the carbothioamide group, analogue **4h** which bears the hydrazine group, and analogue **4l** which bears 5-methylthio-2-trifluoromethyl phenylimino group. While analogue **4d**, **4e**, **4i**, **4k**, **4m**, **4n**, and **4o** were considered moderately active. The structure-activity relationship study revealed that the presence of the carboxamide group in analogue **4b**, the presence of the 2,4-dinitrophenyl group in analogue **4c**, the presence of trifluoromethyl group at *meta* position in the molecular structure of analogue **4g**, and the presence of an acidic group at *meta* position in the molecular structure of analogue **4j** reduced the activity of these compounds so lower that they are ranked as inactive against AGES in the series. When safety measures of the analogs **4a-4o** were conducted by MTT against HePG2 cell lines their safety profile reveals that analogs **4a**, **4e**, **4f**, **4i**, **4l**, **4m**, and **4o** were nontoxic concerning doxorubicin as a standard drug, Analogues **4d**, **4h**, **4k** and **4n** were found fairly toxic while inactive analogues were not subjected in this study. The molecular docking study conducted on the best potent analogues, **4a**, **4f**, and **4h** showed excellent results. From these results we can infer that our approaches to preparing the synthetic analogues of the smaller, natural, and relatively non-toxic molecule are successful. The analogues are significantly active against AGES and non toxic and can be used as lead molecules in the future for the treatment of diabetic-associated complications. The docking study of these analogs reveals that they were not potent only in *in-vitro* but also best in legend-protein based interaction as well.

6. CONFLICT OF INTREST

Authors declare no conflict of interest.

7. REFERENCES

- Ahmad S, Moinuddin, Dixit K, Shahab U, Alam K, Ali A. Genotoxicity and immunogenicity of DNA-advanced glycation end products formed by methylglyoxal and lysine in presence of Cu²⁺. *Biochem Biophys Res Commun* [Internet]. 2011 Apr 15;407(3):568–74. Available from: [<URL>](#).
- Twarda-Clapa A, Olczak A, Białkowska AM, Koziolkiewicz M. Advanced Glycation End-Products (AGEs): Formation, Chemistry, Classification, Receptors, and Diseases Related to AGEs. *Cells*

[Internet]. 2022 Apr 12;11(8):1312. Available from: [<URL>](#).

- Lin J, Wu C, Lu C, Hsia S, Yen G. Glycative stress from advanced glycation end products (AGEs) and dicarbonyls: An emerging biological factor in cancer onset and progression. *Mol Nutr Food Res* [Internet]. 2016 Aug 25;60(8):1850–64. Available from: [<URL>](#).

- Peppia M, Vlassara H. Advanced glycation end products and diabetic complications: A General overview. *Hormones* [Internet]. 2005;4(1):28–37. Available from: [<URL>](#).

- International diabetes federation. *Diabetes Atlas* [Internet]. Brussels: Belgium: International Diabetes Federation; 2015. Available from: [<URL>](#).

- Yeh WJ, Hsia SM, Lee WH, Wu CH. Polyphenols with antiglycation activity and mechanisms of action: A review of recent findings. *J Food Drug Anal* [Internet]. 2017 Jan 1;25(1):84–92. Available from: [<URL>](#).

- Arya SS, Rookes JE, Cahill DM, Lenka SK. Vanillin: a review on the therapeutic prospects of a popular flavouring molecule. *Adv Tradit Med* [Internet]. 2021 Sep 7;21(3):415–33. Available from: [<URL>](#).

- Cade WT. Diabetes-Related Microvascular and Macrovascular Diseases in the Physical Therapy Setting. *Phys Ther* [Internet]. 2008 Nov 1;88(11):1322–35. Available from: [<URL>](#).

- Rondeau P, Bourdon E. The glycation of albumin: Structural and functional impacts. *Biochimie* [Internet]. 2011 Apr 1;93(4):645–58. Available from: [<URL>](#).

- Eble AS, Thorpe SR, Baynes JW. Nonenzymatic glucosylation and glucose-dependent cross-linking of protein. *J Biol Chem* [Internet]. 1983 Aug 10;258(15):9406–12. Available from: [<URL>](#).

- Schmidt AM, Yan S Du, Wautier JL, Stern D. Activation of Receptor for Advanced Glycation End Products. *Circ Res* [Internet]. 1999 Mar 19;84(5):489–97. Available from: [<URL>](#).

- Guariguata L, Whiting DR, Hambleton I, Beagley J, Linnenkamp U, Shaw JE. Global estimates of diabetes prevalence for 2013 and projections for 2035. *Diabetes Res Clin Pract* [Internet]. 2014 Feb 1;103(2):137–49. Available from: [<URL>](#).

- Vlassara H, Uribarri J. Glycooxidation and Diabetic Complications: Modern Lessons and a Warning? *Rev Endocr Metab Disord* [Internet]. 2004 Aug;5(3):181–8. Available from: [<URL>](#).

- O'Brien J, Morrissey PA, Ames JM. Nutritional and toxicological aspects of the Maillard browning reaction in foods. *Crit Rev Food Sci Nutr* [Internet]. 1989 Jan 1;28(3):211–48. Available from: [<URL>](#).

- Abbas G, Al-Harrasi AS, Hussain H, Hussain J, Rashid R, Choudhary MI. Antiglycation therapy: Discovery of promising antiglycation agents for the

- management of diabetic complications. *Pharm Biol* [Internet]. 2016 Feb 8;54(2):198–206. Available from: [<URL>](#).
16. Ahmad S, Shahab U, Baig MH, Khan MS, Khan MS, Srivastava AK, et al. Inhibitory Effect of Metformin and Pyridoxamine in the Formation of Early, Intermediate and Advanced Glycation End-Products. Agarwal PK, editor. *PLoS One* [Internet]. 2013 Sep 4;8(9):e72128. Available from: [<URL>](#).
17. Ahmad S, Khan MS, Akhter F, Khan MS, Khan A, Ashraf JM, et al. Glycooxidation of biological macromolecules: A critical approach to halt the menace of glycation. *Glycobiology* [Internet]. 2014 Nov 1;24(11):979–90. Available from: [<URL>](#).
18. Goh SY, Jasik M, Cooper ME. Agents in development for the treatment of diabetic nephropathy. *Expert Opin Emerg Drugs* [Internet]. 2008 Sep 2;13(3):447–63. Available from: [<URL>](#).
19. da Silva CM, da Silva DL, Modolo L V., Alves RB, de Resende MA, Martins CVB, et al. Schiff bases: A short review of their antimicrobial activities. *J Adv Res* [Internet]. 2011 Jan 1;2(1):1–8. Available from: [<URL>](#).
20. Neelakantan M, Esakkiammal M, Mariappan S, Dharmaraja J, Jeyakumar T. Synthesis, Characterization and Biocidal Activities of Some Schiff Base Metal Complexes. *Indian J Pharm Sci* [Internet]. 2010 Feb 1;72(2):216–22. Available from: [<URL>](#).
21. Liang C, Xia J, Lei D, Li X, Yao Q, Gao J. Synthesis, in vitro and in vivo antitumor activity of symmetrical bis-Schiff base derivatives of isatin. *Eur J Med Chem* [Internet]. 2014 Mar 3;74:742–50. Available from: [<URL>](#).
22. Fugu MB, Ndahi NP, Paul BB, Mustapha AN. Synthesis, characterization, and antimicrobial studies of some vanillin schiff base metal (II) complexes. Available online www.jocpr.com *J Chem Pharm Res* [Internet]. 2013;5(4):22–8. Available from: [<URL>](#).
23. Song WJ, Cheng JP, Jiang DH, Guo L, Cai MF, Yang HB, et al. Synthesis, interaction with DNA and antiproliferative activities of two novel Cu(II) complexes with Schiff base of benzimidazole. *Spectrochim Acta Part A Mol Biomol Spectrosc* [Internet]. 2014 Mar 5;121:70–6. Available from: [<URL>](#).
24. Jhaumeer-Laulloo S, Gupta Bhowon M, Mungur S, Fawzi Mahomoodally M, Hussein Subratty A. In vitro Anti-glycation and Anti-oxidant Properties of Synthesized Schiff Bases. *Med Chem (Los Angeles)* [Internet]. 2012;8(3):409–14. Available from: [<URL>](#).
25. Rakshit S, Lakshminarasimhan T, Guturi S, Kanagavel K, Kanusu UR, Niyogi AG, et al. Nitration Using Fuming HNO₃ in Sulfolane: Synthesis of 6-Nitrovanillin in Flow Mode. *Org Process Res Dev* [Internet]. 2018 Mar 16;22(3):391–8. Available from: [<URL>](#).
26. Ribeiro TS, Freire-de-Lima L, Previato JO, Mendonça-Previato L, Heise N, Freire de Lima ME. Toxic effects of natural piperine and its derivatives on epimastigotes and amastigotes of *Trypanosoma cruzi*. *Bioorg Med Chem Lett* [Internet]. 2004 Jul 5;14(13):3555–8. Available from: [<URL>](#).
27. Shah MS, Rahman MM, Islam MD, Al-Macktuf A, Ahmed JU, Nishino H, et al. Synthesis, antimicrobial and antioxidant evaluation with in silico studies of new thiazole Schiff base derivatives. *J Mol Struct* [Internet]. 2022 Jan 15;1248:131465. Available from: [<URL>](#).
28. Jahan H, Siddiqui NN, Iqbal S, Basha FZ, Shaikh S, Pizzi M, et al. Suppression of COX-2/PGE2 levels by carbazole-linked triazoles via modulating methylglyoxal-AGEs and glucose-AGEs – induced ROS/NF- κ B signaling in monocytes. *Cell Signal* [Internet]. 2022 Sep 1;97:110372. Available from: [<URL>](#).
29. Naganagowda G, Meijboom R, Petsom A. Synthesis and Antimicrobial Activity of New Schiff Base Compounds Containing 2-Hydroxy-4-pentadecylbenzaldehyde Moiety. *Adv Chem* [Internet]. 2014 Jul 21;2014(1):1–9. Available from: [<URL>](#).
30. Ul-Haq Z, Khan A, Ashraf S, Morales-Bayuelo A. Quantum mechanics and 3D-QSAR studies on thienopyridine analogues: inhibitors of IKK β . *Heliyon* [Internet]. 2020 Jun 1;6(6):e04125. Available from: [<URL>](#).
31. Halgren TA. Merck molecular force field. I. Basis, form, scope, parameterization, and performance of MMFF94. *J Comput Chem* [Internet]. 1996 Apr;17(5–6):490–519. Available from: [<URL>](#).
32. Haider S, Barakat A, Ul-Haq Z. Discovery of Potential Chemical Probe as Inhibitors of CXCL12 Using Ligand-Based Virtual Screening and Molecular Dynamic Simulation. *Molecules* [Internet]. 2020 Oct 20;25(20):4829. Available from: [<URL>](#).
33. Pettersen EF, Goddard TD, Huang CC, Couch GS, Greenblatt DM, Meng EC, et al. UCSF Chimera—A visualization system for exploratory research and analysis. *J Comput Chem* [Internet]. 2004 Oct 1;25(13):1605–12. Available from: [<URL>](#).
34. Ali M, Barakat A, El-Faham A, Al-Rasheed HH, Dahlous K, Al-Majid AM, et al. Synthesis and characterisation of thiobarbituric acid enamine derivatives, and evaluation of their α -glucosidase inhibitory and anti-glycation activity. *J Enzyme Inhib Med Chem* [Internet]. 2020 Jan 1;35(1):692–701. Available from: [<URL>](#).



The Effect of Different Accelerators on the Vulcanization of EPDM Rubber

Murat Teker^{1,*} , Esra Öztürk¹ , Ayşe Usluoğlu¹ 

¹Department of Chemistry, Faculty of Art and Science, Sakarya University, 54187, Sakarya, Turkey.

Abstract: EPDM (ethylene propylene diene monomer) is a type of synthetic rubber. The products of rubber have great importance in every part of life. EPDM rubber has high tensile strength, high tension, toughness, and is weather resistant. Therefore, EPDM (ethylene-propylene-diene rubber) is widely used in many fields. The aim of this study is to examine the effect of accelerator type on mechanical properties and vulcanization characteristics of EPDM rubber. We used the accelerators; thiazole, sulfonamides, dithiocarbamate, thiuram, and guanidine groups. The results show that the fastest cure time and the best tensile strength are achieved with dithiocarbamates for EPDM rubber.

Keywords: EPDM, Accelerator, Vulcanization.

Submitted: January 8, 2024. **Accepted:** June 14, 2024.

Cite this: Teker M, Öztürk E, Usluoğlu A. The Effect of Different Accelerators on the Vulcanization of EPDM Rubber. JOTCSA. 2024;11(3): 1267-74.

DOI: <https://doi.org/10.18596/jotcsa.1416132>

***Corresponding author's E-mail:** teker@sakarya.edu.tr

1. INTRODUCTION

Elastomers are the most important raw materials used in the rubber industry, as they have a wide area of use in many sectors such as food, textiles, healthcare, military, automotive industry, construction, etc. (1).

Ethylene Propylene Rubber (EPDM/EPM) is a copolymer of ethylene and propylene. EPDM is extremely heat, ozone, and weather resistant (2, 3). Due to these properties, this rubber is widely used in many applications (4, 5, 6).

Vulcanization is one of the most significant technologies in modern industry. During the process of vulcanization, when we add sulphur to rubber, the C-H bonds get broken and replaced by C-S bond (7). The discovery of sulphur vulcanization of rubber by Goodyear and independently by Hancock more than 150 years ago was the genesis of one of the most important classes of engineering materials.

Accelerators are defined as the chemicals added to a rubber compound to increase the speed of vulcanization and to permit vulcanization to proceed at a lower temperature and with greater efficiency (8). Accelerator also decreases the quantity of sulphur necessary for vulcanization, thus improving the 'aged' properties of the vulcanized rubber.

Accelerator choice is both important and critical (9). Selecting the best accelerator system is very difficult. Many parameters, such as raw rubber storage stability, processability, scorch, crosslinking, and cured rubber, come into consideration.

There are, principally, what we called prescriptions, such as rubber, sulphur, zinc oxide, oil acid, accelerator, extender, softener, and anti-oxidant. In this study, the features of vulcanization of the mixtures of EPDM (ethylene propylene diene) rubber by using different accelerators and the features of these after vulcanization was examined. Also, it was investigated how physical characteristic of the mixture of EPDM rubber can be changed with varied amounts of accelerators during and after vulcanization.

2. EXPERIMENTAL SECTION

2.1. Used Materials

It is used Dutralter 4038 as EPDM. Carbon blacks are also FEF N 550 and HAF N 330. Despite these, accelerators are MBT (2-mercapto benzimidazole), MBTS (dibenzimidazole sulphur), CBS (N-cyclohexyl- 2 benzimidazole sulfonamide), MBS (2-benzimidazole- N-sulphene morpholine), TBBS (N-tertiary butile-2 benzimidazole sulfonamide), TMTD (Tetramethyl thiuram disulfide), TMTM (Tetramethylthiuram monosulfide), ZDMC (Zinc

dimethyl dithiocarbamate), ZDEC (Zinc diethyl dithiocarbamate), ZEPC (Zinc ethyl phenyl dithiocarbamate), DPG (Diphenyl-guanidine).

2.2. Preparation of Rubber Mixtures

The mixture was prepared in the open laboratory on a two-cylindrical shaft. (ASTM D3182). EPDM rubber, various accelerators, and a series of mixtures were

attained. It contains EPDM rubber 100 phr, carbon black 109.4 phr, paraffinic oil 54.0 phr, zinc oxide 4.0 phr, stearic acid 2.70 phr, sulphur 2.50 phr, different accelerators (MBT, MBTS, CBS, MBS, TBBS, TMTD, TMTM, ZDCM, ZDEC, ZEPC, and DPG) 2.50 phr. The combinations of EPDM prepared with different kinds of accelerators are shown in Table 1 (10).

Table 1: The Combination of EPDM prepared with different kind of accelerators.

Raw Materials (phr)	Accelerator (phr)											
	MBT	MBTS	CBS	MBS	TBBS	TMTD	TMTM	ZDCM	ZDEC	ZEPC	DPG	TMTM
EPDM rubber	100	100	100	100	100	100	100	100	100	100	100	100
Carbon black	109.4	109.4	109.4	109.4	109.4	109.4	109.4	109.4	109.4	109.4	109.4	109.4
Paraffinic oil	54.0	54.0	54.0	54.0	54.0	54.0	54.0	54.0	54.0	54.0	54.0	54.0
Zinc Oxide	4.00	4.00	4.00	4.00	4.00	4.00	4.00	4.00	4.00	4.00	4.00	4.00
Stearic acid	2.70	2.70	2.70	2.70	2.70	2.70	2.70	2.70	2.70	2.70	2.70	2.70
Sulfur	2.50	2.50	2.50	2.50	2.50	2.50	2.50	2.50	2.50	2.50	2.50	2.50
Accelerator	2.50	2.50	2.50	2.50	2.50	2.50	2.50	2.50	2.50	2.50	2.50	2.50
Total	275.1	275.1	275.1	275.1	275.1	275.1	275.1	275.1	275.1	275.1	275.1	275.1

phr: Parts per one hundred rubber.

2.3. Used Devices and Features

Rheometer: It is used to measure the vulcanization characteristics of mixtures and to save the vulcanization curve. It also applies oscillating stretch into mixture under high temperature and pressure, and as a consequence of an increase in the cross-

link's intensity, an increment in torque is shown as a function of time. The unit of torque is N-m or lb-in (pounds inch), Figure 1. The vulcanization state, which is made ready with each distinctive accelerator, was gauged by MDR-2000 rheometer device (ASTMD 5289).

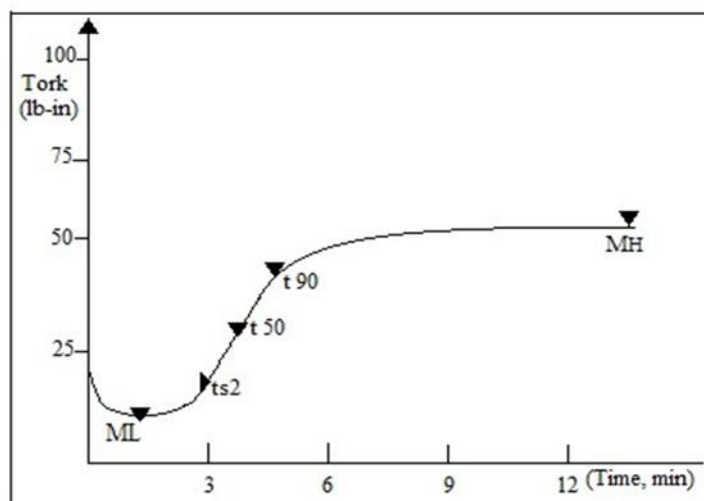


Figure 1: Graphic of curve of vulcanization.

The feature of the curve of vulcanization can be explained in such a way.

ts2; Beginning time of hardening, unit is minutes or minutes: seconds. ts2 is helpful to determine safety of procedure.

ML: Minimum torque, units N-m and ya Ib-in (pounds-inch).

MH: Maximum torque, unit is N-m or Ib-in (pounds-inch). It is related to properties such as tensile, tear, and tensile strength.

t90, Time to reach maximum cook time, unit is minutes or minutes: seconds. The t90 is helpful in determining the press time during production (11-12).

Shoremeter: The toughness of rubber materials, in general speaking, is the measurement of resistance against immersion of metal rod, marble, or needle into them. In this effort, shore type is the durometer measuring toughness, kind A. In durometers, the tip of immersion is not only marble but also frustocone. Toughness should be measured after the device's surface of measurement contacts the sample for a

maximum of 3 minutes. The prepared mixtures were hardened in the hydrolytic press at 150°C. Following of vulcanization, the toughness measurement was carried out with a Shore A Durometer, whose brand is Braiss. (ASTM D2240).

Tensiometer: This apparatus gives an indication of both the extension of the product at the time of failure and the fracture resistance of the product after vulcanization. The thickness of the sample cut as a bow-tie was measured from three different parts, and it was hanged between two wangs of tensiometer, and the power was applied to the sample. At the time of sample failure, the tensiometer saves the failure-extension curve and gives its values.

Fracture Point: The ratio of forces between the time of failure and the beginning. (MPa or N/mm²).

Breaking Elongation: The ratio of length between changing at the failure and changing at the beginning. (%)

Modulus: The amount of unit surface for the force applying to a specific extension. (MPa or N/mm²).

3. RESULTS AND DISCUSSION

Vulcanization characteristics of EPDM rubber mixture prepared with different accelerators obtained after rheometer test were compared with the physical features of the ones obtained by tensiometer test after vulcanization.

In reference to outcomes from rheometer test, it is concluded that for the maximum ML value for EPDM rubber DPG and MBS is the best choice (Figure 2). However, the minimum value is by TMTM.

In Figure 3, the upper limit of MH values is reached with thiuram and dithiocarbamates, but the lower limit is related to DPG and mercapto groups. Similar results were obtained with previous studies. The highest MH values were obtained with TBBS and TMTM, while the lowest MH value was obtained with DPG (13).

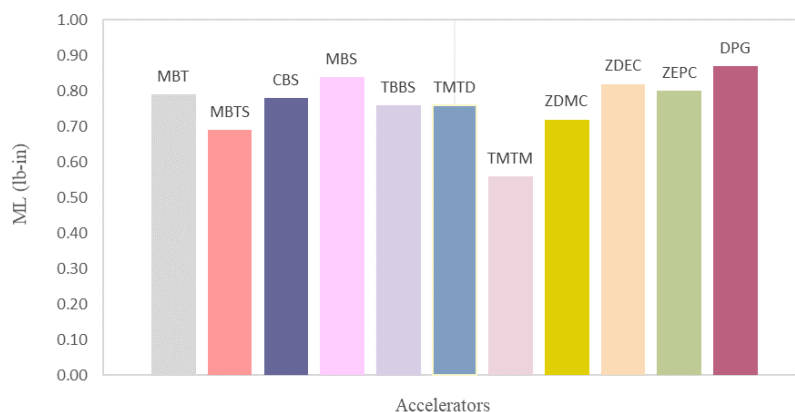


Figure 2: The effect of accelerators in EPDM mixtures on the value of ML.

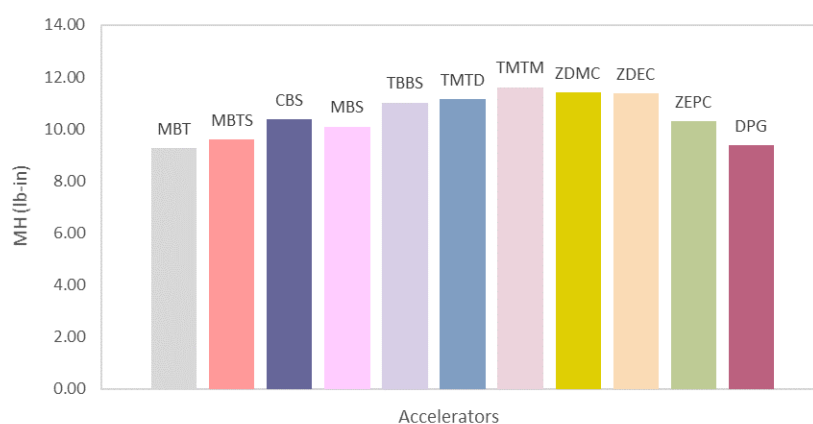


Figure 3: The effect of accelerators in EPDM mixtures on the value of MH.

In Figure 4, the lowest hardening time, i.e., providing the fastest hardening group, belongs to TMTD and ZDMC. The longest hardening times are given by MBT and MBTS. For EPDM mixture, the earliest hardening time is with thiuram and dithiocarbamates. Whereas the latest one is from the mercaptos, which are medium level accelerators. It has been observed that

similar results have been achieved in previous studies (14).

The longest ts₂ value is by MBTS, and the shortest one is by dithiocarbamates. MBTS has the safest processing, with the highest value of ts₂. Dithiocarbamide groups are the fastest ones to start hardening. Similar results were seen in the study of

Alam et al. (15). Dithiocarbamate accelerators are used as ultra-fast accelerators for rubber compounds (16).

The comparison of toughness values after vulcanization is shown in Figure 6. According to that, the lowest is with DPG. Whereas the highest toughness value is with TMTD. Thiurams and ZDMC

have also shown a high hardness value. The crosslink density of rubber vulcanizate also affects the hardness value. The higher the crosslinking density, the lower the chain mobility (17). Their high stiffness was caused by the decreased mobility of polymer chains, which was also confirmed by the values of hardness and elongation-at-break (18).

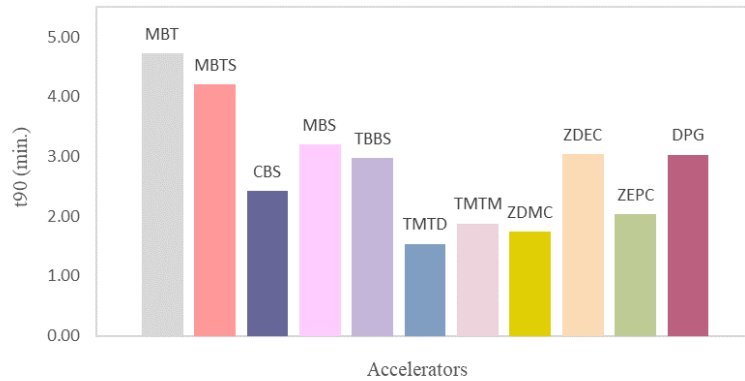


Figure 4: The effect of accelerators in EPDM mixtures on the value of t90.

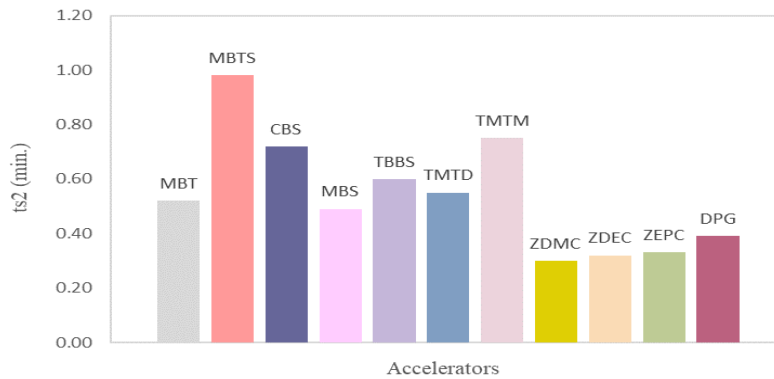


Figure 5: The effect of accelerators in EPDM mixtures on the value of ts2.

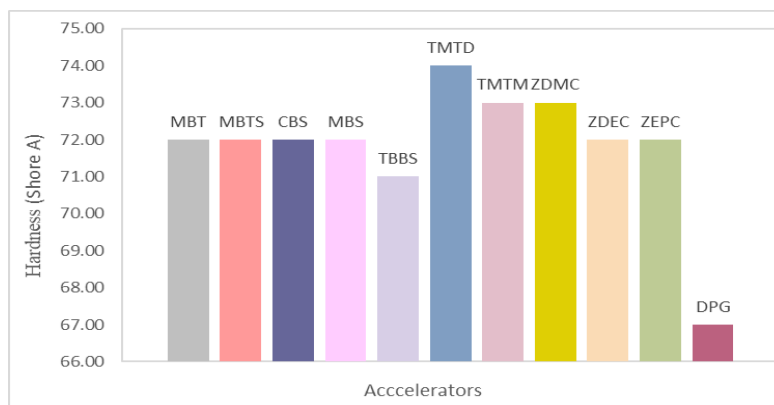


Figure 6: The effect of accelerators in EPDM mixtures on the value of toughness.

As specified in Figure 7 above, the highest modulus value is provided by dithiocarbamates and thiurams. The lowest modulus value is obtained with DPG. However, it is realised that the strengthening properties of DPG, used generally as a secondary accelerator, are low. This is due to the chemical structure of DPG (14).

In Figure 8, ultimate breaking strength is reached with thiurams and dithiocarbamates. The lowest breaking strength value is obtained with MBS and

DPG. Similar results have been obtained in previous studies. It was found that mixtures made with TMTD had higher tensile strength values (19).

In case the elongation values are checked, there is a higher elongation value when DPG whose breaking strength is not good enough is used. TMTM and mercaptanes are the second-best alternatives, providing the highest elongation after DPG (Figure 9).

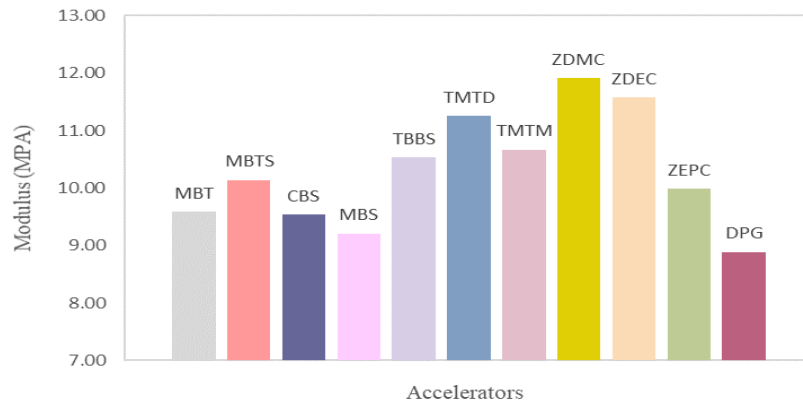


Figure 7: The effect of accelerators in EPDM mixtures on the value of Modulus.

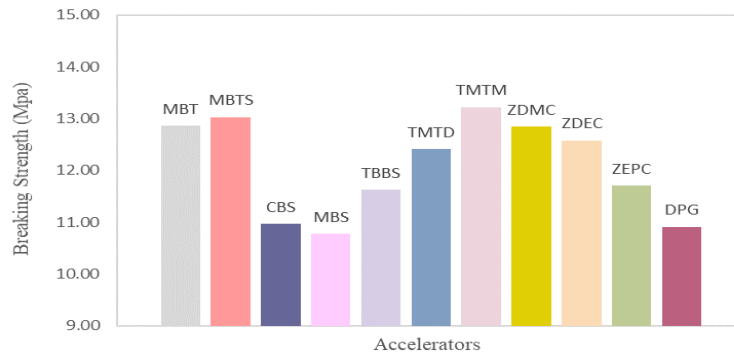


Figure 8: The effect of accelerators in EPDM mixtures on the value of Breaking Strength.

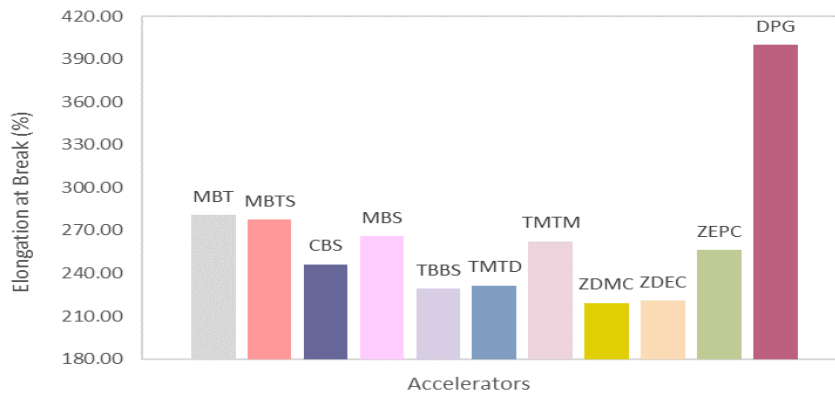


Figure 9: The effect of accelerators in EPDM mixtures on the value of Elongation.

Table 2: The feature of vulcanization of EPDM mixture prepared with different type of accelerators.

	MBT	MBTS	CBS	MBS	TBBS	TMTD	TMTM	ZDMC	ZDEC	ZEPC	DPG
ML (Ib-in)	0.79	0.69	0.78	0.84	0.76	0.76	0.56	0.72	0.82	0.80	0.87
MH (Ib-in)	9.25	9.60	10.37	10.09	11.02	11.15	11.61	11.41	11.37	10.30	9.37
t90 (min.)	4.72	4.20	2.42	3.20	2.98	1.54	1.88	1.74	3.04	2.03	3.03
ts2 (min.)	0.52	0.98	0.72	0.49	0.60	0.55	0.75	0.30	0.32	0.33	0.39
Hardness (Shore A)	72	72	72	72	71	74	73	73	72	72	67
Modulus (MPa)	9.59	10.14	9.54	9.21	10.53	11.26	10.67	11.91	11.58	9.99	8.89
Breaking Strength (MPa)	12.86	13.03	10.97	10.78	11.63	12.41	13.22	12.85	12.58	11.71	10.91
Elongation at Break (%)	281.00	277.60	246.30	266.05	229.25	231.50	262.40	219.30	220.97	256.15	400.15

According to Table 2, as the hardness increases, the breaking strength increases, while the elongation decreases. High hardness can be evaluated as providing a high crosslink density for these groups. The high crosslink density causes the molecular chains to move less. Similar results have been presented in previous published studies. The highest modulus values and the lowest elongation values are observed with dithiocarbamates (20). When DPG was used, the lowest modulus value and the highest elongation value were obtained.

4. CONCLUSION

Thiurams and dithiocarbamates forming high intensity of cross-linking bonds in EPDM rubbers provide great MH, breaking strength, modulus value, and toughness value. Thiurams and dithiocarbamates are known to have the lowest t90 values which is the time of hardening. Since dithiocarbamates react as rapidly as possible, they have the lowest ts2 values. Furthermore, MBTS from the mercapto groups recognized as providers of late activation expresses high ts2 values. Although the strengthening behaviour of DPG is quite marginal, the best elongation levels are provided by DPG. The reason for that is that DPG has a polysulphite capacity as high as possible. Finally, while the cross-linking intensity increases, breaking strength, modulus, and toughness values also rise. Increment in this texture is generally directly proportional to the augmentation in MH value. When t90 is short enough, MH becomes dominant, so the intensity of the cross-linking bond of rapid accelerators is greater. Elongation portions for EPDM rubbers except dithiocarbamate groups generally decrease as the time of vulcanization become shorter.

5. REFERENCES

1. Fazli A, Rodrigue D. Recycling Waste Tires into Ground Tire Rubber (GTR)/Rubber Compounds: A Review. *J Compos Sci* [Internet]. 2020 Jul 31;4(3):103. Available from: [<URL>](#).
2. Akpınar Borazan A. Preparation and Characterization of EPDM Rubber Mixture for a Heat Resistant Conveyor Belt Cover. *Anadolu Univ J Sci Technol A - Appl Sci Eng* [Internet]. 2017 Sep 30;18(2):507–20. Available from: [<URL>](#).
3. Arayaprane W, Rempel GL. Effects of cashew nut shell liquid as a plasticizer on cure characteristics, processability, and mechanical properties of 50 : 50 NR/EPDM blends: A comparison with paraffin oil. *J Appl Polym Sci* [Internet]. 2007 Nov 15;106(4):2696–702. Available from: [<URL>](#).
4. Nabil H, Ismail H, Azura AR. Compounding, mechanical and morphological properties of carbon-black-filled natural rubber/recycled ethylene-propylene-diene-monomer (NR/R-EPDM) blends. *Polym Test* [Internet]. 2013 Apr;32(2):385–93. Available from: [<URL>](#).
5. Ulusoy H, Demir F. Investigation of Rheological and Mechanical Properties of Rubbers Produced by Sulfur Vulcanization from EPDM Rubbers with

Different Ethylene Ratios. *Osmaniye Korkut Ata Üniversitesi Fen Bilim Enstitüsü Derg* [Internet]. 2022 Feb 23;5:216–26. Available from: [<URL>](#).

6. Bartosik D, Szadkowski B, Kuśmierk M, Rybiński P, Mirkhodzhaev U, Marzec A. Advanced Ethylene-Propylene-Diene (EPDM) Rubber Composites Filled with Raw Silicon Carbide or Hybrid Systems with Different Conventional Fillers. *Polymers* [Internet]. 2022 Mar 29;14(7):1383. Available from: [<URL>](#).

7. Sing G, Mahajan A, Kumar M. Review Paper on Vulcanization of Rubber and It's Properties. *Glob J Eng Sci Res*. 2015;2(8):1–4.

8. Wang M, Zhu J, Zhang S, You G, Wu S. Influencing factors for vulcanization induction period of accelerator / natural rubber composites: Molecular simulation and experimental study. *Polym Test* [Internet]. 2019 Dec;80:106145. Available from: [<URL>](#).

9. Yang S yan, Jia Z xin, Liu L, Fu W wen, Jia D min, Luo Y fang. Insight into vulcanization mechanism of novel binary accelerators for natural rubber. *Chinese J Polym Sci* [Internet]. 2014 Aug 26;32(8):1077–85. Available from: [<URL>](#).

10. Ozturk E. Farklı kauçuk karışımlarının vulkanizasyonuna hızlandırıcıların etkisi. [Sakarya]: University of Sakarya; 2008.

11. Alam MN, Mandal SK, Roy K, Debnath SC. Synergism of novel thiuram disulfide and dibenzothiazyl disulfide in the vulcanization of natural rubber: curing, mechanical and aging resistance properties. *Int J Ind Chem* [Internet]. 2014 Mar 25;5(1):8. Available from: [<URL>](#).

12. Keklikcioğlu Çakmak N, Engin YE. Synthesis and Characterization of Ethylene Propylene Diene Monomer (EPDM) Rubber Mixture. *Omer Halisdemir Univ J Eng Sci* [Internet]. 2019 Jul 31;8(2):1299–306. Available from: [<URL>](#).

13. Setyadawi NM, Mayasari HE. Curing Characteristic of Various Accelerators on Natural Rubber/Chloroprene Rubber Blends. *J Din Penelit Ind* [Internet]. 2020;31(2):154–62. Available from: [<URL>](#).

14. Formela K, Waşowicz D, Formela M, Hejna A, Haponiuk J. Curing characteristics, mechanical and thermal properties of reclaimed ground tire rubber cured with various vulcanizing systems. *Iran Polym J* [Internet]. 2015 Apr 10;24(4):289–97. Available from: [<URL>](#).

15. Alam MN, Kumar V, Potiyaraj P, Lee DJ, Choi J. Synergistic activities of binary accelerators in presence of magnesium oxide as a cure activator in the vulcanization of natural rubber. *J Elastomers Plast* [Internet]. 2022 Feb 10;54(1):123–44. Available from: [<URL>](#).

16. Samarasinghe I, Walpalage S, Edirisinghe D, Egodage S. Study on sulfur vulcanized natural rubber formulated with nitrosamine safe diisopropyl xanthogen polysulfide/tertiary butyl benzothiazole

- sulphenamide binary accelerator system. *Prog Rubber, Plast Recycl Technol* [Internet]. 2021 Aug 11;37(3):190–202. Available from: [<URL>](#).
17. Nghiem TT, Nguyen BL, Huyen LT, Kawahara S. A novel approach to prepare self-healing vulcanized natural rubber using tetramethylthiuram disulfide. *Polym J* [Internet]. 2023 Oct 11;55(10):1097–102. Available from: [<URL>](#).
18. Nabil H, Ismail H, Azura AR. Optimization of accelerators on curing characteristics, tensile, and dynamic mechanical properties of (natural rubber)/(recycled ethylene-propylene-diene monomer) blends. *J Vinyl Addit Technol* [Internet]. 2015 Jun 26;21(2):79–88. Available from: [<URL>](#).
19. Marković G, Radovanović B, Marinović-Cincović M, Budinski-Simendić J. The Effect of Accelerators on Curing Characteristics and Properties of Natural Rubber/Chlorosulphonated Polyethylene Rubber Blend. *Mater Manuf Process* [Internet]. 2009 Oct 19;24(10–11):1224–8. Available from: [<URL>](#).
20. Erbek Cömez E, Öztürk S. Investigating Rheological, Mechanical and Heat Aging Effects of Different Accelerator Systems at EPDM Compounds. *Int J Eng Res Dev* [Internet]. 2023 Jun 2;15(2):654–64. Available from: [<URL>](#).



The Effect of Different Methacrylation Amounts on Physical Properties of Gelatin Methacryloyl Biomaterials: Machine Learning Approach

Sena Çakıcı¹ , Rumeysa Tutar^{2*} 

¹Department of Chemical Engineering, Faculty of Engineering, Istanbul University-Cerrahpaşa, Avcılar, Istanbul, 34320, Turkey.

²Department of Chemistry, Faculty of Engineering, Istanbul University-Cerrahpaşa, Avcılar, Istanbul, 34320, Turkey.

Abstract: The rational design process for biomaterials is time-consuming. Machine learning (ML) is an efficient approach for reducing material synthesis and experimentation in terms of cost and time. Among the emerging biopolymers for tissue engineering applications, methacrylic anhydride (MA)-functionalized gelatin (GelMA), which was chosen as the model biomaterial for this study, has assumed a promising role owing to its excellent tunable properties and biocompatibility. The ML approach was used to determine the efficiency of the MA amounts selected for GelMA synthesis. In addition, the effect of different methacrylation amounts on the molecular structure of GelMA was indicated in terms of its physical properties. This modeling was performed to generate predictions based on 20 mL of MA. The prediction output was obtained as a result of four data models from the 20 mL MA column. First, data were collected with experimental applications for swelling and degradation ratios, and then the data processing phase was applied. The most suitable ML model, decision tree regression, was selected, and the results were interpreted graphically. The experimental results were compared with the ML results, and the efficiency of ML is shown in detail. The Mean Squared Error (MSE) value for degradation was calculated as 10.16, with a Root Mean Squared Error (RMSE) of 3.1885, Mean Absolute Error (MAE) of 2.6667, and Mean Absolute Percentage Error (MAPE) of 14.66%. For swelling, the MSE value was calculated to be 1821.25, with an RMSE of 3.1885, MAE of 2.6667, and MAPE of 14.66%. In future studies, it is anticipated that the performance of the model will improve with the expansion of the experimental dataset for swelling measurements.

Keywords: Methacrylic anhydride, Gelatin, GelMA, Physical properties, Data analysis, Machine learning.

Submitted: April 26, 2024. **Accepted:** July 6, 2024.

Cite this: Çakıcı S, Tutar R. The Effect of Different Methacrylation Amounts on Physical Properties of Gelatin Methacryloyl Biomaterials: Machine Learning Approach. JOTCSA. 2024;11(3): 1275-86.

DOI: <https://doi.org/10.18596/jotcsa.1473948>

***Corresponding author's E-mail:** rumeysa.tutar@iuc.edu.tr

1. INTRODUCTION

A rational design process for biomaterials can be time-consuming. The prepared biomaterial needs to have the desired functionality while mimicking human physiology. Biomaterials are used for biomedical applications; therefore, all details are important (1,2). In particular, the development of biocompatible biomaterials requires rational designs. The development of biomaterials using the traditional approach involves a long, trial-and-error cycle. It is becoming increasingly important to improve this process in terms of time and cost (3). The purpose of machine learning (ML) in biomaterial production and design is to accelerate the process and obtain accurate models.

Machine learning emulates human learning. ML is an important field of science that operates through the development of various algorithms and techniques (1). The primary objective of machine learning is to derive inferences and obtain predictions from data. ML aims to save time in data analysis and engineering. The most efficient form of the material can be achieved using ML (4). In recent years, the field of data science has seen numerous advancements in data analysis owing to the proliferation of data. Interest in this field has increased significantly to save time in concluding data as quickly as possible. The basic logic of machine learning is to learn the pattern and statistical correlation of data (5). The expected results and interpretations differ depending on the

data type. Applying an incorrect model resulted in inaccurate results and poor performance.

One machine-learning algorithm is called supervised learning. It teaches a computer to understand the relationship between input data, which are the variables provided, and output, which is the desired result (6). This approach is used in many applications, particularly for data collection and image processing (7). They can be used in language processing, medicine, finance, and many other fields. Some supervised learning methods are classified into linear regression, decision trees, random forests, and artificial neural networks. Another important ML algorithm is unsupervised learning, which is used to understand a dataset. It describes the pattern of the data in the dataset and the correlation between the data. Unsupervised learning can be classified into data collection, clustering (7,8), dimensionality reduction (9,10), and feature engineering. In particular, these two ML algorithms are most commonly used in the biological and material fields.

The input and output data are important for supervised machine learning. The model was divided into training and testing sets using the input data. It learns with the training dataset and checks it with the inputs, which it divides into a test set (11). In addition to the importance of the input and output information in supervised learning, it is recommended for situations where known data are available for the output of the data to be predicted. Supervised learning uses classification and regression techniques (12). In decision trees, a dataset can be divided into a smaller training set with a feature selected from the training data. The results are formed in this way to create branches. At this point, the results were divided into questions asked at the root nodes of the separation. Branches were created as a pure subset of the training dataset. Decision tree methods can be classified using regression analysis (13,14). It is preferable to interpret the dataset in regression according to the results of the data in the new clusters created in the regression analysis because the dataset is numerical, and the results are analyzed according to variable parameters. In the present study, the variables were the time and degree of methacrylation of the GelMA biomaterial. A dataset was created from the results of the degradation and swelling measurements based on these two variables. The model was applied using decision trees, and branching under small clusters was examined using regression analysis. In general, the aim is to use decision trees with regression analysis on the dataset.

Hydrogels are polymer materials that can absorb and retain large amounts of water without degrading their structure (15). Hydrogels are used in various applications, such as tissue engineering and environmental engineering. Many physical properties of hydrogel biomaterials, such as swelling and degradation ratios, can be experimentally determined. Gelatin methacryloyl (GelMA), often abbreviated as GelMA, is a derivative of gelatin containing primarily methacrylamide and minor methacrylate groups (2,16,17). Methacrylic groups

were introduced from methacrylic anhydride (MA) onto the active amine and hydroxyl groups of GelMA. GelMA is called very high GelMA, high/medium GelMA, or low GelMA based on the addition of MA. The amount of methacrylamide-functionalization is an important parameter that affects the polymerization and crosslinking processes of GelMA hydrogel structures (16-18). The incorporation of methacrylate groups into the amine-containing side chains of gelatin enabled photopolymerization, resulting in a stable hydrogel that remained intact at 37 °C. The variation in the degree of methacrylation allows precise control over the physical properties of GelMA, offering a customizable spectrum of swelling characteristics tailored to various applications (18).

Researchers have explored hydrogel stiffness through the application of machine-learning techniques. It has been established that the stiffness of hydrogels is intricately related to their physical properties. Altering the reaction conditions induces changes in the physical, chemical, and morphological attributes of hydrogels (19,20). Researchers have mostly investigated the effect of photocrosslinking conditions on hydrogel stiffness based on the mechanical properties (21). Photocrosslinking conditions are directly related to photoinitiators. Therefore, researchers have applied artificial intelligence (AI) to overcome the limitations associated with experimental optimization. For instance, a group developed an artificial neural network (ANN) model to predict the effects of Eosin Y, triethanolamine (TEA), and N-vinyl-2-pyrrolidone (NVP) concentrations on stiffness and gelation time (22). In a previous study, GelMA hydrogels were fabricated with different DS values (49.8%, 63.8%, and 73.2%) using 1, 5, and 10 molar ratios of MA, respectively. It was observed that the average porosity of the dried hydrogels, as determined by scanning electron microscopy (SEM), decreased with higher substitutions (23,24). Considering these approaches, the present study is the first of its kind in this context. Investigating the effects of different degrees of methacrylation on GelMA biomaterials will provide researchers with different perspectives.

Our study focused on the importance of the amount of methacrylate in GelMA preparations and its physical properties, such as swelling and degradation. This is important for the application of GelMA hydrogels in tissue engineering applications. To date, 8 mL of MA has been experimentally investigated for different organs in tissue engineering applications of GelMA (2,16-18). We aimed to obtain physical property data according to varying amounts of methacrylation during the synthesis of GelMA using a machine-learning approach. The dataset was created by considering changes in the parameters as a result of the synthesis. This parameter determines the physical properties of the hydrogel structure based on the swelling and degradation ratios. In this study, there were multiple independent variables (features) in the dataset because GelMA was synthesized with different amounts of methacrylation (4, 8, 12, and 20 mL MA). Swelling and degradation data were experimentally collected for each degree of

methacrylation. For four different degrees of methacrylation (four distinct variables), 10 data points were used in the swelling studies, whereas nine data points were used in the degradation studies. Experimental results were initially obtained using a 20 mL methacrylation degree as a sample. Subsequently, the results were presented by comparing the experimental data with machine learning data for the 20 mL methacrylation degree.

Decision tree regression was chosen as the method. This model is based on the principle of continuously partitioning data fields and creating a prediction model for each partition. This partitioning creates decision trees graphically. The decision tree machine learning method was employed to perform a regression analysis on two distinct datasets and establish more specific relationships between the data. Decision tree regression analysis allows the dataset to be interpreted in smaller groups using branches. Another reason for choosing decision-tree methods is their inherent simplicity and ease of understanding.

2. EXPERIMENTAL SECTION

2.1. Materials and Instruments

Type A porcine gelatin (300 g Bloom), methacrylic anhydride (MA purity >94%), triethanolamine (TEA purity >99%), N-vinyl caprolactam (VC purity >98%), Eosin Y disodium salt, cellulose dialysis membranes (12–14 kDa molecular weight cutoff), and phosphate-buffered saline (PBS) tablets were purchased from Sigma-Aldrich. Dulbecco's phosphate-buffered saline (DPBS) was purchased from Gibco (Life Technologies). Attenuated total reflectance-Fourier transform infrared (ATR-FTIR) spectra of all studied samples were recorded between 4000 and 500 cm^{-1} using a Jasco FT/IR 6700 spectrophotometer. A JEOL ECZ500R (11.75 Tesla) spectrometer and high-performance Ultrashield TM 500 MHz superconducting magnet were used for NMR analysis. Scanning electron microscopy (SEM) micrographs were acquired at different magnifications using an SEM (JEOL JSM 5600).

2.2. GelMA Synthesis and Characterization

Gelatin was methacrylated based on previous literature (16,17). Different amounts of MA (4, 8, 12, and 20 mL) were used to prepare GelMA biomaterials. Briefly, 10 g of gelatin was dissolved in DPBS at 50 °C under constant stirring. After the gelatin was completely dissolved, MA was added dropwise to the gelatin solution. The reaction was allowed to continue for 2 h. Subsequently, a cellulose dialysis membrane was used to remove unreacted chemicals from the GelMA solution. After dialysis, the solution was placed in a glass container, frozen, and freeze-dried using a TeknoSEM brand lyophilizer device. ATR-FTIR spectroscopy and $^1\text{H-NMR}$ characterization were used to identify pristine gelatin and the prepared GelMA materials.

2.3. Hydrogel Preparation and Characterization

Hydrogels were prepared using a visible-light photoinitiator system. Visible light crosslinker solutions (PIs) were prepared using Eosin Y disodium

salt (0.5 mM), VC (1.25 w/v%), and TEA (1.875 w/v%) (2,16). To determine the physical properties, 10% w/v GelMA was dissolved in a PI solution to prepare the hydrogels. A small LED light source (VALO Light Curing Device, Ultradent, USA) was used to crosslink hydrogels. Visible light was applied for 120 s to the GelMA solutions, which were then placed in a polydimethylsiloxane (PDMS) mold (diameter: 9 mm and depth: 7 mm) to fabricate crosslinked hydrogel discs of the same size. The resulting GelMA hydrogel discs were frozen overnight and dried using a lyophilizer. Dry hydrogel discs were then used to determine the physical properties of GelMA.

2.4. Morphological Characterization

The SEM surface morphologies of the methacrylate-modified samples and hydrogels after crosslinking were examined using scanning electron microscopy. The samples and scaffolds were placed on a double-sided graphite tape, attached to a metal surface, and sputter-coated with gold for 10 s.

2.5. Physical Properties of GelMA Hydrogels

After preparing the hydrogel discs via visible-light crosslinking, the physical properties of the GelMA hydrogels were characterized based on their swelling and degradation ratios. The physical properties of GelMA were obtained by adding 4, 8, 12, and 20 mL of methacrylic anhydride in four different GelMA syntheses, which were tested using appropriate methods. The obtained data were used to create the dataset.

2.5.1. Swelling Ratio

The swelling capacity of the prepared GelMA hydrogels was evaluated in DPBS at 37 °C following previously reported procedures (2). The hydrogel discs were prepared using a freeze-drying method. Dry hydrogel discs were weighed and recorded to obtain their initial dry weight (W_i). Then, all weighed hydrogel samples were soaked in DPBS and placed in an incubator. They were then weighed after removing excess water at specific time points to determine the wet weight at each interval (W_s). The time intervals were set to 1 h, 3 h, 5 h, 7 h, 24 h, 168 h, and 336 h. The swelling ratios were calculated using the ratio of the increase in mass to the mass of the swollen samples. A minimum of six samples were tested for each case.

$$\text{Swelling (\%)} = (W_s - W_i) / W_i * 100 \quad (1)$$

W_i = initial weight before swelling.

W_s = swollen weight of the materials.

2.5.2. Degradation Ratio

The in vitro degradation behavior of the scaffolds was analyzed using collagenase type II solution at 37 °C (2). The freeze-dried hydrogel discs were weighed to determine their initial weights. The dried samples were then immersed in collagenase II solution. Samples were removed from the solution at checkpoints of 1 h, 3 h, 5 h, 7 h, 24 h, and 168 h of incubation. The hydrogel discs were then frozen and lyophilized. The dry weights were recorded at each time point. The degradation ratios of the hydrogel discs were calculated using the following equation:

$$\text{Lost weight (\%)} = (W_i - W_d)/W_i \times 100 \quad (2)$$

W_i = initial dry weight before degradation, and W_d = final dry weight after the operation.

2.6. Machine Learning (ML) Study

Visual Studio Code is a stand-alone source code editor compatible with Windows, macOS, and Linux operating systems. It is freely accessible and provides seamless internet connectivity. For our study, we utilized the Conda virtual environment, which is both free and easily integrated with the Visual Studio Code editor alongside the Python programming language. The Decision Tree Regression model was employed to demonstrate data prediction within the supervised learning domain of machine learning. Through data pre-processing, the dataset was rendered suitable and subsequently partitioned into training and testing subsets. Prior to the model implementation, normalization was applied to standardize the data, followed by the application of the model to the data frame. Hyperparameter tuning was conducted to optimize the model fit and enhance performance. Mean square error (MSE) values were computed to evaluate error performance. Finally, the predicted data were compared with the actual data displayed on the screen, and the results were analyzed.

3. RESULTS AND DISCUSSION

The bands based on methacrylation of the GelMA structures were used for characterization, as shown in Figure 1. FTIR spectra were used to identify the chemical composition of the fabricated samples. To conduct this analysis, pristine gelatin and GelMA were directly used. They were exposed to infrared waves in the range $4000\text{--}400\text{ cm}^{-1}$ using a Jasco FT/IR-6700 spectrometer. The band at 1210 cm^{-1} was assigned to the secondary (amide) group, $\nu(\text{C-N})$, in the spectra of Gelatin and GelMA. The spectra of GelMA with different methacrylated ratios showed peak shifts. For GelMA containing 8 mL MA, a shift in the C-N band occurred. The bands at 1640 cm^{-1} and 1540 cm^{-1} correspond to C=O and N-H bending, respectively. While there is C=O stretching (amide I) in the gelatin structure, C=C groups are formed in the GelMA structure owing to the methacrylated anhydride (25,26). The peaks of both groups were very close to each other. The -NH_2 groups in the gelatin structure exist as -NH groups in GelMA after methacrylation. The broad amide A band observed at approximately 3300 cm^{-1} as a characteristic medium absorption peak can be attributed to the stretching vibrations of O-H and N-H. The -NH_2 bands in the gelatin structure are shadowed by the -OH band. A widespread peak was observed (2,26).

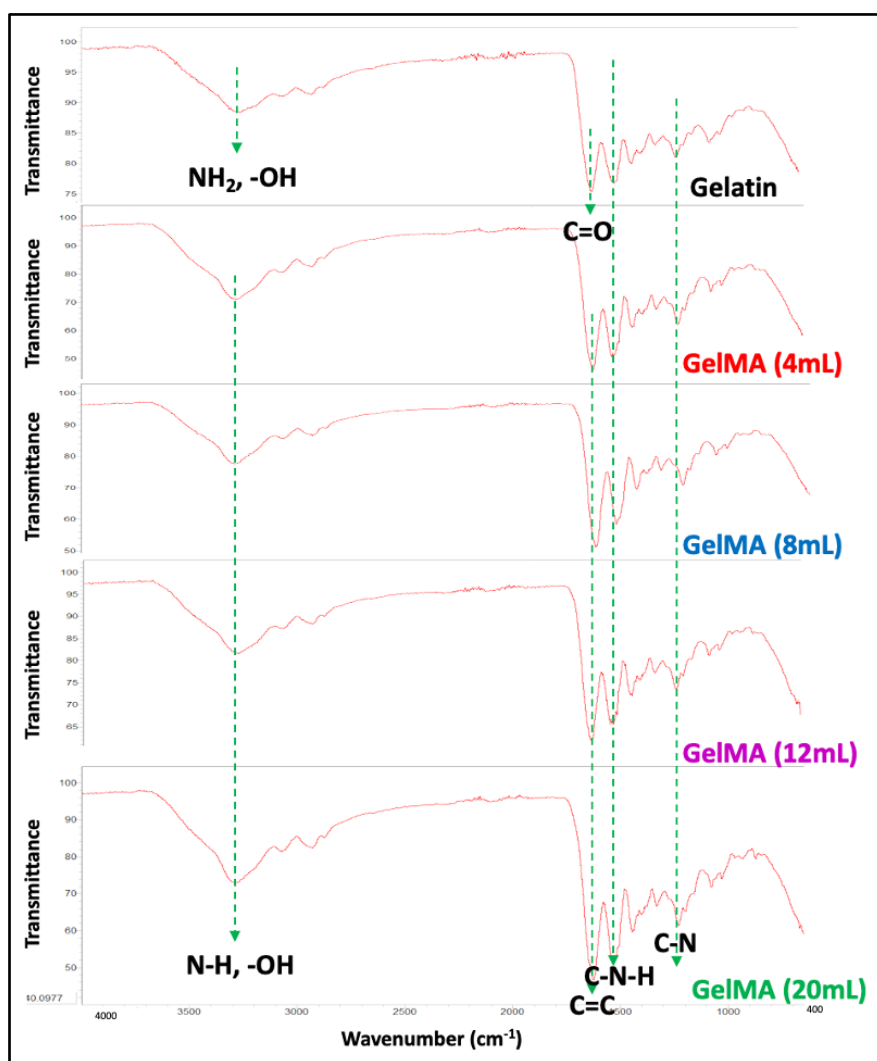


Figure 1: The ATR-FTIR spectra of pristine Gelatin and GelMA samples.

In $^1\text{H-NMR}$ spectra of pristine gelatin and four different methacrylated GelMA samples are shown in Figure 2. Deuterium oxide (D_2O) was used to prepare solutions for the measurements at room temperature. Because of the methacrylation reaction, two main peaks (belonging to the magnetically different protons at vinyl groups, $\text{CH}_2=\text{C}$) were observed at 5.4-5.6 ppm in the GelMA

spectrum (2,27). This indicated that the methacrylic group was successfully connected to the gelatin. GelMA hydrogels were fabricated with different degrees of methacrylation (DM), which were calculated based on Equation 3 (14.3%, 28.6%, 71.4%, and 86%) by employing 4, 8, 12, and 20 mL of MA, respectively (16,27).

$$\text{Degree of methacrylation (DM) \%} = \frac{\text{Area under curve of GelMA signal at 2.9 ppm}}{\text{Area under curve of Gelatin signal at 2.9 ppm}} * 100 \quad (3)$$

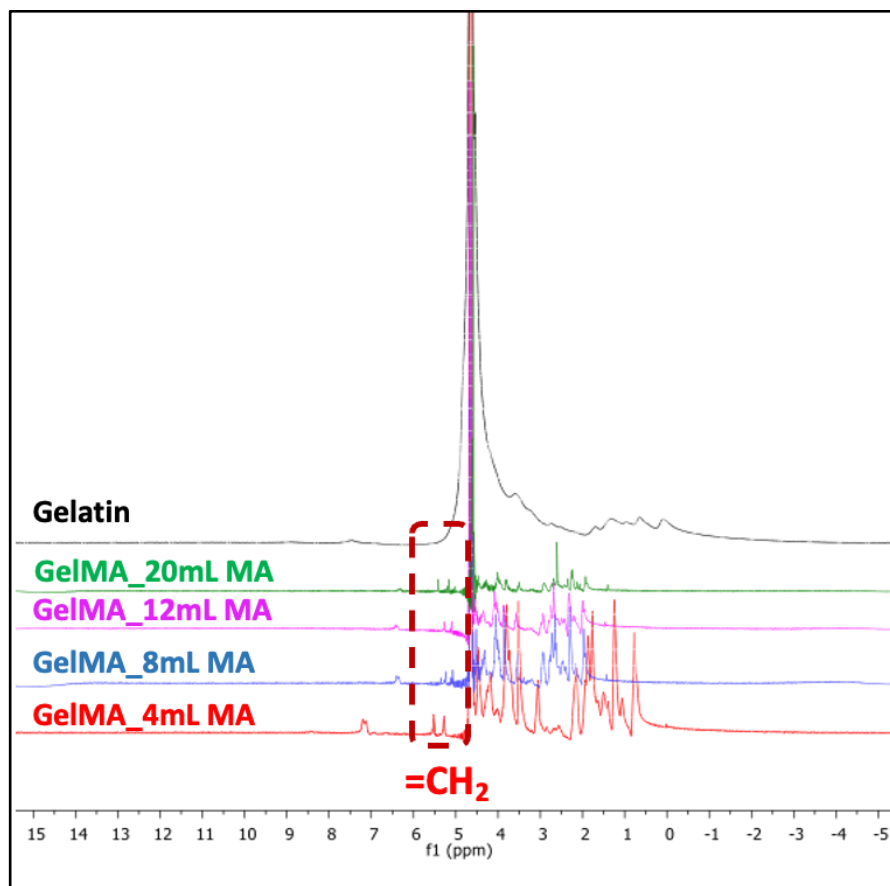


Figure 2: $^1\text{H-NMR}$ Analysis of pristine Gelatin and GelMA samples.

The morphological characterization, distribution, and variations in the porosities of the four hydrogels and samples are shown in Figure 3.

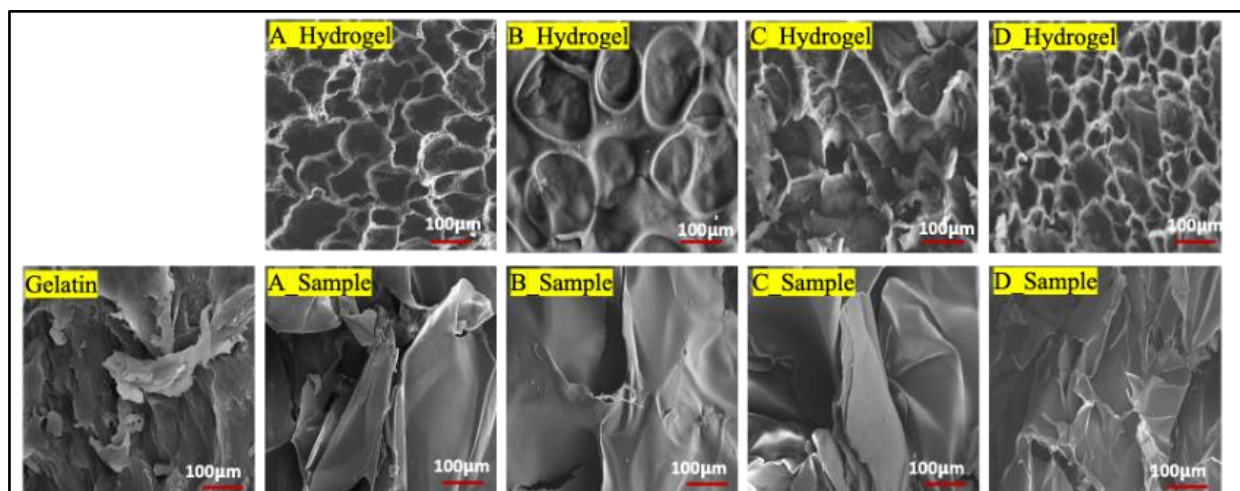


Figure 3: The SEM images of different amounts of methacrylated modified gelatin hydrogels (GelMA) (A-4 mL, B-8 mL, C-12 mL, D-20 mL) and samples (Gelatin, A-4 mL, B-8 mL, C-12 mL, D-20 mL).

The microstructure and porosity of the synthesized GelMA hydrogels and samples at four different MA concentrations (4 mL, 8 mL, 12 mL, and 20 mL) were investigated using SEM, as shown in Figure 3. The porosity of GelMA hydrogels is inversely correlated with GelMA concentration and cooling rate (23), and the hydrogel porosity can be controlled by adjusting the substitution amount of MA (24,28). According to the images in Figure 3, an increase in DM% does not result in any increase in porosity and uniformity.

The data collection is also explained in detail. Two datasets are obtained. Data were obtained at different methacrylation degrees and at different

times for the physical properties, which were separated by the swelling and degradation ratios of the GelMA biomaterials. For each specific time point, the average of six measurements was obtained and processed as one data point.

First, data processing was applied to model the degradation properties of the GelMA hydrogels. A panda library was imported to create a data frame (Figure 4). Subsequently, the degradation results were entered according to the time of the experiment and transferred to Python. Data processing was started to load the data into the Python environment.

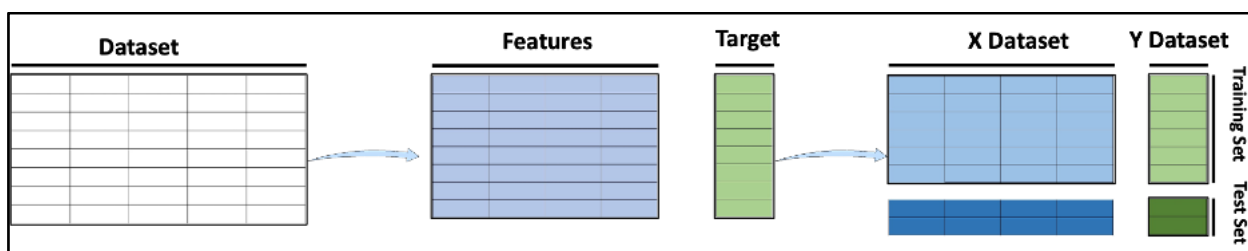


Figure 4: Train test data split.

The dataset was divided into variable data and columns to be predicted. Independent variables and allocated columns were divided into test and training data.

Actual and Predicted values are indicated. The data obtained from the application of the machine learning model are compared with the real values in Figure 5.

The graph for the degradation properties of the GelMA hydrogels was written in Python and was the result of the machine learning model. This helped us interpret the results of the model. Residuals were defined as the difference between observed and predicted values. A symmetric bell-shaped histogram, which was evenly distributed around zero, indicates that the normality assumption was likely to be true. Positive values on the y-axis indicate that the estimates were too low. Negative values indicated that the estimate was too high. A value of zero indicated that the prediction was correct.

The data obtained from the laboratory are presented in a table according to hours in Figure 5 (A). These values are written in Python. All Python codes used in this study are provided in detail in the Supplementary Information (EIS).

```
import pandas as pd
data = {
    'Hour': [1, 2, 3, 4, 5, 6, 7, 24, 168],
    '4ml': [19, 23, 22, 20, 19, 25, 20, 20, 23],
    '8ml': [23, 24, 24, 19, 26, 23, 23, 22, 23],
    '12ml': [20, 22, 20, 20, 16, 24, 22, 20, 22],
    '20ml': [15, 21, 17, 19, 15, 20, 22, 18, 15]
}
df = pd.DataFrame(data)
```

The train_test_split operation was used to split the data from the scikit-learn (sklearn) library. By

assigning "x" and "y" variables, train and test sets were separated for each variable. Our "X" variable must be an independent variables. Our "y" variable was the set of variables from which wanted to obtain results and from which predictions to be used in machine learning were created. When the dependent variable was separated from the independent variables while separating the data, it was called the "y" column because the prediction was made on target 20 (mL) data.

X_train: This was part of the learning of the values predicted by the model. This was used to understand the relationship between the data during the learning process of the model.

X_test: This allows data trained with independent variables to be tested to evaluate the performance of the model.

Y_train was used to measure the performance of the model. In the x_train section, the learned relationship was compared with y_train, and the success of the model was determined.

Y_test: Used together with "X_test" data to measure how well the model works and the success of its predictions. The model's success was calculated by comparing its predictions with "y_test" data (such as the mean square error (MSE)).

Test_size=0.4 means 60% train and 40% reserved for test.

When Random_state is not defined in the code for each run, the results may vary. When the random_state = "constant integer" was entered, the training data were constant for each run.

```
from sklearn.model_selection import train_test_split
X = df.drop(['Hour', '20ml'], axis=1)
```

```
y = df['20ml']
X_train, X_test, y_train, y_test = train_test_split(X,
y, test_size=0.4, random_state=42)
```

Scaling was used to scale the features in the dataset and to improve the performance of the model. The main purpose was to transfer data to a specific range, such as between 0 and 1 or between -1 and 1 (29).

```
from sklearn.preprocessing import MinMaxScaler
scaler = MinMaxScaler()
X_normalized = scaler.fit_transform(X)
X_normalized = pd.DataFrame(X_normalized,
columns= X columns).
```

In decision tree modeling, specifically the chosen empirical tree model, data are partitioned using a repeated division method (30). A regression model was selected because of its ability to explore the relationships between the dependent variable and a series of independent variables. The code sequence used to implement the model is outlined below:

```
from sklearn.tree import DecisionTreeRegressor
model = DecisionTreeRegressor()
```

One of the factors that enhanced the model's performance was the hyperparameter setting (1). A key reason for using this method is its efficiency in handling large numbers of hyperparameters, particularly in complex datasets, thereby reducing time loss. Hyperparameter tuning has been

employed in tree-based machine learning models and deep neural network modeling. The grid search method, a common approach in hyperparameter tuning, involves creating hyperparameter values on a preset grid and then using and validating the model for each combination. Consequently, combinations of hyperparameters that yielded the highest model performance were identified (31). This process was automated using Scikit-learn's GridSearchCV, which facilitated selection and implementation of the best model.

```
from sklearn.model_selection import GridSearchCV
param_grid = {'max_depth': [None, 5, 10, 15, 20,
25],
'min_samples_split': [2, 5, 10],
'min_samples_leaf': [1, 2, 4]}
grid_search = GridSearchCV(model, param_grid,
cv=5, scoring='neg_mean_squared_error')
grid_search.fit(X_train_normalized, y_train)
best_model = grid_search.best_estimator_
```

Values were printed on the screen in this way to observe the actual and estimated values at 20 mL according to the hours in:

Output:
Hours: 24, Actual 20ml: 18, Predicted 20ml: 18.666666666666668
Hours: 2, Actual 20ml: 21, Predicted 20ml: 16.0
Hours: 6, Actual 20ml: 20, Predicted 20ml: 18.666666666666668
Hours: 1, Actual 20ml: 15, Predicted 20ml: 18.666666666666668

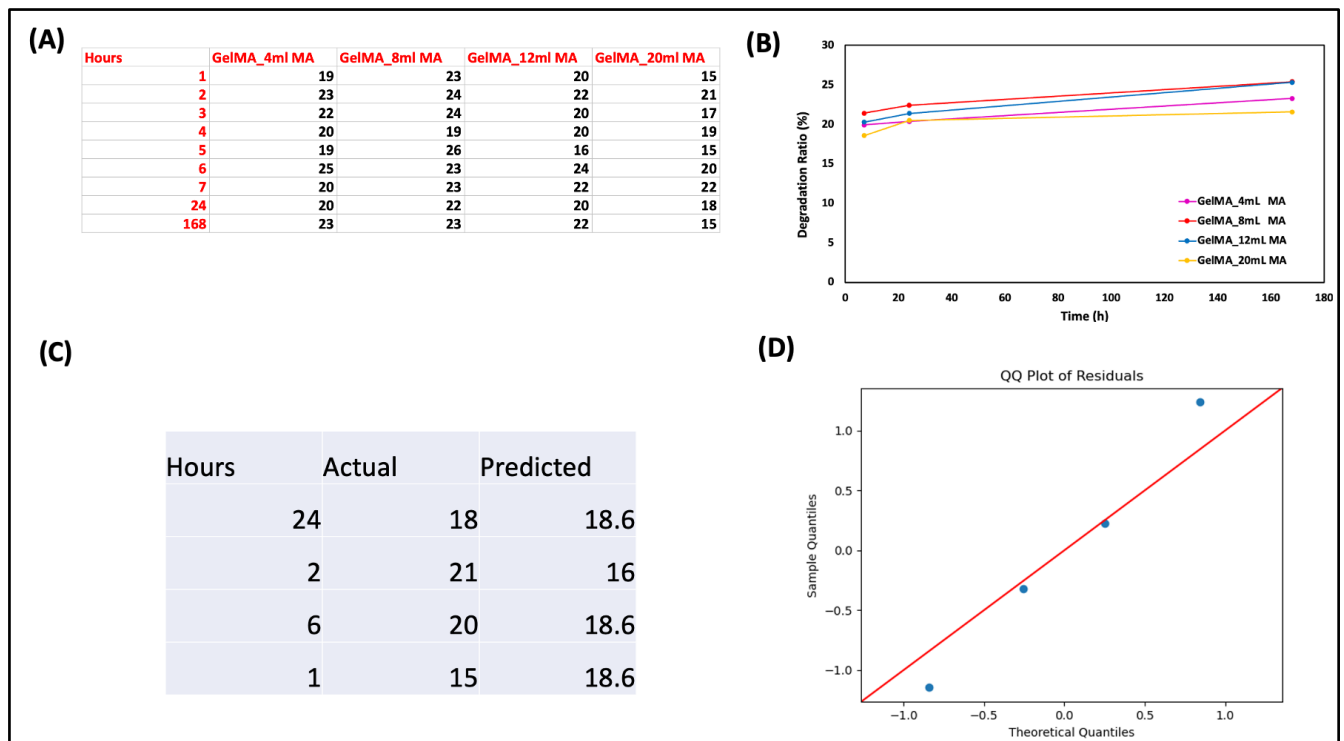


Figure 5: Degradation data (A) and ratios (%) (B) were obtained according to time. Actual and Predicted Values (C). QQ Plot of Residuals (D).

A Q-Q Plot of residuals was used to assess whether the residuals were normally distributed. Ideally, these points should be close to the line. In the QQ Plot of Residuals, the percentiles of the theoretical normal distribution are on the x-axis, and the

percentiles of the model's errors are on the y-axis. The histogram (Figure 5 (D)) shows the spread and evaluation of its success.

Second, data processing was applied to model the swelling properties of the GelMA hydrogels. The results of the swelling physical measurements were modeled by making inferences from the machine learning performed in the degradation physical measurement. Physical measurement of swelling was based on the results of the two methacrylation degrees and hours.

Actual and Predicted values are indicated. After machine learning modeling was performed to observe the results, the y_{test} set was estimated. The results were compared with real values, as shown in Figure 6.

Data Pre-processing began by importing the pandas library. The data obtained from the experiment were written in the form of a data frame according to the given time (Figure 6 (A)).

```
import pandas as pd
data = {
    'Hour': [1, 2, 3, 4, 5, 6, 7, 24, 168, 336],
```

```
'4ml': [225, 230, 234, 319, 250, 288, 274, 242,
276, 274],
'8ml': [199, 219, 229, 253, 202, 243, 193, 224,
228, 238],
'12ml': [199, 190, 227, 180, 220, 182, 202, 279,
299, 325],
'20ml': [255, 304, 293, 307, 261, 381, 276, 208,
250, 225]
}
df = pd.DataFrame(data)
```

After applying the model, the results were printed on the screen to compare the predicted values for 20 mL with the actual values according to the given hours. In addition, these values are listed in the table for comparison and observation.

Output: Actual vs Predicted 20 mL Values:
Hours: 168, Actual 20ml: 250, Predicted 20ml: 208.0
Hours: 2, Actual 20ml: 304, Predicted 20ml: 307.0
Hours: 6, Actual 20ml: 381, Predicted 20ml: 307.0
Hours: 1, Actual 20ml: 255, Predicted 20ml: 261.0

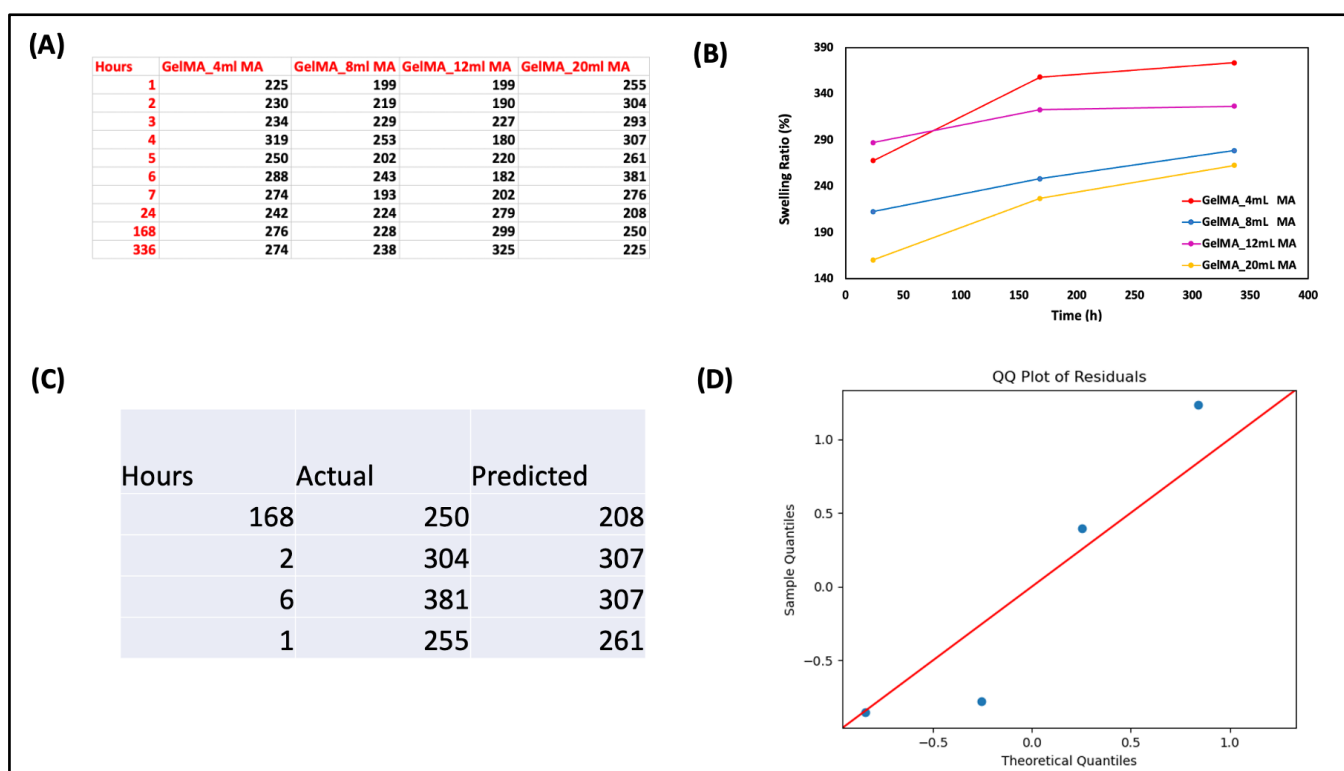


Figure 6: Swelling data (A) and ratios (%) (B) were obtained according to time. Actual and Predicted Values (C). QQ Plot of Residuals (D).

While designing this study, we asked the following questions.

- How does the variation in methacrylation amount during GelMA synthesis affect the physical changes in the GelMA molecule structure?
- Can hydrogel-based materials be designed using machine learning?
- Can a machine learning algorithm be created by creating a GelMA synthesis dataset?

We hypothesized that increasing and/or decreasing the amount of methacrylamide in the GelMA hydrogel would alter the physical properties of the prepared hydrogel. A model developed using machine learning

methods can predict the physical properties of a hydrogel by taking the amount of methacrylic anhydride in the GelMA hydrogel as input.

In this study, multiple independent variables (features) were obtained from different degrees of methacrylation in the dataset. Different datasets for the physical properties, swelling, and degradation were created and evaluated using different models. When many machine learning models were compared for degradation measurements, their performance was determined using the Mean Squared Error (MSE) (32). All details are included in the Supplementary Information (ESI). The MSE is the

difference between the actual and predicted values, and the square of the errors is calculated; thus, the performance of the regression model is calculated. Many methods can be used to measure model performance; examples of these methods include Mean Square Error (MSE), Root Mean Squared Error (RMSE), Mean Absolute Error (MAE), and Mean Absolute Percentage Error (MAPE). In this study, the calculations were performed using the MSE value. MSE is the mean of the squares of the errors, that is, the difference between the actual and predicted values (4). It is expected that the resulting amount of data will not be very high. It is understood that performance is good when the result is close to zero. For the RMSE and MAPE performance results, z' was the predicted value. z is the measured value, and N is the total number of observations. The lowest RMSE value indicated the highest performance (33,34). For the MAPE calculation, the performance result is obtained as a percentage, and a low percentage is a measure of good performance (35,36). MAE properties are commonly referred to as absolute errors (5).

When the data structure was observed, there were four different variables, and each variable had nine data points for the degradation results. In addition, there were four different variables, and each variable had 10 data points for the swelling results. The most suitable model for this dataset is the decision tree regressor (31,37). This modeling was performed to create predictions of 20 mL. The prediction output was obtained as a result of four data modeling from column 20 mL. After the modeling was applied, the MSE values were checked to evaluate the performance.

It should be noted that this dataset was small. The present research aims to demonstrate how the applications aimed in this study can be carried out. As this was a small dataset, it was anticipated that the margin of error would be high. This study aimed to demonstrate the applicability of modeling and obtain prediction results.

Scaling and hyperparameter adjustments were performed in Python to minimize the errors made by the model and avoid overfitting. The MSE, RMSE, MAE, and MAPE were evaluated based on a hyperparameter application to test the performance of the model.

4. CONCLUSION

This study aimed to measure the physical properties according to different degrees of methacrylation, create a dataset with the results, and interpret them by modeling them using machine learning. Swelling and degradation data were experimentally collected for each degree of methacrylation. For four different degrees of methacrylation (four distinct variables), 10 data points were used in the swelling studies, whereas nine data points were used in the degradation studies. Experimental results were initially obtained using a 20 mL methacrylation degree as a sample. Subsequently, the results were presented by comparing the experimental data with

machine learning data for the 20 mL methacrylation degree. After determining the predicted values, a decision tree regressor was applied, which was selected as the appropriate model. Performance metrics were calculated to assess the accuracy of the results. To visualize the model's outcomes, the predicted values were observed, and graphs were generated. Following data processing and partitioning, a machine-learning model was applied. The performance metrics were computed after the implementation of the model. To visually interpret the results, a graph displaying the actual versus the predicted values was generated. Numerically, predicted and actual values were documented in code, facilitating result analysis.

As a result, the degradation and swelling physical properties of the GelMA biomaterial for different degrees of methacrylation were experimentally studied, and data were obtained. The obtained data were compared with experimental results using machine learning and decision tree regression for a 20 mL methacrylation degree. The Mean Squared Error (MSE) value for degradation was calculated as 10.16, with a Root Mean Squared Error (RMSE) of 3.1885, Mean Absolute Error (MAE) of 2.6667, and Mean Absolute Percentage Error (MAPE) of 14.66%. For swelling, the MSE value was calculated to be 1821.25, with an RMSE of 3.1885, MAE of 2.6667, and MAPE of 14.66%. In future studies, it is anticipated that the performance of the model will improve with the expansion of the experimental dataset for swelling measurements. When the results were compared, it was determined that the accuracy of the study increased as the experimental dataset increased. As the number of data points increases, the resulting performance increases. In addition, it is important to avoid overfitting in machine learning, that is, the situation in which machine learning imitates the data exactly.

5. CONFLICT OF INTEREST

The authors declare that they have no affiliations with or involvement in any organization or entity with any financial interest in the subject matter or materials discussed in this manuscript.

6. ACKNOWLEDGMENTS

The TUBITAK 2209-A University Student Research Project Support Program supported this study. Project number: 1919B012307651.

7. DATA ACCESS STATEMENT

Research data supporting this publication are available from the Visual Studio Code, Python, and Conda repositories located at <https://code.visualstudio.com/download>.

8. REFERENCES

1. Meyer TA, Ramirez C, Tamasi MJ, Gormley AJ. A user's guide to machine learning for polymeric biomaterials. ACS Polym Au [Internet]. 2023 Apr 12;3(2):141–57. Available from: [<URL>](#).

2. Tutar R, Koken SY, Tuncaboşlu DC, Çelebi-Saltık B, Özeroğlu C. In situ formation of biocompatible and ductile protein-based hydrogels via Michael addition reaction and visible light crosslinking. *New J Chem* [Internet]. 2023;47(22):10759–69. Available from: [<URL>](#).
3. Basu B, Gowtham NH, Xiao Y, Kalidindi SR, Leong KW. Biomaterialomics: Data science-driven pathways to develop fourth-generation biomaterials. *Acta Biomater* [Internet]. 2022 Apr;143:1–25. Available from: [<URL>](#).
4. Greener JG, Kandathil SM, Moffat L, Jones DT. A guide to machine learning for biologists. *Nat Rev Mol Cell Biol* [Internet]. 2022 Jan 13;23(1):40–55. Available from: [<URL>](#).
5. Inza I, Calvo B, Armañanzas R, Bengoetxea E, Larrañaga P, Lozano JA. Machine learning: An indispensable tool in bioinformatics. In 2010. p. 25–48. Available from: [<URL>](#).
6. Peng GCY, Alber M, Buganza Tepole A, Cannon WR, De S, Dura-Bernal S, et al. Multiscale modeling meets machine learning: What can we learn? *Arch Comput Methods Eng* [Internet]. 2021 May 17;28(3):1017–37. Available from: [<URL>](#).
7. Castelli V, Cover TM. On the exponential value of labeled samples. *Pattern Recognit Lett* [Internet]. 1995 Jan 1;16(1):105–11. Available from: [<URL>](#).
8. Reddy YCAP, Viswanath P, Reddy BE. Semi-supervised learning: a brief review. *Int J Eng & Technology* [Internet]. 2018;7(1):81–5. Available from: [<URL>](#).
9. Li Y. Deep Reinforcement Learning: An Overview [Internet]. 2017. 85 p. Available from: [<URL>](#).
10. Ayodele TO. Types of Machine Learning Algorithms. In: *New Advances in Machine Learning* [Internet]. InTech; 2010. Available from: [<URL>](#).
11. Mahesh B. Machine learning algorithms - A review. *Int J Sci Res* [Internet]. 2020 Jan 5;9(1):381–6. Available from: [<URL>](#).
12. Aery MK, Ram C. A review on machine learning: Trends and future prospects. *An Int J Eng Sci* [Internet]. 2017;25:89–96. Available from: [<URL>](#).
13. Pathak S, Mishra I, Swetapadma A. An assessment of decision tree based classification and regression algorithms. In: *Proceedings of the International Conference on Inventive Computation Technologies (ICICT-2018)* [Internet]. 2018. p. 92–5. Available from: [<URL>](#).
14. Myles AJ, Feudale RN, Liu Y, Woody NA, Brown SD. An introduction to decision tree modeling. *J Chemom* [Internet]. 2004 Jun 4;18(6):275–85. Available from: [<URL>](#).
15. Süren SM, Tutar R, Özeroğlu C, Karakuş S. Versatile multi-network hydrogel of acrylamide, sodium vinyl sulfonate, and N,N'-methylene bisacrylamide: A sustainable solution for paracetamol removal and swelling behavior. *J Polym Environ* [Internet]. 2024 Jan 20;32(1):164–81. Available from: [<URL>](#).
16. Tavafooghi M, Sheikhi A, Tutar R, Jahangiry J, Baidya A, Haghniaz R, et al. Engineering tough, injectable, naturally derived, bioadhesive composite hydrogels. *Adv Healthc Mater* [Internet]. 2020 May 24;9(10):1901722. Available from: [<URL>](#).
17. Van Den Bulcke AI, Bogdanov B, De Rooze N, Schacht EH, Cornelissen M, Berghmans H. Structural and rheological properties of methacrylamide modified gelatin hydrogels. *Biomacromolecules* [Internet]. 2000 Mar 14;1(1):31–8. Available from: [<URL>](#).
18. Nichol JW, Koshy ST, Bae H, Hwang CM, Yamanlar S, Khademhosseini A. Cell-laden microengineered gelatin methacrylate hydrogels. *Biomaterials* [Internet]. 2010 Jul;31(21):5536–44. Available from: [<URL>](#).
19. He J, Sun Y, Gao Q, He C, Yao K, Wang T, et al. Gelatin methacryloyl hydrogel, from standardization, performance, to biomedical application. *Adv Healthc Mater* [Internet]. 2023 Sep 15;12(23):2300395. Available from: [<URL>](#).
20. Noshadi I, Hong S, Sullivan KE, Shirzaei Sani E, Portillo-Lara R, Tamayol A, et al. In vitro and in vivo analysis of visible light crosslinkable gelatin methacryloyl (GelMA) hydrogels. *Biomater Sci* [Internet]. 2017;5(10):2093–105. Available from: [<URL>](#).
21. O'Connell CD, Zhang B, Onofrillo C, Duchi S, Blanchard R, Quigley A, et al. Tailoring the mechanical properties of gelatin methacryloyl hydrogels through manipulation of the photocrosslinking conditions. *Soft Matter* [Internet]. 2018;14(11):2142–51. Available from: [<URL>](#).
22. Karaoglu IC, Kebabci AO, Kizilel S. Optimization of gelatin methacryloyl hydrogel properties through an artificial neural network model. *ACS Appl Mater Interfaces* [Internet]. 2023 Sep 27;15(38):44796–808. Available from: [<URL>](#).
23. Van Vlierberghe S, Dubruel P, Schacht E. Effect of cryogenic treatment on the rheological properties of gelatin hydrogels. *J Bioact Compat Polym* [Internet]. 2010 Sep 4;25(5):498–512. Available from: [<URL>](#).
24. Chen Y, Lin R, Qi H, Yang Y, Bae H, Melero-Martin JM, et al. Functional human vascular network generated in photocrosslinkable gelatin methacrylate hydrogels. *Adv Funct Mater* [Internet]. 2012 May 23;22(10):2027–39. Available from: [<URL>](#).
25. Tutar R, Yüce-Erarslan E, İzbudak B, Bal-Öztürk A. Photocurable silk fibroin-based tissue sealants with enhanced adhesive properties for the treatment of corneal perforations. *J Mater Chem B* [Internet]. 2022;10(15):2912–25. Available from: [<URL>](#).
26. Rahali K, Ben Messaoud G, Kahn C, Sanchez-Gonzalez L, Kaci M, Cleymand F, et al. Synthesis and

- characterization of nanofunctionalized gelatin methacrylate hydrogels. *Int J Mol Sci* [Internet]. 2017 Dec 10;18(12):2675. Available from: [<URL>](#).
27. Claaßen C, Claaßen MH, Truffault V, Sewald L, Tovar GEM, Borchers K, et al. Quantification of substitution of gelatin methacryloyl: Best practice and current pitfalls. *Biomacromolecules* [Internet]. 2018 Jan 8;19(1):42–52. Available from: [<URL>](#).
28. Lee Y, Lee JM, Bae P, Chung IY, Chung BH, Chung BG. Photo-crosslinkable hydrogel-based 3D microfluidic culture device. *Electrophoresis* [Internet]. 2015 Apr 24;36(7–8):994–1001. Available from: [<URL>](#).
29. Jamal P, Ali M, Faraj RH, Ali PJM, Faraj RH. Data normalization and standardization: A technical report. *Mach Learn Tech Reports* [Internet]. 2014;1(1):1–6. Available from: [<URL>](#).
30. Tso GKF, Yau KKW. Predicting electricity energy consumption: A comparison of regression analysis, decision tree and neural networks. *Energy* [Internet]. 2007 Sep;32(9):1761–8. Available from: [<URL>](#).
31. Yang L, Shami A. On hyperparameter optimization of machine learning algorithms: Theory and practice. *Neurocomputing* [Internet]. 2020 Nov;415:295–316. Available from: [<URL>](#).
32. Hodson TO. Root-mean-square error (RMSE) or mean absolute error (MAE): when to use them or not. *Geosci Model Dev* [Internet]. 2022 Jul 19;15(14):5481–7. Available from: [<URL>](#).
33. Polat K, Güneş S. Automatic determination of diseases related to lymph system from lymphography data using principles component analysis (PCA), fuzzy weighting pre-processing and ANFIS. *Expert Syst Appl* [Internet]. 2007 Oct;33(3):636–41. Available from: [<URL>](#).
34. İnal M. Determination of dielectric properties of insulator materials by means of ANFIS: A comparative study. *J Mater Process Technol* [Internet]. 2008 Jan;195(1–3):34–43. Available from: [<URL>](#).
35. Amid S, Mesri Gundoshmian T. Prediction of output energies for broiler production using linear regression, ANN (MLP, RBF), and ANFIS models. *Environ Prog Sustain Energy* [Internet]. 2017 Mar 7;36(2):577–85. Available from: [<URL>](#).
36. Willmott CJ, Matsuura K. Advantages of the mean absolute error (MAE) over the root mean square error (RMSE) in assessing average model performance. *Clim Res* [Internet]. 2005 Dec 19;30(1):79–82. Available from: [<URL>](#).
37. Loh W. Classification and regression trees. *WIREs Data Min Knowl Discov* [Internet]. 2011 Jan 6;1(1):14–23. Available from: [<URL>](#).



Assessment of Biochemical Changes of Four *Aspergillus* Species Grown on the Medium from Agricultural Wastes

Nadia Khuder^{1*} , Adnan Ali-Nizam¹ 

¹Damascus university, Department of plant biology, Faculty of science, Damascus, Syrian Arab Republic.

Abstract: Hazardous disposal of agricultural wastes (AW) has adverse environmental consequences, including water and air pollution and the potential for disease outbreaks. On the other hand, the utilization of AW represents a missed opportunity to harness a valuable economic resource. This study was conducted with the objective of utilizing a composite medium comprising agricultural waste to cultivate *Aspergillus* species and assessing its impact on the species' internal chemical composition compared to malt extract media (ME). Our findings demonstrate that the agricultural waste-based medium is abundant in essential nutrients, including soluble proteins and sugars, and is also enriched with a variety of secondary metabolites. Consequently, this change in the growth medium induces changes in the physical characteristics of fungal biomass, such as color and texture, along with a high content of biomass proteins and secondary metabolites, including phenols, flavonoids, carotenoids, and antioxidants. The *A. avenaceus* gave the highest biomass (1.1412 ± 0.4 g), while the *A. niger* gave the highest value of proteins (16.06 ± 0.4 mg/g), phenols (33.37 ± 0.8 mg/g), flavonoids (4.84 ± 0.4 mg/g), carotenoids (1.131 ± 0.09 mg/g). *A. carbonarius* gave the highest value of antioxidants ($IC_{50} = 0.28 \pm 0.06$ mg/mL). In contrast, using malt extract as a growth medium results in high carbohydrate and lipid production; *A. flavus* showed the highest value for fats (56.6 ± 0.9 mg/g), whereas *A. carbonarius* showed the highest value for sugars (167.1 ± 6.2 mg/g). Additionally, the malt extract medium contributed to low levels of secondary metabolites, which was offset by an increase in the protein bands of the fungal species. This research recommends the use of agricultural wastes to grow fungi species as an environmentally and economically important microbiological application.

Keywords: Agricultural waste, Medium, *Aspergillus*, Secondary metabolites.

Submitted: October 19, 2023. **Accepted:** June 5, 2024.

Cite this: Khuder N, Ali-Nizam A. Assessment of Biochemical Changes of Four *Aspergillus* Species Grown on the Medium from Agricultural Wastes. JOTCSA. 2024;11(3): 1287-96.

DOI: <https://doi.org/10.18596/jotcsa.1378393>

***Corresponding author's E-mail:** nadia.khuder@damascusuniversity.edu.sy

1. INTRODUCTION

Beyond the immediate concerns related to waste disposal and the mitigation of visual and olfactory nuisances, environmentalists are deeply preoccupied with the overarching issue of ecological damage affecting our forests, terrestrial landscapes, and crucial water resources. This concern is underscored by historical records, notably from 1967 and 1969, when agricultural practices emerged as the second most substantial source of pollution, primarily evidenced by significant fish mortality. Notably, the culpability did not predominantly rest with fertilizers but rather with insecticides and food production processes, which not only compromised water quality but also catalyzed the propagation of diseases within adjacent regions. This historical perspective amplifies the urgency of addressing these multifaceted environmental challenges and

underscores the imperative of seeking more sustainable solutions (1).

A significant quantity of agricultural residues resulting from crop cultivation and food processing, including materials like straw, cobs, and remnants from fruit and vegetable processing, is regularly produced. The methods used for managing, treating, and disposing of these agricultural wastes have the potential to negatively impact the quality of air, water, and soil. Unfortunately, a substantial portion of these waste materials is presently disposed of in landfills or released into rivers, thus causing notable environmental hazards (2).

Plant biomass serves as a fundamental feedstock for various industrial applications due to its richness in lignocellulosic materials and other valuable compounds. These resources can be effectively

harnessed through physical, chemical, and biotechnological treatments. As a result of these processes, a range of useful products can be derived, including extracts with applications in the food and pharmaceutical industries and platform chemicals such as organic acids produced through fermentation, biofuels, energy sources, and fiber residues suitable for use in bio-composite materials (3).

Biological waste treatment processes involve a blend of microorganisms with the ability to break down organic waste materials. Within certain bounds, these microorganisms can adapt to fluctuating organic loads and environmental factors like temperature and pH levels. However, the presence of extreme temperatures, elevated concentrations of metal ions, or toxic chemicals can impede or entirely inhibit their activity.

The composition of microorganisms in different biological treatment systems varies and can encompass bacteria, fungi, algae, protozoa, rotifers, Crustacea, bacteriophage, worms, and insect larvae, depending on the prevailing environmental conditions (4,5).

Fungi are truly remarkable organisms found in diverse ecosystems, exhibiting the ability to thrive on both living and deceased organic matter, including agricultural plant residues and municipal solid waste. Many fungi are adept at colonizing solid substrates, secreting extracellular enzymes to break them down, and subsequently reabsorbing the resulting nutrients through their fungal hyphae (6).

Aspergillus species are among the first fungal organisms cultivated on artificial media and studied for their biochemical properties. They inhabit a wide range of environments, with some being common saprophytes in the soil while others are found on stored food items (7). These species are known for producing a diverse array of secondary metabolites that are of industrial significance and therapeutic relevance, including antibiotics and lovastatin. As a result, they have garnered considerable attention within the scientific research community (8).

Given their filamentous nature, extrinsic factors such as water availability, temperature, pH levels, and the composition of the nutrient medium exert a substantial influence on the growth and biosynthesis of secondary metabolites in *Aspergillus* species (9).

In our research, we investigated the chemical composition of a specially formulated agricultural waste medium. We then examined how this medium affected the growth of *Aspergillus* species, their biomass production, and the physical characteristics of their hyphae. Furthermore, we assessed its impact on the efficiency of primary and secondary metabolite production, drawing comparisons with a commonly used commercial malt extract medium.

2. EXPERIMENTAL SECTION

2.1. Collection and Preparation of Agricultural Waste

Agricultural waste materials were collected, including potatoes, eggplant fruit, zucchini fruit, orange peels, corn peels, bean pod peels, bean leaves, and bean stems. To prepare these materials, they underwent a series of steps: first, they were thoroughly washed, followed by drying and chopping into smaller pieces. Subsequently, the chopped materials were allowed to air-dry in the shade. Once sufficiently dried, samples were finely ground using an electric mixer, sieved to ensure uniformity, and then stored in plastic bags at room temperature in a dry environment for future use (10).

2.2. Chemical Analysis and Preparation of Agricultural Waste Medium

The agricultural waste (AW) medium was meticulously prepared as follows: 2 grams of each plant powder were added to 500 mL of distilled water, and the mixture was then sterilized using an Autoclave. After sterilization, the medium underwent filtration, and its pH was carefully measured and adjusted to 5.6 before undergoing another round of sterilization. To determine the protein content of the medium, the Bradford assay method was used by the Coomassie blue detector; the bovine serum albumin was employed to make the standard curve (11). The phenol sulfuric acid method was employed for the assessment of soluble sugars, as described by Dubois et al. in 1956. The glucose equivalent was utilized to establish the standard curve for this purpose (12).

The total phenol content was quantified by adding 1 mL of medium broth to 0.5 mL of 50% Folin-Ciocalteu and 1.5 mL of 20% Na₂CO₃, with the final volume adjusted to 5 mL using distilled water (13). The samples were then incubated in darkness for one hour, and their absorbance was subsequently measured at 760 nanometers. The gallic acid equivalent was employed to construct the standard curve.

Lastly, the concentration of dissolved salts was determined using a pH meter. For comparative purposes, the same analytical procedures were applied to the Malt (M) medium broth (14).

2.3. Fungal Strains Used

The *Aspergillus* strains employed in this study were originally sourced from the soil of pine forests in Syria. 1 g of the soil was diluted in 99 mL distilled sterile water. Several dilutions were prepared to get ⁵10 concentrations. 1 mL of ⁵10 solution was grown on a potato dextrose agar (PDA) petri dish and incubated at 28°C for three days. This process was repeated several times. The genus *Aspergillus* was verified based on colony characteristics and microscopic characteristics. These strains underwent a purification process and were ultimately cultivated Malt extract agar and subjected to an identification protocol as per established methods (15,16).

2.4. Preparation of Fungi Culture

The *Aspergillus* species were grown on PDA for about one week at 28 ± 2 °C. The spore suspension was collected in tween 0.05% and was enumerated by a qualified hemocytometer.

1 mL spore suspension of each fungal strain (10^6 spores/mL) was added to 1 L of agricultural waste broth medium and malt extract broth medium (17).

The medium was put at 28 °C while shaking at 150 rpm for three days. The Fungal biomass was separated, water-washed, and oven-dried at 100 °C until constant weight had been reached. Dry Fungal biomass was crushed in a mortar and then Stored in a -80°C freezer (18).

2.5. Preparation and Extraction of Fungal Metabolites

500 mL of 80% methanol was Added to fungal biomass and sonicated in an ultrasonic bath sonicator for 180 min. After that, the samples were stirred vigorously for two days by using a magnetic stir bar and magnetic stirrer. The extracts were filtered with vacuum filtration and evaporated in a rotary evaporator, then put into a pre-weighed 20 mL glass vial. The weight of the dried samples was obtained using a scale to calculate the yield in mg. The dried extract was stored in a -20 °C freezer (19).

2.6. Determination of Total Sugar (Carbohydrate) and Total Phenols in Fungal Extract

The carbohydrate content was determined by the phenol sulphuric acid method, and the phenol content was determined by the Folin-Ciocalteu method.

2.7. Determination of Total Flavonoids in Fungal Extract

The TFC of the fungal extracts was determined by an aluminum chloride colorimetric assay. 500 μL of methanolic extract 80% was added to 150 μL of NaNO_3 5% and incubated in the dark for 5 minutes. One hundred fifty microliters of AlCl_3 10% were added to the extract and incubated in the dark for 6 minutes. 1 mL of NaOH 1M was added and incubated for 15 minutes in the dark. The absorbance of each mixture was determined at 510 nm. Quercetin equivalent was employed to make the standard curve (20).

2.8. Determination of Total Carotenoids in Fungal Extract

The fungal extract was diluted in methanol absolute to get a concentration of 1 mg/mL; chlorophyll a, chlorophyll b, and total carotenoids were determined by the following equation using a spectrophotometer resolution range 1-4 nm:

$$C_a = 15.65 A_{666} - 7.34 A_{653} \quad (\text{Eq. 1})$$

$$C_b = 27.05 A_{653} - 11.21 A_{666} \quad (\text{Eq. 2})$$

$$C_{x+c} = (1000 A_{470} - 2.86 C_a - 129.2 C_b)/221 \quad (\text{Eq. 3})$$

C_a is total chlorophyll a, C_b is total chlorophyll b, and C_{x+c} is total carotenoids by concentration $\mu\text{g/mL}$ (21).

2.9. Determination of DPPH Radical-scavenging Activity in Fungal Extract

A series of the different concentrations (0.1 – 2 mg/mL) of each methanolic extract 80% was prepared, and 200 μL of the fungal extract was added to 2 mL of 1, 1- diphenyl-2-picryl hydrazyl (DPPH) reagent. The samples were incubated in the dark for 30 minutes; the absorbance was measured at 517 nm. The ability to scavenge the DPPH radical was calculated using the following equation: DPPH scavenging effect (%) = $((A_0 - A_1/A_0) \times 100)$, where A_0 was the absorbance of the control reaction, and A_1 was the absorbance in the presence of the sample. The percentage of scavenging activity obtained was subsequently plotted against the sample concentration. The IC_{50} value, defined as the amount of antioxidant necessary to decrease the initial DPPH concentration by 50%, was calculated from the results and used for comparison. A lower value of IC_{50} indicates a higher efficiency of scavenging free radicals. The results were compared to Ascorbic acid (Vitamin C), which was prepared as standard with different concentrations (0.01, 0.02, 0.03, 0.04, 0.05 mg/mL) (22).

2.10. Preparing of Crude Extracts and Measuring of Protein Values

The Tris-HCl 6.8 0.5 M with phenylmethylsulphonyl fluoride (PMSF) 0.5 mM was prepared. 1 mL of this solution was added to 0.5 g of fungal biomass. Then, the biomass was crushed in a mortar. The crude extracts were separated from the cell walls, remaining by centrifugation at 25000 rpm for 30 min, and then were processed through three stages. The protein content was determined using Bradford's method. The bovine serum albumin was employed to make the standard curve. The supernatants were kept in microtubes in a -20 °C freezer (23).

2.11. Sodium Dodecyl Sulphate-polyacrylamide Gel Electrophoresis

The fungal protein extracts were analyzed using the SDS-PAGE method with %13 separating gel and %4 stacking gel (Sigma) at a constant voltage of 90 V for one hour and 120 V for two hours.

The extracts were boiled for 5 min with a loading buffer containing 4% sodium dodecyl sulfate (SDS), 20% glycerol, 10% 2-mercaptoethanol, 0.004% Bromophenol Blue, and 0.125 mol/L Tris-HCl 6.8.

35 μL of each sample was loaded on a gel. Along with the standard protein marker (blue plus, trance. China). The gel was stained with 0.25% Coomassie Brilliant blue R 250 (Sigma) (24).

2.12. Determination of Total Lipids

The fungal biomass was prepared for extraction by grinding the dried material into a powder using a mill. For hexane extraction, 300 mL of n-hexane was added to 4 grams of fungal biomass powder. Conical flasks were sealed with aluminum foil to prevent solvent evaporation. Then, all extraction mixtures

were subjected to one hour of sonication using an ultrasonic bath sonicator. Following sonication, they were agitated at 200 rotations per minute at room temperature for 24 hours.

To remove cellular residue, the mixture was centrifuged at 25,000 rotations per minute for 30 minutes. The hexane phase was collected and evaporated in a rotary evaporator, and each extract was collected in a pre-weighed flask. The flask was subsequently heated to dryness in an oven at 60°C to enable gravimetric quantification of the lipid extract.

The resulting crude lipid was re-dissolved in hexane and transferred into a sealed glass vial for storage in a -20 °C freezer (25).

2.13. Statistical Analyses

Data were analyzed using the IBM SPSS Statistics software (Version 22.0)—the experimental design involved four groups. To investigate the effects of two factors (independent variables) and their interaction with the dependent variable, a two-way Analysis of Variance (ANOVA) was performed. This statistical approach is ideal for understanding how each factor contributes to the observed outcomes and whether their effects are independent or interactive. Results were deemed statistically significant at a p-value less than 0.05. All data are reported as means \pm standard deviations (SDs).

3. RESULTS AND DISCUSSION

The agricultural waste medium exhibited a dark brown color with a pH of 5.8, while the malt extract medium was a transparent yellow with a pH of 5.5. The agricultural medium was rich in nutrients, containing significant amounts of soluble proteins and sugars, as well as a high concentration of salts and plant-derived secondary metabolites such as phenols (see Table 1) (26). In contrast, the malt medium had slightly higher levels of soluble sugars and proteins but lower concentrations of salts and phenols (Table 1). Statistical analysis revealed significant differences in the average chemical compositions of the two media ($p < 0.001$).

These variations in medium composition influenced the growth characteristics of the fungi. Four fungal species were identified through macroscopic observations (colony diameter and color) and microscopic examinations (vesicle, metula, phialides, and conidia shapes and sizes): *Aspergillus niger*, *Aspergillus flavus*, *Aspergillus carbonarius*, and *Aspergillus avenaceus* (16). Both media supported robust fungal growth, resulting in significant biomass production with noticeable differences in color and texture (27). The fungi on malt medium generally showed light, creamy colors with a cohesive, rubbery texture, whereas those on agricultural waste were darker and more fragile (see Figure 1).

Table 1: Chemical composition of the tested media.

Medium g/L	Protein	Sugars soluble	Phenols	Dissolved salts ($\mu\text{g/cm}$)
ME	0.17 \pm 0.01	2.9 \pm 0.2	0.69 \pm 0.09	507 \pm 12
AW	0.10 \pm 0.02	2.2 \pm 0.1	1.4 \pm 0.05	915 \pm 2

Notably, the agricultural waste medium appeared to promote high biomass production, coinciding with a low in stored fat. This phenomenon can be attributed to fungi primarily utilizing carbon from the medium for cellular growth and repair, with the surplus being allocated to fat storage (28). Among the species studied, *A. avenaceus* displayed the highest biomass production, with values of 1.1412 \pm 0.09 g and 0.8261 \pm 0.06 g on the agricultural waste and malt extract media, respectively. Statistical analysis

indicated significant differences in mean biomass between the species across the two media.

The dark brown color of the mycelium is attributed to the presence of pigments like carotenoids (see Table 2). The fragility of the mycelium may result from the medium's high salt content. The high salt prompts the fungi to develop thin cell walls with greater porosity, facilitating exchange processes with the environment (29-31).

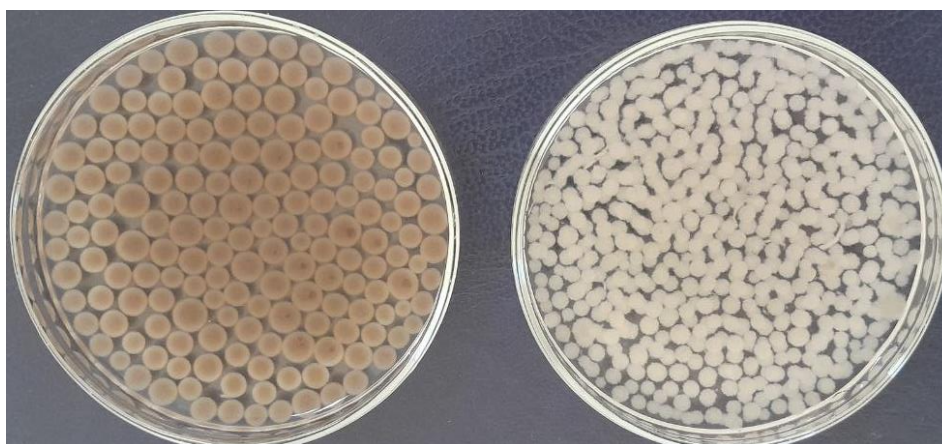


Figure 1: The Biomass of *A. niger* on agricultural waste and malt extract media, in order from the left.

The chemical composition of the medium significantly impacted lipid and carbohydrate synthesis in the fungal biomass (32). Malt medium, being richer in nutrients, showed slightly higher lipid and carbohydrate levels. Although total lipid content showed no significant variation among individuals, *A. flavus* recorded the highest production in both media ($47.4 \pm 0.2 - 56.6 \pm 0.9$ mg/g; Table 2), aligning

with findings from similar studies (33). In terms of carbohydrates, *A. carbonarius* produced the most in malt extract, measuring 167.1 ± 6.2 mg/g (Table 2), a finding consistent with other reports (34). Statistical analysis confirmed significant differences in the average total lipids and carbohydrates between species on both media at p -value=0.014 and p -value<0.001, respectively.

Table 2: The Basic chemical composition of fungal species on the tested media.

Medium	Biomass (g)		Proteins (mg/g)		Lipids (mg/g)		Carbohydrates (mg/g)	
	ME	AW	ME	AW	ME	AW	ME	AW
<i>A. niger</i>	0.434 ± 0.08	0.544 ± 0.04	2.247 ± 0.3	16.06 ± 0.4	24.2 ± 0.5	14.7 ± 0.3	84.21 ± 7.1	29.17 ± 4
<i>A. carbonarius</i>	0.1852 ± 0.06	0.5083 ± 0.03	3.483 ± 0.3	15.169 ± 0.3	13.4 ± 0.6	11.7 ± 0.3	167.1 ± 6.2	57.86 ± 4
<i>A. flavus</i>	0.365 ± 0.04	0.5211 ± 0.06	1.573 ± 0.1	4.045 ± 0.2	56.6 ± 0.9	47.4 ± 0.2	52.69 ± 5.5	48.55 ± 5.6
<i>A. avenaceus</i>	0.8261 ± 0.06	1.1412 ± 0.09	4.270 ± 0.2	4.494 ± 0.3	24.7 ± 0.5	19.3 ± 0.3	103.52 ± 3	60.83 ± 2

In contrast, the agricultural waste medium directed the species to synthesize high levels of proteins, phenols, flavonoids, and carotenoids (Table 3), which are antioxidant compounds and anti-stress factors. In fact, fungi use these compounds for cellular construction and repair and to resist pressure factors (9, 35).

Protein production differed between species in both media. The best species producing proteins on the agricultural waste medium was *A. niger* 16.06 ± 0.4 mg/g. The species that was not affected by changing the medium is *A. avenaceus*, which also was the best in producing protein on the malt extract medium (Table 2). These results are comparable to those obtained in similar studies (36).

The production of phenols and flavonoids, and carotenoids differed among the species on

agricultural waste medium, and the best species in production was *A. niger* by 33.37 ± 0.8 mg/g – 4.84 ± 0.42 mg/g – 1.131 ± 0.09 µg/g for phenols, flavonoids, and carotenoids respectively. The results are coherent with other studies (37-39).

The species grown on the agricultural waste medium (except for *A. flavus*) displayed lower IC₅₀ values, revealing a higher antioxidant activity; these species also exhibited greater phenol levels compared to those grown on malt medium (Table 3). The species showing the highest antioxidant activity was *A. carbonarius*, with a half-maximum inhibitory concentration of 0.28 ± 0.06 mg/mL (Table 3). These results agreed with those of previous studies (20,40). The averages of the total proteins, phenols, flavonoids, and carotenoids between the species on both media were significantly different at p -value<0.001.

Table 3: The Secondary chemical composition of fungal species on the tested media.

Medium	Phenols mg/g		Flavonoids mg/g		Carotenoids µg/g		IC ₅₀ of antioxidant activity mg/mL	
	ME	AW	ME	AW	ME	AW	ME	AW
<i>A. niger</i>	18.70 ± 0.2	33.37 ± 0.8	0.27 ± 0.03	4.84 ± 0.4	0.276 ± 0.05	1.131 ± 0.09	1.42 ± 0.09	0.38 ± 0.04
<i>A. carbonarius</i>	13.86 ± 0.4	29.84 ± 0.4	0.33 ± 0.02	4.02 ± 0.3	0.134 ± 0.03	0.797 ± 0.06	0.47 ± 0.05	0.28 ± 0.06
<i>A. flavus</i>	11.67 ± 0.3	11.19 ± 0.5	0.17 ± 0.05	1.51 ± 0.3	0.294 ± 0.04	0.418 ± 0.05	0.87 ± 0.04	1.47 ± 0.03
<i>A. avenaceus</i>	10.3 ± 0.3	13.51 ± 0.3	0.51 ± 0.1	1.73 ± 0.2	0.227 ± 0.04	0.426 ± 0.05	0.77 ± 0.07	0.63 ± 0.04

(Ascorbic acid IC₅₀: 0.0467 mg/mL = 0.00026 mM/mL)

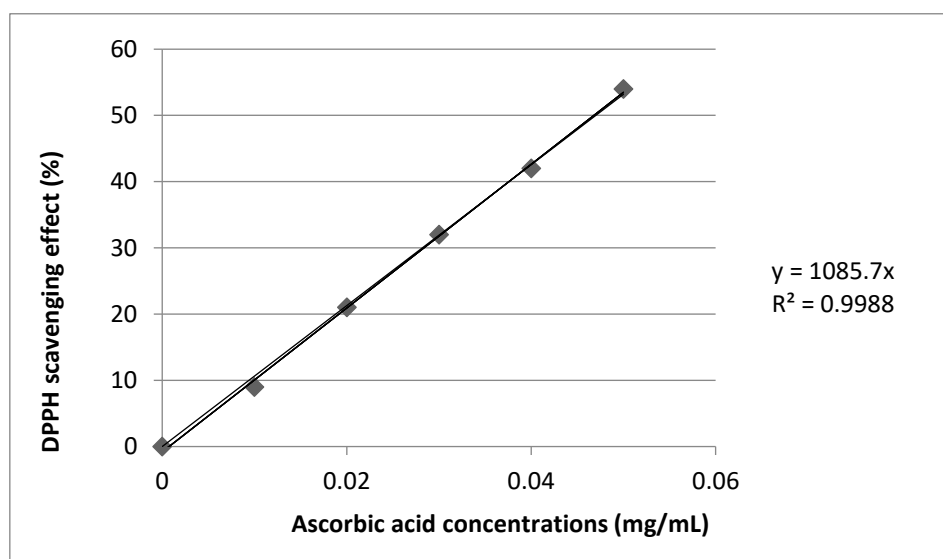


Figure 2: Standard calibration curves of Ascorbic acid.

The qualitative Electrophoretic protein pattern for every species was different after cultivating them on malt extract medium and agricultural waste medium.

The highest number of protein bands for the species on the malt extract medium and agricultural waste medium was 20 and 18 bands for *A. flavus*, respectively. *A. carbonarius* exhibited the lowest number of protein bands on both media, 12 and 10 bands, respectively. In general, the high number of protein bands in the species was associated with low

production of phenols, flavonoids, and antioxidant capacity.

The resulting bands could be stress proteins or antioxidant enzyme protein groups produced by the fungi to improve their adaptability to the medium (41-43). *A. avenaceus* with the same number of bands for both media shows a small change in the efficiency of its production of phenols and flavonoids (Table 3-4).

Table 4: The frequency of protein bands obtained from *Aspergillus* species (kilodalton) on the tested media.

Species Medium	<i>A. niger</i>		<i>A. carbonarius</i>		<i>A. flavus</i>		<i>A. avenaceus</i>	
	ME	AW	ME	AW	ME	AW	ME	AW
Proteins Bands Number	14	10	12	10	20	18	17	17
190		+			+	+	+	+
114		+			+	+	+	+
112	+		+	+				
111.8	+			+	+	+	+	+
89.4			+		+	+		
83.8				+				
82.9							+	+
80.3							+	+
78.2	+		+		+	+		
77.8	+							
70						+	+	
67.4	+	+					+	+
67.1			+	+				
64.8					+			
62.4	+				+		+	+
59.4	+	+			+			
56.5					+			
55						+	+	+
52	+							
50.5			+	+	+			
46.6			+		+	+		+
44.8	+							
43							+	+
42.1			+	+				
41.2		+			++	+		
38.5					++	+		
37.6							+	+
36.7							+	+
34.1	+	+	+	+				
31.9							+	+
28.7			+		+	+		
28							+	+
26.7	+	+	+	+				
25.3	+	+	+	+	+	+		
24.3							+	+
18.5					+	+		
16.2					+	+		
15.4					+	+	+	+
10.7	+	+			+	+	+	+
10	+	+	+	+	+			

4. CONCLUSION

Our findings highlight the potential utilization of agricultural waste, previously considered detrimental to the environment and economically wasted. By formulating a medium enriched with soluble proteins and sugars, we demonstrated its suitability for fostering the growth of *Aspergillus* species. This medium also induced distinctive physical attributes, including color and texture, in addition to boosting biomass, protein content, and the production of secondary metabolites, particularly phenols, due to the stress factors introduced during cultivation, such as high salt and phenol concentrations.

Conversely, the use of malt extract medium was associated with high primary compounds such as carbohydrates and lipids.

5. CONFLICT OF INTEREST

There is no conflict of interest with any institution.

6. ACKNOWLEDGMENTS

The authors acknowledge to express my gratitude to the Laboratory of the Plant Biology Department for facilitating work matters.

7. FUNDING

Funding information: This research is funded by Damascus University, and the funding number is 501100020595.

8. REFERENCES

1. Loehr RC. Agricultural waste management: problems, processes, and approaches. London: Academic Press Inc.; 2012.
2. Poltronieri P, D'Urso OF. Biotransformation of Agricultural Waste and By-Products [Internet]. Amsterdam, Netherlands: Elsevier; 2016. Available from: [<URL>](#).
3. Hussain CM, Hait S. Advanced Organic Waste Management: Sustainable Practices and Approaches [Internet]. Amsterdam, Netherlands: Elsevier; Available from: [<URL>](#).
4. Ali Nizam A, Ayed H. Efficiency of Actinobacteria Isolated from Quateena and Roman bridge Lakes in Growth in media polluted by OMWW and crude oil. Tishreen Univ Journal-Biological Sci Ser [Internet]. 2016;38(3):195-209. Available from: [<URL>](#).
5. Rathour RK, Sharma D, Sharma N, Bhatt AK, Singh SP. Engineered microorganisms for bioremediation Current Developments in Biotechnology and Bioengineering. Amsterdam, Netherlands: Elsevier; 2022.
6. Cohen R, Hadar Y. The roles of fungi in agricultural waste conversion. In: Fungi in Bioremediation [Internet]. Cambridge University Press; 2001. p. 305-34. Available from: [<URL>](#).
7. Smith JE. *Aspergillus* [Internet]. New York: Springer; 1994. Available from: [<URL>](#).
8. Vadlapudi V, Borah N, Yellusani KR, Gade S, Reddy P, Rajamanikyam M, et al. *Aspergillus* Secondary Metabolite Database, a resource to understand the Secondary metabolome of *Aspergillus* genus. Sci Rep [Internet]. 2017 Aug 4;7(1):7325. Available from: [<URL>](#).
9. Cary JW, Gilbert MK, Lebar MD, Majumdar R, Calvo AM. *Aspergillus flavus* Secondary Metabolites: More than Just Aflatoxins. Food Saf [Internet]. 2018;6(1):7-32. Available from: [<URL>](#).
10. Christabel O, Dorcas E, Elizabeth U. Suitability of food crop wastes in the formulation of laboratory media used for the cultivation of soil fungi. Int J Food Sci Microbiol. 2016;4(3):137-41.
11. de Oliveira RL, da Silva SP, Converti A, Porto TS. Production, Biochemical Characterization, and Kinetic/Thermodynamic Study of Inulinase from *Aspergillus terreus* URM4658. Molecules [Internet]. 2022 Sep 28;27(19):6418. Available from: [<URL>](#).
12. DuBois M, Gilles KA, Hamilton JK, Rebers PA, Smith F. Colorimetric Method for Determination of Sugars and Related Substances. Anal Chem [Internet]. 1956 Mar 1;28(3):350-6. Available from: [<URL>](#).
13. Yadav M, Yadav A, Yadav JP. In vitro antioxidant activity and total phenolic content of endophytic fungi isolated from *Eugenia jambolana* Lam. Asian Pac J Trop Med [Internet]. 2014 Sep;7:S256-61. Available from: [<URL>](#).
14. Rhoades JD. Soluble Salts. In 1982. p. 167-79. Available from: [<URL>](#).
15. Samson RA, Pitt JI. Integration of Modern Taxonomic Methods For *Penicillium* and *Aspergillus* Classification [Internet]. Samson RA, Pitt JI, editors. London: CRC Press; 2003. Available from: [<URL>](#).
16. Samson RA, Varga J, Frisvad JC. Taxonomic studies on the genus *Aspergillus*. Stud Mycol [Internet]. 2011 Jun;69(1). Available from: [<URL>](#).
17. Atallah OO, Mazrou YSA, Atia MM, Nehela Y, Abdelrhim AS, Nader MM. Polyphasic Characterization of Four *Aspergillus* Species as Potential Biocontrol Agents for White Mold Disease of Bean. J Fungi [Internet]. 2022 Jun 12;8(6):626. Available from: [<URL>](#).
18. Rodrigues JC, Lima da Silva W, Ribeiro da Silva D, Maia CR, Santos Goiabeira CV, Figueiredo Chagas HD, et al. Antimicrobial Activity of *Aspergillus* sp. from the Amazon Biome: Isolation of Kojic Acid. Comi G, editor. Int J Microbiol [Internet]. 2022 May 17;2022:4010018. Available from: [<URL>](#).
19. Pinheiro EAA, Carvalho JM, dos Santos DCP, Feitosa A de O, Marinho PSB, Guilhon GMSP, et al. Antibacterial activity of alkaloids produced by endophytic fungus *Aspergillus* sp. EJC08 isolated from medical plant *Bauhinia guianensis*. Nat Prod Res [Internet]. 2013 Sep;27(18):1633-8. Available from: [<URL>](#).
20. Almanaa TN, Rabie G, El-Mekkawy RM, Yassin MA, Saleh N, EL-Gazzar N. Antioxidant, antimicrobial and antiproliferative activities of fungal metabolite produced by *Aspergillus flavus* on in vitro study. Food Sci Technol [Internet]. 2022;42:e01421. Available from: [<URL>](#).
21. Wellburn AR. The Spectral Determination of Chlorophylls a and b, as well as Total Carotenoids, Using Various Solvents with Spectrophotometers of Different Resolution. J Plant Physiol [Internet]. 1994 Sep;144(3):307-13. Available from: [<URL>](#).
22. Cui Y, Li J, Deng D, Lu H, Tian Z, Liu Z, et al. Solid-state fermentation by *Aspergillus niger* and *Trichoderma koningii* improves the quality of tea dregs for use as feed additives. Šiler BT, editor. PLoS One [Internet]. 2021 Nov 12;16(11):e0260045. Available from: [<URL>](#).
23. Jacobs DI, Olsthoorn MMA, Mailliet I, Akeroyd M, Breestraat S, Donkers S, et al. Effective lead selection for improved protein production in *Aspergillus niger* based on integrated genomics. Fungal Genet Biol [Internet]. 2009 Mar;46(1):S141-52. Available from: [<URL>](#).
24. Azar S, Leila S, Alireza K, Mansour B, Amir B. Determining Protein Patterns for Three Fungus Species *Aspergillus fumigatus*, *Asp. Flavus* and *Asp. Niger*, Obtained from Outdoor Air in Iran. Glob Vet [Internet]. 2010;4(2):130-4. Available from: [<URL>](#).
25. Halim R, Gladman B, Danquah MK, Webley PA. Oil extraction from microalgae for biodiesel production. Bioresour Technol [Internet]. 2011 Jan;102(1):178-85. Available from: [<URL>](#).
26. Abdullah N, Chin NL, Mokhtar MN, Taip FS. Effects of bulking agents, load size or starter cultures in kitchen-waste composting. Int J Recycl Org Waste Agric [Internet]. 2013 Dec 17;2(1):3. Available from: [<URL>](#).
27. Christensen M. A Synoptic Key and Evaluation of Species in the *Aspergillus Flavus* Group. Mycologia [Internet]. 1981 Nov 12;73(6):1056-84. Available from: [<URL>](#).
28. Meeuwse P, Tramper J, Rinzema A. Modeling lipid accumulation in oleaginous fungi in chemostat cultures: I. Development and validation of a chemostat model for *Umbelopsis isabellina*. Bioprocess Biosyst Eng [Internet]. 2011 Oct 3;34(8):939-49. Available from: [<URL>](#).

29. Trevithick JR, Metzberg RL. Genetic Alteration of Pore Size and Other Properties of the Neurospora Cell Wall. *J Bacteriol* [Internet]. 1966 Oct;92(4):1016–20. Available from: [<URL>](#).
30. Shu CH. Fungal Fermentation for Medicinal Products. In: *Bioprocessing for Value-Added Products from Renewable Resources* [Internet]. Elsevier; 2007. p. 447–63. Available from: [<URL>](#).
31. Afroz Toma M, Rahman MH, Rahman MS, Arif M, Nazir KHMNH, Dufossé L. Fungal Pigments: Carotenoids, Riboflavin, and Polyketides with Diverse Applications. *J Fungi* [Internet]. 2023 Apr 7;9(4):454. Available from: [<URL>](#).
32. Tereshina VM, Kovtunenka A V., Memorskaya AS, Feofilova EP. Effect of Carbohydrate Composition of the Cytosol of *Aspergillus niger* Conidia on Their Viability During Storage. *Appl Biochem Microbiol* [Internet]. 2004 Sep;40(5):454–9. Available from: [<URL>](#).
33. Nemeč T, Jernejc K, Cimerman A. Sterols and fatty acids of different *Aspergillus* species. *FEMS Microbiol Lett* [Internet]. 2006 Jan 17;149(2):201–5. Available from: [<URL>](#).
34. Ianutsevich EA, Danilova OA, Groza N V., Tereshina VM. Membrane lipids and cytosol carbohydrates in *Aspergillus niger* under osmotic, oxidative, and cold impact. *Microbiology* [Internet]. 2016 May 16;85(3):302–10. Available from: [<URL>](#).
35. Kim Y, Nandakumar MP, Marten MR. Proteome map of *Aspergillus nidulans* during osmoadaptation. *Fungal Genet Biol* [Internet]. 2007 Sep;44(9):886–95. Available from: [<URL>](#).
36. Anupama, Ravindra P. Studies on production of single cell protein by *Aspergillus niger* in solid state fermentation of rice bran. *Brazilian Arch Biol Technol* [Internet]. 2001 Mar;44(1):79–88. Available from: [<URL>](#).
37. Saleh A, Elrefaie H, Hashem A, EL-Menoufy H, Mansour N, El-Beih A. Chemical Investigations and Optimization Studies on *Aspergillus terreus*-18 Showing Antioxidant Activity. *Egypt J Chem* [Internet]. 2018 Sep 28;62(2):215–30. Available from: [<URL>](#).
38. Tawfik E, Alqurashi M, Aloufi S, Alyamani A, Baz L, Fayad E. Characterization of Mutant *Aspergillus niger* and the Impact on Certain Plants. *Sustainability* [Internet]. 2022 Feb 8;14(3):1936. Available from: [<URL>](#).
39. Sanjay KR, Kumaresan N, Manohar B, Kumar SU, Vijayalakshmi G. Optimization of Carotenoid Production by *Aspergillus Carbonarius* in Submerged Fermentation Using a Response Surface Methodology. *Int J Food Eng* [Internet]. 2007 Nov 3;3(5). Available from: [<URL>](#).
40. Arora DS, Chandra P. Assay of antioxidant potential of two *Aspergillus* isolates by different methods under various physio-chemical conditions. *Brazilian J Microbiol* [Internet]. 2010 Oct;41(3):765–77. Available from: [<URL>](#).
41. Kniemeyer O, Lessing F, Brakhage AA. Proteome analysis for pathogenicity and new diagnostic markers for *Aspergillus fumigatus*. *Med Mycol* [Internet]. 2009 Jan;47(s1):S248–54. Available from: [<URL>](#).
42. Miskei M, Karányi Z, Pócsi I. Annotation of stress-response proteins in the aspergilli. *Fungal Genet Biol* [Internet]. 2009 Mar;46(1):S105–20. Available from: [<URL>](#).
43. Fountain JC, Bajaj P, Nayak SN, Yang L, Pandey MK, Kumar V, et al. Responses of *Aspergillus flavus* to Oxidative Stress Are Related to Fungal Development Regulator, Antioxidant Enzyme, and Secondary Metabolite Biosynthetic Gene Expression. *Front Microbiol* [Internet]. 2016 Dec 21;7:2048. Available from: [<URL>](#).



Half-metallic Ferromagnetism in Fe-doped and Zn-vacancy Defected ZnSe: First-Principles Investigation

Vusala N. Jafarova^{1,2*} [ORCID](#), Aynur N. Jafarova¹ [ORCID](#), Asmer A. Abdullayeva¹,
Musaver A. Musaev¹ [ORCID](#)

¹Azerbaijan State Oil and Industry University, 20 Azadlig Ave., AZ-1010, Baku, Azerbaijan.

²Khazar University, 41 Mehseti Str., AZ1096, Baku, Azerbaijan.

Abstract: The magnetic properties of defected ZnSe wurtzite systems were theoretically investigated using Density Functional Theory and Local Spin Density Approximation. From this first principal study, it was determined that pure ZnSe is a non-magnetic direct band gap semiconductor. Investigations show that adding the iron and the presence of a single Zn vacancy defect leads to the magnetization of ZnSe. The results of total energy calculations show that a ferromagnetic state is favorable when Zn is replaced with Fe. The ferromagnetic alignment in Fe-doped ZnSe wurtzite compound behaves in high-spin and half-metallic states.

Keywords: ZnSe: Fe, Magnetic properties, Ferromagnetism, Half-metallic.

Submitted: January 25, 2024. **Accepted:** July 12, 2024.

Cite this: Jafarova VN, Jafarova AN, Abdullayeva AA, Musaev MA. Half-metallic Ferromagnetism in Fe-doped and Zn-vacancy Defected ZnSe: First-Principles Investigation. JOTCSA. 2024;11(3): 1297-302.

DOI: <https://doi.org/10.18596/jotcsa.1425866>

***Corresponding author's E-mail:** vcafarova@beu.edu.az

1. INTRODUCTION

Diluted magnetic semiconductors (DMSs) attract research interest for the semiconducting and magnetic properties in the same compound (1-4). 3d transition-metal (TM=V, Cr, Mn, Fe, Co, Ni) doped II-VI Zn-based semiconductor compounds have revealed their potential for technical application according to their wide band gap of 2.70 eV (5). ZnSe is ideally appropriate for the fabrication of photodetectors, CO₂ laser focusing lenses, sensors, solar cells, and other photovoltaic applications (5,6). This material can be applied for the production of optoelectronic devices such as light emitters and detectors (7-9).

DMSs based on II-VI group compounds have been attracting great interest as promising materials for new spin electronic devices because these compounds show ferromagnetism, whose Curie temperature depends on the carrier concentration (10,11). For industrial applications of DMSs, room-temperature ferromagnetism is strongly required.

The DMSs' first-principles studies have allowed the production of new types of materials with possible technological applications in Engineering, Medicine, and Environmental Chemistry.

In Refs. (12,13) reported that Fe-doped and as-grown ZnSe solid solutions show a paramagnetic nature at low temperatures. In theoretical work (14), the authors predicted lower FM properties and the presence of a spin-glass state for ZnSe: Fe solid solutions. In (15), reported results are in contradiction with the prediction of antiferromagnetic (AFM), paramagnetic, and spin-glass (SG) magnetic states in Zn(Fe)Se zinc-blende crystal. D.P. Rai and co-workers studied (16) 5 Zn vacancies in the monolayer hexagonal ZnSe 18-atom supercell modeled by 3×3×1 transferred based on the DFT. They reported that the Zn vacancy makes the FM state of ZnSe. Nevertheless, there is no common opinion about the mechanism of magnetism in iron-doped ZnSe, and the views of different researchers are opposite.

This work is based on the DFT-LSDA+U; a detailed theoretical study of magnetic properties for Fe²⁺ doped ZnSe structure is provided. In our previous work (17), we obtained that the calculated energy band gap (2.7 eV) of ZnSe is closer to the known experimental results. The results of magnetic properties of Zn_{1-x}Fe_xSe (x=1/8, 1/16) systems also provide useful information for future research studies to understand the origin of ferromagnetism

in these systems. However, a lower energy state in the FM state compared to the AFM state indicates a stable magnetic state.

2. THEORETICAL SECTION

2.1. Investigation Method

The calculations were carried out for the Zn(Fe)Se systems with 32 and 96 atoms by the DFT method (18) within Local Spin Density Approximation (LSDA) (19) implemented Atomistix ToolKit code within incorporated Mulliken population analysis. The interactions between the electrons and ions, as well as exchange correlation, were described by the Fritz-Haber-Institute ion pseudopotentials (20). The Kohn-Sham wave functions (21) are solved in a linear combination of atomic orbitals (LCAO), and the cutoff of kinetic energy for electrons is 150 Ry. The supercells containing dopant atoms and vacancies were geometry optimized, and the force and stress tolerances are about less than 0.01 eV/Å and 0.01 eV/Å³, respectively. The reciprocal space integration was performed with a 5×5×5 Monkhorst-Pack grid (22). To simulate the antiferromagnetic states of DMS systems, cations (Zn) were replaced randomly by Fe[↑]_{x/2} (for spin-up) and Fe[↓]_{x/2} (for spin-down) ions.

3. RESULTS AND DISCUSSION

3.1. Magnetic Properties of Fe-doped ZnSe

Using the DFT-LSDA method within Hubbard U correction, the magnetic properties from Mulliken Population analysis were studied using Atomistic ToolKit software. In work (23), the authors summarized the results of magnetic properties of TM-doped ZnSe nanosheet using the DFT-GGA method. They reported that the magnetic moment for Fe atom doped nanosheet is about 4.89 μ_B. In the present case, the model used for TM²⁺ doped ZnSe is a 5×5×5 MP grid for 32 and 96-atom supercells with one or two Zn atoms substituted by TM dopant atoms. In order to calculate magnetic properties, iron atoms have been modeled to replace the site of Zn atoms, as shown in Figure 1. In all figures of spin-polarization structures, the magnetic moments of atoms are described by green arrows.

For recent simulations, the FM and AFM states of Fe-doped ZnSe supercells can be described as Zn_{1-x}Fe[↑]_xSe and Zn_{1-x}Fe[↓]_{x/2}Fe[↑]_{x/2}Se, correspondingly. Moreover, in order to check the stability of these phases, the differences in energy between both states (ΔE=E_{AFM} - E_{FM}) of these systems have been calculated. The obtained values are given in Table 1.

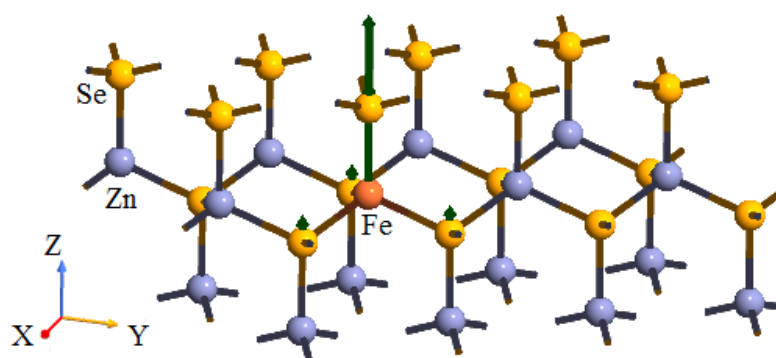


Figure 1: The spin-polarization for Zn₁₅Fe₁Se₁₆ supercell (Zn-gray, Se-yellow, Fe-brown).

Table 1: The DFT-LSDA+U results for different Zn_{1-x}Fe_xSe supercells.

Supercell	<i>x</i>	μ(Fe), μ _B per Fe	(E _{AFM} -E _{FM})/2, meV per Fe
Zn ₁₅ Fe ₁ Se ₁₆	0.0625	4.004	-
Zn ₁₄ Fe ₂ Se ₁₆	0.125	4.0	0.205
Zn ₄₇ Fe ₁ Se ₄₈	0.0208(3)	4.0	-
Zn ₄₆ Fe ₂ Se ₄₈	0.04166	3.9975	0.035

The first-principles results of the total energy differences ΔE show that the antiferromagnetic (AFM) state is more stable than the ferromagnetic (FM) spin ordering one when Fe²⁺ substitutes on Zn sites. Similar behavior is reported for TM co-doping ZnSe cubic structures in Ref. (24).

Current studies show that a single Fe(Zn) substitution leads to magnetization, and the magnetic moment for 96-atom systems is around 4 μ_B, which is consistent with the band structure results. This value corresponds to the GGA obtained result (4.89 μ_B) for Fe-doped ZnSe nanosheet (23).

In the case of Fe(Zn), Zn atoms have a less weakening effect on the magnetic field (~ -0.05 μ_B), the magnetization created mainly by the impurity atom (~ 3.5 μ_B from Fe atom including 3.359 μ_B from *d*-electrons). The positive magnetic moments of all Se atoms (~ 0.6 μ_B) are small in magnitude.

3.2. ZnSe:Fe with Zn Vacancy-defect

In this section, we investigated two cases of Zn vacancy-defect positions in ZnSe systems. The presence of Zn vacancy and Fe-doped ZnSe systems (Figure 2) lead to significant changes. The Se atoms, which are located neighboring the vacancy position

and chemically bonded to the iron, create a positive magnetic moment and make up for the negative moment of the zinc atoms.

For Fe(Zn) replacement and availability of one Zn vacancy positioned far from the impurity atom, the computed total moment of the 96-atom supercell is $5.594 \mu_B$, with main partial magnetic moments from Fe ($3.607 \mu_B$) and 48 Se atoms ($2.774 \mu_B$). The significant contributions relate to the 4 Se atoms nearby and chemical bonding with impurity atom ($0.704 \mu_B$) and 4 Se with dangling bonds from nearly the vacancy position ($1.265 \mu_B$). 46 Zn atoms weaken the total magnetic moment of the system ($-0.787 \mu_B$). Thus, the total magnetization of the supercell increases by the amount of $\sim 1.6 \mu_B$ due to the defect.

In the second case, the vacancy site is chosen in such a way that one of the host selenium atoms bonded with an impurity atom loses one chemical bond due to the vacancy. We obtain the strength of the magnetization by $0.353 \mu_B$. The impurity iron atom makes great moment ($3.605 \mu_B$), and 46 Zn atoms weaken total magnetization by the quantity $-0.37 \mu_B$. The basic contributions from 48 Se atoms: $2.712 \mu_B$ (4 Se atoms bonding with impurity atom ($0.525 \mu_B$), 4 Se atoms losing the chemical bond due to vacancy ($1.275 \mu_B$)). In comparison with the vacancy-free case, total magnetic field strengthening is $\sim 1.95 \mu_B$.

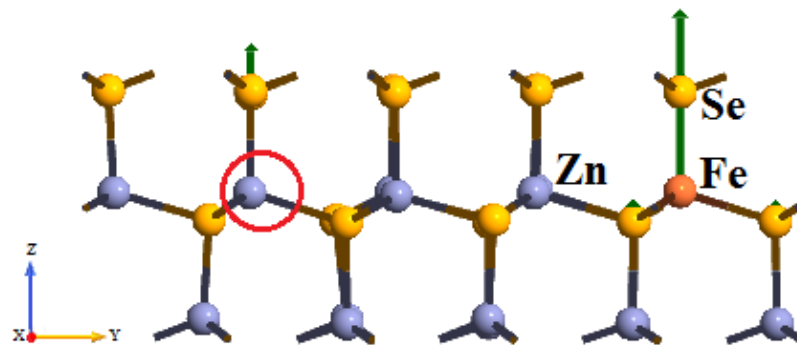


Figure 2: The spin polarization structure for $Zn_{14}Fe_1Se_{16}$ with one Zn vacancy.

The first-principles results for the wide band gaps of 32-atom ZnSe supercells are 2.60/2.60 eV and 1.22/1.39 eV for up and down states, correspondingly. The total magnetic moment for the $Zn_{14}Fe_1Se_{16}$ system is $\sim 5.9 \mu_B$.

Figures 3 and 4 show the calculated spin-polarized band structures and total density of states for the Fe-doped and Zn-vacancy-defected $Zn_{46}Fe_1Se_{48}$ 96-atom supercell.

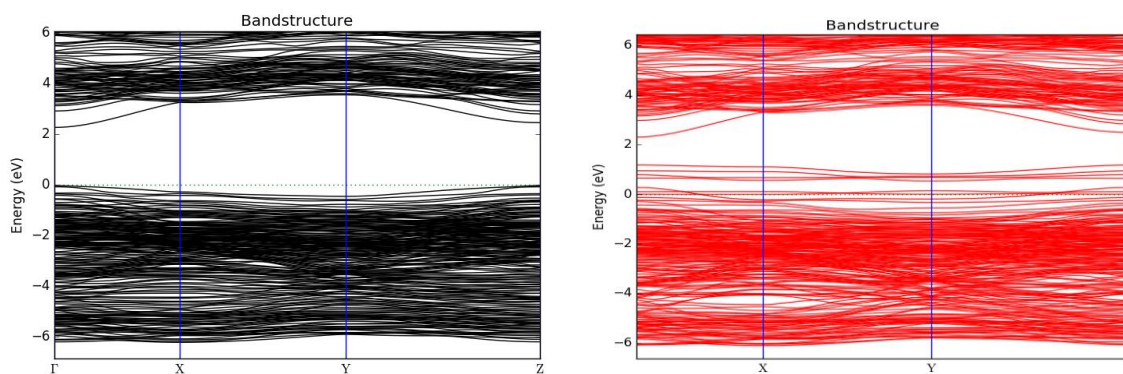


Figure 3: The obtained band structures for Fe-doped and Zn-vacancy defected $Zn_{46}Fe_1Se_{48}$ for spin-up (black color) and spin-down states (red color).

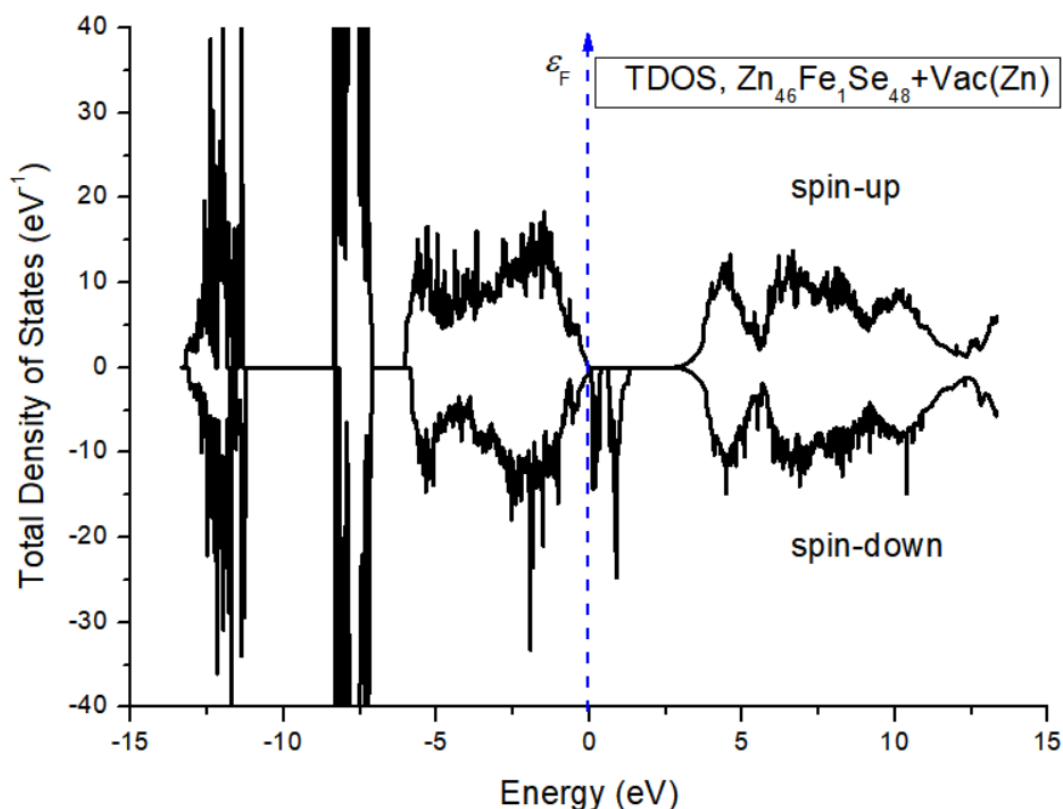


Figure 4: The DFT-LSDA+U calculated TDOS of $\text{Zn}_{46}\text{Fe}_1\text{Se}_{48}$ system with Zn vacancy.

DFT-LSDA+U calculations revealed that Fe(Zn) replacement and the availability of one Zn defect in the ZnSe supercell is the most effective for strengthening the magnetization. Thus, the shift of moment of the system due to one Zn vacancy side is $(1.6 \div 1.9) \mu_B$, depending on the chosen location of the defect.

4. CONCLUSION

In summary, the magnetic properties of iron-doped ZnSe systems are studied by DFT using the LSDA+U method. The investigations performed for 32- and 96-atom Fe-doped ZnSe supercells show that Zn substitutions by Fe lead to a ferromagnetic spin ordering. The FM alignment in the Zn(Fe)Se systems behaves as semi-metallic ferromagnetism manifests itself in a significant density of impurity states. The band gap energy of ZnSe supercells is observed to increase after the Fe atom replaces Zn and leads to the magnetization of systems. The results of total energy calculations of ZnSe almost present a stable antiferromagnetic state when Fe^{2+} ions are substituted on Zn sites.

In this work, we hope to contribute significantly to the investigation of DMSs and their possible technological applications for society's benefit.

5. CONFLICT OF INTEREST

The authors declare that they have no known competing financial interests or personal relationships that could have appeared to influence the work reported in this paper.

7. REFERENCES

1. Munekata H, Ohno H, von Molnar S, Segmüller A, Chang LL, Esaki L. Diluted magnetic III-V semiconductors. *Phys Rev Lett* [Internet]. 1989 Oct 23;63(17):1849–52. Available from: [<URL>](#).
2. Ohno H, Shen A, Matsukura F, Oiwa A, Endo A, Katsumoto S, et al. (Ga,Mn)As: A new diluted magnetic semiconductor based on GaAs. *Appl Phys Lett* [Internet]. 1996 Jul 15;69(3):363–5. Available from: [<URL>](#).
3. Dietl T. A ten-year perspective on dilute magnetic semiconductors and oxides. *Nat Mater* [Internet]. 2010 Dec 23;9(12):965–74. Available from: [<URL>](#).
4. Dietl T, Ohno H. Dilute ferromagnetic semiconductors: Physics and spintronic structures. *Rev Mod Phys* [Internet]. 2014 Mar 24;86(1):187–251. Available from: [<URL>](#).
5. Neumark GF, Park RM, Depuydt JM. Blue-green diode lasers. *Phys Today* [Internet]. 1994 Jun 1;47(6):26–32. Available from: [<URL>](#).
6. Karzel H, Potzel W, Köfferlein M, Schiessl W, Steiner M, Hiller U, et al. Lattice dynamics and hyperfine interactions in ZnO and ZnSe at high external pressures. *Phys Rev B* [Internet]. 1996 May 1;53(17):11425–38. Available from: [<URL>](#).
7. Adetunji BI, Adebambo PO, Adebayo GA. First principles studies of band structure and electronic properties of ZnSe. *J Alloys Compd* [Internet]. 2012 Feb;513:294–9. Available from: [<URL>](#).

8. Haase MA, Qiu J, DePuydt JM, Cheng H. Blue-green laser diodes. *Appl Phys Lett* [Internet]. 1991 Sep 9;59(11):1272–4. Available from: [<URL>](#).
9. Eason DB, Yu Z, Hughes WC, Roland WH, Boney C, Cook JW, et al. High-brightness blue and green light-emitting diodes. *Appl Phys Lett* [Internet]. 1995 Jan 9;66(2):115–7. Available from: [<URL>](#).
10. A. Medvedkin G, Takayuki Ishibashi TI, Takao Nishi TN, Koji Hayata KH, Yoichi Hasegawa YH, Katsuaki Sato KS. Room temperature ferromagnetism in novel diluted magnetic semiconductor $Cd_{1-x}Mn_xGeP_2$. *Jpn J Appl Phys* [Internet]. 2000 Oct 1;39(10A):L949. Available from: [<URL>](#).
11. Ohno H. Properties of ferromagnetic III–V semiconductors. *J Magn Magn Mater* [Internet]. 1999 Oct;200(1–3):110–29. Available from: [<URL>](#).
12. Mayer AM. Lecture notes in physics. 1982;152:109–19. Available from: [<URL>](#).
13. Furdyna JK. Diluted magnetic semiconductors. *J Appl Phys* [Internet]. 1988 Aug 15;64(4):R29–64. Available from: [<URL>](#).
14. Katayama-Yoshida H, Sato K. Spin and charge control method of ternary II–VI and III–V magnetic semiconductors for spintronics: theory vs. experiment. *J Phys Chem Solids* [Internet]. 2003 Sep;64(9–10):1447–52. Available from: [<URL>](#).
15. Khan MS, Shi L, Zou B. Impact of vacancy defects on optoelectronic and magnetic properties of Mn-doped ZnSe. *Comput Mater Sci* [Internet]. 2020 Mar;174:109493. Available from: [<URL>](#).
16. Rai DP, Laref A, Khuili M, Al-Qaisi S, Vu T V., Vo DD. Electronic, magnetic and optical properties of monolayer (ML) hexagonal ZnSe on vacancy defects at Zn sites from DFT-1/2 approach. *Vacuum* [Internet]. 2020 Dec;182:109597. Available from: [<URL>](#).
17. Jafarova V., Musaev M. First-principles study of structural and electronic properties of ZnSe with wurtzite structure. *Tech Rom J Appl Sci Technol* [Internet]. 2023 Feb 9;6:42–6. Available from: [<URL>](#).
18. Hohenberg P, Kohn W. Inhomogeneous electron gas. *Phys Rev* [Internet]. 1964 Nov 9;136(3B):B864–71. Available from: [<URL>](#).
19. Parr RG, Yang W. Density-functional theory of atoms and molecules [Internet]. New York: Oxford University Press; 1989. Available from: [<URL>](#).
20. Fuchs M, Scheffler M. Ab initio pseudopotentials for electronic structure calculations of poly-atomic systems using density-functional theory. *Comput Phys Commun* [Internet]. 1999 Jun;119(1):67–98. Available from: [<URL>](#).
21. Lundqvist S, March NH. Theory of the Inhomogeneous Electron Gas [Internet]. Lundqvist S, March NH, editors. Boston, MA: Springer US; 1983. 425 p. Available from: [<URL>](#).
22. Monkhorst HJ, Pack JD. Special points for Brillouin-zone integrations. *Phys Rev B* [Internet]. 1976 Jun 15;13(12):5188–92. Available from: [<URL>](#).
23. Chen XL, Huang BJ, Feng Y, Wang PJ, Zhang CW, Li P. Electronic structures and optical properties of TM (Cr, Mn, Fe or Co) atom doped ZnSe nanosheets. *RSC Adv* [Internet]. 2015;5(128):106227–33. Available from: [<URL>](#).
24. Behloul M, Salmani E, Ez-Zahraouy H, Benyoussef A. Theoretical investigation of electronic, magnetic and optical properties of ZnSe doped TM and co-doped with MnTM (TM: Fe, Cr, Co): AB-initio study. *J Magn Magn Mater* [Internet]. 2016 Dec;419:233–9. Available from: [<URL>](#).



Digital Image Colorimetric Detection of H₂O₂ Utilizing PEG/Ag/AgO Nanoparticles Derived from Tangerine Leaf Extract

Emre Yılmazoğlu^{1*} 

¹Istanbul University-Cerrahpaşa, Faculty of Engineering, Department of Chemical Engineering, 34320, Avcılar, Istanbul, Türkiye.

Abstract: Recent developments in biosensors based on digital platforms have primarily focused on enhancing rapid detection, flexibility, and selectivity through the utilization of nanomaterials. Despite these advances, the complexity of image colorimetric measurements continues to be a subject of interest. This study focused on the development of a new digital image colorimetric biosensor for real-time quantification of hydrogen peroxide (H₂O₂). The designed nanostructure-based sensor showed excellent selectivity and sensitivity, utilizing polyethylene glycol/Silver/Silver(II) oxide nanoparticles obtained from tangerine leaf extract (TLE/PEG/Ag/AgO NPs). The sensor's performance was validated using Ag/AgO NPs derived from tangerine leaf extract (TLE), demonstrating remarkable selectivity and sensitivity using a Red-Green-Blue (RGB)--based approach. Based on digital image colorimetric measurements of TLE/PEG/Ag/AgO NPs, a system for determining H₂O₂ was established in a linear range of 2.0–100.0 µmol/L with a low limit of detection (LOD) of 1.82 µmol/L. This study not only presented a facile strategy for the design of the digital image colorimetric TLE/PEG/Ag/AgO NPs-based biosensor but also shed light on the remarkable potential of smartphone sensing devices based on nanosensor technology. These sensors offer fresh perspectives and multidisciplinary approaches to visually sensitive sensing in a range of applications, such as biomedical diagnostics, security screening, and environmental monitoring.

Keywords: Digital biosensor, Image colorimetric sensor, Silver nanoparticles, Green sensor.

Submitted: February 19, 2024. **Accepted:** July 1, 2024.

Cite this: Yılmazoğlu E. Digital Image Colorimetric Detection of H₂O₂ Utilizing PEG/Ag/AgO Nanoparticles Derived from Tangerine Leaf Extract. JOTCSA. 2024;11(3): 1303-12.

DOI: <https://doi.org/10.18596/jotcsa.1439951>

***Corresponding author's E-mail:** emre.yilmazoglu@iuc.edu.tr

1. INTRODUCTION

Nanotechnology involves the creation and utilization of materials that are one, two, or three-dimensional and range in scale from 1 to 100 nm, with high performance in physical, chemical, biological, optical, electrical, etc., for various purposes, especially in fields such as medicine, electronics, and the environment (1). These nanoscale materials have the advantage of being easily incorporated into the structure or metabolism of bulk materials due to their small volume. In addition, their high energy and surface area make it easier and less expensive for them to exhibit desired qualities than it would be to change the bulk material's attributes (2,3).

Both organic and inorganic structures, such as metals or metal oxides, as well as polymers, lipids, and carbohydrates, can be used in the design of advanced NPs (4-6). High selectivity and stability are well-known characteristics of metal or metal oxide-

based NP sensors. Depending on their composition and form, these nanoparticles may also possess magnetic, fluorescent, anticancer, antibacterial, antifungal, antiviral, anti-inflammatory, and wound-healing properties (7,8). These properties render them extremely valuable in a multitude of applications, such as medical imaging, biomedical device coatings, wound dressings, and drug delivery systems.

The development of biosensors based on inorganic nanoparticles (NPs) has garnered significant attention in recent years in biomedical applications. These sensors, surpassing traditional counterparts, offer distinct advantages, especially in the early diagnosis of diseases. Key benefits encompass fast response times, portability, sensitivity, selectivity, reusability, and affordability (9-11). Nanostructure-based biosensors exhibit effectiveness in detecting a broad spectrum of biomolecules, ranging from antibodies, proteins, and carbohydrates to enzymes,

hormones, nucleic acids, and microorganisms. The integration of nanoparticles into biosensor design plays a crucial role in enhancing the sensitivity and selectivity of measurements, significantly elevating biosensor performance. It is known that Ag NPs possess a broad application potential, particularly in the realms of medicine and electronics, owing to their conductivity, antimicrobial properties, and biocompatibility (12-14). Numerous research have studied the usage of Ag NPs in biological contexts, examining their various forms and sizes. Specifically, a multitude of studies have reported on the sensitive detection of biomarkers associated with the early diagnosis of cancer using Ag NPs. H_2O_2 is among the most prevalent reactive oxygen species in medical metabolism research. Imbalances in reactive species induce oxidative stress in the body, potentially resulting in various illnesses, including those related to the immune system, such as cancer. Thus, a prompt and cost-effective measurement of chemical concentrations, such as H_2O_2 , in biological settings provides a distinct advantage for diagnosing illnesses.

With the advent of green chemistry, the utilization of biological sources for nanoparticle synthesis has grown in popularity. Microorganisms and plant extracts are used to create abundant, affordable, biodegradable, and biocompatible compounds through green synthesis. This green synthesis, which uses a bottom-up methodology, involves using the functional groups found in biological components to produce nanoparticles from metal ions. Especially biological wastes containing compounds with capping/reducing effects can be used for this purpose, increasing the added value. Moringa (*Moringa oleifera*), ginger (*Zingiber officinale*), thyme (*Thymus vulgaris*), oregano (*Origanum vulgare*), rice (*Oryza sativa*), Mexican poppy (*Argemone mexicana*), *Alpinia katsumadai*, blue pea (*Clitoria ternatea*), black nightshade (*Solanum*

nigrum), China hibiscus (*Hibiscus rosa-sinensis*), Aniseed (*Pimpinella anisum*), ivy gourd (*Coccinia grandis*), Indian gooseberry (*Phyllanthus emblica*), satsuma mandarin (*Citrus unshiu*), mandarin (*Citrus reticulata*), sweet orange (*Citrus sinensis*), lemon (*Citrus limon*) and many other plants can be used in the green synthesis of Ag nanoparticles (15-31).

In this study, green Ag/AgO NPs were synthesized using a simple sonochemical method, incorporating biowaste tangerine leaf extract (TLE) and biodegradable polyethylene glycol (PEG). The biodegradable TLE/PEG/Ag/AgO NPs were characterized using transmission electron microscopy (TEM), Fourier-transform infrared spectroscopy (FTIR), and X-ray diffraction (XRD) methods. The performance of the proposed H_2O_2 -sensitive biosensor was assessed through the RGB method, employing a mobile phone with a digital color approach. This approach aimed to develop a sensor that is both sensitive to H_2O_2 and environmentally friendly.

2. EXPERIMENTAL SECTION

2.1. Materials

Mandarin (*Citrus reticulata*), sourced from Mersin, Turkey, was obtained from a local market in Istanbul. Various materials, including ethyl alcohol, PEG400, epichlorohydrin, $AgNO_3$, acetone, hexane, toluene, glucose, isopropyl alcohol (IPA), and H_2O_2 , were purchased from Merck Company (Germany).

2.2. Preparation of TLE/PEG/Ag/AgO NPs

The mandarin leaves underwent a thorough cleansing with distilled water and was subsequently dried in an oven at 80 °C for an hour. Following this, 40 g of dry plant material was treated with a 100 ml solution consisting of 80% (v/v) ethyl alcohol and water, employing an ultrasonic bath at 50 °C for 2 hours. The extracts were filtered with filter paper.

Table 1: Variations in composition for the preparation of green TLE/PEG/Ag/AgO NPs.

Code	Extract	PEG400	Epichlorohydrin	$AgNO_3/NaOH$
TLE/PEG	20 mL	-	-	-
TLE/PEG	20 mL	0.1 g	0.02 g	-
TLE/PEG/Ag/AgO NPs	20 mL	0.1 g	0.02 g	0.012 M/0.1 M

Different samples with distinct compositions were prepared (Table 1). Initially, TLE extracts were procured, followed by the addition of 0.1 g PEG400 to 20 mL of the extract in a sequential step. Subsequently, 0.02 g of epichlorohydrin was introduced and stirred at 700 rpm using a magnetic stirrer. Finally, to obtain TLE/PEG/Ag/AgO NPs, 10 mL of 0.012 M $AgNO_3$ and 2 mL of 0.1 M NaOH solution were added, and the sample was sonicated for 30 minutes. Remarkably, a discernible color change was observed in all solutions within the latest 5 minutes of the process.

2.3. Characterization

The morphology and chemical properties of the synthesized TLE/PEG/Ag/AgO NPs were evaluated through various characterization techniques. High-resolution transmission electron microscopy

(HRTEM) with an acceleration voltage of 100 kV, utilizing the HighTech HT7700 instrument, was employed for morphological analysis. X-ray diffraction analysis (XRD) was conducted using Malvern Panalytical Aeris 600W, with Cu K α radiation at 40 kV and 15 mA, providing insights into the crystallographic structure. Fourier transform infrared spectroscopy (FTIR) was performed in the frequency range of 400 to 4000 cm^{-1} to assess the functional groups present in the synthesized TLE/PEG/Ag/AgO NPs.

The TEM images were processed and analyzed using ImageJ software to determine the particle dispersion of TLE/PEG/Ag/AgO NPs. For assessing the RGB color channels of smartphone cameras, we employed a Casper VIA F20 (Türkiye) smartphone equipped with cameras featuring resolutions of 48MP-5MP-2MP-

2MP. Additionally, the XRD data were utilized to calculate the crystallite size of the TLE/PEG/Ag/AgO NPs using the Debye-Scherrer equation (2.1) (32).

$$\tau = K\lambda/\beta\cos\theta \quad (2.1)$$

where β is the full width at half-maximum (FWHM), K is the form factor equal to 0.9, and θ is the experimental Bragg angle of the diffraction peak of TLE/PEG/Ag/AgO NPs.

2.4. Calculations

In digital colorimetric analyses, diverse compounds such as acetone, hexane, toluene, glucose, IPA, and H_2O_2 were examined in concentrations ranging from 2.0 to 100.0 $\mu\text{mol/L}$. In a transportable box (20 cm*20 cm*5 cm), the sample and the smartphone camera were separated by 10 cm. Using the automated option without close-up or filter, the specimen was centered in the image. A high-quality image with a comparable light effect appeared after around ten seconds. Using the RGB color assessment, all digital-colorimetric observations of 2 mL of the green TLE/PEG/Ag/AgO NPs-digital biosensor were performed for 1 minute at 25 °C against 10 μM of the target analyte. Utilizing a camera-integrated colorimetric TLE/PEG/Ag/AgO NPs-biosensor on an F20 model smartphone, all photos were used to study the selective detection of H_2O_2 at a resolution of 1600 \times 1200 pixels, with data falling between for black color value [0,0,0] and for white color value [255,255,255]. An ImageJ color software was used to examine every image of the biosensors that had been developed. Using Eqs. 2.2–2.6 (33), the prepared TLE/PEG/Ag/AgO NPs-based biosensor's Euclidean distance (ΔE), response (S), limit of detection (LOD), and limit of quantification (LOQ) values were determined for the selective digital colorimetric detection of H_2O_2 .

$$\Delta E = \sqrt{(R_i - R_0)^2 + (G_i - G_0)^2 + (B_i - B_0)^2} \quad (2.2)$$

$$S = 100 \frac{X_c - X_0}{X_0 - X_{ref}} [\%] \quad (2.3)$$

$$S(\%) = m \log(C) + n \quad (2.4)$$

$$LOD = 3.3\sigma/m \quad (2.5)$$

$$LOQ = 10\sigma/m \quad (2.6)$$

Sample color values for red, green, and blue colors are represented as R_i , G_i , and B_i , respectively. R_0 , G_0 , and B_0 are the reference values for the colors. X_c is the concentration-related raw sensor signal, X_0 is the signal measured at zero concentration, and the X_{ref} is the reference signal value for each color channel (is equal to 255 for red and green, to 0 for blue). n is the intercept and m is the slope of the line equation between response (S) and base-10 logarithm of the concentration of the analyte (C). σ is the standard deviation value of the response.

3. RESULTS AND DISCUSSION

3.1. Characterization of the TLE/PEG/Ag/AgO NPs

By employing HRTEM, XRD, and FTIR techniques, we thoroughly examined the surface and chemical attributes of the synthesized TLE/PEG/Ag/AgO NPs. A noteworthy application aimed at advancing image analysis involves leveraging artificial intelligence (AI) for surface analysis. Within this investigation, HRTEM imaging of the fabricated NPs was conducted using a dual 8-bit RGB colored mode, subsequently applied to the AI-assisted TEM micrograph of the TLE/PEG/Ag/AgO NPs. In Figure 1, the TEM micrograph and the AI-assisted TEM micrograph of TLE/PEG/Ag/AgO NPs were presented.

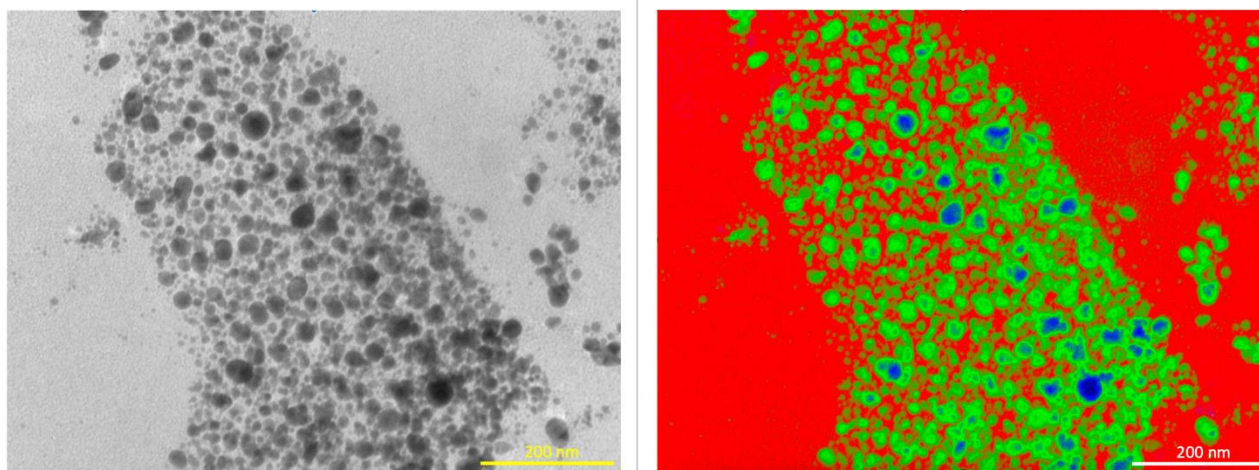


Figure 1: (a) TEM micrograph and (b) AI-assisted TEM micrograph of TLE/PEG/Ag/AgO NPs.

The homogeneous dispersion of Ag/AgO NPs within the TLE/PEG matrix is confirmed by TEM analysis, as shown in Fig. 1(a), demonstrating a homogenous particle distribution. According to TEM results, we observed that the NPs have a spherical geometry, and their diameters vary between 10-20 nm. However, considering that NPs below 10 nm are difficult to image, a digital image processing

approach was applied by applying ImageJ software to TEM images to overcome this difficulty (Fig. 1(b)). With this method, the morphology and diameters of the green/blue colored NPs could be determined more easily and effectively. The advantages provided by the ImageJ digital image processing approach helped us achieve more sensitive and precise results, especially in the detection of Ag/AgO NPs with a

diameter of sub-10 nm. In our analysis of the red, green, and blue channels within the AI-assisted TEM digital image using RGB evaluation, we observed that agglomerated Ag/AgO NPs were identified in the blue channel. Concurrently, the green-colored channel highlighted the presence of more uniformly distributed Ag/AgO NPs. The decreasing intensity of

the green color suggested that the Ag/AgO NPs may have an undetectable particle diameter. In the literature, image-processing software supported by artificial intelligence is suggested as an economical method for detecting nanostructures by evaluating microscopic results (34,35).

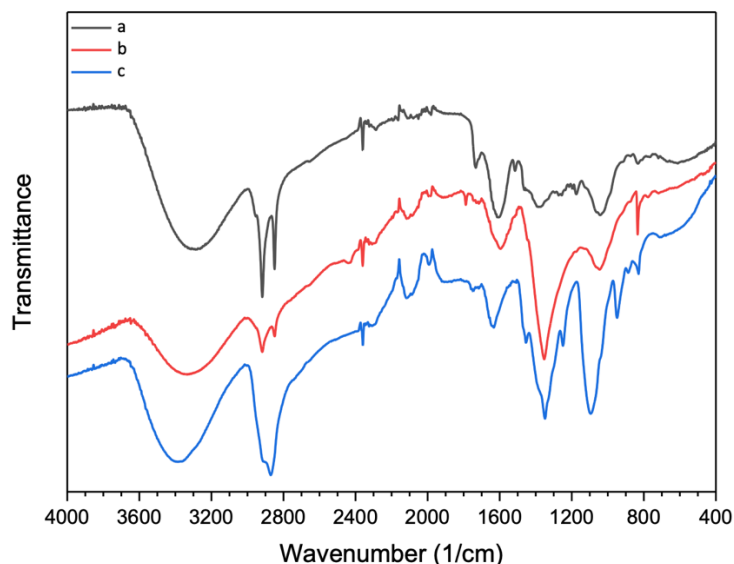


Figure 2: FTIR spectra of (a) TLE, (b) TLE/PEG, and (c) TLE/PEG/Ag/AgO NPs.

The TLE/PEG/Ag/AgO nanoparticles were found to have possessed unique functional groups according to the FTIR technique. Fig. 2 displayed the FTIR spectra of TLE, TLE/PEG, and TLE/PEG/Ag/AgO NPs. The FTIR results of TLE (Fig. 2.a) revealed distinctive peaks at specific wavenumbers: 3314 cm^{-1} (OH stretching), 2917 cm^{-1} (-CH symmetric stretching band), 2850 cm^{-1} (-CH asymmetric stretching band), 1606 cm^{-1} (C-O stretching), and 1042 cm^{-1} (C-O stretching vibrations). Additionally, a cluster of bands between 1293 to 1175 cm^{-1} corresponds to C-O-C, C-O, and O-H groups (36). In Fig. 2.b, the FTIR spectra of the TLE/PEG, it was found to have the characteristic bands at 3400 cm^{-1} (OH stretching), 2918 cm^{-1} (-CH symmetric stretching band), 2849 cm^{-1} (-CH asymmetric stretching band), 1595 cm^{-1} (C-O stretching), and 1045 cm^{-1} (C-O stretching vibrations). In this study, we attributed the low-intensity peak around 2917 cm^{-1} -2850 cm^{-1} and the highly intense peak at 1045 cm^{-1} to the formation of the prepared TLE/PEG polymeric blend (37). In Fig. 2.c, depicting the FTIR spectra of the TLE/PEG/Ag/AgO NPs, characteristic bands were identified at 3400 cm^{-1} (OH stretching), 2902 cm^{-1} (-CH symmetric stretching band), 2871 cm^{-1} (-CH asymmetric stretching band), 1663 cm^{-1} (C-O stretching), 1095 cm^{-1} (C-O stretching vibrations), 830 cm^{-1} (Ag-O), 713 cm^{-1} (Ag-O), and 535 cm^{-1} (Ag-O) (38). Compared with the FTIR spectrum of TLE/PEG, the spectrum of TLE/PEG/Ag/AgO NPs

shows observable shifts in the C-O stretching peak (from 1595 to 1663 cm^{-1}) and peaks (from 1045 to 1095 cm^{-1}). Additionally, the FTIR spectrum of TLE/PEG/Ag/AgO NPs exhibits a more intense hydroxyl peak of around 3400 cm^{-1} . The weak broadband at 2120 cm^{-1} in the FTIR spectrum of TLE/PEG/Ag/AgO NPs may be attributed to -CO-Ag (39).

These changes suggest that the NPs are synthesized and stabilized by carboxyl groups. In summary, the FTIR results of TLE, TLE/PEG, and TLE/PEG/Ag/AgO NPs show small differences; all exhibit the characteristic FT-IR spectrum of TLE/PEG. This indicates that the TLE/PEG encapsulates the NPs, effectively covering the TLE/PEG. These findings are consistent with the XRD results.

X-ray diffraction pattern analysis was used to confirm the crystallinity and phase purity of the synthesized TLE/PEG/Ag/AgO NPs, as shown in Fig. 3. The XRD data showed the effective production of TLE/PEG/Ag/AgO NPs. The cubic crystal structure of Ag NPs was identified as the source of the diffraction peaks at 2θ values of 38.24° (1 1 1), 44.50° (2 0 0), 64.76° (2 2 0), and 77.65° (3 1 1) (ICDD Card No. 01-087-0718) (40). AgO NPs' tetragonal crystal structure was also identified by peaks at 2θ values of 32.45° (2 0 2), 55.02° (2 2 4), and 67.50° (2 0 6) (ICDD Card No. 01-076-1489) (41).

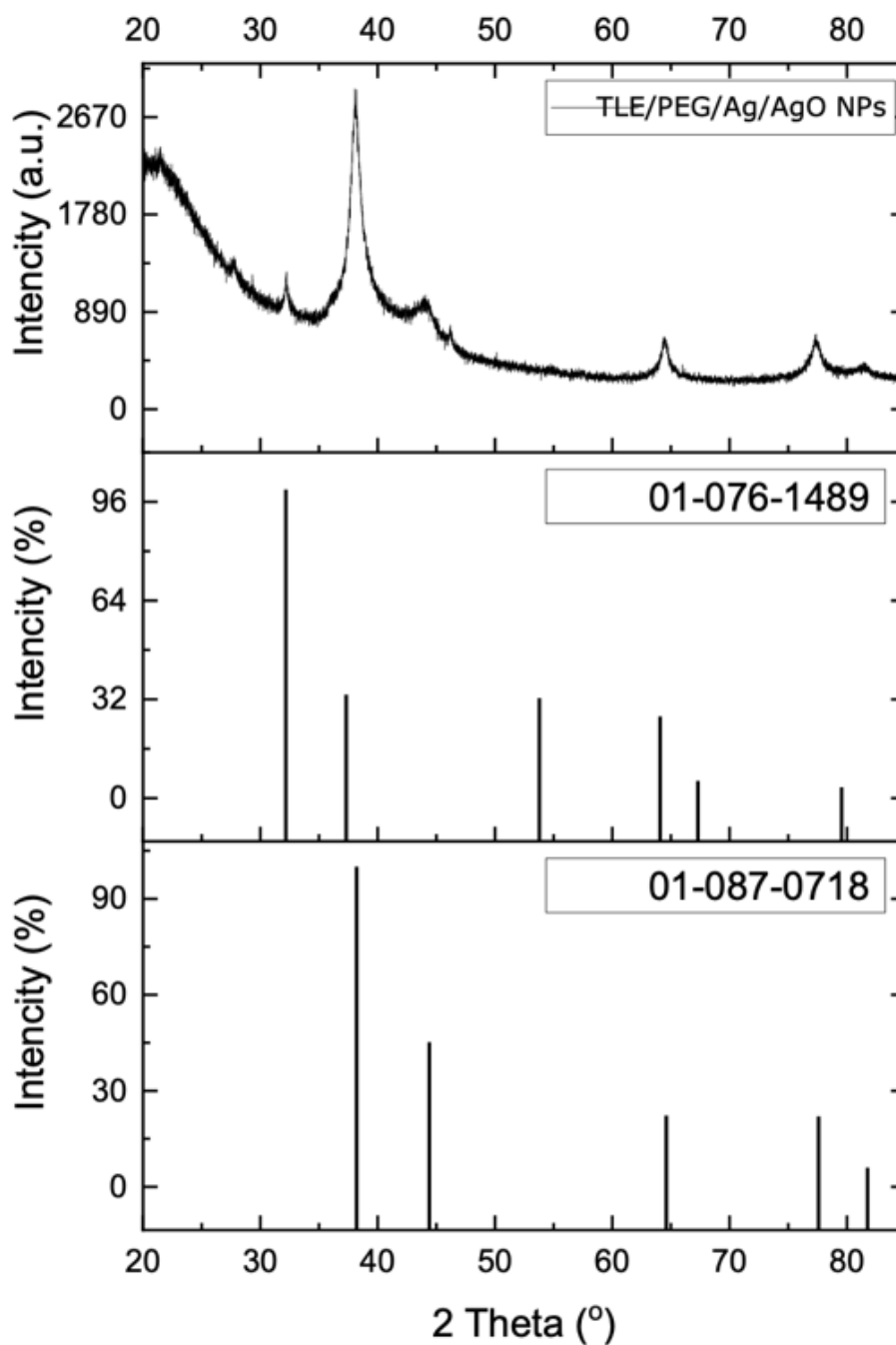


Figure 3: XRD graph of TLE/PEG/Ag/AgO NPs.

3.2. Green TLE/PEG/Ag/AgO NPs-based digital image colorimetric sensor for the detection of H_2O_2

This study employed an innovative digital image colorimetric sensor based on TLE/PEG/Ag/AgO NPs

for the detection of H_2O_2 . The digital colorimetric outcomes were analyzed through cumulative RGB histograms, and subsequently, each sample image (H_2O_2 , acetone, hexane, toluene, glucose, and IPA) was quantified using Pantone color values.

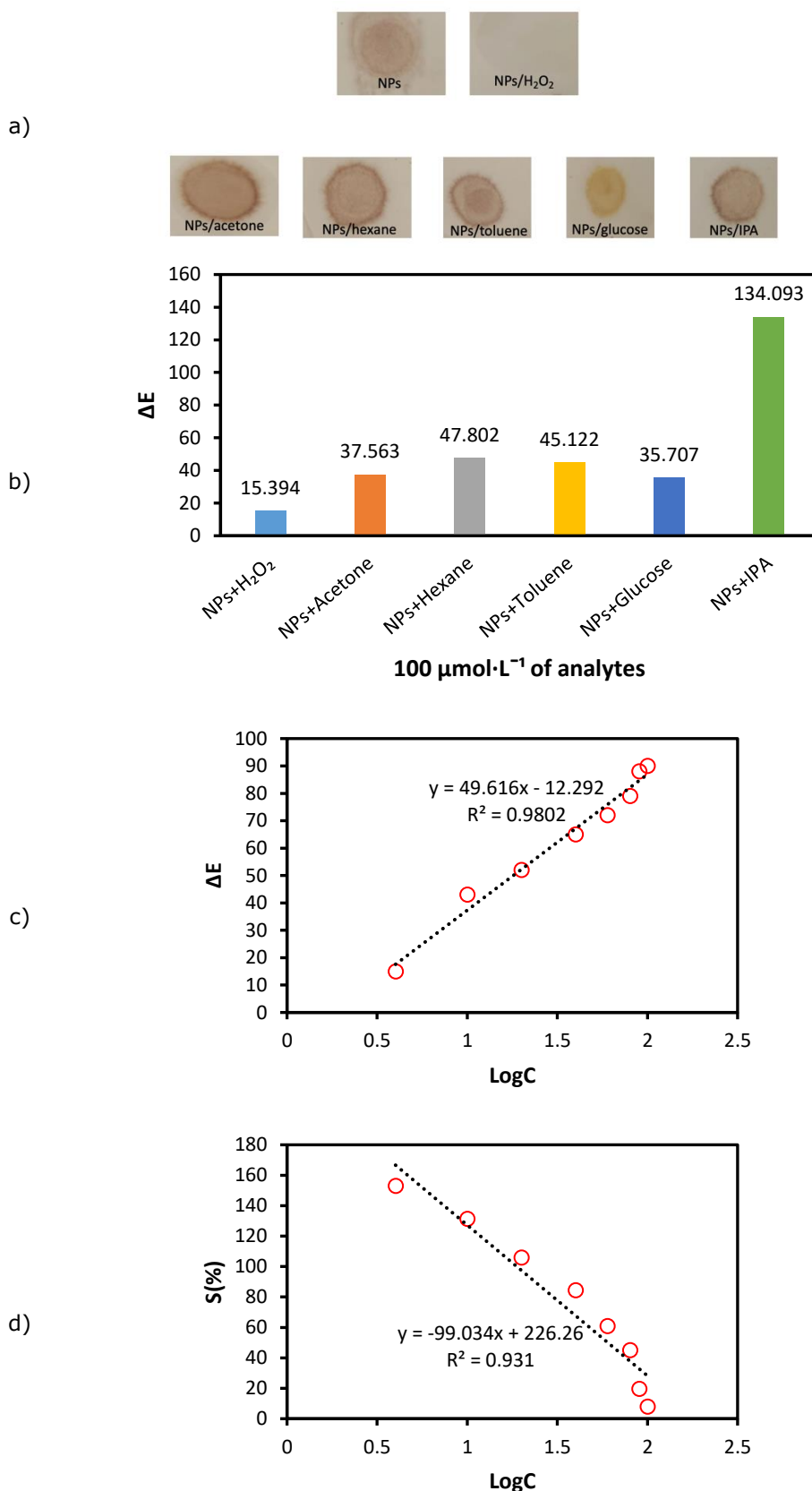


Figure 4: a) and b) Selectivity of the TLE/PEG/Ag/AgO NPs-based sensor in 100.0 μmol/L of different analytes such as H₂O₂, acetone, hexane, toluene, glucose, and IPA, the graphs of c) Log C–ΔE and (d) Log C–S (%) in a concentration range of 2.0 to 100.0 μmol/L of H₂O₂.

Figure 4 displayed various studies that demonstrated the selectivity of the TLE/PEG/Ag/AgO NPs-based sensor. The sensor's behavior towards several analytes, such as H₂O₂, acetone, hexane, glucose, and IPA, each at a concentration of 100.0

μmol/L, was depicted in Figure 4.a. The TLE/PEG/Ag/AgO NPs-based sensor's overall selectivity was summarized in Figure 4.b, highlighting its capacity for discrimination over a range of analytes and concentrations. Additional

evidence of the selectivity was provided by the graphical displays in Figures 4.c and 4.d, which showed the relationship between Log C- ΔE and Log C-S (%), respectively.

In this study, also, the color change of the analyte and the response of the colorimetric sensor were also characterized by the rate of change of the blue color (ΔB) in the RGB color channels. In control experiments, since there was no change in the blue color channel between TLE/PEG (B channel value: 155) and TLE/PEG + H₂O₂ (B channel value: 155), this was determined as the control group. Additionally, the blue color change it caused on other analytes is presented in Table 2. As can be seen, the extract containing NPs provided a higher change rate in the blue color value when applied to H₂O₂. This comparison also showed that the NPs-free extract is ineffective in detecting H₂O₂.

Table 2: Changes in blue color intensity across studied analytes.

Sample + Analyte	ΔB values
TLE + H ₂ O ₂	0
TLE/PEG + H ₂ O ₂	0
TLE/PEG/Ag/AgO NPs + H ₂ O ₂	38
TLE/PEG/Ag/AgO NPs + Acetone	20
TLE/PEG/Ag/AgO NPs + Hexane	11
TLE/PEG/Ag/AgO NPs + Toluene	7
TLE/PEG/Ag/AgO NPs + Glucose	28
TLE/PEG/Ag/AgO NPs + IPA	17

In this study, it was focused on investigating the detection of additional compounds such as IPA, H₂O₂, acetone, hexane, toluene, and glucose. The TLE/PEG/Ag/AgO NPs-based sensor, known for its sensitivity and selectivity, was utilized with the user-friendly ImageJ software. In the presence of H₂O₂, the sensitive detection exhibited a noticeable color shift, while other analytes (acetone, hexane, toluene,

glucose, and IPA) displayed a substantial color change (Fig. 4.a). The digital colorimetric TLE/PEG/Ag/AgO NPs-based sensor employed the RGB method for the detection of H₂O₂.

According to Fig.4a-d, the sample color changed from green to yellow after one minute and within the range of 2.0 to 100.0 $\mu\text{mol/L}$ of H₂O₂ concentration. The TLE/PEG/Ag/AgO NPs-based sensor's ΔE values for H₂O₂, acetone, hexane, toluene, glucose, and IPA were determined to be 15, 37, 47, 45, 35, and 134, respectively, based on the RGB data. Additionally, throughout a broad concentration range of 2.0 to 100.0 $\mu\text{mol/L}$, the ΔE values of the TLE/PEG/Ag/AgO NPs-based sensor showed a colorimetric change, ranging from 15 to 90. The TLE/PEG/Ag/AgO NPs-based sensor's colorimetric data demonstrated its extremely selective performance, with an LOD of 0.27 $\mu\text{mol/L}$ within the concentration range of 2.0 to 100.0 $\mu\text{mol/L}$. Table 3 presented various performance parameters of the Ag-contributing nanostructures designed for H₂O₂ sensing.

The experimental results reported in this work demonstrated the great potential of the TLE/PEG/Ag/AgO NPs-based sensor for H₂O₂ detection. With its large dynamic range of 2.0 to 100.0 $\mu\text{mol/L}$, sensitivity, and selectivity, it emerged as a promising option for various real-world applications. The sensor's high sensitivity was crucial for accurate detection even at low concentrations, as evidenced by its low LOD of 0.27 $\mu\text{mol/L}$. The digital colorimetric data further emphasized the sensor's rapid response, qualifying it for real-time applications. In particular, the noticeable color shift within a minute was remarkable. The colorimetric variations over a wide concentration range and the reported ΔE values for several analytes demonstrate the versatility and potential for selective detection of the sensor.

Table 3: Various performance parameters of the Ag-contributing nanostructures designed for H₂O₂ sensing.

Electrode	Potential (V)	Measurement Range (mmol/L)	LOD ($\mu\text{mol/L}$)	Sensitivity ($\mu\text{A/mM/cm}^2$)	Reference
AgNPs/3DG	-0.65	0.03-16.21	14.9	1.094	(41)
AgNPs-rGO-PANI/GCE	-0.4	0.01-1	0.05	14.7	(42)
AgNPs/CS/GE	-0.3	-	6.6	115.2	(43)
AgNPs/N-G/GCE	-0.3	0.1-126	1.2	4.46	(44)
AgNPs-rGO/ITO	-0.3	0.1-100	1.6	-	(45)
Ag/PSi/CPE	-0.45	0.0016-0.5	0.45	-	(46)
Nafion/Gr-CCS-AgNPs/GCE	-0.2	0.02-5.02	2.49	-	(47)
MWCNT/Ag nanohybrids/Gold electrode	-0.2	0.05-17	0.5	1.42	(48)
GC/rGO-Nf@Ag	-0.65	1-30	0.535	0.4508	(49)
AgNPs-MWCNT-rGO/GCE	-0.35	0.1-100	0.9	-	(50)
AgNPs/Cu-TCPP/CCE	-0.25	0.0037-5.8	1.2	21.6	(51)
AgNPs/NDs/GCE	-0.2	0.0001-0.0034	0.01	0.00159	(52)
MnO ₂ -Ag nanowire/GCE	-0.5	0.1-4	0.24	-	(53)
(PDA/AgNPs)/GCE	-0.6	0.05-1.75	6.5	-	(54)
TiO ₂ NTs/rGO/AgNPs/GCE	-0.6	0.05-15.5	2.2	1151.98	(55)
SPE/rGO@CeO ₂ -AgNPs	-0.3	0.0005-12	0.21	-	(56)
Ag-TiN/SMS	-0.3	0.00005-2.1	0.0077	33.25	(57)
Ag-HNTs-MnO ₂	-0.3	0.002-4.71	0.7	11.9	(58)

4. CONCLUSION

In conclusion, the TLE/PEG/Ag/AgO NPs-based sensor has demonstrated significant promise for H₂O₂ detection, as indicated by the study's findings. Its noteworthy features, encompassing a broad dynamic range from 2.0 to 100.0 µmol/L, excellent sensitivity, and remarkable selectivity, are underscored by the published experimental results. With a low LOD at 0.27 µmol/L, the sensor emerges as a valuable choice for numerous practical applications, showcasing its capacity for precise detection even at minute concentrations. The colorimetric data's swift response, including a discernible color shift within a minute, further accentuates its potential for real-time applications. The observed ΔE values for various analytes and the demonstrated adaptability in colorimetric fluctuations over a wide concentration range highlight the sensor's effectiveness and promise for selective detection. Overall, these results affirm that the TLE/PEG/Ag/AgO NPs-based sensor is a viable and versatile tool for accurate cancer biomarker (H₂O₂) detection, with implications for a variety of real-world applications.

5. CONFLICT OF INTEREST

There is no conflict of interest.

6. REFERENCES

- Xu J, Ma J, Peng Y, Cao S, Zhang S, Pang H. Applications of metal nanoparticles/metal-organic frameworks composites in sensing field. *Chinese Chem Lett* [Internet]. 2023 Apr;34(4):107527. Available from: [<URL>](#).
- Qanash H, Bazaid AS, Alharazi T, Barnawi H, Alotaibi K, Shater ARM, et al. Bioenvironmental applications of myco-created bioactive zinc oxide nanoparticle-doped selenium oxide nanoparticles. *Biomass Convers Biorefinery* [Internet]. 2024 Aug 1;14(15):17341–52. Available from: [<URL>](#).
- Lu N, Shao C, Li X, Miao F, Wang K, Liu Y. CuO nanoparticles/nitrogen-doped carbon nanofibers modified glassy carbon electrodes for non-enzymatic glucose sensors with improved sensitivity. *Ceram Int* [Internet]. 2016 Jul;42(9):11285–93. Available from: [<URL>](#).
- Zhang W, Hong C, Pan C. Polymerization-Induced Self-Assembly of Functionalized Block Copolymer Nanoparticles and Their Application in Drug Delivery. *Macromol Rapid Commun* [Internet]. 2019 Jan 2;40(2):1800279. Available from: [<URL>](#).
- Hulsey S, Absar S, Choi H. Investigation of simultaneous ultrasonic processing of polymer-nanoparticle solutions for electrospinning of nanocomposite nanofibers. *J Manuf Process* [Internet]. 2018 Aug;34:776–84. Available from: [<URL>](#).
- Afzali M, Mostafavi A, Shamspur T. Developing a novel sensor based on ionic liquid molecularly imprinted polymer/gold nanoparticles/graphene oxide for the selective determination of an anti-cancer drug imiquimod. *Biosens Bioelectron*

[Internet]. 2019 Oct;143:111620. Available from: [<URL>](#).

- Alavi M, Varma RS. Phytosynthesis and modification of metal and metal oxide nanoparticles/nanocomposites for antibacterial and anticancer activities: Recent advances. *Sustain Chem Pharm* [Internet]. 2021 Jun;21:100412. Available from: [<URL>](#).
- Shashiraj KN, Hugar A, Kumar RS, Rudrappa M, Bhat MP, Almansour AI, et al. Exploring the Antimicrobial, Anticancer, and Apoptosis Inducing Ability of Biofabricated Silver Nanoparticles Using *Lagerstroemia speciosa* Flower Buds against the Human Osteosarcoma (MG-63) Cell Line via Flow Cytometry. *Bioengineering* [Internet]. 2023 Jul 10;10(7):821. Available from: [<URL>](#).
- Dissanayake NM, Arachchilage JS, Samuels TA, Obare SO. Highly sensitive plasmonic metal nanoparticle-based sensors for the detection of organophosphorus pesticides. *Talanta* [Internet]. 2019 Aug;200:218–27. Available from: [<URL>](#).
- Zhai D, Liu B, Shi Y, Pan L, Wang Y, Li W, et al. Highly Sensitive Glucose Sensor Based on Pt Nanoparticle/Polyaniline Hydrogel Heterostructures. *ACS Nano* [Internet]. 2013 Apr 23;7(4):3540–6. Available from: [<URL>](#).
- Ghosh G. Early detection of cancer: Focus on antibody coated metal and magnetic nanoparticle-based biosensors. *Sensors Int* [Internet]. 2020;1:100050. Available from: [<URL>](#).
- Gholami M, Koivisto B. A flexible and highly selective non-enzymatic H₂O₂ sensor based on silver nanoparticles embedded into Nafion. *Appl Surf Sci* [Internet]. 2019 Feb;467–468:112–8. Available from: [<URL>](#).
- Teodoro KBR, Migliorini FL, Christinelli WA, Correa DS. Detection of hydrogen peroxide (H₂O₂) using a colorimetric sensor based on cellulose nanowhiskers and silver nanoparticles. *Carbohydr Polym* [Internet]. 2019 May;212:235–41. Available from: [<URL>](#).
- Ismail M, Khan MI, Akhtar K, Khan MA, Asiri AM, Khan SB. Biosynthesis of silver nanoparticles: A colorimetric optical sensor for detection of hexavalent chromium and ammonia in aqueous solution. *Phys E Low-dimensional Syst Nanostructures* [Internet]. 2018 Sep;103:367–76. Available from: [<URL>](#).
- Mohammed GM, Hawar SN. Green Biosynthesis of Silver Nanoparticles from *Moringa oleifera* Leaves and Its Antimicrobial and Cytotoxicity Activities. Ali S, editor. *Int J Biomater* [Internet]. 2022 Sep 19;2022:4136641. Available from: [<URL>](#).
- Judith Vijaya J, Jayaprakash N, Kombaiyah K, Kaviyarasu K, John Kennedy L, Jothi Ramalingam R, et al. Bioreduction potentials of dried root of Zingiber officinale for a simple green synthesis of silver nanoparticles: Antibacterial studies. *J Photochem Photobiol B Biol* [Internet]. 2017 Dec;177:62–8. Available from: [<URL>](#).
- Aldosary SK, El-Rahman SNA, Al-Jameel SS, Alromihi NM. Antioxidant and antimicrobial activities

of *Thymus vulgaris* essential oil contained and synthesis thymus (*Vulgaris*) silver nanoparticles. *Brazilian J Biol* [Internet]. 2023;83:e244675. Available from: [<URL>](#).

18. Hambardzumyan S, Sahakyan N, Petrosyan M, Nasim MJ, Jacob C, Trchounian A. *Origanum vulgare* L. extract-mediated synthesis of silver nanoparticles, their characterization and antibacterial activities. *AMB Express* [Internet]. 2020 Dec 5;10(1):162. Available from: [<URL>](#).

19. Mirzajani F, Askari H, Hamzelou S, Schober Y, Römpf A, Ghassempour A, et al. Proteomics study of silver nanoparticles toxicity on *Oryza sativa* L. *Ecotoxicol Environ Saf* [Internet]. 2014 Oct;108:335–9. Available from: [<URL>](#).

20. Singh A, Jain D, Upadhyay MK, Khandelwal N, Verma HN. Green synthesis of silver nanoparticles using *Argemone Mexicana* leaf extract and evaluation of their antimicrobial activities. *Dig J Nanomater Biostructures* [Internet]. 2010;5(2):483–9. Available from: [<URL>](#).

21. He Y, Wei F, Ma Z, Zhang H, Yang Q, Yao B, et al. Green synthesis of silver nanoparticles using seed extract of *Alpinia katsumadai*, and their antioxidant, cytotoxicity, and antibacterial activities. *RSC Adv* [Internet]. 2017;7(63):39842–51. Available from: [<URL>](#).

22. Malabadi RB, Mulgund GS, Meti NT, Nataraja K, Vijaya Kumar S. Antibacterial activity of silver nanoparticles synthesized by using whole plant extracts of *Clitoria ternatea*. *Res Pharm* [Internet]. 2012;2(4):10–21. Available from: [<URL>](#).

23. Anushaa A, Pushpa A, Vijaya KG, Thippareddy K. Green synthesis of non-cytotoxic silver nanoparticles using *Solanum nigrum* leaves extract with antibacterial properties. *GSC Biol Pharm Sci* [Internet]. 2021 Jun 30;15(3):262–71. Available from: [<URL>](#).

24. Lu L, Zhuang Z, Fan M, Liu B, Yang Y, Huang J, et al. Green formulation of Ag nanoparticles by *Hibiscus rosa-sinensis*: Introducing a navel chemotherapeutic drug for the treatment of liver cancer. *Arab J Chem* [Internet]. 2022 Feb;15(2):103602. Available from: [<URL>](#).

25. Zayed MF, Mahfoze RA, El-kousy SM, Al-Ashkar EA. In-vitro antioxidant and antimicrobial activities of metal nanoparticles biosynthesized using optimized *Pimpinella anisum* extract. *Colloids Surfaces A Physicochem Eng Asp* [Internet]. 2020 Jan;585:124167. Available from: [<URL>](#).

26. Yasmin H. M, Veerendra C. Y. Synthesis of *Coccinia grandis* (L.) Voigt extract's silver nanoparticles and its in vitro antidiabetic activity. *J Appl Pharm Sci* [Internet]. 2021 Aug 5;11(8):108–15. Available from: [<URL>](#).

27. Renuka R, Devi KR, Sivakami M, Thilagavathi T, Uthrakumar R, Kaviyarasu K. Biosynthesis of silver nanoparticles using *phyllanthus emblica* fruit extract for antimicrobial application. *Biocatal Agric Biotechnol* [Internet]. 2020 Mar;24:101567. Available from: [<URL>](#).

28. Niluxsshun MCD, Masilamani K, Mathiventhan U. Green Synthesis of Silver Nanoparticles from the Extracts of Fruit Peel of *Citrus tangerina*, *Citrus sinensis*, and *Citrus limon* for Antibacterial Activities. *Ciccarella G*, editor. *Bioinorg Chem Appl* [Internet]. 2021 Feb 2;2021:695734. Available from: [<URL>](#).

29. Hussain M, Raja NI, Mashwani Z, Naz F, Iqbal M, Aslam S. Green synthesis and characterisation of silver nanoparticles and their effects on antimicrobial efficacy and biochemical profiling in *Citrus reticulata*. *IET Nanobiotechnology* [Internet]. 2018 Jun 21;12(4):514–9. Available from: [<URL>](#).

30. Mogole L, Omwoyo W, Viljoen E, Moloto M. Green synthesis of silver nanoparticles using aqueous extract of *Citrus sinensis* peels and evaluation of their antibacterial efficacy. *Green Process Synth* [Internet]. 2021 Dec 7;10(1):851–9. Available from: [<URL>](#).

31. Basavegowda N, Rok Lee Y. Synthesis of silver nanoparticles using Satsuma mandarin (*Citrus unshiu*) peel extract: A novel approach towards waste utilization. *Mater Lett* [Internet]. 2013 Oct;109:31–3. Available from: [<URL>](#).

32. Sekkat A, Liedke MO, Nguyen VH, Butterling M, Baiutti F, Sirvent Veru J de D, et al. Chemical deposition of Cu₂O films with ultra-low resistivity: correlation with the defect landscape. *Nat Commun* [Internet]. 2022 Sep 9;13(1):5322. Available from: [<URL>](#).

33. Engel L, Benito-Altamirano I, Tarantik KR, Pannek C, Dold M, Prades JD, et al. Printed sensor labels for colorimetric detection of ammonia, formaldehyde and hydrogen sulfide from the ambient air. *Sensors Actuators B Chem* [Internet]. 2021 Mar;330:129281. Available from: [<URL>](#).

34. Thompson NBA, O'Sullivan SE, Howell RJ, Bailey DJ, Gilbert MR, Hyatt NC. Objective colour analysis from digital images as a nuclear forensic tool. *Forensic Sci Int* [Internet]. 2021 Feb;319:110678. Available from: [<URL>](#).

35. Karakuş S, Özbaş F, Baytemir G, Taşaltın N. Cubic-shaped *corylus colurna* extract coated Cu₂O nanoparticles-based smartphone biosensor for the detection of ascorbic acid in real food samples. *Food Chem* [Internet]. 2023 Aug;417:135918. Available from: [<URL>](#).

36. Boughendjioua H, Mezedjeri NEH, Idjouadiene I. Chemical constituents of Algerian mandarin (*Citrus reticulata*) essential oil by GC-MS and FT-IR analysis. *Curr Issues Pharm Med Sci* [Internet]. 2020 Dec 1;33(4):197–201. Available from: [<URL>](#).

37. Georgieva M, Gospodinova Z, Keremidarska-Markova M, Kamenska T, Gencheva G, Krasteva N. PEGylated Nanographene Oxide in Combination with Near-Infrared Laser Irradiation as a Smart Nanocarrier in Colon Cancer Targeted Therapy. *Pharmaceutics* [Internet]. 2021 Mar 22;13(3):424. Available from: [<URL>](#).

38. Rita A, Sivakumar A, Dhas SSJ, Dhas SAMB. Structural, optical and magnetic properties of silver oxide (AgO) nanoparticles at shocked conditions. *J*

- Nanostructure Chem [Internet]. 2020 Dec 24;10(4):309–16. Available from: [<URL>](#).
39. Bhagyaraj S, Krupa I. Alginate-Mediated Synthesis of Hetero-Shaped Silver Nanoparticles and Their Hydrogen Peroxide Sensing Ability. *Molecules* [Internet]. 2020 Jan 21;25(3):435. Available from: [<URL>](#).
40. Jaiswal KK, Banerjee I, Dutta S, Verma R, Gunti L, Awasthi S, et al. Microwave-assisted polycrystalline Ag/AgO/AgCl nanocomposites synthesis using banana corm (rhizome of *Musa sp.*) extract: Characterization and antimicrobial studies. *J Ind Eng Chem* [Internet]. 2022 Mar;107:145–54. Available from: [<URL>](#).
41. Zhan B, Liu C, Shi H, Li C, Wang L, Huang W, et al. A hydrogen peroxide electrochemical sensor based on silver nanoparticles decorated three-dimensional graphene. *Appl Phys Lett* [Internet]. 2014 Jun 16;104(24):243704. Available from: [<URL>](#).
42. Kumar V, Gupta RK, Gundampati RK, Singh DK, Mohan S, Hasan SH, et al. Enhanced electron transfer mediated detection of hydrogen peroxide using a silver nanoparticle-reduced graphene oxide-polyaniline fabricated electrochemical sensor. *RSC Adv* [Internet]. 2018;8(2):619–31. Available from: [<URL>](#).
43. Dodevska T, Vasileva I, Denev P, Karashanova D, Georgieva B, Kovacheva D, et al. Rosa damascena waste mediated synthesis of silver nanoparticles: Characteristics and application for an electrochemical sensing of hydrogen peroxide and vanillin. *Mater Chem Phys* [Internet]. 2019 Jun;231:335–43. Available from: [<URL>](#).
44. Tian Y, Wang F, Liu Y, Pang F, Zhang X. Green synthesis of silver nanoparticles on nitrogen-doped graphene for hydrogen peroxide detection. *Electrochim Acta* [Internet]. 2014 Nov;146:646–53. Available from: [<URL>](#).
45. Moradi Golsheikh A, Huang NM, Lim HN, Zakaria R, Yin CY. One-step electrodeposition synthesis of silver-nanoparticle-decorated graphene on indium-tin-oxide for enzymeless hydrogen peroxide detection. *Carbon N Y* [Internet]. 2013 Oct;62:405–12. Available from: [<URL>](#).
46. Ensafi AA, Rezaloo F, Rezaei B. Electrochemical sensor based on porous silicon/silver nanocomposite for the determination of hydrogen peroxide. *Sensors Actuators B Chem* [Internet]. 2016 Aug;231:239–44. Available from: [<URL>](#).
47. Wang H, Wang H, Li T, Ma J, Li K, Zuo X. Silver nanoparticles selectively deposited on graphene-colloidal carbon sphere composites and their application for hydrogen peroxide sensing. *Sensors Actuators B Chem* [Internet]. 2017 Feb;239:1205–12. Available from: [<URL>](#).
48. Zhao W, Wang H, Qin X, Wang X, Zhao Z, Miao Z, et al. A novel nonenzymatic hydrogen peroxide sensor based on multi-wall carbon nanotube/silver nanoparticle nanohybrids modified gold electrode. *Talanta* [Internet]. 2009 Dec 15;80(2):1029–33. Available from: [<URL>](#).
49. Yusoff N, Rameshkumar P, Mehmood MS, Pandikumar A, Lee HW, Huang NM. Ternary nanohybrid of reduced graphene oxide-nafion/silver nanoparticles for boosting the sensor performance in non-enzymatic amperometric detection of hydrogen peroxide. *Biosens Bioelectron* [Internet]. 2017 Jan;87:1020–8. Available from: [<URL>](#).
50. Lorestani F, Shahnava Z, Mn P, Alias Y, Manan NSA. One-step hydrothermal green synthesis of silver nanoparticle-carbon nanotube reduced-graphene oxide composite and its application as hydrogen peroxide sensor. *Sensors Actuators B Chem* [Internet]. 2015 Mar;208:389–98. Available from: [<URL>](#).
51. Ma J, Bai W, Zheng J. Non-enzymatic electrochemical hydrogen peroxide sensing using a nanocomposite prepared from silver nanoparticles and copper (II)-porphyrin derived metal-organic framework nanosheets. *Microchim Acta* [Internet]. 2019 Jul 27;186(7):482. Available from: [<URL>](#).
52. Habibi B, Jahanbakhshi M. Sensitive determination of hydrogen peroxide based on a novel nonenzymatic electrochemical sensor: silver nanoparticles decorated on nanodiamonds. *J Iran Chem Soc* [Internet]. 2015 Aug 4;12(8):1431–8. Available from: [<URL>](#).
53. Han Q, Ni P, Liu Z, Dong X, Wang Y, Li Z, et al. Enhanced hydrogen peroxide sensing by incorporating manganese dioxide nanowire with silver nanoparticles. *Electrochem Commun* [Internet]. 2014 Jan;38:110–3. Available from: [<URL>](#).
54. Wang F, Han R, Liu G, Chen H, Ren T, Yang H, et al. Construction of polydopamine/silver nanoparticles multilayer film for hydrogen peroxide detection. *J Electroanal Chem* [Internet]. 2013 Oct;706:102–7. Available from: [<URL>](#).
55. Wang W, Xie Y, Xia C, Du H, Tian F. Titanium dioxide nanotube arrays modified with a nanocomposite of silver nanoparticles and reduced graphene oxide for electrochemical sensing. *Microchim Acta* [Internet]. 2014 Aug 27;181(11–12):1325–31. Available from: [<URL>](#).
56. Yao S, Xu J, Wang Y, Chen X, Xu Y, Hu S. A highly sensitive hydrogen peroxide amperometric sensor based on MnO₂ nanoparticles and dihexadecyl hydrogen phosphate composite film. *Anal Chim Acta* [Internet]. 2006 Jan;557(1–2):78–84. Available from: [<URL>](#).
57. Chu Y, Huang Z, Wang X, Zhou M, Zhao F. Highly dispersed silver imbedded into TiN microspheres for electrochemical detecting of hydrogen peroxide. *Sci Rep* [Internet]. 2020 Dec 17;10(1):22126. Available from: [<URL>](#).
58. Zhang S, Sheng Q, Zheng J. Synthesis of Ag-HNTs-MnO₂ nanocomposites and their application for nonenzymatic hydrogen peroxide electrochemical sensing. *RSC Adv* [Internet]. 2015;5(34):26878–85. Available from: [<URL>](#).



Elucidation of Cu-AMT Structure by Voltammetric Method

Kübra Gençdağ Şensoy¹ [ORCID](#), Ali Ersin Karagözler² [ORCID](#)

¹Department of Food Processing, Köşk Vocational High School, Aydın Adnan Menderes University, Aydın, Turkey.

²Department of Chemistry, Faculty of Science, Aydın Adnan Menderes University, Aydın, Turkey.

Abstract: The long-term anthropogenic release of metals has increased their distribution and concentration in ecosystems, leading to sustained interest in their behavior and impact. Metals are not biodegradable and are converted from one chemical state to another. Even in low concentrations, heavy metals carry high danger. Therefore, the need for continuous control of trace metals in the environment is increasing. In this technique, the metal to be analyzed is deposited on the electrode surface in the form of metal complexes, and determinations are made using the peak currents obtained by potential scanning in the cathodic or anodic direction. The sensitivity and selectivity of the assay are increased by the choice of the ligand used as the complexing agent. In the study carried out to elucidate the structure of the complex formed by Cu(II) with 5-amino-1,3,4-thiadiazole-2-thiol (AMT), it was estimated that the complex structure could probably be in the ratio of 1:1. In addition, studies have been carried out to determine the stability of the complexes to be formed in various environments since the stability of the complex is related to the species in the solution comprising the medium, its concentration and the pH of the solution.

Keywords: 5-amino-1,3,4-thiadiazole-2-thiol, Trace element, Adsorptive stripping voltammetry (AdSV), Mercury drop electrode, Stoichiometry.

Submitted: December 7, 2023. **Accepted:** July 23, 2024.

Cite this: Gençdağ Şensoy K, Karagözler AE. Elucidation of Cu-AMT Structure by Voltammetric Method. JOTCSA. 2024;11(3): 1313-20.

DOI: <https://doi.org/10.18596/jotcsa.1401623>

***Corresponding author's E-mail:** kubra.genccdag.sensoy@adu.edu.tr

1. INTRODUCTION

Environmental control is one of the main applications of electroanalytical chemistry, and its importance in the determination of pollutants is increasing day by day. Electrochemical measuring devices are of great importance in controlling contaminants in situ, as they allow the instrument to be taken to the sample rather than to the laboratory. Progress in miniaturization technology has allowed the development of sensitive and sensitive electrochemical devices for in situ and instant measurement (1). Electrochemical sensors and detectors are well suited for on-site control of primary pollutants. These devices meet most of the requirements of on-site environmental analysis.

Copper is critical in environmental studies due to its widespread occurrence, potential toxicity, and ecological significance. Its presence in environmental samples can indicate pollution from various sources, including industrial processes, agriculture, and urban runoff.

Several analytical techniques are used to determine copper in environmental samples, each offering different levels of sensitivity, selectivity, and precision. When the literature studies in recent years are examined, spectroscopic methods (inductively coupled plasma-optical emission spectrometry, inductively coupled plasma mass spectrometry, flame atomic absorption spectroscopy (2-4), electrochemical techniques (voltammetry) (5), and portable analytical tools (X-ray fluorescence) are widely used.

The voltammetric determination of copper has undergone significant advancements, driven by the increasing demand for precise, rapid, and cost-effective analytical techniques. Voltammetry, known for its high sensitivity and selectivity in detecting trace metal ions, has been enhanced through various innovations, making it a vital tool in environmental monitoring, industrial applications, and biomedical research.

One key innovation is the development of advanced electrode materials. Traditional mercury-based

electrodes, which pose environmental and health risks, are being replaced by eco-friendly alternatives such as bismuth, carbon nanotubes, and graphene-based electrodes. These materials not only mitigate health and environmental concerns but also improve detection limits and analytical performance (5).

Another significant advancement is the integration of microfluidic systems and the miniaturization of voltammetric devices. These portable and on-site systems enable real-time monitoring of copper levels in various environmental matrices, providing critical data for timely decision-making in pollution control and remediation efforts (6).

Additionally, improvements in software and computational methods have revolutionized data analysis and interpretation in voltammetry. The incorporation of machine learning algorithms and advanced signal processing techniques has enhanced the accuracy and reliability of copper determination, allowing for better handling of complex datasets (7).

These innovations, ranging from advanced electrode materials to portable devices and sophisticated data analysis tools, have significantly expanded the capabilities of voltammetric techniques. They play a crucial role in addressing contemporary challenges in environmental science, public health, and industrial quality control, ensuring precise and efficient monitoring of copper in diverse settings.

The interaction between AMT (5-amino-1,3,4-thiadiazole-2-thiol) and Cu^{2+} (copper (II) ion) generally occurs in the form of a complex formation. AMT interacts with copper (II) ions as a strong complexing agent and forms complexes with high stability.

AMT contains a triazole compound, and the nitrogen and sulfur atoms in this ring connect coordinative bonds with copper (II) ions. Copper (II) ions are generally systems of four- or six-coordinated complexes. Depending on the structure of AMT, these complexes can be four-coordinated, and coordinative bonds occur between the nitrogen and sulfur atoms of AMT and copper (II) ions.

In recent years, electrochemical techniques based on stripping analyses have attracted attention for the in situ determination of selected metals (8–10). For example, a method based on stripping potentiometry (for traces of copper, cadmium, lead, and zinc) and adsorptive stripping voltammetry (for traces of chromium) has been used successfully to study metal contamination in soils and sediments at hazardous waste sites (11). In these in situ measurements, the concentration values measured by stripping analyses were found to be close to those obtained by the Environmental Protection Agency (EPA). The very low detection limits achieved by anodic stripping voltammetry (ASV) are due to the concentration of the analyte in the sample solution during the deposition step. Unlike techniques such as atomic absorption spectrometry and inductively coupled plasma emission spectrometry, which determine only the total metal concentration, ASV detects not only

the total metal concentration but also the reactive metal, which is a fraction of the total metal concentration. High sensitivity, portability, and low cost make stripping analyses attractive for the identification of contaminated sites and in situ analysis of selected metals during their remediation. There are not many examples in the literature of the use of AMT in the study for analytical purposes. Three of these few studies are about immobilizing AMT on silica gel and removing heavy metals from water with immobilized particles (11–13).

Other studies demonstrate the electrocatalysis, selectivity, and signal-enhancing effects of 5-amino-1,3,4-thiadiazole-2-thiol thin-film electrodes, which are generally formed by electropolymerization on carbon electrodes (14–20).

In this study, using the adsorptive stripping voltammetry (AdSV) technique, trace levels of the Cu element were complexed with 5-amino-1,3,4-thiadiazole-2-thiol (AMT), deposited on the mercury drop electrode, and then applied in the appropriate direction. The aim was to determine the amount of the trace element by stripping it from the electrode and performing a potential scan. To avoid the interference effect of other metals, pH, accumulation potential, and accumulation time were adjusted during voltammetric analysis to increase the selectivity of Cu^{2+} detection. These parameters are optimized to support the formation and detection of Cu^{2+} complexes relative to other metals. The fact that 5-amino-1,3,4-thiadiazole-2-thiol has been used for the first time in stripping voltammetry in the determination of Cu will contribute to the emergence of a new field of study in this field.

2. EXPERIMENTAL SECTION

2.1. Reagent and Solutions

All reagents used were analytical reagent grade, and all solutions were prepared using ultrapure water. 10^{-2} M Cu^{2+} stock solution: It was prepared by dissolving 0.1705 g $\text{CuCl}_2 \cdot 2\text{H}_2\text{O}$ in 100 mL ultrapure water.

5-amino 1,3,4-thiadiazole 2-thiol (AMT): This was prepared daily at a concentration of 10^{-2} M. 0.0133 g of AMT was dissolved in 10 mL of dimethylformamide (DMF).

Preparation of 0.1 M Britton-Robinson buffer solution: Ultrapure water by mixing 6.1830 g H_3BO_3 , 6.75 mL H_3PO_4 (85%, $d=1.71$ g/mL), 5.75 mL CH_3COOH (100%, $d=1.05$ g/mL) and 7.45 g KCl made up to 1000 mL. The pH was adjusted to the desired value by adding dropwise 2 M NaOH solution onto 250 mL portions of the prepared stock buffer solution. pH=2.0, 5.0, 7.0, and 9.0 Britton-Robinson (BR) buffer solutions were obtained, and studies were carried out on these pHs.

2.2. Apparatus

Voltammetric measurements were carried out by using the IVIUM Compact Stat Plus Module. The three-electrode system consisted of a mercury drop electrode working electrode (Bioanalytical Systems, Inc.), an Ag/AgCl/KCl reference electrode (BAS,

Model RE-5B, W. Lafayette, USA), and a platinum wire as the auxiliary electrode.

Fourier transform infrared (FT-IR, Measurement mode: ATR, Resolution: 4 cm^{-1} , four scans) spectroscopy was employed to characterize liquid Cu, AMT, and Cu-AMT complex within the range of $4000\text{--}450\text{ cm}^{-1}$ (Perkin Elmer, spectrum two, USA).

2.3. Removal of Mercury

Dirty mercury was taken into falcon tubes, approximately 5 mL each. Up to 40 mL of tap water was added and vortexed. This process was repeated at least five times. The mercury fractions through which the tap water was passed were collected in a single tube and vortexed again (to ensure homogeneity). The same procedures were repeated by adding 2 M HNO_3 . The mercury fractions vortexed with HNO_3 were vortexed with distilled water until their acidity was removed. The deacidified mercury was taken into a clean beaker and dried on filter paper at $50\text{ }^\circ\text{C}$ in the oven. It was checked voltammetrically whether the mercury taken into the mercury chamber contained impurities.

2.4. Removal of Dissolved O_2 from Analysis Solutions

Oxygen creates the following problems in voltammetric studies because it gives a wide range of reduction waves and is a strong oxidant;

- Reduction of O_2 creates an additional faradaic current.
- O_2 reduction waves interfere with analyte waves because they cover a wide potential range.
- Some analytes can react with oxygen. For example, in the presence of heavy metal ions, metal oxides are formed or cause oxidation of the metal collected in anodic stripping voltammetry.

For these reasons, it is necessary to remove dissolved O_2 from the analysis solutions. The most convenient method for removing oxygen is by bubbling pre-purified nitrogen gas through the analysis solution. For solutions with high analyte concentration, nitrogen directly from the tank can be used. However, direct use of tank nitrogen is not suitable for solutions with low analyte concentration. With the oxygen cleaning system, the oxygen in the nitrogen gas must also be removed beforehand.

There are different methods for this final purification process, with varying levels of ease of use. The most common of these methods is the use of vanadium chloride solution, which was applied in this study.

This solution consists of boiling two grams of ammonium metavanadate with 25 mL of concentrated hydrochloric acid, then diluting it with water to 250 mL and reducing it by adding a few grams of zinc amalgam. When nitrogen gas containing traces of oxygen is passed through the blue or green vanadium solution obtained, it is reduced to the vanadium (II) stage, and the solution becomes clear purple.

Once depleted (as evidenced by the disappearance of the purple color), vanadium chloride solutions can be reconstituted by adding a few mL of concentrated hydrochloric acid or zinc powder mixed with more mercury.

3. RESULTS AND DISCUSSION

Classically, the most common method used for the voltammetric determination of trace metals is anodic stripping voltammetry. In this method, metals are deposited on the mercury drop to form an amalgam with mercury at a potential more negative than the reduction potential and then oxidized from the electrode by an anodic scan. The differential pulse technique is generally used as the scanning technique. Metals can also be determined by scanning in the cathodic direction. Since there is no accumulation step in this approach, the detection limit of the method is higher than that of ASV.

Adsorptive stripping voltammetry is an alternative detection approach used for the determination of trace metals whose detection limit is not low enough or which are outside the potential window of the electrode used in the determination of redox potential or at potentials close to the anodic/cathodic potential limits. The concentration of the metal is determined by the voltammetric peaks observed as a result of the anodic or cathodic scans of the complex, which is formed in the solution or on the electrode surface, with the metal to be determined and adsorbed on the electrode surface.

3.1. Cyclic Voltammetric Behaviors of AMT and Cu-AMT Complexes

The voltammograms obtained on the suspended mercury drop electrode of 10^{-5} M AMT solution in four different pH environments are shown in Figure 1. While anodic and cathodic peaks are not observed at low pH, especially cathodic peaks that occur at $\text{pH}=7$ and 9, with an increase in pH ($\text{pH}=9$), the cathodic peak becomes more pronounced and shifts to more positive potentials.

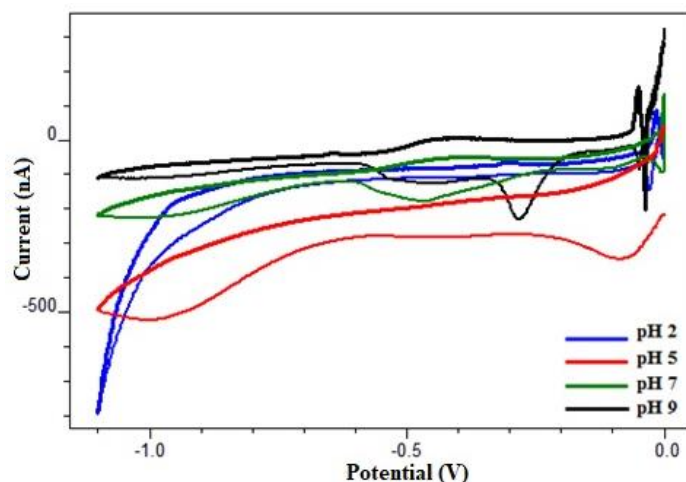


Figure 1: Comparison of cyclic voltammograms of 10^{-5} M AMT taken in pH=2.0, 5.0, 7.0, and 9.0 BR buffer.

Figure 2 shows the cyclic voltammetric behavior of solutions containing 10^{-6} M Cu and 10^{-5} M AMT (1:10 Cu: AMT mole ratio) obtained at different pHs on a suspended mercury drop electrode. At this stage, it is not possible to determine precisely whether the

small peaks that appear in the cathodic scanning, depending on the pH of the environment in four different pH environments, are caused by AMT itself or a possible Cu: AMT complex.

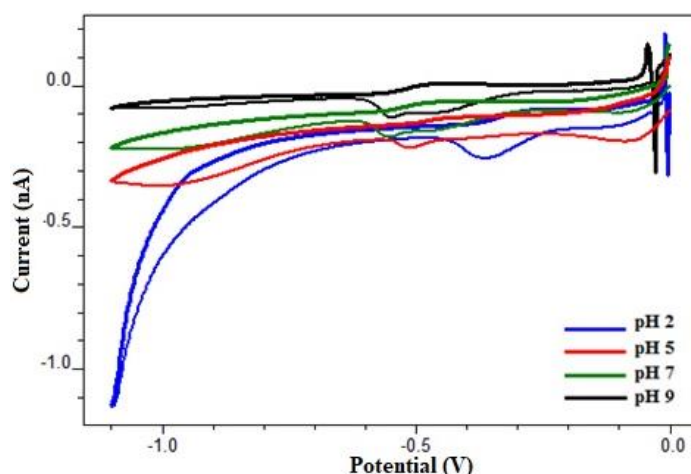


Figure 2: Comparison of cyclic voltammograms of Cu-AMT (1:10) complex taken in BR buffer pH=2.0, 5.0, 7.0, and 9.0.

3.2. Effect of Cu and Cu-AMT Complex on Cathodic Scanning, Anodic Scanning and Anodic Stripping Peaks

When the peak heights and positions in voltammograms taken with pure AMT, Cu, and Cu: AMT (1:10) complex solutions at four different pHs were examined, it was observed that Cu^{2+} formed a complex with AMT only in pH 2 BR buffer.

When Figure 3 is examined, Cu^{2+} at pH=2 gives a small (34 nA) reduction peak in the cathodic scan. In the anodic scans, the copper peaks are higher (84 and 405 nA). It is expected that the anodic stripping peak (405 nA) is this high, as Cu^{2+} is concentrated by forming amalgam on the mercury drop for 60 seconds in the stripping mode. The fact that the Cu^{2+} peak in the anodic direction is larger than the peak in the cathodic direction (84 nA > 34 nA), without precipitation step, is Cu^{2+} with the negative potential effect applied to the electrode in a short time from -

1.1 V, which is the beginning of the anodic scanning until the Cu^{2+} peak appears (-0.388 V). This can be explained by the accumulation of mercury on the electrode surface.

The histogram drawn for the copper metal clearly shows that the Cu-AMT complex is formed at this pH, and the peak of this complex causes a peak of about ten times ($336/34 \sim 10$ times) size compared to the pure copper peak in the cathodic scan. On the other hand, the peak obtained by the anodic stripping technique in the presence of AMT is higher than the peak obtained in the absence of ligand in the medium ($469 \text{ nA} > 405 \text{ nA}$).

The results in the pH=2 environment of copper metal clearly show that the presence of AMT allows the obtaining of higher peak currents by both cathodic scanning and anodic stripping voltammetry.

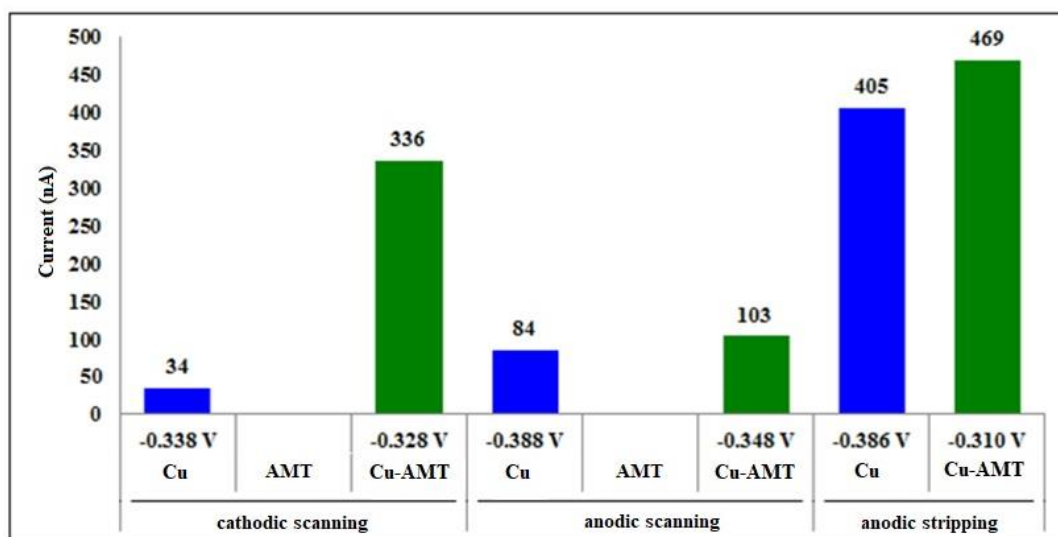


Figure 3: Peak heights measured from differential pulse voltammograms taken in pH 2 BR buffer of Cu^{2+} (10^{-6} M), AMT (10^{-5} M), and Cu: AMT 1:10 (10^{-6} M Cu^{2+} and the solution containing 10^{-5} M AMT) and comparison of their location.

3.3. Elucidation of the Structure of the Complex

To elucidate the Cu-AMT complex structure, cathodic scans were carried out in a series of solutions in which the mole ratios of Cu-AMT were changed systematically. The peak heights measured from the cathodic scanning voltammograms obtained by adding at least 10 μL of 10^{-6} M Cu solution to the 10^{-5} M AMT solution each time were plotted in Figure 4 on a bar chart.

Both the volumes of Cu^{2+} solution added, and the mole ratios of Cu-AMT are shown on the horizontal axis of the graph. When the graph is examined, it is seen that the Cu-AMT complex peak increases regularly until the mole ratio of Cu-AMT is roughly 1. Therefore, it can be said that the resulting complex is a 1:1 complex.

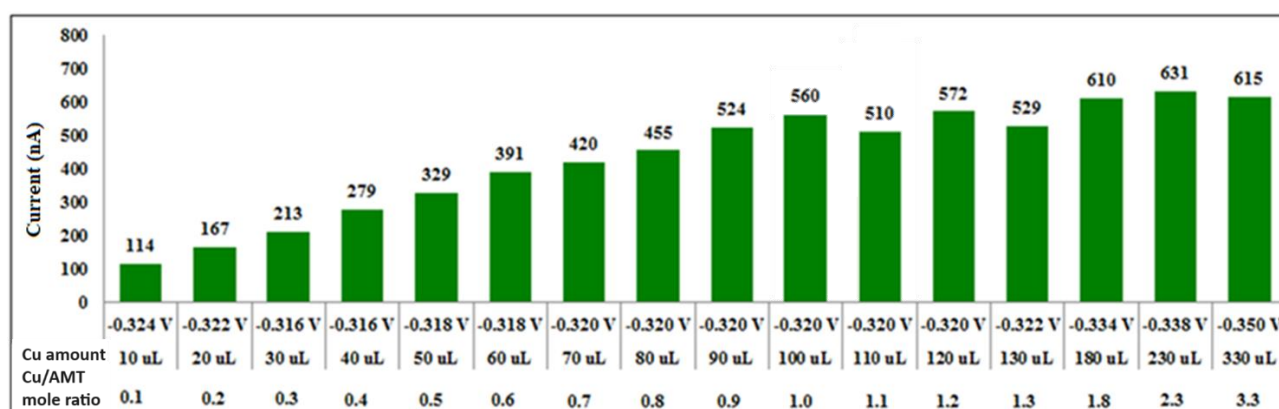


Figure 4: Histogram giving the responses of cathodic scanning voltammograms taken in pH 2 BR buffer after each addition of at least 10 μL of 10^{-6} M Cu solution to 10^{-5} M AMT solution.

3.4. Characterization of Cu, AMT, and Cu-AMT complex by FT-IR

The chemical characterization was investigated using FT-IR. The FTIR spectra were recorded in the range of $4000\text{--}450\text{ cm}^{-1}$.

The peak seen in the Cu and Cu-AMT spectra around 3400 cm^{-1} belongs to O-H stretching vibrations. O-H stretching is generally a vibration that gives a wide and intense signal. In the AMT spectrum, the bands between 3000 and 2800 cm^{-1} indicate NH_2 stretching vibration. Bands in the range of $1500\text{--}1000\text{ cm}^{-1}$ can

be assigned to CN, CN, NN, and CS stretching vibrations, respectively. When the band between $700\text{--}400\text{ cm}^{-1}$ in all three spectra is examined, the change in AMT suggests that Cu forms a complex with AMT.

In the previous study in the literature, the structure of the complex was elucidated with IR, and its stoichiometry was found to be 1:1 (21). It is consistent with our study.

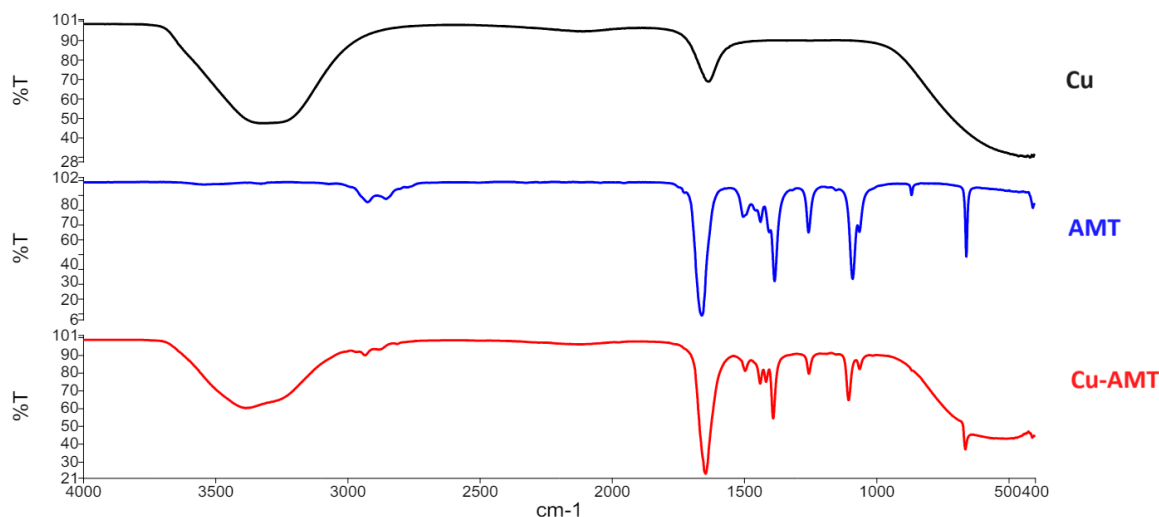


Figure 5: FT-IR spectra taken for characterization of Cu, AMT, and Cu-AMT complex.

3.5. Detection Limit of Cu Determination

The limit of detection (LOD) and quantification (LOQ) for electrochemical Cu determination was calculated by measuring the signal of Cu at different concentrations ranging from 1×10^{-6} to 1×10^{-5} M (Figure 6). According to the procedure reported by

Miller and Miller (22), the LOD and LOQ of Cu were calculated using the regression equations ($y = 5E+07x + 71,6$, $R^2 = 0,995$), and it was found to be $0,68 \mu\text{M}$ and $2,2 \mu\text{M}$ respectively.

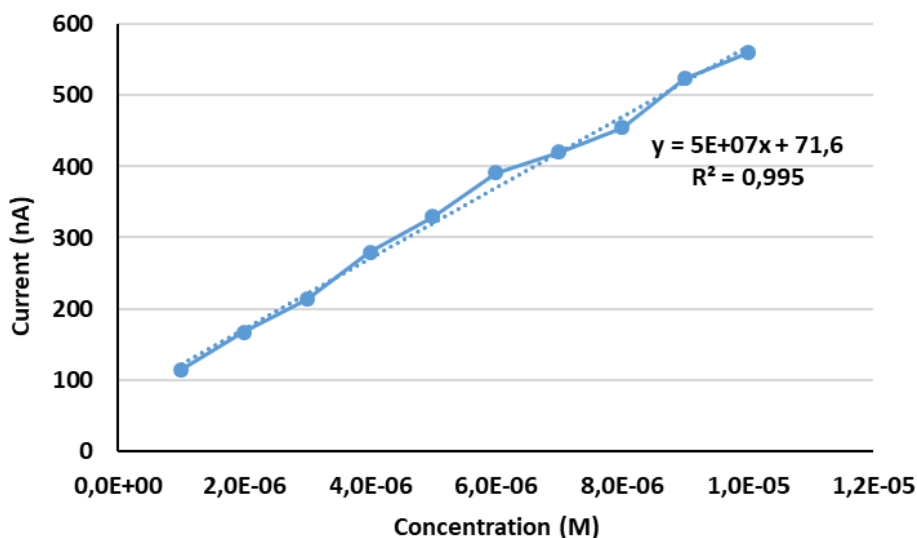


Figure 6: The calibration graph illustrates the oxidation signal of Cu obtained at various concentrations from 1 to 10 μM .

4. CONCLUSION

When designing an electrochemical sensor for copper determination, the detection mechanism plays a crucial role in ensuring sensitivity, selectivity, and reliability. One of the most widely used and effective detection mechanisms is anodic stripping voltammetry (ASV).

ASV is particularly suitable for detecting trace levels of copper due to its high sensitivity and low detection limits. The mechanism involves a two-step process: first, copper ions are pre-concentrated onto the electrode surface by applying a negative potential, causing the ions to be reduced and deposited as a metallic layer. In the second step, the potential is swept in the positive direction, causing the copper to oxidize and strip back into the solution. The current produced during this stripping process is directly

proportional to the concentration of copper in the sample.

In the study carried out to elucidate the structure of the complex formed by Cu(II) with AMT, it was estimated that the complex structure could probably be in the ratio of 1:1.

5. CONFLICT OF INTEREST

The authors possessed no relevant financial or non-financial interests.

6. REFERENCES

1. Thongngamdee S. Novel electrochemical sensors for environmental monitoring [Internet]. [New Mexico]: New Mexico State University; 2006. Available from: [<URL>](#).

2. Hou X, Jones BT. Inductively Coupled plasma/optical emission spectrometry. In: Meyers RA, editor. Encyclopedia of Analytical Chemistry [Internet]. Chichester: John Wiley & Sons Ltd; 2000. p. 9468–85. Available from: [<URL>](#).
3. Chen S, Liu C, Yang M, Lu D, Zhu L, Wang Z. Solid-phase extraction of Cu, Co and Pb on oxidized single-walled carbon nanotubes and their determination by inductively coupled plasma mass spectrometry. J Hazard Mater [Internet]. 2009 Oct 15;170(1):247–51. Available from: [<URL>](#).
4. Tautkus S, Kazlauskas R, Kareiva A. Determination of copper in tea leaves by flame atomic absorption spectrometry. Chemija [Internet]. 2004;15(4):49–52. Available from: [<URL>](#).
5. Ariño C, Serrano N, Díaz-Cruz JM, Esteban M. Voltammetric determination of metal ions beyond mercury electrodes. A review. Anal Chim Acta [Internet]. 2017 Oct 16;990:11–53. Available from: [<URL>](#).
6. Aryal P, Hefner C, Martinez B, Henry CS. Microfluidics in environmental analysis: Advancements, challenges, and future prospects for rapid and efficient monitoring. Lab Chip [Internet]. 2024 Feb 27;24(5):1175–206. Available from: [<URL>](#).
7. Ramachandran R, Chen TW, Chen SM, Baskar T, Kannan R, Elumalai P, et al. A review of the advanced developments of electrochemical sensors for the detection of toxic and bioactive molecules. Inorg Chem Front [Internet]. 2019 Dec 3;6(12):3418–39. Available from: [<URL>](#).
8. Fleet B, Gunasingham H. Electrochemical sensors for monitoring environmental pollutants. Talanta [Internet]. 1992 Nov 1;39(11):1449–57. Available from: [<URL>](#).
9. Tercier M -L., Buffle J. In situ voltammetric measurements in natural waters: Future prospects and challenges. Electroanalysis [Internet]. 1993 Apr 9;5(3):187–200. Available from: [<URL>](#).
10. Olsen KB, Wang J, Setiadji R, Lu J. Field screening of chromium, cadmium, zinc, copper, and lead in sediments by stripping analysis. Environ Sci Technol [Internet]. 1994 Nov 1;28(12):2074–9. Available from: [<URL>](#).
11. Tzvetkova P, Vassileva P, Nickolov R. Modified silica gel with 5-amino-1,3,4-thiadiazole-2-thiol for heavy metal ions removal. J Porous Mater [Internet]. 2010 Aug 7;17(4):459–63. Available from: [<URL>](#).
12. Dogan CE, Akcin G. Sorption and Desorption of Lead on 5-Amino-1,3,4-Thiadiazole-2-Thiol Immobilized Silica Gel by Flame Atomic Absorption Spectrometry (FAAS). Instrum Sci Technol [Internet]. 2008 Jul 25;36(5):476–92. Available from: [<URL>](#).
13. Padilha P de M, Gomes LA de M, Padilha CCF, Moreira JC, Filho NLD. Determination of metal ions in natural waters by flame-AAS after preconcentration on a 5-amino-1,3,4-thiadiazole-2-thiol modified silica gel. Anal Lett [Internet]. 1999;32(9):1807–20. Available from: [<URL>](#).
14. Kalimuthu P, John SA. Simultaneous determination of epinephrine, uric acid and xanthine in the presence of ascorbic acid using an ultrathin polymer film of 5-amino-1,3,4-thiadiazole-2-thiol modified electrode. Anal Chim Acta [Internet]. 2009 Aug 4;647(1):97–103. Available from: [<URL>](#).
15. Kalimuthu P, Abraham John S. Highly sensitive and selective amperometric determination of nitrite using electropolymerized film of functionalized thiadiazole modified glassy carbon electrode. Electrochem Commun [Internet]. 2009 May 1;11(5):1065–8. Available from: [<URL>](#).
16. Kalimuthu P, Abraham John S. Selective electrochemical determination of paracetamol using nanostructured film of functionalized thiadiazole modified electrode. Electroanalysis [Internet]. 2010 Feb 22;22(3):303–9. Available from: [<URL>](#).
17. Kalimuthu P, Abraham John S. Selective determination of 3,4-dihydroxyphenylacetic acid in the presence of ascorbic and uric acids using polymer film modified electrode. J Chem Sci [Internet]. 2011 May 29;123(3):349–55. Available from: [<URL>](#).
18. Kannan P, John SA. Ultrasensitive detection of L-cysteine using gold-5-amino-2-mercapto-1,3,4-thiadiazole core-shell nanoparticles film modified electrode. Biosens Bioelectron [Internet]. 2011 Dec 15;30(1):276–81. Available from: [<URL>](#).
19. Revin SB, John SA. Electropolymerization of 3-amino-5-mercapto-1,2,4-triazole on glassy carbon electrode and its electrocatalytic activity towards uric acid. Electrochim Acta [Internet]. 2011 Oct 1;56(24):8934–40. Available from: [<URL>](#).
20. He JB, Qi F, Wang Y, Deng N. Solid carbon paste-based amperometric sensor with electropolymerized film of 2-amino-5-mercapto-1,3,4-thiadiazole. Sensors Actuators B Chem [Internet]. 2010 Mar 4;145(1):480–7. Available from: [<URL>](#).
21. Chufán EE, Pedregosa JC, Borrás J. Spectroscopic behaviour of metal-drug complexes. Infrared spectra of Cu(II) complexes with 5-amino-1,3,4-thiadiazole-2-thiol (Hatm). Vib Spectrosc [Internet]. 1997 Dec 1;15(2):191–9. Available from: [<URL>](#).
22. Miller JN, Miller JC. Statistics and chemometrics for analytical chemistry [Internet]. 6th ed. Gosport: Pearson Education Limited; 2010. Available from: [<URL>](#).



Investigation of Peroxidase-Like Activity of Flower-Shaped Nanobiocatalyst from *Viburnum Opulus L.* Extract on the Polymerization Reactions

Berkant Kalayci¹ , Naime Kaplan² , Muge Mirioglu¹ , Seyma Dadi³ , Ismail Ocsoy⁴ ,
Ersen Gokturk^{1*} 

¹Department of Chemistry, Hatay Mustafa Kemal University, Hatay, 31001, Turkey.

²Department of Chemistry, Gaziantep University, Gaziantep, 27310, Turkey.

³Department of Nanotechnology Engineering, Abdullah Gül University, Kayseri, 38080, Turkey.

⁴Department of Analytical Chemistry, Faculty of Pharmacy, Erciyes University, Kayseri, 38039, Turkey.

Abstract: Here, we report the effects of peroxidase-mimicking activity of flower shaped hybrid nanobiocatalyst obtained from *Viburnum-Opulus L.* (Gilaburu) extract and Cu²⁺ ions on the polymerization of phenol and its derivatives (guaiacol and salicylic acid). The obtained nanoflowers exhibited quite high catalytic activity upon the polymerization of phenol and guaiacol. The yields and the number average molecular weights of the obtained polymers were significantly high. Due to solubility issue of salicylic acid in aqueous media, polymerization of salicylic acid resulted in very low yields. Free-horseradish peroxidase (HRP) enzyme is known to be losing its catalytic activity at 60 °C and above temperatures. However, the synthesized nanoflowers exhibited quite high catalytic activity even at 60 °C and above reaction temperatures. This provides notable benefits for reactions needed at high temperatures, and it is very important to use these kinds of nanobiocatalysts for both scientific studies and industrial applications.

Keywords: Enzymatic polymerization, Peroxidase, *Viburnum Opulus L.* extract, Phenol derivatives, Organic-inorganic hybrid nanobiocatalyst.

Submitted: March 12, 2024. **Accepted:** July 1, 2024.

Cite this: Kalayci A, Kaplan N, Mirioglu M, Dadi S, Ocsoy I, Gokturk E. Investigation of Peroxidase-Like Activity of Flower-Shaped Nanobiocatalyst from *Viburnum Opulus L.* Extract on the Polymerization Reactions. JOTCSA. 2024;11(3): 1321-28.

DOI: <https://doi.org/10.18596/jotcsa.1451444>

***Corresponding author's E-mail:** ersengokturk@gmail.com

1. INTRODUCTION

Enzyme catalyzed polymerization reactions have been extensively studied due to being environmentally benign and simple procedure for different purposes (1,2). Peroxidase enzymes oxidize proton donor compound using hydrogen peroxide (H₂O₂), and two moles of water are released. Peroxidases, such as horseradish peroxidase (HRP) and soybean peroxidase (SBP), typically consist of iron (Fe) ions in their active centers (3). These centers initiate radical polymerization reactions of vinyl monomers and some aromatic compounds, including phenol, aniline, etc (4).

Dordick and coworkers were the first group reporting the enzymatic polymerization of phenol (5). A variety of organic and inorganic electron donating compounds, including phenols, amines, indoles,

phenolic acids, and sulfates, could be oxidized by peroxidase enzymes (6,7). Therefore, different kinds of polymers could be manufactured in good yields. Even though the enzymatic polymerization method is known to be environmentally benign and simple procedure for different studies, there are some limitations to use enzymes in industrial scale applications. In addition to the high cost of enzymes, their instability and decreased catalytic activity in aqueous solutions are known to be important drawbacks for enzymatic polymerization reactions (8,9). Immobilization of enzymes is applied to solve these drawbacks and has been partially successful. Enzyme immobilization increases the stability of enzymes and makes them reusable (1). However, most enzymes lose their catalytic activity after immobilization due to inappropriate conformation and mass transfer limitations between enzyme and substrate (10,11). Because of this reason, it is very

important to apply a suitable immobilization technique in order to use enzymes efficiently in many applications or to discover new generation catalysts that can show similar catalytic activities as enzymes.

Hybrid organic-inorganic flower shaped nanobiocatalysts were first reported by Ge and coworkers (12). Different proteins as organic sources and Cu(II) ions as inorganic constituent were used to generate hybrid nanoflowers. Complexation between protein and Cu²⁺ ions generated flower-shaped micrometer-sized particles. Even though these particles were micrometer-sized, they were named nanoflowers because of their nanoscale properties. The obtained protein-Cu²⁺ nanoflowers showed very high catalytic activity and stability. These nanoflowers showed 2.5 times higher catalytic activity compared to the free laccase enzyme on the oxidation of epinephrine. While free-laccase enzyme lost 50% of its catalytic activity within 10 days, the nanoflowers showed higher than 95% of catalytic activity even after 2 months. There are limited numbers of studies in the literature related to the utilization of hybrid nanoflowers in polymerization studies. Gokturk and coworkers synthesized flower shaped hybrid HRP-Cu²⁺ nanoflowers from free-HRP enzyme and Cu²⁺ ions (13). Obtained HRP-Cu²⁺ nanoflowers exhibited quite high catalytic activity and stability towards polymerization of hydroquinone, catechol, and resorcinol. Up to 95% of polymerization yield was observed. The nanoflowers also showed very good catalytic activity even at 60 °C reaction temperature without denaturation. Another interesting study about the formation of hybrid nanoflowers and their applications in the polymer synthesis was also reported by Gokturk and coworkers. In this study, the complexation between green tea extract as an organic component and Cu²⁺ ions as an inorganic component was accomplished, and flower shaped green tea-Cu²⁺ nanobiocatalyst was observed (4). Obtained green tea-Cu²⁺ nanoflowers exhibited peroxidase-mimicking activity towards polymerization of phenol derivatives. Polymerization of phenol using green tea-Cu²⁺ nanoflowers was achieved at 60 °C reaction temperature with 82% of yield. Green tea-Cu²⁺ nanoflowers also showed very good catalytic activity and stability up to 60 °C reaction temperature in which free-HRP enzyme denatures.

In this study, the effects of peroxidase-mimicking activity of hybrid nanobiocatalyst obtained from *Viburnum-Opulus L.* (Vib.-Op. L.) extract and Cu²⁺ ions on the polymerization of phenol and its derivatives (guaiacol and salicylic acid) were investigated. The obtained nanoflowers exhibited quite high catalytic activity upon the polymerization of phenol and guaiacol. The yields and the number average molecular weights of the obtained polymers were significantly high. Due to the solubility issue of salicylic acid in aqueous media, polymerization of salicylic acid resulted in very low yields. Even though free-HRP enzyme starts losing its catalytic activity at 60 °C, the synthesized nanoflowers exhibited quite high catalytic activity even at 60 °C and above reaction temperatures. This provides notable

benefits for reactions needed at high temperatures, and is very important to use these nanoflowers for both scientific and industrial applications.

2. EXPERIMENTAL SECTION

2.1. Instrumentation

Bruker-Instruments-NMR (DPX-400) 400 MHz spectrometer was used for the ¹H and ¹³C nuclear magnetic resonance (¹H and ¹³C NMR) spectra of the products. Scanning electron microscope (SEM) images were monitored using Zeiss Gemini 500 instrument. Shimadzu IRAffinity-1S spectrometer was utilized for FT-IR analyses of the products. Thermogravimetric analyses were carried out with a Mettler-Toledo TGA/DSC 1 Star system instrument under nitrogen (N₂) at 10 °C/min heating rate from room temperature (RT) to 1000 °C. Differential scanning calorimetry (DSC) analyses were performed with a Mettler-Toledo DSC 1 Star system instrument with a heat cycle at 10 °C/min from 0 °C to 500 °C under N₂. Shimadzu LC-20AD instrument was used for the gel permeation chromatography (GPC) analyses of the polymers at 40 °C using HPLC grade N,N'-dimethylformamide (DMF) mobile phase at 1 mL/min flow rate. Narrow polydispersity polystyrene (PS) standards were used for the calibration. TGA, DSC, and GPC analyses results were given in supporting information.

2.2. Extraction of Vib.-Op. L.

20 g of dry Vib.-Op. L. fruits (gilaburu) were powdered by porcelain mortar and pestle. It was then extracted in 200 mL of methanol at RT for 3 days. Collected extract was first filtered (Whatman filter paper# 1, pore size 25 µm), and then solvent was evaporated. The dried extract was kept in the refrigerator at +4 °C for nanobiocatalyst production (14).

2.3. Synthesis of Vib.-Op.-Cu²⁺ Nanoflowers

Viburnum Opulus L. extract at a concentration of 0.1 mg/mL was poured into 50 mL of a mixture consisting of 10 mM pH 7.4 PBS buffer and 0.8 mM CuSO₄.5H₂O (copper sulfate pentahydrate). The resulting solution was vortexed and kept in the refrigerator at +4 °C for 3 days. The mixture was then centrifuged to collect blue-colored precipitate and washed with water 3 times to eliminate impurities. The blue solid product was then dried and kept in the refrigerator at +4 °C for polymerizations (14).

2.4. Representative Polymerization Procedure

100 mg of phenol derivative monomers (phenol, guaiacol, and salicylic acid) and the nanoflowers were put in 5.0 mL of buffer solution. In order to ensure solubility in the polymerization of salicylic acid, 0.2 mL of THF was also added to the mixture. The reaction was adjusted to the desired temperature. Then, polymerization was initiated by adding 70 µL of hydrogen peroxide (H₂O₂) to the mixture at 10 minutes intervals for 15 times. At the end of polymerization, the black precipitate was centrifuged, washed with water and methanol, and dried. The optimum polymerization condition was determined by performing the polymerization

reactions at different pH (pH: 7.0, 7.4, and 8.0), with different weight percentages (7.5, 10.0, and 15.0%) of catalyst loadings and at different temperatures (40, 50, 60, and 70 °C) (13).

FT-IR (ATR) spectrum of polyphenol (entry 7 in Table 1): 3400 cm^{-1} (O–H stretch), 1720 cm^{-1} and 1620 cm^{-1} (C=C aromatic stretch), 1195 cm^{-1} (C–O), 950 cm^{-1} , 650 cm^{-1} . ^1H NMR spectrum of polyphenol (entry 7 in Table 1) (400 MHz, DMSO- d_6 , δ , ppm): 6.67-6.70 (5H, m, Ar-H). ^{13}C NMR spectrum of polyphenol (100 MHz, DMSO- d_6): δ 145.7 (Ar-O), 129.8, 119.7, 116.1, 100.0 (Ar-CH).

FT-IR (ATR) spectrum of polyguaiacol (entry 9 in Table 1): 3500 cm^{-1} (O–H stretch), 1712 cm^{-1} and 1604 cm^{-1} (C=C aromatic stretch), 1195 cm^{-1} (C–O), 817 cm^{-1} , 763 cm^{-1} . ^1H NMR spectrum of polyguaiacol (entry 9 in Table 1) (400 MHz, DMSO- d_6 , δ , ppm): 6.84 (4H, m, Ar-H), 3.75 (3H, s, OCH₃). ^{13}C NMR spectrum of polyguaiacol (100 MHz, DMSO- d_6): δ 145.6 (Ar-O), 119.8, 116.1, 100.0 (Ar-CH), 56.4 (OCH₃).

FT-IR (ATR) spectrum of polysalicylic acid (entry 10 in Table 1): 3500 cm^{-1} (O–H stretch), 1705 cm^{-1}

(C=O), 1160 cm^{-1} (C–O), 816 cm^{-1} , 964 cm^{-1} . ^1H NMR spectrum of polysalicylic acid (entry 10 in Table 1) (400 MHz, DMSO- d_6 , δ , ppm): 12.48 (1H, s, COOH), 6.55-8.65 (4H, m, Ar-H). ^{13}C NMR spectrum of polysalicylic acid (100 MHz, DMSO- d_6): δ 161.6 (COOH), 135.9 (Ar-O), 130.7, 119.5, 117.4, 100.0 (Ar-CH).

3. RESULTS AND DISCUSSION

Scanning electron microscope (SEM) images of the Vib.-Op.-Cu²⁺ nanoflowers obtained from the complexation between *Viburnum-Opulus L.* extract and Cu²⁺ ions were illustrated in Figure 1. The Vib.-Op.-Cu²⁺ nanobiocatalyst has a spherical morphology and snowball appearances just like *Viburnum Opulus L.* flower seen on the right corner of Figure 1a. The average diameter of flower shaped spheres was found to be approximately 10 μm , and these flowers showed narrow size distributions. Although the size of the obtained Vib.-Op.-Cu²⁺ particles are micrometer-scale, these flowers are named nanobiocatalysts because they show nanoscale characteristics as mentioned in the literature (12).

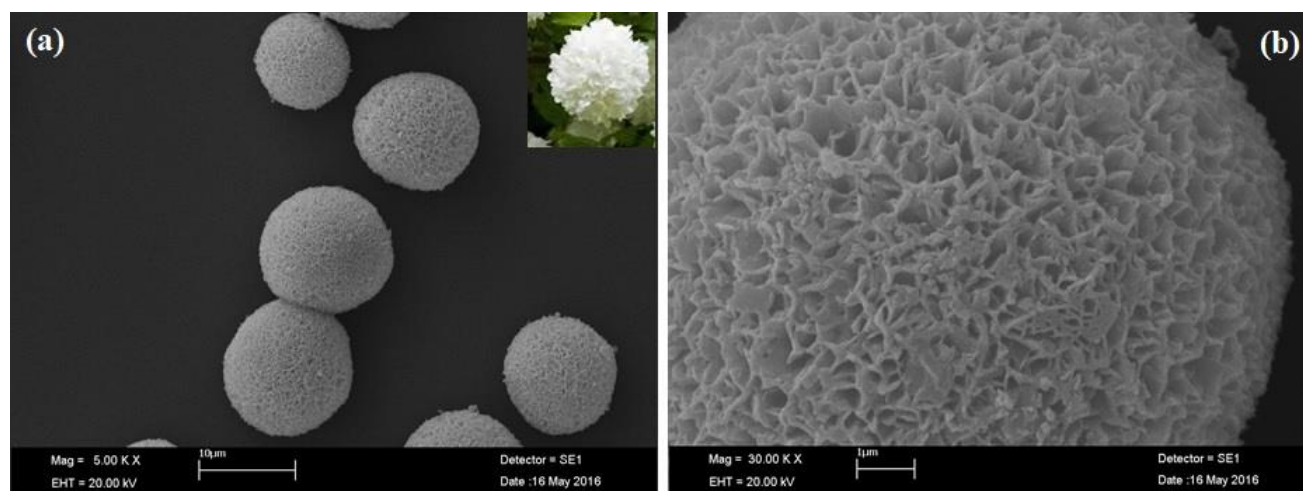


Figure 1: The spherical morphology of Vib.-Op.-Cu²⁺ nanoflowers.

The results of the polymerization of phenol derivatives in the presence of hybrid nanoflowers (Vib.-Op.-Cu²⁺) are given in Table 1. The reaction temperature, solution pH, and catalyst amount were first optimized in the polymerization of phenol using Vib.-Op.-Cu²⁺ nanoflowers (Figure 2). All polymerizations were performed in buffer media. In order to examine the influence of solution pH on the polymerization of phenol, three different buffer solutions (pH: 7.0, 7.4, and 8.0) were used in the

reactions. The results showed that polymerizations performed in pH 7.4 buffer at 50 °C (Table 1, entry 1) resulted in the highest yield and molecular weight of the polyphenol compared to the other buffers. Polymerizations in pH 7.0 (Table 1, entry 4) and pH 8.0 (Table 1, entry 5) buffers also showed high yields, but both yields and molecular weights of the polymers were lower than the product obtained at pH 7.4.

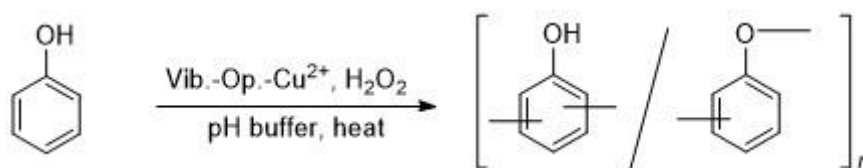


Figure 2: Polymerization of phenol using hybrid Vib.-Op.-Cu²⁺ nanoflowers in the presence of H₂O₂.

In order to optimize the amount of nanoflowers, polymerization of phenol was accomplished with three different catalyst loadings: 7.5 wt% (Table 1, entry 1), 10 wt% (Table 1, entry 2), and 15 wt% (Table 1, entry 3) at 50 °C in pH 7.4 buffer. The highest polymer yield was 78% obtained with 15 wt% of catalyst loading relative to phenol (Table 1, entry 3). The polymerization yield with 7.5 wt% of catalyst loading was 74%, which is slightly lower

than that of 15 wt% of catalyst loading. However, thermal stability and the average molecular weight of the obtained polymer with 7.5 wt% of catalyst loading were considerably higher than that of the polymer obtained with 15 wt% of catalyst loading. Due to the observation of better thermal properties and higher molecular weight, the optimum amount of catalyst loading for the polymerization of phenol was determined to be 7.5 wt%.

Table 1: Polymerization of phenol and its derivatives by Vib.-Op.-Cu²⁺ nanoflowers in the presence of H₂O₂.

Entry	Weight% Vib.-Op.-Cu ²⁺	pH	T _p (°C)	Yield (%)	T ₅₀ (°C)	Residue (%) at 1000 °C	M _n (Da)	Đ
1 ^a	7.5	7.4	50	74	630	23.8	122000	2.86
2 ^a	10.0	7.4	50	76	540	18.0	104000	2.75
3 ^a	15.0	7.4	50	78	489	2.7	77000	3.43
4 ^a	7.5	7.0	50	73	614	18.6	71000	2.99
5 ^a	7.5	8.0	50	67	450	2.6	66000	2.75
6 ^a	7.5	7.4	40	61	477	7.2	80000	3.23
7 ^a	7.5	7.4	60	81	620	29.1	202000	2.26
8 ^a	7.5	7.4	70	74	612	28.8	118000	3.25
9 ^b	7.5	7.4	60	37	628	28.9	90000	3.02
10 ^c	7.5	7.4	60	10	431	2.0	49000	3.13

^a100 mg of phenol in different pH buffers were polymerized in the presence of H₂O₂, ^b100 mg of guaiacol was polymerized in the presence of H₂O₂, ^c100 mg of salicylic acid was polymerized in the mixture of 4.8 mL of pH 7.4 buffer and 0.2 mL of THF in the presence of H₂O₂, T_p= reaction temperature, T₅₀= temperature at 50% residue, M_n: the number average molecular weight, Đ: polydispersity index (M_n and Đ values for the polymers were given in supporting information).

The influence of reaction temperature on the polymerization yield and the number average molecular weights of the synthesized polymers were also examined as the last optimization parameter. Four different temperatures between 40 °C and 70 °C were tried to detect the optimum polymerization temperature. The highest yield was accomplished at 60 °C (Table 1, entry 7). HRP enzyme is known to denature and lose its catalytic activity at 60 °C and above temperatures (15). Obtained successful outcomes indicated that Vib.-Op.-Cu²⁺ nanoflowers showed very high catalytic activity even at 70 °C reaction temperature (Table 1, entry 8), and provided 74% of polymer yield. This suggests that Vib.-Op.-Cu²⁺ nanoflowers can be used for some radical polymerization reactions requiring high temperatures. All these optimization parameters for the polymerization of phenol using Vib.-Op.-Cu²⁺ catalyst showed that 7.5 wt% catalyst loading in pH 7.4 buffer at 60 °C reaction temperature (entry 7 in Table 1) resulted in 81% of yield, and the molecular weight of the polyphenol was 202000 Da. In the literature, free-HRP enzyme catalyzed polymerization of phenol was isolated up to 95% of yield under pH 6.9 buffer at RT (16). According to our findings, Vib.-Op.-Cu²⁺ nanoflowers showed lower catalytic activity towards polymerization of phenol compared to the free-HRP enzyme. However, lower cost and showing very high stability at high reaction temperatures are noticeable properties of Vib.-Op.-Cu²⁺ nanoflowers compared with HRP enzyme. Thermal analysis results of this polymer under

nitrogen (N₂) atmosphere showed that polyphenol lost 50% of its weight at 620 °C, and carbonaceous residue at 1000 °C was 29% (Figure S7, supplementary information). The polydispersity index was found to be 2.26, and this shows that polyphenol has partially narrow molecular weight distribution. Differential scanning calorimetry (DSC) analysis of polymer 7 (entry 7 in Table 1) is shown in Figure S11 (supplementary information). A broad peak was observed at 110 °C due to the thermosetting property of the polyphenol (13). Carbon-oxygen (oxy-ortho or oxy-para) and carbon-carbon (ortho-ortho or ortho-para) couplings occur during the polymerization of phenol, and therefore, cross-linking properties could be observed due to these couplings in the polymer repeating units.

FT-IR, ¹H and ¹³C NMR analyses were carried out for the structural characterizations of the obtained polymers. According to the FT-IR spectrum of the polyphenol obtained from entry 7 in Table 1, the broad band detected around 3400 cm⁻¹ belongs to the hydroxyl (-OH) stretching vibration (Figure 3a). The peaks observed around 1720 and 1620 cm⁻¹ indicate aromatic (-C=C-) stretching vibrations. The C-O absorption band is observed at 1195 cm⁻¹ (17). The vibration bands observed at 650 and 950 cm⁻¹ indicate 1,2 and 1,4 substitutions occurred in the polyphenol structure, proving that polymerization takes place at *ortho*- and *para*- positions of phenol (18).

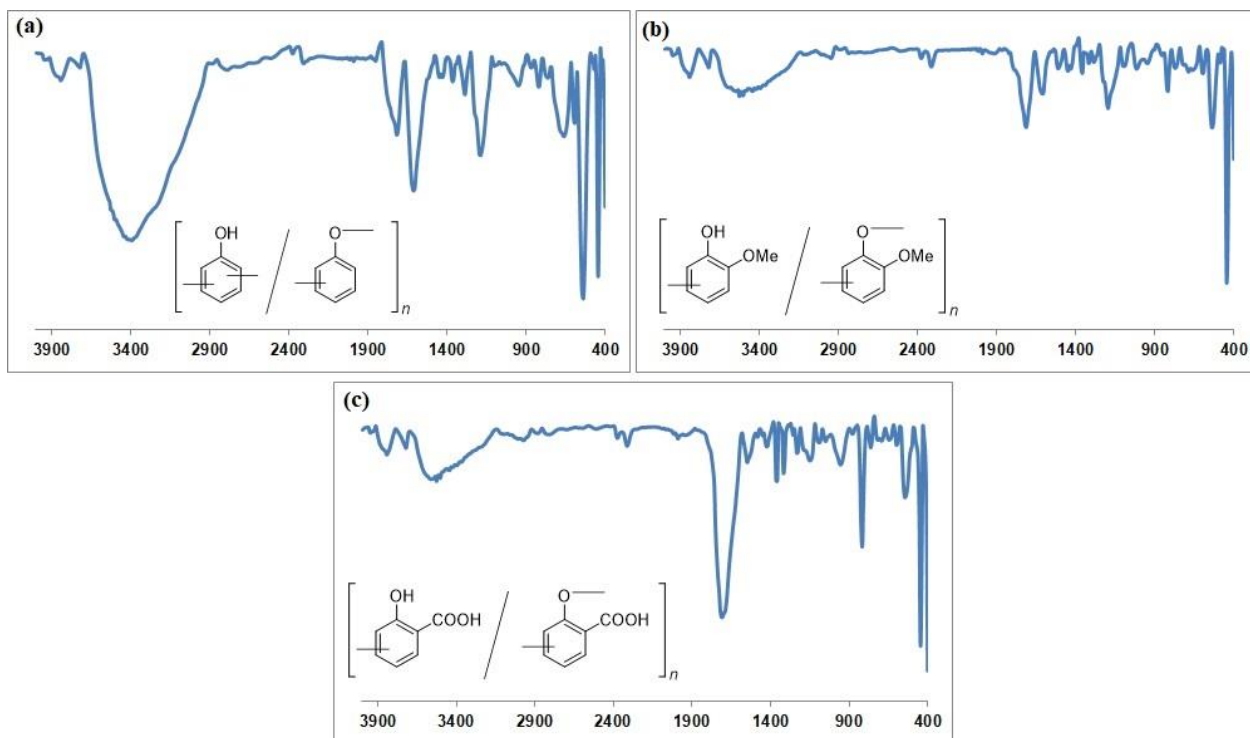


Figure 3: FT-IR spectra results of (a) polyphenol (entry 7 in Table 1), (b) polyguaiacol (entry 9 in Table 1), (c) polysalicylic acid (entry 10 in Table 1).

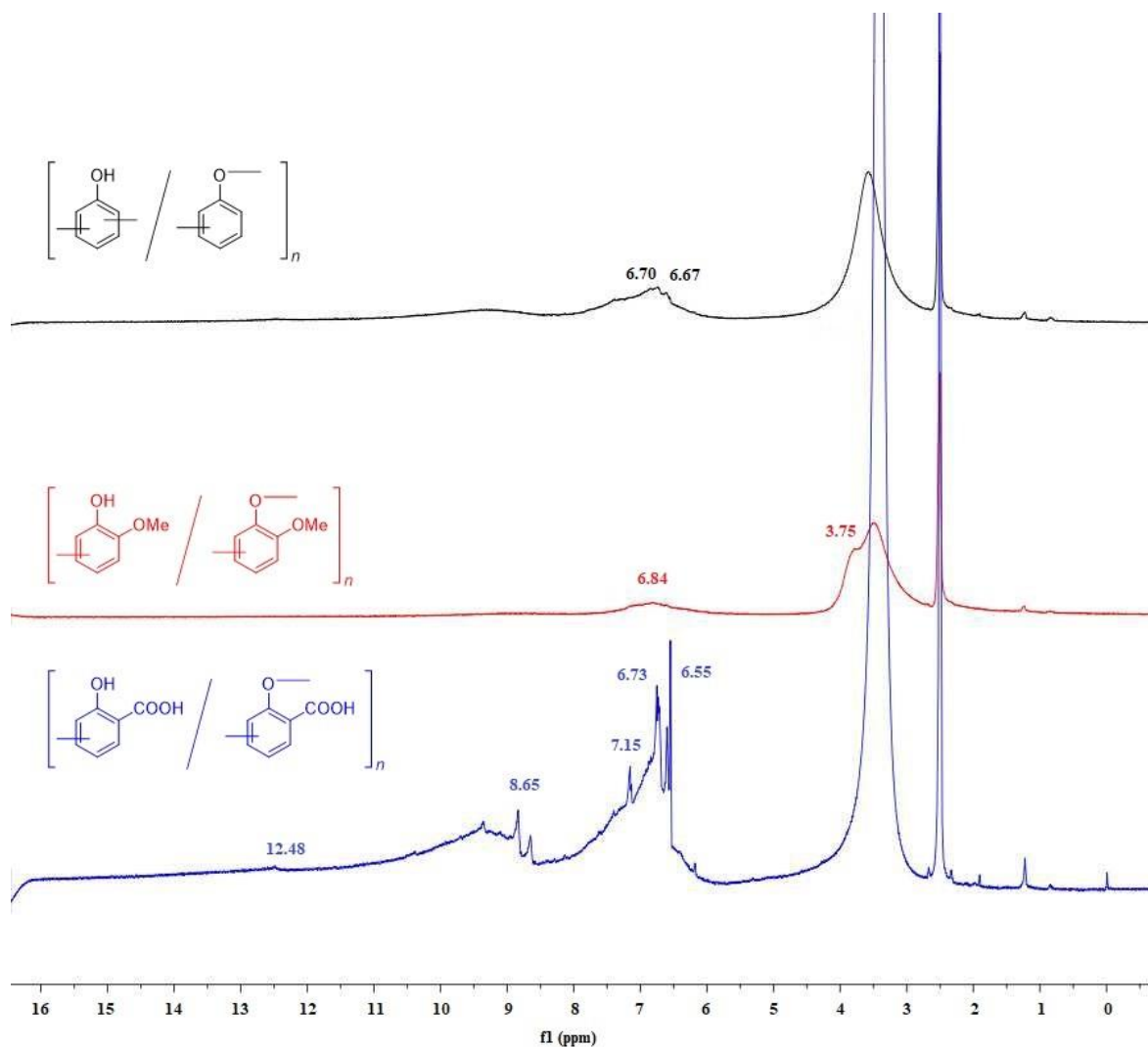


Figure 4: ¹H NMR spectra results of polyphenol (top, entry 7 in Table 1), polyguaiacol (middle, entry 9 in Table 1), polysalicylic acid (bottom, entry 10 in Table 1).

In addition to the FT-IR results, ^1H and ^{13}C NMR analyses were also performed to verify the structure of the obtained polymer. ^1H NMR spectrum of polymer 7 (entry 7 in Table 1) showed only aromatic protons due to the polyphenol structure (Figure 4). The broad peak observed between 6.67 ppm and 6.70 ppm belongs to aromatic C-H protons. The broadening of the peaks observed in the spectrum is due to the formation of polymeric structure. Phenolic hydroxyl (-OH) proton was not observed in the ^1H NMR spectrum. Presumably, the hydroxyl (-OH) peak

cannot be seen due to the polymerization proceeding through oxy-phenylene couplings from the phenolic hydroxyl (-OH) group. In addition to that, exchange of hydrogen and deuterium atoms in the $\text{DMSO-}d_6$ NMR solvent of the polyphenol sample might be the reason for this observation (13). ^{13}C NMR spectrum of polymer 7 (entry 7 in Table 1) also confirms the ^1H NMR spectrum. The peaks detected in the aromatic region between 100.0-145.7 ppm proved the presence of aromatic carbons in the structure (Figure 5).

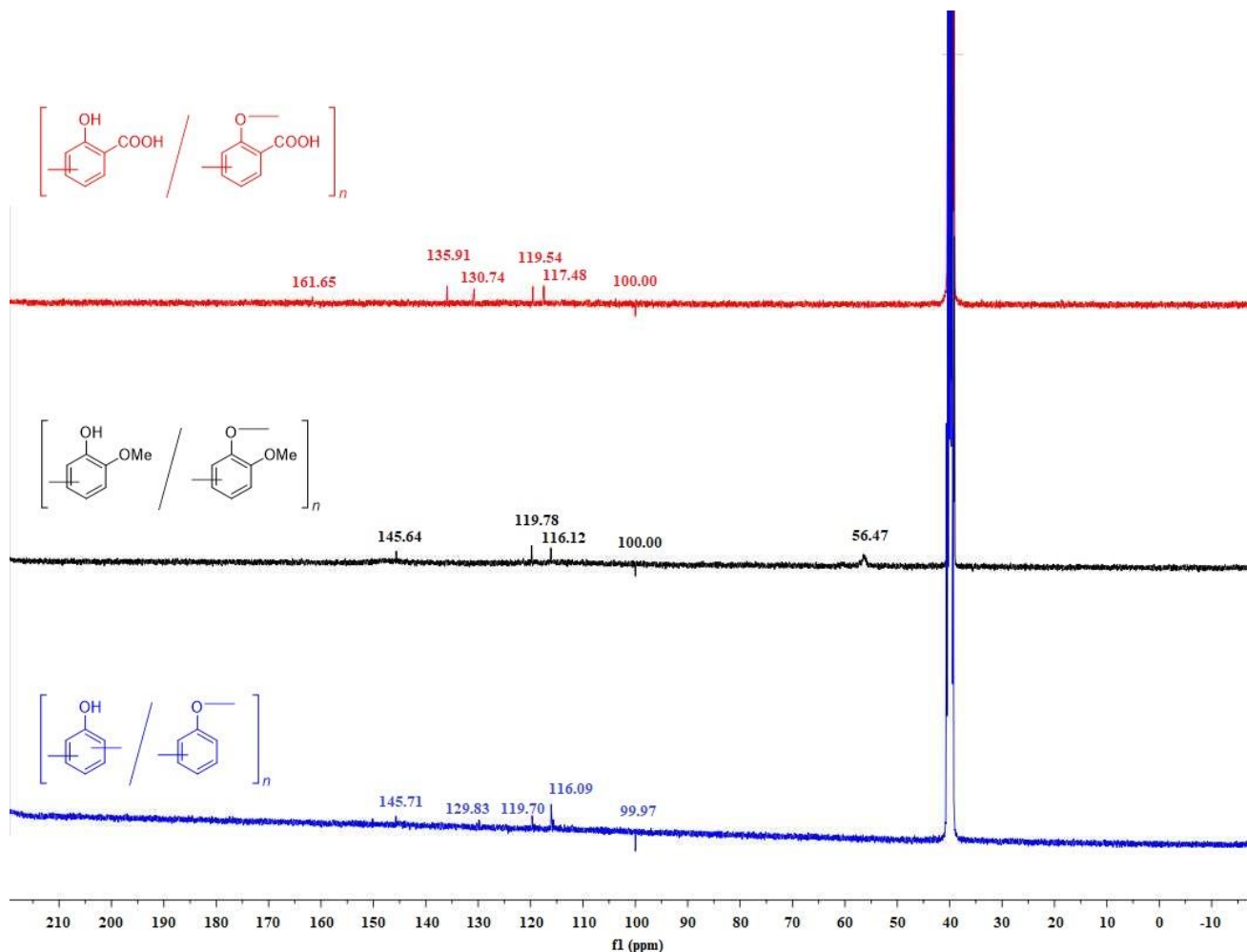


Figure 5: ^{13}C NMR spectra results of polyphenol (bottom, entry 7 in Table 1), polyguaiacol (middle, entry 9 in Table 1), polysalicylic acid (top, entry 10 in Table 1).

The optimal reaction condition (entry 7 in Table 1) was also tried for the polymerizations of guaiacol and salicylic acid monomers (Figure 6 and 7). Polymerization of guaiacol using Vib.-Op.- Cu^{2+} nanoflowers resulted in 37% of yield, and the average molecular weight of polyguaiacol was 90000 Da (entry 9 in Table 1). Polydispersity index was 3.02. We previously reported polymerization of guaiacol by free-HRP enzyme in the presence of H_2O_2 in pH 7.4 PBS at 30 °C, and highest polymerization yield was 51% (19). The highest polyguaiacol yield using Vib.-Op.- Cu^{2+} nanoflowers in pH 7.4 at 60 °C was 37%. This result showed that Vib.-Op.- Cu^{2+} nanoflowers demonstrated slightly lower catalytic

activity towards polymerization of guaiacol compared with the free-HRP enzyme. According to the thermal analysis results, the polymer lost 50% of its weight at 628 °C under N_2 atmosphere, and pyrolysis residue of the polymer at 1000 °C was detected to be 28.9% (Figure S9, supplementary information). DSC thermogram of the polyguaiacol (entry 9 in Table 1) is shown in Figure S12 (supplementary information). A broad peak was observed at 110 °C due to the thermosetting property of the polymer. An exothermic broad peak observed at 390 °C is related to the decomposition temperature of polyguaiacol (13).

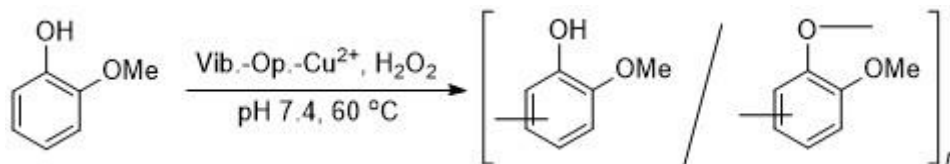


Figure 6: Polymerization of guaiacol using hybrid Vib.-Op.-Cu²⁺ nanoflowers in the presence of H₂O₂ at 60 °C.

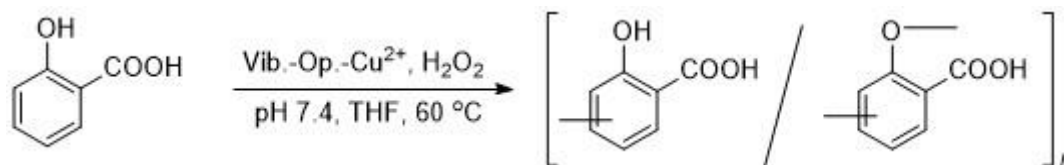


Figure 7: Polymerization of salicylic acid using hybrid Vib.-Op.-Cu²⁺ nanoflowers in 4.8 mL of pH 7.4 buffer and 0.2 mL of THF mixture in the presence of H₂O₂ at 60 °C.

FT-IR spectrum of the product (entry 9 in Table 1) indicated that an absorption band of hydroxyl (-OH) stretching vibration appeared around 3500 cm⁻¹ (Figure 3). The peaks observed at 1712 and 1604 cm⁻¹ indicated aromatic (-C=C-) stretching vibrations. C-O absorption band was also observed at 1195 cm⁻¹. Vibration bands at 817 and 763 cm⁻¹ show 1,2,4 substitution patterns of the phenyl rings in the polymer repeat units, indicating that polymerization occurred at *ortho*- and *para*- positions of guaiacol.

Figure 4 also shows the ¹H NMR spectrum of the product (entry 9 in Table 1). A proton peak appeared at 3.75 ppm as a shoulder can be attributed to methyl group of the methoxy group (-OCH₃) in the polyguaiacol structure. Chemical shifts of aromatic protons were observed around 6.84 ppm as a broad peak. Phenolic hydroxyl (-OH) proton in the ¹H NMR spectrum of polyguaiacol was not also detected as mentioned in the ¹H NMR spectrum of polyphenol (19). ¹³C NMR spectrum of polymer 9 (entry 9 in Table 1) is illustrated in Figure 5. The existence of the methoxy group (-OCH₃) in the polyguaiacol structure was also proved by ¹³C NMR spectrum. The ¹³C peak observed at 56.47 ppm indicates the presence of methyl carbon in the methoxy group (-OCH₃). The ¹³C peaks detected between 100.0-145.6 ppm are due to aromatic carbons in the polymer structure.

Entry 7 in Table 1 condition was also applied for the polymerization of salicylic acid (Figure 7). However, salicylic acid was not polymerized due to its insolubility in the buffer solutions. Thus, a small amount of water-soluble organic solvent (tetrahydrofuran, THF) was added into the buffer solution. 4.8 mL of pH 7.4 buffer and 0.2 mL of THF mixture was used in the polymerization of salicylic acid (entry 10 in Table 1). After applying this solvent mixture, 10% of polymer yield was obtained. Increasing the amount of THF resulted in no polymer product, probably due to the decomposition of the nanoflowers in organic solvents (20). Therefore, the optimum amount of THF was determined to be 0.2 mL. The average molecular weight of polysalicylic acid was 49000 Da. Polydispersity index of the polymer was 3.13. 50% mass loss of this polymer

occurred at 431 °C, and the carbonaceous residue at 1000 °C was 2% (Figure S10, supplementary information). According to DSC thermogram of polysalicylic acid (entry 10 in Table 1), a broad peak at 85 °C is attributed to the thermosetting property of the polymer. Exothermic broad peaks observed at 290 °C and 390 °C are related to the decomposition temperatures of the polymer (Figure S13, supplementary information).

Figure 3 also shows FT-IR spectrum of the product (entry 10 in Table 1). Stretching vibration of hydroxyl (-OH) group was observed around 3500 cm⁻¹. Absorption band related to the carbonyl (C=O) group was observed at 1705 cm⁻¹. The C-O vibration band appeared at 1160 cm⁻¹. Peaks detected at 817 and 964 cm⁻¹ indicated 1,2,4 substitution patterns of the phenyl ring, indicating that the polymerization occurred at *ortho*- and *para*- positions of phenolic hydroxyl group of salicylic acid. ¹H NMR spectrum of polysalicylic acid (entry 10 in Table 1) is also shown in Figure 4. Aromatic protons of polysalicylic acid were observed between 6.50 and 8.65 ppm. A proton detected at 12.48 ppm was attributed to the carboxylic acid proton (-COOH). Figure 5 shows the ¹³C NMR spectrum of polysalicylic acid (entry 10 in Table 1). The presence of the carbonyl carbon belonging to the carboxylic acid group was also proved by ¹³C NMR spectrum. ¹³C peak observed at 161.6 ppm indicates the presence of carbonyl carbon in the carboxylic acid (-COOH) functional group. ¹³C peaks observed between 100.0-135.9 ppm are due to aromatic carbons in the polymer structure.

4. CONCLUSION

In conclusion, the effects of Vib.-Op.-Cu²⁺ hybrid nanoflowers on the polymerization of phenol derivatives (phenol, guaiacol, and salicylic acid) were investigated. The results showed that hybrid Vib.-Op.-Cu²⁺ nanobiocatalyst demonstrated HRP enzyme-mimicking catalytic activity towards polymerization of phenol derivatives. The yields and the number average molecular weights of the obtained polymers were significantly high. Due to solubility issue of salicylic acid in aqueous media, polymerization of salicylic acid resulted in very low yields. Polymerizations carried out using Vib.-Op.-

Cu²⁺ nanobiocatalyst resulted in very high yields of polymer products without degradation of the catalysts, even at reaction temperatures as high as 60 °C in which peroxidase enzymes can be denatured. This provides notable benefits for reactions needed at high temperatures, and it is very important to use these types of nanoflowers for both scientific studies and industrial applications. Discovery of similar kinds of nanoflowers from proteins (or plant extracts) and metal ions may also expand their utilization in polymer chemistry as promising catalytic reagents for radical polymerizations. Future studies will focus on understanding the origin of catalytic activity of Vib.-Op.-Cu²⁺ nanoflowers, and similar kinds of nanostructures will be tried to synthesize from the isolated active components of *Viburnum Opulus L.* extract.

5. CONFLICT OF INTEREST

The authors have no conflicts of interest to declare.

6. ACKNOWLEDGMENTS

This project was supported by the Scientific Research Projects Coordination Unit at Hatay Mustafa Kemal University. Project Number: 20.M.048.

7. REFERENCES

- Altinkaynak C, Tavlasoglu S, İydemir N, Ocsoy I. A new generation approach in enzyme immobilization: Organic-inorganic hybrid nanoflowers with enhanced catalytic activity and stability. *Enzyme Microb Technol* [Internet]. 2016 Nov;93-94:105-12. Available from: [<URL>](#).
- Ocsoy I, Dogru E, Usta S. A new generation of flowerlike horseradish peroxidases as a nanobiocatalyst for superior enzymatic activity. *Enzyme Microb Technol* [Internet]. 2015 Jul;75-76:25-9. Available from: [<URL>](#).
- Hollmann F, Arends IWCE. Enzyme initiated radical polymerizations. *Polymers* [Internet]. 2012 Mar 6;4(1):759-93. Available from: [<URL>](#).
- Kalayci B, Kaplan N, Dadi S, Ocsoy I, Gokturk E. Production of flower-shaped nanobiocatalysts from green tea and investigation of their peroxidase mimicking activity on the polymerization of phenol derivatives. *Polym Adv Technol* [Internet]. 2024 Jan 13;35(1):e6272. Available from: [<URL>](#).
- Dordick JS, Marletta MA, Klibanov AM. Polymerization of phenols catalyzed by peroxidase in nonaqueous media. *Biotechnol Bioeng* [Internet]. 1987 Jul 18;30(1):31-6. Available from: [<URL>](#).
- Isci I, Gokturk E, Turac E, Sahmetlioglu E. Chemoenzymatic polymerization of hydrazone functionalized phenol. *Polym Sci Ser B* [Internet]. 2016 Jul 12;58(4):411-20. Available from: [<URL>](#).
- Kumbul A, Gokturk E, Turac E, Sahmetlioglu E. Enzymatic oxidative polymerization of para -imine functionalized phenol catalyzed by horseradish peroxidase. *Polym Adv Technol* [Internet]. 2015 Sep 4;26(9):1123-9. Available from: [<URL>](#).
- Ahmad R, Sardar M. Enzyme immobilization: An overview on nanoparticles as immobilization matrix. *Biochem Anal Biochem* [Internet]. 2015;4(2):1000178. Available from: [<URL>](#).
- Zhang Y, Ge J, Liu Z. Enhanced activity of immobilized or chemically modified enzymes. *ACS Catal* [Internet]. 2015 Aug 7;5(8):4503-13. Available from: [<URL>](#).
- Gupta MN, Mattiasson B. Unique applications of immobilized proteins in bioanalytical systems. In 1992. p. 1-34. Available from: [<URL>](#).
- Hanefeld U, Cao L, Magner E. Enzyme immobilisation: fundamentals and application. *Chem Soc Rev* [Internet]. 2013;42(15):6211-2. Available from: [<URL>](#).
- Ge J, Lei J, Zare RN. Protein-inorganic hybrid nanoflowers. *Nat Nanotechnol* [Internet]. 2012 Jul 3;7(7):428-32. Available from: [<URL>](#).
- Gokturk E, Ocsoy I, Turac E, Sahmetlioglu E. Horseradish peroxidase-based hybrid nanoflowers with enhanced catalytic activities for polymerization reactions of phenol derivatives. *Polym Adv Technol* [Internet]. 2020 Oct 4;31(10):2371-7. Available from: [<URL>](#).
- Ildiz N, Baldemir A, Altinkaynak C, Özdemir N, Yilmaz V, Ocsoy I. Self assembled snowball-like hybrid nanostructures comprising *Viburnum opulus L.* extract and metal ions for antimicrobial and catalytic applications. *Enzyme Microb Technol* [Internet]. 2017 Jul;102:60-6. Available from: [<URL>](#).
- Topal Y, Tapan S, Gokturk E, Sahmetlioglu E. Horseradish peroxidase-catalyzed polymerization of ortho-imino-phenol: Synthesis, characterization, thermal stability and electrochemical properties. *J Saudi Chem Soc* [Internet]. 2017 Sep;21(6):731-40. Available from: [<URL>](#).
- Oguchi T, Tawaki S ichiro, Uyama H, Kobayashi S. Soluble polyphenol. *Macromol Rapid Commun* [Internet]. 1999;20(7):401-3. Available from: [<URL>](#).
- Kumbul A, Gokturk E, Sahmetlioglu E. Synthesis, characterization, thermal stability and electrochemical properties of ortho-imine-functionalized oligophenol via enzymatic oxidative polycondensation. *J Polym Res* [Internet]. 2016 Mar 18;23(3):52. Available from: [<URL>](#).
- Kocak A, Kumbul A, Gokturk E, Sahmetlioglu E. Synthesis and characterization of imine-functionalized polyphenol via enzymatic oxidative polycondensation of a bisphenol derivative. *Polym Bull* [Internet]. 2016 Jan 4;73(1):163-77. Available from: [<URL>](#).
- Göktürk E. Flowerlike hybrid horseradish peroxidase nanobiocatalyst for the polymerization of guaiacol. *TURKISH J Chem* [Internet]. 2020 Oct 26;44(5):1285-92. Available from: [<URL>](#).
- Yildirim P, Gokturk E, Turac E, Demir HO, Sahmetlioglu E. Chemoenzymatic polycondensation of para-benzylamino phenol. *Chem Pap* [Internet]. 2016 Jan 30;70(5):610-9. Available from: [<URL>](#).



The Extraction of Antioxidant Compounds from *Coriandrum sativum* Seeds by Using Green Solvents

Özge Demir¹ , Aslı Gök¹ , Şah İsmail Kırbaşlar¹ 

¹Istanbul University-Cerrahpasa, Engineering Faculty, Chemical Engineering Department, Avcilar, 34320, Istanbul, Turkey.

Abstract: In this study, bioactive compounds from *Coriandrum sativum* seeds were extracted by microwave assisted extraction (MAE) using natural deep eutectic solvents (NADESs). The total antioxidant capacity (TAC) of extracts was determined by using cupric reducing antioxidant capacity (CUPRAC) method. 2,2-diphenyl-1-picrylhydrazyl (DPPH) and 2,2'-azino-bis(3-ethylbenzothiazoline-6-sulfonic acid) (ABTS) analyses have been employed to measure the free radical scavenging ability of the sample extracts. Five different deep eutectic solvents, using choline chloride in combination with hydrogen bond donors (three polyalcohols and two organic acids) were firstly scanned. Choline chloride and 1,4-butanediol at the molar ratio of 1:4 was the best solvent of choice to extract natural antioxidants to achieve the best level of TAC. The response surface methodology (RSM) was applied to achieve the most advantageous conditions. The optimal process conditions for the maximum TAC value were as follows: 326 watt microwave power, 88 second extraction time, and 10 liquid/solid (L/S) ratio. In this study, we report an efficient, rapid, and green method to extract natural antioxidants from Turkish *Coriandrum sativum* seeds.

Keywords: *Coriandrum sativum* seed, deep eutectic solvent, antioxidant activity, CUPRAC, DPPH, ABTS.

Submitted: January 17, 2024. **Accepted:** July 14, 2024.

Cite this: Demir Ö, Gök A, Kırbaşlar Şİ. The Extraction of Antioxidant Compounds from *Coriandrum sativum* Seeds by Using Green Solvents. JOTCSA. 2024;11(3): 1329-38.

DOI: <https://doi.org/10.18596/jotcsa.1421371>

***Corresponding author's E-mail:** ozge.demir@iuc.edu.tr

1. INTRODUCTION

Coriandrum sativum (commonly known as coriander) is one of the oldest and widespread crop species, dating back to around 1550 BC (1). *Coriandrum sativum* is widely distributed in Mediterranean countries (2). The plant has a very distinct flavor and is highly aromatic (3). It is used in the manufacture of detergents, emulsifiers, soaps, and softeners (4). The leaves and seeds are used in many food products, such as liquors, teas, meat, pickles, fish, and bakery (2,3,5). The plant is known for its potential healing properties (3). It has been used as a therapeutic target for treating respiratory disorders, urinary disorders, and digestive ailments such as indigestion, nausea, dyspepsia, and dysentery (2-5). The seeds have been reported to possess pharmaceutical properties such as antidiabetic, antimicrobial, antibacterial, antifungal, analgesic, anti-inflammatory, anticancer, and antiseptic properties (1-3,5-7). The seeds are a potent source of antioxidant compounds like polyphenols, particularly phenolic acids and flavonoids, which are important nutrients in the human diet (8).

Oxygen free radicals in biological cells weaken the immune system and cause several diseases. On the other hand, antioxidants deactivate free radicals before they attack the cell and they eventually leave the body. Lots of studies in epidemiology demonstrated that compounds having antioxidant properties can inhibit the emergence of numerous conditions such as cancer, diabetes, cardiovascular diseases, and Alzheimer's disease (9). Besides, when antioxidants are added to food products, the formation of toxic oxidation products is retarded as well as the shelf life of food is increased (10). A high nutritional quality is provided with the addition of antioxidants to the food products.

Chemical engineers make great efforts to create eco-friendly solvent systems that have low cost and low toxicity. Volatile organic solvents like methanol, hexane, ethanol, chloroform, and acetone have been broadly utilized to extract bioactive components from plants (11). Despite their increased solvation and extraction capability, the toxicity of conventional solvents might pose an environmental and public health threat. Besides, using these solvents leads to

undesirable solvent residues in the extracts. Recently, natural deep eutectic solvents (NADESs) have taken the place of conventional solvents. NADESs were discovered at the beginning of the 21st century as new types of green solvents. NADESs have several benefits such as low cost, biodegradability, easy preparation and pharmaceutically acceptable toxicity (12). NADESs are generally prepared by mixing hydrogen bond donors (HBDs), such as urea, organic acids and polyols with hydrogen bond acceptors (HBAs) (13). The components of NADES interact with each other via hydrogen bonds. One component acts as a hydrogen bond donor, while the other component acts as a hydrogen bond acceptor. NADES has a lower melting point than its individual components. This is owing to the intermolecular hydrogen bonding between the components of NADES (14,15). Choline chloride (ChCl) is a cost effective, biodegradable and non-toxic quaternary ammonium salt. ChCl-based NADESs have been mostly studied for the separation of bioactive materials from plants (16-18).

Extraction is the first step in separating bioactive compounds from plants. The extraction method is important since it affects the efficiency and operational cost. Ultrasound-assistant extraction (UAE), maceration extraction, soxhlet extraction, and microwave-assisted extraction (MAE) are extraction techniques that were extensively used for the recovery of natural products from plant matrices (19,20). Among them, MAE is the fastest technique (21). MAE provides high extraction efficiency and consumes less solvent. Microwave radiation affects the moisture of solid material. The evaporated moisture applies pressure to the cell wall. Eventually, the plant cell wall is broken down, so that target molecules leach out (22).

In this study, natural antioxidants from *Coriandrum sativum* seed were extracted by ChCl-based NADESs. The most important extraction parameters (liquid/solid ratio (L/S), extraction time and microwave power) were optimized by response

surface methodology (RSM). Ethanol (EtOH) was used as benchmark solvent to compare the results. The total antioxidant capacity (TAC) of *Coriandrum sativum* peel extracts was ascertained by using cupric reducing antioxidant capacity (CUPRAC) method. The free radical scavenging (FRS) activity was measured by 2,2-diphenyl-1-picrylhydrazyl (DPPH) and 2,2'-azino-bis(3-ethylbenzothiazoline-6-sulfonic acid) (ABTS) analyses. The results of this research will be the first to examine the antioxidant features of *Coriandrum sativum* seed extracts utilizing NADESs so far, thus being noteworthy in the field of green and sustainable chemistry.

2. MATERIALS AND METHODS

2.1. Plant Material

The Turkish coriander was obtained from a local market (Istanbul, Turkey). The air-dried coriander was ground in a laboratory mill to a screen size of 0.5 mm in order to obtain uniform particle size. The seeds were kept in the freezer until the experiments.


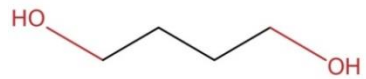
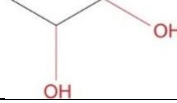
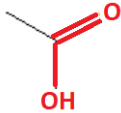
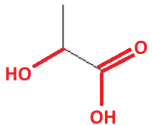
2.2. Chemicals

ChCl, 1,4-butanediol, 1,2-propanediol, ethylene glycol, acetic acid, lactic acid, EtOH, methanol, neocuproine, trolox (TR), ammonium acetate, copper(II) sulfate, DPPH, ABTS, and potassium persulfate were purchased from Sigma Aldrich, USA. Every chemical compound in this study was of analytical grade.

2.3. NADES Preparation

The NADES preparation was carried out by simply mixing two components according to the molar ratios given in Table 1. Water was added to carboxylic acid-based NADESs to decrease the viscosity. First, ChCl and HBDs were weighed on an analytical balance (Mettler Toledo). Next, ChCl and HBDs were mixed at desired molar ratios. The mixture was heated at 333.2 K with stirring until a transparent and homogeneous liquid NADES was formed. The prepared NADESs were stored in the room temperature environment.

Table 1: The composition of ChCl-based NADESs.

HBD	HBD structure	ChCl:HBD molar ratio	Water content (v/v)	Ref
Ethylene glycol		1:4	-	(23)
1,4-butanediol		1:4	-	(21,23)
1,2-propanediol		1:4	-	(23)
Acetic acid		1:2	30%	(22)
Lactic acid		1:2	30%	(16)

2.4. The Extraction Procedure and Instrumentation

The ground *Coriandrum sativum* seeds were put into a 50 mL flask, and NADESs were added into the flask. Except NADESs, ethanol and water were used as the conventional solvents. The flask was placed in the microwave oven (Milestone NEOS-GR). Microwave extractions were performed at different microwave power levels (250 W-350 W), microwave times (60-90 seconds) and liquid-to-solid (L/S) ratios (10-20 mL to 1 g). The experiments were repeated three times. After extractions, the mixtures were left to cool down at room temperature. Finally, the extracts were filtered through a 45 µm nylon filter before UV-Vis analyses. UV-Vis measurements were carried out with a Varian CAY Bio 100 UV-Vis spectrometer (Agilent, USA).

2.5. Statistical Analyses

The variables were systematically investigated with Box-Behnken design (BBD) of RSM. Microwave power (A), time (B), and L/S ratio (C) were the independent variables, and TAC (Y) was the response. TAC values of *Coriandrum sativum* seed extracts were analyzed using a second order polynomial equation (24-26). An analysis of variance (ANOVA) test was applied to analyze results (27).

2.6. TAC Analyses

TAC of *Coriandrum sativum* seed extract was analyzed by CUPRAC method (27-29). CUPRAC method is based on the reduction of cupric neocuproine complex (Cu(II)-Nc) to yellow-orange colored cuprous chelate (Cu(I)-Nc) in the presence of antioxidants. First, x mL extract was added to the test tube, including 3 mL of reagent mixture (1 mL of 10 mM CuCl₂, 1 mL of 7.5 mM Nc and 1 mL of 1 M NH₄Ac buffer). Then, (1.1-x) mL H₂O was added to the mixture, which made up to a final volume of 4.1 mL. The mixture tube was capped. After 30 min, the absorbance was read at 450 nm (A₄₅₀) against a reagent blank. The absorbance is linearly correlated with the antioxidant capacity (30). TAC is expressed as TR equivalent (mmol TR/g-dried sample (DS)) as given in Eq. 1 below (27-29,31):

$$\text{TAC (mmol TR/g - DS)} = \frac{A_s}{\epsilon_{TE}} \frac{V_m}{V_s} D_f \frac{V_E}{m} \quad (1)$$

where A_s refers to the recorded absorbance value, V_s indicates the sample volume, V_e is the extract volume, V_m signifies the total volume, ε_{TE} refers to the molar absorptivity coefficient in TR equivalent, D_f is the dilution factor (when needed), and m refers to the mass of the DS.

2.7. Determination of DPPH Free Radical Scavenging Activity

DPPH free radical scavenging assay is one of the most popular antioxidant assays, which was reported by Sánchez Moreno et al (32). DPPH free radical scavenging activity of sample extract was ascertained based on its ability to react with stable DPPH free radical. Antioxidants in sample extract reduce the stable purple-colored radical DPPH into the yellow-colored DPPH-H by donating hydrogen atoms to the DPPH free radical, thereby neutralizing

its toxic effect (33). DPPH method is as follows: First, x mL sample extract was added into a test tube, including (2-x) mL methanol and 2 mL 0.2 nM DPPH. The tube was stoppered and left to stand for 30 min in the dark. After 30 min, the absorbance was read at 515 nm against MeOH. All the assays were replicated three times. Findings were given in mean ± standard deviation. Corrected absorbance values (Δ_A) were utilized to determine DPPH free radical scavenging activity by using the following equation (29,31):

$$\Delta_A = A_{DPPH} - (A_E - A_0) \quad (2)$$

where A_{DPPH} is the absorbance of DPPH reagent without the sample, A_E is the absorbance of the extract, and A₀ is the absorbance of the extract without DPPH reagent.

DPPH free radical scavenging activity is expressed as mmol TR/g-DS based on the TR standard calibration curve. The DPPH free radical scavenging activity was derived from the following equation (29):

$$\text{DPPH free radical scavenging activity (mmol TR/g-DS)} = \frac{\Delta_A}{\epsilon_{TE}} \frac{V_m}{V_s} D_f \frac{V_E}{m} \quad (3)$$

2.8. Determination of ABTS Free Radical Scavenging Activity

The ABTS⁺ free radical has been widely used as a tool to determine the free radical scavenging activity of antioxidants. ABTS assay is based on the reduction of chromogenic reagent ABTS⁺ in the presence of antioxidants. Chromogenic ABTS⁺ solution is prepared by the following procedure. ABTS⁺ (50 nM) is diluted with distilled water to a final concentration of 7.0 nM. K₂S₂O₈ is added to the solution, the final concentration of K₂S₂O₈ is 2.45 nM in the solution. The obtained ABTS⁺ solution is left for 12-16 hours at ambient temperature. The application of ABTS assay is as follows: x mL sample extract is mixed with (4-x) mL methanol and 1 mL ABTS⁺ solution (1:10 diluted with methanol). The absorbance is read at 734 nm against ethanol after ABTS⁺ addition. The corrected absorbance value, Δ_A, is calculated by the equation below

$$\Delta_A = A_{ABTS} - (A_E - A_0) \quad (4)$$

where A_{ABTS} refers to the absorbance of ABTS⁺ reagent without the sample, A_E is the absorbance of the extract, and A₀ is the absorbance of the extract without ABTS⁺ reagent.

ABTS free radical scavenging activity is determined with the following equation (29):

$$\text{ABTS free radical scavenging activity (mmol TR/g-DS)} = \frac{\Delta_A}{\epsilon_{TE}} \frac{V_m}{V_s} D_f \frac{V_E}{m} \quad (5)$$

ABTS free radical scavenging activity is expressed as mmol TR/g-DS based on the TR standard calibration curve.

3. RESULTS AND DISCUSSION

3.1. DES Selection

Five different types of NADES were synthesized to determine the most potent NADES. NADES combinations were prepared based on the published data (34). Molar ratios are written in Table 1. ChCl salt was chosen as HBA. Several polyols and organic acids were selected as HBD, which are considered to be renewable, nontoxic, and biodegradable (35). To evaluate the extraction capability of NADES, pure ethanol and water were used as the benchmark solvents.

ChCl:alcohol ratio (1:4) was used according to the literature data. Mahmood et al. studied the antioxidant activity of *Chlorella vulgaris* plant extracts. In that study, polyols were tested as HBDs. Among different ChCl to HBD ratios (1:1, 1:2, 1:3, 1:4), the 1:4 ratio was determined as the most ideal ratio for all the NADES combinations (35). ChCl:alcohol ratio of 1:1 is not suitable to use due to the high viscosity and high surface tension of ChCl (36). Therefore, a ChCl-to-alcohol ratio of 1:4 is chosen to keep the interactions going well (37).

NADES extraction capacity is mainly affected by the following factors: H-bonding interactions, polarity, viscosity, and pH (21,38). High viscosity is one of the most important disadvantages of NADES because high viscosity leads to the mass transfer resistance of molecules entering the liquid surface. Carboxylic acid-based NADESs possess high viscosity. The addition of water in carboxylic acid-based NADESs would reduce the viscosity (39). Cui et al. emphasized that 30 % water content (v/v) in NADESs decreases the viscosity. However, an excessive amount of water breaks the hydrogen bond network in the eutectic solution, thereby reducing the hydrogen bonding interactions between NADES and polyphenolics (40,41).

From all different type of NADESs, ChCl:1,4-butanediol (1:4) provided the best TAC value. Apparently, ChCl:1,4-butanediol has the most favorable electrostatic and hydrogen-bond interactions with the target molecule (35). Besides, alcohol-based NADESs showed better TAC values than carboxylic acid-based NADESs. The high performance of alcohol-based NADESs is associated with multiple hydrogen bonding networks, which interact with target molecules and establish strong connections (42). Ethanol extract showed relatively low antioxidant activity, which may be due to the non-synergistic effects with the target molecules (43). Similarly, flavonoid extraction from *Flos Sophora imaturus* plant has been conducted by

Wang et al. and the team reported that ChCl:1,4-butanediol (1:4) is the best solvent among all ChCl-based NADESs (including glycerol, glycol, 1,3-butanediol, citric acid, lactic acid, glucose and sucrose as the HBDs) (44).

The positions of -OH groups in HBD is also a significant factor affecting the extraction capability of the solvent. For example, 1,2-propanediol and 1,4-butanediol have the same number of -OH groups (see Table 1). However, -OH groups of 1,2-propanediol are at vicinal position, which is unfavorable for 1,2-propanediol. Here, 1,2-propanediol produces steric hindrance, which results in the reduced possibility of interactions with the target molecules. On the other hand, 1,4-butanediol has -OH groups at terminal position, which overcome the intermolecular forces, and thereby mass transfer limitations (45). Moreover, 1,4-butanediol has a longer alkyl chain than ethylene glycol and 1,2-propanediol. 1,4-butanediol here seemed to be less affected by intermolecular repulsions due to the alkyl chain length (35). To sum up, HBD structure is an important factor for solute-solvent interactions and should be considered in the solvent selection (17).

Polarity is also an important factor affecting the efficiency. Polyphenolic compounds are highly polar compounds. According to the "like dissolves like" principle, solvents with high polarity are better for polyphenolic extractions (33). Although water molecules are highly polar and have a relatively low TAC value (46).

3.2. TAC Optimization

The extraction parameters, including time, microwave power, and L/S ratio, were optimized by using BBD. The levels of variables and their actual values were given in Table 2. The outcomes were fitted to a quadratic polynomial equation by using multiple regression analysis given below as Eq. 6.

$$\text{TAC} = 0.036 + (7.125\text{E}-003)\text{A} + 0.016\text{B} - (8.875\text{E}-003)\text{C} - (9.000\text{E}-003)\text{AC} \quad (6)$$

The ANOVA test was performed to discover the interactions between the variables and the optimum process conditions (see Table 3). The model F value of 14.20 and p value less than 0.05 imply that the model is important (47). The terms having p values less than 0.05 are considered important. In these circumstances A, B, C, and AC are important model terms (40). The small coefficient of variation (C.V. % =18.42) value also proved the remarkable reliability of the model. The adequate precision is 12.304, pointing out that the model could be used to navigate the design space (36,43,48).

Table 2: The levels of variables and their actual values.

Run	Power (A) Watt	Time (B) Second	L/S ratio (C) -	TAC (Y) mmol TR/g-DS
1	250.00	75.00	20.00	0.036
2	300.00	90.00	20.00	0.031
3	300.00	75.00	15.00	0.034
4	250.00	75.00	10.00	0.027
5	300.00	60.00	10.00	0.034
6	350.00	75.00	10.00	0.062
7	300.00	75.00	15.00	0.034
8	250.00	60.00	15.00	0.014
9	250.00	90.00	15.00	0.042
10	300.00	90.00	10.00	0.064
11	350.00	60.00	15.00	0.012
12	300.00	60.00	20.00	0.014
13	300.00	75.00	15.00	0.034
14	350.00	75.00	20.00	0.035
15	300.00	75.00	15.00	0.034

Table 3: The results of ANOVA test.

Source	Sum of Squares	df	Mean Square	F Value	p-value Prob > F
Model	3.697E-003	6	6.162E-004	14.20	0.0002
A-power	4.061E-004	1	4.061E-004	9.36	0.0121
B-time	2.113E-003	1	2.113E-003	48.70	< 0.0001
C-Liquid/Solid	6.301E-004	1	6.301E-004	14.53	0.0034
AB	1.822E-004	1	1.822E-004	4.20	0.0675
AC	3.240E-004	1	3.240E-004	7.47	0.0211
BC	4.225E-005	1	4.225E-005	0.97	0.3470
Residual	4.338E-004	10	4.338E-005		
Lack of Fit	4.338E-004	6	7.230E-005		
Pure Error	0.000	4	0.000		
Cor Total	4.131E-003	16			
<i>Statistical parameters</i>					
Std. Dev.	6.586E-003				
Mean	0.036				
C.V. %	18.42				
PRESS	2.166E-003				
R-Squared	0.8950				
Adj R-Squared	0.8320				
Pred R-Squared	0.4756				
Adeq Precision	12.304				

3-D response surface curves were plotted to visualize the relationship between the factors and the response (40,43). As seen from Figs. 1a and 1b, increasing microwave power enhanced the response. Apparently, increasing temperature reduced the surface tension and viscosity of the solvent, so that solvent could effectively penetrate into the cell matrix (35,39,41,48).

As seen from 1b, at different microwave powers, the TAC value was increased as the microwave time increased. In the optimization study, microwave time was kept under 90 seconds because bioactive compounds decomposed after 90 seconds due to the prolonged irradiation (33). Keeping irradiation times short reduces energy consumption at the same time (33,43).

As understood from Fig. 1c, the TAC value increased as L/S ratio decreased at different microwave time levels. It is clear that an adequate solvent amount enhances the contact area between the cell matrix and the solvent, which increases the mass transfer rate (36). On the other hand, increasing the solvent amount more than it is supposed to be shall break the interactions between the solvent and the focused compounds, thereby decreasing the efficiency (33,49,50).

The optimum conditions for the highest TAC value (TAC: 0.070 mmol TR/g - DS) were determined as follows: 326.10 Watt microwave power, 88.40 second extraction time, and 10.03 L/S ratio. For practical convenience, the verification experiment was performed under the conditions of 326 Watt microwave power, 88 second microwave time, and 10 L/S ratio. The verification experiment confirmed the accuracy of the predicted model with less than 0.02 % error (39).

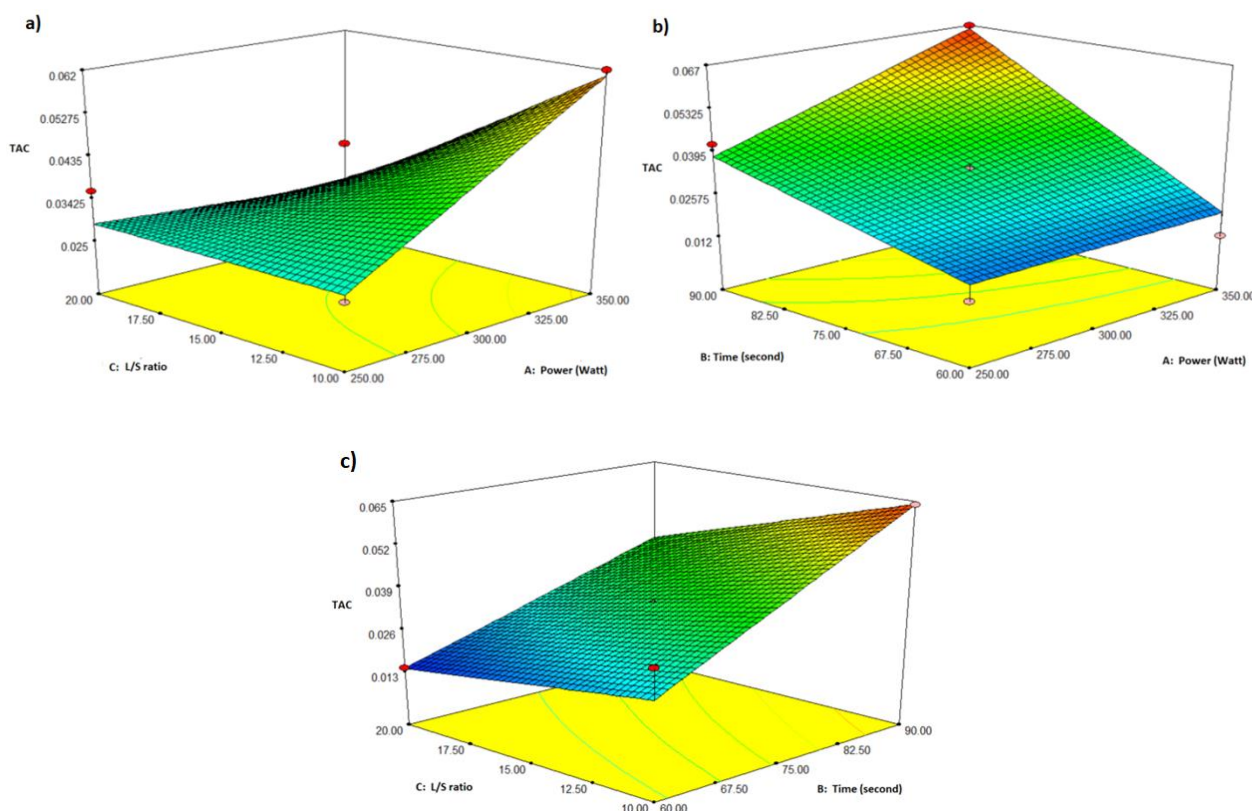


Figure 1: The plots of a) L/S ratio versus power, b) time versus power, c) L/S ratio versus time.

3.3. Comparisons of TAC measurements with DPPH and ABTS Free Radicals Scavenging Assays

DPPH and ABTS free radical scavenging activities of the seed extract were determined at the optimum extraction conditions and compared with EtOH extract. Antioxidant capacity findings are written in Table 4 and shown in the graph Fig. 2. As seen, TAC values were higher than DPPH and ABTS free radical scavenging values, which can be explained by the fact that lipophilic antioxidants were not able to donate a hydrogen atom or an electron to stabilize DPPH and ABTS free radicals by converting them to

the non-radical species (30). The TAC value and radical scavenging activity values of ethanol extract were less than those obtained by ChCl:1,4-butanediol extract. Obviously, ChCl:1,4-butanediol extract is a better free radical scavenger than ethanol extract in the ranges of studied MAE conditions (30). This might be owing to strong hydrogen bonding interactions between the NADES and the extract (14). More specifically, the interactions between -OH group of phenolic compounds and the anion of choline chloride salt might be the main motivation behind DES-based separation (29,42).

Table 4: TAC, ABTS and DPPH values of *Coriandrum sativum* seed extracts.

Solvent	Extraction conditions	TAC mmol TR/g-DS	DPPH mmol TR/g-DS	ABTS mmol TR/g-DS
DES	MAE (326 W, 88 second, 10 L/S)	0.070	0.013	0.045
EtOH	MAE (326 W, 88 second, 10 L/S)	0.024	0.009	0.006

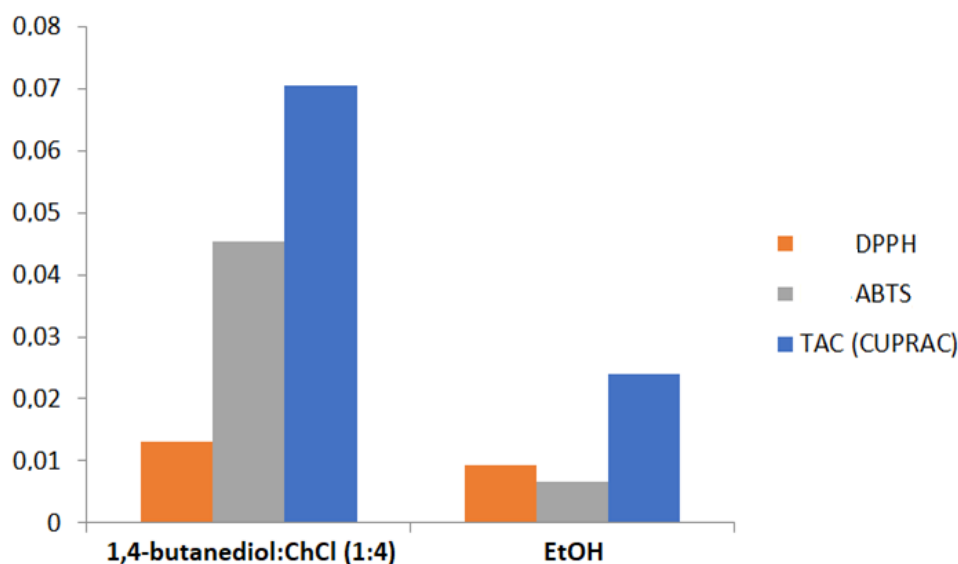


Figure 2: Graphical representation of antioxidant assay results.

4. CONCLUSION

In this study, ChCl:1,4-butanediol (1:4) was selected as the most efficacious solvent system to extract antioxidant compounds from *Coriandrum sativum* seed using MAE. Under the optimum conditions of 326 Watt microwave power, 88 second extraction time and 10 L/S ratio, TAC value was obtained as 0.070 mmol TR/g – DS. ChCl:1,4-butanediol (1:4) has yielded better results than conventional solvent ethanol at the optimum conditions in terms of CUPRAC, ABTS and DPPH assays. In the present work, we show a rapid, green, efficient and cost-effective method for the extraction of natural antioxidants from Turkish *Coriandrum sativum* seeds. This study is significant as being the first time to introduce the extraction of natural antioxidants from Turkish *Coriandrum sativum* seeds by using the green solvents of 21st century called NADESSs.

Declarations

Ethical approval

There are no ethical approvals required for the research.

Consent to Publish

Consent to publish was obtained from all participants.

Consent to Participate

All participants were consented to participate in this study.

Funding

The authors have not received any financial support and have no conflict of interest to report in the preparation of this manuscript.

Competing Interest

The authors declare no competing interests, financial or otherwise.

Availability of data and materials

All data and materials are available in this manuscript.

5. REFERENCES

- Abbassi A, Mahmoudi H, Zaouali W, M'Rabet Y, Casabianca H, Hosni K. Enzyme-aided release of bioactive compounds from coriander (*Coriandrum sativum* L.) seeds and their residue by-products and evaluation of their antioxidant activity. J Food Sci Technol [Internet]. 2018 Aug 23;55(8):3065–76. Available from: [<URL>](#).
- Zeković Z, Vidović S, Vladić J, Radosavljević R, Cvejin A, Elgndi MA, et al. Optimization of subcritical water extraction of antioxidants from *Coriandrum sativum* seeds by response surface methodology. J Supercrit Fluids [Internet]. 2014 Nov 1;95:560–6. Available from: [<URL>](#).
- Bhat S, Kaushal P, Kaur M, Sharma HK. Coriander (*Coriandrum sativum* L.): Processing, nutritional and functional aspects. African J Plant Sci [Internet]. 2014 Jan 31;8(1):25–33. Available from: [<URL>](#).
- Senrayan J, Venkatachalam S. Optimization of ultrasound-assisted solvent extraction (UASE) based on oil yield, antioxidant activity and evaluation of fatty acid composition and thermal stability of *Coriandrum sativum* L. seed oil. Food Sci Biotechnol [Internet]. 2019 Apr 17;28(2):377–86. Available from: [<URL>](#).
- Laribi B, Kouki K, M'Hamdi M, Bettaieb T. Coriander (*Coriandrum sativum* L.) and its bioactive constituents. Fitoterapia [Internet]. 2015 Jun 1;103:9–26. Available from: [<URL>](#).
- Asgarpanah J, Kazemivash N. Phytochemistry, pharmacology and medicinal properties of *Coriandrum sativum* L. African J Pharm Pharmacol [Internet]. 2012 Aug 22;6(31):2340–5. Available from: [<URL>](#).

7. Deepa B, Anuradha C V. Antioxidant potential of *Coriandrum sativum* L. seed extract. Indian J Exp Biol 2011 [Internet]. 2011;49:30–8. Available from: [<URL>](#).
8. Zeković Z, Kaplan M, Pavlič B, Olgun EO, Vladić J, Canlı O, et al. Chemical characterization of polyphenols and volatile fraction of coriander (*Coriandrum sativum* L.) extracts obtained by subcritical water extraction. Ind Crops Prod [Internet]. 2016 Sep 1;87:54–63. Available from: [<URL>](#).
9. Soto-Vaca A, Gutierrez A, Losso JN, Xu Z, Finley JW. Evolution of phenolic compounds from color and flavor problems to health benefits. J Agric Food Chem [Internet]. 2012 Jul 11;60(27):6658–77. Available from: [<URL>](#).
10. Dżiki D, Różyło R, Gawlik-Dżiki U, Świeca M. Current trends in the enhancement of antioxidant activity of wheat bread by the addition of plant materials rich in phenolic compounds. Trends Food Sci Technol [Internet]. 2014 Nov 1;40(1):48–61. Available from: [<URL>](#).
11. Azmir J, Zaidul ISM, Rahman MM, Sharif KM, Mohamed A, Sahena F, et al. Techniques for extraction of bioactive compounds from plant materials: A review. J Food Eng [Internet]. 2013 Aug 1;117(4):426–36. Available from: [<URL>](#).
12. Zainal-Abidin MH, Hayyan M, Hayyan A, Jayakumar NS. New horizons in the extraction of bioactive compounds using deep eutectic solvents: A review. Anal Chim Acta [Internet]. 2017 Aug 1;979:1–23. Available from: [<URL>](#).
13. Skarpalezos D, Detsi A. Deep eutectic solvents as extraction media for valuable flavonoids from natural sources. Appl Sci [Internet]. 2019 Oct 4;9(19):4169. Available from: [<URL>](#).
14. Jurić T, Mičić N, Potkonjak A, Milanov D, Dodić J, Trivunović Z, et al. The evaluation of phenolic content, in vitro antioxidant and antibacterial activity of *Mentha piperita* extracts obtained by natural deep eutectic solvents. Food Chem [Internet]. 2021 Nov 15;362:130226. Available from: [<URL>](#).
15. García A, Rodríguez-Juan E, Rodríguez-Gutiérrez G, Rios JJ, Fernández-Bolaños J. Extraction of phenolic compounds from virgin olive oil by deep eutectic solvents (DESS). Food Chem [Internet]. 2016 Apr 15;197:554–61. Available from: [<URL>](#).
16. Altunay N, Elik A, Gürkan R. Preparation and application of alcohol based deep eutectic solvents for extraction of curcumin in food samples prior to its spectrophotometric determination. Food Chem [Internet]. 2020 Apr 25;310:125933. Available from: [<URL>](#).
17. Xu H, Peng J, Kong Y, Liu Y, Su Z, Li B, et al. Key process parameters for deep eutectic solvents pretreatment of lignocellulosic biomass materials: A review. Bioresour Technol [Internet]. 2020 Aug 1;310:123416. Available from: [<URL>](#).
18. Tang B, Bi W, Zhang H, Row KH. Deep Eutectic Solvent-Based HS-SME Coupled with GC for the analysis of bioactive terpenoids in *Chamaecyparis obtusa* leaves. Chromatographia [Internet]. 2014 Feb 28;77(3–4):373–7. Available from: [<URL>](#).
19. Dhanani T, Singh R, Shah S, Kumari P, Kumar S. Comparison of green extraction methods with conventional extraction method for extract yield, L-DOPA concentration and antioxidant activity of *Mucuna pruriens* seed. Green Chem Lett Rev [Internet]. 2015 Apr 3;8(2):43–8. Available from: [<URL>](#).
20. Bimakr M, Rahman RA, Taip FS, Ganjloo A, Salleh LM, Selamat J, et al. Comparison of different extraction methods for the extraction of major bioactive flavonoid compounds from spearmint (*Mentha spicata* L.) leaves. Food Bioprod Process [Internet]. 2011 Jan 1;89(1):67–72. Available from: [<URL>](#).
21. Liu JZ, Lyu HC, Fu YJ, Jiang JC, Cui Q. Simultaneous extraction of natural organic acid and flavonoid antioxidants from *Hibiscus manihot* L. flower by tailor-made deep eutectic solvent. LWT [Internet]. 2022 Jun 15;163:113533. Available from: [<URL>](#).
22. Chanioti S, Tzia C. Extraction of phenolic compounds from olive pomace by using natural deep eutectic solvents and innovative extraction techniques. Innov Food Sci Emerg Technol [Internet]. 2018 Aug 1;48:228–39. Available from: [<URL>](#).
23. Meng Z, Zhao J, Duan H, Guan Y, Zhao L. Green and efficient extraction of four bioactive flavonoids from *Pollen Typhae* by ultrasound-assisted deep eutectic solvents extraction. J Pharm Biomed Anal [Internet]. 2018 Nov 30;161:246–53. Available from: [<URL>](#).
24. Yalçın Ö, Baylan N, Çehreli S. Adsorption of levodopa onto Amberlite resins: equilibrium studies and D-optimal modeling based on response surface methodology. Biomass Convers Biorefinery [Internet]. 2022 Apr 9;12(4):1281–94. Available from: [<URL>](#).
25. Lalikoglu M, Aşçı YS, Sırma Tarım B, Yıldız M, Arat R. Hydrophobic deep eutectic solvent effect on acrylic acid separation from aqueous media by using reactive extraction and modeling with response surface methodology. Sep Sci Technol [Internet]. 2022 Jul 3;57(10):1563–74. Available from: [<URL>](#).
26. Lalikoglu M. Separation of butyric acid from aqueous media using menthol-based hydrophobic deep eutectic solvent and modeling by response surface methodology. Biomass Convers Biorefinery [Internet]. 2022 Apr 14;12(4):1331–41. Available from: [<URL>](#).
27. Doldolova K, Bener M, Lalikoğlu M, Aşçı YS, Arat R, Apak R. Optimization and modeling of microwave-assisted extraction of curcumin and antioxidant compounds from turmeric by using natural deep

- eutectic solvents. Food Chem [Internet]. 2021 Aug 15;353:129337. Available from: [<URL>](#).
28. Esin Çelik S, Özyürek M, Güçlü K, Çapanoğlu E, Apak R. Identification and anti-oxidant capacity determination of phenolics and their glycosides in elderflower by On-line HPLC-CUPRAC Method. Phytochem Anal [Internet]. 2014 Mar 10;25(2):147–54. Available from: [<URL>](#).
29. Bener M, Şen FB, Önem AN, Bekdeşer B, Çelik SE, Lalikoglu M, et al. Microwave-assisted extraction of antioxidant compounds from by-products of Turkish hazelnut (*Corylus avellana* L.) using natural deep eutectic solvents: Modeling, optimization and phenolic characterization. Food Chem [Internet]. 2022 Aug 15;385:132633. Available from: [<URL>](#).
30. Altun M, Çelik SE, Güçlü K, Özyürek M, Erçağ E, Apak R. Total antioxidant capacity and phenolic contents of Turkish hazelnut (*Corylus Avellana* L.) kernels and oils. J Food Biochem [Internet]. 2013 Feb 1;37(1):53–61. Available from: [<URL>](#).
31. Bener M. Modeling and optimizing microwave-assisted extraction of antioxidants from *Thymra Spicata* L. and characterization of their phenolic constituents. Food Sci Biotechnol [Internet]. 2019 Dec 11;28(6):1733–45. Available from: [<URL>](#).
32. Sanchez-Moreno C, Larrauri JA, Saura-Calixto F. A procedure to measure the antiradical efficiency of polyphenols. J Sci Food Agric [Internet]. 1998;76:270–6. Available from: [<URL>](#).
33. Ozturk B, Parkinson C, Gonzalez-Miquel M. Extraction of polyphenolic antioxidants from orange peel waste using deep eutectic solvents. Sep Purif Technol [Internet]. 2018 Nov 29;206:1–13. Available from: [<URL>](#).
34. Barbieri JB, Goltz C, Batistão Cavalheiro F, Theodoro Toci A, Igarashi-Mafra L, Mafra MR. Deep eutectic solvents applied in the extraction and stabilization of rosemary (*Rosmarinus officinalis* L.) phenolic compounds. Ind Crops Prod [Internet]. 2020 Feb 1;144:112049. Available from: [<URL>](#).
35. Wan Mahmood WMA, Lorwirachsutee A, Theodoropoulos C, Gonzalez-Miquel M. Polyol-based deep eutectic solvents for extraction of natural polyphenolic antioxidants from *Chlorella vulgaris*. ACS Sustain Chem Eng [Internet]. 2019 Mar 4;7(5):5018–26. Available from: [<URL>](#).
36. Zheng B, Yuan Y, Xiang J, Jin W, Johnson JB, Li Z, et al. Green extraction of phenolic compounds from foxtail millet bran by ultrasonic-assisted deep eutectic solvent extraction: Optimization, comparison and bioactivities. LWT [Internet]. 2022 Jan 15;154:112740. Available from: [<URL>](#).
37. Wang M, Wang J, Zhang Y, Xia Q, Bi W, Yang X, et al. Fast environment-friendly ball mill-assisted deep eutectic solvent-based extraction of natural products. J Chromatogr A [Internet]. 2016 Apr 22;1443:262–6. Available from: [<URL>](#).
38. Duan L, Dou LL, Guo L, Li P, Liu EH. Comprehensive evaluation of deep eutectic solvents in extraction of bioactive natural products. ACS Sustain Chem Eng [Internet]. 2016 Apr 4;4(4):2405–11. Available from: [<URL>](#).
39. Cui Q, Liu JZ, Wang LT, Kang YF, Meng Y, Jiao J, et al. Sustainable deep eutectic solvents preparation and their efficiency in extraction and enrichment of main bioactive flavonoids from sea buckthorn leaves. J Clean Prod [Internet]. 2018 May 20;184:826–35. Available from: [<URL>](#).
40. Cui Q, Peng X, Yao XH, Wei ZF, Luo M, Wang W, et al. Deep eutectic solvent-based microwave-assisted extraction of genistin, genistein and apigenin from pigeon pea roots. Sep Purif Technol [Internet]. 2015 Aug 17;150:63–72. Available from: [<URL>](#).
41. Loarce L, Oliver-Simancas R, Marchante L, Díaz-Maroto MC, Alañón ME. Implementation of subcritical water extraction with natural deep eutectic solvents for sustainable extraction of phenolic compounds from winemaking by-products. Food Res Int [Internet]. 2020 Nov 1;137:109728. Available from: [<URL>](#).
42. Zannou O, Koca I. Greener extraction of anthocyanins and antioxidant activity from blackberry (*Rubus* spp) using natural deep eutectic solvents. LWT [Internet]. 2022 Mar 15;158:113184. Available from: [<URL>](#).
43. Alsaud N, Shahbaz K, Farid M. Application of deep eutectic solvents in the extraction of polyphenolic antioxidants from New Zealand Manuka leaves (*Leptospermum Scoparium*): Optimization and antioxidant activity. J Mol Liq [Internet]. 2021 Sep 1;337:116385. Available from: [<URL>](#).
44. Wang G, Cui Q, Yin LJ, Zheng X, Gao MZ, Meng Y, et al. Efficient extraction of flavonoids from *Flos Sophorae Immaturus* by tailored and sustainable deep eutectic solvent as green extraction media. J Pharm Biomed Anal [Internet]. 2019 Jun 5;170:285–94. Available from: [<URL>](#).
45. Cao J, Chen L, Li M, Cao F, Zhao L, Su E. Efficient extraction of proanthocyanidin from *Ginkgo biloba* leaves employing rationally designed deep eutectic solvent-water mixture and evaluation of the antioxidant activity. J Pharm Biomed Anal [Internet]. 2018 Sep 5;158:317–26. Available from: [<URL>](#).
46. Xu M, Ran L, Chen N, Fan X, Ren D, Yi L. Polarity-dependent extraction of flavonoids from citrus peel waste using a tailor-made deep eutectic solvent. Food Chem [Internet]. 2019 Nov 1;297:124970. Available from: [<URL>](#).
47. Evlik T, Aşçı YS, Baylan N, Gamsızkan H, Çehreli S. Reactive separation of malic acid from aqueous solutions and modeling by artificial neural network (ANN) and response surface methodology (RSM). J Dispers Sci Technol [Internet]. 2022;43(2):221–30. Available from: [<URL>](#).

48. Lin S, Meng X, Tan C, Tong Y, Wan M, Wang M, et al. Composition and antioxidant activity of anthocyanins from *Aronia melanocarpa* extracted using an ultrasonic-microwave-assisted natural deep eutectic solvent extraction method. *Ultrason Sonochem* [Internet]. 2022 Sep 1;89:106102. Available from: [<URL>](#).

49. Rashid R, Mohd Wani S, Manzoor S, Masoodi FA, Masarat Dar M. Green extraction of bioactive compounds from apple pomace by ultrasound

assisted natural deep eutectic solvent extraction: Optimisation, comparison and bioactivity. *Food Chem* [Internet]. 2023 Jan 1;398:133871. Available from: [<URL>](#).

50. Liu Y, Li J, Fu R, Zhang L, Wang D, Wang S. Enhanced extraction of natural pigments from *Curcuma longa* L. using natural deep eutectic solvents. *Ind Crops Prod* [Internet]. 2019 Nov 15;140:111620. Available from: [<URL>](#).